

Cristian Andreescu  
Adrian Clenci *Editors*

# Proceedings of the European Automotive Congress EAEC- ESFA 2015

 Springer

Proceedings of the European Automotive  
Congress EAEC-ESFA 2015

Cristian Andreescu · Adrian Clenci  
Editors

# Proceedings of the European Automotive Congress EAEC-ESFA 2015

 Springer

*Editors*

Cristian Andreescu  
University Politehnica of Bucharest  
Bucharest  
Romania

Adrian Clenci  
University of Pitești  
Pitești  
Romania

ISBN 978-3-319-27275-7

ISBN 978-3-319-27276-4 (eBook)

DOI 10.1007/978-3-319-27276-4

Library of Congress Control Number: 2015955888

Springer Cham Heidelberg New York Dordrecht London

© Springer International Publishing Switzerland 2016

This work is subject to copyright. All rights are reserved by the Publisher, whether the whole or part of the material is concerned, specifically the rights of translation, reprinting, reuse of illustrations, recitation, broadcasting, reproduction on microfilms or in any other physical way, and transmission or information storage and retrieval, electronic adaptation, computer software, or by similar or dissimilar methodology now known or hereafter developed.

The use of general descriptive names, registered names, trademarks, service marks, etc. in this publication does not imply, even in the absence of a specific statement, that such names are exempt from the relevant protective laws and regulations and therefore free for general use.

The publisher, the authors and the editors are safe to assume that the advice and information in this book are believed to be true and accurate at the date of publication. Neither the publisher nor the authors or the editors give a warranty, express or implied, with respect to the material contained herein or for any errors or omissions that may have been made.

Printed on acid-free paper

Springer International Publishing AG Switzerland is part of Springer Science+Business Media  
([www.springer.com](http://www.springer.com))

# Foreword



The European Automotive Congress was thought to be a common scientific event of the traditional biannual European Automotive Engineers Cooperation (EAEC) Congress (this year at its 14th edition) and the Annual International Conference of the Society of Automotive Engineers of Romania (SIAR)—ESFA.

The Congress was organized by the SIAR and the Automotive Engineering Department of the University “Politehnica” of Bucharest in cooperation with EAEC under the patronage of Fédération Internationale des Sociétés d’Ingénieurs de Techniques d’Automobile (FISITA).

The motto of the Congress (*Academia, Industry and Government: together for automotive engineering development*) was an indication of the organizers belief that there is a need for meetings and discussions about the current and future challenges of the automotive world in order to find the best solutions. In other words, we are convinced that the challenges of the future can only be overcome if these tripartite discussions occur permanently.

The papers included in this volume are selected by the Scientific Committee among the almost 130 technical papers proposed to be presented at the Congress.

The authors of these articles are experts from research, industry, and universities coming from 14 countries among which nine from Europe. Their papers are covering the latest issues such as fuel economy and environment, automotive safety and comfort, automotive reliability and maintenance, new materials and technologies, traffic and road transport systems, advanced engineering methods and tools, advanced powertrains, and hybrid and electric drives.

Therefore, we hope these papers will generate fruitful discussions about an exciting topic: the automotive engineering in the light of the future challenges.

Prof. Cristian Andreescu  
EAEC-ESFA 2015 Congress Chairman

Assoc. Prof. Adrian Clenci  
SIAR President

# Scientific Committee

Prof. Cornel Stan, West Saxon University of Zwickau (President of the Scientific and Technical Committee)

Prof. Cristian Andreescu, University “Politehnica” of Bucharest, Romania

Prof. Gabriel Anghelache, University “Politehnica” of Bucharest, Romania

Dr. Rodica Baranescu, Former President, Society of Automotive Engineers, USA

Prof. Alexandru Boroiu, University of Pitesti, Romania

Prof. Nicolae Burnete, Technical University of Cluj-Napoca, Romania

Prof. Anghel Chiru, “Transilvania” University of Brasov, Romania

Assoc. Prof. Adrian Clenci, University of Pitesti, Romania

Prof. Grigore Danciu, University “Politehnica” of Bucharest, Romania

Prof. Vasile Dragu, University “Politehnica” of Bucharest, Romania

Prof. Cedimir Duboka, President, Yugoslav Society of Automotive Engineers (JUMV)

Prof. Victor Gheorghiu, Hamburg University of Applied Sciences, Germany

Assoc. Prof. Danut Grosu, Military Technical Academy, Romania

Brigadier Ret. Prof. Gunther Hohl, Austria

Prof. Daniel Iozsa, University “Politehnica” of Bucharest, Romania

Prof. Nicolae Ispas, “Transilvania” University of Brasov, Romania

Prof. Florian Ivan, University of Pitesti, Romania

Prof. Eden Mamut, University Ovidius of Constanta, Romania

Prof. Laurentiu Manea, University Ovidius of Constanta, Romania

Assoc. Prof. Danut Marinescu, University of Pitesti, Romania

Assoc. Prof. Marin Marinescu, Military Technical Academy, Romania

Prof. Viorel Mateescu, University “Politehnica” of Bucharest, Romania

Prof. Niculae Negurescu, University “Politehnica” of Bucharest, Romania

Prof. Mircea Oprean, University “Politehnica” of Bucharest, Romania

Dr. Pierre Podevin, Conservatoire National des Arts et Métiers de Paris, France

Assoc. Prof. Plamen Punov, Technical University of Sofia, Bulgaria

Prof. Edward Rakosi, Technical University “Gheorghe Asachi” of Iasi, Romania

Assoc. Prof. Adrian Sachelarie, Technical University “Gheorghe Asachi” of Iasi, Romania

Dan Stancioiu, Ph.D., Lecturer, Liverpool John Moores University  
Prof. Ion Tabacu, University of Pitesti, Romania  
Prof. Stefan Tabacu, University of Pitesti, Romania  
Prof. Daniela Vasiliu, University “Politehnica” of Bucharest, Romania  
Prof. Nicolae Vasiliu, University “Politehnica” of Bucharest, Romania  
Dr. Ludwig G.E. Vollrath, FISITA Vice President, Europe



# Contents

<b>Investigation of a Mechanism Through a Transient Thermal Analysis and an Equivalent Steady-State Thermal Analysis. . . . .</b>	1
Alexandra-Raluca Moisescu, Stefan Sorohan and Gabriel Anghelache	
<b>Inter-cylinder Distribution of Di-Ethyl-Ether Injected into the Intake Manifold of a Diesel Engine Using CFD Simulation . . . . .</b>	9
Victor Iorga-Siman, Adrian Clenci, Rodica Niculescu and Alina Trică (Tuță)	
<b>Analysis of Complex Planetary Mechanisms Used in Nine Speed Automatic Transmissions of Cars . . . . .</b>	21
Neacsu Eugen, Banca Gheorghe and Oloeriu Florin	
<b>DUSTER ZERO—Electric Vehicle Research 4WD . . . . .</b>	37
Danut Gabriel Marinescu, Viorel Nicolae, Cristian Liviu Popescu, Liviu Calin and Nicusor Mierloiu	
<b>The Thermal Characterisation of a Disc Brake Rotor at Reduced Scale with Particular Reference to Pad Aspect Ratio . . . . .</b>	51
Varun S. Prabhu, Abdulwahab A. Alnaqi and Peter C. Brooks	
<b>Experimental Identification of the Automotive Magnetorheological Shock Absorbers. . . . .</b>	61
Nicolae Vasiliu, Anton Hadăr, Alexandru Dobre, Constantin Călinoiu and Cristian Andreescu	
<b>Application of Fuzzy Topsis and Ahp Method in Evaluating Vehicle Roadworthiness Performance. . . . .</b>	69
Jakimovska Kristina, Duboka Čedomir and Karastoyanov Dimitar	
<b>Concept Design of Twin-Sheet Thermoplastic Cellular Structures for Vehicle’s Bumper System . . . . .</b>	81
Stefan Tabacu, Claudiu Diaconescu and Alexandru Oltean	

<b>On the New Concept and Advantages of the Integrated Shock Absorber—Air Spring—“Isas”</b> . . . . .	93
Adrian Ioan Niculescu, Antony Jankowski, Mirosław Kowalski and Tudor Sireteanu	
<b>Forces Involved in Small Overlap Crash</b> . . . . .	105
Xavier Da Silva and Núria Parera	
<b>State of the Sm-Art Components Used on Autonomous Platforms for Sustainable Mobility</b> . . . . .	117
Valerian Croitorescu and Yassine Ruichek	
<b>Passenger Cars Exhaust Emissions Under Real Driving Conditions</b> . . . . .	127
Jerzy Merkisz and Jacek Pielecha	
<b>Studies Regarding the Influence of Exhaust Backpressure on the Performances of a Compression Ignited Engine</b> . . . . .	141
Nicolae Burnete, Dan Moldovanu, Doru-Laurean Baldean and Levente Kocsis	
<b>A Study of Waste Heat Recovery Impact on a Passenger Car Fuel Consumption in New European Driving Cycle</b> . . . . .	151
Plamen Punov, Nikolay Milkov, Quentin Danel and Christelle Perilhon	
<b>Modeling of Electric Vehicles for Driveability Control Applications</b> . . . . .	165
Ionut Alexandru Stoica, Marius Valentin Bataus and Ioan Mircea Oprean	
<b>Making of Safer Network Operating System Components</b> . . . . .	175
Arun S Nair and Jaideep Save	
<b>Statistical Decision in the Automotive Material Selection</b> . . . . .	189
Cristian Andreescu, Adrian Stere Paris, Cristian Dragomirescu and Constantin Târcolea	
<b>Effects Analysis of Zone 30 Based on Recognition, Age and Accident Experience</b> . . . . .	197
Ryosuke Ando, Yasuhide Mimura, Keiichi Higuchi and Marehiro Mukai	
<b>New Technology for Composite Materials Parts</b> . . . . .	209
Anghel Chiru and Lucian Eugen Rad	
<b>Tyre Dynamics: Model Validation and Parameter Identification</b> . . . . .	219
Andreas Hackl, Wolfgang Hirschberg, Cornelia Lex and Georg Rill	
<b>Smart Solutions for Vehicle Chassis</b> . . . . .	233
Mihai Florea, Valerian Croitorescu and Mircea Oprean	
<b>Study for an Electrified UTV Platform</b> . . . . .	245
Grigore Danciu	

**Measurement of Fuel Consumption for an Off-road Vehicle With Conventional and Hybrid Powertrain. . . . .** 259  
 Gabriel Anghelache, Alexandra-Raluca Moisescu and Ioan Mircea Oprean

**Security in Connected Cars . . . . .** 267  
 Mushabbar Hussain

**The Development of New Evaluation Criteria for Supercharged Engines Based on Elasticity and Adaptability at Traction . . . . .** 277  
 Ivan Florian, Mihai Stelian Niculae and Dragoş Constantin Neacşu

**The Comparative Study of Engine Vehicles Functioning With Petrol and Liquefied Petroleum Gas. . . . .** 285  
 Ramona-Monica Stoica, Marian-Eduard Rădulescu, Irinel Dinu, George Ene, Daniel Neagu and Ion Copae

**Maintenance Costs Statistics for Urban Cars . . . . .** 297  
 Adrian Stere Paris, Cristian Andreescu, Cristian Dragomirescu and Constantin Târcolea

**Investigation of Third Body Phenomenon in Model Braking Using Infrared Camera. . . . .** 307  
 Zbigniew Skorupka and Antoni Jankowski

**Modelling and Simulation of the Dynamic Behaviour Automotive’s Suspension By AMESim . . . . .** 317  
 Alexandru Dobre, Anton Hadăr, Daniela Vasiliu, Nicolae Vasiliu and Cristian Andreescu

**Study Concerning the Loads Over Driver’s Heads in Cases of Cars Crashes with Involved Cars of the Same or Different Generation . . . . .** 325  
 Nicolae Ispas and Mircea Nastasoiu

**Use of GPS/INS Devices for Experimental Study of Vehicle Dynamics . . . . .** 337  
 Dinu Covaciu, Ion Preda, Dragoş-Sorin Dima and Anghel Chiru

**Study of the Dynamic Behavior of a Car Body for Mounting the Rear Axle . . . . .** 349  
 Ştefan-Ionescu Romeo, Petrache Gheorghe, Ionel Vieru, Viorel Nicolae and Pârlac Sebastian

**Simulation of the Air Conditioning Curtains with Turbulent Circular Jet Flows Inside the Cabin Vehicle Using ANSYS CFD. . . . .** 357  
 Vasile Caunii and Adrian Sachelarie

**The Influence of Exhaust Backpressure Upon the Turbocharger’s Boost Pressure . . . . .** 367  
 Levente-Botond Kocsis, Dan Moldovanu and Doru-Laurean Bâldean

<b>Investigating Maintenance Procedures for Engine Air Filters . . . . .</b>	<b>375</b>
Marius Toma	
<b>Fatigue Analysis for the Primary Shaft of a Mechanical Gearbox of a Car . . . . .</b>	<b>385</b>
Mario Trotea, Dumitru Neagoie, Loreta Simniceanu and Augustin Constantinescu	
<b>Optimizing Combustion in an Single Cylinder GDI SI Engine. . . . .</b>	<b>395</b>
Stelian Tarulescu, Radu Tarulescu and Cristian-Ioan Leahu	
<b>On The Possibility to Reduce Diesel Engines Emissions by Operating with Biodiesel B20 in PPC Mode . . . . .</b>	<b>405</b>
Alexandru Racovitza, Bogdan Radu, Mohanad Aldhaidhawi and Radu Chiriac	
<b>Public Transport—Feasible Solution for Sustainable Urban Mobility . . . . .</b>	<b>419</b>
Vasile Dragu, Eugen Roșca and Aura Ruscă	
<b>Uncertainty in the Study of Automotives Dynamics and Analysis and Reconstruction of Car Crashes . . . . .</b>	<b>431</b>
Ramona-Monica Stoica, Marian-Eduard Rădulescu, Irinel Dinu, George Ene, Daniel Neagu and Ion Copae	
<b>Assessment of Effective Elastic Properties of Honeycomb Cores by Modal Finite Element Analyses . . . . .</b>	<b>443</b>
Ștefan Sorohan, Dan Mihai Constantinescu, Marin Sandu and Adriana Georgeta Sandu	
<b>Model Preparation for Structural FEA on Main Components of an Internal Combustion Engine . . . . .</b>	<b>455</b>
Dan Mihai Dogariu, Cristian Tănăsie, Anghel Chiru, Cristian-Ioan Leahu and Vlad Ștefan Stancu	
<b>Dynamics of a Crank-Shaft Mechanism with Multiple Clearances by a Multibody Approach . . . . .</b>	<b>463</b>
Stănescu Nicolae–Doru	
<b>Research Applied to Exhaust Gas After-Treatment Systems in 1.6 L Zsg 416 Ford Engine . . . . .</b>	<b>475</b>
Lucian-Vasile Crișan-Lupa, Adela-Ioana Borzan, Dan Moldovanu and Levente-Botond Kocsis	
<b>Development of a Water Rankine System to Improve Diesel Engine Efficiency . . . . .</b>	<b>485</b>
Bogdan Radu, Alexandru Racovitza and Radu Chiriac	

**Traffic Modeling Aspects Using Visum Software and Effects on the Traffic Optimization** . . . . . 495  
 Horea George Crişan and Nicolae Filip

**Performance Evaluation of Complex Intersections by Micro-simulation.** . . . . . 507  
 Sorin Ilie, Gabriela Mitran, Viorel Nicolae and Amalia Ana Dascăl

**Drag Phenomena Within a Torque Converter Driven Automotive Transmission—Laminar Flow Approach** . . . . . 517  
 Marin Marinescu, Octavian Alexa, Radu Vilau, Constantin-Ovidiu Ilie and Valentin Vinturis

**Analysis of Crashes at Intersections in Bucharest** . . . . . 529  
 Şerban Raicu, Dorinela Costescu and Ştefan Burciu

**The NVH Behaviour of a Powertrain Fixed on a Measurement Bench.** . . . . . 541  
 Andrei Daniel Calin, Nicolae Enescu, Radu Chiriac and Nicolae Orasanu

**Composite Materials Testing Method Steering Column Bracket Test** . . . . . 553  
 Lucian Eugen Rad, Anghel Chiru, Cristian Leahu and Dan Mihai Dogariu

**Calculation of the Steering Column Bracket Made of Composite Materials Reinforced with Continuous Fibers.** . . . . . 567  
 Lucian Rad, Anghel Chiru and Cristian Leahu

**A Method for 3D Geometry Scanning of a Combustion Chamber** . . . . . 577  
 Dan Mihai Dogariu, Ciprian Andrei, Bogdan Tiberiu Vieru, Radu Adrian Plămădeală and Anghel Chiru

**Researches to Improve the Reliability of Clutches with Dual-Mass Flywheel.** . . . . . 585  
 Valentin Nişulescu, Gheorghe Bancă, Marius Bâzgå and Alexndru Boroiu

**Theoretical and Practical Analysis of the in-Cylinder Tumble Motion** . . . . . 595  
 Dan Moldovanu and Adela Ioana Borzan

**Optimized Automotive Spark Ignition Engine.** . . . . . 605  
 Edward Rakosi, Sorinel Talif and Gheorghe Manolache

**Aspects Regarding the Evolution of the Depollution Norms and Test Cycles in Order to Determine Polluting Emissions** . . . . . 619  
 Gheorghe Bancă, Valentin Nişulescu and Gheorghe Frăţilă

<b>Measurement Equipment for Research of the Pressure Wave Compressors</b> . . . . .	633
Cristian-Ioan Leahu, Dan Mihai Dogariu, Anghel Chiru, George-Radu Toganel and Gabriel Mitroi	
<b>Friction Analysis of a Two Stroke Engine</b> . . . . .	641
Sebastian Radu, Horia Abăitâncei, Adrian Tușinean, Gheorghe-Alexandru Radu and Marton Iakab-Peter	
<b>Independent Suspension—The Equivalence of Model and Vehicle Parameters</b> . . . . .	651
Ion Preda	
<b>Studies About Behavior of the Human Cervical—Head System During Frontal Crash Impact</b> . . . . .	665
Stefanita Ciunel and Bebe Tica	
<b>Considerations on the Vehicles Identification and Classification in Traffic by the Length Criterion</b> . . . . .	677
Nicolae Filip, Adrian Dohotari and Jacint Kovacs	
<b>Aspects Regarding Priority Settings in Unsignalized Intersections and the Influence on the Level of Service</b> . . . . .	687
Dumitru Ilie, Matei Lucian, Vîntorului Matei, Racilă Laurențiu and Oprica Theodor	
<b>Influence of Tyre Pressure and Weight Distribution on Axles on the Theoretical Speed Ratio in the Running Gear System of Four-Wheel Drive Tractors</b> . . . . .	695
Mircea Nastasoiu and Nicolae Ispas	
<b>The Development of a New Thermal Comfort Indexes</b> . . . . .	703
Catalin Adrian Neacsu and Mariana Ivanescu	
<b>The Correlation Between the Tests and the Calculation Method in the Case of an Engine Mount</b> . . . . .	715
Gîrbovan Daniel, Nicolae Viorel and Vieru Ionel	
<b>Dummy Kinematic Behaviour and Head Injuries Analysis in Frontal Collisions</b> . . . . .	723
Oana Victoria Oțăt, Ștefan Cristian Castravete and Victor Oțăt	
<b>Theoretical and Experimental Research on the Torque Variation of the Body Passing Through Landmarks</b> . . . . .	733
Dumitru Neagoie, Dumitru Bolcu, Loreta Simniceanu and Mario Trotea	
<b>The Simulation of the Vehicle Motion Based on Generalized Mathematical Model of Vehicle Motion</b> . . . . .	741
Loreta Simniceanu, Victor Otat, Trotea Mario and Mihaela Bogdan	

**Research Regarding Night-Time Pedestrian Visibility . . . . . 749**  
Bogdan Tolea, Daniel Trusca and Csaba Antonya

**Research Regarding the Effects of Emergency Vehicle Braking upon  
Its Occupants . . . . . 757**  
Alexandru-Ionut Radu, Daniel-Dragos Trusca, Bogdan-Adrian Tolea  
and Corneliu Cofaru

**Effect of Water Injection at Inlet of Turbocharger on Compressor  
Performances . . . . . 765**  
Podevin Pierre, Périlhon Christelle, Danlos Amélie, Punov Plamen,  
Nouri Hussain, Wagner Marc, Massouh Fawaz and Mansilla Raul

# Abbreviations

AEM	Advanced engineering methods and tools (CAD-CAM-CAE)
APT	Advanced power trains (engine and transmission)
ARM	Automotive reliability and maintenance
FEP	Fuel economy and pollution control
HEV	Hybrid and electric vehicles
MAT	New materials and technologies (lightweight solutions)
NVH	Noise vibration and harshness (NVH)
TTS	Traffic and road transport systems (including automated and cooperative driving and future sustainable mobility concepts)
VDS	Vehicle dynamics safety and comfort



# Investigation of a Mechanism Through a Transient Thermal Analysis and an Equivalent Steady-State Thermal Analysis

Alexandra-Raluca Moisescu, Stefan Sorohan and Gabriel Anghelache

**Abstract** The thermal analysis of a rotary engine mechanism requires taking into consideration the transfer of heat from the combustion gas to the engine parts, which include rotating parts and fixed parts, as well as the transfer of heat to the environment. During an engine mechanism rotation, the conditions of convective heat transfer are variable, and the surfaces of fixed parts exposed to combustion gas are continuously changing. In this case, the transient thermal analysis using the finite elements method is very complex because of the permanent modification of surfaces covered with combustion gas, as a consequence of mechanism rotation. Therefore, in the current paper, an equivalent model for steady-state thermal analysis is developed, so that the same results are obtained as in the long transient thermal analysis, but with significantly smaller requirements of time and computational resources. The transient thermal analysis performed for a large number of rotations, which provides the stationary thermal conditions of mechanism parts, is compared with the equivalent steady-state thermal analysis performed using the equivalent film coefficients and the equivalent convection temperatures. The distributions of fixed part temperature and heat flux obtained from the steady-state thermal analysis are compared to those obtained from the transient thermal analysis, and very good similarities are ascertained. In conclusion, the equivalent steady-state thermal analysis provides similar results, compared with the transient thermal analysis, but with significantly lower computational effort.

**Keywords** Finite elements · Thermal analysis · Heat transfer · Film coefficient · Temperature

---

A.-R. Moisescu (✉) · S. Sorohan · G. Anghelache  
University Politehnica of Bucharest, Splaiul Independentei 313, 060042 Bucharest, Romania  
e-mail: raluca.moisescu@upb.ro

© Springer International Publishing Switzerland 2016  
C. Andreescu and A. Clenci (eds.), *Proceedings of the European Automotive Congress EAEC-ESFA 2015*, DOI 10.1007/978-3-319-27276-4\_1

## Introduction

The development of a rotary engine involves simulation, performed using the finite element method, of mechanism behaviour under thermal and mechanical loads during engine cycles. The simulation provides the temperature distribution of engine parts, so that thermal expansion can be investigated in conjunction with mechanical loads applied on engine mechanism parts.

The thermal analysis requires taking into consideration the transfer of heat from the combustion gas to the engine parts, which include rotating parts and fixed parts, as well as the transfer of heat to the environment (Heywood 1988). Both the rotating and the fixed parts are exposed to combustion gas over an interval of the mechanism rotation. Throughout this interval, the conditions of convective heat transfer are variable, and the surfaces of fixed parts exposed to combustion gas are continuously changing. In this case, the transient thermal analysis using the finite elements method (Kurowski 2004) is very complex because of the permanent modification of surfaces covered with combustion gas, as a consequence of mechanism rotation. Furthermore, the transient thermal analysis needs a large number of engine cycles to be performed, in view of obtaining quasi-constant temperatures for each point of the mechanism (Reddy and Gartling 2010).

Therefore, an equivalent model for steady-state thermal analysis has to be developed, so that the same results are obtained as in the transient thermal analysis, but with significantly smaller requirements of time and computational resources. The temperature distribution from this steady-state thermal analysis must correspond to the results from the transient thermal analysis, which provides the stationary thermal conditions of mechanism parts.

## Mechanism Model for Transient Thermal Analysis

The hypothetical mechanism, shown in Fig. 1, consists of a cylindrical rotor inside a fixed part. The 300 mm diameter rotor has a pocket on 90° of its circumference. The fixed part has been modelled as a cylindrical ring with 300 mm inner diameter and 330 mm outer diameter. Both rotor and fixed part are made of aluminium, with the following properties: density 2700 kg/m<sup>3</sup>, thermal conductivity 200 W/(m K), specific heat capacity 800 (W s)/(kg K). The rotor angular speed corresponds to rated engine speed 60 min<sup>-1</sup>, and each mechanism rotation corresponds to an entire engine cycle.

Heat is generated in the cavity corresponding to the rotor pocket (considered combustion chamber), on an angular interval between 0° and 90° of mechanism rotation, as shown in Fig. 2. Throughout the interval of combustion process, convective heat transfer of combustion gas (with film coefficient 300 W/(m<sup>2</sup> K) and temperature 800 °C) towards the fixed part is considered on the inner surface corresponding to the rotor pocket, and neglected on the rest of the fixed part inner surface. Throughout the remaining interval of mechanism rotation, heat transfer is

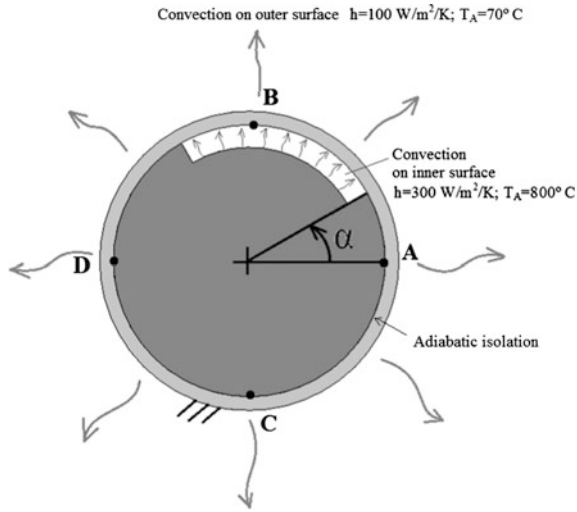


Fig. 1 Model for thermal analysis of a simplified rotary engine mechanism

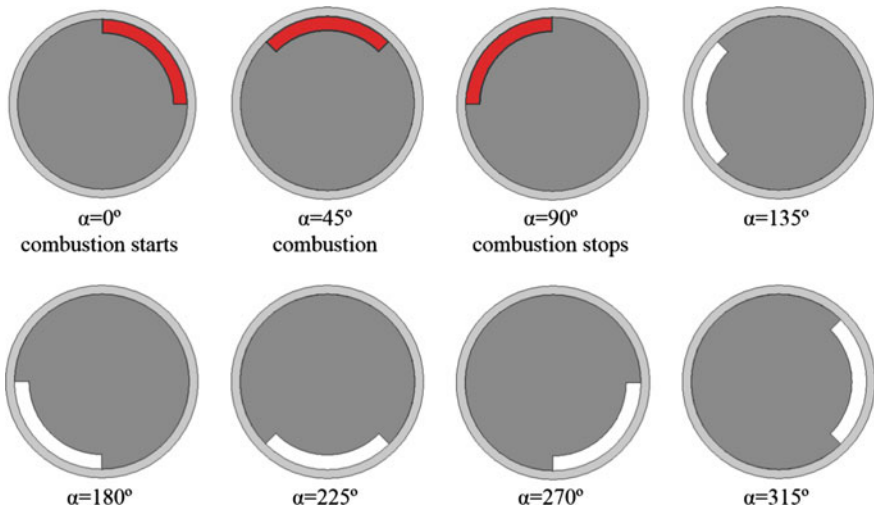
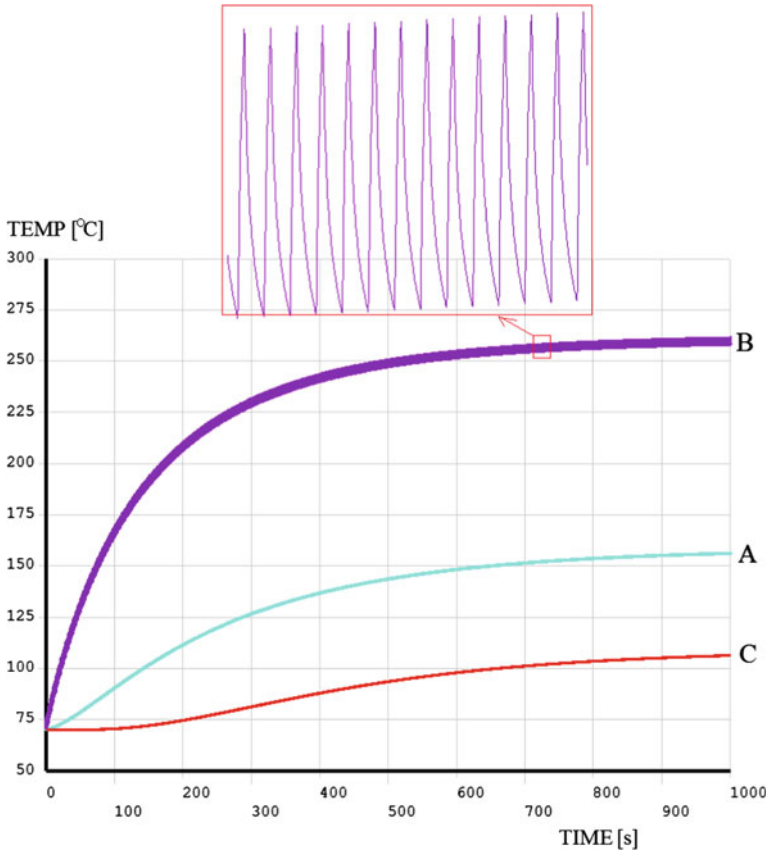


Fig. 2 Combustion phase with respect to rotor position throughout mechanism rotation

neglected on the entire inner surface of the fixed part. Convective heat transfer (with film coefficient  $100 \text{ W}/(\text{m}^2 \text{ K})$  and temperature  $70 \text{ }^\circ\text{C}$ ) is considered constant on the outer surface of fixed part.

The transient thermal analysis is performed for 1000 rotations, in view of obtaining quasi-constant temperatures for each point of the mechanism after many



**Fig. 3** Evolutions of temperatures during transient thermal analysis

engine cycles. The evolutions of temperatures for points A, B, and C of the fixed part during this analysis are shown in Fig. 3. It can be noticed that point B has pulsating temperature variation, but all three points tend to stabilize to quasi-constant temperature values.

### **Equivalent Mechanism Model for Steady-State Thermal Analysis**

As the transient thermal analysis requires extended time and computing resources, an equivalent model is necessary for steady-state thermal analysis.

The heat flux of a point or an area element located on the fixed part inner surface is defined as an average considering its variation over an entire mechanism rotation:

$$q_m = h_m(T_0 - T_m) = \frac{\int_0^{360} q(\alpha) d\alpha}{360^\circ}, \quad (1)$$

where

- $q_m \left[ \frac{\text{W}}{\text{m}^2} \right]$  is the average heat flux of the point over an entire rotation,  
 $h_m \left[ \frac{\text{W}}{\text{m}^2 \text{K}} \right]$  is the equivalent film coefficient for the point over an entire rotation,  
 $T_m [\text{K}]$  is the equivalent convection temperature for the point over an entire rotation,  
 $T_0 [\text{K}]$  is the resulting quasi-constant temperature of the area element,  
 $q(\alpha) \left[ \frac{\text{W}}{\text{m}^2} \right]$  is the variation of heat flux of the point as a function of rotor angle over an entire rotation,  
 $\alpha [^\circ]$  is the rotor angle position.

The variation of heat flux of the abovementioned point as a function of rotor angle over an entire rotation is defined as:

$$q(\alpha) = h(\alpha)[T_0 - T(\alpha)], \quad (2)$$

where

- $h(\alpha) \left[ \frac{\text{W}}{\text{m}^2 \text{K}} \right]$  is the variation of film coefficient for the point as function of rotor angle over a rotation,  
 $T(\alpha) [\text{K}]$  is the variation of convection temperature for the point over an entire rotation.

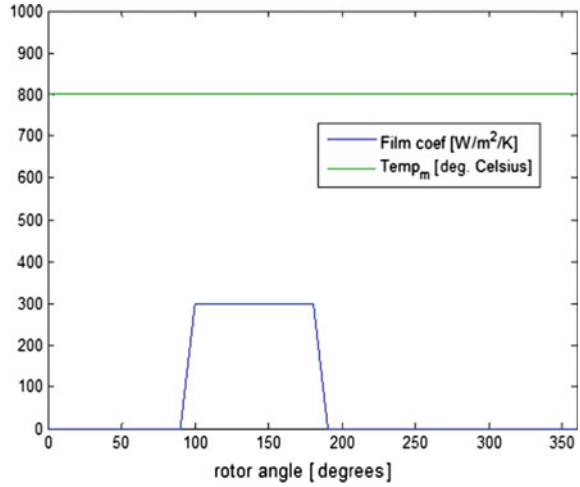
From (1) and (2), the following equation can be obtained:

$$T_0 360 h_m - 360 h_m T_m = T_0 \int_0^{360} h(\alpha) d\alpha - \int_0^{360} h(\alpha) T(\alpha) d\alpha. \quad (3)$$

Therefore the equivalent film coefficient for the mentioned point over an entire rotation is:

$$h_m = \frac{\int_0^{360} h(\alpha) d\alpha}{360}, \quad (4)$$

**Fig. 4** Variations of convection temperature and film coefficient for point B during a mechanism rotation



and the equivalent convection temperature for the same point over an entire rotation is:

$$T_m = \frac{\int_0^{360} h(\alpha)T(\alpha)d\alpha}{h_m 360}. \quad (5)$$

The Eqs. (4) and (5) allow that the transient thermal analysis, which tends to stationary thermal conditions, is replaced with an equivalent steady-state thermal analysis, which no longer requires  $\alpha(t) [^\circ]$  the rotor angle as a variable.

For example, during an entire mechanism rotation the point B undergoes variations of convection temperature and film coefficient as shown in Fig. 4.

The average values of the film coefficient and convection temperature for the point B situated on the fixed part at  $\alpha = 90^\circ$  (which has the longest exposure to combustion gas) are  $h_m = 75 \text{ W}/(\text{m}^2 \text{ K})$  and  $T_m = 800 \text{ }^\circ\text{C}$ . The area elements A and D situated on the fixed part at  $\alpha = 0^\circ$  and at  $\alpha = 180^\circ$  have practically no convective heat transfer, and therefore on the angular intervals  $[0^\circ; 90^\circ]$  and  $[90^\circ; 180^\circ]$  linear variations of the film coefficient and convection temperature are obtained.

## Comparison of Results from Transient and Steady-State Thermal Analysis

The transient thermal analysis performed for 1000 rotations is compared with the steady-state thermal analysis. The distribution of temperatures on the fixed part obtained from the steady-state thermal analysis is shown in Fig. 5 next to the distribution of temperatures obtained from the transient thermal analysis, and very

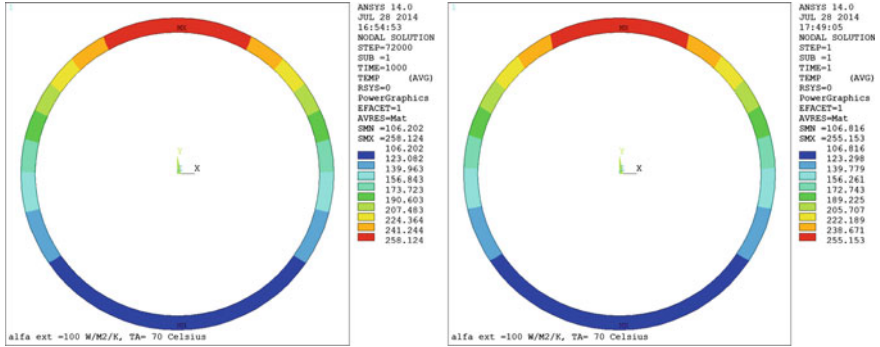


Fig. 5 Temperatures of fixed part obtained from the transient (left) and steady-state (right) thermal analysis

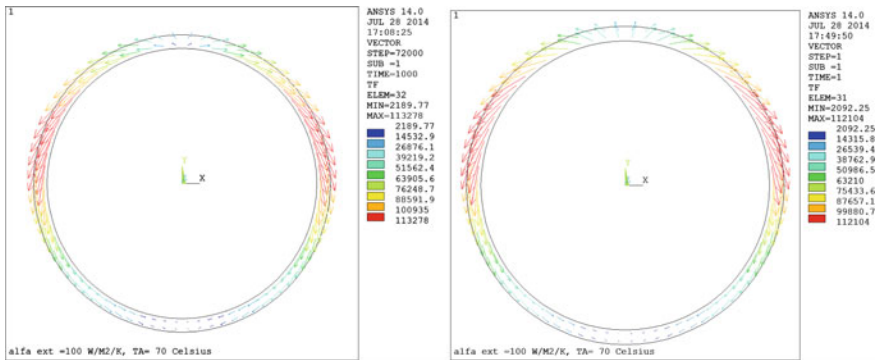


Fig. 6 Heat flux of the fixed part obtained from the transient (left) and steady-state (right) thermal analysis

good similarities are ascertained. Also, the results obtained from the two analyses for the heat flux of the fixed part are quite similar, as shown in Fig. 6.

## Conclusions

The transient thermal analysis takes into account the permanent modification of surfaces covered with combustion gas, as a consequence of mechanism rotation, but requires a large number of engine cycles to obtain quasi-constant temperatures for each point of the mechanism. The complexity of the transient thermal analysis makes it inappropriate for simulations of a realistic rotary engine mechanism, with many parts and complicated geometry.

The equivalent model for steady-state thermal analysis is developed based on the definition of heat flux as an average considering its variation over an entire mechanism rotation. This assumption allows expressing the equivalent film coefficient over an entire rotation and the equivalent convection temperature over an entire rotation. Thus, the transient thermal analysis, which tends to quasi-constant temperature distributions, can be replaced with an equivalent steady-state thermal analysis, which no longer requires the rotor angle as a variable.

The comparison of fixed part temperature and heat flux proves that the steady-state thermal analysis performed using the equivalent film coefficients and the equivalent convection temperatures provides very similar results, compared with the transient thermal analysis, but with significantly lower computational effort.

**Acknowledgments** The research presented in this paper has been performed within the scientific research project No 266059 funded under the European Union Programme FP7-TRANSPORT.

## References

- Heywood JB (1988) Internal combustion engine fundamentals. McGraw-Hill, New York  
Kuroski PM (2004) Finite element analysis for design engineers. SAE International, Warrendale  
Reddy JN, Gartling DK (2010) The finite element method in heat transfer and fluid dynamics. CRC Press, Boca Raton



# Inter-cylinder Distribution of Di-Ethyl-Ether Injected into the Intake Manifold of a Diesel Engine Using CFD Simulation

Victor Iorga-Siman, Adrian Clenci, Rodica Niculescu and Alina Trică (Tuță)

**Abstract** This paper is a consequence of a study on assessing the cold-starting performance of a compression ignition engine fuelled with different blends of fossil diesel fuel and biodiesel. Through experimental investigations, it was found that the engine starting at  $-20\text{ }^{\circ}\text{C}$  was no longer possible in the case of using B50 (50 % diesel + 50 % biofuel made from sunflower oil). In order to determine the engine starting in this particular situation, Di-Ethyl-Ether (DEE) was injected into the intake manifold. DEE being a highly flammable substance, the result was a sudden and explosive engine starting, the peak pressure in the monitored cylinder in the first successful engine cycle being almost twice the one which is usually considered as normal. As a consequence of this observation, we wondered what happened in the other 3 engine's cylinders which were not monitored with pressure sensors. Since the cause of the sudden and explosive engine starting was the DEE, our question is in which way the DEE injected into the intake manifold was distributed to each of the 4 cylinders of the engine. Does the extremely high peak of pressure occur in the other 3 cylinders, as well? Since only one cylinder was monitored with a pressure sensor, the method which was used to find the answer to the question mentioned before was to use a CFD approach. Thus, this paper's objective is to present the method used in order to find the inter-cylinder distribution of the injected DEE.

**Keywords** Biodiesel · Cold start · DEE · DEE inter-cylinder distribution · CFD

## Notations

Bx Biodiesel blend ratio (*i.e.* for  $x = 0$ , B0, meaning no biodiesel; for  $x = 100$ , B100, meaning no diesel fuel)  
CAD Computer Aided Design  
CFD Computational Fluid Dynamics

---

V. Iorga-Siman · A. Clenci (✉) · R. Niculescu  
University of Pitesti, Pitesti, Romania  
e-mail: adrian.clenci@upit.ro

A. Trică (Tuță)  
Renault Technologie Roumanie, Ilfov, Romania

CO	Carbon monoxide
CO <sub>2</sub>	Carbon dioxide
DEE	Di-Ethyl-Ether
HC	Unburned hydrocarbons
NO <sub>x</sub>	Nitric Oxides
Pmax	In-cylinder absolute pressure peak, [bar]
PM	Particulate Matter
PN	Particulate Number

### **Turbulence model notations**

Z	Normalized wall-normal velocity scale
$\kappa$	Turbulent Kinetic Energy, TKE [ $\text{m}^2 \text{s}^{-2}$ ]
$\nu$	Fluid kinematic viscosity
$\omega$	Turbulent dissipation
f	Elliptic relaxation function
RNG	Re-normalisation Group
SST	Shear Stress Transport
y	Dimensionless wall distance

## **Introduction**

The main challenges of today's automotive transport are first the reduction of pollution (CO, HC, NO<sub>x</sub>, PM and PN) and then the reduction of greenhouse emissions (e.g. CO<sub>2</sub> emissions). The reduction of the energetic dependency on petroleum products is another challenge. And finally, the transportation industry needs to find a solution in acceptable economic conditions; therefore biofuels appear to be a good answer.

In 2010, biofuels represented about 3 % of the worldwide energy consumption in the automotive transport. In the future, several scenarios are proposed going from 5 to 15 % in 2025. In Europe 10 % of energy for the transport sector should be renewable in 2020.

The work presented in this paper is part of a larger research program that is running at the University of Pitesti (Niculescu and Clenci 2009–2011). Its purpose is to highlight one of the problems encountered when blending biodiesel with commercial petroleum diesel: the deterioration of the cold starting performance of the compression ignition engine. Worldwide there are many areas where really low sub-zero ambient temperatures are encountered during winter (countries at high latitudes, regions at high altitudes and far from the moderating effect of the open sea). In this case, the engine start time and repeatability become the key performance attributes.

In this context, one goal of the authors was to assess the starting performance at  $-20\text{ }^{\circ}\text{C}$  of a common automotive compression ignition engine, fuelled with different blends of fossil diesel fuel and biodiesel. Another goal was to determine the biodiesel blend ratio limit at which the engine would not start at  $-20\text{ }^{\circ}\text{C}$ , and subsequently, to investigate the impact of di-ethyl-ether (DEE) injection into the intake manifold on the engine's start (Clenci et al. 2014a).

Figure 1 presents the results obtained during a starting test at  $-20\text{ }^{\circ}\text{C}$ . For each of the tests performed (commercial petroleum diesel fuel, B30, B50), the glow plug states were the same i.e. all off, preheat, wait for cranking, cranking, post heat on, post heat finished.

As shown in Fig. 1, the engine did not manage to start with B50. Therefore, as already mentioned, the solution used to help the engine to start was the injection of 150 mg of DEE into the intake duct just before the air filter and before pushing the engine's start button. Concerning the effect of DEE on engine behavior, Fig. 1 shows that two cycles with very high peak pressures ( $>200\text{ bar}$ !) were recorded. As seen, it was enough to help the engine to start but at the cost of generating extreme mechanical stress. It is for this reason that the actuation of glow plugs is not recommended when using DEE as ignition improver.

As a consequence of this observation, we wondered what happened in the other 3 engine's cylinders which were not monitored with pressure sensors. Since the cause of the sudden and explosive engine starting was the DEE, our question is in which way the DEE injected into the intake manifold was distributed to each of the 4 cylinders of the engine. Does the extremely high peak of pressure occur in the other 3 cylinders, as well? Since only one cylinder was monitored with a pressure sensor, the method which was used to find the answer to the question mentioned

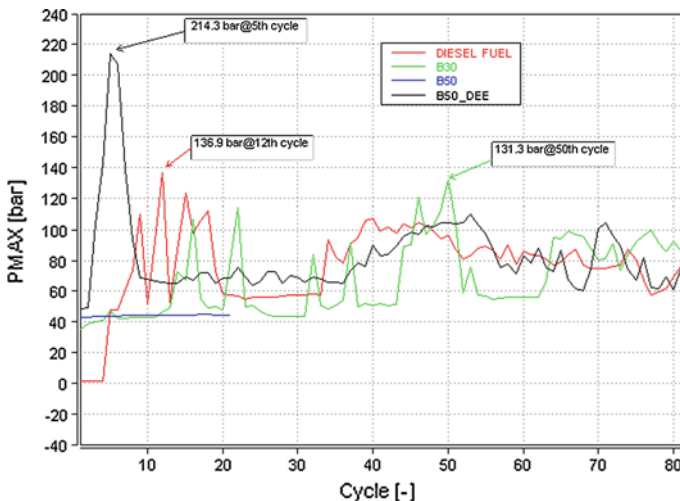


Fig. 1 Pressure peaks cyclic evolution, Clenci et al. (2014a)

before consisted in a CFD approach. Thus, this paper's main objective is to present the method used in order to find the inter-cylinder distribution of the injected DEE.

Our paper is organized in 2 sections, followed by the conclusions drawn from the study and future works. After this first section framing the work in the current context, Sect. 2 presents the Computational Fluid Dynamics (CFD) approach, which has been used in order to find the inter-cylinder distribution of the DEE injected into the intake manifold. This area is divided in two subsections: in the first one, the simulation is described and in the second one, the results are presented and discussed in detail.

## Computational Fluid Dynamics Simulation

Computational fluid dynamics, usually abbreviated as CFD, is a branch of fluid mechanics that uses numerical methods and algorithms to solve and analyze problems that involve fluid flows. The fundamental basis of almost all CFD problems are the Navier–Stokes equations, which define any single-phase (gas or liquid, but not both) fluid flow. Despite considerable advances in computer technology and mathematical modeling during the past twenty years, this numerical method only aims to provide approximate results because the exact resolution of the Navier-Stokes equations under specified boundary conditions is still an impossible task. However the numerical approach is a good alternative in fluid flow study.

According to Clenci et al. (2014b), the experimental techniques of fluid flows investigation are able to provide high quality results (even the spatial structure and the temporal revolution of the velocity field) but require good optical access for large fields of view, high speed photography, innovative data analysis methods, and state-of-the-art equipment, which makes them quite expensive. Performing flow measurements in an engine can therefore be difficult because of the complexity of the equipment involved. The advantage of numerical investigations is that an expensive and time-consuming measurement set-up is not necessary. Thanks to the increasing power of computers, nowadays the processes occurring in an internal combustion engine can be modeled more and more accurately and simulated faster. One may note, however, that even the numerical simulations need significant computational cost.

In the current study, the CFD simulation was performed AVL-Fire® 2013 software. FIRE® is a powerful multi-purpose thermo-fluid dynamics software with a particular focus on handling fluid flow applications related to internal combustion engines and powertrains.

The details of the computer used to simulate the flow phenomena of the air-DEE mixture flow into the intake manifold of our engine are presented in Table 1.

As mentioned before, the aim of the simulations is to have an idea of the inter-cylinder distribution of the injected DEE; thus, to extrapolate on the effect of DEE in each of the engine's 4 cylinders.

**Table 1** Specification of used computer

System	Manufacturer	Dell
	Type	X64
OS		Windows 7.6.1
Processor	Type	Intel Xeon X5650
	Speed	2.67 GHz
	# CPU(s)	6
RAM		24 GB

**Table 2** Technical characteristics of the engine

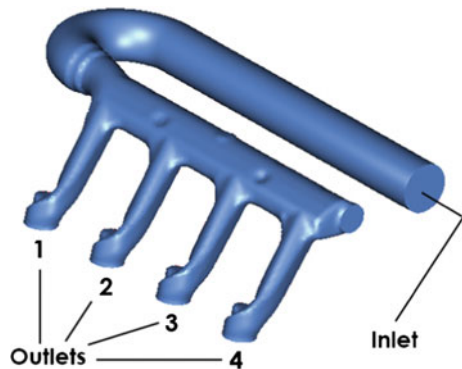
Characteristics	Values
# Cylinders	4
Total capacity (cm <sup>3</sup> )	1461
Volumetric compression ratio	17.9
Max. power (kW) @ speed (rpm)	48 @ 4000
Max. torque (Nm) @ speed (rpm)	160 @ 1700
Number of injector holes/hole diameter (mm)	5/0.15
Injection pressure (bar)	100–1400

The technical characteristics of the engine are presented in Table 2. Some of these technical characteristics are used in the AVL Fire tool calibration.

### *Mesh Generation and Simulation Description*

The intake manifold has been previously designed using commercial CAD software (CATIA)—Fig. 2. As seen from this figure, there is one inlet that corresponds to the injection surface. In reality, the DEE is injected before this surface, actually, at the entrance in the air filter. Thus, we considered the whole inlet surface as the injection

**Fig. 2** Description of the volume—Inlet/outlets



surface in order to obtain the largest cloud of DEE. The outlets correspond to the intake of the four cylinders and are numbered from 1 to 4 (the first being the nearest to the bend of the intake manifold, and the fourth, the farthest).

The first step is to mesh the computational domain. In order to study the effect of the meshing on the results, two different meshes have been made and analyzed: a coarse mesh, containing 96,863 cells and a fine mesh of 351,000 cells. For both cases, the structured grid with hexahedral shape cells was used. The numerical results are fairly close. However, the computational time and the average time per step are very different (Fig. 3). Generally, the mesh is a trade-off resulted from the need to obtain good results in reasonable simulation time.

Several selections in addition to inlet/outlets are required to study the inter-cylinder distribution of DEE. Indeed, the software is not able to calculate the mass fraction of DEE in a surface selection because the additional formula accounts for the volume of the cells. So, four cells selections have been added (Fig. 4): the finer the meshing is, the smaller these four volumes are.

The chosen turbulence model is the  $\kappa-\zeta-f$  recently developed by Hanjalic et al. (2004). It is a robust modification of the elliptic relaxation model. The aim is to improve numerical stability of the original  $\bar{v}^2-f$  model by proposing an eddy viscosity model, which solves a transport equation for the normalized wall-normal velocity scale  $\zeta = \bar{v}^2/k$  instead of  $\bar{v}^2$ . This turbulence variable ( $\zeta$ ) can be regarded as the ratio of the two time scales: scalar  $k/\varepsilon$  (isotropic), and lateral  $\bar{v}^2/k$  (anisotropic). It also introduces a more robust wall boundary condition for  $f$  equation, this time  $f_{wall}$  is proportional to  $1/y^2$  ( $y$  is a dimensionless wall distance) instead of  $1/y^4$  in the original  $\bar{v}^2-f$  model.

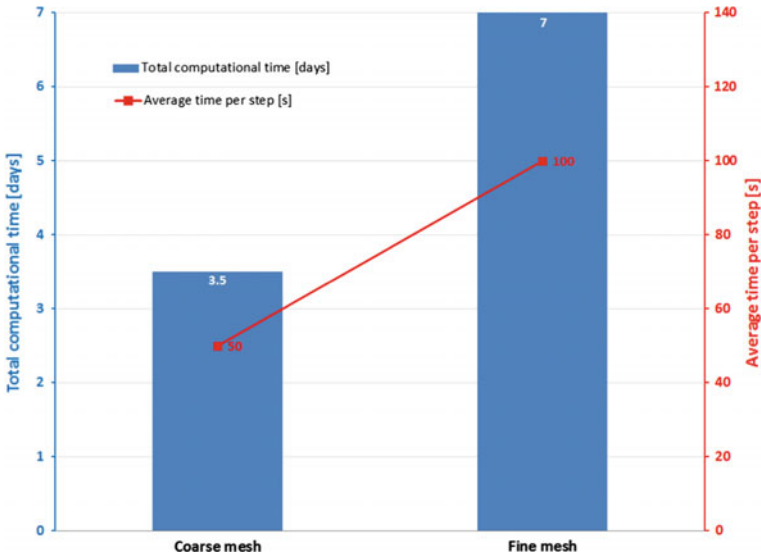
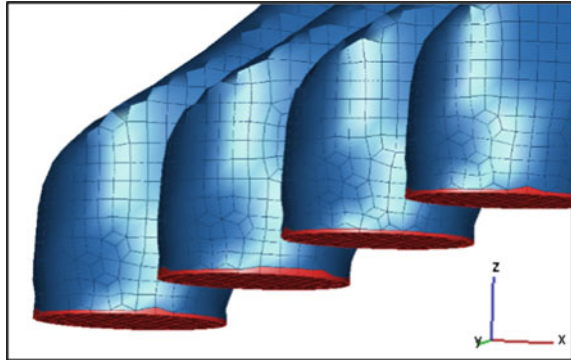


Fig. 3 Effect of the mesh on computational time

**Fig. 4** Description of the additional selections



Since there are numerous turbulence modeling approaches (e.g.  $k-\omega$  model with its two declinations:  $k-\omega$  *standard* and  $k-\omega$  *SST* and  $k-\epsilon$  model with its three declinations:  $k-\epsilon$  *standard*, *realizable*  $k-\epsilon$  and  $k-\epsilon$  *RNG*), in order to sustain the one chosen, several CFD simulations should have been carried out to see which the best

**Table 3** Details of simulation

	Parameters	Values	Comments
Run mode	Run mode	Time step	–
	Calculation time step, $\Delta t$ [ms]	0.5	–
	End time [s]	3.0	The equivalent of 15 cycles @ 600 rpm (based on experimental results, it is expected that DEE to be consumed in this time)
Boundary conditions	Inlet/outlets/wall temperature [°C]	–20	Based on the experimental conditions
	Inlet static pressure [Pa]	100,000	Based on the experimental conditions
	Outlets mass flow [g/s]	2.3	Based on an engine speed of 600 rpm
Spray	Type of fluid	DEE	DEE was introduced in fire's database by user defined functions
	Fluid temperature [°C]	–20	Based on the experimental conditions
	Injected mass [mg]	150	Based on the experimental conditions
	Injection duration [s]	1	Based on the experimental conditions
	Velocity [m/s]	0.5	Based on the experimental conditions
	Number of cloud particles per second	200,000	Arbitrary value

is. However, taking into account the long computational time (Fig. 3) and the novelty of the  $\kappa-\zeta-f$  model, we have decided for this stage to not explore the results of other turbulence models.

As for the boundary conditions, spray details and setup of the simulation, Table 3 presents the data.

Concerning the DEE spray, it is underlined that it is injected in a static environment for 1 s. After this injection, the flow is activated by imposing the mass flow boundary condition through the outlets based on the timing resulted from operating the engine at 600 rpm.

### ***Simulation Results. Discussion***

This section will present only the inter-cylinder distribution of DEE obtained when using the fine mesh of 351,000 cells and the 1–3–4–2 cylinder filling order.

The CFD software is able to provide numerous 2D and 3D results. For instance, Fig. 5 present the life time of spray droplets and the mass fraction of the gaseous DEE obtained at certain moments in time.

In the above pictures, the four circles corresponding to the four cylinders, represent the opening and closing of the intake valves, i.e. when a circle is black the valves are closed (the air-DEE mix is not sucked into the cylinder), while when a circle is white, the valves are opened (the corresponding cylinder sucks the air-DEE mix). These results are presented just to show an example of post-processing.

Detailed results concerning the DEE inter-cylinder distribution were obtained by using the four additional cells selections created to calculate the mass fraction of DEE passing through each of the intake manifold's outlets (Fig. 4). Thus, Fig. 6 presents the percentage of the evaporated DEE found in each of the 4 cylinders, starting from the 1st cycle till the 10th cycle.

In the figure above, only 10 cycles were taken from the 15 simulated due to the fact that in the 11th engine cycle there is almost no more DEE in the intake manifold.

Now, by summing up the DEE quantities found in each cylinder after these first 10 cycles, one may obtain the DEE inter-cylinder distribution during the duration of the 10 engine cycles (Fig. 7).

By analyzing Figs. 6 and 7, it is obvious that cylinder number 1 (this is the one that was monitored with pressure sensor during the cold starting tests) is absorbing more DEE compared to the others 3 engine's cylinders.

Thus, coming back to the goal of this study (*What happened in the other 3 engine's cylinders which were not monitored with pressure sensors? Does the extremely high peak of pressure occur in the other 3 cylinders, as well?*), by extrapolating the results, one may say that the extremely high pressure peak of 214.3 bar (see Fig. 1) did not occur in the other 3 cylinders. Certainly, higher pressure peaks than the ones obtained with diesel fuel occurred when DEE was used but apparently not at the extent of the one recorded in the 1st cylinder. For



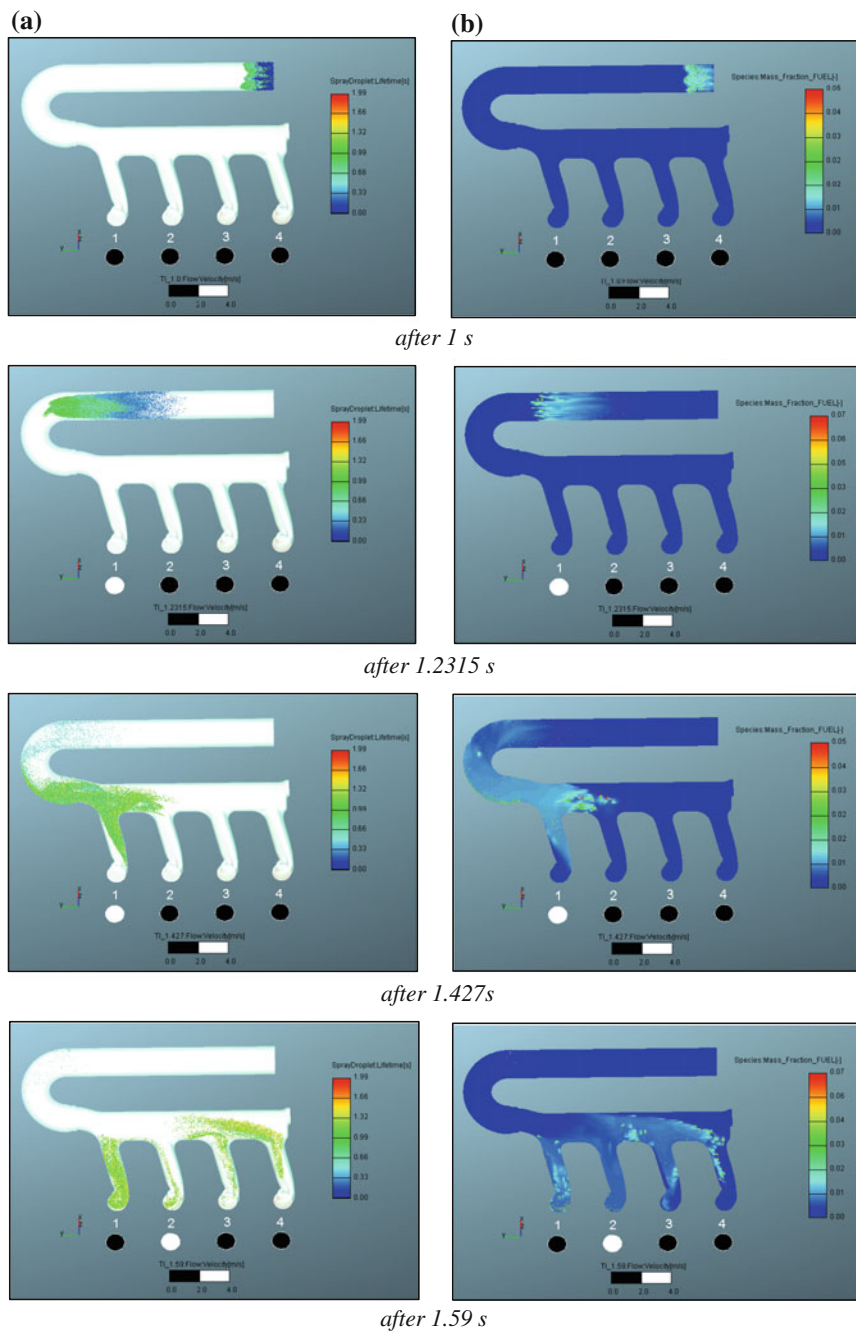


**Fig. 5** a Spray droplets lifetime. b Mass fraction of gaseous DEE

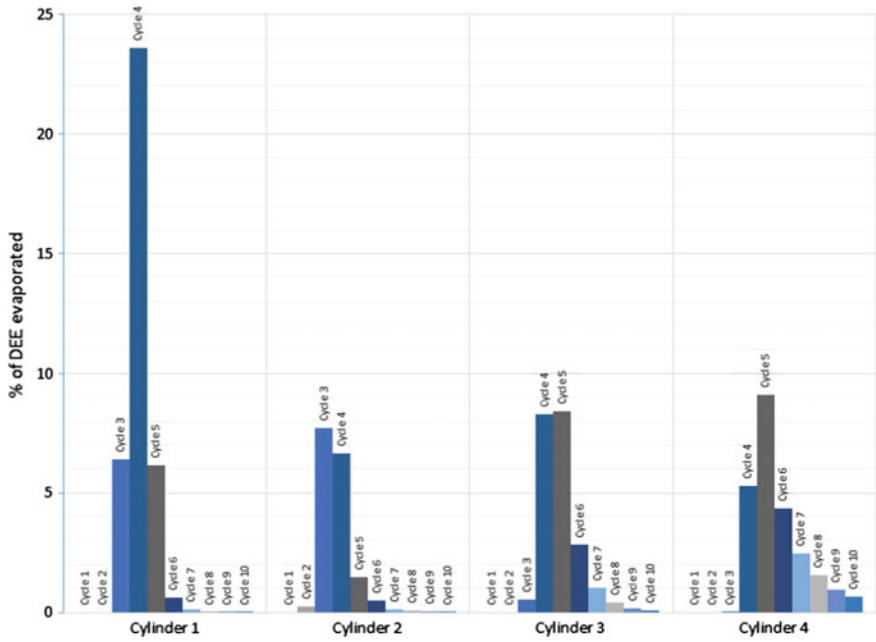


Fig. 6 DEE absorption per cylinder and engine cycle

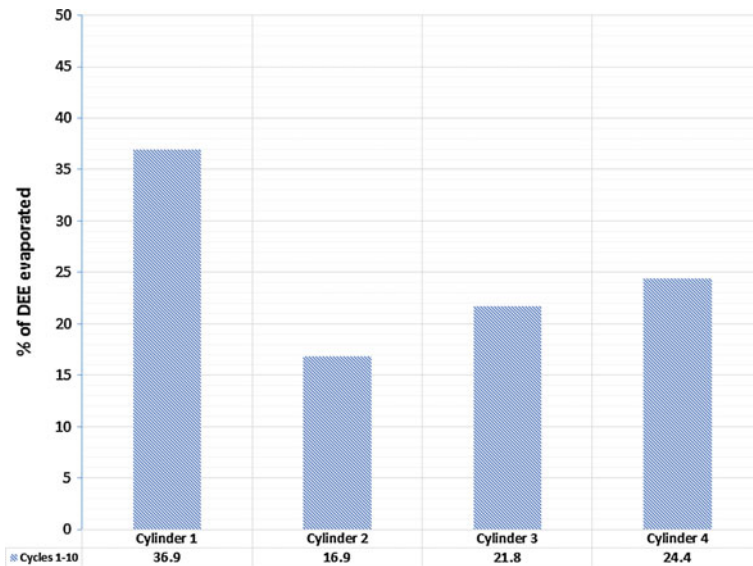


Fig. 7 Total absorption of DEE per cylinder and during 10 cycles

instance, if one associates the 4th engine cycle from the 1st cylinder (see Fig. 6) with the extremely high pressure peak mentioned before, then, the conclusion is that this kind of peak values does not occur in any of the other cylinders or cycles.

## Conclusions and Future Works

The CFD simulation helped to understand what would be the impact in each cylinder of the DEE which was used as an ignition improver for engine cold starting.

The simulation showed that the 1st cylinder is taking the highest quantity of DEE, therefore, this represents the worst case scenario regarding in-cylinder's peak pressures.

This kind of simulation should be enough to determine the needed quantity of DEE able to still start the engine when using B50 (for instance) but on the condition of respecting the maximum allowable cylinder pressure capable of ensuring the wanted engine's reliability.

For the validation of the simulation's results, the authors will soon perform once again the cold starting tests, this time by using in-cylinder pressure sensors for each of the 4 cylinders. Obviously, the validation will be a qualitative one since the pressure peaks from each cylinder should be in the same relation as the DEE inter-cylinder distribution shown in Figs. 6 and 7.

The mesh type and the turbulence model are amongst the key points of the CFD simulation. Usually, in order to be sure that the converged solution is trustworthy, the numerical solution must be independent of the mesh size and turbulence model. Therefore, in order to accomplish this goal the authors are currently running other simulations on this particular topic.

**Acknowledgments** The authors would like to express their gratitude to the Romanian Council for Scientific Research in Higher Education for their financial grant in the period 2009–2011. Thanks are also due to Renault Technologie Roumanie which provided the cold room for the tests. Equally helpful was the involvement in the CFD study of our intern (Mylène Oberson) from Ecole de Mines de Saint Etienne.

## References

- Niculescu R, Clenci A (2009–2011) *Research regarding the developing of a method for improving the cold starting performance of biodiesel fuelled compression ignition engines (in Romanian)*, Research grant CNCSIS 696
- Clenci A, Niculescu R, Iorga-Simăn V, Descombes G, Podevin P (2014a) *Biofuels and cold starting: application on a diesel engine (in French)*. Colloque Francophone sur l'Énergie, Environnement, Économie et Thermodynamique, COFRET'14, Paris, France

- Clenci A, Iorga-Simăn V, Deligant M, Podevin P, Descombes G, Niculescu R (2014b) A CFD study on the effects of operating an engine with low intake valve lift at idle corresponding speed. *Energy* 71:202-217. doi: [10.1016/j.energy.2014.04.069](https://doi.org/10.1016/j.energy.2014.04.069) (ISSN: 0360-5442, 2014)
- Hanjalic, Popovac, Hadziabdic (2004) About the  $\kappa$ - $\zeta$ - $f$  turbulence model. AVL Fire Documentation

# Analysis of Complex Planetary Mechanisms Used in Nine Speed Automatic Transmissions of Cars

Neacsu Eugen, Banca Gheorghe and Oloeriu Florin

**Abstract** This paper presents a kinematic and dynamic analysis of two planetary geared nine-speed automatic transmission ZF9HP and W9A700, on which numerical results are used to compare their level of performance. The study of these two transmissions aims to highlight the advantages and disadvantages of both constructive solutions, knowing that through kinematic synthesis process seeks to choose the optimal final architecture by a high number of feasible kinematic schemes.

**Keywords** Powerflow · Planetary mechanism · Synthesis · Kinematic scheme

## Introduction

In the powertrain system of the motor vehicles, the main function of the transmission is to adjust the running states and operating characteristic of the engine at driving conditions of the vehicle, in order to optimize fuel consumption and dynamic driving characteristic so as to maintain the vehicle controllable and safe, as well as to enhance passengers comfort. In mechanical discrete transmissions the gear ratio is defined by the speed stage of gearbox and changed depending on

---

N. Eugen (✉)

Technic Department, General Inspectorate of Romanian Border Police, Bucharest, Romania  
e-mail: neacsu\_eugen\_cosmin@yahoo.com

B. Gheorghe

Engine Control and Calibration Department, Renault Technologie Roumanie, Titu, Romania  
e-mail: banca\_2004@yahoo.com

O. Florin

Military Automotive Engineering and Transportation Department, Military Technical Academy, Bucharest, Romania  
e-mail: oloeriuflorin@yahoo.com

operating parameters of the engine and vehicle, carried out by the driver, according to the driving conditions.

In the designing phase of mechanical transmission of motor vehicle, the most important steps are the setting of gear ratios, a process known as the setting of speed range of gear stage of gearbox and choosing the suitable kinematic drivetrain, a process known as synthesis of kinematic schemes. The speed-ratio arrangement of gearbox involves the determination of kinematic characteristics and establishing of gear ratios after reports about the dynamic and traction performances of vehicle or according to criteria related to fuel consumption (Stoicescu 2007). The lowest and highest gear ratios values of gearbox are determined, in general, in order to obtain required acceleration or traction performance and respectively to achieve an imposed maximum speed. Usually, the number and values of intermediate gear ratios are determined in order to obtain equal ranges of the engine speed or vehicle speed in each gear, and to obtain equal intervals of traction force variation in neighboring gears.

The fuel consumption of an internal combustion engine represent a function dependent on vehicle speed and loading conditions as rolling parameters, that taking in account gear ratios, can be transformed into a function dependent on load and engine speed. Studies on the influence of gear ratios establishment on fuel consumption (Stoicescu 1998; Golebiewski and Stoeck 2012), reveals that by increasing the number of gears and use as much possible the higher gear stages, generate a significant reduction in fuel consumption and thus emissions, due to placement of operating speeds in the economic range of the engine speed.

Increasing the number of gear steps, especially by adding of overdrive speed-ratios, given the presented advantages, is an obvious tendency of manufacturers of gearboxes, so that currently exist cars equipped with automatic transmissions with a number of eight and even nine gears. These may include eight-speed automatic transmissions ZF8HP and AISIN TL 80SN both with two overdrive gears and nine-speed automatic transmissions W9A700 and ZF9HP with three, respectively four overdrive gears.

## **Analysis Methodology of Gearbox Kinematic Scheme**

The synthesis process of kinematics structures based on graph theory elements (Hsu et al. 1994) significantly reduce the number of mathematically possible variants at a number of functional variants called feasible variants. Choosing the optimal kinematic scheme of a number of feasible variants involves analysis of all these constructive solutions.

Analysis of kinematic schemes for a planetary gearbox is an absolutely necessary stage in the synthesis process, because in order to establish the optimum kinematic scheme that leads to required speed ratios and to fulfill certain constructive requirements is needed to comparing parameters that must be determined and that are interested in functional terms. Usually, in the conceptual phase of gearbox

design the necessary constructive requirements are linked to compactness, mass, volume, overall dimensions and robustness.

The kinematic structures of nine-speed automatic transmissions ZF9HP and W9A700 developed and manufactured by ZF Friedrichshafen AG, respectively Daimler AG, presented in Figs. 1 and 2, are the result of analysis and synthesis process of complex compound planetary mechanisms with four degree of mobility. The difference between the presented automatic transmissions in terms of kinematic structures prove the imposition by the manufacturers of different construction requirements and various functional restrictions that may be highlighted by analyzing these kinematic schemes.

The functional parameters calculation of presented kinematic structures can be done based on algebraic or matrix methods, which involves to successively follow several defined stages (Ciobotaru et al. 2005). Matrix based method that is applied in this case, provide complete informations about powerflow circulation and allows to use mathematical programs in a iterative way that reduce the time for the calculations. The working procedure is presented in the following stages.

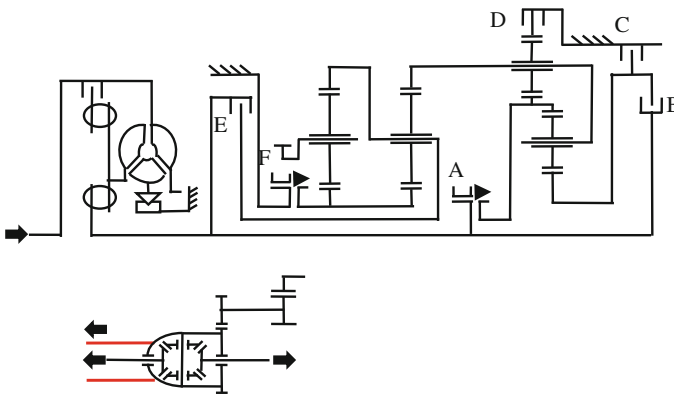


Fig. 1 Kinematic structure of ZF9HP gearbox

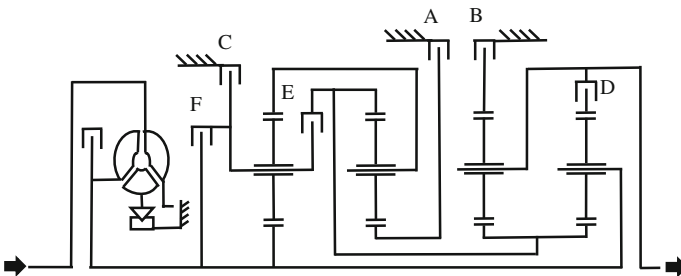


Fig. 2 Kinematic structure of W9A700 gearbox





**Table 3** Calculus relations and acquired numerical values of simple planetary gearsets constant K

ZF9HP		W9A700	
Calculus relation of $K$	$K$ value	Calculus relation of $K$	$K$ value
$K_1 = \frac{i_2}{i_2 - i_3}$	2.053	$K_1 = i_2 - 1$	2.132
$K_2 = \frac{i_1}{i_3} - 1$	1.461	$K_2 = \frac{i_8}{1 - i_8}$	2.274
$K_3 = \frac{i_4}{i_3 - i_4}$	2.65	$K_3 = \frac{i_3}{i_2 - i_3}$	2.333
$K_4 = \frac{1}{i_4 - 1}$	2.591	$K_4 = \left(\frac{i_1}{i_2} - 1\right) \cdot \left(1 + \frac{i_3}{i_2 - i_3}\right)$	2.534

**Fig. 3** Network structure of ZF9HP gearbox

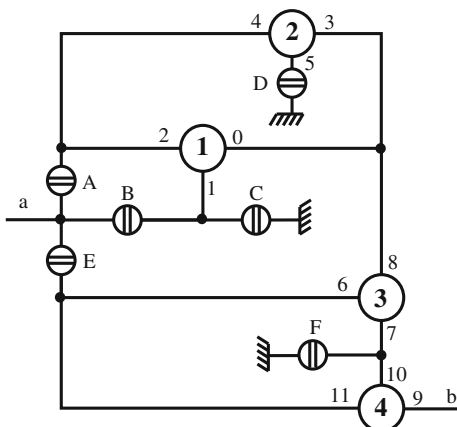
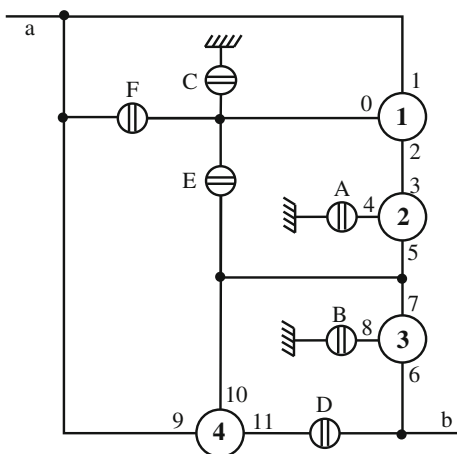


**Fig. 4** Network structure of W9A700 gearbox



external elements of planetary gearsets, coupling or braking elements and input or output elements of kinematic scheme (Figs. 3 and 4).

3. Number external elements for all  $m$  simple planetary gearsets of kinematic structure according to rules contained in Table 4.

**Table 4** Representation of planetary gerset elements and numbering rules of elements in a kinematic structure

Type of external elements in simple planetary gerset nr. $j$	Symbol	Allocated number
Sun gear	1	$3j - 2, j = \overline{1, m}$
Ring gear	2	$3j - 1, j = \overline{1, m}$
Planet carrier	0	$3j - 3, j = \overline{1, m}$

4. Identify connected external elements according to kinematic or equivalent nodal structure; the link between any two external elements connected  $p$  and  $q$  leads to equations of the form:

$$\omega_p - \omega_q = 0 \quad (1)$$

wherein  $p, q \in [0, 3m - 1]$

5. Identify external element connected to the input shaft of gearbox and initializes his angular velocity value with the unit value:

$$\omega_p = \omega_a = 1 \quad (2)$$

6. Identify external element connected to the output shaft of gearbox.
7. With coefficients of angular velocities and free terms it builds the matrices  $C_V$ , respectively  $T_V$  for each gear stage. The matrix  $C$  it has a quadratic form and comprise a number of rows and columns equals to the number of external elements of all planetary gearsets. The first  $m$  rows of coefficients remains the same for all gears, wherein the coefficients of other rows are changed according to the equation corresponding to angular velocities restrictions introduced by the shifting elements. The general kinematic equations of simple planetary gearsets that form the kinematic structure of gearbox are under the form of:

$$\omega_{3j-2} + K_j \omega_{3j-1} - (1 + K_j) \omega_{3j-3} = 0 \quad (3)$$

8. To form a gear stage is needed to engage certain coupling or braking elements. The number of engaged elements must be one unit smaller than the number of kinematic structure degree of freedom. In this case, the angular velocities restrictions are under the form of:

$$\omega_p = 0 \text{ for braking elements} \quad (4)$$

$$\omega_p - \omega_q = 0 \text{ for coupling elements} \quad (5)$$

wherein  $p, q \in [0, 3m - 1] = 0$ .

The presented relations forms a determined algebraic equations system with matrix form:

$$C_V \times V = T_V \quad (6)$$

wherein  $V$  is the angular velocity matrix values of external elements of planetary gearsets.

Finally, are determined the angular velocity matrix for each gear stage:

$$V = C_V^{-1} \times T_V \quad (7)$$

9. To calculate the distribution of power flow, with coefficients of torque and free terms it builds the matrices  $C_T$ , respectively  $T_T$  for each gear stage. In the construction of matrix  $C_T$  are used the relations of torque equilibrium and distribution on planetary gearsets elements, the relations of torque equilibrium on nodal scheme joints and the restrictive relations introduced by shifting elements.

The torques that loads external elements of planetary gearsets satisfies the equation pairs:

$$\{-K_j M_{3j-2} + M_{3j-1} = 0 \quad (8)$$

$$\{M_{3j-2} + M_{3j-1} + M_{3j-3} = 0 \quad (9)$$

For identified joints the equilibrium equations are under the form of:

$$\sum M_r = 0 \quad (10)$$

wherein  $r \in [0, 3m + n_{cb}]$  and  $n_{cb}$  are the number of all coupling and braking elements. In the calculation, the torque that loads the input element, corresponding to the input shaft, are initialised with unit value:

$$M_a = 1 \quad (11)$$

In this case, the restrictions are imposed by the coupling and braking elements that remain disconnected in each gear stage, and are represented by cancellation of their load torques:

$$M_f = 0 \quad (12)$$

wherein  $f \in [0, n_{cb}] = 1$ .

The matrix of torques values that loads external elements of planetary gearsets and shifting elements in each gear stage are:

$$M = C_T^{-1} \times T_T \quad (13)$$

In the following sections of paper are presented graphic representations of results acquired by application of presented methodology, whose interpretation allows to identify the functional particularities and efficiency grade of both constructive solutions.

### *Gearboxes Angular Speed Analysis*

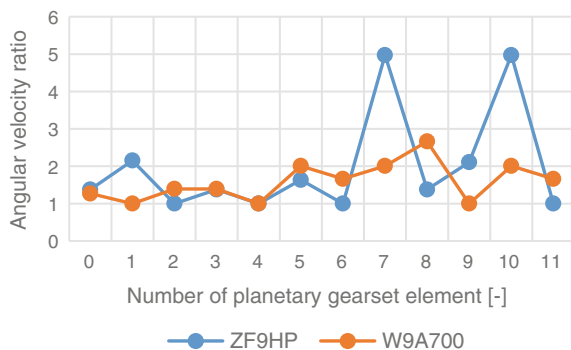
In the synthesis process of kinematic structure of automatic gearbox the angular velocity of planetary gearset elements represent an selective criteria of feasible kinematics schemes, because operating angular speed are limited to a critical value. The limited speed  $n_{cr}$  can be imposed by thermal and dynamic safe operating condition, but based on practical experience (Schaeffler Technologies GmbH 2014) can be taken into account additional criteria such as smooth running, sealing function and centrifugal forces, even if are provided favorable conditions of lubrication and cooling.

The determination of angular velocities of elements and further of radial acceleration and maximum centrifugal forces, allows to compare the level of bearing loads and to evaluate the level of comfort in terms of operating noise produced by the gearboxes.

The analysis of angular velocities of planetary gearsets elements highlights that the ZF9HP gearbox, in eight gear stage, realise the angular velocity multiplication of elements 7 and 10, both of them representing the commonly sun gear of planetary gearsets 3 and 4, with a ratio of 4.995 related to the input shaft. The maximum angular velocity ratio of W9A700 gearbox are acquired in the same gear stage, at the element 8 that represent ring gear of planetary gearset 3, and according with Fig. 5, it is a value of 2.663.

The graphic representations of maximum angular velocity of planet gears in each gear stage are presented in Fig. 6. The maximum values of it, reported to the angular velocity of input shaft, are 4.831 for ZF9HP at planetary gearset 3 and 3.506 for W9A700 at the same planetary gearset number.

**Fig. 5** Maximum angular velocity ratios of the PG elements



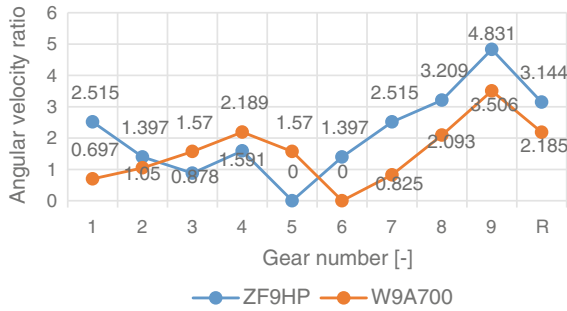


Fig. 6 Maximum angular velocity ratios of planet gear in each stage

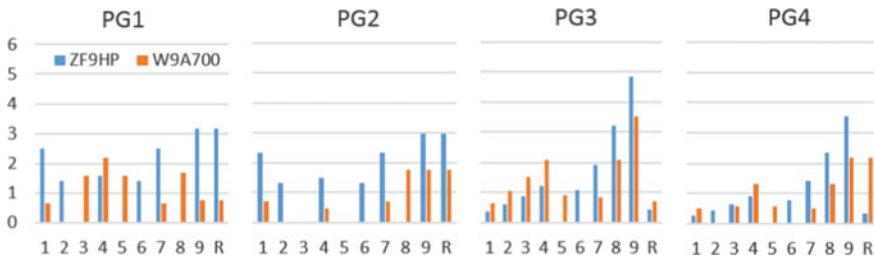


Fig. 7 Angular velocity ratios of planet gears for all planetary gearsets (PG) in each gear stage

From Fig. 7 it can be remarked that the planet gears of each planetary gearset of ZF9HP gearbox are higher angular velocities than in the case of W9A700 gearbox.

In the operation of gearbox, the difference between angular velocities of coupling elements has a major influence on the parameters regarding to passengers comfort and dynamic performance of vehicle when gearshifts occurs and also, represent an appreciation factor of drag torque loss in open multi-plate clutches or brakes.

The power loss through friction in open shifting element  $P_{fr}$  and drag torque  $T_{fr}$  are defined by mathematical relations (Dong et al. 2015):

$$P_{fr} = T_{fr} \Delta\omega \tag{14}$$

$$T_{fr} = \frac{N\pi\Delta\omega\mu}{2h} \cdot (r_o^4 - r_i^4) \tag{15}$$

wherein  $N$  is the number of friction facings,  $\mu$  is the lubricant dynamic viscosity,  $h$  is the lubricant thickness,  $\Delta\omega$  is relative angular velocity difference,  $r_o$  is the outer radius of friction plate and  $r_i$  is the inner radius of friction plate.

The level of comfort during each gearshift depends on relative angular velocity of friction plates of the coupling element and can be translated in jerk and variations of vehicle acceleration.

The graphic representations shows in Figs. 8, 9 and 10 provides informations about relative angular velocity ratio during gearshifts. It turns out that the maximum relative velocity ratios of shifting elements are recorded in the case of ZF9HP gearbox, on dog clutch A, at shifting by the driving mode in reverse mode and backward. According to Table 1 that shows the shifting elements logic, result that the dog clutches A and F are released one-by-one at upshifts 4–5, respectively 7–8,

**Fig. 8** Relative angular velocity ratio for upshifts sequence

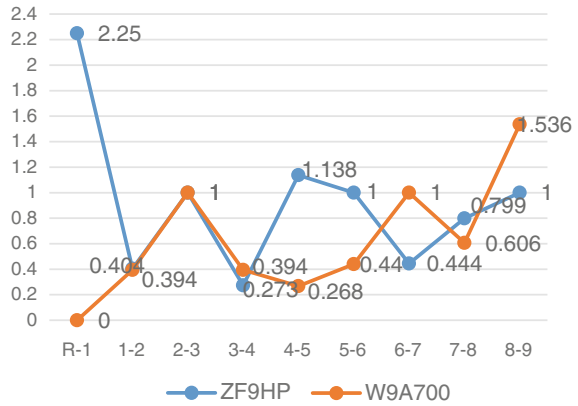


**Fig. 9** Relative angular velocity ratio for downshifts sequence

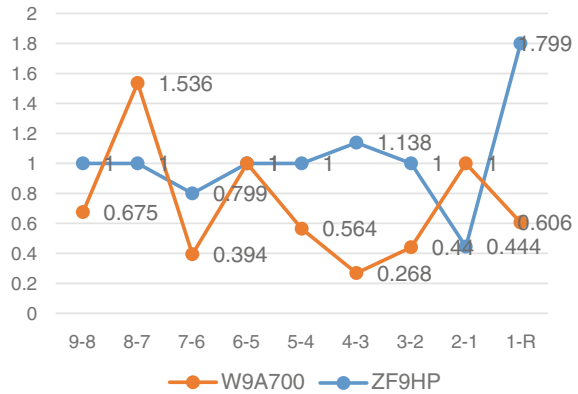
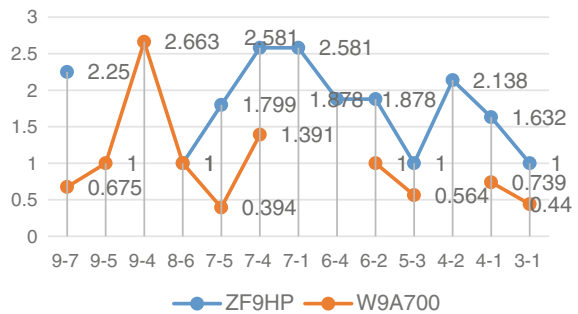


**Fig. 10** Relative angular velocity ratio for “kick-down”



situations where the transmission will be in complete neutral mode for a short time and will lead to a brief interruption of torque delivery. The engagement of dog clutches A and F occurs at downshifts 9–7, 8–7, respectively 7–4, 6–4, 5–4. According to Fig. 10, the downshifts 9–7, 7–4 and 6–4 occurs at high values of relative angular velocity of 2.35, 2.581, respectively 1.878. Due to the design of the shifting elements A and F and their special conditions for synchronising at high relative speed, the program of ZF9HP transmission control unit allows downshifts with just over a gear step jumps. Therefore, are allows downshifts 9–7, 8–6, 7–5, 5–3, 4–2, 3–1, and the exclusion by program of downshift 6–4 is due to high relative speed at engagement of dog clutch A. It detects a high ratio of relative angular velocity of 2.138 at downshift 4–2, but this is allowed because it doesn't involve engagement of any other dog clutch.

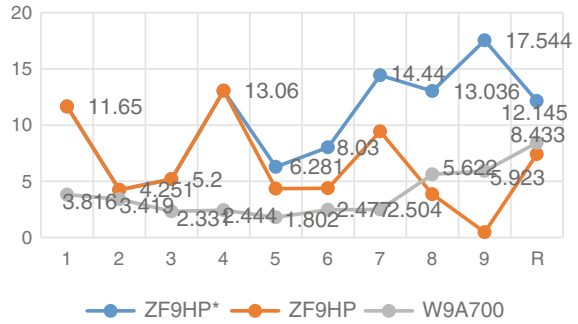
The downshifts with 3, 4 or 5 gear stages jumps are eliminated from shift pattern due tot the difficulty in synchronisation process, especially in situations 8–5, 8–4 or 9–5 which implies simultaneously engagement of both dog clutches. The downshift 9–7 with a high relative angular speed ratio is absolutely necessary to obtain high acceleration performance of vehicle during high speed passing maneuvers through kick-down shift, but involves a long shift time due the synchronisation process.

The advanced algorithms for downshifts 9–7, 8–7, 7–5, 1-R and shift R-1 comprise a complex logic of synchronising process. If the transmission control module starts to select a shift that requires one of the dog clutches, it send an information at electronic control unit of engine in order to adjust the engine to a specific angular speed. To assist speed synchronisation of the two dog clutch component, the engine increase or decrease torque and angular speed. In situation which are needed to increase angular speed, the transmission control unit commands the slip of one or more friction clutches until the components of the dog clutch are moving at the same speed. The actions of complex control algorithms embedded in controller software, during synchronisation, are translated into higher wear of friction elements that affect reliability of transmission, and also in limiting of dynamic performances of vehicle, both of these consequences forming a disadvantage compared to W9A700 transmission.

To comparative analysis of losses due to the frictions of open shifting elements, according with Eq. (15), the drag torque depends on number of friction faces and overall dimensions of friction plates, which in turn are calculated to transmit or to resist at maximum torque achieved in operation. Therefore, taking in account assumptions that both gearboxes use types of lubricants with the same value of dynamic viscosity and the thickness of lubricants of plates in disengaged state are the same, is considered that the product between relative angular velocity ratio and maximum torque transmitted to the shifting elements represent a comparison parameter of friction loss level.

The graphic representation on Fig. 11 shows the level of friction losses in both gearboxes in each gear stage. To highlight the potential of reduction of losses by using of dog clutches, also is presented the situation of losses level in the gearbox namely ZF9HP\* in which A and F are multi-plate clutches. Note that, including the

**Fig. 11** The level of drag torque in all open shifting elements



use of dog clutches, in seven of ten gear stages the ZF9HP gearbox are higher losses than W9A700.

### *Gearboxes Torque Loads Analysis*

The torques acquired in operating conditions loads the gears, shafts and shifting elements, and their maximum values, according to calculation of resistance, are those that dictate overall dimensions of internal organs. Regarding the torques that loads shifting elements, as shown in Fig. 12, finds that the kinematic structure of W9A700 gearbox is advantageous because it achieves a maximum torque ratio of 2.775 at brake D, compared with maximum value of 3.852, at brake B, of ZF9HP gearbox. Also, four by six shifting elements of W9A700 are loads with lower values of torque than ZF9HP gearbox. The maximum values of torque that loads each gear element of planetary gearsets and its corresponding shaft are presented in Fig. 13.

**Fig. 12** Maximum torque ratios of shifting elements

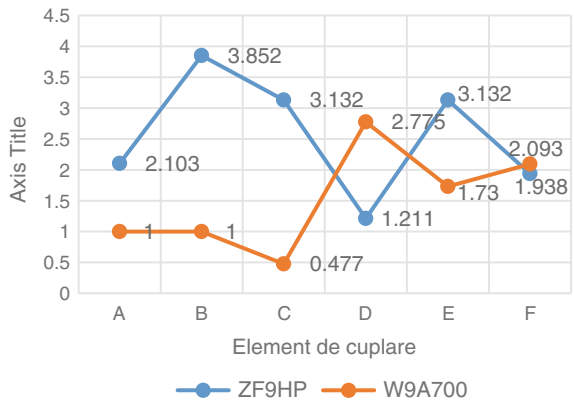
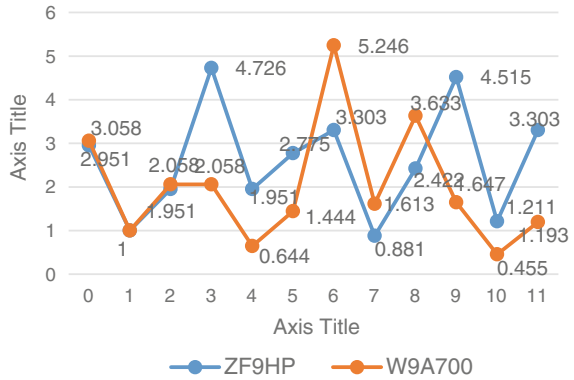




**Fig. 13** Maximum torque ratios of planetary gearsets elements



### Gearboxes Powerflows and Efficiency Grade Analysis

For a more detailed analysis of operating situations of gearboxes, in Figs. 14 and 15 are shown the powerflows in gear stages with speed ratio different by one unit.

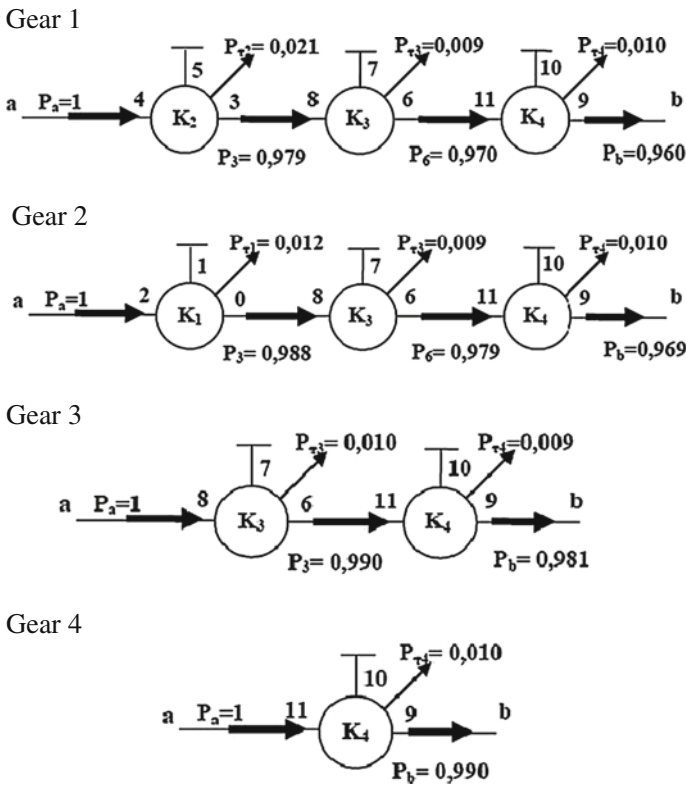


**Fig. 14** Powerflows of ZF9HP gearbox in each gear stage

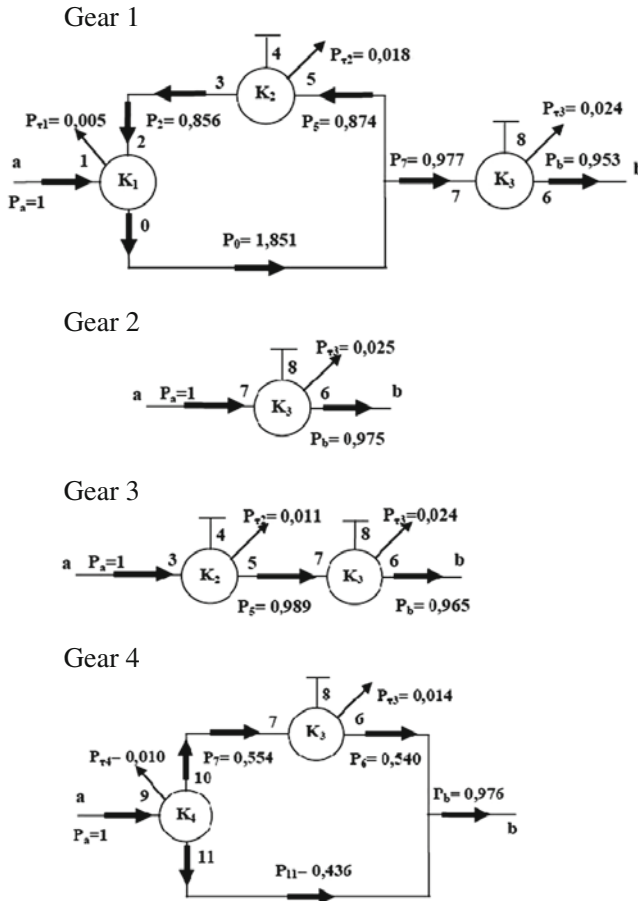
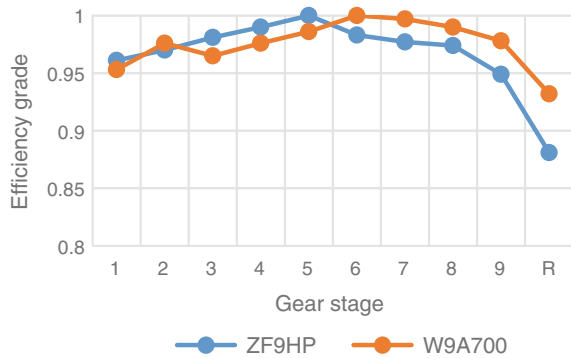


Fig. 15 Powerflows of W9A700 gearbox in each gear stage

The ZF9HP gearbox provides a gear stage using a single planetary gearset, two gear stages using two simple planetary gearsets, four gear stages using three simple planetary gearsets and two gear stages using all four simple planetary gearsets. In the gear stages 6, 7, 8, 9 and reverse the powerflow is transmitted on two or more circuits. It stands the overload of simple planetary gearset 1 in reverse gear stage by a power ratio of 1.491 and a internal parasite powerflow that causes drastic reduction of efficiency. Internal parasite powerflow are also in gear stages 6, 7 and 9.

The W9A700 gearbox provides two gear stages using a single planetary gearset, three gear stages using two simple planetary gearsets and four gear stages using three simple planetary gearsets. In gear stage 1, appears an internal parasite powerflow and the overloading of simple planetary gearset 1 with a power ratio of 1.851. Also, in gear stages 5 and 7 it appears an internal parasite powerflows and

**Fig. 16** Efficiency grade of gearboxes



the overloading of planetary gearset 4 with power ratios of 1.647, respectively 1.214.

Power losses due to gear meshing, as presented in equivalent nodal schemes of gear stages are dependent on powerflow modes. Knowing that the directions of powerflows in each gear stage, mechanically efficiency grade was determined, the results being presented in Fig. 16.

It finds that the ZF9HP gearbox is more efficient in lower gear stages, for example 1, 3, 4 and 5, while the W9A700 gearbox are more efficient in higher gear stages 6, 7, 8, 9, and in reverse gear.

According to presented methodology, because the input angular velocity and torque were initialised as one unit, the values obtained through calculation for functional parameters doesn't represent real values, but ratios of this parameters reported to input variables.

For example, the output power presented in Figs. 14 and 15 represent the power ratio that is the same with efficiency grade values.

## Conclusions

For determination of functional parameters values is applied a matrix-based analysis method, which allows to use a mathematical software in a systematic mode by passing through well establish steps. The functional parameter results shows that the synthesis of kinematic schemes in order to fulfill constructive requirements leads to kinematic structures that doesn't provides maximum performances related to operating conditions and backwards. The design requirements of ZF9HP transmission regarding to space installation optimization, and in particular the transmission length limitation, in order to allow using in vehicles with transverse engine, provide a kinematic structure with two complex Ravigneaux and Simpson planetary gearsets. This arrangement of simple planetary gearsets and the placement mode of shifting elements in kinematic structure provide difficile operating condition that limit performances compared to W9A700 transmission due to the high value of

functional parameters like angular speed, radial acceleration, torque loads and relative angular speed of internal elements. Due to the relative higher angular speed and to the integration of dog clutches in shifting elements that are need to synchronisation in engaging process, can't be used certain shifting possible sequences, from shift pattern being eliminated 6–4 downshift, so that are limited dynamic performance in terms of vehicle acceleration in condition of high speed passing manoeuvres.

The need of dog clutch synchronisation at high value of relative angular speed, like situation of 9–7 downshift, impose using of advanced control algorithms and leads to decrease level of comfort due to the jerk, variation of linear acceleration of vehicle and engine torque limitation during certain gearshifts.

**Acknowledgements** The work has been funded by the Sectoral Operational Programme Human Resources Development 2007–2013 of the Ministry of European Funds through the Financial Agreement POSDRU 187/1.5/S/155420.

## References

- Ciobotaru T et al (2005) *Transmisii planetare pentru autovehicule militare*. Editura Academiei Tehnice Militare, Bucuresti
- Dong P et al (2015) A method of applying two-pump system in automatic transmissions for energy conservation. *Adv Mech Eng* 7:1687814015590306
- Golebiewski W, Stoeck T(2012) Effect oh high-speed traction gearbox ratio on vehicle fuel consumption. *Teka Comm Monit Energ Agric* 41–46
- Hsu C-H et al (1994) Automatic synthesis of displacement graphs for planetary gears. *Math Comput Model* 67–81
- Schaeffler Technologies GmbH (2014) *Planetary gear bearing arrangements in industrial gearboxes*
- Stoicescu AP (1998) *On the capability of the fixed-ratio transmissions to reduce the automobile fuel consumption in driving cycle with constant accelerations*. Paris, s.n
- Stoicescu AP (2007) *Proiectarea performantelor de tractiune si de consum ale automobilelor*. Editura Tehnica, Bucuresti

# DUSTER ZERO—Electric Vehicle Research 4WD

**Danut Gabriel Marinescu, Viorel Nicolae, Cristian Liviu Popescu,  
Liviu Calin and Nicusor Mierloiu**

**Abstract** This paper presents the new aspects regarding a full electric vehicle, all wheels drive developed within the Automotive Engineering Research Centre, University of Pitesti, Romania on the mechanical platform DACIA DUSTER 4WD. The conversion was made by implementing a new electric powertrain that contains Renault ZE components already launched on the market for commercialized vehicles. For reasons of cost, the architecture of the electric drive is mono-motor type and includes a synchronous electric motor type, 44 kW, a robotized gears box with two speeds (L—Low for all terrain and H—High for the road) and the classic mechanical all-wheel drive system. This system allows three different driving modes: 2WD front-wheel drive for maximum electric energy efficiency, Auto, in which the rear-wheel drive is engaged automatically and Lock, whereby 50 % of torque is consistently fed through the rear axle. The traction battery, divided into two stacks is lithium-ion technology type, 400 V, 22 kWh. The performances are: maximum speed: 130 km/h; autonomy (NEDC) (estimated): 160 km; standard charging: 6–8 h with home WALL BOX; fast charging: 0.5–1 h with public and quick charger.

**Keywords** Dacia DUSTER 4WD · Electric vehicle · 4WD

---

D.G. Marinescu (✉) · V. Nicolae  
Automotive Engineering Research Centre, University of Pitesti, Pitesti, Romania  
e-mail: dan.marinescu@upit.ro

V. Nicolae  
e-mail: viorel.nicolae@upit.ro

C.L. Popescu · L. Calin  
Renault Technologie, Voluntari, Roumanie  
e-mail: liviu.popescu@renault.com

L. Calin  
e-mail: liviu.calin@renault.com

N. Mierloiu  
Akka Romserv, Voluntari, Romania  
e-mail: mierloiu\_nicusor@yahoo.com

## Abbreviations

4WD	Four wheel drive
ABS	Anti-lock braking system
AC	Air conditioning
BMS	Battery management system
CATIA	Computer aided three dimensional interactive application
CBC	Connexion box and traction battery charger
DC	Direct current
EBA	Emergency brake assist
EBD	Electronic brake force distribution
EM	Electric machine
ESC	Electronic stability control
EV	Electric vehicle
GEP	Group electric pump
HV	High voltage
HVAC	Heating, ventilation, and air conditioning
IE	Internal combustion-engine
MCU	Motor control unit
NEDC	New European driving cycle
PEB	Power electronic box
UV	Ultraviolet
ZE	Zero emission
ZERO	Zero emission ROmanian concept

## Introduction

The current restrictions on the pollutant emissions concern also the SUV (Sport Utility Vehicle) type vehicle sector characterized by high levels of emission. In these circumstances many producers have developed projects that reduce these emissions through partial electrification (hybrid propulsion) or total electrification (electric propulsion).

In this direction, in the *Automotive Engineering Research Centre, Alternative Propulsion System and Renewable Energies* laboratory of the University of Pitesti, two projects were developed based on the successful market model Dacia *DUSTER 4WD*. This low cost crossover car is made by the Automobile Dacia—Group Renault, at their plant located near Pitesti city, Romania. These two projects are: The *DUSTER Hybrid E4WD*, named *GRAND HAMSTER Electricway 4WD* (Marinescu et al. 2012) developed during 2011–2013 and the *DUSTER Electric 4WD* (Fig. 1) named *DUSTER ZERO 4WD* (ZERO—Zero Emission ROmanian concept) developed during 2013–2016 (Marinescu et al. 2015).



**Fig. 1** DUSTER Z.E.R.O. 4WD—Full electric vehicle and the our car’s symbol (taken over from the “Vidraru” hydropower monument on the Arges River)

Both *GRAND HAMSTER E4WD* and *DUSTER ZERO 4WD* are light SUV developed in order to create greens Dacia all-wheels drive vehicles, usable for the special applications in areas with restrictions on pollution.

These studies are academic projects and have no connection with the projects or future car models of Dacia-Group Renault.

### ***DUSTER ZERO 4WD Architecture***

Unlike the previous concept *DUSTER Hybrid E4WD*, named *Grand Hamster Electricway 4WD* (Fig. 2), where only the new rear axle was driven in the electric mode, the *DUSTER ZERO 4WD* concept is an entirely battery electric vehicle, all-wheel drive (Fig. 3).

For reasons of cost, the architecture of the electric drive 4WD is a mono-motor type and it includes an electric drive train placed in the front side of the vehicle and a transmission all-wheel drive type.

The traction battery assembly with two stacks is located in the central and rear sides

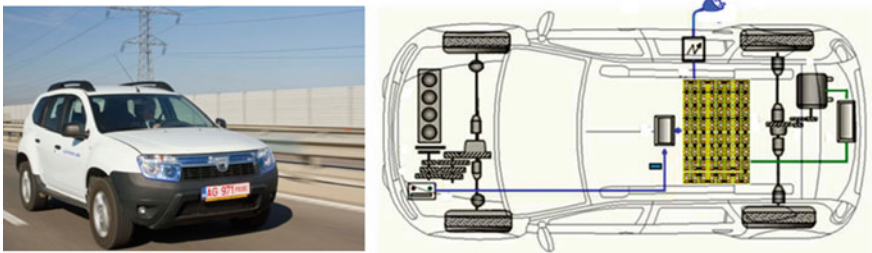


**Fig. 2** *DUSTER Hybrid E4WD* concept with the electric powertrain on the rear side (Marinescu et al. 2012)

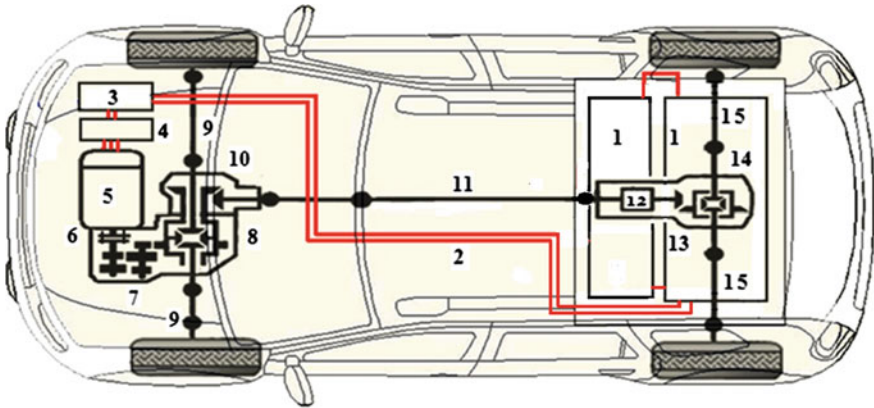


**Fig. 3** Architecture of the *DUSTER ZERO 4WD*, full electric vehicle

The architecture of the *DUSTER ZERO 4WD* is presented in Fig. 3. When the driver presses the accelerator pedal, the lithium-ion battery 1 transmits energy to the electric machine 5 via the high voltage conductors 2, the connexion box 3 and the power electronic box 4.

The battery charges whenever the vehicle decelerates. When the driver lifts his foot from the accelerator pedal, the vehicle's kinetic energy is recovered by the electric machine 5 (*generator* mode) which converts it into electric current. The current generated is stored in the traction battery 1. The architecture of the transmission includes: a new coupling motor/gear input shaft 6, a new gearbox with two speeds 7, and the classic components: front differential 8, front drive shafts 9, transfer gear box 10, propeller shaft 11, electric controlled coupling 12, conical gear 13, rear differential 14, rear drive shafts 15.

## Electric Drive System 4WD

The power electric drive components are located in the front side of the vehicle, in transverse position (Fig. 4). It includes: the Connection Box and the Charger, on the top, the Power Electronic Box with the DC/DC converter and the inverter box, on the middle and the electric machine (the electric motor) on below.

They are joined by a specific frame. Mounted on the car body and on the transmission (Fig. 5). To connect the electric machine with the new front gearbox it was necessary to adapt the stator housing in the transmission side. The electric motor is fixed to the gearbox through an adapter plate.

The transfer of the power from the electric motor shaft to the input transmission shaft is made by an original coupling device with vibration damper.



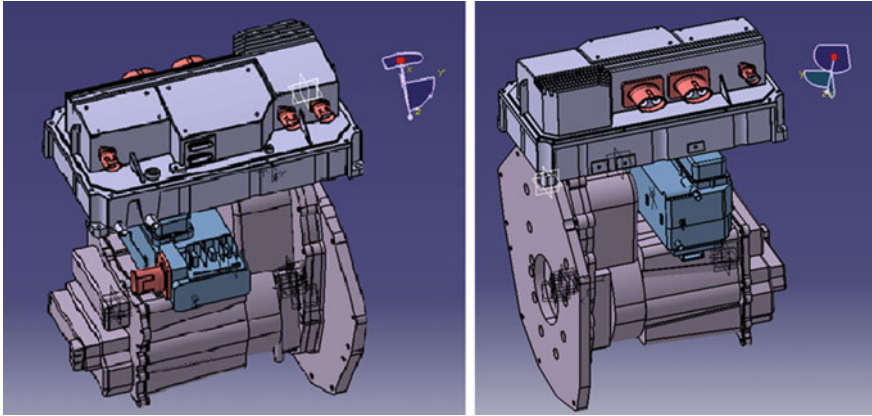


**Fig. 4** The power electric equipment assembly: connection box-charger, power electronic box, electric machine (the electric motor) (CATIA modelling)

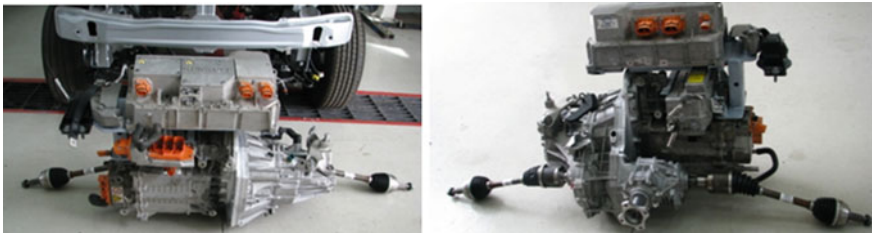


**Fig. 5** The front electric powertrain with 2 speed gearbox of the *DUSTER ZERO 4WD*

To integrate this assembly in the engine compartment from Dacia Duster 4WD we used a new arrangement of the components, different from the Renault ZE solutions (Fig. 6).

The liquid-cooling system for the electric machine inverter and the battery charger is in a closed circuit with the radiator, two pumps (one for the main electric motor and inverter and the second one for the battery charger), and the thermostat and the relief valve. The fan is bi-speed.

### ***Connexion Box and Traction Battery Charger (CBC)***

This assembly made by LEAR company is placed on the top of the power-train. In the charging mode (Fig. 7) it receives the energy from the charging socket and

distributes it to the traction battery charger. In the traction mode it receives the energy from the traction battery and distributes it to the inverter to the electric motor.

### ***Power Electronic Box (PEB): Inverter, DC/DC Converter and Excitation***

This assembly made by Continental company, fluid cooling is a powerful electronic for electric machines in hybrid and electric vehicles versions. It is compact in size and weight, and it has a very high power density. The inverter drives the electric machine in motor and generator mode.

The DC/DC Converter transforms the electricity from HV traction battery and conventional 14 V power net. The output power: up to 3 kW.

### ***Motor Control Unit (MCU)***

The Motor Control Unit is made by Continental company. It realizes: the driver demand acquisition; the powertrain torque management; the brake pedal management; the recuperation/regeneration; the HV energy management; the traction battery charge management; the 14 V battery charge management; the thermal management e.g. heating, air conditioning and pre-conditioning; the E-power-train system cooling (electric water pumps) and communication gateway Central safety management.



**Fig. 6** *DUSTER ZERO 4WD* motor compartment

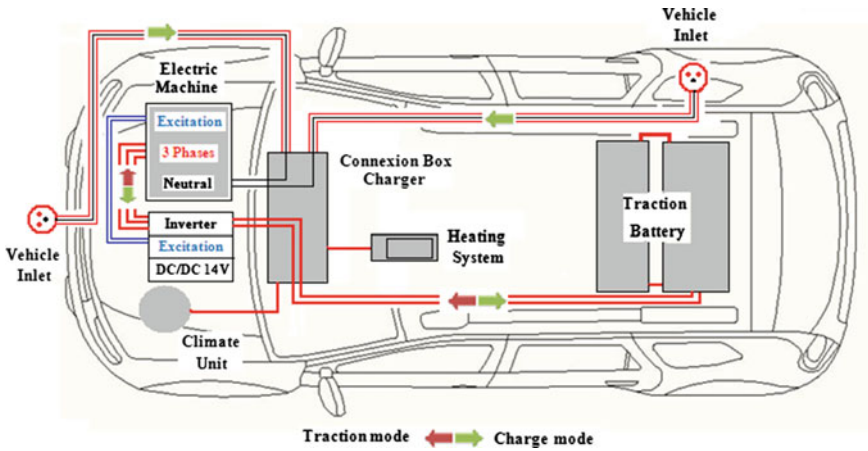


Fig. 7 The electrical power circuit of the *DUSTER ZERO 4WD*

### *Electric Machine (EM)*

DUSTER ZERO 4WD concept is powered by an electric machine 5AM40 type, made by Continental-Renault which also equips Renault Kangoo ZE vehicle. It is a synchronous electric motor with rotor coil, high speed machine, high power density and high efficiency (Vignaud and Fennel 2012). Its peak power is 44 kW at 1856–10500 rpm and the maximum torque is 226 Nm at 480–1856 rpm.<sup>1</sup> The electric motor characteristics are shown in Fig. 6.

### *Transmission 4WD Type*

The new transmission of the DUSTER ZERO 4WD was made starting from the mechanical *DUSTER 4WD* transmission, internal combustion-engine version, the TL8 type. Due to the favorable characteristics of the electric motor (Fig. 8) the new transmission does not require clutch, gearbox or reverse gear. Thus *DUSTER ZERO 4WD* can be driven similarly to a vehicle with automatic transmission.

The selector lever (Fig. 9) has four positions. P: park; R: reverse; N: neutral; D: drive. The drive mode switch is given the command by a cable (for the forward, the neutral and the reverse mode) and the Parking Lock device. The display of the instrument panel (Fig. 9) shows these modes.

However, to have similar performance as the thermal vehicle, we adopted a reducer with two speeds. The change of the speeds, L—Low, for all terrain and H—High for the roads, is made by a servo-motor controlled by the driver by a button.

<sup>1</sup>[www.renault-ze.com](http://www.renault-ze.com).

**Fig. 8** Electric motor 5AM40 characteristics

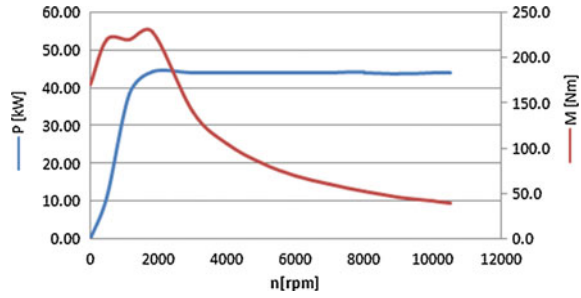


**Fig. 9** The DUSTER ZERO 4WD cockpit



The new Parking Lock device is mounted in the reducer housing.

Depending on the road conditions, similar as the internal combustion-engine version the mechanical all-wheel drive system can provide three different driving modes by another button:

- *2WD*, where the transmission is locked into front-wheel drive for maximum electric energy efficiency and maximum autonomy. This mode is used on dry roads with good grip, and is indicated on the new instrument panel;
- *Auto*, in which the rear-wheel drive is engaged automatically. The operating principle “AUTO” distributes the electric motor torque between the front and the rear axles, according to the road conditions and the vehicle speed. This position optimizes the road holding. This mode is used on any type of road: dry, snow covered, slippery, etc. This mode is not indicated on the instrument panel and it is not available yet;
- *4WD Lock*, whereby 50 % of torque is consistently fed through the rear axle. The operating principle “4WD Lock” mode distributes the electric motor torque between the front and rear axles in order to optimize the performance capacity of the vehicle in off-road situations. This mode is used only in extreme driving conditions (mud, steep slopes, sand). This mode is indicated on the new instrument panel.

## Traction Battery and Battery Charging System

### *Traction Battery Design*

The traction battery, lithium-ion, air cooled contents two stacks of 24 modules, serial coupled: the first stacks are located in a central position beneath the rear seats and the second one is located above the rear axle. This new architecture (Fig. 10) was chosen to boast the same carrying capacity as the internal combustion-engine version.

The capacity of *DUSTER ZERO 4WD*'s traction battery is 22 kW/h and its weight is approx 260 kg (Teyssot 2012).

In addition to the modules package the battery box includes: the internal cooling system, the electrical circuit computer and connection box, the BMS box, the signal wiring “low voltage” and the general contactor.

An energy recovery system enables the battery to be charged when the car decelerates.

### *Battery Charging System*

The *DUSTER ZERO 4WD* is charged via a socket located in the front side of the vehicle (Fig. 11). The actual variant (without additional heating) has a secondary socket located in the lateral rear side, behind the flap of the fuel tank (Fig. 11).

It will be possible to charge the battery of *DUSTER ZERO 4WD* in one of the following two ways:

- **A household mains supply** using a 10A @ 220 V, power 2.2 kW or 16A @ 220 V, power 3.5 kW which will fully charge the battery in between 6 and 8 h.

**Fig. 10** The traction battery of the *DUSTER ZERO 4WD* (CATIA modelling)  
DUSTER ZERO 4WD

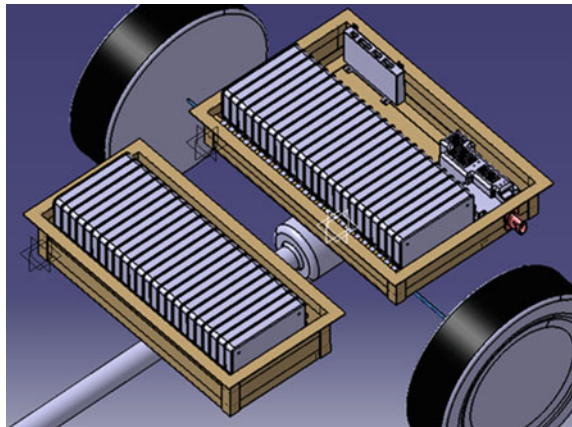




**Fig. 11** Front socket and supplementary rear socket of the *DUSTER ZERO 4WD*

This method is particularly suitable for vehicles which are charged during the workday or at night, since it allows owners to benefit from the off-peak rates available in certain countries. This standard charging is made with home WALL BOX type;

- **At fast charge** stations using a 32A @ 400 V, power supply which enables the battery to be charged in approximately 30–60 min. This semi-fast charging is made with public and quick charger.

## Vehicle Conversions

### *DUSTER ZERO 4WD's Suspension*

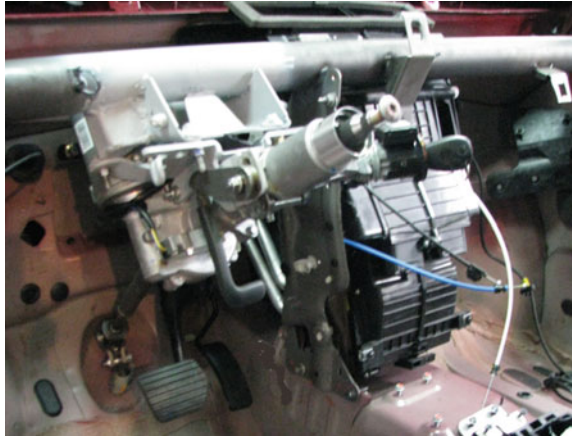
In order to adapt the *DUSTER ZERO 4WD* to the new weight distribution, the suspension has been revised. The front axle is an independent pseudo Mac Pherson type, with helicoidal springs, hydraulic telescopic shock absorbers and anti-roll bar. The front suspension setting is softer, since electric motors are lighter than all the internal combustion engines available for *DUSTER 4WD*.

The rear axle is an independent pseudo Mac Pherson type with lower pulled arm with helicoidal spring's, hydraulic telescopic shock absorbers and anti-roll bar. Meanwhile, the rear suspension has been revised to cope with the heavier weight, due to the presence of the supplementary mass of the traction battery.

### *DUSTER ZERO 4WD's Steering*

An important change to the vehicle was the adapting of an electric power steering system, variable rate, column-assist type (Fig. 12). This system, a brushed DC motor was integrated in the steering column; the motor was located in the passenger compartment.

**Fig. 12** The electric power steering system column-assist type of the *DUSTER ZERO 4WD*



Compared with the traditional hydraulic steering systems, with GEP (Group Electric Pump) mounted on the Dacia cars and *DUSTER Hybrid E4WD*, the Electric Power Steering system offers assistance to the driver directly and it has the advantages of energy economy, handiness, easy adjustment, less noise and waste and the working principle of ESP system.

### ***DUSTER ZERO 4WD's Braking***

The braking system is similar to the diesel version and includes: ventilated discs on the front axle with 280 mm disc diameter, drum in the rear axle 9 in. diameter, ABS (Anti-lock Braking System) Bosch 8.1, EBD—Electronic Brake force Distribution, EBA (Emergency Brake Assist) and ESC (Electronic Stability Control).

For the assist system a new vacuum pump HELLA, electric type was installed in the engine compartment behind the 12 V auxiliary battery.

### ***DUSTER ZERO 4WD's Interior***

The range management is a key factor when it comes to electric vehicles, and has taken significant steps to make this aspect as straight forward and efficient as possible.

A specific dashboard display (Fig. 9) has been adapted to ensure that the driver is kept informed about the remaining battery charge and the operational range:

- A gauge alongside the speedometer indicates how much battery charge remains;
- An “Econo”-meter provides the driver with an indication of energy consumption based on a system that employs three colors: light blue depicts normal use, dark

blue reveals optimal energy use, while red informs the driver when he is using excessive energy in a way that will have a negative effect on the vehicle's operational range;

- The speedometer needle moves across a turquoise arch;
- The trip computer's functions are adapted to the needs of electric vehicles. It displays the remaining range and the remaining battery energy (kWh), as well as real-time and average energy consumption.

An *Eco Mode* function is available on *DUSTER ZERO 4WD*. Activating this function limits the operation of the air conditioning and the heating system and it results in increasing the range by up to 10 %.

### ***DUSTER ZERO 4WD's Climatization***

Similar to the Renault electric vehicles *DUSTER ZERO 4WD* is equipped with a HVAC system with an electric compressor AC DENSO and an electric heating device.

The system with a specific architecture serves to cooling/heating the interior of the car and cooling/heating the traction battery. The liquid circuit is equipped with one radiator for the interior climatization and one radiator for the external battery climatization and the two pumps.

When the car is plugged in, the driver can program pre-conditioning system, pre-heating or pre-cooling of the cabin.

In order to increase the cooling and heating efficiency, and cuts down on heat entering or leaving, thus also reducing the air-conditioning's power consumption the following measures were taken:

- The thermal insulation of the roof with aluminum foil and a hollow layer, similar to Nissan leaf<sup>2</sup>;
- The thermal insulation of the windows with anti UV foil, turquoise color;
- The rear window was replaced with a Rear Hatch Glass to lower the access surface of luggage compartment.

### **Vehicle Performances**

For the *DUSTER ZERO 4WD* we are expecting the following performances:

Range (NEDC cycle): 160 km

Top speed: 130 km.

---

<sup>2</sup>[www.nissan-global.com](http://www.nissan-global.com).



## Conclusions

*DUSTER ZERO 4WD* (ZERO—Zero Emission Romanian concept), the full electric Dacia 4WD vehicle was built on the mechanical platform *DACIA DUSTER 4WD*, by implementing a new electric drive with *Renault ZE* components, already launched on the market for commercialized vehicles.

The electric version of Dacia *DUSTER 4WD* features the same practical functions as the internal combustion-engine version, i.e.: the same carrying capacity and the same high standard of comfort. On top of that, it delivers a silent ride, responsive performance, immediate availability of torque as soon as it starts, automatic transmission, and low running costs and, of course, the satisfaction of owning a zero-emissions vehicle in the areas of use.

*DUSTER ZERO 4WD* concept includes several innovative solutions: 4WD Electric Drive with two speeds; a specific dashboard display with specific EVs board computer; an electric power steering system, variable rate, column-assist type, a new HVAC system adapted for the passenger compartment and traction battery.

The project will be finalized in the beginning of the 2016.

**Acknowledgments** This project has been realized in the *Automotive Engineering* Research Centre, *Alternative Propulsion System and Renewable Energies* laboratory, University of Pitesti. We have benefited from the technical support offered by *RENAULT TECHNOLOGIE ROUMANIE, LEAR ROMANIA*, to whom we express our gratitude.

## References

- Marinescu DG, Tabacu I, Serban F, Nicolae V, Tabacu S, Vieru I (2012) Plug-in hybrid vehicle with a lithium iron phosphate battery traction type. In: SAE China and FISITA (eds) Proceeding of the FISITA 2012 world automotive congress, lecture notes in electrical engineering, Vol 191 LNEE, Issue Vol. 3, Springer-Verlag, Berlin, Heidelberg, pages 449–461, ISBN: 978-3-642-33777-2\_36
- Marinescu DG, Popescu LC, Tabacu I, Nicolae V, Serban FI, Vieru I, Tabacu St, Iorga A (2015) A full electric vehicle 4WD. EVS28, the 28th international electric vehicle symposium and exhibition, KINTEX, Korea, May 3–6, 2015
- Teyssot A (2012) Battery key parameters and their impact on EV application. SHC Day, Gothenburg, May, 7th, 2012
- Vignaud A, Fennel H (2012) Efficient electric powertrain with externally excited synchronous machine without rare earth magnets using the example of the Renault system solution. Vienna Motor Symposium, April, 27th, 2012

# The Thermal Characterisation of a Disc Brake Rotor at Reduced Scale with Particular Reference to Pad Aspect Ratio

Varun S. Prabhu, Abdulwahab A. Alnaqi and Peter C. Brooks

**Abstract** An integral part of the development of a disc brake system is associated with the physical test of the foundation brake using a brake dynamometer. Testing undertaken at full scale is both costly and time consuming and recent work, for example Prabhu et al. (2015), has shown that reduced scale testing is capable of replicating the tribological conditions at the interface such that the thermal response of the rotor approaches that of its full scale counterpart. The same work also demonstrated experimentally the connection between pad aspect ratio and rotor response and this had been omitted from the formal scaling methodology. This paper extends the scaling theory to reflect the presence of pad aspect ratio through the use of a validated finite element model of the reduced scale brake. The results show that for the given reduced scale brake, there exists a pad aspect ratio at which the thermal response of the rotor is at a minimum. The conclusions drawn apply equally to the behaviour of the rotor at full scale.

**Keywords** Disc brake · Scale testing · Dynamometer · Finite element model · Pad aspect ratio

## Introduction

A foundation brake plays a key role within the brake system of a passenger car since it is the means through which energy, linked to the forward motion of the vehicle, is reliably and consistently converted into heat. This is subsequently dissipated through the rotor and pad combination at the friction interface.

---

V.S. Prabhu · P.C. Brooks (✉)  
University of Leeds, Leeds, UK  
e-mail: p.c.brooks@leeds.ac.uk

A.A. Alnaqi  
Department of Automotive and Marine Engineering Technology, College of Technological Studies, PAAET, Adiliya, Kuwait

The associated brake torque appears between the tyre and ground as the brake force that causes the vehicle to either slow or maintain its forward speed (Limpert 1999). The foundation brake development process is lengthy and consideration of the whole system is required to ensure that all demands are met. In addition, manufacturers of vehicles face continual pressure from both the customer and legislation to reduce cost and weight whilst safeguarding functionality and safety.

Part of the development process necessitates the physical evaluation of the brake using a dynamometer. A dynamometer is a versatile test platform that can take several forms which provide the means to characterise the behaviour of a brake under carefully controlled conditions. An inertial dynamometer can be used to undertake the evaluation of a full size foundation brake and such tests are costly and time consuming. At the other end of the scale, a pin on disc tribometer can be used to investigate the performance of the friction pair. This will typically use a single pad of friction material pushed against one side of a rotating disc although some studies have used setups involving two pads that are diametrically opposed. Other approaches that fall between these extremes have involved the use of FAST machines to screen for friction stability in combination along with CHASE dynamometers to monitor the friction material and several scaling procedures (Kermc et al. 2005; Tsang et al. 1985; Alnaqi et al. 2014a, 2014b; Desplanques et al. 2007; Newcomb 1959; Sanders et al. 2001).

One of these alternative approaches is presented in Alnaqi et al. (2014a) and employs a formal scaling methodology to accelerate the development process. The methodology relies upon a scaling factor that is defined as the ratio of pad area between the full and reduced scale systems. It results in a small scale dynamometer that not only preserves the full scale sliding velocity, pad pressure and energy density but also employs a realistic brake caliper, in which the pads of friction material are applied to each side of the rotor. Alnaqi et al. (2014a), also describes an experimental setup that shows a practical application of the methodology.

Prabhu et al. (2015), uses the scaling and experimental approach of Alnaqi et al. (2014a), to explore the impact of pad aspect ratio on the thermal response of the brake rotor. The principal driver for this came from the earlier work of Desplanques et al. (2007) who suggest that the ratio of the area of the frictional rubbing surface on the disc to that of the pad be preserved between the full and reduced scale brakes. This is the so-called similitude rule. Prabhu et al. (2015), demonstrated a strong dependency of the scaled rotor temperature on pad aspect ratio and was also able to show how this factor impacts on the brake design at full scale.

This paper first reviews the scaling process of Alnaqi and extends the theory to formally take into consideration the concept of similitude or pad aspect ratio. It then makes use of the mathematical model, developed and validated in Prabhu et al. (2015), to explore in detail the thermal response of the scaled rotor as a function of change in pad aspect ratio.

## The Scaling Process

A factor,  $S$ , is the basic quantity that is used to drive the brake scaling process and its use permits the specification of a small scale brake directly from its full scale counterpart. The method ensures that the tribological and thermal conditions at the friction interface remain fixed across the scales. Since the level of interface friction is the key characteristic of the friction pair to maintain at each scale, it is necessary to force equivalence of both sliding speed and pressure. This in turn ensures that the interface temperatures are comparable. Alnaqi et al. (2014a), proposes that the scaling factor,  $S$ , is defined as the ratio the full scale pad area,  $A_F$ , to that of the reduced scale pad,  $A_S$ . The subscripts  $F$  and  $S$  refer to the full scale and reduced scale setups. Consequently, consideration of the energy balance equation along with the assumption that the change in temperature experienced by the full and reduced scale brake is the same indicates that the rotor mass,  $M$ , also scales linearly with the scaling factor  $S$ :

$$\frac{A_F}{A_S} = \frac{M_F}{M_S} = S \quad (1)$$

The mean rubbing radius of the brake,  $r_m$ , is a parameter that must also be subject to scaling and this scales with  $S^{0.5}$ :

$$\frac{r_{mF}}{r_{mS}} = S^{0.5} \quad (2)$$

Brake torque is a function of the mean rubbing radius, the contact pressure, pad area and the coefficient of friction and since this is assumed constant across the scales, the necessary brake torque relationship has the form:

$$\frac{T_F}{T_S} = S^{1.5} \quad (3)$$

The angular velocity of the dynamometer,  $\omega$ , is subject to scaling and is a function of the sliding velocity and the mean rubbing radius and is shown by Alnaqi to be:

$$\frac{\omega_F}{\omega_S} = S^{-0.5} \quad (4)$$

The geometry of the rubbing surface of a pad varies from one design to another and this feature of the real brake is not considered in Alnaqi et al. (2014a). For the purpose of this work it is necessary to consider the pad area to be rectangular, of width  $W$  and length  $L$ . A rectangular area was also used in Prabhu et al. (2015) as this simple shape facilitated the straightforward manufacture of the scaled pads of

friction material used in the experimental work. Consequently, at each scale the area of each pad is:

$$A_F = L_F W_F \quad A_S = L_S W_S \quad (5)$$

and the corresponding aspect ratios,  $AR$ , are given by:

$$AR_F = \frac{W_F}{L_F} \quad AR_S = \frac{W_S}{L_S} \quad (6)$$

Equation (1) implies that length scales with  $S^{0.5}$  and so the geometry of the reduced scale pad can be written in terms of the full scale equivalent:

$$L_S = L_F S^{-0.5} \quad W_S = W_F S^{-0.5} \quad (7)$$

Combination of Eqs. (6) and (7) show that the pad aspect ratio is independent of scale:

$$AR_S = \frac{W_S}{L_S} = \frac{W_F S^{-0.5}}{L_F S^{-0.5}} = \frac{W_F}{L_F} = AR_F = AR \quad (8)$$

and implies that the aspect ratio at full scale be mirrored at the reduced scale.

## The Methodology

The experimental findings contained in Prabhu et al. (2015) form the basis of the extended numerical simulation that is presented in this paper. The experiments were conducted using a scaled version of a medium sized passenger car disc brake with a scaling factor of 5.47. Four sets of Wilwood brake pads, termed Pad A, B, C and D were used against the scaled brake rotor. Each pair of pads had a different aspect ratio but retained the same area. Table 1 shows the essential pad geometry that was used in the original experimental work and the subsequent numerical simulations undertaken as part of this study.

Figure 1 illustrates the pad geometry that is tabulated in Table 1. Details of the chosen pads can be found in the Wilwood catalogue<sup>1</sup>. A sequence of drag brake events were replicated using the dynamometer. This led to each aspect ratio undergoing 9 tests, Table 2. Tests were stopped once the rotor temperature reached 300 °C for reasons of health and safety.

The finite element model used to predict the maximum disc rotor temperature is the same as that found in Prabhu et al. (2015) and is depicted in Fig. 2. It is comprised of 4 noded heat transfer elements, set in a regular rectangular mesh of

<sup>1</sup>Wilwood Brake Pads, <http://www.wilwood.com/Calipers/CaliperList.aspx?subname=PS1>.

**Table 1** Essential pad geometry

Pad designation	Mean rubbing radius ( $r_m$ ) (mm)	Pad length (L) (mm)	Pad width (W) (mm)	Aspect ratio (W/L)	Equivalent arc angle ( $^\circ$ )	Pad area (A) (mm <sup>2</sup> )	Scale factor (S) (-)
Full scale	117	74	39	0.53	36.9	2886	-
<i>Experimental</i>							
Pad A	50	24	22	0.91	27.8	528	5.47
Pad B	50	26.5	20	0.75	30.7	530	5.45
Pad C	50	29.5	18	0.61	34.3	531	5.44
Pad D	50	44	12	0.27	52.2	528	5.47
<i>Numerical</i>							
1	50	24	22.0	0.92	27.8	528	5.47
2	50	24.56	21.5	0.88	28.4	528	5.47
3	50	25.14	21.0	0.84	29.1	528	5.47
4	50	25.76	20.5	0.8	29.9	528	5.47
5	50	26.4	20.0	0.76	30.6	528	5.47
6	50	27.08	19.5	0.72	31.4	528	5.47
7	50	27.79	19.0	0.68	32.3	528	5.47
8	50	28.54	18.5	0.65	33.2	528	5.47
9	50	29.33	18.0	0.61	34.1	528	5.47
10	50	30.17	17.5	0.58	35.1	528	5.47
11	50	31.06	17.0	0.55	36.2	528	5.47
12	50	32.0	16.5	0.52	37.3	528	5.47
13	50	33.0	16.0	0.48	38.5	528	5.47
14	50	34.06	15.5	0.46	39.8	528	5.47
15	50	35.2	15.0	0.43	41.2	528	5.47
16	50	36.41	14.5	0.4	42.7	528	5.47
17	50	37.71	14.0	0.37	44.3	528	5.47
18	50	39.11	13.5	0.35	46.0	528	5.47
19	50	40.62	13.0	0.32	47.9	528	5.47
20	50	42.24	12.5	0.3	50.0	528	5.47
21	50	44.0	12.0	0.27	52.2	528	5.47

0.25 mm thickness. The model can represent change in the pad aspect ratio through combination of the direct change in the parameter  $W$ , that reflects the width of the pad and the duration of the pulse of heat that is applied to the model once per revolution. This reflects the so-called ‘rotating heat source’ effect and is captured through the angular velocity of the dynamometer and the equivalent arc angle of the pad, Table 1, that is derived from the length of the pad,  $L$ , and the mean rubbing radius,  $r_m$ . The transient thermal analysis therefore comprises a series of alternate heating and cooling steps. The heat partition ratio between the rotor and pad was

**Fig. 1** Pad geometry

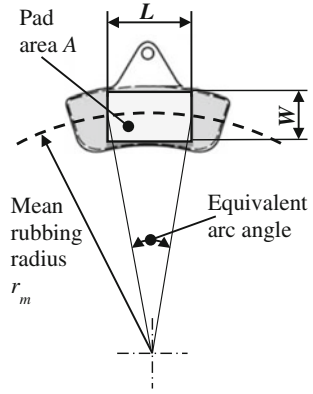
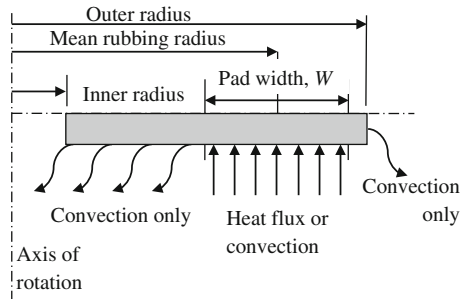


**Table 2** Speed—pressure matrix for experimental programme (Prabhu et al. 2015) (modified)

Speed			Pressure		
Level	kmph	rpm	Low (1.5 bar)	Medium (2.5 bar)	High (4.5 bar)
Low	5.2	185	Low energy Fig 3(a)		
Medium	15.5	545			
High	25.8	925			High energy Fig 3(b)

**Fig. 2** Outline of finite element model (Prabhu et al. 2015) (modified)



determined to be 0.9. Radiative heat transfer was assumed negligible whilst a convective heat transfer coefficient of  $30 \text{ W/m}^2\text{K}$  was used. The grey cast iron rotor was assigned a specific heat of  $460 \text{ J/kgK}$  and a thermal conductivity of  $51 \text{ W/mK}$ . It was validated by Prabhu et al. (2015), against the experimentally derived results linked to Pad C and an interface coefficient of friction of 0.5.

## Results and Discussion

The experimental work of Prabhu et al. (2015) demonstrated that pad aspect ratio has an impact on the thermal response of the rotor, which is evident from the temperature time histories contained in Fig. 3. Figure 3a illustrates data from the low energy test whilst Fig. 3b presents data from the high energy test. The time taken to reach the target temperature of 300 °C varies considerably and Pad C runs the coolest. The rate of increase in disc surface temperature varies with pad aspect ratio with Pad C the least aggressive (Fig. 3a) whilst pads A and D are the most aggressive.

Prabhu et al. (2015), also defined additional measures with which to interrogate the experimental data. A length ratio:

$$\text{Length Ratio} = \frac{\text{Length of full scale brake pad } (L_F)}{\text{Length of scaled pad } (L_S)} \tag{9}$$

a width ratio:

$$\text{Width Ratio} = \frac{\text{Width of full scale brake pad } (W_F)}{\text{Width of scaled pad } (W_S)} \tag{10}$$

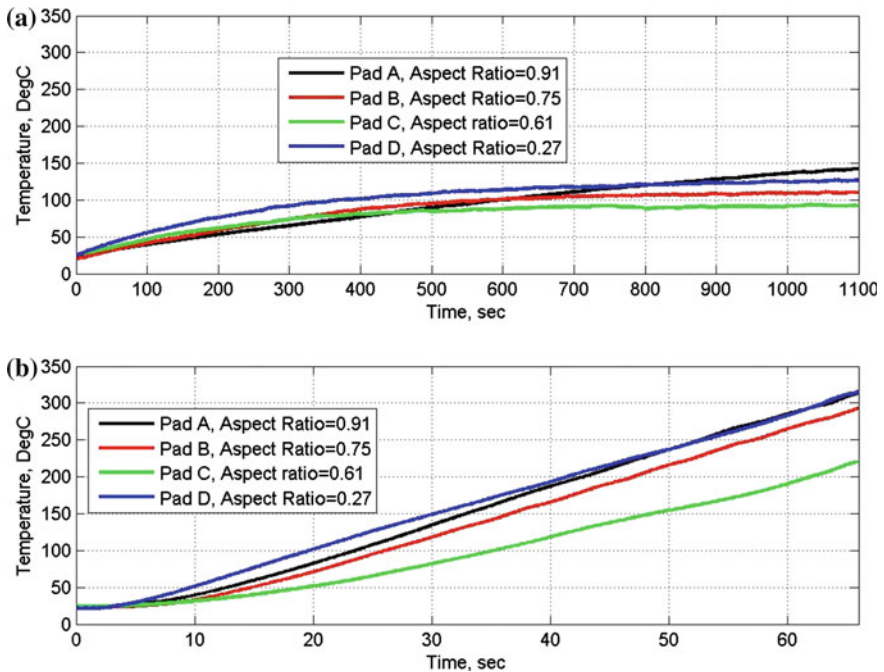


**Fig. 3** Selected temperature time histories from experimental programme, **a** low energy (1.5 b, 185 rpm) rotor time histories, **b** high energy (4.5 b, 925 rpm) rotor time histories



**Table 3** Comparison between full and reduced scale pads

Pad designation	Pad length (L) (mm)	Pad width (W) (mm)	Aspect ratio (W/L)	Length ratio ( $L_F/L_S$ )	Width ratio ( $W_F/W_S$ )	$\Delta$	$T_s$ ( $^{\circ}\text{C}$ )
Full scale	74	39	0.52	–	–	–	–
Pad A	24	22	0.92	3.08	1.77	1.31	298
Pad B	26.5	20	0.75	2.79	1.95	0.84	278
Pad C	29.5	18	0.61	2.50	2.16	0.34	205
Pad D	44	12	0.27	1.68	3.25	1.57	300

and a parameter  $\Delta$ , found from the absolute difference between (9) and (10):

$$\Delta = \left| \frac{L_F}{L_S} - \frac{W_F}{W_S} \right| \quad (11)$$

in which  $\Delta$  tends towards 0 as the scaled geometry approaches that of the full scale brake. The results in Table 3, show a connection between the response of a scaled pad and that of the full scale equivalent. The response is least favourable with Pads A and D (the rotor surface temperature,  $T_s$  is at a maximum and  $\Delta > 0$ ) whereas Pad C yields the most favourable response ( $T_s$  is at a minimum and  $\Delta$  is tending towards 0).

The experimental results, from pads A to D show that the maximum surface temperature of the rotor,  $T_s$ , varies with aspect ratio and that  $T_s$  will be minimised for a particular value of aspect ratio. The finite element model of the rotor was therefore used at the reduced scale to predict estimates of  $T_s$  as a function of aspect ratio between the limits of 0.27 and 0.92. Intermediate values of aspect ratio were determined through incremental increase in the width of the pad,  $W$ , whilst preserving the desired area, Table 2.

To permit comparison, each model was run for a period of 60 s and the maximum temperature,  $T_{s,60}$ , noted at the end of each simulation. The quantity  $\text{Del } T_{s,60}$ , defined as the absolute difference between the simulated rotor temperature and the target temperature of 300  $^{\circ}\text{C}$ ,

$$\text{Del } T_{s,60} = |(T_{s,60} - 300)| \quad (12)$$

permits identification of the aspect ratio of interest and is plotted against pad aspect ratio in Fig. 4 along with  $T_{s,60}$ .

The results follow the pattern alluded to by the experimental data and show that the rotor temperature is minimised at an aspect ratio that lies somewhere between 0.48 and 0.52. The aspect ratio of the full scale pad is 0.53, Table 1, which suggests that some attempt to minimise the thermal response of the full scale rotor may have been undertaken during the development process.

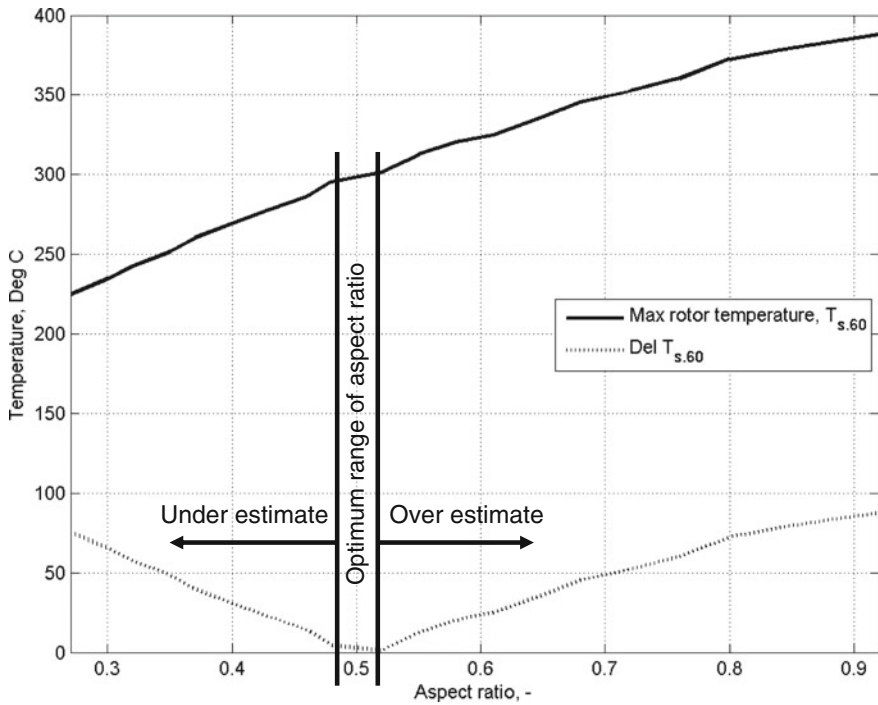


Fig. 4 Simulated scaled rotor response as a function of aspect ratio

The data linked to  $Del T_{s,60}$  provides a ready indication of the importance that attaches to the use of the correct pad aspect ratio when replicating the full scale brake at a reduced scale. If an aspect ratio is used that is less than the full scale, then the thermal response will be underestimated whilst if the aspect ratio is greater than the full scale value, the response will be overestimated.

The response of the full scale brake was assessed using the finite element model and the resulting 60 s time history compared with that of the equivalent reduced scale model with aspect ratio 0.52. The maximum temperature at full scale was 307 °C whilst that at reduced scale was 301 °C, a difference of 2 %, which demonstrates good agreement and gives confidence to the scaling methodology.

## Conclusions

A simple extension to the scaling methodology presented by Alnaqi et al. (2014a), that has defined the area of the pad in terms of a simple rectangle, was used to show that pad aspect ratio can be treated as a quantity that is independent of scale. The set of experimental results performed in Prabhu et al. (2015) for a series of drag brake

events were reviewed and employed to underpin a numerical study into the influence of pad aspect ratio on the thermal response of the reduced scale rotor. The simulated scaled rotor response was shown to be sensitive to change in pad aspect ratio, predicting a change in rotor temperature of approximately  $\pm 29\%$  around the  $300\text{ }^{\circ}\text{C}$  target temperature. The results also confirmed the hypothesis that there exists an aspect ratio that tends to minimise the rotor temperature. This aspect ratio was predicted to lie within the range  $0.48 < \text{AR} < 0.52$ . As aspect ratio was shown to be independent of scale, this trend will apply equally to the full scale brake and the full scale brake pad has an aspect ratio of 0.53 which lies close to range. The thermal response of the associated full scale brake rotor was used to demonstrate the near equivalence of the simulated thermal response across the scales.

Further experimental investigation is required to strengthen the findings of this work and should, as a minimum include a study based around a constant g stop. The experimental work at small scale should also use the same pad material that is used in the full scale brake.

## References

- Alnaqi AA, Barton DC, Brooks PC (2014a) Reduced scale thermal characterization of automotive disc brake. *Appl Therm Eng* 75: 658–668
- Alnaqi AA, Shrestha S, Brooks PC, Barton DC (2014b) Thermal performance of PEO coated lightweight brake rotors compared with grey cast iron. *Eurobrake 2014*, France
- Desplanques Y, Roussette O, Degallaix G, Copin R, Berthier Y (2007) Analysis of tribological behaviour of pad-disc contact in railway braking—Part 1. Laboratory test development, compromises between actual and simulated tribological triplets. *Wear* 262:582–591
- Kermc M, Kalin M, Vizintin J, Stadler Z (2005) A reduced-scale testing machine for tribological evaluation of brake materials. *Life Cycle Tribol* 48: 799–806
- Limpert R (1999) Brake design and safety. Society of Automotive Engineers, Troy
- Newcomb TP (1959) Transient temperatures attained in disk brakes. *Br J Appl Phys* 10:339–340
- Prabhu VS, Alnaqi AA, Brooks PC (2015) The thermal characterisation of a disc brake rotor at reduced scale with particular reference to pad aspect ratio. *EuroBrake 2015*, Germany
- Sanders PG, Dalka TM, Basch RH (2001) A reduced-scale brake dynamometer for friction characterization. *Tribol Int* 34:609–615
- Tsang PHS, Jacko MG, Rhee SK (1985) Comparison of chase and inertial brake dynamometer testing of automotive materials. *Wear* 103:217–232

# Experimental Identification of the Automotive Magnetorheological Shock Absorbers

Nicolae Vasiliu, Anton Hadăr, Alexandru Dobre, Constantin Călinoiu  
and Cristian Andreescu

**Abstract** The effectiveness of the shock absorbers in terms of comfort and automotive manoeuvrability is closely linked to the free and forced vibrations generated by the road irregularities and the driver's orders (acceleration, braking etc.). The passengers mass, the sprung mass parties (car body), the free parties mass (wheels and a part of the suspension), the stiffness and the damping coefficient of the various elements of the car are involved in this process. In the road vehicles' suspensions field, the dampers control through the valves is an extremely difficult target due to the unpredictable flow's variation and the pressure difference generated inside them. This was the main reason for developing and using magneto rheological fluids as dampers fluids. The authors have designed and built a complex test bench in order to compare the behaviour of a classical dampers and a magneto rheological one. A high speed National Instruments data acquisition system was used to obtain information about the correlation between the damping force, stroke, and speed, control current, temperature etc. The results were compared with the similar ones supplied by some top level manufacturers.

**Keywords** Magneto rheological shock absorbers (MR) · Experimental identification · Numerical simulations · AMESIM

## Introduction

The damper is an important component of any suspension system, because it determines the damping level of the vibrations of the car body generated by the irregularities of the road. A magneto rheological (MR) damper has the ability to change the viscosity of the fluid, when it is subjected to the action of a magnetic

---

N. Vasiliu (✉) · A. Hadăr · A. Dobre · C. Călinoiu · C. Andreescu  
University Politehnica of Bucharest, Splaiul Independenței, no. 313, Sector 6,  
Bucharest, Romania  
e-mail: vasiliu1946@gmail.com

field. The development of this relatively new technology wasn't easy. The first commercial use of the magneto rheological fluid in a semi-active suspension system was implemented on passenger cars at the beginning of the 2000s: MagneRide™ developed by Delphi Automotive Systems and Corp/BWI Group. The first passenger car, equipped with such a shock absorber was Cadillac Seville STS in 2002, followed by Audi A8 in 2006.

There are a lot of papers concerning the MR dampers. Different kinds of models have been developed: quasi-static and dynamic, parametric and non-parametric, phenomenological and heuristic ones, based on a set of well suited functions (Kasprzyk et al. 2014). An extensive overview on different types of models of the MR damper as well as some identification and validation methods can be found in Wang and Liao (2011). In a simple MR damper, the variation of the electric current in a coil placed in the piston changes the physical properties of the fluid. MR dampers are widely used in vibration control systems: from automobiles to civil structures such as buildings or bridges (Sapinski 2006).

## Test Bench Description

The test bench is composed of a high stiffness frame, which at the top level is provided with a flexible bushes for connecting the force transducer with the damper, and on the bottom with another flexible bushes for coupling with the hydraulic servo cylinder (Fig. 1).

**Fig. 1** The frame of the test bench for shock absorbers



The driving system was designed by the authors and manufactured by AEROTEH SA from ROMANIA. It can use any type of high speed servo valves (aerospace, industrial, proportional type etc.). A high speed piezo ceramic force transducer (MTS) is used to measure the damping force developed by the shock absorber. The velocity of the stroke piston is measured by an inductive contactless transducer (SCHEWITZ). The test bench control is performed by NI LabVIEW software set up on a NI PXI high speed controller. The driving system can supply 21kN for a maximum speed of 1 m/s, working at 21 MPa.

### Preliminary Experimental Results

The first step in defining the behaviour of a *classical* damper is the use of a sine input signal with a small frequency, for example  $f = 0.5$  Hz (Fig. 2). Some of the experimental results are presented in the Figs. 2, 3 and 4. The damping force follows and velocity with some distortion generated. The maximum force reaches around 550 N for a velocity of 60 mm/s.

The main features which define the behavior of a hydraulic shock absorber are  $F(x)$  and  $F(v)$ , shown in Figs. 3 and 4 for different frequencies.

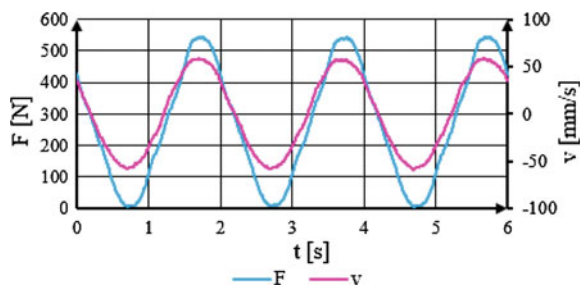
A high frequency signal leads to the increasing of the hysteresis loop of the damping characteristic of the shock absorber.

For the behaviour of the magneto rheological damper study was used a sine signal having the frequency  $f = 0.5$  Hz. A part from the experimental results are presented in the Figs. 5, 6 and 7. In Fig. 5 it can be observed how varies the damping force in time for different values of the electric current.

The main features which define the behaviour of a MR shock absorber are presented in Figs. 8 and 9, for a sine input signal of 0.5 Hz. Naturally, this kind of damper generates an increased force compared to the classical one considered as reference.

Most of modern researches concerning the complex behaviour of the MR dampers (Savaresi et al. 2010; Gołdasz et al. 2015; Choi et al. 2015; Laura et al. 2000) show similar results. The maximum damping force depends in a parabolic manner on the electric current. The control damping force is always increasing with

**Fig. 2** The damping force and velocity depending on the time, for a classical damper



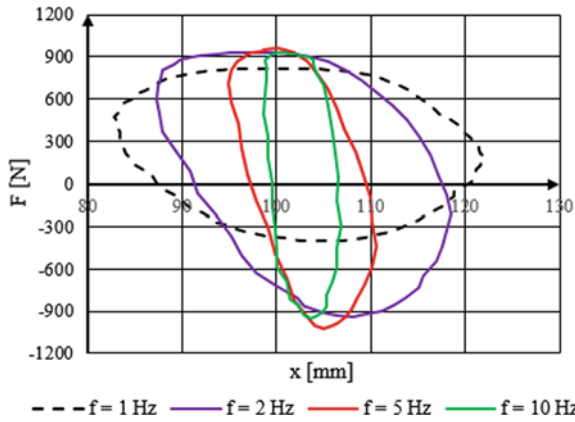


Fig. 3 The damping force and displacement depending on the time, for a classical damper

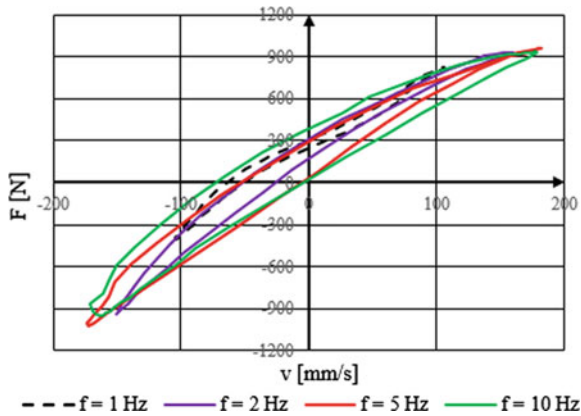


Fig. 4 The damping force depending on the velocity, for a classical damper

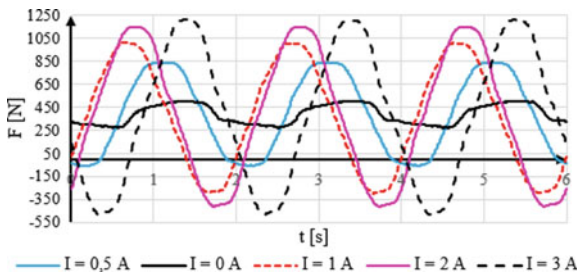
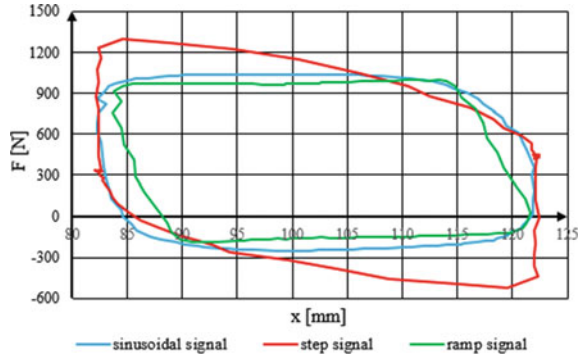
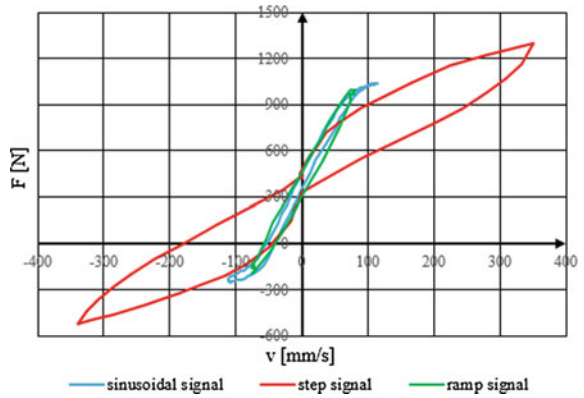


Fig. 5 The damping force depending on the time, for a MR damper for different values of the electric current

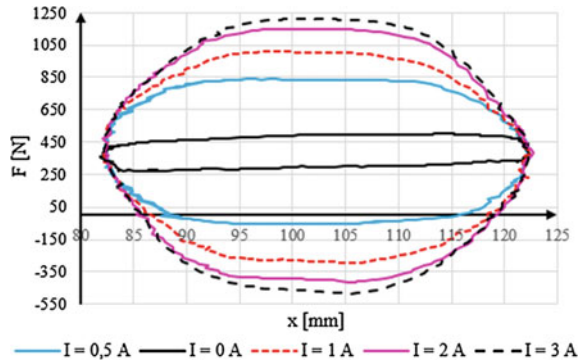
**Fig. 6** The variation of damping force according to the displacement for different types of signals,  $f = 1$  Hz,  $I = 0.5$  A



**Fig. 7** The variation of damping force versus velocity for different types of signals ( $f = 1$  Hz, and  $I = 0.5$  A)



**Fig. 8** The damping force versus the displacement generated by a MR damper supplied by different currents



the current value, but the fluid magnetic saturation limits the force. For a coil impedance of about  $1 \Omega$ , the saturation occurs when the current reaches about 3 A (Fig. 10).



**Fig. 9** The damping force versus velocity, for a MR damper supplied by different current

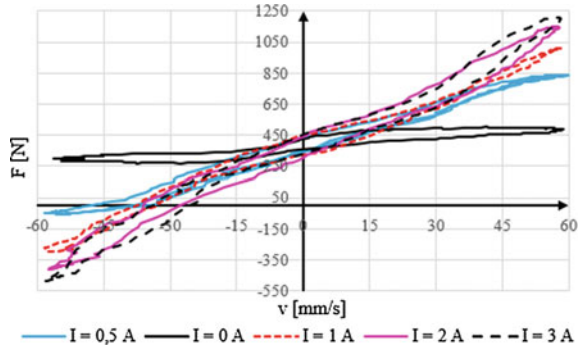
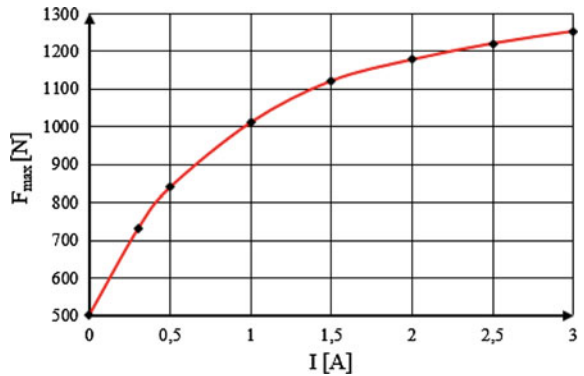


**Fig. 10** The maximum damping force depending on the electric current



## Conclusions

The behaviour of the MR dampers can improve the passengers comfort and the holding road in a significant measure. The damping force can be increased using a MR damper in the same mechanical conditions as the classical one. Usually, the control of a MR damper is done by changing the average electric current value by the aid of a PWM controller. This control manner avoids the shocks introduced by the sudden changes of the current. The average value of the current during a sine or ramp control signal seems to be the best control strategy.

A lot of problems have to be solved in the implementation of the MR technology in a series of cars. A strong improvement of the passengers comfort needs a very sophisticated fuzzy controller.

Increasing the intensity of the electric current applied to the magneto rheological shock absorber leads to the damping force increasing, improving the comfort. For example, for a sinusoidal input signal with a frequency of 0.5 Hz and a current of 3 A, the damping force increased by 2.4 times compared with the case “unpowered”.

**Acknowledgements** The work has been funded by the Sectoral Operational Program Human Resources Development 2007–2013 of the Ministry of European Funds through the Financial Agreement POSDRU/159/1.5/S/134398. The authors are also grateful to AEROTEH SA Romania, ICPEST SRL Romania, and NATIONAL INSTRUMENTS Romanian Branch companies for their technical and technological support.

## References

- Choi SB, Han YM (2015) Magnetorheological fluid technology-applications in vehicle systems. CRC Press, Boca Raton, ISBN:978-1-4398-5673-4
- Gołdasz J, Sapiński B (2015) Insight into Magnetorheological Shock Absorbers. Springer, Berlin, ISBN:978-3-319-13232-7
- Jansen LM, Dyke SJ (2000) Semi-active control strategies for mr dampers: a comparative study. ASCE J Eng Mech 126(8):795–803
- Kasprzyk J, Wyrwał J, Krauze P (2014) Automotive MR damper modelling for semi-active vibration control. In: 2014 IEEE/ASME international conference on advanced intelligent mechatronics (AIM), Besançon, France, July 8–11, 2014
- Sapinski B (2006) Magnetorheological dampers in vibration control. AGH University of Science and Technology Press, Cracow, Poland
- Savaresi SM, Poussot-Vassal C, Spelta C, Sename O, Dugard L (2010) Suspension control design for vehicles. Elsevier, Amsterdam, ISBN:978-0-08-096678-6
- Wang DH, Liao WH (2011) Magneto rheological fluid dampers: a review of parametric modelling. Smart Mater Struct 20(2):023001

# Application of Fuzzy Topsis and Ahp Method in Evaluating Vehicle Roadworthiness Performance

Jakimovska Kristina, Duboka Čedomir and Karastoyanov Dimitar

**Abstract** Roadworthiness itself can be achieved in a combination of two ways, by ‘Keep Vehicles Roadworthy’ and by ‘Produce Roadworthy Vehicles’. One can not keep a vehicle roadworthy, if it is not produced to be and to remain roadworthy. The other way around is that one doesn’t need to produce a roadworthy vehicle, if no one keeps it roadworthy. First, this study proposes fuzzy AHP (Analytic Hierarchy Process) method to gain real values for the vehicle roadworthiness indicators. Within the proposed methodology, a decision group and vehicle roadworthiness framework containing 14 indicators are firstly established. Optimal MCDM method i.e. fuzzy TOPSIS (The Technique for Order of Preference by Similarity to Ideal Solution) method was chosen for the evaluation of vehicle roadworthiness performance of motor vehicles depending on their condition and that assessment is presented through Vehicle Roadworthiness Performance Index—VRWPI of a motor vehicle in operation. This study also proposes fuzzy TOPSIS method to combine the vehicle roadworthiness indicators into one overall index. The results demonstrate the engineering practicability and effectiveness of AHP and

---

J. Kristina (✉)

Institute of Information and Communication Technologies, Bulgarian Academy of Sciences,  
Acad. G. Bonchev str. bl. 2, 1113 Sofia, Bulgaria  
e-mail: kristina.jakimovska@mf.edu.mk

and

J. Kristina

Faculty of Mechanical Engineering—Skopje, Ss. Cyril and Methodius University,  
Karposh II bb, P.O.Box 464, 1000 Skopje, Macedonia

D. Čedomir

Faculty of Mechanical Engineering, University of Belgrade, Kraljice Marije 16,  
35, Pf. 34 Belgrade, Serbia  
e-mail: cduboka@eunet.rs

K. Dimitar

Institute of Information and Communication Technologies, Bulgarian Academy of Sciences,  
Acad. G. Bonchev str. bl. 2, 1113 Sofia, Bulgaria  
e-mail: dkarast@iinf.bas.bg

TOPSIS method in vehicle roadworthiness evaluation also importance of the weights on the various indicators are being illustrated.

**Keywords** Composite indicator · Fuzzy TOPSIS · Fuzzy AHP · Vehicle roadworthiness performance index—VRWPI

## Introduction

Many studies about the effect of technical defects on road traffic accidents have been conducted. There is a high level of variation in the results. It starts out at almost no influence of technical defects on accidents and ends at 28 % (DEKRA Automobil GmbH—Road safety report 2008; DEKRA Automobil GmbH—Verkehrssicherheitsreport Landstrassen 2013). The problem of the condition of vehicles with regard to their safety is especially evident in the case of accidents when formally and essentially there is a need to determine their cause. Although international experiences show that a large percentage of such events (from 85 to 95 %) are caused by driver error, or because of the human factor, the condition of the vehicle that was involved in the accident is a very important element.

## Vehicle Roadworthiness

Many vehicle owners do not adequately maintain their vehicles so significant numbers of defective vehicles are in use, a matter of concern as poor vehicle condition has an adverse affect on safety and the environment<sup>1</sup>. The level of defects in vehicles in use in Europe remains high and shows no signs of improving with the introduction of new technologies and manufacturing systems. The information collected in<sup>2</sup> was analysed and collated into a common format in order to establish a picture of the current state of knowledge of roadworthiness enforcement generally, how it is performed and organised in all member states of the European Union and with what results. Roadworthiness itself can be achieved in a combination of two ways, by ‘Keep Vehicles Roadworthy’ and by ‘Produce Roadworthy Vehicles’. One can not keep a vehicle roadworthy, if it is not produced to be and to remain roadworthy. The other way around is that one doesn’t need to produce a roadworthy vehicle, if no one keeps it roadworthy. ‘Keep Vehicles Roadworthy’ (may also be called ‘roadworthiness Assurance’) splits up into two parts, which are the forced way ‘Roadworthiness Enforcement’ and the voluntary way ‘Voluntary Inspection’. Roadworthiness can be achieved in different ways (see Footnote 2).

---

<sup>1</sup>AUTOFORE project WP 300: Vehicle technology / Diagnostic technology.

<sup>2</sup>AUTOFORE project WP200: Current situation of roadworthiness enforcement on E.U.

### Vehicle Roadworthiness Indicators

The choice of the vehicle roadworthiness performance indicators was based on the guidelines given in vehicle roadworthiness Directives (Council Directive 96/96/EC of 20 December 1996; Council Directive 2009, 2010) and the studies presented in Duboka (2010, 2011). The final selection of vehicle roadworthiness performance indicators is shown in Table 1. Each of the vehicle roadworthiness performance indicators is further explained. Two sets of indicators to evaluate the vehicle roadworthiness are proposed in this study and for each of the indicators are assigned unique items I to XV (indicators from V to XIII are pooled in one indicator XV).

Each of these vehicle roadworthiness indicators take part in smaller or bigger percentage in vehicle safety assessment according to their condition i.e. grade/valuation in vehicle roadworthiness (Jakimovska 2014).

*The age of the vehicle*, expressed in years is always influential parameter of vehicle safety, and thus the vehicle roadworthiness. This indicator is inversely proportional with increasing age of the vehicle reduces vehicle roadworthiness performance.

*Mileage* (expressed in number of traveled kilometers) indicator that is considered here is included only by amount, and not regarding the conditions of exploitation. It should be noted that this indicator certainly have important influence on vehicle roadworthiness.

*The history of maintenance* is an influential factor, since this indicator monitors the condition of the vehicle throughout its lifespan. Whether performed preventive maintenance, corrective or a combination of both, of great importance is that the maintenance is performed in an authorized service of the manufacturer, where there is certainty that the maintenance is done according to the manufacturer's

**Table 1** Vehicle roadworthiness indicators

Vehicle roadworthiness indicators	
Variant A	Variant B
I vehicle age (years)	I vehicle age (years)
II vehicle mileage (km)	II vehicle mileage (km)
III maintenance history	III maintenance history
IV accident involvement history	IV accident involvement history
V repair history	XV proper vehicle systems and devices
VI proper braking condition	
VII proper steering condition	
VIII proper tyre condition	
IX proper lighting condition	
X proper belt and components for fastening child seats condition	
XI proper emission control	
XII overall safety status	
XIII number of defects per failed vehicle	
XIV vehicle modifications	

instructions and using original parts and materials. Recently, the authorities in our country and worldwide increasingly introduce frequent checks for fraud in keeping with used vehicles.

*History of involvement in accidents* is an indicator that shows how often a vehicle for his lifetime will be involved in a car accident.

When a technical malfunction or an accident happens, repairs that are performed on the vehicle are recognized in the indicator *History of repair*. The condition of the vehicle after the repair depends largely on whether it is done professionally or not, and its consequences are described in detail by Berg et al. (2008).

*Braking condition* in many papers is associated with the safety of the entire vehicle. By reducing its accuracy, proportionally the vehicle roadworthiness is also reduced.

*Steering condition, tyre condition, lighting condition, belt and components for fastening child seats condition and emission control* are also parameters that reflect the safety condition of the vehicle and are also evaluated during the periodic control of the vehicle.

The *overall safety status* indicator evaluate the safety of the vehicle in terms of the number of available advanced safety systems (ABS/ASR, SRS, ESS, ACC, etc.) that are included in the vehicle.

*Number of defects per failed vehicle* expresses the number of simultaneous failures of vehicle malfunction.

*Modifications to the vehicle* are common and have a significant stake in vehicle roadworthiness performance (Berg et al. 2009).

## Assigning Indicator Weights by Fuzzy Ahp

The essence of the AHP—method is in comparison of pairs of stacking attributes values. It is performed by making comparisons between pairs of values of certain indicators, while asking which of the two compared indicators is more important and how. The scale of the relative importance to measure comparison is expressed using a scale from 9 to 1/9. Value 1 indicates equality between two individual indicators, while the value 9 or 1/9 indicates that the relevant indicator is 9 times more important than the other or 9 times less important than the other (Kahraman 2008).

The inability of AHP—method to deal with uncertainty and subjectivity in the process of pairwise comparison can be overcome by using fuzzy AHP—method, where instead of well-defined values, the fuzzy AHP—method used a range of values that would be able to cover the uncertainty of the decision (Sezhian et al. 2011). For that reason, fuzzy AHP—method is chosen for the calculation in the current research. The calculation of the weight factor with fuzzy AHP method can be described in the following steps:

- Step 1: Comparison of factors  
Based on expert opinion the pairwise comparison of factors is being prepared. The experts are required to compare each factor in pairs in a matrix form with

**Table 2** Comparisons of the experts are in a scale of 9 values

Linguistic value	Real value	Fuzzy value
Absolutely strong	9	(8, 9, 9)
Very strong	7	(6, 7, 8)
Fairly strong	5	(4, 5, 6)
Slightly strong	3	(2, 3, 4)
Equal	1	(1, 1, 1)
Slightly weak	1/3	(1/4, 1/3, 1/2)
Fairly weak	1/5	(1/6, 1/5, 1/4)
Very weak	1/7	(1/8, 1/7, 1/6)
Absolutely weak	1/9	(1/9, 1/9, 1/8)

size  $n \times n$ , where  $n$  is the number of factors. Comparisons of the experts are in a scale of 9 values (Table 2) and are denoted by  $r_{ij}$ . The results of the comparison of the experts are grouped into a pairwise comparison matrix using the average mean.

$$R = \begin{matrix} & A_1 & A_2 & \cdots & A_n \\ \begin{matrix} A_1 \\ A_2 \\ \vdots \\ A_n \end{matrix} & \begin{bmatrix} r_{11} & r_{12} & \cdots & r_{1n} \\ r_{21} & r_{22} & \cdots & r_{2n} \\ \vdots & \vdots & \ddots & \vdots \\ r_{n1} & r_{n2} & \cdots & r_{nn} \end{bmatrix} \end{matrix} \tag{1}$$

Comparing values in pairs expressed by fuzzy linguistic values (see Table 2).

- Step 2: Perform the test of consistency

In order to control the consistency of subjective opinions and accuracy of the weight factors, it is necessary to calculate the factor of consistency—CF who is defined:

$$CF = (\lambda_{\max} - n)/(n - 1) \tag{2}$$

where  $\lambda_{\max}$  is the maximum eigenvalue of the matrix  $R$ , and  $n$  is the number of factors. If the consistency factor is less than 0.1 it is regarded that the pairwise comparisons are acceptable.

- Step 3: Converting parameters in fuzzy numbers

The values of the pairwise comparison matrix are converted into triangular fuzzy numbers in accordance with the rules for conversion (in Table 2)

$$\tilde{R} = \begin{matrix} & A_1 & A_2 & \cdots & A_n \\ \begin{matrix} A_1 \\ A_2 \\ \vdots \\ A_n \end{matrix} & \begin{bmatrix} \tilde{r}_{11} & \tilde{r}_{12} & \cdots & \tilde{r}_{1n} \\ \tilde{r}_{21} & \tilde{r}_{22} & \cdots & \tilde{r}_{2n} \\ \vdots & \vdots & \ddots & \vdots \\ \tilde{r}_{n1} & \tilde{r}_{n2} & \cdots & \tilde{r}_{nn} \end{bmatrix} \end{matrix} \tag{3}$$

- Step 4: Calculation of fuzzy weight factor dimensions  
Fuzzy weight factor dimensions can be calculated with the formula:

$$\tilde{u}_i = (\tilde{r}_{i1} \odot \tilde{r}_{i2} \odot \dots \odot \tilde{r}_{in})^{1/n} \tag{4}$$

- Step 5: Calculate of final fuzzy weight factors  
Final fuzzy weight factors for every criterion can be obtained with:

$$\tilde{w}_i = \tilde{u}_i \odot (\tilde{u}_{i1} \oplus \tilde{u}_{i2} \oplus \dots \oplus \tilde{u}_{in})^{-1} \tag{5}$$

- Step 6: Calculation of the true values of the weight factors  
Final fuzzy weight factors of every criterion can be obtained with:

$$w_i = [(w_i^u - w_i^l) + (w_i^m - w_i^l)]/3 + w_i^l \tag{6}$$

by using the values from  $\tilde{w}_i = (w_i^l, w_i^m, w_i^u)$

## Composite Indicator and Fuzzy Topsis Method

TOPSIS is a *multi-criteria decision analysis method*, which was originally developed by Hwang and Yoon in 1981 with further developments by Yoon in 1987 and Hwang, Lai and Liu in 1993. TOPSIS is based on the concept that the chosen alternative should have the shortest geometric distance from the positive ideal solution and the longest geometric distance from the negative ideal solution. It is a method of compensatory aggregation that compares a set of alternatives by identifying weights for each criterion, normalizing scores for each criterion and calculating the geometric distance between each alternative and the ideal alternative, which is the best score in each criterion. An assumption of TOPSIS is that the criteria are *monotonically* increasing or decreasing. *Normalization* is usually required as the parameters or criteria are often of incongruous dimensions in multi-criteria problems (Kahraman 2008). Compensatory methods such as TOPSIS allow trade-offs between criteria, where a poor result in one criterion can be negated by a good result in another criterion (Hermans 2009).

A composite indicator (CI) is an mathematical aggregation of a set of individual indicators that measure multi-dimensional concept. There are  $m$  comprised alternatives, each alternative consist  $n$  sub-indicators  $x_{ij}$ . For each alternative is evaluated CI. CI is used for performance measurement, benchmarking, via providing an aggregated performance index in various fields such as Human Development Index, Road Safety Development Index—RSDI (Al Haji 2005).The graphical representation of CI construction is illustrated on Fig. 1,  $C_1 - C_n$  means criteria.

The TOPSIS method is used to analyze a multi-criteria decision making problem with  $m$  alternatives with  $n$  criteria. In TOPSIS method, the best alternative should



$$\begin{matrix} & C_1 & C_2 & \dots & C_n \\ A_1 & \begin{bmatrix} x_{11} & x_{12} & \dots & x_{1n} \end{bmatrix} \\ A_2 & \begin{bmatrix} x_{21} & x_{12} & \dots & x_{2n} \end{bmatrix} \\ \vdots & \begin{bmatrix} \vdots & \vdots & \ddots & \vdots \end{bmatrix} \\ A_m & \begin{bmatrix} x_{m1} & x_{m2} & \dots & x_{mn} \end{bmatrix} \end{matrix} \rightarrow \begin{bmatrix} CI_1 \\ CI_2 \\ \vdots \\ CI_m \end{bmatrix}$$

**Fig. 1** Construction of composite indicator

have the shortest Euclidean distance from the positive ideal solution (PIS) and the longest distance from the negative ideal solution (NIS). The PIS is a hypothetical solution which maximum values from database of all alternatives, the NIS is a hypothetical solution which minimum values from database of all alternatives (Hui et al. 2010; Javadian and Kazemi 2009). TOPSIS defines an index called relative closeness to the PIS and remoteness from the NIS. This index can be used as a CI of alternatives. The main procedure of the TOPSIS method is described in the following steps:

- Step 1: Define a decision matrix  
The decision matrix  $D$  of  $m \times n$  dimension consists of values of  $n$  sub-indicators for  $m$  alternatives:
- Step 2: Normalize the decision matrix  
The values of sub-indicators are normalized to scale 0-1. In case of “benefit type” indicators, what means a higher value is better, is used formula:

$$x'_{ij} = \frac{x_{ij} - \min_i \{x_{ij}\}}{\max_i \{x_{ij}\} - \min_i \{x_{ij}\}} \tag{7}$$

“Cost type” sub-indicators, what means the lower value is better, are normalized in the following way:

$$x'_{ij} = \frac{\max_i \{x_{ij}\} - x_{ij}}{\max_i \{x_{ij}\} - \min_i \{x_{ij}\}} \tag{8}$$

- As a result is obtained the normalized decision matrix  $D'$ .
- Step 3: Compute the weighted normalized decision matrix  
Elements of the normalized decision matrix  $D'$  are multiplied by weight vector  $W$ , which consist  $n$  weight factors  $w$ . These factors express the relatively importance of criteria. The elements of weighted normalized decision matrix  $V$  are expressed as:

$$v_{ij} = w_j x'_{ij} \tag{9}$$

- Step 4: Identify the PIS and NIS

The positive ideal solution  $A^+$  and the negative ideal solution  $A^-$  can be expressed as:

$$A^+ = \left( \max_i \{v_{i,1}\}, \dots, \max_i \{v_{i,n}\} \right) = (v_1^+, \dots, v_n^+) \tag{10}$$

$$A^- = \left( \min_i \{v_{i,1}\}, \dots, \min_i \{v_{i,n}\} \right) = (v_1^-, \dots, v_n^-) \tag{11}$$

- Step 5: Calculate the distance to PIS and NIS

For each alternative  $i$  the Euclidean distance  $d_i^+$  to the positive ideal solution and distance  $d_i^-$  to the negative ideal solution is defined (Nardo et al. 2005).

- Step 6: Compute the relative closeness data to CI

Values  $d_i^+$  and  $d_i^-$  are combined to relative closeness index  $C_i$ :

$$C_i = \frac{d_i^-}{d_i^+ + d_i^-} \tag{12}$$

The  $C_i$  is a composed indicator—CI of alternative  $i$ .

To express the subjectiveness and imprecision of the evaluation process, the sub-indicators and weights are represented by a triangular fuzzy number (Bo and Klir 1995). A triangular fuzzy number  $\tilde{n}$  can be define by a triplet  $(a, b, c)$  shown in Fig. 2. The membership function  $\mu_{\tilde{n}}$  is defined

$$\mu_{\tilde{n}}(x) = \begin{cases} \frac{x-a}{b-a}, & a \leq x \leq b \\ \frac{c-x}{c-b}, & b \leq x \leq c \\ 0, & \text{otherwise} \end{cases} \tag{13}$$

where  $a < b < c$ . The  $b$  is the most possible value of fuzzy number. Similarly as in the case of real numbers, operations of positive fuzzy numbers can be defined (Bo and Klir 1995).

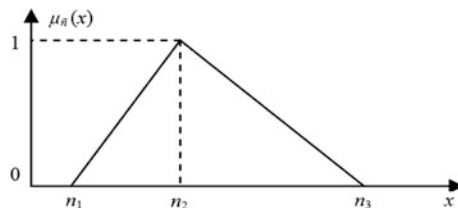


Fig. 2 A triangular fuzzy number  $\tilde{n}$

**Table 3** The 7-level scale of fuzzy numbers expressed in linguistic terms

Real value $x$	Linguistic value	Fuzzy value $\tilde{n}$
$0 \leq x < 1/7$	Very low	$(0, 0, 1/6)$
$1/7 \leq x < 2/7$	Low	$(0, 1/6, 2/6)$
$2/7 \leq x < 3/7$	Medium low	$(1/6, 2/6, 3/6)$
$3/7 \leq x < 4/7$	Medium	$(2/6, 3/6, 4/6)$
$4/7 \leq x < 5/7$	Medium high	$(3/6, 4/6, 5/6)$
$5/7 \leq x < 6/7$	High	$(4/6, 5/6, 1)$
$6/7 \leq x \leq 7/7$	Very high	$(5/6, 1, 1)$

The distance between fuzzy numbers can be defined:

$$D(\tilde{n}_1, \tilde{n}_2) = \sqrt{\frac{1}{3} [(a_2 - a_1)^2 + (b_2 - b_1)^2 + (c_2 - c_1)^2]} \tag{14}$$

In step 1 decision matrix is generated, in step 2 this matrix is normalized. After normalization, the real values in the decision matrix and weight values are converted into fuzzy numbers. The 7-level scale of fuzzy numbers expressed in linguistic terms is used (Table 3).

The calculations in step 3 are proceeded with the fuzzy values. In step 4, the fuzzy values of PIS and NIS is identified and in step 5 is calculated the distance to PIS and NIS by formula (14), in step 6 the relative closeness is estimating by (12).

## Results of the Calculations

Calculations of the weight factors with fuzzy AHP are shown in Table 4. Assigned weights of the criteria were applied to fuzzy TOPSIS model and Table 5 presents the results of the calculations.

**Table 4** Calculations of the weight factors with fuzzy AHP

Indicator	Fuzzy value	Real value
I	$(0.07; 0.09; 0.12)$	0.092
II	$(0.14; 0.20; 0.26)$	0.198
III	$(0.051; 0.065; 0.076)$	0.062
IV	$(0.15; 0.20; 0.29)$	0.176
XIV	$(0.04; 0.06; 0.08)$	0.06
XV	$(0.34; 0.41; 0.55)$	0.412

**Table 5** Vehicle Roadworthiness Performance Index—VRWPI

Experts	VRWPI with TOPSIS	VRWPI with fuzzy TOPSIS
1	0	0
2	0.515	0.503
3	0.645	0.408
4	0.770	0.860
5	0.642	0.720
6	0.440	0.496
7	0.442	0.400
8	0.575	0.592
9	0.597	0.700
10	0.453	0.640
11	0.522	0.667
12	0.564	0.440
13	0.700	0.815
14	0.528	0.775
15	1.000	1.000

## Conclusions

A composed indicator has been accepted as a useful tool in many non-technical areas, such as economy, society and environment. In this paper is presented application of CI in the field of technical sciences. Among numerous methods of multi-criteria decision making, the fuzzy AHP is very suitable for evaluating alternatives when qualitative and quantitative advertence are expressed only with linguistic vagueness. The contribution of this paper is to propose an efficient and effective decision framework for evaluation of vehicle roadworthiness using fuzzy AHP method. A fuzzy TOPSIS method was also realized to deal with the subjective kind of uncertainty of data (i.e. linguistic variables given by experts) and proved valuable in creating Vehicle Roadworthiness Performance Index—VRWPI. The construction process of this method is transparent and can be used to support the desired policy.

**Acknowledgments** The author gratefully acknowledge the support by the project AComIn: Advanced Computing for Innovation funded by the FP7 Capacity Programme Research Potential of Convergence Regions, grant number 316087.

## References

Jakimovska K (2014) Development of methodology for condition based vehicle assessment. PhD thesis, University Ss. Cyril and Methodius—Faculty of Mechanical Engineering—Skopje  
 AUTOFORE project WP 200: Current situation and trends in roadworthiness enforcement

- AUTOFORE project WP 300: Vehicle technology/ Diagnostic technology  
 AUTOFORE project WP200: Current situation of roadworthiness enforcement on E.U
- Al Haji G (2005) Development of an International Index to Measure Road Safety Performance. Dissertation thesis, Department of Science and Technology, Campus Norrköping, Linköping University Norrköping, Sweden
- Bo Y, Klir G (1995) *Fuzzy Sets and Fuzzy Logic—Theory and Applications*. Prentice Hall PTR
- Berg FA, Rucker P, Leimbach F, Schmorte U, Chirwa EC, Chinnaswamy GK (2008) The effects of unprofessional repairs on quality and safety of road vehicles subjected to crash loading. Proceedings of ICRASH Kyoto, Japan
- Berg FA, Rucker P, Leimbach F, Kiebach H (2009) The project fair repair—a contribution to highlight possible impacts of non-professional repair on the quality and safety of vehicles. XXII Science and Motor Vehicles Conference Belgrade, Serbia
- Council Directive 96/96/EC of 20 December 1996—Official Journal of the European Communities  
 Council Directive 2010/48/EC of 5 July 2010—Official Journal of the European Communities  
 Council Directive 2009/40/EC of 6 May 2009—Official Journal of the European Communities
- Duboka Ć (2010) Vehicle condition-based roadworthiness performance indicator. World Automotive Congress FISITA Budapest, Hungary
- Duboka Ć (2011) Vehicle safety performance indicators and indexes. XXIII Science and Motor Vehicles Conference Belgrade, Serbia
- DEKRA Automobil GmbH—Road safety report 2008—Strategies for preventing accidents on Europa's roads
- DEKRA Automobil GmbH—Verkehrssicherheitsreport Landstrassen 2013—Strategien zur Unfallvermeidung auf den Strassen Europas
- Hermans E (2009) A methodology for developing a composite road safety performance index for cross-country comparison. PhD thesis—University of Hasselt, Belgium
- Hui S, Zhiqing F, Ye S, (2010) Research on comprehensive evaluation of Urban public transportation competitiveness in Hebei province based on TOPSIS. IEEE
- Javadian N, Kazemi M (2009) A general fuzzy TOPSIS based on New Fuzzy positive and negative ideal solution. IEEE IEEM
- Kahraman C (2008) *Fuzzy multi-criteria decision making-theory and applications with recent developments*, Vol 16
- Nardo M, Saisana M, Saltelli A, Tarantola S, Hoffman A, Giovannini E (2005) *Handbook on constructing composite indicators: methodology and user guide*. OECD Statistics Working Paper Vol 3
- Sezhian MV, Muralidharan C, Nambirajan T, Deshmukh SG (2011) Performance measurement in a public transport sector passenger bus transport company using fuzzy TOPSIS, fuzzy AHP and ANOVA—a case study. *Int J Eng Sci Technol*

# Concept Design of Twin-Sheet Thermoplastic Cellular Structures for Vehicle's Bumper System

Stefan Tabacu, Claudiu Diaconescu and Alexandru Oltean

**Abstract** The 2013 World Health Organization's Report on road safety shows that from 1.24 million fatalities recorded each year there are 270,000 pedestrian related events. Although the most severe injuries are produced when the pedestrian's head is striking the bonnet or the area surrounding the windshield, lower limbs injuries do commonly result. The present study is focused on the development of an energy absorbing structure based on cellular configurations manufactured by vacuum forming thermoplastic sheets that finally define a unitary part. A parametric analysis is performed in order to evaluate internal energy accumulated during deformation. The numerical model of the front end structure of 2001 Ford Taurus model with the EC No 78/2009 specialised legform impact was investigated and the results discussed. Two configuration for energy absorber were defined and investigated using numerical simulation. The first configuration uses a single layer of four rows of cellular structures, while the second configuration uses a double layered structure of twin sheet cells on three rows. For the first case of cellular structure the bending angle of the impactor recorded a value of  $19^\circ$  while for the second case the value decreased to  $14^\circ$ . In all cases the shear displacement was well below the maximum accepted value. The maximum acceleration recorded during simulation using the single layer cellular structure was of 122 g while for the double layered structure the value was of 106 g. Compared to the original solution in both cases there was an improvement of the impactor's response.

**Keywords** Pedestrian protection · Twin-sheet forming · Cellular structures · Impact performance

---

S. Tabacu  
University of Pitesti, Târgu Din Vale, 1, 110040 Pitesti, Romania

S. Tabacu (✉) · C. Diaconescu · A. Oltean  
Alseca Engineering, 24, Soseaua de Centura, Tunari, Romania  
e-mail: stefan.tabacu@upit.ro; stefan.tabacu@alseca.com

C. Diaconescu  
e-mail: claudiu.diaconescu@alseca.com

A. Oltean  
e-mail: alexandru.oltean@alseca.com

## Introduction

In 2013 World Health Organization released the latest Report on road safety (WHO 2013a) accompanied by a document dedicated to pedestrian safety (WHO 2013b). By summarizing the outlines of the Report (WHO 2013b), it shows that from 1.24 million fatalities recorded each year, there are 270,000 pedestrian related events thus special measures are required, perhaps mandatory, in order to increase the safety.

Although the most severe injuries are produced when the pedestrian's head is striking the bonnet or the area surrounding the windshield (Shojaeefard et al. 2014), lower limbs injuries do commonly result in case of a vehicle–pedestrian impact (Mo et al. 2014). The European Parliament and the Council released in 2009 *Regulation (EC) No 78 on the type approval of motor vehicle with regard to the protection of pedestrians and other vulnerable road users* (European Commission 2009) that states the required structural response in case of a vehicle–pedestrian impact. As a consequence, by 24th of February 2013, the bumper systems of M1 type vehicles should fall under the following prescriptions: the maximum dynamic knee bending angle shall not exceed 19.0°; the maximum dynamic knee shearing displacement shall not exceed 6.0 mm; and the acceleration measured at the upper end of the tibia shall not exceed 170 g.

Literature and patent data were reviewed by Schuster (2004) and the following trends for safety improvement were identified: bumper mounted sensors and pedestrian airbags; alternative energy absorbers; flexible beams and bull bars. Regarding the development process of a vehicle bumper beam, the rigid structure behind the frontal fascia, the work of Davoodi et al. (2012) summarizes the major requirements. Although steel is the most preferred construction material for the bumper beam, composite materials were investigated by Belingardi et al. (2013) and Davoodi et al. (2011) as a viable, alternative, solution. The energy absorbers can be adapted to various configurations of existing solutions. This may be a reliable and less expensive solution, for existing vehicle, meant to comply with the prescriptions of EC Regulation 78/2009.

## Cellular Twin Sheet Structures

Cellular or patterned structures are of a particular interest due to impact performances. Cellular configurations provide good energy absorption characteristics while maintain a low specific weight as shown by Bartl et al. (2008), Kathiresan et al. (2012), Zou et al. (2009) and Sashikumar et al. (2012). The egg-box structures prove to be a reliable solution for energy absorption devices as presented by Lam et al. (2004) for thermoplastic composites, Yoo and Chang (2008) for fabric composites and Chung et al. (2007) for carbon/glass fibre reinforced polymers.

A specialized cellular structure that uses the SKYDEX<sup>®</sup> material was investigated by Zhu et al. (2014).

Twin sheet thermoplastic structures are highly efficient solutions that provide outstanding performance by means of using small amounts of materials (shaped in rather complex geometry) and high-tech, low energy consumption equipments. The structures are manufactured using vacuum formed sheets that finally define a unitary structure. The manufacturing process is presented in Fig. 1.

Although a wide range of patterns can be formed, the structures with circular frusta were investigated using numerical methods. Akisanya and Fleck (2006), Gupta et al. (2006), Gupta and Venkatesh (2007) and Mamalis et al. (2001) investigated the deformation process and structural performances of conical frusta structures providing the background of the present study. A Matlab (Matlab Inc. 2009) code was developed in order to define the numerical model for the design analysis. The numerical simulations were performed using the general-purpose finite-element explicit-solver LS-Dyna (Hallquist 2003) (available in the ANSYS ACADEMIC RESEARCH LS-Dyna package).

The following parameters were investigated (Fig. 2): cell size (the diameter of the cone is half length of a cell); sheet thickness; draft angle and column height. The length of the cell ranges from 20 to 35 mm, the draft angle is set to 5° and 10° while the thickness of the formed part ranges from 0.5 to 2.0 mm. The following parameters were investigated: cell size (the diameter of the cone is half length of a cell); sheet thickness; draft angle and column height. The length of the cell ranges from 20 to 35 mm, the draft angle is set to 5° and 10° while the thickness ranges from 0.5 to 2.0 mm.

Material parameters (Young modulus, yield stress and failure strain) were identified from available material databases (<http://www.matweb.com/>—accessed on 17.09.2014). For the numerical simulation a simple material model (isotropic with kinematic hardening—\*MAT\_003) was selected and a value of 1.0 GPa was

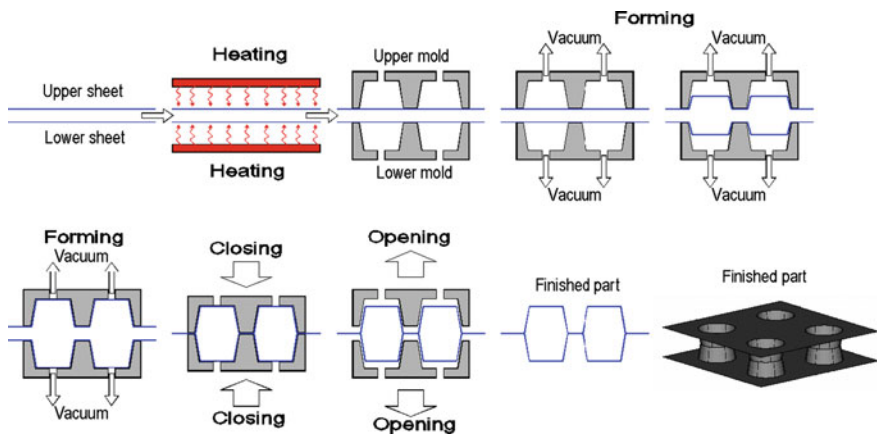
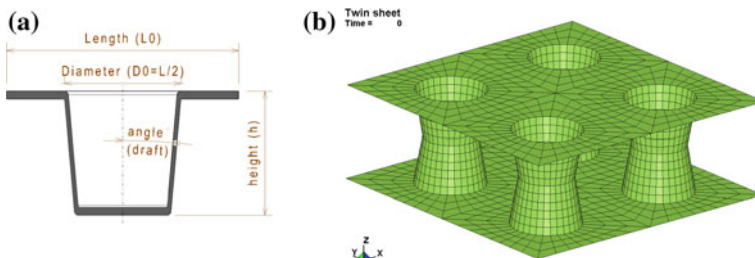


Fig. 1 Twin sheet structures. Manufacturing process





**Fig. 2** The numerical model of the cellular structure **a** main dimensions; **b** model for the design analysis ( $2 \times 2$  cells pattern)

assigned to the Young’s modulus, 0.020 GPa for the yield stress and 1.5 (150 %) for the strain at failure. The cellular structure was crushed by a flat rigid wall, travelling with a constant velocity of 1.0 m/s. It was found that the mean crush force is dependant of the value of yield stress and part’s dimensions (Abramowicz and Jones 1986; Jones 1989; Wierzbicki et al. 1992). The value of the strain at failure gives the amount of internal energy accumulated by the structure. Figure 3 presents the internal energy accumulated by the structure during crushing. Results are represented as a function of total height of the cell ( $2 \cdot h$ ) and wall thickness.

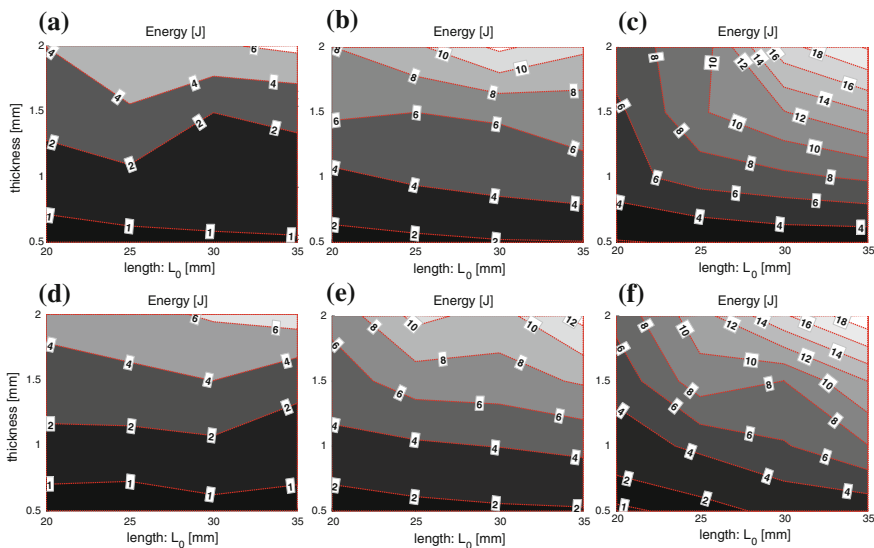


**Fig. 3** Internal (deformation) energy. **a**  $H = 10$  mm;  $\theta = 5^\circ$ ; **b**  $H = 20$  mm;  $\theta = 5^\circ$ ; **c**  $H = 30$  mm;  $\theta = 5^\circ$ ; **d**  $H = 10$  mm;  $\theta = 10^\circ$ ; **e**  $H = 20$  mm;  $\theta = 10^\circ$ ; **f**  $H = 30$  mm;  $\theta = 10^\circ$

## Results

### *Numerical Model Overview*

For the investigation of the pedestrian protection a specialized impactor should be used as prescribed by Regulation 78 of the European Commission. The legform impactor is a complex experimental device for system protection analysis as presented by Teng and Nguyen (2010) and Abvabi et al. (2010) and requires special validation as presented by Matsui et al. (2004) and Matsui (2014).

In conjunction with the impactor model, the numerical analysis was performed using the finite element model of the Ford Taurus developed by National Crash Analysis Center. The current release of the numerical model, available from November 2014, shows very good performance for the impact cases used for the validation.

For the pedestrian protection analysis, in order to improve the runtime, a reduced model of the vehicle was used (Fig. 4).

Once the ground level was set using the numerical model of the vehicle the legform model was positioned at 25 mm above this level according to the test requirements.

### *Analysis of the Existing Bumper System*

The vehicle features an energy absorber made of foam. The absorber is placed between the bumper fascia and bumper frame, fixed on the late mentioned structure. Figure 5a shows the numerical model used for the first case. The energy absorber can be identified in the figure and the material information are presented in Fig. 5b. On the midsection of the bumper frame there is an additional metallic structure used to support and guide the absorber.

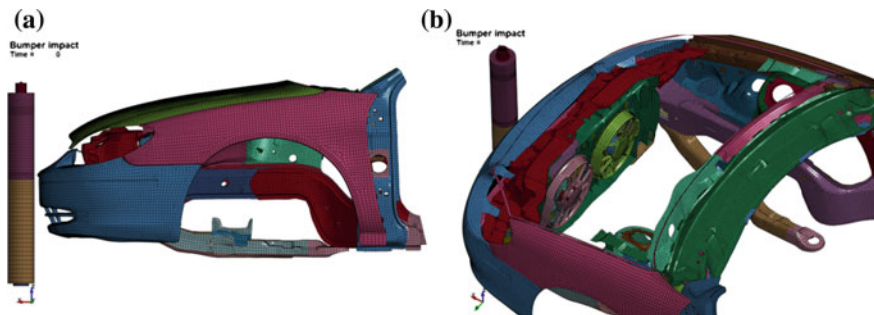


**Fig. 4** Numerical model. **a** Side view; **b** view of the engine compartment

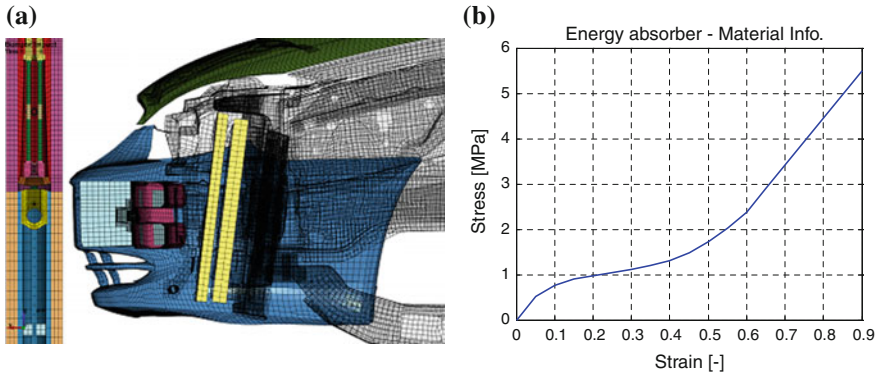


**Fig. 5** Numerical model of the existing vehicle. **a** Numerical model; **b** energy absorber—material information

Using this numerical model the maximum acceleration recorded for the tibia was of 153 g, a shear displacement of 2.65 mm and a maximum bending angle of 27.33° (0.477 rad). Although the maximum acceleration and shear displacement fall within the prescription of Regulation (EC) No. 78/2009 the maximum bending angle exceeds the maximum value. No penalty should be addressed given the fact that it represents the Ford Taurus model released in 2001.

### *Model Without the Energy Absorber*

The foam absorber and the auxiliary structure were removed from the existing model in order to investigate the structural performances of the vehicle front end when the pedestrian protection is evaluated. Figure 6a presents the results, at the

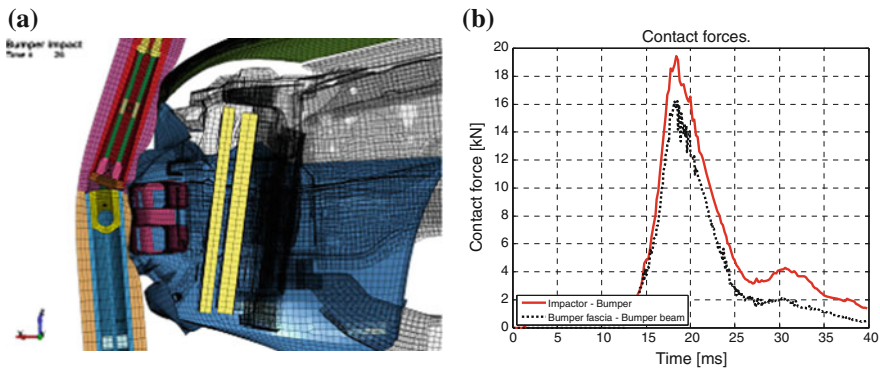


**Fig. 6** Numerical model. Model without absorber. **a** Deformed structure (maximum bending angle); **b** interface/contact forces

time step when the maximum bending angle of the impactor was recorded, obtained during the simulation.

Using this numerical model the maximum acceleration recorded for the tibia was of 177 g, a shear displacement of 2.56 mm and a maximum bending angle of  $23.26^\circ$  (0.406 rad). Compared to the previous set of results it can be noticed that the acceleration increased while the shear displacement and the bending angle decreased. This shows that due to the presence of the foam made energy absorber there is a reduced deformation of the bumper. Although it has a cushioning effect it keeps the impactor on an extreme position allowing the upper section of the legform impactor to bend over the hood. The maximum impact force is of 19.5 kN (Fig. 6b) while the energy absorbed by the vehicle structures is about 260 J (from which about 40 J are restored during the rebound phase). This shows that a large amount of energy must be consumed by the legform structures giving the acceleration and bending values. Maximizing the energy consumed by the legform can be a solution to improve the values of the parameters giving the pedestrian protection performance.

### ***Model with Twin Sheet Structure.***

The area, measured at the level of the bumper fascia, where the maximum longitudinal displacement was recorded spans over a length of 150 mm (according to diameter of the impactor). The height of the bumper beam is of 130 mm giving the area of the structure recording the major deformations.

Based on the deformed area, deformation energy and contact forces and using the results of the parametric analysis the cell dimensions can be defined. The goal is to maximize the energy absorbed by the structure while maintaining a low crushing force. The analysis pointed to a cell dimension of 35 mm giving a configuration of  $4 \times 4$  cells.

The thickness of the structure was set to 1.0 mm. This configuration is also supported by the manufacturing process as larger cells are easier to manufacture. The forces required to crush the structure is 12 kN less than the maximum computed force when the foam absorber is absent (Fig. 7b). The cellular structure, with a height of 30 mm, was placed on the bumper frame facing the bumper fascia. Figure 7a shows the deformed structure when the maximum bending angle was recorded.

An additional 130 J are consumed by the cellular structure. Based on the results from the parametric analysis the  $4 \times 4$  cells highly deformed by the impactor were supposed to consume  $(4 \times 4) \text{ cells} \cdot 8 \frac{\text{J}}{\text{cell}} = 128 \text{ J}$ . Same time the energy consumed by the bumper fascia decreased due to the smaller deformations of the structure. Figure 7b presents the computed contact forces. The maximum forces decreased with an important influence of the dynamics of the legform impactor. The maximum acceleration was of 122 g, maximum shear displacement of 1.53 mm and the

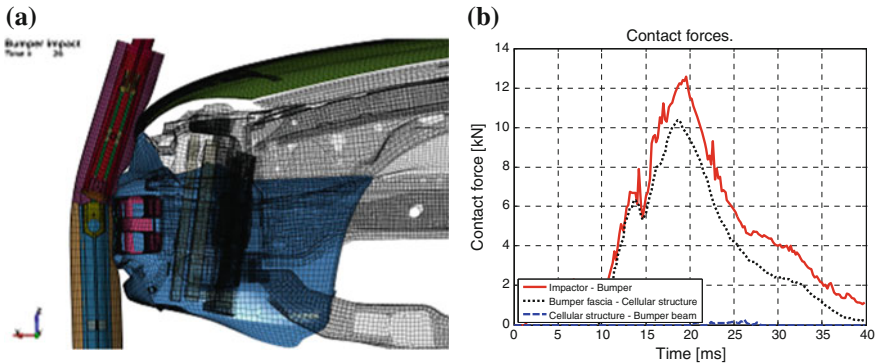


**Fig. 7** Numerical model. Model with cellular structure. **a** Deformed structure (maximum bending angle); **b** interface/contact forces

bending angle of 19° (0.33 rad). These values falls within the prescribed values when the pedestrian protection is addressed although the value of the bending angle equal with the maximum accepted value. The real vehicle may show an improved value due to the fact that some parts on the vehicle’s front end were not modelled.

A second configuration was used. The second configuration was designed as a two layers cellular structure with three cells on a row. Figure 8a presents the deformed structure when the maximum bending angle was recorded.

The total energy consumed by the structure is of 210 J with a total energy consumed by the vehicle’s structures of about 380 J. Based on the results from the parametric analysis the  $2 \times 4 \times 3$  cells highly deformed by the impactor were supposed to consume  $2 \text{ layers} \times (4 \times 3) \frac{\text{cells}}{\text{layer}} \cdot 8 \frac{\text{J}}{\text{cell}} = 192 \text{ J}$ . Same time, due to the layered configuration of the cellular structure the impact force does not exceeds 10 kN (Fig. 8b). The maximum acceleration was of 106 g, maximum shear

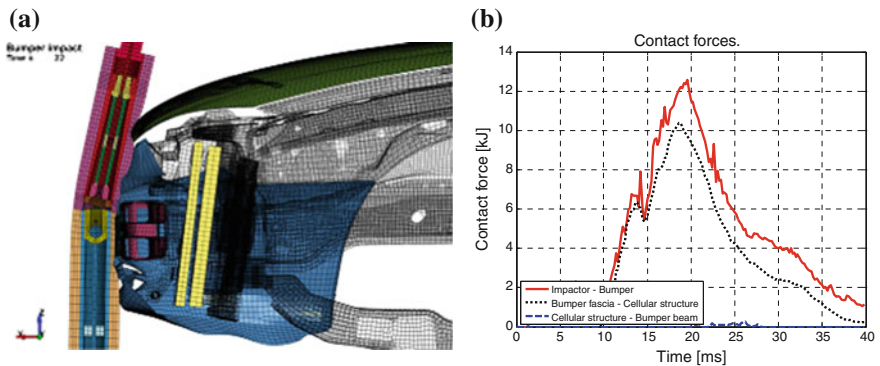


**Fig. 8** Numerical model. Model with double layered cellular structure. **a** View of the model (without the energy absorber); **b** interface/contact forces

displacement of 1.45 mm and the bending angle of  $14^\circ$  (0.244 rad). These values falls within the prescribed values showing an adequate level of protection.

## Conclusions

Twin sheet forming process is mainly focused on forming closed structures with high stiffness and low weight as vacuum forming is a highly productive industrial process. Although it presents some limitations related to the complexity of the geometry of the finished part it can be easily applied for simple parts. Using a custom code developed in MATLAB a tool for parametric design of structures was developed. A set of cellular structures with a conical frusta were investigated in order to define add-on devices for enhanced pedestrian protection. The dimensions of the cells ranges between 20 and 35 mm while the total height of the structure was set to 10, 20 and 30 mm. For the conical section the draft angle was set to  $5^\circ$  and  $10^\circ$  close to the cylindrical shape. Using the average and maximum crush force plots and considering the amount o internal energy that can be accumulated by the structure during deformation a cellular structure was defines.

The numerical model of the front end structure of 2001 Ford Taurus model with the specialised legform impact was investigated. Starting from the original model that features a foam energy absorber the pedestrian protection was evaluated. As a second step the foam absorber was removed and a simulation performed. Results were used in order to define the cellular structure used as an energy absorbing device.

The first configuration used a single layer of four rows of cells. Compared with the model without energy absorber the bending angle decreased from  $23^\circ$  to  $19^\circ$  while the acceleration decreased from 177 to 122 g. For the defined range of cell's dimensions there were no other configurations able to provide a substantial improvement.

As a consequence a cellular structure with two layers was defined. The bending angle recorded a value of  $14^\circ$  while the maximum acceleration recorded a value of 106 g giving a good level of protection for the pedestrians.

Based on the numerical model the foam absorber has a mass of 1.39 kg while the single layer structure has a mass of 0.45 kg while the layered structure has a mass of 0.62 kg. Just adding the highly efficient thermoforming process, the proposed structure for energy absorbing devices may be a reliable solution. One limitation of the single layer configuration may be identified of the thinning of the wall that points to the thickness of the raw sheet used to manufacture the parts that may add some constrains to the manufacturing process. Moreover due to the smaller dimensions of the cells the structure can be easily adapted to other parts (interior trims, dashboard) in order to provide increased protection.

## References

- Abramowicz W, Jones N (1986) Dynamic progressive buckling of circular and square tubes. *Int J Impact Eng* 4:243–270
- Abvabi A, Nasr A, Noorpoor A, Saeed Kisat M (2010) Investigation on the effect of impact location height on pedestrian safety using a legform impactor dynamic model. *Safety Sci* 48:660–671
- Akisanya AR, Fleck NA (2006) Plastic collapse of thin-walled frusta and egg-box material under shear and normal loading. *Int J Mech Sci* 48:799–808
- Bartl F, Klaus H, Dallner R, Huber O (2008) Material behaviour of a cellular composite undergoing large deformations. *Int J Impact Eng* 36:667–679
- Belingardi G, Beyene AT, Koricho EG (2013) Geometrical optimization of bumper beam profile made of pultruded composite by numerical simulation. *Compos Struct* 102:217–225
- Chung JG, Chang SH, Sutcliffe MPF (2007) Deformation and energy absorption of composite egg-box panel. *Compos Sci Technol* 67:2342–2349
- Davoodi MM, Sapuan SM, Ahmad D, Aidy A, Khalina A, Jonoobi M (2011) Concept design of car bumper beam with developed hybrid bio-composite material. *Mater Des* 32:4857–4856
- Davoodi MM, Sapuan SM, Aidy A, Abu Osman NA, Oshkour AA, Wan Abas WAB (2012) Development process of a new bumper beam for passenger car: a review. *Mater Des* 40:304–313
- European Commission (2009) Regulation (EC) No 78 on the type approval of motor vehicle with regard to the protection of pedestrians and other vulnerable road users
- Gupta NK, Mohamed Sheriff N, Velmurugan R (2006) A study of buckling of thin conical frusta under axial loads. *Thin Wall Struct* 44:986–996
- Gupta NK, Venkatesh (2007) Experimental and numerical studies of impact axial compression of thin-walled conical shells. *Int J Impact Eng* 34:708–720
- Hallquist JO (2003) LS-DYNA keyword user's manual. Version 970. Livermore Software and Technology Corporation, Livermore CA
- Jones N (1989) *Structural impact*. Cambridge University Press, Cambridge
- Kathiresan M, Manisekar K, Manikandan V (2012) Performance analysis of fibre laminated thin conical frusta under axial compression. *Compos Struct* 94:3510–3519
- Lam SW, Tao XM, Yu TX (2004) Comparison of different thermoplastic cellular textiles composites on their energy absorption capacity. *Compos Sci Tech* 13–14:2177–2184
- Mamalis AG, Manolacos DE, Ioannidis MB, Kostazos PK, Hassiotis G (2001) Finite element simulation of the axial collapse of thin-wall square frusta. *Int J Crashworthiness* 6:155–164
- Matsui Y, Ishikawa H, Sasaki A, Kajzer J, Günter S (2004) New biofidelic corridor and biofidelity test procedure for pedestrian legform impactors. *Traffic Inj Prev* 5:390–397
- Matsui Y (2014) Safety assessment characteristics of pedestrian legform impactors in vehicle-front impact tests. *Accident Anal Prev* 73:65–72
- Mo F, Arnoux PJ, Cesari D, Masson C (2014) Investigation of the injury threshold on knee ligaments by the parametric study of car-pedestrian impact conditions. *Safety Sci* 62:58–67
- Sashikumar S, Chirwa EC, Myler P, Qian P, Matsika E (2012) Numerical investigation of the collapse behaviour of an aluminium egg-box under quasi-static loading. *Int J Crashworthiness* 17:582–590
- Schuster P (2004) Current trends in bumper design for pedestrian impact: a review of design concepts from literature and patents. American Iron and Steel Institute
- Shojaeefard MH, Najibi A, Ahmadabadi MR (2014) Pedestrian safety investigation of the new inner structure of the hood to mitigate the impact injury of the head. *Thin Wall Struct* 77:77–85
- Teng TL, Nguyen TH (2010) Assessment of the pedestrian friendliness of a vehicle using subsystem impact tests. *Int J Auto Tech—KOR* 11:67–73
- The MathWorks, Inc. (2009) MATLAB. Natick, Massachusetts, USA
- Wierzbicki T, Bhat SU, Abramowicz W, Brodtkin W (1992) Alexander revisited—a two folding elements model of progressive crushing of tubes. *Int J Solids Struct* 29:3269–3288

- World Health Organization (WHO) (2013a) Global status report on road safety 2013: supporting a decade of action
- World Health Organization (WHO) (2013b) Pedestrian safety: a road safety manual for decision-makers and practitioners
- Yoo SH, Chang SH (2008) An experimental study on energy absorbing structures made of fabric composites. *Compos Struct* 86:211–219
- Zhu F, Dong L, Ma H, Chou CC, Yang KH (2014) Parametrized optimal design of a novel cellular energy absorber. *Int J Mech Sci* 86:60–68
- Zou Z, Reid SR, Tan PJ, Li S, Harrigna JJ (2009) Dynamic crushing of honeycombs and features of front shock. *Int J Impact Eng* 36:165–176



# On the New Concept and Advantages of the Integrated Shock Absorber—Air Spring—“Isas”

**Adrian Ioan Niculescu, Antony Jankowski, Miroslaw Kowalski and Tudor Sireteanu**

**Abstract** The paper reveal for the first time the novel concept of integrate shock-absorber-air spring, called shortly ISAS, and its advantages based simulations on quarter car model realized with ADAMS software-View module. ISAS is an easy and cheap solution for vehicle trim correction easy-going or in real time, to increase stability, comfort, passing capacity, handling, cruise speed and active security, reducing the risk of undercarriage damage. The novelty is to create a controllable buoyant force under the damper dust shield, by sliding closing the area between dust shield and outer cylinder and filling it with compressed gas/air at proper pressure. Comparative to the known solution realize with rubber sleeve/bellows the new proposed solution is more compact, reliable and resistant at high pressure, thus having possibility to fully eliminate the steel spring, his function being full taken by the air spring device contained by the ISAS product, situation reducing the cost comparative to the classic suspension. The “ISAS” trim corrector, has applicability on front and rear suspension including to the Macpherson solution, each vehicle kind including motorcycles, cars, buses, trucks, trains, military and racing vehicles, improving performances, comfort and transport security. The same the novel trim corrector has applicability in vehicle seats and cabin, increasing the

---

A.I. Niculescu (✉)

Institute of Solid Mechanics of the Romanian Academy, 15 Constantin Mille,  
1st District, Bucharest, Romania  
e-mail: adrian\_ioan\_niculescu@yahoo.com

A. Jankowski

Institute of Aviation, Warsaw, Poland  
e-mail: antonijankowski@yahoo.com

M. Kowalski

Air Force Institute of Technology, Warsaw, Poland  
e-mail: mirosław.kowalski@itwl.pl

T. Sireteanu

Institute of Solid Mechanics of the Romanian Academy, Bucharest, Romania  
e-mail: siretimsar@yahoo.com

comfort, visibility and thus the transport security. The ISAS solutions are in patent application no. A2015/00368—OSIM Romania. The ISAS concept advantages are demonstrates based simulation on a complex quarter car model equipped with rebound and compression stopper buffers and shock absorber equipped with adjustable pneumatic spring.

**Keywords** Trim corrector · Shock absorber · Air spring · Integrated · ISAS

## How Realize Integrated Shock Absorber—Air Spring

To realize ISAS uses a standard damper and apply some minor modifications, presented below:

- Step 1 replace the standard dust shield with other one resistant to pressure
- Step 2 apply an annular body on the outer cylinder, the annular body containing one or more channels with one or more seal elements, their sealing lip/sliding sealing on the inner surface of the new dust shield
- Step 3 seal new resistant dust shield against rod with a seal member
- Step 4 apply an air filling valve on the dust shield and connect it to a pressure air source, respectively to a compressed air tank or a compressor
- Step 5 adjust manually or automatically the vehicle trim, by modifying the gas/air pressure

Figure 1 shows evolution from standard damper to integrated damper-air spring.

The components presented in Fig. 1 are explained in Table 1.

The elements 1 ÷ 8 are commune elements for both variants.

The washer 18 is utilized when the support shoulder of the rod 3 is enough.

In Fig. 2 are presented other two sealing solutions against the rod and filler rod solution.

In the Fig. 3 is presented solution for full trim control.

The main elements presented in Fig. 3 are:

- 206 air spring units  $C_1, C_2, C_3, C_4$ , controlling each semi-axle
- 117 pressure transducers
- 176 position transducers
- 14 source of pressured gas/air
- 209 pressured gas/air reservoir
- 205 electro-valves
- 145 analysis, command and control unit
- 149, 150, 206, 207 indicators for pressure, position, pitch and roll

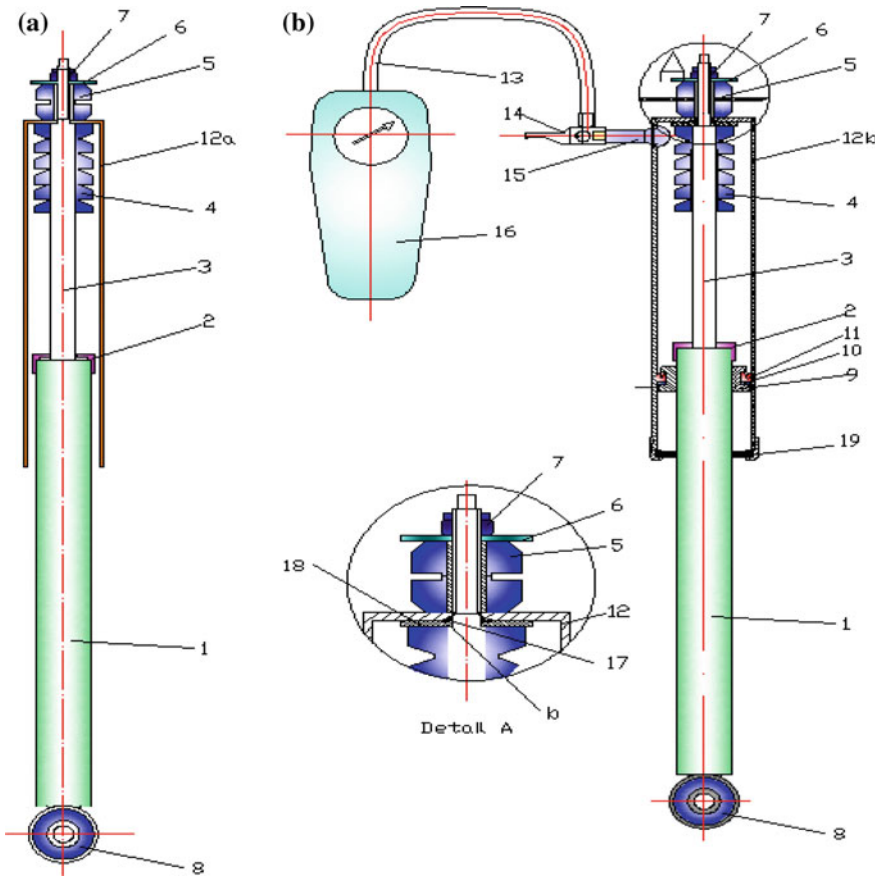


**Fig. 1** The genesis of integrated shock absorber-air spring based a standard shock absorber. **a** The standard shock absorber. **b** Integrated shock absorber-air spring, realized based standard shock absorber from position A

**Table 1** The components of standard damper and of integrated spring-damper

1	Shock absorber outer cylinder	11	Sliding sealing element
2	Annular anvil	12a	Dust shield
3	Rod	12b	Reinforced dust shield
4	Stopper buffer on compression	13	Pressure hose
5	Gripping pads	14	Quick plug
6	Washer	15	Quick valve
7	Self-locking nut	16	Compressor/pressure gas tank
8	Gripping bushing	17	Seal element
9	Annular piston	18	Special washer
10	Pusher ring (optional)	19	Dust brush

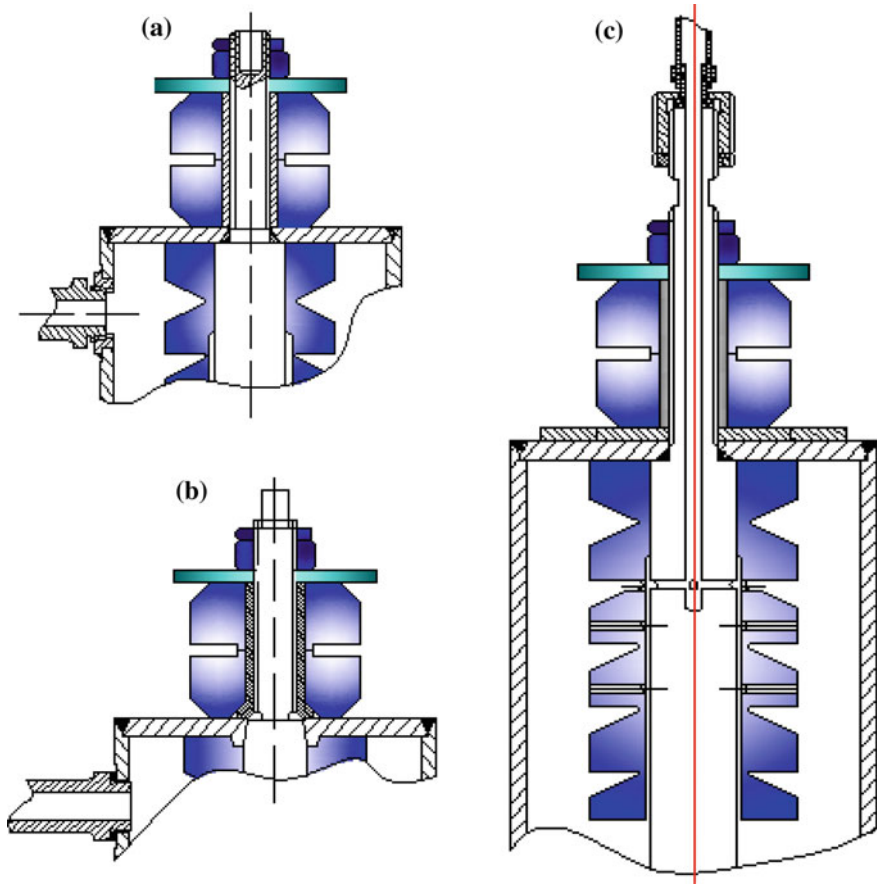


**Fig. 2** Other sealing and filling solutions. **a** Sealing when the rod shoulder is enough. **b** Sealing by conical fit. **c** Filler rod solution

### The Realized Integrated Shock Absorbers—Air Springs

The elements are the same presented in Fig. 1 and explained in Table 1, excepting the positions 19, 20, representing (Fig. 4):

- 20 centering ring
- 21 protecting seal

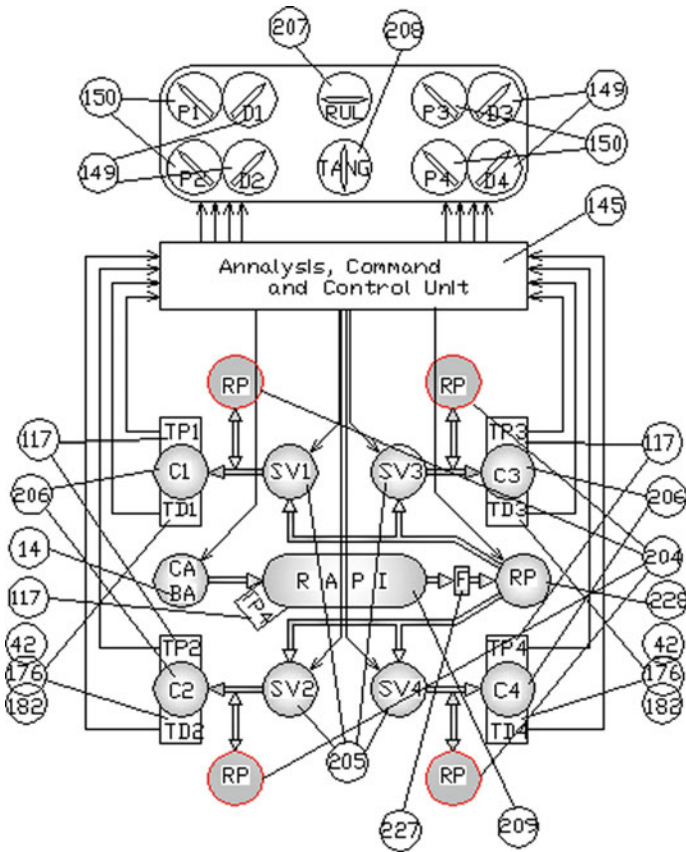


Fig. 3 The block diagram for step by step or in real time vehicle trim control

### The Quarter Car Model Realized in Adams-View Module

The quarter car model realized with ADAMS, module View is presented in the Fig. 5.

The damping characteristic is defined by damping forces at different speed for each strokes respectively one for rebound and other for compression.

The contact force road-wheel (CONTACT\_1) is defined based on the tire rigidity.

The stopper buffer forces on compression (CONTACT\_2) and rebound (CONTACT\_3) are defined based on the each specific rigidity characteristics.

The road excitation is realized with a function generator.

The software allow the model evolution visualisation in real time, also generating the diagrams of displacements, forces, accelerations, speeds, for each elements or for relative evolution between diverse elements.

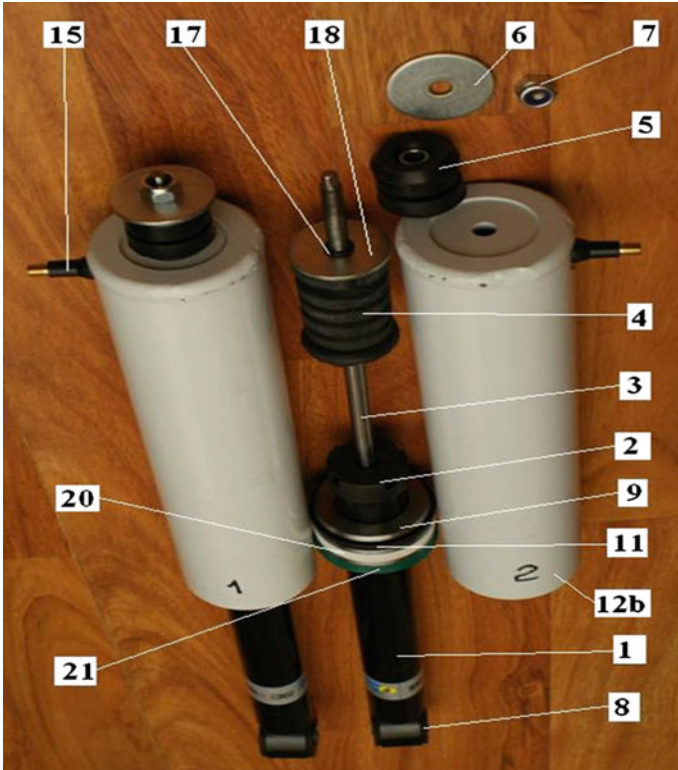


**Fig. 4** The realized trim corrector devices

The elements are:

1	Vehicle body
2	Translational joint for sprung mass
3	Integrated spring-damper
4	Main suspension spring
5	Compression stopper buffer
6	Axle
7	Translational joint for axle
8	Rebound stopper buffer
9	Road
10	Translational joint for road
11	Under body bottom level

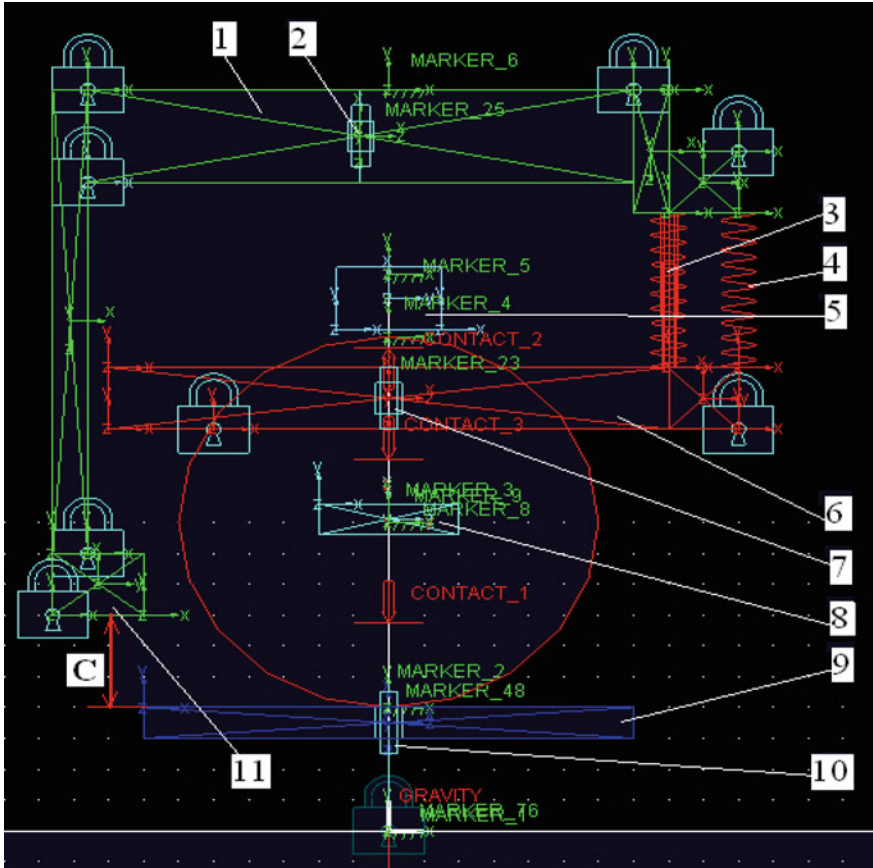


Fig. 5 The quarter car model with integrated spring-damper and standard spring

In the figure the padlocks represents the fixed joints linking the elements belongs to the each parts.

C—body-ground clearance.

The model covers both solutions, respectively solution:

- with two springs e.g. mains suspension spring (4) and correction spring included in integrated spring-damper (3);
- with one spring e.g. only spring included in integrated spring-damper (3), this spring taking the role of the main suspension spring, but being adjustable, situation in which the spring (4) has null rigidity.

**Table 2** The springs forces and lengths used for trim corrector efficiency evaluation

Loaded state	Sprung mass [kg]	Sprung weight [N]	Trim correction value [m]	Spring force [N]	Spring length [m]	
					Normal position	Corrected
Fully	360	3530	0.00	3530	0.2265	–
Fully	360	3530	0.04175	3530		0.26825
Fully	360	3530	0.06	3530		0.2865

## The Tested Corrections

The springs forces and lengths used for trim corrector evaluation are presented in the Table 2.

## Numerical Application

The road/car vertical interaction has been simulated using ADAMS software View module.

The considered car has the following characteristics:

$m_U = 240$ [kg]	sprung mass at unloaded
$m_F = 360$ [kg]	sprung mass at fully loaded
$m_{US} = 35$ [kg]	unsprung mass
$l = 0.236$ [m]	the overall suspension stroke
$d_{RB} = 0.014$ [m]	the rebound stopper buffer deformation, under 5000 [N]
$d_{CB} = 0.040$ [m]	the compression stopper buffer deformation, under 1000 daN
$k_1 = 14085$ [N/m]	the suspension rigidity
$k_T = 2.1810^8$ [N/m]	the maximal tire rigidity at the deformation of 0.06 [m]
$k_2 = 14085$ [N/m]	the trim corrector rigidity (took identically with main spring)
$k_{CB} = 245166$ [N/m]	the compression stopper buffer rigidity
$k_{TD} = 350237$ [N/m]	the rebound stopper buffer rigidity
$\delta_{U-F} = 0.0835$ [m]	the suspension stroke between unloaded to fully loaded state

$$\delta_{U-F} = \frac{G_F - G_U}{k_S} = \frac{(360 - 240) \cdot 9.80665}{14085} = 0.0835 \text{ [m]} \quad (1)$$

## Test Conditions

The simulation was realized for fully loaded car using a road generated by a sum of harmonic functions presented in Eq. (2).



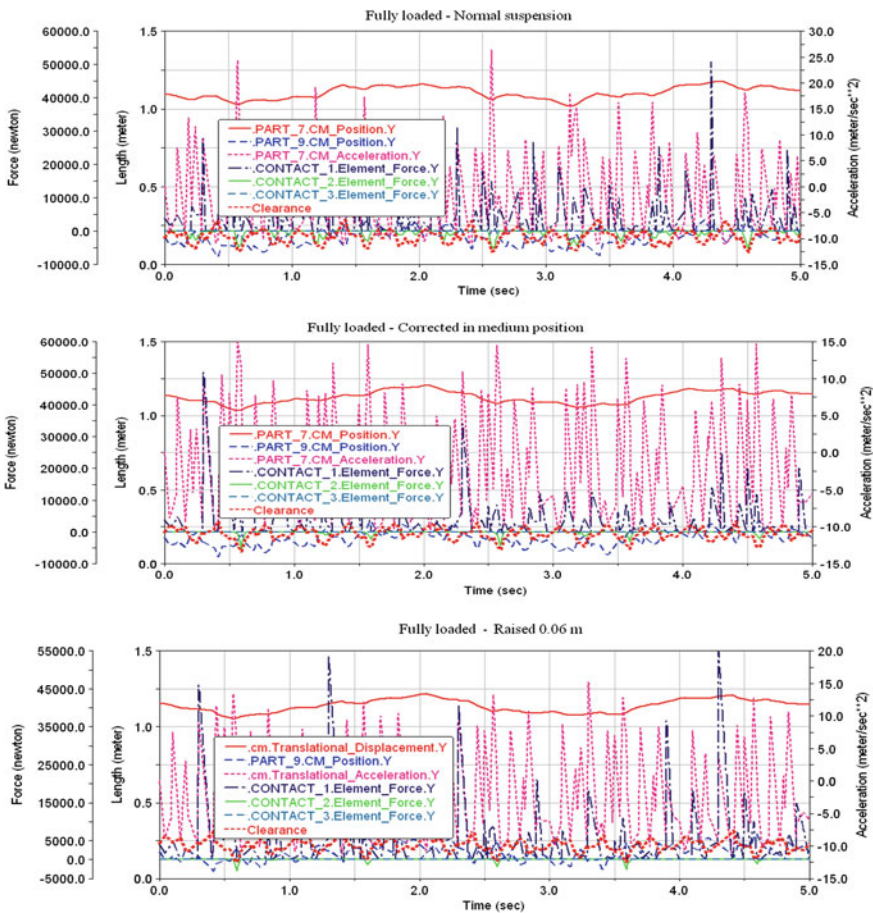
The excitation covers the specific frequencies area, being under the body frequencies up to the wheel proper frequencies.

$$h = 0.05 \sin(2\pi \cdot 0.4 \cdot t) + 0.04 \sin(2\pi \cdot 3 \cdot t) + 0.03 \sin(2\pi \cdot 8 \cdot t) + 0.02 \sin(2\pi \cdot 15 \cdot t) \quad (2)$$

## Results

The simulation were realized for the suspension no trim corrector action and with trim corrector lifting the car body 0.04175 [m] (representing medium stroke position) and 0.06 [m], the result being presented in the Table 3.

**Table 3** The simulation results



The parameters for behavior evaluation are:

- Body-road clearance, evaluated by RMS and minimal values
- Comfort, evaluated by RMS and maximal car body vertical accelerations;
- Adherence, evaluated by wheel-road RMS contact force;
- Body and axles protection, evaluated by RMS and maximal buffer strike force

Where: RMS—root mean square

In the diagrams:

- PART\_7.CM\_Position.Y—represents the vertical body position
- PART\_7.CM\_Acceleration.Y—represents the vertical body acceleration
- PART\_9.CM\_Position.Y—represents the longitudinal road profile
- (CONTACT\_1), (CONTACT\_2) and (CONTACT\_3) were defined previous

In the Table 4 are presented the performances improvement, due to the trim corrector action.

The evaluation is realized comparing each result with value corresponding situation without trim corrector.

**Table 4** The performances improvement, due to the trim corrector action

Fully loaded						
Parameter		Normal position	Raised in medium position		Raised 0.06 m	
		Values	Values	Improvement (%)	Values	Improvement (%)
Body-ground clearance [m]	RMS	0.179	0.204	14	0.219	22.32
	Minimal	0.079	0.082	4.4	0.106	34.39
Vertical body acceleration [m/s <sup>2</sup> ]	RMS	8.444	7.781	7.85	7.743	8.31
	Maximal	26.342	14.939	43.3	15.149	42.49
Adherence [N]	RMS	8927.932	7303.795	-18.19	10235.58	14.65
Force in compression buffer [N]	RMS	1401.342	745.963	46.77	0	100
	Maximal	5666.359	5139.972	9.29	2941.499	48.1

## Conclusions

The simulations confirm the trim corrector increases the suspension performances, thus for the analyzed case the trim corrector increase simultaneous:

• Body-ground clearance	—evaluated by RMS values	between 14 ÷ 22.3 %
	—evaluated by minimal value	between 4.4 ÷ 34.4 %
• Body comfort	—evaluated by RMS values	between 7.9 ÷ 8.3 %
	—evaluated by maximal body acceleration	between 43.3 ÷ 42.5 %
• Adherence	—evaluated by RMS wheel-ground contact force	between -18.2 ÷ 14.7 %
• Body/axles protection	—evaluated by RMS buffer force	between 46.8 ÷ 100 %
	—evaluated by maximal buffer force	between 9.3 ÷ 48.1 %

The novel trim corrector solutions can be applied even on the Macpherson variants improving performances on all variants by trim correction step by step or for better behavior in real time trim control.

On good roads, by reducing body-ground clearance, decreases pitch and roll axes and thus increasing stability at pitch and roll, increasing stability and cruise speed.

On bed roads, by increasing body-ground clearance, increasing passing capacity and body protection.

## Reference

ADAMS Handbook

# Forces Involved in Small Overlap Crash

Xavier Da Silva and Núria Parera

**Abstract** Recent crashworthiness studies in the EU and the USA found higher severity (deformation and occupant injuries) in frontal crashes when the vehicle was loaded outboard (small overlap). IIHS began a small overlap front crashworthiness evaluation in 2012. Two strategies to deal with the problems of cage intrusion and lateral motion were followed by manufacturers: sliding away from the barrier with lateral translation or absorbing energy with rotation. After several crash test and crashworthiness analyses, IDIADA determined the importance of identifying the forces applied in each structural element involved in small overlap crash. A need to know about how vehicles react to small overlap impact was identified, and in order to help manufacturers with vehicle development a small overlap barrier able to record forces was built. This barrier could obtain force information of each important structural vehicle element such as hinge pillar, footwell, rocker panel, etc. during the crash. The instrumented barrier helps to correlate simulation and improve elements in order to reduce cage intrusion and reduce occupant injuries. The load cells in the barrier are tri-axial in order to obtain information from the X, Y and Z axes; this being especially important at the corner of the barrier where the translation and rotation of the vehicle takes place. The results will help to analyse the forces involved in vehicle structural areas and the influence of energy absorption and lateral motion strategies will be analysed in order to have a better knowledge of the vehicle response under this crash situation.

**Keywords** Impact test · Accident analysis · Barrier · Data analysis

---

X. Da Silva (✉) · N. Parera  
Applus+IDIADA, L'Albornar, PO Box 20 E-43710, Santa Oliva (Tarragona), Spain  
e-mail: xavier.dasilva@idiada.com

N. Parera  
e-mail: nuria.parera@idiada.com

## Introduction

New systems such as ESP, crash avoidance and line control have helped in the mitigation of frontal crashes. Additionally, the quality of crashworthiness data in the EU and the USA has increased due to the awareness of the value of this data in helping to have better knowledge in accidentology in terms of occupant injuries and intrusion patterns. Focusing on more severe frontal crashes, a large percentage of fatalities was found in newer vehicles in which engagement of frontal structures was limited. State of art small overlap frontal and oblique crashes are a new research priority for NHTSA (2009), Brumbelow and Zuby (2009) as was previously introduced by IIHS.

IDIADA initiated a development program with the aim of creating a new design of fully instrumented barrier to identify forces involved in small overlap crashes. After several crash tests and crashworthiness analyses, IDIADA identified the importance of the forces applied in each structural element involved in a small overlap crash. A need for knowledge about how vehicles react to SOI (small overlap impact) was identified and in order to help manufacturers with vehicle development a small overlap barrier able to record forces was developed. Better structural designs will lead to lower intrusions and decreased fatalities on the road.

## Crashworthiness Data

Currently the SOI test is only implemented in US consumer tests and therefore it is only applicable to vehicles sold in the US market. However, Lindquist et al. (2004) identified that 34 % of fatal frontal crashes in Sweden were SOI. Moreover, accident data from FIMCAR (Lenard 2006) showed that nearly 20 % of the frontal crashes analysed corresponded to an overlap lower than 25 % (Fig. 1).

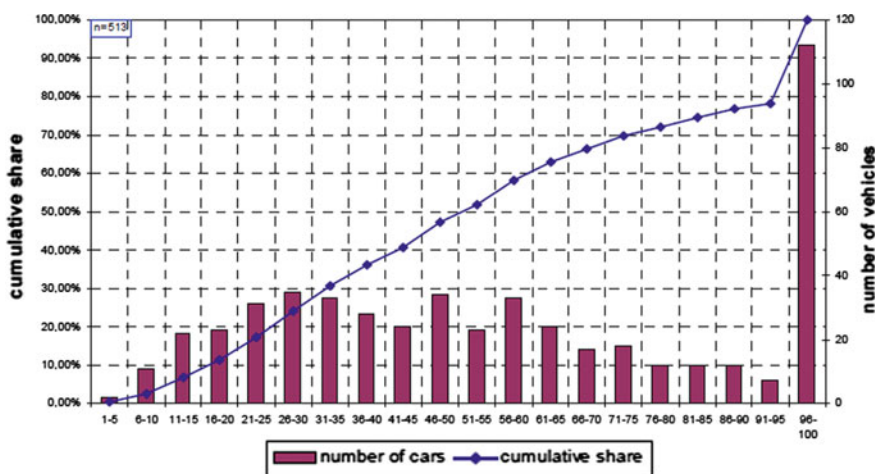
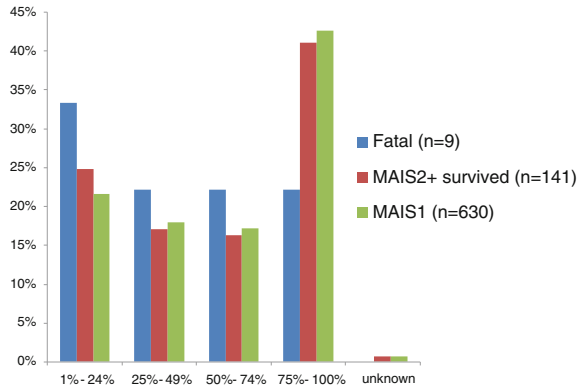


Fig. 1 Level of overlap in the PENDANT cases. Source Lenard (2006)

**Fig. 2** Outcome severity depending on the impact overlap. *Source* Thompson et al. (2011)



Results from FIMCAR project (Thompson et al. 2011) using GIDAS accident data show a higher rate of fatal outcome for lower overlap rates (Fig. 2).

### Small Overlap Impact Test

IIHS (Insurance Institutes of Highway Safety) introduced small overlap as a consumer test in the US after crashworthiness research with new cars with good results in full frontal and offset (40 %) crash test (Insurance Institute for Highway Safety 2012). Results showed a new scenario of fatal accidents without engagement of structural elements designed for frontal crash (Da Silva and Ferrer 2014). A test was carried out to reproduce real small overlap crashes. Vehicle was propelled at 64.4 km/h toward a rigid barrier; this was designed to replicate what happens in field cases when the front corner of a vehicle collides with another vehicle or an object such as a tree or utility pole. The test vehicle is aligned with the rigid barrier such that the right edge of the barrier face is offset to the left of the vehicle centreline by  $25 \pm 1$  % of the vehicle width. In most cases this causes the barrier to strike directly in outboard zone of its longitudinal structural members.

IIHS is an independent, non-profit, research and communications organization that is influential in the American market, which follows IIHS vehicle results and updates over social networks and on TV. For example, in 2014 the IIHS website was in the top 10 referring websites in the USA. Due to this fact OEM’S take seriously all the requirements and specifications that IIHS demands in their crash test protocols. Recent studies reveal an influence on sales depending on small overlap results (Brumbelow and Zuby 2009). Vehicles with good performance in IIHS’s small overlap frontal crash test had positive consumer opinion and sales results compared with other vehicles with marginal or poor. Improving vehicle

design to increase crashworthiness not only improves vehicle safety but also increases sales.

## Implications of SOI Test to Vehicle Design

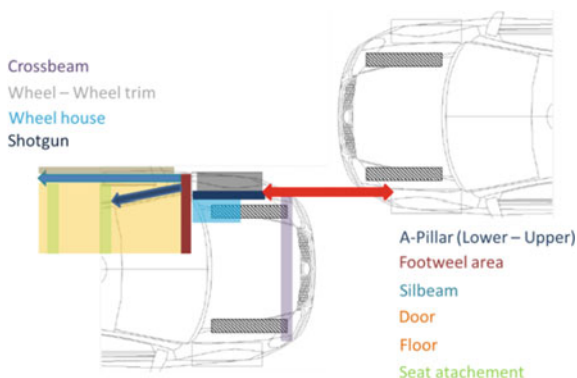
Structural elements designed for energy absorption do not interact directly with the intrusive force in small overlap crashes. This fact cause higher damage in the footwell zone, A-Pillar and rocker panel. Frequently vehicles suffer oblique kinematics, and interaction along the struck side of the vehicle increasing the chances of injuries from outboard components such as the door and A-pillar.

A detailed review of injuries shows that KTH (Knee-Thigh-Hip) and pelvis injuries frequently occur in the absence of femur fractures AIS 3+ (70 %) especially in a small overlap due to higher intrusions. Behaviour of footwell and Lower A-pillar is very important in preventing the high intrusions in lower body area. The upper body region has the second area with more percentage in AIS 3+ (42 %) in small overlap crashes, specifically in the chest area. These injuries have been caused by the contact with the belt, door and steering wheel. To improve the assessment of the dummy, modifications in restraint systems should be made to prevent and control lateral motion of dummy during the crash kinematics (Fig. 3) (Sherwood et al. 2009; Rudd et al. 2011).

Vehicle manufacturers are responding quickly to the structural challenges associated with the IIHS small overlap test. Different combinations of structural improvements for small overlap were found to be effective in reducing occupant compartment intrusion.

Countermeasures included vehicle structure modifications to promote stronger occupant compartments and new elements to absorb crash forces and reduce intrusions. However, the high pulse caused by a very stiff structure demands more reaction of the restraint system to dissipate the increase of energy.

**Fig. 3** Structural elements involved in small overlap crash



## Testing Barrier Necessity

IDIADA used an IIHS model barrier to design a new acquisition system following the protocol criterion for small overlap test. This barrier was redesigned with load cell (X, Y and Z) in frontal part. Several crashes were performed by IDIADA with this barrier, but after analysis and research of crash energies and forces, more information of the barrier should be recorded. More research and innovation adds another step forward to achieving improved barrier in order to determine the role of each structural element in barrier corner.

After an internal study of the small overlap testing results, it was seen that a large amount of information was lost during the final part of the test. This lack of information was due to rotation and translation at the barrier’s corner and that part of the barrier has no acquisition system. Energy observed for vehicle structure due the rotation and translation added another important component in structural elements used to absorb energy only in X axis. For this reason Y and Z component played another relevant scenario in this type of crash necessary to evaluate and implement countermeasures.

Figure 4 approximately represents the sum of forces registered in each delimited area by contact with barrier. Placing a vehicle without frontal bumper provided a general view of elements involved in each barrier load cell. These results showed forces involved for each structural element in frontal barrier face during crash. As can be appreciated, applied forces give a general view of loads for each set of elements or body block. However, relevant energy applied on corner by heavy

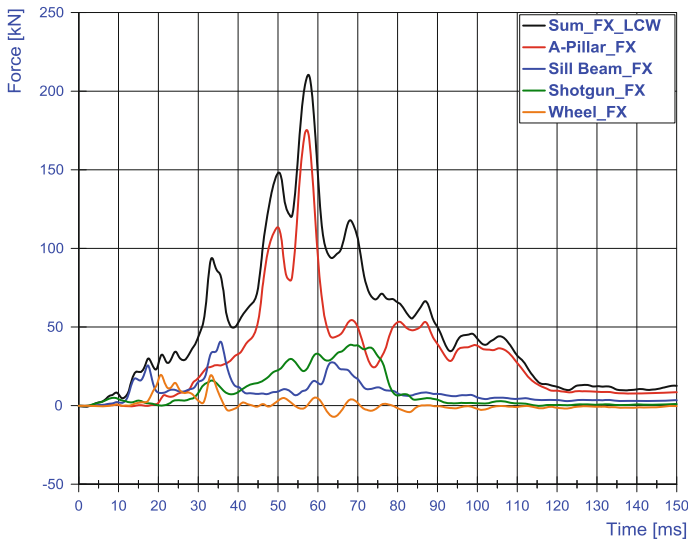


Fig. 4 Sum of the barrier’ forces obtained



components such as rocker panel or A-pillar during rotation and translation were not recorded or identified.

Additionally, in order to quantify approximately the force of the vehicle recorded during the crash and compare it with the total force ( $F_t = m * a^2$ ) assuming all limitations by friction, differences of mass and mechanical losses, a simple calculation was done. Equivalent “force” was represented by acceleration of non-structural side (B-pillar) plus weight of vehicle. The red line of Fig. 5 represents the appropriate force (in a perfect scenario) of the vehicle and the green line represents the overall forces of the small overlap barrier registered. The yellow zone represents the period of test time when the data obtained by the barrier is lower than the supposed force applied by the vehicle.

Part of the theoretical force was not recorded by the actual acquisition system. In order to know the amount of energy that was dissipated by the vehicle’s absorption mechanisms and the real energy registered by the barrier during the test, several calculations were made. From the forces registered by the barrier, the vehicle has been considered as a rigid body and the energy has been obtained by following the work equation:

$$W = \int_A^B F dx$$

Some calculus had been made in order to obtain the theoretical displacement of the vehicle and the displacement obtained by the barrier at the test. After that, the forces shown in Fig. 5 have been integrated and represented versus the time, obtaining the results shown in Fig. 6.

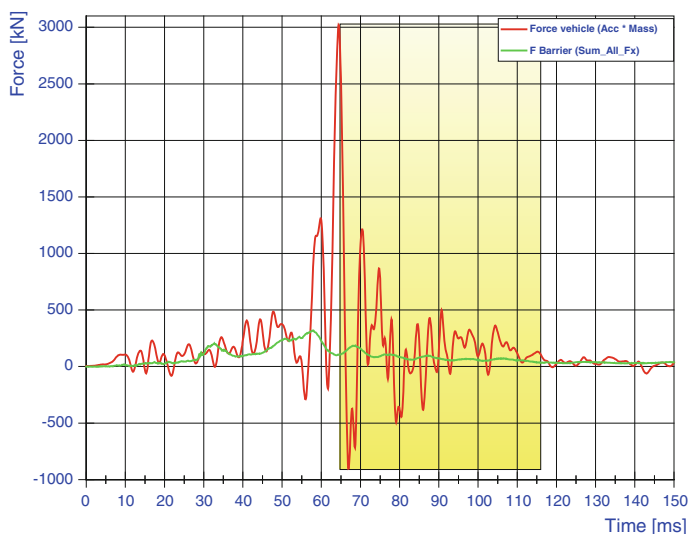


**Fig. 5** Comparison between the barrier and theoretical vehicle force

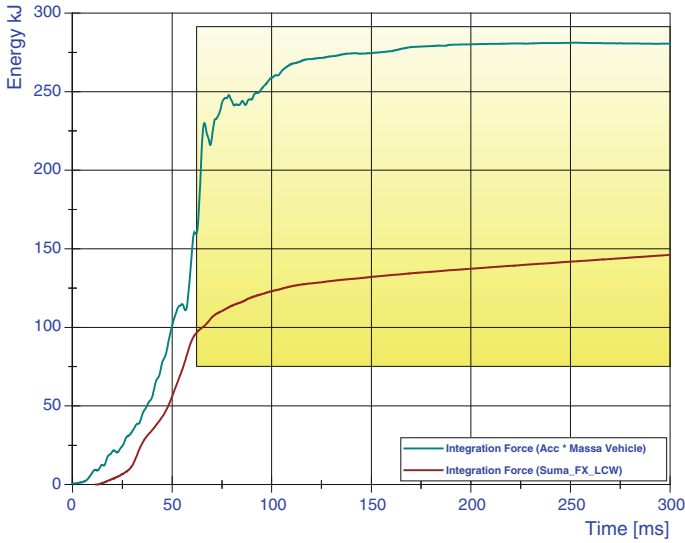


**Fig. 6** Comparative of Barrier’s energy versus equivalent vehicle energy

As can be seen in Fig. 6, the difference between the theoretical energy of the vehicle (green) and the energy registered by the barrier (red) coincides with the results of Fig. 5. A gap of energy between the lines that should not be this big (both lines should be similar) can be seen. This gap is due to the amount of data that cannot be obtained due to the lack of load cells at the corner of the barrier.

The instrumentation of the corner will give data of the maximum forces produced during the test at the corner and will obtain more information about which forces make the vehicle rotate, deform and the role of each structural element. Also, the full instrumentation of the barrier will offer new data about the wheel’s kinematics during the test. This will imply new test data not available before that will help to have a better knowledge of one of the most important structural parts of the vehicle. Knowing this data will be extremely important to improving the structural mechanism to absorb energy during the crash and know how elements involved in wheel disconnection or wheel intrusion behave.

### Testing Improvement

The barrier has been redesigned at Applus+IDIADA adding load cells to the previous barrier which only had load cells at the front. A new acquisition system has been implemented at the corner of the barrier ensuring non-deformation. Triaxle load cells have been set along the centre of the barrier and at the corner, obtaining

**Fig. 7** Small overlap barrier acquisition system



information during all vehicle contact with barrier at all testing time in X, Y, Z directions.

The triaxle cells will offer more information such as the vehicle's kinematics during the test and at the rotation and translation at the corner (Fig. 7).

Also, the structure was redesigned to guarantee no deformation or rupture due to the new load cells and was reinforced at the frontal and corner area to protect the acquisition system. The load cells in corner fulfil IIHS protocol and provide a continuous reading during crash. In order to protect the load cells placed at the centre and at the corner, special tools were designed and developed to create a uniform surface for the entire barrier.

Also, these tools offer the possibility to replace each load cell one by one without taking all of them out. Load cell shields in frontal area have square and radial shape in corner. Tooling built can be seen in Fig. 8.

The tool for the corner had to be round, and the screws that fixed the tool to the barrier were specially designed in order to guarantee a perfect and uniform surface at the corner.

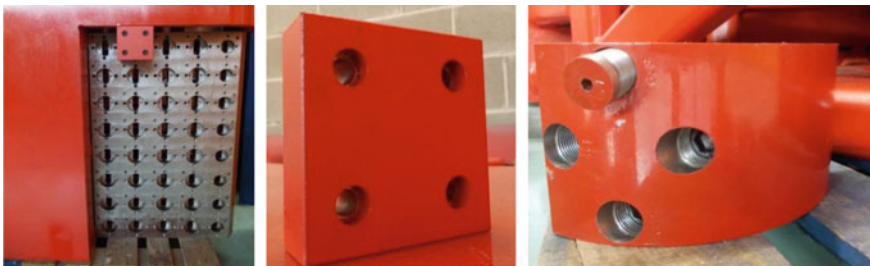


**Fig. 8** Square tool for the centre of the barrier and corner of the barrier

## Results

A test validation was carried out with a similar structural vehicle in order to be able to compare the data obtained between the old barrier and the new one. Vehicles had similar weight, but due to confidentially, no testing information can be attached. A force diagram was elaborated by the acquisition system of the barrier. As can be seen in Fig. 9, the first impact of the car is almost not noticed by the old barrier while the new barrier has valuable data.

Because the vehicle tested with the old barrier was slightly different (both SUV with similar weights) from the one tested with the new barrier, it can be seen that the timing of the tests was different. For example at 29 ms in the old test the vehicle's wheel impacted the barrier while with the new barrier it did not. However the importance of the validation test is to compare in time the differences in forces and distribution (Fig. 10).

At 36 ms both vehicles' wheels impacted the barrier. However, the information obtained by the new barrier is more accurate and has a wider range (Fig. 11).

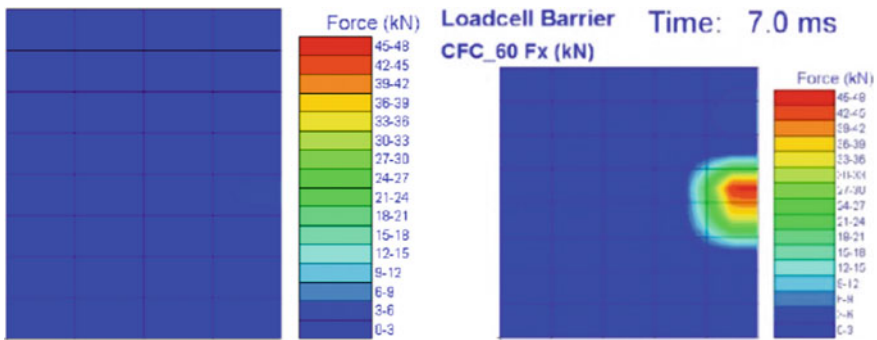


Fig. 9 Old barrier (left) versus new barrier (right) at 7 ms

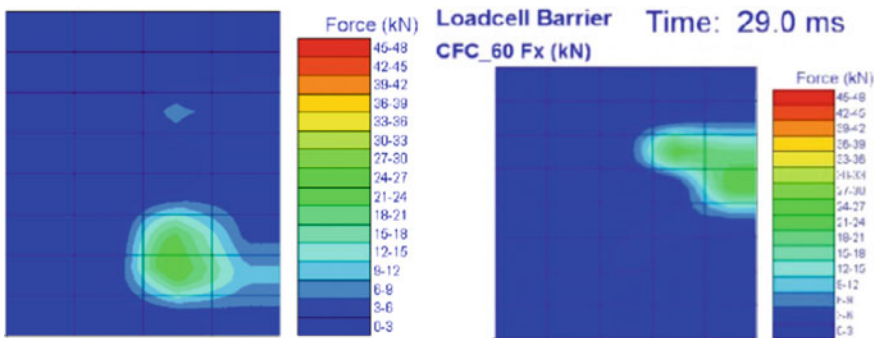


Fig. 10 Old barrier (left) versus new barrier (right) at 29 ms

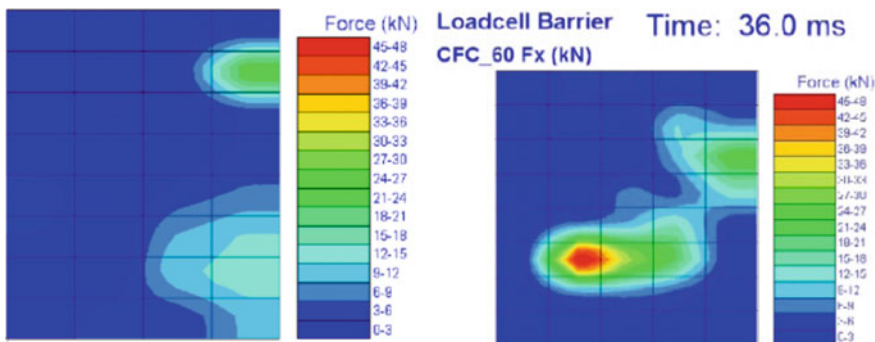


Fig. 11 Old barrier (left) versus new barrier (right) at 36 ms

While wheel block and rocker panel impacted the barrier at 60 ms, higher forces can be seen in the new barrier than the older one. The new results show that the only high forces present in the lower part of the diagram are the ones created by the wheel.

Also, high forces are present at the upper part of the barrier’s corner due the interaction of shotgun and junction with upper A-pillar. These forces are relevant to controlling the vehicle trajectory and slide it off the barrier according to the manufacturer’s strategy (Fig. 12).

At 69 ms the forces applied by vehicle on barrier affirm increase of red forces at starting oblique movement. Influence on upper A-pillar will help to identify intrusive forces that lead to deformations in engine compartment. These intrusions affect cross car beam and steering column changing restraint system behaviour leading to reduced airbag interaction with occupants (Fig. 13).

The new acquisition system provides more information from the beginning of the test until the end of the vehicle’s separation. In the validation test of the new barrier, no vehicle front structure or response measures were measured.

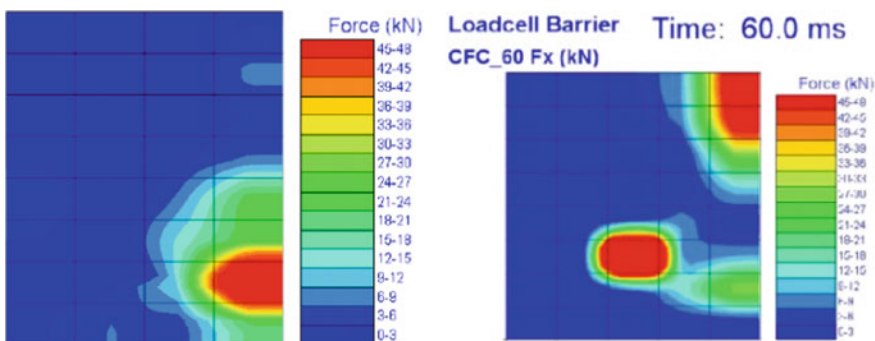


Fig. 12 Old barrier (left) versus new barrier (right) at 60 ms

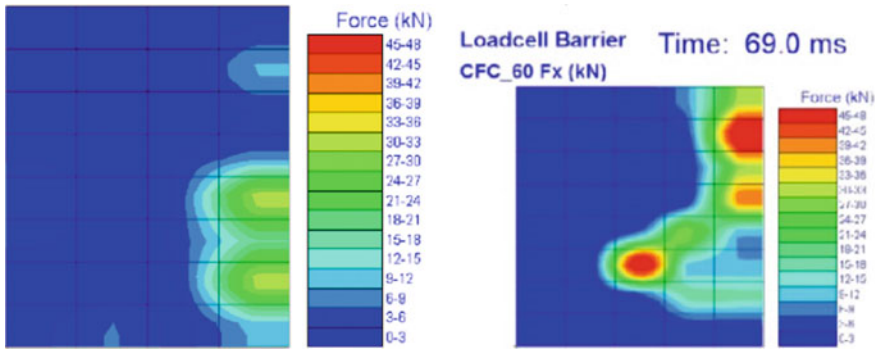


Fig. 13 Old barrier (left) versus new barrier (right) at 69 ms

### Conclusion

The comparison between the new acquisition system barriers data provides more information to improve the testing equipment for critical translations and oblique movements in vehicles for small overlap test. More information during a crash test contributes to a better understanding of the structural element’s behaviour under compression and rotation forces. Due to this, new countermeasures in multiple vehicle structures to promote stronger occupant compartments were introduced to absorb the crash forces. Implementation of new structural crush areas will reduce harmful intrusions in occupant compartment.

Different combinations of structural improvements for small overlap were found to be effective in reducing occupant compartment intrusions and improving dummy kinematics in the IIHS small overlap test. Better testing tools give information to manufacturers to improve the state of art under this testing scenario.

The obtainment of better correlations in forces during crash provides essential information to face the challenges involved in new testing procedures. These improvements cannot be done without a fully instrumented barrier, which is able to record and analyse all the available data during the test and correlate the effectiveness of each structural improvement. The development of new testing tools has importance, most of all to improve and develop vehicles and offer a better level of safety to road users.

**Acknowledgments** This work was supported by IDIADA Automotive Technology and all co-workers involved in the project.

## References

- Brumbelow ML, Zuby DS (2009) Impact and injury patterns in frontal crashes of vehicles with good ratings for frontal crash protection. Paper no. 09-0257. In: Proceedings of the 21st international technical conference on the enhanced safety of vehicles. National Highway Traffic Safety Administration, Washington, DC
- Da silva X, Ferrer A (2014) Study of the similarity between small overlap impact (SOI) crashworthiness tests and real SOI accidents in Spain. SAE Brasil
- Insurance Institute for Highway Safety (2012) Small overlap frontal crashworthiness evaluation crash test protocol (ver. II). Arlington, VA
- Jakobsson L, McNally G, Axelson A, Lindman M, Kling A, Broberg T, Fermér M, Wågström L (2013) Severe frontal collisions with partial overlap: two decades of car safety development. SAE technical paper 2013-01-0759. SAE International, Warrendale, PA
- Lenard J (2006) PENDANT: a European crash injury database. In: 2nd expert symposium on accident research. Hannover
- Lindquist M, Hall A, Björnstig U (2004) Car structural characteristics of fatal frontal crashes in Sweden. *Int J Crashworthiness* 9:587–597
- NHTSA (2009) Research priority plan 2009–2011 published in Nov 2009
- Rudd R, Scarboro M, Saunders J (2011) Injury analysis of real-world small overlap and oblique frontal crashes. In: 22nd ESV conference, Paper. NO. 11-0384
- Sherwood C, Nolan J, Zuby D (2009) Characteristics of small overlap crashes. In: Proceedings of 21st international ESV technical conference [book on CD-ROM]. National Highway Traffic Safety Administration, Washington, DC
- Thompson A, Edwards M, Wisch M, Adolph T, Krusper A, Thomson R, Johannsen H (2011) Report detailing the analysis of national accident databases. FP7 European Commission FIMCAR project. GA no. 234216

# State of the Sm-Art Components Used on Autonomous Platforms for Sustainable Mobility

Valerian Croitorescu and Yassine Ruichek

**Abstract** Mobility is fundamental to our society and economy. It must be sustainable to assure a prosperous future for everybody. While supporting economy, meeting travel needs and ensuring a long-term viability for the transport systems, the natural environment needs preservation for mobility upgrade. The revolution of the mobility will be assured by vehicle electrification and autonomous driving. The mobility of the future will provide various options to address and will implement the main aspects of sustainability. Cities all around Europe must be well-prepared for the changes that will be initiated by these two fast developing technological fields in order to gain a maximum benefit towards sustainable mobility. This paper emphasizes the basis of an autonomous vehicle in terms of design and its functional behavior following certain goals. Once implemented inside a university campus, the possibility for replicating all the activities is just around the corner.

**Keywords** Autonomous driving • Modular platform • Virtual design • Electric vehicles • Smart mobility

---

V. Croitorescu (✉)

Scientific Research and Continuous Training Center for Sustainable Automotive Technologies, Faculty of Transport, University POLITEHNICA of Bucharest, 313 Splaiul Independentei St., 6th Sector, Bucharest, Romania  
e-mail: valerian.croitorescu@upb.ro

Y. Ruichek

IRTES (Institut de Recherche sur les Transports, l'Énergie et la Société)—SET Laboratory (Laboratoire Systèmes et Transports), University of Technology of Belfort-Montbéliard, Rue Thierry Mieg, 90010 Belfort Cedex, France  
e-mail: yassine.ruichek@utbm.fr



## **Introduction**

More than 66 % of the world population will be living in urban areas by 2020, while nowadays urban areas are responsible for about one quarter of CO<sub>2</sub> emissions from transport. According to the Impact Assessment SEC(2011) 358 of the European Commission, without efficient steps towards sustainable mobility the CO<sub>2</sub> emissions from transport would remain one third higher than their 1990 level by 2050. According to the “White Paper on Transport”, one of the requirements is to achieve a reduction of the greenhouse gas emission with at least 60 % by 2050 in the transport sector of the European Union (EU) with respect to 1990.

Due to the increased pollution, the costs related to fossil fuels usage and because vehicles are crowding the urban areas, the transition to the ‘low carbon’ or ‘no carbon’ vehicles is mandatory. The quality of life, low harmful emissions and decongestion inside cities are increasing their importance, more than ever.

Sustainable electric mobility needs to be tackled on all major urban areas, supporting also the cities both for becoming smart and innovative and citizens friendly. The problems regarding the urban environmental concerns is represented by the most important task in terms of mobility. Using one solution available, the electric mobility, a forward step for a cleaner urban environment is made. As a response to these issues, all vehicles manufacturers are harnessing cutting edge technologies to enable sustainable vehicles in urban environments.

In addition, futuristic tasks are also taken into account. The autonomous driving represents another key element that will revolutionize the future mobility while providing various options to address and implement the main aspects of sustainability.

Local administrations and governments all around Europe must be well-prepared for the changes that will be initiated by the fast developing technological fields in order to gain a maximum benefit towards sustainable mobility.

The objective of the paper is to highlight the possibility of using autonomous driving feature on electric vehicles in urban areas, their functional behavior and part of the components that are mandatory for a basic utilization.

## **Mobility in Terms of Vehicle Technology and Innovative Applications**

Electric vehicles development plays an important role for all global car-manufacturers since this is a key-technology to reach the goals of CO<sub>2</sub> reduction. Both hybrid and electric vehicles are already available for commercial use. However, research and new developments in these fields are necessary to make electric vehicles more efficient and affordable.

The autonomous driving represents another important development that is meant to increase the possibility for the mobility management dimension. The citizens will

benefit substantially from using autonomous driving systems since they gain more freedom of individual mobility and they have the option of spending the time with other tasks while the vehicles are self-driven. From futuristic autonomously parking to light public transport as a primary step, other tasks are able to be performed by autonomous vehicles that can be used for freight transport or public services. The functional needs for the autonomous driving vehicles include the precise controllability, which can be easily offered by the electric vehicles due to their electrified actuators.

The combination of the two technologies, electric vehicles and autonomous driving, offers a promising possibility to achieve viable innovative solutions towards sustainable mobility. *Higher efficiency in public transport* is achieved, also for short distances at vehicles low velocities, taking into account the decongestion into urban city centers and the usage inside private campuses, large exhibitions, inside big parking lots and shopping centers, close to big transport hubs (train-bus-metro-airport) allowing linking the surrounding stations. *Higher efficiency in light freight transport* is achieved by using adequately the public space and the daily working hours, not to over jam the existing activities, for mailing delivery and goods transport. *Higher efficiency in parking* is achieved, by gaining more vehicle storage inside parking lots and by increasing the safety, taking into account also the autonomous 'valet-parking'. *Higher efficiency in public services* is achieved for maintenance services, by day or by night, avoiding the rush hours.

The technology has been accelerated following these reasons, being able to meet the goals for better mobility.

## The Legislative Boundaries

The electric vehicles regulations stated by the European Commission require considerable research and technology development investments on the present trend, when better energy efficiency and less greenhouse gas emissions are mandatory. The regulations can be divided for the different equipment needed for the electric vehicles, including also the grid connectivity and compatibility. Standardization is needed for the charging infrastructure, for the vehicle to grid connection and for the safety and test cycles. The connection to the power network has to follow comprehensive standards and normative in order to permit recharging the energy storage system, preferable using common interfaces agreed worldwide, not to fragment the market with incompatible solutions and to reduce the costs. An intensive work on standardization is running regarding the connectors, charging stations and communication interfaces by the International Standardization Organization (ISO), International Electrotechnical Commission (IEC) and European Committee for Electrotechnical Standardization (CENELEC). United Nations Economic Commission for Europe (UNECE) Regulation 100 provides norms for users' safety on high voltage vehicles equipment.

Not only the technological limitations represent boundaries difficult to pass, but also current regulations like the Vienna Convention on Road Traffic represent an obstacle in front of autonomous driving vehicles usage on European roads. This topic is already addressed by the United Nations Economic Commission for Europe (UNECE) where regulatory action is currently going on. In order to promote this new technology and all its advantages, even if on private roads and private places their operation is set and is already available, their operation in a first step only at low velocities on public roads represent a reasonable approach to start establishing autonomous driving in application with low risk.

## The Infrastructure Boundaries

The current available infrastructure dedicated to electric vehicles is less than needed in most European countries. As the economic and the technological barriers are addressed, the market penetration with regard to electric vehicles is increasing and the infrastructure for the power supply is continuously developing, the potential customers are accepting the mobility patterns.

One issue is related to the energy consumption by the electric vehicles and their need to recharge the energy storage. Although, the grid capacity is not considered as impediment to that, as only a fraction of the total energy will be consumed. But, for a large number of energy storage systems used on vehicles, additional energy quantities will be needed. The capabilities of a charging station include the prevention system for peak loads. The intelligent billing systems are also required in order to encourage the potential users, being part of the infrastructure. The appropriate infrastructure has to provide the available and the necessary density for the requested recharging. The installation has to include private and public places, to use desired interfaces and to ensure interoperability and connectivity with the electricity supplier. The safety risks and the electromagnetic compatibility has to be also considered. (Croitorescu 2012)

Directly related to the infrastructure availability, the batteries are following the latest technologies. Different materials are used for producing batteries, being added to various architectures possible to be adopted. Several further technologies are under development and could be available soon for vehicle applications. The batteries target is the autonomy/driving range given, and a complementary adequate charging time and low power losses during it. The costs are the major decision factor, beside the volume and the weight of the battery packages. The battery should be used as a possible 'feeder' of the electricity system on a later date. Therefore, their design should follow the paths for at least keeping their lifetime untouched (Croitorescu 2012).

The existing infrastructure is approachable for using autonomous driving vehicles, but better developed communication are needed. Vehicle to vehicle, vehicle to infrastructure and vehicle to human are subjects for continuously research and innovation activities. For safety operations, the advanced driving systems that are

already used on current vehicles have to be adapted to the ‘no driver’ option (Croitorescu 2014).

## The Vehicle Architecture

The vehicle is designed on a modular platform, using a dedicated chassis structure, for easily different configurations selection. The electric powertrain contains the electric machine, the battery package, the power electronics and the autonomous driving dedicated systems. All these equipment are placed inside the chassis structure, not disturbing the body shape of the vehicle, neither the passengers nor baggage compartments.

In the framework of CPER 2006–2013 (Contrat Pan Etat Région) at UTBM, the IRTES-SET laboratory has developed an experimental platform composed with automated electrical vehicles, equipped with different sensors for perception and localization (cameras, LIDARS, GPS, IMU, etc.), and communication interfaces (Fig. 1). Running with low speeds, the vehicles are dedicated to be automated and instrumented for autonomous driving in urban areas. The sensors are gathered as a network of sensors to develop data fusion architecture. This allows to acquire data coming from different sensors with a synchronous manner. Basing on redundancy, data fusion is fundamental to achieve more precise, robust and reliable perception and localization for autonomous vehicles.

## The Challenges and the Dedicated Equipment

The technological challenges are connected to several related scientific issues in order to obtain ‘smart vehicles’ and mobility.

Developing advanced driving assistance systems needs to develop new collaborative approaches for a more secure and comfortable driving (better information to



**Fig. 1** SetCar: experimental platform of the IRTES-SET laboratory of UTBM

the driver, more autonomy for the vehicle, intelligent and ergonomic access to embedded services) and to develop systems for monitoring risks (crossings, schools exit).

The vehicle integration in the traffic regulation process is important in terms of negotiating the rights of way and courses reservation, having the goal to develop traffic ‘smart’ regulation.

The eco-driving can be accomplished by the integration of information extracted from the vehicle environment, to optimize driving in terms of energy consumption (vehicle tracking, behavior modification approach to the tri-color lights), to develop information systems providing services that help reducing energy consumption (avoiding traffic jams).

New approaches to mobile location ensuring availability, integrity and accuracy, through the combination of multiple sources of information including the new Galileo constellations are needed to localize the vehicles in real time (Marais et al. 2014).

The autonomous driving vehicles take part from one of the five levels of development, defined by the National Highway Traffic Safety Administration (NHTSA). Each level corresponds to the ability to drive with or without partial intervention from the driver. Based on these definitions, an autonomous driving vehicle can include different equipment and systems, used for the tasks from the driver is privileged, briefly explained in the following. Level 0 is dedicated only to vehicle with driver’s complete control. Level 1 is meant when not more than two safety activities are assisted by automatic systems, for example the automatic braking and the electronic stability control, but the driver still have the complete final decision. Level 2 allows to use at least two automatized functions together, for situations close to limits, for example the adaptive cruise control and the lane keeping system, but the driver has the entire responsibility for the vehicle state of functioning. Level 3 is represented by the existence of many automatized systems, as many as the vehicle configuration support, that are not asking the driver intervention for their activities, these systems taking the complete decision for the tasks to be done, but being ready to let the command to the driver and to seize him immediately in order to have the time to action. Level 4 is characterized by no intervention from the driver, the vehicle is able to operate by itself in any conditions, for any driving scenarios, by anticipating the road and the obstacles during the travel, using the information given by the driver regarding the destination; at this level the vehicle can run without any human presence inside the vehicle.

In order to accomplish the automated driving function, several equipment are mandatory to be used. Among the equipment needed, the key components consist in the Radio Detection And Ranging (RADAR), the 2D/3D Light Detection And Ranging (LIDAR), mono-vision systems (with one video camera), multi-vision systems (two or more video cameras), the Global Positioning System (GPS), the inertial navigation systems, etc.

The *RADAR* is able to determine the geometrical position, the speed and the direction of an object using radio waves, being able to monitor the presence of other vehicles, any obstacles and/or pedestrians. The ‘blind-spot detection’, the adaptive

cruise control' and the 'autonomous parking' systems are able to work only if the radar is operating correctly.

*The LIDAR* is able to determine the distance to and between obstacles using laser scanning technologies and analyzing the reflected light, with high precision. Based on the resulted information, road maps are able to be defined.

*The GPS* is a global navigation system that receives radio waves and uses them as reference points on the ground. The precise geometrical position can be determined.

*The vision systems* deliver contextual information (forms, colors and texture of objects) compared to RADAR and LIDAR sensors. They allow through image processing and analysis to estimate motion, 3D structure and recognition of objects in dynamic scenes.

The best way to use these different sensorial systems is to put them in a data fusion framework. For example, combining LIDAR and vision systems has become a popular approach for environment perception. For vehicle localization, last developments are based on combining GPS and vision/LIDAR systems for improvement in terms of precision and mitigation.

## Inside Campus Implementation and Operation

The IRTES-SET laboratory has implemented several projects on perception and localization for intelligent vehicles and autonomous driving. In (Li 2013), a method for occupancy Grid Map (OGM) construction is proposed for vehicle environment representation. The method is based on LIDAR information and disparity map extracted from stereovision. Moving objects are detected and segmented using visual odometry and U-disparity. The detected objects are also classified and recognized (pedestrians, cyclists, cars) using special features extracted by a method based on Kernel Principal Component Analysis. Figure 2 illustrates OGM construction. This work was part of the IGV project (Intelligence of Ground Vehicles), which was part of CPER 2006–2013 at UTBM.

In (Marais et al. 2014), a data fusion method for vehicle localization is proposed to take into account GNSS signal propagation conditions. This type of analysis is needed particularly in dense environments. Indeed, within dense environments, GNSS signals could be reflected depending on the structure of the environment surrounding the GPS receiver. This problem has an effect on to the position estimation. To tackle this situation, the environment of the GPS receiver need to be characterized. For that, a fisheye camera close to the GPS receiver to observe the sky was installed. The acquired images are segmented and the regions are classified into two classes: sky and no-sky using color and/or texture information. The satellites are then projected onto the image to detect satellites that are received directly and those that are blocked or received indirectly. The position can be then estimated by using only the visible satellites from the received and/or using also those received through multi-path following different models.

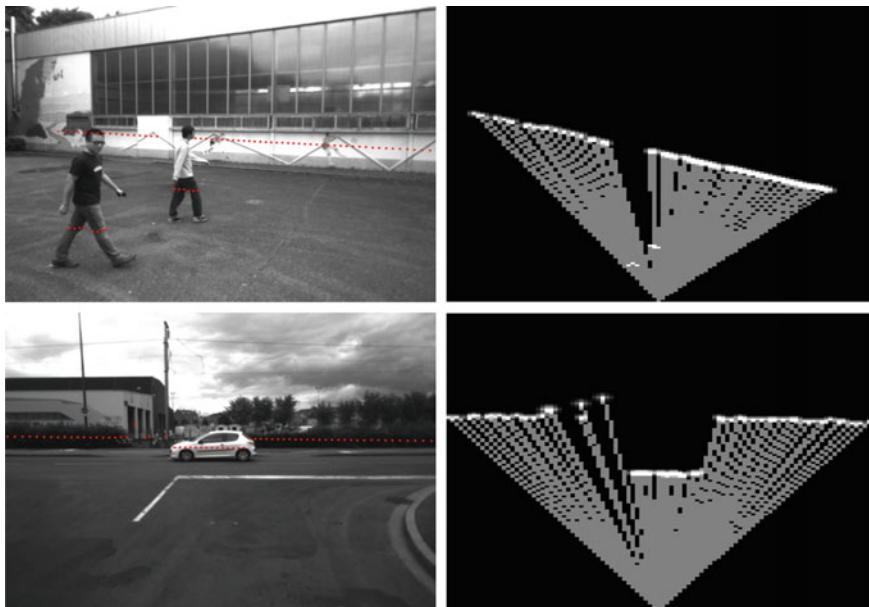


**Fig. 2** OGM construction using LIDAR and stereovision

This work was part of the CAPLOC project (Combination of image analysis and Signal Propagation Knowledge for localization), supported by the PREDIT (Programme de Recherche et d'Innovation dans les Transports Terrestres), and developed jointly with IFSTTAR (Institut Français des Sciences et Technologies des Transports, de l'aménagement et des réseaux). Figure 3 shows some results about the sky and no-sky detection and satellite position projection.

In the framework of the SafePlatoon project (Safe Platoon of Autonomous Vehicles), supported by the ANR (Agence Nationale de la Recherche), IRITES-SET has conducted research on autonomous platooning. The objective is to put vehicles within a chain and the objective is that all the vehicles follow autonomously one of them, the first one in the case of road traveling (linear configuration). The



**Fig. 3** Segmentation/classification (sky and no-sky regions) and satellite position projection

**Fig. 4** Platooning of autonomous vehicles—the head vehicle is driven manually and the others follow it autonomously



developed approach is based on Multi-Agent Systems Paradigm (Dafflon et al. 2013). Figure 4 illustrates the concept of platooning.

## Conclusions and Discussions

The future prediction include most of the vehicles manufacturers' plans in terms of mobility. Mercedes intend to introduce the 'Autobahn Pilot' system that allows vehicles driving without the driver intervention at all. Mobileye Company waits the urban and interurban roads improvement for supporting the autonomous driving approaches until 2018. Volvo optimism is revealed with the plans to avoid any car accidents and no human being to be heart from 2020 by using their autonomous driving vehicles. Navigant Research expect that autonomous driving vehicles will overcome 95.4 million units each year until 2035, while Institute of Electrical and Electronics (IEEE) estimates that 75 % of the vehicles will be autonomous until 2040.

Therefore, the future is constrained to research and innovation for the sustainable mobility in term of autonomous vehicles.

**Acknowledgements** The present paper contains parts from the project proposal "Autonomous Electric Modular Platform", PN-II-RUTE-2014-4-2674, under the RUTE Sub-Program competition, supported by Romanian Ministry of Education and Research. It reports also parts from CPER 2006–2013 (Contrat Plan Etat Région) at UTBM, CAPLOC project, supported by PREDIT, and SafPlatoon project, supported by ANR.

## References

- Croitorescu V (2012) Modern drives using unconventional energy storage devices—hybrid electric vehicles. Ph.D. thesis, Bucharest, Romania
- Croitorescu V (2014) Project proposal PN-II-RU-TE-2014-4-2674, Program PNCDI 2007-2014, Subprogram RUTE 2014



- Dafflon B, Gechter F, Gruer P, Koukam A (2013) Vehicle platoon and obstacle avoidance: a reactive agent approach. *IET Intell Transp Syst J* 7(3):257–264
- Li Y (2013) Stereo vision and Lidar based dynamic occupancy grid mapping: application to scenes analysis for intelligent vehicles. Ph.D. thesis, UTBM, France, Dec 2013
- Marais J, Meurie C, Attia D, Ruichek Y, Flancquart A (2014) Toward accurate localization in guided transport: combining GNSS data and imaging information. *Transp Res C* 43:188–197

# Passenger Cars Exhaust Emissions Under Real Driving Conditions

Jerzy Merkisz and Jacek Pielecha

**Abstract** This paper presents the preliminary concept research to develop the test used in the measurement of emissions in real traffic conditions for passenger vehicles. In the applied models of total exhaust emissions from transport, the emission rate is adopted based on maximum admissible values prescribed in an exhaust emission homologation standard. In such a scenario, the results obtained from the models are only estimates, whose applicability may be restricted. It is thus necessary to seek new possibilities to assess vehicle exhaust emissions such as real driving measurements. The measurements are performed under actual vehicle operating conditions and they use the PEMS (Portable Emission Measurement System) equipment. The research carried out at Poznan University of Technology with the use of this method attempts to answer questions regarding the exhaust emissions, their variability and relation to the engine and vehicle operating parameters. The paper presents several vehicles investigated for exhaust emissions under actual traffic conditions—RDE (Real Driving Emissions).

**Keywords** Exhaust emissions · Vehicle testing · Real driving emissions

## Introduction

A fundamental factor leading to technology development in all branches of industry is the need to reduce its negative impact on the natural environment. Transport is one of the most dynamically changing fields of industry, particularly due to the ever-changing exhaust emission levels. Increasing emphasis is put on the

---

J. Merkisz (✉) · J. Pielecha

Faculty of Machines and Transportation, Poznan University of Technology, Piotrowo 3,  
60-965 Poznań, Poland

e-mail: jerzy.merkisz@put.poznan.pl

J. Pielecha

e-mail: jacek.pielecha@put.poznan.pl

measurements of exhaust emissions, from combustion engines of machines and vehicles especially under actual operating conditions. These measurements much better reflect the environmental situation than the tests only simulating actual conditions of operation used thus far or stationary tests. These measurements became possible due to a significant advancement in the area of measurement techniques in recent years (Merkisz et al. 2014).

Passenger vehicles are subject to intermittent inspections at inspection stations, however the inspections are carried out for a limited (much lower than in real traffic) operating range of the engine. The assessment of the environmental performance of the vehicles may also be carried out on a chassis dynamometer. It is quite opposite for heavy-duty vehicles, in which case, in order to assess the in-service emissions, the engine must be removed from the vehicle for testing. Statistical research on a chassis dynamometer may sometimes be performed on vehicles of different applications, while the tests used in the methodology designed to assess the emissions are not at all different. The proposal for tests utilizing portable measurement systems is a universal solution as it can be used for vehicles of different applications but fitted with the same engines (Merkisz et al. 2015).

Exhaust emissions measurements from passenger cars are conducted during type-approval tests on chassis dynamometers, during road tests in real traffic conditions and on vehicle inspection stations (at the stations it is the concentration of the exhaust components not their emission that is measured). The type-approval measurements are performed on chassis dynamometers according to strictly determined procedures and are used only for new passenger cars. The aim of the NEDC (New European Driving Cycle), WLTP (Worldwide harmonized Light vehicles Test Procedures) and the American US06 (Federal Test Procedure) type-approval tests (Fig. 1) for a fixed speed profile is to control the compliance of

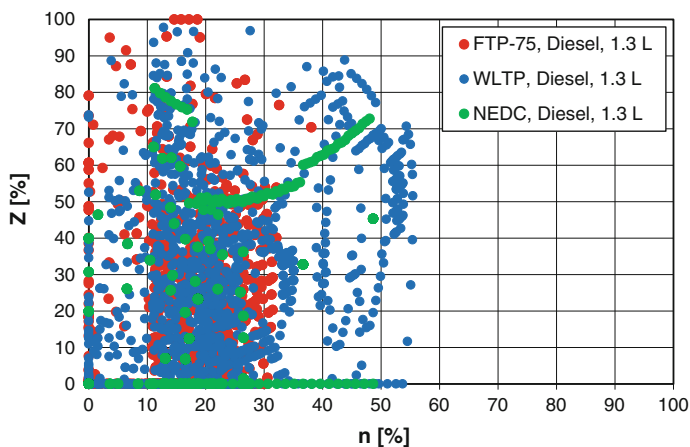


**Fig. 1** Engine operating parameters in various emissions tests (based on Fontaras et al. 2013)

the vehicles with environmental requirements (European Commission 2011, 2012). Road exhaust emissions tests of passenger vehicles are not yet legislated compared to heavy-duty vehicles, for which the NTE (Not to Exceed) test has already been designed (a test checking whether the vehicle exceeds the limit values) (Ligterink et al. 2013).

Recent research on pollutant emissions under real traffic conditions performed using mobile devices (Bougher et al. 2010) reflects the state of ecological vehicles very well. Most attention is paid to the possibility of using such research to calibrate engines (Bergmann 2013), in such a way so as to limit emissions not only during the emission test, but also in the whole operating range of the engines (Kruttsch et al. 2011). Comparative studies conducted in laboratories (Fontaras et al. 2013) indicate compliance with the emission limits for operating vehicles with petrol engines, it also indicates that vehicles with diesel engines significantly exceed the permissible emissions of nitrogen oxides (Weiss et al. 2013). Attention is drawn to significant emissions of particulate matter, mainly in the form of nanoparticles from combustion engines (Myung and Park 2012) and the dependence of such research results on terrain topography (Merkisz and Pielecha 2015). The results of such studies are currently not presented independently, but they are confirmed by articles which encompass several years of studies (Chen and Borken-Kleefeld 2014) and comprehensive summaries of vehicles researched in real traffic conditions (Franco et al. 2013, 2014). An innovative approach described in the article is the proposed emission correction coefficients, which have thus far not yet been published.

## **Portable Emissions Measurement System**

The most desirable are on-road emission tests as this is the only way to measure the actual emission level. The biggest disadvantage of this method is the price of the equipment and its adaptation to individual vehicles. Following the latest trends, the Institute of Combustion Engines and Transport equipped its Combustion Engines laboratories with modern research tools such as the system of Semtech DS, Ecostar and M.O.V.E exhaust emission analyzers with measuring probes (exhaust flow meters) manufactured by Sensors Inc. and AVL. The system of analyzers measures the exhaust emissions from combustion engines fitted in all types of machines and vehicles under the conditions of their real operation (Figs. 2 and 3).

Since 2008 a series of passenger vehicle emission tests was initiated under urban and extra urban driving conditions. A portable exhaust emission analyzer was fitted inside the vehicle and the measuring probe outside the vehicle. The tests consisted of a continuous measurement of the emissions while the vehicle was in motion on a preset road portion.

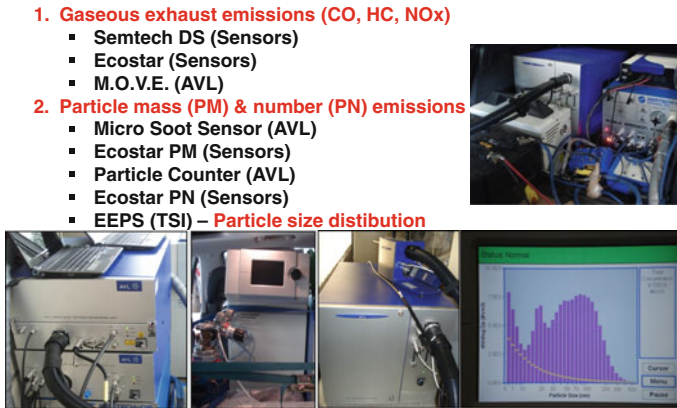


Fig. 2 The test potential under real operating conditions (analyzer Semtech DS)

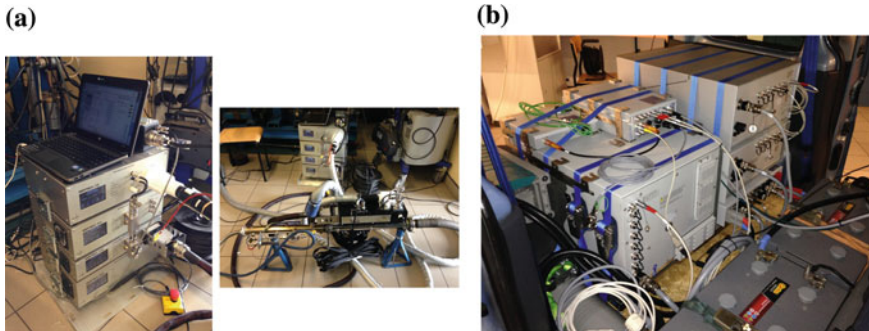


Fig. 3 The view of the analyzer for on-road emission testing of vehicles: a ecostar by sensors, b M.O.V.E by AVL

### Proposal to Define the Exhaust Emissions Indexes

The authors of the paper propose an introduction of an exhaust emissions correction coefficient ( $k$ ) denoting the multiple of the increase or decrease of the exhaust emissions under actual traffic conditions compared to the values in homologation tests. Such an index has been defined for a given exhaust component ( $k$ —exhaust emission correction coefficient):

$$k_j = \frac{E_{real,j}}{E_{NEDC(FTP-75,WLTP),j}} \tag{1}$$

where:

- $j$  exhaust component for which the emission index was determined,
- $E_{real,j}$  emission under actual traffic conditions [g/km],
- $E_{NEDC,j}$  emission measured in the NEDC test [g/km] or other tests such as FTP75 or WLTP

The authors of the paper propose an introduction of exhaust emission correction coefficient ( $k$ ), correcting the values of the homologation emissions to the value obtained under actual operation for passenger vehicles and light-duty trucks (up to 3500 kg):

$$m = KENS$$

where:

- $m$  mass of the pollutant [g],
- $k$  exhaust emission correction coefficient,
- $E$  emission of a vehicle according to the Euro standard ([g/km]),
- $N$  number of vehicles,
- $S$  vehicle mileage [km],

Exhaust emission correction coefficients (relating to specific pollutants) can usually be calculated as the value relating to the entire test, which is the ratio of emission of the pollutant in the road test performed under real traffic conditions to the normative value. The conditions under which road tests were carried out were characterized by the following features:

- test duration—no longer than 90 min;
- 33 % of the test time spent in urban conditions, where the vehicle speed did not exceed 50 km/h,
- 33 % of the test time spent in extra urban conditions—vehicle speed in the range of 50–90 km/h,
- 33 % of the test time spent in highway conditions—vehicle speed in the range of 90–130 km/h (should not exceed 140 km/h).

Such vehicle working conditions—expressed in units of absolute speed—don't necessarily have to match the identical operating conditions of the engine itself. For this reason the requirements for vehicle engines have also been specified:

(1) with regards to gasoline engines:

- 40 % minimum share of engine operating conditions in the relative speed range ( $n_{rel}$ ), defined as:

$$n_{rel} = \frac{n - n_{min}}{n_{max} - n_{min}} \tag{3}$$

in the range  $n_{rel} = 0-40$  % and relative load in the range  $Z = 0-20$  %;

- 30 % minimum share of engine operating conditions in the relative speed range  $n_{rel} = 0-50$  % and relative load in the range  $Z = 0-60$  %, excluding the previously specified areas;
  - 10 % minimum share of engine operating conditions in the relative speed range  $n_{rel} = 0-100$  % and relative load in the range  $Z = 0-100$  %, excluding the previously specified areas;
- (2) with regards to Diesel engines:
- 40 % minimum share of engine operating conditions in the relative speed range  $n_{rel} = 0-20$  % and relative load in the range  $Z = 0-40$  %;
  - 30 % minimum share of engine operating conditions in the relative speed range  $n_{rel} = 0-40$  % and relative load in the range  $Z = 0-50$  %, excluding the previously specified areas;
  - 10 % minimum share of engine operating conditions in the relative speed range  $n_{rel} = 0-100$  % and relative load in the range  $Z = 0-100$  %, excluding the previously specified areas.

## Tested Vehicles

The presented emission results are the result of 9-year-long research as a part of the study of passenger vehicles in real traffic conditions. These studies were made on a group of more than 150 passenger cars with different technical characteristics (Fig. 4). The study involved vehicles powered by gasoline engines as well as diesel engines, with various displacement (from 1.3 to 3.0 dm<sup>3</sup>) and taking into account the different exhaust aftertreatment systems. The data presented in the article, in the road tests results section relate to cars with varying mileage (from 20,000 km to 500,000 km) and various technical parameters (various layouts of petrol and diesel power supply systems). The results are divided into the categories of the emission regulations of Euro 4, Euro 5 and Euro 6 omitting the results for vehicles with lower



**Fig. 4** Vehicles used for tests (example)

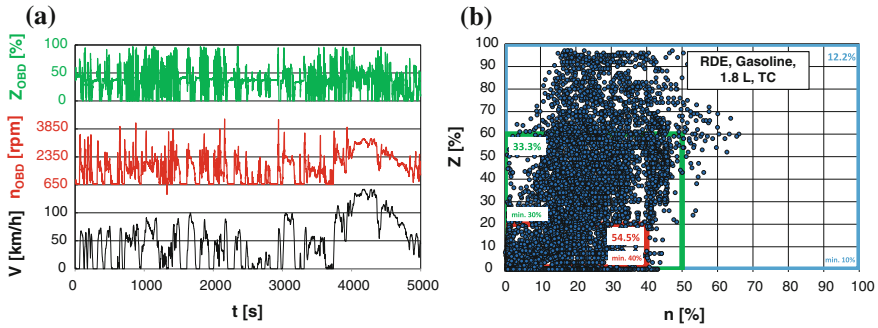


**Fig. 5** Operating conditions of a gasoline engine vehicle in road tests: **a** the registration of vehicle speed, load and engine speed, **b** engine operating points on a characteristic of the relative speed and load

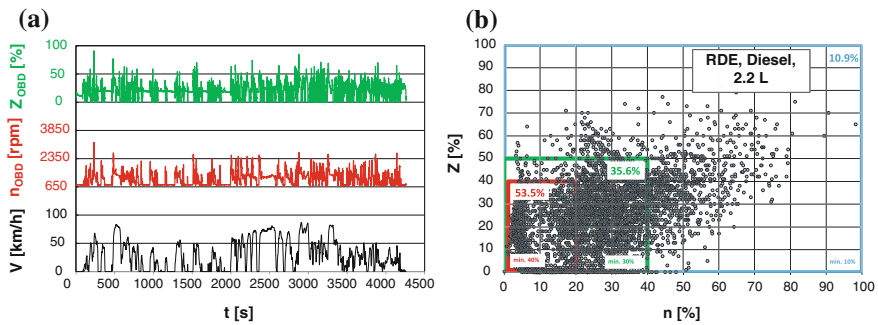


**Fig. 6** Operating conditions of a diesel engine vehicle in road tests: **a** the registration of vehicle speed, load and engine speed, **b** engine operating points on a characteristic of the relative speed and load

emission classes. The results of road emissions were ranked from lowest to highest value and only the extreme values were given (values that were obtained in conditions not satisfying the requirements of the screening test described previously have been discarded).

Figures 5 and 6 show examples of the results of road emission tests while maintaining the required areas of operation of engines: a petrol engine that meets the above requirements (Fig. 5), and the partial results of a vehicle powered by a diesel engine, which also meets such requirements (Fig. 6).

### Research Apparatus

The testing apparatus is shown in Fig. 7. For the measurement of the exhaust emissions from vehicles the portable Semtech DS analyzer (Fig. 7a) was used. It allowed measurements of the exhaust emissions—carbon monoxide, carbon



dioxide, hydrocarbons and nitrogen oxides (Johnson 2014). For the measurement of the particle mass (Fig. 8) the portable AVL 483 Micro Soot Sensor analyzer (Fig. 8a) was used. To measure the particle number the particle counter AVL 439 (Fig. 8b) was used, and for measurements of the distribution of diameters of solid particles the EEPS 3090 mass spectrometer by TSI Incorporated (Fig. 8c) was used.

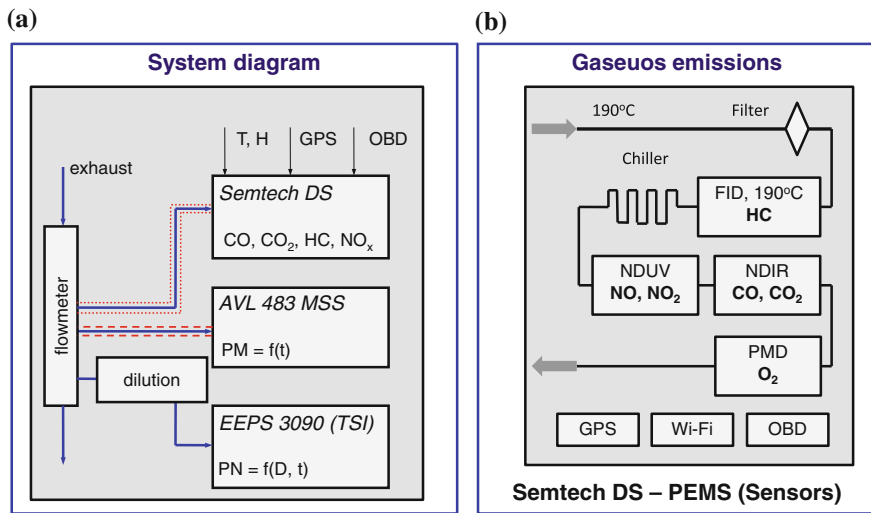


Fig. 7 The measurement system used for emission tests in real traffic conditions

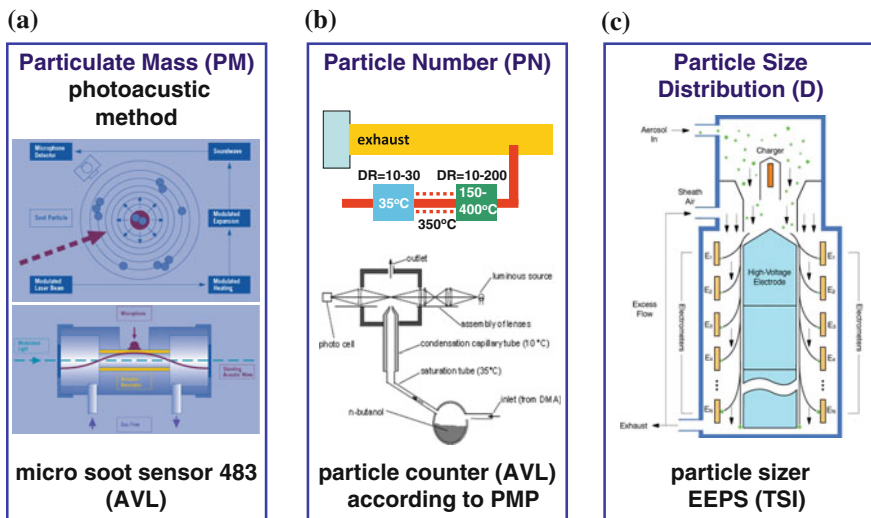
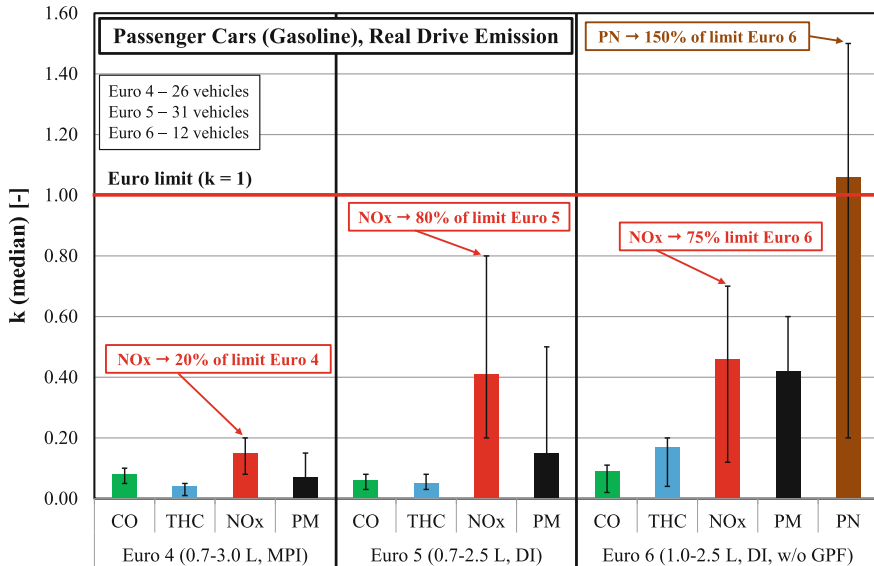


Fig. 8 Measurement system used for testing particulate emissions: **a** the analyzer for measurement of the particle mass concentration—AVL 483 Micro soot sensor, **b** the particle counter AVL 439, **c** the mass spectrometer EEPS 3090 by TSI for measurement of the size distribution of particles

## Results Analysis

Values of exhaust emission correction coefficient of pollutants obtained in road tests were the following:

- (1) for passenger vehicles powered by gasoline engines (Fig. 9):
  - those complying with Euro 4 regulation (vehicles with displacements of 0.7–3.0 dm<sup>3</sup> with multi-point fuel injection were measured): emission correction coefficient of carbon monoxide  $k_{CO}$  remained within 0.05–0.1 with the median value equal to 0.08; the median value of hydrocarbon emissions correction coefficient  $k_{HC}$  was 0.04, while the emission correction coefficient of nitrogen oxides  $k_{NOx}$  was in the range of 0.08–0.2 (median 0.15), and the correction coefficient for particulate emissions did not exceed the value of 0.15, with a median of 0.07 (as a limit value for particulate emissions the limit of 5 mg/km has been accepted—the same as for vehicles with Euro 5 emission class);
  - those complying with Euro 5 regulation (vehicles with displacements of 0.7–2.5 dm<sup>3</sup> with direct fuel injection were measured) emission correction coefficient of carbon monoxide  $k_{CO}$  remained within 0.03–0.08 with the median value equal to 0.06; the median correction coefficient of hydrocarbon emissions  $k_{HC}$  was 0.05 (with the limit values—the minimum and maximum amounting to 0.03 and 0.08 respectively), while the correction coefficient of emissions of nitrogen oxides  $k_{NOx}$  in the range of 0.2–0.8



**Fig. 9** The values of the exhaust emission correction coefficient for passenger cars equipped with gasoline engines of Euro 4, Euro 5 and Euro 6 emission class (based on 69 vehicles tested)

(median 0.41), and the correction coefficient for particulate emissions not exceeding the value of 0.5 (median 0.15); vehicles with emission classes Euro 4 and Euro 5 did not register emissions in real traffic conditions that would exceed the emission standards;

- those complying with Euro 6 regulation (vehicles with displacements of 1.0–2.5 dm<sup>3</sup> with direct fuel injection, without a particulate filter for petrol engines were measured): the median emission correction coefficient of carbon monoxide  $k_{CO}$  value was 0.09 (with limit values of 0.02 and 0.11); the median rate of hydrocarbon emission correction coefficient  $k_{HC}$  was 0.17 (with limit values—the minimum and maximum amounting respectively to 0.04 and 0.2), and the emissions correction coefficient of nitrogen oxides  $k_{NOx}$  was in the range of 0.12–0.7 (with a median of 0.46); while the emission correction coefficient of particle matter by mass  $k_{PM}$  did not exceed the value of 0.6 (median 0.42); whereas the value of the emission correction coefficient for particle number differed significantly, the median was 1.06 (with limit values ranging between 0.2 and 1.5); for vehicles powered by petrol engines with Euro 6 emission class the particle number emissions exceeded the set limits in relation to the emission standards by a maximum of 50 % (the maximum value of the emission correction coefficient is 1.5).

(2) for passenger vehicles powered by diesel engines (Fig. 10):

- those complying with Euro 4 regulation (vehicles with displacements of 1.3–2.2 dm<sup>3</sup> without particulate filter were measured): emission correction coefficient of carbon monoxide  $k_{CO}$  remained within 0.01–0.05 and the

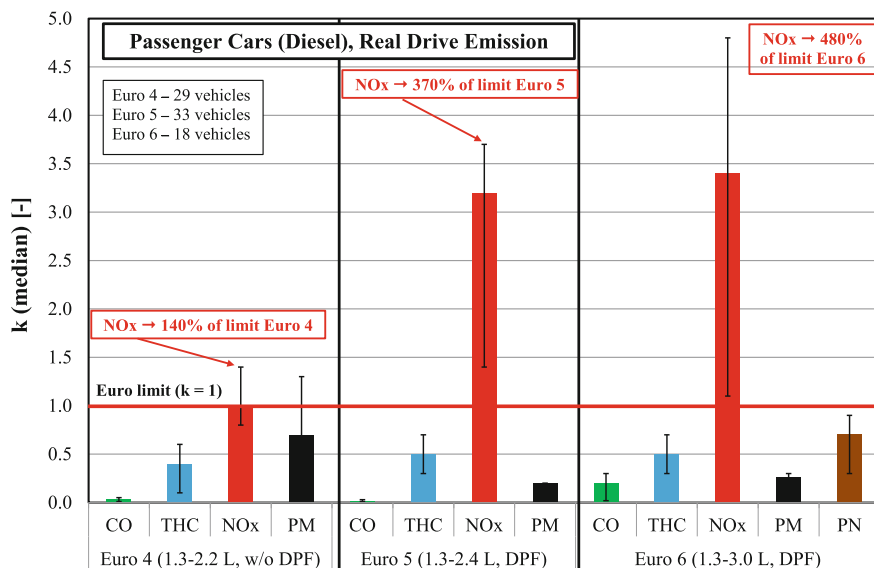


**Fig. 10** The values of the emission correction coefficient for passenger cars equipped with diesel engines with Euro 4, Euro 5 and Euro 6 emission class (based on 80 vehicles tested)

median value was equal to 0.04; the median correction coefficient of hydrocarbon emissions  $k_{\text{HC}}$  was 0.4, while the emission correction coefficient of nitrogen oxides  $k_{\text{NO}_x}$  was in the range of 0.8–1.4 (maximum excess emissions of nitrogen oxides by 40 % over the norm; with a median of 1.0), emission correction coefficient for particulate matter did not exceed the value of 1.3 with a median of 0.7 (thus exceeding the allowed emissions by 30 %);

- those complying with Euro 5 regulation (vehicles with displacements of 1.3–2.4 dm<sup>3</sup> with a particulate filter were measured); emission correction coefficient of carbon monoxide  $k_{\text{CO}}$  remained within 0.01–0.03 with a median value of 0.02; the median correction coefficient of hydrocarbon emissions  $k_{\text{HC}}$  was 0.5 (with the limit values—the minimum and maximum of 0.3 and 0.7 respectively), while the emission correction coefficient of nitrogen oxides  $k_{\text{NO}_x}$  was in the range of 1.4–3.7 (median 3.2—exceeding the nitrogen oxide emissions by more than 3-fold compared to the Euro 5 limit), the emission correction coefficient of particulate matter by mass does not exceed the value of 0.2 (median 0.15); for this class the biggest issue is the emission of nitrogen oxides—exceeding the norm by over 3 times;
- those complying with Euro 6 regulation (vehicles with displacements of 1.3–3.0 dm<sup>3</sup> with a DPF were measured); the median ratio of carbon monoxide  $k_{\text{CO}}$  value of 0.2 (with extreme values of 0.02 and 0.3); the median correction coefficient of hydrocarbon emissions  $k_{\text{HC}}$  was 0.5 (with the limit values—the minimum and maximum amounting to 0.3 and 0.7 respectively), and the emission correction coefficient of nitrogen oxides  $k_{\text{NO}_x}$  was in the range of 1.1–4.8 (a median of 3.4); while the emission correction coefficient of particulate matter by mass  $k_{\text{PM}}$  did not exceed the value of 0.3 (median 0.26); the value of the emission correction coefficient for particle number with the median of 0.71 was similar (with limit values ranging between 0.3 and 0.9); for vehicles powered by diesel of Euro 6 emission class a significant excess in emissions of nitrogen oxides in relation to the emission standards was found, with its value exceeding the limit more than 3.5-fold (maximum value of the correction coefficient equal to 4.8).

## Conclusions

The investigations led to developing exhaust emissions correction coefficients defined as a fraction equal to the value of exhaust emissions in real operating conditions to those registered in the homologation test. From the performed analysis it can be concluded that gasoline powered passenger vehicles meet the emission

requirements and diesel vehicles significantly exceed their respective admissible emission limits of nitrogen oxides.

As seen in road tests the emission correction coefficients—depending on the weight of the vehicle and the technical solutions used—for gasoline engines in Euro 4 and 5 emission class reach the value of up to  $k_j = 0.8$  for all exhaust gas components. In contrast, for vehicles with Euro 6 emission class powered by gasoline with a direct injection the obtained values of correction coefficient of particulate emissions (in terms of number of particulates) exceed the values obtained in homologation tests. In road tests, the average value of the emission correction coefficient of particle number was  $k_{PN} = 1.06$  (with a maximum value of about 1.5).

The values of exhaust emissions correction coefficients for vehicles powered with diesel engines shape differently: on road tests, it has been shown, that the values of the emission correction coefficients of carbon monoxide and hydrocarbons are less than 1 (meeting the regulation of exhaust emissions), while the emission correction coefficient of nitrogen oxides reached values ranging between  $k_{NOx} = 0.7\text{--}4.8$  (limit values are shown). Likewise for the determination of particulate emissions (in terms of particle mass the emission correction coefficient ranged between  $k_{PM} = 0.2\text{--}1.3$ , and in terms of particle number between  $k_{PN} = 0.3\text{--}0.9$ ).

## References

- Bergmann D (2013) Developing the technology innovation process for further emissions reduction. In: 6th integer diesel emissions conference and diesel exhaust fluid forum. Atlanta
- Bougher T, Khalek I, Trevitz S, Akard M (2010) Verification of a gaseous portable emissions measurement system with a laboratory system using the code of federal regulations part 1065, SAE paper series 2010-01-1069
- Chen Y, Borken-Kleefeld J (2014) Real-driving emissions from cars and light commercial vehicles—results from 13 years remote sensing at Zurich. *Atmos Environ* 88:157–164
- European Commission (2011) Regulation (EU) No. 582/2011, implementing and amending regulation (EC) No. 595/2009 of the European parliament and of the council with respect to emissions from heavy-duty vehicles (Euro VI) and amending annexes I and III to directive 2007/46/EC of the European parliament and of the council, 25 May 2011
- European Commission (2012) Regulation No. 64/2012, amending regulation (EU) No. 582/2011 implementing and amending regulation (EC) No. 595/2009 of the European parliament and of the council with respect to emissions from heavy-duty vehicles (Euro VI), 23 Jan 2012
- Fontaras G, Franco V, Dilara P, Martini G, Manfredi U (2013) Development and review of Euro 5 passenger car emission factors based on experimental results over various driving cycles. *Sci Total Environ* 468–469:1034–1042
- Franco V, Kousoulidou M, Muntean M, Ntziachristos L, Hausberger S, Dilara P (2013) Road vehicle emission factors development: a review. *Atmos Environ* 70:84–97
- Franco V, Posada Sánchez F, German J, Mock P (2014) White paper: real-world exhaust emissions from modern diesel cars. Part 2: detailed results. The international council on clean transportation
- Johnson T (2014) Vehicular emissions in review. SAE paper series 2014-01-1491

- Krutzsch B, Weibel M, Steiner R, Schmeißer V (2011) System simulation of modern powertrain concepts—from an industrial perspective. Cross-cut lean exhaust emissions reduction simulations, crosscut workshop on lean emissions reduction simulation. University of Michigan, Dearborn
- Ligterink N, Kadijk G, van Mensch P, Hausberger S, Rexeis M (2013) Investigations and real world emission performance of Euro 6 light-duty vehicles. TNO Report R11891:1–53
- Merkisz J, Pielecha J (2015) Real driving emissions—vehicle tests in variable terrain. In: European science society of powertrain and transport publication. *J KONES Powertrain Transp* 22(1):217–225
- Merkisz J, Pielecha J, Radzimirski S (2014) New trends in emission control in the European union. Springer tracts on transportation and traffic, p 1–170
- Merkisz J, Pielecha J, Fuc P (2015) LDV and HDV vehicle exhaust emission indexes in PEMS-based RDE Tests. *Fortschritt-Berichte VDI Verlag*, vol 12, no 783, pp 240–265
- Myung C, Park S (2012) Exhaust nanoparticle emissions from internal combustion engines: a review. *Int J Automot Technol* 13(1):9–22
- Weiss M, Bonnel P, Hummel R, Steininger N (2013) A complementary emissions test for light-duty vehicles: assessing the technical feasibility of candidate procedures (No. EUR 25572 EN). European commission, JRC scientific and policy reports, pp 1–56

# Studies Regarding the Influence of Exhaust Backpressure on the Performances of a Compression Ignited Engine

Nicolae Burnete, Dan Moldovanu, Doru-Laurean Baldean  
and Levente Kocsis

**Abstract** This paper presents some of the researches made on a compression ignited engine, in order to establish the influence of the exhaust backpressure (that can be caused by the existence or clogging of the catalytic converter, or by the SCR catalyst or the particle filter or by the noise reduction tubing itself) on the performances of a CI engine. The research was made on a ultramodern test bed inside the TestEcoCel Laboratory (Test, Research and Certification of Internal Combustion Engines) that work on biodiesel, of the Automotive and Transport Department, Technical University of Cluj-Napoca, Romania. Graphs, values and results were obtained through experimental measurements on the test bed and evaluated using specific software.

**Keywords** Engine power · Engine torque · Exhaust backpressure

## Introduction

There are studies (Bolt et al. 1973; Cong et al. 2011; Schubiger et al. 2001) that show an important influence of the exhaust backpressure on existing systems (EGR), emissions, performance and most of all, air consumption. Therefore to know the most significant influences on an existing compression ignited engine, a series of measurements must be made.

The role of active and passive ways of depollution has risen due to more severe normative and the need to respect them. Fortunately, some of the most important active and passive ways of depollution are placed on the exhaust system of the internal combustion engine, and this influences in a negative way the exhaust gas flow, with direct effect on the fresh fluid admission.

With the grow of the exhaust backpressure (due to the resistance of burned exhaust gases on the exhaust pipes) the residual burned gas also grows in quantity

---

N. Burnete (✉) · D. Moldovanu · D.-L. Baldean · L. Kocsis  
Technical University of Cluj-Napoca, Cluj-Napoca, Romania  
e-mail: nicolae.burnete@auto.uteluj.ro

(the pumping diagram is modified), and this has a negative effect on the intake of fresh fluid inside the cylinders (due to the reduction of the available volume inside the cylinder and also due to the mixing with the high temperature burned gases that lower the density of the resulting mixed fluid).

It is known (Bataga et al. 1995; Cristea 2009, Grünwald 1980, Şugar and Banica 2014) that the fill coefficient (fill efficiency) is defined as a ratio between the number of kilo-moles of fresh load inside the cylinder at the end of the intake process,  $N_p$  and  $N_o$  ( $N_s$ ), the number of kilo-moles that may theoretically fill the cylinder at a certain pressure  $p_o$  and temperature  $T_o$  (or  $p_s$  and  $T_s$ ):

$$\eta_u = \frac{N_p}{N_o}, \quad (1)$$

and, the residual gas coefficient  $\gamma_r$  is the ratio between the number of kilo-moles  $N_r$  of residual gases and  $N_p$ , the number kilo-moles of fresh load.

On the other side, the perfection of the exhaust system is characterized by the evacuation coefficient  $\eta_{ev}$  of the burned exhaust gases from the cylinder (Grünwald 1980).

$$\eta_{ev} = \frac{1}{1 + \gamma_r}, \quad (2)$$

which shows that  $\eta_{ev}$  varies inversely with the residual gas coefficient  $\gamma_r$ .

At the same time, if the following equation is taken into consideration (Grünwald 1980):

$$\gamma_r = \frac{p_r T_o}{p_o T_r} \frac{1}{\eta_u (\varepsilon - 1)}, \quad (3)$$

where  $p_r$  and  $T_r$  are the pressure and the temperature of the in-cylinder gases then the piston is at TDC (the end of exhaust process), and  $\varepsilon$  is the compression ratio, it can be seen that  $\gamma_r$  and  $\eta_u$  are inversely proportional, the residual gas coefficient being inversely proportional with the compression ratio (that influences directly  $p_r$  and  $T_r$ ).

The dependence of the effective power of the engine  $P_e$  with the air consumption  $C_a$  (Grünwald 1980):

$$P_e = k \frac{Q_i}{L_{min}} \frac{\eta_i \eta_m}{\lambda_a} C_a, \quad (4)$$

explains the efforts of filling the cylinders with a well determined quantity of fluid, and the greater the quantity, the better, and also underlines the importance of relations 1 through 3 (in relation number 4,  $Q_i$  is the inferior calorific power of the fuel,  $\eta_i$  indicated efficiency of the engine,  $\eta_m$  mechanical efficiency of the engine,  $C_a$  the air consumption,  $L_{min}$  the minimum air quantity for the complete burn of one kilogram of fuel,  $\lambda_a$  air excess coefficient,  $k$  constant that depends on the used measure units).



In the case of the compression ignited engine, the oxidation catalytic converter, SCR Catalyst, particle filter and the noise reduction tubing, are elements that prevent the free flow of exhaust gases (because they are big dynamic resistances) and their clogging has a direct effect on the proper working of the engine, also for example the regeneration of the particle filter is not always made at optimum parameters. More than that, the clogging of the particle filter is due to different reasons: the thermal regime of the engine too low, injection system faults, supercharging system faults, quality of the fuel, lubrication oil that does not respect the specifications of the engine producer, use of the engine at low loads (working in urban areas), DPF sensor faults, intercooler faults, and so on.

## Objectives

The study is based on the determination of the performances of a CI engine, when there is a flap placed on the exhaust system and it can be automatically controlled to produce a backpressure in the exhaust, to simulate the chemical and noise depollution devices that produce the same effect. Also, the influence of the backpressure on the main indices of the compression ignited engine can be determined.

## Methodology

To reach the goals of the research, the TestEcoCel Laboratory (Test, Research and Certification of Internal Combustion Engines of the Automotive and Transport Department, Technical University of Cluj-Napoca—TÜV Certificated Laboratory and national RAR certified), was used.

The Laboratory has high performance equipment that ensure high precision, that is why the measurements were made on the test bed shown in Fig. 1 (test bed equipped with a compression ignited engine connected to an active dynamometer,

**Fig. 1** The test bed used for the measurements



opacimeter mounted on the exhaust and the flap that induces the backpressure in the exhaust system.

The main characteristics of the engine are presented in Table 1. To create the specific conditions of the backpressure, a flap was used, presented in Fig. 2.

As modifications brought to the main exhaust system, the only original element is the catalytic converter, then the flap was mounted to create the backpressure (and replaces the original noise reduction system) and an exhaust tubing that has three meters in length with a diameter of 50 mm.

The opening/closing of the flap was controlled by the automation system of the Laboratory, PUMA Open (V14.1), the backpressure values vary between 0 and 570 millibars. The pressure in the exhaust system was measured by using a Kistler sensor.

In order to ensure the repetitive nature of the measurements, the ambient temperature was controlled inside the test chamber and maintained constant throughout the measurements: temperature ( $\pm 3\%$ ), atmospheric pressure ( $\pm 3\%$ ), and the relative humidity was measured (Fig. 3).

A test cycle was made, with 10 measurement steps for 10 different speeds of the engine (speeds vary from 1400 rot/min to 3400 rot/min) and the effective power, engine torque, fuel consumption, exhaust gas opacity, cooling liquid temperature when entering and exiting the engine, intake pressure, exhaust pressure, intake air

**Table 1** Technical characteristics of the IC engine

Nomenclature	Value	Unit
Bore	79.5	mm
Stroke	95.5	mm
Compression ratio	19	–
Displacement	1900	cm <sup>3</sup>
Valves per cylinder	2	–
Power	63	kW
Torque	240	Nm
Fueling system	VE injection pump	

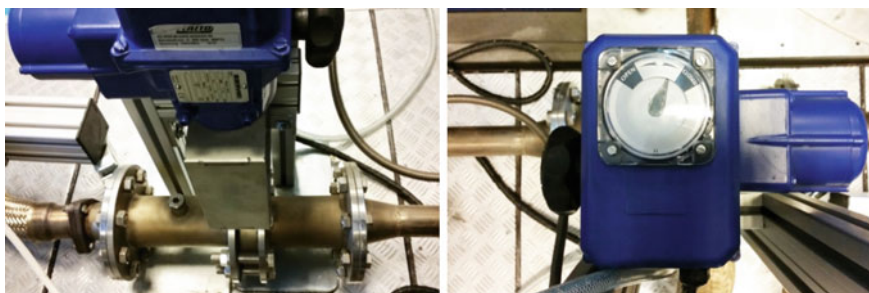


**Fig. 2** The mounted flap on the exhaust system



Fig. 3 Control interface of the conditioning system

temperature (before and after intercooler), exhaust gas temperature, oil temperature inside the inferior carter of the engine.

The conceived test cycle (Fig. 4) was run automatically and presumes following 10 steps of speed from 1400 rot/min to 3400 rot/min at full load ( $\chi = 100\%$ ), with a period of 50 s for stabilization and 10 consecutive measurements per step measurement, and recording of the average of the 10 measurements for every step (underlining the minimum, maximum and average values, so that there are no deviations greater than 0.5%—in case of greater spreads, the values are not recorded).

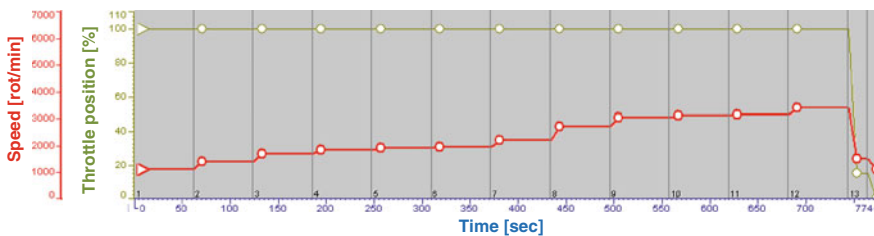


Fig. 4 The automatic test cycle implemented in puma open

## Results and Discussions

Based on the implemented test cycle, the established values were measured and stored (like seen in Fig. 5), and then they were processed and analyzed. The automation software Puma Open and the test control systems allowed the obtaining of the measurements, organized in tables and graphs.

The obtained results (from experimental research) underline the fact that the Engine Power ( $P_e$ ) (Figs. 6 and 7), the Engine Torque ( $M_e$ ) (Fig. 8) and the exhaust gas opacity (Fig. 9) are strongly influenced by the exhaust backpressure (Fig. 10).



Fig. 5 Control room panels (puma open)

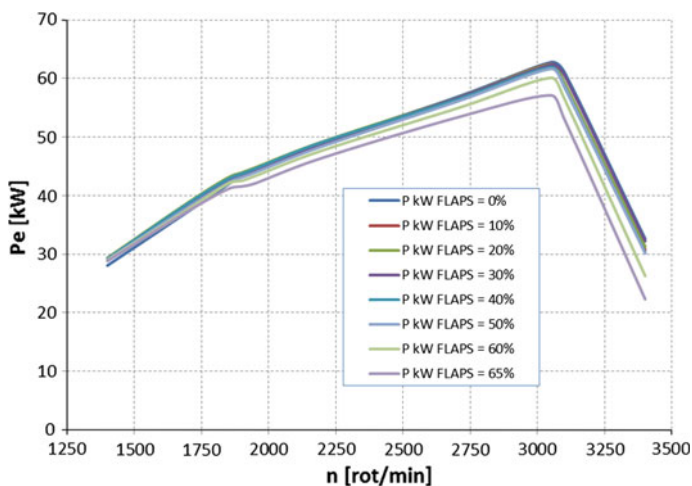


Fig. 6 Engine power variation (vs. engine speed) for different flap position

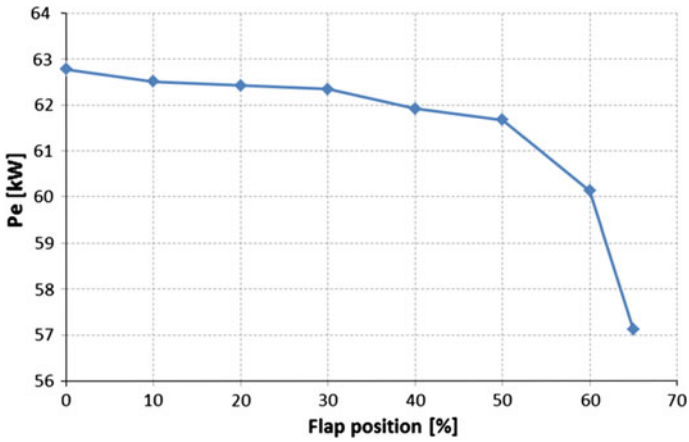


Fig. 7 Maximum engine power variation for different flap position

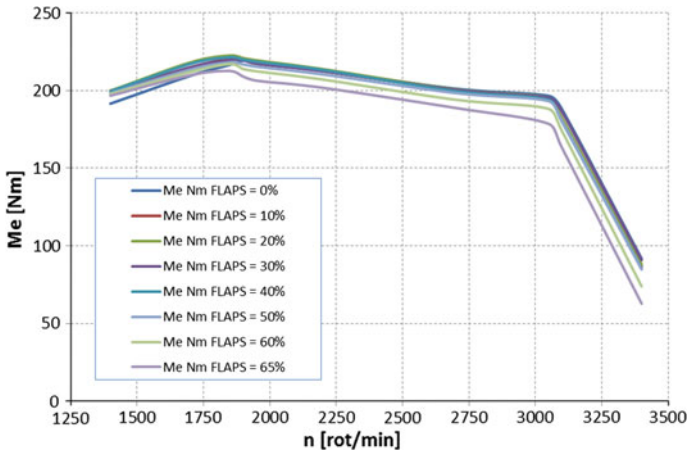


Fig. 8 Engine torque variation (vs. engine speed) for different flap position

For lower speeds (1400 rot/min), the Engine Power does not present major variations, by creating the exhaust backpressure, at a speed of 3050 rot/min (Rated Engine Power Speed) a decrease of 8.99 kW was found, only by closing the exhaust back pressure flap from 0 to 65 % (more is not recommended to ensure the integrity of the measuring devices). The biggest decrease of power was found at 3400 rot/min, when, by closing the flap at 65 %, the power decreased by 31.63 %.

By closing the flap at 65 %, the Engine Torque is decreased with 4.69 % (at a speed of 1900 rot/min), and at maximum speed, 3400 rot/min, it decreases with 31 %.

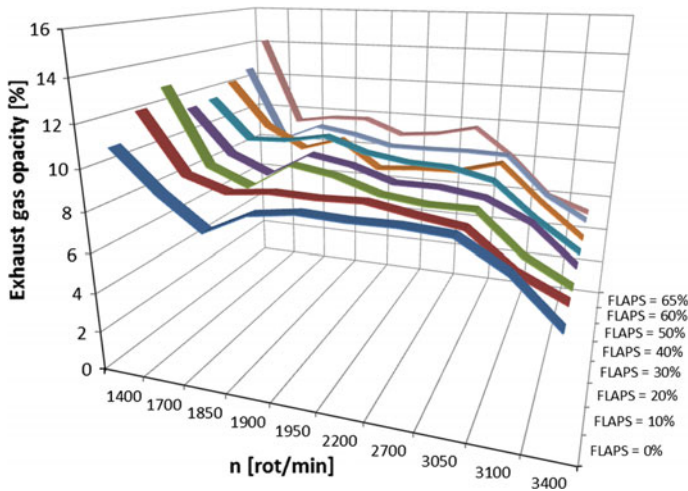


Fig. 9 Gas opacity variation (vs. speed) for different flap positions

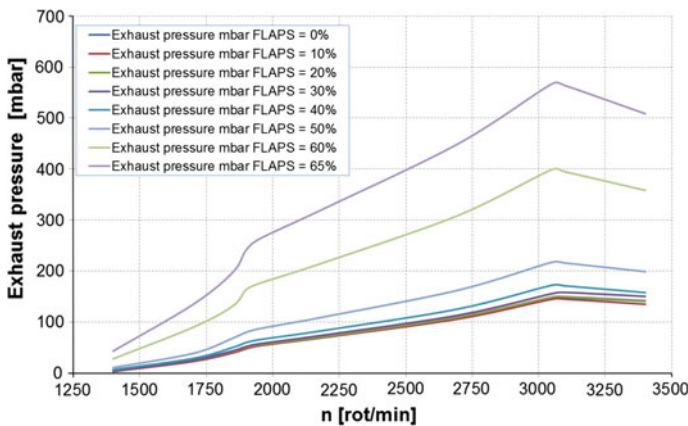


Fig. 10 Backpressure variation (vs. engine speed) at different flap positions

Exhaust gas opacity is lower by raising the speed (between 51.6 and 62.7 %), more precisely, if the exhaust system is open (0 % flaps opening), the gas opacity drops from 10.91 (at 1400 rot/min) to 5.28 (at 3400 rot/min), and when the flap is closed 65 %, the gas opacity drops from 14.15 (at 1400 rot/min) to 5.27 (at 3400 rot/min). At lower speeds (under 2000 rot/min) an opacity raise is clearly observed as the backpressure is raised (because of the flap closing), at over 3000 rot/min the opacity varies within close limits.

The Engine Torque and Engine Power have a normal variation, in accordance with relation 3 and 4. By raising the exhaust backpressure, the fresh air mass that

enters the engine cylinders is smaller, because the residual gases reduce the effective volume of the cylinder—volume that should be available for fresh air.

The exhaust backpressure raises the necessary pumping work (exhaust gases), so it reduces the fill efficiency.

Reducing the fresh air quantity and by raising the temperature of the fresh air (because of the existence of burned gases in the cylinder) leads to the chain reaction inhibition and reduce a little ignition delay (by raising  $\gamma_r$ , the temperature at the end of the intake process also raises); due to this fact, the opacity of the exhaust gases have the tendency to grow.

## Conclusions

After the evaluation of the experimental research a clear conclusion can be formulated: the exhaust backpressure clearly influence the Engine Torque and Power of the compression ignited engine, backpressure that exists because of the clogging of the depollution devices on the exhaust (oxidation catalytic converter, SCR catalyst, particle filter, and noise reduction system).

To improve the performance indices of the compression ignited engine, it is mandatory to study also the influence of the backpressure on all pollutants, especially because TestEcoCell Laboratory allows the measuring of 24 compounds of the exhaust gases, depending on the fuel (pure diesel or mixtures of diesel and biodiesel).

## Bibliography

- AVL Pressure Sensor, <https://www.avl.com/web/guest/-/canopen-pressure-transducer-c-fem-p>
- Bataga N et al (1995) Motoare cu ardere interna, Ed. Didactica si Pedagogica, Bucharest. ISBN 973-30-4922-0
- Bolt JA, Stephen PB, Frederick JV (1973) The influence of the exhaust back pressure of a piston engine on air consumption, performance, and emissions. No. 730195. SAE technical paper
- Cristea D (2009) Cai de optimizare a motoarelor cu ardere interna, Ed. Universitatii din Pitesti. ISBN 978-973-690-910-8
- Cong S, Garner CP, McTaggart-Cowan GP (2011) The effects of exhaust back pressure on conventional and low-temperature diesel combustion. Proc Inst Mech Eng D J Automobile Eng 225(2):222–35
- Grünwald B (1980) Teoria, calculul si constructia motoarelor pentru autovehicule rutiere, Ed. Didactica si Pedagogica, Bucharest
- Schubiger R, Andrea B, Konstantinos B (2001) Influence of EGR on combustion and exhaust emissions of heavy duty DI-diesel engines equipped with common-rail injection systems. No. 2001-01-3497. SAE technical paper
- Şugar IR, Banica M (2014) Experimental study regarding the computation of the effective power of a spark-ignition. Appl Mech Mater 657:704-707. ISSN 1662-7482
- WEINLLICH test bench, Volkswagen diesel engine AVM type, <http://www.weinlich.de/gb/mpgb/pv04gb.htm>

# A Study of Waste Heat Recovery Impact on a Passenger Car Fuel Consumption in New European Driving Cycle

Plamen Punov, Nikolay Milkov, Quentin Danel  
and Christelle Perilhon

**Abstract** In this article the effect of waste heat recovery (WHR) system by means of Organic Rankine cycle (ORC) on passenger car engine fuel consumption was studied. A vehicle driving model was developed in order to determine the engine operating points in New European Driving Cycle (NEDC). In order to evaluate exhaust gases enthalpy and fuel consumption at engine operating points corresponding to the driving cycle the engine was experimentally tested in steady mode. The exhaust gases temperature was measured at a location situated 1.5 m downstream the exhaust valves considering that place as the inlet of ORC heat exchanger. A simulation model of ORC was developed using R245fa as a working fluid. Numerical results revealed that maximum recovered power was 1.69 kW. The contribution of the WHR system on the vehicle fuel consumption was assessed by reduction in cumulated fuel consumption for a NEDC. Applying an ORC to engine exhaust gases reduces cumulated fuel in a NEDC test from 0.441 to 0.414 kg. In relative values this reduction accounts to 5.9 %.

**Keywords** Diesel engine · Passenger car · Fuel consumption · Waste heat recovery · Organic rankine cycle

---

P. Punov (✉) · N. Milkov  
Department of Combustion Engines, Automobiles and Transport,  
Technical University of Sofia, 1000 Sofia, Bulgaria  
e-mail: plamen\_punov@tu-sofia.bg

N. Milkov  
e-mail: nikolay.milkov@tu-sofia.bg

Q. Danel · C. Perilhon  
Cnam - Conservatoire National des Arts et Métiers Laboratoire CMGPCE, Paris, France  
e-mail: quentin.danel@outlook.fr

C. Perilhon  
e-mail: christelle.perilhon@cnam.fr



## Introduction

Reduction of CO<sub>2</sub> emissions for light-duty vehicle by 41 % in 2020 in comparison with 2006 is the target for European Union (EU). The new target level measured by New European Driving Cycle (NEDC) will be 95 g/km (Daccord et al. 2013). In order to meet the future restriction of CO<sub>2</sub> emissions for passenger cars, it is necessary to reduce significantly the engine fuel consumption by developing more advanced technologies.

Despite modern technologies such as high pressure direct injection, variable valve lift and timing, stratified mixture in gasoline engines, turbocharging, down-sizing and others, overall efficiency of automobile engines still remains below 40 % (Milkov et al. 2014; Zhang et al. 2013; Taylor 2008). In reciprocating engines more than 60 % of fuel energy is lost as a form of heat in exhaust gases and cooling system. A number of studies (Domingues et al. 2013; Katsanos et al. 2012; Kölsch and Radulovic 2015; Yang et al. 2014; Barrieu et al. 2013; Boretti 2012) revealed that WHR from exhaust gases by means of Rankine cycle (RC) and ORC is the most prospective way to increase engine efficiency.

A study conducted on a passenger car revealed that RC applied to engine exhaust system can reduce the vehicle fuel consumption within the range from 1.5 to 7.57 % at cruising speed range from 80 to 160 km/h (Punov et al. 2015a). It was stated that at low engine speed and load the energy of exhaust gases is not enough to provide evaporation of the water in the RC which means not output power is produced.

Performance and economic optimization of an ORC for a gasoline hybrid vehicle was also reported (Dimitrova et al. 2015). The optimization was carried out at different driving cycles. For NEDC a reduction by 24 % in engine fuel consumption was estimated. In combination with pneumatic hybridization the reduction accounted to 38.4 %.

The aim of this article is to study the influence of WHR from exhaust gases on passenger car fuel consumption in NEDC. It is important to assess the contribution of WHR technologies due to the fact that NEDC is still used in EU for light-duty vehicle test procedure in homologation.

## Vehicle Driving Model

In this study we needed to define the engine operating points corresponding to vehicle speed defined by NEDC. The vehicle is a mechanical system that interacts with the road surface. At any moment the sum of forces applied to the vehicle must be zero. Thus, the dynamic model in flat road is presented in Fig. 1.

The engine power was determined by taking into consideration the vehicle motion power and transmission mechanical efficiency as follows:

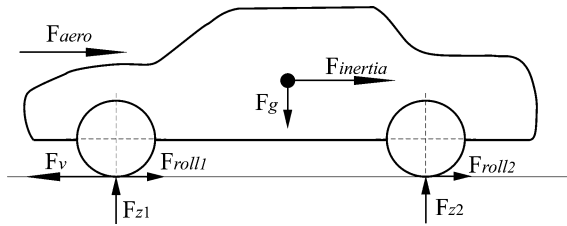


Fig. 1 Vehicle dynamic model

$$P_e = P_v \cdot \eta_{tr} \tag{1}$$

The power needed for motion as a function of the vehicle speed was determined by the longitudinal power balance. Then the motion power was estimated by multiplying the traction force by the vehicle velocity, as proposed in (Genta and Morello 2008):

$$P_v = F_v \cdot V \tag{2}$$

where  $F_v$  is the traction force to the driving wheels and  $V$  is the vehicle speed. The following correlation was used to determine  $F_v$ , both in steady and transient operation mode (Millo et al. 2011):

$$F_v = F_{roll} + F_{aero} + F_a + F_{inertia} + F_{gx} \tag{3}$$

As the current study was conducted without load slope the grade resistance  $F_{gx}$  is zero. The rolling resistance was determined as follows:

$$F_{roll} = M_v \cdot g \cdot (f_0 + k \cdot V) \tag{4}$$

The aerodynamic resistance  $F_{aero}$  depends on the air density, vehicle frontal area, aerodynamic drag coefficient and vehicle speed. (Millo et al. 2011) proposed a correlation determining aerodynamic resistance as follows:

$$F_{aero} = \frac{1}{2} \rho_a S_v C_x V^2 \tag{5}$$

Inertial force depends on vehicle mass and acceleration. Thus, the force can be estimated as follows:

$$F_{inertia} = M_v \cdot \dot{V} \tag{6}$$

In order to determine the engine operating points in NEDC test, a medium size saloon car was studied. Some data needed to estimate the engine power were taken from the car technical documentation while the rest were taken from the data

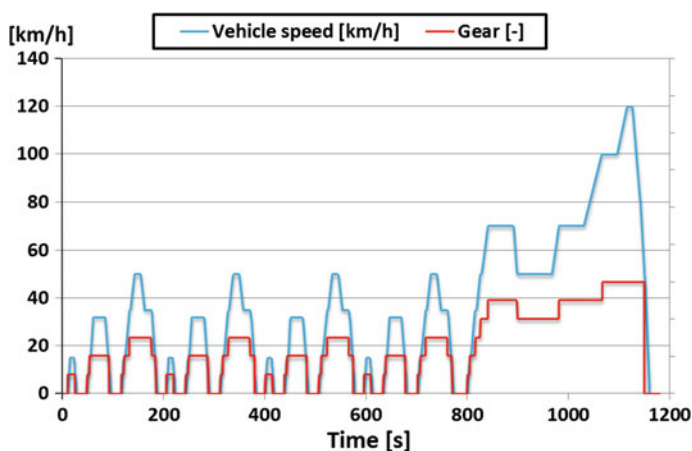
**Table 1** Vehicle main data

Vehicle type	Medium size	$\eta_{tr}$	0.93
<i>Seats</i>	5	$i_{final}$	4.305
$M_v$ , kg	1486	$i_{tr1}$	0.534
<i>Tyres</i>	225/60R16	$i_{tr2}$	0.647
$f_o$	0.008	$i_{tr3}$	0.795
$k$	$6 \cdot 10^{-6}$	$i_{tr4}$	1.121
$S$ , $m^2$	2.25	$i_{tr5}$	1.783
$C_x$	0.3	$i_{tr6}$	3.416

analysis presented in the literature (Genta and Morello 2008), concerning cars in the same class. The parameters are listed in Table 1.

## Determination of Engine Operating Points in NEDC

Since 2000 in EU the NEDC has been used for approval testing of emission and fuel consumption for light-duty vehicle ([www.unece.org/fileadmin/DAM/trans/main/wp29/wp29regs/r083r4e.pdf](http://www.unece.org/fileadmin/DAM/trans/main/wp29/wp29regs/r083r4e.pdf)). The cycle consists of urban driving cycle (UDC) and extra urban driving cycle (EUDC). After cold start of the engine and 10 s idling operation the UDC is repeated four times. The UDC corresponds to a vehicle operation at low speed and idling, the driving condition typical for the cities. The EUDC is added after the fourth repetition of UDC. This part represents more aggressive high speed driving mode with higher exhaust gases temperature. The NEDC is presented in Fig. 2.

**Fig. 2** NEDC for vehicles with 6-gear transmission

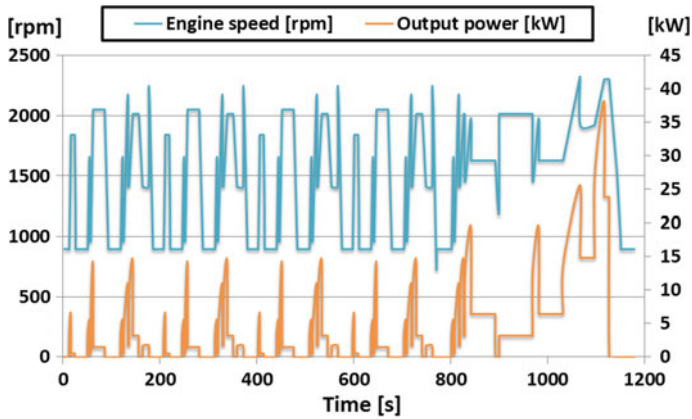


Fig. 3 Engine speed and output power over NEDC

The engine speed was estimated by means of vehicle speed and transmission ratio in respect to the gear. It was assumed that the engine operates at 900 rpm at idling mode and not a start-stop system is used. In order to determine engine load the engine power was estimated by means of Eq. (1). Thus, the brake mean effective pressure (BMEP) was defined over the test cycle as follows:

$$BMEP = \frac{120 \cdot P_e}{V_h \cdot n} \tag{7}$$

It was assumed that the engine output power, respectively the BMEP is zero during deceleration and idling. Both engine speed and output power in the NEDC are presented in Fig. 3.

The engine outputs data have been already studied numerically over engine operating map (Punov et al. 2015a). The operating points in respect to NEDC are shown on the engine map in Fig. 4. It can be seen that the engine operates within the speed range from 900 to 2330 rpm and BMEP ranged from 0 to 10 bar. Maximum engine power of 38.2 kW is needed for acceleration from 100 to 120 km/h.

In that operating point the brake specific fuel consumption (BSFC) is approximately 210 g/kWh. However, the engine operates with BSFC less than 300 g/kWh at a short time period. The numerical results presented in Fig. 4 have not been experimentally proven. For that reason in this paper the engine was experimentally studied at operating points previously defined by the vehicle simulation in NEDC.

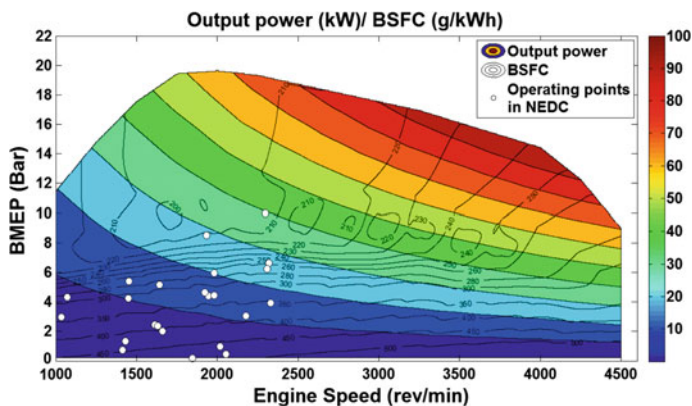


Fig. 4 Engine operating points in NEDC presented on the engine map

## Experimental Test

The engine under study is a 2.0 l four-cylinder high-pressure direct injection (HDI) diesel engine developed by PSA Peugeot Citroen. The maximum output power is 101 kW at 4000 rpm and the maximum torque is 320 Nm at 2000 rpm. The engine is equipped with a variable geometry turbocharger. The boost pressure is limited to 1.3 bar. The Common rail system of the engine is produced by Delphi. The maximum injection pressure is 1600 bar. The engine is also equipped with an exhaust gas recirculation (EGR) system and post treatment system including a catalytic converter and diesel particulate filter (DPF). The cylinder is equipped with four valves per cylinder. The main geometrical parameters of the engine are listed in Table 2.

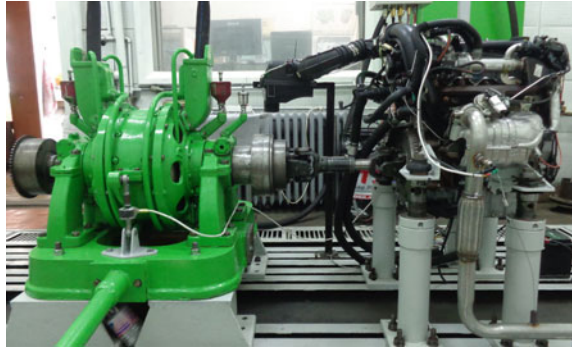
The experimental study was conducted at Department of combustion engines, automobiles and transport of Technical university of Sofia. The test facility includes an engine test bed equipped with hydraulic brake, flexible diesel engine management system and data acquisition system for data analysis. The engine test bed is shown in Fig. 5.

The engine is mechanically coupled to hydraulic brake D4. The maximum power absorption from the brake is 257 kW at 4500 rpm. A strain gauge sensor is used in order to measure the brake force. The sensor was produced at Technical university of Sofia for operating range from 0 to 1500 N. Two mechanically controlled valves are used to control the brake.

Table 2 Main engine data

Engine type	Cylinders	Volume	Bore (mm)	Stroke (mm)	$\varepsilon$	Valves/cylinder
HDI	4	2L	85	88	17.2	4

**Fig. 5** Engine test bed facility



In order to assess the possibilities of WHR from exhaust gases as well as the fuel consumption reduction we needed to measure the exhaust gases parameters (temperature and mass flow rate) and fuel consumption, respectively. We estimated the exhaust mass flow measuring the intake mass flow and fuel mass flow. An intake mass flow sensor produced by Bosch, based on thermo anemometry principal was used in order to measure the intake mass flow. Fuel consumption was estimated measuring the volumetric flow while the density of the fuel was previously defined to be  $0.840 \text{ g/cm}^3$ . We used Rotronics RCC101 volumetric fuel flow measurement technic with two flow sensors—one in delivery line and one in return line. The exhaust temperature was measured by means of K type thermocouple located at exhaust pipe 1.5 m downstream the exhaust valves. We considered this location is suitable as inlet section of a Rankine cycle heat exchanger.

In our experimental research the engine operation was controlled by means of Real Time controller produced by National Instruments and specialized modules for control and measurement produced by Drivven. A Lab View project was developed in order to control the engine operation. The entire system provides very large functionality for measurement and control such as: injection process control with up to five separate injections per cycle, injection pressure control, boost pressure control, exhaust gas recirculation (EGR) control, closed-loop control of injection by means of wide band oxygen sensor in exhaust gases etc. Moreover, the system can be adapted for diesel engines with up to 6 cylinders in case of solenoid injectors and up to 4 cylinders in case of piezo injectors. The front panel of the project host application and the system hardware are shown in Fig. 6.

The experimental research was conducted at engine steady operating mode. Twenty five operating points was observed corresponding to idling, constant vehicle speed and acceleration. These operating points were defined based on vehicle simulation in NEDC in previous section. During the test the engine was heated up to normal cooling temperature. The ambient temperature was  $18 \text{ }^\circ\text{C}$  while the barometric pressure was 955 mbar. Then, the values of intake mass flow, fuel flow and exhaust gases temperature were recorded. Variation of exhaust gases parameters in NEDC is shown in Fig. 7.



Fig. 6 Engine management

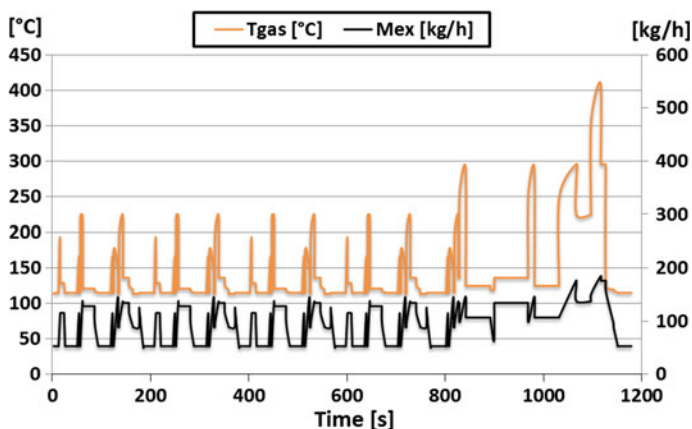


Fig. 7 Exhaust gases temperature and mass flow in NEDC

Measurement of fuel mass flow provided to us opportunities to estimate cumulated fuel consumption of the engine during the vehicle test in NEDC. It was done by integration of fuel mass flow. We observed cumulated fuel consumption of 0.441 kg at the end of the cycle. The cumulated fuel consumption was estimated to be 0.207 and 0.233 kg in UDC and EUDC, respectively.

## Organic Rankine Cycle Simulation

The RC system consists of a tank, pump, heat exchanger (evaporator), expander and condenser (Fig. 8a). The pump increases the fluid pressure. Then the fluid is heated by exhaust gases in three different stages: preheating, evaporation at constant temperature and overheating. By means of expansion of superheated vapour mechanical power is produced on the expander output shaft. The last stage of the

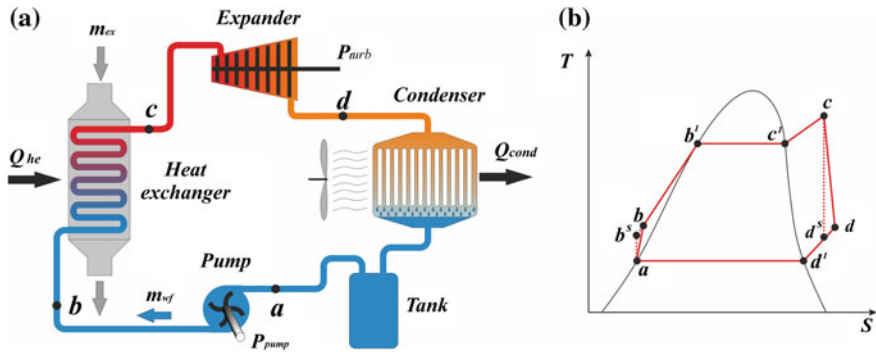


Fig. 8 ORC applied to engine exhaust system

cycle is the condensing process in the condenser. The variation in working fluid thermodynamic parameters is presented in Fig. 8b.

This thermodynamic cycle can operate with different working fluids such as: water, ethanol, CO<sub>2</sub>, organic fluids etc. The RC with organic fluids is also called ORC. Based on our previous research a RC with water is not the best solution for low exhaust gases enthalpy which is typical for NEDC. Due to the low temperature of the gases the overall evaporation of the water cannot be occurred in the exchanger. In order to protect the expansion machine from damages the working fluid has to be pass outside. In other words at low engine load and speed the RC output power is near zero (Punov et al. 2015a).

For that reason we chose in this study an organic fluid R245fa. This fluid has a low evaporation temperature and provides higher efficiency than other organic fluids (Punov et al. 2015b).

In order to estimate the ORC output power a steady model was developed. Thus, the power consumed by the pump was estimated as follows:

$$P_{pump} = \frac{\dot{m}_{wf}(h_{b^s} - h_a)}{\eta_{pump}} \tag{8}$$

Heating of the working fluid by exhaust gas occurs at constant pressure—process *b-c*. At point *c* the fluid is in the form of superheated vapour. The fluid specific enthalpy at the outlet of the heat exchanger was calculated by means of the following equation:

$$h_c = h_b + \frac{Q_{he}}{\dot{m}_{wf}} \tag{9}$$

The heat flow rate transferred by the heat exchanger was estimated by means of a discretized heat exchanger model. Thus, total heat flow rate by the heat exchanger was estimated as:



$$Q_{he} = \sum_{i=1}^n Q_{he(i)} \quad (10)$$

It was assumed that the fluid parameters vary only as a function of tube length. Heat transfer to the ambient air and pressure drop at the heat exchanger were neglected. Then the heat flow rate at finite volume was estimated as:

$$Q_{he(i)} = A_i \cdot U_i \cdot (T_{gas(i)} - T_{wf(i)}) \quad (11)$$

Due to the fact that the exchanger design was not studied here the constant value of heat transfer coefficient for each zone of the exchanger was used.

The output power of the expander is calculated by means of following equation:

$$P_{ex} = \dot{m}_{wf} \cdot (h_c - h_{d^s}) \cdot \eta_{ex} \quad (12)$$

Lastly, the power recovered by the ORC can be estimated as the difference between the power produced by the expander and the power consumed by the pump:

$$P_{RC} = P_{ex} - P_{pump} \quad (13)$$

The working fluid specific enthalpy was defined by means of the open-source platform CoolProp integrated in Python (x, y). The parameters of exhaust gases at the inlet section of the heat exchanger (mass flow, temperature and specific heat capacity) were taken from engine experimental test.

In ORC simulation two parameters of the systems were adjusted: working fluid mass flow rate and pressure in the system. Our target was to provide maximal efficiency of the cycle as well as to avoid the droplets at the outlet of heat exchanger. Considering these conditions ORC output power was simulated and results are presented in Fig. 9. Over UDC we observed a maximum output power of 0.61 kW while in EUDC the maximum was 1.69 kW.

Finally, the effect of the ORC on engine fuel consumption was evaluated. We assumed that ORC output power can be added to the engine crankshaft through a mechanical system as mechanical losses were neglected. Also, the engine load was reduced in a way that the sum of engine output power and ORC output power is enough to provide demanded speed of the vehicle in NEDC. Due to the fact that engine power reduction is not more than 6.8 % the same BSFC values in respect to operating points were used.

The results for fuel consumption are shown in Fig. 10. We observed positive effect of the ORC on the cumulated fuel consumption. The new value is 0.414 kg which is reduction by 5.96 %.

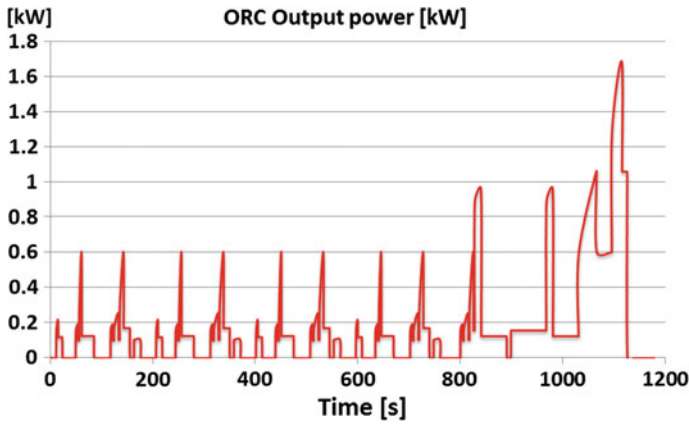


Fig. 9 ORC output power in NEDC

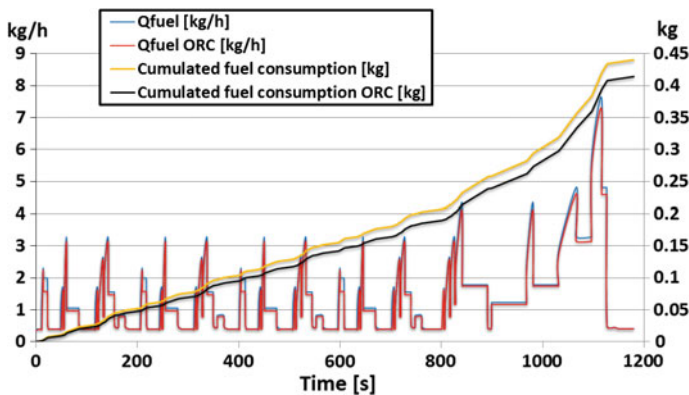


Fig. 10 Engine fuel consumption in NEDC

## Conclusions

The impact of waste heat recovery from automotive engine exhaust gases on fuel consumption was studied in NEDC test procedure. A medium class passenger car powered by 2.0 l diesel engine was chosen as a prototype. A vehicle driving model was used in order to determine the engine operating parameters. In NEDC the maximal engine power demanded by the car was estimated to be 38.2 kW at 2300 rpm. It was observed that the engine operating points are located at engine speed below 2330 rpm and engine load below 10 bar.

The engine was tested at laboratory condition in steady operating mode. A flexible engine management system produced by National Instrument and Drivven was used as well as a data acquisition system. Engine output power,

torque, fuel mass flow, air mass flow, exhaust gasses temperature were measured at twenty five operating points in respect to NEDC. Thus, exhaust gases enthalpy and cumulated fuel consumption were estimated. Total cumulated fuel in NEDC was estimated to be 0.441 kg which corresponds to average fuel consumption of 4.88 l/100 km.

A steady model of ORC including discretized heat exchanger model was developed. Organic fluid R245fa was chosen due to better performance in low temperature heat source. Simulating results of WHR system revealed that maximum recovered power was 1.69 kW. This value was observed at EUDC while in UDC the maximum value was 0.61 kW.

The contribution of WHR was assessed as cumulated fuel consumption estimated without ORC was compared with that obtained with ORC applied to exhaust gases. The comparison revealed reduction in fuel consumption by 5.96 % in case WHR is applied.

This study was conducted with steady simulation model of the ORC. In order to increase the accuracy of research a dynamic simulation has to be carried out. The most critical components in WHR system is the heat exchanger. Usually, the heat exchanger is massif which causes thermal inertia. In other words accumulated heat in the exchanger can be used to evaporate the working fluid at the time when the engine runs on idle. From another hand after engine cold start the ORC output power will be zero during the heating up period.

**Acknowledgements** The research presented in this article received financial support from the Research and development department of the Technical University of Sofia—Internal funding session 2015.

## References

- Barriou E, Hergott J, Rossi A (2013) Power from wasted heat: challenges and opportunities of Rankine based systems for passenger vehicles. In: ICE powertrain electrification & energy recovery. Rueil-Malmaison
- Boretti A (2012) Recovery of exhaust and coolant heat with R245fa organic Rankine cycles in a hybrid passenger car with a naturally aspirated gasoline engine. *Appl Therm Eng* 36:73–77. doi:[10.1016/j.applthermaleng.2011.11.060](https://doi.org/10.1016/j.applthermaleng.2011.11.060)
- Daccord R, Melis J, Kientz T, Darnedru A, Pireyre R, Brisseau N, Fonteneau E (2013) Exhaust heat recovery with Rankine piston expander. In: ICE powertrain electrification & energy recovery. Rueil-Malmaison
- Dimitrova Z, Lourdais P, Maréchal F (2015) Performance and economic optimization of an organic rankine cycle for a gasoline hybrid pneumatic powertrain. *Energy* 86:574–588. doi:[10.1016/j.energy.2015.04.047](https://doi.org/10.1016/j.energy.2015.04.047)
- Domingues A, Santos H, Costa M (2013) Analysis of vehicle exhaust waste heat recovery potential using a Rankine cycle. *Energy* 49:71–85. doi:[10.1016/j.energy.2012.11.001](https://doi.org/10.1016/j.energy.2012.11.001)
- Genta G, Morello L (2008) The automotive chassis: volume 2: system design. Springer
- Katsanos CO, Hountalas DT, Pariotis EG (2012) Thermodynamic analysis of a Rankine cycle applied on a diesel truck engine using steam and organic medium. *Energy Convers Manag* 60:68–76. doi:[10.1016/j.enconman.2011.12.026](https://doi.org/10.1016/j.enconman.2011.12.026)

- Kölsch B, Radulovic J (2015) Utilisation of diesel engine waste heat by organic Rankine cycle. *Appl Therm Eng* 78:437–448. doi:[10.1016/j.applthermaleng.2015.01.004](https://doi.org/10.1016/j.applthermaleng.2015.01.004)
- Milkov N, Punov P, Evtimov T, Descombes G, Podevin P (2014) Energy and exergy analysis of an automotive direct injection diesel engine. In: Scientific Conference BulTrans-2014, Sozopol, pp 149–154
- Millo F, Rolando L, Andreatta M (2011) Numerical simulation for vehicle powertrain development. *Numer Anal Theor Appl*. doi:[19452](https://doi.org/10.1016/j.nat.2011.01.002)
- Punov P, Evtimov T, Milkov N, Descombes G, Podevin P (2015a) Impact of Rankine cycle WHR on passenger car engine fuel consumption under various operating conditions. In: Paper presented at the 28th international conference on efficiency, cost, optimization, simulation and environmental impact of energy systems—ECOS, Pau
- Punov P, Lacour S, Périlhon C, Podevin P, Descombes G, Evtimov T (2015b) Numerical study of the waste heat recovery potential of the exhaust gases from a tractor engine. In: Proceedings of the institution of mechanical engineers, part d: journal of automobile engineering. doi:[10.1177/0954407015577530](https://doi.org/10.1177/0954407015577530)
- Taylor AMKP (2008) Science review of internal combustion engines. *Energy Policy* 36(12):4657–4667. doi:[10.1016/j.enpol.2008.09.001](https://doi.org/10.1016/j.enpol.2008.09.001)  
[www.unece.org/fileadmin/DAM/trans/main/wp29/wp29regs/r083r4e.pdf](http://www.unece.org/fileadmin/DAM/trans/main/wp29/wp29regs/r083r4e.pdf)
- Yang F, Dong X, Zhang H, Wang Z, Yang K, Zhang J, Wang E, Liu H, Zhao G (2014) Performance analysis of waste heat recovery with a dual loop organic Rankine cycle (ORC) system for diesel engine under various operating conditions. *Energy Convers Manag* 80:243–255. doi:[10.1016/j.enconman.2014.01.036](https://doi.org/10.1016/j.enconman.2014.01.036)
- Zhang HG, Wang EH, Fan BY (2013) A performance analysis of a novel system of a dual loop bottoming organic Rankine cycle (ORC) with a light-duty diesel engine. *Appl Energy* 102:1504–1513. doi:[10.1016/j.apenergy.2012.09.018](https://doi.org/10.1016/j.apenergy.2012.09.018)

# Modeling of Electric Vehicles for Driveability Control Applications

Ionut Alexandru Stoica, Marius Valentin Bataus  
and Ioan Mircea Oprean

**Abstract** One of the key issues of modern passenger cars is the customer-perceived performance. This paper aims to investigate the drivability issues of an electric vehicle with emphasis on the dynamic transient response during tip-in maneuvers. Different models of a medium class electrical vehicle are discussed and tested in order to determine the appropriate one for use in drivability studies.

**Keywords** Electric vehicle · Powertrain · Modeling · Drivability

## Introduction

Modern road vehicles are considered to be one of the most complex multidisciplinary dynamic systems having numerous coupled translational and rotational motions of vehicle body, wheels, propulsion system and other subsystems. Moreover, considerable challenges on road vehicle system design and development are arising from the strong coupling of the different performance measures associated with vehicle ride, handling, stability, energy efficiency, packaging and road-friendliness.

The wide variety of levels of perceptual abilities, physical skills and technological understanding of automobile drivers makes these systems unique, and increase the difficulty to transfer standard control theory directly to the automotive field (Canudas-de-Wit et al. 2005). All automotive manufacturers use modeling and simulations coupled with bench and road tests in order to develop and tune the automotive control. In recent years the model base development is preferred due to lower costs and development times (Kokalj et al. 2012).

---

I.A. Stoica · M.V. Bataus (✉) · I.M. Oprean  
Department of Automotive Engineering, University Politehnica of Bucharest, București,  
Romania  
e-mail: mvbataus@yahoo.com

Almost all studies estimate that electric drives represent an alternative power source for the vehicles from which quiet, emission-free operation is required and when relatively modest performance levels and operating range are sufficient (Czapnik 2013). This paper aims to investigate different levels of electric vehicle (EV) modeling in order to estimate the proper complexity needed for the given application. The models are investigated using a middle class passenger car as case study.

The models are implemented using the 1D multi-domain simulation platform LMS Imagine.Lab AMESim. This platform is particularly suited for powertrain applications (Bataus et al. 2010).

The digital control use extensively because of its numerous advantages, has some limitations which if are overlooked in the design process can induce instability and therefore faults in the control system (Tanasa et al. 2013). To address that issue LMS. Imagine.lab AMESim comprises a Matlab/Simulink interface that allows the use of a continuous solver for the plant model and a discrete solver for the control model. Moreover, it is adequate for HiL (Hardware-in-the-Loop) simulation having submodels compatible with real time simulation and analysis tools needed to prepare the a real time model (Bataus et al. 2010; Hayat et al. 2003).

## Electric Vehicle Configurations

There are a diversity of possible EV configurations given by the combination of electric propulsion characteristics and energy sources.

Compared with a conventional propulsion system the clutch can be eliminated and a fixed gearing can replace the multispeed gearbox when an electric motor with constant power in a long speed range is used. This solution not only reduces the size and weight of the mechanical transmission, but also simplifies the drive train control by eliminating the gear shifting.

The electric motor, the fixed gearing and the differential can be integrated into a single transaxle assembly and the whole drive train is further simplified and compacted. The electric drive and the inverter can be packaged in a similar manner with a conventional powertrain (internal combustion engine and gearbox) and supported in the engine compartment in the same way with a minimum of alterations, Fig. 1.

This solution is preferred when a vehicle body carry-over is done from a conventional propelled vehicle. The use of a commune platform with conventional powertrains is cost effective and is considered to be the near future solution.

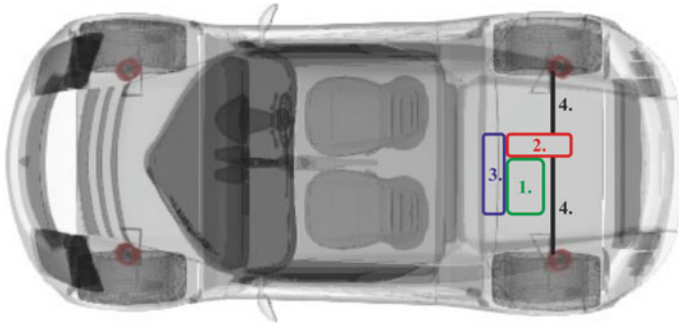


**Fig. 1** Integrated electric vehicle drive: 1. Electric motor; 2. Fixed gearing and differential; 3. Inverter; 4. Driveshafts

## Modeling of Electric Vehicles

Three methods are employed for powertrain studies (Guzzella and Sciarretta 2005):

- Average operating point;
- Quasistatic simulation;
- Dynamic simulation.

These methods are usually applied using numerical computer tools. For control problems only quasistatic and dynamic simulation can be applied.

The quasistatic models are useful for studying the energy management strategies. They can be used to study the influences of key parameters (vehicle mass, motor efficiency etc.) on energy consumption and also to estimate the impact of different methods for energy economy improvement. The simulation is fast and the results files are reduced making this very advantageous for batch runs.

The dynamic approach uses an accurate mathematical description of the system that can describe many dynamic effects. The powertrain model is formulated using sets of ordinary differential equation on the state-space form and can also include partial differential equations or algebraic differential equations. Not all of these effects are relevant for energy consumption estimation others are not. The majority of the relevant effects for energy consumption are relatively slow. The fast effects are usually important for the analysis of comfort and drivability.

Four modeling levels of the vehicle and the mechanical part of the powertrain are investigated in conjunction with an electrical drive model and a simple control. The models used for the components are referred as submodels.

### Basic Electric Vehicle Model

Basic submodels needed for performance and energy consumption studies already exist in IFP Drive library. Using this library is easy to construct a complete powertrain model of an EV as shown in Fig. 2 (model 1).

The model includes submodels of: vehicle, transmission, motor, battery and control unit. A more detailed modeling of electrical subsystem is possible but this was considered unnecessary for the present study. The driver and the mission profile submodels allow the following of a testing cycle.

Because a fixed gearing is used it is possible to include the effect of the motor rotor and the transmission inertias in the vehicle model. The equivalent vehicle mass accounting for rotor, transmission and wheel inertia effect in linear motion is:

$$m_{evch} = m_{veh} + J_m \cdot i^2 / r_w^2 + J_t / r_w^2 + 4 \cdot J_w / r_w^2 \tag{1}$$

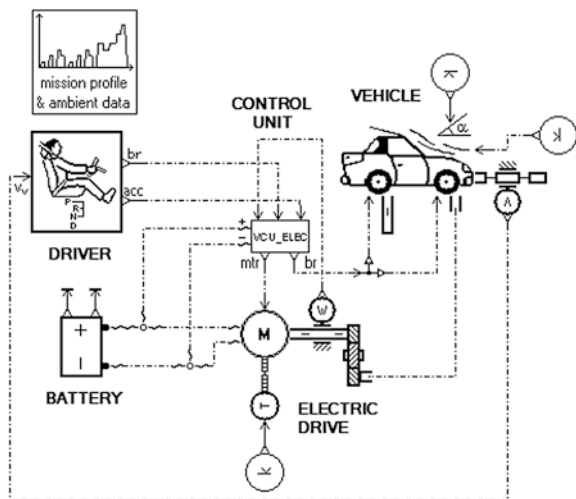
where  $m_{evch}$  is the equivalent vehicle mass,  $m_{veh}$  is the vehicle mass,  $J_m$ ,  $J_t$ ,  $J_w$  are the inertia of the rotor, transmission and wheel,  $i$  is the gear ratio and  $r_w$  is the dynamic wheel radius.

In order to use this model for drivability studies is important to introduce the stiffness of the drivetrain. This can be easily introduced by separating the motor inertia and adding a *rotary spring-damper* that consider the equivalent drivetrain stiffness, Fig. 3 (model 2).

The inertia of the rotor is separated by adding a *rotary load* submodel at the motor shaft. The equivalent drivetrain stiffness is computed with the formula:

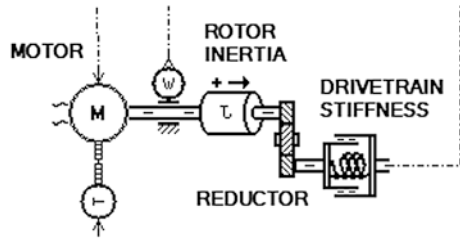
$$\tau_{dt} = \tau_{is} \cdot \tau_{hs\_e} / (\tau_{is} + \tau_{hs\_e}) \tag{2}$$

Fig. 2 Powertrain model for fuel consumption





**Fig. 3** Electric drive model for drivability studies



where  $\tau_{dt}$  is the equivalent drivetrain stiffness,  $\tau_{is}$  is the transmission input shaft stiffness and  $\tau_{hs\_e}$  is the half-shafts equivalent stiffness.

The formula used to compute the equivalent stiffness of the half-shafts was deduced taking into account the influence of the differential.

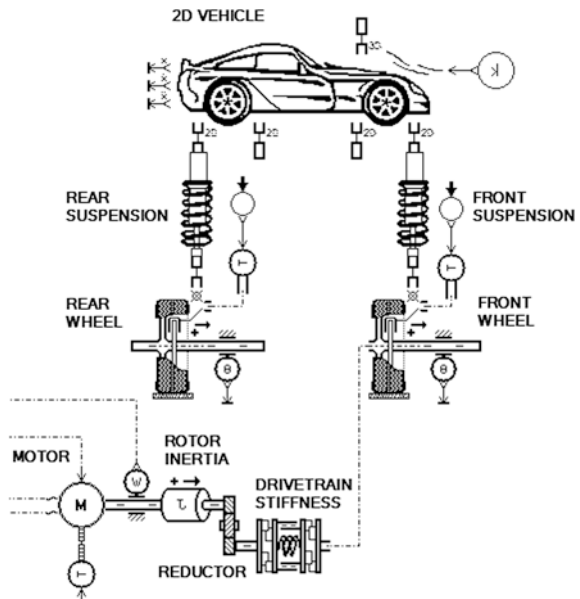
$$\tau_{hs\_e} = 4 \cdot \tau_{hs} \cdot \tau_{rhs} / (\tau_{lhs} + \tau_{rhs}) \tag{3}$$

where  $\tau_{lhs}$  is the left half-shaft stiffness and  $\tau_{rhs}$  is the right half-shaft stiffness.

### Two Dimensional Planar Vehicle Model

The one dimensional vehicle model can be replaced with a two dimensional one. This makes possible the inclusion of the vehicle suspension in the model, Fig. 4 (model 3).

**Fig. 4** Two dimensional vehicle model



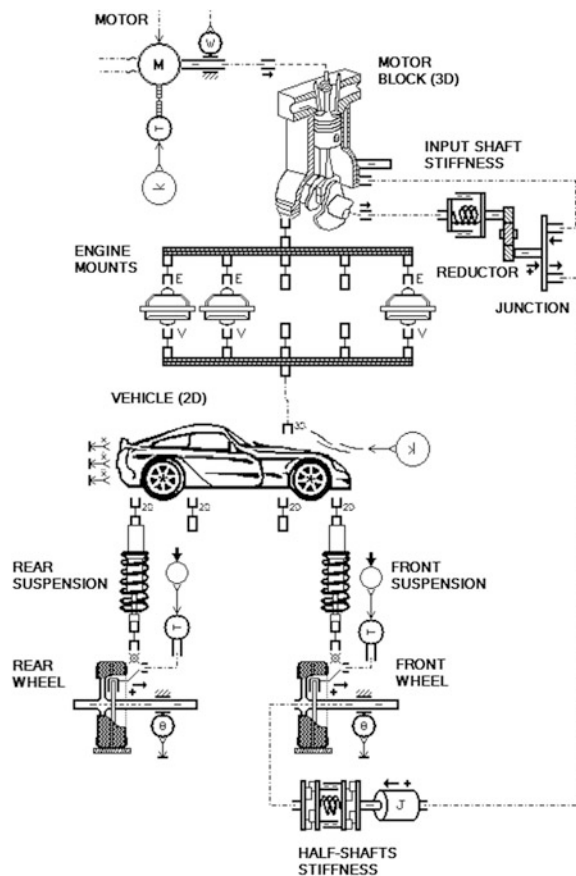
The unsprung masses of front and rear axle are subtracted from the vehicle mass and introduced in suspension submodels. For this model is necessary to first bring the vehicle in equilibrium by setting the initial preload of the suspensions.

### Powertrain Mounts

For the considered electric vehicle configuration the electric drive is packaged in a similar manner with a conventional powertrain and supported in the engine compartment by means of elastic mounts. To see the influence of this solution on the drivability a model was developed, Fig. 5 (model 4).

The motor is now connected with the transmission through a motor block unit that includes also his rotational inertia. This is the same submodel as that used for

Fig. 5 Two dimensional vehicle model with powertrain on elastic mounts



conventional powertrains. It provides the powertrain 6° of freedom and ensures the coupling between powertrain mass, vehicle mass and engine mounts.

A stabilization process is necessary in order to obtain the equilibrium position (the electric motor on the mounts and the vehicle body on the suspension).

A junction is needed in order to return the reaction torque. To ensure this connection it is necessary to break the drivetrain equivalent stiffness in the input shaft stiffness and half-shafts equivalent stiffness. The inertia is also redistributed on two separate ones.

## Results

The models are tested using the “tip-in” maneuver. This is one of the most common maneuvers used to characterize the motor vehicle drivability (Millo et al. 2003). This maneuver consists in a sudden pressing of the acceleration pedal operated from conditions of low speed and low load. The abrupt change of the torque delivered by the motor excites the torsional natural frequencies of the driveline, causing vehicle jerking and acceleration fluctuations which are primarily responsible for the driver’s and passengers’ perception and assessment of performance and comfort.

Usually, to avoid the vehicle oscillations filters are used to modulate the torque demand that is first computed from the driver command. For this study a low-pass first order filter is used.

The low-pass first order filter implements the following transfer function:

$$H(s) = 1/(1 + T \cdot s) \quad (4)$$

where  $s$  is the complex variable and  $T$  is the time constant.

When applied in an elastic drivetrain the effect on the torque output is also influenced by the motor torque characteristic. To properly test the models two values of the velocity are considered, one (10 km/h) in the constant torque zone and another (50 km/h) in the constant power zone of the electric motor.

The vehicle longitudinal acceleration for models with different complexity is compared in Figs. 6, 7, 8 and 9.

Figure 6 describes the comparison of the tip-in maneuver for the basic, one-dimension, powertrain model of the EV (model 1) and the same model equipped with equivalent drivetrain stiffness (model 2). Figure 7 represents the comparison of evolution of the longitudinal acceleration during the same maneuver for model 2 and the two-dimensional powertrain model of the EV (model 3).

Figures 8 and 9 depict the evolution of the longitudinal acceleration during the tip-in maneuvers starting from 10 km/h, respectively 50 km/h, for models 3 and 4.

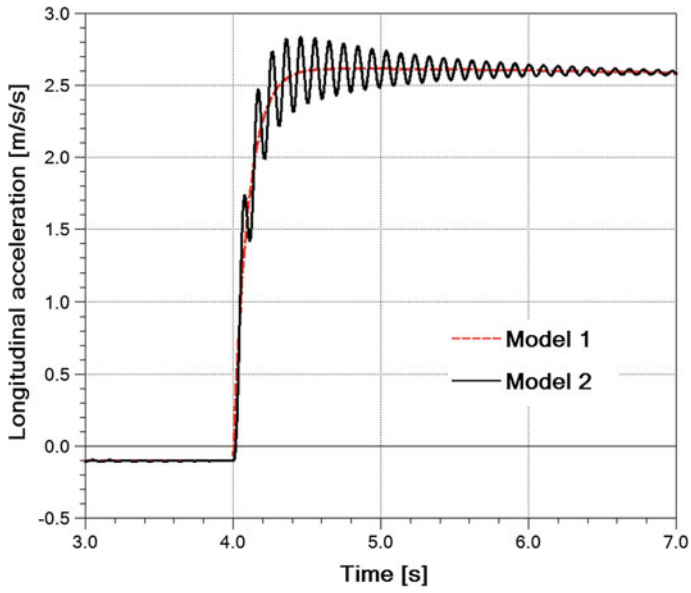


Fig. 6 Tip-in from 10 km/h (model 1 versus model 2)

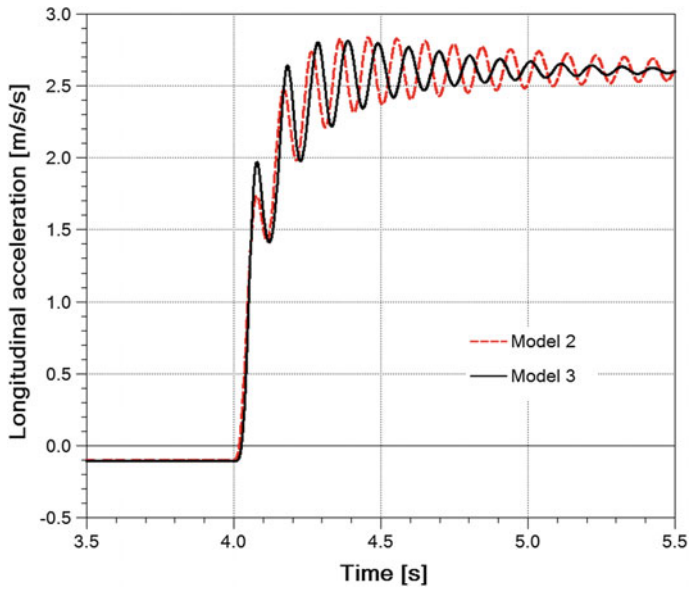


Fig. 7 Tip-in from 10 km/h (model 2 versus model 3)

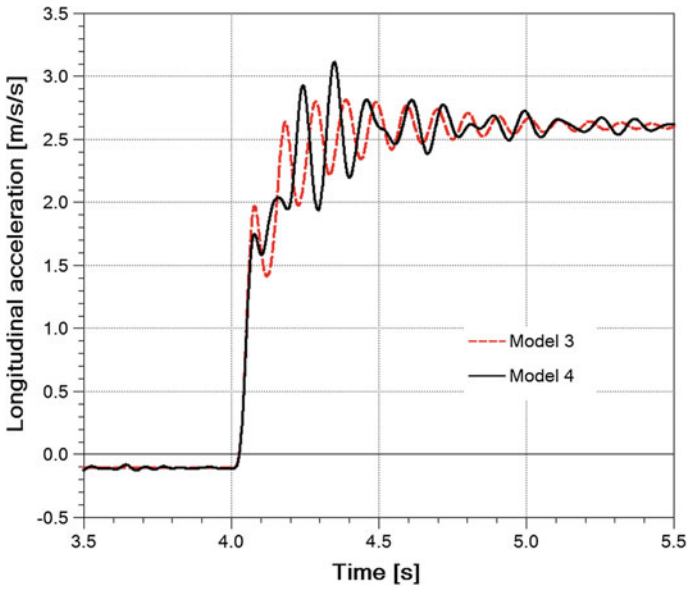


Fig. 8 Tip-in from 10 km/h (model 3 versus model 4)

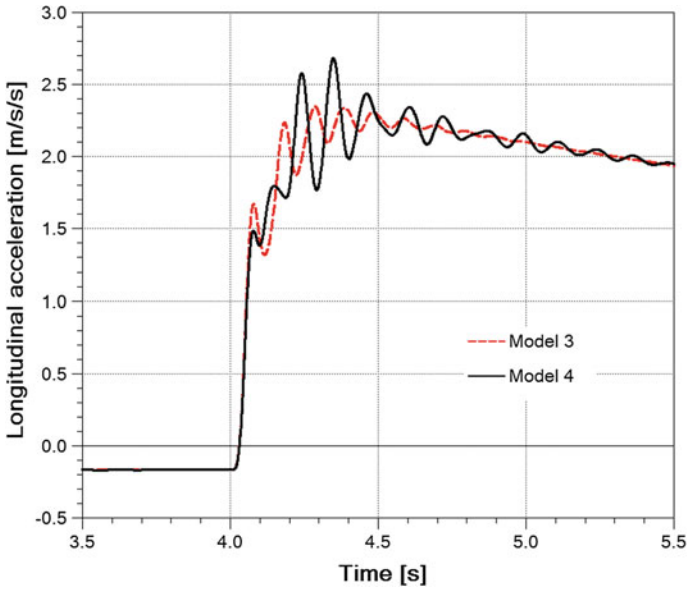


Fig. 9 Tip-in from 50 km/h (model 3 versus model 4)

## Conclusions

Analysis of simulation results showed substantial difference between the four models. Even that the correct distribution of the inertias and mass ensures the same level of average acceleration, the frequency and oscillations amplitudes are changed. Difference of peak-to-peak amplitude comprised between 0.25 and 0.45 m/s<sup>2</sup> are registered.

A basic electric vehicle model developed for performance and energy consumption studies is totally inadequate for the drivability studies.

When the drivetrain stiffness is included the model can be used for electric vehicles with dedicated drivetrain support. Even that some quantitative difference appears with the introduction of a two dimensional vehicle model and of the suspension the simpler one dimensional model can be use for qualitative studies.

For the applications where the electric drive is packaged and supported in a similar manner with a conventional powertrain it is compulsory to use a model that considers the mounting stiffness and geometry.

Having established the proper electric vehicle model for drivability control application, the future work will focus on the drivability strategies needed for the electric vehicles.

## References

- Bataus M, Maciac A, Oprean M, Vasiliu N (2010) Real time simulation of complex automatic transmission models. In: Proceedings of 2010 virtual powertrain creation. ATZ Live, Munich
- Canudas-de-Wit C, Bechart H, Claeys X, Dolcini P, Martinez JJ (2005) Fun-to-Drive by feedback. *Eur J Control* 11:353–383
- Czapnik B (2013) Synthesis, analysis and evaluation of drive concepts. In: 12th International CTI symposium, Berlin
- Guzzella L, Sciarretta A (2005) Vehicle propulsion systems introduction to modeling and optimization. Springer, Berlin, pp 31–40
- Hayat O, Lebrun M, Domingues E (2003) Powertrain driveability evaluation. In: Analysis and simplification of dynamic models, SAE paper no. 2003-01-1328. SAE 2003 World Congress & Exhibition, Detroit
- Kokalj G, Lewis J, Zach C (2012) Significant reduction of powertrain calibration effort in production programs. Automated calibration of driveability on chassis dyno and powertrain testbed. In: The 8th international conference on automotive engineering (ICAE-8), Bangkok
- Millo F, Ferraro CV, Mallamo F, Pilo L (2003) Numerical simulation to improve engine control during tip-in manoeuvre, 2003-01-0374 technical paper. SAE World Congress & Exhibition, Detroit
- Tanasa V, Chiriac A, Popescu D (2013) Errors estimation and refining methods for the numerical computation in real-time control systems. In: Proceedings of the 17th IEEE, international conference on system theory, control and computing, ICSTCC2013. Sinaia, Romania, pp 521–526

# Making of Safer Network Operating System Components

Arun S Nair and Jaideep Save

**Abstract** There are conflicting paradigms on the adoption of functional safety within AUTOMOTIVE software domain as its inherent nature being top-down approach versus the reusable software components. Reusable software component delivers faster time-to-market and with improved stability. Safety Element out of Context of ISO 26262 standard is the boon for such reusable software components. However there are problematic aspects and challenges in implementing Safety Element out of Context approach for automotive domain. This case study paper is the voyage of a reusable off-the-shelf software ‘Network Operating Systems—CAN stack’ to meet the challenge of make it ready for using it in Automotive Safety Integrity level B ECU software.

**Keywords** Automotive safety integrity level B (ASIL B) · Functional safety · Network operating systems (NOS) · Software element out of context (SEooC) · Seven step safety process (SSSP)

## Introduction

The pursuit of comfortable means to humankind resulted in greater inventions in car industry. Now with advent of connected cars and intelligent transport systems, the needs of connectivity with the amalgamation of different networking protocols within the car increased beyond the imagination. Network operating software are standardized software platform systems, that are existing in the car industry to facilitate the communication through various protocols and it helps the ECU software developer from gritty-nutty details of controller features, protocol and etc.

---

A. S Nair (✉) · J. Save  
KPIT Technologies, Bangalore, India  
e-mail: arun.nair@kpit.com

J. Save  
e-mail: jaideep.save@kpit.com

Many vehicles are coming on the road day-by-day, and hence accidents are inevitable. Anywhere from 85 to 90 % of traffic crashes involved some sort of driver error, which attributed to reckless driving such as consumption of alcohol, usage of mobiles and speed. However, there are number of cars accidents from 4 to 5 %, attributed to vehicle faults or equipment failure (Edgar Snyder & Associates 2009). With increasing dependency on electronics it is becoming necessary to ensure safety into components to detect and handle the random hardware failures that arise as a result of the hardware degrading over a period of time or enhance development process to manage the systematic failures. It also prompts for the overall safety within the system and allows to work in safer but may be degraded performance irrespective of equipment or operator errors, hardware faults or environment changes. Thus, the needs of reliable fail safe driving paves the way for functional safety guidelines and ISO 26262 specifications. Functional Safety Standard ISO 26262 is an adaptation of the Functional Safety standard IEC 61508.

This paper discusses how the Network Operating System (NOS) software was enhanced using Safety Element out of Context (SEooC) approach in accordance with the ISO 26262 standards. It also details how the software safety requirements and mechanisms were derived and implemented in the NOS and usage of tools that were used to automate certain safety related process areas. Thus, this case study paper is the voyage of Network Operating Systems—CAN stack (NOS CAN) to meet the goals of ISO 26262 ASIL B standards. This paper recommends the usage of seven step safety process (SSSP) for reusable/off-the-shelf software components, such that it overcome the challenge of making it to work with an ASIL ECU Software.

## **Safer Network Operating Systems**

### ***Software Market: Top Down Versus Reuse/Bottom up***

Market is driven with conflicting paradigms—Top Down and Reuse. Safety approach of ECU development and the distribution of safety across the value chain is top down approach, where the safety requirements with respect to the system arrived and it flows down to the each and every components including software within the system. Thus, the distribution of safety related activities among the stakeholders of the supply chain is the greatest challenge with respect to standard driven by TOP DOWN approach.

However, the pressure of time-to-market requires the reuse of off-the-shelf components. Thus, it mandated to have the component including software elements should made available even before the system design initiated. Thus, concept of a Safety Element out of Context (SEooC) development appears on ASIL 26262 standard context. As observed by (Schneider et al. 2012), there are problematic aspects and challenges in implementing such an approach for automotive domain.



This case study paper demonstrates the process and technical implementation followed in a software product—Network Operating System (NOS)—that is intended to work on production environment.

### Network Operating Systems

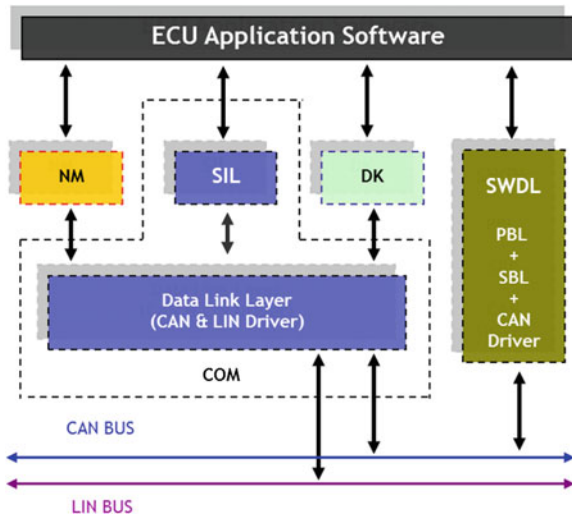
Network Operating System is the platform software required for CAN and LIN based Automotive ECU software. It provides standardized platform Software, consists of APIs to facilitate the communication of messages irrespective of protocol (CAN or LIN) or the underlying controller within it implemented (Fig. 1).

Network Operating System consists of CAN/LIN communication stack, Network Management and Unified Diagnostic Services Diagnostics Kernel (UDS DK). Network Communication Stack (NOS COM) provides Application Programming Interface (API)

- Facilitates communication over CAN and LIN Protocols
- Facilitates connect as well as disconnect to CAN and LIN bus
- Facilitates the communication of messages
- Provides the facility to read and write signals by application software

Network Management (NOS NM) provides the Application Programming Interface (API) to connect and disconnect network, monitor the status of network and switching over to the suitable application frame mode based on the network status. NOS NM handles the connection management, configuration management, sleep/wakeup handling and bus-off recovery process. Unified Diagnostic Service (UDS) kernel logs and manages the fault occurred during the vehicle operation.

Fig. 1 Network operating systems



Thus, Network operating systems provides an off-the-shelf software modules to develop ECU software without having the hassles of interacting with controller/compiler setup as well as protocol used (e.g. CAN and LIN).

The scope of this paper is to describe the technical implementation and the process of enhancing Network Operating System software to make it feasible to use ECU software that requires the adherence to ISO 26262 Functional Safety.

### *Network Operating System Software—Safety Element Out of Context*

Network Operating System Software is an off-the-shelf-software which is reused and ported at a later stage whenever the system is realized. Major part of the software is generic in nature and not developed in the context of a particular vehicle. The safety requirements and the environment in which this software may be used can only be assumed during development.

ISO 26262 has taken into consideration scenarios for such generic hardware and software components and provided guidelines for development of such components for safety applications (Fig. 2).

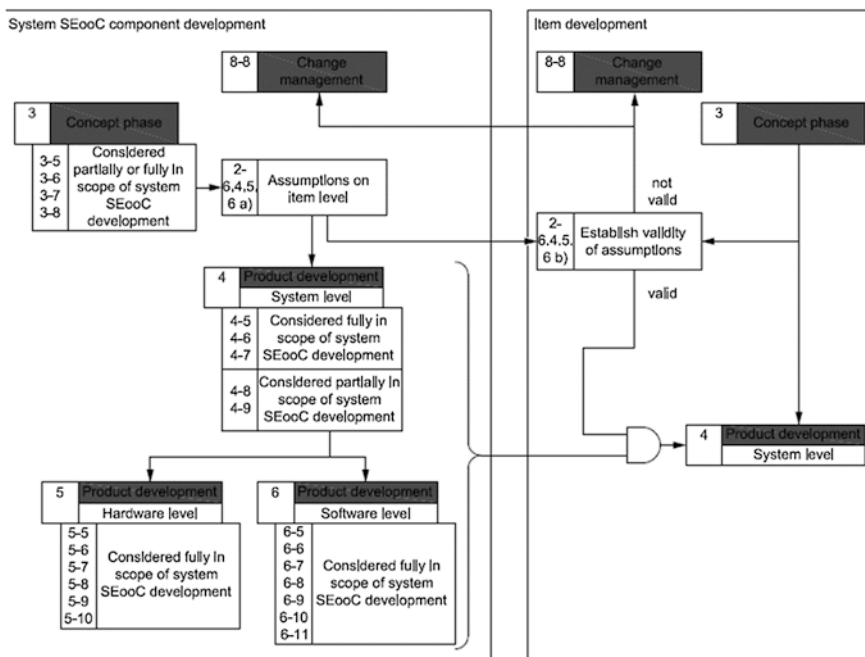


Fig. 2 Safety element out of context development (ISO 26262 Standard 2012)

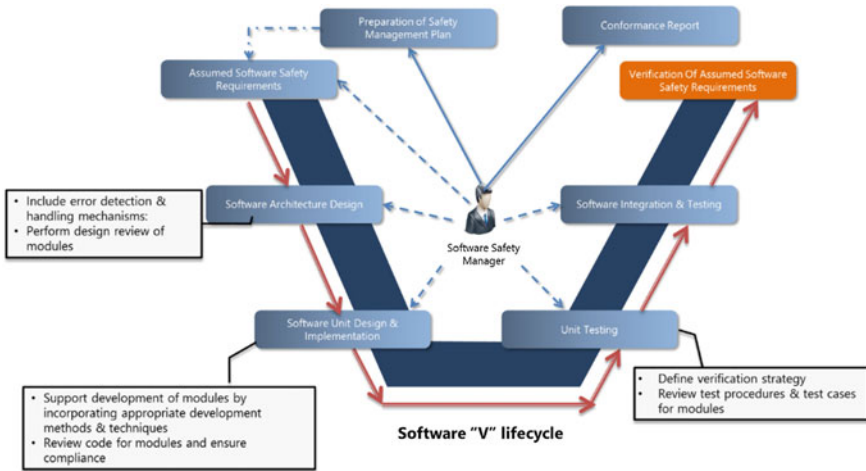


Fig. 3 Software V life cycle—safety process

As Eckhardt (2013) confirms SEooC Development has 3 stages—Requirements assumption, Context assumption and work product Provision. The extended V Safety Lifecycle process was adopted to use for the enhancement of Network Operating System software (Fig. 3).

For NOS product enhancement, devised out a Seven Step Safety Process (SSSP) to enhance the off-the-shelf software components to make suitable to work with ECU software those are functionally safer. These steps are generic enough to adopt as a strategy for any similar product development, wherever the enhancement of existing product is required.

### Seven Step Safety Process for Reusable Components

In this section of case study paper, describes the implementation and results of the Seven Step Safety Process developed in accordance with ISO 26262 framework. The outcome of these steps is to confirm the usage of NOS components to cater the automotive software integrity level requirements of ECU software. The Seven Steps are:

1. Generate assumed safety requirement for an assumed environment
2. Architecture Analysis
3. Tool qualification
4. Technical Implementation
5. Verification and confirmation measures
6. Item requirement validation
7. Ensuring a proper Safety Case

Thus, Seven Step Safety Process provides the practical approach to safety for existing components by an innovative frame work with suitable tools, guidelines and templates.

### ***Step 1: Generate Assumed Safety Requirements for an Assumed Environment***

This step is to perform the safety analysis on an assumed system and identify the safety features of the chosen software component (i.e.; Network Operating Systems). The outcome of this step is to have analyzed and documented safety requirements for the software component. This step includes the following:

- Analyze an assumed system to have probable safety features of the component: Part of this stud identified the system was evaluated to identify the safety requirements system and the set of requirements of NOS component is derived from the same. The other inputs for this study includes the Network Operating Systems specification and assumed Hardware Interface document.
- Perform DFMEA on the existing software component: Unlike typical Design Failure Mode and Effect Analysis (DFMEA), for existing reusable component DFMEA should be carried out in earlier phase of project execution, instead of design phase and with a provision to be revisited/reconfirm during the architecture analysis phase. This activity is carried out with the inputs such as OEM and standard specifications, Lessons Learnt and assumed behavior of the component. It serves as a detailed design review to erase the weakness out of the component design.
- Identify Safety Requirements of NOS: Component specific software safety requirement document and the mapping of Technical Speciation Requirements was documented during this activity.

The phase outcome provided the list of safety functional requirements to be incorporated in-addition to the existing safety and non-safety features of component (Fig. 4).

**Step 1 Outcome:** Per the analysis, identified the facilities to be provided to existing Network Operating Systems software for having the end-to-end verification of messages.

### ***Step 2: Architecture Analysis***

As the safety requirements identified for Network Operating System components, the obvious next step is to incorporate the features within the component design (Fig. 5).

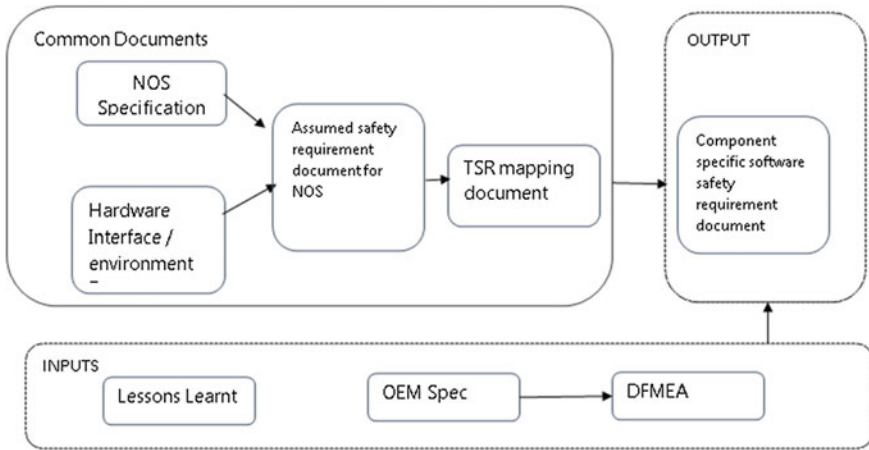


Fig. 4 Network operating systems—safety element out of context

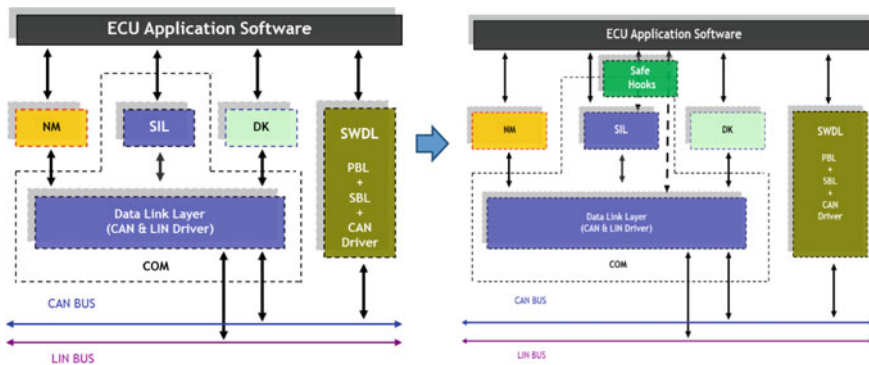


Fig. 5 Network operating systems—architecture analysis

**Step 2 Outcome:** Thus considering the purpose of end-to-end verification and also to provide the maximum flexibility to user, it is decided to provide the callback facility to ECU software instead of Application Programming Interfaces (APIs) within the component. Thus, the callbacks with the intention of upper layer intimation of pre-transmission, post transmission, reception and DLC error was identified.

- void Com\_TxCbk (c\_net\_handle n, C\_UINT32 can\_id, C\_UINT8 COM\_DATA \* DataPtr, C\_UINT8 dlc\_val)  
 Inputs: c\_net\_handle n, C\_UINT32 can\_id, C\_UINT8 COM\_DATA \*Dataptr C\_UINT8 dlc\_val  
 Output: None

**Rationale:** This call-back function is invoked during the beginning of the transmission of every frame by COM layer. This callback provides the data present in the primary buffer and hence this is responsibility of the application developer to enhance the data with required counter or checksum to the transmission buffer. Thus, this is possible to have additional information before transmitting the message to the bus.

- `void Com_TxConfirmation_success (c_net_handle n, C_UINT32 can_id, void*)`

Inputs: `c_net_handle n, C_UINT32 can_id, void *DataPtr`

Output: None

**Rationale:** This callback function is invoked by the application in order to confirm the transmission of every frame on to the CAN bus. This assists to increment the counter to have a flow monitoring by the end-to-end library.

- `void Com_RxCbk (c_net_handle n, C_UINT32 can_id, C_UINT8 COM_DATA *DataPtr, C_UINT8 dlc_val`

Inputs: `c_net_handle n, C_UINT32 can_id, void *DataPtr, C_UINT8 dlc_val`

Output: None

**Rationale:** This call-back function is invoked on reception of frames by COM layer. Correctness and completeness of the received data should be verified by the application upon the reception of data, either of following mechanisms—counters, checksum or signal validation in end-to-end library.

- `void Com_DLCErr_Cbk (c_net_handle n, C_UINT32 can_id, C_UINT8 dlc_val, C_UINT8 conf_dlc, C_UINT8 COM_DATA *DataPtr)`

Inputs: `c_net_handle n, C_UINT32 can_id, void *DataPtr, C_UINT8 dlc_val`

Output: None

**Rationale:** This call-back function is invoked on reception of frames when the received DLC is not equal to the configured DLC in signal database. Upon the data reception, DLC mismatch notification is received if any mismatch and thus, the end-to-end library shall perform the corrective actions

### ***Step 3: Tool Qualification***

In this step, based on the tool error detection (TD) and tool impact (TI) matrix, confidence level of signal database generator tool is evaluated (Fig. 6).

As part of Tool Impact analysis, the impact of the tool generated files on the component behavior was evaluated. This evaluation categorically verified following scenarios of tool generated files.

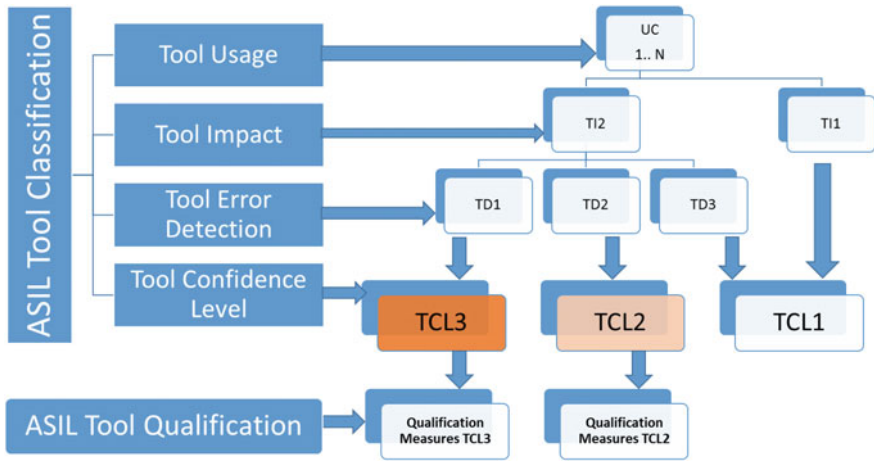


Fig. 6 Signal database generation tool classification scheme

- No output
- Syntactically wrong output
- Semantically wrong output
- Incomplete Output
- Output does not compile (match) with respect to configuration (Data Mismatch)

Thus, this should be categorized as TI1 or TI2. If no impact (TI), then tool is classified with Tool Confidence Level 1 (TCL1) and there is no additional qualification measures is required. In case of TI2, the error detection method should be classified.

As part of error detection analysis, the detection capability of the concern is surfaced on tool generated files was analyzed.

- What are the verification procedures? Sufficiency of them
  - MISRA analysis
  - Desktop Review/Manual Inspection
  - Tool based Interface interference Analysis
- What are the existing validation mechanisms?
- Is it detectable based on existing validation procedure?
  - Detection of syntax errors by compilation
  - Detection of semantic errors by validation procedure
- What are the recommendations of component usage with respect to the assigned safety level?
- Sufficiency existing process to claim the strong error detection mechanism?

Based on the analysis, the tool detection mechanism will be categorized TD1, TD2 or TD3, where TD3 has the highest detection capability. The increasing level of tool error detection capability  $TD1 < TD2 < TD3$ .

As the Generation tool's claim of the development by ISO Part 6 requirements with Risk Analysis/FEMA/Safety management is an item difficult to be convinced. Thus, based on the analysis it was decided to have tool driver kit, in addition to the existing approaches of in-depth verification, validation and usage recommendations. However, if the ECU requirements is beyond ASIL B (i.e., ASIL C or ASIL D), the system output should be verified with another separate tool framework too.

**Step 3 Outcome:** Based on the tool error detection (TD) and tool impact (TI) matrix, confidence level of signal database generation tool determined as "TCL2". Hence, as per the recommendations of ASIL B ECU software, the tool qualification kit was enhanced with addition usage scenarios.

### ***Step 4: Technical Implementation***

In this step, existing component was enhanced with suitable hooks to facilitate the end-to-end latency of the system. The greatest challenge is the compatible usage of safer NOS component within legacy application. Hence, the enhancement of NOS with safer hooks should be within the viability of the component usage.

Let us examine few scenario of safety feature needs within ECU software for the data communication integrity.

- Adding suitable parity mechanisms while sending or publishing the data
- Verification of the completion of data transmission
- Verification of Data Length code (DLC) of incoming data
- Timeout mechanism of expected data arrival
- Confirmation of received data for the correctness (E.g. CRC/Parity check upon reception)
- Valid conversion of raw data to suitable engineering measurements

**Step 4 Outcome:** The enhancement of NOS with safer hooks is required to have safer ECU software application, those required similar features. In addition to the Throughput (RAM/ROM usage) and Performance (CPU load) should be within stipulated limit per requirements of production intended software.

### ***Step 5: Verification and Confirmation Measures***

Standard verification processes recommended by ISO 26262 are followed. An independent safety team with separate reporting structure ensures proper safety standards are followed by performing confirmation reviews, audits and assessments periodically.



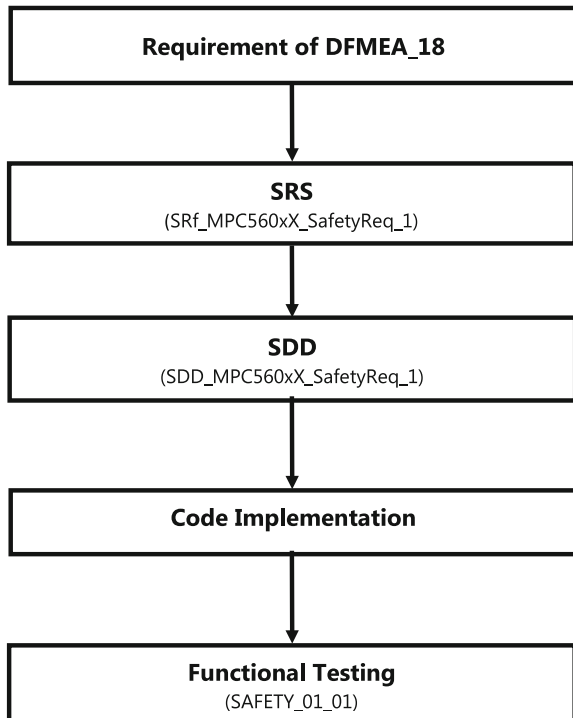
**Step 5 Outcome:** This step ensures that all the safety documentation is adequate and complete to adhere to ISO26262 recommendations. Development and safety review of process artifacts such as safety conformance reports, safety audits and safety assessment reports was carried out during NOS product enhancement.

**Step 6: Item Requirement Validation**

During integration with the item a safety requirement comparison is done to validate that the assumed safety requirements are in line with the item requirements. In case there is any discrepancy, then the NOS assumed safety requirements and/or the item needs to undergo a change in order to ensure that both are consistent (Fig. 7).

**Step 6 Outcome:** Safety testing and related documentation was completed during this step. Also the NOS safety documentation with recommendations and prerequisites with respect to the components design and reusable component usage was documented for the customer use.

**Fig. 7** Network operating system—safety requirement validation



2.1.	DETAILS SAFETY ELEMENTS .....	9
2.1.1	SRS SAFETY ELEMENTS .....	9
2.1.2	SDD SAFETY ELEMENTS.....	9
2.1.3	TEST CASE SAFETY ELEMENTS.....	9
3.	SAFETY CASE .....	10
3.1.	DETAILS SAFETY ELEMENTS .....	10
3.2.	SRS PHASE (PLEASE REFER PC16_COM_SRS_FREESCALE_MPC5602DMLL4_CW_V10.5.DOC) 11	
3.3.	DESIGN PHASE(PLEASE REFER PC16_COM_SDD_FREESCALE_MPC5602DMLL4_CW_V10.5.DOC) .....	11
3.4.	CODING PHASE.....	11
3.5.	TESTING PHASE .....	13
	(PLEASE REFER PC16_COM_STP_FREESCALE_MPC5602DMLL4_CW_V10.5.XLS) .....	13

Fig. 8 Network operating system—safety case document

### Step 7: Ensure a Proper Safety Case

A safety case produced by component vendor to ECU Supplier. It describes the safety management system and measures in place to ensure the controls are effectively and consistently applied. The safety case would consist of all necessary documentary proofs to show how safety in the product has been achieved (Fig. 8).

**Step 7 Outcome:** NOS Safety Case document was prepared and made available for the end-user confirmation.

### Conclusion

Enhanced existing network operating system with safer hooks was implemented. Those safety hooks is made usable by ECU Software developer to make end-to-end data correctness. The throughput and CPU Load measured for Safe NOS and compared with legacy NOS. It was observed that there is slight increase in CPU Load (~0.5 %) for typical set of communication matrix. However, the deployment of NOS within production intended systems was acceptable.

In addition to that, it paves the way for having strong safety culture within the organization. Also devised seven step safety process (SSSP) became the defacto process framework for the reusable off-the-shelf software component development. Thus, this case study provides the experience by a software component vendor to a systematic approach of developing safer reusable components.

## References

- Eckhardt H (2013) Practical issues in safety critical component reuse in the automotive industry. Slides accessed at [www.kpit.com/downloads/medini-analyze/3-esa-workshop-2013.pdf](http://www.kpit.com/downloads/medini-analyze/3-esa-workshop-2013.pdf) on 10 Oct 2015
- Edgar Snyder & Associates (2009) Car accident statistics. <http://www.edgarsnyder.com/car-accident/statistics.html>. Accessed 30 May 2015
- ISO 26262-1 (2012)(e) Road vehicles—functional safety—part 10: guideline on ISO 26262. International Standardization Organization, Geneva, p 50
- Schneider R, Brandstaetter W, Born M, Kath O et al (2012) Safety element out of context—a practical approach. SAE Technical Paper 2012-01-0033. doi:[10.4271/2012-01-0033](https://doi.org/10.4271/2012-01-0033)

# Statistical Decision in the Automotive Material Selection

Cristian Andreescu, Adrian Stere Paris, Cristian Dragomirescu  
and Constantin Târcolea

**Abstract** The objective of the research is the ranking of materials applied to an example from the automotive industry (material candidates for the car body construction). The variety of properties/attributes imposes different evaluations for metrical/ordinal scales and the necessary statistical calculus. Heterogeneity of the characteristics imposes the separation of the attributes into mainly two classes: functional (mechanical, physical, etc.), usually with metric scale and technological and environmental attributes with frequently ordinal scale. The paper analyses a practical case of the material for the car body by Multi Criteria Decision Making (MCDM) procedures like primary ranking and preference index value applied to mechanical, technological and ecological, respective all attributes, etc. All these methods are principally based on the variance, viewed as a risk measure. The final comparison has as result the most valuable materials: Titanium sheet, Glass Reinforced Plastics (GRP) and Carbon Fiber Composite.

**Keywords** Materials ranking · Correlation · Variance analysis

## Introduction

In multicriteria processes, different methods may produce a ranking of the alternatives of a decision that is normally in the same way. Anyway a variability in ranking should be possible on the basis of requirements, respectively weights and is, therefore, acceptable, to arrive at a compromise or consensus. Numerous authors have investigated problems of ranking and decision: (Kemeny and Snell 1962; Cook 2006; Heiser and D'Ambrosio 2013; Singh and Kumar 2012) etc., including the material selection (Ashby 2002; Târcolea and Paris 2008; Paris and Târcolea 2009). The continued development of automotive industry implied the extended

---

C. Andreescu (✉) · A.S. Paris · C. Dragomirescu · C. Târcolea  
University Politehnica Bucharest, Bucharest, Romania  
e-mail: saparis2015@gmail.com

study of new materials utilized for parts production and many researches for a better decision: (Wilhelm 1993; Antunes and Lopes de Oliveira 2014; Davies 2012; Fuchs et al. 2008; Savkin et al. 2014).

## Practical Material Ranking

The general idea of this paper is to present a simpler method (Singh and Kumar 2012; Paris and Târcolea 2015), developing an example for automotive material selection. Material candidates for the car body construction are: Forming grade steel EN 10130 DCO4 + Z, HSS EN 10292 H300YD + Z, UHSS—martensitic, Aluminium 5xxx, Aluminium 6xxx, Magnesium sheet, Titanium sheet, Glass Reinforced Plastics (GRP) and Carbon Fiber Composite. The considered attributes (properties) are: Yield Strength (YS) [MPa], Ultimate Tensile Strength (UTS) [MPa], Elongation A80 [%], Elasticity Modulus (EMod) [MPa], and Density (D) [ $\text{kg}/\text{dm}^3$ ], Forming, Joining, Paint, CO<sub>2</sub> + emis, Disposal and Costs (Davies 2012). The variety of those attributes imposes different evaluation for metrical/ordinal scales. The mechanical properties took into account cover a metrical scale (numerical values of the attributes) and the others use an ordinal scale.

The technological attributes are based on range: 1—difficult to process; 10—production without difficulty. The ecological properties are evaluated on ease with which prevailing legislation can be met: 1—extensive development required; 10—without difficulty. Not all attributes are shown and it is easy to subdivide any of the columns shown (Davies 2012).

For a real model the values must be reordered; there are properties for which the greatest value is the best (for example the tensile strength), and others with the smallest value as the best (for example density); this is a reason for the handling of the marks from 1 to 10 (10 is the best) for an a priori elimination of these inadventences. Another possibility is the Likert scale, analog to the German scores system, with the marks from 1 to 5 (1 is the best), which will indicate directly the position in the hierarchy.

In the present case the solution can be easy perceived because the materials are well known and only a few and it is useful if the number of the objects and attributes is very high, very different and less known. When the Sheller-Globe Corporation, maker of heavy truck cabs, wanted to design a new cab, asks the potential customers to rank the opposition on seven scales covering gasoline mileage, case of steering, durability, etc. (Toffler 1991).

The ranking of the analyzed materials can be obtained rigorously using statistical tools. In the paper it is applied computer aided correlation and variation analysis. The general idea to reduce the calculus volume imposes the study of the correlation matrix of the attributes, to avoid the possible redundancies. So the first step is the calculus of the correlation matrix of the attributes (without costs).

A brief analysis of results shows that some attributes are strong correlated. As working hypothesis it will be:

**Materials’ Ranking Considering Mechanical Properties (YS, UTS, A80, EMod and D)**

The properties YS and UTS have a very good correlation, equivalent with a redundancy, and it permits the elimination one of them. In the same way are EMod si D, and finally it is enough to use only 3 properties: YS (max), A80 (min) and D (min).

To continue the analysis it is necessary to reorder the properties so that they will vary in the same logic, with maximal the best, and then, keeping in mind that A80 and D are minimal the best attributes, the values were inverted.

The applied algorithm (Singh and Kumar 2012; Paris and Târcolea 2014) contains: normalized of the values, the computing of the variances and weights of the characteristics (Table 1, column 2) (the weighting is an important step for the decision maker); it results the ranking of materials (Table 1 column 3).

**The Materials’ Ranking Based on Technological and Ecological Properties**

The considered technological properties are: Forming, Joining, Painting and the ecological properties are: CO<sub>2</sub>+emis and Disposal. The elementary ranking is based on the sum of range values (Table 2).

The scoring of the material employing technological and ecological properties, with the same algorithm (preference index) (Table 3), furnishes another ranking: Forming grade steel EN 10130 DCO4 + Z, HSS EN 10292 H300YD + Z and Carbon Fiber Composite, with comparable results with the elementary ranking (Table 2).

**Table 1** Ranking by 3 selected mechanical properties

Materials	Weights	Rank
Forming grade steel EN 10130 DCO4 + Z	0.024191	9
HSS EN 10292 H300YD + Z	0.03759	8
UHSS—martensitic	0.129931	4
Aluminum 5xxx	0.044398	7
Aluminum 6xxx	0.044822	5
Magnesium sheet	0.084647	4
Titanium sheet	0.193059	3
GRP	0.21365	2
Carbon fiber composite	0.227713	1

**Table 2** Elementary ranking based on technological and ecological properties

Materials	Sum	Elementary rank
Forming grade steel EN 10130 DCO4 + Z	42	1
HSS EN 10292 H300YD + Z	39.5	2
UHSS—martensitic	36.5	6
Aluminum 5xxx	37	4
Aluminum 6xxx	37	4
Magnesium sheet	30.5	9
Titanium sheet	33	8
GRP	36	7
Carbon fiber composite	37	4

**Table 3** Ranking based on technological and ecological properties

Materials	Preference index rank
Forming grade steel EN 10130 DCO4 + Z	1
HSS EN 10292 H300YD + Z	2
UHSS—martensitic	7
Aluminum 5xxx	5.5
Aluminum 6xxx	5.5
Magnesium sheet	9
Titanium sheet	8
GRP	4
Carbon fiber composite	3

### ***The Ranking of Materials upon the Two Groups of Properties (Mechanical, Technological and Ecological)***

It is obvious that the two rankings are completely different, practically opposed. The shortest way is to average the two rankings. A more consistent solution is to compute ranking considering the eight above mentioned properties (Table 4).

The ranking is identical with the one of the mechanical properties because of the significant bigger variance of this kind of properties.

### ***Ranking Including Costs Too***

The analysis based on the nine selected properties makes use of weights and ranks (Table 5).

**Table 4** Ranking with all analyzed properties

Materials	Weights	Rank
Forming grade steel EN 10130 DCO4 + Z	0.05436264	9
HSS EN 10292 H300YD + Z	0.060251017	8
UHSS—martensitic	0.124384837	4
Aluminum 5xxx	0.061893473	7
Aluminum 6xxx	0.06220602	5
Magnesium sheet	0.084416164	4
Titanium sheet	0.167786358	3
GRP	0.187007522	2
Carbon fiber composite	0.197692421	1

**Table 5** Material ranking including costs

Materials	Weights	Rank
Forming grade steel EN 10130 DCO4 + Z	0.040276	9
HSS EN 10292 H300YD + Z	0.04462	8
UHSS—martensitic	0.090397	4
Aluminum 5xxx	0.052236	7
Aluminum 6xxx	0.054685	6
Magnesium sheet	0.067999	5
Titanium sheet	0.251218	1
GRP	0.148718	3
Carbon fiber composite	0.24985	2

### *Ranking Based on 11 Properties*

The analysis based on the eleven selected attributes (Table 6).

To find out the best ranking it is necessary a comparison of the five rankings with the correlation matrix. The results permits the remark that the arranging upon the technological + ecological properties is discordant, as it was already explain. In automotive industry, steel is still very used as consequence of the big weight of the implicit costs, but there is a significant trend to reduce its importance.

The quality of the selection as a whole is assessed by estimating its internal consistency reliability with Cronbach’s alpha test (Wessa 2015).

For each omitted property (V1–V11, Table 7) the coefficients score is over the minimum reliability of 0.7, which consolidates the general Cronbach’s alpha score, which indicates over a 70 % consistency in the scores that are produced in the model.



**Table 6** Material ranking with 11 properties

Materials	Weights	Rank
Forming grade steel EN 10130 DCO4 + Z	0.040884	9
HSS EN 10292 H300YD + Z	0.046639	8
UHSS—martensitic	0.101436	7
Aluminum 5xxx	0.059089	6
Aluminum 6xxx	0.061176	5
Magnesium sheet	0.078856	4
Titanium sheet	0.221089	2
GRP	0.160051	3
Carbon fiber composite	0.230779	1

**Table 7** Measure of the internal consistency reliability

Cronbach alpha and related statistics		
Items	Cronbach alpha	Std. alpha
All items	0.7773	0.8367
V1 excluded	0.7263	0.8273
V2 excluded	0.7073	0.8069
V3 excluded	0.7295	0.8
V4 excluded	0.7801	0.8632
V5 excluded	0.7815	0.8372
V6 excluded	0.7778	0.8073
V7 excluded	0.7805	0.8249
V8 excluded	0.7557	0.792
V9 excluded	0.7516	0.8078
V10 excluded	0.7316	0.83
V11 excluded	0.8008	0.843

## Conclusion

The ranking of the analyzed materials can be obtained rigorously using statistical tools. The variety of those attributes imposes different evaluation for metrical, ordinal scales or both. The general consideration of the properties points out Carbon Fiber Composite as the best, and only the technological and ecological properties reveal steel on the first place, but with Carbon Fiber Composite on the third place. It is of interest the whole comparison, but for practical applications only the first places are important, like in the sports competitions. For the classical materials the selection has usually a simple solution, but for new materials and many properties the ranking is very difficult and unclear without statistical tools. Another possibility of measure of the variation of attributes is the computing of the eigenvalues. Essential for the hierarchy are the properties with the big variance, where the ranking becomes more consistent. The paper should be seen as a technique that

learns by example. The statistical tools applied in the paper seems here to complex for the materials range, however they offer a more exactly image for rational decisions.

## References

- Antunes RA, Lopes de Oliveira MC (2014) Materials selection for hot stamped automotive body parts: an application of the Ashby approach based on the strain hardening exponent and stacking fault energy of materials. *Mater Des* 63:247–256
- Ashby MF (ed) (2002) *Materials selection in mechanical design*. Butterworth-Heinemann Edition, Oxford
- Cook WD (2006) Distance-based and ad hoc consensus models in ordinal preference ranking. *Eur J Oper Res* 172:369–385
- Davies G (ed) (2012) *Materials for automobile bodies*, chapter 3. *Materials for consideration and use in automotive body structures*. Ed. Butterworth-Heinemann, p 99
- Fuchs ERH, Field FR, Roth R, Kirchain RE (2008) Strategic materials selection in the automobile body: economic opportunities for polymer composite design. *Compos Sci Technol* 68: 1989–2002
- Heiser WJ, D'Ambrosio A (2013) Clustering and prediction of rankings within a Kemeny distance framework. In: Berthold L, Van den Poel D, Ultsch A (eds) *Algorithms from and for nature and life*. Springer, Berlin, pp 19–31
- Kemeny JG, Snell JL (1962) Preference rankings: an axiomatic approach. In: Kemeny JG, Snell JL (eds) *Mathematical models in the social sciences*. Blaisdell, New York, pp 9–23
- Paris AS, Târcolea C (2009) Computer aided selection in design processes with multivariate statistics. In: *Proceedings of the international conference on manufacturing system*, vol 4. ICMaS, Bucharest, pp 335–338
- Paris AS, Târcolea C (2014) Materials ranking by means of multiattribute decision making. In: *7th international conference on advanced manufacturing technologies—ICAMaT, IMST, UPB*
- Paris AS, Târcolea C (2015) Multivariate statistic decision design. In: *The eight international working conference “total quality management—advanced and intelligent approaches”*. Ed. Univ. Belgrad, Serbia, pp 295–300
- Savkin AN, Andronik AV, Gorunov AI, Sedov AA, Sukhanov MA (2014) Advanced materials of automobile bodies in volume production, European transport/Trasporti Europei. *Int J Transp Econ Eng Law* 56(10):1–27
- Singh H, Kumar R (2012) Selection of material for bicycle chain in Indian scenario using MADM approach. In: *Proceedings of the world congress on engineering*, V. III. London, pp 1377–1381
- Târcolea C, Paris AS (2008) The Joreskog technique applied for materials design, In: *Proceedings of the 17th international conference on manufacturing systems—ICMaS*, Ed. Acad. Romane, University Politehnica of Bucharest, Machine and Manufacturing Systems Department Bucharest, pp 309–312
- Toffler A (1991) *Powershift: knowledge, wealth, and violence at the edge of the 21st century*. Bantam Press
- Wessa P (2015) Free statistics software, office for research development and education, version 1.1.23-r7, URL <http://www.wessa.net/>
- Wilhelm M (1993) Materials used in automobile manufacture—current state and perspectives. *J de Physique IV (C7):C7-31–C7-40*

# Effects Analysis of Zone 30 Based on Recognition, Age and Accident Experience

Ryosuke Ando, Yasuhide Mimura, Keiichi Higuchi  
and Marehiro Mukai

**Abstract** This study was made to answer the question that the recognition for Zone 30 is necessary for the drivers to drive cars safer or not? We conducted some surveys to analyze influences of the recognition for Zone 30. As the target district, Motoshiro district in Toyota City in Japan, where Zone 30 had been put into implementation, was chosen. As the results, there are statistically significant differences between the recognition people and the rest regarding the maximum driving speed. It is known that the maximum speed when driving in the Zone 30 district is reduced more when the drivers recognized the Zone 30 implementation. Then, the analyses were applied for the comparison among the elderly people and the others. The elderly people tend to make higher evaluation for the Zone 30 measures. Moreover, further analysis shew that the Zone 30 related measures have higher potential for the people who experienced traffic accidents than that having no accident experience.

**Keywords** Traffic safety · Zone 30 · Effects · Elderly drivers · Accident experience

---

R. Ando (✉) · K. Higuchi  
Research Department, TTRI (Toyota Transportation Research Institute),  
Motoshiro-Cho 3-17, 471-0024 Toyota, Aichi, Japan  
e-mail: ando@ttri.or.jp

Y. Mimura  
Nagoya Branch, International Development Consultants Co. Ltd, Sakae 2-12-12, Naka-Ku,  
Nagoya, Aichi 460-0008, Japan  
e-mail: y.mimura@idec-inc.co.jp

M. Mukai  
School of Psychology, Chukyo University, Yagoto Honmachi 101-2, 466-8666 Showa-Ku,  
Nagoya, Aichi, Japan  
e-mail: mmukai@lets.chukyo-u.ac.jp

## Introduction

Recently, autonomous driving technology is a very hot issue in the world. A concrete approach is ITS (intelligent transport systems) which include vehicle and infrastructure and V2V (vehicle to vehicle) cooperative driving. However, to step into a real safe automotive society, the enforcement countermeasures cannot be switched off. In this viewpoint, the research on the effects of the enforcement is continually important issue regarding the automobile development.

In order to promote traffic speed limits regulation, WHO (2008) published a famous guideline. Several years later, a new traffic safety program, named the Ninth Fundamental Traffic Safety Program of Japan, was released (Cabinet Office 2011). In which, the National Police Agency (2011) decided that a traffic safety countermeasure, so-called Zone 30 (Vis and Dijkstra 1992; TRL 2003), would be promoted in all prefectures of Japan. In order to make Zone 30 spread easily, the regulations on the necessary road environment conditions had been relaxed. Therefore, there are some districts where planned and developed measures of Zone 30 are different even though the districts may be managed by same police office and local government office. This situation brought up a result that road users, especially drivers, may not recognize Zone 30 in some districts.

Ando and Mimura (2014) discussed the entrance design of the Zone 30 district considering Japanese consciousness to compare with the other countries (IRTAD 2011). Mimura et al. (2014) reported that the recognition for Zone 30 may make the drivers drive cars safer. To understand the effects of the Zone 30 and the related measures further, in this paper, the effects of Zone 30 and the related measures are analyzed on the basis of the recognition, the age and the traffic accident experience.

Two kinds of surveys were carried out in 2012. As the target district, the Motoshiro district (Fig. 1) in Toyota City in Japan, where the Zone 30 and the

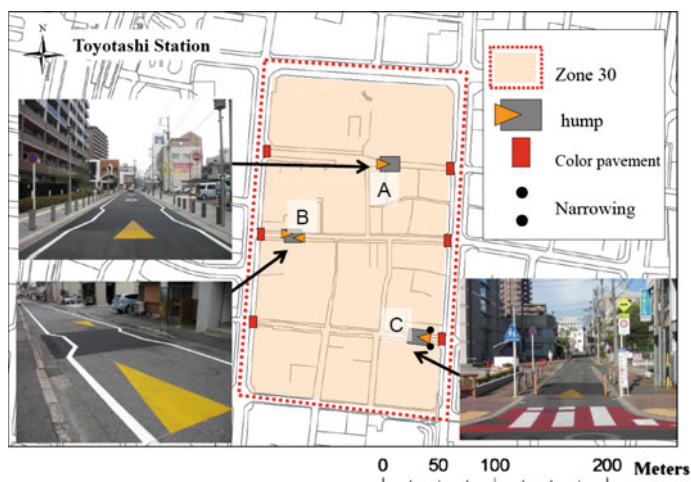
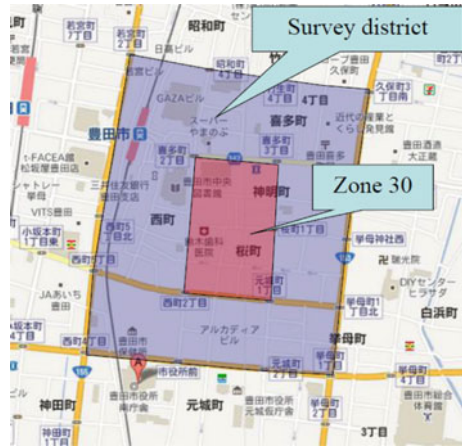
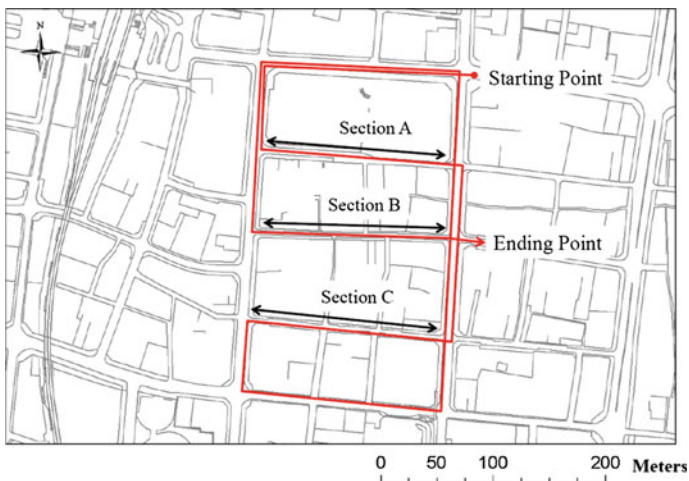


Fig. 1 Zone 30 and the related measures in Motoshiro district

**Fig. 2** Questionnaire survey district



related measures were implemented first time in Toyota City, was chosen. The first survey is a questionnaire survey targeted residents in and rounding the Zone 30 district as shown in Fig. 2. The survey was conducted after the implementation of Zone 30. The answers from 338 households of 1305 in total were obtained. The representative person who drives a car the most frequently at his/her household was asked about the recognition of the Zone 30, change of their driving behaviors and so on. Another survey was based on the test drives which had been conducted on the route given in Fig. 3. Thirty people including 15 persons being 65 years or older took part in the test drives. The test drives have been done twice: before and after the implementation of Zone 30. During the test drives, log data including the



**Fig. 3** Test drives route

position and drive speed et al. and video data focusing to the front view to know the vehicles ahead and parking situation et al. were collected.

### Effects of Recognition on Zone 30

On the basis of the first survey described above, the people can be divided into two groups: one in which the people knew that Zone 30 had been implemented and another one in which the people didn't know that. Figure 4 shows the difference between these two groups. The same thing is there is no one thought the traffic safety were worse. Comparing to the "didn't know" group, the different things are more people in the "knew" group thought the traffic safety became better than before, and less people answered "don't know".

On the other hand, regarding the negative influence, the traffic congestion, which had been commented by many people before the Zone 30 measures were implemented, the percentage of the "no" answer given by the "knew" group doubled that of the "didn't know" group as shown in Fig. 5. Furthermore, the "yes" and "don't know" answers given by the "knew" group are much less that of "didn't know" group. That is, the people who recognized the Zone 30 measures implementation can make a more clear evaluation and their evaluation is more positive.

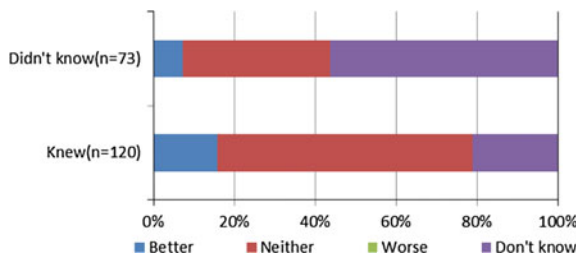


Fig. 4 Evaluation on the traffic safety after zone 30 measures were implemented

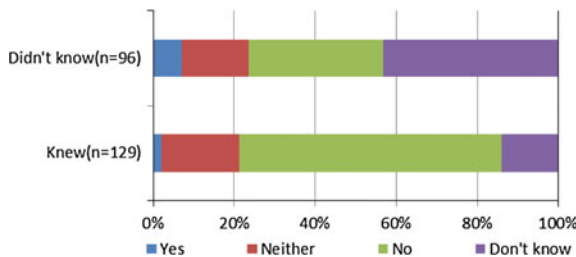


Fig. 5 Evaluation of the traffic congestion rounding the zone 30 district

**Table 1** Factors affecting maximum speed within each section (translated from Mimura et al. 2014)

Factor/Variable	Partial regression coefficient	Standard error	Standard partial regression coefficient	T-value	P-value	Judgement
Zone 30 recognition dummy (knew)	-3.633	1.531	-0.380	-2.373	0.021	*
Gender dummy (male)	-2.929	1.331	-0.280	-2.200	0.032	*
Age dummy (elderly)	-2.306	1.562	-0.246	-1.476	0.146	
Being conscious of speed limit dummy (yes)	-2.584	1.715	-0.255	-1.507	0.138	
Section C dummy (yes)	-5.097	1.319	-0.504	-3.864	0.000	**
Section B dummy (yes)	-2.026	1.282	-0.203	-1.580	0.120	
Constant	40.720	2.334		17.448	0.000	**

Note Sample number = 58,  $R^2 = 0.35$ , Durbin Watson ratio = 2.22, AIC = 334.66, \*\*1 % significant, \*5 % significant

In terms of the second survey described above, the factors which may affect the maximum driving speeds have been analyzed. The results are given in Table 1. There, the Zone 30 recognition dummy shows a 5 % statistically significant coefficient, which means that the recognition may reduce the maximum speed. Furthermore, another 5 % statistically significant result tells us that the male people tend to make their speeds down. Moreover, a negative coefficient with the 1 % statistical significance let us know that the color pavement and the narrowing measures at the section C make the speed decreased effectively.

### Comparison Among the Elderly People and the Others

Japan is the most representative country being the rapidly ageing society in the World. To make the evaluation of the Zone 30 and the related traffic measures, here a comparative analysis is made. The people can be divided three groups: elderly being 65 years old and over, youth being under 30 years old and middle age being between 30 and 64 years old. Considering the recognition, Fig. 6 shows there are not big differences among the three groups.

Figure 7 shows the evaluation on the traffic safety after Zone 30 measures were implemented. The same thing is there is no one thought the traffic safety were worse. On the other hand, the elderly people evaluated “better” much more than the other two groups although these differences are not statistically significant.

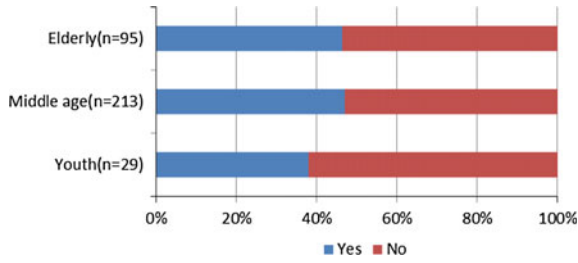


**Fig. 6** Recognition of the zone 30 implementation by the age group

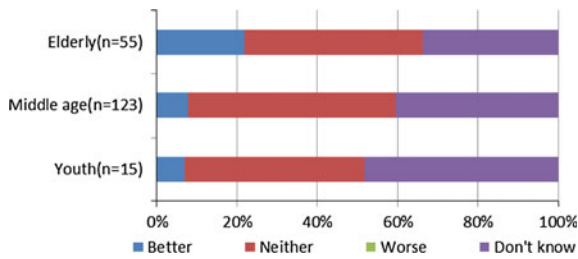


**Fig. 7** Evaluation on the traffic safety after zone 30 measures were implemented by the age group

Figures 8, 9 and 10 show the evaluations of the related three kinds of traffic safety measures by the age group on the effects to make the passing through behavior less, the effects to make the speeds down and the total traffic safety effects respectively.

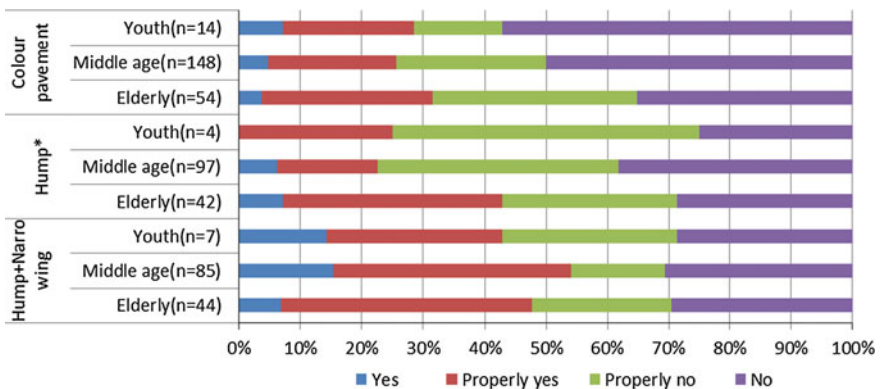


**Fig. 8** Evaluation on the effects to make the passing through behavior less by the age group. *Note* \*10 % significant when making the fisher's exact test (degree of freedom = 2)



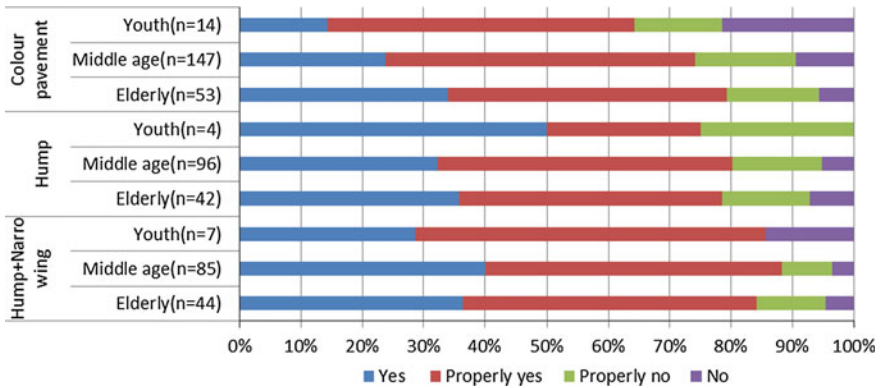


Fig. 9 Evaluation on the effects to make the speeds down by the age group

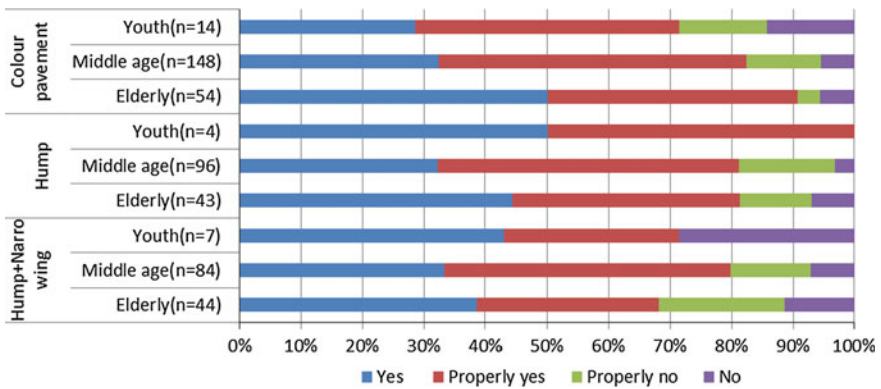


Fig. 10 Evaluation on the total traffic safety effects by the age group

Regarding the effects limiting the passing through in Fig. 8, the hump shows a 10 % statistically significant differences among the three age groups. The elderly people make the greatly positive evaluation. As for the other measures, the elderly people make the relatively higher positive evaluation on the color pavement compared with the other two age groups although there is no statistically significance. Furthermore, the hump+narrowing measures obtain the relatively greater support by all three age groups although they are not statistically significant.

## Comparison by Considering the Traffic Accident Experiences

The most important purpose of the Zone 30 and the related traffic safety measures is to make the traffic accidents decreased. From this viewpoint, the analysis by considering the traffic accident experiences is conducted here.

Figure 11 shows the recognition situation of the Zone 30 implementation. There is no clearly difference between the people who experienced the traffic accidents in the past and the people who have no traffic accident experience.

Figure 12, where the evaluation on the traffic safety after Zone 30 measures were implemented is shown, tells us that the traffic experienced people give a higher “better” percentage. That, the Zone 30 has a more positive effect for the people who experienced the traffic accidents, means an excited result with the high potential to make the traffic accidents decreased.

Figures 13, 14 and 15 show the evaluations of the related three kinds of traffic safety measures by considering the accident experience on the effects to make the passing through behavior less, the effects to make the speeds down and the total traffic safety effects respectively.

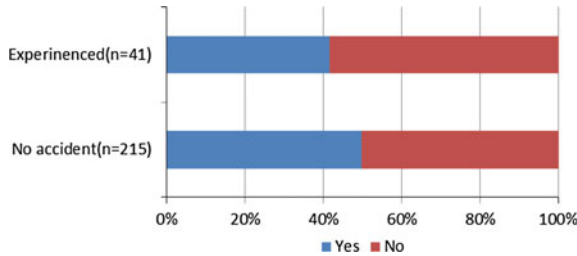


Fig. 11 Recognition of the zone 30 implementation by considering the accident experience

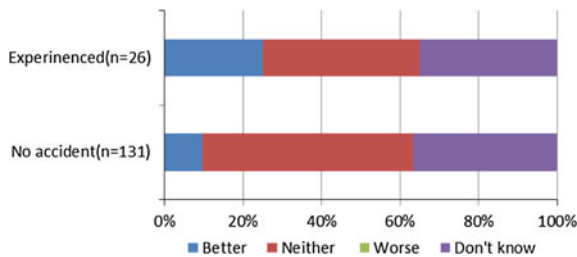
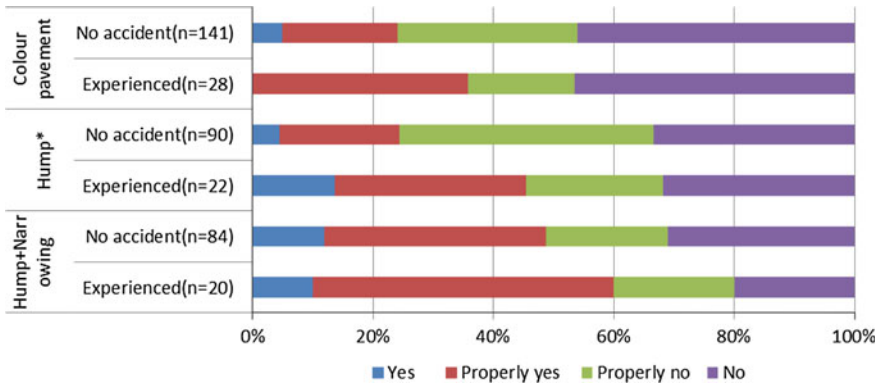


Fig. 12 Evaluation on the traffic safety after zone 30 measures were implemented by considering the accident experience



**Fig. 13** Evaluation on the effects to make the passing through behavior less by considering the accident experience. *Note* \*10 % significant when making the Fisher’s exact test (degree of freedom = 2)

Regarding the effects limiting the passing through in Fig. 13, the hump shows a 10 % statistically significant differences between the two groups. The traffic accident experienced people make the greatly positive evaluation. As for the other measures to limit the passing through, although there is no statistically significance, the traffic accident experienced people make the relatively higher positive evaluation, too. However, on the effects to make the speeds down, there seems no difference between the two groups with all three types of measures as shown in Fig. 14.

Furthermore, regarding the total traffic safety effects given by Fig. 15, the hump +narrowing measures obtain the greater support by the traffic accident experienced people and this difference is a 10 % statistically significant result. Moreover, the

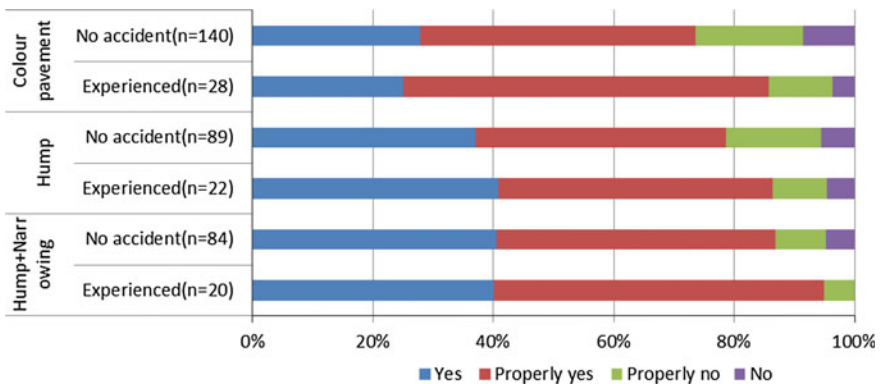


**Fig. 14** Evaluation on the effects to make the speeds down by considering the accident experience

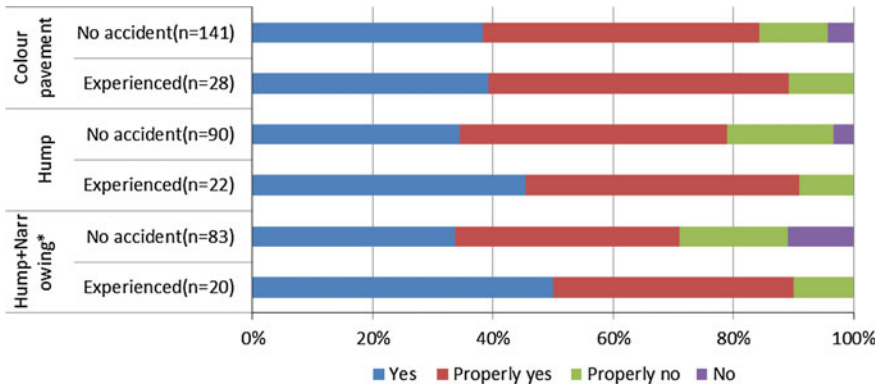


**Fig. 15** Evaluation on the total traffic safety effects by considering the accident experience. *Note* \*10 % significant when making the Fisher’s exact test (degree of freedom = 2)

traffic accident experienced people make the relatively higher positive evaluation also with the other measures.

### Conclusions

This study made an analysis on the effects of the Zone 30 and the related traffic safety measures focusing on the recognition, the elderly and the traffic accident experience.

In terms of the two surveys conducted in Toyota, Japan and then the data analysis based on their results, there are differences between the recognition people and the rest regarding the traffic safety effects of the Zone 30 implementation. It should be emphasized that the maximum speed when driving in the Zone 30 district are reduced more with the drivers recognized the Zone 30 implementation, with the male drivers and with the hump+narrowing road environment.

Regarding the differences among the elderly people and the others, the elderly people evaluated the hump significantly higher to limit people passing through the Zone 30 districts.

Furthermore, as for the differences between the traffic accident experienced people and the others, the traffic accident experienced people evaluated the hump measure significantly higher to limit people passing through the Zone 30 districts and the hump + narrowing measure significantly higher in the viewpoint of total effects.

Since 2011, the Zone 30 measure has been treated as an important and effective traffic safety measure for the community roads and the residential areas. The outputs obtained from the analysis in this study will be supplied to the public and applied for the further promotion and implementation in Japan.

**Acknowledgments** This study was partly supported by JSPS KAKENHI Grants Number 26540076. Furthermore, we would like sincerely to express our thanks to the cooperation provided by Toyota City Government, Toyota Policy Office and the related Citizen Organization.

## References

- Ando R, Mimura Y (2014) A study on entrance of speed limit zone based on users' consciousness in Japan. *Procedia Soc Behav Sci* 111:88–97
- Cabinet Office (2011) Ninth fundamental traffic safety program. Government of Japan
- IRTAD (2011) Road safety annual report. <http://internationaltransportforum.org/irtadpublic/pdf/11IrtadReport.pdf>
- Mimura Y, Higuchi K et al (2014) Relationship of safe driving behavior and cognition of Zone 30, *J JSCE Jpn Soc Civ Eng D3* 70(5):I\_597–I\_604
- National Policy Agency (2011) Report on promotion of zone countermeasures for the community roads. Government of Japan
- TRL (2003) Review of 20mph zones in London boroughs. [http://www.eltis.org/sites/files/case-studies/documents/review\\_of\\_20\\_mph\\_zones\\_in\\_london\\_boroughs\\_full\\_report\\_3.pdf](http://www.eltis.org/sites/files/case-studies/documents/review_of_20_mph_zones_in_london_boroughs_full_report_3.pdf)
- Vis AA, Dijkstra A (1992) Safety effects of 30 km/h zones in the Netherlands. *Accid Anal Prev* 24 (1):75–86
- WHO (2008) Speed management—a road safety manual for decision makers and practitioners

# New Technology for Composite Materials Parts

Anghel Chiru and Lucian Eugen Rad

**Abstract** The paper makes an analysis of automotive manufacturing processes in composite materials. The novelty is the new process of winding space which can obtain small parts with complex geometry (console steering column) using composite materials.

**Keywords** Composite materials · Space winding technology · Manufacturing process

## Introduction

Weight reduction in automotive industry it means to reduce the fuel consumption and fulfill international requirements in CO<sub>2</sub> emissions. Development of light-weight construction, will be analyzed, based on requirements which consist of design concepts and new manufacturing processes, vehicle steering column (steering column console).

The starting point of this new manufacturing method it is the classical process of winding for rotation symmetrical components (Heitz 2013).

Because we discuss about the production of parts with complex geometry used in the automotive industry, this technology should be automatized for large series production >50.000 units/year.

The element that characterizes the new method is to use one or two robots, which allows additional degrees of freedom that allow winding space technology used for obtaining complex parts.

Steering column components are shown in Fig. 1:

---

A. Chiru (✉) · L.E. Rad

Material Science Department, Transilvania University of Brasov, Brasov, Romania  
e-mail: achiru@unitbv.ro

L.E. Rad

e-mail: lucian.rad@unitbv.ro

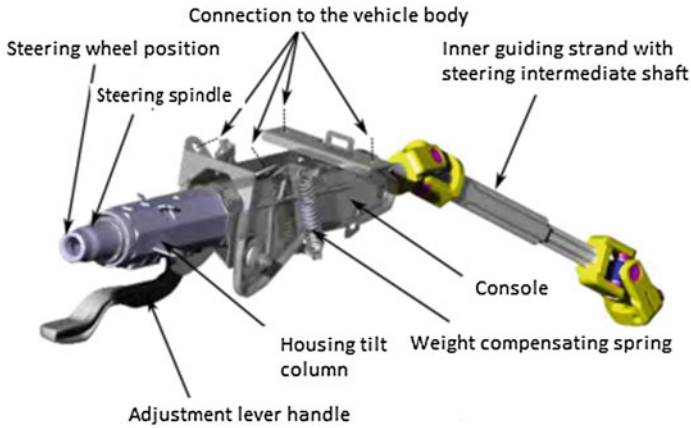


**Fig. 1** Steering column components

We chose as a component for production the steering column bracket VW Golf 6.

Requirements that must be fulfilled steering columns were extracted from the specification of the VW Golf 6:

- Natural frequency:
  - Vertical  $>50$  Hz;
  - Horizontal  $>50$  Hz.
- Stiffness:
  - Vertical  $\leq 1.6$  mm;
  - Horizontal  $\leq 1$  mm.
- Weight saving.
- Force control in climatic conditions of  $-30$  to  $+ 80$  °C
- Locking way and blocking force of action lever, including acoustic and a haptic behavior
- Maximum permissible torsional moment
- Torsional stiffness

Unconventional materials (composite materials based on carbon fiber) have a high potential for use in industry, due to low weight and high rigidity, successfully replacing traditional materials. Manufacture technologies of composite materials are varied and reflect how increasing levels of automation affect freedom in design (Fig. 2).

With increasing levels of automation, the cost of production per piece decreases, depending on the number of components produced annually and manufacturing method used.

For restore the design of structural components of the steering column is important to make considerations of both integral and differential methods of

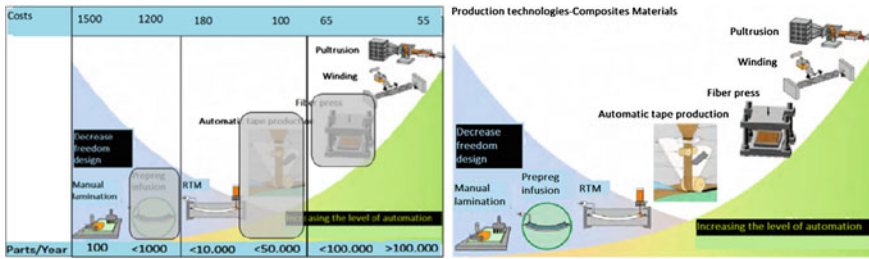


Fig. 2 Different production technologies and estimated costs (Source Heitz 2013)

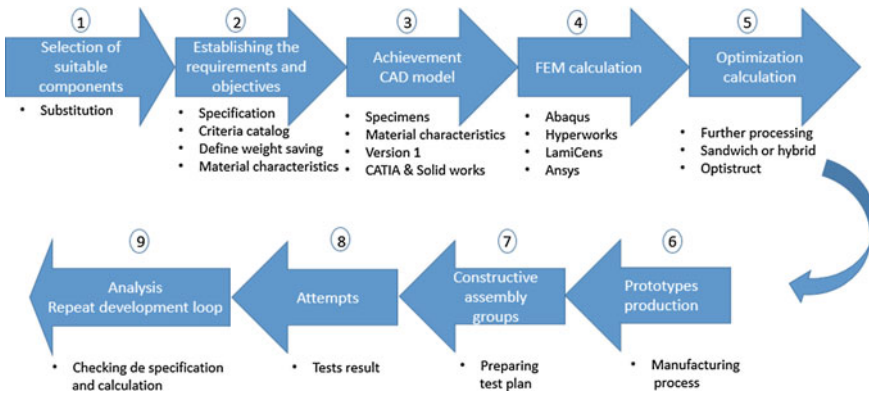


Fig. 3 Product development methodology

design, in terms of the economy and the manufacturing process (Heitz and Chiru 2011).

The methodology for the development of a product is described in Fig. 3.

Following this methodology, we developed a new design for the steering column VW Golf 6, using Catia and Solidworks and using space winding manufacturing process.

### Space Winding Technology

Newly developed method allows through the use of robots, making additional degrees of freedom to the above, even in combination with metal inserts. This process for produce structural components of the steering column with its special requirements on flexural and torsional rigidity and functional integration, limiting the movement of longitudinal reinforcement to absorb collision energy was innovative developed.



The advance is the complexity component of 0.5–1 m/min. With this clock during manufacturing to a length of 300 mm is 20–40 s. The winding space technology is suitable for mass production, with >50,000 pcs./Year. The process is not generated scrap/waste during production or after post processing and have a low volume. A big advantage of this newly developed method is to be submitted by roving, fiber directions consistent with the flow of forces.

For creating parts using space winding technology, we need the following components: carbon fiber roving support, carbon fiber roving, impregnation bath, tensioner, guidance system, two robots, tool, epoxy matrix, oven, de- moulding agent (Fig. 4).

Carbon fiber is mounted on the roving. Then carbon fiber passes through the impregnation bath where he mixed with epoxy resin, excess resin is squeezed. In order to have a constant tension of the fiber, I used a tensioner. The fiber passes through the guide which is mounted on the winding robot arm.

The roving is wrapped in starting point of the forming device that is mounted on the handling robot arm, to ensure self-fixing. While the winding robot performs the winding space, the handling robot is ready with a new forming device. In this way, after winding is completed for forming device, it is led to the oven. Meanwhile, the handling robot already start winding process for a new forming device of the robot. Thus ensuring continuity of production.

**Designing and developing forming device** The construction of the forming device is a real challenge for the new winding space process, because at the winding we need to avoid collisions between parts of the device. After winding, the device is removed from the robot, it is checked possible defects occurs winding the console.

Subsequently, the polymerization process of the console is carried out in the closed form, in a furnace pre-heated to 80 °C. Then the console is removed from the mold.

Because of problems regarding the geometric shape of console and hard demoulding using forming device with pressure plates (Fig. 5), we were developed a new forming device with pressure hose (Fig. 6). If we make a comparison

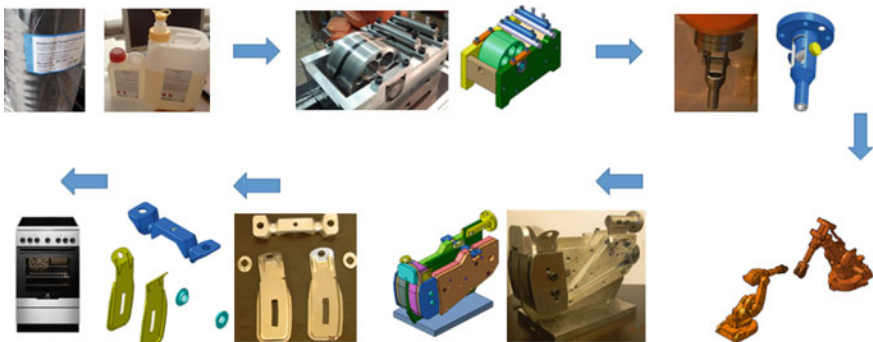
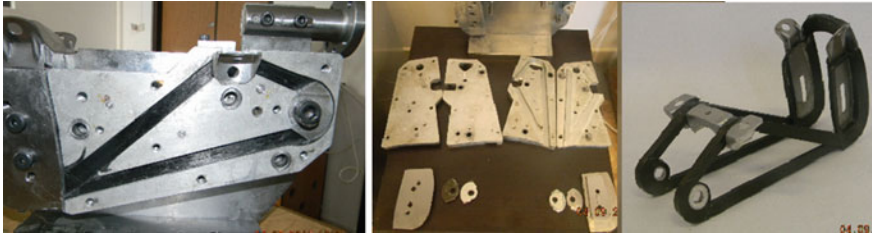
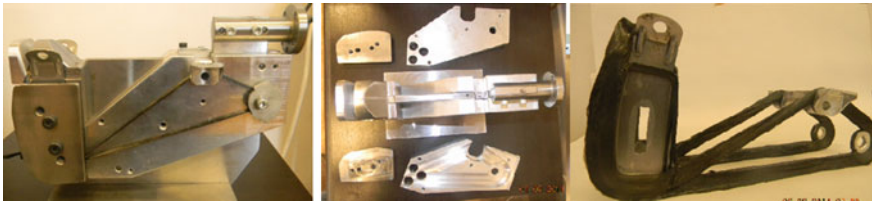


Fig. 4 Winding space technology



**Fig. 5** Forming device with pressure plates for steering column console



**Fig. 6** Forming device with pressure hose for steering column console

between two forming device, will see that, production time decrease with 30 min/part but the most important is the easy-way demoulding because of opportunity to not destroy the part (Table 1).

Due insert metal sites, construction console as a hybrid structure is more complex, because in addition to fiber orientation changes should be taken into account

**Table 1** Comparison between the two forming device regarding production time

	Pressure plates Time (min)	Pressure hose Time (min)
<i>Tool preparation</i>		
Cleaning	15	10
Resources separation application	20	20
Total duration of preparing	35	30
<i>Production</i>		
Winding time	15	15
Closing pressure plates	5	5
Hardining time 10 min/80 ° C + 2 h/100 °C	130	130
Air cooling after hot extraction	60	60
Demoulding	30	5
Total duration of production	240	215
Total time production	275	245

the inserts. In this way results in a new composite material. It was accepted the existence of overlapping but they have little influence on the deposit component due under tensile fibers. Overall reduce weight is 639 g and 52 % decrease from steel version

**Design and implementation impregnation bath** Carbon fiber, before being wound on the forming, have to be impregnated with resin. Thus, we designed a resin impregnation and squeezing additional fiber by means of a squeezing cylinder (Fig. 7). After the carbon fiber is out of the impregnation bath, it must be sufficiently squeezed so that in the winding process does not appear resin spraying forming device.

This additional resin sprinkled on the forming device, is hardening, which leads to additional cleaning operation with direct impact on the total production time per piece.

**Design and implementation guidance system** Guidance system is mounted to the robot flange being the element which guide the impregnated fiber on forming device. There has been several models for guidance system (Fig. 8), but we chose the one which had the fiber outlet as small as possible to prevent the return fiber during winding process.

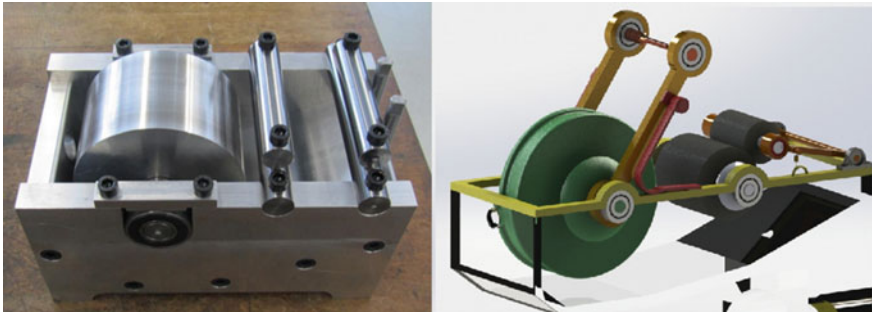
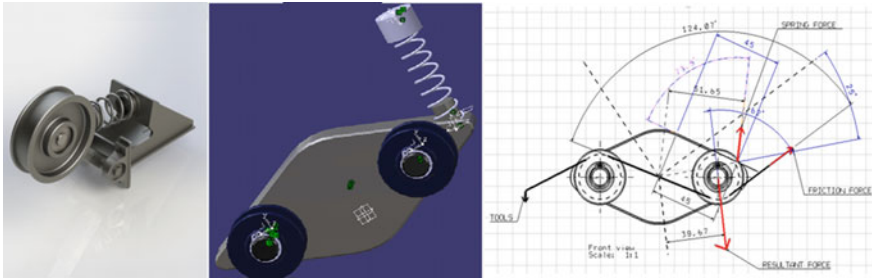


Fig. 7 Impregnation bath with fix squeeze cylinders (left) and rotating cylinders (right)



Fig. 8 Different versions for guidance system



**Fig. 9** Carbon fiber tensioner and calculus tensioner scheme

**Tensioner** Because the quality of part is depending to fiber tensioning during the winding process, we need a tensioner which will provide an constant tension in the fiber ( $T = 20 \text{ N}$ ) (Fig. 9).

The most important thing is that we need a rotational moment for roving support which does not allow the carbon fiber to unwind from the bobbin such that in any moment of the movement the carbon fiber remains tensioned.

In the most tensed position of the system (in the maximum compression point of the spring) there is 25 grades between vertical plan and system position.

It is suppose that the coefficient of friction is not important between the carbon fiber and rollers, because it was used rollers on bearing ( $\mu = 1$ ).

$$F = 2T \cos a = 2 * 20 * \cos 62^\circ = 18.77 \text{ N} \tag{1}$$

Determination of necessary spring force for balance between resultant force and spring force:

$$M = 2F * l_1 = 2 * 18.77 * 40 = 1501.6 \text{ N mm} \tag{2}$$

$$M = F^{spring} * l_2 \gg F^{spring} = M/l_2 = 1501.6/51.6 = 29 \text{ N} \tag{3}$$

F necessary force spring to maintain constant 20 N in fiber

$\alpha$  is the angle between fiber direction and spring direction

$l_1$  distance between mechanism center and rolling center

$l_2$  distance between mechanism center and spring center

The necessary force spring to maintain an constant tension ( $T = 20 \text{ N}$ ) in carbon fiber, is 29 N.

**Roving support** the purpose of roving support is to hold the carbon fiber bobbin, to assure a easy mounting of bobbin, to maintain moment of friction such that provide constant tension in fibre of 20 N.

$$M^{torque} = T * R = 2F * l^1 = 20 * 38.5 = 770 \text{ N mm} \tag{4}$$

$$M^{friction} = F_x * \mu * r \text{ for } M^{torque} = M^{friction}, F_x = M^{torque} / \mu * r = 46 \text{ N} \tag{5}$$

- R bobbine radius (38.5 mm)
- M friction coefficient between brake pad and plastic
- r radius of brake pad (44.5 mm)
- $F_x$  pressure force of brake pad

### Conclusion

We realized a part of composite material and to estimate the quality of the results obtained we can make a comparison between different materials and processes for the same part.

In order to respect the requirements of VW (Fig. 10) regarding the stiffness, natural frequency and weight saving, it's easy to conclude that composite materials based on carbon fiber and space winding technology, could be a solution to create small parts with complex geometry, cheap and for mass production.

One of the great advantages of this newly developed process is the possibility to be executed using roving bobbins sites with good price and the fibers of the roving can be submitted in accordance with the flow paths defined and lines of force (Taca and Paunescu 2012). Irregularities in the roving layer deposition can be tolerated within certain limits so that in the event of winding techniques irregularities in laying the fibers free permit ensuring a proper quality. The new process, developed in this work allows additional degrees of freedom winding space by using a robot. This new process has now been announced to be patented. With production assembly described we can achieve a continuous production with a production cycle of under 2 min/piece. Weight bracket obtained, using composite materials, is lower by 48 % compared to steel bracket (Fig. 11).

	Requirements	SeriesSteel	Carbon(Autoclave)	Carbon RTM	Carbon Space winding
Weight [g]	Console+Case	622+600	268+231	258+258	325+258
Stiffness					
Vertical F=600N [ mm]	≤1,6	1	3,65	1,56	1,58
Horizontal F=250N [ mm]	≤1	0,46	2,68	1,2	0,98
Natural frequency -wheel position-fully extended/down:					
Vertical [ Hz]	>50 Hz	65,8	39,3	52,6	59
Horizontal [ Hz]	>50 Hz	54,2	26,1	48,2	54

**Fig. 10** Comparison between different technologies and different materials for steering column console



**Fig. 11** Steering column bracket steel (*left*) and carbon fiber (*right*)

Developing new components for composites technology, we can create parts with complex geometries, light-weight and with strong material properties.

This opens up the potential in the field of lightweight construction in vehicles technique that can be used in future for other segments. Test results on specimens help choosing the correct material composition, mode of settlement of the fibers, their orientation, etc. With the help of computer programs AlphaLam, LamiCens, LAP can calculate the dimensional characteristics of different stratifications. This technology allows for the construction of any automotive part by simply replacing the tool.

Is brought into question the existence of a concept for economic production in large series of structural components of the steering column. To achieve such production is necessary to meet the requirements of the customers and for large series (over 50,000 pcs./Year) to obtain a maximum delta costs 20 Euro, additional costs, together with a reduction in weight 1 kg, without affecting functionality.

## References

- Heitz T (2013) The physical-mechanical properties of structural components made of fiber composite materials in the application of steering columns in cars. Doctoral Thesis, Brasov, Romania
- Heitz T, Chiru A (2011) Analysis of using CFK material for steering columns components in passenger vehicles—part 2. FISITA, 13 EAEC Automotive Congress, Valencia
- Taca C, Paunescu M (2012) Composite materials. MatrixRom, Bucuresti. ISBN 9789737558440

# Tyre Dynamics: Model Validation and Parameter Identification

Andreas Hackl, Wolfgang Hirschberg, Cornelia Lex and Georg Rill

**Abstract** The present paper deals with the experimental validation of tyre dynamics approaches as it is widely applied in tyre models for vehicle dynamics and handling. Firstly it gives a brief derivation of two modelling principles regarding the deflection velocity in the considered direction of the tyre's deformation. This is then followed by a brief description of the performed measurement procedure. From the measurements, a set of model parameters of the considered tyre, depending on different manoeuvre speeds and frequencies, is identified, where no particular fitting parameters for the tyre dynamics are needed. Based on these model parameters, the related dynamic simulations are carried out. The comparisons show that the applied first-order model describes the behaviour quite well within a certain operation range, whereas the second-order approach cannot deliver better results in spite of the longer computational time. However, for investigations within an enlarged frequency range of the steer input and at high slip angles, a more detailed model is recommended.

**Keywords** Tyre dynamics modelling · Semi-physical model · Tyre testing · Vehicle dynamics · Handling

---

A. Hackl (✉) · W. Hirschberg · C. Lex  
Graz University of Technology, Inffeldgasse 11/II, A-8010 Graz, Austria  
e-mail: andreas.hackl@tugraz.at

W. Hirschberg  
e-mail: wolfgang.hirschberg@tugraz.at

C. Lex  
e-mail: cornelia.lex@tugraz.at

G. Rill  
OTH Regensburg University of Applied Science, Regensburg, Germany  
e-mail: georg.rill@oth-regensburg.de

## Introduction

Modelling and simulation of safety relevant Driver Assistance Systems (DAS) and Vehicle Dynamics Controllers (VDC) which act in standard and limit situations lead to increasing accuracy demands in the description of dynamic reactions of tyre contact forces, e.g. (Hirschberg et al. 2000; Lex and Eichberger 2011). For that purpose, first-order approaches are widely applied in this field of vehicle dynamics and handling, which originate from (Schlippe and Dietrich 1942), were modified by (Pacejka 2006) and later on refined by Rill (2012). This approach is typically characterised by the first-order differential equation

$$\tau_{x,y} \dot{F}_{x,y}^D + F_{x,y}^D = F_{x,y}^S, \quad (1)$$

where the superscripts  $D$  and  $S$  distinguish between dynamic and static tyre forces and the subscripts  $x$  and  $y$  indicate the longitudinal and lateral directions of the tyre forces  $F$ . However, the coefficient  $\tau$  which corresponds to a relaxation length is not constant, but depends on the wheel load  $F_z$  and the tyre slips  $s_x$  and  $s_y$  respectively.

The line of modelling of the visco-elastic mechanism of tyre deformation is the key of a proper description of  $\tau$ . Based on previous researches, e.g. (Hackl et al. 2015), the scope of the present paper is to investigate two different approaches for the above mentioned modelling method. One is the modelling principle regarding to the semi-physical tyre model TMeasy (Hirschberg et al. 2007; Rill 2012) and the other one, named here TMmass, refers to (Pacejka 2006). This is done by comparison of selected simulation results with corresponding measurement data from an extensive laboratory testing programme. With the aim to run vehicle dynamics models on uneven, but not rough roadways, a frequency range of at least 4 Hz was considered. Due to the research project's current focus on lateral vehicle dynamics, the evaluation of the correspondent relations in longitudinal direction will be dealt with on a later occasion.

## Modelling Aspects

A common model approach to dynamic tyre forces and torques takes the compliance of the tyre in lateral, longitudinal, and circumferential directions into account, Fig. 1. According to (Pacejka 2006), a mass representing an appropriate part of the tyre belt in contact is considered too.

Then, the dynamic lateral force  $F_y^D$  is modelled by

$$F_y^D = c_y y_e + d_y \dot{y}_e, \quad (2)$$



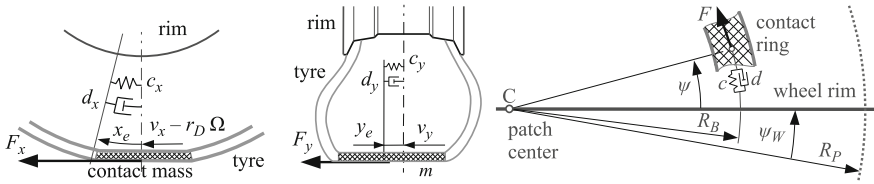


**Fig. 1** Tyre deflection in the longitudinal, lateral and circumferential directions

where  $y_e, \dot{y}_e$  follow from

$$m\ddot{y}_e + d_y\dot{y}_e + c_y y_e = F_y^S(v_y + \dot{y}_e). \tag{3}$$

Within this approach  $m$  denotes the corresponding belt mass,  $c_y$  and  $d_y$  are the stiffness and damping properties of the tyre, and  $F_y^S$  describe the lateral tyre characteristics evaluated at the dynamic sliding velocity  $v_y + \dot{y}_e$ . This model is named tyre model with mass TMmass for further investigations in the present paper under numerical solution of Eq. (3).

The corresponding belt mass is supposed to be quite small, and may therefore be neglected in favour of computational efficiency and reduced model parameterisation effort. In case of neglecting the belt mass,  $y_e, \dot{y}_e$  then follow from

$$d_y\dot{y}_e + c_y y_e = F_y^S(v_y + \dot{y}_e), \tag{4}$$

representing a first-order tyre dynamics model, which is used within the TMeasy tyre model. As shown in (Rill 2006, 2012; Hackl et al. 2015), the implicit first order differential equation is analytically expanded from  $F_y^S(v_y + \dot{y}_e)$  into a Taylor Series. In contrast to Eq. (3), the formulation in Eq. (4) finally leads to a closed description of  $\tau$  to be used in Eq. (1). In this article, the difference between TMmass as described in Eq. (3) and the approach within TMeasy as described in Eq. (4) will be compared.

## Test Bench Setup and Tyre Measurement Programme

Measurements have been carried out on a brake and suspension test rig, which was developed for investigation of durability and fatigue of components of quarter vehicle suspensions, (Harrich et al. 2006). For the present experiments, the wheel assembly consisting of tyre, rim and wheel carrier were mounted to the test bench using a rigid suspension. No spring and damper elements were attached between wheel and test bench.

The test bench has a drum with an outer diameter of 1.219 m. It can be pivoted around the vertical axis to generate a slip angle  $\alpha$  between  $\pm 15$  deg with a maximum

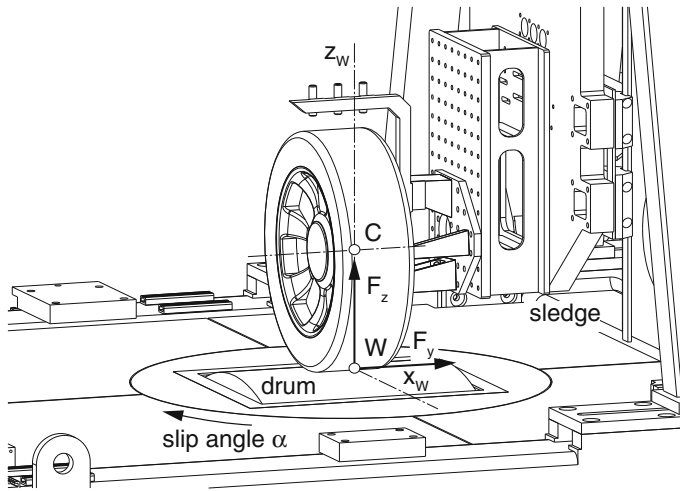


**Fig. 2** Test bench setups to parametrise and validate the non-linear first-order tyre dynamics approach

rotational velocity of 25 %/s, see Fig. 2. The drum speed can be varied between 0 and 1,300 rpm. The vertical tyre load is set using a vertical hydraulic cylinder with a maximum cylinder force of 25 kN. Depending on the weight of the test assembly and the required travel range, a maximum pulse frequency of 35 Hz can be achieved with this cylinder. The maximum actuator speed is 1.1 m/s, the maximum actuator acceleration is 10 m/s<sup>2</sup>.

The resulting forces and torques in the wheel hub are measured using a high-precision Kistler (2015) wheel force transducer (WFT), applied on a radial tyre size of 205/55 R16. Three non-contact temperature sensors were used to measure the tyre surface temperature directly after the outlet of the tyre contact patch. The internal tyre pressure was set at operational temperature of 20°. In addition, the drum steer angle  $\alpha$ , the drum roll speed  $\Omega_{drum}$ , the vertical travel  $z_C$  of the wheel carrier and the ambient temperature during the tests are measured. All signals discussed in the following were recorded at a sample rate of 1 kHz.

### ***Tyre Measurement Manoeuvres***

To investigate the non-linear tyre dynamics and validate the characteristics of the lateral spring  $c_y$  and damper  $d_y$  properties, two different measurement programmes are defined. The first is used to parametrise the steady state lateral tyre characteristics which are implemented in the tyre models and also needed for the optimisation, see Sect. “[Steady State Tyre Characteristics](#)”. Secondly, high dynamic manoeuvres are performed to validate the non-linear tyre dynamics and examine the

**Table 1** Overview of the measured conditions to parametrise and validate the non-linear tyre model behaviour

Tyre load $F_z$	3,600	N
Tyre pressure $p$	2.75	bar
Sine slip angle amplitude $\alpha$	1, 2, 4 and 6	°
Sine slip angle frequency $f$	0.125, 0.25, 0.5, 1, 2 and 4	Hz
Drum circumferential speed $v_x$	20, 60, 100 and 130	km/h

influences on different drum speeds and frequencies on the lateral spring and damper properties. To cover vehicle dynamics on uneven roadways, a frequency range up to 8 Hz is supposed to be covered by the model.

To fulfill all requirements and include the physical limits of the test bench, a sine slip angle input with different frequencies and amplitudes and a constant normal force  $F_z$  was used for both measurement programmes. In detail, a frequency range in steps from 0.125 to 4 Hz and an amplitude range of the slip angle  $\alpha$  from 1 to 6° were carried out. With the target of keeping a constant tyre load, a hydraulic pump with a maximum force of  $F_{z,max} = 10,000$  N is installed. A side slip-frequency-drum speed-matrix, with respect to the manoeuvre ranges, was set up for the parametrisation.

Table 1 gives a summary of the measured conditions used in present paper. For a detailed list of performed measurements see (Hackl et al. 2015).

## Steady State Tyre Characteristics

To validate the dynamic behaviour depending on the frequency and wheel speed of the tyre, a steady state tyre model is needed. This basic tyre model is parametrised with step steer inputs during constant drum speed of 60 km/h, described in (Hackl et al. 2015). Starting from this basic tyre model, the steady state characteristics have been adapted using quasi-stationary sine manoeuvres with a frequency of 0.125 Hz, speed of 60 km/h and different slip angle amplitudes listed in Table 1. This was necessary because the tyre showed a changed behaviour due to tyre wear during these tests.

As mentioned in the literature, cf. (Rill 2012), two main characteristics are changing during the lifetime of a tyre. The main change of characteristics is an increase of the lateral stiffness because of the reduced tyre tread depth. Secondly, the force maximum is moving to a smaller slip angle value. These two factors are especially important for manoeuvres performed with a slip angle  $\alpha$  less or equal to 6°, which have been used for these investigations.

The values of the lateral spring  $c_y$ , lateral damper  $d_y$  and the model mass  $m$ , all described in Sect. “Modelling Aspects”, are used from (Hackl et al. 2015) and (Pacejka 2006). Together, with the parameters of the steady state tyre characteristics adapted to the tyre wear, these parameters are summarised in Table 2. As seen in

**Table 2** Parameters to describe the lateral steady state tyre characteristics with  $F_{z,Nom} = 3,600$  N, for a parameter definition see (Rill 2012), and the dynamic model parameters as described in Sect. “Modelling Aspects”

Initial slope	$dfy0$	75,600	N/-
Maximum force	$fym$	4,000	N
Slip $s$ where $f(s) = fm$	$sym$	0.1125	–
Sliding force	$fys$	3,700	N
Slip $s$ where $f(s) = fs$	$sys$	0.5	N/-
Frictitious velocity	$v_N$	0.01	m/s
Lateral spring init	$c_{y0}$ (Hackl et al. 2015)	126640.6	N/m
Lateral damper init	$d_{y0}$ (Hackl et al. 2015)	1770.7	Ns/m
Contact mass init	$m_0$ (Pacejka 2006)	1	kg

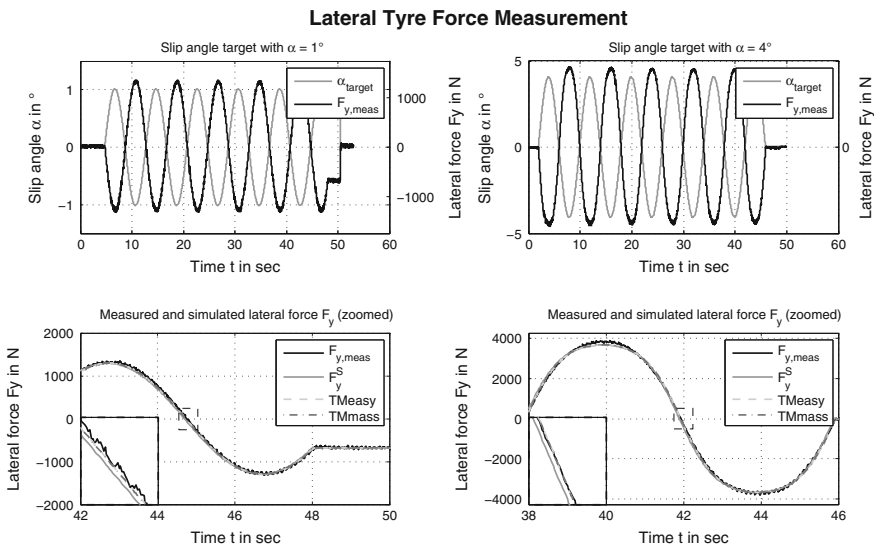


**Fig. 3** Validation of the steady state tyre characteristics by comparing measurements  $F_{y,meas}$  to simulations with a steady state model, the dynamic TMeasy model and the enhanced dynamic model TMmass. A quasi-stationary sine manoeuvre with a sine frequency  $f = 0.125$  Hz, tyre load  $F_z = 3,600$  N, drum speed  $v_x = 60$  km/h and two different slip angle amplitudes  $\alpha = 1^\circ$  (left) and  $\alpha = 4^\circ$  (right) were used

Fig. 3, a validation with two different slip angle amplitudes was carried out, an amplitude target of  $\alpha = 1^\circ$  shown in the left and with  $\alpha = 4^\circ$  shown in the right column.

On the upper two figures, the slip angle target is shown with a constant tyre load  $F_z = 3,600$  N, drum speed  $v_x = 60$  km/h, and the measured lateral Force  $F_{y,meas}$ . In the figures below, the comparison between measured and simulated force is presented. It can be seen that there is nearly no difference between the simulation with the tyre model TMeasy and the enhanced mass model TMmass, described in

Sect. “Modelling Aspects”. There is just a small delay between the steady state tyre characteristics  $F_y^S$  and the two dynamic models, which are traceable to the dynamic behaviour also on just a small frequency.

## Comparison and Validation of the Simulation with Measurement Data

In this main part of the paper, the simulation with the two tyre models, both described in Sect. “Modelling Aspects”, is presented and compared with measurement data. The principal focus was to investigate the influences of different frequencies and drum speeds on lateral spring  $c_y$  and damper  $d_y$  properties. Therefore, an optimiser was used to minimize the least squares error between the two models and the manoeuvres, with respect to the two parameters. In addition, these two models were compared with respect to optimisation/calculation time and accuracy.

To find the minimum between the measurement and the simulation deviation, a stochastic method called *Particle Swarm Optimisation* based on (Eberhart and Kennedy 1995) and (Kennedy and Eberhart 1995) with an extension from (Liu et al. 2005) was used. In addition, for all optimisations a constant number of iteration steps and swarm particles were used.

### Variation of the Frequency

The first part of the validation describes the influences of the frequency  $f$ . Therefore, manoeuvres with a constant speed  $v_x = 60$  km/h, slip angle amplitude of  $\alpha = 2^\circ$  and a frequency range from  $f = 0.125$ –4 Hz were applied.

Figure 4 shows an example of the optimisation with a frequency  $f = 1$  Hz. On the upper left subfigure, the slip angle target  $\alpha_{target}$  and the measured lateral force  $F_{y, meas}$  is shown. On the two right subfigures, the good agreement between the simulated and measured lateral force is presented with different zoom factors. Also the behaviour between the steady state and the dynamic characteristics can be seen in the below right subfigure. A second representation, with the lateral deflection versus the lateral force, is presented in subfigure four, as can be seen left below, to show the small deviation between the two models.

In Table 3, the average, the maximum and minimum results from ten independently executed optimisations for a manoeuvre frequency of  $f = 1$  Hz are written. The biggest difference between the tyre model TMeasy and TMmass is seen in the calculation time by an increase of up to about 350 % for the model TMmass. Therefore, the model with the enhanced mass may be theoretically more accurate, but at a cost of higher calculation time. In both cases the simulation was

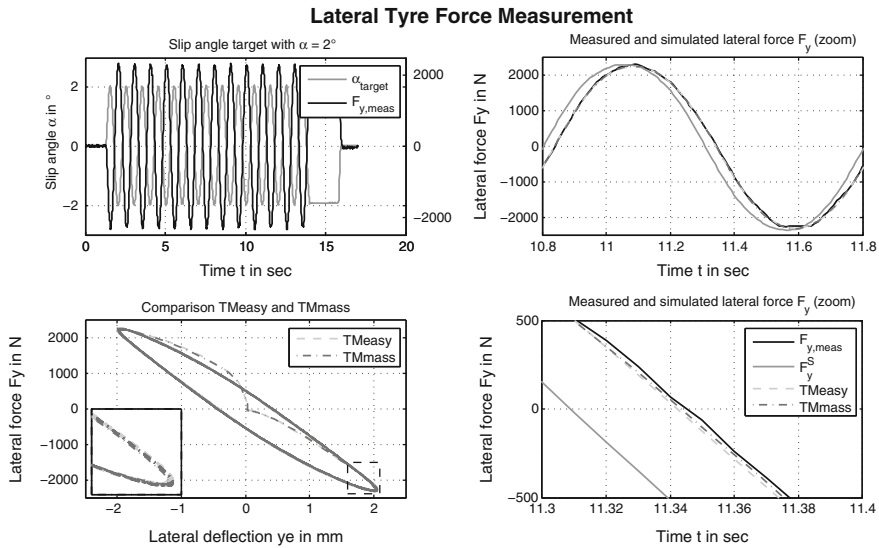


**Fig. 4** Comparison of the two optimised tyre models TMeasy and TMmass using measurements of a sine manoeuvre with a sine frequency  $f = 1$  Hz, tyre load  $F_z = 3,600$  N, drum speed  $v_x = 60$  km/h and a slip angle amplitude  $\alpha = 2^\circ$

**Table 3** Parameter results of the optimisation from the manoeuvres with a sine frequency  $f = 1$  Hz, tyre load  $F_z = 3,600$  N, drum speed  $v_x = 60$  km/h and a slip angle amplitude  $\alpha = 2^\circ$

	$c_y$ in N/m	$d_y$ in Ns/m	$m$ in kg	$t_{sim}$ in % (approx.)
Tyre model TMeasy				
Minimum value	131.454	1.072	–	–
Average value	132.166	1.316	–	100
Maximum value	133.204	1.489	–	–
Tyre model TMmass				
Minimum value	123.707	1.230	1	–
Average value	124.348	1.327	1	350
Maximum value	125.499	1.442	1	–

obtained by using the Matlab-Solver ode15 s that applies implicit multi-step formulas with step-size and order control.

Regarding the spring characteristics  $c_y$ , it can be seen that in both tyre models, the three values are in a quite small range and it can be assumed that a good minimum was found. But the damper characteristics, especially in the tyre model TMeasy, show a higher deviation. Therefore, the influences of the two parameters with respect to the optimisation result were investigated separately.

Using the initial parameters from Table 3, and changing the spring characteristics with  $\pm 25\%$  and the damper characteristics by multiply and dividing by 5, a

parameter study with the tyre model TMeasy was done. The results of this parameter study, presented in Fig. 5, shows that the influence of the damper value is quite smaller compared to that of the spring, which mirrors the results from Table 3. Comparing the deviations of the different simulations shows that a small change of the spring causes a much higher change in the lateral force characteristics than changing the damper properties. The tyre model with the enhanced mass showed the same behaviour, and thus is not presented. To minimize the influence of the damper on optimisations and focus on the spring properties, a constant damper value during the sine frequency variation was further assumed.

The results presented in Fig. 6 show the optimised spring parameter  $c_y$  for different frequencies. The solid line represents the average and the grey hatching the whole area of results of the carried out optimisations for the two different tyre models.

The main aspect shown in this figure is the increasing behaviour of the spring characteristics which reflects the results from (Hackl et al. 2015) that there is an influence of the frequency on the dynamic tyre behaviour. It seems there is a degree of dynamic hardening of the lateral stiffness with decreasing frequency. To investigate this effect, a more detailed model is needed.

Summarized, in this subsection it was shown that the spring parameter influences the dynamic behaviour to a higher degree than the damper. In addition, it was presented that the spring properties of the used models are not constant with respect to the frequency. Both models can describe the behaviour of the lateral force for a fixed frequency with optimised parameters.

It was shown that the inclusion of the mass may theoretically bring a more accurate calculation of the dynamic lateral force, but, like within the tyre model TMeasy, it does not solve the measured influences of different frequencies on the

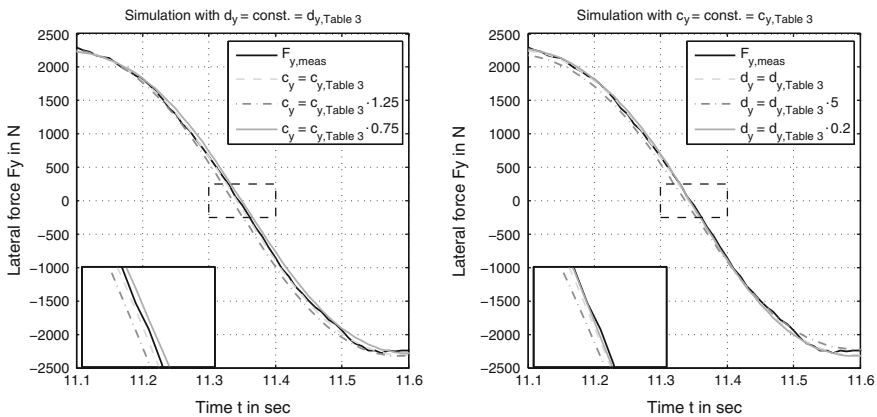


**Fig. 5** Comparison of measurement and simulation results by using different values for spring parameter  $c_y$  (left subfigure) and damper parameter  $d_y$  (right subfigure) values on the sine manoeuvres with a sine frequency  $f = 1$  Hz, tyre load  $F_z = 3,600$  N, drum speed  $v_x = 60$  km/h and a slip angle amplitude  $\alpha = 2^\circ$

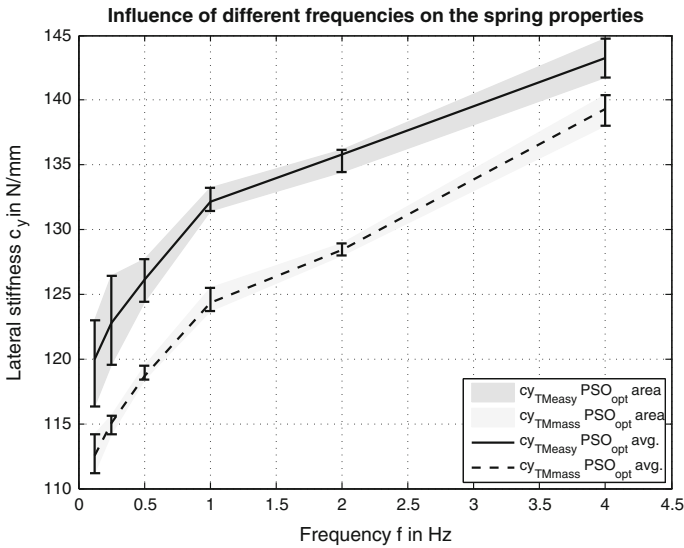


**Fig. 6** Results of the influence of different sine-slip angle frequencies on the spring characteristics  $c_y$  with a manoeuvre with constant tyre load  $F_z = 3,600$  N, drum speed  $v_x = 60$  km/h and a slip angle amplitude of  $\alpha = 2^\circ$

spring characteristics. To describe these effects with constant parameters a more detailed model is needed. Another aspect between the two models is the different calculation time, which should not be neglected, especially with regard to real time applications.

### *Variation of the Speed*

To validate and with the aim to enhance a tyre model to describe the dynamic behaviour in more detail, the influence of the speed should be additionally investigated. Therefore, the influence of different drum speeds from  $v_x = 20$ – $130$  km/h on the lateral spring and damper properties are investigated and presented in this chapter. Starting from the results in Table 3, the drum speed was varied. In Fig. 7, the results of the drum speed variation is presented. Just three drum speeds are presented because of a measurement error during the 100 km/h measurements.

It can be seen that both the lateral stiffness and the lateral damper properties increase with a higher drum speed. It has to be mentioned that the damper characteristics of the tyre model TMeasy for a drum speed of 130 km/h seems slightly too high and should be checked with further measurements. It is also shown that the results of the optimisations are quite equal to that of the investigations on the



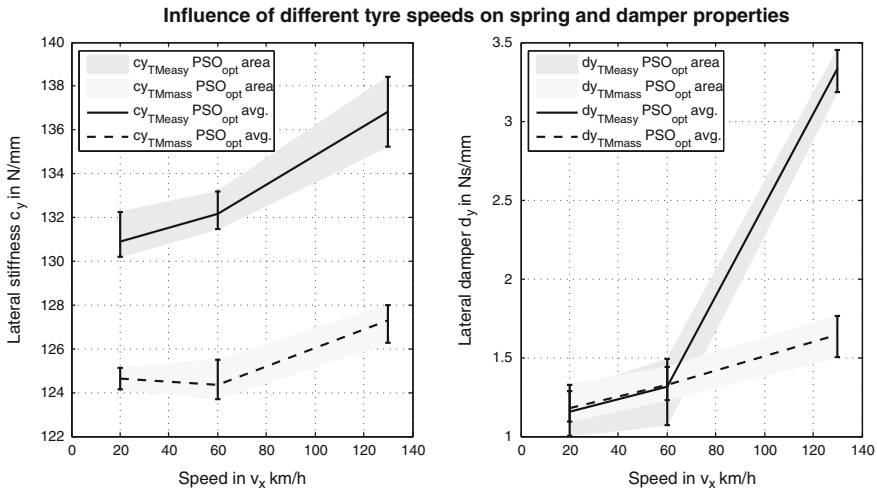


**Fig. 7** Results of the influence of different drum speeds  $v_x$  on spring  $c_y$  and damper  $d_y$  characteristics with a sine manoeuvre under constant tyre load  $F_z = 3,600$  N, a slip angle amplitude of  $\alpha = 2^\circ$  and a slip angle frequency  $f = 1$  Hz

frequency dependency. The deviations of the spring properties are in a smaller range in comparison to the damper.

In summary, it is presented that there is an influence of the speed on the parameters that characterise the dynamic tyre behaviour. Both models are not able to handle the influence without adapting the model parameters to the speed. In the near future, new measurement manoeuvres with a higher range of speed values and smaller steps between the values are planned to investigate the influence in more detail.

### *Mass Variation in the Enhanced Tyre Model $TM_{mass}$*

In Sects. “[Variation of the Frequency](#)” and “[Variation of the Speed](#)” it was shown that an enhanced model is needed to describe the influence of the frequency and the speed. In the last part of this article, the mass variation of the enhanced model is considered. The goal was to investigate the influences of the mass parameter on the spring and damper properties and validate this approach for further research in the area of tyre dynamics. Therefore, the influence of varied mass  $m = 0.1\text{--}10$  kg on the lateral tyre force behaviour is done with respect to the optimised spring and damper characteristics for a fixed manoeuvre. For this manoeuvre, a constant speed  $v_x = 60$  km/h, tyre load of  $F_z = 3,600$  N, slip angle amplitude of  $\alpha = 2^\circ$  and a frequency  $f = 1$  Hz was used.

In Table 4 and Fig. 8, the results for different mass variations are shown. On the left side, the influences on the spring, and on the right on the damper characteristics

**Table 4** Parameter average results of the optimisation with different model masses with a sine manoeuvre and sine frequency  $f = 1$  Hz, tyre load  $F_z = 3,600$  N, drum speed  $v_x = 60$  km/h and a slip angle amplitude of  $\alpha = 2^\circ$

	$m$ in kg	$c_y$ in N/m	$d_y$ in Ns/m	$t_{sim}$ in % (approx)
Enhanced model with mass TMmass				
	0.1	124.3826	1.3157	385
	0.5	124.3182	1.2611	385
	1	124.3480	1.3270	350
	2	124.4516	1.3479	315
	10	124.3585	1.6930	260

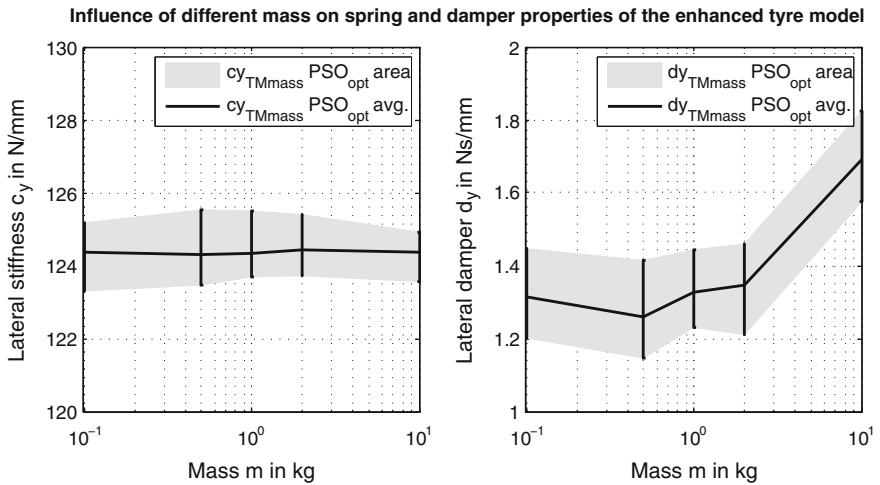


**Fig. 8** Results of the influence of model mass in the enhanced tyre model TMmass on spring  $c_y$  and damper  $d_y$  characteristics using a sine manoeuvre with constant tyre load  $F_z = 3,600$  N, a slip angle amplitude  $\alpha = 2^\circ$  and a slip angle frequency  $f = 1$  Hz

is presented. As can be seen on the left, there is nearly no influence on the spring characteristics. Regarding the damper characteristics, it seems to slightly increase with a higher mass. The larger deviation of the damper in the optimisation is attributed to the smaller influence of the damper behaviour on the lateral force behaviour compared to the spring.

## Conclusion

The present paper investigates the tyre dynamic approaches as they are widely applied in tyre models for vehicle dynamics and handling simulation. Firstly, two modelling principles are briefly described which consider different methods to obtain a proper description of the tyre's relaxation behaviour, particularly depending on the tyre load and the amount of the acting slip. Therein, the tyre stiffness and the viscous damping parameters are included in the relaxation functions. How these effects are implemented distinguishes the tyre model TMeasy from an alternative approach, named here TMmass, which includes an additional mass for the description of the visco-elastic deformation of the tyre in the contact area. This represents a second-order approach for the computation of the tyre deflection. However, in order not to exceed the extent, only the lateral relations were considered in this article.

An extended measurement programme on a test bench under laboratory conditions was carried out to validate both the above mentioned modelling approaches. The testing conditions are briefly documented, where particularly sine inputs on the slip angle with different amplitudes and frequencies under different tyre speeds were applied. Advantageously the results shown in the paper are restricted to a nominal tyre load of 3,600 N.

The essential model parameters in tyre dynamics are the tyre stiffness and damping with respect to the particular direction of deformation. Both these properties are carefully identified using measurement results. As already previously mentioned, their variability with respect to the excitation frequency, amplitude and rolling speed does not allow linear modelling, but requires more detailed models for stiffness and damping. Also, the hyper-elasticity seems to be worth to be taken into consideration.

In addition, the results of this investigation demonstrate that the additional model mass introduced in TMmass, which is considered in the calculation of the tyre's deformation velocity, only weakly influence the resulting model accuracy. Summing up, one may conclude that this artificial mass, which significantly extends the computational effort, may not have real relevance for the mentioned dynamic tyre modelling.

## References

- Eberhart RC, Kennedy J (1995) A new optimizer using particle swarm theory. In: Proceedings of the 6th international symposium on micromachine human science, pp 39–43
- Hackl A, Hirschberg W, Lex C, Rill G (2015) Experimental validation of a non-linear first-order tyre dynamics approach. In: Proceedings of the 24th international symposium on dynamics of vehicles on roads and tracks, Graz (Aug 17–21, 2015)

- Harrich A, Tonchev A, Hirschberg W (2006) Der neue dynamische Bremsen- und Radaufhängungsprüfstand an der TU Graz. In: Proceedings of the braking technology. TÜV SÜD, Munich (Dec 7–8, 2006)
- Hirschberg W, Weinfurter H, Jung C (2000) Ermittlung der Potenziale zur LKW-Stabilisierung durch Fahrdynamiksimulation, VDI-Berichte 1559, Düsseldorf, pp 167–188
- Hirschberg W, Rill G, Weinfurter H (2007) Tire model TMeasy. Veh Syst Dyn 45(Suppl 1):101–119
- Kennedy J, Eberhart RC (1995) Particle swarm optimization. Proc IEEE Int Conf Neural Netw 4:1942–1948
- Kistler GmbH (2015) Measuring systems and sensors to meet extreme challenges. <http://www.kistler.com/at/de/product/force/9267A1>. Accessed 01 Oct 2015
- Lex C, Eichberger A (2011) Der Reifen als Einflussgröße für Fahrerassistenzsysteme und Fahrdynamikregelungen. OEAMTC Symposium Reifen und Fahrwerk, Vienna
- Liu B, Wang L, Jin YH, Tang F, Huang DW (2005) Improved particle swarm optimization combined with chaos. Chaos, Solitons Fractals 25:1261–1271
- Pacejka HB (2006) Tire and vehicle dynamics. Butterworth-Heinemann, Oxford
- Rill G (2006) First order tire dynamics. In: III European conference on computational mechanics: solids, structures and coupled problems in engineering, Lisbon
- Rill G (2012) Road vehicle dynamics, fundamentals and modeling. CRC Press, Taylor & Francis Group, Boca Raton
- von Schlippe B, Dietrich R (1942) Zur Mechanik des Luftreifens. Zentrale für wissenschaftliches Berichtswesen der Luftfahrtforschung (ZWB), Berlin-Adlershof  
<http://www.ftg.tugraz.at>. Accessed 01 Oct 2015

# Smart Solutions for Vehicle Chassis

Mihai Florea, Valerian Croitorescu and Mircea Oprean

**Abstract** So far parts of the chassis are designed specifically for each type of vehicle, so manufacturing and assembly processes are feasible only for a very large number of units produced each type of model, but they do not allow their adaptation to different desired configurations. Therefore, to minimize production costs and to give the possibility to adapt a different chassis for multiple-body design solutions, a modular structure should be developed. This paper highlights the possibility of developing new modular chassis using different various assemblies and sub-assemblies. The modular platform provides the ability to use the same components and modules for different vehicles. This solution is not limited in using for modular platforms; it can be used in the construction industry and other fields that require scalability and low masses.

**Keywords** Modular platform · Vehicle chassis · Virtual design · Electric mobility

## Introduction

Electric mobility becomes a very viable alternative due to reduction of the fossil fuel resources. Moreover, legislative bodies require different rules and demand the car manufacturers to consider a greener approach for their vehicles.

---

M. Florea · V. Croitorescu (✉) · M. Oprean  
Scientific Research and Continuous Training Center for Sustainable Automotive Technologies, University POLITEHNICA of Bucharest, Faculty of Transport, Room JC004, 313 Splaiul Independentei St., 6th Sector, Bucharest, Romania  
e-mail: valerian.croitorescu@upb.ro

M. Florea  
e-mail: mihai\_florea@live.com

M. Oprean  
e-mail: mircea.oprean@upb.ro

Pollution is increasingly evident especially in urban areas where it has become a pressed companionship. Thus, the existing companies involved in the production of motor vehicles will have to consider moving to the next stage, the electrification.

Most automobile companies are trying to adopt the conversion solution—so the designers face the challenges to replace the old conventional propulsion system with a hybrid one or with an electric one.

Designing a hybrid or an electric powertrain, taking into account that the vehicles become more and more advanced, may require a new design for the entire car, possibly using other body design solutions to better integrate the additional systems and the electrical components. But such an approach will change the concept of a car in a meaningful way (Croitorescu 2014).

The structure of an electric vehicle must be realized in the most economical way and can be easily integrated as a wide range of such as vehicles, light public transport and light freight transport vehicles. Powertrain electrification involves redesigning the chassis as an essential part of the vehicle.

To develop a chassis that covers a wide range of vehicles and to minimize the costs involves two ways: to reduce the production costs for each model, or to develop a modular platform that can be suited for all the models.

The modular platform provides the ability to use the same components and modules for different vehicles. These similarities lead to reduced costs despite the relatively small number of developing each vehicle separately (Croitorescu 2014).

The objective of the paper is to find a suitable solution for designing and manufacturing a modular platform equipped with an electric powertrain. This should provide supporting various assemblies and subassemblies of an electric vehicle with a different design and general organization. It must have a “SMART” construction/design: it should have minimum weight, as much as possible, it should be very simple and it should have a more efficient body shape in terms of energy efficiency/design. Therefore, it is necessary to develop a suitable platform for producing and assembling the various modules required for meeting various design conditions (Croitorescu 2014).

## **Modular Platform Overview**

### ***The Components***

The modular platform consists in three main systems (Fig. 1): the structural frame and the electric powertrain (including wheels).

Taking into account the boundaries that may be met while covering the design and development stages, the frame can be considered as a single body composed of beam elements assembled by welding, riveting or bolted.

The most important parts of an electric powertrain are the electric motor, the transmission, the high-voltage batteries and the power electronics.

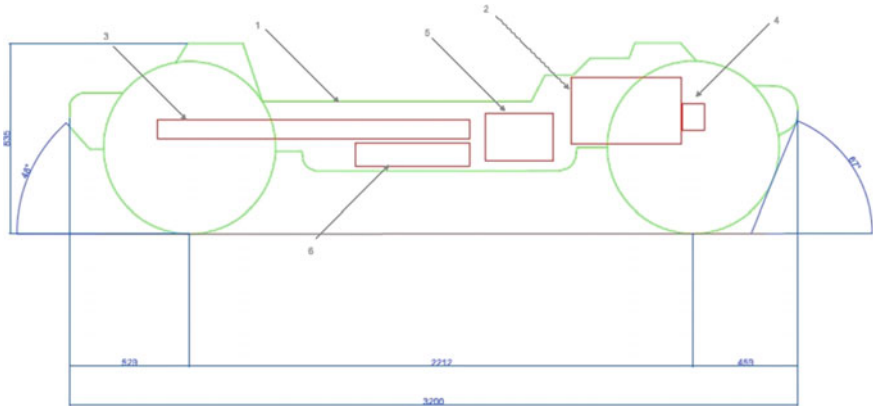


**Fig. 1** The modular platform’s main parts (Florea 2015, [www.tribology-abc.com/calculators/uts.htm](http://www.tribology-abc.com/calculators/uts.htm)) (1 Structural frame, 2 electric motor, 3 high voltage batteries, 4 transmission, 5 power electronics, 6 cooling system)

### *The Exterior Dimensional Parameters*

After investigating all the needed parts’ capacities, the exterior dimensions of the frame were chosen, as presented in Table 1:

The height of the frame is not the same as the total height of the platform or the vehicle. The length or width of the frame are the same as for the platform and can be the same as for the vehicle.

### *The Intended Use*

This platform can equip different types of vehicles, including autonomous electric cars and small city cars, with overall flexible organization that can adapt to various needs of the designer. It should be able to permit the assembling of different systems like the ones that compose the powertrain and the ones that are specific for the vehicle destination.

**Table 1** The exterior dimensions of the frame

Length (mm)	Width (mm)	Height (mm)
3200	1600	350

## **The Structural Frame**

### ***The Constructive Solution***

After several investigations regarding the solution to be adopted, the most suitable constructive solution revealed to be the ‘Space Frame’ construction. This classic solution can be easily applied for hybrid and electric vehicles. The Space Frame construction type structure is made of steel or aluminum tubes placed in a triangular format to support the weight of the suspension, engine, passengers, etc. The elements of this structure include stress strain and compression, without any torsion or bending loads. The chosen design has several advantages. Its modularity allows easily adapting to different solutions and different sizes needed for additional components. The inside volume space can be used for housing the battery package and the power electronics, offering high protection in case of accident. The structure can easily be disassembled, the elements can be removed and replaced with other elements, not mandatory to keep their external dimensions, and therefore, both the exterior and the interior sizes can vary. The structure gravity center is very close to the geometrical center of the platform, which gives easiness in maneuvering. The manufacturing processes are facilitated by the existence of different elements, with predefined dimensions.

### ***Materials Used for Manufacturing the Structural Frame***

In order to manufacture the structural frame several materials have to be taken into account. The materials were selected following several criteria, including elastic coefficients, durability of the material, recycling properties, costs, and the weight.

The structural steel is one of the considered materials was. In recent decades there have been significant advances in terms of this material, managing to make the processing easier, stiffer and more durable (<http://cordis.europa.eu/growth/calls/top2-5.htm>). It is not used only for body parts of conventional vehicles; it is also found in internal combustion engine components, shafts, wheels etc. It is an important material for the majority of vehicle components, offering the low cost advantage.

During recent years, the development of new technologies has allowed to some steels to have lower mass by 19 % and to have a much better dynamic behavior, like Ultralight Steel Auto Body (ULSAB). But, the ability to absorb impact energy represent the main reason for using steels.

Aluminum was considered also as a possible material to be used. Aluminum is used for many subassemblies used on conventional vehicles and beyond: elements of the internal combustion engine, transmission components, and chassis or body parts are just some of them. By using aluminum in vehicle design reduces curb weight. Aluminum benefit of several advantages, including lower specific density, high energy absorption at impact, high specific strength, does not corrode etc.



**Table 2** Characteristics of the material EN—AW—7075 (<http://gleich.de/de/produkte/aluminium-walzplatten/al-walzplatten—en-aw/en-aw-7075#sheet>)

Ultimate tensile strength ( $\sigma_p$ ):	Min. 480 MPa
Hardness:	Min. HB 160
Tensile Yield Strength ( $\sigma_e$ ):	Min. 390 MPa
Modulus of elasticity (E):	72,000 N/mm <sup>2</sup>
Module of stiffness (G):	27,000 N/mm <sup>2</sup>
Poisson's ratio ( $\nu$ ):	0.3

New research has shown that the aluminum use in bodywork construction instead of steel can reduce the weight by up to 50 %; which would reduce the curb weight of a vehicle by up to 20–30 %.

The main disadvantage of this material may be considered the cost: its price is high and unstable at the world's market prices.

Magnesium was considered the third material to be used. The magnesium has low specific density, having smaller mass for the same occupied volume. It is 33 % lighter than aluminum and 75 % lighter than steel. Magnesium components have many disadvantages in terms of its mechanical characteristics; it requires a special design of its own for automotive applications. The magnesium specific hardness is lower compared to aluminum, and its thermal expansion coefficient is higher. Its advantages consist in better manufacturing and higher life expectancy.

Due to poor mechanical characteristics, pure magnesium must be alloyed with other elements. The most common elements alloyed within are the Aluminum (Al) and Zinc (Zn), known to form alloys like Mg–Al–Zn.

After the analysis of the possible materials needed for the structural frame, aluminum was the chosen material. It is lighter than steel (has a lower specific density), does not corrode and it is more malleable. Compared to magnesium, it is more resistant. More specific, the aluminum EN—AW—7075 was chosen. Its characteristics are shown in Table 2.

## Modelling the Structure

Starting from this high aimed demand, several possibilities for the structure were investigated. Several shapes for the structure modules were taken into account. Three types of elements with identical profiles and different lengths were used to develop the chassis.

Critical stresses are involved while designing and testing the chassis. The analysis can be performed either by finite element method either by using empirical formulas. Some assumptions were made where necessary. The chosen method for designing the chassis was based on finite element modeling and analysis, using both ANSYS and CATIA. Following the needs of an elaborate study, the method is using more than one level of design.

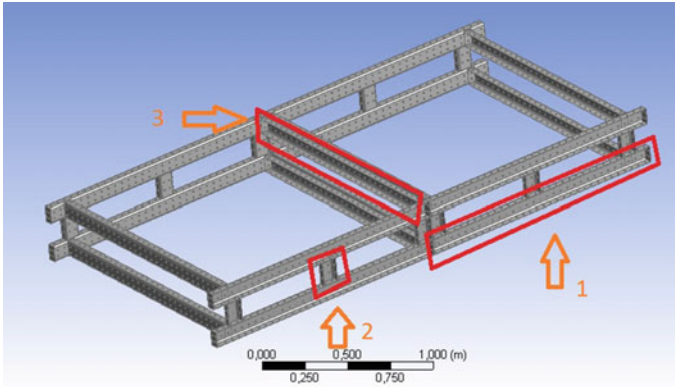


**Fig. 2** The 3D model of the structural frame

**Table 3** Total number of elements

No.	Element	Number of elements
1	X-axis beam (1)	8
2	Z-axis beam (2)	12
3	Y-axis beam (3)	8

Based on the frame's length, width and height, the dimensions of the structural elements were determined, considering their position. Thus, the 3D model (Fig. 2) was developed. A total of 28 elements resulted. The number of elements is presented in Table 3. The profile of every element (Fig. 3) has a length of 100 mm and a width of 50 mm.

The length of each element is presented in Table 4.

To ensure the modularity, symmetric holes were applied on each face for all the elements (Fig. 4). The holes diameter was adopted to 10 mm, and the spacing between the centers of two enclosed holes was set to 50 mm.

### *The Mass*

The total mass approximated after modelling the structure was 29.425 kg. This reduced weight of the frame was obtained due to the existing holes in the structure and the use of aluminum, being 3 times lighter than steel. The advantages deriving from mass reduction are listed: lower drag resistance, lower inertia and the possibility to obtain a higher autonomy of the electric platform.

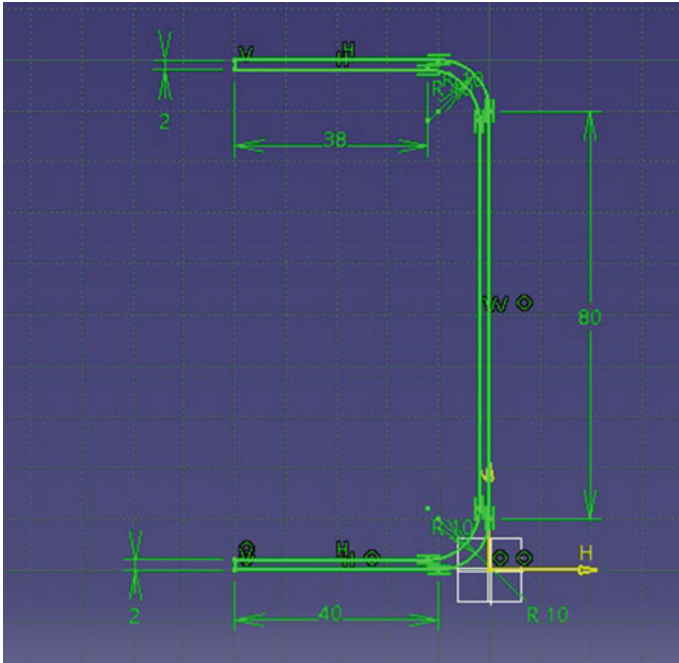
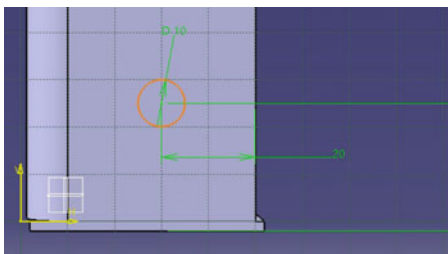


**Fig. 3** The dimensions of the profile of every element

**Table 4** Length of each element

No.	Element	Length (mm)
1	X-axis beam (1)	1600
2	Z-axis beam (2)	150
3	Y-axis beam (3)	1400

**(a)**



**(b)**

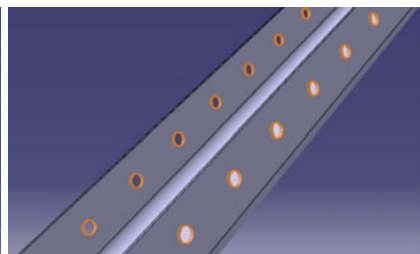


**Fig. 4** The applied holes. **a** Lateral view. **b** Isotropic view

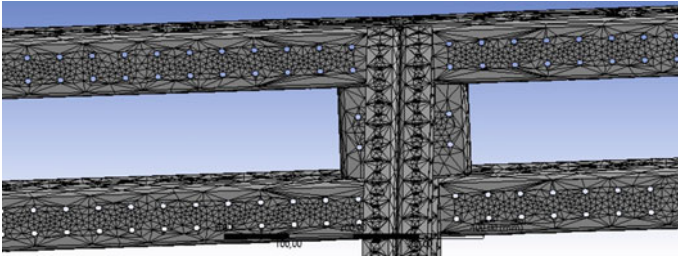


**Fig. 5** The mesh detail

### ***The Finite Element Model***

The structure was modeled through a numerical analysis using dedicated software. Due to the geometrical constraints and the complexity of the 3D model of the structure and the limitation of the post-processing levels, the initial meshed model was simplified. The initial model contained a number of at least 170,000 elements and more than 364,000 nodes. Taking into account that the entire chassis structure needs a huge number of elements (starting from the initial value multiplied for each bar ‘x’ times), beam elements have been used (Fig. 5). The beam elements have the same cross sections.

### **Results**

The results include the possibility of testing different shapes and modules for the chassis elements, during different scenarios. A static analysis of the chassis results along with the forces that act in each module individually and in the entire body. The final geometrical dimensions, shapes and the used material type were established.

Also, different types of loading were taken into account. Stress state of the chassis, at different levels of loadings required the presented approach.

### ***The analysis of the vertical symmetric loads was performed***

The dynamic load depends on the mass and gravitational acceleration and it was introduced in the simulation as follows.

$$P_{zs} = m_{zs} \cdot G_s \quad (1)$$

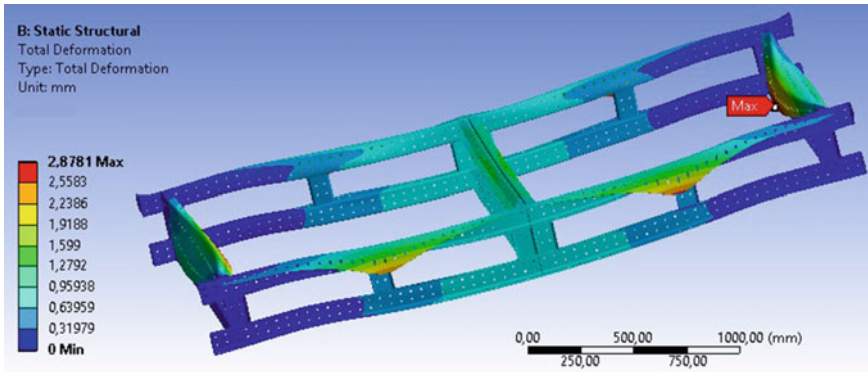


Fig. 6 Maximum deformation (vertical symmetric loads)

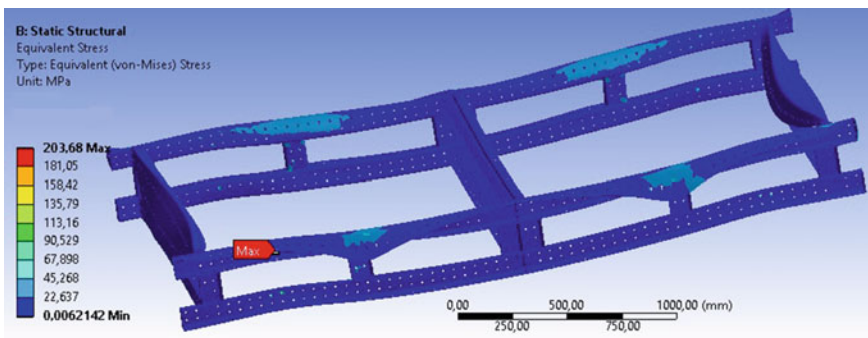


Fig. 7 Von-Mises Stress (vertical symmetric loads)

$m_{zs}$  dynamic load coefficient [-];  
 $G_s$  total weight of the platform [N]

For this analysis, the dynamic load coefficient ( $m_{zs}$ ) was chosen to be equal to 2 due to its destination. The total weight of the platform included the weight of the powertrain components with an added mass of 450 kg. The model returned a maximum deformation of 2.87 mm (Fig. 6) and a maximum von-Mises stress of 203 MPa, less than 2/3 times of the yield strength of the material (Fig. 7).

***The analysis in case of elevating the platform was performed***

If settled on the elevator, the load acting on the structural frame is considered to be equal to the weight of the electric platform and the added load; in fact, the vehicle

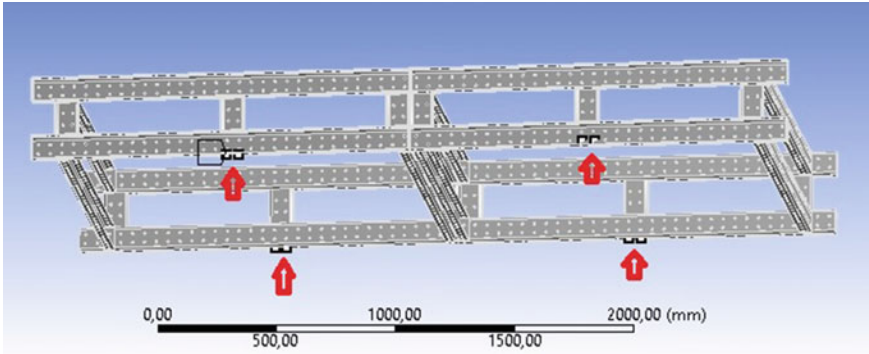


**Fig. 8** Supporting surfaces

weight. The surfaces on which the structure supports were fixed on the axis of the Z-axis beams (Fig. 8).

The maximum deformation in this case (Fig. 9a), of 1.17 mm, is smaller than the one from the vertical symmetric analysis. The average deformation is about 0.5 mm. The maximum von-Mises stress (Fig. 9b) is 209 MPa, bigger with 6 MPa than the one from the vertical symmetric analysis, but still less than 2/3 times of the yield strength of the material.

### *Torsional Stiffness*

The torsional stiffness is the most common method of verifying the structural frame's rigidity of a vehicle. For this method the calculation of torsional stiffness coefficient is needed and it is determined as follows:

$$K_{\text{torsrig}} = \frac{M}{\varphi} [\text{Nm}/^\circ] \quad (2)$$

- $K_{\text{torsrig}}$  torsional stiffness coefficient [-];
- $M$  torsion moment [Nm];
- $\varphi$  torsion angle [°]

After computing, the torsional stiffness coefficient obtained was 4464 Nm/°, suitable for the platform destination (Fig. 10).

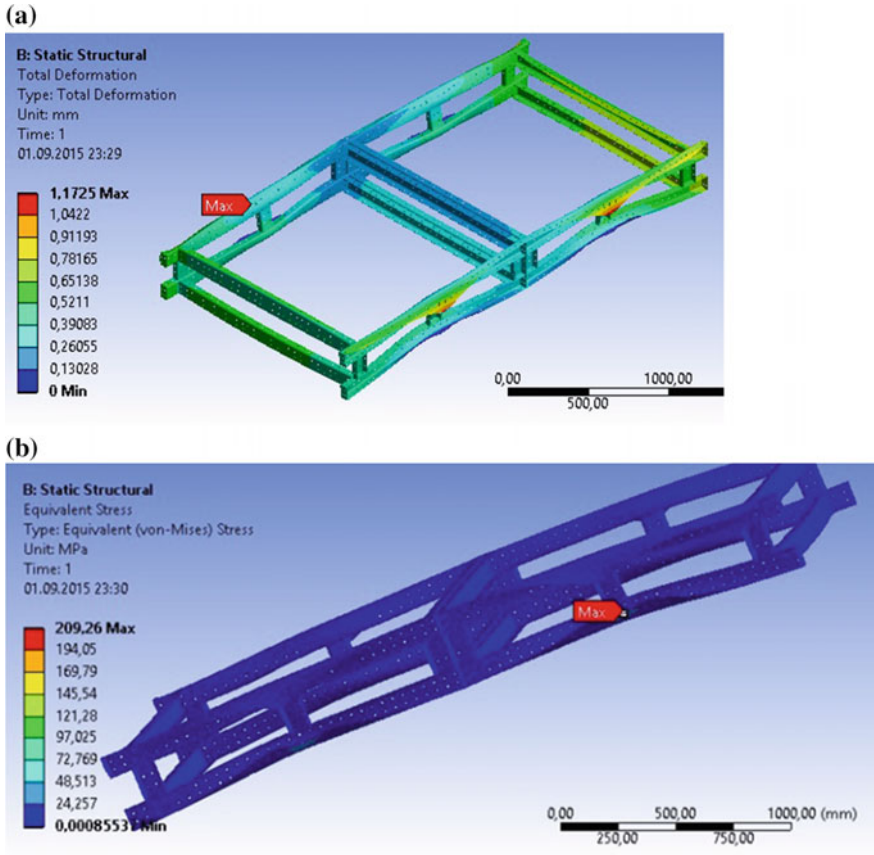


Fig. 9 a Maximum deformation (elevator case). b Von-Mises Stress (elevator case)

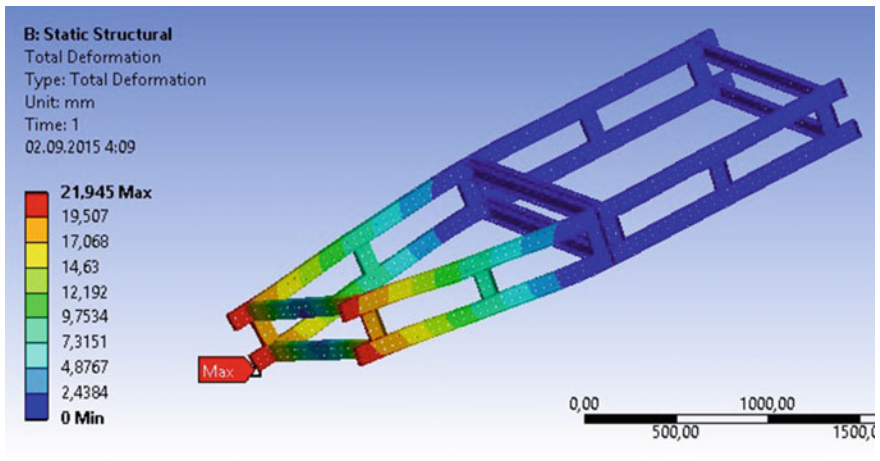


Fig. 10 Total deformation (torsional stiffness determination)

## Conclusions and Discussions

The structural frame was designed in order to be easily integrated in a vehicle chassis. The structure developed has a simple design, being symmetrical in all three orthogonal views. The structure is made of 28 elements, relatively low compared to other similar models. The mass of the platform is about 29.5 kg.

This model has been introduced in various simulations, as close to real conditions; the results were satisfactory, no deformation was significant and no stress exceeded the yield stress of the used material.

This structure can be widely used in various fields of interest, with various destinations, from light public transport or light freight transport, to being used in areas of industry by installing various specific subassemblies. Basically, this solution is not limited to be used for modular platforms; it can be used in the construction industry and in other fields that require scalability and low masses.

## References

- Croitorescu V (2014) Project proposal PN-II-RU-TE-2014-4-2674, subprogram RUTE 2014, program PNCDI 2007-2014
- Florea M (2015) Proiectarea structurii de rezistență a unui șasiu utilizat pentru o platforma modulară de vehicul electric și elementele de prindere ale subansamblurilor corespunzătoare sistemului de propulsie electric (The chassis structure design and development used for an electric vehicle modular platform, the sub-assemblies and fasteners design for the electric propulsion system). Diploma Project, Scientific Coordinator: Univ.As.Prof. Valerian Croitorescu, University Politehnica of Bucharest



# Study for an Electrified UTV Platform

Grigore Danciu

**Abstract** This paper presents a design study for electrification of a Utility Task Vehicle (UTV). It starts with the state-of-the-art and motivations for UTV. Then, it presents a design model for the vehicle electrification, based on the dynamic model of the power-train. Many implementation solutions are discussed. Based on this model, a practical selection is done, concerning the necessary equipment: motor, controller, transmission, battery, and charger. Conclusions present a short analysis of this design.

**Keywords** Electric vehicle · UTV · Electrification design

## Introduction

Environmental protection by using renewable energy and mainly in its electrical form is a must of our society, as presented in EU-Directive (2009), by International Energy Agency-IEA (2015) or Romanian Ministry of Environment (2012). On the other hand, mobility is also a must with a very fast growing. Combining these, the rational towards the move to electrical mobility is now well described in a large number of documents and trends can be summarized by the following points:

- Radical cut of green-house gas (GHG) emissions all across Europe, independently from where and how the electricity is produced. With respect to the internal combustion engine vehicles (ICEV), comparable electric vehicles (EVs) would achieve on average up to 50 % GHG reduction per equal kilometers run. This reduction is very likely to remain stable all along the forthcoming decade, which makes that by 2020 both the 95gCO<sub>2</sub>/km target per

---

G. Danciu (✉)

Faculty of Transportation, University Politehnica of Bucharest,  
313 Splaiul Independentei, Bucharest, Romania  
e-mail: danciu@ieee.org

average fleets based on ICEVs only and the EU-Directive (2009) on Renewable Energies will be met only with EV contribution;

- Cancellation of noxious emissions in cities recognized to be the cause of a higher number of deaths than those caused by road fatalities (in EU of the order of 35,000/year);
- Avoid the use of the most critical primary energy source (petroleum);
- Rapid convergence of the technologies developed for renewable energy with those adopted for electrical mobility (power electronics, energy storage, etc.);
- Either first generation bio-fuels or third generation ones (algae), have not been proved to have a Life Cycle satisfactory positive energy balance and appear to be desperate solutions against the challenges posed by oil. While technologies to low cost cellulosic bio-ethanol (second generation bio-fuels), although having a rather positive energy return, they still need to be further developed before they could meet the cost parity with petroleum based fuels;
- Further improvements of ICEs are possible, but another 5 % improvement of the peak efficiency will not change the challenge posed by liquid fuels whose world demand are supposed to grow on average 1.3 %/year until 2035, as presented by IEA (2015);
- In the year 2000, Light Electrical Vehicles (LEVs) such as bicycles, scooters, tricycles, mopeds, quad-cycles, and UTVs accounted for a global production of the order of 100,000/year while in the 2015 they are expected to be produced in several tens of millions/year. To support these developments there is an ongoing replacement of lead-acid batteries with much more efficient and cleaner technologies, like Li-ion; China, Korea, and Japan are rolling out large scale production, addressing manufacturing cost issues;
- LEVs are now evolving to micro cars and conventional mid-sized cars. European companies will then be exposed to a novel vertically organized supply chain supported by large nations where regulations are made by fast acting Governmental Institutions. This is having and will have an ever increasing impact on the relations amongst Tier1-2 suppliers and OEMs, which is likely to be reflected on heavy industrial restructuring. European industries are then faced to manage the effects caused by this radical change of the supply chain adopting quickly and properly sized competing instruments that could avoid the move of the European productions to the new high tech countries;
- The demand of new forms of mobility is spreading all over the world reflecting people awareness on the ever increasing problems to provide primary energy and raw materials, on climate change, and on the impact of noxious emissions on health. Rather than offering forms of mobility based on ever increasing prices, the industry is now faced to satisfy a rationale demand of mobility. Not only clean, low energy consume, and safe vehicles, but it needs vehicles requiring less energy to be produced, using recyclable and eventually self disposable materials-systems.

In this context, the present paper proposes a study of Utility Task Vehicle (UTV) electrification. Detailed information and pictures for UTV may be found at

dealers or producers as UTVGuide (2015), Polaris (2015) or TITANUTV (2015). UTV is known also as Side by Side or Recreational Off-road Vehicle (ROV) and is bigger than ATV (All-Terrain Vehicle), has a higher payload capability (400–800 kg) and a side-by-side seating arrangement, with roll-over protection. It has a lot of applications but some are in urban locations such maintenance works in gardens and car parks, streets and industrial locations, sport and recreational activities, etc. In such applications, a dedicated EV is the best solution, but in some case an acceptable solution could be the electrification or retrofitting of an existing ICEV.

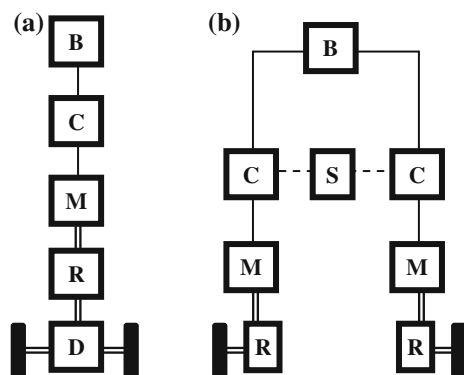
## Electrification Design

### Architecture

The power-train of a full electric vehicle (FEV) which is the case of this study could have a very flexible architecture, as presented by Racicovschi et al. (2007). The Fig. 1a presents the simplest solution, where power electrical link is with solid line, low power coordination is with dash line, and mechanical link is with double line. It is similar to the ICEV propulsion. The driving axle has the usual differential, D. It is mechanically coupled with the reduction gear, R. Usually it has a fix reduction ratio, but the new trend is to use a two steps gear. The electric machine, M, is reversible and works both as motor and generator. It was initially a DC machine, but the trend is to replace it with an AC machine such:

- (i) a permanent magnet (PM) synchronous machine fed with sinus currents (vector controlled) or with rectangular currents, known as Brushless DC. In the first case the control algorithm is more complex and needs a high resolution position transducer, but has a higher efficiency and lower torque ripple.

**Fig. 1** EV architectures  
**a** With differential;  
**b** Independent driving wheels  
*B* Battery; *C* Controller;  
*M* Motor; *R* Reduction gear;  
*D* Differential



- (ii) an induction machine which is cheap and very robust, but has a complex control algorithm(vector controlled) and position transducer.
- (iii) a switched reluctance machine which is the most robust and cheap but has some disadvantages in specific torque and power, and torque ripple. It is not widely used.

Always, the electric machine is fed by a digital controller, C. It controls the torque by controlling the currents and thus controls the position, speed and acceleration. It also monitors and controls the machine status (temperature, maximum torque, etc.). Finally, the energy source or storage, B, could usually be a rechargeable battery, a supercapacitor, or a fuel cell. This paper does not discuss catenary solutions. The batteries are the main supply solution. Despite the lithium chemistry is widely used on cars and buses, many electric UTVs still use lead batteries. In Fig. 1b, the mechanical differential is replaced by independent driving wheels. Each wheel has a gear, motor and controller, supplied from the same storage. The axle's wheels are coordinated by a supervisor, S, which commands the two controllers. It can implement, also, advanced dynamic strategies such ABS/ASR/ESP functions, thus increasing the axle effectiveness. Other solutions are possible, too. One could present two driving axles, each having a differential, a gear and a motor with controller, supplied from the same battery. The two controllers are coordinated by a supervisor. Other solution could have four independent driving wheels, each having a gear and a motor with controller, supplied from the same battery and coordinated by a single supervisor, etc.

### ***Power-Train Design***

Based on a given architecture, this point finds specific parameters for the power-train components, M, C, R, and S. This step is based on the main power-train performance specifications: gross mass,  $m_a$  (kg), maximum speed,  $v_{\max}$  (km/h), maximum slope,  $p_{\max}$  (%), speed at maximum slope,  $v_p$  (km/h), equivalent wheel radius,  $r_r$  (m), and range,  $S$  (km).

### **Maximum Motor Power and Motor Selection**

The necessary power increases with the vehicle speed. Therefore the maximum necessary power is usually obtained combining two limit criteria: maximum speed and maximum slope. In all cases, this state must be reach for long time, and so, continuous power has to be considered.

In steady conditions, which is the case at maximum speed or constant uphill speed, the traction force  $T_f$ , must balance the total resistances, that is the sum of

drag force,  $R_a$ , rolling  $R_r$  resistance, and slope resistance,  $R_p$ , all measured in (N) as presented by Gillespie (1992) and Stoicescu (2007):

$$T_f = R_a + R_r + R_p \quad (1)$$

The *drag force* in air, without wind is:

$$R_a = 1/2 * d_{air} * C_x * A * v^2 \quad (2)$$

where,

A is the projected frontal area of the vehicle ( $m^2$ );

v is vehicle speed (m/s);

$d_{air}$  is the air density, equal at sea level to  $1.225 \text{ kg/m}^3$

$C_x$  is the drag coefficient, specific to each vehicle

So, if the vehicle speed is expressed in (km/h), the air drag results:

$$R_a = 0.047 * C_x * A * v^2 \quad (2a)$$

The *rolling resistance* is:

$$R_r = f * g * m_a * \cos\alpha_p \quad (3)$$

where:

f is a dimensionless rolling coefficient, specific to each tire;

g is the gravitational acceleration in ( $m/s^2$ );

$\alpha_p$  is the slope angle and p (%) the slope,  $\alpha_p = \text{arctg}(p/100)$

The slope resistance is:

$$R_p = m_a * g * \sin\alpha_p \quad (4)$$

The corresponding necessary power, in (kW), results multiplying forces by speed in (km/h):

$$P_{nec} = v * T_f / 3600 \quad (5)$$

- (a) Then, in horizontal conditions ( $\alpha_p = 0$ ), without wind and at maximum speed,  $v_{max}$ , the necessary traction force is:

$$T_{f\text{ hor-vmax}} = R_a + R_r = 0.047 * C_x * A * v_{max}^2 + f * g * m_a \quad (6)$$

and the necessary power is:

$$P_{nec-hor} = v_{h-max} * (0.047 * C_x * A * v_{max}^2 + f * g * m_a) / 3600 \quad (7)$$

- (b) On a positive slope road, the traction force and power at a given speed,  $v_p$ , are respectively:

$$\begin{aligned} T_{fp} &= R_a + R_{rp} + R_p \\ &= 0.047 * C_x * A * v_p^2 + f * g * m_a * \cos\alpha_p + m_a * g * \sin\alpha_p \end{aligned} \quad (8)$$

$$\begin{aligned} P_{nec-p} &= v_p * (0.047 * C_x * A * v_p^2 + f * g * m_a * \cos\alpha_p + m_a * g \\ &\quad * \sin\alpha_p) / 3600 \end{aligned} \quad (9)$$

The resultant necessary power is the maximum from (7) and (9):

$$P_{nec} = \max\{P_{nec-hor}, P_{nec-p}\} \quad (10)$$

*NOTICE: This algorithm is fully appropriate for a multi-ratio gear-box. For a fix ratio gear, the necessary torque must also be taken into consideration, usually by an appropriate simulation. For a good dynamic, it is possible to increase the necessary power or to introduce a multi-ratio gear.*

The necessary motor power results considering the transmission efficiency,  $\eta_t$ :

$$P_{mot} \geq P_{nec} * \eta_t \quad (11)$$

From this, considering the option for a specific motor type, and considering particular conditions (temperature and cooling possibilities, vibrations, dust, water, mud, price and commercial conditions, reliability, etc.) it is possible to select an existing motor from the market.

## Controller Selection

Usually, the motor producer suggests an appropriate controller, too. It is strongly recommended to follow this suggestion. Also, this producer gives the working conditions for the assembly motor-controller and mainly the rated DC voltage and peak current,  $V_{DC}$  and  $I_{DCpeakmax}$  respectively. Montage conditions must be taken carefully into consideration and respected in this selection, such as cooling, water-protection, vibration level, safety, etc.

## Reduction Gear Selection

For fixed reduction gear the reduction coefficient,  $i_R$ , usually results from the performances imposed. At the given vehicle speed,  $v_{ref}$ , the necessary power  $P_{nec-ref}$  is calculated from (10). For the selected motor, the corresponding motor reference

speed  $n_{ref}$ , results from the power-speed diagram, given in Fig. 1. If many values are possible, the higher one is usually chosen, in order to maximize the torque. On the other hand, the vehicle speed,  $v$ , and the motor speed,  $n$ , expressed respectively in (km/h) and (rev/min), are given by the relation:

$$v = \frac{2\pi}{60} * \frac{n}{i_R} * r_r * 3600/1000 = 0.3768 * \frac{n * r_r}{i_R} \quad (12)$$

From here, the total reduction coefficient,  $i_R$ , results as:

$$i_R = 0.3768 * \frac{n_{ref} * r_r}{v_{ref}} \quad (13)$$

The coefficient  $i_R$  usually contains the reduction gear and differential coefficients. It must simultaneously satisfy both conditions for maximum speed and slope.

For the practical selection of the gear, beside reduction coefficient,  $i_R$ , other parameters must be also considered such as the maximum input torque,  $T_{max}$ , (which is the peak torque of the motor), and the maximum motor speed, working conditions, etc.

## Battery

Concerning batteries, different chemistries are available, but the majority of new UTV designs use lead or lithium technologies. The lithium battery has a much higher specific energy and power, but is very expensive and more delicate in exploitation, concerning vibration resistance, cooling, balancing, etc. Battery selection has the following steps:

- (a) Selection of the battery technology;
- (b) Calculation of the units' number (cells or modules),  $N$ . Usually the manufacturers offer two solutions: individual cells or battery modules, composed of many cells internally connected. The rated voltage of the cell depends of the technology. For instance, Li-NMC oxide cell (short from nickel, manganese and cobalt) has 3.7 V, LiFePO<sub>4</sub> has 3.2 V, and lead has 2 V/cell. The rated module voltage,  $V_{N1}$ , could be 6, 12 V or higher. The total necessary battery voltage,  $V_{DC}$ , is given by the controller-motor producers as presented in Sect. [Reduction Gear Selection](#). It results:

$$N = V_{DC}/V_{N1} \quad (15)$$

- (c) The battery capacity (or energy) is calculated considering that the necessary battery energy is used for propulsion and for auxiliary services like lighting, heating, servo, etc.

$$W_{nec} = W_{prop} + W_{aux} \quad (16)$$

- (c1) The necessary propulsion energy,  $W_{prop}$ , is usually calculated based on the given range on a horizontal road, at constant speed, close to the average traffic speed,  $v_{traffic}$ . Usually, this speed is 50–60 % of the maximum speed. For instance, for a car with  $v_{max} = 100$  km/h,  $v_{traffic} = 60$  km/h. A more complicated cycle model could be used, but this solution needs a computer model and is not considered here. Consequently, the propulsion energy for the range,  $S$ , and constant speed,  $v_{traffic}$ , measured respectively in (kWh), (km), (km/h), is:

$$W_{traffic} = S * T_{pvtraffic} / 3600 \quad (17)$$

where  $T_{pvtraffic}$  is the traction force corresponding to the vehicle resistances at traffic speed,  $v_{traffic}$ . It results by replacing  $v_{h-max}$  with  $v_{traffic}$  in relation (6). Considering the efficiencies of the motor, controller and transmission, respectively  $\eta_m$ ,  $\eta_c$  and  $\eta_t$ , the propulsion energy is:

$$W_{prop} = \frac{W_{traffic}}{\eta_m * \eta_c * \eta_t} \quad (18)$$

- (c2) The auxiliary energy depends of the necessary average power,  $P_{aux}$  and the travel duration,  $t_s$  for the range  $S$ , and speed  $v_{traffic}$ :

$$t_s = S / v_{traffic}, W_{aux} = P_{aux} * t_s \quad (19a)$$

- (d) On the other hand, the working cycle of a battery does not involve all its capacity. A full charge of the battery, especially at lithium could overheat the battery. A deep discharge can also damage the battery. Consequently each battery has maximum and minimum acceptable values for the depth of discharge (DOD) coefficients. Usually, for lithium  $DOD_{max}$  is about  $\sim 0.8$  (discharged) and  $DOD_{min} \sim 0.1$  (fully charged), but for lead the range is higher. It results:

$$W_{tot} = \frac{W_{nec}}{DOD_{max} - DOD_{min}} \quad (20)$$

- (e) The battery capacity measured in [Ah] can be obtained as:

$$C_{tot} = 1000 * W_{tot} / V_{DC} \quad (21)$$



Special attention must be paid to the battery location to avoid safety problems (explosion or electric shocks) especially in the event of an accident, and axles' loading balance.

### Charger and BMS

The new battery technologies, and especially lithium, need a special attention to control and monitor the battery. This is made by an electronic device, known as Battery Management System (BMS). It measures the current, voltages and temperatures for each cell or module and communicates with the charger and controller in order to keep an appropriate battery state and to extend battery life. It also does the necessary periodic balance of the battery elements. Usually BMS is recommended by the battery producer or even is incorporated in the battery unit.

The on-board charger is also recommended by the controller manufacturer or the battery producer. Its principal parameters are: cooling and charging methods, rated input voltage and current, rated output voltage and current and the maximum and minimum values for these, battery technology, charging algorithm permitted, etc.

### Practical Design Exercise

For this purpose of this exercise it was selected a very popular UTV, Polaris Ranger 400, model 2012, available on Romanian market, too. Its principal specifications are given in Table 1, based on UTV Guide (2015) information. For this exercise, a simple electrification solution was to replace the conventional power-train with an electrical one, keeping the original architecture. That is to replace the engine and gear box with a motor and reduction gear, and fuel supply system (tank, pump, etc.) with batteries and charger.

**Table 1** Ranger 400 parameters from UTVGuide (2015)

Dimensions (L × W × h)	cm	297 × 147 × 185 (108" × 56.5" × 73")
Engine power	kW	21.6 (29 HP) 455 cc-1 cylinder
Dry mass	kg	476 (1050 lbs)
Max. payload	Kg	454 (1000 lbs)
Towing rating	kg	567(1250 lbs)
Tires Front/Rear		25 × 8-12; 25 × 10-12
Ground clearance	cm	25.4 (10")
Top speed	km/h	64 (40 mph)
Transmission		Automatic PVT

## ***Electrified Vehicle Principal Parameters Estimation***

The electric vehicle has a higher weight, due mainly to the batteries. Based on experience with other EVs, for instance given by Titan (2015), the dry mass could be estimated to 787 kg. Keeping a payload of 453 kg (1000 lbs), results a gross mass,  $m_a = 1240$  kg. Usual for such EV, the top speed on horizontal road is  $v_{\max} = 40$  km/h. In this case the vehicle has usually no trailer. For slope, practical off-road conditions need access to difficult roads, carrying the maximum load (towing load) at reasonable speed. Practical values are a maximum inclination of  $p = 15\%$  at a maximum speed of  $v_{p\max} = 25$  km/h. In this case the combined gross mass,  $m_{ap}$  is composed of the dead-weight, the towing load and the driver (usually 75 kg). Taking the usual value of UTV hitch tow capacity which is 1500 lbs (680 kg), it results  $m_{ap} = 1540$  kg. On the other hand, the axles loading is increased and better balanced due to the batteries. So, we select the same tire type for front and rear, accepting a higher loading, for instance the tire type  $25 \times 9-12$ , which has the  $t_{\text{height}} = 25''$ ,  $t_{\text{width}} = 9''$  and wheel diameter =  $12''$ . The rolling resistance coefficient for this tire is around 0.2, as results from HPWizard (2015), combined with Bosch (2007).

## ***Electric Motor, Controller and Gear Selection***

As discussed in Sect. [Maximum Motor Power and Motor Selection](#) two conditions are taken into account:

- (a) *maximum speed on horizontal road.* In this case, the gross mass is  $m_a = 1240$  kg and the gravitational acceleration is  $9.81 \text{ m/s}^2$ , and the rolling resistance depends of a lot of conditions, but as presented above, for these tires, an usual coefficient is  $f = 0.02$ . The aerodynamic coefficient was selected also from the literature, close to the value declared by Renault (105) for Twizy,  $C_x = 0.65$ . Considering the low speed of this vehicle, its influence is not significant. The projected frontal area was estimated on geometrical bases, approximating the vehicle shape with regular geometrical figures, function of vehicle height,  $V_h$ , width,  $V_w$ , ground clearance,  $V_{gc}$ , and tire width,  $t_w$ :

$$A = V_w * (V_h - V_{gc}) + 2 * t_w * V_{gc} = 2.46 \text{ m}^2 \quad (22)$$

From (6)–(7) it results at  $v_{\max} = 40$  km/h, that:

$$\begin{aligned} R_a &= 0.047 * 0.65 * 2.46 * 40 * 40 = 120.24 \text{ N}; & P_a &= R_a * v / 3600 = 1.34 \text{ kW} \\ R_{r-hor} &= 0.02 * 9.81 * 1240 = 243.29 \text{ N}; & P_{r-hor} &= R_{r-hor} * v / 3600 = 2.7 \text{ kW} \\ T_{fhor-vmax} &= R_a + R_{r-hor} = 363.53 \text{ N}; & P_{nec-hor} &= P_a + P_{r-hor} = 4.04 \text{ kW} \end{aligned} \quad (23)$$

- (b) *on slope*. In this case the gross mass is higher, due to the tow load, but the speed is significantly reduced, but enough for a reasonable traffic attitude. So,  $m_{ap} = 1540$  kg, and  $v_p = 25$  km/h. The considered inclination is according to usual off-road conditions,  $p = 15$  %. From (8)–(9) it results:

$$\begin{aligned} R_a &= 46.97 \text{ N}; R_{rp} = 298.81 \text{ N}; R_p = 2241.04 \text{ N}; T_{fp} = 2586.82 \text{ N} \\ P_a &= 0.33 \text{ kW}; P_{rp} = 2.08 \text{ kW}; P_p = 15.56 \text{ kW}; P_{nec-p} = 17.97 \text{ kW} \end{aligned} \quad (24)$$

At this point, some important conclusions are:

- the rolling resistance is considered constant with speed which can be accepted here, at low speed;
- the air drag is very low and can be practically neglected. It does not depend of slope angle. The aerodynamic coefficient,  $C_x$  has low importance and the vehicle shape could be chosen from practical considerations;
- the slope driving force,  $R_p$  is the most important element in this case, due to the high inclination and towing load. It is constant with speed.
- the necessary driving power results from (10),  $P_{nec-max} = 17.97$  kW, and is in climbing service. The motor power must be higher, due to the transmission efficiency, as in (11). In this case, for a 2WD is reasonable to take the efficiency  $\eta_t = 0.6$  and for 4 WD a lower value, around 0.94. It results that the motor needs to have a continuous power:

$$P_{motor} > 19.12 \text{ kW} \quad (25)$$

Despite many DC motors are available on market, the best solution at a low price difference, but having better performances and reliability, is to use an AC motor. Considering (25) the selected motor is AC-50 from HPEVS (2015). It is an 8" AC motor designed for automotive and utility applications. This motor can be supplied at different voltages with different specifications. In order to have the optimum specific power, torque and efficiency in the limited room offered by this UTV, it was selected the '72 V—vented and fan cooled' application. Its performance results from the power-speed diagram presented in Fig. 2 for continuous service. The maximum continuous torque is  $T_{max} = 59$  Nm–3000 rpm and power  $P_{max} = 22$  kW–4000 rpm, with top speed,  $n_{top} = 7000$  rpm. At lower voltage the current is too high and decreases the efficiency. At higher voltage the battery pack is difficult to organize, and so many manufacturers prefer to use 48 V. The peak service has a maximum speed  $n_{top-peak} = 8000$  rpm, with two currents at different peak times: (a)  $I_{max} = 650$  A<sub>DC</sub>,  $P_{maxpeak} = 41.49$  kW–2800 rpm, and  $T_{Npeak} = 149.8$  Nm–2700 rpm; (b)  $I_{max} = 550$  A<sub>DC</sub>,  $P_{maxpeak} = 39.38$  kW–3150 rpm,  $T_{Npeak} = 125$  Nm–2900 rpm.

The working point was chosen for the worse case, that is climbing the hill at 25 km/h in continuous service. The necessary power is  $P_w = 19.12$  kW and from

**Fig. 2** AC-50 motor mechanical diagram, based on HPEVS (2015)

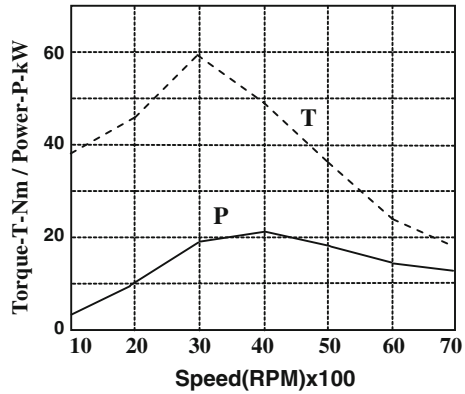


Fig. 2, the corresponding speed is  $n_{ref} \approx 4200$  rpm. The rated tire radius is  $r_n = \text{tire}_{height}/2 = 12.5'' = 0.3175$  m. Considering a small tire working deformation, the equivalent wheel radius is  $r_r = 0.97 * r_n = 0.308$  m. The total reduction coefficient results from (13),  $i_R = 19.96$ . To implement this, HPEVS recommends the trans-axle model Graziano UTV 900 from Graziano (2015), and intermediates this acquisition. A custom value for the reduction coefficient could be negotiated with the producer. Other parameters for gear selection result from the peak diagram of AC-50 and are the maximum torque  $T_{gear} = T_{Npeak} = 150$  Nm, and maximum speed,  $v_{gear-input} = 1.1 * 8000$  rpm  $\sim 9000$  rpm, considering a possible 10 % over-speed. With this gear, the maximum vehicle speed of 40 km/h is produced at  $n = 6720$  rpm, less than the motor maximum speed, and the necessary power of  $4.3/0.94 = 4.57$  kW is much lower than 13 kW, the motor power at that speed, verifying a proper design.

Concerning the controller, HPEVS recommends for the AC-50 motor at 550A peak and 72 V, the model 1238-6501, produced by Curtis Instruments Inc. (2015).

## Battery Selection

The chemistry proposed is the common solution for UTV, the lead battery. Considering the rated DC voltage required by the motor,  $V_{DC} = 72$  V, and 12 V battery units, the number of series connected batteries from (15) is  $N = 6$ . If consider the average traffic speed  $v_{traffic} = 20$  km/h, and usual range  $S = 70$  km  $\sim 45$ mi, from (6) the traction force in steady state on horizontal road is,  $T_{pvtraffic} = 273.35$  N. Thus, from (17), the necessary energy is  $W_{traffic} = 5.31$  kWh. Considering the efficiencies of motor and inverter, provided by the manufacturers, about 0.85 each, and transmission 0.94, the propulsion energy taken from the battery is from (18),  $W_p = 7.82$ kWh. The auxiliary power for such a vehicle considering lighting and other small loads is about 250 W. The traveling time taken from (19) is  $t_s = 3.5$  h, and the auxiliary energy from (19a) is  $W_{aux} = 0.875$ kWh.

So, the total necessary energy is  $W_{nec} = 8.7$  kW. For lead, the minimum discharging coefficient is about  $DOD_{min} = 0.02$  and the maximum  $DOD_{max} = 0.85$ . Then, from (20) the total energy stored in the battery pack is  $W_{tot} = 10.48$  kWh, and from (21), the capacity of a battery unit is 145.6 Ah. For this, it is selected a deep cycle lead battery of type US185HC XC2 produced by US Battery (2015). It has reserve capacity of 117 min at 75 A, resulting a capacity of 146.25 Ah, practically the battery capacity in working conditions, where UTV current at 20 km/h is 77 A. For this battery, at  $DOD_{max} = 0.85$ , the expected lifecycle is about 650 cycles, and the 20 h capacity is  $C_{20} = 220$  Ah. The total battery pack weight is  $m_{bat} = 54.4$  kg \* 6 = 326 kg.

For charging, a recommended on-board charger is SCO7220 from Quick Charge (2015) providing a smart charging at 72 V/20 A at a weight of  $m_{charger} = 42$  lbs = 19 kg.

## Conclusions

The present study has some important conclusions such:

1. UTVs are a cheap and practical solution for a lot of small urban and off-road activities.
2. The electric solution is already present, as demonstrated by Titan (2015), but electrification of a classical UTV could be a practical solution, too.
3. A design algorithm for power-train electrification has been proposed and clear solutions given.
4. Considering that the weight of removed components such engine, tank, gear box is comparable with the weight of motor, controller, fix gear and charger the difference in weight between the Ranger 400 and the electrified vehicle is just the battery pack weight, which validate the study. This is confirmed by the electric version of this producer, Ranger EV, given in Polaris (2015).
5. On horizontal road the vehicle has a high power and torque reserve, allowing for a good dynamic.

## References

- BOSCH (2007) Automotive handbook, 7th edn. SAE, Warrendale  
 DIRECTIVE 2009/28/EC—Official Journal of EU-5.6.2009-L140/16-62  
 Gillespie TD (1992) Fundamentals of vehicle dynamics. SAE, Warrendale  
[http://www.utvguide.net/polaris\\_ranger\\_400.htm](http://www.utvguide.net/polaris_ranger_400.htm). Accessed 08 Oct 2015  
<http://www.titanutv.com/resources/pdf/2014-analysis.pdf>. Accessed 08 Oct 2015  
<http://hpwizard.com/tire-friction-coefficient.html>. Accessed 09 Oct 2015  
<http://www.polaris.com/en-us/ranger-utv/ranger-ev-avalanche-gray/specs>. Accessed 10 Oct 2015  
<http://www.quickcharge.com/on-board-chargers-standard.html>. Accessed 10 Oct 2015

- <http://usbattery.com/products/12-volt-batteries/us-185hc-xc2/>. Accessed 10 Oct 2015
- <http://curtisinstruments.com/?fuseaction=Products.home#/motorcontrollers/64>. Accessed 10 Oct 2015
- <http://www.oerlikon.com/graziano/en/products/automotive/transfer-cases-for-full-electric-zero-emission-vehicles-2/>. Accessed 10 Oct 2015
- [http://www.autoevolution.com/moto/polaris-ranger-400-2009.html#aeng\\_polaris-ranger-400-2009-455](http://www.autoevolution.com/moto/polaris-ranger-400-2009.html#aeng_polaris-ranger-400-2009-455). Accessed 12 Oct 2015
- <http://www.hpevs.com/catalog-ac-50.htm>. Accessed 12 Oct 2015
- <http://www.renault.fr/gamme-renault/vehicules-electriques/twizy/twizy/caracteristiques-techniques.jsp>. Accessed 12 Oct 2015
- International Energy Agency—Tracking\_Clean\_Energy\_Progress\_2015. [http://www.iea.org/publications/freepublications/publication/Tracking\\_Clean\\_Energy\\_Progress\\_2015.pdf](http://www.iea.org/publications/freepublications/publication/Tracking_Clean_Energy_Progress_2015.pdf)
- Racicovschi V et al (2007) Electric and hybrid vehicles (in Romanian). Electra, Bucharest
- Romanian Ministry of Environment and Water and Forests. [http://www.mmediu.ro/beta/wp-content/uploads/2012/06/2012-06-12\\_dezvoltare\\_durabila\\_nsdenglish12112008.pdf](http://www.mmediu.ro/beta/wp-content/uploads/2012/06/2012-06-12_dezvoltare_durabila_nsdenglish12112008.pdf). Accessed 06 May 2015
- STOICESCU A (2007) Automobile traction and consumption performances design. ET, Bucharest

# Measurement of Fuel Consumption for an Off-road Vehicle With Conventional and Hybrid Powertrain

Gabriel Anghelache, Alexandra-Raluca Moiescu  
and Ioan Mircea Oprean

**Abstract** The hybrid powertrain of an off-road vehicle allows reducing fuel consumption and exhaust emissions. For a small off-road vehicle, the development of a prototype hybrid powertrain has been achieved. One of the possibilities to quantify the efficiency of hybridization consists of comparing the fuel consumption for the vehicle with conventional powertrain and for the same vehicle with prototype hybrid transmission. The comparison has been made through experimental investigation of fuel consumption. Fuel consumption measurements have been performed using portable equipment with high-precision volumetric flowmeters. A data acquisition system with specially developed LabVIEW applications has been mounted on-board the vehicle for real-time measurement of fuel flow. During road rolling, the measuring system has also allowed real-time monitoring and adjustment of vehicle speed according to the NEDC (New European Drive Cycle). Vehicle speed measurement in road conditions has been performed using an optical speed transducer. For the vehicle with conventional powertrain, the measurement of fuel consumption has been performed both in real road conditions and on the chassis dynamometer, at variable speed according to the urban drive cycle NEDC. For the vehicle with hybrid powertrain, the measurement of fuel consumption has been performed on the chassis dynamometer, at variable speed according to the urban drive cycle NEDC. The hybrid powertrain measurement results have been compared to those obtained for the vehicle with conventional powertrain, and a decrease of fuel consumption has been ascertained.

**Keywords** Fuel economy · Off-road vehicle · Hybrid powertrain · Data acquisition

---

G. Anghelache · A.-R. Moiescu (✉) · I.M. Oprean  
University POLITEHNICA of Bucharest, Splaiul Independentei 313,  
060042 Bucharest, Romania  
e-mail: raluca.moiescu@upb.ro

## Introduction

In the current context characterized by alarming global warming, strong local pollution in large urban areas and rapid evolution of regulations regarding vehicle emissions, the automotive manufacturers are increasingly concerned on hybrid vehicles, considered as one of the solutions for reducing fuel consumption and implicitly exhaust emissions. The main feature of hybrid vehicles is that they include components able to recover the kinetic energy of the vehicle during deceleration and store this energy, in view of ulterior use during acceleration or constant speed rolling. Thus the hybrid powertrain of a vehicle allows reducing fuel consumption and exhaust emissions, as stated in Erjavec (2013), Hodgkinson and Fenton (2001), Mi et al. (2011).

The development of a prototype hybrid powertrain for a small off-road vehicle with spark-ignition engine, shown in Fig. 1, has been achieved at the Automotive Engineering Department of the University POLITEHNICA of Bucharest. The hybrid powertrain has parallel architecture, with reversible electric unit and 55 kg battery pack.

One of the possibilities to quantify the efficiency of hybridization consists of comparing the fuel consumption for the vehicle with conventional powertrain and for the same vehicle with prototype hybrid transmission. The comparison has been made through measurements of fuel consumption.

## Fuel Consumption Measurement System

Experimental investigations of fuel consumption have been performed using portable equipment with high-precision volumetric transducers, able to quantify the flow through the fuel pressure line and through the fuel return line. In addition to

**Fig. 1** Small off-road vehicle with prototype hybrid powertrain developed at the automotive engineering department of the university POLITEHNICA of Bucharest





the fuel inlet and outlet measurements, the following physical quantities have been taken into account: vehicle longitudinal speed, distance on longitudinal direction, and time. An optical transducer has been used for accurately measuring vehicle speed and distance. A National Instruments portable system with PXI cards has performed the data acquisition for the abovementioned parameters using counters and analog inputs. The measuring system components are presented schematically in Fig. 2 and shown on board the vehicle in Fig. 3.

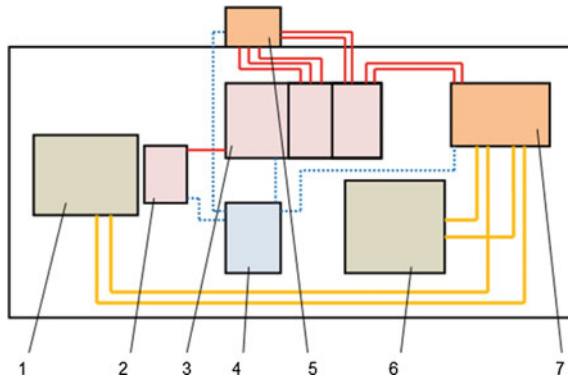


**Fig. 2** Fuel consumption measuring system set-up: 1 Internal combustion engine, 2 touch-screen monitor, 3 National Instruments system with PXI data acquisition cards, 4 supplementary 12 V battery, 5 optical transducer for vehicle speed and distance, 6 vehicle fuel tank, 7 measuring equipment with high-precision volumetric flowmeters



**Fig. 3** Measuring system on board the vehicle

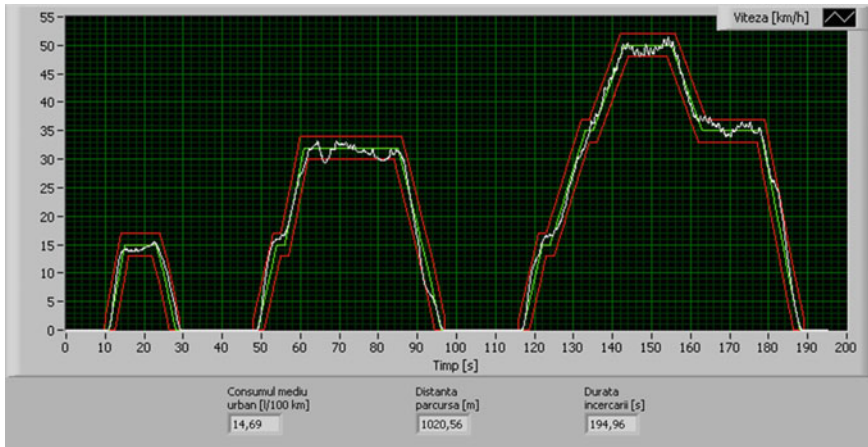


**Fig. 4** Data acquisition and processing application specially developed in LabVIEW showing results measured on the road for the vehicle with conventional powertrain

In addition to the measurements of flow through fuel pressure and return lines, of vehicle speed and distance, the measuring system has been required to allow real-time on-board monitoring of vehicle speed, so that the vehicle driver can follow standardized drive cycles or maintain controlled speed during consumption measurements. This has been achieved by using a real-time data acquisition and data processing application specially developed in LabVIEW environment, shown in Fig. 3 (middle above) and in Fig. 4, which allows measuring and displaying vehicle speed on a touch-screen monitor on-board the vehicle. With the help of this application, the real-time variation of speed is graphically displayed live on the monitor, superimposed on the standardized drive cycle, thus allowing the driver to track and correlate vehicle speed with the required cycle. From the measured time variations of fuel quantity, travelled distance, and vehicle speed, the specially developed LabVIEW application computes the average and instantaneous fuel consumption.

## Results of Fuel Consumption Experimental Investigations

The measurement of fuel consumption has been performed for the vehicle with conventional powertrain both in real road conditions and on the chassis dynamometer, at variable speed according to the urban portion of the NEDC (New European Drive Cycle) stated in UN ECE (2015) Regulation No. 83. For the vehicle with hybrid powertrain, the measurement of fuel consumption has been performed on the chassis dynamometer, at variable speed according to the urban NEDC. The variations of speed and instantaneous fuel consumption versus time measured on the chassis dynamometer are shown in Fig. 5 for the vehicle with conventional powertrain, and in Fig. 6 for the vehicle with hybrid powertrain.

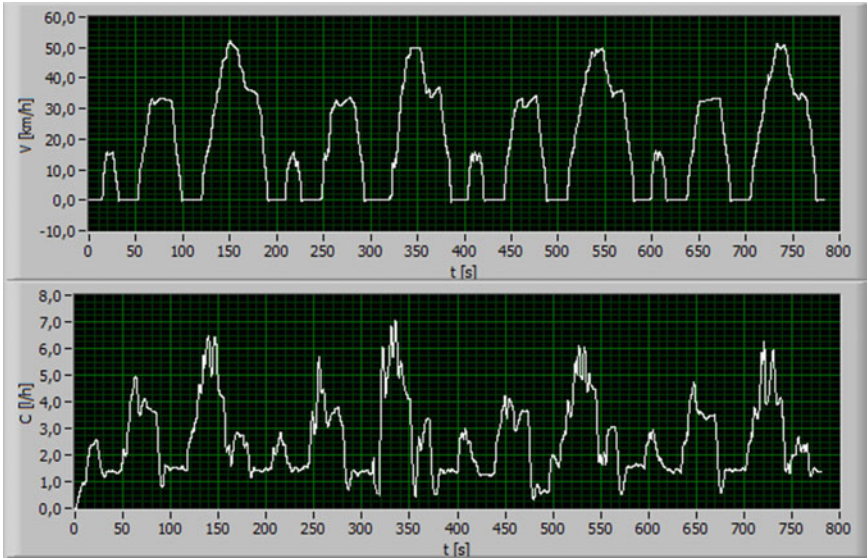


**Fig. 5** Vehicle speed and instantaneous fuel consumption measured on chassis dynamometer for the vehicle with conventional powertrain

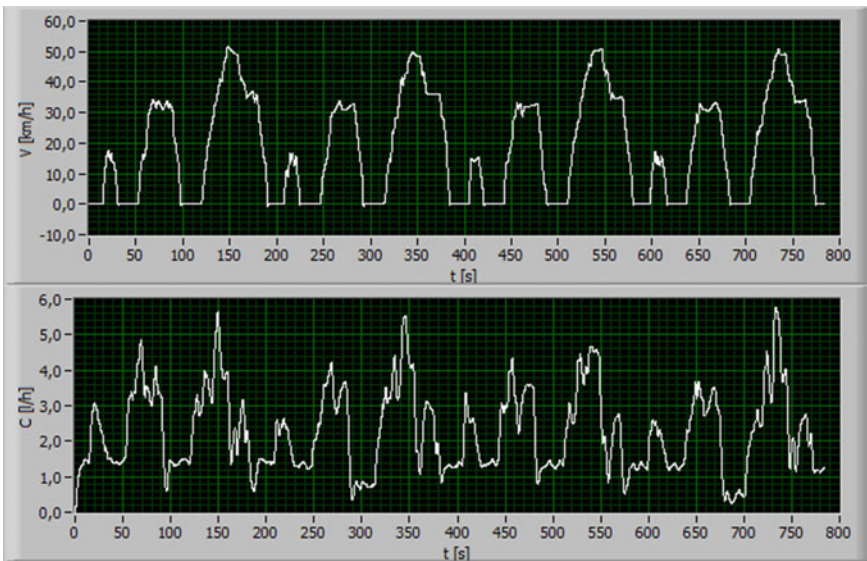


**Fig. 6** Vehicle speed and instantaneous fuel consumption measured on chassis dynamometer for the vehicle with hybrid powertrain

**Table 1** The average fuel consumption measured at variable speed according to the urban NEDC

Powertrain	Conventional	Conventional	Hybrid
Vehicle rolling conditions	Road	Chassis dynamometer	Chassis dynamometer
Average fuel consumption (l/100 km)	14.7	13.5	12.3

The values of average fuel consumption measured at variable speed according to the urban NEDC for the vehicle with conventional powertrain and with hybrid powertrain are presented in Table 1. For the vehicle with conventional powertrain, there is a decrease in average fuel consumption when rolling on the chassis dynamometer, due to the difference in vehicle and rolling conditions (test road surface and profile, climate, tyres, etc.).

The comparison of measurements on chassis dynamometer shows that the average fuel consumption has decreased by 9 % in the case of hybrid powertrain with respect to the case of conventional powertrain. This achievement could be improved through further refinement of hybrid transmission, and control software evolution.

## Conclusions

The measurement system developed for investigating the fuel consumption acquires simultaneously vehicle speed, distance, flow through the fuel pressure line and flow through the fuel return line. The system allows mounting without modifying the normal operation of the vehicle. It is also able to display real-time vehicle speed, so that the vehicle driver can follow standardized drive cycles or maintain controlled speed during consumption measurements.

The measurement system allows investigating the fuel consumption both in real road conditions and on the chassis dynamometer; it provides vehicle instantaneous fuel consumption, and also average fuel consumption during drive cycles such as the NEDC.

For the vehicle with conventional powertrain, the average fuel consumption shows a decrease as a consequence of rolling on chassis dynamometer, due to the difference in vehicle and rolling conditions.

The average fuel consumption measured on chassis dynamometer is lower in the case of hybrid powertrain with respect to the case of conventional powertrain, thus proving the efficiency of hybridization.

## References

- Erjavec J (2013) Hybrid, electric and fuel-cell vehicles. Delmar, Clifton Park
- Hodkinson R, Fenton J (2001) Lightweight electric/hybrid vehicle design. Butterworth-Heinemann, Oxford
- Mi C, Masrur MA, Gao DW (2011) Hybrid electric vehicles: principles and applications. Wiley, Chichester
- UN ECE (2015) Regulation no 83: uniform provisions concerning the approval of vehicles with regard to the emission of pollutants according to engine fuel requirements. <http://www.unece.org/fileadmin/DAM/trans/main/wp29/wp29regs/R083r5e.pdf>. Accessed 15 Oct 2015

# Security in Connected Cars

Mushabbar Hussain

**Abstract** This article provides an overview about the probable security threats in modern automotive systems, and possible counter measures to safeguard the vehicle from potential attacks. This paper attempts to describe few prominent use cases in the automotive context and potential threats associated with each of them, followed by possible security mechanisms to provide a secure environment. The main focus of this paper is to discuss about the security threats in connected cars and possible security solutions to counter the attacks. Further this article briefly discusses about hardware cryptographic solutions and the advantages of hardware security for realizing real-time solutions. Finally provides a realtime illustration of how security concepts can be applied to automotive usecases. The paper concludes by highlighting the importance of having security built into the products right from the concept phase.

**Keywords** Cybersecurity · Connected cars · Automotive security · Key management · V2X communication · HSM

## Introduction

The classic cars were much simpler, and so was the electronics in them. The components of a classic cars were discrete and unconnected to each other, they were more of a closed systems without much interaction with the external world. With advances in technology, the modern automotive systems have become more sophisticated, more software-intensive, more complex, and highly connected systems making them highly vulnerable to security attacks. A modern automobile can have up to 80 embedded microcontrollers on board running tens of millions of lines of code within them. The embedded ECU's control almost every function of the car

---

M. Hussain (✉)

KPIT Technologies, Sarjapura Outer Ring Road, Bangalore 560103, India  
e-mail: mushabbar.hussain@kpit.com

including safety-critical vehicle applications such as braking, engine control, steering, airbag functions, navigation systems etc. Therefore security attacks are not just limited to disclosure and loss of sensitive data but also affect the safety critical functions of the car.

Recent studies and Experiments conducted by Independent research organizations from EUROPE/US (Checkoway et al. 2015) have demonstrated that once a hackers gain access to the in-vehicle network of the car, could control everything; from controlling the acceleration, to applying/releasing brakes, playing songs of their choice, locking/unlocking the doors. These experiments have demonstrated that security plays an important role in automotive systems because security threats might not only cause nuisance and disclose of sensitive data but also affect the safety critical functions of the car. This mean without security there is no safety.

## Security Threats in Connected Cars

A connected (or autonomous) car is a driverless car or self-driving car which is capable of sensing its environment and navigating without human input. Autonomous cars are fully connected vehicles that use a combination of wireless technologies (such as radar, lidar, GPS) and advanced sensors (stereo cameras and long- and short-range RADAR) for its operation. These cars are expected to have a permanent connection to the Internet and to the cloud for fetching various kinds of information such as current road situation, weather conditions, or the parking situation at the destination. Benefits of autonomous cars include zero accidents, reduced traffic violations, productive commute time, elimination of human errors, improved energy efficiency (Silberg and Wallace 2014).

In order to operate in real time, autonomous cars may use wireless technologies to communicate with the grid, the cloud, with other vehicles (V2V) and to infrastructure (V2I). An enormous amount of data will becomes available on the air. This essentially means that someone—a hacker, terrorists, and unauthorized parties can have means to capture data, alter records, instigate attacks on systems and track every movement of vehicle. The hackers can gain access to the vehicle sensors that control airbags, breaking systems, door lock operations and virtually control or disable the car. They could provide false information to drivers, use denial-of-service attacks to bring down the in-vehicle network, illicitly reprogram the ECUs with a malware and even can download incorrect navigation maps to mislead the driver. Therefore, system security will undoubtedly become a paramount issue which the automakers need to address before putting the autonomous cars on the road (Fig. 1).

The current automobiles today are not quite capable to detect and prevent hackers from gaining access to the vehicle network, detecting and rejecting malicious commands injected into the ECU (Barry and Philpot 2011).

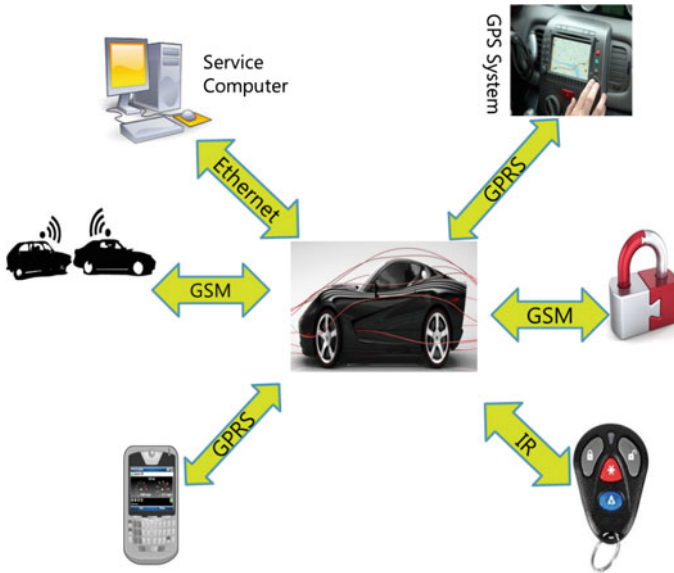


Fig. 1 Typical vehicle network of a modern vehicle

**Here are some of the security threats to modern automobiles:**

- Inducing forged traffic into the in-vehicle network
- Downloading of malicious applications into the ECU
- Gaining access to ECU resources by launching a brute force attack on the system
- Illegal Odometer Tuning
- Tuning/Manipulation protection
- Attack on Tire Pressure Monitoring System (TPMS)
- Inducing forged traffic into a navigation system
- Breaking Antitheft systems such as central locking, immobilizers
- Corruption of rewriteable flash memory
- Execution of unauthorized commands

**The security system inside autonomous vehicle shall ensure:**

- Technology in a self-driven car works 100 % of the time without compromising on the safety-critical functionality.
- Internal as well as external communication interfaces are properly secured
- Enable Secure software download
- Detect and prevent malware from running on the ECU's
- Enable secure access to secret keys and confidential data
- Electronic immobilizer;
- Software and hardware integrity
- Protection from theft and forgery



## Realization of Security Solutions in Automotive Systems

In this section provides a general overview of some of the important automotive features, and discuss about possible security measures that can be applied to make the vehicle functions secure from cyber attacks (Fig. 2).

### *Main Automotive Usecases*

- **Target Authentication**

Target authentication involve authentication of entities and communication partners before allowing access to its internal resources. For ex, authentication of entities requesting read/write access to ECU internal data—ex, diagnosis testers, remote clients

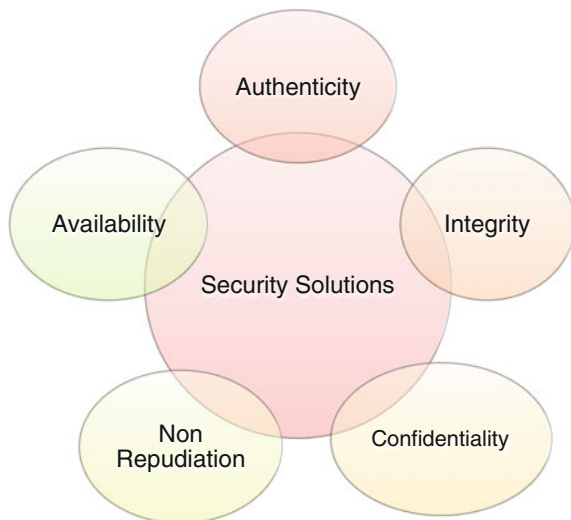
- **Secure Communication**

The system shall ensure authenticity and integrity of the data communicated over internal/external interfaces. Ex: Secure OnBoard, Secure Off-Board communications

- **Secure Boot**

The objective of the secure boot is to ensure the integrity of code/software stored in the flash has not been compromised. Secure boot validates the flash contents by computing the digital signature of the flash software component and compare it with the pre-configured value. Popularly implemented with the help of hardware security peripheral

**Fig. 2** Security elements of interest



- **Secure Flashing**

Secure flashing helps to prevent malicious content from getting flashed on the ECU. Secure Software flash-loaders employ security mechanisms such as application authentication (using MAC, Digital Signatures), application integrity check (using CRC, hash) to ensure the authenticity and integrity of software being flashed into the ECU memory

- **Key management functions**

Key management is the management of security keys in a cryptosystem. This involves key generation, exchange, storage, use, update, deletion of keys. It includes technology, policies and procedures for managing all the cryptographic keys—symmetric and asymmetric

- **V2X Communication**

V2X (Vehicle-to-Vehicle or Infrastructure) communication involves exchange of information between vehicles, with the roadside infrastructure (ex traffic signals, warning signs), with remote systems such as e-call center, with the GPS systems etc. V2X plays an important role in the development of Intelligent Transport System (ITS) and connected cars.

- **Secure Storage**

Secure storage of confidential data such as secret seeds, keys, keying material, security logs, and configuration/calibration data

In order to secure the vehicles from cyber-attacks, the system shall implement appropriate security mechanisms based on software and hardware cryptography. The security system must ensure that data is protected during its transit, while it is stored & accessed, and have mechanism in place to ensure both unauthorized (malicious hackers) and unintended modifications do not go undetected.

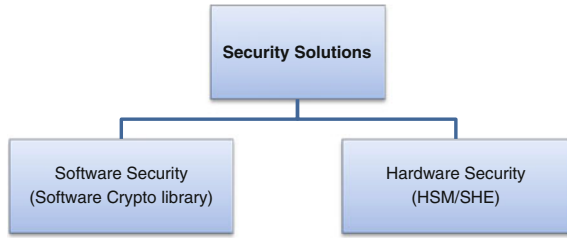
Here are some of the crypto services that help in realization of security solutions in automotive systems:

- Digital Signature generation/verification
- Message Digest generation/validation
- MAC generation/verification
- Random Number generators
- Data Encryption/Decryption based on Symmetric and Asymmetric keys
- Secure Hash

### ***Security Solutions can be Realized by Both Hardware and Software Crypto Mechanisms***

In order to harden ECUs against security attacks, security mechanisms (to prevent successful manipulation of software, data, keys and keying material) must be rooted in hardware (Fig. 3).

**Fig. 3** Security solutions broadly level classification



Hardware security solutions are realized with the help of hardware security peripherals such as HSM (Hardware Security Module) based on EVITA, and SHE (Secure Hardware Extension) based on SHE specifications. EVITA and SHE are major security initiatives in the auto industry that define security standards, EVITA specification targets both Hardware & Software solutions

### *Introduction to SHE/HSM*

SHE/HSM are on-chip security peripherals embedded within an automotive MCU. HSM/SHE are dedicated security modules specifically developed and designed for security use-cases. They are designed to move cryptographic functions from SW to HW domain (The Evita Project) (Fig. 4).

SHE/HSM usually provides a fixed set of cryptographic services to the application layer. The basic cryptographic services can be used to realize complex automotive security use-cases

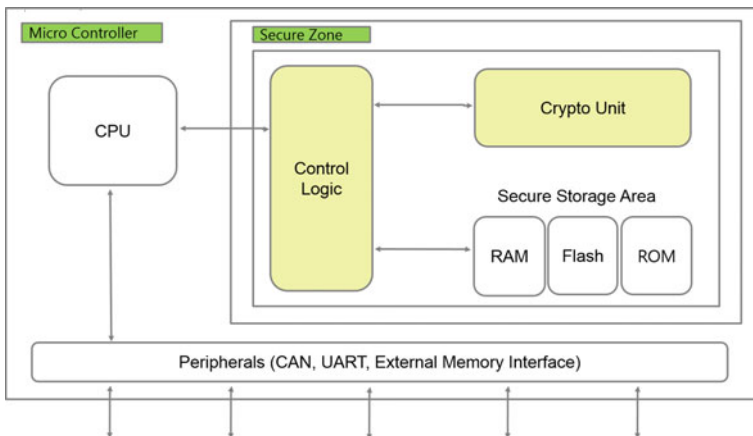


**Fig. 4** Simplified logical structure of a hardware security peripheral

**Main Features/Functions:**

- Symmetric key Encryption based on AES-128
- CMAC generation & verification
- Random number generation for secure generation of cryptographic keys
- Application/Boot loader verification
- Secure storage of secrets keys and keying material
- On-chip Flash/ROM read-out protection against unauthorized access

**Advantages of SHE/HSM:**

- Onboard secure cryptographic key generation
- Onboard secure cryptographic key storage and management
- Offloading application servers for complete asymmetric and symmetric cryptography.
- Hardware acceleration

**A Sample Case Study**

In this section we look at practical use case of a Secure Bootloader in the automotive context and see how security concepts can be applied to make the software download more secure (Fig. 5).

**Main features of a Secure Flash loader:**

- **Application Authentication:** To ensure the authenticity of data downloaded to the ECU (verify that software originated from known source)
- **SW Integrity check**—Verify that the SW has not been altered during transit
- **Secure Boot:** Software authenticity verification during ECU start-up
- **Secure Access:** Ensures that only authorized Testers can unlock the ECU to perform critical tasks such as application flashing, vehicle diagnostics etc.
- **Secure Storage:** For secure storage of ECU confidential data such as secret seed/keys, keying material (Fig. 6).

***Illustration of Application Authentication***

To enable application authentication and integrity check, signature of the application software is computed (ex, using CMAC, RSA-2048) and attach to the software that is downloaded.

ECU Side:

- ECU re-computes the signature of the downloaded software:  $S'$
- Compares computed signature( $S'$ ) with the attached signature( $S$ )

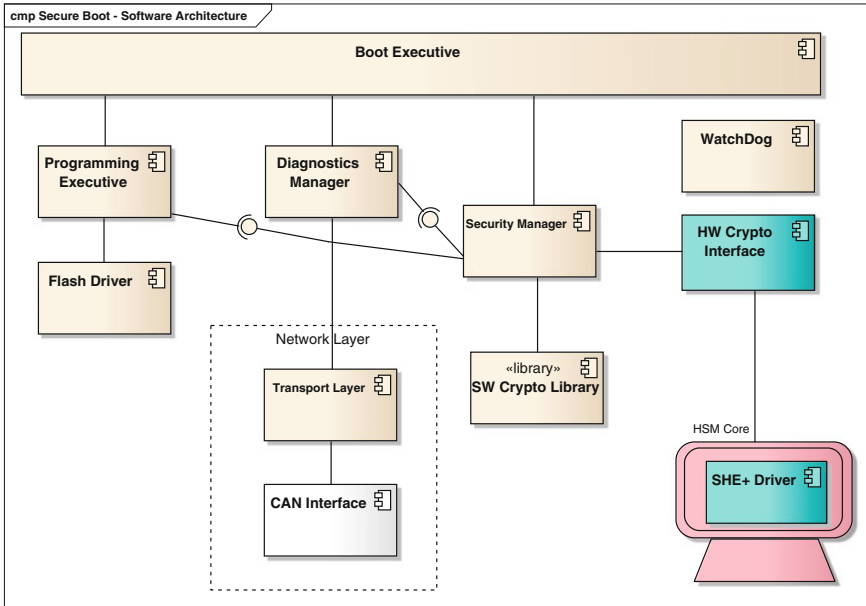


Fig. 5 Secure bootloader architecture

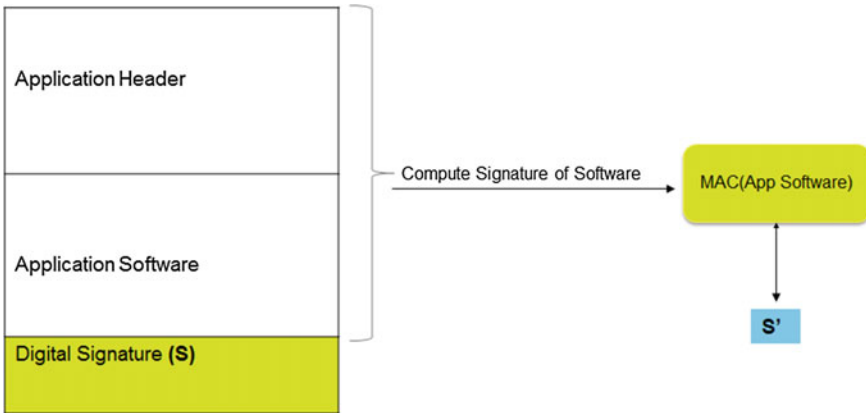


Fig. 6 Application authentication example

- If  $S = S'$   $\rightarrow$  application is authentic

The above example illustrations demonstrates how security concepts can be applied to verify the authenticity and integrity of software before flashing them into the ECU.

## Conclusions

With modern automotive systems getting connected to the internet, the security is no more an optional feature. In the last decade, the automobile industry has been focusing more on improving safety aspects of the car and this decade the focus would be to build more secure and safer vehicles. As the security threats can endanger life of the passengers designing more secure products is an absolute necessity.

Building secure products cannot happen overnight, it should start from the early days of software development life cycle. Security should be built into the design and into the code. Developers should start designing and implementing security based on threat analysis results of their systems, address the vulnerabilities (security holes) in a phase wise manner. Lastly consider industry standards such as NIST (National Institute of Standards and Technology), ENISA (European Union Agency for Network and Information Security), FIPS (Federal Information Processing Standards), EVITA, SHE, in building crypto/security solutions rather than going with proprietary security mechanisms

Currently many organizations are involved in doing research related to security in connected cars. Most of the research has focused on identifying the security problems and only to a lesser extent towards presenting solutions. Much remains to be done. One of the greatest challenges in adding security to the connected car would be to adapt the security solutions to the very high safety requirements, under the constraints of very limited hardware, software and power resources.

## References

- Barry K, Philpot C (2011) Can your Car be hacked? <http://www.caranddriver.com/features/can-your-car-be-hacked-feature>
- Checkoway S, McCoy D, Kantor B, Anderson D, Shacham H, Savage S (2015) Comprehensive experimental analyses of automotive attack surfaces. University of California, San Diego; Koscher K, Czeskis A, Roesner F, Kohno T University of Washington
- Digital signature. [http://en.wikipedia.org/wiki/Digital\\_signature](http://en.wikipedia.org/wiki/Digital_signature)
- Information security. [http://en.wikipedia.org/wiki/Information\\_security](http://en.wikipedia.org/wiki/Information_security)
- Potlapally N (2008) Secure embedded system design. [http://palms.ee.princeton.edu/PALMSopen/dissertations/Nachiketh\\_Potlapally\\_phdthesis.pdf](http://palms.ee.princeton.edu/PALMSopen/dissertations/Nachiketh_Potlapally_phdthesis.pdf)
- Silberg G, Wallace R (2014) Self-driving cars: the next revolution. <https://www.kpmg.com/US/en/IssuesAndInsights/ArticlesPublications/Documents/self-driving-cars-next-revolution.pdf>
- The Evita project. <http://www.evita-project.org/objectives.html>

# The Development of New Evaluation Criteria for Supercharged Engines Based on Elasticity and Adaptability at Traction

Ivan Florian, Mihai Stelian Niculae and Dragoş Constantin Neacşu

**Abstract** This paper aims to outline supercharged engines from the perspective of elasticity and adaptability, starting with the curves of power and torque. As is already known, the diagram of supercharged engine is not similar with the one of natural aspirated engine. As a result, classic coefficients are not suitable for this type of engines, because they can't define in a proper way how the engine is running. Beginning with the particularities of the supercharged engine, in the paper are defined new coefficients which allows to appreciate in a correct way the engine behavior on the vehicle. As a result, are defined the following coefficients: the coefficient of torque diagram flattening, the coefficient of power diagram flattening, the coefficient of stability, the coefficient of instability, the coefficient that define the field of use, the coefficient of adaptability, the coefficient of elasticity, the coefficient of torque reserve, the coefficient of power reserve. Using these coefficients, the authors defined an equation of optimization, termed equation of efficiency, which allows to evaluate in a global way a wide variety of supercharged engines.

**Keywords** Engine diagram · Elasticity · Adaptability · Equation of efficiency · The field of use

## Study Motivation

Over time, internal combustion engines for vehicles have progressed more and more from the perspective of dynamic economic and ecologic performances.

---

I. Florian · M.S. Niculae (✉) · D.C. Neacşu  
University of Piteşti, Piteşti, Romania  
e-mail: mihainiculae92@yahoo.com

I. Florian  
e-mail: florianivan2002@yahoo.com

D.C. Neacşu  
e-mail: neacsudragos54@yahoo.com

The behavior of an engine is evaluated usually by using elasticity and adaptability coefficients

### *Natural Aspirated Engine*

For the natural aspirated engine, as is already known the stability operating area is defined by the maximum torque engine speed and maximum power engine speed (Fig. 1).

Corresponding to this area are defined the classic coefficients of adaptability  $k_a$  and elasticity  $k_e$ .

$$k_e^{na} = \frac{n_M}{n_P} \quad (1.1)$$

$$k_a^{na} = \frac{M_{e_{max}}}{M_P} \quad (1.2)$$

$M_{e_{max}}$ —maximum torque;  $M_P$ —maximum torque at maximum power;  $n_M$ —maximum torque engine speed;  $n_P$ —maximum power engine speed; na—stands for natural aspirated

Manufacturers aims to achieve the lower value possible for the coefficient of elasticity and a value equal to 1 for the coefficient of adaptability.

The authors of this paper consider that the classic coefficients are not entirely suitable for a proper analysis of the potential of an internal combustion engine.

Therefore are proposed two new coefficients:

- (a) The coefficient of torque reserve:

$$r_M^{na} = \frac{M_{rez}}{M_{e_{max}}} = \frac{M_{e_{max}} - M_P}{M_{e_{max}}} = 1 - \frac{1}{k_a} \quad (1.3)$$

$M_{rez}$ —Torque reserve

- (b) The coefficient of power reserve:

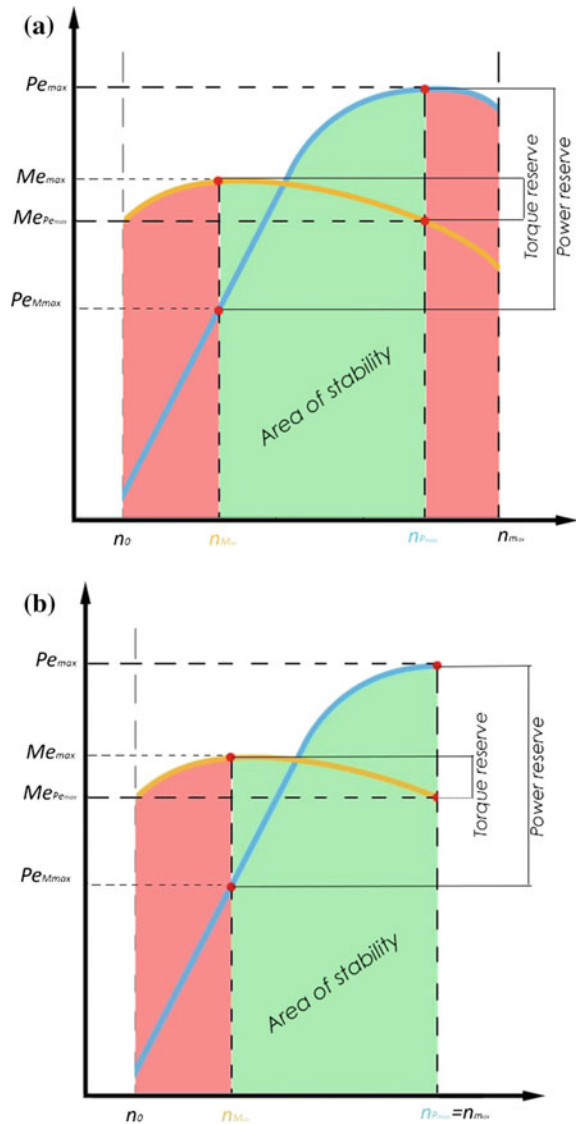
$$\begin{aligned} r_P^{na} &= \frac{P_{rez}}{P_{e_{max}}} = \frac{P_{e_{max}} - P_M}{P_{e_{max}}} = 1 - \frac{P_M}{P_{e_{max}}} = 1 - \frac{M_{e_{max}} \cdot \frac{\pi \cdot n_M}{30}}{M_P \cdot \frac{\pi \cdot n_P}{30}} = 1 - \frac{M_{e_{max}}}{M_P} \cdot \frac{n_M}{n_P} \\ &= 1 - k_a^a \cdot k_e^a \end{aligned} \quad (1.4)$$

$P_M$ —Maximum power at maximum torque;  $P_{rez}$ —Power reserve;  $P_{e_{max}}$ —Maximum power

Obvious for these coefficients are desired lower values possible.



**Fig. 1** Engine diagram of a natural aspirated engine (Ivan 2014). **a** M.A.S. **b** M.A.C

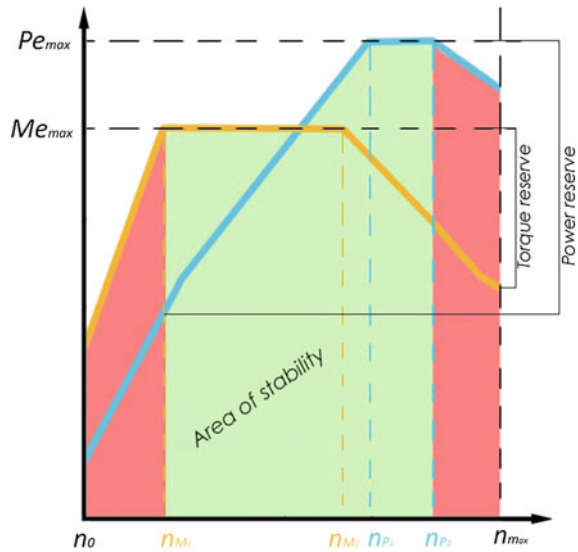


### Supercharged Engine

Experience has shown that in case of the supercharged engine the power and torque diagrams are not similar with the diagrams of the natural aspirated engines.

In technical literature are not known coefficients that can define the particularities of a supercharged engine diagram.

**Fig. 2** Engine diagram of a supercharged engine (Ivan 2014)



Therefore the authors of this paper redefined the coefficients from above for the supercharged engine case (Fig. 2).

The coefficients are:

- (a) The coefficient of elasticity:

$$k_e^s = \frac{n_{M1}}{n_{P2}} \tag{1.5}$$

$n_{M1}$ —minimum engine speed where the maximum torque is achieved;  $n_{P2}$ —maximum engine speed where maximum power is achieved; s—stands for supercharged

- (b) The coefficient of adaptability:

$$k_a^s = \frac{M_{emax}}{M_{P2}} \tag{1.6}$$

$M_{P2}$ —torque obtained at maximum power engine speed;

The coefficient of torque reserve:

$$r_M^s = \frac{M_{rez}}{M_{emax}} = \frac{M_{emax} - M_{P2}}{M_{emax}} = 1 - \frac{1}{k_a^s} \tag{1.7}$$

(c) The coefficient of power reserve:

$$\begin{aligned}
 r_P^s &= \frac{P_{rez}}{P_{emax}} = \frac{P_{emax} - P_M}{P_{emax}} = 1 - \frac{P_M}{P_{emax}} = 1 - \frac{M_{emax} \cdot \frac{\pi \cdot n_M}{30}}{M_p \cdot \frac{\pi \cdot n_p}{30}} = 1 - \frac{M_{emax}}{M_p} \cdot \frac{n_M}{n_p} \\
 &= 1 - k_a^s \cdot k_e^s
 \end{aligned}
 \tag{1.8}$$

$P_{M1}$ —maximum power obtained at maximum engine speed

Therefore because the engine torque and power diagrams are flattened, are defined two new coefficients for the supercharged engine.

The flattened area highlights a better behavior of the engine from the perspective of elasticity and adaptability.

(d) The coefficient of torque diagram flattening:

$$a_M = \frac{n_{M2} - n_{M1}}{\frac{n_{M2} + n_{M1}}{2}} = \frac{2(n_{M2} - n_{M1})}{n_{M2} + n_{M1}}
 \tag{1.9}$$

It is desired that this coefficient to have high values. This coefficient give us information about the capability of the vehicle to climb a ramp in a superior gear without changing gears.

It can be observed that the denominator highlights the area where the curve is flattened.

For example if a vehicle is designed to be a taxi, the flattened area should be preferable in the low engine speed range.

(e) The coefficient of power diagram flattening

$$a_P = \frac{n_{P2} - n_{P1}}{\frac{n_{P2} + n_{P1}}{2}} = \frac{2(n_{P2} - n_{P1})}{n_{P2} + n_{P1}}
 \tag{1.10}$$

It is also desired to have high values, because it give us information about engine capacity to accelerate in a specific gear.

It can be observed that the denominator highlights the area where the curve is flattened.

Researching the diagrams of a variety of cars it can be observed that the power curve is narrowed than torque curve. (4 times arrowed than the torque curve)

In some cases engines don't have a flattened power curve. Even more, the flattening power curve is situated in the maximum engine speed area.

As a result this area it has no essential significance in terms of dynamic performance. (the differences between a flattened power curve and a classic power curve are not significant)

The authors suggest that this parameter called “the coefficient of power diagram flattening” to not be integrated in the equation of an objective function which allows to appreciate the influence of the supercharged engine diagram over the dynamic performance of a car.

### The Function of Efficiency

The dispersion of the values obtained for these coefficients require defining an objective function which allows an overall assessment over the performances developed by an engine.

This function should be capable to allow to compare a wide range of engines from the perspective of elasticity and adaptability.

The equation that was developed by the authors is named function of engine efficiency—FEE.

- natural aspirated engine:

$$FEE^{na} = \frac{1}{k_e^{na} \cdot k_a^{na} \cdot r_M^{na} \cdot r_P^{na}} \tag{2.1}$$

- supercharged engine:

$$FEE^s = \frac{a_M}{k_e^s \cdot k_a^s \cdot r_M^s \cdot r_P^s} \tag{2.2}$$

The comparison between engines that equip Unimog trucks:(Figs. 3 and 4; Tables 1 and 2)

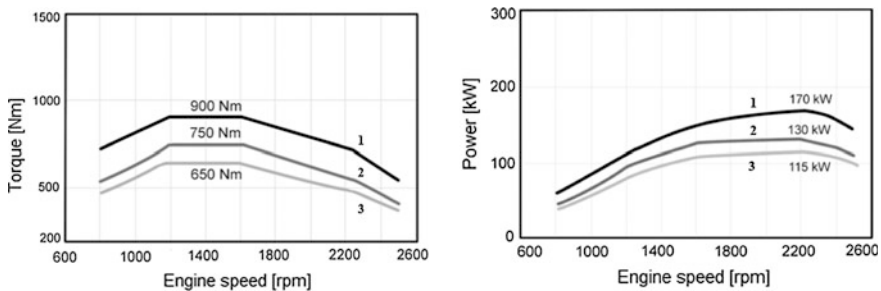


**Fig. 3** Engine diagrams of 4 cylinder version (Technical Manual for Unimog implement carrier BlueTec 6)

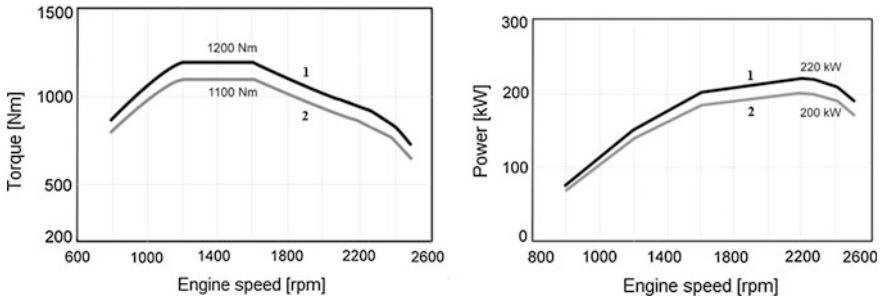


**Fig. 4** Engine diagrams of 4 cylinder version (Technical manual for Unimog implement carrier BlueTec 6)

**Table 1** Engine characteristics

Engine	OM 934 LA	OM 934 LA	OM 934 LA	OM 936 LA	OM 936 LA
Version	934.971	934.971	934.972	936.971	936.971
Number of cylinders and alignment	L4	L4	L4	L6	L6
Maximum power (kW)	115	130	170	200	220
Maximum torque (Nm)	650	750	900	1100	1200
Engine speed at maximum power (rpm)	2200	2200	2200	2200	2200
Idle speed (rpm)	720	720	720	720	720
Total displacement (cm <sup>3</sup> )	5132	5132	5132	7698	7698
Displacement unit (cm <sup>3</sup> )	1283	1283	1283	1283	1283
Compression ratio	17.6	17.6	17.6	17.6	17.6
Minimum engine speed where the maximum torque is achieved (rpm)	1200	1200	1200	1200	1200
Maximum engine speed where maximum power is achieved (rpm)	1600	1600	1600	1600	1600
Maximum torque at maximum power (Nm)	500	650	750	800	980
Maximum engine speed (rpm)	2500	2500	2500	2500	2500

Technical Manual for Unimog Implement Carrier BlueTec 6

**Table 2** Obtained values

Engine	OM 934 LA	OM 934 LA	OM 934 LA	OM 936 LA	OM 936 LA
Version	934.971	934.971	934.972	936.971	936.971
$k_e^s$	0.55	0.55	0.55	0.55	0.55
$k_a^s$	1.30	1.15	1.20	1.38	1.22
$r_M^s$	0.23	0.13	0.17	0.27	0.18
$r_P^s$	0.29	0.37	0.35	0.25	0.33
$a_M^s$	0.29	0.29	0.29	0.29	0.29
FEE	6.00	<b>9.19</b>	7.58	5.59	7.03

## Conclusions

The optimal version between all engines is OM934-LA (4L), which has a medium supercharge ratio and between the 6 cylinders versions, the optimal engine is OM936 LA which also has a medium supercharge ratio.

As can be seen, engines have the same constructive characteristics, but different types of supercharge ratio.

The proposed method can be applied to any type of supercharged engine and allows selection of the optimal variant from the perspective of dynamic, economic and ecologic performances.

## Bibliography

- Golloch R (2005) Downsizing bei Verbrennungsmotoren. Springer, Berlin  
 Heisler H (1995) Advanced engine technology. SAE, Warrendale  
 Ivan FI (2014) Processes and characteristics of internal combustion engines—lecture notes. University of Pitesti, Pitesti  
<http://www2.mercedes-benz.co.uk-Technical> Manual for Unimog Implement Carrier BlueTec 6

# The Comparative Study of Engine Vehicles Functioning With Petrol and Liquefied Petroleum Gas

Ramona-Monica Stoica, Marian-Eduard Rădulescu, Irinel Dinu,  
George Ene, Daniel Neagu and Ion Copae

**Abstract** The main purpose of this paper is to present the comparative analysis of fuel saving performances in different functioning situations. In order to achieve such thing all the parameters with major influence on engine functioning must be identified. The comparative study of engine vehicles functioning implies establishing harmonic components with high energetic contribution from experimental dynamic series. For a quantitative highlighting of targeted parameters influence on engine functioning are being used the correlation analysis, variance analysis, informational theory and sensitivity analysis. Other purposes of the paper are to study energy efficiency for both fuels and make a comparison between engine performances by using the two fuels.

**Keywords** Engine · Energy efficiency · Information theory · Variance analysis · Time-frequency analysis

---

R.-M. Stoica (✉) · I. Copae  
Military Technical Academy, 39th–49th George Cosbuc Bd., Bucharest, Romania  
e-mail: monyk\_dep@yahoo.com

I. Copae  
e-mail: copaeion@yahoo.com

M.-E. Rădulescu  
Technical Expert F-L, 10Ath Răcari Str., Bucharest, Romania  
e-mail: radulescu1961@yahoo.com

I. Dinu  
Insurance Company Astra S.A., 3rd Nerva Traian Str., Bucharest, Romania  
e-mail: irinel.dinu@astrasig.ro

G. Ene  
S.C. Insurance S.R.L., 21st Nicolae Grigorescu Bd., Bucharest, Romania  
e-mail: ene\_george@yahoo.com

D. Neagu  
Carpatica Insurance S.A., 72nd Unirii Bd., Bucharest, Romania  
e-mail: daniel.neagu@carpaticaasig.ro

## Introduction

Saving energetical resources currently represents a major attention for all field specialists. In this general context, in automotive field are being developed unceasing research for using unconventional fuels, alternative to classical one of oiler type which are about to be exhausted. Using liquefied petroleum gas represents one of the alternative to classical fuels which leads to the decrease of their exhausting process (Copae 2006).

## Experimental Research

Experimental research were conducted with a Skoda Octavia automotive, fitted with petrol injection engine 1.6 MPI with 4 cylinders (Fig. 1a), with a maximum power of 75 kW at 5600 rev/min engine speed; maximum engine torque is 148 Nm, at 3800 rev/min engine speed. Petrol consumption is 10 L/100 km for urban cycle, 5.8 L/100 km for extra-urban cycle and 7.4 L/100 km for combined cycle (Wojnar 2012).

In addition, the automotive is fitted with a liquefied petroleum gas power plant (Fig. 1a), which consists of a multipoint injection equipment with 4 injectors (Fig. 1b).

Automotive functional parameters registration was made with the Panasonic tester (Fig. 2), specialized in automotive diagnosis including those of Skoda kind.

For the development of experiments, the tester was connected to automotive diagnostic socket and the transfer of data from tester's memory to computer was made through a VCDS application (Fig. 2b), used at automotives from class VW, Audi, SEAT, Skoda. VCDS, acronym from VAG-COM Diagnostic System, represents a Windows based software and it is produced by Ross-Tech enterprise

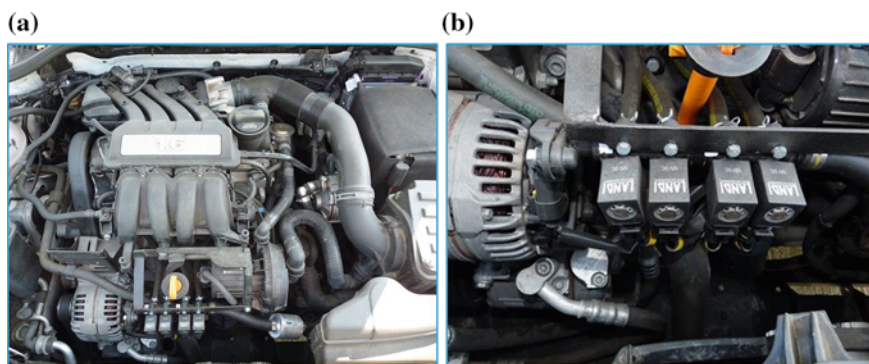


**Fig. 1** Automotive engine and LPG injection equipment



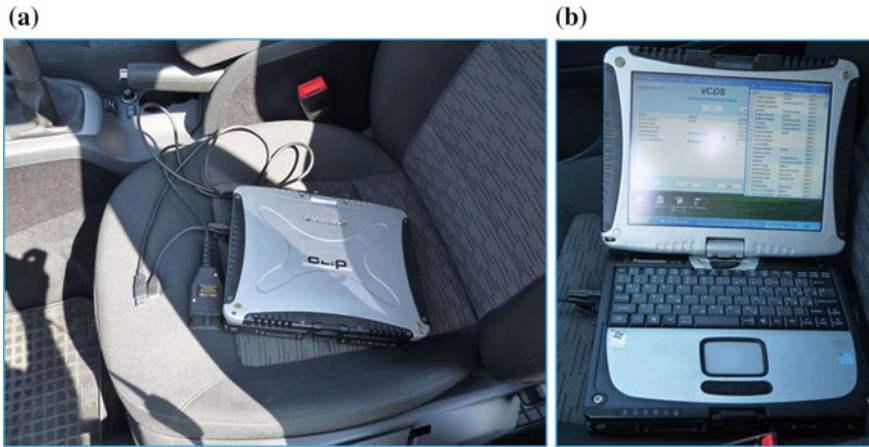


Fig. 2 Interface with on-board computer, Panasonic tester and VCDS software

(Sevart 2012). This software offers values of measured parameters, technical parameters (braking system status, oil engine level, catalytic converter status, air-conditioning status etc.), diagnostic parameters etc.

Figure 3 shows automotive speed values  $V$ , in continuous representation and discrete representation. Discrete representation, the real one, allows an easier visualization of ranges with the most values of the targeted parameter. For example, from Fig. 3 results that much more that a half of speed values (68.2 and 62 %) are in the range 40–70 km/h. Graphs also show minimum, average and maximum values for all tests.

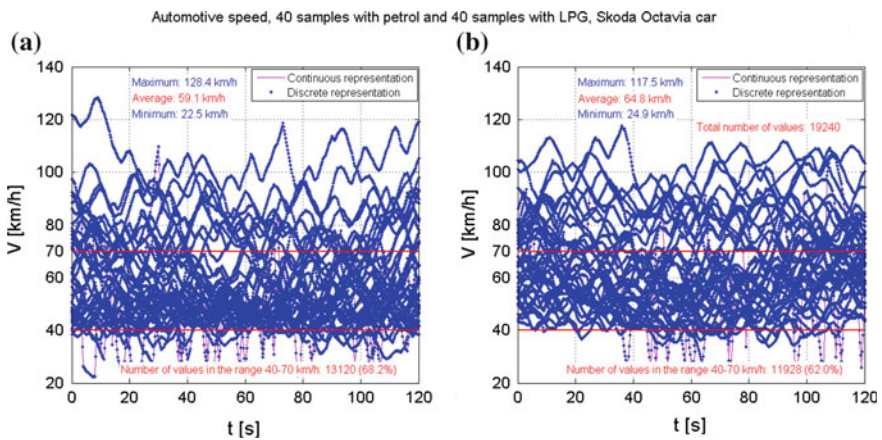
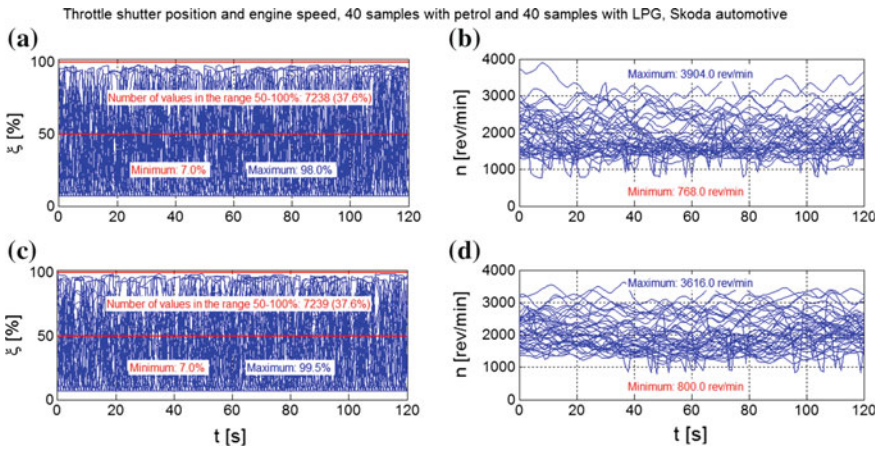


Fig. 3 Automotive speed. a With petrol, speed. b With LPG, speed



**Fig. 4** Throttle shutter’s position and engine speed. **a** With petrol, throttle shutter position. **b** With petrol, engine speed

Figure 4 presents another two measured parameters, throttle shutter’s position (engine load) and engine speed at functioning with both fuels, in graphs are also shown minimum and maximum values for all tests.

The graphs on the left also show that the engine ran almost identically at average and high loads ( $\zeta = 50\text{--}100\%$ ), number of associated values is the same for both fuels (37.6 % of all samples).

Figure 5 presents average values of each sample and average value of all samples for fuel consumption at 100 km  $C_{100}$  and hourly fuel consumption  $C_h$  for both fuels. From upper graphs is observed that in case of petrol, average

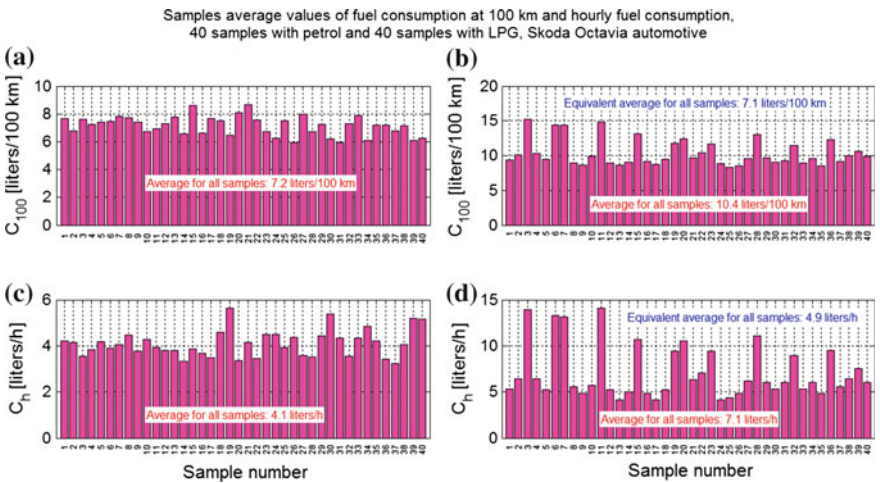


**Fig. 5** Average values of each sample and of all samples for fuel consumption. **a** Fuel consumption at 100 km, petrol. **b** Fuel consumption at 100 km, LPG. **c** Hourly fuel consumption, petrol. **d** Hourly fuel consumption, LPG

consumption at 100 km for all 40 samples is 7.2 L/100 km, and in case of LPG is 10.4 L/100 km. From lower graphs results that in case of petrol the average hourly consumption for all samples is 4.1 L/h, and in case of LPG is 7.1 L/h. However it must be highlighted the fact that in case of LPG also exists an equivalent consumption, meaning in proportion to petrol.

Equivalent fuel consumption at 100 km  $C_{100e}$  and hourly equivalent consumption  $C_{he}$  (index  $e$ —equivalent) is calculated with formulas:

$$C_{100e} = C_{100} \frac{P_g \rho_b Q_{ib}}{P_b \rho_g Q_{ig}}; \quad C_{he} = C_h \frac{P_g \rho_b Q_{ib}}{P_b \rho_g Q_{ig}} \tag{1}$$

In formulas (1) index “ $b$ ” belongs to petrol and index “ $g$ ” to LPG. These formulas show that LPG is favoured regarding price ( $P_b = 6.01$  ron/liter;  $P_g = 2.85$  ron/liter when tests took place), but is disadvantaged regarding density ( $\rho_b = 0.74$  kg/L;  $\rho_g = 0.54$  kg/L) and low calorific power ( $Q_{ib} = 47,300$  kJ/kg;  $Q_{ig} = 45,000$  kJ/kg); in conclusion, first parameter increases equivalent consumption, and the other two decreases. In these circumstances, Fig. 5 determines that in case of LPG the equivalent consumption at 100 km is less then in case of petrol (7.1 L/100 km as opposed to 7.2 L/100 km), and hourly equivalent consumption nears that of petrol (4.9 L/h as opposed to 4.1 L/h).

A similar situation appears when is targeted the  $k_c$  ratio between automotive kinetic energy  $W_{cin}$  and input energy due to fuel  $W_i$ , as well as  $k_s$  proportion between input energy due to fuel  $W_i$  and vehicle’s covered distance  $S$ :

$$k_c = \frac{W_{cin}}{W_i}; \quad k_s = \frac{W_i}{S} \tag{2}$$

whose sample values and entire set values are found in Fig. 6. In the graphs on the right also appear equivalent proportion values, established with formulas such as (1):

$$k_{ce} = k_c \frac{P_g \rho_b Q_{ib}}{P_b \rho_g Q_{ig}}; \quad k_{se} = k_s \frac{P_g \rho_b Q_{ib}}{P_b \rho_g Q_{ig}} \tag{3}$$

As it can be seen from upper graphs, the equivalent proportion value  $k_{ce}$  is higher if LPG is used (0.38 as opposed to 0.23), and the equivalent proportion value  $k_{se}$  is lower if LPG is used (3.0 as opposed to 3.4); both aspects confirm the advantage of using LPG, obviously due to it’s lower price.

Must be highlighted the fact that this criterion is the most important thing in estimating **energy efficiency**, due to the fact that in the definition formula of  $k_c$  proportion is used the automotive kinetic energy, which represents the energy spent for actual movement, but also input energy due to fuel; this criterion consists of a dynamics constituent  $W_{cin}$  and a fuel saving constituent  $W_i$ .

Finally, must be observed that in Formula (2) the two energies are established with formulas:

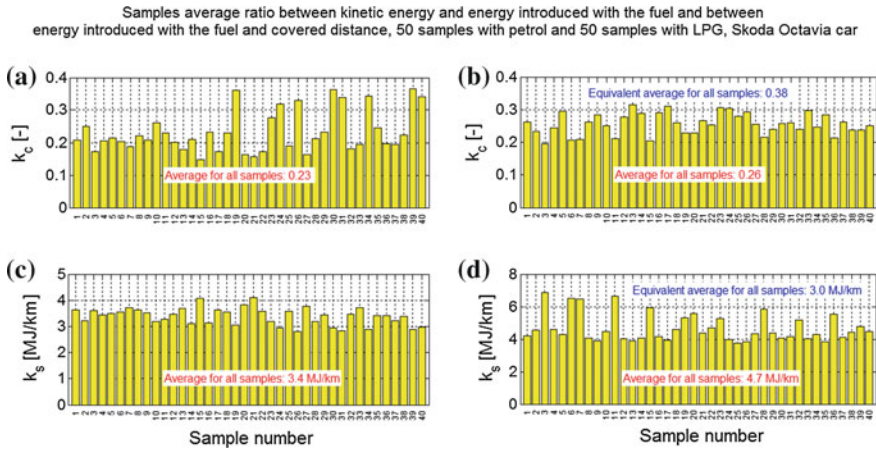


**Fig. 6** Automotive energy efficiency. **a** Kinetic energy/fuel energy ratio, petrol. **b** Kinetic energy/fuel energy ratio, LPG. **c** Fuel energy/distance ratio, petrol. **d** Fuel energy/distance ratio, LPG

$$W_{cin} = \frac{m_a v^2}{2}; \quad W_i = \frac{\rho Q_i C_{100} S}{100} \quad (4)$$

where:  $m_a$ —automotive mass;  $v$ —speed.

## Factors Influence on Engine Functioning

The more and more strictly requests regarding dynamics and fuel saving performances that are currently set to automotives engines need a thorough study of different parameters influence on its functioning. In specialty literature are found appreciations, both quantitative but especially qualitative, regarding functional parameters influence like adjustment, design and exploitation on automotives performances. It must be mentioned that in specialty literature the study of different parameters influence is made after a restrictive methodology namely: for the study of a certain factor is considered that all the other remain constant, which obviously is unconformably to reality. The study performed within this paper eliminates the mentioned restriction, that all other factors, beside the targeted one, remain constant, especially because in case of automotives fitted with on-board computer exists pronounced functional interdependence. For a quantitative highlighting of targeted parameters influence on engine functioning are being used the correlation analysis, variance analysis, informational theory and sensitivity analysis (Brissaud 2005; Carey 1998; Clarke 2003; Gray 2007; Langsrud 2003; Schneider 2007).

At **correlation analysis**, for highlighting if functional parameters are independent or not and establishing the character of the dependence (linear or non-linear), the **correlation coefficient**  $\rho$  is frequently used and is defined by formula (Copaе 2006):

$$\rho_{xy} = \frac{R_{xy}(0)}{\sqrt{R_{xx}(0)R_{yy}(0)}} \tag{5}$$

with values  $\rho \in [-1; 1]$ , a perfect linear dependency is reached for  $\rho^2 = 1$ . If  $\rho = 1$  then there is a perfectly direct linear dependency, and if  $\rho = -1$  then there is a perfectly indirect linear dependency; if  $0 < \rho \leq 1$  there is a direct non-linear dependency, and if  $-1 \leq \rho < 0$  there is an indirect non-linear dependency. Finally, if  $\rho = 0$ , then the two sizes  $x$  and  $y$  are independent; obviously, if  $\rho \neq 0$  sizes are dependent. In addition, in Formula (5), the numerator is an intercorrelation function with discrete time as origin, meaning for  $\tau = 0$ , and under the radical are auto-correlation functions still for  $\tau = 0$ .

For example, Fig. 7 presents sample values of correlation coefficients for the two fuels; factorial sizes (influence factors) are throttle shutter’s position  $\xi$  and engine speed  $n$ , and the resulting size, engine power  $P_e$ .

As it can be seen from Fig. 7, there is no experimental sample at which the correlation coefficient is null so, targeted sizes are not independent, which was functionally expected. Also, because at all samples correlation coefficients are subunitary, results that between these sizes are more or less emphasized the non-linear dependencies; between the two, the most emphasized non-linear dependency is between engine power and engine speed (lower graphs), correlation coefficients have smaller values, including the average for all samples. The presence of non-linear dependencies leads to the conclusion that engine functioning must be described by non-linear mathematical models in order to assure a high accuracy.

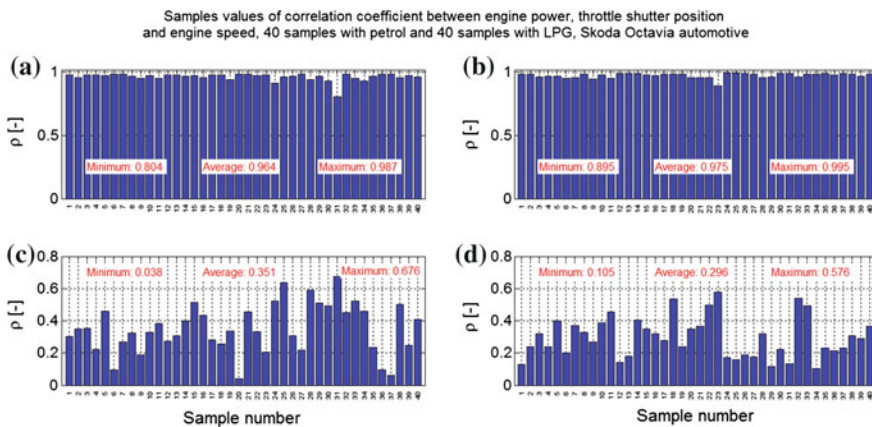


**Fig. 7** Correlation analysis. **a** Engine power–shutter position, petrol. **b** Engine power–shutter position, LPG. **c** Engine power–engine speed, petrol. **d** Engine power–engine speed, LPG

In addition, graphs from Fig. 7 show that between targeted sizes there are direct dependencies and all correlation coefficients have positive values. So, from upper graphs results that when throttle shutter opens more, engine power increases and backwards. Likewise, from lower graphs results that when engine speed increases, it's power increases and backwards; this means that the engine runs on the ascending part of power curve, in other words the maximum power is never reached.

**Informational analysis** of engine functioning, based on experimental data obtained at tests, allows establishing relevant sizes, meaning those factors with the highest influence on targeted sizes. Informational analysis of engine functioning is based on two main concepts from information theory: entropy and information (Brissaud 2005; Copae 2006; Gray 2007; Schneider 2007). So, *entropy* represents the product between probability  $p$  and information  $I$  for the entire events  $x_i \in X$ :

$$H(X) = \sum_{i=1}^n p(x_i)I(x_i) \Rightarrow H(X) = - \sum_{i=1}^n p(x_i) \log_2 p(x_i) \quad (6)$$

and *mutual information* is established with a formula that involves conditional entropy:

$$I(X; Y) = H(X) - H(X|Y) \quad (7)$$

Mutual information is a basic concept for the study of systems dynamics (of engine functioning) and represents a measure of interdependencies between variables. For this reason, the variables with the highest influence are the ones defined by the highest mutual information; these are called relevant variables, attached to the concept of relevance. For mentioned reasons, it is considered that information theory represents a generalization of classical correlation, and mutual information is a measure of relevance.

For example, Fig. 8 presents the graph with results of informational analysis for the case when cyclic flow of fuel is a resulting size (placed in upper part) and there are considered six factorial sizes (influence factors): throttle shutter's position  $\zeta$ , engine speed  $n$ , injection period (injection time)  $t_i$ , intake air pressure  $p_a$ , ignition advance  $\beta$  and excess air coefficient  $\lambda$ .

In graph's joints from Fig. 8 are shown entropy values  $H$ . On graphs bend are written mutual information values between two sizes  $I$ . It is observed that the first two relevant variables (with the highest influence on cyclic flow of fuel) are throttle shutter's position (mutual information with a cyclic flow of 1.211 bits) and injection time ( $I = 1.095$  bits).

Figure 8 also shows mutual information between 6 factorial sizes; it is determined that the highest mutual information is between throttle shutter's position and injection period, of 2.249 bits, which exceeds the ones above. This aspect confirms the necessity that in engine functioning study is also targeted the mutual influence between different targeted factors, not only between them and the resulting size; as

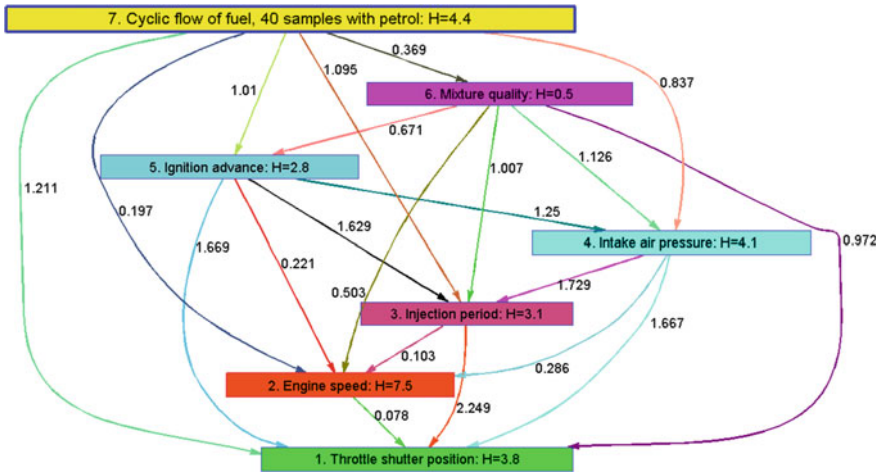


Fig. 8 Informational analysis

a matter of fact the graph shows that other factors interdependencies are more pronounced than the two relevant ones.

The study of different factors influence also uses *variance analysis* (ANOVA—Analyse Of Variance, MANOVA—Multivariate Analyse Of Variance); dispersion has a remarkable importance in the analysis of different factors influence on the development of a dynamic process (Carey 1998; Clarke 2003; Langsrud 2003).

The English statistician and mathematician Ronald Fisher, founder of variance analysis, proved that by estimating dispersion of a characteristic, influenced by a factor, then by eliminating the influence and comparing the two dispersions, there are obtained quantitative informations about this influence. In consequence, variance analysis means comparing two types of dispersion, factorial and residual. If factorial dispersion is bigger than residual dispersion, then the current factor has a noticeably influence on the targeted process. Backwards, if factorial dispersion (individual or interaction with another factor) is smaller than the residual one, then the factor has a sloppy influence on the targeted process. Practically, this comparison can be made by establishing percentage contribution for every factor and the residual for total dispersion.

For example, in Fig. 9 are presented the results after applying generalized MANOVA algorithm (are being considered the targeted factors and interactions between them), through the study of influence on cyclic flow of fuel for 6 factors, including the interactions between them. From Fig. 9 is determined that in both cases, throttle shutter's position has the biggest contribution to total dispersion (35.77 and 43.44 %). Hereinafter come engine speed in case of using petrol (25.21 % contribution) and injection time in case of using LPG (with 38.38 %). The third largest contribution factor to total dispersion is injection period in case of using petrol (cu 14.77 %) and engine speed in case of using LPG (with 6.3 %).

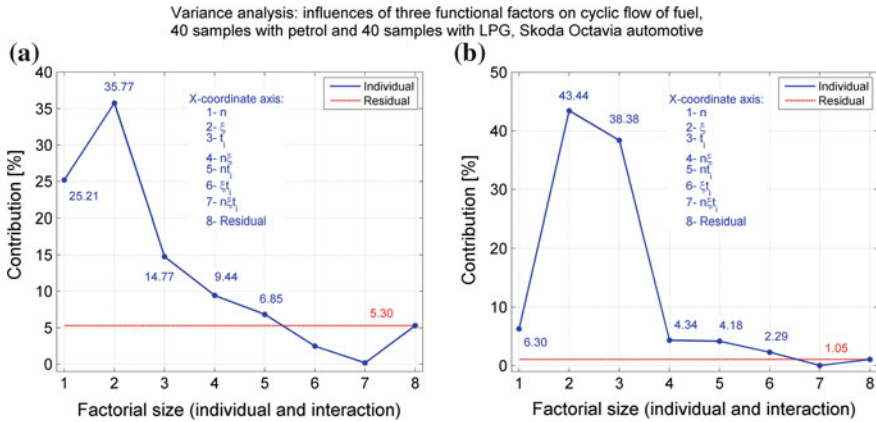


**Fig. 9** Variance analysis. **a** Running with petrol. **b** Running with LPG

From the two graphs is determined that there are also some interactions between factors with higher values contributions to total dispersion than the residual. For example, in case of petrol from Fig. 9a the sum of the two interactions is 16.29 % (engine speed-shutter’s position with 9.44 %, engine speed-injection period with 6.85 %), value that exceeds the contribution of injection period (14.77 %) which is why it can not be disregarded. So, it is confirmed the need that during some factors’ influence study on engine functioning are also taken into account the interactions between them.

Given the above, another aspect must be mentioned. If we compare the results from variance analysis (Fig. 9) and from informational analysis (Fig. 8) we can observe some differences in some factors influence order. So, in variance analysis the first three influence factors are throttle shutter’s position, engine speed and injection time, while in informational analysis are throttle shutter’s position, injection time and ignition advance.

These differences appear because variance analysis, as the name, relates only to dispersion (so to targeted size deviation towards average value), and informational analysis relates to the whole process (dispersion and mean).

### Spectral Analysis of Engine Functioning

From engine functioning study based on experimental data, also present interest the harmonic components with high energy intake, but also their time spacing.

So, a spectral analysis is necessary, meaning a classical frequency analysis (Fourier) and a time-frequency analysis, for example, the last one uses Stockwell transform (Copae 2006). Figure 10 presents an example, the graph shows both harmonic components with high energy intake (in the range 0–12 Hz), and their time spacing (around the values  $t = 12$  s,  $t = 28$  s,  $t = 42$  s,  $t = 66$  s,  $t = 80$  s).



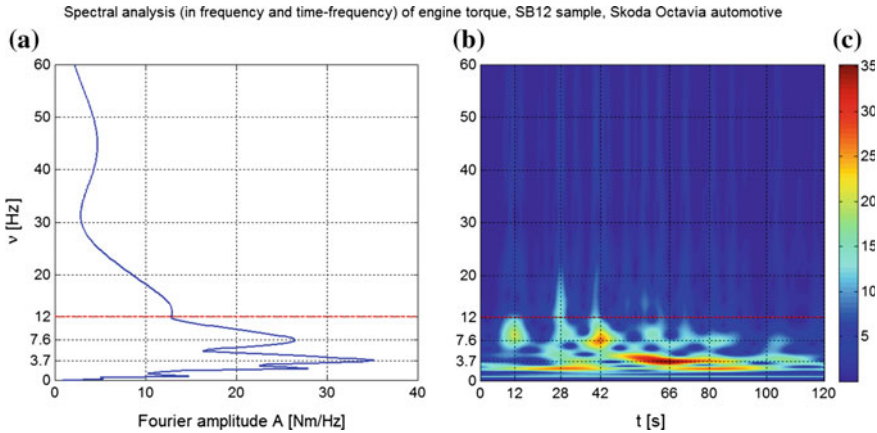


**Fig. 10** Spectral analysis. **a** Frequency analysis (Fourier). **b** Time-frequency analysis (Stockwell)

## Conclusions

The study of automotive engine functioning based on experimental data allows highlighting some different features if methods and algorithms specific to systems dynamics are being used.

From the above results that the study of different factors influence on engine functioning must also take into account both interactions between factors and the aspect that factorial sizes vary simultaneously during functioning, these two are the main differences towards classical study from specialty literature.

## References

Brissaud J (2005) The meanings of entropy. Faculty of Sciences, Rabat, Morocco  
 Carey G (1998) Multivariate analysis of variance (MANOVA). Colorado State University, Fort Collins  
 Clarke B (2003) Analysis of multivariate and time series data. Colorado State University, Fort Collins  
 Copae I, Lespezeanu I, Cazacu C (2006) Dinamica autovehiculelor. Editura ERICOM, București  
 Gray R (2007) Entropy and information theory. Stanford University, New York  
 Langsrud Ø (2003) MANOVA for Matlab. Division of Statistics, Department of Mathematics, University of Oslo, Norway  
 Schneider T (2007) Information theory primer. University of Colorado, Fort Collins  
 Wojnar B (2012) Skoda Octavia. Manual de utilizare. Skoda Auto, București  
 Severt J (2012) VCDS. User’s manual. Diagnostic software for VW/Audi/SEAT/Skoda. Ross-Tech, LLC

# Maintenance Costs Statistics for Urban Cars

Adrian Stere Paris, Cristian Andreescu, Cristian Dragomirescu  
and Constantin Târcolea

**Abstract** A central economic problem in urban traffic is the total maintenance costs (failure replacements and preventive maintenance), as an important competitive level. The paper has, as main result, the statistical analysis of the dependence between the traffic urban mileage and the total maintenance costs. The variation of these costs depending on the mileage is very useful for any driver and employer. The paper uses some statistical models to evaluate the possibilities of calculation the maintenance costs and their schedule. The most important working tool in the paper is the regression analysis between the independent variable—mileage (measured in kilometres) and the dependent one—the maintenance costs. This statistical function can be used for prognoses and schedules of maintenance costs. Another statistical practical applications used for data modelling are power fit, modified geometric, cubic and normal models; the traffic urban mileage, and respective maintenance costs, has an univariate normal distribution (Shapiro-Wilk test); the derived distribution of both variables is a bivariate Gaussian model (Henze-Zirkler and Royston tests). Numerical adequate examples for automotive operation were processed with specialised software.

**Keywords** Car maintenance costs · Regression · Normality tests

## Introduction

The paper uses the capabilities of some specialized software, mainly applying the regression analysis of experimental data and some numerical examples and extends the discussion to stochastic modeling. The tendency in the statistical research is to use more adaptive models, to represent features of the data as adequately as possible and to adapt them to the realistic assumptions.

---

A.S. Paris (✉) · C. Andreescu · C. Dragomirescu · C. Târcolea  
University Politehnica Bucharest, Bucharest, Romania  
e-mail: saparis2015@gmail.com

The novelty of the paper is to study that power fit, modified geometric and the normal functions are adaptive distributions for describing the maintainability costs of systems, because these sets of elements contain symmetric and skewed models.

The activity interruption is intolerable in the high competing world. Reducing cars downtimes and assuring quality have become increasingly important as the demand of today's business environment.

Throughout the years, the importance of the maintenance functions, and therefore also of maintenance management, has grown. The widespread automatisaton has reduced the number of production personnel and has increased the capital employed in production equipment. As a result the fraction of employees working in the maintenance area has grown, as well as the fraction of maintenance spending on the total operational costs.

A large number of authors have studied models for equipment's maintenance: (Osaki 2002), (Dekker 1996), (Mobley 2013), Higgins and Mobley (2001), etc.

Many efforts have been made to maintainability applications for automotive systems: (Bertsche and Lechner 2004), (Eberlin and Hock 2014), (Muralidharan and Syamsundar 2012), (Hochgräf 2015), etc.

The particular interest for maintenance costs is also reflected by the recording and processing of those costs: (Barnes and Langworthy 2003), (Victoria Transport Policy Institute 2013), etc.

The weight of every repair type, in the whole program of maintenance, should be determinate by prognosis techniques. During the automotive's life span the weights of every type of repairs are changing randomly.

Maintenance cost can be a significant factor in an organization's profitability. In manufacturing, maintenance cost could consume 2–10 % of the company's revenue and may reach up to 24 % in the transport industry (Payne et al. 2005).

## Practical Analysis of Maintenance Costs

The experiment was conceived to be carried out on a sample of 100 modern Romanian passenger cars working as taxi in Bucharest (Grad et al. 2010). The monitoring of the cars lasted about two years, in which period each car covered 85,000–140,000 km. This period is an important part of such a car life, during which practically all types of failure occur for the most of the car systems and parts: infant failures (in the first stage of life), random failures (during the useful life) and wear-out failures (at the end of life) and the maintenance costs. The compared costs for different drivers and car life periods were tested with ANOVA method and the practical results confirm the homogeneity of data. In other words the null hypothesis should not be rejected.

A further step for a deep statistical analysis is to test for heteroskedasticity (Goldfeld–Quandt test), that involves examining the regression residuals. The hypothesis to be tested is that the variances of the errors of the regression model are

**Table 1** The Goldfeld-Quandt test results

Meta analysis of Goldfeld-Quandt test for Heteroskedasticity			
Description	Significant tests		OK/NOK
1 % type I error level	0	0	OK
5 % type I error level	0	0	OK
10 % type I error level	0	0	OK

not constant, but instead are monotonically related to a pre-identified explanatory variable.

The values of the Table 1 indicate a strong rejection of the hypothesis of the heteroskedasticity.

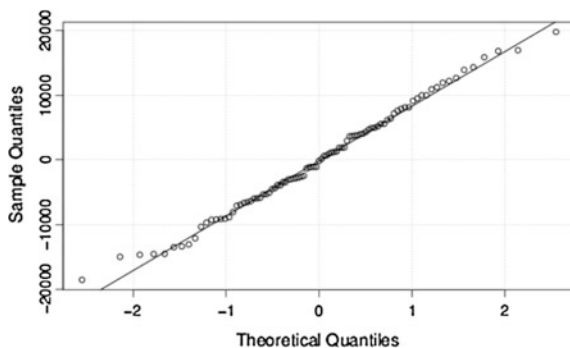
Also it should be checked the homoscedasticity and normality of residuals with the Q-Q-Plot of theoretical and sample quantiles (Fig. 1). The plot indicates that in resulted regression there is no tendency in the error terms.

After these preliminary analyses of data, the linkage is tested by the correlation coefficient and shows an adequate value. The existence of dependence between mileage and maintenance costs was tested with the Student test. The resulted Pearson product-moment correlation coefficient,  $r = 0.74308$ , with the number of degrees of freedom 91, and the empirical statistics is  $t = 10.593$ , and as result the existence of correlation between these two characteristics is verified.

A general tendency in the statistical research is to use more flexible models, to represent features of the data as adequately as possible and to reduce unrealistic assumptions (Azzalini and Capitanio 1999). The ranges of canonical distributions are usually unbounded, while the lifetime of the products is a bounded interval. The present paper analyses some of laws and focuses the study of new adequate models, for the given experimental automotive industry data. The parameters of the proposed functions were estimated from the experimental data. These models are used for predicting the maintainability of the systems.

The complete processing of data concerning the relation between total maintenance costs  $C_2$  considering the traffic urban mileage  $C_1$  is given by different regression functions:

**Fig. 1** Residual normal Q-Q plot



Power Model

$$C_2 = 1.6 * 10^{-6} * C_1^{1.87}; s = 734; r = 0.742$$

Gaussian Model

$$C_2 = 6079e^{-((C_1-153441)^2)/2*53905^2}; s = 738; r = 0.743$$

Cubic Model

$$C_2 = 11165 - 0.3976C_1 + 0.000005C_1^2 - 1.8 * 10^{-11} C_1^3; s = 748 r = 0.743;$$

Modified Geometric Model

$$C_2 = 25582 C_1^{-16745/C_1}; s = 734; r = 0.743 \text{ (Fig. 2),}$$

where r is a determination coefficient and s, standard error, is a measure of the variance (Fig. 2).

The apparent variety of the regression functions is statistically not significant different on the considered domain.

In Fig. 3 ( $C_1 = \text{km}$  and  $C_2 = \text{maintenance costs}$ ) the confidence interval, CI, shows the likely location of the true population parameter, while the prediction interval, PI, must account for both the uncertainty in knowing the value of the population mean, plus data scatter, so that the last interval is always wider than the first one.

With the cubic processed model should be computed the 95 % confidence and prediction intervals for a estimated value, for example if  $C_1 = 100,000 \text{ km}$  gives the value  $C_2 = 3713.4 \text{ lei}$  and:

- 95 % confidence interval:  $3527.2 \leq C_2 \leq 3899.6$
- 95 % prediction interval:  $2243.1 \leq C_2 \leq 5183.8^*$ ,

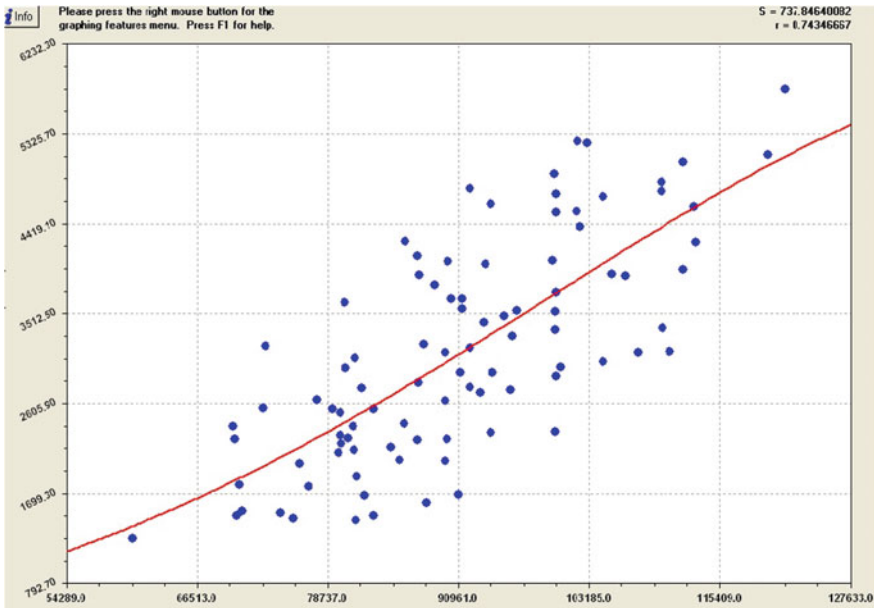


Fig. 2 The modified geometric model

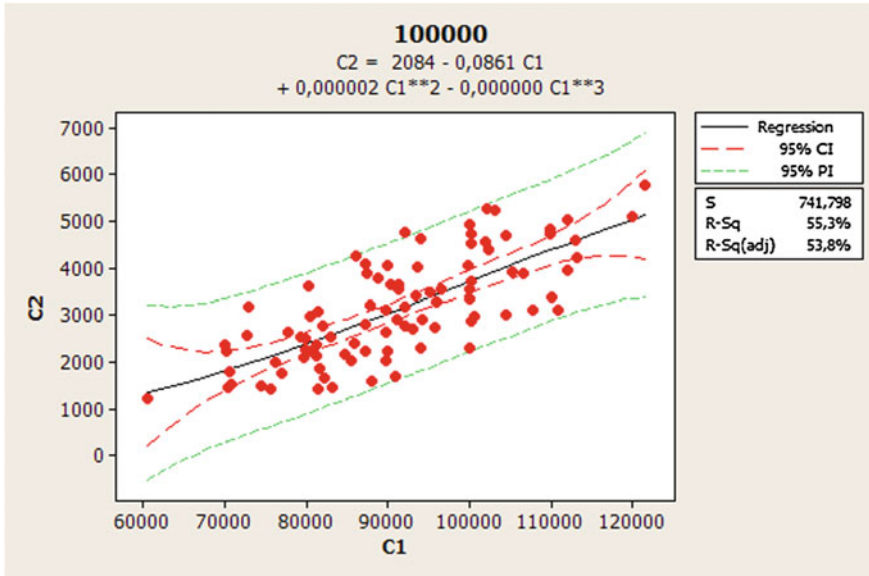


Fig. 3 Confidence (CI) and prediction (PI) intervals for the cubic fitted data

and for  $C_1 = 150,000$  km gives the value  $C_2 = 6946.7$  lei and:

- 95 % confidence interval:  $6215.9 \leq C_2 \leq 7677.4$
- 95 % prediction interval:  $5315.3 \leq C_2 \leq 8578.0^*$

\*interval limits denote a point that is an extreme outlier in the predictors.

A precondition for many statistical applications is an assessment of the normality of data, because normal data is an underlying hypothesis in engineering applications. The normal distribution has important relevancies to reliability and manufacturing or both. Mechanical devices are frequently subject to wear and their reliability is closed to a normal distribution, because their life depends on many factors. On the other hand the variability of manufactured parts and the quality control procedures are usually modeled by the normal distribution. In these conditions it is useful to verify the adequacy of the experimental data with this distribution, considering the big existing number of statistical applications and software solutions for this one. Consequently in the first step, the normality of the data for the millage of the cars will be verified. The applied test is Shapiro-Wilk for univariate normality, with the results:

$$W = 0.9791; p\text{-value} = 0.1161.$$

On the basis of these values the null hypothesis is accepted: the millage data can be modeled with normal repartition (Fig. 4).

**Fig. 4** Normal Q-Q plot for millage data

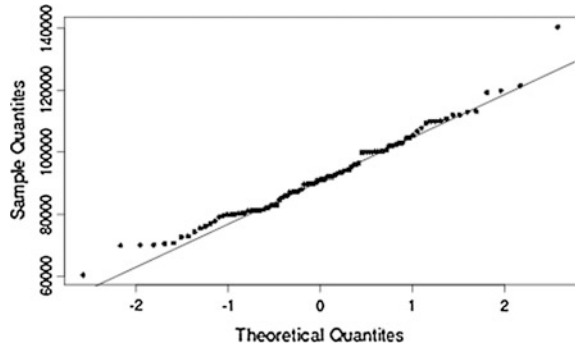
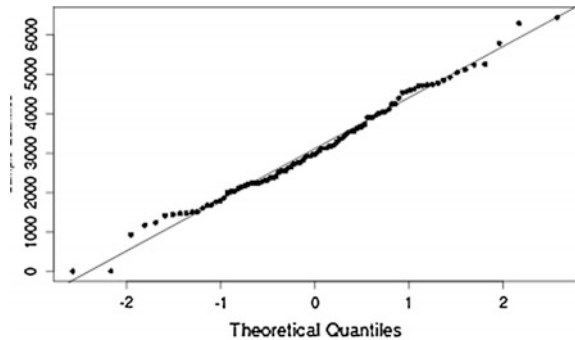


**Fig. 5** Normal Q-Q plot for maintenance costs data



In the second step the normality for the maintenance costs of the cars will be verified. The applied test is Shapiro-Wilk for univariate normality with the results:

$W = 0.9883$ ;  $p\text{-value} = 0.5395$ . On the basis of these values the null hypothesis is accepted: the costs data can be modeled with normal repartition (Fig. 5).

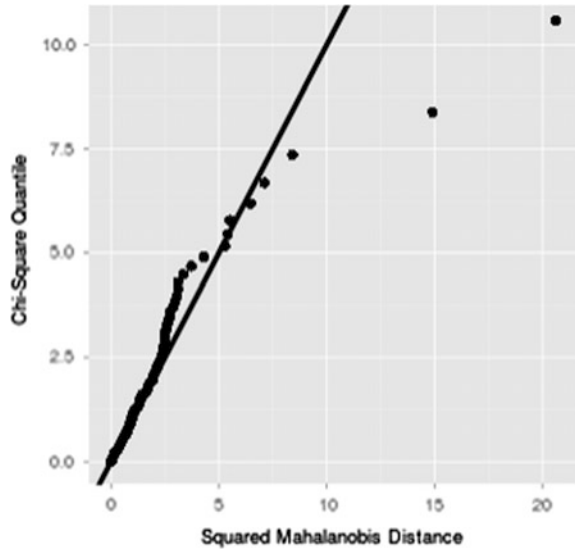
The each random variable, millage and respectively maintenance costs, follows an univariate normal distribution, but they are not independent. With modern data collection system and computers used for on-line process monitoring and fault identification in manufacturing and economic processes, it is common to monitor more than one correlated process variables simultaneously. If each variable of a set of correlated variables is controlled by an univariate control chart independently, it should lead to wrong conclusions (Montgomery 2005). Instead Multivariate Statistical Process Control is used for monitoring processes where there are several correlated quality variables. A step further is to verify the bivariate normality of analyzed data.

An applied test for bivariate normality is Henze-Zirkler, with the results:

$$HZ = 0.7361117; p\text{-value} = 0.1921784.$$

On the basis of these values the null hypothesis is accepted: the data should be modeled with a multivariate normal repartition (Fig. 6).

**Fig. 6** Chi square Q-Q plot for processed data (Henze-Zirkler test)

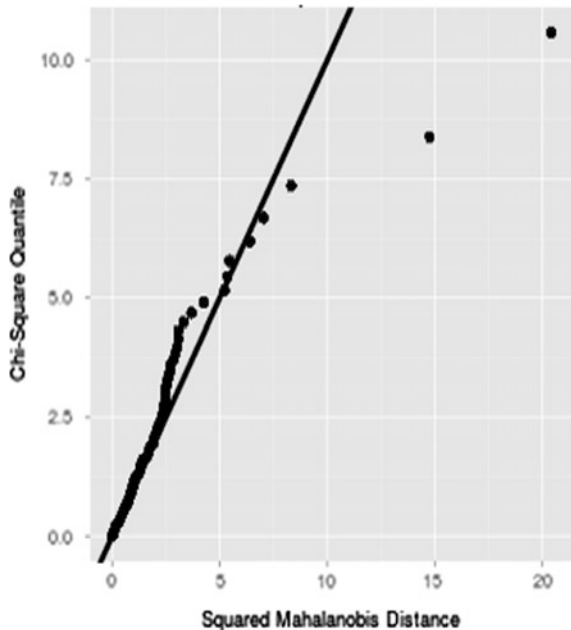


Another test for bivariate normality is Royston, with the results:

$$H = 3.624267; p\text{-value} = 0.1607907$$

On the basis of these tests the null hypothesis is accepted: these two variables, mileage and costs, are represented by a bivariate normal distribution (Fig. 7). The random vector of both variables should be described as a multivariate normal.

**Fig. 7** Chi square Q-Q plot for processed data (Royston test)





## Conclusions

The main result of the paper is the statistical analysis of the regression between the traffic urban mileage and the total maintenance costs. The use of statistical tools offers multiple possibilities to evaluate and optimize the preventive and corrective maintenance costs, to help buyers and owners to determine the direct and indirect costs of a product or system (Total Cost of Ownership—TCO), here buying, owning and operating a car. Sometimes, when comparing cars (particularly vehicles in different classes), the TCO data is a valuable wake-up call for car shoppers. During the two years of monitoring the passenger cars working as taxi, the description of all the failures and their moments of occurrence as well as the parts preventive replacements and the costs were registered in a data base (Grad et al. 2010). Estimations and prognoses with the statistical models of the paper make possible multiple comparisons with different brands and producers. For example the average total maintenance costs per kilometer are around 0.33 lei for recorded data.

Another novelty of the paper is to introduce power fit, modified geometric and the normal functions, adaptive distributions for describing of the maintainability costs of systems. These proposed models allow the simulation and prediction of the lifetime's costs of the products. In the paper new statistical models for total maintenance costs have been obtained considering the traffic urban mileage. This is an economical expansion of authors' early studies on automotive reliability (Târcolea et al. 2011).

To consider the popular applications of the normal distribution it was analysed the validity of the Gaussian model for the processed data with positive results and a final bivariate normal repartition.

## References

- Azzalini A, Capitanio A (1999) Statistical applications of the multivariate skew normal distribution. *J Roy Stat Soc* 61:579–602
- Barnes G, Langworthy P (2003) The per-mile costs of operating automobiles and trucks, final report 2002 to 2003. *Transp Res Rec J Transp Res Board* 1864(1):71–77
- Bertsche B, Lechner G (2004) *Zuverlässigkeit im Fahrzeug- und Maschinenbau, Ermittlung von Bauteil- und System-Zuverlässigkeiten*. Springer, Berlin
- Dekker R (1996) Applications of maintenance optimization models: a review and analysis. *Reliab Eng Syst Saf* 51:229–240
- Eberlin S, Hock B (2014) *Zuverlässigkeit und Verfügbarkeit technischer Systeme, Eine Einführung in die Praxis*, Springer Vieweg
- Grad A, Panait T, Andreescu C (2010) Some aspects concerning the reliability and maintenance of the braking and rolling systems of taxi passenger cars. In: International conference ESFA 2009, Bucharest, *Ingenieria automobilului*, nr 15, iunie: 17–19
- Higgins LR, Mobley RK (2001) *Maintenance engineering handbook*. McGraw-Hill Classic, New York City
- Hochgräf M (2015) *Untersuchungen zur Lebensdauer und Zuverlässigkeit von Elektrofahrzeugen*. Kassel University Press GmbH, Germany

- Mobley K (2013) Maintenance engineering handbook. McGraw-Hill Education, New York City
- Montgomery D C, (2005), Introduction to Statistical Quality Control, John Wiley
- Muralidharan K, Syamsundar A (2012) Statistical methods for quality, reliability and maintain-ability. PHI Learning Pvt. Ltd., New Delhi
- Osaki S (2002) Stochastic models in reliability and maintenance. Springer, Berlin
- Payne AC, Chelson JV, Reavill LRP (2005) Management for engineers. Wiley, New York
- Târcolea C, Paris AS, Andreescu C (2011) The reliability and maintenance of the braking and rolling systems of transport vehicles. In: 11th international congress on mechnization and energy in agriculture, TRAKAGENG 2011, Istanbul. In: Proceedings of 11th international congress on mechanization and energy in agriculture, Namik Kemal University, Ed Ankoglu Madbaacilik, Istanbul, Turkey, pp 261–264, 21–23 Sept 2011
- Victoria Transport Policy Institute (2013) Transportation cost and benefit analysis II—vehicle costs. <http://www.vtpi.org/tca/tca0501.pdf>

# Investigation of Third Body Phenomenon in Model Braking Using Infrared Camera

Zbigniew Skorupka and Antoni Jankowski

**Abstract** During the braking process there are several phenomena that influence whole process in many ways. One of them is existence of the intermediate layer called third body, which exists between connecting surfaces of the friction pair. The third body phenomenon is very hard to classify, describe, and what is most important, to see. Most obvious and visible sign of the third body existence is debris left after friction. Using standard camera or naked eye it is not possible to observe any particles during braking process due to their small size (dust like) and high temperature. However it was performed by the use of thermal camera, which can record particles' heat signatures and made possible their observation during braking process. All of the tests and investigations were made using inertial type test stand designed for friction material testing in repeatable conditions. Two sets of data were obtained as the results of the study. One set from electrical measurements of the braking torque, braking force and rotational speed. Second one was recorded film using the infrared camera. When compared together, it was clearly seen that emission of the particles occurred during braking process can be linked with the braking torque behaviour. The novelty of the proposed method is to use of the infrared camera in the observations of the existence and amount of the third body phenomenon. Infrared based investigations base on the assumption that particles (and gases) are emitted from the friction area and intensity of the emission is linked with the braking torque changes. In the authors' opinion connection between thermal observation and braking torque measurement proves influence of the third body on the braking torque in friction interaction (braking).

**Keywords** Brakes · Friction pair · Material tests · Model braking · Third body

---

Z. Skorupka · A. Jankowski (✉)  
Institute of Aviation, al. Krakowska 110/114, 02-256 Warsaw, Poland  
e-mail: antoni.jankowski@ilot.edu.pl

Z. Skorupka  
e-mail: zbigniew.skorupka@ilot.edu.pl

## Introduction

Third body phenomenon is based on existence of intermediate layer between friction pair components. This occurs mostly in friction brakes where dynamics and energy of the process is high and results in significant wear of the friction pair's materials (Ścieszka 1998). In most cases third body consists of friction products i.e. particles of separated material. Sometimes it is a gas, resulting from high temperature chemical reactions taking place during high energy braking, or mix of particles and gas.

Particles that form third body during friction are the by-product of the process connected to the wear of the friction pair. Mentioned by-products are created by the separation of particles of the less hard material in friction pair, for example composite brake pad abraded by the cast iron disc brake. Abrasion of the softer material is intended and ensures proper operation of the brake.

Third body in the friction process is not desirable due to creation of intermediate layer in the friction pair changing frictional engagement between materials. Almost always it results in undesirable reduction of friction coefficient—in most cases it drops dramatically. Furthermore particles of abraded material can stick to the surface of the materials in friction pair changing its properties more or less permanently.

The particles trapped in the friction zone can be disposed in several ways—by the sets of grooves on the disc brake surface (cars) or by making segment disc brakes (aviation). Unfortunately it is not possible to dispose of all the particles (in this case the third body) from the friction zone so problem stays. Furthermore trapped particles not always leave friction zone during braking even when proper mechanical means exist.

Observation of the third body phenomenon is quite hard to perform. During braking or the other types of frictional engagement is not possible to directly see what is really happening in the contact zone. Particle type third body can be observed after the friction process ends. Visible results of phenomenon existence can be described as inclusions stuck to the material surface or particles of the material scattered near the brake. Gas existence is even harder to prove and often is only a guess, which is based on the knowledge of the material properties and/or reached process temperature.

Result of the third body existence can be verified in laboratory testing when the friction coefficient fluctuation occurs during friction, without any significant change of the temperature. Friction coefficient fluctuations can be subtle or hard. In the first case it is hard to tell about origins of the phenomenon because it can be caused either by the third body existence or regular friction material wear. When change is hard and time stretched or permanent it is most likely that something else than normal frictional engagement is present. Of course, one has to remember that this explanation is inconclusive and incomplete due to the number of other, than third body, phenomena occurring during braking. It is also necessary to state that friction coefficient observation in third body phenomenon is valid only if the temperature

influence is excluded. When temperature rises over the permissible level, friction coefficient will change and this cannot be connected to the third body phenomenon.

The best way of investigating of the third body phenomenon is to observe it both by friction coefficient change and by methods showing existence of particles or gas. One can think that the simplest way is to observe and record the process using camera or visual observation. In theory it is possible but in reality it is unlikely to see so small particles (not mentioning gas) in the friction zone by the regular optical means.

The best way is to use alternative optical method providing expanded view on the phenomenon. According to the friction process nature, products of friction reach high temperature, higher than ambient, what makes use of thermography the right choice.

In the next chapters thermographic camera work principle, friction materials laboratory testing and third body phenomenon investigation using infrared observation technique is described.

## Thermographic Camera

Thermographic camera (infrared camera, thermal imaging camera) is mainly used to measure infrared radiation of object. Radiation quantity of the object's surface depends on actual body temperature. Intensity of radiation on the other hand depends on material out of, which body is made and is called emissivity. Emissivity as material constant is defined as body's ability to emission of radiation energy. Most of the materials have emissivity well known and easy to find in engineering sources. It is necessary to remember that metallic materials (in opposition to most of non-metallic ones) change its emissivity due to surface state or treatment.

Emissivity can change from 0 up to 100 %, depending on material type, colour and its surface state. For example "black body" has emissivity is equal to 1.0 (100 %) as the ideal source of radiation unlike mirror that has emissivity as low as 0.1 (10 %).

Most of the materials change its emissivity with the temperature changes what result in simultaneous change in amount of radiation and its value. This makes precise temperature measurement challenging or impossible. Sample average emissivity values of several materials are shown in Table 1.

Every thermographic device has two main components (except main wave detector), which determine its measurement capabilities, namely optics and spectral filter. Optics or optical system is defining optical range of camera, its zooming capabilities, and amount of light, which is transferred to the detector and view area to be covered during measurement. Spectral filter is a device used to filter and to allow only selected wavelengths, important for temperature evaluation, to pass to the wave detector. Typical waveband is between 1 and 20  $\mu$ .

**Table 1** Sample average emissivity values of several materials

Material	Surface treatment	Average emissivity
Aluminium	Not oxidized	0.02–0.1
	Polished	0.02–0.1
	Rough	0.1–0.3
	Oxidized	0.2–0.4
Steel	Polished	0.1
	No rust	0.1–0.8
	Raw	0.4–0.6
	Cold rolled	0.7–0.9
	Coated	0.7–0.9
Cast iron	Not oxidized	0.05–0.2
	Rusty	0.5–0.7
	Oxidized	0.5–0.9
	Forged, rough	0.9
Asbestos	–	0.95
Carbon	Not Oxidized	0.8–0.9
	Graphite	0.7–0.8
Water	–	0.93

Wave detector and its control system is used to converting infrared signal to electrical impulses, which are later directed to acquisition system usually external computer with proper analysis/recoding software.

Main advantage of thermographic camera is ability to record image of studied object. Cameras record temperature of every separate pixel of wave detector within measurement range where the number of separate points/pixels is defined by detector resolution. It results in possibility of very flexible temperature evaluation

**Table 2** Selected technical data of FLIR SC645 camera ([FLIR SC64 user manual](#))

Name	Value/description
Temperature measurement range	–20 to +150 °C 0 to +650 °C
Spectral range/accuracy	7.5–13 μm/±2 °C or ±2 % indication
Thermal sensitivity	<0.05 °C w + 30 °C/50 mK
Detector resolution	17 μm
Resolution/detector type	640 × 480 pix./focal plane array (FPA), non-cooled
Response time	8 ms, typical
Optics	Focal point 24.5 mm, F = 1.0 min. sharpening 0.4 m
Field of view	25° × 18.8°
Optical transmission correction	Automatic
Manual emissivity correction	0.01–1.0 (program)
Measurement correction	Global (program)
Data interface	USB, LAN 1 Gbit

(ex. in areas, single points, colour visualization of temperatures, evaluating maximal, minimal and/or average temperature). Another advantage of thermographic camera use is possibility of record and visualise thermal phenomena not to be seen by naked eye due to their aspects or due to possible danger to observer.

In described research FLIR SC645 camera (25 fps), FLIR ResearchIR software for data recording and MS Excel for analytical analysis and graph drawing was used. Main technical data of the camera is shown in Table 2.

## Test Equipment Used

All tests were carried out using IL-68 (Fig. 1; Table 3) inertial type test stand. IL-68 is designed for friction materials testing mainly for brake use. The specificity of the IL-68 tests lies in fact that one tests covers full braking from start velocity  $V_{max}$  to full stop ( $V_{end} = 0$ ). Typical test campaign is (Skorupka and Grygorcewicz 2013) a combination of 5 to 8 bed-ins for proper geometry cohesion of friction pair in contact zone (for maximal use of friction area) and 10-qualification test that are carried out in order to evaluate various properties of braking process. Tests performed using IL-68 provide information about materials' friction coefficient, wear, temperature or braking time in designated conditions.

Test object in model tests is a set of samples (sectors) made out of real friction pair materials (Fig. 2).

**Fig. 1** IL-68 test stand side view

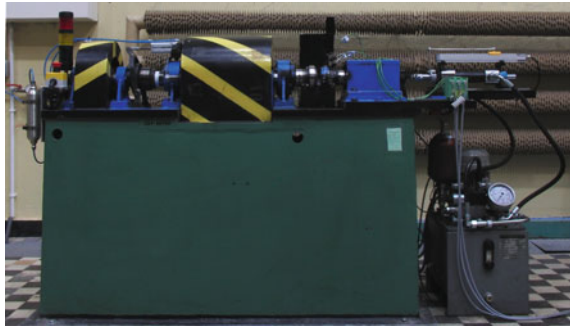


**Table 3** Selected technical parameters of IL-68 test stand

Name	Value/Description
Shaft maximal rotational speed	9000 rpm (150 rps)
Maximal torque	$0.154 \div 1.54 \text{ kg (m/s)}^2$ ( $0.098 \text{ kg (m/s)}^2$ step)
Maximal clamping force	5.88 kN

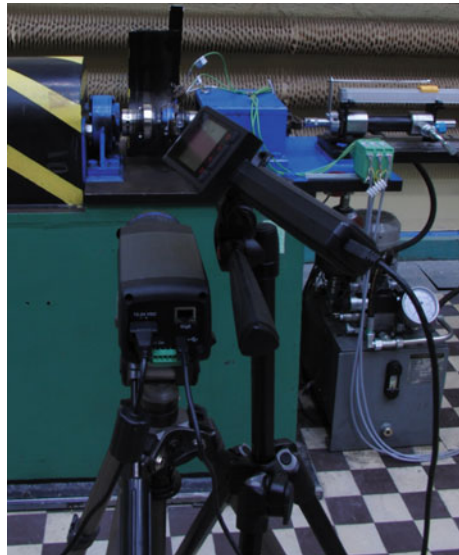


**Fig. 2** Example of model friction pair used in IL-68 tests (*right* friction material samples, *left* cast iron countersample)

IL-68 test stand allow to measure and to record number of test parameters: braking torque, braking force, braking time, and rotational speed of samples. These parameters are used not only for measurement purposes but also as internal control signals for IL-68. All of measurements are recorded for further analysis.

Thermographic camera was used to record area of tests in order to measure both during braking trial as well as to visualise phenomena not to be seen by the naked eye (Skorupka 2015). Camera position during tests is shown in the Fig. 3.

**Fig. 3** Thermographic camera position during tests





## Investigations

As it was written above, thermographic camera allows recording temperatures in whole area covered by its optical system. During tests several temperatures were monitored: average temperature of friction area, temperatures of selected points on both test samples (friction pair) near contact area. As this article is not dedicated to temperature measurement, this topic will not be further described.

Thermographic camera also allowed to record of the hot particles release from the friction pair contact area. Due to their size and short cooling time, usually it is not possible to see them directly. Sample images where hot particles can be seen are shown (Fig. 4). Release of the hot particles can be connected to the third body phenomenon. As it was described in Chap. 1, third body can be the layer of the loosen particles trapped in contact area of the friction pair.

Third body phenomenon is known from its influence on friction coefficient. In most cases friction coefficient drops when intermediate layer is created. It happens because loosen particles start to roll between friction pair surfaces creating bearing like effect. Until the time when particles are released from the contact area, friction coefficient is decreasing and in extreme can drop to zero. Usually release of third body from the contact area results in the friction coefficient restore to the previous level.

It is justified to say that mentioned phenomenon can be directly seen on friction coefficient or braking torque recordings. In the Fig. 5 one can see temperature, rotational speed and, braking torque versus time. There is a strong disorder on the braking torque graph time stamp 10–12 s resulting dynamic drop and return to the more less previous state. When this anomaly is matched to the frames from infrared camera of the same timestamp it can be seen that strong release of friction products is connected to the braking torque “heal” process seen right after its sudden drop. If not critical temperature is taken to the equation, everything starts to prove the third body emission. Unfortunately it is not possible to see the third body grow process

**Fig. 4** Hot particles leaving friction contact during IL-68 test (sample frame from thermographic camera recording)



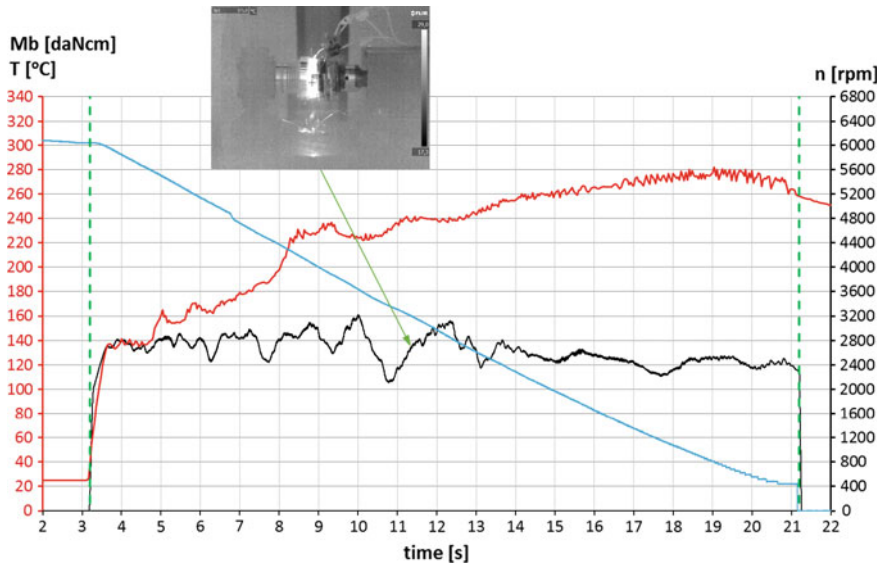


**Fig. 5** Braking torque ( $M_b$ ), temperature ( $T$ ), and rotational speed ( $n$ ) recording. Note the correlation to particles emission

due to the nature of it (it happens in the contact area, too small and too hidden for direct observation) but release of hot particles from the contact area is seen perfectly. Such possibility given by the use of infrared camera combined with the braking torque and temperature acquisition is helpful to determine if third body phenomenon occurs.

On the other hand there is a similar process called brake fade. This phenomenon shows the same drop in braking torque with the difference that change is permanent. Brake fade is temperature induced and is connected to the destruction of friction material. Its presence can be seen when temperature of the brake rise to the over critical values, which are beyond friction material's resistance.

## Conclusions

Thermographic camera was invaluable aid in order to evaluate phenomenon involving particle emission from the friction contact area that can be identified as release of the third body.

Use of infrared imaging gave the possibility to see particles emission in the first place, but also it helped to determine intensity of the phenomenon.

Sudden temperature rise and permanent braking torque or friction coefficient drop can be identified as brake fade. Brake torque drop and immediate rise during

the braking process (drop and rise must be noticeable and hard) without any temperature abnormalities identifies third body phenomenon existence.

## References

FLIR SC645 user manual

Ścieszka S (1988) Hamulce Cierne. Gliwice-Radom

Skorupka Z (2015) Pomiar temperatury pary czarnej w badaniach modelowych, *Logistyka*, 3

Skorupka Z, Grygorcewicz P (2013) Badania laboratoryjne hamulców ciernych w laboratorium badań podwozi lotniczych. *Technika Transportu Szybowego*

# Modelling and Simulation of the Dynamic Behaviour Automotive's Suspension By AMESim

Alexandru Dobre, Anton Hadăr, Daniela Vasiliu, Nicolae Vasiliu and Cristian Andreescu

**Abstract** The main objective of this paper consists in the preliminary analyse of the dynamic behaviour of an automobile's suspension using a model built in AMESim simulation program. For the dynamic study of a car suspension the authors have used a full vehicle model with 15 degrees of freedom, hear including the steering system. A strong nonlinear model was used in order to optimize the performance of the suspension by a long series of numerical simulations. The entirely research has shown that AMESim offers a real aid in the suspension study, because it significantly reduces the working time. Once created a model, and validated by experimental measurements, it can be used to study any type of similar suspension.

**Keywords** Suspension · Simulation · Comfort · Automobile

## Introduction

When driving an automobile on a driveway, which usually is not perfectly smooth, having a series of irregularities, shocks and vibrations are occurring due to the wheels interaction with the driveway irregularities, but also oscillations of the sprung and unsprung masses that characterize the comfort. The excitations are directly responsible for production of the automobiles oscillations. The main excitations which have major implications on comfort are given by the driveway irregularities, plus the excitations due to non-uniformity and wheel disequilibrium. Excitations can be also given by the movement regime change (acceleration, braking, cornering), but these have low implications on the comfort.

Ageing of some components from the automobile's transmission is intensifying due to vibrations and oscillations, but also the possibility of failure by breaking at

---

A. Dobre · A. Hadăr · D. Vasiliu · N. Vasiliu (✉) · C. Andreescu  
Splaiul Independenței, no. 313, Sector 6, Bucharest, Romania  
e-mail: vasiliu1946@gmail.com

fatigue of some of these due to the dynamic loads encountered in transmission. These also affect the integrity of the transported commodities. They adversely affect comfort, stability, maneuverability and also reliability of the driveway.

The parameters of the suspension are usually fixed: they can't be adapted to the road surface. The modern researches has showed that the active suspension offers better performance than the passive or semi-active suspension (Khan 2014).

## The Full Vehicle Model

The chassis model is the central module for car dynamics modelling to which all car sub modules can be connected (suspension—spring, shock absorber, end stop, antiroll bar—aerodynamic module, tire, road, sensors, engine, brakes, steering system, powertrain module, external load etc.). The full model is dedicated especially for the vehicle longitudinal and lateral dynamics study. The car body solid is rigid and is capable of full 3D motion (LMS Imagine. Lab 2013).

The full vehicle model can take into account all the important inputs encountered in the vehicle dynamics: road model, tire model, elastokinematics axles model, rack displacement model, engine torque, road adherence, braking torque, aerodynamic model, suspension system with antiroll bar (Andreescu 2010; Vasiliu and Vasiliu 2005).

The full vehicle model is a multibody system, which contains the following components: car body, steering rack, spindle, wheel and all the mechanical joints between these elements (Fig. 1). A part of results are presented in Figs. 2, 3, 4 and 5.

The system identification consists in determination a model of the dynamical process by using the information obtained from experimental data with that derived from an a priori knowledge of the physical behaviour of the system (Juang 1994). Generally, the system or the physical process which must be modelled can be of any kind, even though applied system identification usually considers only deterministic processes (Buchacz 2007; Guidaa et al. 2010).

This multibody model is a mechanism described with 15 DOF and related kinematic constraints between the bodies. The complex axle kinematics is introduced to model the specific joint between sprung and unsprung masses. The major improvements with respect to the core model are the antiroll effects and the end stops that are compressed by large suspension strokes. Antiroll bar has indeed a strong influence on the rolling motion of the car body and handling capabilities. The steering rack displacement shows some small vibrations on the back stroke (Figs. 6 and 7).

The optimisation of the suspensions is obtained not only via a careful design and by tuning the springs and the shock absorbers, but also by improving the design of the other components of the suspensions. So the designer can better exploit their damping properties in order to get an overall ride improvement. Also, an appropriate design of the suspension geometry such as: links, arms, levers (Guglielmino et al. 2005, 2008; Stăncioiu 2003) can offer some improvements.

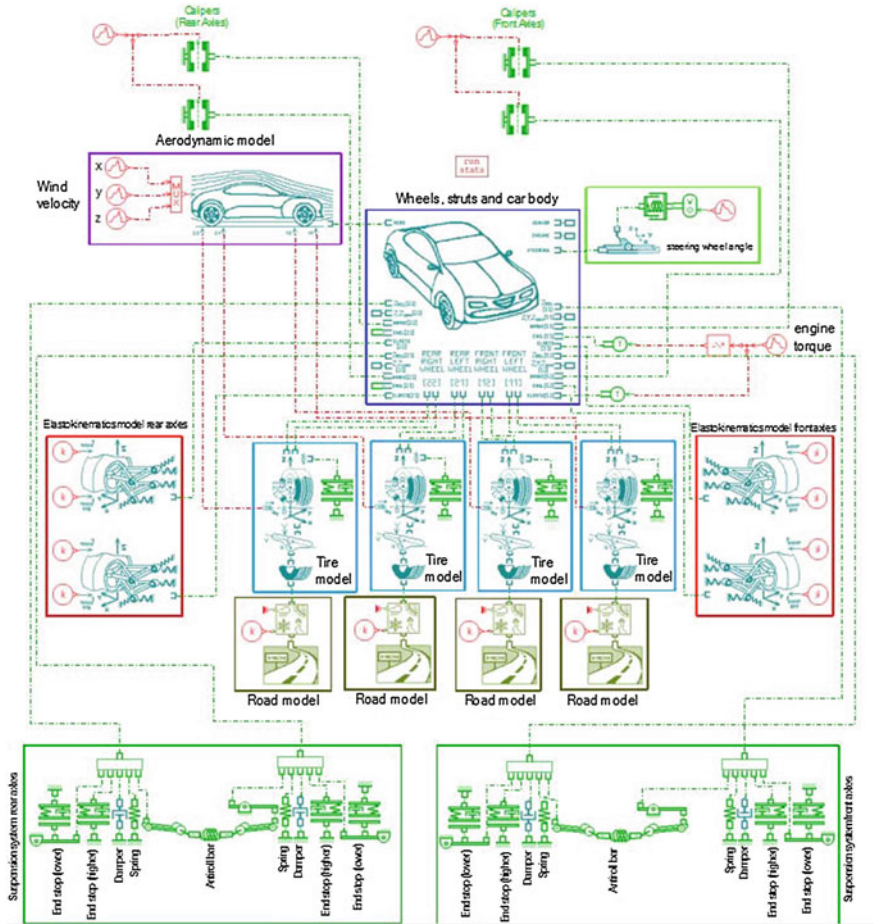


Fig. 1 The full vehicle modelled with AMESim program

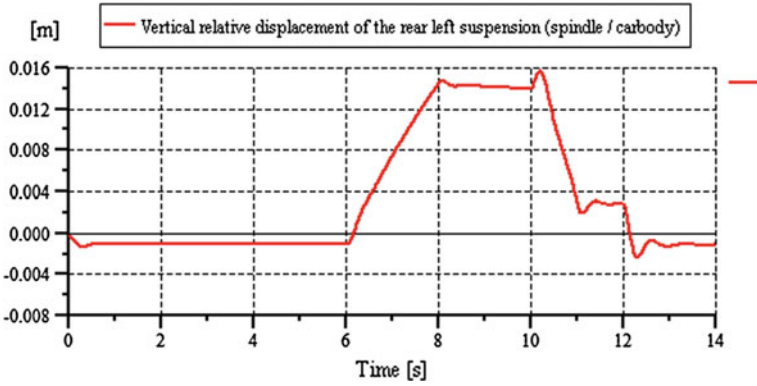


Fig. 2 Vertical relative displacement of the rear left suspension versus time

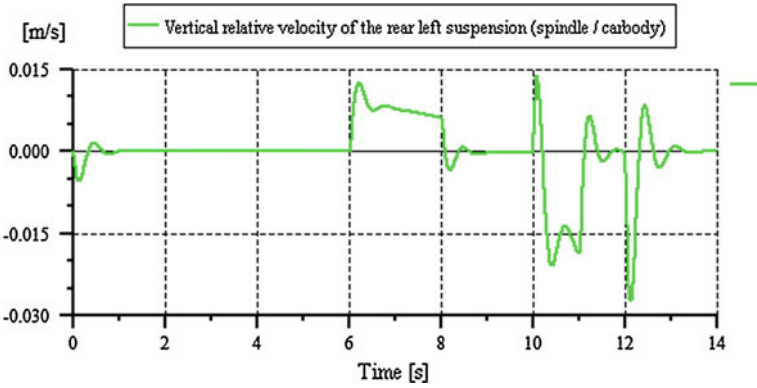


Fig. 3 Vertical relative velocity of the rear left suspension versus time

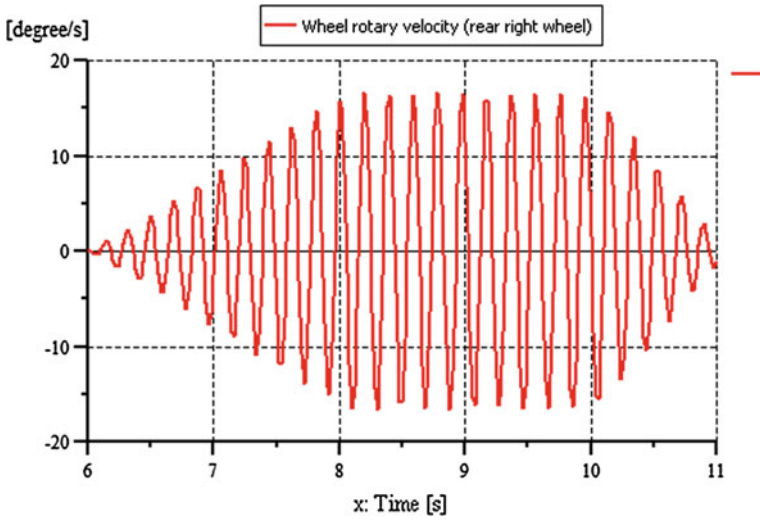


Fig. 4 Wheel rotary velocity for rear right wheel versus time

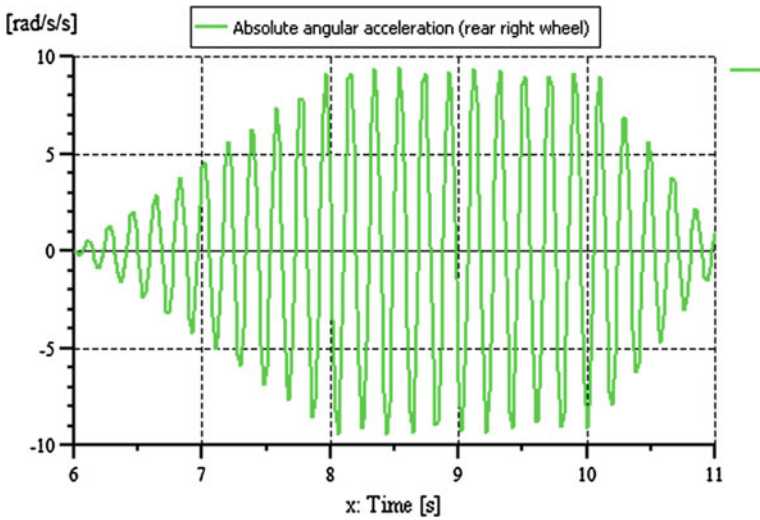


Fig. 5 Wheel absolute angular acceleration of the rear right wheel versus time



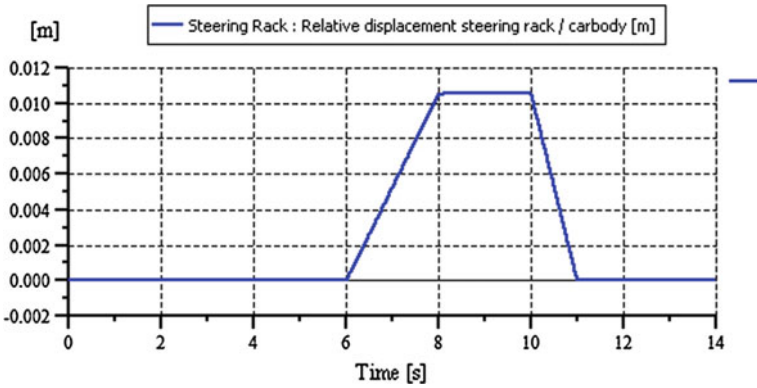


Fig. 6 Relative displacement of the steering rack/car body versus time

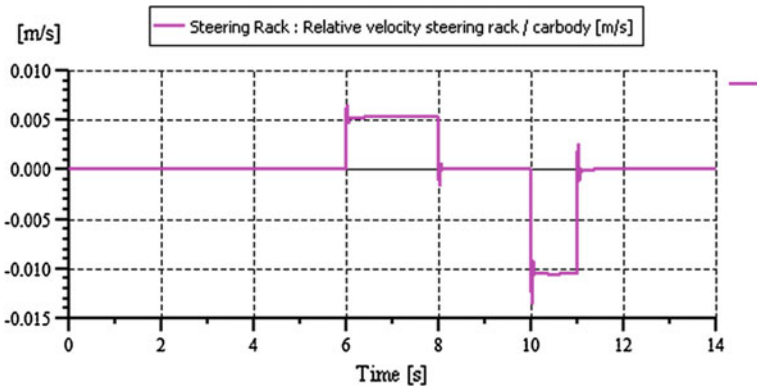


Fig. 7 Relative velocity steering rack versus time

## Conclusions

The simulation performed by AMESim program allows an easily adjustment the suspension’s parameters in order to obtain a higher comfort. The study can be adapted easily to any type of suspension due to fast model response. The dynamic behavior of the conventional suspension is limited from the point of view of comfort comparative with the other suspension types. The comfort is harder to estimate. Although some standards which quantifies the comfort are legal, its evaluation is still a disputed problem. Therefore, each type of a new car needs an extensive research study.

**Acknowledgments** The work has been funded by the Sectoral Operational Program Human Resources Development 2007–2013 of the Ministry of European Funds through the Financial Agreement POSDRU/159/1.5/S/134398.

## References

- Andreescu CN (2010) Automotive dynamics, vol I. Politehnica Press, Bucharest (in Romanian). ISBN 978-606-515-107-9
- Buchacz A (2007) Modelling, synthesis, modification, sensitivity and analysis of mechanic and mechatronic systems. *J Achiev Mater Manuf Eng* 24(1):198–207
- Guglielmino E, Stammers CW, Stăncioiu D, Sireteanu T (2005) Conventional and non-conventional smart damping systems. *Int J Veh Auton Syst* 3(2/3/4):216–229
- Guglielmino E, Sireteanu T et al (2008) Semi-active suspension control—improved vehicle ride and road friendliness. Springer, New York (e-ISBN: 978-1-84800-230-2)
- Guidaa D, Nilvetti F, Pappalardo CM (2010) Parameter identification of a full-car model for active suspension design. *J Achiev Mater Manuf Eng* 40(2):138–148
- Juang J-N (1994) Applied system identification. Prentice Hall, Upper Saddle River
- Khan L, Qamar S, Khan MU (2014) Comparative analysis of adaptive neurofuzzy control techniques for full car active suspension system. *Arab J Sci Eng* 39:2045–2069. doi: [10.1007/s13369-013-0729-4](https://doi.org/10.1007/s13369-013-0729-4)
- LMS Imagine.Lab—Mechatronic simulation software for model—based systems engineering. <http://www.plm.automation.siemens.com/>
- Stăncioiu D, Sireteanu T, Guglielmino E, Giuclea M (2003) Vehicle road holding and comfort improvement using controlled dampers. In: 7th International conference on economicity, safety and reliability of the vehicle, Bucharest, Romania, pp 1195–2002
- Vasiliu N, Vasiliu D (2005) Fluid power systems, vol I. Technical Press House, Bucharest

# Study Concerning the Loads Over Driver's Heads in Cases of Cars Crashes with Involved Cars of the Same or Different Generation

Nicolae Ispas and Mircea Nastasoiu

**Abstract** Car occupant protection in traffic accidents is a main target of today cars designers. Known as active or passive safety, many technological solutions were developing over the time for an actual better car's occupant safety (Henn in *Teach Math Appl* 17:162–170, 1998). In the real world, in traffic accidents are often involved cars from different generations with various safety historical solutions. The aims of these papers are to quantify the influences over the car driver head loads in cases of different generation of cars involved in side crashes. Both same and different cars generations were used for the study. The paper's experimental results were obtained by support of DSD, Dr. Steffan Datentechnik GmbH—Linz, Austria. The described tests were performed in full test facility of DSD Linz, in "Easter 2015 PC-Crash Seminar". In all crashes we obtaining results from both dummy placed in impacted and hits car. The novelty of the paper are the comparisons of data set from each of driver (dummy) of two cars involved in six of seven experimental crashes performed. In the first six crash cases are also analyzed the delays between drivers heads acceleration from strike and impacted cars (DSD Crash Test 2015). Another novelty of this paper consists in possibilities to analyze the influences of structural historical cars solutions over deformation and loads in cases of traffic accidents involved. Paper's conclusions can be future used for car passive safety improvement.

**Keywords** Crash test · Traffic accident · Head injury · Occupant safety

---

N. Ispas (✉) · M. Nastasoiu  
Automotive and Transportation Department, Transilvania University of Braşov,  
Braşov, Romania  
e-mail: inicu@unitbv.ro

M. Nastasoiu  
e-mail: m.nastasoiu@unitbv.ro

## Introduction

During the DSD facility experiments, seven 90° collisions against a standing vehicle will be performed. The DSD full-scale facility accelerates the driving vehicles to the appropriate test velocity. Approximately 10 m in front of the collision point, the vehicle will be disconnected from the guiding sled and the vehicle crashes against the stationary car. The impact speeds were 20, 40, 60 and 80 km/h. The ignition of the vehicles was turned on (DSD Crash Test 2015) (Fig. 1).

## Experimental Research

Seven 90° crash tests were performed according with EN1317 and EN12767. In each of them, except of last one was used dummy as car driver in both in crash cars. Complex accelerometers were mounted for dummy’s head, chest, neck and pelvis. Accelerations, velocities and rotations of the cars were also measured.

In the Figs. 2, 3, 4, 5, 6, 7 and 8 on see a brief description of each crash together with heads acceleration data.

<p><b>P01</b> Chrysler PT Cruiser L4 Length: 4288 mm Width: 1748 mm Mass: 1613 kg Year: 2007</p>		<p><b>P05</b> Fiat 176 Punto 60/75 Length: 3760 mm Width: 1630 mm Mass: 935 kg Year: 1994</p>	
<p><b>P02</b> Fiat 176 Punto 55 Length: 3760 mm Mass: 875 kg Year: 1994</p>		<p><b>P06</b> Opel Astra Length: 4655 mm Width: 1815 mm Mass: 1410 kg Year: 2013</p>	
<p><b>P03</b> Fiat 176 Punto 55 Length: 3760 mm Width: 1630 mm Mass: 875 kg Year: 1994</p>		<p><b>P07</b> Fiat 176 Punto 55 Length: 3760 mm Width: 1630 mm Mass: 875 kg Year: 1994</p>	
<p><b>P04</b> Fiat 176 Punto 55 Length: 3760 mm Width: 1630 mm Mass: 875 kg Year: 1994</p>		<p><b>P08</b> Honda Accord 4D Length: 4595 mm Width: 1750 mm Mass: 1272 kg Year: 2002</p>	
		<p><b>P09</b> VW Golf 1,4 Length: 4149 mm Width: 1735 mm Mass: 1137 kg Year: 1998</p>	

Fig. 1 The cars were used in experimental crashes

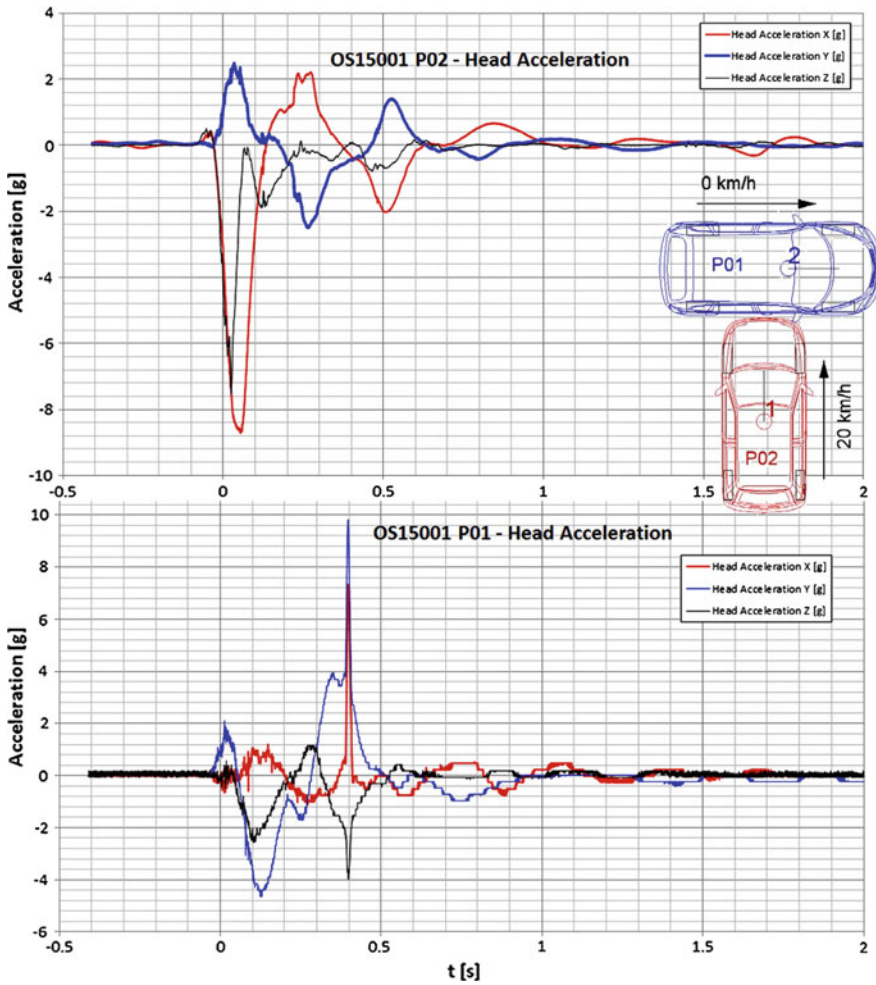


**Fig. 2** First collision—Fiat Punto P02 crashes into *right* side of Chrysler PT Cruiser P01 in the *right B* pillar area. Dummies are present in both vehicles. Head accelerations for moving vehicle driver are on *top* of figure

The dummy instrumentation is showed in Fig. 9, for all impact situations, including accelerometer for the dummy head (Zellmer 2010).

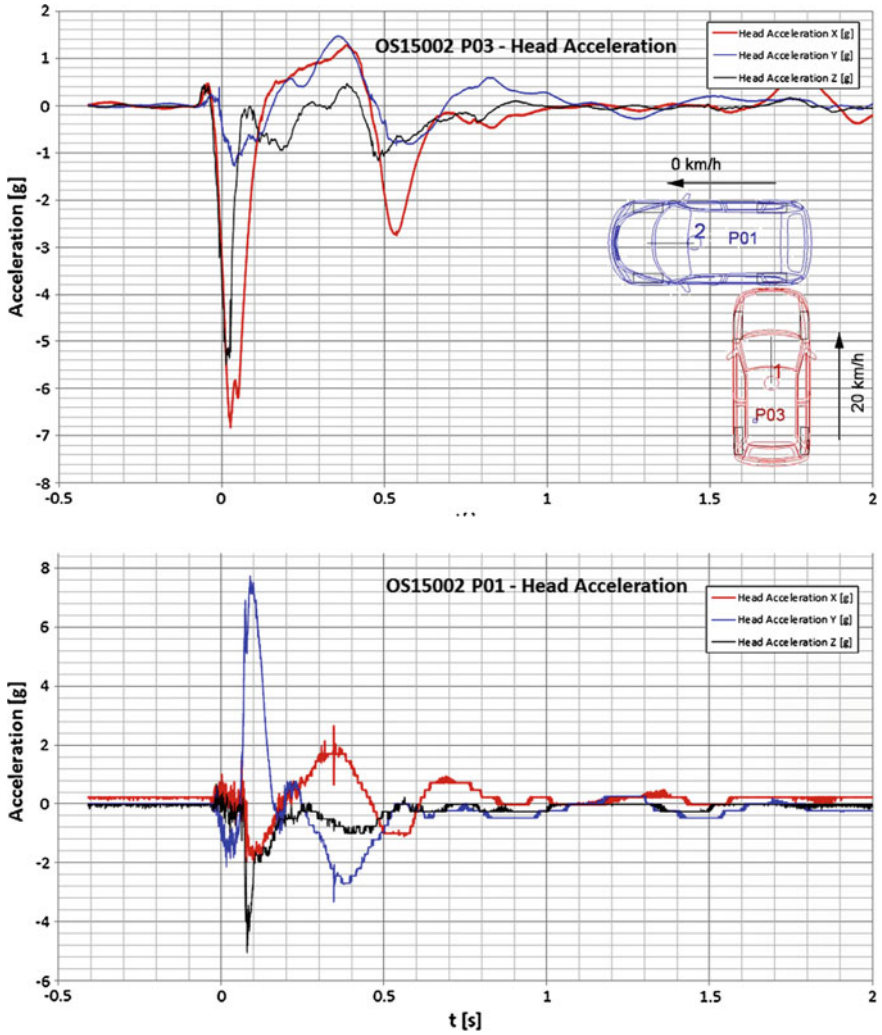


Fig. 3 Second collision—Fiat Punto P03 crashes into Chrysler PT Cruiser P01 in the left rear area. Dummies are in both vehicles. Head accelerations for moving vehicle driver are on top

### Results and Discussions

In the real world, crash tests are strong tools for improve both occupants and road vehicle safety. Compatibility between cars has for a long time been reduced to the simple image of heavy against light cars. Over the past years vehicle stiffness has been increased thanks to improved restraint systems. We also have a better understanding of the front end design energy absorption. Front end design is at the cross road of numerous contradictory constraints: self-protection of occupants,

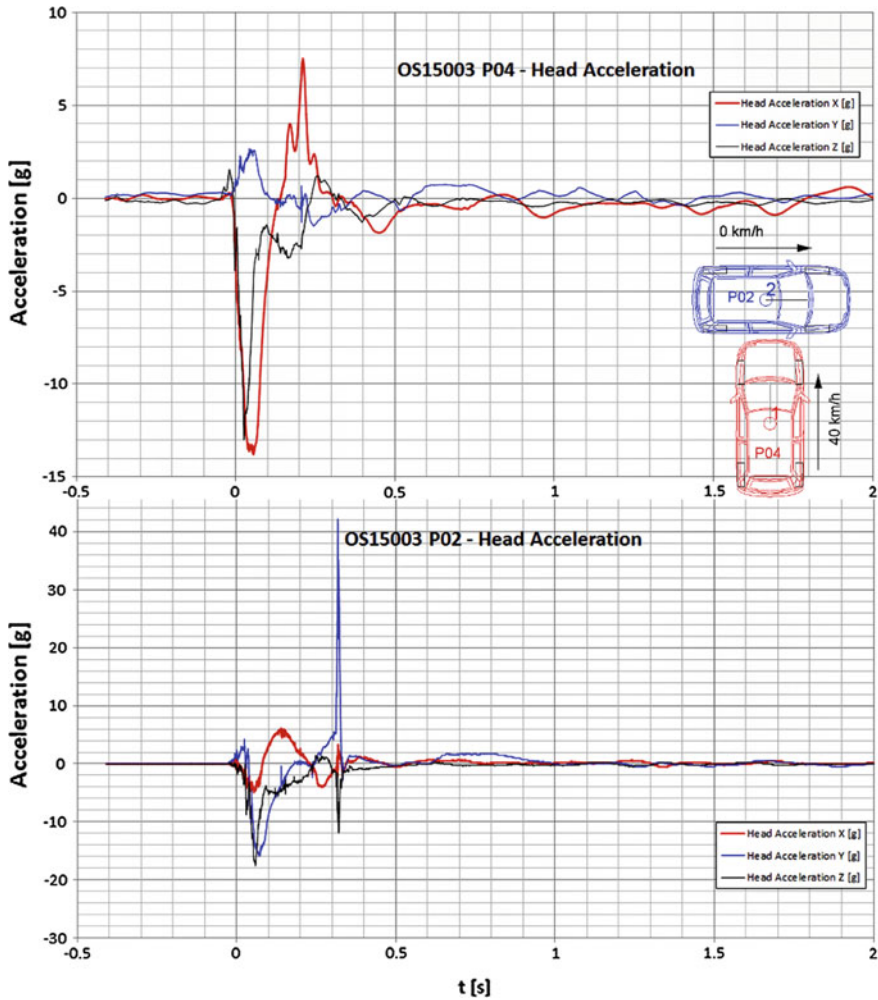
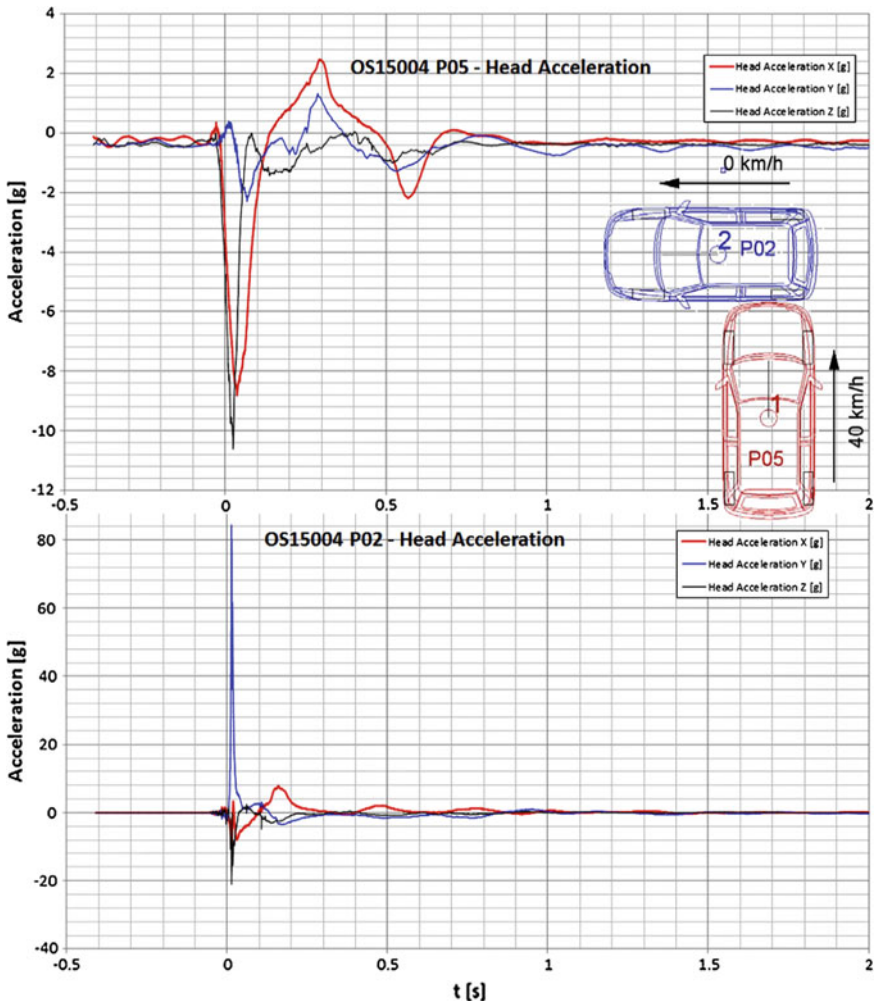


Fig. 4 Third collision—Fiat Punto P04 crashes into Fiat Punto P02 in the *right B* pillar area. Dummies are in both vehicles. Head accelerations for moving vehicle driver are on *top* of figure

protection of vulnerable users such as pedestrians, reparability, styling, aerodynamics, engine cooling and so on. Therefore, each manufacturer has developed its own solution to solve this difficult equation which resulted in a wide variety of front end designs, structure and stiffness regardless of the overall mass of the vehicle. Solutions however have been optimized against a rigid wall or soft obstacle but not in car to car configuration (Delannoy and Faure 2003).

Using for each crash case cars with or without technical/age compatibility, we can write the followers main conclusions:



**Fig. 5** Fourth collision—Fiat Punto P05 crashes into Fiat Punto P02 in the *left* rear area. Dummies are in both vehicles. Head accelerations for strikes vehicle driver are on *top*

#### A. First crash test:

1. Cars crash was at low impact speed (19.4 km/h) between vehicles from different generation (Fiat Punto 55—from year 1996 vs. Chrysler PT Cruiser from year 2006);
2. The cars are dissimilar weights (Fiat Punto 55–895 kg, Chrysler PT Cruiser–1470 kg);
3. For 2006 year car generation the car side from neighborhood of “B” pillar is more stiffness compared with stiffness of the same zone from a cars made in 1996;



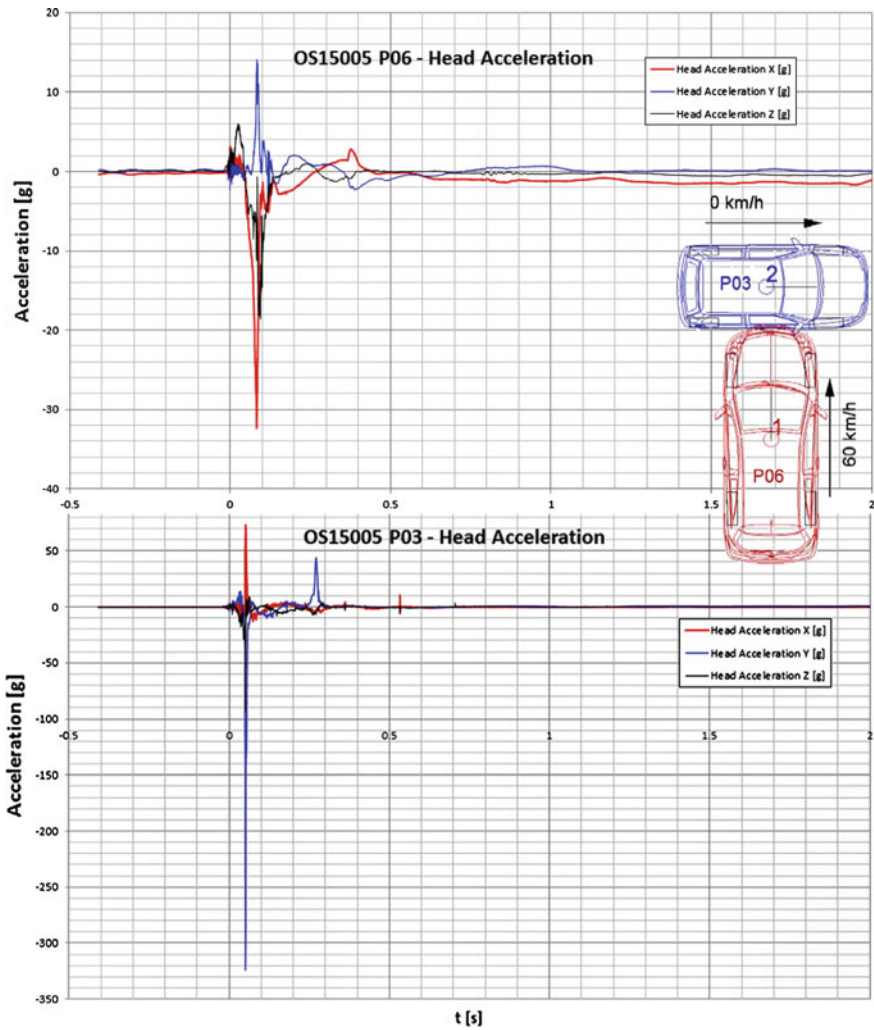


**Fig. 6** Fifth collision—Opel Astra P06 crashes into Fiat Punto P03 in the *right B* pillar area. Dummies are in both vehicles. Head accelerations for strikes vehicle driver are on *top* of figure

4. The Fiat Punto car is made with a low absorber of crash energy in the car front structure;
5. The maximum absolute amounts of accelerations of Fiat Punto car driver head were 7.6 g on “Z” direction and 8.7 g on “X” direction;
6. The maximum absolute amounts of accelerations of P01 car driver head were 4 g on “Z” direction and 9.8 g on “Y” direction.

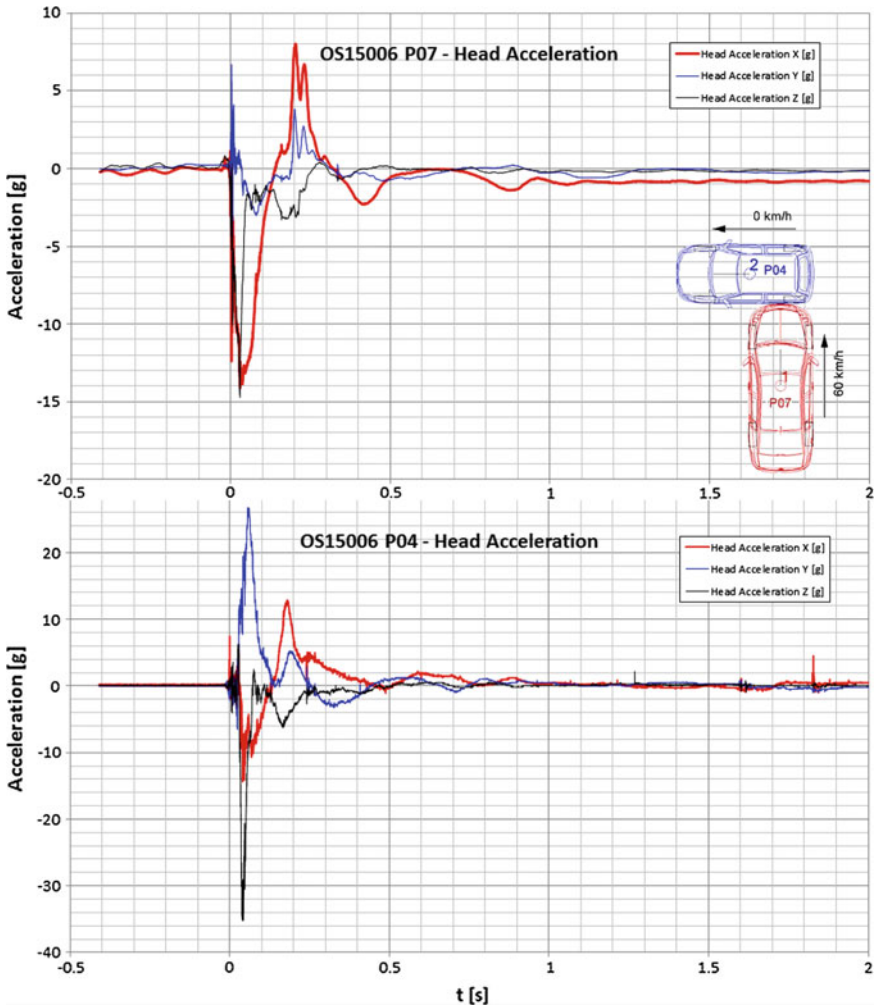
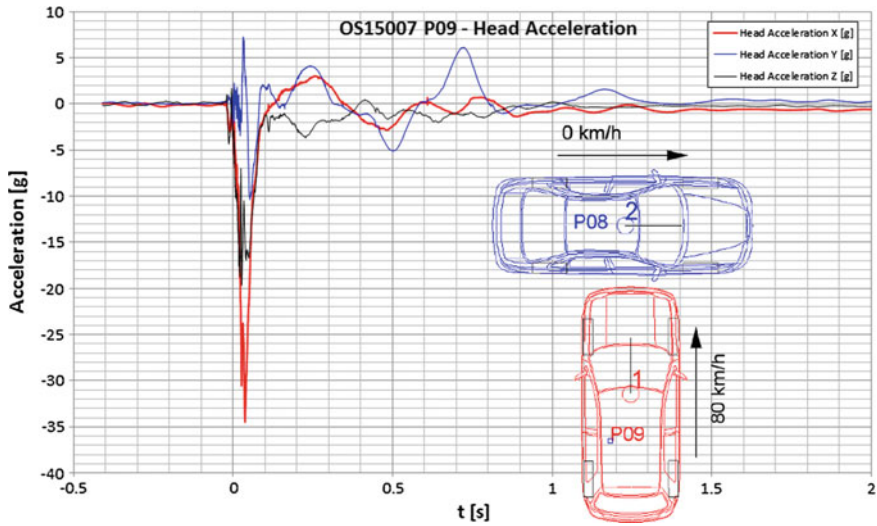


Fig. 7 Sixth collision—Fiat Punto P07 crashes into Fiat Punto P04 in the left rear area. Dummies are in both vehicles. On top on see head accelerations for strikes vehicle driver

B. Second crash test:

1. Cars crash was at low impact speed (19.3 km/h) between vehicles from different generation (Fiat Punto 55—from year 1994 vs. Chrysler PT Cruiser from year 2006);
2. The cars are dissimilar weights(Fiat Punto 55–850 kg, Chrysler PT Cruiser-1470 kg);



**Fig. 8** Seventh collision—VW Golf (P09) crashes into Honda Accord (P08) in the *right B* pillar area. Dummy was in VW car. Collision speed was 80 km/h

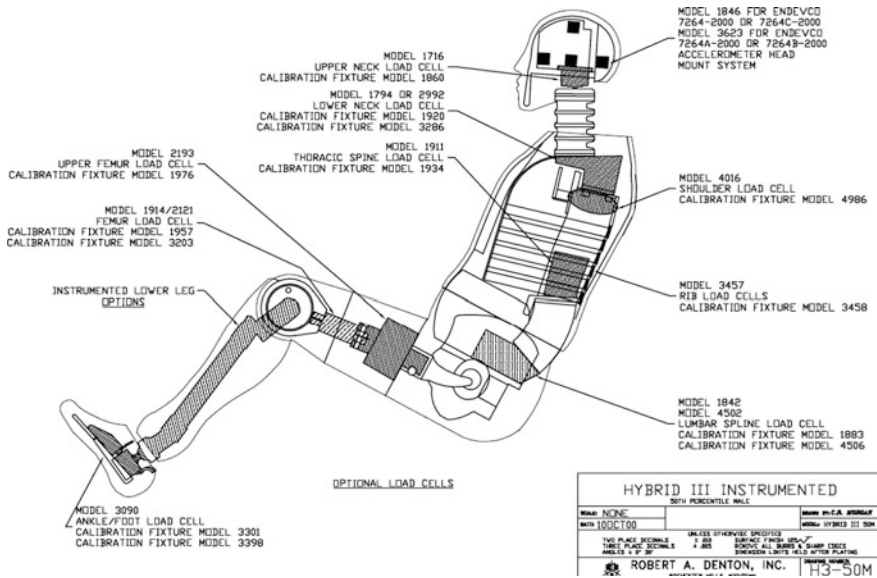


**Fig. 9** Dummy instrumentation for all crash cases (Zellmer 2010)

3. For 2006 year car generation the car side from neighborhood of “C” pillar and rear axle is more stiffness compared with stiffness of the same zone from a cars made in 1994;
  4. The Fiat Punto car is made with a low absorber of crash energy in the car front structure;
  5. The maximum absolute amounts of accelerations of Fiat Punto car driver head were 5.5 g on “Z” direction and 6.82 g on “X” direction;
  6. The maximum absolute amounts of accelerations of P01 car driver head were 5 g on “Z” direction and 7.85 g on “Y” direction.
- C. Third crash test:
1. Cars crash was at relatively low impact speed (40.7 km/h) between vehicles from the same generation (Fiat Punto 55—from year 1996 vs. Fiat Punto 55—from year 1997);
  2. The cars are similar weights (Fiat Punto 55, 1997—830 kg, Fiat Punto 55, 1996—895 kg);
  3. For 1996 year car generation the stiffness of front door is the same compared with stiffness of the front door of a cars made in 1997;
  4. Both Fiat Punto cars are made with a low absorber of crash energy in the car front structure;
  5. The maximum absolute amounts of accelerations of Fiat Punto 1996 year car driver head were 13 g on “Z” direction and 13.9 g on “X” direction;
  6. The maximum absolute amounts of accelerations of P02 car driver head were 12 g on “Z” direction and 42 g on “Y” direction.
- D. Fourth crash test:
1. Cars crash was at relatively low impact speed (40.7 km/h) between vehicles from the same generation (Fiat Punto 55—from year 1994 vs. Fiat Punto 55—from year 1996);
  2. The cars are similar weights (Fiat Punto 55, 1994—890 kg, Fiat Punto 55, 1996—895 kg);
  3. For 1994 year car generation the neighborhood of “C” pillar and rear axle have the same stiffness compared with stiffness of the same zone from a cars made in 1996;
  4. Both Fiat Punto cars are made with a low absorber of crash energy in the car front structure;
  5. The maximum absolute amounts of accelerations of Fiat Punto 1994 year car driver head were 10.6 g on “Z” direction and 8.8 g on “X” direction;
  6. The maximum absolute amounts of accelerations of P02 car driver head were 22 g on “Z” direction and 85 g on “Y” direction.

## E. Fifth crash test:

1. Cars crash was at medium impact speed (59.4 km/h) between vehicles from very different generation (Opel Astra from year 2014 vs. Fiat Punto 55—from year 1994);
2. The cars are dissimilar weights (Opel Astra from year 2014—1440 kg, Fiat Punto 55 from year 1994—850 kg);
3. For 1994 year car generation the front side door is less stiffness compared with stiffness of the same zone from a cars made in 2014;
4. The Opel Astra car is made with a high absorber of crash energy in the car front structure;
5. The maximum absolute amounts of accelerations of Fiat Punto car driver head were 18.5 g on “Z” direction and 33 g on “X” direction;
6. The maximum absolute amounts of accelerations of P03 car driver head were 325 g on “Y” direction and 73 g on “X” direction.

## F. Sixth crash test:

1. Cars crash was at relatively medium impact speed (60.7 km/h) between vehicles from the same generation (Fiat Punto 55—from year 1997 vs. Fiat Punto 55—from year 1994);
2. The cars are similar weights (Fiat Punto 55, 1997—890 kg, Fiat Punto 55, 1994—830 kg);
3. For 1997 year car generation the stiffness of the side in place of rear axle is the same compared with stiffness of the side rear axle from a car made in 1994;
4. Both Fiat Punto cars are made with a low absorber of crash energy in the car front structure;
5. The maximum absolute amounts of accelerations of Fiat Punto 1996 year car driver head were 14.8 g on “Z” direction and 14 g on “X” direction;
6. The maximum absolute amounts of accelerations of P04 car driver head were 35 g on “Z” direction and 27 g on “Y” direction.

## G. Seventh crash test:

1. Cars crash was at relatively high impact speed (80 km/h) between vehicles from the same generation (VW Golf 1.4—from year 1998 vs. Honda Accord 4D—from year 2002);
2. The cars are similar weights (VW Golf 1.4, 1998—1137 kg, Honda Accord 4D, 2002—1272 kg);
3. For 2002 year car generation the stiffness of the side in B pillar area is comparable with stiffness of the side from a car made in 1998;
4. The maximum absolute amounts of accelerations of VW Golf (P09) year car driver head were 35 g on “X” direction and 7 g on “Y” direction.

## References

- Delannoy P, Faure J (2003) Compatibility assessment proposal close from real life accident. SAE Technical Papers, paper #: 14 June 2003, published: 19 May 2003
- DVD-ROM (2015) DSD Crash Tests April 2015, “Easter 2015 PC-Crash Seminar”, © DSD, Linz 2015
- Henn H-W (1998) Crash test and the head injury criterion. *Teach Math Appl* 17(4):162–170
- Zellmer H (2010) Dummy design and issues. In: *International course on transportation planning and safety*, New Delhi

# Use of GPS/INS Devices for Experimental Study of Vehicle Dynamics

Dinu Covaciu, Ion Preda, Dragoş-Sorin Dima and Anghel Chiru

**Abstract** The goal of this study is to use different data acquisition devices based on GPS (global positioning system) receivers and/or IMU (inertial measuring unit) sensors for ascertaining the vehicle's dynamics performances. The acquisition systems used were with two GPS receivers, one GPS receiver and one inertial unit, and two GPS receivers and one inertial unit. The parameters that can be determined include velocity, longitudinal and lateral acceleration, slip angle, yaw rate, turning radius. Raw data are filtered using digital filters like CFC (Channel Frequency Class) or Kalman, and values measured with one device are used to improve the quality of data taken with another device. The tests performed involved accelerating, braking and turning. The collected data are processed using the proprietary software of the commercial acquisition systems, and also some original developed software applications.

**Keywords** Vehicle dynamics · Inertial sensors · Vehicle attitude · Data filter

## Introduction

The use of GPS and INS (inertial navigation system) devices in the study of vehicle dynamics was quite spread during the last years. A frequent approach consists in the use of a vehicle motion model in combination with a Kalman filter applied on data collected from IMU, to estimate vehicle states when noisy GPS and IMU data are available. Sumeet et al. (2013) extend the GPS/IMU sensor fusion to include dead reckoning through the OBD speed data, so that good estimation, including vehicle trajectory, can be obtained using a low cost GPS, IMU and OBD (on-board diagnostics) scan tool. Many researchers, like Yoon and Peng (2010), Grewal et al. (2007), Ryu et al. (2002) and Grip et al. (2009), use GPS units with single or dual antenna and inertial sensors. The principles are presented in Grewal et al. (2007).

---

D. Covaciu (✉) · I. Preda · D.-S. Dima · A. Chiru  
Transilvania University of Braşov, Braşov, Romania  
e-mail: dinu.covaciu@unitbv.ro

Recently, Phondeenana et al. (2014) shows that using the PPP (precise-point-positioning) technology it is possible to obtain a higher accuracy of GPS measurements.

Using GPS receivers and IMU devices, the following values can be measured directly:

- with GPS receivers: time, position (latitude, longitude, altitude), speed, course;
- with IMU (inertial) devices: yaw, pitch and roll rates, accelerations on three axes.

Then many other values can be calculated based on the measured ones:

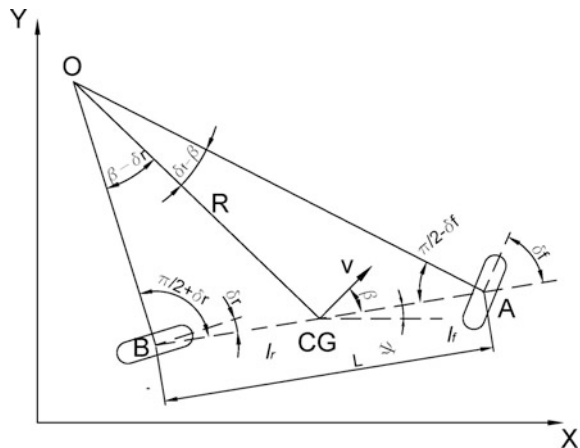
- based on GPS measurements: longitudinal acceleration, lateral acceleration, radius and center of turn, yaw and yaw rate;
- based on IMU: velocities and distances on the three axes (the unit is in this case integrated in an inertial navigation system, or INS).

The yaw rate can be measured with a gyroscope, or can be calculated based on the vehicle course given by a GPS receiver, but for the vehicle sideslip are required accurate measurements of the ground speed of two different points on the vehicle. The sideslip can be measured directly with a two-antenna GPS system (Yoon and Peng 2010), combined if possible with IMU sensors.

## The Model

The model that is probably the most frequently used in the study of the lateral dynamics of a vehicle is the single-track vehicle model (the “bicycle model”) Rajamani (2011), Preda and Ciolan (2012) (Fig. 1). Both front wheels are

**Fig. 1** The single track vehicle model used for study of vehicle kinematics





represented by one single wheel at point A, and both rear wheels are represented by one single central rear wheel at point B.

The notation in the figure are as follows:

- the steering angles for the front and rear wheels:  $d_f$  and  $d_r$ ;
- the center of gravity of the vehicle is at point CG;
- the distances of points A and B from the CG of the vehicle are  $l_f$  and  $l_r$ ;
- the wheelbase of the vehicle is  $L = l_f + l_r$ ;
- X, Y are inertial coordinates describing the location of the CG;
- $\Psi$  is the the yaw angle and indicates the orientation of the vehicle (heading);
- the velocity at the CG of the vehicle is V and makes an angle b with the longitudinal axis of the vehicle.

The angle b is called the slip angle of the vehicle.

As per Fig. 1, the following equations can be deduced (Covaciu et al. 2014):

$$\frac{\sin(\delta_f - \beta)}{l_f} = \frac{\sin(\frac{\pi}{2} - \delta_f)}{R} \quad \frac{\sin(\beta - \delta_r)}{l_r} = \frac{\sin(\frac{\pi}{2} + \delta_r)}{R} \tag{1}$$

The rate of change of the vehicle heading (the yaw rate of the vehicle body) is:

$$\dot{\Psi} = \frac{v}{R} \tag{2}$$

and the overall equations of motion will be (Preda and Ciolan 2012):

$$\dot{X} = v \cdot \cos(\Psi + \beta) \quad \dot{Y} = v \cdot \sin(\Psi + \beta) \tag{3}$$

$$\dot{\Psi} = \frac{v \cdot \cos(\beta)}{l_f + l_r} (\tan(\delta_f) - \tan(\delta_r)) \tag{4}$$

Some of the variables on these equations can be measured and are input data, others will be calculated. Which values are measured and which are calculated depends on the measuring devices used.

## Acquiring and Processing Data

The test track is presented in Fig. 2, as it is represented in a CAD environment, composed by points and lines. Each point entity has attached custom data recorded with the GPS receiver. The vehicle driven on this track was equipped with various sensors (Fig. 3), including Speedbox (from Race Technology), PIC-DAQ (from DSD) and DS-5 (Covaciu et al. 2011).

Speedbox is a family of high precision data acquisition devices for automotive applications, that use inertial (IMU) and GPS technology for measurement of

**Fig. 2** Test track, shown as point and lines in CAD environment

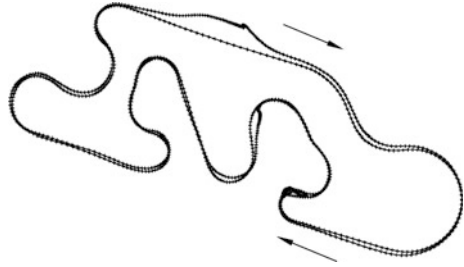


**Fig. 3** Instrumented vehicle



vehicle performance. The system used has a dual GPS RTK (real time kinematics) antenna layout. The INS option uses complex algorithms and Kalman filtering to cross reference the GPS data with the inertial data. As it is stated on the manufacturer's website (Race\_Technology), "this makes it ideal for real world road testing as well as test tracks".

PIC-DAQ is a data acquisition platform based on a PIC microcontroller, and with one gyroscope and two accelerometers, all of them working on three axes. The recorded accelerations and angular velocities describe the movement. The system can take also data from a GPS sensor, through a serial interface. Only the speed is taken from GPS, extracted from one of the NMEA 0183 sequences.

DS-5 is an in-house built data acquisition system, based on the GPS 18x-5 Hz sensor from Garmin, that offers very precise position and velocity information. Data are sent to a computer through a serial interface, as NMEA 0183 sequences. The sequences are logged as text files, using a custom developed software. Two GPS sensors were used in this experiment, mounted at front and rear of the vehicle's roof. Each sensor sends its own position, time, speed and heading information to the logger, and these are then used to compute the accelerations, yaw and slip of the vehicle.

For a GPS receiver, the position as latitude and longitude coordinates is known. These coordinates are transformed to cartesian coordinates and from three consecutive points, using the equation of a circle described by three points, the radius of turn can be calculated, and also the center of the turn. Using only data given by the GPS receivers, the longitudinal and lateral acceleration can be calculated as:

$$acc_x = dv/dt \quad acc_y = v^2/R \tag{5}$$

where  $acc_x$  is the longitudinal acceleration,  $acc_y$  is the lateral acceleration,  $v$  is the measured speed,  $R$  is the calculated radius of turn and  $t$  is the time given also by the GPS receiver. The calculated acceleration values are affected by GPS positioning errors and low sampling rate. In case of longitudinal acceleration, the positioning information is not used, only the speed and time, which are very accurate (speed is measured using the doppler effect). When a higher sampling rate is needed, the solution is to use accelerometers (IMU).

The longitudinal and lateral accelerations measured with IMU for the track shown in Fig. 1 are presented in Fig. 4. The values used for these diagrams are not filtered (acceleration values given in  $g$ ).

The basic (raw) data obtained from each GPS receiver is the speed, represented in Fig. 5 for the same recorded track.

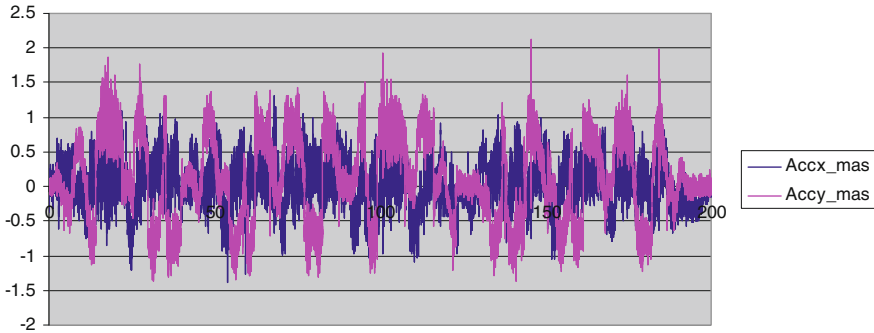


Fig. 4 Longitudinal and lateral acceleration, measured with IMU, as raw data (g)

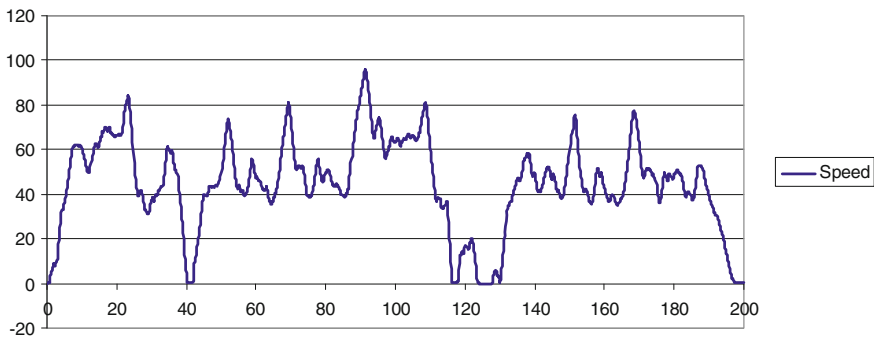


Fig. 5 Speed obtained from a GPS receiver

## Data Filters

Since the values in Fig. 5 are smooth enough, it is obvious that the values used to generate the diagrams in Fig. 4 need to be filtered. The noise has a frequency higher than those of the signal, so it should be used a low-pass filter. The simplest digital low-pass filter is equivalent with the electronic first-order RC filter (composed by just one resistor and one capacitor). The transfer function of the discrete digital filter will be:

$$y(t) = y(t - 1) + a(x(t) - y(t - 1)) \quad (6)$$

where  $y(t)$  is the current output,  $y(t - 1)$  is the previous output,  $x(t)$  is the current input and  $a$  is a smoothing coefficient with values between 0 and 1. When the smoothing coefficient is closer to 0, the attenuation of high frequency will be more pronounced, but there are chances to lose some of the useful signal amplitude.

More complex filters were developed for special applications, like the CFC filter and the Kalman filter. CFC (Channel Frequency Class) filter is used especially in impact tests, as stated in the SAE J211 standard (SAE 1995). The J211 standard establish four channel frequency classes of low-pass filters and specifies acceptable frequency response for each filter class. The four filters are designated as CFC 60, 180, 600, and 1000. The filter is derived from analog Butterworth filters whose corner frequency (the 3 dB limit frequency) is equal to the CFC designation divided by 0.6. The minimum sampling frequency for CFC 60 is 600 Hz. The standard is not applied for lower sampling rates, but the filter can be defined also outside those four classes. The transfer function of the CFC filter is:

$$y(t) = a_0x(t) + a_1x(t - a) + a_2x(t - 2) + b_1y(t - 1) + b_2y(t - 2) \quad (7)$$

and the filter coefficients  $a_0$ ,  $a_1$ ,  $a_2$ ,  $b_1$ ,  $b_2$  are calculated with formulas defined in J211, depending by the filter class and sampling frequency.

A filter class 5 applied to the longitudinal acceleration diagram will result in the red graph shown in Fig. 6.

It is obvious that a lower class is required to filter the acceleration recorded with a sampling rate of 100 Hz. The result is shown in Fig. 7.

The Kalman filter comprises a measurement update and a time update (Ryu and Gerdes 2004). The evolution from the state  $t - 1$  to the current state  $t$  is described by the equation:

$$x_t = F_t x_{t-1} + B_t u_t + w_t \quad (8)$$

where  $x_t$  is the state vector containing the terms of interest (e.g. acceleration) at time  $t$ ,  $u_t$  is the vector containing any control inputs,  $F_t$  is the state transition matrix which applies the effect of each state parameter at time  $t - 1$  on the state at time  $t$ ,  $B_t$  is the control input matrix which applies the effect of each control input parameter in the vector  $u_t$  on the state vector, and  $w_t$  is the vector containing the process noise

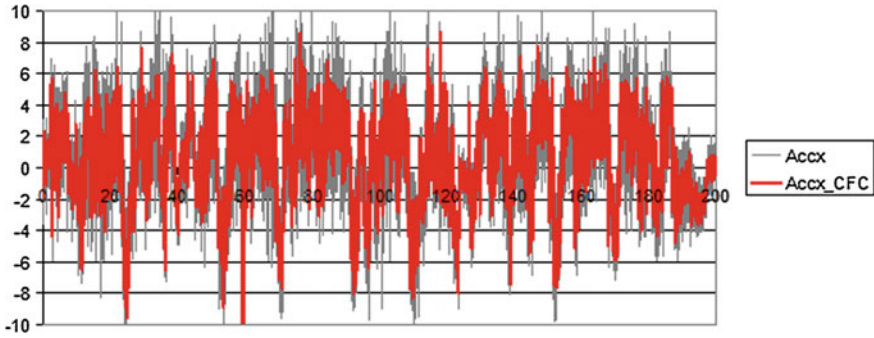


Fig. 6 Longitudinal acceleration, filtered CFC5 (m/s<sup>2</sup>)

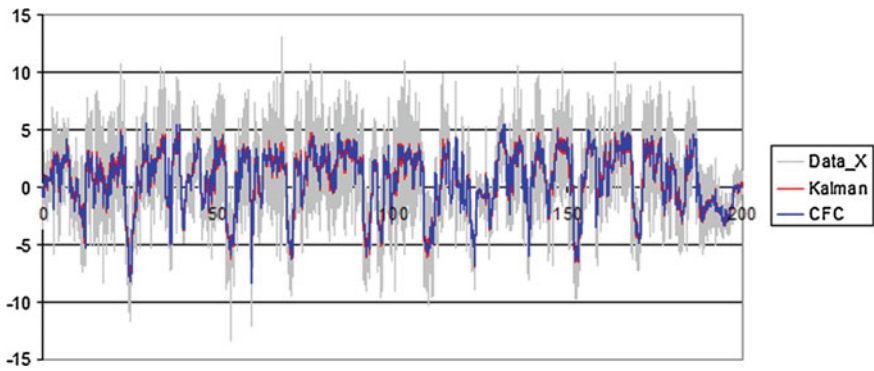


Fig. 7 Longitudinal acceleration, CFC1 and Kalman filters (m/s<sup>2</sup>)

terms for each parameter in the state vector (Faragher 2012). The measurements can be expressed as:

$$z_t = H_t x_t + v_t \tag{9}$$

where  $z_t$  is the vector of measurements,  $H_t$  is the transformation matrix and  $v_t$  is the vector containing the measurement noise terms for each observation in the measurement vector.

The value of  $x_t$  is a linear combination of its previous value plus a control signal  $u_t$  and a process noise. We can assume that in case of many measurements there is no control signal (like the case when we measure only the acceleration using an accelerometer). In this case the equation of the filter can have a simplified form:

$$\hat{x}_t = k_t \cdot z_t + (1 - k_t) \cdot \hat{x}_{t-1} \tag{10}$$

where  $\hat{x}_t$  is the current estimation of the variable and  $\hat{x}_{t-1}$  is the previous estimation of the analysed variable;  $z_t$  is the measured value and  $k_t$  is the Kalman gain, which is also updated at each iteration. The Eq. (10) is quite similar with the Eq. (6) of the low-pass filter, except that the Kalman gain is calculated again at each iteration.

The implementation of the filter as an iterative process includes the measurement update as follows:

$$\begin{aligned} k &= p/(p+r) \\ y(t) &= y(t-1) + k \times (x(t) - y(t-1)) \\ p &= (1-k) \times p \end{aligned} \quad (11)$$

and the kalman filter prediction is calculated as:

$$\begin{aligned} y(t-1) &= y(t) \\ p &= p + q \end{aligned} \quad (12)$$

The filter Eqs. (11) and (12) are applied with each measurement and initialized with the process noise  $q$ , the sensor noise  $r$ , the initial estimated error  $p$  and the initial value  $y(t)$  considered as equal with the measured value  $x(t)$ . The initial values for  $p$  and  $x$  are not very important because both are updated during the process.

The resulted diagram, with a Kalman filter applied with a process noise ( $q$ ) of 0.1 and a sensor noise ( $r$ ) of 10, is shown in Fig. 7, and it can be seen that the curve is quite close to those filtered with CFC1 (also in Fig. 8).

## GPS Versus INS Measurements

A portion of the diagram of longitudinal acceleration is presented in Fig. 8. Similarly, the lateral acceleration, Kalman filtered, is shown (as detail) in Fig. 9. The acceleration calculated from GPS data ( $dv/dt$ ) is represented in Fig. 10, for the same time interval. The differences between diagrams in Figs. 8 and 10 are caused in part by the measurement errors, but also the reference systems are different (the vehicle system in case of INS device and an external reference system in case of GPS). The lateral acceleration measured with the accelerometer on y axis is part of the acceleration calculated from GPS data. The direction of travel is different by the direction of vehicle's longitudinal axis (x axis), and this is proven also by the diagrams in Figs. 8, 9 and 10—when there are notably differences between the diagrams in Figs. 8 and 10, it can be noticed also a change of lateral acceleration in Fig. 9.

The differences between the values of accelerations determined with the GPS and INS devices are also noticeable when the vehicle speed is calculated from measured acceleration. The accelerometer bias will lead to an increasing speed. The difference is visible also in Fig. 11, where the diagram of calculated speed (red) is corrected with the speed given by GPS.

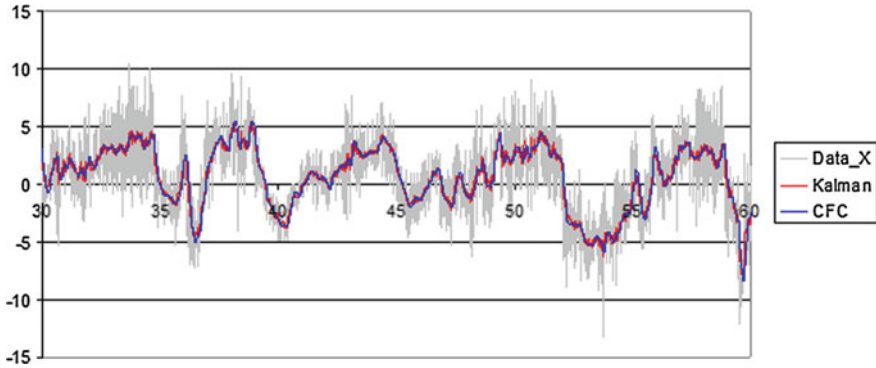


Fig. 8 Diagram of longitudinal acceleration, filtered—detail

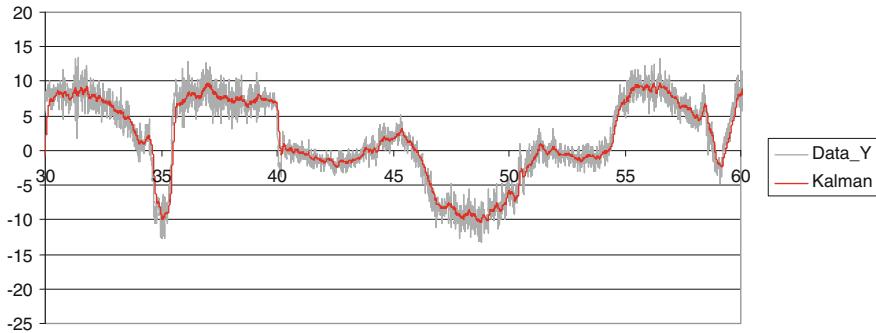


Fig. 9 Diagram of lateral acceleration, filtered—detail

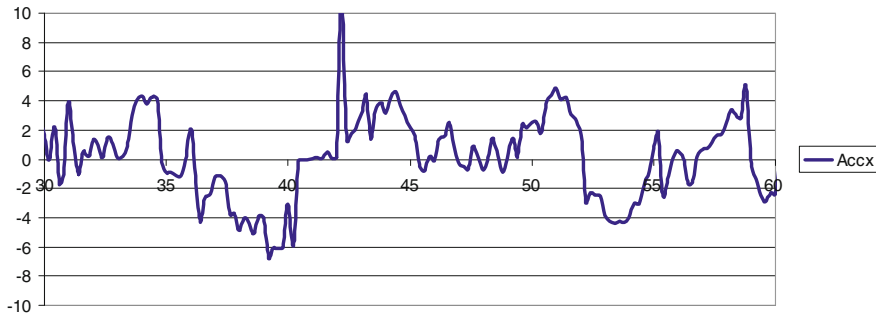


Fig. 10 Diagram of lateral acceleration, calculated from GPS data

A vehicle state parameter that can be also ascertained from both GPS and INS measurements is the yaw (and yaw rate). The yaw rate can be measured directly with the INS, if the device includes also a gyroscope, and can be also calculated

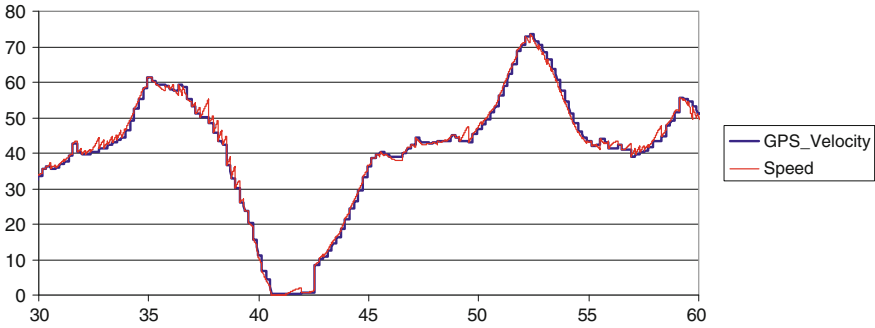


Fig. 11 Vehicle speed, measured with GPS and calculated from acceleration

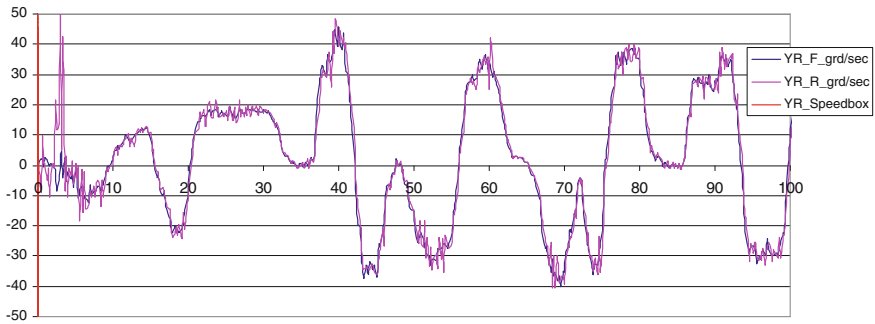


Fig. 12 Yaw rate given by Speedbox and two independent GPS receivers

starting from the vehicle speed and the turning radius. Also the yaw rate can be estimated as the variation of the heading of the vehicle. An example of the yaw rate calculated as heading variation, for two independent GPS receivers placed on front and rear of vehicle roof, and also measured with the Speedbox system, is presented in Fig. 12. When the yaw rate value results from vehicle heading, it can be calculated the radius of turn, and the lateral acceleration (as the speed multiplied with the yaw rate).

## Conclusion

Data measured with IMU devices and GPS receivers, independently or together, can be used to estimate the vehicle attitude. When using IMU devices, the collected data are strongly influenced by measurement noise and appropriate filtering needs to be used. Filters like CFC and Kalman were experimented and the results were quite similar, but depends by the filter parameters. Using also a GPS receiver will improve the accuracy, and will give also positioning information. However, when



multiple sources of data are used, the process is nonlinear and an extended Kalman filter should be used.

Among the parameters measured and calculated in this study, there are also many others that define the vehicle state and can be estimated satisfactorily from the GPS data and inertial sensors data. The side slip angle can be defined as the difference between the vehicle yaw angle and the direction of the velocity. Both yaw and direction of velocity can be obtained using GPS and INS, and so the vehicle slip angle can be calculated.

**Acknowledgements** This work was partially supported by the strategic grant POSDRU/159/1.5/S/137070 (2014) of the Ministry of Labor, Family and Social Protection, Romania, co-financed by the European Social Fund—Investing in People, within the Sectoral Operational Programme Human Resources Development 2007–2013.

## References

- Covaciu D, Preda I, Ciolan G (2011). GPS based data acquisition system for mobile applications. *Acta Technica Jaurinensis* 4(4):453–464
- Covaciu D, Preda I, Dima DS, Chiru A (2014) Study on the possibility to estimate the vehicle side slip using two independent GPS receivers. In: 3rd international congress science and management of automotive and transportation engineering SMAT2014. University of Craiova, Craiova, Romania
- Faragher R (2012) Understanding the basis of the Kalman filter via a simple and intuitive derivation. *EEE Sig Process Mag* 29:128–132
- Grewal MS, Weill LR, Andrews AP (2007) *Global positioning systems, inertial navigation, and integration*. Wiley, Hoboken
- Grip HF, Imsland L, Johansen TA, Kalkkuhl JC, Suissa A (2009) Vehicle sideslip estimation: design, implementation, and experimental validation. *IEEE Control Syst* 29:36–52
- Phondeenana P, Thitipatanapong R, Klongnaivai S, Noomwongs N, Chantranuwathana S (2014) Driver behavior detection based on PPP-GNSS technology. *SAE Technical Paper* 2014-01-2006
- Preda I, Ciolan G (2012) Vehicle mathematical model for the study of cornering. *Annals of the Oradea University. Fascicle of Management and Technological Engineering, XI (XXI):1.22–1.32*
- Race\_Technology. Speedbox [Online]. [Accessed May 2015]
- Rajamani R (2011) *Vehicle dynamics and control*. Springer Science & Business Media, Berlin
- Ryu J, Gerdes JC (2004) Integrating inertial sensors with global positioning system (GPS) for vehicle dynamics control. *J Dyn Syst Meas Control* 126:243–254
- Ryu J, Rossetter EJ, Gerdes JC (2002) Vehicle sideslip and roll parameter estimation using GPS. In: *International symposium on advanced vehicle control (AVEC), 2002 Hiroshima, Japan*, pp 373–380
- SAE (1995) *Instrumentation for impact test—part 1: electronic instrumentation*. SAE paper no. J211/1. Society of Automotive Engineers, Warrendale, PA
- Sumeet K, Paefgen J, Wilhelm E, Sarma SE (2013) Integrating on-board diagnostics speed data with sparse GPS measurements for vehicle trajectory estimation. In: *The SICE Annual Conference*
- Yoon JH, Peng H (2010) Vehicle sideslip angle estimation using two single-antenna GPS receivers. In: *ASME 2010 dynamic systems and control conference*, pp 863–870

# Study of the Dynamic Behavior of a Car Body for Mounting the Rear Axle

Ștefan-Ionescu Romeo, Petrache Gheorghe, Ionel Vieru,  
Viorel Nicolae and Pârlac Sebastian

**Abstract** This paper presents a dynamic analysis of the car body for mounting the rear axle. It was performed a study on the frequency response by determining the values for the inertances. The calculated values were compared with those provided by the specifications. FEM (Finite Element Method) was used as calculation method and the results were compared with those determined experimentally on the test bench.

**Keywords** Dynamic analysis · Frequency response · Inertance · FEM

## Introduction

The carrying structure is an assembly of the car body that takes direct the mechanical stress due to its own weight, payload and other parts. It is the element which take over the mechanical stress in all car travel modes, following all the conditions imposed to a mounting base for the engine, transmission and axles for moving stable on any type of trajectory or path, provided in the specification of each project.

---

Ș.-I. Romeo (✉) · P. Gheorghe  
RTR, Voluntari, Romania  
e-mail: romeo.stefan-ionescu@renault.com

P. Gheorghe  
e-mail: gheorghe.petrache@renault.com

I. Vieru · V. Nicolae · P. Sebastian  
University of Pitesti, Pitesti, Romania  
e-mail: ionel.vieru@upit.ro

V. Nicolae  
e-mail: viorel.nicolae@upit.ro

P. Sebastian  
e-mail: seby\_kwo@yahoo.fr

Transmission of the rolling noise from the road to the passenger compartment is performed via assembled axles, mounting brackets or support of bridges on the car body and body frames (roof, floor, windshield, tailgate, deck).

The dynamic stiffness of the car body supports must have values that provide good filtration of the vibration from the axles.

## The Calculation Model

The carrying structure is called the “body in white”, a suggestive name considering its functional role. Currently, the construction of the car body considered self-supporting are those where the body includes as a subset the self-supporting structure (framework, systems of rack and plates that take the mechanical aforementioned stress, having attached by hinge parts bearing doors, hood etc).

Preparation of the model was done according to the study objectives by the following steps:

- the geometry was imported from the database;
- the geometry was prepared for finite element meshing;
- finite element meshing;
- materialization of links between parts (bolts, welds, sealants, solder points etc.).

Meshing the car body for the “body in white” is based on the geometry of the car shown in Fig. 1.

Table 1 presents the characteristics of the car body materials used for calculation.

The stucked connections (structure/mastic) is represented by volume elements of HEXA type; the battery and its mass (17.13 kg) is defined by elements of volume.

Representation of threaded connections (RBE2) integrates the diameter of seat washer that meets its technical definition. Representation of welds is carried out by

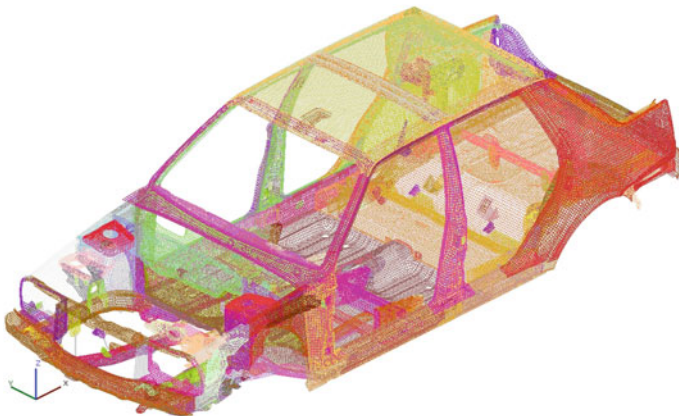


**Fig. 1** Meshing of car body

**Table 1** Characteristics of car body materials

Material	Modulus of elasticity (E) (N/mm <sup>2</sup> )	Poisson coefficient (ν)	Density (ρ) (kg/m <sup>3</sup> )
Steel	$2.1 \times 10^5$	0.29	$7.89 \times 10^3$
Aluminium	$7 \times 10^4$	0.33	$2.7 \times 10^3$
Glass	$6 \times 10^4$	0.22	$2.6 \times 10^3$
Sealant for windscreen	$3.2 \times 10$	0.45	$1.8 \times 10^3$
Sealant for roof	25	0.45	$1.8 \times 10^3$

the principle “non-coincident nodes”, integrated into the ANSA pre-processor software. These links are of type: RBE3—HEXA—RBE3 (Donley et al. 2002a).

## The Dynamic Study

The dynamic analysis involves the following steps:

- description of axle’s fixing points on “body in white”;
- analysis of inertances the points of stress input on the axles;
- analysis of vibrator transfer functions based on excitation points (axle’s supports), to the main areas of the car body.

Analysis of the modal base of a car body model was realised by calculations in the (0–250 Hz) frequency range. Calculations were performed with NASTRAN (SOL 103 and SOL 108), integrating the static adjustment of global modes, to consider their own modes with a constant reduction in value of 3 % (Donley et al. 2002b).

For each account (inertances, transfers, flexibility), it was applied a unified stress on three directions OX, OY, OZ.

The excitation points of the car body on the rear axle are shown in Fig. 2.

Next will be presented only to the analysis related to “bearing point A”, which is considered representative for the results and conclusions of study.

The experimental data acquisition was performed in the three directions of the excitation zones, and Fig. 3 presents these determinations for the bearing point A (Conti et al. 1992).

The inertance of a point is the rate between local acceleration and force ( $\frac{\gamma_i}{F_i}$ ) from the same point for all directions.

The axle support behaves like a resort and the inertance in this point is:

$$\frac{\gamma_i}{F_i} = \frac{\omega^2 \cdot x}{k \cdot x} = \frac{\omega^2}{k} \quad (1)$$

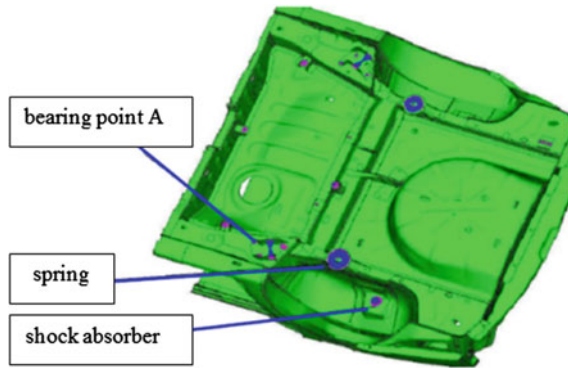


**Fig. 2** The excitation points of the car body for the rear axle area

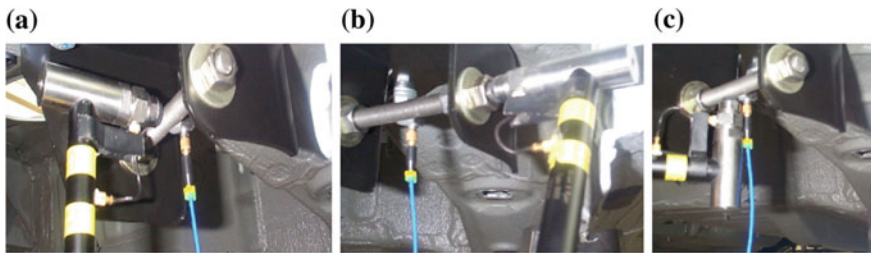


**Fig. 3** Experimental determinations for the point A. **a** OX direction. **b** OY direction. **c** OZ direction

The inrtance represented in decibels is expressed by the relation:

$$R\gamma(dB) = 20 \cdot \log\left(\frac{\gamma}{F}\right) \tag{2}$$

with  $\gamma$  representing the acceleration in  $(m \cdot s^{-2})$  and  $F$  representing the excitation force in  $(N)$ .

Knowing the magnitude of the acceleration at the points of resonance, it could be determined the flexibility of the structure at this points, expressed in meters.

The inrtances were calculated starting from an excitation unit in the three directions of the rear axle mounting points on the car body.

The synthesis of these results is presented in Table 2.

To estimate the importance of the calculated or measured inrtance, it is compared with the curve of ISO equivalent stiffness; this curve corresponds to an average calculated rate for a structure that has a variable stiffness depending on frequency.

**Table 2** Car body stiffness in the mounting points of the rear axle

Point A	Direction	Calculated dynamic stiffness (N/m)	Calculated average stiffness (N/m)
Right bearing of the rear axle	OX	2.23E + 07	8.64E + 06
	OY	3.37E + 06	5.36E + 06
	OZ	1.37E + 07	9.63E + 06

This curve is drawn using the following formula:

$$R_k(\text{dB}) = 20 \cdot \log\left(\frac{\omega^2}{K}\right) \tag{3}$$

with:

- $R_k$  stiffness (dB)
- $\omega = 2\pi v$  pulsation (Hz)
- $K = \text{ISO}$  stiffness (N/m)

A value of “ISO-stiffness” of  $10^7$  N/m is a value frequently used by carmakers for fastening supports of axles on the car body.

The inertance’s median curves must be under the dynamic stiffness imposed by the rules, as could be observed in Figs. 4, 5 and 6 presented the curves of inertance of the rear axle mounting bracket on the body for three directions OX, OY, OZ.

Figure 7 shows the curve of flexibility in the mounting support of the rear axle to the car body for OZ axis.

Analyzing the curves of flexibility it was obtained maximum deformation amplitudes for frequency of 25 Hz on direction OX and OY and 22 Hz on direction OZ. Thus, none of the three flexibilities is not signaled, by computing, to be dangerous in overcoming the elongation or the elastic limit of the board.

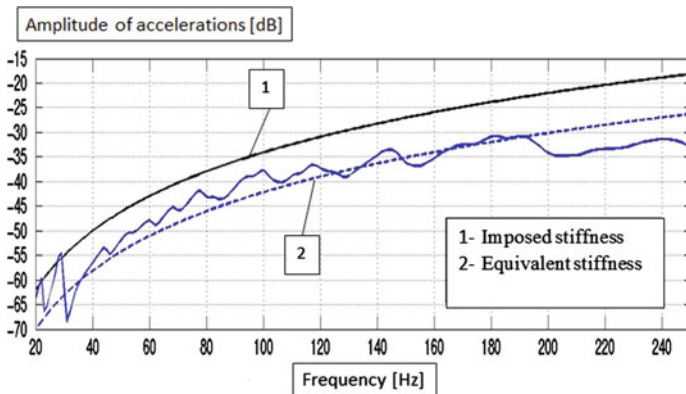


**Fig. 4** Inertance’s curves of the mounting support of the rear axle to the car body for OX axis

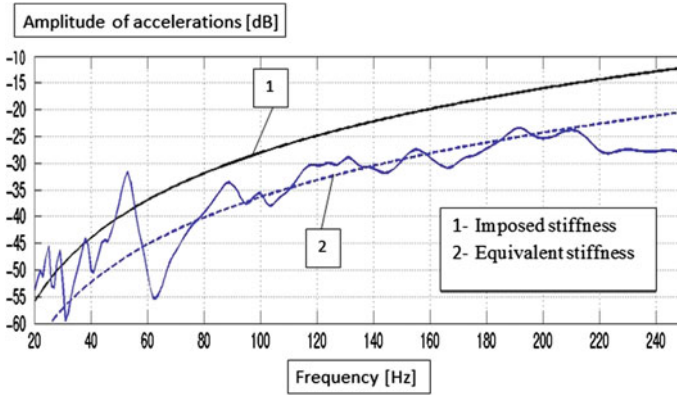


Fig. 5 Inertance’s curves of the mounting support of the rear axle to the car body for OY axis

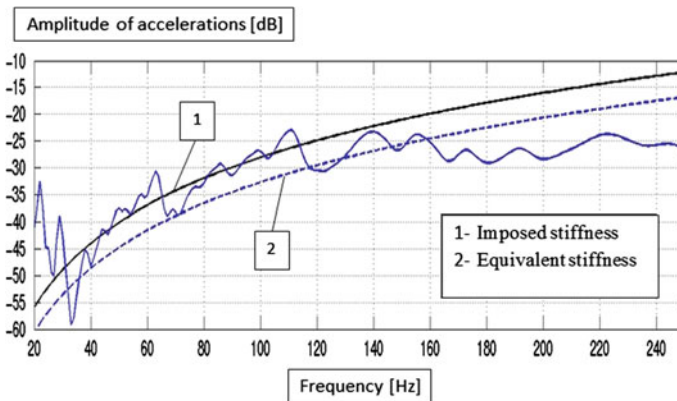


Fig. 6 Inertance’s curves of the mounting support of the rear axle to the car body for OZ axis

The greatest flexibility is on the direction OZ of  $7.2 \times 10^{-5}$  m.

Given the elastic limit of steel of 0.2 %, it is obtained a deformation of  $3 \times 10^{-3}$  % for a 1.5 mm thick sheet used in this mounting of the rear axle.

The flexibility of  $7.2 \times 10^{-5}$  m is well below the elastic limit of 0.2 % for treated steels and of 2 % for untreated steels.

Calculation of frequency response allows predicting the dynamic behavior of structures subjected to a forced excitation. The inertance characterizes the dynamic rigidity of the system in some points, being defined by an acceleration induced to a point by an unitary excitation in this point.

Knowing the inertance is so important at the points of excitation or fixation for a functional structure, where appears the main vibrator transfer. In the excitation or fixation points there are inserted filter elements in order to alleviate the amplitude of vibration depending on frequency.

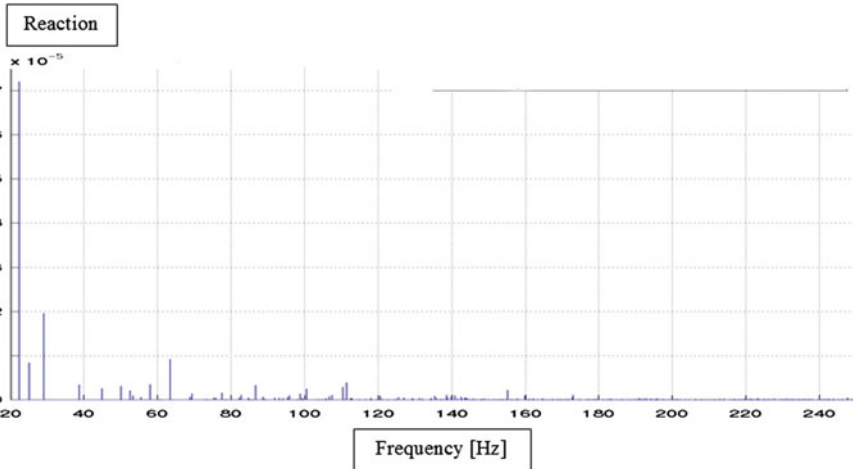


**Fig. 7** The curve of flexibility in the mounting support of the rear axle to the car body for OZ axis

The analysis of frequency response consisted in validating the structure in relation to the level of vibration to ensure that the frequency response is not too high during a forced stress. The analysis also allow the identification of areas sensitive to excitations entering in the structure and to estimate its ability to filter them.

## Conclusions

Calculation of frequency response allowed estimating the dynamic behavior of a structure subjected to a forced excitation. In most of Renault specifications, this calculation is called “inertance” and characterizes the dynamic or acoustic stiffness of a system in some points. It is defined by the induced acceleration of a point by a unit excitation at this point. The inertance is an important parameter because it allows evaluation of the power induced in the structure that is transmitted to the rest of the structure.

The results of calculation were compared with those determined experimentally on the test bench and with those stipulated by the specifications. To estimate the significance of calculated or measured inertance, it was compared with some equivalent stiffness curve, corresponding to an average level foreseen for that structure.

Determination of inertance is important at the points of excitation or fixing a functional structure, where the main transfer is carried vibrator. Such frequency response calculation therefore consisted in validating structure in relation to the level of vibration and ensure that it (frequency response) is not too high a forced



request. It also allows identification of sensitive areas excitations that enters the structure and assess its ability to filter them.

## References

- Donley M et al. (2002a) MSC Nastran Enciclopedia  
Donley M et al. (2002b) Basic dynamic analysis user guide, MacNeal Schwendler Corporation, Santa Ana  
Conti P et al. (1992) Test/analysis correlation using frequency response functions. IMAC X, San Diego, USA

# Simulation of the Air Conditioning Curtains with Turbulent Circular Jet Flows Inside the Cabin Vehicle Using ANSYS CFD

Vasile Caunii and Adrian Sachelarie

**Abstract** Under the current economic conditions, the simulation of the operation of an assembly with the help of a dedicated software is of a great importance for all the automobile manufacturers. This saves money substantially, because it no longer performs physical prototypes, and it will be known from the beginning whether or not it functions within the required parameters. The implementation of an HVAC air system with turbulent circular jet flows for a car is a challenge, as it embeds refrigeration system and heating system components, and last but not least the system mixing the hot air and cold air with the system of the air jet curtains. It is very important to know how the air currents will circulate inside the binnacle, and a solution to this problem is the simulation in ANSYS CFD.

**Keywords** HVAC · Simulation · ANSYS CFD · Air curtain system

## Introduction

Under the conditions of the fierce competition in the market of the HVAC ventilation and air conditioning systems, it is intensely sought a solution for reducing the time and cost of design, and for its development and implementation. A decisive factor is the CFD (Computational Fluid Dynamics) simulation, as it allows us to view the operation of the system without having to build a prototype, to perform various tests and optimizations.

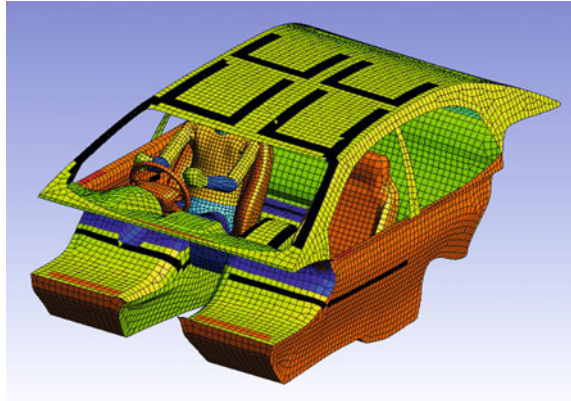
---

V. Caunii · A. Sachelarie (✉)

Department Automotive and Mechanics, Technical University  
“Gheorghe Asachi” of IASI, Bd, Dimitrie Mangeron Nr.43,  
700116 Iasi, Romania  
e-mail: adrian.sachelarie@tuiasi.ro

V. Caunii  
e-mail: vasilecaunii@gmail.com

**Fig. 1** Layout of the air conditioner curtains with turbulent circular jet flows



It was thus necessary to build and test a ventilation and air conditioning system for a car, to allow the independent cooling and heating of each seat inside a car by using air conditioning curtains with turbulent circular jet flows.

The principle scheme of such a system is presenting in Fig. 1.

## Study Description

The study analyses, from the point of view of the flow and speed, the air conditioning jets in an HVAC system with turbulent circular jet flows mounted inside a test vehicle, on the upper side and also on the lower side of the cabin, Fig. 2.

This air conditioning system has been designed in order to offer the maximum thermal comfort for each seat of the car, depending on the occupant's preference. We wanted every room to be heated or cooled independently, the close areas to influence each other as little as possible, and in case a seat is not occupied, the air curtains with turbulent circular jet flows are supplied with air from the outside up to a point, then they use the recirculated air in order to save energy.

**Fig. 2** Air curtains with turbulent circular jet flows, upper side



For the design we started from the mathematical model of a turbulent circular jet flow, which was extended to a model of air jet curtain. After calculating the numerical values for the sizing of the turbulent circular air jet curtain, we started to simulate their operation by using software ANSYS.

### The Mathematical Model of a Turbulent Circular Jet Flow

The turbulent circular jet flow appears when a fluid passes through a circular hole in another fluid, like in the Fig. 3.

Laboratory observations showed that all the turbulent circular jet flows have the same opening angle, opening hole (d) and injection speed (U) irrespectively of the fluid (water, air or other). The universal value is 11.8°, the result being a radius/distance ratio of 1/5 (Cushman-Roisin et al. 2013):

$$\tan 11.8^\circ \approx \frac{1}{5} \tag{1}$$

Therefore, for all the turbulent jets we will have:

$$R = \frac{1}{5} \cdot x \tag{2}$$

where: R—jet radius at distance x.

If the nozzle diameter is d, then the initial radius of the jet will be d/2. To simplify the shape of the above mentioned formula, the origin of the jet shall be at the distance:

$$\frac{5 \cdot d}{2} = 2.5 \cdot d \tag{3}$$

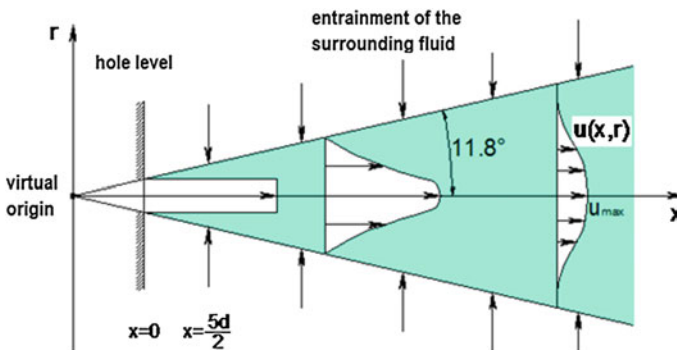


Fig. 3 Scheme of a turbulent circular jet flow (Cushman-Roisin et al. 2013)

The origin of  $x$  axis can be considered as being the virtual origin of the jet starting from a precise point.

The structure of the speed along a turbulent circular jet is shown in Fig. 4a and b, where:  $d$ —hole diameter;  $x$ —distance along the jet centreline;  $r$ —radial distance from the centreline;  $r_{1/2}$ —radial distance where the speed decreases to the half of the centreline;  $U$ —average speed as a function of distant  $x$ , along the jet;  $U_j$ —jet speed in the hole;  $U_0$ —jet speed along the centerline depending on  $x$ .

So, the speed profile inside the jet is expressed as:

$$\frac{5 \cdot d}{2} = 2.5 \cdot du(r) = u_{\max} \cdot \exp\left(-\frac{r^2}{2 \cdot \sigma^2}\right) \tag{4}$$

representing the profile of the bell curve with the standard deviation  $\sigma$  and the maximum value of  $u_{\max}$ .

The speed along the jet centerline varies inversely compared to the distance along the jet, so the average speed is:

$$\bar{u} = \frac{1}{\pi \cdot R^2} \cdot \int_0^\infty u \cdot (2 \cdot \pi \cdot r \cdot dr) = U \cdot \frac{5 \cdot d}{2 \cdot x} = \frac{u_{\max}}{2} \tag{5}$$

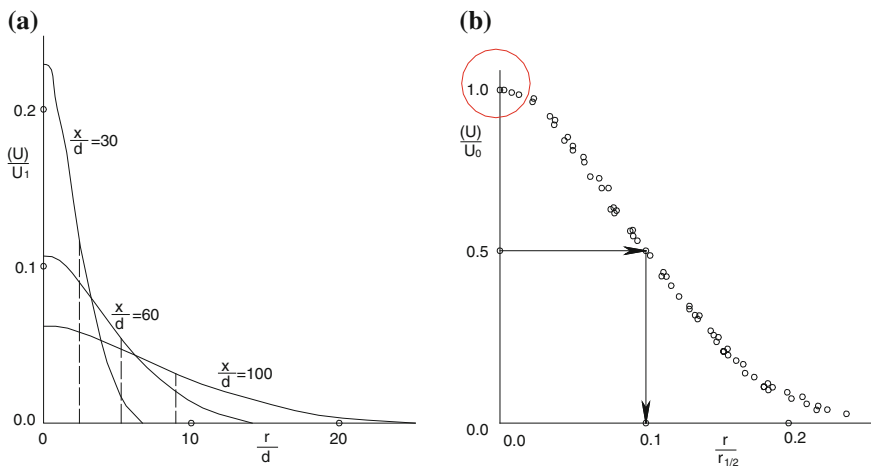


**Fig. 4** **a** Radial profiles of the axial average speed in a turbulent circular jet and **b** axial average speed compared to distant radial in a turbulent circular jet (Cushman-Roisin et al. 2013)

### Model of the Curtain with Turbulent Circular Air Flows

Starting from a turbulent circulant jet of air we can have an air curtain composed of jets if we accomplish the following conditions: the air jets originate along the same axis; the air outlet holes are equal; the distance between the holes is equal and it allows the overlapping of the jets; the initial velocity of the jet must be sufficient to ensure its propagation Fig. 5.

Starting from these conditions, the following is requested:

- The minimum distance between the turbulent circular jets that should form de curtain is 10 cm = 0.1 m;

$$R = \frac{1}{5} \quad x = \frac{1}{5} \cdot 0.1 = 0.02 \text{ m} \tag{6}$$

- In order to obtain the maximum thermal comfort the jet speed must be between 0.1 m/s and 0.4 m/s;
- The maximum x distance at which the air curtain should operate is 0.5 m.

Under the condition that:

$$\frac{x}{d} = 100 \tag{7}$$

It results:

$$d = \frac{x}{100} = \frac{0.05}{100} = 0.005 \tag{8}$$

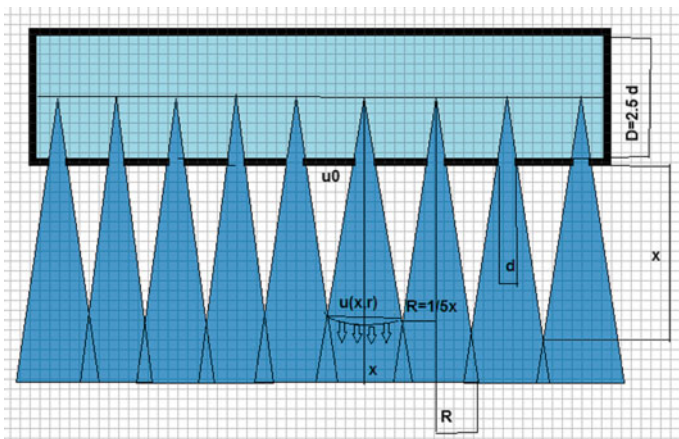


Fig. 5 Creation of the air conditioning curtain with turbulent circular jets

The initial jet speed must be 0.4 m/s and it can descend until 0.1 m/s in order to be within the thermal comfort limits according to the above figure.

Due to the condition that the origin of the jet should be at  $2.5 \times 0.005$  (hole diameter) = 0.0125 m, we choose for the upper curtain the diam.  $D = 40$  mm or 0.04 m and for the lower curtain  $D_1 = 30$  mm or  $D_1 = 0.03$  m. Both diameters allow that the virtual origin should be as close as possible to the pipe axis.

## Simulation in ANSYS

In this paper we present the simulation of the air conditioning curtains with circular turbulent jets of air conditioning at the top, above the hand because the distance from the body segments (arm, forearm, hand) is very different. In this case we used a model of the hand consisting of 3 segments: arm, forearm and hand to view properly the flow of the turbulent circular air conditioning jets. We have been particularly interested in viewing the jets' speed and how they interact with the hand.

In order to get a sense of human thermal comfort the simulation must meet the following conditions: the speed while exiting the holes should be 0.4 m/s; the distance between the arm and the tubing must be up to 0.4 m; the distance between the holes must be of 0.025 m in order to have a curtain of air condition circular and turbulent jets.

The results of the analyses are reported in the Figs. 6, 7, 8, 9, 10 and 11.

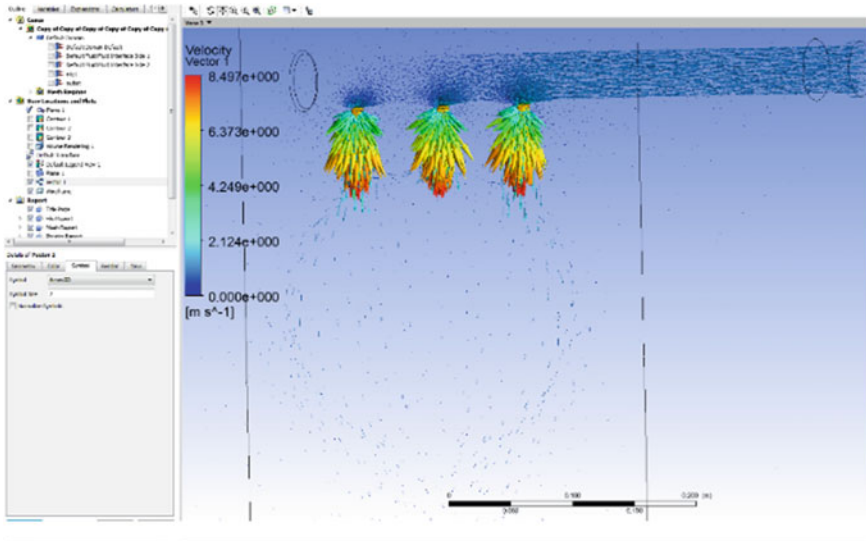
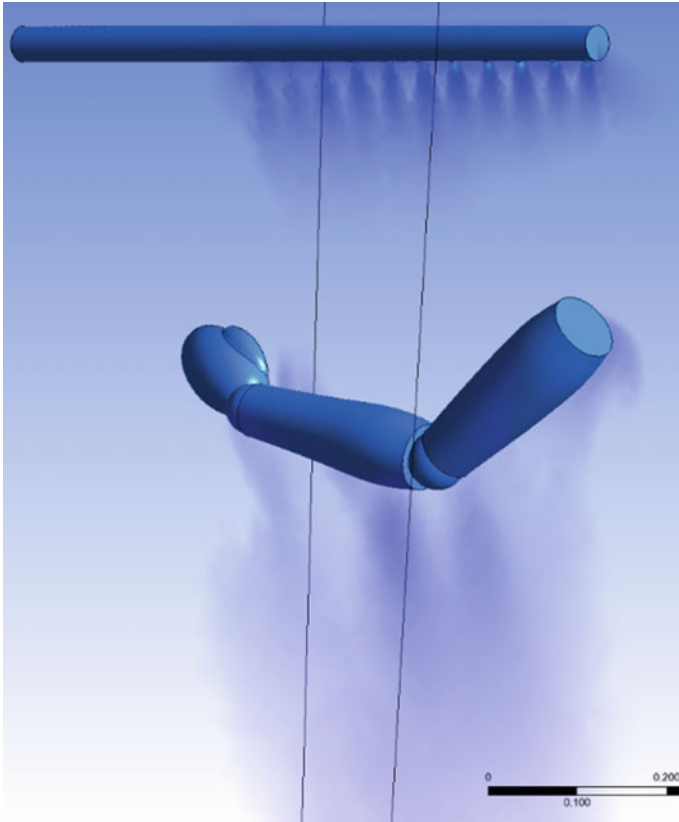


Fig. 6 Tubing of the air curtain with turbulent circular air jets



**Fig. 7** Creation of the curtain from turbulent circular jets

In Fig. 7 we can see how the turbulent circular jets are combined and they make a curtain at a distance of about 0.1 m.

In Fig. 8 we have the interaction way of the air currents of the curtain with turbulent circular conditional air jets with the hand at a distance of 0.4 m (the least favorable case).

In Fig. 9 the simulation in ANSYS shows us a cross-sectional view of the curtain with turbulent circular air jets and the way in which the air wraps the hand.

In Fig. 10 we can see the variation of the air conditioning pressure jets of the curtain relative to the contact surfaces. Note that the pressure has a uniform distribution and this is another advantage of this air distribution system.

Another analysis performed in ANSYS is the analysis of the velocity of the air jets and of how they interact with the hand. This analysis is shown in Fig. 11 and we see that the curtain jets keep their speed relatively constant.



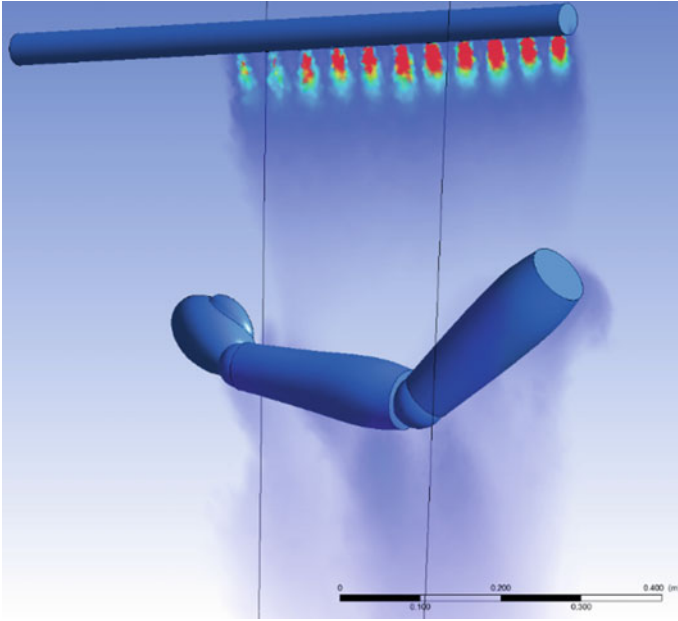


**Fig. 8** Interaction between the turbulent circular jets curtain and the hand

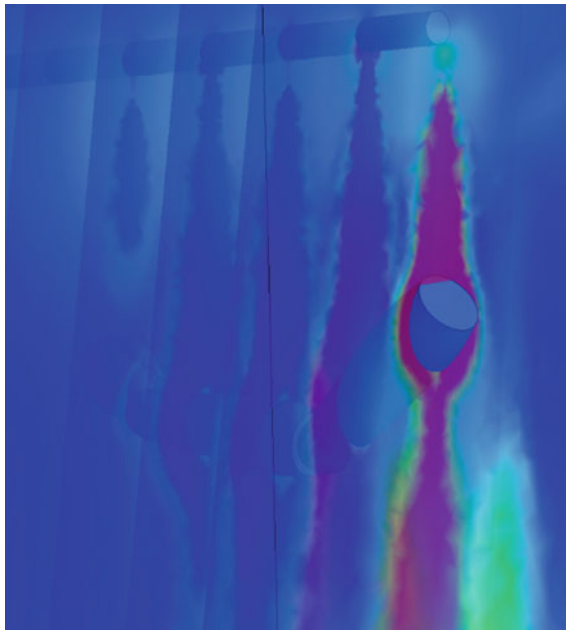


**Fig. 9** Cross-sectional view of the curtain's jets

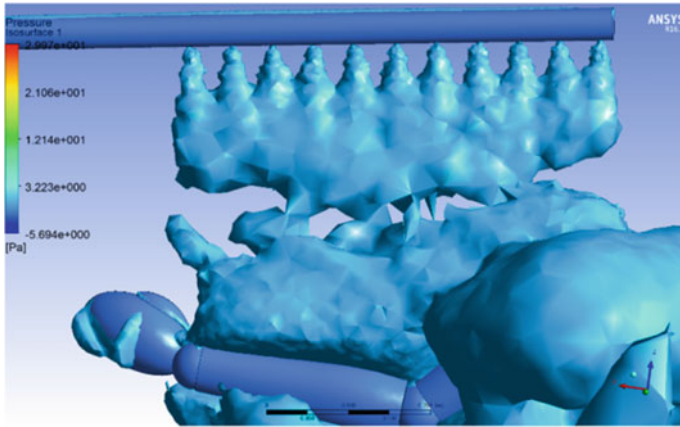


Fig. 10 Pressure of the air conditioning jets curtain regarding the contact surfaces

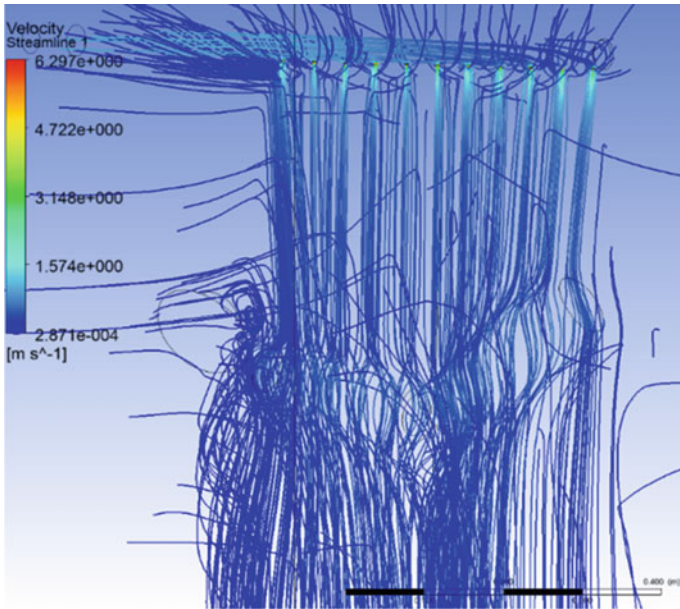


Fig. 11 Flow of the turbulent circular jets—side view

## Conclusions

The CFD simulation in general, and in ANSYS FLUENT in particular, makes available a very strong and efficient tool that, in addition to saving time and money, offers us a quite complete vision of the phenomena taking place in such a project.

The system of the curtains with turbulent circular air conditioning jets offer the following advantages:

Simple construction.

High thermal comfort due to the almost ideal speed of the air currents.

The inner volume is equally covered with jets having the same intensity and temperature.

The thermal comfort sensation will also be enhanced by the fact that this system lacks the effects of the air current or the dry-eye syndrome.

The solution of the air conditioning curtains results in the simplification of the construction of the HVAC unit (the unit that mixes warm air with cold air).

## References

Cushman-Roisin B, Gualtieri C, Mihailovic, TD, (2013) Environmental fluid mechanics: current issues and future outlook in fluid mechanics of environmental interfaces, 2nd ed. CRC Press, Boca Raton, pp 35– 39

Information on: <http://www.ansys.com/Products/Simulation+Technology/>

Information on: <http://www.ansys.com/staticassets/ANSYS/staticassets/>

# The Influence of Exhaust Backpressure Upon the Turbocharger's Boost Pressure

Levente-Botond Kocsis, Dan Moldovanu and Doru-Laurean Băldean

**Abstract** The authors present their studies that were conducted in order to analyze the behavior of the turbocharger of a compression ignition engine while the exhaust was obstructed at different levels to simulate the influence of different levels of exhaust backpressure upon the charging device. The goal was to measure in what way and to what extent is the behavior of the turbocharger influenced by the backpressure caused by a flap, introduced in the exhaust line of the analyzed engine. Tests were carried out on a four cylinder 1.9 dm<sup>3</sup> turbocharged Diesel engine fitted to an active dyno. A special flap in the exhaust line, operated by PUMA Open was used to simulate different backpressure values from 0 up to 570 mbar additional pressure. During the test, at each engine speed power, torque, fuel consumption, intake pressure, room pressure, intake pressure and temperature before and after turbocharger was measured and stored. The results of the investigations show a clear dependence of the exhaust backpressure related to turbocharger performances. Exhaust lines can be tuned for certain engine speed domains which are given by the internal combustion engine's destination.

**Keywords** Turbocharged engine · Backpressure · Boost pressure · Engine speed

## Introduction

Engine exhaust backpressure is defined as the exhaust gas pressure that is produced by the engine to overcome the hydraulic resistance of the exhaust system in order to discharge the gases into the atmosphere.

At increased backpressure levels, the engine has to compress the exhaust gases to a higher pressure which involves additional mechanical work and/or less energy extracted by the exhaust turbine which will affect intake manifold boost pressure.

---

L.-B. Kocsis (✉) · D. Moldovanu · D.-L. Băldean  
Technical University of Cluj Napoca, Cluj Napoca, Romania  
e-mail: levente.kocsis@auto.utcluj.ro

The increased exhaust temperature can result in overheating of exhaust valves and the turbine. An increase in NO<sub>x</sub> emissions is also possible due to the increase of engine load (Kesgin 2005).

Turbochargers typically use engine lubricating oil as their lubricating and cooling medium. Excessive exhaust pressures can increase the likelihood of failure of turbocharger seals, resulting in oil leakage into the exhaust system. VERT recommended back pressure limits are given for a range of engines sizes (Mayer 2004).

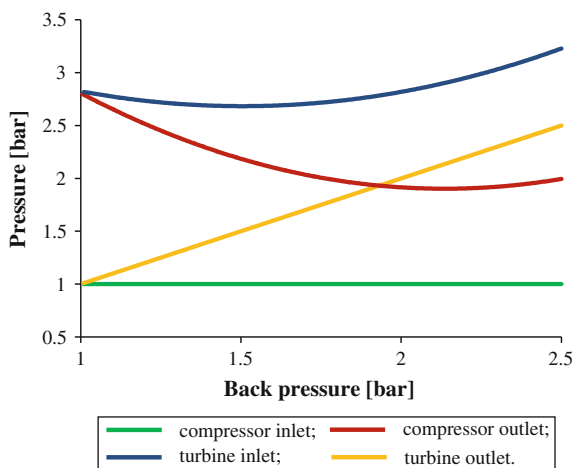
Peter Hield concludes in his main findings (Hield 2011) that by raising the backpressure in the exhaust, the pressure ratios across the turbocharger compressor and turbine decreases, reducing the mass flow of air through these components and thus the air available to the engine. He also states that the compressor and turbine operating points describe distorted ellipses approximately centered on the steady state operating point, this being due to the inertia of the rotor. The shapes of the orbits follow the shapes of the compressor and turbine maps, and the distortion becomes increasingly pronounced as the amplitude of the fluctuations in the exhaust increases (Watson and Janota 1982).

One of the main conclusion of his study is that exhaust gas temperature increases significantly with increasing back pressure due to the increased power required (to overcome the additional pumping work) and the reduced air flow (Grünwald 1980). In addition, imposed back pressure fluctuations cause large exhaust temperature fluctuations, which further increases the maximum temperature and also induces thermal cycling. These effects lead to increased wear and reduced reliability, and can cause thermal failures (Heywood 1988).

In case of operating steady state, the pressures at the inlet and outlet of the compressor and turbine versus backpressure will take the shape shown in Fig. 1.

The important quantity in Fig. 1 for both the compressor and the turbine is the pressure ratio, which decreases in both cases. The reduced turbine pressure ratio means that less power can be extracted from the flow, resulting reduced temperature

**Fig. 1** Pressure curves operating steady state (Hield 2011)



difference and reduced mass flow. This then means that the power provided to the compressor will be reduced, reducing the increase in gas pressure across the compressor, further reducing the mass flow through the engine.

## Objectives

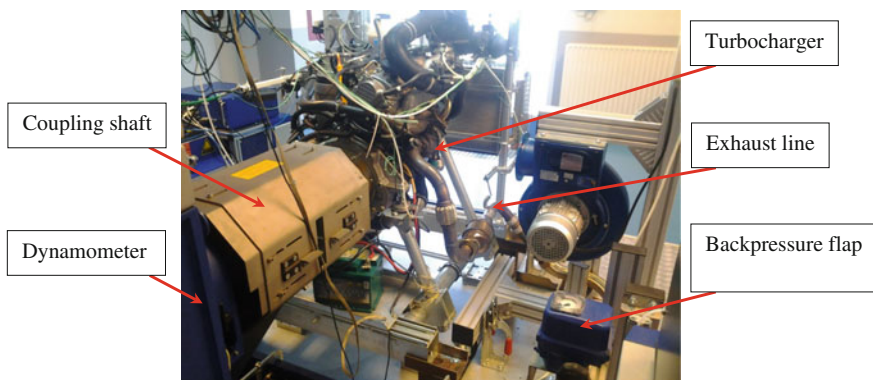
The main goal was to measure and analyze in what way and to what extent is the behavior of the turbocharger influenced by the value of backpressure caused by a flap, introduced in the exhaust line of the analyzed engine, which can simulate the backpressure caused by exhaust line geometry.

## Methodology

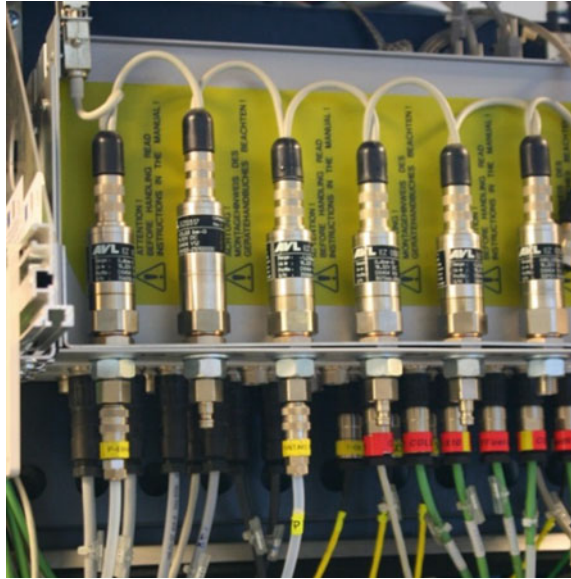
Tests were carried out in the new test facility of the Technical University of Cluj Napoca, commissioned with the latest generation test equipment. Equipment used includes a four cylinder 1.9 dm<sup>3</sup> turbocharged Diesel engine (AWM code) fitted to an active dynamometer (Fig. 2).

In order to be able to quantify the net difference in performance, the mufflers, which induced a total backpressure of about 400 mbar at its highest point, were separated from the exhaust. To control the throttle an AVL THA 100 was used, while fuel conditioning and metering was done by AVL's 735 and 753 units. The pressure sensors used were AVL pressure transducers (Fig. 3), with ranges from 0.25 to 6 bar absolute pressure, their characteristics being shown in Table 1.

The whole test room was air conditioned, having a quasi-static room temperature. Each equipment, sensor and the engine itself was controlled by the PUMA



**Fig. 2** Experimental setup

**Fig. 3** Pressure transducers**Table 1** Technical data for APT100 pressure transducers

Parameter	Value
Typ. total error band (TEB)	0.35 % F.S. at 0 to +60 °C
Rise time	Approx. 1 ms; 10 to 90 % PN
Long term stability in service	Typ. 0.1 % F.S. in 18 months at 25 °C
Ambient temperature	-40 to +120 °C
Temperature of the medium	-40 to +120 °C
Output signal	4–20 mA
Electrical connection	DIN 43650-A (IP65)
Pressure connection	G 1/4 inch female
Protective class	IP 65 according to DIN 40050
Supply	9–2 V DC

Open main operating system. A special flap in the exhaust line (Fig. 4), operated by PUMA Open was used to simulate different backpressure values from 0 up to 570 mbar additional pressure. This was the highest recorded backpressure value before malfunction of the test rig appeared. The unit is used to set the exhaust backpressure of combustion engines up to a power of 400 kW, with operating temperature up to a maximum of 650 °C. The exhaust gas pressure was adjusted during full load operation of the actual tested engine (Fig. 5).

In order to assure repeatability of the power test, a test cycle was conceived. This cycle included 10 measurements at different engine speeds according to the engine's specification of idle speed, maximum torque speed, maximum power



Fig. 4 Backpressure control flap (Zagorski 2003)

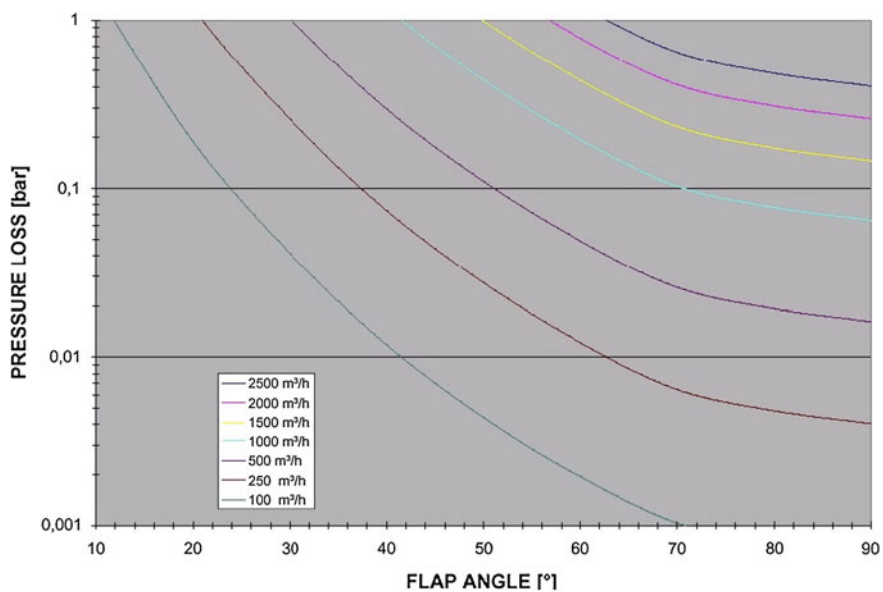


Fig. 5 Pressure loss characteristics, depending on flap angle and exhaust flow rate (Zagorski 2003)



speed and maximum speed of the engine. During the test, at each engine speed power, torque, fuel consumption, intake pressure, room pressure, intake pressure and temperature before and after turbocharger was measured and stored. The measured data was then processed with specialized software and interpreted.

## Results and Discussions

The current study was limited to steady state operation, to avoid the simultaneous change of multiple parameters such as EGR rate, thermal inertia of different systems, etc. Furthermore, the study is not able to give an answer on how will the performance of the turbocharger be affected when any of the exhaust emissions reducing equipment is positioned upstream or downstream of the turbocharger.

As one would predict, measured backpressure rises as flap angle gets closer to 90°, but backpressure value is also a function of engine speed and gas flow, that is why, as it can be seen in Fig. 6, the shape of backpressure curve is influenced by torque curve. At peak engine torque injected fuel quantity per cycle reaches maximum level, resulting in high gas flow values, while after reaching peak power (at 3100 rpm), ECU lowers fuel supply value resulting in lower mass flow values and lower backpressure values as well.

By the turbocharger view of point the results of the investigations show a clear dependence between the exhaust backpressure and turbocharger performances. However, this is not a linear variation. Compressor outlet pressure rises until peak torque is reached, then the wastegate valve maintains the pressure qvazi-constant up to peak power point.

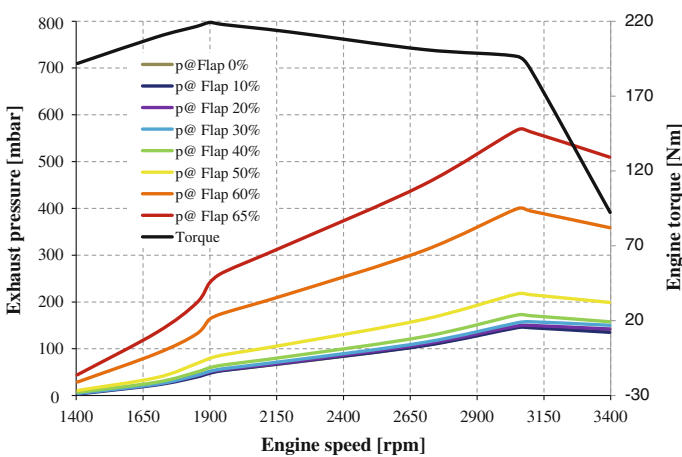


Fig. 6 Backpressure versus flap angle

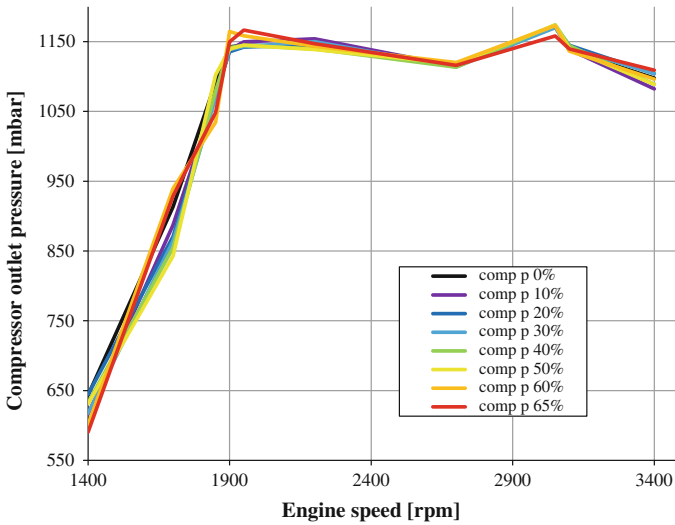


Fig. 7 Compressor outlet pressure versus engine speed, depending on flap angle

While with no initial backpressure in the exhaust line the boost pressure curve raises constantly (Fig. 7), almost linear up to the maximum torque speed, adding some backpressure introduces a deflection from the initial curve, lowering the boost pressures with 8 % at most, for a backpressure greater with 50 % than initial. In this engine speed range, when the backpressure was further raised up to 250 % of the initial value, behavior of the turbocharger changed and two inflection points appeared (Fig. 8). Boost pressure was beginning at a lower value, but then was

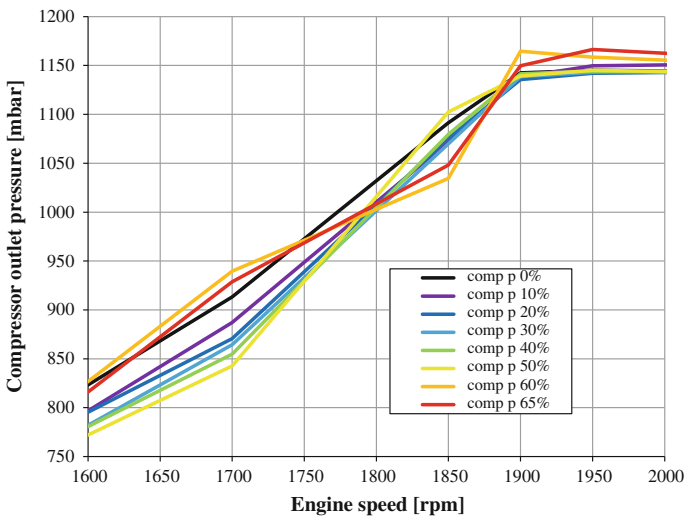


Fig. 8 Compressor outlet pressure restricted to a narrow engine speed domain

growing rapidly and for 100 rpm it was higher than with no initial backpressure. It was swinging back again and became lower than the reference boost pressure, so that it had culminated in greater values again, at maximum torque speed, where wastegate was beginning to open. Up to 2600 rpm boost pressure was somewhat greater for backpressures up to 10 % higher than reference and up to the maximum power engine speed all pressure curves except one were tending to meet in one point. The boost pressure curve belonging to the highest backpressure reached at this point a value 2 % less than all the other.

## Conclusions

Although boost pressure in the studied points and conditions did not have values all the way lower or greater than the reference, it can be stated that backpressure influences turbocharger performance at a great extent. The investigations reveal that exhaust lines can be tuned for certain engine speed domains which are given by the internal combustion engine's destination.

## References

- Grünwald B (1980) Teoria—Construcția și Calculul Motoarelor pentru Autovehicule Rutiere. Editura Didactică și Pedagogică, București
- Heywood JB (1988) Internal combustion engine fundamentals. McGraw-Hill, New York
- Hield P (2011) The effect of back pressure on the operation of a diesel engine. Maritime Platforms Divisions, Defence Science and Technology Organisation, Canberra
- Kesgin U (2005) Effect of turbocharging system on the performance of a natural gas engine. Energy Convers Manag 46:11–32
- Mayer A (2004) Number-based emission limits, VERT-DPF-verification procedure and experience with 8000 retrofits. VERT, Switzerland
- Watson N, Janota M (1982) Turbocharging the internal combustion engine. The Macmillan Press Ltd, Houndmills
- Zagorski CH (2003) AVL AT1619 5490M00B exhaust back pressure unit, AVL operating manual

# Investigating Maintenance Procedures for Engine Air Filters

Marius Toma

**Abstract** Most vehicles in operation are equipped with air filters made of cellulose fiber. Dust particles that are not retained by the air filter reach inside the engine, intensifying its wear. The air filter condition affects economic performance, power and reliability of the internal combustion engine. Properly maintenance of the air filters positively affects engine durability and reduces maintenance costs. The air filter condition is assessed by the restriction generated. This paper investigates to what extent the air filters replaced according to the maintenance schedule recommended by the manufacturer (depending on the distance traveled by the vehicle while using the air filter or the operating time of the air filter) were replaced at the appropriate time. Restriction values generated by seven types of new and used air filter are being presented. The results show that replacing filters according to the maintenance manual and repair is made in most cases prematurely or too late. The paper also draws attention on the default mounting of the air filter that could lead to its damage and consequently allowing unfiltered air entering the engine.

**Keywords** Air filters • Restriction • Filters damage • Maintenance

## Introduction

Most vehicles in operation are equipped with air filters made of cellulose fiber. These are original or aftermarket air filters. Maintenance procedures for engine air filters refer to the regular activity of removing and mounting the filters into their housing. In literature, engine intake filters have a recommended service life of 48,000 km under normal driving condition (Barris 1995; Bugli and Green 2005). The recommendations provided in the maintenance and repair handbooks regarding air filter replacement intervals varies widely. Air filters that fit a vehicle' engine are

---

M. Toma (✉)

University Politehnica of Bucharest, Splaiul Independentei 313, Bucharest, Romania  
e-mail: marius.toma@upb.ro

original or aftermarket ones and have different constructive particularities. However, the replacement of air filters is usually made every year or after 15,000 km (Toma and Bobâlca 2015) without taking into account their real technical condition.

Another aspect regarding maintenance activity is related to removal and then mounting the air filter. Mounting the air filter into filter housing had to be done properly in order to ensure a good seal between filter and its housing to prevent unfiltered air entering into the engine cylinders.

According to ISO 5011 (2000), “restriction” is defined as being the static pressure measured immediately downstream of the unit under test. Multistage air cleaner—air cleaner consisting of two or more stages, the first usually being a precleaner, followed by one or more filter elements.

## Literature Overview

Air filters maintenance has two components; the mounting and removing action of the filters and determining their replacement criteria meaning the useful life of the air filters. The mounting and removing action depends on the design of air filtration system and is mentioned in the maintenance and repair handbooks of each vehicle. To determine when to replace filters multiple criteria are being used. For air filters that equip light and medium vehicles, the most used criteria are based on the distance traveled by the vehicle using that filter followed by time as the air filter has been in use. These criteria are also specified in the vehicles’ maintenance and repair handbooks and the values vary from one manufacturer to another. Toma (2014, 2015) showed that the replacement depending on these two criteria do not ensure a complete usage of air filters, although it complies with the maintenance schedule.

Typical service interval of air filters for light/medium duty vehicles under normal driving conditions is about 48,000 km (Barris 1995; Bugli and Green 2005; Thomas et al. 2013). Normal usage conditions is defined as driving on paved roads, with a dust concentration in the environment between 0.010 and 0.139 mg/m<sup>3</sup> (Barris 1995).

Another criterion for filter replacement depends on the restriction rise produced by the filter. In order to apply this criterion, air filtration system that equips motor vehicle must be equipped with a special transducer.

Bugli (2001) states that air filter should be changed when restriction rise reaches values between 1 and 2.5 kPa for light and medium vehicles and papers (Bugli 1997, 2000; Bugli and Green 2005; Norman et al. 2009) at values of 2.5 kPa.

For heavy-duty vehicles, (Bugli 2001) recommends changing the air filter when restriction reaches 6.25–7.5 kPa.

For a 6.7 l diesel engine, the value of total restriction is 3.5 kPa for new filters and 6.5 kPa for used filters that need replacement (Powertrain Technologies N67 2009); for three diesel engines of 2, 3 and 6.7 l, air filter should be replaced when restriction reaches ~5–7 kPa at the maximum air flow point (Thomas et al. 2013).

The restriction limits are set by the engine manufacturer that recommends the total restrictions values depending on the engine type (Donaldson air intake accessories 2013). These values range between 3.7 and 7.5 kPa for large diesel engines (Jaroszczyk et al. 2004; Donaldson air intake accessories 2013).

## Preparing and Conducting the Experimental Tests

The study refers to measuring the restriction generated by new and used air filters and if they were correctly mounted into their housing. The results are used to determine if air filters were properly replaced and at the appropriate time.

The experimental tests were made on a specialized rig in laboratory conditions. The rig main parts are the air filter system, the exhaust system, air flow measurement system and air flow adjustment system. The air filter system is the one that equip Renault K9K engines and consists of the air filter housing and the intake air duct. The schematic diagram of the test rig is detailed in paper (Toma and Fileru 2015). The laboratory rig allows measuring the restriction produced by the filters, ensuring an airflow that can be measured and adjusted between 0 and 280 m<sup>3</sup>/h. Temperature, humidity and ambient air pressure are also determined.

During experimental research, air filters that equips Renault K9K engine, the 792 (50 kW), 796 and 830 (63 kW), 838 and 890 (60 kW) types were tested. These engines meet Euro 3 and Euro 4 emission standards and equip Dacia Logan vehicles produced between 2005 and 2010. For this type of vehicles, air filter replacement should be made every 15,000 km or one year for models manufactured until 2008 and every 20,000 km or two years for models manufactured after 2008 according to the maintenance and repair handbook (Dacia Logan Maintenance Manual 2006, 2009). The manufacturer requires halving the distance traveled for replacing the filters that are being used in special conditions, for example when the vehicles is operating in a dusty environment or more than 1000 km/year on vehicle track. Also, there are different recommendations regarding the replacement interval of air filters in the service stations. Not least, we must take into account that beyond the warranty period, the customer has the last word regarding the moment when air filter should be replaced.








30 air filters were tested, out of which nine were new and 21 were used. The tested air filters are classified as follows:

- By producer—there are original air filters, further labeled with OE and after-market air filters from several manufacturers, further labeled with A, B, C, D, E and F;
- By condition—there are new filters further labeled with “N” and used filters labeled with “U”.

The main characteristics of tested air filters are listed in Table 1.

For the two types of filters with precleaner, EO and E, the precleaner is not take into account in setting the filtering surface. The filtering area is represented by the

**Table 1** The main characteristics of tested air filters

Filter	Number of pleats	Filter height (mm)	Filtering material thickness (mm)	Cellulose filtering material area (m <sup>2</sup> )	Multistage air cleaner	Appearance
OE	135	70	0.41	0.60	Yes (sponge)	
A	132	58	0.41	0.71	No	
B	123	65	0.32	0.66	No	
C	126	45	0.25	0.56	No	
D	115	57	0.28	0.65	No	
E	110	63	0.31	0.62	Yes (nonwoven fiber)	
F	109	57	0.31	0.59	No	

**Table 2** The real operating data of used air filters

Filter	Exploitation conditions			Filter	Exploitation conditions		
	Mileage (km)	Operating time	Travel area		Mileage (km)	Operating time	Travel area
OE-U-1	–	1 year	Urban	B-U-3	20,000	1 year	Mixed
OE-U-2	–	1 year	Mixed	C-U-1	20,000	1 year	Mixed
OE-U-3	15,000	1 year	Mixed	C-U-2	20,000	1 year	Mixed
OE-U-4	–	1 year	Mixed	D-U-1	–	1 year	Mixed
A-U-1	9000	2 years	Extra urban	D-U-2	15,000	1 year	Mixed
A-U-2	20,000	1 year	Mixed	D-U-3	–	1 year	Mixed
A-U-3	–	1 year	Mixed	E-U-1	–	1 year	Mixed
A-U-4	–	1 year	Mixed	E-U-2	20,000	1 year	Mixed
A-U-5	14,000	2 years	Extra urban	F-U-1	5000	1 year	Urban
B-U-1	–	1 year	Mixed	F-U-2	10,000	1 year	Mixed
B-U-2	12,000	1 year	Mixed				

“–” Data not available

cellulose filtering material only. Table 1 shows the characteristics and appearance of the seven types of tested air filters. Although they are mounted on the same housing for the same engine family, they have very different characteristics.

The used filters were collected from vehicles in operation that arrived to service stations for preventive maintenance actions. Collection of used filters was made directly from their housing. After removing the air filter from the housing, the filters were placed and kept sealed in plastic bags to prevent water absorption from atmospheric air and losing the dust by shaking the filter. Table 2 shows data regarding filters usage and the environment in which the vehicle traveled using the filters.

During collection campaign, 79 used air filters were collected. The test results for 38 of them are presented in paper (Toma and Fileru 2015). Out of the 79 filters, six had deformed and broken sealing surface. This was due to incorrect mounting of new filters into their housing. The appearance of two of these filters is shown in Fig. 1. Default installation of air filters leads to damaged seal, allowing air with impurities to reach inside engine cylinders with serious consequences for engine's wear. Filters with damaged sealing surface are both original and aftermarket filters and were not tested further.

Renault K9K 792 engine with 50 kW maximum power consumes of 298.5 kg/h airflow at maximum power regime and 156 kg/h at maximum torque regime (Pană et al. 2012). The tests were made at 87.8 % of the maximum air flow consumed by the engine. Although ISO 5011 standard recommends that tests should be made at maximum air flow consumed by the engine, during this research a lower air flow was adopted for two reasons: the exhaust system of the test rig allows maximum 282 kg/h for new filters and consequently we adopted a lower rate of 262 kg/h so that used filters could also be tested. Another reason is related to the fact that under



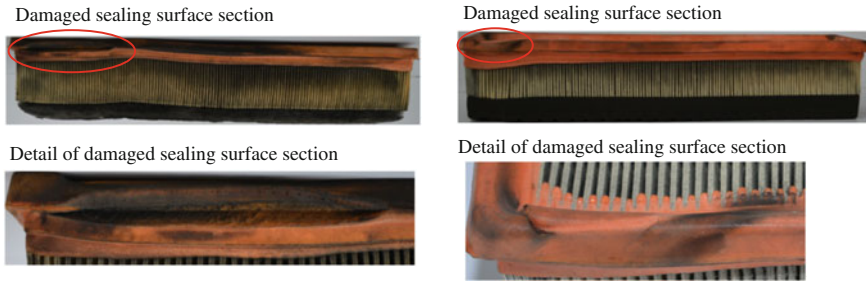


Fig. 1 Examples of damaged air filters

normal operating conditions, vehicles are rarely or never used at maximum power regime (Norman et al. 2009) and consequently we adopted an air flow adequate to high power regime, close to engine’s maximum power. Air filters have been tested in similar conditions as in paper (Toma and Fileru 2015).

ISO 5011 recommends that restriction values should be adjusted depending on the temperature and air pressure. Therefore, the temperature and ambient pressure were measured during tests.

## Results and Discussions

During experimental tests, pressure restriction produced by each filter was measured. The restriction values are plotted in Fig. 2.

New filters have produced a restriction between 3.5 and 4.7 kPa. This difference of 1.2 kPa is high given that paper (Toma 2015) recommends replacing air filters

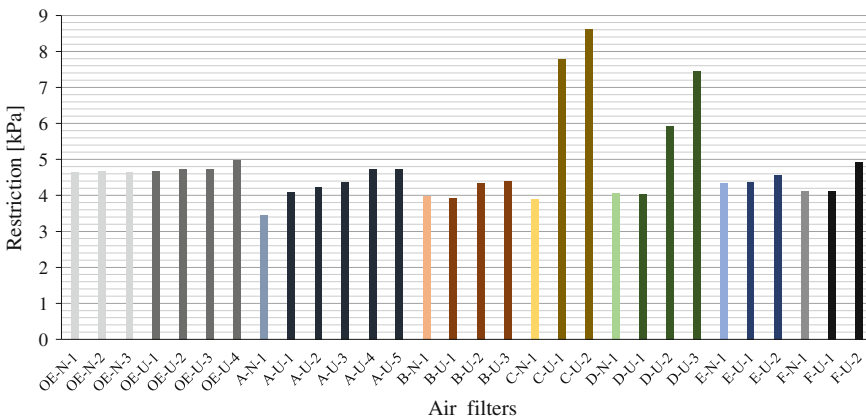


Fig. 2 Restriction generated by the air filters

when restriction increase with 1–2.5 kPa for light and medium vehicles engines. The new filter OE-U-4 produces a restriction that corresponds with the replacement time of A type used filters. The seven new filters generated restriction values in a widely range due to constructive particularities. As expected, the highest values were generated by the air filters with precleaner OE-N-2 = 4.7 kPa E-N-1 = 4.3 kPa; the restrictions of air filters without precleaner ranged between 3.5 and 4.1 kPa. The restriction value of 3.5 kPa for new filters is also mentioned in paper Pana et al. (2012). The lowest restriction was produced by filter A-N-1 = 3.5 kPa, A type filters having the largest filtering area of all tested filters and no precleaner. Yet, there could not be traced a proportional dependence between the size of the cellulose filtering surface and restriction produced by each filter.

For the same type air filters, used filters restriction is higher than that of new filters. The observation is valid for six of the seven types of filters. Regarding B type air filters, B-N-1 produced a restriction 0.057 kPa lower than B-U-1 used filter. This behavior of the filters has been presented in paper (Toma 2013) where have been tested filters that equip K7M Renault engines. This behavior is explained by the fact that new filters were tested on the laboratory rig for a short time so that the flowing passages through the filtering material could not fully form. The B-U-1 used filter is known to have been used in urban and extra urban area but no information about traveled distance were available.

The OE used filters produced a restriction rise of maximum 0.337 kPa compared to OE-N-1 filter. These filters produced low restrictions, far below of the 2.5 kPa recommended in the literature for filter replacement. UE type used filters replaced according to the maintenance schedule, were prematurely replaced before reaching their full capacity of usage.

The five used air filters A type generated restrictions between 0.647 and 1.286 kPa. A-U-4 and A-U-5 filters were replaced when they reached 1 kPa higher restriction compared to new filters. According to (Bugli 2001) these filters were replaced at the appropriate time. Still, most authors consider that replacement should be made after an increase of 2.5 kPa (Bugli and Green 2005; Bugli 1997, 2000; Norman et al. 2009). The other A type used filters were prematurely replaced. The B type used filters produced a restriction rise of maximum 0.4 kPa compared to new filters, E type of maximum of 0.238 kPa and F type maximum 0.797 kPa. These filters were replaced too early, when they could still be used.

A series of filters OE-U-1, B-U-1, D-U-1, E-U-1 and F-U-1 generated restrictions very close or even lower than restriction produced by new filters of the same type, as B-N-1 filter. F-U-1 was used only 5000 km and for the other filters there were no information available about the traveled distance. These filters can be considered almost new.

D-U-2 filter generated a restriction 1.9 kPa higher compared to new filter and is considered to have been replaced at the right time. D-U-3 filter produced a restriction 3.4 kPa higher compared to new filter, far above the recommended value for replacement in the literature. D-U-3 filter was replaced too late.

A special behavior had the C type filters. The two used filters tested showed restrictions rise with 3.88 kPa and respectively 4.72 kPa compared to that produced

by the new filter. It should be noted that these restrictions were not achieved at 262 m<sup>3</sup>/h air flow, but at a lower value of 167 m<sup>3</sup>/h. Air flow rate of 262 m<sup>3</sup>/h could not be reached by the exhaust system. These filters were severely clogged and their replacement was made too late. It should be pointed that the filtering surface of these filters is the smallest of all tested filter types. In similar operating conditions, these filters will record the fastest load with impurities.

Of the 21 used filters that were tested, 15 were prematurely replaced, A-U-4, A-U-5, D-U-2 were replaced at the right time and C-U-1, C-U-2 and D-U-3 were replaced too late.

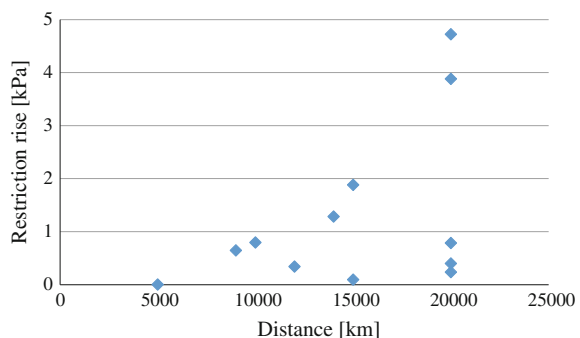
Replacing air filters prematurely affects the filtering efficiency besides the additional cost implications. (Marty 1995; Zemaitis 1998) showed that filters are increasing their efficiency as they are used, thereby engine protection against abrasive wear is increasing too. This is particularly important, since it is estimated that in 80 % of cases, the life of internal combustion engines is limited by wear consequences (Marty 1995).

Late replacement of air filters leads on the one hand to the significant increase of gaso-dynamic resistances in the air intake system of the engine. Depending on the engine type, restriction rise above the recommended limits in the literature leads to poorer dynamics performances of the vehicle. On the other hand, it occurs the risk of damaging the filtering material and the seal, leading to significantly reduced filtering efficiency.

Figure 3 shows the dependence between the restriction generated by the filters and the distance traveled by the vehicles using these filters. A slight increase trend of the restriction is noticed when traveled distance increases. Also, the filters that were used 20,000 km generated restrictions rises in a very wide area. This is explained on the one hand by the constructive particularities of the filters and on the other hand by the different environmental conditions and road infrastructure where filters were used.

Replacing air filters according to traveled distance or operating time criteria do not ensure a timely replacement, increasing maintenance costs and reducing engine's protection against abrasive wear. The replacement must be made depending on restriction rise. This is measured with a specialized transducer

**Fig. 3** Restriction depending on the travelled distance



installed into the air intake system of the engine. The transducer must be calibrated so that the restriction value indicated for filter replacement will not produce a reduction of maximum power by more than 2–3 %. This power decrease is considered acceptable in the work (Lisowski 2009).

For Renault K9K engine family, Euro 5 and Euro 6, the manufacturer fitted the air filter housing with a transducer that visually indicates the charge level of the filter with impurities. During the research, we noticed that service stations ignored this transducer indications and filters replacement was still made according to traveled distance or operating time criterion. This attitude is explained by the mistaken belief that a new air filter is better than a used one, as showed in paper (Toma and Bobâlcă 2015).

## Conclusions

Incorrect mounting of the air filter into its housing, ignoring the steps indicated in the maintenance and repair handbooks, is leading to air filter damage during its use, reducing the filtering efficiency and intensifying abrasive wear into the kinematic couplings of the engine.

New filters produced a wide range of restriction values due to constructive particularities.

New filters with precleaner produced higher restrictions than those without precleaner.

The lowest restriction was produced by the new filter with the largest filtering area. No proportional dependence is observed between the size of the surface of the filtering material and the restriction produced by each filter.

For filters of the same type, six of the seven types generated higher restrictions for used filters compared to the restriction generated by new filters.

Filters OE-U-1, B-U-1, D-U-1, E-U-1 and F-U-1 generated very similar restrictions to the new filters of the same type. These filters can be considered almost new.

Of the 21 used filters that were tested, 15 were prematurely replaced, three were replaced at the right time and another three were replaced too late.

Replacing air filters prematurely involves additional maintenance costs and reduces engine protection against abrasive wear.

A slight increase trend of the restriction is noticed when traveled distance increases.

Replacing air filters according to traveled distance or operating time criteria do not ensure a proper replacement, increasing maintenance costs and reducing engine's protection against abrasive wear.

Air filter replacement should be made according to the indication received from a specialized transducer installed into the air intake system of the engine.

**Acknowledgments** The work has been funded by the Sectoral Operational Programme Human Resources Development 2007–2013 of the Ministry of European Funds through the Financial Agreement POSDRU/159/1.5/S/134398.

## References

- Barris MA (1995) The influence of filter selection on engine wear, emissions, and performance. SAE Technical Paper Series, 952557
- Bugli NJ (1997) Filter performance requirements for engine air induction systems. SAE Technical Paper Series, 970556
- Bugli NJ (2000) Service life expectations and filtration performance of engine air cleaners. SAE Technical Paper Series, 2000-01-3317
- Bugli NJ (2001) Automotive engine air cleaners—performance trends. SAE Technical Paper Series, 2001-01-1356
- Bugli NJ, Green GS (2005) Performance and benefits of zero maintenance air induction systems. SAE Technical Paper Series, 2005-01-1139
- Dacia Logan Maintenance Manual (2006)
- Dacia Logan Maintenance Manual (2009)
- Donaldson Air intake accessories (2013) Filter indicators and gauges, filter service indicators maximize filter life
- International Standard ISO 5011 (2000) Inlet air cleaning equipment for internal combustion engines and compressors—performance testing, 2nd edn., 2000-12-01. Corrected and reprinted 2001-07-15
- Jaroszczuk T, Pardue C, Holm E (2004) Recent advance in engine cleaners design and evaluation. J KONES Intern Combust Engines 11:259–275
- Lisowski M (2009) Evaluation of air filters in truck vehicle engines. TEKA Kom Mot Energ Roln. OL PAN 9:155–163
- Marty M (1995) Total filtration TM, the influence of filter selection on engine wear, emissions, and performance. SAE Technical Paper Series, 952557
- Norman K, Huff S, West B (2009) Effect of intake air filter condition on vehicle fuel economy
- Pana C, Negurescu N, Popa MG et al (2012) Ecologic automotive diesel engine achieved by LPG fueling. J Environ Prot Ecol 13(2):688–699
- Sprinkler Applications (2009) FTP, Powertrain Technologies, N67 MNT
- Thomas J, West B, Huff S (2013) Effect of air filter condition on diesel vehicle fuel economy. SAE Technical Paper, 2013-01-031
- Toma M (2013) Researches on the influence of maintenance activity of air filters on the dynamic performances of automotive internal combustion engines. PhD Thesis, University Politehnica of Bucharest
- Toma M (2014) A study of the air filters' maintenance for internal combustion engines. Sci Bull Ser D 76:101–110
- Toma M (2015) Some aspects concerning the period of automotive air filters replacement on the basis of their technical conditions. Appl Mech Mater 809–810:1181–1186
- Toma M, Bobâlcă C (2015) Research on drivers' perception on the maintenance of air filters for internal combustion engines. In: 9th International conference interdisciplinarity in engineering, INTER-ENG 2015, 8–9 October 2015, Tirgu-Mures, Romania
- Toma M, Fileru I (2015) Research on the air filters' maintenance for diesel engines. In: 9th International conference interdisciplinarity in engineering, INTER-ENG 2015, 8–9 October 2015, Tirgu-Mures, Romania
- Zemaitis W (1998) Stacked panel filter for engine air intake systems. SAE Technical Paper Series, 980868

# Fatigue Analysis for the Primary Shaft of a Mechanical Gearbox of a Car

Mario Trotea, Dumitru Neagoe, Loreta Simniceanu  
and Augustin Constantinescu

**Abstract** The paper presents the fatigue analysis of the primary shaft of a mechanical gearbox with three axles for a SUV car. For the analytical fatigue calculation the Soderberg method was used for finding the global fatigue safety factor. The numerical fatigue analysis was performed using Ansys software for the maximum load case of the primary shaft using Soderberg mean stress theory from Ansys Fatigue Tool.

**Keywords** Fatigue · Soderberg method · Numerical analysis · Safety factor

## Introduction

Compared to static load cases, variable loads repeated a significant number of times have an adverse effect on the strength capacity of the material of the resistance elements. This can cause unexpected breakage of parts although in terms of strength of materials were properly designed. Breaks occur at much lower stress than the stress value corresponding to static loads. This phenomenon of premature rupture at stresses below the limit is known as *material fatigue*.

In this paper analytical fatigue calculation is performed for the primary shaft of a manual gearbox whose design is similar with the R380 gearbox of Land Rover

---

M. Trotea (✉) · D. Neagoe · L. Simniceanu · A. Constantinescu  
University of Craiova, Craiova, Romania  
e-mail: mtrotea@yahoo.com

D. Neagoe  
e-mail: neagoe\_dumitru@yahoo.com

L. Simniceanu  
e-mail: lsimniceanu@yahoo.com

A. Constantinescu  
e-mail: gusti\_constantinescu@yahoo.com

Discovery II ([http://www.landroverresource.com/docs/R380\\_Gearbox\\_Overhaul\\_Manual.pdf](http://www.landroverresource.com/docs/R380_Gearbox_Overhaul_Manual.pdf)).

In comparison, there is a numerical fatigue analysis by finite element method using ANSYS program.

## Analytical Fatigue Calculation for Primary Shaft

Fatigue calculation is to determine the safety factor to fatigue and comparison with recommended values. This calculation requires determining loading regime and determining the influencing factors of the material fatigue.

### *Establishing Loading Scheme and the Shaft Material*

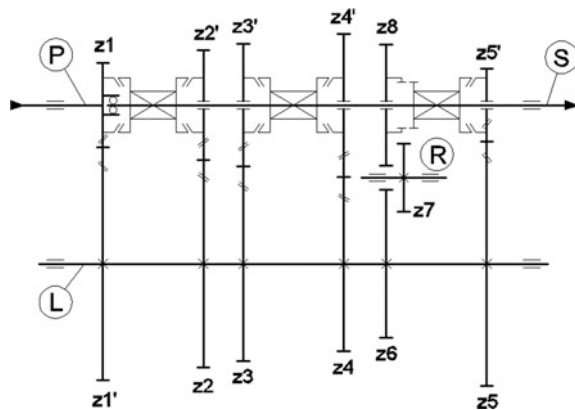
Kinematic scheme of the gearbox shown in Fig. 1 is used to determine the shafts loads due to the gears forces.

The adopted material for shaft is 18MoNiCr17 STAS 11512-91. This is a carburizing steel for gears. Since the gear and the shaft is in one piece construction, the shaft will be made of this material.

Loading scheme of primary shaft and bending moment diagrams in horizontal and vertical plane is shown in Fig. 2a, b, c. The diagrams are drawn for 1st, 2nd, 3rd and 5th gear for corresponding bending  $M_I$ ,  $M_{II}$ ,  $M_{III}$  and  $M_V$ .

Maximum bending moment on the shaft is for the fifth gear as shown in the diagrams of bending moments. At the distance of 140 mm from the left end of the shaft is the connecting fillet for which the fatigue calculation is made with bending moments in the two planes:  $M_H = -202,361$  Nmm and  $M_V = -145,038$  Nmm.

**Fig. 1** Kinematic scheme of the gearbox



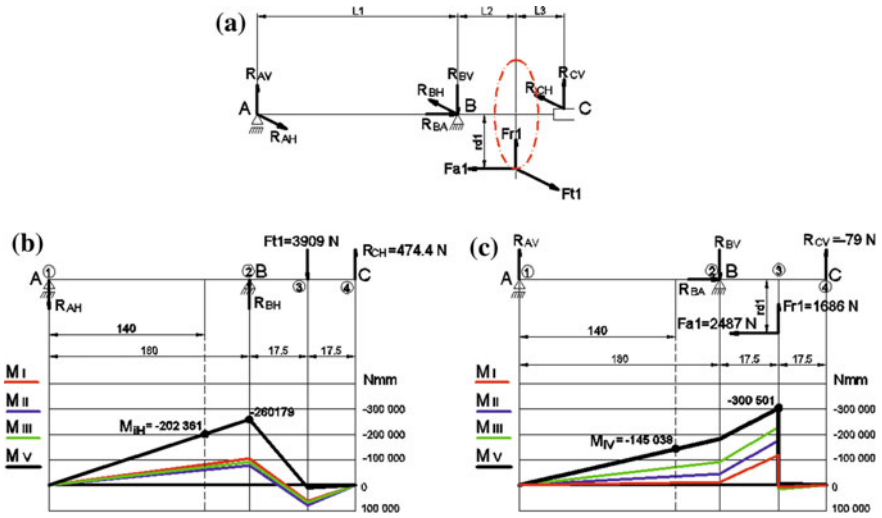


Fig. 2 Loading scheme of primary shaft and bending diagrams a loading scheme; b horizontal bending diagram; c vertical bending diagram

The shaft shape and the dimensions of interest area for the fatigue calculation are shown in Fig. 3.

### Fatigue Safety Factor Calculation

The variable load that the shaft is subjected to is a composed load with bending, having an alternating symmetric cycle, and torsion with a pulsating cycle.

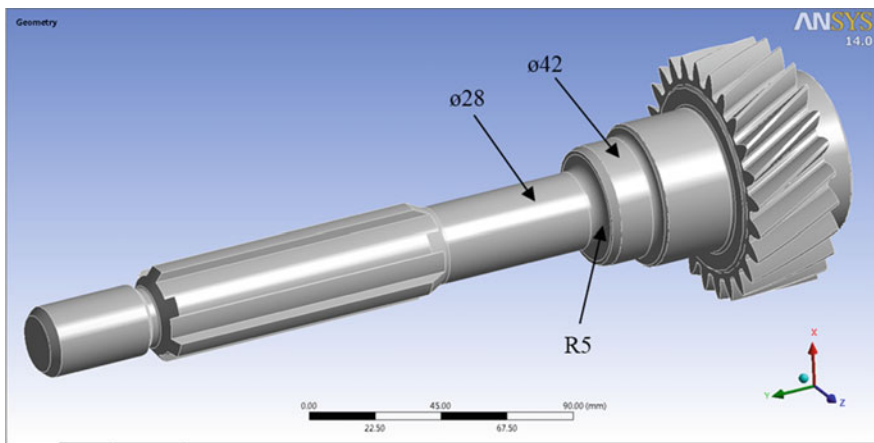


Fig. 3 The solid model of the primary shaft



The fatigue calculation will use partial safety coefficients  $c_\sigma$  and  $c_\tau$ , corresponding to normal stress and shear stress, accordingly.

The fatigue calculation is performed for stress concentrator zone from diameter of 28–42 mm diameter corresponding to the rotation sleeve, as shown in Fig. 3.

Fatigue safety factor for bending load, using Soderberg schematization, is (Buzdugan 1986; Deutsch 1976):

$$c_\sigma = \frac{1}{\frac{K_\sigma}{\varepsilon \cdot \gamma_\sigma} \cdot \frac{\sigma_a}{\sigma_{-1}} + \frac{\sigma_m}{\sigma_c}} \quad (1)$$

where:

$K_\sigma$  is effective coefficient of concentration for variable bending;

$\varepsilon$  is dimensional coefficient,  $\varepsilon = 0.74$  (Buzdugan 1986)

$\gamma_\sigma$  is coefficient of surface quality,  $\gamma_\sigma = 0.75$  (Buzdugan 1986)

$\sigma_a$  is bending amplitude stress;

$\sigma_m$  is mean stress (for fully reversing cycle  $\sigma_m = 0$ );

$\sigma_c$  is yield tensile strength,  $\sigma_c = 780$  MPa

$\sigma_{-1}$  is fatigue strength for fully reversed bending (Buzdugan 1986),  $\sigma_{-1} = (0.4 \div 0.6) \cdot \sigma_r$ ,  $\sigma_{-1} = 0.6 \cdot \sigma_r \cong 710$  MPa,  $\sigma_r = 1200$  MPa);

The effective coefficient of concentration for variable bending loads is (Buzdugan 1986):

$$K_\sigma = 1 + c(K'_\sigma - 1) \quad (2)$$

where:

$K'_\sigma$  is fatigue coefficient of concentration for changing in diameter with fillet radius,  $K'_\sigma = 1.75$  (Buzdugan 1986);

$c$  is correction coefficient (Buzdugan 1986),  $c = 0.77$ . Thus,  $K_\sigma = 1.5772$

Stress amplitude is:

$$\sigma_a = \frac{M_i}{W_z} \quad (3)$$

where

$M_i$  is bending moment for the section with the fillet radius;  $M_i = 290,465$  Nmm ( $M_i = \sqrt{M_{iH}^2 + M_{iV}^2}$ , see Fig. 2b, c);

$W_z$  is the strength modulus for this section;  $W_z = \frac{\pi \cdot d^3}{32}$

The stress amplitude is:  $\sigma_a = 122.8$  N/mm<sup>2</sup>.

The value of fatigue safety factor for bending stress, determined with relation (1) is:  $c_\sigma = 2.033$ .

Fatigue safety factor for torsion load is calculated with (Buzdugan 1986):

$$c_\tau = \frac{1}{\frac{K_\tau}{\varepsilon \cdot \gamma_\tau} \cdot \frac{\tau_a}{\tau_{-1}} + \frac{\tau_m}{\tau_c}} \tag{4}$$

where:

- $K_\tau$  is effective coefficient of concentration for variable torsion load;
- $\varepsilon$  is dimensional coefficient,  $\varepsilon = 0.74$ , previously determined;
- $\gamma_\tau$  is coefficient of surface quality,  $\gamma_\tau = 0.6 \cdot \gamma_\sigma + 0.4$ , so  $\gamma_\tau = 0.85$
- $\tau_a$  is tangential stress amplitude;
- $\tau_{-1}$  is fatigue strength for zero-based cycle for torsion,  $\tau_{-1} = (0.55 - 0.58) \cdot \sigma_{-1}$   
 $\sigma_{-1} \quad \tau_{-1} \cong 0.56 \cdot \sigma_{-1} \cong 400 \text{ MPa}$  (Buzdugan 1986);
- $\tau_m$  mean stress for torsion, for zero-based cycle,  $\tau_m = \frac{\tau_a}{2}$ ;
- $\tau_c$  shear yield strength,  $\tau_c \cong 0.6 \cdot \sigma_c$  (Buzdugan 1986, Deutsch 1976)

$$\tau_c \cong 0.6 \cdot \sigma_c = 460 \text{ MPa}$$

The effective coefficient of concentration for variable torsion loads is (Buzdugan 1986):

$$K_\tau = 1 + c(K'_\tau - 1) \tag{5}$$

where:

- $K'_\tau$  is fatigue coefficient of concentration for changing in diameter with fillet radius (Buzdugan 1986),  $K'_\tau = 1.3$ ;
- $C$  is correction coefficient (Buzdugan 1986),  $c = 1$ . Thus,  $K_\tau = 1.3$

The tangential stress amplitude is:

$$\tau_a = \tau_{tmax} = \frac{M_t}{W_p} \tag{6}$$

where:

- $M_t$  is the torque applied to the principal shaft,  $M_t = 300,000 \text{ Nmm}$
- $W_p$  is polar strength modulus for this section,  $W_p = \frac{\pi \cdot d^3}{16}$ , ( $d = 28 \text{ mm}$ )

In this case, the tangential stress amplitude is:  $\tau_a = 69.6 \text{ N/mm}^2$ .

The value of fatigue safety coefficient for torsion is:  $c_\tau = 2.297$ .

The global fatigue safety coefficient is (Buzdugan 1986; Deutsch 1976):

$$c = \frac{c_\sigma \cdot c_\tau}{\sqrt{c_\sigma^2 + c_\tau^2}} \tag{7}$$

Replacing the values for  $c_\sigma$ ,  $c_\tau$  in relation (7), we have:  $c = 1.52$ . This value correspond to recommendations from (Buzdugan 1986; Deutsch 1976), which give the value for global fatigue safety coefficient as  $c = 1.5 \dots 1.7$ .

## Numerical Fatigue Analysis

The numerical analysis for fatigue calculation is realised using the finite element analysis program ANSYS 14, starting from the solid model construction of the gearbox shaft, shown in the Fig. 3.

For structural fatigue analysis was used an equivalent material for the 18MoNiCr17 alloyed steel, namely SNCM420 (0.20C-1.8Ni-0.5Cr-0.2Mo). For this material both the mechanical properties and the fatigue test results are known (<http://smds.nims.go.jp/MSDS/sheethtml/F51J.html>).

The finite element model shown in the Fig. 4 contains more than 613,000 tetrahedron type elements and more than 115,000 nodes.

The boundary conditions of the shaft were made according to the loading scheme and are shown in the Fig. 5, where: A—radial bearing with axial displacement; B—radial bearing without axial displacement; C—the resultant force of horizontal reaction and vertical reaction of the interior bearing; D—the torque transmitted from the engine crankshaft through the clutch driven disc; E—pinion rotation lock; F—the resultant force of radial and axial forces from permanent gear.

Using the static structural analysis it is obtained the value of equivalent stress  $\sigma_{ech} = 127.02 \text{ N/mm}^2$  for the fillet area between 28 mm diameter shaft and 42 mm diameter shaft, as it shown in Fig. 6.

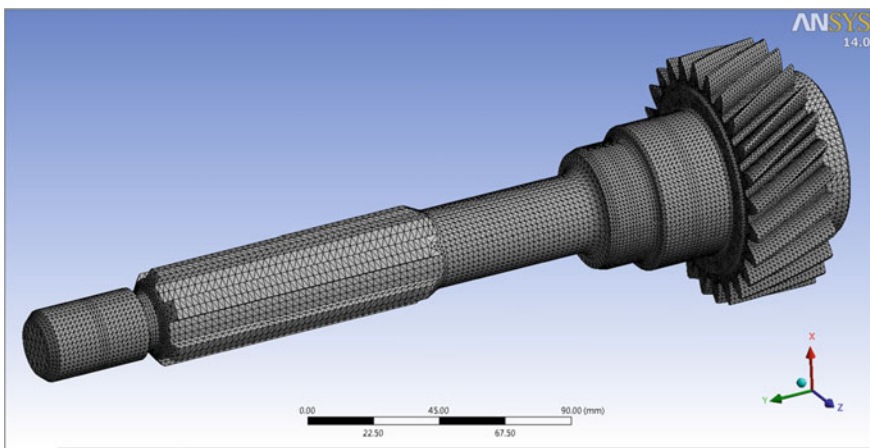


Fig. 4 Finite element model

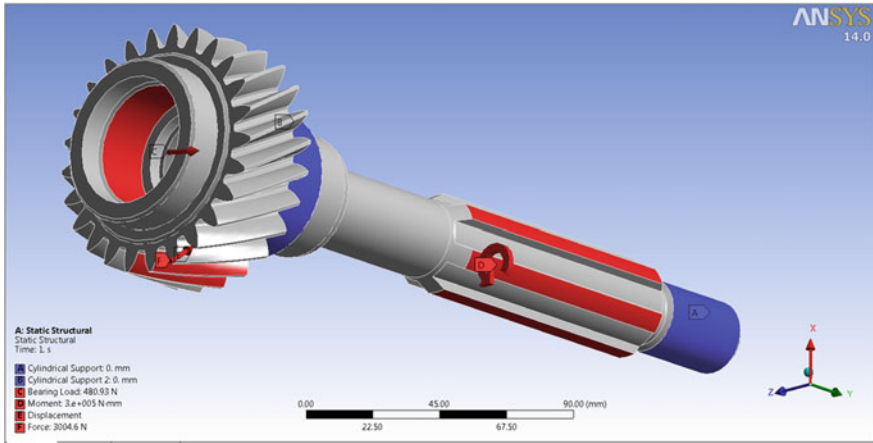


Fig. 5 Boundary conditions

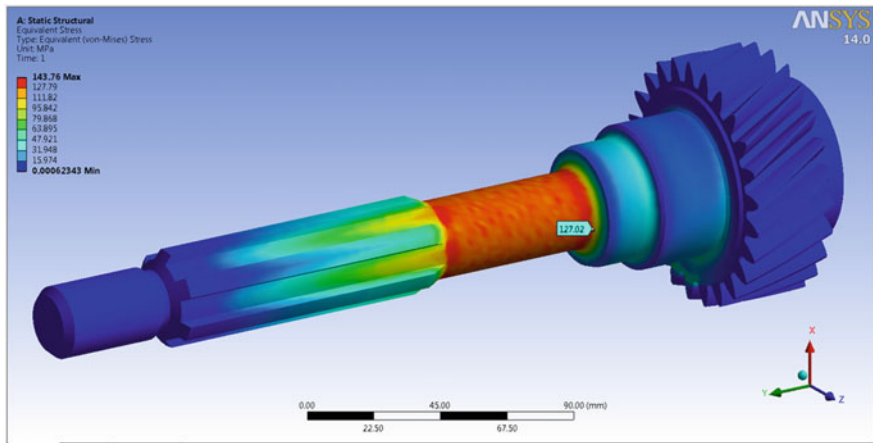


Fig. 6 The equivalent stress in the fillet area, 127.02 MPa

Analysing the type of stresses of the fillet area using the biaxiality indicator (BI) it is observed that for this area we have only the pure shear for fatigue calculation (that is  $BI = -1$ ), as it is shown in the Fig. 7.

This indicates that for this area we can taking into account only the shear stress and for this reason the fatigue analysis uses a variable pulsed load with the Soderberg schematization. The  $K_f$  fatigue factor  $K_f$  is adopted as the value for the torsion load determined by the classical method for  $c_\tau$  and this is  $K_f = \frac{c_\tau \gamma_\tau}{K_\tau} = 0.48$ .

The value of fatigue strength factor for the fillet area is  $c_{analysis} = 2.3765$ , as it is shown in Fig. 8.

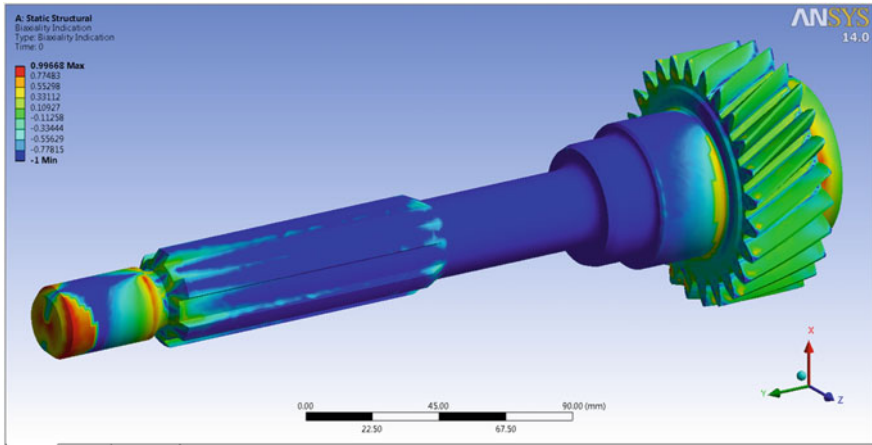


Fig. 7 Biaxiality indication

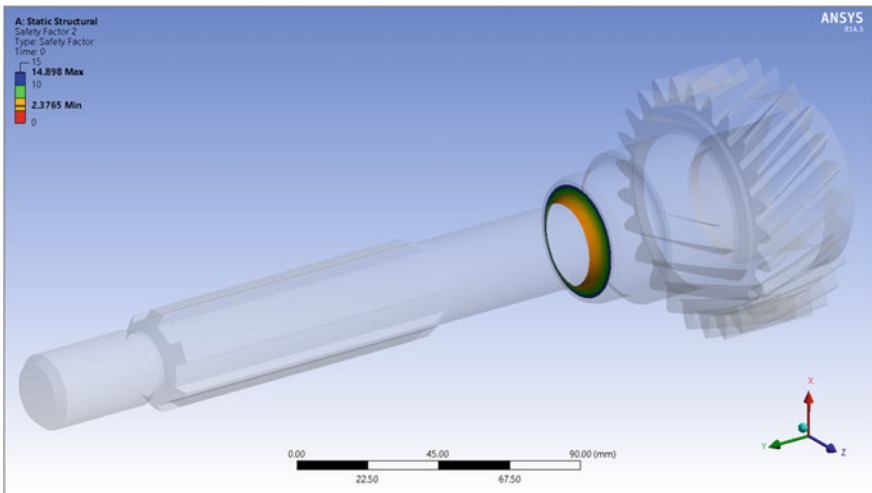


Fig. 8 Minimum fatigue safety factor, 2.3765

## Conclusions

Considering the comparative analysis of the results obtained by the two methods it is observed that the value of fatigue strength coefficient obtained by the finite element method is greater than the value of the fatigue strength coefficient obtained by the classical method. This is because the values of stress values determined analytically, using simplified hypothesis, are appreciably different from the finite element method values for the same load conditions. Also, the classical analysis is

using the choice of same material characteristics based on general relations that are valid under certain condition.

Taking into account these considerations, it may be appreciated that the 3.46 % relative error value between the previous two fatigue strength coefficients is acceptable ( $c_\tau = 2.297$  and  $c_{analysis} = 2.3765$ ), and this can validate the numerical method analyses results.

## References

- Buzdugan Gh (1986) Rezistența materialelor. Editura Academiei Republicii Socialiste România, București, pp 375–420
- Deutsch I (1976) Rezistența materialelor. Editura Didactică și Pedagogică, București, pp 438–459

# Optimizing Combustion in an Single Cylinder GDI SI Engine

Stelian Tarulescu, Radu Tarulescu and Cristian-Ioan Leahu

**Abstract** Throughout the world, many efforts are being made to improve the thermal efficiency of automotive internal combustion engines (Sellnau et al. in GDCI multi-cylinder engine for high fuel efficiency and low emissions 2015). In this paper, the AVL 475 cc GDI Single Cylinder Research Engine 5405 was tested over a range of steady-state operating conditions using a modern injection system. Calibration mapping was conducted over a wide range of operating conditions, in order to optimize the combustion. The tests was made at Transilvania University of Braşov, ICDT—Research & Development Institute. This tests include simulations for different engine loads and regimes, modifying one by one the engine’s intake parameters, operational parameters and atmospheric conditions. The mixture formation and combustion processes of the fuel will be monitored through the test bed component software, AVL FIRE Commander 7.06c—IAV, AVL PUMA Open Test Bed Automation and AVL Indicom software. In order to optimize the combustion, the engine map was modified. The main parameters that was changed are: the amount of fuel per cycle, ignition timing for first and second injection, excess air factor  $\lambda$ , for different intake pressures, engine speeds and loads. In the next figure is presented the engine map for the analyzed engine.

**Keywords** Combustion · Optimize · Engine · Gasoline

---

S. Tarulescu (✉) · R. Tarulescu · C.-I. Leahu  
Transilvania University of Brasov, Eroilor Boulevard, 29, 500036 Brasov, Romania  
e-mail: s.tarulescu@unitbv.ro

R. Tarulescu  
e-mail: radu.tarulescu@unitbv.ro

C.-I. Leahu  
e-mail: leahu.cristian@unitbv.ro

## Introduction

The new Euro 6 regulations regarding CO<sub>2</sub> emissions and regulated emissions including NO<sub>x</sub>, CO, HC, and particulate matter (PM) are demanding advanced internal combustion engines with greatly improved combustion processes. While diesel engines are already very efficient, they are challenged to meet future emissions standards at reasonable cost. Gasoline engines are preferred by customers, but the efficiency of gasoline engines is relatively low (Ghadikolaei 2014).

Gasoline Direct Injection (GDI) is an increasingly popular type of fuel injection system employed in modern four-stroke gasoline engines. The gasoline is highly pressurized, and injected by high voltage driven injectors via a common rail fuel line directly into the combustion chamber of each cylinder, as opposed to conventional single or multi-point fuel injection that happens in the intake manifold tract, or cylinder port. The major advantages of a GDI engine are lower emission levels, increased fuel efficiency and higher engine power output. In addition, the cooling effect of the injected fuel and the more evenly dispersed combustion mixtures and temperatures allow for improved ignition timing settings which are an equally important system requirement. Emissions levels can be more accurately controlled with the GDI system. The lower levels are achieved by the precise control over the amount of fuel, air and ignition settings which are varied according to the engine load conditions and ambient air temperature (Gajbhiye and Chincholkar 2013).

In order to obtain data and optimize solutions for GDI engines, a research program was developed at Transilvania University of Braşov, ICDT—Research & Development Institute. The research stand is an AVL single cylinder test bed for gasoline and diesel engines (Fig. 1). For the present paper, the tests was made on a AVL 475 cc GDI Single Cylinder Research Engine 5405. The single cylinder can be setup in several configurations (with multipoint injection, with direct injection, with turbocharger). There will be tested the fuel mixture formation combustion process and the influence of turbocharged engine. The engine with transparent quartz cylinder is built for the visualization of internal processes from outside using a high speed movie camera. The piston with quartz head allows filming the internal processes with the help of a system of mirrors. The mixture formation and combustion processes of the fuel will be monitored through the test bed component software, AVL FIRE Commander 7.06c—IAV (AVL 2013).

## Methodology

In the present study were made tests in order to improve the combustion for one research engine. The results can be used to improve the processes of GDI gasoline engines in order to reduce the exhaust emissions and fuel consumption (Verlag 2014).

Single Cylinder Research Engine 5405 specifications are: Bore: 82 mm; Stroke: 90 mm; Displacement: 475 ccm; Max. speed: 6000 rpm; Rated power: 20 kW



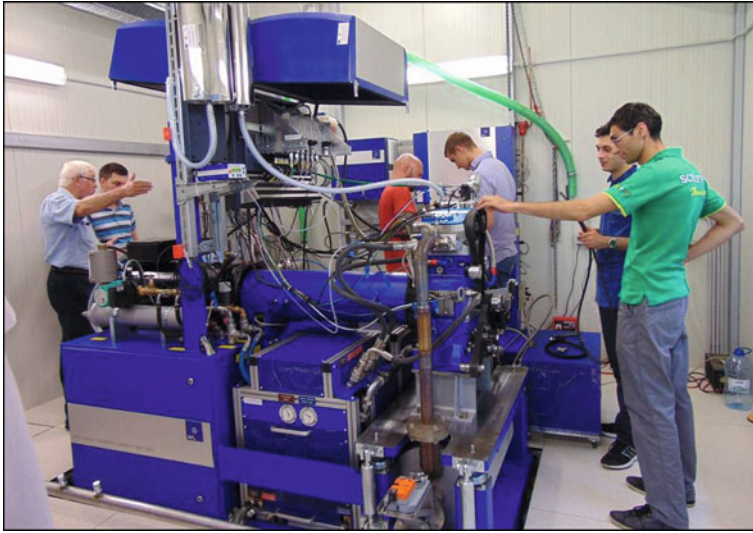


**Fig. 1** AVL single-cylinder compact test bed used for GDI research

natural aspirated; Rotation inertia approx.  $0,4 \text{ kgm}^2$ ; Combustion concept: Homogeneous,  $\lambda = 1$ ; Compression ratio: 11.5:1.

The test bed have some other components and systems: Balancer System for SCRE; MPFI Conversion Kit, Conversion kit for AVL Gasoline Direct Injection SCRE from GDI to Multi Point Fuel Injection (MPFI) operation; Conversion Kit: Optical Topworks 514 Gasoline GDI; Mirror Unit for Optical Measurements; AVL Engine Control Unit (AVL ETU 427); Coolant and conditioning Unit 577; AVL Fuel mass flow meter—Type Flex Fuel; AVL Fuel temperature control; Intake Air Consumption Measurement Device; Particle Evaluation—Micro Soot Sensor Continuous Measurement of Soot Concentration; AVL PUMA Open Test bed Automation; Exhaust Gas analyzer, Model GA-21plus (AVL 2013).

The used software used for intake and combustion process optimization is AVL FI2RE Commander 7.06c—IAV. AVL FIRE was developed to solve the most demanding flow problems in respect to geometric complexity and chemical and physical modeling. FIRE offers a comprehensive computational fluid dynamics solution: a powerful set of modules, features and capabilities, pre-and post-processing integrated in a common environment and workflows and methods effectively supporting the use of the software to solve any problem accurately (AVL 2013).

The software used for engine parameters monitoring is AVL Indicom software. During cycle based data acquisition the value of cycle time must vary all the time.

For combustion tests several parameters will be monitored: engine speed, intake fuel pressure, cylinder maximum pressure, intake air pressure, spark ignition time,

**Table 1** Engine parameters

SPEED (rpm)	IMEP (bar)	P <sub>MAX</sub> (bar)	AI 50 % (°CA)	P Intake (mbar)	SA (°CA)	SOI (CA)	DOI (ms)	P RAIL (bar)	T EXH (°C)	Lambda (-)
1000	3.00	17.40	25.00	-303.5	-20	-280	1850	100	240	1.00

injection start moment, injection time, rail pressure, exhaust temperature and mixture ratio (Excess Air— $\lambda$ ). They are presented in the Table 1.

The first set of tests was made using a standard engine map (in AVL FI2RE). For following tests the spark ignition time and air excess coefficient were optimized. The tests was made for different engine loads and engine speeds. Also, one set of tests was made for one direct injection per cycle and other set of tests was made for two injections per cycle (First DI injection and Second DI injection). The setup was made in AVL FI2RE software as is showed in Fig. 2 (AVL 2013).

In Fig. 3 is presented the main menu used for intake and combustion parameters optimization. The engine load is controlled through manifold

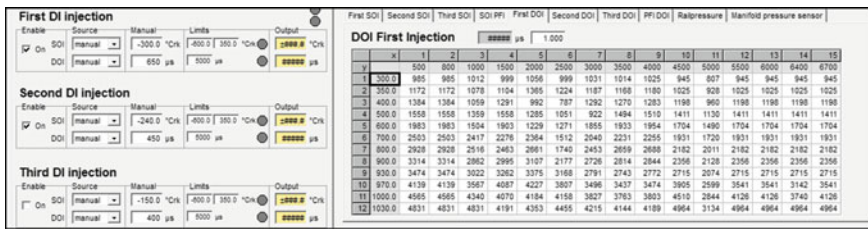


**Fig. 2** AVL FI2RE working sheet—number of injections/cycle and duration of injection

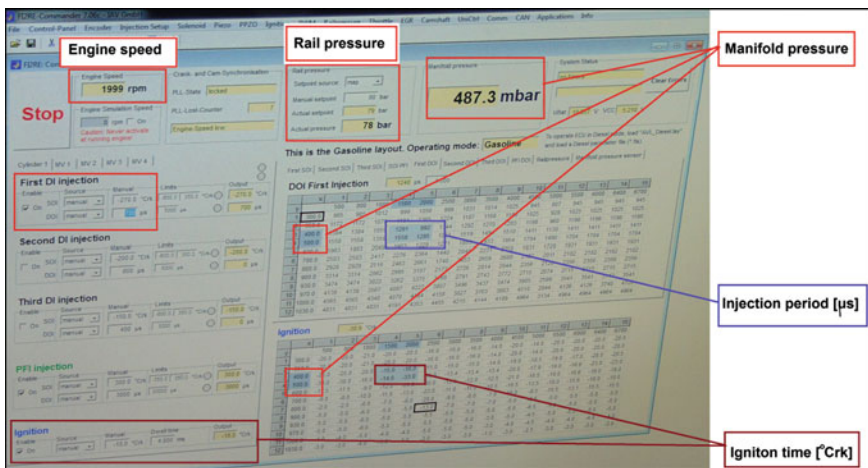


**Fig. 3** AVL FI2RE menu—engine map parameters

pressure. The engine speed is set using the main control system (AVL Puma interface). The intake parameters are controlled by set the number of injections (first, second or third direct injection and one indirect injection). The fuel mixture can be adjusted by varying the amount of fuel injected per cycle (injection period—(μs)). The ignition time is also set in crank angle degrees before top dead center.

The parameters changes were made to obtain an optimal single cylinder pressure curve and more optimal combustion (no detonations). In the Fig. 4 are presented the intake, ignition and combustion features for 475 cc GDI Single Cylinder Research Engine.

Tests were done for one specific engine speed and one engine load by modifying the following parameters: number of injections, amount of fuel injected per cycle and ignition time (spark moment) before top dead center (TDC).

In order to control the quality of the combustion and exhaust emission level it was used exhaust gas analyzer, Model GA-21plus. For each test (in order to optimize intake and combustion parameters) were recorded values of the main pollutants (as seen in the example working page in Fig. 5) (GA-21 plus 2013).

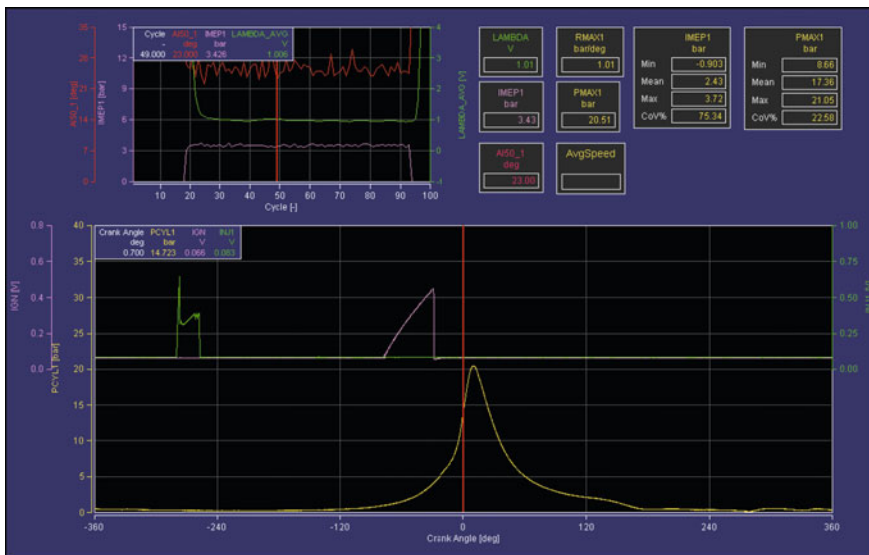


Fig. 4 Engine parameters monitoring with AVL Indicom software

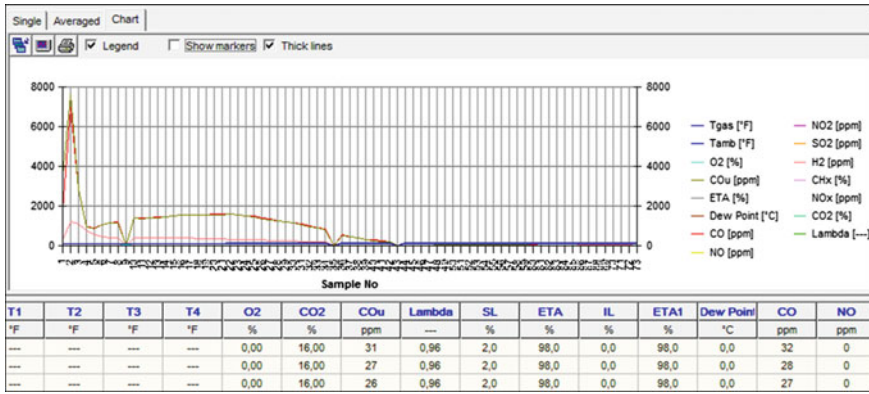


Fig. 5 Interface for exhaust gas analyzer model GA-21plus—parameters

### Results

In order to achieve an engine map for optimal functioning were tested several values for the ignition moment (crank angle) and the amount of fuel injected per cycle. Tests were made for a big range of engine speeds and throttle positions (engine loads). For example we chose a set of tests made under the following conditions: engine speed ~2000 rpm; manifold pressure ~500 mbar; spark moment before TDC: -18 → -26 °CA; injection period: 900 → 1300 μs; intake with one injection or two injections per engine cycle.

For each test, there were measured the emissions to determine optimum combustion and pollution level. The results are presented in Figs. 6, 7, 8, 9, 10 and 11.

The lowest levels of CO<sub>2</sub> were recorded for the values of the spark advance angle before TDC of 20 to 22 °CA, when the duration of injection was selected 1200 μs. Also, for a selected value of 22 °CA, when injection time/engine cycle is variable, the lowest value of CO<sub>2</sub> is registered for 1100 μs.

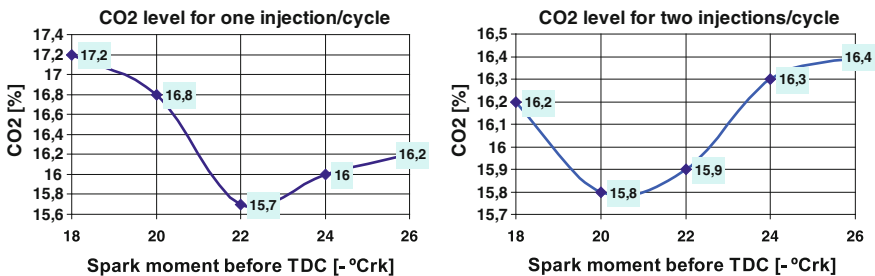


Fig. 6 Variation of CO<sub>2</sub> with spark advance to TDC for one and two injections/cycle

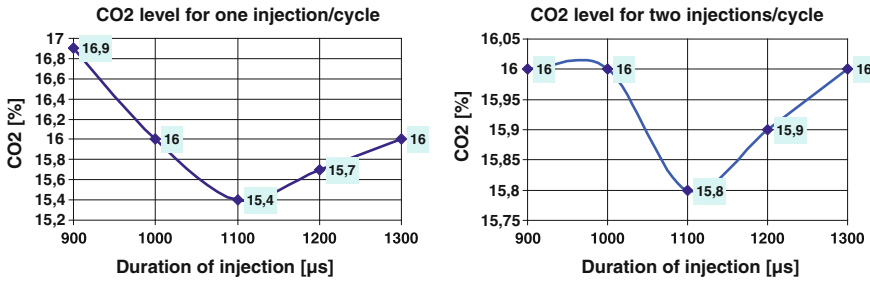


Fig. 7 Variation of CO<sub>2</sub> with duration of injection/cycle for one and two injections/cycle

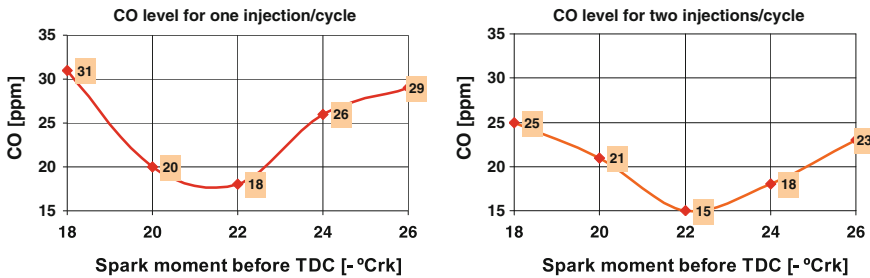


Fig. 8 Variation of CO with spark advance to TDC for one and two injections/cycle

The lowest values of CO were recorded for 22 °Crk, when the duration of injection was selected 1200 µs. Also, for a selected value of 22 °Crk, when injection time/engine cycle is variable, the lowest value of CO is registered for 1100 and 1200 µs.

The lowest values of NO<sub>x</sub> were recorded for 24 and 26 °Crk, when the duration of injection was selected 1200 µs. Also, for a selected value of 22 °Crk, when injection time/engine cycle is variable, the lowest value of CO is registered for 900 and 1100 µs.

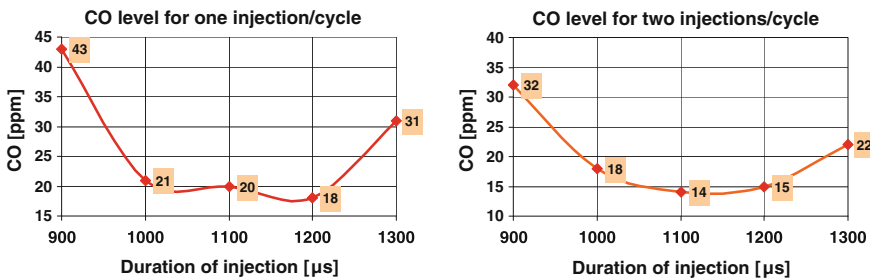


Fig. 9 Variation of CO with duration of injection/cycle for one and two injections/cycle

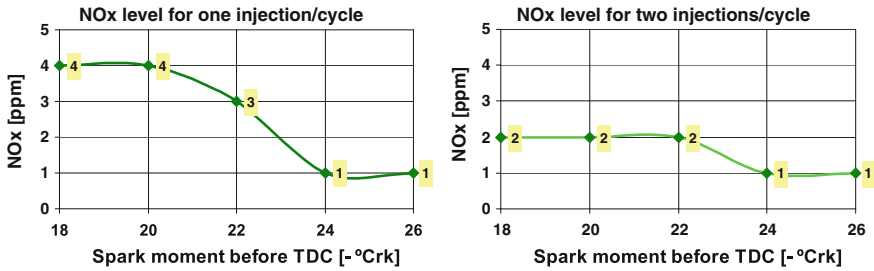


Fig. 10 Variation of NO<sub>x</sub> with spark advance to TDC for one and two injections/cycle

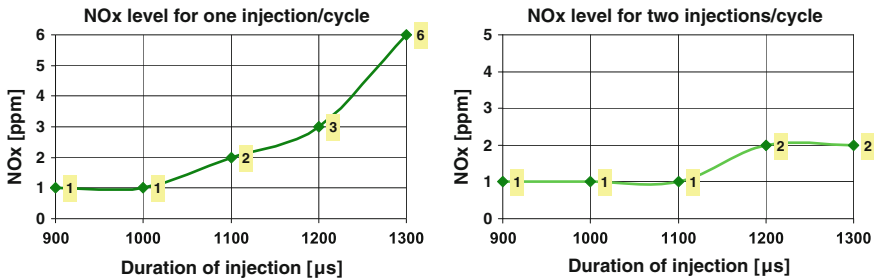


Fig. 11 Variation of NO<sub>x</sub> with duration of injection/cycle for one and two injections/cycle

It can be concluded that for optimum combustion and reduced emission values at exhaust pipe will choose the spark advance angles of 20 to 22 °Crk and injection times per cycle of 1100–1200 μs. Also, an intake with two injections per cycle, one pilot and a main injection would be the best solution for optimum performance.

In order to achieve a complete map of the engine, will optimize intake and combustion parameters for as many speeds and engine loads as possible.

## Conclusions

Using the previous researches and extensive simulation work, a vast set of tests was made on an experimental single cylinder engine with gasoline direct injection (GDI). Central to these tests was a fuel injection system and injection strategy combined with engine parameters optimization. This produced robust ignition with very clean, efficient, and stable combustion.

In order to achieve an engine map for optimal functioning were tested several values for the ignition timings and the amount of fuel injected per cycle. Tests were

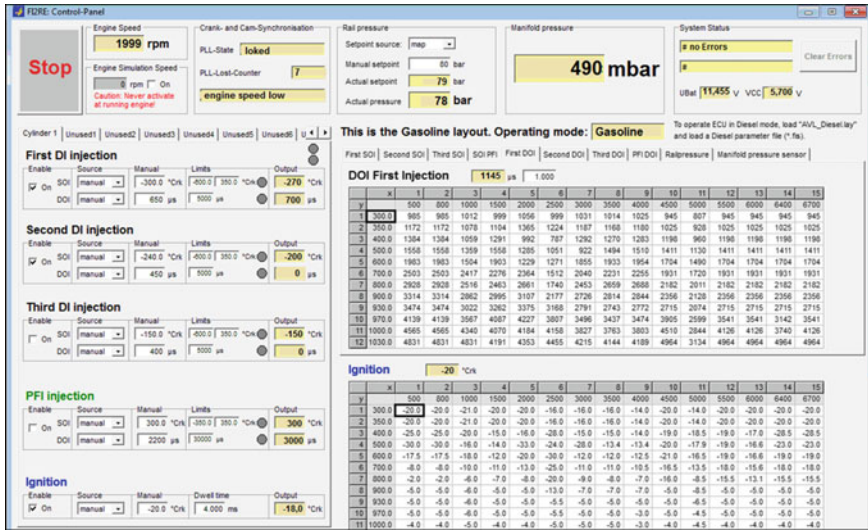


Fig. 12 Engine map—intake and combustion parameters

mader for a big range of engine speeds and loads. For a complete map of the engine, there will be optimize intake and combustion parameters for as many speeds and engine loads as possible. An engine map example is presented in Fig. 12.

**Acknowledgments** We hereby acknowledge the structural funds project PRO-DD (POS-CCE, O.2.2.1., ID 123, SMIS 2637, ctr. No 11/2009) and Transilvania University of Brasov for providing the infrastructure used in this work.

**References**

AVL (2013) Tutorials and books for engines test cell equipments usage  
 Flue Gas Analyser GA-21 plus (2013) Operating manual, Madur electronics. Vienna—Austria  
 Gajbhiye PK, Chincholkar SP (2003) Review on electronically assisted gasoline direct injection 4-stroke single cylinder engine system. Int J Sci Res (IJSR). India Online ISSN: 2319-7064  
 Sellnau M, Moore W, Sinnamon J, Hoyer K, Foster M, Husted H (2015) GDCI multi-cylinder engine for high fuel efficiency and low emissions. Copyright © 2015 SAE International, Published 14 Apr 2015  
 Ghadikolaie MA (2014) History of Gasoline Direct Compression Ignition (GDCI) engine—a review. IJRET Int J Res Eng Technol 03(01). eISSN: 2319-1163, pISSN: 2321-7308, Available @ <http://www.ijret.org>  
 Verlag Europa-Lehrmittel (2014) Modern automotive technology, 2nd edn. Nourney, Vollmer GmbH & Co. KG, Germany, ISBN 978-3-8085-2302-5

# On The Possibility to Reduce Diesel Engines Emissions by Operating with Biodiesel B20 in PPC Mode

Alexandru Racovitza, Bogdan Radu, Mohanad Aldhaidhawi  
and Radu Chiriac

**Abstract** Using diesel-biodiesel blends in Diesel engine has been highlighted to offer a good opportunity in reducing the exhaust emissions for particular engine operating conditions. The blended diesel-biodiesel with up to 20 % biodiesel in petroleum diesel fuel (B20) is in production and available for use in USA being considered as viable path to be followed in the effort to reduce the effect of the greenhouse gas emissions issued by the operation of heat engines. Although previous studies investigating the effect of B20 on engines emissions led to some contradictory results, the life cycle analysis performed on the well-to-wheel base shown that 35 % reductions of CO<sub>2</sub> emission, in respect to fossil fuels operation are possible. The association of this alternative fuel use with some new combustion concepts as homogeneous charge compression ignition (HCCI) premixed charge compression ignition (PCCI) or partially premixed combustion modes (PPC) may amplify these potential reductions. The present study continued the investigation on B20 effects by performing a set of comparative experimental tests on a conventional direct injection tractor diesel engine running alternatively with B20 and petroleum diesel fuel at 2400 rpm speed and 60 % load. The possibilities to enhance the effects of B20 fuel by PPC combustion operation mode were explored by numerical simulations using the AVL BOOST v2013.2 code. It was basically found that further improvements in decreasing emissions of Diesel engines operating with B20

---

A. Racovitza · B. Radu (✉) · M. Aldhaidhawi · R. Chiriac  
Department of Thermodynamics, Engines, Thermal and Refrigerant Machines,  
Faculty of Mechanical Engineering, University Politehnica of Bucharest,  
Splaiul Independentei nr. 313, Sector 6, 060042 Bucharest, Romania  
e-mail: bobitaradu@yahoo.com

A. Racovitza  
e-mail: alexandru\_racovitza@yahoo.com

M. Aldhaidhawi  
e-mail: mohanadhamazah@gmail.com

R. Chiriac  
e-mail: raduchiriac2001@yahoo.com



can be obtained without significant changes in Diesel engines structure and adjustments.

**Keywords** Biodiesel · Diesel engine · Partially premixed combustion · Emissions · Efficiency

## Introduction

PPC (Partially Premixed Combustion) operating mode for CI (compression ignition) engines has been promoted as an intermediary stage between HCCI (homogenous charge compression ignition) mode, in which the entire fuel quantity is premixed with the air (almost like for classic SI engines) and Diesel classic injection operating method, for which combustion turns to its diffusive characteristic (Tanov et al. 2014). Every mode of air fuel mixture formation proves its benefits or disadvantages, as these different modes are illustrated in Fig. 1, separated by different injection timings. Operating in HCCI mode means that SOI (start of the injection) is very early positioned on cycle and combined with the use of a fuel with higher auto-ignition resistance conducts to an almost complete homogeneity of the vaporized fuel in the combustion air. This could adjust the rough engine operation and its noise together with the NO<sub>x</sub> emissions level, but it strongly encourages the knock (for low octane number fuels) CO and smoke to occur

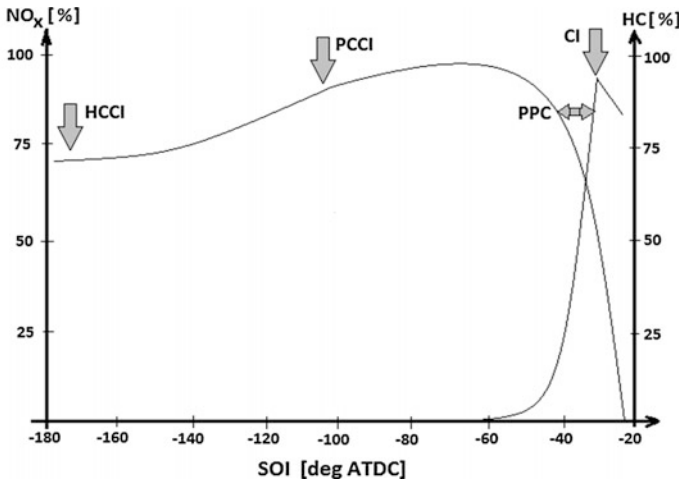


**Fig. 1** Different modes in CI engines operation with regard to emissions levels (Tanov et al. 2014)

(Kalgatgi et al. 2011). On the contrary, standard diesel injection timings, followed by rapid and then diffusive combustion increases the rate of the cycle heat release together with the gases temperature, leading to the rise of the NO<sub>x</sub> emissions, if not controlled by EGR means (Fridriksson 2011; Maurya and Agarwal 2013). Related to another concept, the gasoline compression ignition concept (GCIC), it has been proven that gasolines with 70 to 75 RON (research octane number) are suitable to be used in CI engines due to their weak resistance, especially when referring to operational conditions consisting in low loads and high speeds (Kim et al. 2014; Manente et al. 2010).

PPC operating mode could be a promising way to get minimized the emissions (soot, CO and NO<sub>x</sub>), keeping the engine in-between its efficiency limits at high loads and speeds either. In case of Diesel (DI) engine, the benefit comparing to HCCI combustion is that the fuel injection timing could be use itself as a main control parameter for the combustion period. Negative valve overlap (NVO) is an operating mode that enables LTC (low temperature combustion) in automotive engines. In addition to retain a large fraction of residuals, NVO operation also enables partial fuel injection during the recompression period as a means of enhancing and controlling main combustion. Thermal effects of NVO fueling on main combustion are well understood, but chemical effects of the products of NVO reactions remain uncertain (Steeper and Davisson 2014). According to other authors, the thermal control of the heat transfer could also be obtained using NVO (negative valve overlap) with symmetric OVC (outlet valve closing) and IVO (inlet valve opening) cycle positions to TDC (top dead center) (Cao et al. 2007).

Using biodiesel and biodiesel-diesel blends as alternative fuels in diesel engines, the above described aspects could be improved regarding the influences of this particular fuel on air-fuel mixture formation and combustion, as it has been highlighted in previous studies (Gharbanpour and Rasekhi 2013). There are evident differences between chemical and thermo-physical properties of biodiesel compared to those of fossil fuel. For example, the higher viscosity of biodiesel can affect the spray characteristics, the air-fuel mixture formation and its combustion. However, the ignition delay when using biodiesel is shortened due to its higher cetane number. The lower heating value and the higher oxygen content for biodiesel conduct to a shorter ignition delay and a shorter combustion duration, reducing the heat release rate and the maximum rate of the pressure rise and finally reducing the engine rated power comparing to the classic Diesel fuel engine operation. Regarding the exhaust emissions, simulation and experimental results showed that the use of biodiesel (B20) in compression engines generally led to lower CO<sub>2</sub>, CO and HC exhaust gas emissions (Voicu et al. 2013).

The present work describes an appropriate way to decrease Diesel main emissions' levels by using both PPC operating mode, by modifying fuel injection timing and the use of B20 diesel-biodiesel blend fuel when testing a direct injected and normal aspirated tractor diesel engine.

## Experimental Infrastructure, Engine Operating Modes and Simulation Procedures

A fully operational test bed equipped with required measurement devices has been adapted on testing the performances and the emissions of the naturally aspirated direct injection tractor diesel engine, with 4 cylinders in line, having the total displacement of 3759 cm<sup>3</sup>, nominal power of 50 kW at 2400 rpm, maximum torque of 228 Nm at 1400 rpm, bore/stroke ratio of 102 mm/115 mm and the compression ratio of 17.5. The schematic of the test bed is showed in Fig. 2 (Chiriac et al. 2015).

The multiple fuels operating test bed has been adapted under the purpose of the present work, allowing the engine fueling alternatively with the both tested fuels, Diesel and biodiesel B20. The standard value for diesel injection timing was -7° CA start of injection (SOI) relative to TDC. The performances and the emissions of the

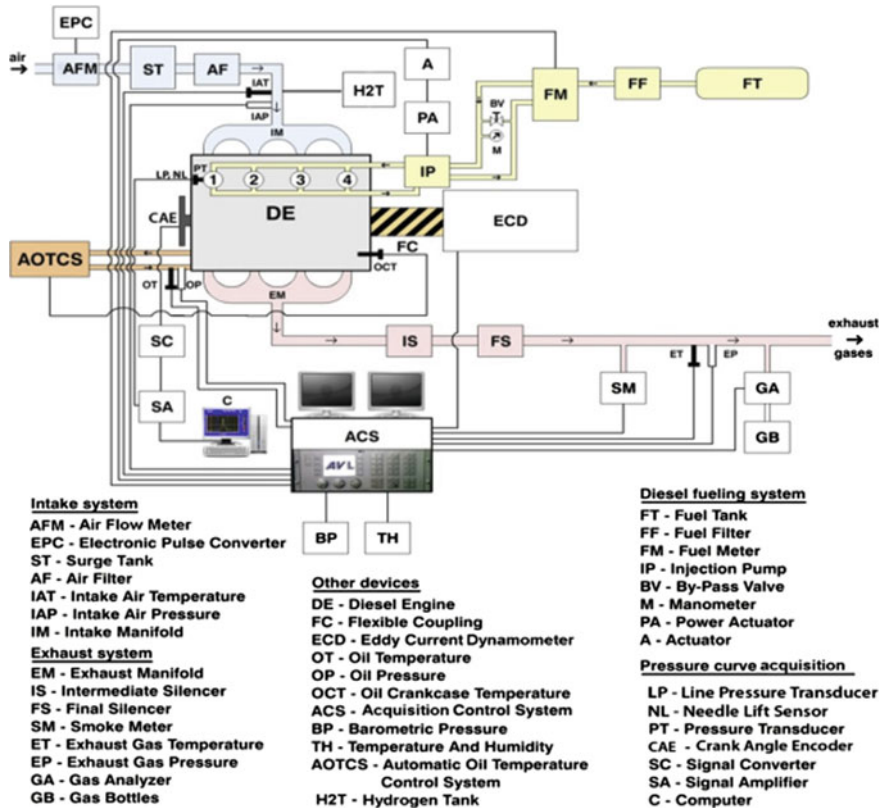
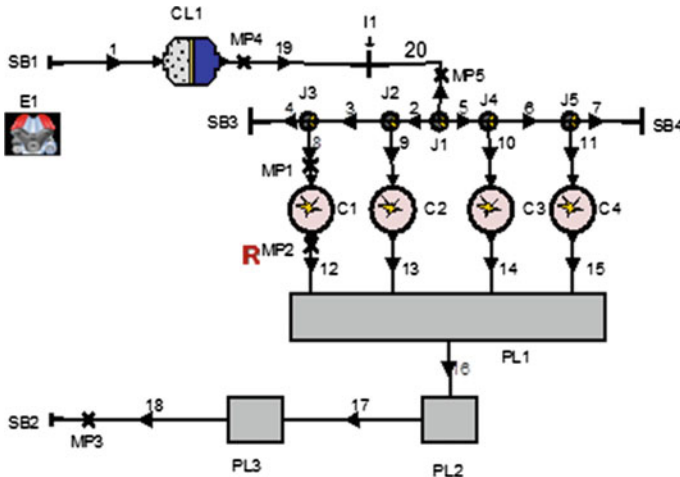


Fig. 2 The schematic of the test bed



**Fig. 3** The schematic of the engine symbolic model (AVL BOOST Theory and AVL BOOST Users Guide)

operated engine were tested at 2400 rpm speed, 60 % load and different injection timings and decreasing SOI points (down to 20 deg) (Voicu et al. 2013).

In order to develop the analysis regarding the engine operation and performances under PPC mode, the engine calibration parameters and cylinder processes simulation were described by using AVL BOOST code v2013.2 (AVL BOOST Theory and AVL BOOST Users Guide). By means of the Boost interface, all the engine components, such as the cylinders, the intake and exhaust manifolds, as well as some auxiliary equipment, the system boundaries, the air filter, the catalyst etc., have been modelled (Chiriac et al. 2015). All the components are linked together by pipes as it can be seen in Fig. 3.

The values of calibration parameters were chosen considering the AVL—MCC combustion model, for which the operating data on injection and combustion characteristics would provide acceptable relative errors. These parameters values are specified in Table 1:

The simulation analysis has considered the engine operating condition previously mentioned: 60 % load, 2400 rpm speed and a series of SOI timings (°CA) starting with -7 (standard) and down to -44, in order to obtain a reasonable approach to the conditions characterizing the PPCC and PPC air-fuel mixture formation modes. The obtained results should highlight a particular value of the injection timing, for which engine emissions (NO<sub>x</sub>, CO, smoke) could register significantly decreasing compared to the standard operating condition, meanwhile preserving engine performance (P<sub>e</sub>) and efficiency (BSFC).

**Table 1** Calibration parameter values

Parameter	Diesel	B20
Number of Injector Holes (-)	5	
Hole Diameter (mm)	0.24	
Discharge Coefficient (DisC) (-)	0.7	
Rail Pressure (RaiP) (bar)	350	
Ignition Delay Calibration Factor (IgnDel) (-)	0.72	0.66
Combustion Parameter (ComPar) (-)	1.62	1.68
Turbulence Parameter (TurPar) (-)	1	
Dissipation Parameter (DisPar) (-)	1	
Premixed Combustion Parameter (PremixPar) (-)	0.91	0.65
NOx Kinetic Multiplier (NOxKM) (-)	2.05	1.17
NOx Post Processing Multiplier (NOxPM) (-)	0.35	0.34
CO Kinetic Multiplier (COKM) (-)	0.0245	0.0241
Soot Production Constant (SPC) (-)	150	290
Soot Consumption Constant (SCC) (-)	330	60
EGR Parameter (EGRPar) (-)	1	
Evaporation Parameter (EvapPar) (-)	0.70353	

## Results and Comments

A first group of results after setting the values of calibration parameters for the calculation model is related to the best approach between the two pressure traces, experimental and simulation for the two fuels operation, pure Diesel fuel and biodiesel B20. Figure 4 shows the comparative variation of the pressure curves

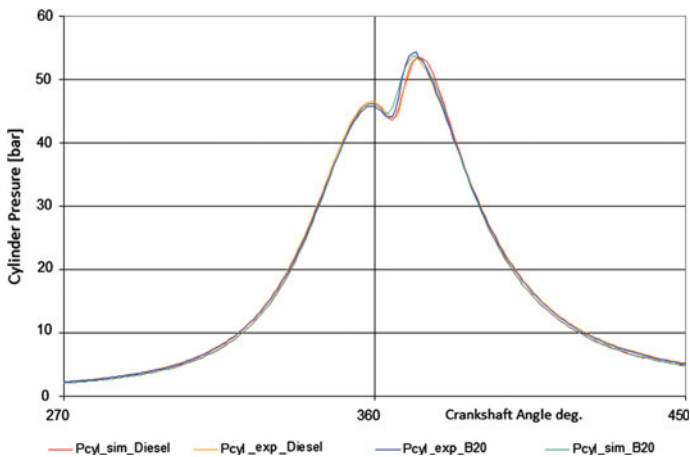


**Fig. 4** Comparison between experimental and simulation pressure traces for 60 % load, 2400 rpm speed and  $-7^{\circ}\text{CA}$ , SOI

plotted when engine operated in reference condition (2400 rpm speed, 60 % load and injection timing corresponding to  $-7$  °CA SOI, Start of Injection).

In Table 2 are listed the simulation results, including the calculated relative deviations concerning engine emissions levels, performance and efficiency indicators, related to the experimental values, for Diesel fuel and biodiesel B20 at reference operating engine condition.

As a consequence of model calibration, the model parameters have been adopted considering acceptable relative deviations of the significant performance and emissions indicators which are in the domain  $-9.5$ ;  $+3.3$  % (see Table 2). The highest values for the relative deviations were registered for soot and CO emission.

The simulation work has been extended to evaluate the engine emissions values (CO, Soot and  $\text{NO}_x$ ) at different injection timings, with SOI values of:  $-32$ ,  $-35$ ,  $-38$ ,  $-41$  and  $-44$  °CA, under the same engine operating conditions of load and speed keeping the values adopted for model parameters which were established in the calibration stage.

Figures 5, 6 and 7 highlight the levels of CO, Soot and respectively  $\text{NO}_x$  as simulation results in comparison with the values obtained for  $-7$  °CA SOI as the reference operating condition. Like a general remark, all the emission values for extended injection timings are significantly lower than the experimental reference values. The lowest values for CO and Soot emissions are related to the injection timing of  $38$  °CA, bTDC (before top dead center). The reduced emissions for both fuels in the range of advanced injection timings ( $-44$  to  $-32$  °CA) could be explained by better homogenization of the air-fuel mixture preventing the occurrence of over rich zones which are responsible for soot formation and carbon incomplete oxidation and also of stoichiometric zones which are involved in the NO formation. In the same time, faster combustion with an increased premixed character associated with reduced residence time diminishes the NO to  $\text{NO}_2$  conversion rate, falling thus the  $\text{NO}_x$  emissions in respect with the reference condition.

The comparison between the two tested fuels emphasizes for biodiesel B20 lower CO values than for pure Diesel in the whole investigated range of injection timings (Fig. 5). This behavior can be attributed to the reduced carbon content of biodiesel which leads for the same air consumptions of the engine to leaner mixtures ensuring thus better carbon oxidation (the rate of CO formation/destruction mechanism is calculated by the group of reactions proposed by Onorati) (Ismail et al. 2013). There is an important decreasing by 10 times when this emission is referred to those obtained for the reference condition.

In the extended injection timings range soot is higher for biodiesel relative to pure Diesel fuel (Fig. 7) although it remains approximately 3 times lower than reference. The model considers two reactions (model of Schubiger which is used for the 2-zone calculation) for the soot formation mechanism that is governed by reaction kinetic mechanisms (Schubiger et al. 2002). The soot formation reaction is attributed to the combustion rate of the diffusion combustion. The oxidation reaction depends on the actual net soot mass in the cylinder and the oxygen availability in the burned zone. The concurrence between these formation-oxidation reactions gives the magnitude of soot emission in the burned gases. The results show an

**Table 2** Comparison between simulation and experimental results at reference condition

	NO <sub>x</sub> (g/kWh)		CO (g/kWh)		Soot (g/kWh)		P <sub>max</sub> (bar)		(dp/dt) <sub>max</sub> (bar/deg)		P <sub>e</sub> (kW)		BSFC (g/kWh)		Lambda (-)		Fuel Cons. (kg/h)	
	Sim	Exp	Sim	Exp	Sim	Exp	Sim	Exp	Sim	Exp	Sim	Exp	Sim	Exp	Sim	Exp	Sim	Exp
Diesel	6.45	6.40	5.75	6.20	0.236	0.23	53.4	53.3	1.46	1.42	26.6	26.83	288.5	285.8	2.29	2.36	7.7	7.66
St. dev.	0.8 %		-7.2 %		2.6 %		0.2 %		2.8 %		-0.5 %		0.9 %		-2.9 %		0.5 %	
B20	6.14	6.24	6.06	6.55	0.181	0.2	53.6	54.3	1.45	1.41	26.7	26.83	295.7	298	2.46	2.38	7.92	7.99
St. dev.	-1.6 %		-7.4 %		-9.5 %		-1.2 %		2.8 %		-0.3 %		-0.5 %		3.3 %		-0.8 %	

**Fig. 5** CO comparison values

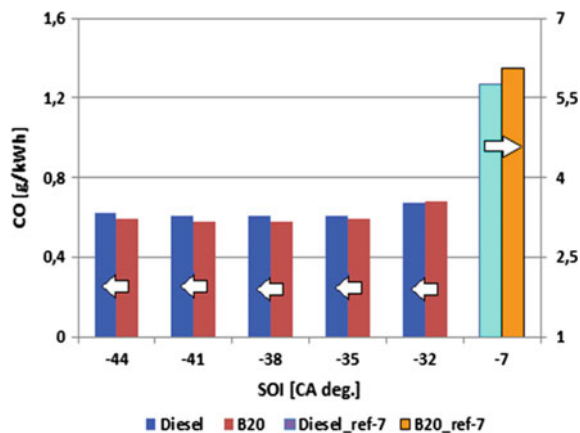


**Fig. 6** Soot comparison values

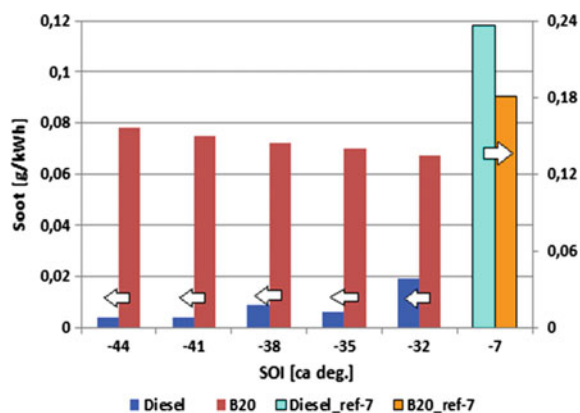
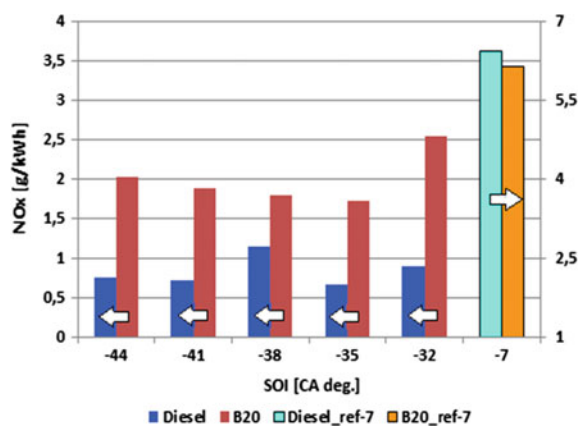


**Fig. 7** NO<sub>x</sub> comparison values





increase of total combustion duration in the case of biodiesel and approximately the same duration for the premixed stage as for Diesel fuel this leading finally to longer diffusion stage for biodiesel B20. In such conditions the formation reaction is stronger than the oxidation one and soot emission becomes higher for biodiesel.

On the contrary, the  $NO_x$  emissions (calculated using Patta and Häfner model based on the extended Zeldovich mechanism) (Gärtner et al. 2004) seem to increase for the same injection timings as a result of temperature rise when a higher pre-mixed degree of the cylinder charge occurs (Fig. 6), but in respect to reference condition it is approximately 3 times lower. Higher peak fire pressure and higher peak temperature burned registered for biodiesel B20 lead to superior  $NO_x$  values.

Figures 8, 9 and 10 reveal the values simulated for effective power ( $P_e$ ), break specific fuel combustion (BSFC) and maximum pressure ( $p_{max}$ ), for the same range of injection timings, keeping the same reference  $-7^\circ CA$ , SOI reported for the engine operation set up.

Fig. 8 Output power comparison values

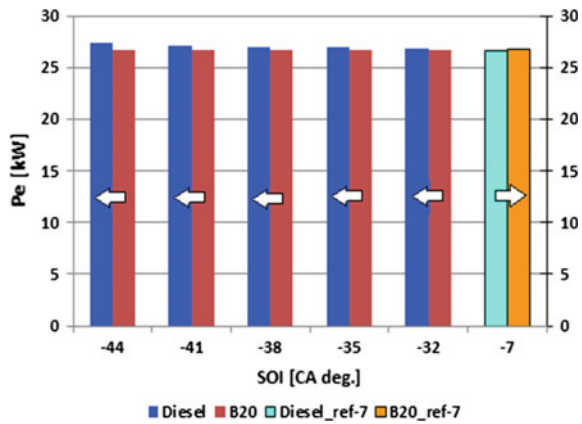
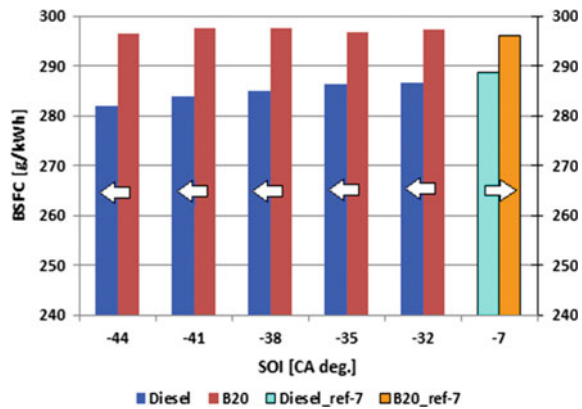


Fig. 9 BSFC comparison values



As a preliminary condition for the calculation model, the effective power was considered to remain practically unchanged (Fig. 8). The resulted values concerning BSFC, for each type of fuel apart, show a small decrease by 3.5 % in the case of Diesel fuel and a small increase by 1 % in the case of biodiesel. The decrease of the engine efficiency when using Biodiesel B20 is related to its LHV (lower heating value) compared to Diesel fuel (Fig. 9). At constant load and speed, the peak fire pressure and peak pressure rise values are higher for earlier injection timings for both fuels because the whole combustion process is shifted towards compression with an increased ignition delay (two times longer) and stronger premixed combustion, two times longer too. Thus for both fuels, the effect of much more accumulated mass of fuel injected in the auto-ignition delay is visible as an approximately two times higher peak fire pressure. This effect diminishes towards superior injection timings where for Diesel fuel maximum pressure levels fall down under biodiesel levels by approximately 5 %. The differences between the tested fuels are evident in absolute values of peak fire pressure (Fig. 10).

In the extended Table 3, there are listed the simulation results for performance and emission indicators at  $-38\text{ }^{\circ}\text{CA SOI}$ , considered as the optimum point in the partially premixed charge operation and the experimental results as reference for  $-7\text{ }^{\circ}\text{CA SOI}$ . The calculated relative deviations for two important changes, fuel nature and injection timing show that CO emission can be substantially reduced by 91.1 %, soot by 64 % and NOx by 71.3 %, keeping the performance parameters almost at initial values, effective power reduced only by 0.7 % and efficiency reduced just by 0.1 %. The important drawback of this operation mode is related to the peak fire pressure which is increased 61.3 % and to the peak pressure rise increased by 201.4 % in condition of similar air-fuel ratio leaned by 3.3 % with reduced fuel consumption by 1 %.

**Fig. 10** Peak fire pressure comparison values

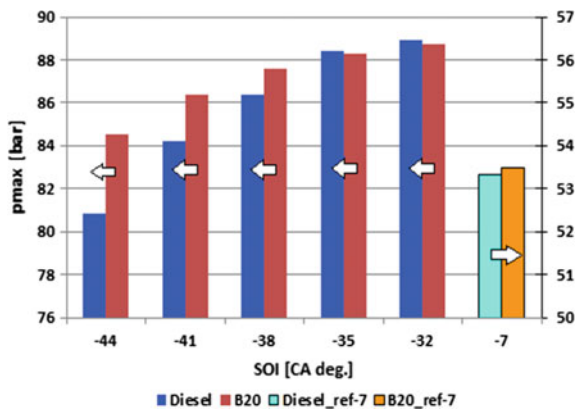


**Table 3** Comparison between simulation and experimental values obtained at 2400 rpm speed and 60 % load

	NO <sub>x</sub> (g/kWh)		CO (g/kWh)		Soot (g/kWh)		P <sub>max</sub> (bar)		(dp/dα) <sub>max</sub> (bar/deg)		P <sub>e</sub> (kW)		BSFC (g/kWh)		Lambda (-)		Fuel Cons. (kg/h)	
	Sim	Exp	Sim	Exp	Sim	Exp	Sim	Exp	Sim	Exp	Sim	Exp	Sim	Exp	Sim	Exp	Sim	Exp
SOI (°CA)	-38	-7	-38	-7	-38	-7	-38	-7	-38	-7	-38	-7	-38	-7	-38	-7	-38	-7
Diesel	1.14	6.40	0.6	5.75	0.099	0.23	86.4	53.3	4.12	1.42	27	26.83	285	285.8	2.3	2.36	7.73	7.66
St. dev.	-82.1 %		-89.5 %		-43.6 %		62.1 %		190.1 %		0.6 %		-0.2 %		-2.5 %		0.9 %	
B20	1.79	6.24	0.58	6.55	0.072	0.2	87.6	54.3	4.25	1.41	26.62	26.83	297.5	298	2.46	2.38	7.91	7.99
St. dev.	-71.3 %		-91.1 %		-64 %		61.3 %		201.4 %		-0.7 %		-0.1 %		3.3 %		-1 %	

## Conclusions

- Simulation tests conducted on the normal aspirated tractor diesel engine at high speed, 2400 rpm and high load, 60 %, have concluded that early start injection process influences the improvement of gas emissions levels comparing to diesel classic injection operation.
- This significant drop of the emissions levels is linked directly to the combustion particularities of the partial premixed mode of air-fuel formation and combustion for both types of fuels, Diesel and biodiesel B20. For this particular combustion mode, hydrocarbons and CO are presumed more likely to be consumed but meanwhile the high rate of fire pressure and temperature rise is leading to NO<sub>x</sub> formation.
- Although biodiesel is renewable, nontoxic, and biodegradable and has low emission profiles, the main drawback of using biodiesel in Diesel engines is still the high proportion of NO<sub>x</sub> emissions at low and medium loads.
- Performance and efficiency of the tested engine maintain their reference values, the only difference consisting in the slight increase of BSFC when using B20 because of its lower LHV comparing to Diesel fuel.
- The significant augment of the peak pressure rise in correspondence with the peak fire pressure at early injection timings has to be further analyzed due to the risk of major engine vibrations and noise which could challenge reasonable limitations.
- Considering the importance of the actual results the potential of proposed solution was confirmed but an experimental and theoretical study has to be extended to other engine operating conditions.

**Acknowledgements** The authors of this paper acknowledge the AVL Advanced Simulation Technologies team for its significant support offered to them in performing the simulation part of this work.

## References

- AVL BOOST Theory and AVL BOOST UsersGuide, <https://www.avl.com/ro/boost>
- Cao L et al (2007) Analysis of controlled auto-ignition/HCCI combustion in a direct injection gasoline engine with single and split fuel injectors. *Combust Sci Technol* 180(1):176–205
- Chiriac R et al (2015) On the possibility to reduce CO<sub>2</sub> emissions of heat engines fueled partially with hydrogen produced by waste heat recovery. *Int J Hydrogen Energy*. doi:10.1016/j.ijhydene.2015.06.064
- Fridriksson H (2011) CFD Investigation of heat transfer in a Diesel engine with diesel and PPC combustion mode. Master thesis, Lund University
- Gärtner U et al (2004) Development and application of a semi-empirical NO<sub>x</sub> model to various HD diesel engines. In: *Thermo-and fluid dynamic processes in diesel engines 2*. Springer, Berlin, pp 285–312

- Gharbanpour M, Rasekhi R (2013) A parametric investigation of HCCI combustion to reduce emissions and improve efficiency using a CFD model approach. *Fuel* 106(2013):157–165 Elsevier
- Ismail HM et al (2013) Development of a reduced biodiesel combustion kinetics mechanism for a CFD modelling for a light-duty diesel engine. *Fuel* 106:388–400 Elsevier
- Kalghatgi GT et al (2011) Auto-ignition quality of gasoline fuels in partially premixed combustion in diesel engines. In: *Proceedings of the combustion institute*, no 33. Elsevier, pp 3015–3021
- Kim K et al (2014) Load expansion of naphtha multiple premixed compression ignition (MPCI) and comparison with partially compression ignition (PPCI) and conventional diesel combustion (CDC). *Fuel* 136(2014):1–9 Elsevier
- Manente V et al (2010) An advanced internal combustion engine concept for low emissions and high efficiency from idle to maximum load using gasoline partially premixed combustion. SAE technical paper 2010-01-2198. doi:[10.4271/2010-01-2198](https://doi.org/10.4271/2010-01-2198), 21 p
- Maurya RK, Agarwal AK (2013) Investigations on the effect of measurement errors on estimated combustion and performance parameters in HCCI combustion engine. *Measurement* 46 (2013):80–88 Elsevier
- Schubiger RA et al (2002) Soot emission from diesel combustion. *MTZ* 63(5):342–353
- Steeper R, Davisson M (2014) Analysis of gasoline negative-valve-overlap fueling via dump sampling. *SAE Int J Engines* 7(2):762–771. doi:[10.4271/2014-01-1273](https://doi.org/10.4271/2014-01-1273)
- Tanov S et al (2014) Combustion stratification with partially premixed combustion, PPC, using NVO and split injection in a LD-diesel engine. *SAE Int J Engines* 7(4):1911–1919. SAE paper no. 2014-01-2677. doi: [10.4271/2014-01-2677](https://doi.org/10.4271/2014-01-2677)
- Voicu I et al (2013) Effects of hydrogen induction in a diesel engine operating with biodiesel B20 at different injection timings. *Termotehnica Revue*, XVII (2), pp 43–54

# Public Transport—Feasible Solution for Sustainable Urban Mobility

Vasile Dragu, Eugen Roșca and Aura Ruscă

**Abstract** Fulfilling the nowadays population's mobility requirements is an acute duty that the policy makers, and mostly those from the public transportation field or local authorities, should solve into a sustainable manner. We travel more and for different purposes, with a lot of travel means, proving a selfish travel behavior. The travel pattern, mainly in the cities, has changed dramatically during the last century, and we assist to an exacerbate use of the personal cars instead of the public transportation or walk. The paper investigates the public transportation system in Bucharest area, outlining the way the public authorities decided to shape its development. Different transport modes (subway, bus, tram, trolleybus) are analyzed, considering their network features and technological procedures. Using dedicated software (VISUM), the public transport levels of service for the city's districts are evaluated. A concordance between the territory system characteristics and the public transport is seek out. Conclusions, to improve the public transport attractiveness and to alleviate the mobility, are proposed.

**Keywords** Urban development · Sustainable mobility · Transport networks · Public transport

---

V. Dragu (✉) · E. Roșca · A. Ruscă  
Faculty of Transport, Department Transport, Traffic and Logistic,  
University Politehnica of Bucharest, Splaiul Independentei Nr. 313,  
sector6, 060042 Bucharest, Romania  
e-mail: v\_dragu@yahoo.com

E. Roșca  
e-mail: eugen.rosca@gmail.com

A. Ruscă  
e-mail: aura\_panica@yahoo.com

## Introduction

Following the industrial revolution, the peoples' life got better and better and the cities began to develop. The industrialization brought a quick increase in passenger cars (PC) number as shown in Table 1.

In 10 cities in Romania the number of passenger cars exceeds 600 PC/1000 inhabitants. Bucharest became a city with more vehicles than Amsterdam, Copenhagen, Prague or Rome (Univers Ingineresc 2015). The Mobility Plan proposed by Bucharest Metropolitan Transport Association (part of the civic society acting in accordance with the municipality) aims to create a complex public transport network to solve the actual congestion problems. As a benchmark, was settled to increase from 20 % to at least 80 % the use of the public transport. This goal has to be realized in the zone having the highest density of population in the country—over 8000 inhab./km<sup>2</sup>.

Despite the other goods, the passenger car possession has consequences beyond the private area. First of all, this could satisfy the mobility needs, enlarging the activities space, and secondly it could reshape the urban form because there is a tight connection between the motorization degree and urbanization. The motorization strengthens the connection among the urban areas (Yeh 2009; Newman and Kenworthy 1996).

**Table 1** Number of passenger cars/inhabitants

Country	1985	1990	1995	2002	2006	GP/inhab. <sup>a</sup>
Germany	450	512	529	580	597	22,670
Belgium	363	419	463	520	538	23,250
France	446	495	520	585	595	22,010
Great Britain	379	454	474	536	571	25,250
Canada	559	617	562	572	585	22,300
USA	708	752	759	785	813	35,060
Japan	375	456	527	576	593	33,550
South Korea	25	71	177	273	322	9930
Taiwan	71	143	208	263	295	13,790 <sup>b</sup>
Argentina	173	180	167	190	181	4060
Brasil	86	87	89	117	124	2850
China	3	5	8	12	23	940
India	3	5	6	8	12	480

Source [www.iru.org](http://www.iru.org), [www.ccfa.fr](http://www.ccfa.fr)

<sup>a</sup>GDP USD/inhab. in 2002 (World Bank 2004)

<sup>b</sup>GDP USD/inhab. in 2002 (General Directorate for Budget and Statistics)

## Sustainable Mobility

In contemporary society the maximum limits of environmental degradation were entered in the form of general valid principles, in terms of eco-development and more recently sustainable development. Quality of life in major cities is being determined by the congestion level, air quality, network vulnerability and traffic safety on the road transport infrastructures (Dragu et al. 2015).

Sustainable development can be considered a cybernetic system, as its definition reveals, as being the development that meets present needs without compromising the ability of future generations to meet their own needs. It is an interconnection covering several future states of relations, and interconnections man—nature having strong interrelated forms of feedback.

The objective of sustainable development of urban transport can be formulated as follows: urban transport networks must achieve consistency between the level of service, limited natural resources, environment and infrastructures capacity.

Classic measures to satisfy mobility needs focused exclusively on developing the road infrastructure leading to the land use, the degradation of the natural landscape, increased risks of accidents and attracting new traffic, which lead again to the congestion and the process is cyclic until the expansion of road infrastructures is no longer possible. Thus a false congestion decrease process is described (Fig. 1).

To ensure sustainable development of mobility and reduce congestion, the traditional measures of enhancing transport infrastructure have to be associated with measures to reduce the social travel needs. Table 2 shows comparatively the urban mobility planning models (Pucher and Buehler 2010).

Since concerns for sustainable development have come to the attention of specialists, the cities development issues and the interaction between their development and mobility have gained more importance. The focus is mainly on economic and social consequences for the environment of the urban system. (Vanco 2011; Allaire 2004).

According to the “White Paper” (revised in 2011), a better integration of modal networks will lead to an increased number of modal choices: airports, ports, railways, metro and bus stations should be more closely linked and transformed into multimodal connection platforms for passengers (exchange poles). Greater use of

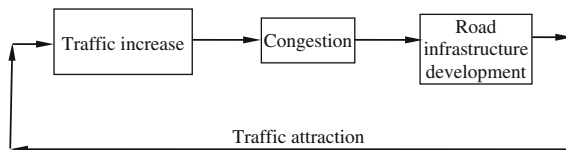


**Fig. 1** False model to decrease congestion (Dragu et al. 2014)



**Table 2** Planning urban mobility (after Pucher and Buehler 2010)

Classic urban mobility planning	Sustainable urban mobility planning
Traffic oriented	Human oriented
Main goal: enhancing traffic conditions	Main goal: enhancing accessibility and quality of life
Political decisions based on specialists studies	Stake-holders involvement
Transportation engineering point of view	Multidisciplinary
Actions towards increasing roads capacity	Actions towards decreasing travel needs, modal allocation and urban logistics
Oriented investments program	Sharing investments among domains providing sustainable mobility
Great and expensive infrastructure projects	Enhancing efficiency of transport
Limited impact in solving urban traffic problems	High and timeless impact in reducing traffic and changing in travel behavior

public transport modes must be accompanied by an appropriate set of passengers' rights (EC 2011).

The overall objective of sustainable development in Romania is the balanced development of the transport system providing modern infrastructures and transport services, sustainable development of the economy and a higher quality of life (Stefanica and Dragu 2013).

Achieving this objective will contribute directly to ensuring sustainable development of the transport sector, the economy and the environment, increase the accessibility of Romania, ensuring co-modality, promoting the balanced development of all modes of transport and improving quality and efficiency in services ([www.gov.ro/ro/obiective/strategii-politici](http://www.gov.ro/ro/obiective/strategii-politici)).

Besides these actions, there are the *traditional* measures aiming to reduce the travel need (Banister 1997, 2008; Raicu et al. 2014; Dragu et al. 2011):

- Access restriction in specific areas;
- Reducing the number of PCs owned by a family and their intensive and distributive (car pooling, car sharing);
- Rescheduling jobs beginning time;
- Priorities for non-motorized transport and for the land-use;
- Subsidies for the non-motorized transport;
- Public relations;
- Park and ride, parking fees, parking control;
- Avoiding congestion during peak-hours;
- Investments in public transport capacities;
- Priority for public transport;
- Subsidies in public transport;
- Traffic restrictions;
- Road use taxation;
- Traffic calming.

There are so many potential measures to reduce the travel needs, which can be combined with the stated policies. These solutions consist of switching and substitution mechanisms through which the trips are changed and reduced.

## State of the Urban Public Transport

Lately, due to social, economic and geographical development of cities, the need of mobility has grown more and more. Citizens from economically developed cities, where congestion and pollution make personal journey unattractive and expensive, understand mobility as a right (Albalade and Bel i Queralt 2009).

Between 1960–1970, the annual number of journeys made by public transport has increased in North America and Western Europe. Although there are differences between countries in these areas, it is encouraging that overall, the number of public transport users has increased despite rising incomes and private car owners.

Between 2005 and 2010, the annual number of journeys made by public transport ranges from 237 trips/year/person in Sweden to 24 trips/year/person in USA. It may seem surprising that after the USA, the Netherlands has the lowest number of trips made by one person in one year by public transport (52), but this is because a huge number of journeys is effectuated by bicycle (Pucher and Buehler 2010).

It is remarkable that in Canada is carried out twice more public transit than in the US likely that the variation in the development of cities (they tend to compact cities), the smaller number of owners of private cars and higher costs with fuel (Filion et al. 2004).

All European countries (Fig. 2) have shown a greater percentage of public transport users than the US, but even so there are notable differences among them.

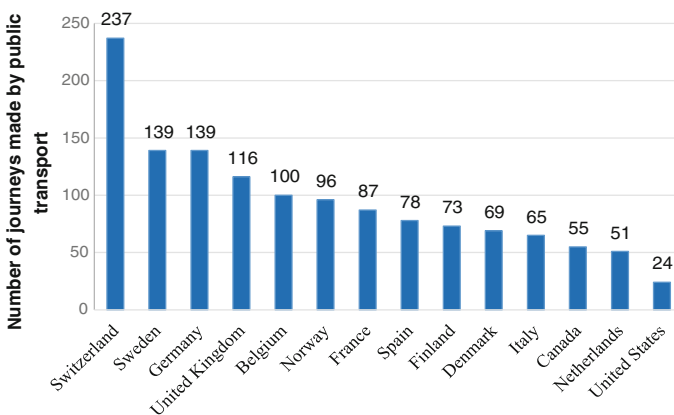


**Fig. 2** Number of journeys by person [journeys/pers./year], in Europe and North America, 2005–2010 (APTA 2012; BFS 2011)

Greater demand for public transport in European countries is due to higher densities of cities, higher fuel and car purchase fees, the small number of available parking spaces, and a large number of restrictions on car use in cities. Overall, European cities offer transport services with a better quality than those in the US (National Research Council 2001). The service quality level in terminals for local, regional and inter-regional transport is determinant for making public transport more attractive (Dragu et al. 2003).

Since 1990, in Romania and especially in Bucharest there has been a constantly growing tendency towards new expensive residential settlements located in the suburbs. Bucharest is a historically developed city and there is no available space to increase the street capacity for cars and traffic. Public transport system which is composed of underground (67 km) and surface network (Table 3) it is a solution to satisfy the need for urban mobility (Popa et al. 2006).

The tram network has three major terminals: Calea Plevnei, Piața Sf. Gheorghe și Piața Unirii. Calea Plevnei terminal is located relatively far away (approx. 1 km from any attraction point). Trams back here frequencies are relatively low. Piața Sf. Gheorghe terminal is well located in relation to major centers of attraction in the city center, but the frequency is reduced or tends to be unbalanced along the corridors most used.

Piața Unirii terminal is centrally located although the access is via pedestrian crossings on high-traffic streets. Frequency of service to Piața Unirii is high and tends to occur only by tram from the SW of the city.

Radial network of tramlines does not offer transiting journeys of the city without correspondence. This possibility is partly covered by a central adjacent line offering alternative routes (e.g. Line 41 highly used). Tram network has a solid surface covering of the city, but has substantial fluctuations in headways. Nowadays, Bucharest Surface Operator (RATB) has 481 trams, network density 1.17 km/km<sup>2</sup>, 23 routes, and a parking capacity in 8 depots of 574 trams.

From the point of view of the operation the headways are between 2 and 54 min. Lead times are reduced on lines 41 and 32 (2–6 min) and the largest intervals 19–54 min are on line 46 (Gara de Nord—Granitului); the greatest range being late hours of the night.

In terms of equipment and comfort of the passengers, trams have different standards, the park consisting of old and new vehicles. Network access is via

**Table 3** Terrestrial transport network features

No.	Network type	Length (km)	
		Network	Routes
1.	Bus	419	1224
2.	Trolley	66	130
3.	Tram	139	242
Total		624	1596

stations, which have a different design depending on the year of construction. Mostly, the access in vehicles is on stairs, leading to inconvenience for the elderly or mobility impairment persons. The weakest point is the lack of opportunities to penetrate and cross the central zone, which would reduce congestion in the area.

Trolleybus network can be shared artificially in three subnets: South network, the network crossing the city and adjacent network. Transport lines which cross the city have a common axis (Bd. Regina Elisabeta, Piața Universității and Bd. Carol I).

Adjacent lines tend to reach that point of interest Gara de Nord, but none of these lines (running Calea Grivitei) reach the downtown area. There is a parallel of the trolley bus lines with M4 metro line.

Southern trolley lines form a network independent from other lines. They are organized and have Piața Sudului as an extremely important correlation and economic center of Berceni area. Lines tend to be well designed and in accordance with the transport demand. In the South area, each trolley line tends to have a parallel bus line route that goes further to the city center. The density of tram network is  $0.6 \text{ km/km}^2$ , the tram fleet counts 297 units, there are 4 depots, 17 routes, depots capacity 404 trams.

In terms of exploitation, especially of fulfilling demand, the headways are between 2 and 64 min. The highest frequency has route 77 (Piața Resita - Alexandru Obregia) with headways ranging from 2 to 8 min, and the lowest frequency route 90 (Arena Națională—Valea Argeșului) between 26 and 64 min. This line has a very long route and its analysis on any segment shows that it is not the only transport option.

Bus network is the most extensive of all networks and is designed to cover areas left free for other modes of transport already analyzed (metro, tram, trolley). However the bus network does not supply the high-capacity urban modes (metro, tram), but bus lines have radial routes to the city center, overlapping in many cases with metro lines, tram and trolley right. Thus it comes to unnecessary and inefficient resource consumption.

The characteristics of the bus fleet and network are: network density  $2.98 \text{ km/km}^2$ , the fleet size 1147, eight depots, 106 public transport routes (including 10 suburban lines), active fleet 862 buses, parking capacity in the 8 depots is 1241 units, leading to 92 % degree of use, given the number of buses in the total fleet inventory, which also must be parked inside depots.

In terms of operating buses and meeting the demand for transport, the headways (and hence hourly capacity) are between 3 and 50 min. The highest frequency has route 139 (Zețariilor—Piața Leu) with headways between 3 and 8 min and the highest headways have routes 216, 106, 122, 124 and others that connect residential areas or new remote commercial areas.

Analyzing the number of vehicles in the fleet inventory and those in the active park is noted that approx. 33 % of the park is inactive fleet which is huge, considering the large amount of expenditure with inactivate park.

With respect to the average speed operation, it no longer exists the classical distinction between the speeds of urban transport modes, due to congestion, and the fact that public transportation runs often in the general traffic—13 km/h for trams,

**Table 4** Trips made by public transport in Bucharest ( $\times 10^6$ )

Year	2013		2012		Difference	Dif. %
	Value	(%)	Value	(%)		
Tram	322	44.35	334	44.47	-12	-3.59
Trolley	72	9.92	74	9.86	-2	-2.70
Bus	332	45.73	343	45.67	-11	-3.21
Total	726	100	751	100	-25	-3.33

Source [www.ratb.ro/statistici.php](http://www.ratb.ro/statistici.php)

11.3 km/h for trolleys and 13.7 km/h for buses (2013 base year). Also in 2013, there is a mean daily transport service approximately of 14.6 to 15.8 h/day (14.7 h/day for trams, 15.8 h/day for trolleys and 14.6 h/day for buses). The value is high which explains the high number of failures and hence high value of the idle fleet.

The number of trips made by urban population of Bucharest, using public transport vehicles is presented in Table 4.

From Table 4 it notes that the number of trips made by public urban transport decreased in 2013 compared to 2012. This can be attributed to the fact that income and willingness to pay for private car use grew or made a shift towards travel by metro. Another cause may be the errors in counting the number of trips made due to the impossibility to identify all passengers using public transport.

Table 5 shows the offer of the Bucharest Surface Operator.

To analyze the degree of public transport serving the population in the areas bounded by the districts of Bucharest, the data in Table 6 were used. It states that information relating to the tram and trolley network characteristics of each sector were obtained using VISUM macro-simulation program.

The dimensional random variables considered and whose linear functional dependence was verified were:

1. Number of inhabitants and tram network length in each sector;
2. Sector surface and tram network length in each sector;
3. Number of inhabitants and trolley network length in each sector;
4. Sector surface and trolley network length in each sector;
5. Population density and tram network length in each sector;
6. Population density and trolley network length in each sector.

**Table 5** Public transport offer in Bucharest (seats.km for a loading degree of 6.5 psg./m<sup>2</sup>) ( $\times 10^6$ )

Mode	Year		Dif. %
	2013	2012	
Tram	4 503.76	4 454.08	+1.12
Trolley	949.39	954.25	-0.51
Bus	4 616.70	4 595.59	+0.46
Total	10 069.85	10 003.92	+0.66

Source [www.ratb.ro/statistici.php](http://www.ratb.ro/statistici.php)

**Table 6** Network and served area features

Sector features		1	2	3	4	5	6
Inhabitants		238,217	304,523	342,541	261,306	241,585	333,422
Surface (km)		68	32	33	30	28	37
Population density (inh./km <sup>2</sup> )		3503.2	9516.4	10,380	8710.2	8628	9011.4
Network length (km)	Tram	24.7	37.8	17.4	7.2	21	30.9
	Trolley	8.8	17.2	6..2	6.2	10.0	17.6
Network density (km/km <sup>2</sup> )	Tram	0.36	1.18	0.53	0.24	0.75	0.84
	Trolley	0.13	0.54	0.19	0.21	0.36	0.48

If  $n$  measurements are made for a bi-dimensional random variable (the measurements being connected to the values for each sector in Bucharest)  $x_1, y_1; x_2, y_2; \dots; x_n, y_n$ , then the correlation coefficient  $r$  is:

$$r = \frac{\sum_{i=1}^n (x_i - \bar{x})(y_i - \bar{y})}{n \cdot s_x \cdot s_y}, \tag{1}$$

where  $\bar{x}$  și  $\bar{y}$  are the means for  $x$  and  $y$ ;  
 $n$  number of measurements  $x_i$  and  $y_i$ ;  
 $s_x$  și  $s_y$  standard deviations for  $x$  and  $y$ .

The correlation coefficient may have a value in the range from  $-1$  to  $1$ . When  $r = 1$ ,  $x$  and  $y$  are linked by a linear functional dependence both sizes vary in the same sense. If  $r = -1$ , there is a reverse dependence in nature.

The significance of dependence between two random variables is determined by assessing the correlation coefficient. In a small volume of selection ( $n$  less than 30 ... 50) it can be used the Romanovski criterion ( $R_r$ ) (Dragu 2001):

$$R_r = |r| \sqrt{n - 1} \geq 3. \tag{2}$$

If inequality (3.2) is satisfied, then the assessment obtained for the correlation coefficient is considered real and correlation exists. Otherwise, this deviation from zero is considered as random.

The calculated values for determining the existence of a linear connection function defining the sizes of the bi-dimensional random variable are presented in Table 7.

**Table 7** Measurements of the bi-dimensional random variables

Measurements Random variables	$\bar{x}$	$\bar{y}$	$S_x$	$S_y$	R	$R_r$
Inhabitants ( $x_i$ )—Tram network length ( $y_i$ )	286,932.40	23.17	42,129.40	9.74	0.30	0.66
Sector surface ( $x_i$ )—Tram network length ( $y_i$ )	38.00	23.17	13.7	9.74	0.16	0.36
Inhabitants ( $x_i$ )—Trolley network length ( $y_i$ )	286,932.40	11.00	42,129.40	4.72	0.36	0.79
Sector surface ( $x_i$ )—Trolley network length ( $y_i$ )	38.00	11.00	13.70	4.72	-0.10	0.22
Population density ( $x_i$ )—Tram network density ( $y_i$ )	8291.50	0.65	2221.00	0.31	0.42	0.94
Population density ( $x_i$ )—Trolley network density ( $y_i$ )	8291.50	0.32	2221.00	0.15	0.48	1.08

## Conclusions

Developed countries are trying to implement a coherent urban transport system where the number of trips by personal car is minimized.

Emerging countries can avoid the situation experienced by developed countries, by direct passage to the stage of public transport and modal shift that could prevail the problems of congestion, stress, pollution of all kinds and traffic (Holden et al. 2013).

From the analysis it appears that many of the weaknesses in the public transport system in Bucharest are still valid. The accelerated growth of the degree of motorization leads, for the common use of the infrastructure by personal cars and public transport, to heavy traffic conditions that affect decision to use the public transport. The conditions offered by the public transport operator are severely affected by external factors (congestion) and the quality perceived by users is not a true reflection of the efforts of the authorities to meet the transport schedule.

Analyzing data listed in Table 4 and those in Table 5, it notes that the number of trips made by public urban transport decreased in 2013 compared with 2012, while the supply of transport has increased. The offer increased in number of seatsxkm, which means that RATB was concerned with qualitative and quantitative increase supply. Quantitative aspect of the number of seats offeredxkm indirectly reflected in the qualitative aspects of the business and increases the attractiveness of public transport.

The analysis of the values shown in Table 7 underlines the conclusion that there is no dependency between variables. This is because the value  $r$  is far from a value of 1 or  $-1$ . Also, disregard of the condition (3.2) leads to the same conclusion that there is no dependency between variables. In practice, a fair service of the territory by the public transport should admit dependence existence between variables.

## References

- Albalade D, Bel i Queralt G (2009) Factors explaining urban transport systems in large European cities: a cross-sectional approach. IREA—working papers, IR09/005
- Allaire J (2004) Mobilité et effet de serre: l'évolution des villes au Nord et les perspectives au Sud. Cahier de recherche, Série EPE 37:2004
- Banister D (1997) Reducing the need to travel. *Environ Plann B* 24:437–450
- Banister D (2008) The sustainable mobility paradigm. *Trans Policy* 15(2):73–80
- BFS (2011) Mobility and transport 2010. Bern: Bundesamt fuer Statistik/Swiss Federal Office for Statistics
- Dickens M, Neff J, Grisby D (2012) APTA 2012 public transportation fact book
- Dragu V (2001) Trafic urban și suburban de călători, Editura BREN, București. ISBN 973-8143-59-4, 152 p
- Dragu V, Rosca E, Rusca F, (2003). Service quality in the terminal joining magistral and urban transport. Transportation faculty. Politehnica University of Bucharest, Rumania, pp 5–7
- Dragu V, Ștefănică C, Burciu Ș (2011) The influence of Bucharest's metro network development on urban area accessibility. *Theor Empirical Res Urban Manage* 6(1):5–18
- Dragu V, Roman VC, Roman EA (2014) Acțiuni asupra cererii de transport orientate către o mobilitate urbană durabilă, *Buletinul AGIR* nr. 2/2014, Editura AGIR, pp 78–83
- Dragu V, Burciu S, Rosca E, Rusca F (2015) Intervention opportunity model within transport studies. *UPB Sci Bull Ser D Mech Eng* 77(1):97–104
- EC European Commission (2011) White paper roadmap to a single European transport area towards a competitive and resource efficient transport system. COM, p 144
- Filion P, Bunting T, McSpurran K, Tse A (2004) Canada-US Metropolitan Density Patterns: Zonal Convergence and Divergence. *Urban Geogr* 25(1):42–65
- Holden E, Linnerud K, Banister D (2013) Sustainable passenger transport: back to Brundtland. *Trans Res A Policy Pract* 54:67–77
- National Research Council (US) (2001) Transportation research board. Committee for an international comparison of national policies and expectations affecting public transit. Making transit work: insight from Western Europe, Canada, and the United States. National Academy Press
- Newman PW, Kenworthy JR (1996) The land use—transport connection: an overview. *Land Use Policy* 13(1):1–22
- Popa M, Raicu S, Costescu D, Rusca F (2006) Effects of a non-motorized transport infrastructure development in the Bucharest metropolitan area. In: 4th international conference on urban regeneration and sustainability (the sustainable city)
- Pucher J, Buehler R (2010) Walking and cycling for healthy cities. *Built Environ* 36(4):391–414
- Raicu S, Dragu V, Burciu S et al (2014) Effects of facility location on urban road traffic. In: Proceedings of the 2nd international conference on traffic and transport engineering (ICTTE), pp 196–202
- Ștefanica C, Dragu V (2013) About the quality of service in a transport terminal. *Metal Int* 18 (9):276
- Univers Ingineresc nr. 17/1–15 septembrie 2015
- Vanco F (2011) Formes urbaines et durabilité du système de transports: Une application par les coûts de la mobilité urbaine des ménages sur l'agglomération Lyonnaise (Doctoral dissertation, Lyon 2)
- [www.gov.ro/ro/obiective/strategii-politici-programe/programul-legislativ-al-guvernului-romaniei-pentru-perioada-2005-2008-principalele-reglementari&page=2](http://www.gov.ro/ro/obiective/strategii-politici-programe/programul-legislativ-al-guvernului-romaniei-pentru-perioada-2005-2008-principalele-reglementari&page=2)
- [www.iru.org](http://www.iru.org)
- [www.cdfa.fr](http://www.cdfa.fr)
- [www.ratb.ro/statistici.php](http://www.ratb.ro/statistici.php)
- Yeh CF (2009) Intermodalité et coûts des déplacements urbains dans les mégapoles. Les cas de Paris, Shanghai et Taipei (Doctoral dissertation, Université Paris-Est)



# Uncertainty in the Study of Automotives Dynamics and Analysis and Reconstruction of Car Crashes

Ramona-Monica Stoica, Marian-Eduard Rădulescu, Irinel Dinu,  
George Ene, Daniel Neagu and Ion Copae

**Abstract** This paper aims to highlight the most used mathematical models as well as the uncertainties resulting from automotive dynamics study and analysis and reconstruction of car crashes. In order to understand the process, a description of basic concepts must be made regarding: value intervals, vectors and matrix with intervals, algebraic systems with intervals and differential equation with intervals. Another purpose of the paper is to establish mathematical models for automotive dynamics study and for the analysis and reconstruction of car crashes in the presence of uncertainties. We also study some parameters' influence on sizes that define automotives dynamics and car crashes. Moreover, other goals of this study are to establish sizes associated with automotives dynamics and car crashes in the presence of uncertainties by applying the concepts and intervals analysis algorithms or by applying the concepts and uncertainty theory's algorithms which is a branch of mathematical statistics complementary to the probability theory.

---

R.-M. Stoica (✉) · I. Copae  
Military Technical Academy, 39th—49th George Cosbuc Bd., Bucharest, Romania  
e-mail: monyk\_dep@yahoo.com

I. Copae  
e-mail: copaeion@yahoo.com

M.-E. Rădulescu  
Technical Expert F-L, 10Ath Răcari Str., Bucharest, Romania  
e-mail: radulescu1961@yahoo.com

I. Dinu  
Insurance Company Astra S.A., 3rd Nerva Traian Str., Bucharest, Romania  
e-mail: irinel.dinu@astrasig.ro

G. Ene  
S.C. Insurance S.R.L., 21st Nicolae Grigorescu Bd., Bucharest, Romania  
e-mail: ene\_george@yahoo.com

D. Neagu  
Carpatica Insurance S.A., 72nd Unirii Bd., Bucharest, Romania  
e-mail: daniel.neagu@carpaticaasig.ro

**Keywords** Road accident · Vehicle dynamics · Interval analysis · Uncertainty theory · Generalized Hukuhara differentiability

## Uncertainties in the Study of Automotive Dynamics

For the study of automotive driving in case of uncertainty is used the well known differential equation which describes it's longitudinal dynamics (Ghiulai 1975); if we consider a driving on a horizontal road, this equation becomes:

$$v' = \frac{g}{\delta G_a} \left( \frac{M_e i_t \eta_t}{r_r} - G_a f - k S v^2 \right) \quad (1)$$

in which the speed  $v$  is unknown, and  $v'$  is it's derivative.

In formula (1) are noted:  $g$ —gravitational acceleration,  $\delta$ —reduced mass coefficient,  $G_a$ —automotive weight,  $M_e$ —engine torque,  $i_t$ —total transmission ratio,  $\eta_t$ —transmission efficiency,  $r_r$ —wheel rolling radius,  $f$ —rolling resistance coefficient,  $k$ —aerodynamic coefficient,  $S$ —automotive frontal area.

For an automobile with multiple gear mechanical transmission, with engine speed  $n$ :

$$i_t = \frac{\pi n r_r}{30 v} \quad (2)$$

Likewise, is also taken into account the formula:

$$S = k_s B H \quad (3)$$

in which  $k_s$  represents shape parameter (which considers that frontal area is not a rectangle),  $B$  automotive track and  $H$  it's maximum height. In conclusion, the differential Eq. (1) becomes:

$$v' = \underbrace{\frac{\pi \eta_t g}{30 \delta G_a} \frac{M_e n}{v}}_{c_1} - \underbrace{\frac{g}{\delta} f}_{c_2} - \underbrace{\frac{k k_s B H g}{\delta G_a}}_{c_3} v^2 \quad (4)$$

In the differential Eq. (4) engine torque, engine speed and driving speed are known from tests of a certain sample. In this formula are noted the coefficients of differential equation  $c_1$ ,  $c_2$  and  $c_3$ , defined by formulas:

$$c_1 = \frac{\pi \eta_t g}{30 \delta G_a}; \quad c_2 = \frac{g}{\delta} f; \quad c_3 = \frac{k k_s B H g}{\delta G_a} \quad (5)$$

In these formulas there are uncertainties regarding the 6 sizes  $\eta_t, \delta, G_a, f, k$  and  $k_s$ , because there are not precisely known, but with values intervals; some of them are adopted from specialty literature ( $\eta_t, \delta, f, k$  and  $k_s$ ), and  $G_a$  according to automotive technical specification at which we add uncertainties regarding fuel quantity, luggage and passengers weight etc. Also, in formulas (4) and (5) is considered that there are no uncertainties regarding gravitational acceleration  $g$  (is adopted  $g = 9.81 \text{ m/s}^2$ ) and  $B$  and  $H$  sizes.

In conclusion the coefficients (5) of differential Eq. (4) also have values within certain intervals, from a minimum value (index  $m$ ) to a maximum value (index  $p$ ), so that formula (4) becomes:

$$v' = [c_{1m}; c_{1p}] \frac{M_e n}{v} - [c_{2m}; c_{2p}] - [c_{3m}; c_{3p}] v^2 \tag{6}$$

Therefore, formula (6) represents a differential equation with coefficients situated in real values intervals which means that theoretically it has an infinity of solutions; in other words, the differential equation has solutions layouted in an interval and can be solved with specific algorithms. Likewise, as it can be determined, the study of automotive dynamics in case of uncertainties uses operations with real values intervals: addition, deduction, multiplication and division.

Because the tests were conducted with a Ford Focus automotive, in the presented formulas, sizes that intervene are adopted with the following instantaneous and average values from the respective interval:

- rolling resistance coefficient for driving on a dry asphalt (how the tests were developed):  $f = [f; \bar{f}] = [0.012; 0.022]$ ;  $m(f) = 0.017$
- reduced mass coefficient:  $\delta = [\delta; \bar{\delta}] = [1.05; 1.4]$ ;  $m(\delta) = 1.225$
- transmission efficiency:  $\eta_t = [\eta_t; \bar{\eta}_t] = [0.82; 0.92]$ ;  $m(\eta_t) = 0.87$
- aerodynamic coefficient:  $k = [k; \bar{k}] = [0.2; 0.3]$ ;  $m(k) = 0.25$
- shape coefficient:  $k_s = [k_s; \bar{k}_s] = [0.85; 0.9]$ ;  $m(k_s) = 0.875$
- automotive weight:  $G_a = [G_a; \bar{G}_a] = [13753.6; 17559.9]$ ;  $m(G_a) = 15656.7$
- sizes:  $B = 1.84 \text{ m}$ ,  $H = 1447 \text{ m}$ .

As it can be determined, adopting such intervals originates from the impossibility of making deterministic forecasts, meaning to operate with unique values; therefore, the use of values intervals show the existence of uncertainties regarding the operating sizes. As it can be seen, from a quantitative point of view, uncertainties can be defined as ***an expectational set of values***.

For example, in specialty literature from auto field, for driving on dry asphalt is considered that rolling resistance coefficient has values in the range  $f = [0.012; 0.022]$ . So, in this case can be written:

$$f = [0.012; 0.022] = 0.017 \pm 0.005 = 0.017 \left( 1 \pm \frac{0.005}{0.017} \right) = 0.017 \left( 1 \pm \frac{0.034}{100} \right) \tag{7}$$

Therefore, as opposed to the values presented in specialty literature, it can be said that for automotives, the average value of rolling resistance coefficient for driving on dry asphalt can be adopted in dynamics calculus as 0.017 with a relative uncertainty of 3.4 % and an absolute uncertainty of 0.034; from the values given for this coefficient  $f = 0.012\text{--}0.022$  results that it's variation range is 83.3 %.

It must be observed that values presented in specialty literature for rolling resistance coefficient are obtained based on previously made measurement. In this case, if tests were conducted with a certain automotive, the real value of rolling resistance coefficient is not precisely known which is why an average/nominal value from specialty literature is adopted. The fair thing to do is to make calculations with *the entire recommended values interval*, this coefficient represents an uncertain variable; obviously, the result is a range of values and not a single value.

As it can be seen, operating with uncertainties requests the use of concepts and algorithms from intervals analysis and differential equations with intervals; in the first case are being used operations with intervals, and in the second case the generalized Hukuhara differentiability. For these ends there can be used the Matlab softwares (with INTLAB toolbox) and Mathematica.

For exemplification, follow-up is being studied the influence of the 6 factors ( $G_a$ ,  $f$ ,  $\delta$ ,  $\eta_t$ ,  $k_s$ ,  $k$ ) on automotive dynamics, but they are analysed only one by one. For this purpose, it will be considered an experimental sample noted F19 (at which  $v$ ,  $M_e$ ,  $n$  are known) and will be solved the differential equation with intervals (6) at which the 3 coefficients vary within the intervals established by interval operations. Figure 1 presents the results obtained in case *all 6 influence factors vary* in ranges presented above.

As it can be seen from formulas (1) from graph, the 6 influence factors have the following variations in the mentioned intervals: automotive weight  $\Delta G_a = 27.7$  %, rolling resistance coefficient  $\Delta f = 83.3$  %, low mass coefficient  $\Delta \delta = 33.3$  %, transmission efficiency  $\Delta \eta_t = 12.2$  %, shape coefficient  $\Delta k_s = 5.9$  %, aerodynamic coefficient  $\Delta k = 34.6$  %. In these circumstances, sample average speed has a variation across the whole interval  $\Delta V_m = 34.6$  %, and maximum speed  $\Delta V_{max} = 26.5$  %.

The graph also shows interval values of the 3 coefficients of differential Eq. (6); therefore, this differential equation is according to Fig. 1:

$$v' = [0.00000349; 0.00000667] \frac{M_e n}{v} - [0.08408571; 0.20554286] - [0.00018062; 0.00048833]v^2 \quad (8)$$

so, all coefficients are shown through real values intervals.

By resolving this differential equation with intervals we obtain speed values in case of uncertainties. Figure 1 presents the two extreme curves, which represent lower curve and upper curve; the solutions of differential equation with intervals, theoretically in infinite number, are placed between the two curves and on top of curves, so in the range marked on graph.

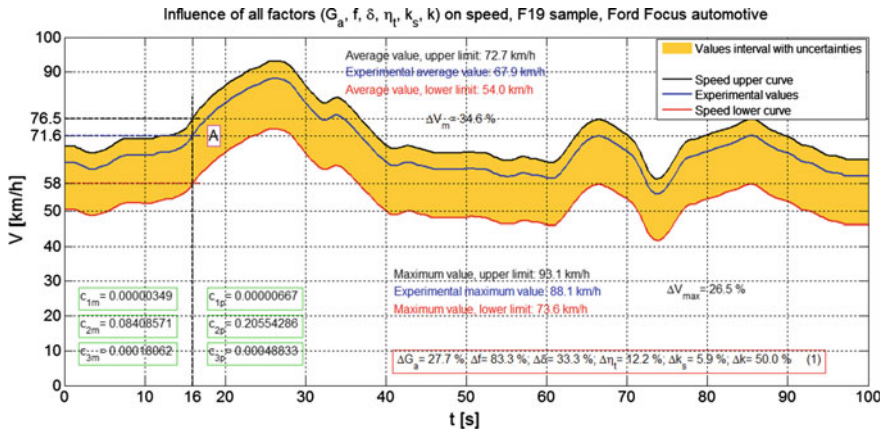


Fig. 1 Simultaneous influence of some factors on driving speed

Between the two curves is also the experimental curve, whose differential equation coefficients (6) are unknown, but they are placed in the respective intervals. As it can be determined from graph, experimental curve is placed more near the upper curve.

Likewise, in graph are also presented values of statistics characteristic for speed sample (average and maximum value), both the experimental and those associated with curves.

In graph is also shown an example with speed values at time  $t = 16$  s (zone A): the experimental value is  $V_e = 71.6$  km/h, the value associated with lower curve is  $\underline{V} = 58$  km/h, and the value associated with upper curve is  $\bar{V} = 76.5$  km/h.

Similarly is also analyzed the separate influence of one by one factor of the targeted 6. Therefore it can be concluded that the six factors have different influences on speed, for each of the 70 samples or for all samples. In order to establish which of the six targeted factors has bigger or smaller influence on speed (meaning on automotive dynamic), Fig. 2 presents the proportion between average speed variation and targeted factor variation, and the proportion between maximum speed variation and analysed factor variation with the name shown in graph.

Graph from Fig. 2 shows that the highest influence on speed variation (through average and maximum value) has the shape coefficient  $k_s$  (meaning the automotive frontal area), followed by transmission efficiency  $\eta_t$ , automotive weight  $G_a$ , reduced mass coefficient  $\delta$ , aerodynamic coefficient  $k$  and rolling resistance coefficient  $f$  (the last one with the smallest influence and off course, taking into account that tests were conducted on a dry asphalt).

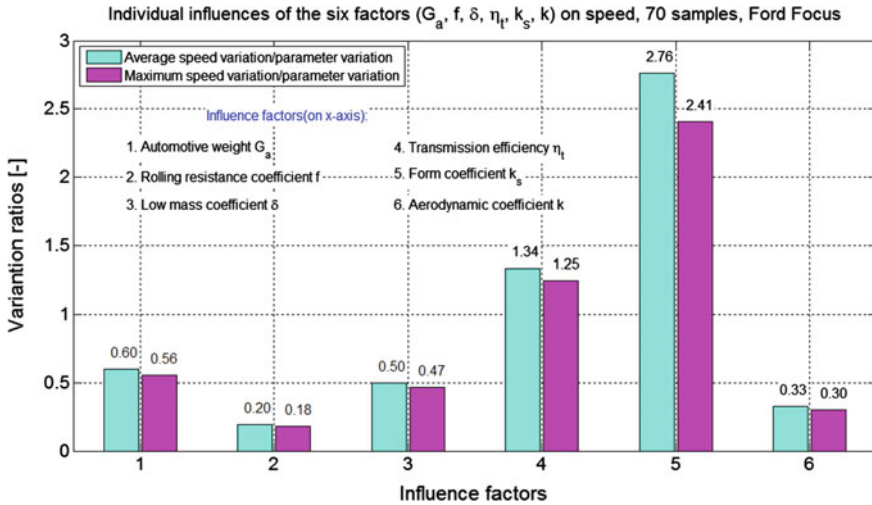


Fig. 2 Separate influence of some factors on speed

### Uncertainties in the Analysis and Reconstruction of Car Crashes

In order to offer some examples from car crashes, there are uncertainties regarding moving vehicles mass, mass moments of inertia, rolling radius, rolling resistance, aerodynamic coefficient, frontal area, adhesion coefficient, centre of gravity position, impact centre position, restitution coefficient, tangential friction coefficient between vehicles, reaction time and driver action etc. As it can be determined, uncertainties are related to the three participant factors at a car crash: the vehicle, the environment and the driver. Also, it can be observed that actually almost nothing is precisely known, that is why operating with unique values does not certify obtaining accurate results; usually, it is also said that the only certain thing is that everything is uncertain.

Follow-up is presented an example of uncertainty that appears in the analysis and reconstruction of car crashes. As it is known, the adhesion coefficient on an used dry asphalt rolling track has values in the range  $\varphi = [0.6; 0.8]$  if driving speed is less than 48 km/h and  $\varphi = [0.55; 0.7]$  if driving speed is higher than 48 km/h (Datentechnik 2013). In the first case it can be written:

$$\varphi = 0.7 \pm 0.1 = 0.7 \left( 1 \pm \frac{0.1}{0.7} \right) = 0.7(1 \pm 0.1428) = 0.7 \left( 1 \pm \frac{14.28}{100} \right) \quad (9)$$

So, in regard to the values presented in specialty literature, it can be said that for driving on an used dry asphalt rolling track, value of adhesion coefficient can be adopted 0.7 with an uncertainty of 14.28 % if automotive speed is less than

48 km/h. From this statement emerges another uncertainty, *if* the automotive speed is less than 48 km/h.

If it were to make a car crash analysis, the real value of adhesion coefficient is not precisely known, that is why is usually adopted the average value of coefficient from specialty literature (meaning 0.7); average value is also known as nominal value. In absence of other information, the accurate thing is to make calculations with *the entire recommended interval of values*, because adhesion coefficient represents an uncertain variable; obviously, it would be obtained an interval of values and not a unique value.

From the necessity of taking into account uncertainties, in specialty literature are presented values intervals of sizes used as initial data, as it can be observed from examples presented like the one above.

In car crash field there are multiple mathematical models (Brach 2011; Burg and Moser 2013; Datentechnik 2013; Franck 2013; Struble 2014; Varat 2008; Wach 2011), which allow making analysis and reconstruction of a car crash (Brach, Ishikawa, Crash3, PC-Crash etc.), but all these does not take into account uncertainties. One of the most used is Brach model, which is a planar model (PIM – Planar Impact Mechanism) of collision between two automotives, which considers linear movement along  $Ox$  and  $Oy$  axes, but also angular movement around vertical axis  $Oz$ ; therefore, the model takes into account only automotives yaw movement.

In *car crash analysis* the model establishes impact final sizes, in the hypothesis that initial sizes are known, but it can also be applied backwards for *car crash reconstruction*, when collision final sizes are known.

The scheme of impact simulation is presented in Fig. 3. There are considered two vehicles  $A_1$  and  $A_2$  of  $m_1$  and  $m_2$  mass, at which we know the mass moments

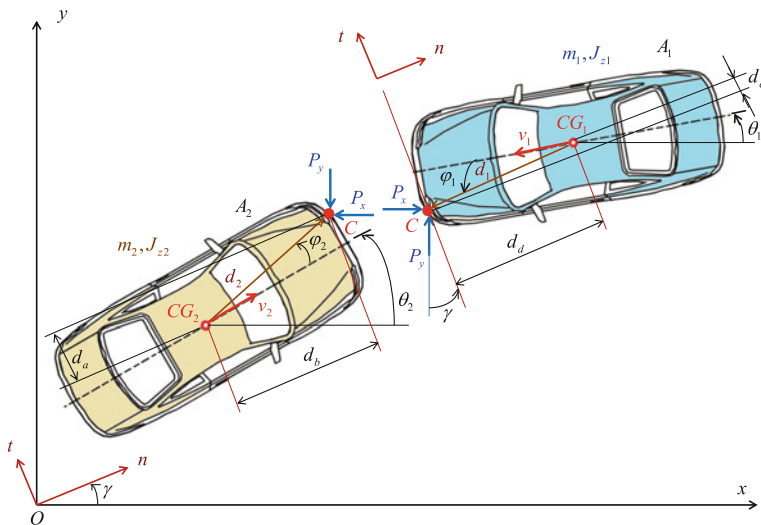


Fig. 3 The scheme of Brach planar impact model

of inertia around vertical axis  $J_{z1}$  and  $J_{z2}$ , but also the common contact point  $C$ , also named as centre of impact or point of impact (POI—Point Of Impact). Likewise, is adopted a local fixed reference coordinate system  $(x, y)$ , attached to the ground. The orientations of the two vehicles in impact moment are given by angles  $\theta_1$  and  $\theta_2$  relative to the fixed system  $(x, y)$ . Centre of impact  $C$  is located relative to centres of gravity  $CG_1$  and  $CG_2$  of vehicles by distances  $d_1$  and  $d_2$ , but also by  $\varphi_1$  and  $\varphi_2$  angles. Also, is adopted a normal and tangential coordinate system  $(n, t)$  relative to centre of impact or deformed surface, which is oriented with a  $\gamma$  angle towards the fixed system  $(x, y)$ .

In scheme also appear axes components of percussion  $P$  ( $P_x$  și  $P_y$ ), as well as distances between centres of gravity and centre of impact  $C$  ( $d_a, d_b, d_c, d_d$ ).

The mathematical algorithm of Brach model can be written in vectorial-matrix form like this (Brach 2011), with sizes related to fixed axis system  $(x, y)$ :

$$\mathbf{A} \cdot \mathbf{x} = \mathbf{B} \cdot \mathbf{x}_0 \tag{10}$$

In *car crash analysis*, final vector  $\mathbf{x}(6 \times 1)$  contains unknown sizes from the end of separation phase (end of collision), noted by convention with capital letters:

$$\mathbf{x} = [V_{x1} \ V_{x2} \ V_{y1} \ V_{y2} \ \Omega_{z1} \ \Omega_{z2}]^T \tag{11}$$

where symbol “ $T$ ” marks the mathematical transposing operation.

Initial vector  $\mathbf{x}_0(6 \times 1)$  contains known sizes from impact phase (start of collision), noted by convention with small letters:

$$\mathbf{x}_0 = [v_{x1} \ v_{x2} \ v_{y1} \ v_{y2} \ \omega_{z1} \ \omega_{z2}]^T \tag{12}$$

The matrix  $\mathbf{A}(6 \times 6)$  from formula (10) has the following form:

$$\mathbf{A} = [\mathbf{A}_{11} \ \mathbf{A}_{12}] \tag{13}$$

in which:

$$\mathbf{A}_{11} = \begin{pmatrix} m_1 & m_2 & 0 \\ 0 & 0 & m_1 \\ 0 & m_2 d_c & m_1 d_d \\ 0 & m_2 d_a & m_1 d_b \\ \cos \gamma & -\cos \gamma & \sin \gamma \\ 0 & m_2(\sin \gamma + \mu \cos \gamma) & m_1(\cos \gamma - \mu \sin \gamma) \end{pmatrix} \tag{14}$$



and:

$$\mathbf{A}_{12} = \begin{pmatrix} 0 & 0 & 0 \\ m_2 & 0 & 0 \\ 0 & J_{z1} & 0 \\ 0 & 0 & J_{z2} \\ -\sin \gamma & d_c \cos \gamma - d_d \sin \gamma & d_a \cos \gamma - d_b \sin \gamma \\ 0 & 0 & 0 \end{pmatrix} \tag{15}$$

Likewise, matrix  $\mathbf{B}(6 \times 6)$  has the form:

$$\mathbf{B} = [\mathbf{B}_{11} \quad \mathbf{B}_{12}] \tag{16}$$

where:

$$\mathbf{B}_{11} = \begin{pmatrix} m_1 & m_2 & 0 \\ 0 & 0 & m_1 \\ 0 & m_2 d_c & m_1 d_d \\ 0 & m_2 d_a & m_1 d_b \\ -e \cos \gamma & e \cos \gamma & -e \sin \gamma \\ 0 & m_2(\sin \gamma + \mu \cos \gamma) & m_1(\cos \gamma - \mu \sin \gamma) \end{pmatrix} \tag{17}$$

and:

$$\mathbf{B}_{12} = \begin{pmatrix} 0 & 0 & 0 \\ m_2 & 0 & 0 \\ 0 & J_{z1} & 0 \\ 0 & 0 & J_{z2} \\ e \sin \gamma & -e(d_c \cos \gamma - d_d \sin \gamma) & -e(d_a \cos \gamma - d_b \sin \gamma) \\ 0 & 0 & 0 \end{pmatrix} \tag{18}$$

in these expressions are present the restitution coefficient  $e$  and tangential friction coefficient between vehicles  $\mu$ .

Matrix Eq. (10) has the solution:

$$\mathbf{x} = \mathbf{A}^{-1} \cdot \mathbf{B} \cdot \mathbf{x}_0 \tag{19}$$

which represents unknown sizes from expression (11).

For example, two automotives A1 and A2 get into a collision like the one shown in Fig. 4 (Brach 2011), where there are also presented initial calculation data according to planar impact mechanism from Fig. 3. Applying Brach impact model, results the speeds from the end of separation phase  $V_1 = 36.02$  km/h and  $V_2 = 51.5$  km/h, without considering uncertainties.

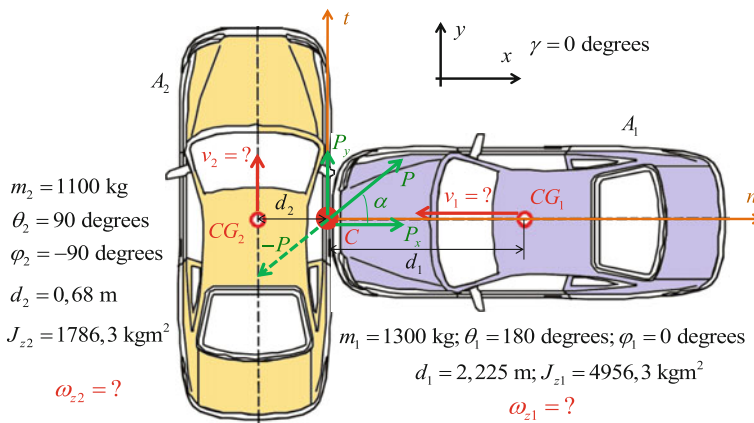


Fig. 4 Example of planar impact between two automobiles

In specialty literature are presented different uncertainties encountered in the analysis and reconstruction of car crashes, all in form of value intervals, of whom only some of them are follow-up presented:

- restitution coefficient has values in the range  $e = [0.1; 0.3]$ , in which case from expressions (16)–(18) is obtained a matrix with intervals;
- tangential friction coefficient is considered to vary within the range  $\mu = [0.4; 0.55]$ , in which case from expressions (13)–(15) is obtained a matrix with intervals;
- mass moments of inertia adopted by NHTSA are established with formulas such as:

$$J_x = k_x m B^2; J_y = k_y m A^2; J_z = k_z m A^2 \tag{20}$$

where  $m$  represents mass,  $B$  track and  $A$  automotive axle base; for automobiles, coefficients from expressions (20) have the following values:  $k_x = 0.1475-0.1725$ ;  $k_y = 0.2-0.227$ ;  $k_z = 0.2225-0.2475$ .

It must be mentioned *a very important aspect from practice* meaning that *uncertainties* always *submit Gauss normal distribution*; the consequence of this hypothesis is that the value with the highest probability of advent is interval arithmetic mean, so it's centre.

Figure 5 presents centralization of results obtained at vehicles separation speeds, by consecutive considering, cumulative, of different uncertainties like it is shown in graph. From Fig. 5 results that if we consider all mentioned uncertainties (other uncertainties can be considered too), then estimated values of sizes from the end of impact (at the end of separation phase) are  $V_1 = 37.55$  km/h,  $V_2 = 54.41$  km/h, which represents centers of intervals obtained by calculus; from graph is determined

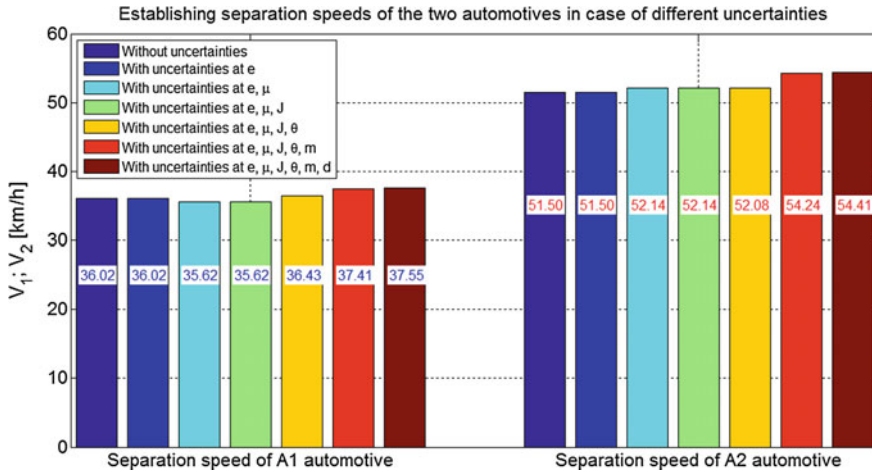


Fig. 5 Separation speeds in case of uncertainties

that if we do not consider any uncertainty, then  $V_1 = 36.02$  km/h,  $V_2 = 51.5$  km/h, meaning the ones obtained at Fig. 4.

## Conclusions

Taking into consideration all uncertainties assures a higher guarantee of the results obtained, because in real case there are never precisely known the sizes that are used.

For the study of automotive dynamics, inclusive those involved in car crashes, it is necessary to use operations with value intervals, vectors and matrix with intervals and differential equations with intervals, which have approaches and specific algorithms.

## References

Brach R, Brach M (2011) Vehicle accident analysis and reconstruction methods. SAE, Warrendale, USA

Burg H, Moser A (2013) Handbook of accident reconstruction. Vieweg & Teubner, Kippenheim, Germany

Datentechnik S (2013) PC-Crash. Operating and technical manual. Mea forensic, USA

Franck H, Franck D (2013) Mathematical methods for accident reconstruction. CRC Press, Boca Raton

Ghiulai C, Vasiliu Ch (1975) Dinamica autovehiculelor. Editura Didactică și Pedagogică, București

Struble D (2014) Automotive accident reconstruction. CRC Press, London

Varat M (2008) Crash reconstruction research. SAE, Warrendale

Wach W (2011) Simulation of vehicle accidents using PC-Crash. Institute of forensic Research Publishers, Cracow, Poland

# Assessment of Effective Elastic Properties of Honeycomb Cores by Modal Finite Element Analyses

Ștefan Sorohan, Dan Mihai Constantinescu, Marin Sandu  
and Adriana Georgeta Sandu

**Abstract** The main issue in analyzing honeycomb structures is the substantial computational effort that has to be spent in modeling and analyzing them with a multi-cell construction core by maintaining the actual geometry. Therefore, the common practice in the finite element modeling is to replace them by an equivalent orthotropic material. The determinations of these equivalent properties of the homogenized core are based on analytical or numerical relationships usually obtained from pure axial and shearing loads. By using these initial estimations of the equivalent properties, a homogenized model works well for in-plane deformations but may give large errors for out-of plane deformations which generally take place in panel or sandwich homogenized structures. This paper presents a numerical method that can be used to correct some of the equivalent elastic properties of the homogenized core to work properly in bending and torsion based on some modal analyses applied first for a real honeycomb panel, to obtain a reference solution, and then on the homogenized orthotropic panel where some of the equivalent elastic constant are iteratively improved by an optimization algorithm to fit the reference solution. The analyzed types of honeycomb cores are the commercial ones in three cell configurations: square, regular hexagonal and re-entrant shapes. The calculations show that some of the equivalent elastic properties obtained in the classical approach must be corrected with factors larger than five as to obtain correct results in bending and torsion loads.

---

Ș. Sorohan (✉) · D.M. Constantinescu · M. Sandu · A.G. Sandu  
Department of Strength of Materials, University Politehnica of Bucharest,  
Splaiul Independenței 313, 060042 Bucharest, Romania  
e-mail: stefan.sorohan@upb.ro

D.M. Constantinescu  
e-mail: dan.constantinescu@upb.ro

M. Sandu  
e-mail: marin.sandu@upb.ro

A.G. Sandu  
e-mail: adriana.sandu@upb.ro

**Keywords** Honeycombs · Homogenization · Equivalent properties · Finite element · Modal analysis

## Introduction

The use of sheet metals or laminate composites as skins and low density cellular materials as cores in sandwich constructions has enabled a very good utilization of the constituent materials also providing structural components with high stiffness and strength to weight ratios. These composite panels are also incorporated in automotive engineering, where, usually, for structural analysis, the finite element method is used. The main problem in analyzing such honeycomb sandwich structures is the substantial computational effort that has to be spent in modeling and analyzing a sandwich structure with a multi-cell construction core by maintaining the actual honeycomb core geometry. Therefore, the common practice in the finite element modeling of honeycomb sandwich structures is to replace the core by an equivalent two or three dimensional orthotropic material. Replacement of the actual honeycomb core by an equivalent continuum model (homogenization) works well, especially in problems involving global structural analysis for deformation, eigenbuckling and vibration analysis.

Due to its construction, the honeycomb core should exhibit orthotropic behavior. Usually the constitutive model approximates the honeycomb core as a homogeneous material rather than a structural assembly of shells. The characterization of a constitutive model for an orthotropic material can be difficult due to the nine distinct parameters that must be determined (three Young's moduli, three shear moduli and three Poisson's ratios). There are some papers which present analytical relationships for these nine constants (Gibson and Ashby 1997; Masters and Evans 1996; Balawi and Abot 2008; Grediac 1993), obtained using the homogenization theory and considering *only axial and pure shearing loads*. It was observed that using these analytical formulae for a relatively small core height, in a homogenized sandwich model which deforms in bending and torsion, the obtained results introduce large errors (Soroşan et al. 2015), therefore, considering the authors' previous experience (Soroşan et al. 2003; Soroşan and Părăuşanu 2005) in this field and some similar papers (Hinnerichs et al. 2006; Jiang et al. 2014), a procedure to extract some of the orthotropic elastic constants of the analyzed honeycombs cores using modal analysis is presented in this paper. In a recent work (Jiang et al. 2014), a similar procedure is used, but for the complete sandwich panel, whereas in (Hinnerichs et al. 2006), a special design of a beam like structure of honeycomb core with two attached masses is considered.

For the analyzed honeycomb cores in this paper, a commercial honeycomb type in three variants (Fig. 1), from an aluminum alloy ( $E_s = 70,000$  MPa;  $\nu_s = 0.33$  and  $\rho_s = 2700$  kg/m<sup>3</sup>) is considered. The cell parameters dimensions are:  $t = 0.1$  mm for all three variants;  $\ell = 5$  mm,  $h = 10$  mm and  $\theta = 0^\circ$  for *square honeycomb*;

$\ell = h = 5.132$  mm and  $\theta = 30^\circ$  for *regular honeycomb* and  $\ell = 8.1407$  mm,  $h = 15.0218$  mm and  $\theta = -30^\circ$  for *re-entrant honeycomb*. Two sets of thicknesses  $b$  are chosen:  $b = 5$  mm, considered as *small thickness* and then  $b = 25$  mm, considered as *large thickness*.

### Analytical Background

For an equivalent *orthotropic material*, which may be a homogenized honeycombs, with the principal directions along the axes of the system OXYZ (Fig. 1), according to the generalized Hooke’s law, it yields  $\bar{\epsilon} = \mathbf{C}\bar{\sigma}$ , where  $\bar{\epsilon}$  and  $\bar{\sigma}$  are the strain and respectively the stress vector of the homogenized structure. The compliance matrix, which includes the equivalent engineering mechanical elastic properties, is (Gibson and Ashby 1997)

$$\mathbf{C} = \begin{bmatrix} \frac{1}{E_1} & -\frac{\nu_{21}}{E_2} & -\frac{\nu_{31}}{E_3} & 0 & 0 & 0 \\ -\frac{\nu_{12}}{E_1} & \frac{1}{E_2} & -\frac{\nu_{32}}{E_3} & 0 & 0 & 0 \\ -\frac{\nu_{13}}{E_1} & -\frac{\nu_{23}}{E_2} & \frac{1}{E_3} & 0 & 0 & 0 \\ 0 & 0 & 0 & \frac{1}{G_{12}} & 0 & 0 \\ 0 & 0 & 0 & 0 & \frac{1}{G_{23}} & 0 \\ 0 & 0 & 0 & 0 & 0 & \frac{1}{G_{13}} \end{bmatrix}. \tag{1}$$

Owing to the symmetry, the following equations must exist:

$$\frac{\nu_{21}}{E_2} = \frac{\nu_{12}}{E_1}; \quad \frac{\nu_{31}}{E_3} = \frac{\nu_{13}}{E_1}; \quad \frac{\nu_{32}}{E_3} = \frac{\nu_{23}}{E_2}. \tag{2}$$

Here Poisson’s ratio  $\nu_{ij}$  is defined as the negative of the strain in the  $j$  direction divided by the strain in the  $i$  direction, for normal loading in the  $i$  direction

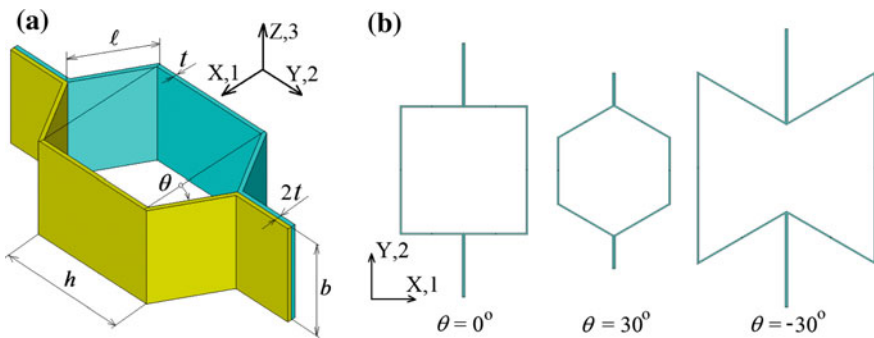


**Fig. 1** A representative volume element and honeycomb parameters (a) and three analyzed configurations of constant relative density  $\rho$  and constant wall thickness  $t$  (b)

( $v_{ij} = -\varepsilon_j/\varepsilon_i$ ). For example  $v_{12}$  correspond to negative ratio of the strains along direction 2 and the strain parallel to direction 1 when the axial loading direction is 1, so  $v_{12} = -\varepsilon_2/\varepsilon_1$ .

The inverse matrix of compliance matrix in (1) is the material stiffness matrix which must be positively defined. This condition can be easily obtained using linear algebra. According to the honeycombs in Fig. 1, where the absolute values of the Poisson's ratios  $v_{21}$ ,  $v_{31}$  and  $v_{32}$  are usually larger than  $v_{13}$  and  $v_{23}$  and close to  $v_{12}$ , it is convenient to consider them as inputs in finite element codes. The condition for a positively defined orthotropic material results as

$$1 - v_{21}^2 \frac{E_1}{E_2} - v_{32}^2 \frac{E_2}{E_3} - (v_{31}^2 + 2v_{21}v_{31}v_{32}) \frac{E_1}{E_3} > 0. \quad (3)$$

The equivalent mechanical properties of honeycombs can be obtained starting with the isotropic constants of the core material:  $\rho_s$ —mass density,  $E_s$ —Young's modulus and  $\nu_s$ —Poisson's ratio. Using the beam theory (Gibson and Ashby 1997), or a more accurate numerical method (Soroşan et al. 2015), all the engineering constants in (1), and supplementary the equivalent mass density  $\rho$ , can be easily computed. The analytical relationships are obtained in the beam theory hypotheses and are valid only for commercial honeycombs (see Fig. 1) with  $t \ll \ell$ , and  $b \gg \ell$  because of supplementary hypotheses used in their derivations. The numerical estimations of the equivalent mechanical properties of honeycombs are more accurate but they can be also obtained only from pure axial and shear load conditions. Even when these accurate equivalent orthotropic constants are used in plates or sandwiches that are loaded in bending and/or torsion, the results may be erroneous as was shown in Soroşan et al. (2015). This means that some of the equivalent orthotropic properties in bending and/or torsion are different from the same properties in axial and/or simple shearing. Due to date, according to the authors' knowledge, there are not accurate analytical relationships for obtaining the equivalent orthotropic Young's moduli  $E_1$  and  $E_2$ , and respectively the shear moduli  $G_{12}$ ,  $G_{23}$  and  $G_{13}$ , from bending and torsion loading conditions.

To justify the chosen analyzed configuration of cells and to better understand the honeycombs behavior a global analysis is presented. If we consider the relation of the mass density of the equivalent commercial honeycomb core (Gibson and Ashby 1997)

$$\rho = \rho_s \frac{\frac{t}{\ell} \left( \frac{h}{\ell} + 1 \right)}{\left( \frac{h}{\ell} + \sin \theta \right) \cos \theta}, \quad (4)$$

and we impose a constant  $\rho$ , choosing a parabolic variation for  $\ell$  by imposing the ratio  $h/\ell$  for three particular shapes, for example corresponding to  $\theta = -30^\circ$ ,  $0^\circ$  and  $30^\circ$ , we can find the values of  $\ell$  and  $h$  functions of  $\theta$  (Fig. 2a). Then, based on the analytical and/or numerical relationships for equivalent elastic properties (Soroşan et al. 2015), we can estimate all the equivalent orthotropic properties of honeycombs (Fig. 2b–d). One can observe than large variation on the elastic properties of





**Table 2** The equivalent properties of large thickness honeycombs ( $b = 25$  mm)

Mechanical property	Square honeycomb		Regular honeycomb		Re-entrant honeycomb	
	Analytical	Numerical	Analytical	Numerical	Analytical	Numerical
$\rho$ (kg/m <sup>3</sup> )	81	81	81	81	81	81
$E_1$ (MPa)	700	737.5	1.193	1.334	0.3338	0.3725
$E_2$ (MPa)	1.117	1.249	1.193	1.334	0.2684	0.2996
$E_3$ (MPa)	2100	2100	2100	2100	2100	2100
$G_{12}$ (MPa)	0.1867	0.2081	0.7176	0.7996	0.04051	0.04509
$G_{23}$ (MPa)	327.4	342.1	400.8	423.8	162.8	168.1
$G_{13}$ (MPa)	218.6	263.2	245.9	243.4	172.0	149.1
$\nu_{12}$ (-)	0	-0.01898	0.9978	0.9983	-1.114	-1.114
$\nu_{21}$ (-)	0	$-3.216 \times 10^{-5}$	0.9985	0.9989	-0.8960	-0.8963
$\nu_{32}$ (-)	0.33	0.33	0.33	0.33	0.33	0.33
$\nu_{31}$ (-)	0.33	0.33	0.33	0.33	0.33	0.33

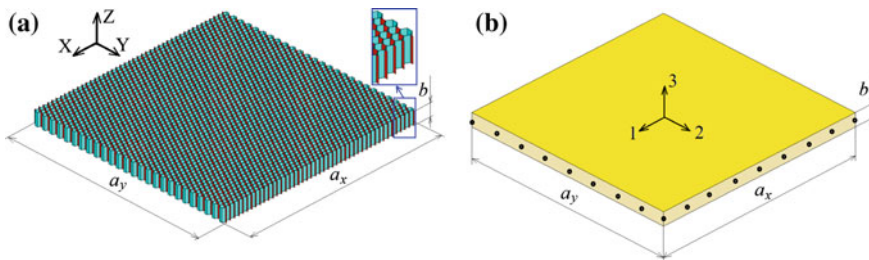


**Fig. 3** A real honeycomb core panel (a) and its equivalent homogenized panel (b). The global dimensions are preserved, also the principal directions of equivalent orthotropic material 123 correspond to global system of coordinate OXYZ. Location of some points for displacements considered in the eigenmodes pairs algorithm, are also presented in (b)

results; anyway small discrepancies exist, but they can be easily explained. In the homogenization of honeycomb cores, the 3D Shell numerical results were used because the reference results for panels are obtained also using a Shell model.

The main idea of homogenization is presented in Fig. 3. The real honeycomb core panel was modeled and analyzed in ANSYS using the Shell181 element type. The main characteristics for six variants of the analyzed honeycombs panels are presented in Table 3.

**Table 3** Main parameters of analyzed honeycomb panels

Honeycomb type	Thickness $b$ (mm)	Number of cells		Global size		Mass (g)
		Along X	Along Y	$a_x$ (mm)	$a_y$ (mm)	
Square	5	40	20	400	400	64.80
	25					324.0
Regular	5	45	26	400	400.3	64.85
	25					324.2
Re-entrant	5	28	18	394.8	394.2	63.04
	25					315.2

### Optimization Algorithm

The natural frequencies, obtained in the reference model (Fig. 3a) and in the homogenized model (Fig. 3b), must be the same, if the equivalent orthotropic elastic constants are correctly obtained from the analytical relationships. But, it was observed that only in-plane normal modes maintain the natural frequencies in the two models. The out of plane normal modes (bending and torsion) present a shift in the natural frequencies from the two sets of models, which means that the elastic equivalent properties in bending and torsion are different from those obtained in axial and shearing loads. If we consider the equivalent elastic properties as design variables, and define an objective function as the sum of these shifts in absolute values for a number of  $N$  arbitrarily out-of-plane normal modes, it is possible to obtain the effective elastic properties in bending by minimizing this objective function. So, the objective function may be also defined as the total absolute relative errors between the reference solutions and the current ones, or called also optimization model solutions, by calculating

$$Obj\_freq = \sum_{i=1}^N c_i \left| \frac{f_{A,i} - f_{X,i}}{f_{A,i}} \right|, \tag{5}$$

where  $c_i$  are weight factors (in this paper  $c_i = 1$ );  $f_{A,i}$  and  $f_{X,i}$  are pairs of natural frequencies from the reference model (or experimental one if possible) and respectively from the optimized model of the homogenized structure.

A main problem in the optimization algorithm is to obtain the correct pairs of natural modes of vibration and for that the MAC (Modal Assurance Criterion) is used. The MAC is a widely used technique to estimate the degree of correlation

between mode shape vectors. The MAC between a reference mode  $\phi_{Aj}$  and a current mode  $\phi_{Xk}$  is defined as

$$MAC_{jk} = \frac{|\phi_{Aj}^T \phi_{Xk}|^2}{\|\phi_{Aj}\|^2 \|\phi_{Xk}\|^2}; \quad j = 1, \dots, n_A; k = 1, \dots, n_X. \quad (6)$$

The value of MAC is between zero and one. A value of one means that one mode shape vector is a multiple of the other. So, if the MAC matrix for equal number of reference and optimized total modes is the identity matrix, the two sets of vectors denote the same mode shapes. It must be mentioned that the degrees of freedom in the two sets must be identically arranged. If for one column (or/and row) there is not a value greater than a limit of correlations, for example 0.5, we can say that there is a mode shape that cannot be paired with the reference set modes. In this paper a minimum  $9 \times 9$  uniformly distributed points in the cores (Fig. 3b) were retained for the modal vectors used in relation (6) to build the MAC matrix.

For the effective optimization was used the Design Optimization module from ANSYS. A general text file for optimization, describing parametrically the homogenized model using APDL commands, was created to be used in sub-problem and first order optimization tools. A special attention in the algorithm was given to relation (3) by the introduction of some particular restrictions, as to obtain the positively defined material stiffness matrix for all combinations of the inputs.

The reference results, that is the first 30 elastic natural frequencies and the corresponding mode shapes, were obtained for all six real geometries presented in Table 3 (see for example Fig. 2a). The models were meshed with four noded Shell element types (over 200,000 finite elements) and the results were saved in text files to be read in the optimization algorithm. The first eight natural modes of vibration for the square honeycomb panel of small thickness, all out-of-plane modes, are presented in Fig. 4, as an example.

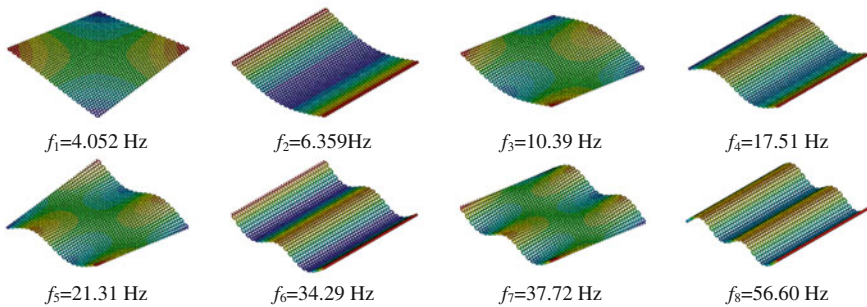


**Fig. 4** First eight natural modes of vibration for the square honeycomb panel ( $b = 5$  mm) obtained from a fine mesh of the reference model using shell type finite element

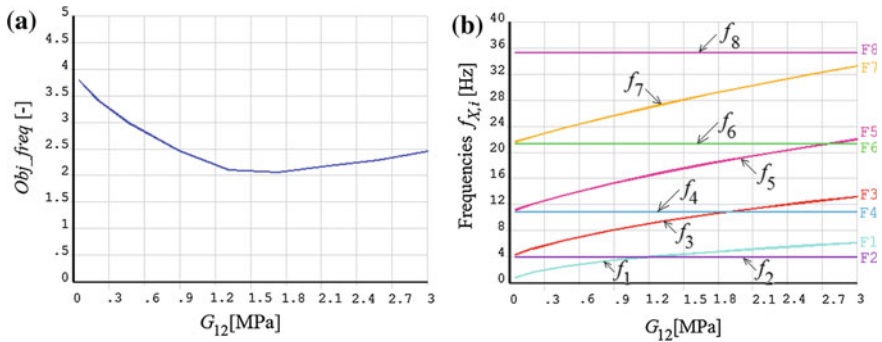


**Fig. 5** Sensitivity curves of parameter  $G_{12}$  for homogenized small thickness ( $b = 5$  mm) square honeycomb panel: Objective function (a) and all first eight elastic natural frequencies (b)

### Sensitivity Analysis

From sensitivity analyses, it was found that only three parameters  $E_1$ ,  $E_2$  and  $G_{12}$  (see for example Fig. 5a) have an important contribution to change the objective function or lower natural frequencies of the homogenized plate model, regardless if this is modeled using Shell, or Brick elements. It was concluded that four, or even eight noded, composite Shell elements are more adequate to be used in the homogenized model due to computation efficiency. For some models, the Poisson ratio  $\nu_{21}$  (or  $\nu_{12}$ ) gives important variation in the objective functions, but it was numerically checked, by the authors of this paper, that de Poisson’s ratios in pure bending do not change relative to their definitions in axial loading, so they were not considered as variable parameters. Also, it is necessary to mention that, the equivalent density of the homogenized honeycomb core is always supposed to be accurately predicted and this is not a variable in optimization.

It can be observed from Figs. 5b and 4, that pure bending modes (mode # 2, 4, 6 and 8) are not depending of  $G_{12}$ , so it is a good practice to include more natural modes into the optimization algorithm.

### Optimization Results and Discussions

All the results reported in Tables 4 and 5, correspond to the case in which only the first eight elastic out-of-plane normal modes of vibrations [ $N = 8$  in Eq. (5)] are fitted to the reference modes using the proposed optimization algorithms for all six different case studies. It can be observed that in bending and torsion, the elastic properties  $E_1$ ,  $E_2$  and  $G_{12}$  are different from their corresponding values obtained from axial and shearing loads. Moreover, as it was mentioned above, the in-plane behavior of the homogenized core is correct. For example, the initial global

**Table 4** The initial estimation and the optimized equivalent bending and torsion properties of small thickness honeycombs ( $b = 5$  mm)

Parameter	Square honeycomb		Regular honeycomb		Re-entrant honeycomb	
	Initial	Optimized	Initial	Optimized	Initial	Optimized
$E_1$ (MPa)	708.8	868.03	1.314	3.4586	0.3639	1.8639
$E_2$ (MPa)	1.229	3.1602	1.314	3.4604	0.2927	1.4999
$G_{12}$ (MPa)	0.2037	1.1300	0.7869	3.4453	0.0438	0.35312
$Obj\_freq$ (%)	342	4.49	384	5.64	479	1.73

**Table 5** The initial estimation and the optimized equivalent bending and torsion properties of large thickness honeycombs ( $b = 25$  mm)

Parameter	Square honeycomb		Regular honeycomb		Re-entrant honeycomb	
	Initial	Optimized	Initial	Optimized	Initial	Optimized
$E_1$ (MPa)	737.5	912.58	1.334	1.4164	0.3725	0.42271
$E_2$ (MPa)	1.249	1.3635	1.334	1.4164	0.2996	0.34001
$G_{12}$ (MPa)	0.2081	0.24874	0.7996	0.89943	0.04509	0.057134
$Obj\_freq$ (%)	38.1	4.68	39.9	7.08	66.1	3.69

absolute relative frequencies ( $Obj\_freq$ ) for first seven in-plane modes, for the small regular honeycomb of 5 mm thickness, is only 4.05 %. The optimized out-of-plane parameters in Tables 4 and 5 are in good agreement with the next eight out-of-plane modes, with some interesting exception for particular modes at high frequency, which supplementary increase the obtained optimized moduli in the first stage (first eight out-of-plane modes).

It can be observed that, at small analyzed core thickness (5 mm) of the re-entrant honeycomb core, the elastic properties in bending  $E_1$  and  $E_2$  may increase with a factor over 5 (1.86/0.36) and over 8 (0.353/0.044) for  $G_{12}$ . These factors decrease, for the large analyzed core thickness (25 mm), and become under 1.3, for all analyzed types of core (maximum is for  $G_{12}$  for the re-entrant type of core 0.057/0.045 = 1.27).

## Conclusions

There are several advantages in using modal testing as a validation procedure for material properties estimations as compared to traditional static material testing. For this modal test structure, a number of modes (usually five to 20) can be easily computed, or better, if possible, measured, thus producing more independent test data from a single static experimental structure to validate the model or to obtain some elastic constants. The modes of vibration are influenced by several of the

elastic constants of the material, thus providing overlapping validation paths for the elastic constants. Using modal testing the analyzed structure can be barely supported, thus accurately simulating free boundary conditions. This is in contrast to material testing, for which the structure has to be gripped with some fixture in order to apply loads producing some unknown or difficult to simulate boundary conditions. In modal tests the honeycomb core deforms dynamically rather than statically, but the assumed model is orthotropic linear elastic and it is not sensitive to variations in strain rate.

The optimization algorithm used to extract the elastic properties of the analyzed honeycomb cores is similar to the algorithm presented by Sorohan and Păraușanu (2005), but in this paper, instead of the experimental determination of modal characteristics of the analyzed cores, they are obtained numerically using a finite element model which replicates completely and accurately the honeycomb cores.

Starting with a unit-cell geometry and using its periodicity, a finite element model of the honeycomb core can be generated and then analyzed in modal analysis for free-free boundary conditions to simulate an experiment. Based on a virtual modal data set of results and a similar simplified orthotropic homogenized shell or solid finite element model, some of the elastic properties of the honeycomb core in bending,  $E_1$ ,  $E_2$  and  $G_{12}$  can be successfully identified based on an optimization algorithm generated in ANSYS APDL. Further, the same concepts can be used to identify other different geometric honeycomb core structures or sandwiches to extend this procedure.

**Acknowledgement** This work was supported by a grant of the Romanian National Authority for Scientific Research, CNDS-UEFISCDI, project number PN-II-PT-PCCA-2011-3.2-0068, contract 206/2012.

## References

- Balawi S, Abot JL (2008) A refined model for the effective in-plane elastic moduli of hexagonal honeycombs. *Compos Struct* 84:147–158
- Gibson LJ, Ashby MF (1997) *Cellular Solids, Structure and properties*. Cambridge University Press, Cambridge, pp 93–174
- Grediac M (1993) A finite element study of the transverse shear in honeycomb cores. *Int J Solids Struct* 30(13):1777–1778
- Hinnerichs TD, Carne TG et al (2006) Characterization of aluminum honeycomb and experimentation for model development and validation. In: Volume II, honeycomb experimentation for model development and validation, Sandia Report Sand 2006–4455
- Jiang D, Zhang D et al (2014) An approach on identification of equivalent properties of honeycomb core using experimental modal data. *Finite Elem Anal Des* 90:84–92
- Masters IG, Evans KE (1996) Models for the elastic deformation of honeycombs. *Compos Struct* 35(4):403–422
- Sorohan S, Sandu A et al (2003) Substructuring technique in finite element analysis of stiffened orthotropic panels. In: Proceedings of the 7th international conference ESFA, Bucharest, 8–9 May, vol 2, Editura Politehnica Press, p 93–102

- Sorohan S, Constantinescu DM et al (2015) The thickness effect of honeycombs on their mechanical response. In: The 2nd edition of new challenges in aerospace science international conference, NCAS 2015, Bucharest, Romania, 5–6 Nov (accepted paper)
- Sorohan S, Părăușanu I (2005) Identification of elastic properties of a composite laminate plate. In: Proceedings of international conference on structural analysis of advanced materials ICSAAM, 15–17 Sept, Bucharest, Romania, p 75–80
- Sorohan S, Sandu M et al (2015) On the evaluation of mechanical properties of honeycombs by using finite element analyses. *INCAS Bull* 7(3):33–49



# Model Preparation for Structural FEA on Main Components of an Internal Combustion Engine

Dan Mihai Dogariu, Cristian Tănăsie, Anghel Chiru,  
Cristian-Ioan Leahu and Vlad Ștefan Stancu

**Abstract** Structural analysis requires generally, a well described case study, in order to perform a correct analysis, which in return, should offer plausible results. In the hypothesis of the case study, different assumptions and simplifications of the geometrical 3D model, proposed for study, are made. For a shorter computing time, simplifications to design are welcomed. Combining the right assumptions with a good robust model, a successful technical analysis can be achieved. The objective of the paper is to present a workflow and several workarounds for building a model for a structural analysis with examples on the main components of an internal combustion engine. This engine belongs to the Research Institute of Transilvania University of Brasov and is used for thermodynamic tests. The paper also presents methods for importing 3D models from CAD to FEA environment without problems or exporting 3D scanned geometry and solidifying surface geometry. The results of the study are presented as the imported and meshed 3D model in FEA environment with mesh verification shown.

**Keywords** FEA · CAD · 3D model · Internal combustion engine

---

D.M. Dogariu (✉) · A. Chiru · C.-I. Leahu · V.Ș. Stancu  
Department of Automotive and Transport Engineering, Transilvania University of Brasov,  
Brasov, Romania  
e-mail: dan.dogariu@gmail.com

A. Chiru  
e-mail: achiru@unitbv.ro

C.-I. Leahu  
e-mail: leahu.cristian@unitbv.ro

V.Ș. Stancu  
e-mail: vladss02@yahoo.com

C. Tănăsie  
Department of Proof of Concept, SC Schaeffler Romania SRL, Brasov, Romania  
e-mail: tanascis@schaeffler.com

## Introduction

The key element in a structural finite element analysis is the geometry, since this type of analysis is used for observing the behavior of a studied component or assembly under force loading. The advantages of such analyses are obvious. Over the years, tools have been developed that prepare the CAD model for efficient meshing (Desktop Engineering 2008).

Supplementary to a good, official geometrical model to study, the analyst must also consider the right material properties and adequate loading situations for the involved components. These loading situations are part of the theoretical assumptions that must be considered during such an analysis.

The first step in creating a FEA model is to fully understand the physical problem being considered (Chang 2015). One of the main required inputs for a Structural Analysis is the geometry. The next step is about simplification and idealization of the problem, due to the complex physical problems that must be solved.

The assumptions are valid for the used FEA software for assuring convergence, but most of all they should be made accordingly to a best reality interpretation. For example symmetry, quarter or pie cuts can be considered instead of the entire model.

The 3D models presented in this paper are based on the main components of an internal combustion engine, which belongs to the Research Institute of Transilvania University of Brasov, where it is used for thermodynamic tests.

## Problem Definition

Meshing, more precisely called discretization, is what converts a mathematical model into a finite element model ready for solution. More complex geometry requires preparation before it can be meshed. In the process of geometry preparation for FEA, a particular geometry is constructed intended specifically for analysis, with the property of being meshable. Furthermore, it must allow for creation of a mesh solvable within a reasonable time.

Often CAD models do not satisfy the requirements for a FEA. Depending on the study, different model modifications can be done on the same product.

The simplifications to the design of the studied components are under the responsibility of the engineer. Such simplifications also reduce computing costs and are especially welcomed when the analysis stops from due to a certain error and several simulations with various parameters are tested. Such geometry simplification may refer to suppressed features like rounds, chamfers, or even modifications that imply major changes in topology, like ignoring channels, bores, and regions with different diameters on a shaft.

On the other hand, in some situations, the components necessary to be subjected to a structural analysis have, in their geometry, bad regions, where the surface is not

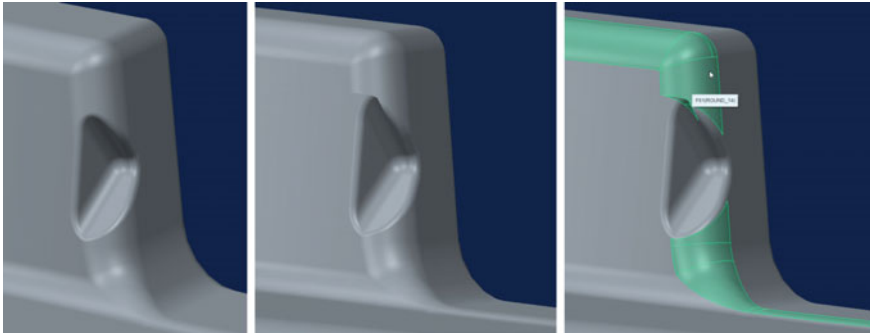


**Fig. 1** Resolving rounds with problems under CAD environment

closed or there are some small surfaces intersecting each other or outside the geometry. Depending on the size of the affected surfaces, the repairing may easily lead to misinterpretations of the design. Such bad geometry areas usually occurs at fillets. An example of a broken fillet and also repairing it can be seen in Fig. 1, the first image from left—the correct fillet, the other two images—the broken fillet and visualizing it by highlight.

In Fig. 1 there is presented a problem with a small pocket with rounds on all edges that may not be removed, due to the fact that the size of the pocket is close to the round radius and it may affect the behavior of this part when subjected to loads. This is an example where the small size of a feature as compared to the overall size of the model does not always justify its exclusion.

The causes for the presence of these bad surfaces are multiple. It can be, for example due to an export error and bad import, or simply because of design error.

In some cases, it is not obvious to spot the possible areas where the geometry might have some errors. This usually happens when dealing with very large objects, or very detailed parts, where it is difficult to observe every square millimeter of surface.

However, any small error in the geometry is most probably going to be the main source of a mesh generation error or warning, when using the involved geometry into a finite element simulation software. It is also possible that the program stops and returns the error even during the import of the geometry. If the import is successful, despite the problematic geometry, during meshing the bad elements are highlighted and so discovered. Then, further repairs are necessary.

## **Geometry Preparation (Preparation of CAD Data)**

Some limitation of FEA, especially on internal combustion engines main components are the imperfections of the finished parts which are not always found in the 3D model. This may affect the structural analysis, so a complete and accurate

3D model must be provided or created. For a great accuracy of the 3D model, a scanned model of the components can be used (Stephenson 2009).

However, using a highly detailed 3D model and also sophisticated modeling approaches and FEA techniques may, on one hand, lead to a more realistic result, but on the other hand, it can be very time-consuming, difficult to verify and to re-produce.

How exactly the simulation time is affected by the model detail level is difficult to predict. This is depending mainly on the solution strategies, whether implicit or explicit solution algorithm (van der Vegte 2004).

After importing the 3D model and before meshing, the de-feature operations should be carried on. Some structural analysis software have a built-in option to highlight the area where very small sector appear and can automatically create virtual features that bypass the problem areas without distortion (Desktop Engineering 2008). In Fig. 2 the imported cylinder head and piston into a FEA software are shown, with highlighted edges where mesh problems may appear.

Some enhancements include element quality checks in real-time during meshing, mesh seeding for optimizing mesh density, and more evolved, adaptive remeshing (both automatic and manual) to adjust the mesh iteratively after running an analysis.

In Fig. 3 the mesh quality of the cylinder head assembly is shown, where mesh warnings are highlighted in yellow. At the left picture it can be observed that the warnings appear to be negligible comparing to the entire volume, but at the right picture during zooming, it can be observed that the warnings appear in the areas of interest. The same thing can be observed in Fig. 4, where the warnings appear the valve areas, where gas exchange phenomena are expected.

These warnings represent excessively distorted elements, considering the aspect ratio of a perfect, tetrahedral element, which was used as mesh type.

Usually, warnings can be diminished when a finer discretization is used, at the cost of extra computing time.

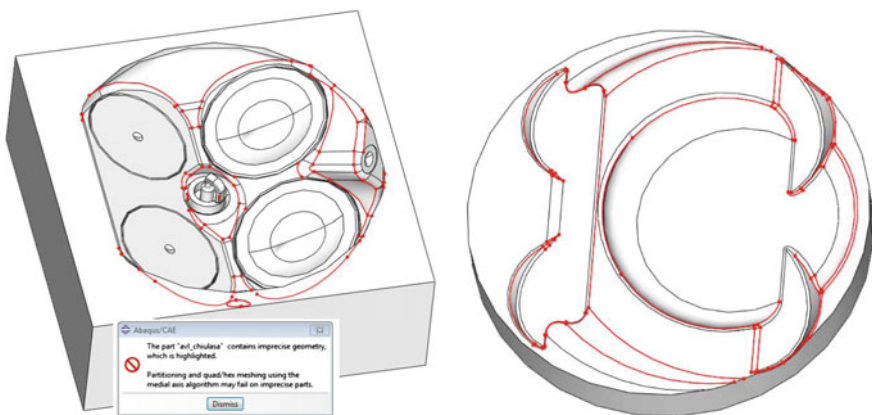


**Fig. 2** The imported cylinder head and piston into a FEA software, where the edges where problems may appear are highlighted in red

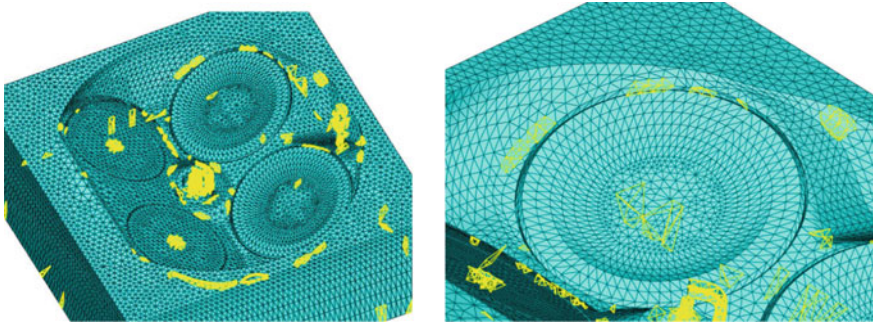


Fig. 3 Mesh quality check on cylinder head assembly

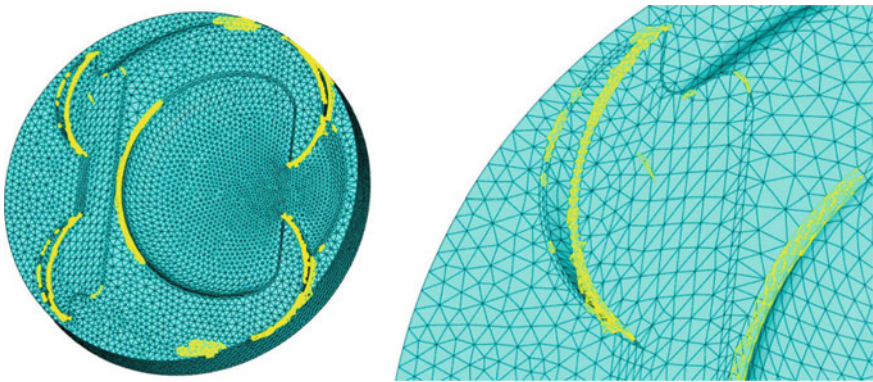


Fig. 4 Mesh quality check on the piston

### Exporting a 3D Model for a FEA

Depending on the FEA case study and on the interaction between the solid or surface modeler and type of FEA, several geometry files formats are available. Examples of the most common geometry model formats used for converting CAD models are presented in Table 1 (About 3D scanning).

Sometimes a STL file format can retain more details than a STEP file, despite the larger file size. This may be advantageous when exporting the geometry for a CFD analysis. Basically, a STL file contains simple planar entities like triangles which are wrapped around the geometrical model (Stereolithography). An advantage of this file format is that the resolution of the geometry which is approximated by triangles can be specified. For example too large triangles will create a small file size, but at the cost of mesh conformation to the actual geometry (Stereolithography). Over-faceted STL files will increase importing time, but not necessarily improve the quality of the final part.

**Table 1** Common file formats containing geometry (About 3D scanning)

ASCII (or ASC)	An X, Y, Z point cloud file in ascii text format
DWG	AutoCad drawing file
DXF	Drawing interchange file—a neutral version of a DWG file
IGES	Initial graphics exchange specification—a neutral format for exchanging CAD data between many different software
OBJ	An open data format that represents the vertices of polygons
PRT	A native CAD format for Pro/ENGINEER
SLDPRT	A native CAD format for SolidWorks
STEP	Standard for the exchange of product model data—(ISO 10303) an advanced neutral format for exchanging CAD data between many different software programs
STL	Standard tessellation language—a polygonal model format similar to OBJ and several others
WRL (VRML)	Virtual reality modeling language—a polygonal file similar to OBJ, STL and several others and can include color

The parameters of the STL file are: tolerance, chord height or facet deviation (AVL FIRE). The chord height specifies the maximum distance between a chord and a surface and is measured in model units. An example on the model of the studied piston with the resulted triangulation affected by the chord height parameter can be observed in Fig. 5.

An example of an assembly of a cylinder head exported as STL file for specific CFD analysis can be seen in Fig. 6. This file format was used for a better conservation of the details in areas of interest. Some CFD software may apply additional geometry mesh refinement during STEP geometry import. This may result in combining small surfaces, which may be very important in some cases, or sometimes can impede the meshing procedure.

In Fig. 7 a CFD analysis was started using the imported STL geometry.

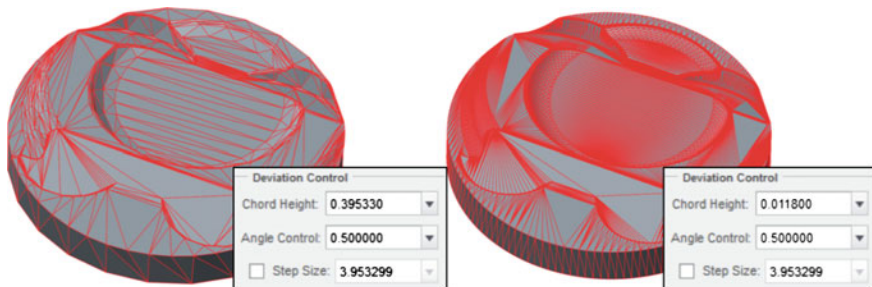


**Fig. 5** Mesh triangulation on the piston surface, with low triangulation quality—*left*, and with high level of triangulation—*right*

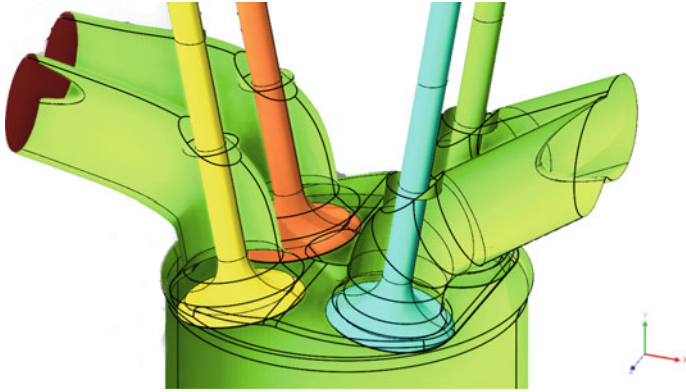


**Fig. 6** Imported assembly as STL file format for CFD analysis

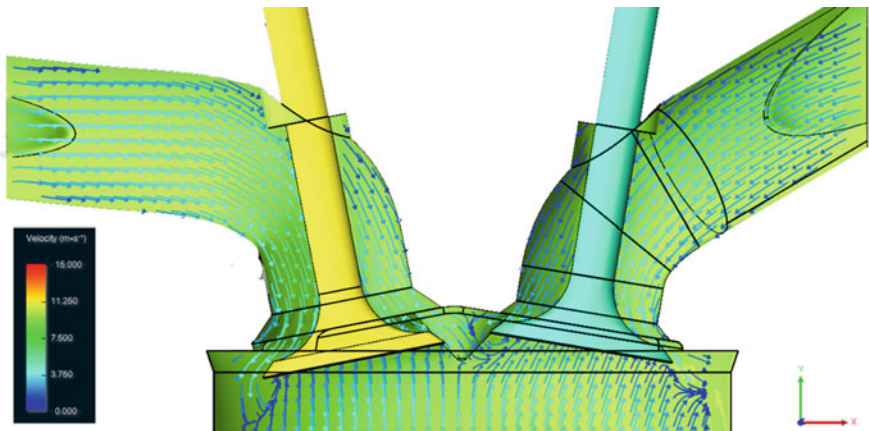


**Fig. 7** Running a CFD analysis on an imported STL geometry

These meshed models will be further used also for different CFD studies, regarding flow phenomena, thermodynamic analyses and combustion processes (Winterbone 2000).

## Conclusion

There are always imperfections and small differences between the finished parts and the original, ideal 3D models, which the designer builds. Depending on the type of simulation, these differences might have an influence on the results.

The scanned geometry offers a great accuracy of the 3D model with respect to the finished parts. When using the models for a CFD analysis, the level of detail for geometry is very important. Thus, the 3D model used for analysis must show a level of detail correspondingly to the case situation.

Nowadays, there are specially built tools that include de-featuring operations that modify the CAD model, often referred to as real operations, and tools for modifying an overlay topology on the original model, referred to as virtual operations (Desktop Engineering 2008).

But, not always simplifying the geometry of the components is realized under the FEA software environment. Most of the time, it is easier to do all geometry modification in a native CAD software and export it from here. Sometimes doing a fast model review direct from CAD, using a visual wireframe analysis can prevent exporting a broken geometry.

A confirmation of a good geometrical model for study is an errorless import of the component, which is entirely meshed in FEA environment with mesh verification shown.

A good, robust model, verified by measurement (3D scanning) may be used for several analyses type, including structural analyses and flow analyses.

## Bibliography

- About 3D scanning <http://www.dirdim.com>  
AVL FIRE (2013) Primer—getting started: intake manifold (900)  
Chang KH (2015) e-design: computer-aided engineering design  
Desktop Engineering (2008) Vol. 13, Issue 12  
Stephenson M (2009) Engine downsizing—an analysis perspective. In: SIMULIA customer conference  
Stereolithography <http://www.stereolithography.com/exporting-stl-files.php>  
van der Vegte GJ (2004) Numerical simulations of the bolted connections: the implicit versus the explicit approach. Connections in steel structures V Amsterdam  
Winterbone DE, Pearson RJ (2000) Theory of engine manifold design. Wave Action Methods for IC Engines, SAE, pp 243–252



# Dynamics of a Crank-Shaft Mechanism with Multiple Clearances by a Multibody Approach

Stănescu Nicolae–Doru

**Abstract** This paper presents an unified matrix equation of motion for the case of the crank-shaft mechanism with clearances. Two type of joints are considered: the revolute joint and the prismatic joint. In the general case there exist three clearances for the three joints of the mechanism. In the present paper we considered that all these three clearances may appear. In this approach the mechanism either can have a unique determined motion, or it can consist in two parts (one formed with one element and the other with two elements), each part having its independent motion, or it can be decomposed in three elements with independent motions. The equation of motion is deduced using a multibody approach and considering that all clearances vanish. The advantageous of this approach is that it is not important which forces and moments act upon the elements of the mechanism. The equation of motion can be also used (with some modifications, by canceling some lines in the matrices) in the case of the existence of one or more clearances. In this situation, the matrix equation splits in some independents matrix equations of motion for each component part of the mechanism. The expressions for the eventual (if the certain clearances vanish) normal reactions are presented too.

**Keywords** Crank-shaft · Clearances · Constraint · Multibody · Motion

## Introduction

The crank-shaft mechanism is intensively studied due to its various applications. Zheng et al. (2015) considers revolute and spherical joints with clearances and with and out lubrication and perform simulations studying the influence of the magnitude of clearance on the behavior of a crank-shaft mechanism. Šika et al. (2012) perform an optimization of a crank-shaft mechanism determining the length of the crank, the

---

S. Nicolae–Doru (✉)

Department of Automotive and Transportation, University of Pitești, Pitești, Romania  
e-mail: doru.stanescu@upit.ro

length of the rod, and the eccentricity. The influence of different parameters on the dynamics of the crank-shaft mechanism with clearance is studied in Goudas et al. (2004). The dynamic response of a crank-shaft mechanism with clearance considering rigid and flexible crank-shaft is analyzed in Zheng and Zhou (2014). Reis et al. (2014) consider the friction and Hertz contact in the study of the dynamic analysis of a crank-shaft mechanism. Daniel and Cavalca (2011) study a crank-shaft mechanism with clearance and hydrodynamic lubrication.

A general multibody approach for the study of the rigid solid with general constraints is given by Pandrea and Stănescu (2015). This approach will be used in the present paper.

### Working Model

We consider the crank-shaft mechanism in Fig. 1, in which the revolute joints at the points  $O_1$  and  $O_3$ , and the prismatic joint are considered with clearances.

One knows the dimensions  $OO_1 = l_1$ ,  $O_{21}C_2 = l_{21}$ ,  $O_{22}C_2 = l_{22}$ , in which  $C_2$  is the center of weight of the shaft, the dimension of the prismatic joint (considered symmetric)  $2e$ , the dimension of the prismatic journal (considered symmetric)  $2d$ , the length of the prismatic joint (also considered symmetric)  $2f$ , the center of weight  $C_3$  of the prismatic joint, and the quote  $h$ .

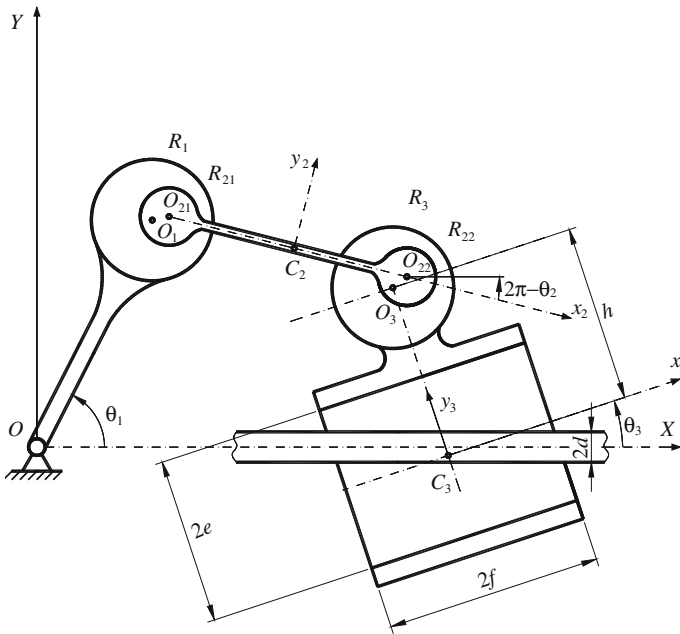


Fig. 1 The working model

The position of the crank is defined by the angle  $\theta_1$  for which is known the law of variation as function of time  $\theta_1 = \theta_1(t)$ .

One also knows the radii  $R_1, r_{21}, r_{22}$ , and  $R_3$  for which the following relations  $R_1 > r_{21}$  and  $R_3 > r_{22}$  hold true.

The position of the shaft is completely defined by the position of the center of weight  $C_2$  (the values  $X_2$  and  $Y_2$  corresponding to the coordinates of the point  $C_2$  with respect to the fixed reference frame  $OXY$ ), and the rotation angle  $\theta_2$  between the mobile axis  $C_2x_2$  and the fixed axis  $OX$  (in figure we represented the positive sense for the angle  $\theta_2$ ).

Corresponding to the rotation of angle  $\theta_2$  one may define the rotational matrix  $[A_2]$  given by

$$[A_2] = \begin{bmatrix} \cos \theta_2 & -\sin \theta_2 \\ \sin \theta_2 & \cos \theta_2 \end{bmatrix}. \tag{1}$$

Analogically, the position of the slider 3 is given by the position of the center of weight  $C_3$  (the coordinates  $X_3$  and  $Y_3$ ), and by the rotation angle  $\theta_3$  to which we assign the rotation matrix

$$[A_3] = \begin{bmatrix} \cos \theta_3 & -\sin \theta_3 \\ \sin \theta_3 & \cos \theta_3 \end{bmatrix}. \tag{2}$$

The mechanical system is acted by a system of forces and moments (not represented in the figure). The given forces that act upon the rigid body 2 reduce to the resultant force  $R_2$  and the resultant moment  $M_2$ , in regard to the center of weight  $C_2$ .

Analogically the system of forces that act upon the rigid body 3 reduces to the resultant  $R_3$  and the resultant moment  $M_3$ , in regard to the center of weight  $C_3$ .

In addition, one knows the mechanical parameters: the masses  $m_2, m_3$ , and the inertial moments  $J_2$ , and  $J_3$  of the rigid bodies 2, and 3, relative to the centers of weight  $C_2$ , and  $C_3$ , respectively.

### The Equations of Motion for the Free (Unconstrained) Rigid Bodies

If there is no contact between the rigid bodies, or the eventual contacts are not constraints (see the next paragraphs), then one may write the equations:

– for the rigid body 2:

$$m_2\ddot{X}_2 = R_{2x}, m_2\ddot{Y}_2 = R_{2y}, J_2\ddot{\theta}_2 = M_2 \tag{3}$$

– for the rigid body 3:

$$m_3\ddot{X}_3 = R_{3x}, m_3\ddot{Y}_3 = R_{3y}, J_3\ddot{\theta}_3 = M_3. \tag{4}$$

The system transforms in a system consisting in three independent rigid bodies having seven degrees of freedom.

### The Case of the Contact Between the Rigid Bodies 1 and 2

Let us denote by  $d_1$  the distance between the points  $O_1$  and  $O_{21}$ . The contact between the two rigid bodies implies the existence of the relation

$$d_1 = R_1 - r_{21}. \tag{5}$$

Between the coordinates  $X_{21}$  and  $Y_{21}$  of the point  $O_{21}$ , and the coordinates  $X_2$  and  $Y_2$  of the center of weight  $C_2$  there exist the relations (Fig. 2)

$$\begin{bmatrix} X_{21} \\ Y_{21} \end{bmatrix} = \begin{bmatrix} X_2 \\ Y_2 \end{bmatrix} + [A_2] \begin{bmatrix} -l_{21} \\ 0 \end{bmatrix}. \tag{6}$$

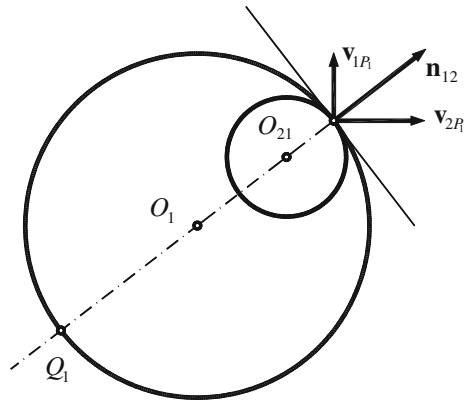
The coordinates  $X_1$  and  $Y_1$  of the point  $O_1$  are given by

$$\begin{bmatrix} X_1 \\ Y_1 \end{bmatrix} = l_1 \begin{bmatrix} \cos \theta_1 \\ \sin \theta_1 \end{bmatrix}. \tag{7}$$

The relation (5) leads to the expression

$$R_1 - r_{21} = \sqrt{(X_{21} - X_1)^2 + (Y_{21} - Y_1)^2}, \tag{8}$$

**Fig. 2** The contact between the bodies 1 and 2



which is exactly the contact condition we have searched.

Let us observe that the expression  $R_1 - r_{21}$  may be also written in the form

$$R_1 - r_{21} = f_1(X_2, Y_2, \theta_2, \theta_1(t)). \quad (9)$$

The straight line  $O_1O_{21}$  has the equation

$$\frac{Y - Y_1}{Y_{21} - Y_1} = \frac{X - X_1}{X_{21} - X_1}, \quad (10)$$

while the circle with the center at the point  $O_1$  and having the radius equal to  $R_1$  is given by

$$(X - X_1)^2 + (Y - Y_1)^2 = R_1^2. \quad (11)$$

The Eqs. (10) and (11) form a system of two nonlinear equations with two unknowns which, in general, has two solutions: the point  $P_1$  of coordinates  $X_{P_1}$  and  $Y_{P_1}$ , and the point  $Q_1$  of coordinates  $X_{Q_1}$  and  $Y_{Q_1}$ . The point  $P_1$  is chosen so that the distance between the points  $P_1$  and  $O_{21}$  is minimum, that is,

$$(X_{P_1} - X_{21})^2 + (Y_{P_1} - Y_{21})^2 \leq (X_{Q_1} - X_{21})^2 + (Y_{Q_1} - Y_{21})^2. \quad (12)$$

The normal  $\mathbf{n}_{12}$  to the circle of center  $O_1$  and radius  $R_1$ , at the point  $P_1$  is given by

$$\mathbf{n}_{12} = \frac{\partial f}{\partial X} \mathbf{i} + \frac{\partial f}{\partial Y} \mathbf{j}, \quad (13)$$

where

$$f(X, Y) = (X - X_1)^2 + (Y - Y_1)^2 - R_1^2 = 0. \quad (14)$$

The velocity of the point  $P_1$  associated to the rigid body 1 reads

$$\begin{bmatrix} v_{1P_{1x}} \\ v_{1P_{1y}} \end{bmatrix} = \begin{bmatrix} \dot{X}_{P_1} \\ \dot{Y}_{P_1} \end{bmatrix}, \quad (15)$$

while the velocity of the point  $P_1$  associated to the rigid body 2 is

$$\begin{bmatrix} v_{2P_{1x}} \\ v_{2P_{1y}} \end{bmatrix} = \begin{bmatrix} \dot{X}_2 \\ \dot{Y}_2 \end{bmatrix} + [\dot{\mathbf{A}}_2] \begin{bmatrix} x_{2P_1} \\ y_{2P_1} \end{bmatrix}, \quad (16)$$

where

$$[\dot{\mathbf{A}}_2] = \begin{bmatrix} -\sin \theta_2 & -\cos \theta_2 \\ \cos \theta_2 & -\sin \theta_2 \end{bmatrix} \dot{\theta}_2, \quad (17)$$

$$\begin{bmatrix} X_{P_1} \\ Y_{P_1} \end{bmatrix} = \begin{bmatrix} X_2 \\ Y_2 \end{bmatrix} + [\mathbf{A}_2] \begin{bmatrix} x_{2P_1} \\ y_{2P_1} \end{bmatrix}, \quad (18)$$

$$\begin{bmatrix} x_{2P_1} \\ y_{2P_1} \end{bmatrix} = [\mathbf{A}_2]^T \left[ \begin{bmatrix} X_{P_1} \\ Y_{P_1} \end{bmatrix} - \begin{bmatrix} X_2 \\ Y_2 \end{bmatrix} \right]. \quad (19)$$

The contact at the point  $P_1$  is a constraint if and only if the difference  $\mathbf{v}_{2P_1} - \mathbf{v}_{1P_1}$  has a non-zero component onto the positive direction of the normal  $\mathbf{n}_{12}$ , which is equivalent to say

$$\left[ \begin{bmatrix} v_{2P_{1x}} \\ v_{2P_{1y}} \end{bmatrix} - \begin{bmatrix} v_{1P_{1x}} \\ v_{1P_{1y}} \end{bmatrix} \right]^T \begin{bmatrix} \frac{\partial f}{\partial X} & \frac{\partial f}{\partial Y} \end{bmatrix} > 0. \quad (20)$$

If the relation (20) is fulfilled, then we have a constraint at the point  $P_1$ ; this constraint is given by the constraint function (9) to which corresponds the relation

$$F_1(X_2, Y_2, \theta_2, \theta_1(t)) = f_1(X_2, Y_2, \theta_2, \theta_1(t)) - R_1 + r_{21} = 0. \quad (21)$$

One obtains a matrix of constraints in the form

$$[\mathbf{B}_1] = \begin{bmatrix} \frac{\partial F_1}{\partial X_2} & \frac{\partial F_1}{\partial Y_2} & \frac{\partial F_1}{\partial \theta_2} & 0 & 0 & 0 \end{bmatrix} \quad (22)$$

and the relation

$$[\mathbf{B}_1]\{\dot{\mathbf{q}}\} = \{\mathbf{C}_1\}, \quad (23)$$

in which

$$\{\mathbf{q}\} = [X_2 \ Y_2 \ \theta_2 \ X_3 \ Y_3 \ \theta_3]^T, \quad (24)$$

$$\{\mathbf{C}_1\} = -\frac{\partial F_1}{\partial \theta_1} \frac{d\theta_1}{dt}. \quad (25)$$

### The Case of the Contact Between the Rigid Bodies 2 and 3

We proceed in an analogous way and obtain (Fig. 3) the function of constraint

$$F_2(X_2, Y_2, \theta_2, X_3, Y_3, \theta_3) = f_2(X_2, Y_2, \theta_2, X_3, Y_3, \theta_3) - R_3 + r_{22} = 0, \tag{26}$$

where

$$f_2(X_2, Y_2, \theta_2, X_3, Y_3, \theta_3) = \sqrt{(X_{22} - X_3)^2 + (Y_{22} - Y_3)^2}, \tag{27}$$

$$\begin{bmatrix} X_{22} \\ Y_{22} \end{bmatrix} = \begin{bmatrix} X_2 \\ Y_2 \end{bmatrix} + [\mathbf{A}_2] \begin{bmatrix} l_{22} \\ 0 \end{bmatrix}. \tag{28}$$

The matrix of constraint has the expression

$$[\mathbf{B}_2] = \begin{bmatrix} \frac{\partial F_2}{\partial X_2} & \frac{\partial F_2}{\partial Y_2} & \frac{\partial F_2}{\partial \theta_2} & \frac{\partial F_2}{\partial X_3} & \frac{\partial F_2}{\partial Y_3} & \frac{\partial F_2}{\partial \theta_3} \end{bmatrix} \tag{29}$$

and verifies the relation

$$[\mathbf{B}_2]\{\dot{\mathbf{q}}\} = \{0\}. \tag{30}$$

### The Case of the Contact Between the Rigid Body 3 and the Guidance

In this case we use the Fig. 4. Let us assume that the contact takes place at the point  $A_1$ .

**Fig. 3** The contact between the bodies 2 and 3

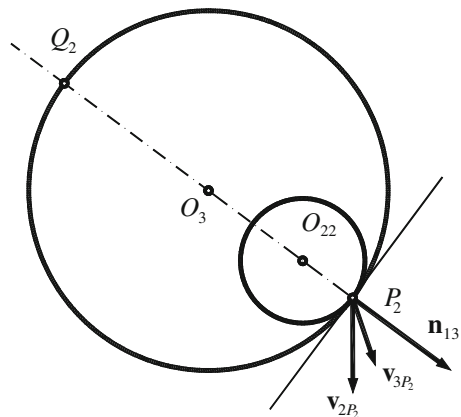
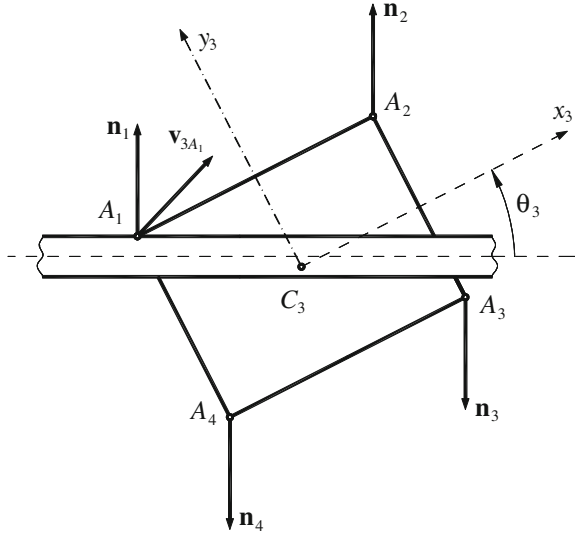


**Fig. 4** The contact between the slider and the guidance



Since (Fig. 1)

$$\begin{bmatrix} X_{A_1} \\ Y_{A_1} \end{bmatrix} = \begin{bmatrix} X_3 \\ Y_3 \end{bmatrix} + [\mathbf{A}_3] \begin{bmatrix} -f \\ e \end{bmatrix}, \tag{31}$$

the existence of the contact at the point  $A_1$  assumes the fulfilling of the condition

$$Y_{A_1} = d, \tag{32}$$

which is equivalent to write

$$d = Y_3 - f \sin \theta_3 + e \cos \theta_3. \tag{33}$$

The velocity of the point  $A_1$  situated on the rigid body 3 is given by

$$\begin{bmatrix} v_{3A_{1x}} \\ v_{3A_{1y}} \end{bmatrix} = \begin{bmatrix} \dot{X}_3 \\ \dot{Y}_3 \end{bmatrix} + [\dot{\mathbf{A}}_3] \begin{bmatrix} -f \\ e \end{bmatrix}, \tag{34}$$

where

$$[\dot{\mathbf{A}}_3] = \begin{bmatrix} -\sin \theta_3 & -\cos \theta_3 \\ \cos \theta_3 & -\sin \theta_3 \end{bmatrix} \dot{\theta}_3. \tag{35}$$



The normal  $\mathbf{n}_1$  to the guidance at the point  $A_1$  has the expression

$$\mathbf{n}_1 = \mathbf{j}. \quad (36)$$

The contact at the point  $A_1$  becomes a constraint if and only if the velocity  $\mathbf{v}_{3A_1}$  has a non-zero component on the negative direction of the normal  $\mathbf{n}_1$ , that is,

$$\begin{bmatrix} v_{3A_{1x}} & v_{3A_{1y}} \end{bmatrix} \begin{bmatrix} 0 \\ 1 \end{bmatrix} < 0. \quad (37)$$

If the last relation is fulfilled, than one gets the constraint function

$$F_3(Y_3, \theta_3) = Y_3 - f \sin \theta_3 + e \cos \theta_3 - d = 0, \quad (38)$$

to which corresponds the matrix of constraint

$$\left[ \mathbf{B}_3^{(1)} \right] = [0 \quad 0 \quad 0 \quad 0 \quad 1 \quad -f \cos \theta_3 - e \sin \theta_3]. \quad (39)$$

Obviously, one may discuss the contacts at the points  $A_2$ ,  $A_3$ , and  $A_4$  in a similar way; it results the matrices of constraints  $\left[ \mathbf{B}_3^{(2)} \right]$ ,  $\left[ \mathbf{B}_3^{(3)} \right]$ , and  $\left[ \mathbf{B}_3^{(4)} \right]$ .

A careful analysis shows that we may have only the following types of contacts:

- contact at a single point  $A_i$ ,  $i = \overline{1, 4}$ ;
- contacts at the points in the form  $A_1$  and  $A_2$ , or  $A_3$  and  $A_4$ ;
- contact at two opposite points in the form  $A_1$  and  $A_3$ , or  $A_2$  and  $A_4$ .

It results that the matrix of constraints  $\left[ \mathbf{B}_3 \right]$  may have one of the following forms:

$$\left[ \mathbf{B}_3 \right] = \left[ \mathbf{B}_3^{(i)} \right], \quad i = \overline{1, 4} \quad (40)$$

$$\left[ \mathbf{B}_3 \right] = \begin{bmatrix} \left[ \mathbf{B}_3^{(1)} \right] \\ \left[ \mathbf{B}_3^{(2)} \right] \end{bmatrix}, \quad \text{or} \quad \left[ \mathbf{B}_3 \right] = \begin{bmatrix} \left[ \mathbf{B}_3^{(3)} \right] \\ \left[ \mathbf{B}_3^{(4)} \right] \end{bmatrix}, \quad (41)$$

$$\left[ \mathbf{B}_3 \right] = \begin{bmatrix} \left[ \mathbf{B}_3^{(1)} \right] \\ \left[ \mathbf{B}_3^{(3)} \right] \end{bmatrix}, \quad \text{or} \quad \left[ \mathbf{B}_3 \right] = \begin{bmatrix} \left[ \mathbf{B}_3^{(2)} \right] \\ \left[ \mathbf{B}_3^{(4)} \right] \end{bmatrix}. \quad (42)$$

## The Matrix Equation of Motion

The matrix of constraints has the form

$$[\mathbf{B}] = \begin{bmatrix} [\mathbf{B}_1] \\ [\mathbf{B}_2] \\ [\mathbf{B}_3] \end{bmatrix}. \quad (43)$$

We denote by  $[\mathbf{M}]$  the matrix

$$[\mathbf{M}] = \begin{bmatrix} m_2 & 0 & 0 & 0 & 0 & 0 \\ 0 & m_2 & 0 & 0 & 0 & 0 \\ 0 & 0 & J_2 & 0 & 0 & 0 \\ 0 & 0 & 0 & m_3 & 0 & 0 \\ 0 & 0 & 0 & 0 & m_3 & 0 \\ 0 & 0 & 0 & 0 & 0 & J_3 \end{bmatrix} \quad (44)$$

and it results the equation of motion

$$\begin{bmatrix} [\mathbf{M}] & -[\mathbf{B}]^T \\ [\mathbf{B}] & [\mathbf{0}] \end{bmatrix} \begin{bmatrix} \{\ddot{q}\} \\ \{\lambda\} \end{bmatrix} = \begin{bmatrix} \{\mathbf{F}\} + \{\tilde{\mathbf{F}}\} \\ \{\dot{\mathbf{C}}\} - [\tilde{\mathbf{B}}]\{\dot{\mathbf{q}}\} \end{bmatrix}, \quad (45)$$

where  $\{\lambda\}$  is the matrix of the Lagrange multipliers; the number of this column matrix is equal to the number of rows of the matrix of constraints  $[\mathbf{B}]$ .

The matrix  $\{\mathbf{F}\}$  is the matrix of the given forces and moments,

$$\{\mathbf{F}\} = [R_{2x} \ R_{2y} \ M_2 \ R_{3x} \ R_{3y} \ M_3]^T. \quad (46)$$

The matrix  $\{\tilde{\mathbf{F}}\}$  has the expression

$$\{\tilde{\mathbf{F}}\} = [0 \ 0 \ L_1 \ 0 \ 0 \ L_2]^T, \quad (47)$$

where the elements  $L_1$  and  $L_2$  are given by

$$L_{i-1} = -[0 \ 0 \ 1] \left[ [\mathbf{Q}_i]^T [\mathbf{J}_i] [\dot{\mathbf{Q}}_i] + [\mathbf{Q}_i]^T [\omega_i] [\mathbf{J}_i] [\mathbf{Q}_i] \right] \left\{ \dot{\beta}_i \right\}, \quad i = 2, 3, \quad (48)$$

with

$$[\mathbf{Q}_i] = \begin{bmatrix} \cos \theta_i & \sin \theta_i & 0 \\ -\sin \theta_i & \cos \theta_i & 0 \\ 0 & 0 & 1 \end{bmatrix}, \quad [\dot{\mathbf{Q}}_i] = \begin{bmatrix} -\sin \theta_i & \cos \theta_i & 0 \\ -\cos \theta_i & -\sin \theta_i & 0 \\ 0 & 0 & 0 \end{bmatrix} \dot{\theta}_i, \quad i = 2, 3, \quad (49)$$

$$[\omega_i] = \begin{bmatrix} 0 & -\dot{\theta}_i & 0 \\ \dot{\theta}_i & 0 & 0 \\ 0 & 0 & 0 \end{bmatrix}, \quad [\mathbf{J}_i] = \begin{bmatrix} 0 & 0 & 0 \\ 0 & 0 & 0 \\ 0 & 0 & J_i \end{bmatrix}, \quad \{\dot{\beta}_i\} = [0 \quad 0 \quad \dot{\theta}_i]^T, \quad i = 2, 3, \quad (50)$$

$$\{\dot{\mathbf{C}}\} = [\{\dot{\mathbf{C}}_1\} \quad 0 \quad 0]^T, \quad (51)$$

$$[\dot{\mathbf{B}}] = \begin{bmatrix} [\dot{\mathbf{B}}_1] \\ [\dot{\mathbf{B}}_2] \\ [\dot{\mathbf{B}}_3] \end{bmatrix}. \quad (52)$$

Obviously, if there is no constraint, then the Eq. (45) takes the form

$$[\mathbf{M}]\{\ddot{q}\} = \{\mathbf{F}\}, \quad (53)$$

which is identical to the Eqs. (3) and (4).

## The Reactions

For the revolute joints (characterized by the matrices of constraints  $[\mathbf{B}_1]$  and  $[\mathbf{B}_2]$ ) the components of the reactions are given by  $\lambda_1 B_{11}$  and  $\lambda_2 B_{21}$ . For the prismatic joint (described by the matrix of constraints  $[\mathbf{B}_3]$ ) the normal reaction is given by  $\lambda_3 B_{35}$  for one contact, or by  $\lambda_3 B_{35}$  and  $\lambda_4 B_{45}$  for the case of two simultaneous contacts.

## Conclusions

The previous study perform the obtaining of the matrix equation of motion for a crank-shaft mechanism with all possible clearances. The equation of motion is obtained by using a multibody approach and it can be used no matter the existence or vanishing of a certain clearance. There exist the following possibilities for the modification of the matrix of constraints:

- there is no contact between the elements 1 and 2, or the contact is not a constraint. In this case the matrix  $[\mathbf{B}]$  loses its first line described by the matrix  $[\mathbf{B}_1]$  and the Lagrange multiplier  $\lambda_1$  vanishes;
- there is no contact between the elements 2 and 3, or the contact is not a constraint. In this case the matrix  $[\mathbf{B}]$  loses its second line described by the matrix  $[\mathbf{B}_2]$  and the Lagrange multiplier  $\lambda_2$  vanishes;

- there is no contact between the element 3 (slider) and guidance, or the contact is not a constraints. In this situation the matrix  $[\mathbf{B}_3]$  disappear in the expression of the matrix  $[\mathbf{B}]$ , while the Lagrange multipliers  $\lambda_3$  and  $\lambda_4$  vanish;
- the contact between the slider and the guidance is realized at a single point, case in which the matrix  $[\mathbf{B}_3]$  loses its second line, the matrix of constraints  $[\mathbf{B}]$  loses its last line and the Lagrange multiplier  $\lambda_4$  vanishes.

Due to the expression of the matrix  $[\mathbf{M}]$  it results that it is always invertible and the procedure for the direct solving of the Eq. (45) described in (Pandrea and Stănescu 2015) can be used in this case.

The expressions for the magnitude of the normal reactions at the constraint points are also presented in the paper.

## References

- Daniel GB, Cavalca KL (2011) Analysis of the dynamics of a slider-crank mechanism with hydrodynamic lubrication in the connecting rod–slider joint clearance. *Mech Mach Theory* 46:1434–1452
- Goudas I, Stavrakis I, Natsiavas S (2004) Dynamics of slider-crank mechanisms with flexible supports and non-ideal forcing. *Nonlinear Dyn* 35:205–227
- Pandrea N, Stănescu ND (2015) Dynamics of the rigid solid with general constraints by a multibody approach. Wiley, Chichester
- Reis VL, Daniel GB, Cavalca KL (2014) Dynamic analysis of a lubricated slider-crank mechanism considering friction and Hertz contact effects. *Mech Mach Theory* 74:257–273
- Šika Z, Grešl N, Valášek M (2012) Synthesis of mechanisms using evolution of associated dissipative systems. *Multibody Sys Dyn* doi:[10.1007/s11044-012-9329-4](https://doi.org/10.1007/s11044-012-9329-4)
- Zheng E, Zhou X (2014) Modeling and simulation of flexible slider-crank mechanism with clearance for a closed high speed press system. *Mech Mach Theory* 70:10–30
- Zheng E, Zhu R, Zhu S, Lu X (2015) A study on dynamics of flexible multi-link mechanism including joints with clearance and lubrication for ultra-precision presses. *Nonlinear Dyn* doi:[10.1007/s11071-015-2315-7](https://doi.org/10.1007/s11071-015-2315-7)

# Research Applied to Exhaust Gas After-Treatment Systems in 1.6 L Zsg 416 Ford Engine

Lucian-Vasile Crişan-Lupa, Adela-Ioana Borzan, Dan Moldovanu and Levente-Botond Kocsis

**Abstract** In the present paper it is synthesized an applied study of the influence that exhaust gas after-treatment systems have upon the power output, engine torque, fuel specific consumption (due to the back-pressure in the exhaust) by testing a modern Ford engine (type ZSG 416), and converting it to a virtual simulation software—Lotus Engine Simulation. The first main objective of the present paper is the comparison of the experimental practical values with the software simulation results and outlining the significant differences. The second main objective is the modification of the initial engine-test-bench by decreasing and also increasing the exhaust back-pressure through the configuration of exhaust gas after-treatment system configuration (minimum back-pressure resistance—no exhaust pipe; standard after-treatment components; clogged catalyst in after-treatment system—high back-pressure) in order to outline the influence on the power and torque curves. In conclusion, the after-treatment system influence on the engine behavior may be altered by catalyst clogging and cleaning (thus the engine operation in all available regimes is needed) and also by mounting an exhaust flaps which can be controlled by modifying its translation inside the gas exhaust pipe.

**Keywords** After-treatment · Automotive · Catalyst · Engine · Exhaust

## Introduction

Spark-ignition and diesel engines (today's international scandal it's a strong proof) are a major source of urban air pollution. The spark-ignition engine exhaust gases contain oxides of nitrogen (nitric oxide, NO, and small amounts of nitrogen dioxide, NO<sub>2</sub>—collectively known as NO<sub>x</sub>, a pollutant that can cause emphysema,

---

L.-V. Crişan-Lupa (✉) · A.-I. Borzan · D. Moldovanu · L.-B. Kocsis  
Technical University of Cluj-Napoca, 103-105 B-dul Muncii, Romania  
e-mail: Lucian.Crisan@auto.uteluj.ro

bronchitis and other respiratory (Ewing 2015) and other pulmonary diseases), carbon monoxide (CO), and organic compounds which are unburned or partially burned hydrocarbons (HC). The relative amounts depend on engine design and operating conditions..., (Grünwald 1980; Roberts et al. 2014). The unburned hydrocarbons exit the cylinder in the bulk-gas flow during blow down and at the end of the exhaust stroke as the piston pushes gas scraped off the wall out of the exhaust valve. Substantial oxidation of the hydrocarbons which escape the primary combustion process by any of the above process can occur during expansion and exhaust (Heywood 1988). All these chemical reactions and physical processes have an influence upon the gas-flow dynamics in the exhaust pipe and after-treatment system. (Rus 2002) Some parameters are studied by simulation (Keynejad and Manzie 2011) or experimental testing (Apostolescu and Taraza 1979).

Simulation is an intrinsic part of the design process. The last one is a significant sequence in realizing a quality product. In the design process, as a result of the development in CAE and CAD systems, it has been achieved the level of virtual designing, simulating and evaluating the products. And this is the most important aspect of the problem, with a strategic influence. Using these types of programs and applications has caused the significant reduction of the costs, because no materials are used at this point (Baldean 2007). L.E.S. (Lotus Engine Simulation) is a simulation tool, having some common features with the rest of similar applications, but it has also many distinct features of its own, which make it particular and promote it higher on the option scale of those who use the computing power as an instrument. It enhances the possibility of transposing in virtual environment the mechanic, hydraulic, electrical and electronic systems (Getting started with LES 2001).

In this paper the standard catalyst in the Ford 1.6 ZSG 416 engine and its influence upon back pressure (and engine performance with and without after-treatment system) were studied, as well as the specific laboratory equipment and methods to research these processes. In the exhaust system takes place all the gas dynamics (Abăitancei et al. 1980). Being a complex phenomenon there are many approaches (Ferenti and Baldean 2013) of studying the effect of catalyst clogging and increasing the back pressure, one of them by measuring and controlling the Exhaust Gas Velocity (EGV) (less destructive, very high costs, high precision), or by designing a flap to slide inside the exhaust pipe (permanently destructive, medium investment, good precision), or by replacing the after-treatment components from exhaust system (temporarily destructive, few investments, good precision), the last one being the highly preferred and suited for this research on the basis of research/investment indicator (Bataga et al. 1995).

By computer simulations and by using advanced engine scanning tools in experimental setup may be achieved an overview of the engine and gas-flow dynamic behavior. Researching through on-board investigation methods in different loading conditions and by experimenting with the after-treatment system may be determined the engine performance (Ferenti and Baldean 2014).

## Material and Methodology

A modern laboratory test-bed (Barabás et al. 2010a, b) with two ways catalyst for the after-treatment system and also a software simulation environment are used in order to develop (both practically and virtually) the process investigation possibilities of the I.C. engine (Burnete et al. 2009). The Ford engine test-bed was configured by the Weinlich Steuerung Company in Germany, using original standard components. The input data are engine speed, engine load, accelerator position, air/fuel consumption; all these values being measured in real time with specific sensors installed on the tested engine and dynamometer, using an electromagnetic dynamometer for braking and loading the working engine (at low engine speeds, at average engine speeds and at maximum speeds), in order to better understand the engine behavior and its relation with the after-treatment system.

The readings of specific installed sensors are taken and analyzed through standard or specially configured diagnosis methods of tested engine systems using Bosch KTS equipment (Baldean et al. 2010a, b).

Researches concerning exhaust gases dynamics for the I.C. engine were developed both through simulation (Baldean et al. 2010a, b) using a utility software for computing the engine cycles and for engine performance predictions, combining variable gas-flow and combustion models, and through experimental tests in laboratory conditions on a specially designed test bed (Fig. 1).

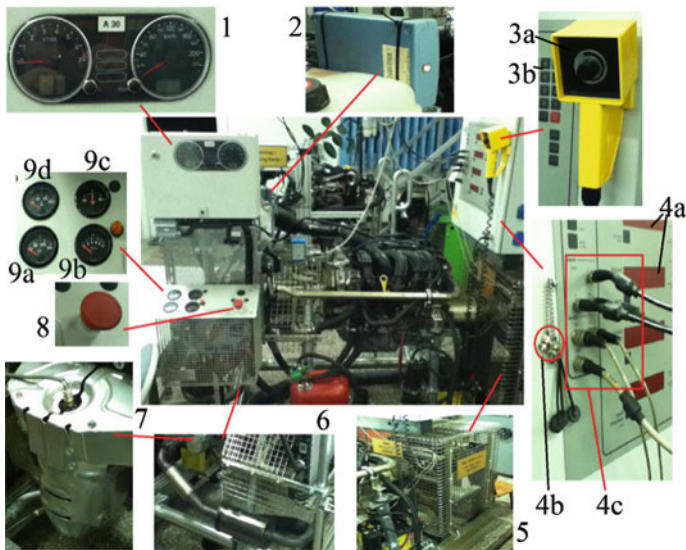


**Fig. 1** Test bed used for experimental determinations. 1 Board panel, 2 picov oscilloscope interface, 3a engine loading handler, 3b dynamometer operating keypad, 4a display, 4b socket covers, 4c data plug-in cables, 5 dynamometer, 6 exhaust system, 7 catalytic converter, 8 emergency stop, 9a oil temperature indicator, 9b oil pressure, 9c ampermeter, 9d coolant temperature indicator

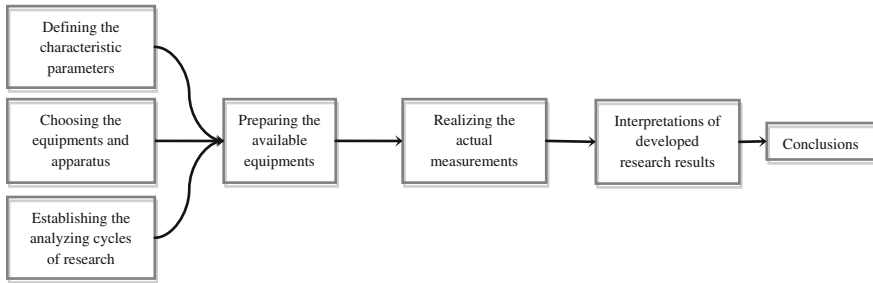


**Fig. 2** Applied research methodology or developing phases of the study

The research simplified methodology is presented in the Fig. 2.

After studying the after-treatment system behavior, there has to be taken into account the optimal operating regime (Crişan et al. 2010). For the different engine speeds and different exhaust/after-treatment system configurations, the engine power and torque were measured at flywheel and crankshaft (idle speed, average engine speeds and at maximum speeds) in 12 points of operation on the nominal characteristic. In order to be as less destructive as possible when configuring the after-treatment system and realizing the experimental tests, a manometer was adapted and fixed to the exhaust system in order to monitor the gas flow. Diagrams were determined and studied.

The intake air temperature, the in-cylinder pressure and the engine temperature were controlled all the time (Bataga et al. 1995). Also a virtual model was built in L.E.S. and simulated in the similar conditions as the real engine installed on the test-bed. After optimizing the exhaust configuration and after-treatment system architecture in L.E.S., the results were implemented in practical test. There were needed some adjustment to be made in order to ensure the proper operation of the reconfigured test-bed (with and without after-treatment system). Also the initial data for engine operation conditions were strictly monitored, atmospheric pressure was yet verified. The tests and simulations were developed as a reference model for standard after-treatment system (one available on Ford engine), to which all other configurations were compared. By analyzing the engine performances with and without after-treatment system, conclusions were issued concerning the optimal behavior and highest economical/energetic point for the studied engine (Bertrand et al. 2012).

## Results

In Fig. 3 it is presented the defining module for dimensions and other characteristics of the exhaust system without any after-treatment components. It may be useful for setting the diameters and the remaining dimensions of the exhaust pipe, silencer, total length, pipe section etc.



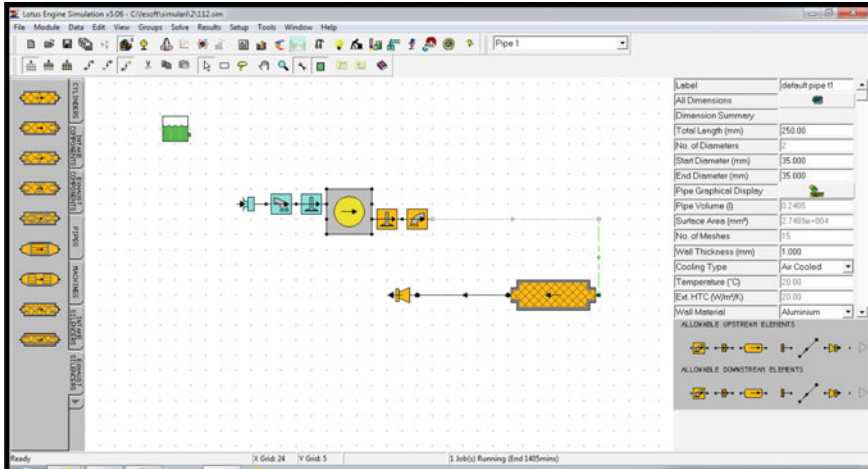


**Fig. 3** Configuration of engine and exhaust components without after-treatment solution

The obtained results were mutually compared and if the after-treatment system is adjusted properly and is not clogged, the practical determinations on the test-bed indicate a smaller fuel consumption (1 ÷ 7 % less) for the standard configuration than the other implemented models and also a maximum 10 % difference related to simulation, but that is may be assumed in the friction coefficient. By introducing an exhaust flaps somewhere in the pipe, the engine power is lowered (above 45 % obstruction).

Graphics of engine performances in three important configurations (a. with no catalytic converter; b. with one catalytic converter; c. with two catalytic converters) are presented in Fig. 4.

In order to outline the influence of some factors upon main indicator parameters of the engine operating cycle (brake mean effective pressure, indicated pressure, indicated fuel specific consumption and indicated efficiency) it is necessary to express these parameters in relation with determining factors (those which manifest the important influence).

Classically the engine effective power ( $P_e$ ) is determined taking into account some structural and operating features in the mathematical expression (Bataga et al. 1995):

$$P_e = \frac{p_e \cdot n \cdot i \cdot V_s}{\tau \cdot 30000} \text{ kW} \tag{1}$$

where:  $p_e$  is brake mean effective pressure (bar);  $n$ —engine speed (rot/min);  $i$ —number of pistons or cylinders;  $V_s$ —cylinder volume defined by the piston displacement;  $\tau$ —number of engine strokes.

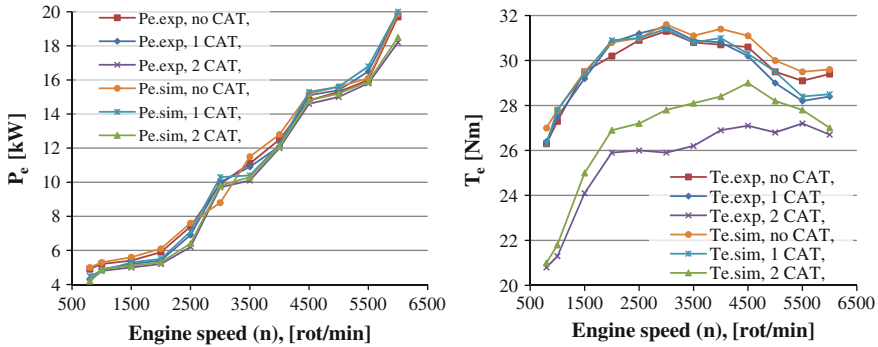


**Fig. 4** Effective power and effective engine torque determined by simulation and experiment. Pe.exp, no CAT—effective power determined experimentally without catalytic converter; Pe.exp, 1 CAT—ef. pwr. exp. with 1 cat. convert.; Pe.exp, 2 CAT—ef. pwr. exp. with 2 cat. convert.; Pe.sim, no CAT—ef. pwr. determined by simulation without catalytic converter; Pe.sim, 1 CAT—ef. pwr. sim. with 1 cat. convert.; Pe.sim, 2 CAT—ef. pwr. sim. with 2 cat. convert.; Te.exp, no CAT—effective torque determined experimentally without catalytic converter; Te.exp, 1 CAT—ef. trq. exp. with 1 cat. convert.; Te.exp, 2 CAT—ef. trq. exp. with 2 cat. convert.; Te.sim, no CAT—ef. trq. in sim. with no catalytic converter; Te.sim, 1 CAT—ef. trq. sim. with 1 cat. convert.; Te.sim, 2 CAT—ef. trq. sim. with 2 cat. convert

In the same fashion effective engine torque in relation with effective engine power is determine by the mathematical expression (Bataga et al. 1995):

$$T_e = 9549.2 \frac{P_e}{n} \text{ Nm} \tag{2}$$

where:  $P_e$  is engine effective power (kW);  $n$ —engine speed (rot/min).

In the research result of the present paper the engine power trend line is defined by a polynomial equation depending on engine speed:

$$P = 2 \times 10^{-7} n^2 + 1.3 \times 10^{-3} n + 3.3591 \text{ kW} \tag{3}$$

and the engine torque also has a polynomial equation:

$$T = 5 \times 10^{-7} n^2 + 3.6 \times 10^{-3} n + 24.898 \text{ Nm} \tag{4}$$

this being also correlated with the engine speed ( $n$ ).

Graphics of engine (hourly and specific) fuel consumptions in the three studied configurations are presented in Fig. 5.

The hourly fuel consumption is defined by a polynomial equation related to engine speed:

$$C_h = 7 \times 10^{-8} n^2 + 3 \times 10^{-4} n + 0.8689 \text{ kW} \tag{5}$$

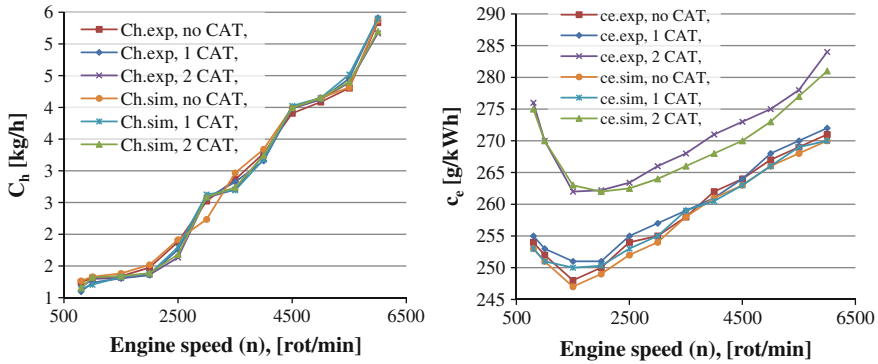


**Fig. 5** Hourly and brake specific fuel consumption determined by simulation and experiment. Ch.exp, no CAT—hourly fuel consumption (HFC) determined experimentally without catalytic converter; Ch.exp, 1 CAT—HFC exp. with 1 cat. convert.; Ch.exp, 2 CAT—HFC exp. with 2 cat. convert.; Ch.sim, no CAT—HFC determined by simulation without catalytic converter; Ch.sim, 1 CAT—HFC sim. with 1 cat. convert.; Ch. sim, 2 CAT—HFC sim. with 2 cat. convert.; Ce.exp, no CAT—brake specific fuel consumption determined experimentally without catalytic converter; Ce.exp, 1 CAT—BSFC exp. with 1 cat. convert.; Ce.exp, 2 CAT—BSFC exp. with 2 cat. convert. Ce.sim, no CAT—BSFC determined by simulation without catalytic converter; Ce.sim, 1 CAT—BSFC sim. with 1 cat. convert.; Ce.sim, 2 CAT—BSFC sim. with 2 cat. convert

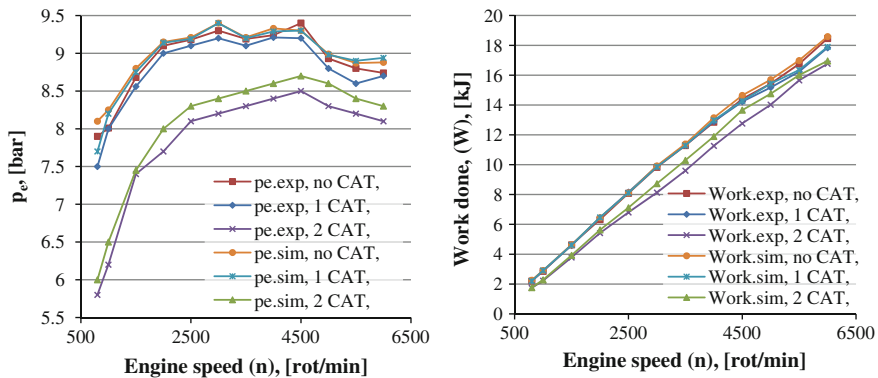


**Fig. 6** Variations of effective pressure and work done by the engine in simulation and experiment.  $p_{e.exp}$ , no CAT—brake mean effective pressure (BMEP) determined experimentally without catalytic converter;  $p_{e.exp}$ , 1 CAT—BMEP exp. with 1 cat. convert.;  $p_{e.exp}$ , 2 CAT—BMEP exp. with 2 cat. convert.;  $p_{e.sim}$ , no CAT—BMEP determined by simulation without catalytic converter;  $p_{e.sim}$ , 1 CAT—BMEP sim. with 1 cat. convert.;  $p_{e.sim}$ , 2 CAT—BMEP sim. with 2 cat. convert.; W.exp, no CAT—Work done exp. without catalytic converter; W.exp, 1 CAT—Work done exp. with 1 cat. convert.; W.exp, 2 CAT—Work done exp. with 2 cat. convert.; W.sim, no CAT—Work done determined by simulation without catalytic converter; W.sim, 1 CAT—Work done sim. with 1 cat. convert.; W.sim, 2 CAT—Work done sim. with 2 cat. convert

and the brake specific fuel consumption also has a polynomial equation:

$$c_e = 8 \times 10^{-7}n^2 + 1.1 \times 10^{-3}n + 252.98 \text{ Nm} \quad (6)$$

being defined in relation to the engine speed ( $n$ ).

The variation graphics of engine mean effective pressure and work done in those three stated and studied exhaust after-treatment configurations are presented in Fig. 6.

## Conclusions and Observations

In order to elaborate the impact of exhaust after-treatment systems on the engine effective power, engine effective torque, hourly fuel consumption, break specific fuel consumption, brake mean effective pressure and work done by the engine, an applied research (both experimentally and by simulation) was carried out in the last months, which was shortly outlined in this paper. Tests and simulation were performed at different loads and speeds. Dynamic and economy performances in three structural configurations (with no after treatment elements, with one catalytic converter and with two catalytic converters) were examined. The results demonstrated that, in the three operating configurations, engine performance and economy consistently decreased with the rising of back-pressure in the exhaust system due to gas flow resistance of catalytic converters and after-treatment increased number of components. Some possible reasons that could reduce the engine performance and economy were further considered. It revealed that increased gas flow resistance led to a lowered quality of air-fuel mixture formation, affecting also the process of combustion, declining specific heat ratio and aggravating ineffectiveness of exhausting system. Thus a multi factor and complex situation contributed to the deterioration of engine performances when it was operating with two catalytic converters and with high back pressure in the exhaust pipe.

Although, at present moment, the number of highly sophisticated exhaust systems with many after treatment components on road vehicles is smaller than that of conventional vehicles (one or none catalytic converters), in the following years it will be an increasing and stringent demand to complicate and develop the after treatment solutions, which further more will affect in some way engine performances, otherwise there will be discussions not only on the “DISELGATE issue” (VW Emissions Scandal 2015), but there will be a matter of automotive development for the future in general. Developing and implementing coping after treatment systems is still very important for the sustainable progress, in particular for European and western countries with stringent polluting policies. Specific legislations for type-approval, certification or in-use conformity of all polluting engines (from now on, knowing what happened with VW case in USA last month) could prevent and discourage engine developers in taking the easy way out with only software tuning for specific operating conditions. Thus a more difficult task is about

to be assumed that of a structural change. It has to be taken down to the roots maybe and start again from the basic phenomena. In particular, a higher compression ratio and development of new materials will be for a considerable period of time other solutions, due to the modified equilibrium with the exhaust back pressure generated by the after treatment components, therefore improving the efficiency and dynamic engine performances of highly complicated or clogged exhaust systems in the case of low polluting configurations.

In conclusion, the after-treatment system influence on the engine behavior may be altered by catalyst clogging and cleaning (thus the engine operation in all available regimes is needed) and also by mounting an exhaust flaps which can be controlled by modifying its translation inside the gas exhaust pipe.

All the obtained result encourage the development of the experimental research concerning the after treatment systems installed or designed for internal combustion engines, in different fuel supply conditions, a situation which may lead to a contribution at air-fuel mixture formation and to a higher combustion efficiency as well as to pollution reduction. This paper outlines the importance of linking the simulation process with experimental research implemented on a test-bed.

In the future works, researches on the different thermal management and operating strategies (even alternative fuels implementation) in the case of emissions and performances of internal combustion engines with complex exhaust systems will be very appreciated.

**Acknowledgements** This paper was supported by Technical University of Cluj-Napoca (Attracting doctoral program). A special recognition is given to the scientific coordinator: Prof. dr. ing. Burnete N.

The authors, previously studied swirl motion inside a CIE, with the paper: **Computational fluid dynamics simulation of a single cylinder research engine working with biodiesel**, published at Thermal Science.

## References

- Abăitancei D et al (1980) Motoare pentru automobile și tractoare, vol 2. Editura Tehnică, București
- Apostolescu N, Taraza D (1979) Bazele cercetării experimentale a mașinilor termice, București, Editura Didactică și Pedagogică
- Bataga N et al (1995) Motoare cu ardere internă, București, Editura Didactică și Pedagogică
- Baldean D (2007) Software for the study of some parameters of gasoline injection process in Otto engines. J. ACTA TECHNICA NAPOCENSIS, Appl Math Mech 6(50), Ed UT Press, ISSN 1221-5872, Cluj-Napoca, Romania
- Burnete N et al (2009) Process investigation possibilities of an internal combustion engine. ESFA 2009. In: The 8th international conference, fuel economy, safety and reliability of motor vehicles, 12–14 Nov, București, Romania, ISSN 2067-1083
- Baldean D, Burnete N, Varga B (2010a) Analysis possibilities through diagnosis of motor vehicles systems using Bosch KTS equipment. J Acta Mecanica 2(3) Technical University of Cluj-Napoca, Romania

- Baldean D, Burnete N, Filip N (2010b) Studies concerning exhaust gases dynamics for an i.c. engine through simulation. In: CONAT, International congress on automotive and transport engineering, 27–29 Oct, Brașov, Romania, vol 5, ISSN 2069-0401
- Barabás I, Todorut IA, Kocsis LB, Baldean DL (2010a) Automated test bench for study of the fuel injection process. *Robot Autom Syst* 166–167:39–44
- Barabás I, Todorut A, Baldean D (2010b) Performance and emission characteristics of an CI engine fueled with diesel-biodiesel-bioethanol blends. *Fuel* 89(12):3827–3832
- Bertrand F, Devals C, Seguianou de Preval C (2012) Towards the simulation of the catalytic monolith converter using discrete channel-scale models. *Catal Today, Modeling of Exhaust-Gas After-Treatment* 188(1):80–86
- Crișan M-A et al (2010) Analysis of some operating parameters of S.I.E. from Seat Leon in different road conditions using a new testing technology. In: CONAT, International congress on automotive and transport engineering, 27–29 Oct, Brașov, Romania. vol 1, ISSN 2069-0401
- Ewing J (2015) Volkswagen C.E.O. Martin Winterkorn Resigns Amid Emissions Scandal. *International Business, New York Times*
- Ferenti I, Baldean D (2013) Studii și cercetări ale unor parametri funcționali și a variației nivelului emisiilor la un motor cu aprindere prin scânteie prin metode avansate de investigație în condiții diferite de încărcare. In: *The 3rd international conference AMMA, Cluj-N., Ed. UT Press*
- Ferenti I, Baldean D (2014) Research of some operating parameters and the emissions level variation in a spark ignited engine through on-board investigation methods in different loading conditions. *Open Eng* 4(2):192–208, ISSN (Online) 2391-5439, DOI: [10.2478/s13531-013-0167-9](https://doi.org/10.2478/s13531-013-0167-9), Published Online: 2014-06-27, Open Access <http://www.degruyter.com/view/j/eng.2014.4.issue-2/s13531-013-0167-9/s13531-013-0167-9.xml?format=INT>
- Grünwald B (1980) *Teoria, Calculul și Construcția motoarelor pentru autovehicule rutiere, București, Editura Didactică și Pedagogică*
- Getting started with Lotus Engine Simulation, 2001
- Heywood JB (1988) *Internal combustion engine fundamentals*, vol 930. McGraw-Hill, New York
- Keynejad F, Manzie C (2011) Cold start modeling of spark ignition engines. *Control Eng Pract* 19 (8):912–925
- Roberts A et al (2014) Internal combustion engine cold-start efficiency: a review of the problem, causes and potential solutions. *Energy Convers Manag* 82:327–350
- Rus I (2002) *Autovehicule rutiere*. Sincron, Cluj-Napoca
- VW Emissions Scandal: Cheating and Outrage. *New York Times, The Opinion Pages*. <http://www.nytimes.com/2015/09/25/opinion/vw-emissions-scandal-cheating-and-outrage.html>

# Development of a Water Rankine System to Improve Diesel Engine Efficiency

Bogdan Radu, Alexandru Racovitză and Radu Chiriac

**Abstract** One way to increase the thermal efficiency of a diesel engine is to recover the waste heat from the exhaust gases and from the cooling system. For the stationary diesel engine, used to generate electrical power, this heat may be converted in useful energy by a cogeneration system, in order to ensure hot water production. For the automotive diesel engine, however, the solution is not applicable therefore a method has to be developed in order to generate mechanical power. In this paper the authors show the design and the simulation performed with the AMESIM software tools for a heat recovery system dedicated to a diesel engine. The engine is simulated with the specific library of the software and the obtained results are used in the second part of the paper concerning the recovery system. The simulation results presented in this paper obviously need to be confronted to the experimental data before validating the prediction capability of the model so that this one could become an important tool in the efforts to emphasize how can be reduced the fuel consumption for truck diesel engines using the on board heat recovery.

**Keywords** Waste heat recovery · Internal combustion engine · Simulation · Rankine cycle

---

B. Radu (✉) · A. Racovitză · R. Chiriac  
Faculty of Mechanical Engineering, Department of Thermodynamics, Engines,  
Thermal and Refrigerant Machines, University Politehnica of Bucharest,  
Splaiul Independentei 313, Sector 6, 060042 Bucharest, Romania  
e-mail: bobitaradu@yahoo.com

A. Racovitză  
e-mail: alexandru\_racovitză@yahoo.com

R. Chiriac  
e-mail: raduchiriac2001@yahoo.com

## Introduction

The new types of diesel engines for heavy duty commercial vehicles convert in average around 40 % of the primary energy into mechanical power. The residual part, that includes friction, coolant, brake work and exhaust gas energy represents almost 60 % from the total energy with a fraction of 27 % in exhaust gases. (Saidur et al. 2012). If at least a fraction of this energy could be harnessed, the efficiency should increase and the global warming could be maintained under control.

There are many technologies that may convert this rejected heat into useful form of energy. The thermoelectric energy conversion may be given as an example in this domain (Saidur et al. 2012). It is used to convert thermal energy from different temperature gradients existing between hot and cold heads of a semiconductor into electric energy. The benefits of this method include free maintenance, silent operation, high reliability and no moving parts. Theoretical economy efficiency could be up to 4.7 %, but the experiments shows an economy of 2 %. Another method is based on adding 2 supplementary strokes for an engine, resulting a six stroke engine (Saidur et al. 2012). The expanded exhaust gas is trapped and recompressed by two additional strokes, with water supply that generate steam to expand the gases and generate power. The exhaust gas could reduce the fuel consumption with a two stage turbocharger. That system includes two devices assembled in serial configuration, with the smaller sized turbocharger used at lower speed in order to produce higher torque to reduce the fuel consumption on the road and the larger one providing boost at higher engine speed. Mechanical turbo-compounding includes a conventional turbocharger which recovers the exhaust engine energy in a turbine to boost the air into the engine. Downstream the turbocharger engine the exhaust gas flows through a second turbine that recovers the energy and converts it into mechanical power (Noor et al. 2014).

The low degree temperature heat from exhaust cannot be efficiently converted into electrical power by using conventional methods as used in industrial waste recovery system. There are various cycles that may be used to produce energy, but the most attractive seems to be the Rankine cycle (Noor et al. 2014). A standard configuration for a system that will generate power is composed from a pump, boiler, expander and condenser (Duparchy et al. 2009). The pump will increase that fluid pressure in system and the fluid will be vaporized into the boiler. The mechanical work is produced in the expander and after that the condenser will transform the vapors back into fluid.

In this system various fluids could be used. If the fluid is organic, the system will be defined as an organic Rankine cycle (ORC). The selection of the fluid in an ORC is related to the operational conditions in order to obtain maximum efficiency (Wang et al. 2011). Thermodynamic properties are important, but for the organic fluids more important is the environmental impact and the comparison made in (Wang et al. 2011) cannot give an optimal solution for a fluid, so there are many fluids to be suitable from different reasons.



Cummins Inc. proposes a system for exhaust energy recovery presented as following (Nelson 2006). The goal for this program is to improve fuel efficiency by 10 % using waste heat energy. The method used is a Rankine cycle with R245fa as operational fluid that extract waste energy from jacket water, charge air, exhaust and EGR.

The solution proposed by DETROIT DIESEL for heavy duty diesel engines (Aneja et al. 2011) includes a boiler, a condenser, a pump, an expander and an electric generator, all mounted on a large truck. The agent fluid selected for this system is ethanol and the expected economy is around 4 %. The authors express the difficulties generated by this system integration on board of the vehicle and by its supplementary weight that will generate a supplementary increase in fuel consumption (around 1 %).

The reduction of the fuel consumption for an automobile is a permanent concern in BMW Group (Obieglo et al. 2011). The authors present a system called Turbosteamer, in fact a Rankine based cycle that uses water as working fluid. For an Otto engine with 160 kW rated power, maximum additional power obtained by heat recovery is about 14 %.

The development of a model that will simulate a heat recovery system with a Rankine cycle may be accomplished with the software AMESIM (Ziviani et al. 2012). In this environment all the elements of an ORC system and the main properties of the working fluid can be defined. The conclusion of this paper was that the ORC simulation model was validated with an average deviation of 2.9 %.

## The Engine Model

The simulation of a heat recovery system must start with a complete description of the internal combustion system in order to provide the input data (Fig. 1). The chosen engine was a large truck diesel with a rated power of 150 kW at 2200 rpm and a bore/stroke ratio of 110/135 mm.

The cruising speed for a 12 tones truck is 90 km/h, the most common speed for highway. At this velocity the necessary power is around 100 kW at 1800 rpm and that represents the output data in the engine model.

For the exhaust gas system the output data for the mentioned power and speed are presented in Figs. 2 and 3.

The average value for the mass flow is 160 g/s and it will be considered as a constant data in the following simulations.

The average exhaust gas temperature to be considered is 450 °C.

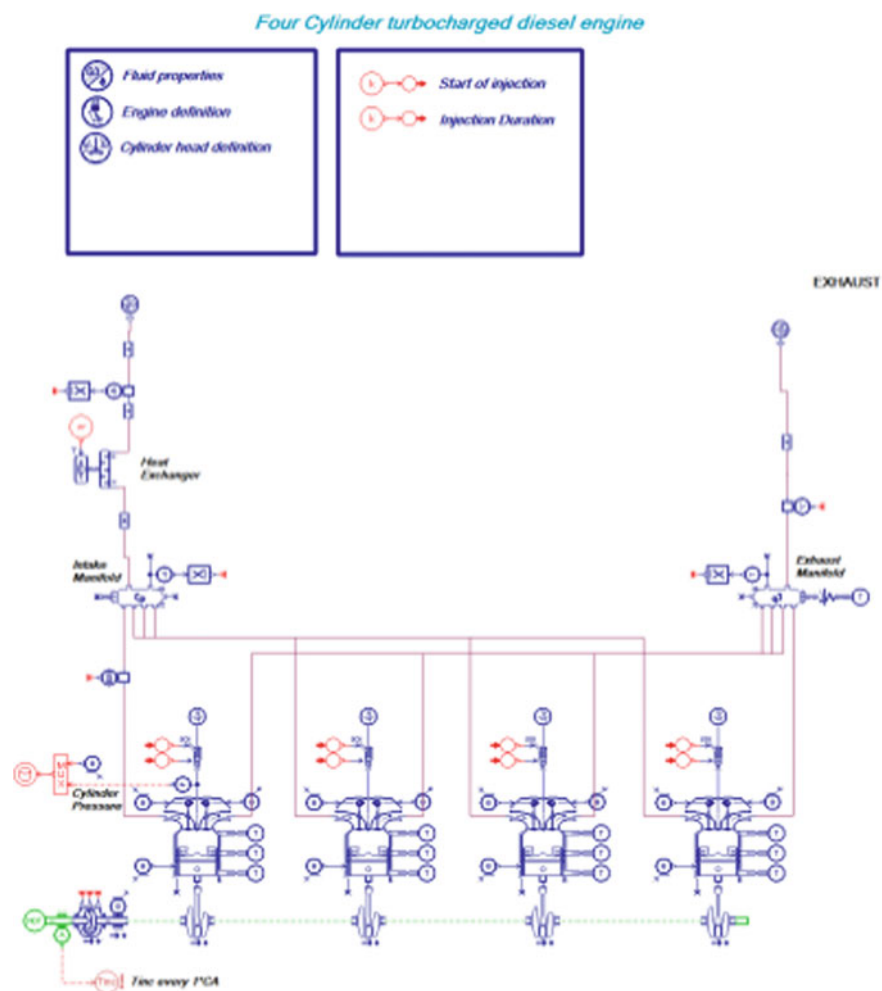


**Fig. 1** The engine model

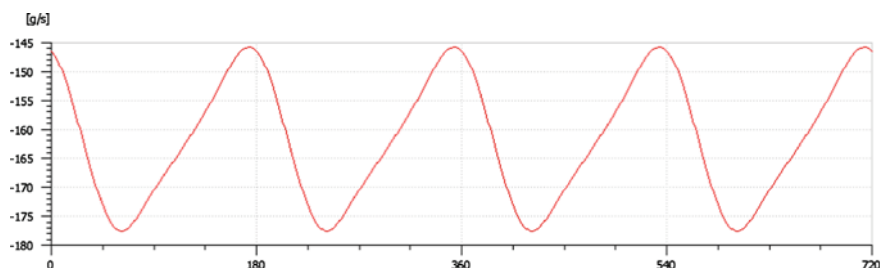


**Fig. 2** Mass flow in exhaust system

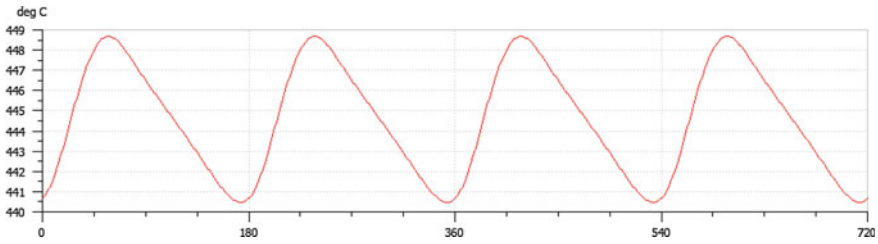


Fig. 3 Temperature in exhaust system

### The Complete Model for Recovery System

The model for a complete water Rankine recovery system is presented in Fig. 4.

It is formed by a series of pipes with the heat transfer capability representing the evaporator. The engine exhaust gas system is modeled as a gas source with constant mass flow and temperature, respecting the results obtained from the engine model. The heat transfer is considered in counter flow, liquid water enters into the system at lowest temperature. The water agent follows its conversion from liquid state into vapors along the system. At the end of these pipes (the evaporator) a turbine together with an energy consumer are also modeled.

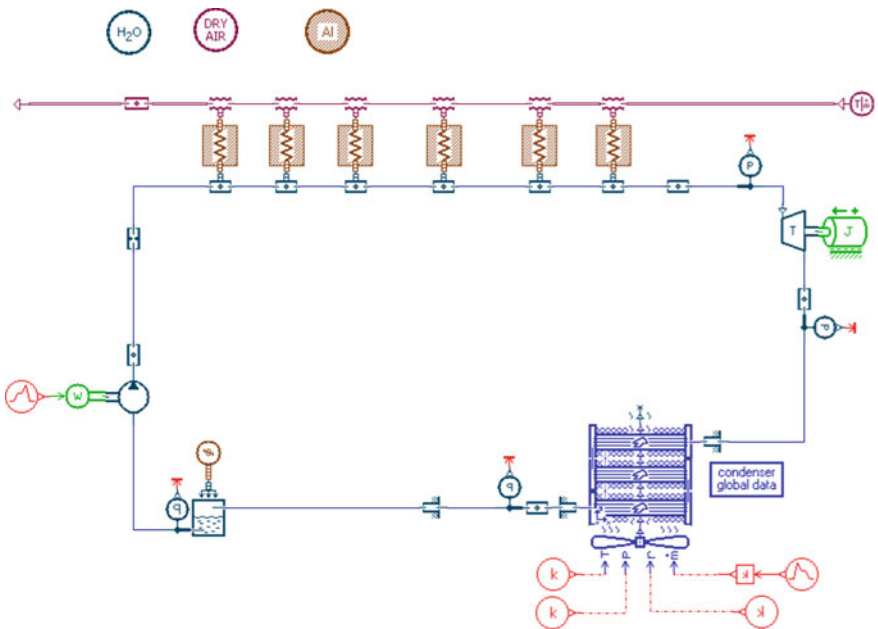


Fig. 4 Complete system model

After the turbine outlet, the low pressure steam is cooled in a condenser and the steam-water mixture is separated inside a separation unit. The pump located after the separator will generate the necessary flowing pressure for the fluid in the system.

This model is far to be complex, but from the mathematical point of view is pretty unstable. Once the steam appears in water or the steam title is under 1, all the agent properties change together with the parameters from the differential equations. AMESIM solve all the differential equations considering time also a variable and a stable solution is obtained after a number of iterations. For this model, on two directions, for the evaporator and for the condenser, the instability propagates along the elements with a high degree of difficulty to obtain a stable solution.

## The Simplified Model

The main goal for this system is to obtain energy at the turbine, so the complete model was simplified considering only the evaporator part (Fig. 5).

The turbine exhaust is considered a source with constant pressure and enthalpy and the pump was also replaced with a water source with constant enthalpy and mass flow. The results obtained from the previous model (unstable solution) offers good approximations for these boundary conditions. The convergence speed increases and results could be obtained using around 200 s integration time.

The main parameters there were taking into account for this model were the pipes length and diameter, water mass flow and turbine outlet diameter. The temperature at pipe no. 1 is around 173 and 343 °C at pipe no. 6 (Fig. 6).

The steam pressure and temperature parameters upstream the turbine are 9.3 bar and 343 °C and the steam expansion will generate a power of about 1.8 kW.

An important parameter in Rankine system design is the water mass flow for the particular turbine dimensions and exhaust gas parameters. Changing the mass water flow values, the pressure remains almost constant, depending especially on the turbine volume. For a turbine volume of 300 cm<sup>3</sup> the system pressure is 9.2 bar.

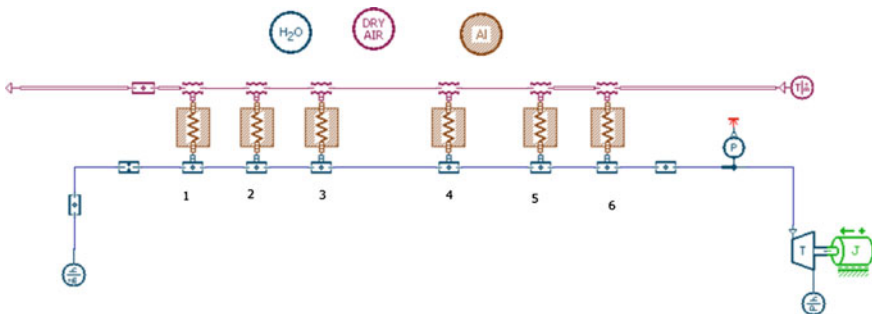


**Fig. 5** The schematic of the simplified model

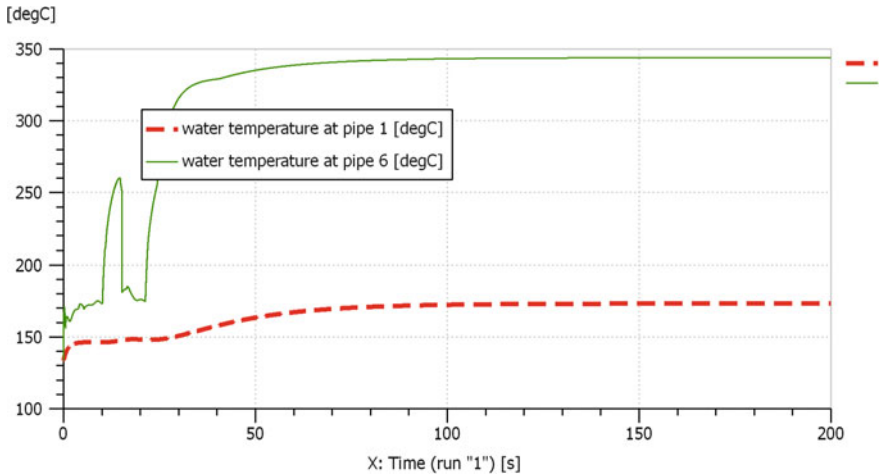


Fig. 6 Temperature variation at pipes no. 1 and no. 6

Temperature at pipe no. 6 significantly varies from 343 to 176 °C in case of operating at larger flow (Fig. 7).

For the last two values of the water temperature corresponding to mass flows of 0.5 and 0.6 kg/min temperature remains almost the same, but the gas mass fraction is different (Fig. 8). The first two values for mass flow will generate steam at pipe no. 6, but for the last two mass flow values the water will not be totally vaporized and the gas mass corresponding fractions are 0.98 and 0.8.

Another important parameter is the pipe length. The six pipes division represents only a mathematical simplification, because the model for the boiling process is

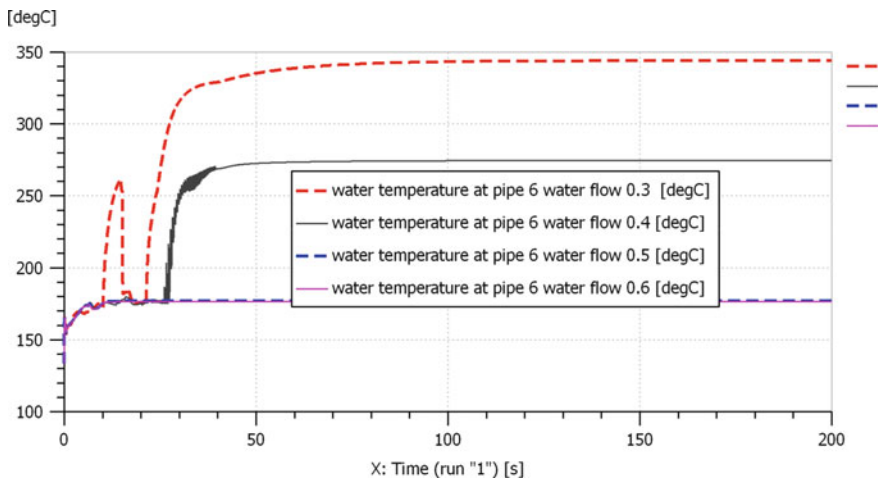
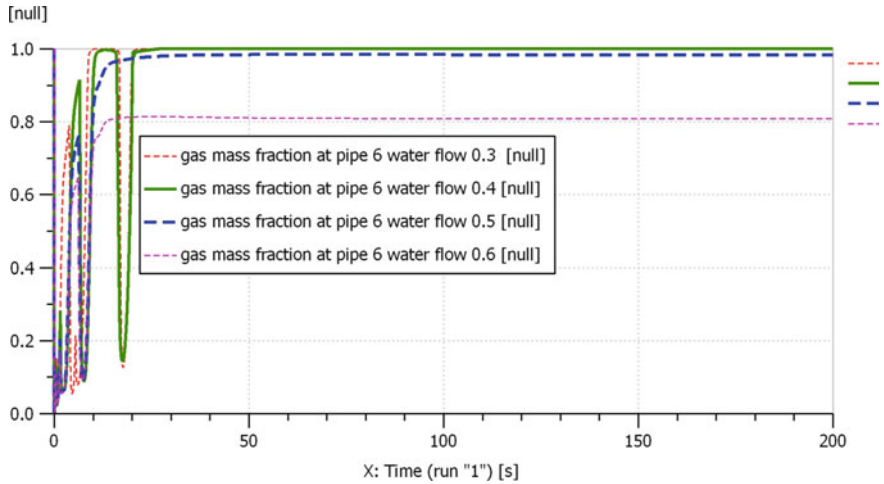


Fig. 7 Temperature at pipe no. 6 under various water flows



**Fig. 8** Gas mass fraction at pipe no. 6 under various water flows

very unstable and this division will accelerate convergence. Considering that all the pipes have the same length, the temperature for a total length of 3 m is 275 °C and 343 °C for 6 m (Fig. 9).

The steam parameters in front of the turbine will generate mechanical power in-between a various range. In Fig. 10 the variation of the obtained turbine mechanical power is plotted as a function of the pipe length, with its increasing correspondence. This power increase is not linear with the pipe length, the maximum increasing rate being obtained between 0.5 and 1 m.

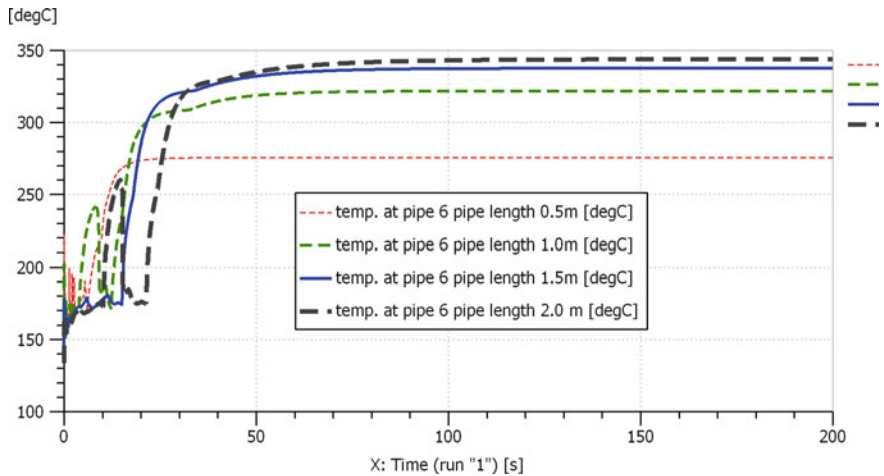


**Fig. 9** Steam temperature at pipe no. 6 with various length values

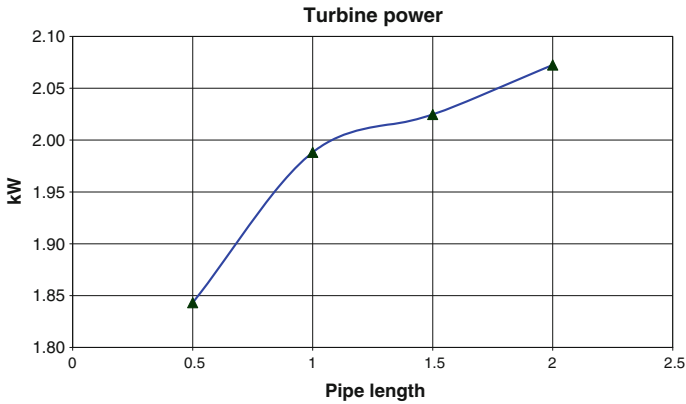


Fig. 10 Turbine power as function of pipe length

The turbine volume is also an important parameter in the system design. Pressure at pipe no. 6 is represented in Fig. 11 versus the turbine volume, at constant water flow. As may be expected, the pressure will decrease with the increase of the turbine volume.

For these specific operation conditions, the mechanical power generated by the turbine reaches its maximum at the minimum turbine volume (200 cm<sup>3</sup>), 1.78 kW, and 1.48 kW for 500 cm<sup>3</sup> turbine volume. These results show that larger steam pressure and temperature values upstream the turbine will generate supplementary power.

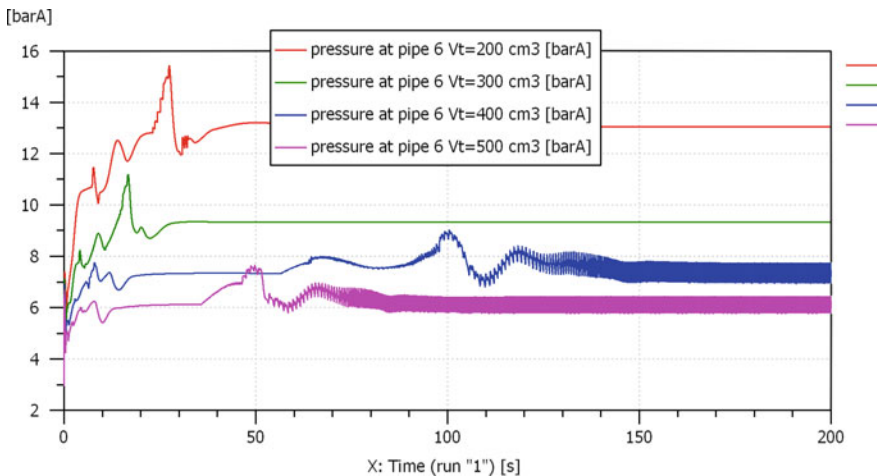


Fig. 11 Pressure at pipe no. 6 versus turbine volume

## Conclusions

The Rankine cycle shows itself to become a promising technique to recover waste heat from internal combustion engines. The heat recovered may be used to generate supplementary mechanical power that could be stored in electrical batteries or used to operate other elements from the truck. By recovering the heat from exhaust gases, the Rankine cycle will influence the engine fuel consumption due to pressure losses in exhaust line that must be determined.

There are many fluids that are taken into account to be used as working fluid. Water is the most common and has no influence on environment.

The thermodynamic 0-D simulation remains a first tool to evaluate the maximum potential for this kind of systems. In practice and based on the assumptions, various conclusions could be taken from those simulations. In this paper a complex model was developed. Obtaining the results for this model simulation require a long computation time because the equations are unstable.

The model was simplified and reduced to the vaporization system and turbine. For these elements a parametric study was implemented to show the influence of some dimensions on the agent pressures and temperatures inside the pipes. These variations also modify the power generated in the turbine and the quantity of the recovered energy.

At a 100 kW diesel engine mechanical output the resulting power recovered is around 2 kW, confirming as percentage value other results (Seher et al. 2012).

## References

- Aneja R et al (2011) Exhaust heat driven rankine cycle for a heavy duty diesel engine. In: DEER 2011
- Duparchy A et al (2009) Heat recovery for next generation of hybrid vehicles: simulation and design of a rankine cycle system. 3. World electric vehicle
- Nelson CR (2006) Exhaust energy recovery. In: DEER conference
- Noor AM et al (2014) Waste heat recovery technologies in turbocharged automotive engine. Rev J Mod Sci Technol 2(1)
- Obieglo A et al (2011) Future efficient dynamics with heat recovery. In: DEER 2011
- Saidur R et al (2012) Technologies to recover exhaust heat from internal combustion engines. Renew Sustain Energy Rev 16:5649–5659
- Seher D et al (2012) Waste heat recovery for commercial vehicles with a rankine process. In: 21 Aachen colloquium automobile and engine technology 2012
- Wang EH et al (2011) Study of working fluid selection of organic rankine cycle (ORC) for engine waste heat recovery. Energy 36:3406–3418
- Ziviani D et al (2012) Development and validation of an advanced simulation model for ORC based system ASME 2012 international mechanical engineering congress and exposition. Houston, Texas, USA



# Traffic Modeling Aspects Using Visum Software and Effects on the Traffic Optimization

Horea George Crişan and Nicolae Filip

**Abstract** The main objectives of this paper consist in presentation of a concrete situations regarding to the traffic modeling in PTV Visum virtual environment. The methodology used consists in developing applications considering the urban mobility plans currently in progress, in the municipalities of Romania. Starting from the current state, it has been developed proposals for traffic optimization which were analyzed in PTV Visum software. The results are based on the restructuring of some road infrastructure elements, with effects on the fluidity of vehicle traffic and hence to reduce the negative effects related to this issue. The work ends with a series of observations on the modeling requirements imposed by the development of urban mobility plans, highlighting the usefulness of carrying out specific applications, in the PTV Visum virtual modeling environment.

**Keywords** Traffic modeling · Visum software · Urban mobility plan

## Introduction

Traffic optimization process is an essential component of the urban mobility phenomenon. Urban mobility represents an attribute of the persons and products movement, into an urban area (O’Flaherty 1997). In this way, the primary role of transport activities is to meet existing mobility demands. In order to meet the conditions for mobility, the urban development must aim at ensuring the highest accessibility and efficiency of private and public transport systems.

The interest aspects of urban mobility are varied. These are related, on the one hand of the transport system, in terms of infrastructure, modes of transport, travel behavior, travel time, etc., and on the other hand, the human activities of various types, locations, accessibility and so on (Boitor 2014). With the continuous

---

H.G. Crişan (✉) · N. Filip

Mechanical Faculty, Automotive Engineering and Transportation Department, Technical University of Cluj—Napoca, B-Dul. Muncii, Nr. 103-105, 400641 Cluj-Napoca, România  
e-mail: crisanhoreageorge@yahoo.com

development of urban environments, urban mobility concept became part of the complex process of urban management, that concern improving the quality of the population life. Urban mobility represents a primary axis of the local administration, in the prioritization order of sustainable urban development.

The structural framework of urban mobility organization strategies, concerns through an urban mobility plan. It is based on current practices of planning, taking into account the principles of integration, participation and assessment. The objective of the urban mobility plan is aimed at the development of an urban transport system, through the fulfillment of conditions, like ([www.eltis.org](http://www.eltis.org)):

- ensuring to the populace of a transport system that allows the access to most important destinations and services;
- increasing the transport safety and security;
- reducing the energy consumption, chemical and sound pollution;
- optimization of persons and products transport systems;
- raising attractiveness and quality of the urban environment, through urban design, for supporting the local community, economy and society in general.

Therefore, fulfilling these minimum conditions, involves the development of a plan for urban mobility, focused to the sustainability aspect. For its implementation, it starts from the analysis of the baseline condition, It establishes the vision, objectives and targets, it choose the necessary policies and measures, monitoring and ongoing assessment of compliance with them in the development and implementation of the sustainable urban mobility plan. The status analysis of transportation system, the behavior of humans, the impact on the environment and the urban traffic, is made by carrying out a traffic study ([www.eltis.org](http://www.eltis.org)). Through this traffic study, are identified major challenges and threats on the transport system and are obtained answers to questions arising from movement in the urban traffic conditions (Pline and James 1999; Timar 2010).

The starting point in the development of a traffic study is the analysis of geographical and demographic situation of the area of study and descriptive analysis of existing urban transport modes (road network, private transport, local public transport, rail, etc.).

The results of these analyses, complemented with the measured traffic values, restore the possibility of analysis the transport demand, at that time, trough realization of the transportation patterns. Achieving the transportation models, involves modeling the traffic deployment, transportation process and the transport demand. Organization of urban movement must take into account the necessity of meeting the current needs, but also by the prospect.

Priorities in the urban circulation organization process, are the people transport (its complications have negative repercussions on the activities of production and services, so the economy as a whole), and the transport of products (with repercussions on the production and supply of services and especially on consumer products necessary for population).

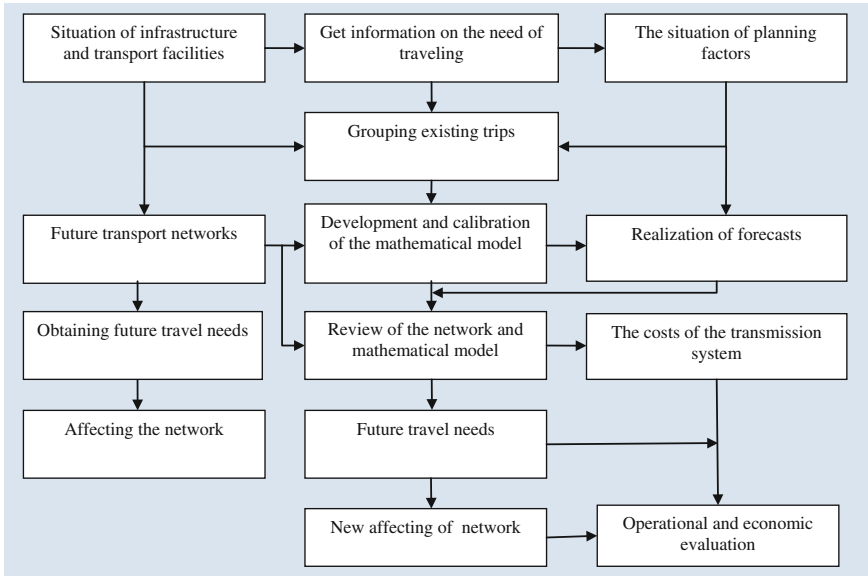


**Fig. 1** The stages of a traffic study

After estimating the demand for transport, it's goes to the elaboration of traffic evolution forecasts and traffic demand, during specified periods of time, resulting the need for optimizing the infrastructure and transport systems (Filip 2010).

A structural sketch of the developing stages of a traffic study, is presented in Fig. 1 (Mitran 2013).

It can be concluded that in the context of present urban mobility plans, carried out as a result of the phenomena of urbanization and continuous development of socio-economic activities, directing attention towards the analysis of continuing growth of the people and products transport needs, is a mandatory condition. Thus, it is found that the share of traffic studies, carried out for the purpose of optimizing the processes of urban transport in the context of urban mobility plans, is significant one.

Facilitating the development of current and perspective transport models, into the traffic studies, requires using of some software applications that offers advantages such as speed of operation, facility of modeling, accuracy and limited errors, achieving graphical layouts based on mathematical models, etc. One of the most widely used computerized applications in studies of application traffic is PTV Visum (Cliath et al., <http://vision-traffic.ptvgroup.com>).

## Achieving the Transport Models Using PTV Visum Application

PTV Visum is an application that allows the virtual modeling of transport processes taking place in the real environment, using mathematical tools such as systems of equations, stochastic processes and calculation algorithms, algebraic and geometric elements. The modeling based on the mathematical structures, allows optimum understanding of phenomena and processes in the transport sector and also allows the development of forecasts related to its future functioning, generating optimization opportunities through (PTV AG 2014; Mitran 2013):

- forecasting of traffic flow;
- estimation of the traffic flows in the absence of some data;
- establishment of transport policies at the micro or macro level;
- correlation of the behavioral link of user and transport system;
- planning routes for transport corridors;
- regulating the modes of using the area;
- the influence of new infrastructure designed elements;
- development of scenarios regarding the traffic organization, the configuration of the transport area, etc.

Development of a model, using PTV Visum software, is made starting from the reality modeled specific data (road infrastructure, traffic rules, measured traffic values, etc.), by formulating associated mathematical relationship, it's producing results that containing data predicted by modeling, following to be subject for validation tests, in relation to the reality corresponding parameters.

A transport model made by using PTV Visum software, is represented in Fig. 2 (Mitran 2013).

The formalization models of the transport offer include the following elements:

- existing transport systems;
- the nodes and arcs of the transport system;
- zoning the territory;
- the public transport lines, routes operated and the circulation programs;

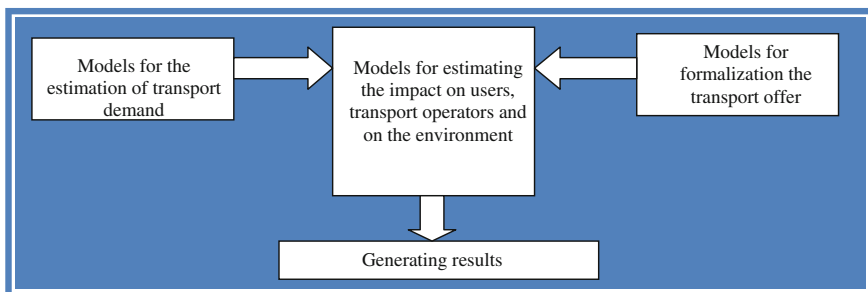
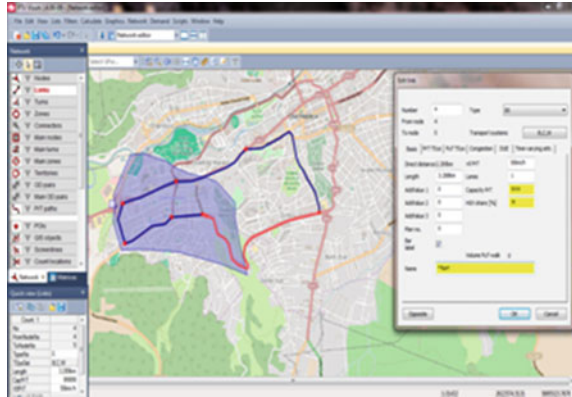


**Fig. 2** The structure of a transport model, conducted in PTV Visum

**Fig. 3** Visum interface and network formalization



In Fig. 3 it presents the interface of the program, representing PTV Visum formalizing transport systems modes (types of transport and vehicles categories) and network elements within the transport offer (nodes, streets, zones), by graphics layout and filling the appropriate values of the designed elements (<http://vision-traffic.ptvgroup.com>).

Models for the estimation of the transportation demand, include:

- origin and destination of passengers;
- the number of travelers recorded on each demand segment;
- temporal distribution of the demand for transport;

For the estimation of transportation demand, PTV Visum application uses the “four steps” method (Mitran 2013). The first step of this method consist of the movements generation, which is used to estimate the number of trips produced and attracted to each area of the territory, over a period of time. The most used mathematical models to generate movements are category index method, (based on the estimation that the generation travel rates are relatively stable over time for the categories of households considered) and the linear regression mathematical method.

The second step consists in the destination travel distribution, generated by each area of traffic, determining the number of shifts between the two traffic zones, bringing the matrix origin-destination (O-D). The most used mathematical models applied, are the rearing factors method (it’s about the determination of future flows of movements between O-D zones) and gravitational model (it is estimated travels for each pair O-D, without using the measured data).

The third step consists in the modal distribution, through the decomposition of the total demand in O-D matrix, for each segment of transport demand, in relation to the usefulness of each transport mode. The mathematical models used are based on probability distribution. The most commonly used models are the Probit (Gauss-Laplace distribution) and Logit.

The final step for estimating the transportation demand, from the four steps model, is the travels affecting. It is to establish a balance between supply and

demand. The mathematical model is based on the Wardrop balance, that knowledge entails a minimum set of input data (transport capacity, traffic speeds, infrastructure, costs, etc.), results minimizing of user transportation costs and a balanced distribution of traffic flows.

An example of a matrix that represents the zone pair distribution by origin-destination is shown in Fig. 4.

Models for estimating the impact on users, transport operators and the environment include:

- travels impaired, calculating the transport service using indicators;
- number of vehicles, the costs and revenues of the carrier;
- chemical and phonic environmental pollution;

Figure 5 (PTV AG 2014) presents the sequence of initiate calculations procedures, input with regard to the transportation systems.

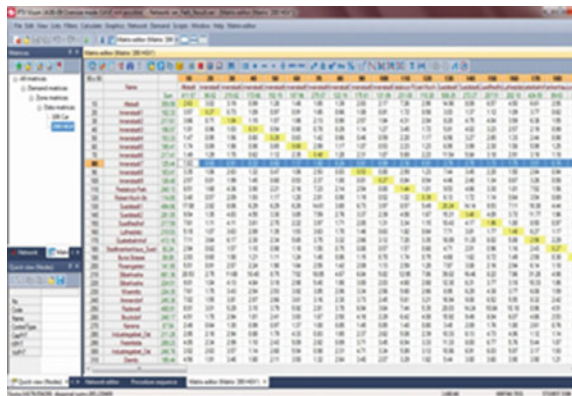
Generating results consists in obtaining:

- statistical data containing the attributes for the objects of the network and public transport routes;
- matrix indicators including travel times, frequency of vehicles circulation;
- graphical representation of traffic flows, isochronous, shortest path, traffic relationships diagram.

In Fig. 6 (<http://vision-traffic.ptvgroup.com>, PTV AG 2014) it presents examples of the results generated, consisting in a graphical layout of an urban public transport system and arrangement of travel time matrix, and in Fig. 7 (PTV AG 2014) it presents graphical examples of traffic flows and isochrones obtained.

Therefore, the PTV Visum software offers opportunities for optimization by determining the impacts of existing or those planned transportation systems, both with respect to the public transport system (under a taxi, mini bus or buses) and private transport system (pedestrians, bikes, cars, heavy vehicles), on urban mobility and quality of the life.

Fig. 4 An O-D matrix representation



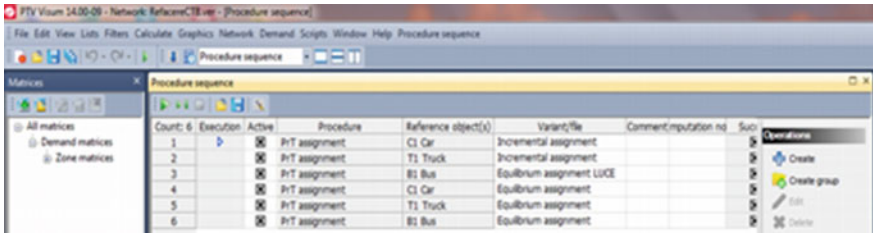


Fig. 5 Sequence of initiate calculations procedures

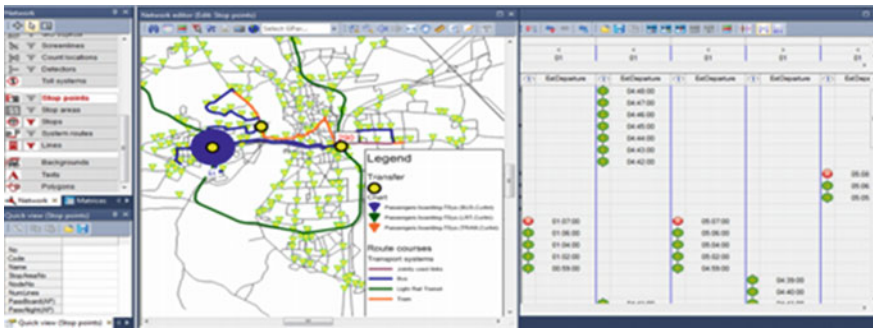


Fig. 6 Examples of mode and travel times results, in the case of a public transportation system



Fig. 7 Examples of results consisting in traffic flows and isochrones

## Optimization of Transport Models Through Case Studies Using PTV Visum

As part of a traffic study, developed over a city from Romania, it was used PTV Visum application for making case studies concerning to the opportunities for optimizing the infrastructure and road traffic deployment. Transportation models

**Fig. 8** The present stage—transportation network loading degree



made using vehicle categories such as cars, trucks and buses. In the first phase it was achieved the current transport model (at the level of the 2015 year), using the measured traffic values and values existing by the road infrastructure construction.

In Fig. 8 is presented the analysis of the degree of transport networks loading, resulting from the ratio of the current network capacity (in red) and the total daily volume of vehicles registered (in blue). Figure 9 presents the analysis of the traffic flow for the three categories analyzed: cars (in red), trucks (in yellow) and buses (in green). It turns out a load with an increase heavy traffic volume, both to the crossing main street but especially to the North city beltway (including the three access roads), and the eastern outward portion of the municipality. It distinguished a low load with heavy traffic in the South-Eastern area of the network.

With the aim of identifying opportunities to streamline the flow of vehicles from the affected areas, and achieving a balanced and uniform distribution of it, in relation to the transport requirements, with the aim of increasing the effectiveness of urban mobility and reducing the level of air pollution, it were made a number of changes to items from the transport network. Subsequently, it has been carried out simulations concerning the redistribution of road traffic, using known traffic values.

The first variant involves building an extension of the Northern belt currently existing in the northeastern area, linking the current belt with the Eastern terminus

**Fig. 9** The present stage—the vehicle flows of cars, trucks, buses

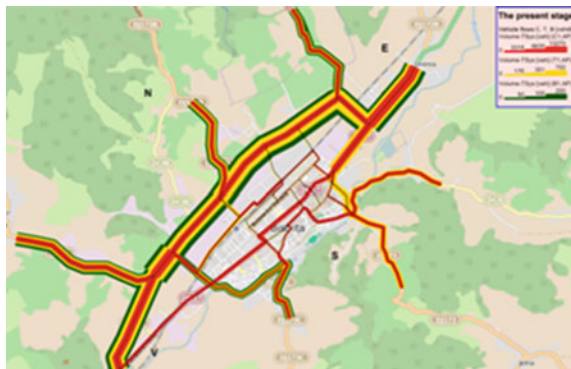




**Fig. 10** The proposed variant II—vehicle flows of cars, trucks and buses



point from outward the city. The flow of vehicles is symbolizing through the red color represent cars, purple the trucks, and yellow the buses. It is found that approximately 78 % of the vehicular traffic of the existing belt will choose this new variant, decongesting traffic from the Eastern exit of the municipality. This variant is shown in Fig. 10.

A second variant, relative to the current state, involves the construction of a new ring belt on the southern side, connected to the city main street by the three new street arms, positioned between the three existing street arms.

The model obtained is shown in Fig. 11. It is found that about 35 % of the traffic from the existing belt will be taken over by the newly-built belt, and about 10 % of the total main street transit traffic, total from which about 18 % is represented through heavy traffic.

The third variant is a combination of the two above variants. It involves a reduction of about 78 % of the 75 % traffic volume by the existing belt. This combined variant is, at the same time, the most costly.

Further, it has conducted an analysis applying the calculation algorithm specific to the chart of traffic relationships “Flow Bundle” (made with the goal of filtering the total flow of vehicles and displaying pairs of origin-destination relationships,

**Fig. 11** The proposed variant I—vehicle flows of cars, trucks and buses



**Fig. 12** Graphical representation of the “Flow Bundle” diagram

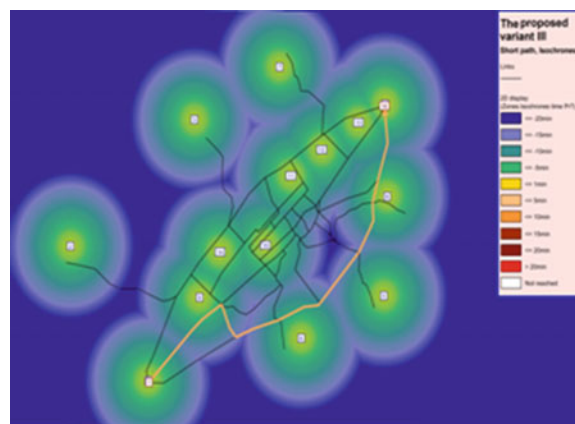


specific to a selected object from the road transportation generated networks), shown in Fig. 12.

So, it is found in this way, that, primordial is necessary to build a new southern ring belt, this one representing a total vehicle flows distribution concentrator. It has been carried out an analysis for the determination the critical road (short path), shown in Fig. 13 (orange color), in relation to the traffic impedance criterion, displayed by the transport times isochrones.

Therefore, it is noticed that the variant of construction the new southern ring road, achieve the aim pursued, consisting of road traffic fluidization on the affected areas, increasing urban mobility, and simultaneously, reducing the degree of air pollution.

**Fig. 13** Short path analysis



## Conclusions

Traffic studies represents a fundamental component by the development of urban mobility plans. Goals pursued consists of optimising transportation processes by streamlining road traffic flows, efficiencies the modes of transport by balancing and offloading traffic flows and reduce the costs of transport and hence reduce the pollution resulted.

To fostering the analyses performed and for obtaining accurate results regarding to the opportunities for improvement the public and private transport processes, it use software applications, based on precise mathematical algorithms.

PTV Visum is one of the most used applications in carrying out traffic studies, providing the possibility of analysis the current status of urban mobility developing, as well as elaborating future scenarios. The results obtained consist in the development of optimal transport models, with the possibility of graphical or tabular analysing and interpreting.

Transportation models resulted, contain data regarding to the travel time matrix indicators and public transport vehicles consecution frequency, with the purpose of optimization the vehicles course, as well as the layout the vehicle flows, time isochrones, shortest road path, traffic relationships diagram, to optimize private transport vehicles and road traffic in general.

With the goal of development a few optimization models with regard to the road vehicles traffic, road infrastructure, with consequences above offloading traffic flows, to improve urban mobility and reduction of atmospheric pollution, it have been carried out case studies using PTV Visum application, included in the traffic study conducted over a city from Romania.

In the first phase, it has been achieved the current stage transportation model, followed by transport models in three new versions. It was analyzed the vehicles flows corresponding to categories of vehicles consists in cars, trucks and buses. Subsequently, it has been carried out the analysis concerning the distribution of the total vehicles flow, "Flow Bundle" and the route of the critical road (short path) shown by the times isochrones.

It has been found that it is necessary to build a new road ring belt, in the southern part of the municipality, which takes up about 35 % of the traffic volume from the existing belt, and about 10 % of the traffic volume from the main line street, from which about 18 % represents heavy vehicles traffic volume. This variant leads to achieving the goal of increasing the degree of urban mobility, through streamlining and balancing the vehicle flows.

## References

- Boitor MR (2014) Strategii alternative pentru îmbunătăţirea mobilităţii urbane în Municipiul Cluj-Napoca. Teză de Doctorat, Cluj-Napoca
- Cliath OA, Trionóide C, Transportation and highway engineering, traffic simulation modelling, The University of Dublin
- Filip N (2010) Ingineria Traficului Rutier, Ed. Mediamira, Cluj-Napoca
- Mitran G, Ilie S (2013) Aplicaţii în modelarea transporturilor—Visum 11.5-, Ed. Matrix Rom, Bucureşti
- O’Flaherty C (1997) Transport planning and traffic engineering. Ed. Elsevier
- PTV AG (2014) Vision traffic suite—tutorial, PTV Visum 14 Quick start, Karlsruhe
- Pline I, James L (1999) Traffic engineering handbook—fifth edition, institute of transportation engineers. Washington D.C, USA
- Timar J (2010) Studii şi cercetări privind optimizarea fluxurilor rutiere urbane. Teză de doctorat, Braşov
- [http://www.eltis.org/sites/eltis/files/BUMP\\_Guidelines\\_RO.pdf](http://www.eltis.org/sites/eltis/files/BUMP_Guidelines_RO.pdf)
- <http://vision-traffic.ptvgroup.com/en-us/products/ptv-visum/>

# Performance Evaluation of Complex Intersections by Micro-simulation

Sorin Ilie, Gabriela Mitran, Viorel Nicolae and Amalia Ana Dascăl

**Abstract** The increase of motorization index, the spatial redistribution of land use functions, the jobs crisis, the degradation of level of service provided by rail mode occurred in Romania in the last two decades have led to increased demand for road transport mode. In the large cities and their suburban areas the phenomenon of congestion occurs, as a consequence of the fact that weren't major interventions in order to increase the transport capacity. An essential stage in the transport planning process is the diagnosis of current situation, because based on its results is possible to propose solutions for improving traffic conditions. To analyze complex intersections or groups of junctions, the measured traffic volumes are insufficient and traffic micro-simulation is required. Micro-simulation takes into account the physical characteristics of the vehicle, the traffic rules and psychological behavior of the driver, achieving a stochastic and dynamic representation of each vehicle in the traffic flow. In this paper is made an analysis of performances offered by the road intersection located in the suburban area of Pitesti City, situated at the junction of three main networks (a highway, two national roads and the urban network), by applying the micro-simulation of traffic flows.

**Keywords** Road intersection · Micro-simulation · Traffic flows · Performance

---

S. Ilie (✉) · G. Mitran · V. Nicolae  
University of Pitesti, Targul din Vale Street, #1, Pitesti, Romania  
e-mail: sorin.ilie@upit.ro

G. Mitran  
e-mail: gabriela.mitran@upit.ro

V. Nicolae  
e-mail: viorel.nicolae@upit.ro

A.A. Dascăl  
Polytechnic University Timisoara, Revolutiei Street, #5, Hunedoara, Romania  
e-mail: amalia.dascal@fih.upt.ro

## Introduction

It is an accomplished fact that in Romania in the last 20 years the evolution which has manifested at the level of land use functions was poorly controlled. The challenge we are facing now is focused on planning in the fields of transport and urbanism so as to satisfy the mobility needs of users, both for the transport of persons, and for the transport of goods.

This reality (meaning uncontrolled development in urban and peri-urban areas) has associated the consequences of manifesting congestion phenomenon, which is reflected through significant negative impact on citizens' quality of life. The main components with negative impact are related to (1) increasing the time spent in travel on relatively short distances, and (2) generating health problems or worsening the existing ones, especially in the case of respiratory and cardiac diseases, due to higher concentrations of pollutants in the atmosphere. Moreover, the environment in which manifests the phenomenon of congestion is characterized by high concentrations of CO<sub>2</sub>, which entails the contribution to enhancing greenhouse effect. Concomitantly with the above mentioned aspects, at the economic level, the deployment of traffic in congestion circumstances lead to increased fuel consumption, fuel that still comes predominantly from non-renewable sources.

Diagnosing the current situation represents an important stage in transport planning process, depending on its results being possible to propose solutions to improve traffic conditions. In this process, the first step consists in collecting real data to identify critical issues at the level of an area of study. In cases in which isolated areas or intersections must be analyzed, traffic volumes measured are sufficient; but for complex intersections or groups of intersections, traffic simulation is required. This method provides visual feedback based on the data collected, facilitating the identification of critical issues and testing the proposals for infrastructure redevelopment.

In the frame of this paperwork the authors present the analysis of performances provided by the road interchange from the suburban area of Pitesti municipality, placed at the junction between the A1 highway, the national roads network and the urban network, by means of traffic flows micro-simulation. For performing the micro-simulation it was used a software that owns comprehensive analysis options, a powerful tool for evaluating and planning the transport infrastructure in urban and extra-urban environment.

## Background

Micro-simulation of traffic flows is based on dynamic and stochastic (random) modeling of the movement of vehicles individually in the frame of a transport system. Each vehicle changes its position in the transport network in every split second depending on (1) its physical characteristics (length, velocity, maximum

acceleration, etc.), (2) the fundamental laws of mechanics and (3) driver's norms of behavior, bearing in mind the road traffic regulation. The microscopic models for simulation the traffic flows require much more data and analysis resources than macroscopic models, but they reproduce with much higher accuracy and fidelity the real traffic conditions, in comparison with macro-simulation case. Sources from specialized literature indicate the advantages and the drawbacks characteristic of this level of traffic flow simulation (Barcelo 2010). The benefits offered by micro-simulation of traffic flows, in the process of traffic analyzing, can be oriented on three main directions: *clarity*, *precision* and *flexibility* (Luk and Tay 2006).

- *Clarity*. The real-time running of traffic flows and graphical interface illustrate the operations performed in traffic in an understandable manner. By visualizing the micro-simulations in 3D format, is facilitated the verification process of sensitivity of modeling the transport network, and the driver's behavior in the frame of the model for micro-simulation the traffic flows.
- *Precision*. In the case of congested networks, by modeling the vehicle at individual level, there is the possibility to simulate with high accuracy the movements performed in intersections. The driver of each vehicle makes decisions individually, regarding speed, traffic lane change and choice of routes, which implies a good representation of the real conditions in comparison with other modeling techniques. For example, the models for simulation at macroscopic and mesoscopic levels use fixed values of saturation flows, under the assumption that all vehicles behave in the same way. Within the micro-simulation models, *the saturation flow* represents an output parameter.
- *Flexibility*. This type of modeling allows the solving of a wide range of problems compared with conventional methods (vehicle—signals activations, demand—dependent on pedestrian amenities, management of waiting queues in intersections, prioritization of public transport, accidents, toll gates, roads works, roundabouts, shock waves etc.). It also allows the representation of the interaction between different vehicle types, as well as their interaction with other transport modes (bus, tram, light rail etc.).

The disadvantages arising from the use of micro-simulation models in the analysis of traffic flows can be grouped into the following categories: *high costs*, *large volumes of input data*, *manifesting characteristic phenomena of traffic lane change* and *extraction of results*.

The fundamentals of traffic micro-simulation were established by authors as Chandler et al. in 1958, Gazis et al. in 1961 (Wilson 2001), Lee in 1966, Bender and Fenton in 1972 (Gipps 1981) within some reference works in the field, in which were developed the analogies of traffic flow with fluid dynamics and circulation of gases through pipelines. Lighthill and Whitman in 1955 and Richards in 1956 postulated that traffic density is a function of position; Newell in 1955 associated the motor vehicle movement along a sparsely used road with gases circulation (Wilson 2001). These models were subjected to improvements in the 1970s (Gipps in 1970

and Wideman in 1974). At present there are tens of software systems for micro-simulation of traffic flows that implement a large variety of theories and behavioral norms of drivers (Algers et al. 2000; Treiber and Kesting 2013).

## Case Study

Within the case study is presented the micro-simulation of traffic at the level of the complex road node where takes place the traffic change between A1 highway (Bucharest—Pitesti), national roads network (represented by DN 7 Stefanesti / Bucharest—Ramnicu Valcea and DN 73 Pitesti—Campulung) and urban network of Pitesti municipality represented by the connection road (bridge over the Arges River) (Fig. 1).

Pitesti municipality is a medium-sized city in Romania, with a population of 177,965 inhabitants in 2014,<sup>1</sup> and which holds the administrative role of the Arges County.<sup>2</sup> The urban transport network is located to the south of the Arges River, which represent a natural barrier on the direction North West—South East. Within the road transport system in the region there is only one crossing over the river through which is realized the connection between the street network and national network. From functional perspective, Pitesti municipality is in close interaction with its peri-urban localities situated to the north of the Arges River:

- localities serviced by DN 7 national road: cities Stefanesti (14,901 inhabitants) and Topoloveni (9602 inhabitants), village Calinesti (11,173 inhabitants),
- localities serviced by DN 73 national road: city Mioveni (34,799 inhabitants), village Maracineni (5186 inhabitants).

The micro-simulation of traffic flows requires knowing the transport supply at an advanced level of particularization (meaning characteristics of infrastructure, as well as characteristics of traffic operating and controlling system), and the transport demand (meaning vehicle characteristics, traffic volumes and selected routes). The relationships between the components of the applied traffic micro-simulation model are shown in Fig. 2.

In order to model the transport supply represented by physical configuration of the network and the traffic control system operating at the level of analyzed road junction, were used information from technical project plan developed for building the A1 highway Bucharest—Pitesti (Fig. 3). As can be seen, this junction road hasn't a configuration which can be framed in the typologies used preponderantly as typical examples of service interchanges: *diamond*, *cloverleaf* and *partly cloverleaf* (CDT 2003). Regarding the traffic control at the level of the road interchange, the access of vehicles is conducted through road signs. Another

<sup>1</sup>National Institute of Statistics, Population and its demographic structure.

<sup>2</sup>Romania's territorial administrative division provides 41 counties.



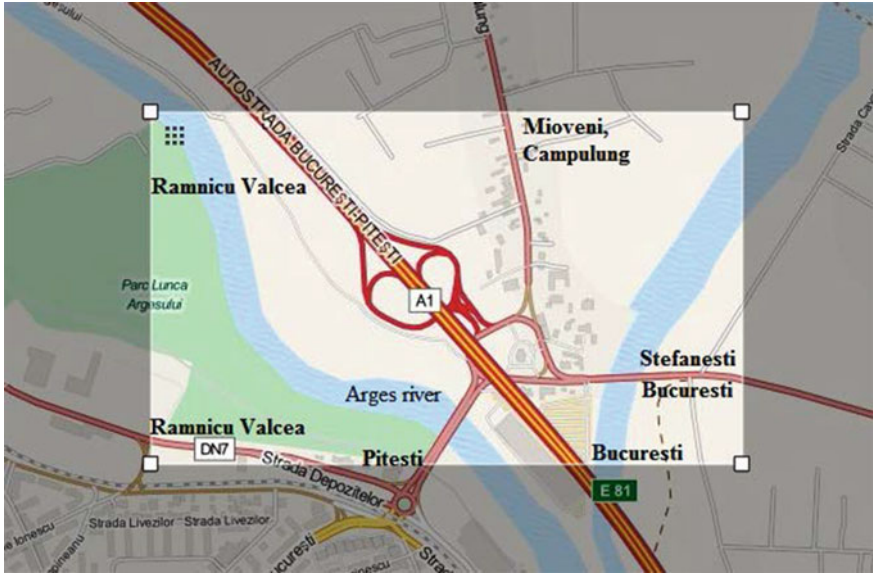
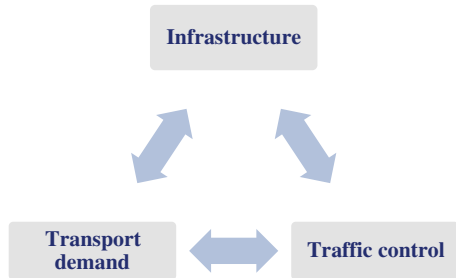


Fig. 1 The study area (Source <https://www.openstreetmap.org>)

Fig. 2 The structure of the traffic micro-simulation model



particularity of the road junction is given by placing a fuelling station inside the ring area, fitted with two entrances and also with parking spaces for heavy duty vehicles.

The transport demand, expressed through Origin—Destination matrices and associated routes, was extracted from macroscopic transport model of Pitesti municipality and its area of influence, developed by authors during other studies (Mitran 2012; Mitran and Ilie 2014).

The calibration and validation of transport model was realized for peak traffic period, determined by measurements made in the key points of the network, in the hourly intervals 7–10 AM and 15–19 AM.

To exemplify, below is presented the variation of traffic flows on the bridge over the Arges River, the road segment linking the studied interchange and the urban street network of Pitesti (Fig. 4).

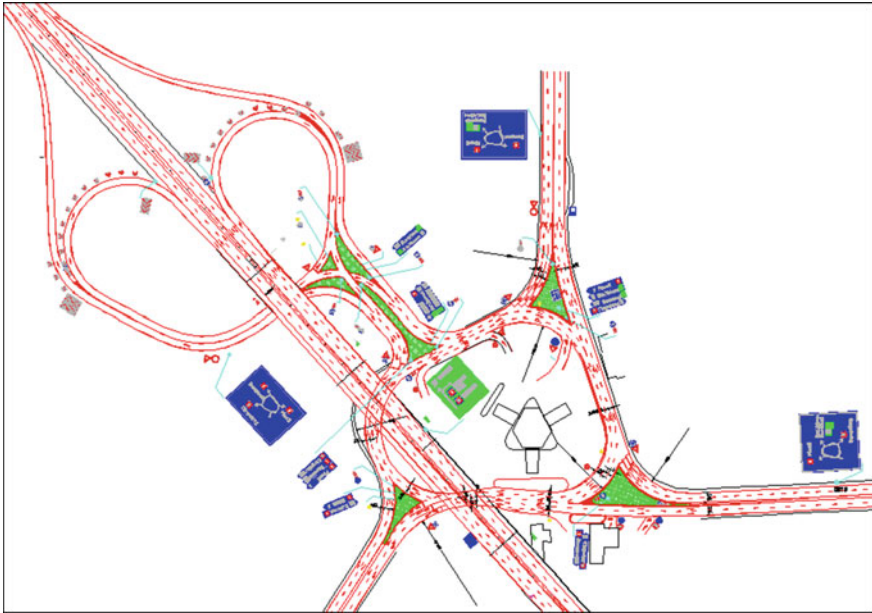


Fig. 3 Representation of the transport supply

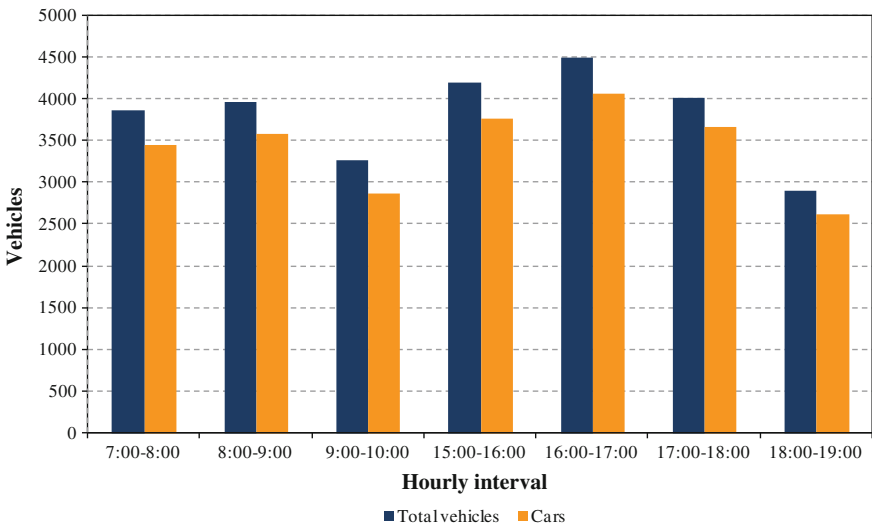


Fig. 4 Hourly traffic flow distribution

The structure of traffic flows in terms of technical characteristics of vehicles represents essential inputs in the simulation process. It is compulsory to define the following characteristics of motor vehicles:

- length;
- acceleration and deceleration rates;
- maximum speed.

In the framework of the performed micro-simulation, the above mentioned technical characteristics were defined for passenger cars and freight motor vehicles.

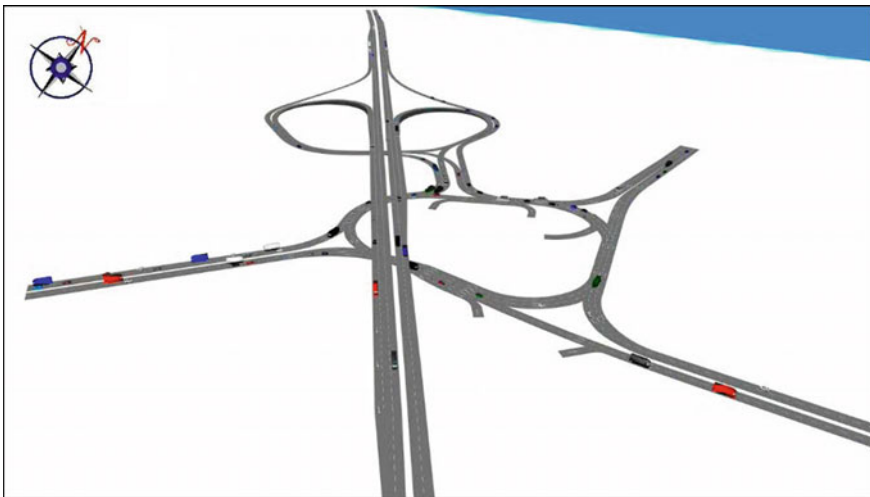
## Results and Discussion

The performance of the complex road interchange was analyzed through simulation at the level of traffic rush hour 16–17 AM, as was highlighted in Fig. 5.

Following the analysis, were determined the values of the following parameters:

- average delay time per vehicle, in seconds;
- average speed, in km/h;
- average number of stops per vehicle;
- number of vehicles that have left the network.

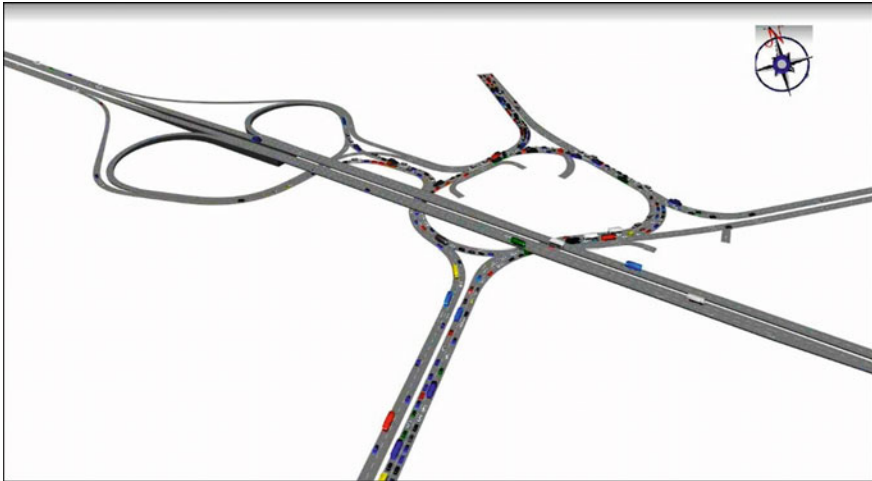
The results of simulations that have been run for 3900 s, including the recommended temporal warm-up period of 300 s [value recommended in specialized literature to obtain results with high accuracy (Manraj et al. 2012)], are shown in Table 1.



**Fig. 5** 3D representation of the realized micro-simulation model

**Table 1** Simulation results

Parameter	Value
Average delay time per vehicle [s]	194.9
Average speed [km/h]	17.5
Average number of stops per vehicle	2.8
Number of vehicles that have left the network	4189

**Fig. 6** Micro-simulation results in the traffic rush hour of a working day

The values of those parameters indicate very low performances recorded at the level of road junction analyzed, which is manifested by congestion at traffic rush hour. The effects of congestion are the waiting queues occurred for crossing this infrastructure sector, each vehicle performing an average of 2.8 stops, the average moving speed being extremely low, only 17.5 km/h, in conditions of a regulated top speed of 50 km/h on that road sector.

An overview on the deployment of circulation extracted from the video recording of the simulation is shown in Fig. 6.

## Conclusions

In this work are highlighted the performances of the transport infrastructure from the peri-urban area of Pitesti municipality, respectively the road interchange which links the network of national roads and highways with local street network, during the traffic rush hour recorded at the level of an average working day of the year (*Annual Average Daily Traffic—AADT*). The analysis of the current situation indicates averages delays of approximately 195 s for a vehicle, which translates into

additional costs incurred by the users of the transport system, resulting from monetary quantification of the values of time required to perform the travel.

Another category of negative effects of the traffic carried in the current circumstances is represented by the emissions of pollutants and CO<sub>2</sub>, associated with the acceleration and deceleration regimes of motor vehicles, imposed by 2.8 average stops which each vehicle performs while crossing through the road junction.

This characterization of traffic deployment in the analyzed area requires identification and implementation of rapid measures in order to improve the circulation conditions. The results obtained following this research will constitute the baseline scenario within future simulations, aiming to identify the best solutions for road traffic fluidization in the analyzed road interchange.

## References

- Algers S, Bernauer E, Boero M et al (2000) Review of micro-simulation models—deliverable D3. SMARTTEST (Simulation Modelling Applied to Road Transport European Scheme Test) project, Institute for Transport Studies, Leeds
- Barcelo J (2010) Fundamentals of traffic simulation. Springer, Berlin
- Connecticut Department of Transportation (CDT) (2003) Highway design manual. Connecticut
- Gipps P (1981) A behavioural car-following model for computer simulation. *Transp Res Part B: Methodol* 15(2)
- Luk J, Tay J (2006) The use and application of microsimulation traffic models. In: Austroads research report. Report AP-R286, Sydney
- Manraj S, Balaji P, Shriniwas A (2012) Modeling of traffic flow on indian expressways using simulation technique. *Procedia—Soc Behav Sci* 43:475–493
- Mitran G (2012) Modelling air pollution generated by traffic flows in urban areas. PhD Thesis, Pitesti
- Mitran G, Ilie S (2014) Transport planning—a component of emergency plan, case study: pitesti metropolitan area. *J Traffic Logistics Eng* 2(1):40–44
- Treiber M, Kesting A (2013) Traffic flow dynamics, data, models and simulation. Springer, Berlin
- Wilson E (2001) An analysis of Gipps' car-following model of highway traffic. *J Appl Math* 66(5):509–537

# Drag Phenomena Within a Torque Converter Driven Automotive Transmission—Laminar Flow Approach

Marin Marinescu, Octavian Alexa, Radu Vilau,  
Constantin-Ovidiu Ilie and Valentin Vinturis

**Abstract** When discussing a torque converter driven, automotive transmission with respect to the vehicle's coasting mode, automotive engineers have to take into account the slip between the converter's propeller and turbine. If the turbine isn't locked to the propeller during coasting process, drag phenomena within the converter's fluid occur and they have to be properly assessed when computing the coasting process dynamics. The best way to make the needed evaluation is to have a separate torque converter and test it on a test bench, if the data provided by the manufacturer, in this respect, weren't available. In the attempt to assess its' coasting dynamic performances, we faced the problem of the reverse rotation of the torque converter that strongly influences the general drag of the vehicle's motion. Hence, this paper tries to provide a method to determine the transmission overall drag considering the torque converter as being its main contributor. The method is based on the experimental research. This method can be successfully used for all type of hydrodynamic components of the transmission under the condition of developing the necessary experimental research. As far as the test were concerned, they were the typical ones designed to determine the mass inertial moments of the transmission components using the "falling weight" principle.

---

M. Marinescu (✉) · O. Alexa · R. Vilau · C.-O. Ilie · V. Vinturis  
Faculty of Mechatronics and Integrated Systems for Armament, Department of Military  
Automotive and Transportation, Military Technical Academy, Bd. George Cosbuc  
nr. 39-49, sector 5, 050141 Bucharest, Romania  
e-mail: marin\_s\_marinescu@yahoo.com

O. Alexa  
e-mail: alexa.octavian@gmail.com

R. Vilau  
e-mail: radu.vilau@yahoo.com

C.-O. Ilie  
e-mail: ovidiuiilie66@yahoo.com

V. Vinturis  
e-mail: vinturisv@yahoo.com

**Keywords** Hydrodynamic transmission • Torque converter • Hydrodynamic friction

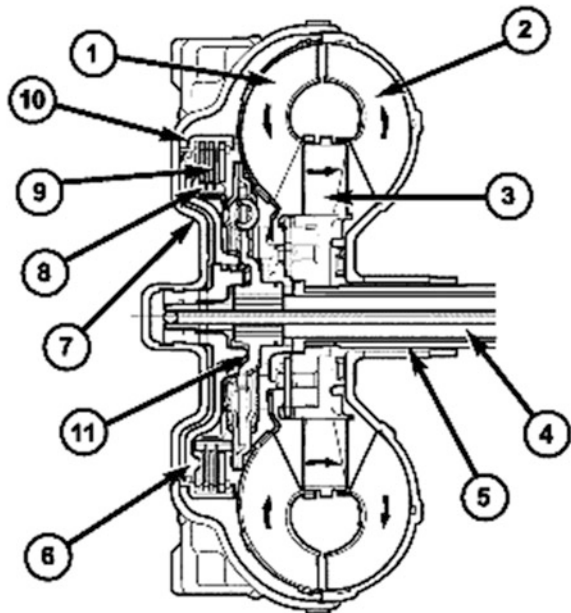
## Introduction

Special vehicles have always been studied from the dynamic point of view. But also, these vehicles require big amounts of money to have their experimental studies developed. Taking into account that a special vehicle is quite expensive (in most of the cases), future development of this kind of products would require even more money. Therefore, simulations would be a better second choice whenever comes about assessing a future product's dynamic features. The issue is quite the same whenever comes about up-to-dating an old product. This is the reason our institution is being involved in several tests with respect to some special vehicles, aiming at determining their dynamic features that could be further used in assessing future vehicles derived from the old ones.

This papers focuses on assessing the coasting parameters of a special tracked vehicle that contains, within its transmission, a hydro torque converter (Fig. 1).

Generally speaking, the dynamic features of the vehicle can be analytically obtained and frequently they overlap the experimental ones, since the theory is well

**Fig. 1** Lockable torque converter 1 turbine, 2 impeller, 3 stator, 4 input shaft, 5 stator shaft, 6 piston, 7 cover shell, 8 internally toothed disc carrier, 9 clutch plate set, 10 externally toothed disc carrier, 11 turbine damper



set in this respect (Alexa 2014; Truta 2014). All in all, the researchers are interested in the take-of stage of the vehicle rather than its braking one, due to the destination of the vehicles we are now discussing about (i.e. military vehicles). Nevertheless, some of the parameters of the taking-off equation are also used in the coasting equations. We don't hereby intend to promote a vehicle's motion equation, they are already well known (Truta 2014). But it should be mentioned that, within both these categories of equation, there is a term that estimates the inertia moments of the moving parts of the vehicle's driveline. When designing the vehicle and manufacturing its transmission's parts, these inertia moments can be easily acquired both from computation or measurements (Alexa 2014; Truta 2014). But assume the vehicle is already built up. It would cost a big deal of money to disassemble it and measure the inertia moments of the parts. Sometimes that is even impossible since the lack of special devices or due some regulations.

This is why we tried to figure out a way to compute the global moments of inertia of a vehicle's transmission. The method itself isn't new at all, as a matter of fact it is well known among the automotive engineers. The principle of the method is depicted in Fig. 2.

The vehicle is missing its tracks on both sides (unlike the one in the picture) so its sprockets, connected to the transmission, are both free. The sprocket on one side of the vehicle hosts a cable, which is coiled around its hub for about 6–7 m long (depending on the crane's height). At the end of the cable, falling down the crane's arm, a weight is hanging. The test itself is quite simple. The sprocket acts like a spool. At the beginning, the weight is uppermost. The driver presses the clutch and depresses the brakes and the weight starts to fall. Knowing the mass of the weight, the spooling radius and the length of the fall, while measuring the falling time, one can find the global moment of inertia of the rotating parts of the driveline. Since the global moment of inertia depends on the gear ratio, the test should be performed for the each vehicle's gear (Fig. 3).



**Fig. 2** Experimental rigging to evaluate a vehicle's transmission moments of inertia



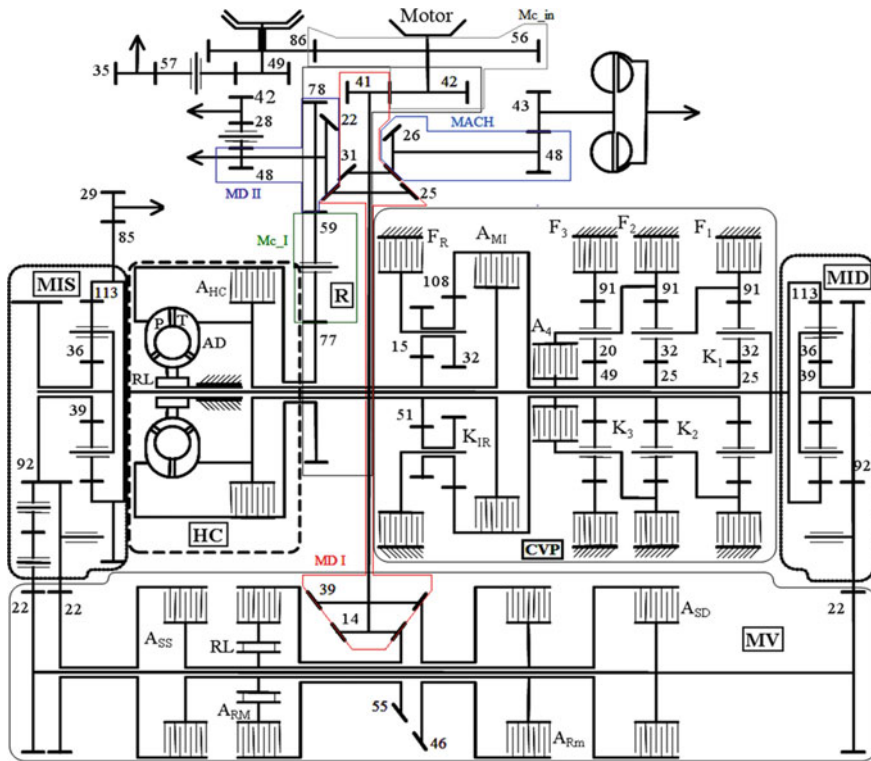


Fig. 3 Transmission’s layout (Alexa 2015)

### Particular Features of the Experiment. Paper’s Goal

As can be easily figured out, the experiment is mainly suitable for the vehicles that have mechanical clutches. When disconnecting the clutch from the engine, the transmission parts are completely free to start rotating (the brake was applied just to keep the parts still, till the operator starts the clock). No friction, except for the one from gearing, occurs. Moreover, this friction can be kept “under control” when evaluating the moments of inertia, since this is rather easy to assess it (its source is mainly the gearing process in oil and can be considered constant for a given temperature of the lubricant).

When a hydro torque converter is involved, beside the above mention sources of friction, another important source comes into being, i.e. the friction of the converter’s fluid. The impeller stands still (it is connected to the engine if the engine doesn’t run) while the turbine starts to rotate, together with the rest of the transmission parts. Moreover, the angular speed of the turbine is different from gear to gear since the total ratio differs from gear to gear. Eventually, for the same gear, the

turbine’s angular speed also varies according to the increasing speed of the accelerated weight on its way down.

In the next pages we’ll try to provide a method to determining the global moment of inertia of a transmission that involves a torque converter, taking into account the liquid friction that occurs between the converter’s turbine and impeller. We’ll start by issuing a mathematical model under some simplifying assumptions then we’ll go on by assessing the moments of inertia for the transmission’s gears, after properly processing the data (Marinescu 2014).

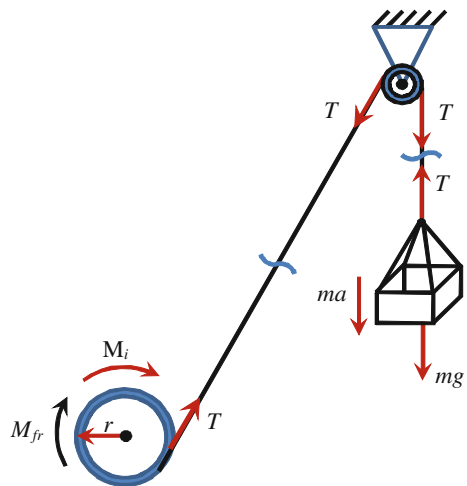
### Mathematical Model of the Phenomenon

Figure 4 depicts the diagram that helped us to issue the mathematical model. The first assumption of our mathematical model was that the whole transmission’s mathematical model is the same as of a ring that replaces the sprocket’s spool with the spooling radius,  $r$ . The liquid friction of the torque converter is assumed to act along the ring’s one side face, at the same radius,  $r$ . Moreover, the rest of the transmission’s friction is considered to be constant, no mater the angular speed or gear ratio and contained by the converter’s frictional torque. Hence, the only friction that varies is the one in the converter, referred as  $M_{fr}$ , that also contains the friction of the rest of the transmission’s components. The moment of inertia  $M_i$  brakes the motion while the load  $mg$  accelerates it (with  $m$  the weight mass).

For the left side of the pulley, the motion equation can be written as:

$$m \frac{dv}{dt} = mg - T \tag{1}$$

Fig. 4 Test’s loading diagram



while for the left side of the pulley, we can write down:

$$Tr = I \frac{d\omega}{dt} + c\omega \quad (2)$$

that assumes a laminar (linear dependency) flow within the converter. Adding the cinematic connection (in the stretched thread) between the two sides of the pulley:

$$\frac{dv}{dt} = r \frac{d\omega}{dt}; \quad v = r\omega \quad (3)$$

we could get system (4). There are some terms in system (4) that need further explanations. Thus,  $a = \frac{dv}{dt}$  is the linear acceleration acting over the right side of the pulley, when the weight of mass  $m$  falls under the gravitational acceleration  $g$ . On the both sides of the pulley,  $T$  is the cable (thread) tension.

$$\begin{cases} m \frac{dv}{dt} = mg - T \\ Tr = I \frac{d\omega}{dt} + c\omega \\ \frac{dv}{dt} = r \frac{d\omega}{dt} \\ v = r\omega \end{cases} \quad (4)$$

The moment of inertia can be written as  $M_i = I \frac{d\omega}{dt}$  where  $I$  is the global kinetic moment of inertia of the transmission and  $\omega$  is the angular speed of the flywheel that stands for the whole transmission. Since the flow inside the torque converter was supposed to be laminar, the frictional moment of resistance (drag moment) can be expressed as  $M_{fr} = c \omega$ , assuming a linear dependence of the drag moment to the angular speed of the equivalent flywheel. In this expression,  $c$  is a constant (actually, the drag coefficient). We also assumed that the drag moment acts as a drag force placed at the  $r$  radius of the flywheel (which, at its turn, was considered to be ring-like flywheel, with a single radius). Eventually,  $t$  is the time (independent) variable of the actual process.

Extracting  $T = mg - m \frac{dv}{dt}$  from the first equation of system (4) and replacing it in the second one we get  $(mg - m \frac{dv}{dt})r = I \frac{d\omega}{dt} + c\omega$ . Yet, taking into account the first cinematic connection in (3) [or the third equation of (4)], it leads to  $mgr - mr^2 \frac{d\omega}{dt} = I \frac{d\omega}{dt} + c\omega$ . Sending all the  $\omega$ -containing terms to the right side of this equation, we get:

$$mgr = (mr^2 + I) \frac{d\omega}{dt} + c\omega \quad (5)$$

This last equation can be further processed, to get some constant terms in front of the angular speed variable and its first derivative:  $\frac{d\omega}{dt} = \frac{mgr}{mr^2 + I} - \frac{c}{mr^2 + I} \omega$ . Having  $\frac{mgr}{mr^2 + I} = b$  and  $\frac{c}{mr^2 + I} = a$  it yields to  $\frac{d\omega}{dt} = b - a\omega$ , or, separating the variables, eventually delivers:

$$dt = \frac{d\omega}{b - a\omega} \tag{6}$$

### Integrating the Equation of Motion

The integration of Eq. (6) is rather simple. The method of integration involves the separation of the variables. Thus, Eq. (6) can be written as:

$$\int_0^t dt' = \int_0^\omega \frac{d\omega'}{b - a\omega'} \tag{7}$$

that yields, for a definite integral, to:

$$t \Big|_0^t = -\frac{1}{a} \ln \left| -\frac{a}{b} \omega + 1 \right| \Big|_0^\omega \tag{8}$$

Since for  $\omega = 0, \ln 1 = 0$  (limit conditions) then for real, positive numbers the solution can be written as  $t = -\frac{1}{a} \ln \left( 1 - \frac{a}{b} \omega \right)$ , or  $-at = \ln \left( 1 - \frac{a}{b} \omega \right)$ . From here, using the exponential function, it turns into  $e^{-at} = 1 - \frac{a}{b} \omega$  that finally provides the solution:

$$\omega = \frac{b}{a} (1 - e^{-at}) \tag{9}$$

Should be appropriate now to replace the previously defined constants,  $a$  and  $b$ , so we can finally get  $\frac{b}{a} = \frac{\frac{mgr}{mr^2+I}}{\frac{c}{mr^2+I}} = \frac{mgr}{c}$  and  $a = \frac{c}{mr^2+I}$ . Therefore, the final solution of the equation, expressing the angular speed evolution of the sprockets' angular speed when the weight is falling under the given circumstances (among we find laminar flow approach of the converters' frictional torque) will be given by:

$$\omega = \frac{mgr}{c} \left( 1 - e^{-\frac{c}{mr^2+I}t} \right) \tag{10}$$

Should be noticed that the equation above has, from the experimental data point of view, two unknown parameters, i.e. the global friction constant  $c$  (met in the moment of global friction expression as  $M_{fr} = c\omega$ ) and the kinetic moment of inertia  $I$ . One way to experimentally find constant  $c$  is to horizontally pull the cable of the sprocket at constant speed (Vilau et al. 2014). Since  $M_{fr} = c\omega$ , while measuring  $M_{fr}$  and knowing the angular speed, the constant will come up, as will be further seen. Eventually, we could compute the kinetic moment of inertia for every gear of the transmission.

## Experimental Data

We have performed several tests with the same falling weight for each gear of the gearbox, except for the 4th gear (a failing transducer prevented in getting reliable results for the last gear (Marinescu 2014); nevertheless, the remaining three sets of results were good and reliable). In the same time, another test has been also performed. It consisted in horizontally pulling the cable from the spool at constant speed while measuring needed force. This test has been performed for each gear and it aimed to experimentally determine the  $c$  constant of the friction moment expression  $M_{fr} = c\omega$ . Since we knew the spooling radius, the pulling speed and force, it was easy to determine the above-mentioned coefficient. The values of the constant  $c$  are given in Table 1, along with other data.

As an example of the achieved data when letting the weight to fall, Fig. 5 depicts the time histories of the measured angular speed for three different tests developed for the third gear of the transmission (due to resolution reasons, only three curves have been plotted). Figure 6 depicts the approximation curves of the experimental data plotted in Fig. 5 [after properly processing (Marinescu 2014)].

Using the *Curve Fitting* module of the Matlab programming environment [3] and considering the motion as developed according the motion law provided by Eq. (10), we tried to compute the most accurate global kinetic moment of inertia of the transmission,  $I$ , for each researched gear ration of the transmission. The *Curve Fitting* module [3] has the ability to provide a value of a researched parameter so the approximation curve would provide the best assessment of the experimental data. Hence, given Eq. (10) and its known, contained parameters, the module provided the global kinetic moment of inertia  $I$  for each gear. The data are given in Table 1.

The data in the table show that the constant affecting the angular speed within the drag moment has a rather small distribution of its values around 110...

**Table 1** Measured and computed parameters of the tests

Gear	Test no.	m (kg)	r (m)	c (s/kg <sup>2</sup> /m)	I (kg m <sup>2</sup> )	Error (%)
I	1	635	0.254	110	8100	7.8
	2			140	7900	6.5
	3			140	8000	5.7
	Average values »			130	8000	6.7
II	1	635	0.254	100	4400	8.5
	2			120	4200	6.8
	3			105	4400	7.6
	Average values »			108	4333	7.6
III	1	635	0.254	100	3300	5.1
	2			100	3200	6.4
	3			100	3000	5.9
	Average values »			100	3167	5.8

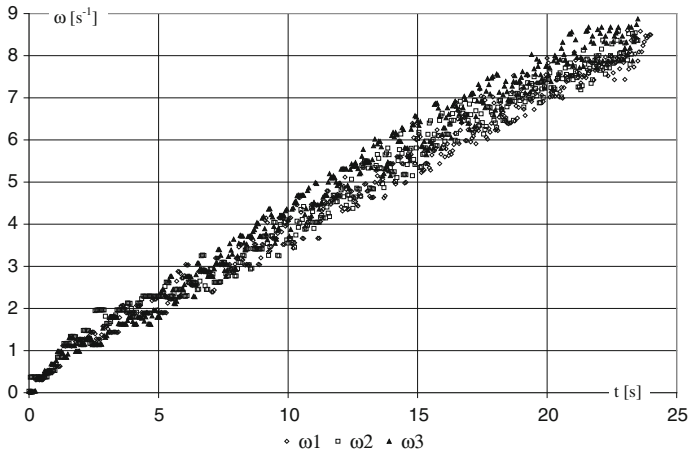


**Fig. 5** Time histories of the measured angular speed for three different tests developed for the third gear of the transmission

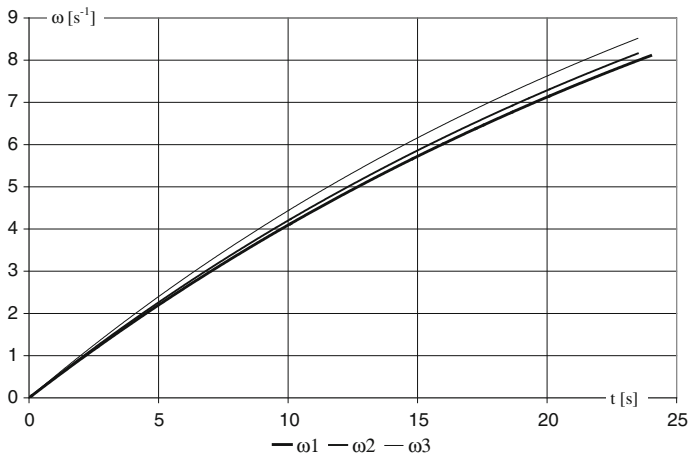


**Fig. 6** The approximation curves of the experimental data plotted in Fig. 5

120  $\text{s/kg}^2/\text{m}$ . That is a proof of the quality of the measurements since it has to keep itself around a certain value (Alexa 2014).

Figure 7 depicts the plotted values and approximation curve of the second test within the first gear as an example of global kinetic moment estimation, curve-fitting procedure.

Another way to check for the accuracy of both the measuring procedures and of the mathematical model and computation was to see if the terminal velocity (angular speed) was the same for every gear of the transmission. Of course, we

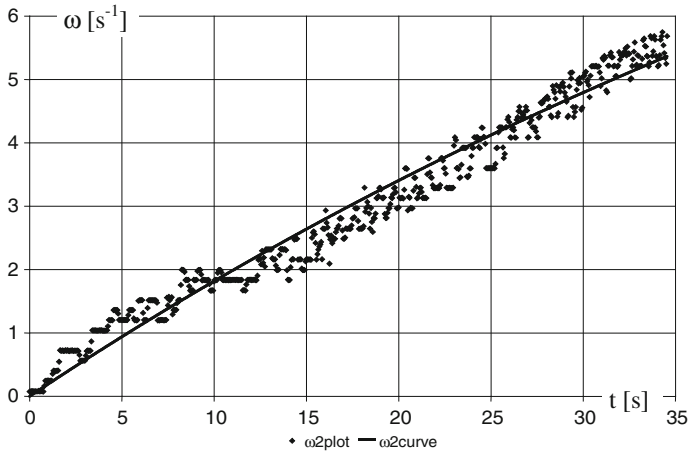


**Fig. 7** Plotted values and approximation curve of the second test within the first gear

couldn't check it for real since the cable was too short, but, pushing forwards the time history of the modeled curves [using Eq. (10)] we have got the results depicted in Fig. 8. We overlapped several curves to determine the value of the terminal angular speed of the sprocket wheel. It came out that the value of the angular speed is about  $15.8 \text{ s}^{-1}$ . It corresponds to a value of about 150 revolutions per minute and it is reached sooner or later, depending on the gear ratio of each gear of the transmission. What is more important is that the vehicle's speed that corresponds to this value is around 15 km/h. So, the engine brake is extremely effective for this vehicle (it is a tracked vehicle).

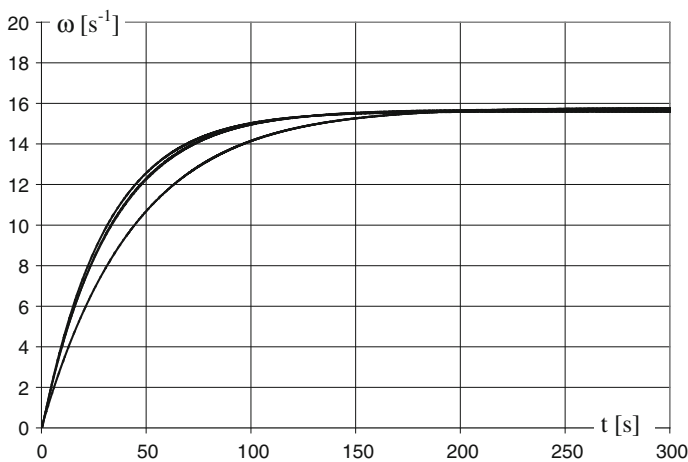


**Fig. 8** Terminal angular speed of the sprocket wheel

## Conclusions

Most of the time one doesn't need using the brakes of the tracked vehicles since their propulsion system is featured by a low efficiency. Nevertheless, the big masses of these special vehicles could imply unevenness of the motion and it would be useful to learn what the coasting regime leads to. The problem with some of these vehicles is that they have hydro-dynamical, automatic transmissions ones, with hydro torque converters. The torque converter's parameters is rather unknown, especially when dragging regimes are involved. We tried to experimentally reveal the dragging behavior of the torque converter and determining the global kinetic moments of the transmission for each gear.

What we learned is that the torque converter has big influence while coasting the vehicle. The ratios of the transmission's gears are also important since they change the angular speed of the converter's turbine from ratio to ratio. The dragging phenomenon starts whenever the terminal speed is overtaken, and that means about 15 km/h for the actual vehicle. Small fluctuation around this terminal velocity may occur due to the different ratios of the transmission. As a matter of fact, it varies between about 12 km/h in the first gear to about 15 km/h in the third one.

The mathematical model of the angular speed variation has been confirmed with enough accuracy [in the terms provided by eq. (10)]. That allowed us to determine the terminal speed. On experimental basis we could never reach that speed, since it would have taken too much time and too much cable for the given mass. Increasing mass won't be possible over a certain limit due to both the labor safety reasons and structure's strength. Moreover, the model allowed us to compute the global kinetic moments of the transmission and their values are quite similar to the theoretical ones. We consider that the model provided in the paper hereby can be further developed using turbulent flow models for the torque converter.

## References

- Alexa O (2015) Contributions to the study of the influence of the mass inertia coefficient on the straight motion dynamics of the tracked military vehicles, Ph.D. Thesis, Military Technical Academy, Bucharest
- Alexa O, Ilie CO, Marinescu M, Vinturis V, Truta M (2014) Simulating the torque and angular speed distribution within a heavy vehicle's planetary gearbox. *Appl Mech Mater* 659:127–132. doi:10.4028 (Trans Tech Publications, Switzerland, ISBN 978-3-03835-272-3)
- Information on <http://mathworks.com>
- Marinescu M, Ilie CO (2014) Filtering the signal of a measured mechanical parameter. In: 10th International conference on communications (COMM), May 29–31, 2014, Bucharest, Romania, conference proceedings. AGIR Publishing House, Bucharest, pp 85–88 (ISBN 978-1-4799-2385-4, IEEE catalog no. CFP1441 J-AR)
- Truță M, Fieraru O, Vilău R, Vinturiș V, Marinescu M (2014) Static and dynamic analysis of a planetary gearbox working process. *Period Adv Mater Res* 837:489–494. doi:10.4028 (ISSN 1022-6680 (print, cd), ISSN 1662-8985 (web), ISBN 978-3-03785-929-2, [www.scientific.net](http://www.scientific.net))
- Vilau R, Marinescu M, Alexa O, Truta M, Vinturis V (2014) Diagnose method based on spectral analysis of measured parameters. *Adv Mater Res* 1036:535–540. doi:10.4028 (Trans Tech Publications, Switzerland, ISBN 978-3-03835-255-6)



# Analysis of Crashes at Intersections in Bucharest

Șerban Raicu, Dorinela Costescu and Ștefan Burciu

**Abstract** Road crashes involve important social and economic consequences and therefore crash analysis and traffic risk represented the topic of many studies. Better understanding of factors that influence the likelihood of crash occurrence could lead to appropriate measures to road safety enhancement. The main objective of this paper is to identify the relationships (i.e., crash-frequency estimation model) between crash frequency and contributing factors related to road infrastructure, traffic and demographic characteristics. The study is implemented for Bucharest, based on crash data over 5 years (2008–2012). The first part of the paper presents the analysis on counted crashes at intersections. The second part describes crash-frequency estimation models developed for different types of intersection, based on negative binomial distribution. The developed models will be useful tools in urban traffic risk assessment at planning phase. In this way, several urban planning alternatives could be analysed and evaluated before important urban and transport infrastructure investment, with negative impact on road safety, are made.

**Keywords** Traffic risk · Crash analysis · Crash-frequency estimation

---

Ș. Raicu · D. Costescu (✉) · Ș. Burciu  
University “Politehnica” of Bucharest, Splaiul Independenței 313,  
060042 Bucharest, Romania  
e-mail: dorinela.costescu@upb.ro

Ș. Raicu  
e-mail: serban.raicu@upb.ro

Ș. Burciu  
e-mail: stefanburciu@yahoo.com

## Introduction

Interdisciplinary research on road safety has identified the main factors contributing to crash occurrence: road user behaviour (drivers and pedestrians), geometrical and technical characteristics of roadway (design characteristics, capacity, pavement type, etc.), traffic characteristics (volume, speed and capacity use) and environmental conditions (Li et al. 2007; Vorko-Jovic et al. 2006). Studies on crashes in urban areas added also land use characteristics (Fleury et al. 2011; Miranda-Moreno et al. 2011; Pulugurtha et al. 2013). The interactions between these mentioned factors determine the occurrence and severity of road crashes. Research on understanding the contributing factors to crash occurrence is necessary in order to identify and develop appropriate road safety measures (European Commission 2010).

The main issue of identifying the relationships between causes and effects of road crashes consists in the lack of detailed data on traffic and driving conditions. Therefore the methods developed in the last decades are limited to statistical models that define the crash frequency at some road network entities (road segment or intersection) or geographic units (traffic analysis zone (TAZ), administrative zones, regional census tracts, country) (Hauer 2001; Lord and Mannering 2010). These models use spatial and temporal elements as explanatory variables (Miaou and Lord 2003). Because the crash incidents are seldom events, the most crash-frequency estimation models are developed based on negative binomial (NB) regression models (Pulugurtha and Sambhara 2011; Lord and Mannering 2010; Persaud and Lyon 2007; Noland and Quddus 2005; Miaou and Lord 2003). In order to overcome the limitation of NB regression models (Lord 2006), recent approaches have proposed finite mixture model that include combination of discrete and continuous representation of data heterogeneity (Park and Lord 2009; Lord and Mannering 2010).

Lord and Mannering (2010) presented the advantages and disadvantages of the different methods applied to crash-frequency estimation. The constant evolution of crash-frequency estimation models enhanced the understanding of contributing factors to crash occurrence. It is assumed that crash-frequency estimation models will represent useful tools in urban and transportation planning (Fleury et al. 2011; Ladron de Guevara et al. 2004).

Unfortunately in Romania there was no concern in collecting and handling crash data in order to estimate crash frequency, useful in quantification of the different factor effects and assessment of road safety measures. Aiming to contribute to road safety enhancement, we have started the study with the analysis of crashes in Bucharest. The focus of this paper is to examine the possible explanatory variables of crash-frequency at intersections.

The available data were the crash-counts in Bucharest for the time period of 2008–2012. We analysed the crash data on different classes of urban road network intersection. In order to better understand the factors affecting crash frequency, it is recommended to define and calibrate distinct models for different type of

intersections (Reurings et al. 2006; Lee and Abdel-Aty 2005). Therefore, for each class of signalized intersection we tried to identify relationships between crash-frequency and predictor variables such as annual average daily traffic (AADT) and demographic attributes (i.e. population density). The signalized intersections with included tram infrastructure and the signalized intersections dedicated only to road traffic were separately analysed. Further, models for 3-way signalized intersections, 4-way signalized intersections and more than 4-way signalized intersections were developed.

## Data and Methodology

The main objective of this study is the development of a set of relationships between urban crash-frequency and their contributing factors, using non-spatial models (i.e. NB models) based on a spatial model of the urban area of Bucharest.

### *Spatial Model of Urban Area of Bucharest*

A GIS model was developed to include the road network characteristics necessary to analyse each class of intersection and to examine the relationships between crash frequency and the explanatory variables. The available data allowed us to analyse two major categories of explanatory variables: (i) traffic characteristics and (ii) demographic factors.

Set of attributes were used in the GIS model to define the characteristics of the urban main road entities. For the analysis presented in this paper we used the next characteristics of intersections:

- Type of signalizing: signalized and unsignalized intersections;
- Type of configuration: 3-way intersections (T-, Y- or skewed Y-intersections); 4-way intersections (regular cross, skewed 4-legged intersections); more than 4-way intersections;
- Type of infrastructure: intersections crossed by trams (with tram tracks included in the road infrastructure); intersections dedicated only to road traffic;
- Existence of public transport stops: without stops at intersection; regular side stops; median tram stops; metro stops.
- Existence of pedestrian crossing: without pedestrian crossing; unsignalized pedestrian crossing; signalized pedestrian crossing; double-signalized pedestrian crossing with median traffic island.

It is usual to use AADT to characterize the traffic in crash-frequency estimation models (Lord and Persaud 2004). Due to the lack of data, using annual average daily traffic represents the best procedure, even though in this way the significant hourly traffic non-uniformities in congested urban areas could not be considered.

In our study we used AADT recorded in 2012 assigned on the major urban road entities.

It was demonstrated that using only traffic flow as single explanatory variable could lead to incorrect estimation of traffic frequencies (Washington et al. 2010). Population has been often used as exposure in crash-frequency estimation, especially for vehicle-pedestrian crashes (Lee and Abdel-Aty 2005). Because 55 % of crashes in the time period of 2008–2012 involved pedestrians, we also analysed as explanatory variables the population and population density for those 80 traffic analysis zones (TAZs) delimited in the Bucharest General Master Plan of Transport (2008). For each TAZ additional attributes characterizing significant motorized vehicle and pedestrian flow generating activities are included in the GIS model (number of commercial centres, number of schools, number of administrative institutions, other interest places).

### *Crash Data*

The available data for our study were the severe traffic crashes counts in Bucharest over 5 years (2008–2012). By using Geographic Information System (GIS) facilities we managed the crash-data and we built geo-database with the location of the crashes in the urban area. We aggregated the crash-frequency for each year of the time period from 2008 to 2012 at urban road network entities (road sections and intersections). Thus, we obtained the overall number of crashes at each network entity over 5 years. This procedure implied the loss of information regarding the yearly non-uniformity of crash-frequency. Nevertheless, taking into account the heterogeneity of entities (especially intersections) of the urban road network in Bucharest, in the next step of the analysis this procedure helped us obtain larger samples of crash counts for the same class of road entities.

The cause of crashes indicated the type of accidents: vehicle-vehicle or vehicle-pedestrian. This way, three categories of road entities resulted: entities where only vehicle-vehicle crashes occurred, entities with only vehicle-pedestrian crashes and entities where vehicle-vehicle but also vehicle-pedestrian crashes occurred. These attributes allowed us to obtain subsets of data for each type of network entities and each category of crashes. The data shows, as we expected, that the percentage of crashes at intersections is substantially higher (81 %) than the percentage of crashes at road sections. Therefore the analysis presented in this paper refers only to crashes at intersections (Fig. 1). There are 191 intersections with recorded accidents, but for further analysis we have selected only 120 intersections located on major roads with available AADT data.

In order to establish the links between traffic and demographic factors with the counts of traffic crashes observed at intersections, we used GIS facilities to select crash data function of the characteristics of road infrastructure. Tables 1 and 2 summarize the results of the several sequential selection procedures applied to signalized, respective unsignalized intersections.

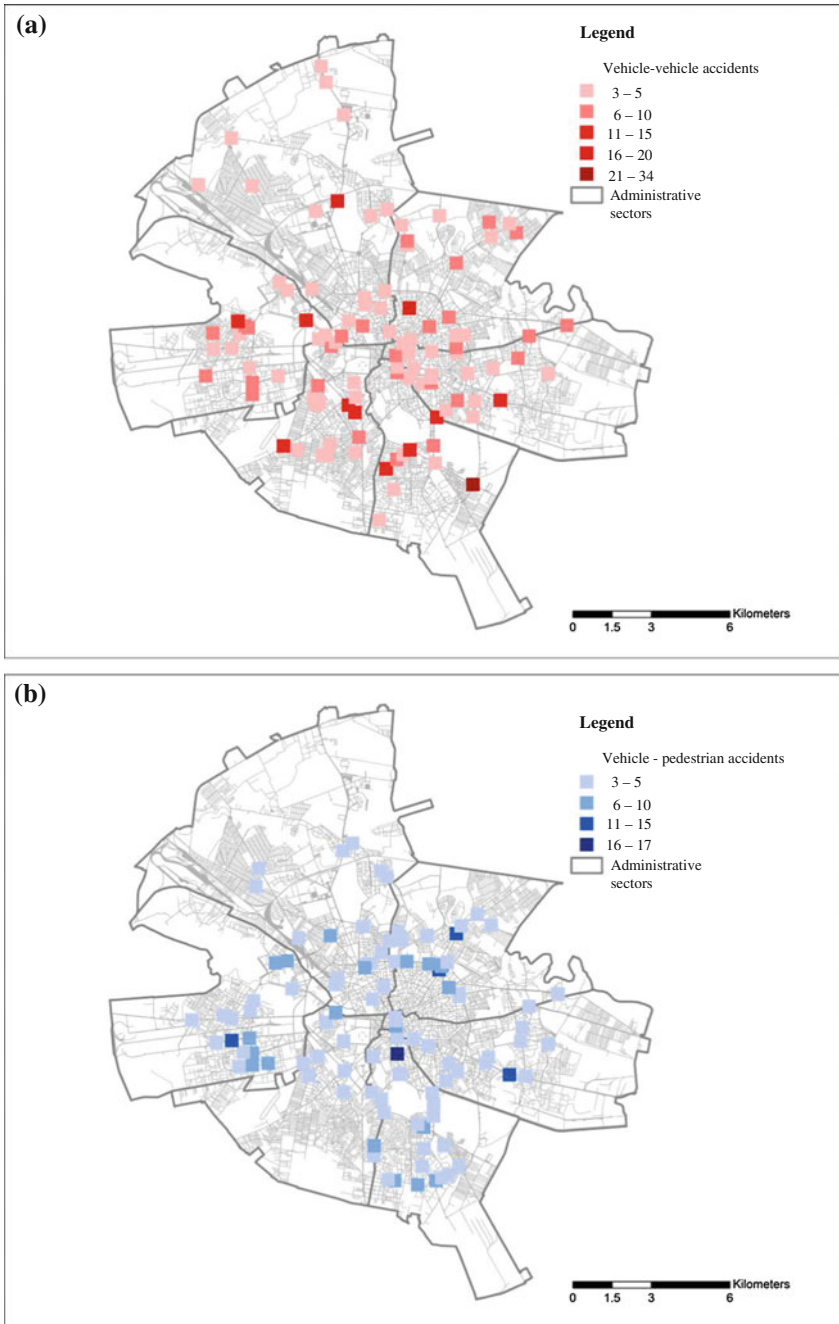


**Fig. 1** Location of road accidents at intersections in Bucharest urban area (2008–2012), **a** vehicle–vehicle accidents (56 %), **b** vehicle–pedestrian accidents (44 %)

**Table 1** Traffic crashes at signalized intersections

Characteristics of intersection		No. of intersections with recorded crashes	Crashes (vehicle-vehicle/vehicle-pedestrian/overall)
1. Type of infrastructure	With tram tracks included in the road infrastructure	51	235–190–425
	Dedicated only to road traffic (without tram facilities)	25	74–39–113
2. Public transport station	With public transport stations at intersection	52	231–194–425
	Without public transport stations	24	78–35–113
3. Type of pedestrian crossing	Pedestrian crossings separated by median traffic island	42	199–167–366
	Pedestrian crossing without separation facilities	30	100–48–149
	Without pedestrian crossing	4	10–13–23
Overall		76	309–228–538

In the case of signalized intersections, the percentage of vehicle-vehicle crashes (57 %) is higher than the percentage of vehicle-pedestrian crashes. But in case of unsignalized intersections, the percentage of vehicle-pedestrian crashes (61 %) is higher than the percentage of vehicle-vehicle crashes. Significant percentages of crashes occurred at intersections with tram facilities, respectively, with public transport stations (79 % in both cases).

**Table 2** Traffic crashes at unsignalized intersections

Characteristics of intersection		No. of intersections with recorded crashes	Crashes (vehicle-vehicle/vehicle-pedestrian/overall)
Type of infrastructure	With tram tracks included in the road infrastructure	22	26–72–98
	Designed only to road traffic (without tram facilities)	22	62–69–131
Public transport station	With public transport stations at intersection	17	39–71–110
	Without public transport stations	27	49–70–107
Type of pedestrian crossing	Pedestrian crossings separated by median traffic island	13	23–51–74
	Pedestrian crossing without separation facilities	–	–
	Without pedestrian crossing	31	65–90–155
Overall		44	88–141–229

Overall, more crashes occurred at the signalized intersections (63 %). Thus, the next section presents the analysis of crash data sets for different classes of signalized intersections.

## Data Analysis

Traffic crashes are complex events, difficult to be estimated. Literature regarding crash-frequency has identified several issues that can lead to incorrect definition and calibration of crash prediction models (Lord and Mannering 2010; Persaud and Lyon 2007; Lord and Persaud 2004). In order to obtain a correct interpretation of factors contributing to crash frequency, distinct examinations for different classes of intersections are recommended (Reurings et al. 2006; Lee and Abdel-Aty 2005). Thus, we selected the crash data for signalized intersections by layout (3-way, 4-way and more than 4-way intersections) (Table 3).

Because small sample sizes resulted for 3-way and more than 4-way intersections, for these classes of intersections we have not managed to obtain a model for crash-frequency estimation. In case of 4-way intersections, the over-dispersion (variance exceeds the mean) has caused issues in defining a model. Over-dispersion is one of the main characteristics of crash data, explained by data clustering, insufficient data to identify temporal correlation or other model miss-specification (Lord and Mannering 2010).

Because we managed the data in GIS environment, we could evaluate the spatial autocorrelation using Moran's I Index (Mitchell 2005). For each sample we obtained low value of Moran's I Index, indicating a random crash spatial distribution. Consequently in case of our study the over-dispersion is not caused by data clustering.

If data are over-dispersed, the negative binomial (or Poisson-gamma) model is recommended (Lord and Mannering 2010; Lord 2006, Reurings et al. 2006). In our study the following equation is initially used:

$$\mu = \beta_0 \cdot Q_1^{\beta_1} \cdot Q_2^{\beta_2} \cdot e^{\sum_j \alpha_j \cdot x_j}, \text{ (accident/year)} \quad (1)$$

**Table 3** Characteristics of traffic crashes at signalized intersections function of layout

Intersection layout	No. of intersections with recorded crashes	Recorded crashes	Crashes/intersection min-max-average-variance
3-way (T-, Y- or skewed Y-intersections)	15	60	3-9-4-2.52
4-way (regular cross, skewed 4-legged intersections)	50	397	3-34-7.9-35.2
more than 4-way intersections	11	81	3-14-7.4-20.7



where

- $\mu$  is the expected number of accidents;
- $Q_1, Q_2$  entering traffic flow in intersection from the major, respective minor road section;
- $x_j$  explanatory variables;
- $\beta_0, \beta_1, \beta_2,$  parameters to be estimated.
- $\alpha_j$

Using the available data on traffic and demographic characteristics, we applied correlation tests in order to identify the explanatory variables for crash-frequency. We used correlation coefficient  $R^2$ , adjusted correlation coefficient  $R^2$ , Akaike information criterion  $AICc$  and variance inflation factor  $VIF$  as evaluators (Mitchell 2005; Cameron and Trivedi 1998).

For the 4-way intersection sample,  $Q_2$  (the minor traffic flow) was identified as the variable with the highest influence on crash-frequency. Nevertheless, we could not obtain an estimation model with adequate correlation coefficients. This issue could be explained by the heterogeneity of traffic flow and land use of Bucharest urban zones (high and low density buildings development use zones, commercial zones etc.).

Therefore, in this stage of the research, we decided to apply additional selection criterion for the available data. The results of the selection are described in Table 4. The obtained models for the 4-way signalized intersections with tram tracks included in the road infrastructure, respective dedicated only to road traffic are presented in the next section.

**Table 4** Characteristics of traffic crashes at 4-way signalized intersections

Type of infrastructure	Type of crash	No. of intersections with recorded crashes	Recorded crashes	Crashes/intersection min-max—average—variance
With tram tracks included in the road infrastructure	Vehicle-vehicle	35	182	0-34-5.2-44.0
	Vehicle-pedestrian		150	0-17-4.28-22.6
	Overall		332	3-34-9.48-42.6
Designed only to road traffic (without tram facilities)	Vehicle-vehicle	15	51	0-9-3.4-6.1
	Vehicle-pedestrian		26	0-7-1.73-4.3
	Overall		77	3-10-5.13-6.6

## Results

For the set of data summarized in the Table 4 we applied several exploratory regression procedure in order to identify the variable with significant contribution to crash-frequency and then to calibrate the model. The model obtained for the 4-way intersections with tram tracks included in the road infrastructure is:

$$\mu_t = 0.14 \cdot Q_1^{1.2} \cdot e^{0.23 \cdot 10^{-4} \cdot \rho_{TAZ} + 0.73 \cdot \rho_{CC}}, \text{ (accident/year)} \quad (2)$$

where

$\mu_t$  is the expected number of accidents at 4-way intersections with tram tracks;  
 $\rho_{TAZ}$  density of population of TAZ where intersection is located;  
 $\rho_{CC}$  density of commercial centres in TAZ where intersection is located.

Equation (2) shows that the minor traffic in intersection has no significant contribution for this class of intersection. A satisfactory correlation coefficient  $R^2$  (0.70) was obtained only by including the density of commercial centres as exposure in the model. This fact indicates that further data on urban activities should be collected and analysed for a better estimation of crash-frequency.

A more complex equation resulted for the 4-way intersections designed only to road traffic, without tram facilities:

$$\mu_r = 0.11 \cdot Q_1^{0.12} \cdot Q_2^{0.033} \cdot e^{-0.6 \cdot 10^{-5} \cdot Q_1 + 0.75 \cdot Q_2 + 0.11 \cdot 10^{-4} \cdot \rho_{TAZ}}, \text{ (accident/year)} \quad (3)$$

where  $\mu_r$  is the expected number of accidents at 4-way intersections designed only to road traffic.

In this case the flow on both interacting ways influences the crash frequency and also the population density. A higher correlation coefficient  $R^2$  (0.76) was obtained. Nevertheless, this result indicates not necessary a better estimation than in the previous case. Rather it is a consequence of the small size sample, an issue emphasized in the literature (Lord and Mannering 2010).

## Conclusions

Many studies have presented methodologies on the topic of crash frequency estimation in the last decades. Several issues related to the development of crash frequency estimation models have been identified and the difficulties in collecting detailed data on traffic crashes limited the improvement of these models.

Nevertheless it is recognized the value of these models as tools in the assessment of the road safety measures and traffic risk for different urban planning alternatives. Therefore we have started our research for the urban area of Bucharest, marked by rapid and radical socio-economic life changes over the last two decades. Besides

major changes in urban commerce structure, new concentration of urban and suburban residential areas, spatial and structural changes of interest places, new motorization indices and traffic flow increase on an inadequate road network lead to traffic congestion and more severe crashes.

Because no previous concern on crash-frequency models existed in Bucharest, the main issues encountered in our research was the collection of data on crashes and explanatory variables. With the available data on AADT for 2012 and demographic data for TAZs we built the urban spatial model. With GIS facilities we processed the data on crashes and we managed to overcome the NB model issues regarding spatial correlation.

The crash-frequency estimation models presented in the previous studies took into account only simple intersection configurations, designed only for road traffic flow. Therefore we had to develop a methodology appropriate to the peculiarities of Bucharest urban road network: heterogeneity of intersection layouts, mixed use of streets by road vehicles and trams.

The road flow, the density of population and the density of commercial centres are identified as explanatory variables of crash-frequency for 4-way signalized intersections. The inclusion of the density of commercial centres in the estimation model emphasized the necessity of detailed data on urban activities directly linked to the generated and attracted vehicle and pedestrian flow.

**Acknowledgments** The work has been funded by the Sectorial Operational Programme Human Resources Development 2007–2013 of the Ministry of European Funds through the Financial Agreements POSDRU/159/1.5/S/132395 and POSDRU/159/1.5/S/132397.

## References

- Bucharest General Master Plan for Urban Transport (2008) Final Rapport, EuropeAid/123579/D/SER/RO
- Cameron AC, Trivedi PK (1998) Regression analysis of count data. Cambridge University Press, Cambridge
- European Commission (2010) Towards a European road safety area: policy orientations on road safety 2011–2020. COM (2010) 389 final, Brussels
- Fleury D et al. (2011) Projets urbains de cohérence fonctions/réseaux, PREDIT Groupe Opérationnel N° 2: Qualité des systèmes de transport. 08 MT S 027 et 08 MT S 028, IFSTTAR-France
- Hauer E (2001) Overdispersion in modeling accidents on road sections and in empirical Bayes estimation. *Accid Anal Prev* 33(6):799–808
- Ladron de Guevara F, Washington SP, Oh J (2004) Forecasting crashes at the planning level: simultaneous negative binomial crash model applied in Tucson, Arizona. *Transp Res Rec* 1897:191–199
- Lee C, Abdel-Aty M (2005) Comprehensive analysis of vehicle–pedestrian crashes at intersections in Florida. *Accid Anal Prev* 37:775–786
- Li L, Zhu L, Sui DZ (2007) A GIS-based Bayesian approach for analyzing spatial–temporal 3 patterns of intra-city motor vehicle crashes. *J Transp Geogr* 15:274–285

- Lord D (2006) Modeling motor vehicle crashes using Poisson-gamma models: examining the effects of low sample mean values and small sample size on the Estimation of the fixed dispersion parameter. *Accid Anal Prev* 38(4):751–766
- Lord D, Mannering F (2010) The statistical analysis of crash-frequency data: A review and assessment of methodological alternatives. *Transp Res Part A* 44:291–305
- Lord D, Persaud BN (2004) Estimating the safety performance of urban road transportation networks. *Accid Anal Prev* 36(4):609–620
- Mitchell A (2005) *The ESRI guide to GIS analysis*, vol 2. ESRI Press, Redlands
- Miaou S-P, Lord D (2003) Modeling traffic crash-flow relationships for intersections: dispersion parameter, functional form, and Bayes versus empirical Bayes methods. *Transp Res Rec* 1840:31–40
- Miranda-Moreno LF, Morency P, El-Geneidy AM (2011) The link between built environment, pedestrian activity and pedestrian–vehicle collision occurrence at signalized intersections. *Accid Anal Prev* 43:1624–1634
- Noland RB, Quddus MA (2005) Congestion and safety: a spatial analysis of London. *Transp Res Part A* 39:737–754
- Park B-J, Lord D (2009) Application of finite mixture models for vehicle crash data analysis. *Accid Anal Prev* 41:683–691
- Persaud B, Lyon C (2007) Empirical Bayes before–after safety studies: lessons learned from two decades of experience and future directions. *Accid Anal Prev* 39(3):546–555
- Pulugurtha SS, Duddu VD, Kotagiri Y (2013) Traffic analysis zone level crash estimation models based on land use characteristics. *Accid Anal Prev* 50:678–687
- Pulugurtha SS, Sambhara VR (2011) Pedestrian crash estimation models for signalized intersections. *Accid Anal Prev* 43:439–446
- Reurings M et al (2006) Accident prediction models and road safety impact assessment: a state-of-the-art. RI-SWOVWP23-R1-V2, RIPCORDER-ISEREST
- Vorko-Jovic A, Kern J, Biloglav Z (2006) Risk factors in urban road traffic accidents. *J Saf Res* 37 (1):93–98
- Washington SP, Karlaftis MG, Mannering FL (2010) *Statistical and econometric methods for transportation data analysis*, 2nd edn. Chapman Hall CRC, FL

# The NVH Behaviour of a Powertrain Fixed on a Measurement Bench

Andrei Daniel Calin, Nicolae Enescu, Radu Chiriac  
and Nicolae Orasanu

**Abstract** The adaptation of a powertrain on an engine test bench could raise some problems concerning the torque transmission solution if it is changed from the classical schema (Fig. 1) (Crankshaft → Internal gearings of the gearbox → Differential → Transmission shafts) to a different configuration needed for the test bench operation (Fig. 2) (Crankshaft → Coupling shaft between the engine crankshaft and user → Eddy current dynamometer). Thus, by making different modifications, various problems can occur, such as NVH and reliability problems. This paper describes the study which was performed for the behavior of the powertrain system of a Dacia Logan K7M710 engine, by keeping the standard mountings of the engine and also by adding an extra fixation on the bench frame in order to stiffen the structure of the test bench. All these were correlated with the measurement on the vehicle.

**Keywords** Bench · Powertrain · NVH · Measurements

---

A.D. Calin (✉) · N. Enescu · N. Orasanu  
Faculty of Biotechnical Systems Engineering, Mechanics Department,  
University Politehnica from Bucharest, Bucharest, Romania  
e-mail: daniel\_calin89@yahoo.com

N. Enescu  
e-mail: enescunicolae875@yahoo.ro

N. Orasanu  
e-mail: norasanu62@yahoo.com

R. Chiriac  
Faculty of Mechanical Engineering and Mechatronics, Internal Combustion Engines  
Department, University Politehnica from Bucharest, Bucharest, Romania  
e-mail: raduchiriac2001@yahoo.com

## Introduction

In this paper it is presented the behavior of a powertrain when it is mounted on a test bench. By keeping the same mountings, but changing the kinematic scheme, the vibration level may increase (Figs. 1 and 2).

Thereby, various situations were studied, in order to see what changes appear and to find the proper method to reduce the vibration level. For safety reasons, an extra bracket was added in the middle area of the powertrain (EB4).

The following configurations were tested:

- The powertrain mounted on the vehicle (reference situation) (Fig. 3);
- The powertrain fixed with the standard mountings on the bench (EB1, EB2, EB3) (Fig. 3);
- The powertrain fixed with the standard mountings + an extra bracket added but not fixed (in order to see the impact of the added mass) (Fig. 4);
- The powertrain fixed on the bench with all four mountings (EB1, EB2, EB3, EB4) (Fig. 4).

The tests were performed with engine running without the break applied, at the following engine speeds: 800, 2000, 3000 and 4000 rpm.

The purpose of this study is to see if, how much and in which way the engine behavior is changing by fix it on the testing bench. For safety reasons, this current, primary study is made in order to see the comporment of the powertrain without inducing the load (by using the Eddy-current break).

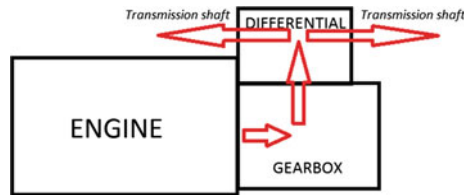


**Fig. 1** Vehicle configuration

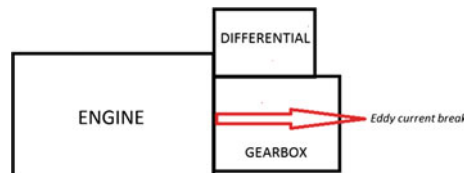


**Fig. 2** Bench configuration

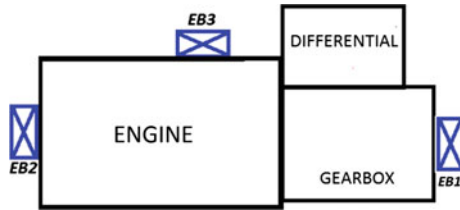


**Fig. 3** Vehicle fixation points. *EB1* Engine bracket 1, *EB2* Engine bracket 2, *EB3* Engine bracket 3, *EB4* Extra bracket (4)

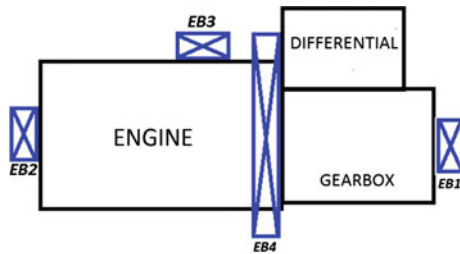


**Fig. 4** Bench fixation points. *EB1* Engine bracket 1, *EB2* Engine bracket 2, *EB3* Engine bracket 3, *EB4* Extra bracket (4)

## Experimental Details

As it is mentioned above, the measurements were made on the K7M710 Renault engine. This is a four cylinders transverse powertrain, with the nominal power of 64 kW, equipped with a 5 speed manual gearbox. In the case of bench measurement, the internal mechanisms are missing, being replaced with a single shaft which connect the crankshaft flange with the Eddy current break.

By measuring the vibration level of the fixing points of the engine and comparing with the initial conditions (vehicle configuration), we can indicate this way if any risk exists for the bench adaptation. The risk implies vibration reliability, fatigue and material stress level which can rise above limits.

All the tests were made using the following equipment (Bruel&Kjaer Magazine 2007)<sup>1,2</sup>:

- Module carrier C Series USB Single Module Carrier NI USB-9162 (Fig. 5);
- Acquisition board National Instruments NI USB-9233 (Fig. 5);

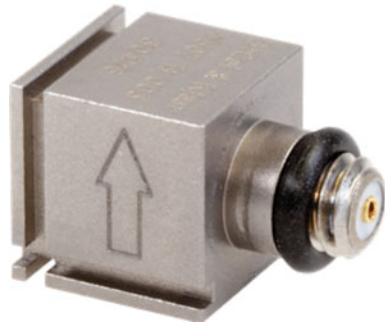
<sup>1</sup>Bruel&Kjaer, “Transducers and conditioning”.

<sup>2</sup>National Instruments, User guide and specifications for data acquisition device NI USB-9223.

**Fig. 5** Data acquisition device (NI-USB-9223) (See Footnote 2)



**Fig. 6** Unidirectional accelerometer (See Footnote 1)



- Accelerometers Bruel&Kjaer (unidirectional) (Fig. 6);
- Acquisition and data processing was made using dB FA Suite 4.8.1 Software.<sup>3</sup>

For each engine mounting, the vibration level was measured x, y and z direction. X direction was considered horizontal and perpendicular on the crankshaft axis, y parallel with the crankshaft axis and vertical (Fig. 7).

For data acquisition and processing was used the software dBFA (signal filtration, integrations, FFT analysis).

## Results and Discussions

The data acquisition was made by recording the vibration level in acceleration ( $m/s^2$ ), using the uni-directional accelerometer placed on each engine bracket (Fig. 7).

A measurement session was performed for each bracket and each engine speed in order to obtain a global image of the vibration level which is inserted in the fixing points (Fig. 10).

---

<sup>3</sup>Software dBFA Suite 4.8.1.



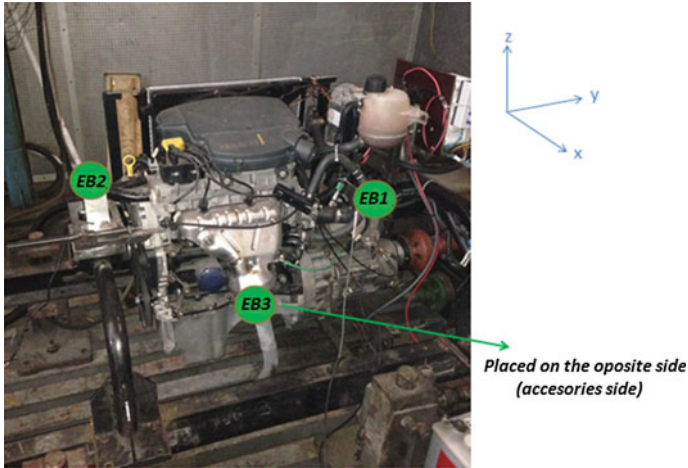


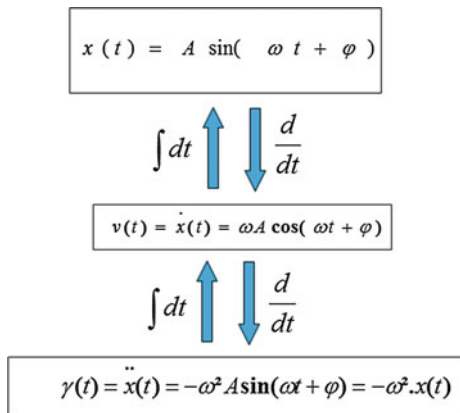
Fig. 7 The measurement bench/coordinates system

The signals were filtered using 2/2 high pass filter (Fig. 9—example for 2000 rpm, EB2, X direction). Also, 2 time integration was applied in order to obtain displacement values (Fig. 8). For the final results, the Fourier transform was applied, and then the RMS values were extracted (Fig. 9) (Orfanidis 2010; Vatterli et al. 2014; Osgood 2009).where

- A signal's amplitude;
- $\omega$  pulsation ( $2\pi f$ );
- $\varphi$  phase.

In order to achieve a global vision of the potential energy level of the engine brackets, the resultant displacement was calculated using the following approach:

Fig. 8 Integration-derivation process (Anghelache 2008; Predoi 2008)



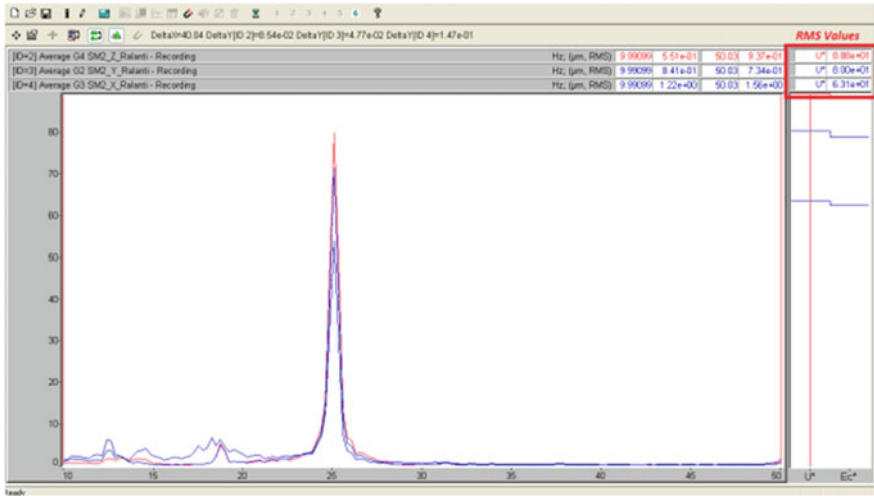


Fig. 9 Spectrum for displacement signals

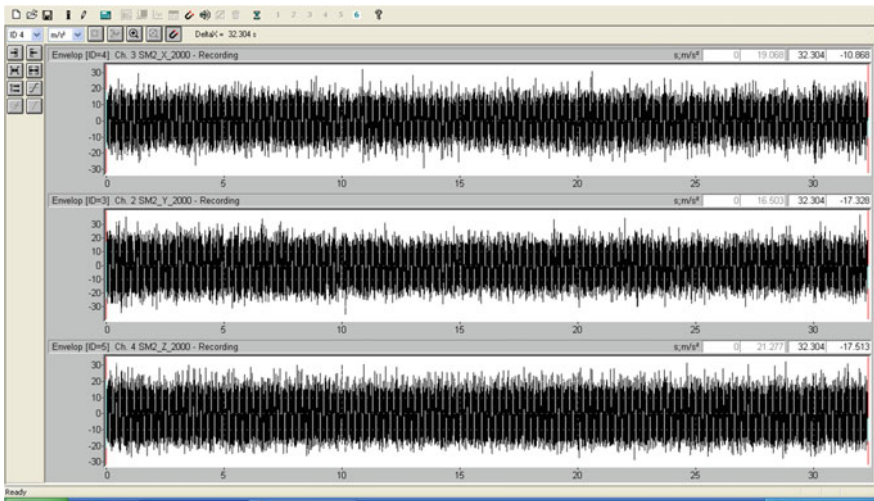


Fig. 10 Acceleration measure signal sample

$$u = \sqrt{x^2 + y^2 + z^2} \tag{1}$$

where

- $u$  resultant displacement value;
- $x, y, z$  RMS values for displacement (Fig. 10).

(a) Vehicle (Figs. 11, 12, 13 and 14, red columns)

The measurement on vehicle represents the reference situation, on which the others calculation are evaluated. The mounting brackets are calculated by the manufacturer according to this situation so the results could be used as a set of specifications.

(b) Bench with standard mountings (Figs. 11, 12, 13 and 14, yellow columns)

As can be observed above, the tendency it is not kept the same for all engine speeds.

Earlier mentioned, the kinematical scheme it's different between the two situations, bench vs. vehicle. A very important role in the vibration behavior is represented by the moving parts. By changing the configuration of the crankline, eliminating the clutch which is a mass added on crankshaft (decreasing de mass → increasing the main frequency) and the internal mechanisms of the gearbox, the

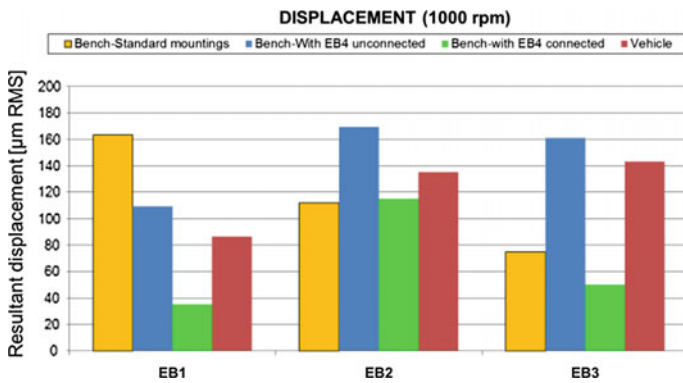


Fig. 11 Resultant displacement 1000 rpm

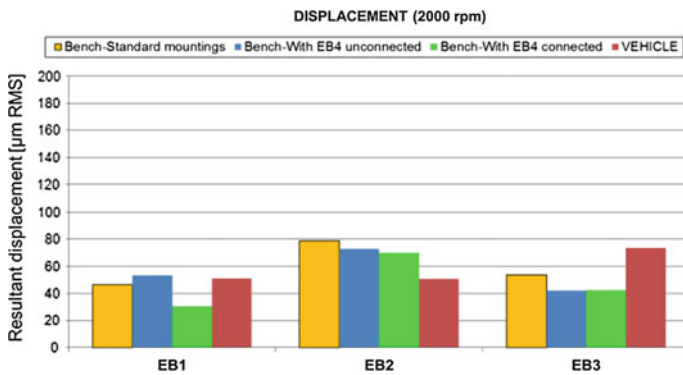


Fig. 12 Resultant displacement 2000 rpm

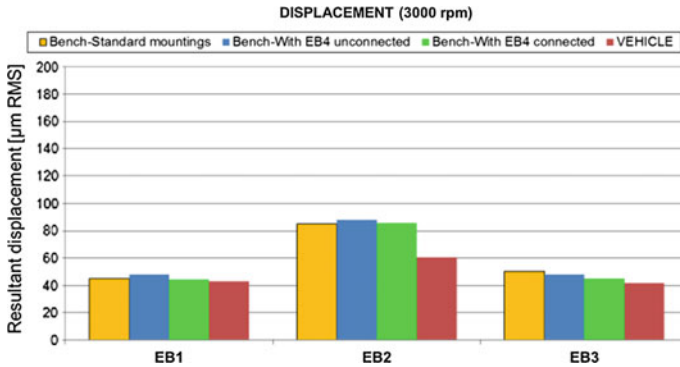


Fig. 13 Resultant displacement 3000 rpm

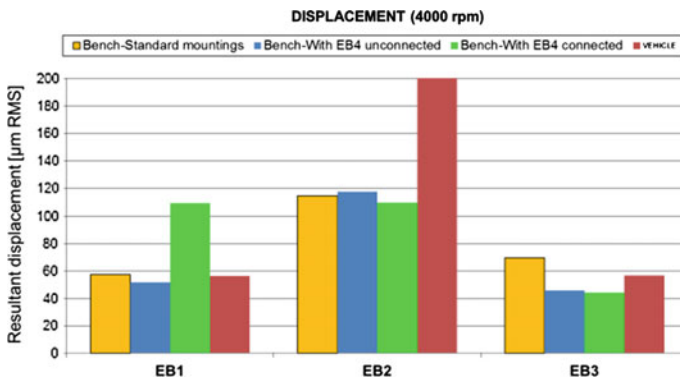


Fig. 14 Resultant displacement 4000 rpm

modal behavior of the crankshaft will change. If the modal behavior is changing, this will be reflected also in the results. Beside this factor, by eliminating parts from the structure, the mass and the stiffness of the powertrain will be different. The consequence will be reflected also in its modal behavior (bending and torsion modes of the engine) also affecting the results.

Considering these, for safety reasons, on the bench it is recommended to obtain a lower or equal energy level on the engine brackets in relation with the vehicle standard configuration.

(c) Bench with EB4-unconnected (Figs. 11, 12, 13 and 14, blue columns)

Because the vibration level was higher in many situation for the bench configuration (especially for EB1, 750 rpm), an extra bracket which connects the gearbox with the bench was added. Before the connection to be done, a measurement was made by fixing the bracket just on the gearbox, without making a rigid connection with the bench. The main idea was to study the effect of compensation mass (EB4

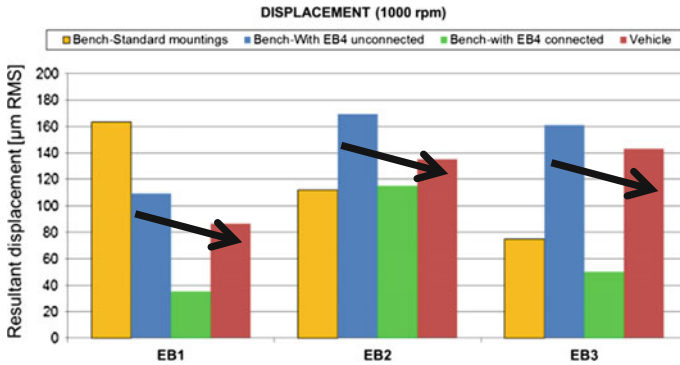


Fig. 15 Effect of EB4 mass 1000 rpm

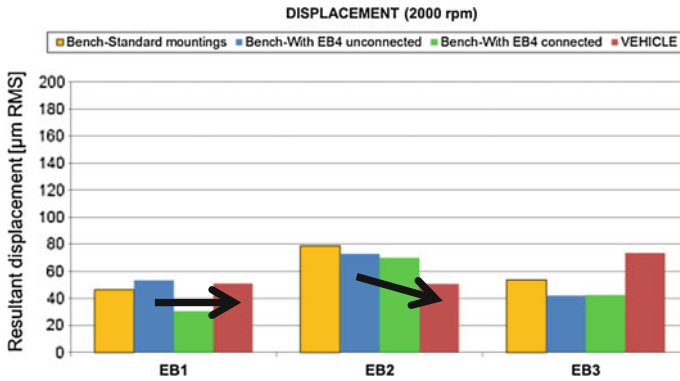


Fig. 16 Effect of EB4 mass 2000 rpm

weight—6 kg) added on the gearbox which is lighter on the bench configuration, without its interior gears.

The main observation that can be taken is that the mass compensate the missing parts from the gearbox and the results get closer to those from the vehicle (Figs. 15, 16, 17 and 18, blue columns versus red columns).

(d) Bench with EB4-connected (Figs. 11, 12, 13 and 14, green columns)

By fixing the EB4 on the bench, an extra fixation point is made, so the powertrain becomes stiffer (Figs. 19 and 20).

For a regular transverse powertrain the inflection point for the bending modes of the powertrain appears on the coupling face area between the gearbox and the engine. By adding this extra fixation (EB4), the amplitude of the powertrain in this area is reduced (Swoboda 1989; Lennström 2006). Although, it was observed also a weak point, the EB1, which doubles its amplitude for the case with the EB4 connected. Therefore, it is recommended to avoid this engine speed as much as

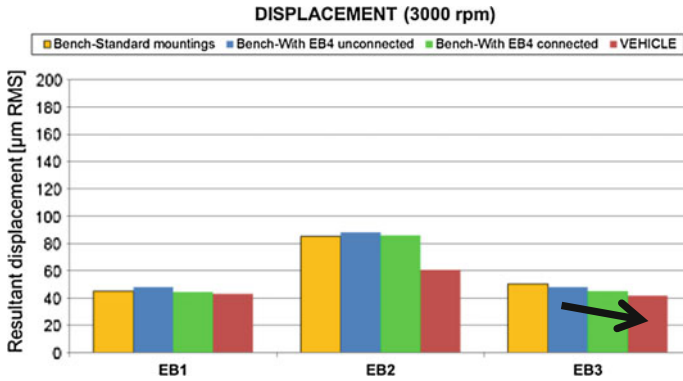


Fig. 17 Effect of EB4 mass 3000 rpm

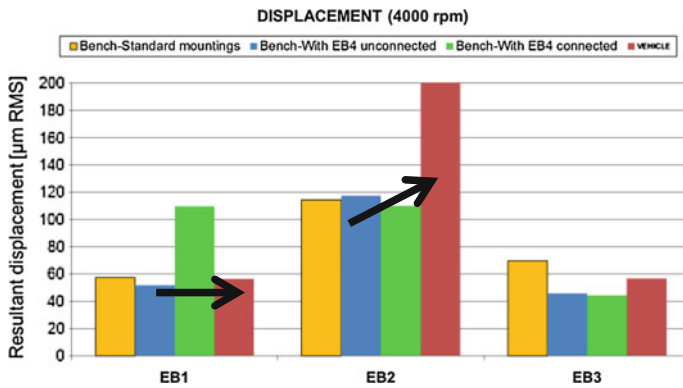


Fig. 18 Effect of EB4 mass 4000 rpm

Fig. 19 Static approach

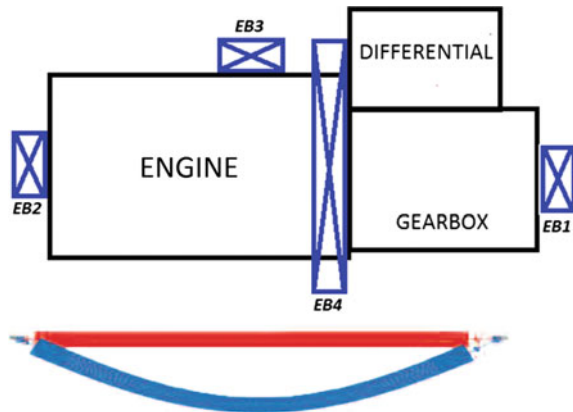
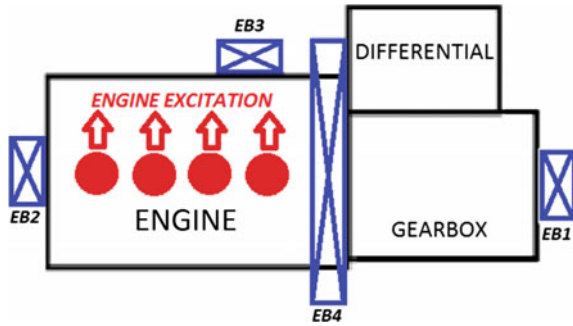


Fig. 20 Dynamic approach



possible because the increase of the stiffness for the EB4, at high engine speeds (the energy distributed on the engine is directly correlated with the square of velocity) lead to large displacements.

### Conclusions

The present study aims to investigate which is the proper NVH solution to apply when mounting a powertrain from vehicle condition to bench condition. Especially for long-time exploitation of the bench, the problems induce by the vibration level could be significantly important. Various problems could occur, in terms of safety (material fatigue or stress for the engine brackets) (Kubo et al. 2015) or in terms of lifecycle of the engine parts (heat-shields or other parts that could break). It is recommended to make this type of analysis, to confront the two situations—real-life conditions (vehicle) vs. adapted situation (bench). This way, could be observed if the new structure needs or not to apply an extra-constraint. Using this extra fixation in the studied case, the vibration level has decreased significantly for most of the fixing points.

As future prospect, measurements need to be done by coupling also the Eddy-current break and observe what happens when the powertrain run in full load conditions. A finite element analysis will be developed also in order to adapt proper solutions without measurement. Also, various software could be used (Hyper works Software Package) in order to develop the best geometry for the extra engine bracket, given some specific conditions (imposed displacement, stress, main frequency, etc.) (Brown et al. 2002).

**Acknowledgments** The work has been funded by the Sectoral Operational Programme Human Resources Development 2007-2013 of the Ministry of European Funds through the Financial Agreement POSDRU/187/1.5/S/155536.

## References

- Anghelache GC (2008) Controlul si atenuarea zgomotelor si vibratiilor autovehiculelor. Notiuni fundamentale. Zgomotul de rulare. Bren Publishing
- Brown JC, Robertson AJ, Serpento ST (2002) Motor vehicle structures. Concepts and fundamentals. SAE Publishing, Warrendale
- Bruel&Kjaer Magazine (2007) The international sound and vibration magazine” from Bruel&Kjaer, No.1
- Kubo P, Paiva C, Ferreira A, Larocca A (2015) Influence of a shock absorber condition on pavement fatigue using relative damage concept. J Traffic Transp Eng (English Edition)
- Lennström D, Olsson M, Wullens F, Nykänen A (2016) Validation of the blocked force method for various boundary conditions for automotive source characterization. Elsevier, Philadelphia
- Orfanidis SJ (2010) Introduction to signal processing. Rutgers University, USA
- Osgood B (2009) The Fourier transform and its applications. Electrical Engineering Department, Stanford University, Stanford
- Predoi MV (2008) Vibratii Mecanice. Modele si aplicatii in Matlab. Matrix Rom
- Swoboda B (1989) Equilibrage des machines alternatives. École Nationale Supérieure du Pétrole et des Moteurs (ENSPM)
- Vatterli M, Kovacevic J, Goyal VK (2014) Foundations of signal processing. Cambridge University Press, Cambridge



# Composite Materials Testing Method Steering Column Bracket Test

Lucian Eugen Rad, Anghel Chiru, Cristian Leahu  
and Dan Mihai Dogariu

**Abstract** Composite material is the most challenging field regarding the complexity phenomenon occurring forming time. The work has a strong practical level, focusing on testing methods for composites based of carbon fiber, using a new technology and the results of tests for components of the steering column made by carbon fiber composites materials.

**Keywords** Composite materials · Space winding process · Carbon fiber

## Introduction

As we known, in contrast to conventional materials, properties of the composites can be controlled to a high extent by the choice of components, the percentage of fiber, fiber orientation and geometry. One of the attributes of composites is that the design engineer can choose the material properties while the optimal shape of the product, arises.

The mechanical properties depends on several variables of the composite (Taca 2012):

- properties of the fiber
- nature of the fiber surface

---

L.E. Rad (✉) · A. Chiru · C. Leahu · D.M. Dogariu  
Department of Material Science, Transilvania University of Brasov, Brasov, Romania  
e-mail: lucian.rad@unitbv.ro

A. Chiru  
e-mail: achiru@unitbv.ro

C. Leahu  
e-mail: cristian.leahu@unitbv.ro

D.M. Dogariu  
e-mail: dogardnm@schaeffler.com

- the material properties of the matrix
- properties of any other phases
- volume fraction of the second phase (and any other phase)
- spatial distribution and alignment of the two phases (including fabric material)
- the nature of the interfaces.

Processing methods—in cycles of temperature, pressure, vacuum and other factors—provide a great variability in the properties of the final product (Hodgkinson 1990).

Ability to create a composite in its final form is effective for production, but complicate the tests. Often there is no clear relationship between the properties of test samples (specimens) and properties of the final product (Iosipescu 1967). Therefore, attempts should be made at different stages of manufacture to measure the properties of both constituent materials and in the final component or structure (Hodgkinson 2000).

## Specific Tests for Console Steering Column

### *Test Equipment*

Typically, each component of the steering column must fulfill several functions. These multi-axial requests can be determined only by testing entire system as a whole.

According to a defined plane, are made various test measurements, listed (Table 1), in order to determine the properties of the steering column. It is perform strength tests/life and/or safety testing of vehicle collisions or other tests. After the tests of resistance/life measurements of the same kind as those before the test are always performed in order to ascertain any change in properties.

Test equipment and computer programs for data processing for testing, test conditions should enable vibration, oscillations, forces and maximum stresses, environmental, durability/reliability.

The tests were made using following equipment:

- MTS Dual Rotary System (DRS)
  - Two torsional stations with single or dual rotary inputs
- Tensile Machine MTS Insight 50
  - 50 kN capability
  - Column spacing of 405 mm
  - Vertical test space of 1100 mm
- NVS (Noise, Vibration, Harshness)/BSR (Buzz, Squeak, Rattle) Testing
  - Electro-dynamic Shaker LDSv890

**Table 1** Standard tests for steering column

Preliminary measurements	Strength tests	Subsequent measurements for strength testing	Vehicle collision tests	Testing for incorrect use	Other tests
Weight	2 K dynamic test	Torque lock release lever	Maintenance force	Torque from incorrect use	Universal joints extraction force
Force lock-release lever	Torsional wear test	Natural frequency horizontal and vertical	Compression tests	Incorrect use of driver lever	Breakout force joints yoke
Natural frequency horizontal and vertical	Wear test of the locking mechanism	Stiffness horizontal and vertical	Freefall test	Limit checking end	Cardan bushings depressing force
Stiffness horizontal and vertical		Strength adjustment in length and height	Body block	The effort required to operate the lever	Shaker test
Strength adjustment in length and height		Maximum moment			
Torsional stiffness		Full rotation			
Maximum moment		Non-uniformity			
Full rotation		Mass flow			
Non-uniformity					

- Environmental Testing
  - Two environmental chambers with a soaking area of 1 m × 0.9 m × 0.9 m
  - Soaking conditions ranging from -55 to 155 °C and 10 to 98 % relative humidity
- Instrumentation
  - Force and torque transducers
  - Pneumatic, hydraulic and electric actuators
- Data Acquisition and Data Analysis
  - MTS data acquisition system
  - Multiple computation models available to aid in system analysis

## Performance Curve Evaluation Torsional Rate, Lash, Stiffness and Damping Structural Lash and Bearing Hysteresis

Besides these standard tests, they can make a series of tests and experiments to explore the behavior of various composite materials and extreme environments. Test results should help the design engineer to correctly calculate different modules and resistant due to the high anisotropy of composite materials based on carbon fibers and to render a representation of the characteristics of composite materials tested.

To perform tests on specimens of composite materials were made plates  $300 \times 300$  mm from which specimens were cut according to the standards. To achieve the plates and specimens using RTM process, we used a standard resin produced by Hunstman standard epoxy resin XB3585 and XB3458 hardener and fiber Toray T700 and Tenax HTS40 (Heitz 2013).

### *Test Results*

To characterize the first two types of material were provided specimens made of Toray T700 fibers and resin hardener XB 3585 fiber Tenax HTS 40 and resin 3458 and hardener XB3585.

In both cases the specimens were produced by RTM process and the volume of the fiber  $\varphi = 51$  %.

The specimens were fixed in special grips on a hydraulic cylinder Zwick and controlled loading and speed testing standards (Fig. 1).

Distance and loading forces were registered by the meter testing device. Tension was read using a laser extensometer with transmitted analog control device and recorded.

The tests required to characterize the behavior of these specimens are:

- Tensile parallel on fiber EN ISO 527
- Tensile perpendicular on fiber EN ISO 527
- Compression parallel on fiber EN ISO 14126
- Compression perpendicular on fiber EN ISO 14126
- Tensile tests ( $\pm 45^\circ$  fibers orientation) for determining shear characteristics DIN 65466

Reasons for traditional materials (steel), to achieve structural components of the steering column, are replaced with composite materials reinforced with carbon fiber, consist advantages of carbon fiber have:

- carbon fibers are very light, their density is  $\rho \approx 1.8 \text{ kg/dm}^3$
- Stiffness and E modulus is high in fiber direction
- fatigue-stiffness to high dynamic loads
- acid-resistance and high biocompatibility
- stressed anisotropic behavior.

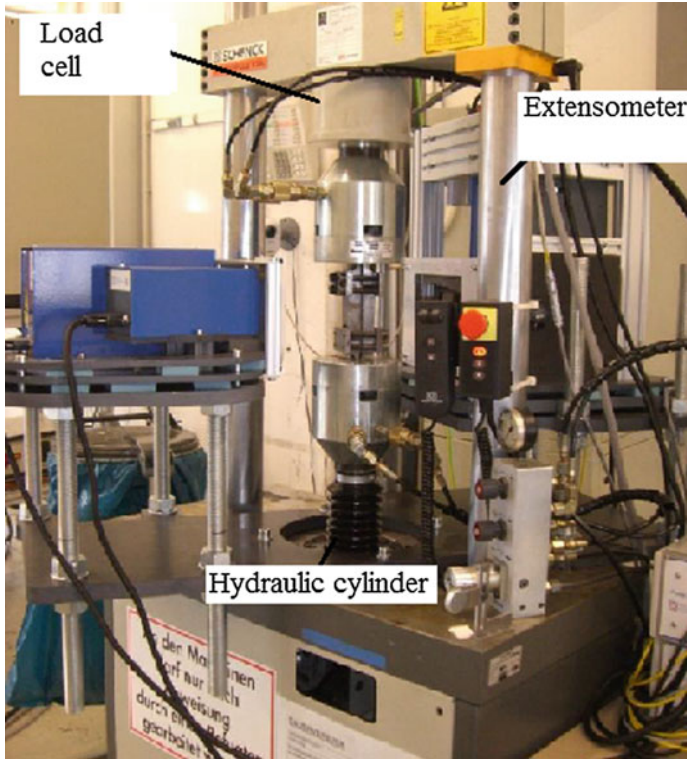


**Fig. 1** Hydraulic testing device

Composites steering column components must be lightweight, have a simple and cheap technology, to meet the requirements of the specifications and bring more innovation in vehicle technology (Heitz and Chiru2011).

The main requirements of the steering column extracted from the specification of the VW Golf 6 are presented below:

- Weight saving
- Natural frequency
  - Vertical  $>50$  Hz
  - Horizontal  $>50$  Hz
- Stiffness
  - Vertical  $\leq 1.6$  mm
  - Horizontal  $\leq 1$  mm
- Force control in climatic conditions of  $-30$  to  $+80$  °C
- Locking way and blocking force of action lever, including acoustic and a haptic behaviour

- Maximum permissible torsional moment
- Torsional stiffness

According to DIN EN ISO 527-1 requires 5 or >5 specimens and test results that the static tests are relevant.

In the following are shown force-displacement curves for the five specimens tested and calculation parameters characterizing composite materials.

### Tensile Parallel on Fiber Direction EN ISO 527

Tensile tests performed on a direction parallel to the fibers, in the same physico-chemical and mechanical conditions, showed a very different behavior of the two composites. It can be seen for HTS 40 crack brush, which indicates its higher rigidity and reduced deformation capacity comparing with T700 fiber (Figs. 2 and 3).

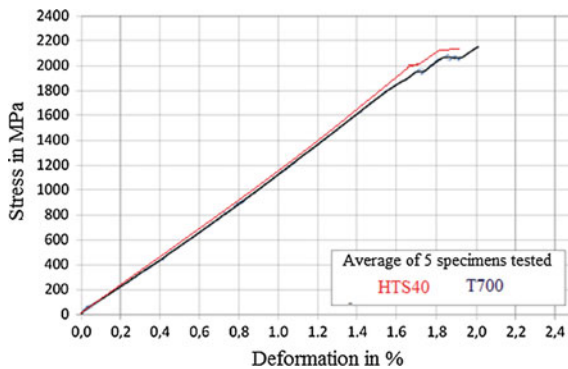


Fig. 2 Tensile stress-strain curve parallel to the fibers direction

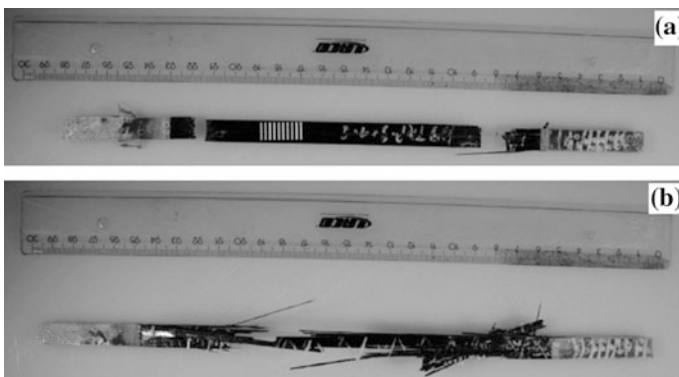


Fig. 3 The typical crack of the specimen T700 (a) and HTS40 (b)

### Tensile Perpendicular on Fiber Direction EN ISO 527

For those tests, the behavior of the two composites was almost identical, which we expect considering that we use the same matrix (Figs. 4 and 5).

### Compression Parallel on Fiber Direction EN ISO 14126

Compressive tests in direction parallel to the fibers produced unexpected results considering that the specimens began to crack to a load 3 times lower than for tensile testing (Figs. 6 and 7).

The variety of measured properties but their accuracy, they may provide information necessary finished product design, fiber placement, type matrix describing

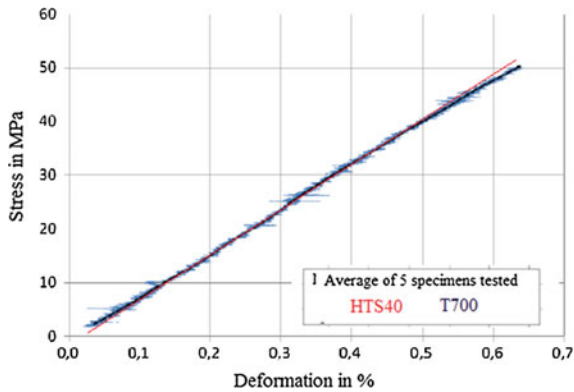


Fig. 4 Tensile stress-strain curve perpendicular to the fibers direction

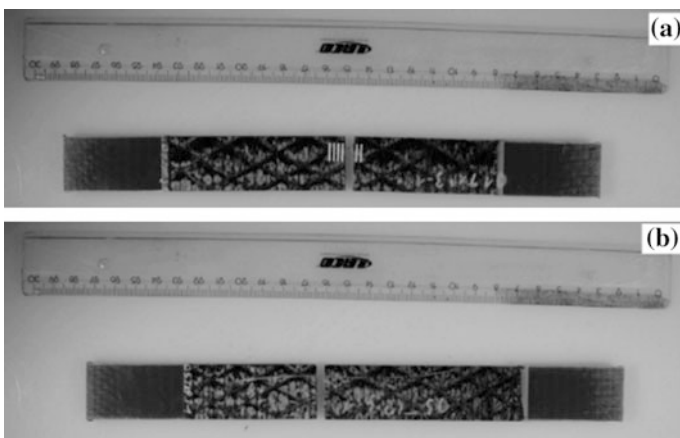


Fig. 5 Tensile typical crack of the specimen T700 (a) and HTS40 (b)

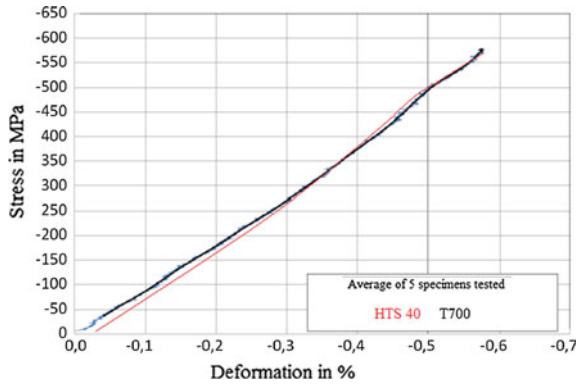


Fig. 6 Compression stress-strain curve parallel to the fibers direction

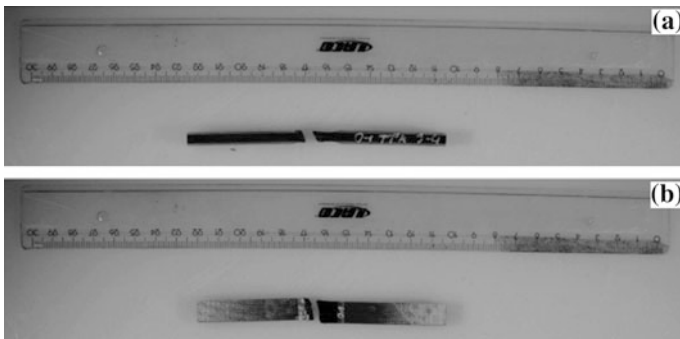


Fig. 7 Compression crack of the specimen T700 (a) and HTS40 (b)

the behavior of finished material information in various work environments and applicability in vehicle components.

Mechanical tests are standardized and that gives us the possibility of comparing different materials in the same terms.

### Compression Perpendicular on Fiber Direction EN ISO 14126

Tests show that, for both laminates, and the values obtained are comparable to the different nature of the fibers does not interfere with the quality of the composite material (Figs. 8 and 9).



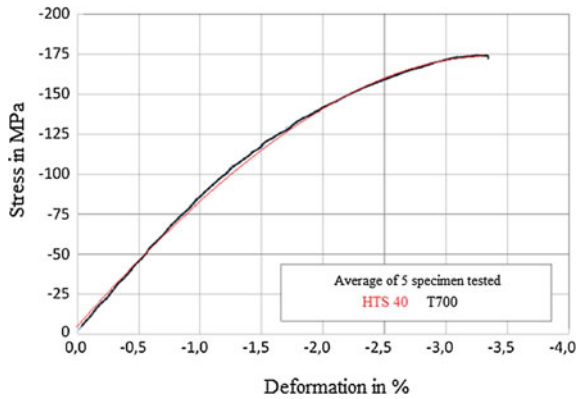


Fig. 8 Compression stress-strain curve perpendicular to the fibers direction

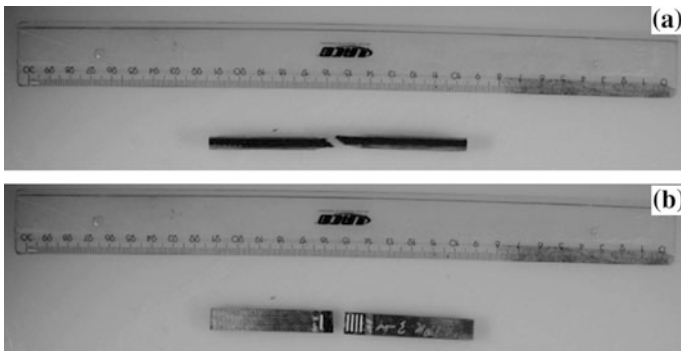


Fig. 9 Compression crack of the specimen T700 (a) and HTS40 (b)

### Tensile Tests ( $\pm 45^\circ$ Fibers Orientation) for Determining Shear Characteristics DIN 65466

The settlement of fibers, gives a high resistance of the composite even if it is subjected to combined loading.

Material behavior in shear loading is largely determined by the quality of the layout matrix and fibers used. Shear behavior of materials, the occurrence of residual stress and return to its original shape, is considered a main theme of research and will not be developed in this exposure.

Composite materials are strong in axial tension, and tensile test specimen, must be gripped in some manner for testing. It is proper to calculate the minor Poisson ratio from the measured transverse modulus, the axial modulus and the major Poisson ratio. For both carbon epoxy laminates, the axial compressive strength was nearly a constant value. The tests shows that, in case of both laminates, the values obtain are comparable

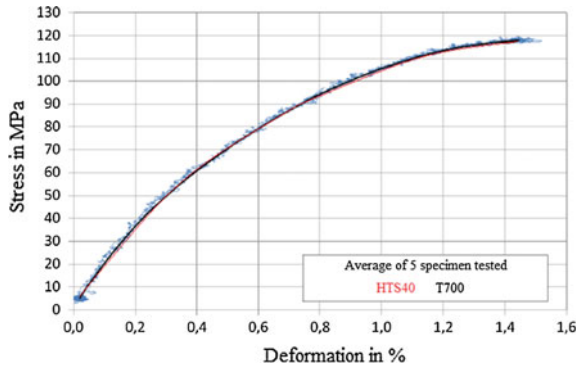


Fig. 10 Tensile stress-strain curve  $\pm 45^\circ$  to the fibers direction

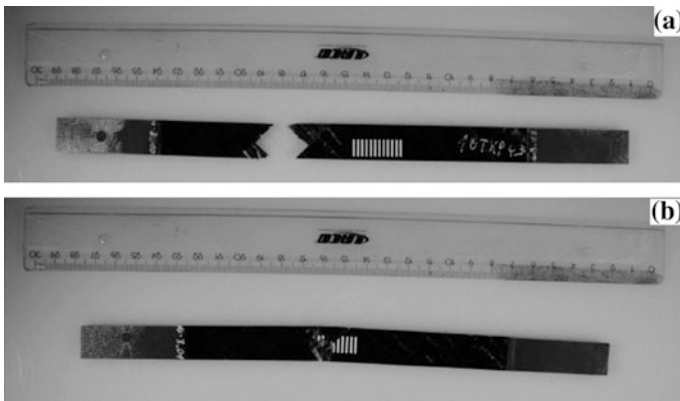


Fig. 11 The most common fracture pattern of the specimen T700 (a) and HTS40 (b)

and the different fiber nature, is not interfere with the quality of the composite material (Figs. 10 and 11). Besides these general tests, depending on the demands of the vehicle manufacturers, component designed specific tests are performed.

### *Console Steering Column Tests*

#### **Stiffness Horizontal and Vertical**

A highly rigid steering column will have its own frequency higher than a less rigid column. As a measure of stiffness is considered ratio force/displacement (N/mm). This report is the equivalent of elastic constant of the steering column. The value of the ratio is higher, we obtained the more rigid steering column. It is therefore desirable to achieve a high rigidity of the steering column. Radial stiffness

**Table 2** Stiffness values measured and FEM values

Stiffness (mm)	Test (mm)	FEM simulation (mm)
BS 1 vertical (<1.6)	±1.47	±0.96
BS 1 horizontal (<1.0)	±0.71	±0.73
BS 2 vertical (<1.6)	±1.45	±1.02
BS 2 horizontal (<1.0)	±0.85	±0.75

**Table 3** Frequency values measured and FEM values

Natural frequency (>50 Hz)	Real test (Hz)	FEM simulation (Hz)
BS 1 vertical	47	45.6
BS 1 horizontal	61.8	58.2
BS 2 vertical	45.3	45.5
BS 2 horizontal	59	57.9

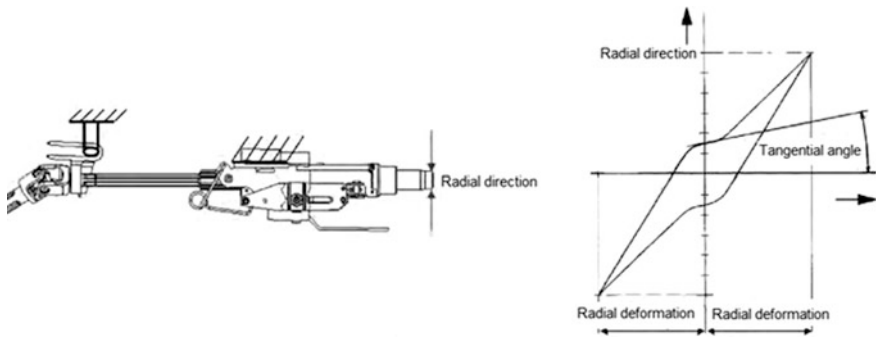


**Fig. 12** Graphical representation of stiffness measurement and the resulting diagram

measurement is made after the vertical and horizontal. Radial forces are applied to the end of the steering pipe. Here deflection is measured (Table 2).

For a defined radial force, resulting deflection should not exceed a certain limit. Tangent curve force/displacement is a measure of movements. The value of tangent at any point of the curve, there should be below a certain limit value (Fig. 12).

### Natural Frequency Horizontal and Vertical

The natural frequency of a complete steering column is measured on the vertical and horizontal Table 3. For this purpose the steering column is mounted on a rigid support. At the end piping steering column mounted a mass equivalent to multiple properties. Then, the steering column is brought into a specific position. On the board applies an acceleration transducer. The excitation frequency is effected by means of an impact hammer (Dirac pulse) in steering piping. If it is desired to measure the natural frequency in the vertical direction, the acceleration sensor is

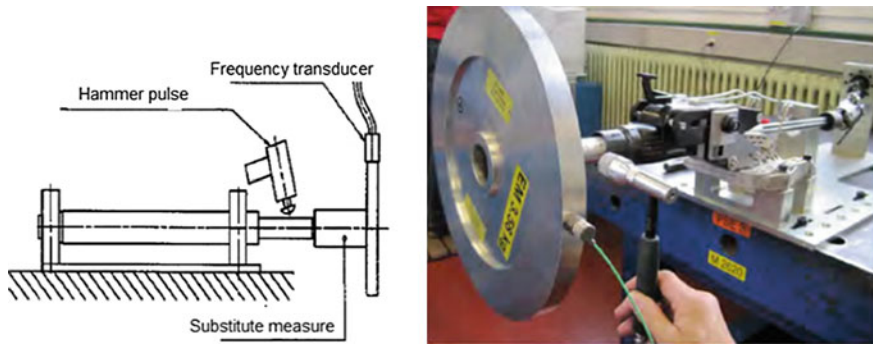


**Fig. 13** Natural frequency measurement

applied to the top or bottom surfaces of the equivalent mass, and the tubing is excited to vibration, to a mechanical impulse in the vertical direction. Measuring direction must correspond to the excitation (Fig. 13).

## Conclusions

The ultimate challenge when it comes to testing, the specimen tested and the component, to behave identically. Of course this depends on many factors, from geometry specimen, type test equipment, software, the results plotting environment in which testings are made.

Although testing devices are technologically evolve and are conducted studies on the behavior of the composite material components in both the specimen and composed, there are differences between the behavior of the specimen subjected to various tests and the results of parts subject to the same tests as the specimen. (Donald 1982).

Testing is the final component values of loads 30 % higher than the component values must resist

Test results of specimens and components in composite materials have shown that traditional materials can be replaced successfully. The quality of parts made of composite materials must be very good and constant in every section of the piece and manufacturing technology should allow the production of parts in high and very high series for automotive parts.

## References

- ASTM (2011) Annual Book of ASTM Standards, Volume 15.03, Space simulation; aerospace and aircraft; composite materials
- ASTM D 4762 (2011) Standard guide for testing polymer matrix composite materials

- Donald F (1982) Adams—CMH-17, composite materials handbook. In: Carlsson LA, Pipes RB (eds) Experimental characterization of advanced composite materials (volume 1). CRC Press, Boca Raton
- Heitz T, Chiru A (2011) Analysis of using CFK material for steering columns components in passenger vehicles—part 2. In: 13th EAEC Automotive Congress, C54, Valancia, FISITA
- Heitz T (2013) Performantele fizico-mecaniceale pieselor din materiale compozite utilizate pentru coloana de direcție a autovehiculului, Teză de doctorat, Brasov, România
- Hodgkinson JM (1990) An experimental comparison of ASTM, BSI and CRAG standard test methods for the determination of mechanical properties of composite materials, the centre for composite materials. Technical report 90/02, Imperial College, London
- Hodgkinson JM (2000) Mechanical testing of advanced fibre composites—published in North and South America. CRC Press LLC, Corporate Blvd, Boca Raton
- Iosipescu N (1967) New accurate procedure for single shear testing of metals. *J Mater* 2:537–566
- Taca C, Paunescu M (2012) Composite materials. MatrixRom, Bucuresti, ISBN 9789737558440

# Calculation of the Steering Column Bracket Made of Composite Materials Reinforced with Continuous Fibers

Lucian Rad, Anghel Chiru and Cristian Leahu

**Abstract** The purpose of this paper is to present calculus models for composite materials structure and their application for console steering column.

**Keywords** Composite materials · Calculus

## Introduction

Due the consistency of components of different nature, the mechanical behavior of composite materials is different from that of conventional materials. In case of composite materials, can't be applied to homogeneous and isotropic environment hypothesis, the study constitutive laws being made in a manner entirely different from that of conventional materials.

Depending on the scale of the analysis is done, the mechanics of composites consists of:

- micro-mechanics, studying the composite material on a microscopic scale, establishing elastic and mechanical characteristics in terms of interaction between phases components;
- macro-mechanics that analyzes the material on a macroscopic scale, assuming homogeneity assumption; phases influence is manifested in macroscopic components through global mechanical characteristics.

The efficiency of a composite material resulting in maximum utilization of physical-mechanical properties of each phase. According to it, we may enunciate assumptions:

- sectional dimensions of the primary elements are minimal reinforcement (reinforcement to consist of fibers);

---

L. Rad (✉) · A. Chiru · C. Leahu  
Transilvania University Braşov, Braşov, Romania  
e-mail: lucian.rad@unitbv.ro

- the volume fraction of fibers to be increased ( $V(f) > 50 \%$ );
- highlight the reinforcement direction so that the phases have a known geometry;

There are several models in the literature that could lead to the calculation of composite materials reinforced with long continuous fibers UD, but closest to our case and that highlights best console behavior, is linear model.

The two components of the composite, fibers and the matrix, take the load in different ways, depending on their rigidity. The way that the force applied is absorbed by components and their movements, depend on the relationship between the phases of the composite.

Both fiber and matrix having a linear elastic behavior can be modeled by the equivalence with resorts assembled in series or in parallel.

In a series assembly, the force is the same in both elements (regardless of cross-sectional shape and size) and displacements are inversely proportional to stiffness.

Assemble parallel shifts assumed equal loads directed along the axis. The force due to each element is proportional to its stiffness.

## Calculation of Composite Materials Steering Column Bracket

For console steering column was considered the model for calculating continuous fiber reinforced composites. This model is closest to the experimental results and has potential if we take into account coefficients of compensation depends largely on how the packaging of the fibers, such as fibers, the type of matrix, how impregnating fibers are and even and the heat treatment for polymerization of the component.

These characteristics are suitable for the landmark steering column that we aim to analyze.

The unit cell parameters for UD reinforced composites are:

- the distance between the fibers;
- the thickness or the distance between fiber layers, where there are several layers;
- an arbitrary size.

Fiber reinforced composite materials are part of heterogeneous and anisotropic material so that their mechanics is a much more complex than traditional materials.

*Environment heterogeneous and anisotropic material is an environment wherein its properties at any point and in any direction, are different.*

In case of hexagonal packing fiber, material will be transverse isotropic and will take only five parameters describing the elastic properties of the composite.

### Determining the Relative Proportions of Fiber $\phi$

Fiber composite material features is highly dependent on volume proportion of fiber, This proportion is defined by:  $M_f = V_f/V$  where  $V$  is the proportion of overall volume. In order to calculate the quantity of fiber and the fiber proportion of the volume, we proceed as follows (Figs. 1 and 2):

1. Select a suitable component manufacturing process.
2. The volume ratio is determined by the process of production, namely by the fiber preform related. Through winding technology it can be achieve a volume ratio standard  $M_f = 0.6$ .
3. Laminate strength calculations shall be made with volume ratio conditioned by the manufacturing process, determining the necessary thickness of the walls.
4. Knowing the wall thickness and fibers volume ratio, it can be determined amount of fiber needed and that the number of roving sites, deposits or fiber layers.
5. For fiber volume ratio it's imposed limitations by the geometric arrangement of the fibers.

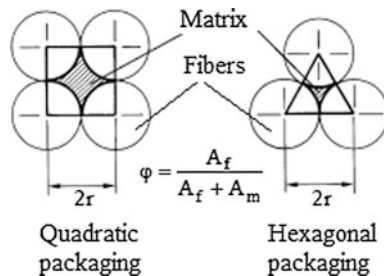


Fig. 1 Methods of packing fibers

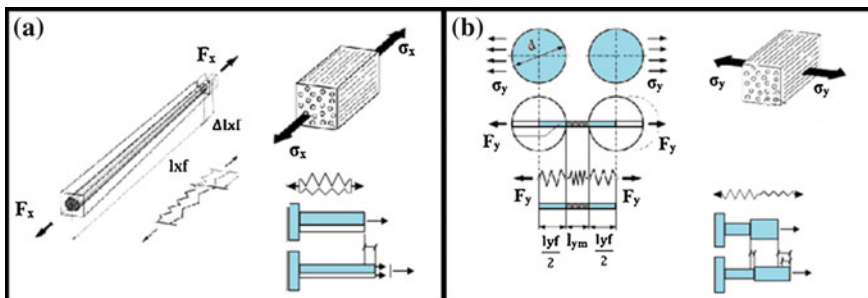


Fig. 2 Equivalence with parallel and series resorts



Thus the maximum fiber ratio volume resulting:

$$\varphi_{patratmax} = \frac{\pi}{4} = 0.79 \tag{1}$$

$$\varphi_{hexmax} = \frac{\pi}{2\sqrt{3}} = 0.91 \tag{2}$$

### Determination of Carbon-Epoxy Characteristics Material

To calculate the composite structure of the console, start from the constituent materials of the composite. The carbon fiber is SGL Sigrafil C30 50 K and the matrix is epoxy resin Epicote LR385 + LH385 (Table 1).

#### The characteristics of the carbon fiber and epoxy resin:

Composite material geometry:

After winding, beam appears as a solid cylinder. Rectangular geometry ( $h = 10 \text{ mm}$ ,  $t = 20 \text{ mm}$ ) is rendered using a tool (Fig. 3). Experimental established that the number of rovings must be 40 for the 24 K (1200 tex) carbon fiber and 15 for 50 K (3200 tex) carbon fiber.

$L$  length of analyzed unit cell (100 mm) (Fig. 4);

$S_f$  surface of the fiber;

$S_m$  surface of the matrix;

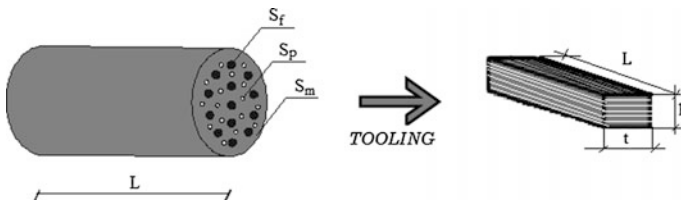
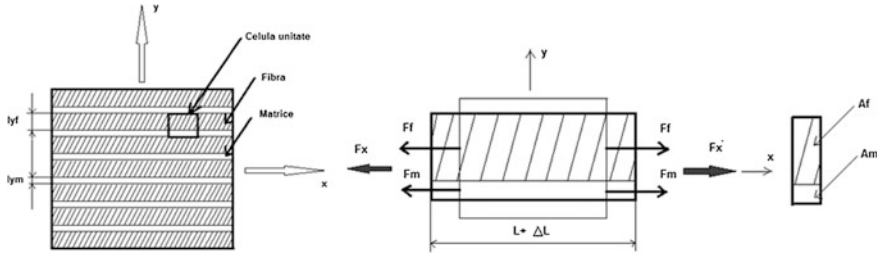


Fig. 3 Composite material geometry and desired geometrical dimension

Table 1 Values for carbon fiber and resin

Density	Carbon fiber		Matrix	
	Sigrafil C 3050 K		Epicote LR 385 + LH385	
	$\rho_f$	1800 kg/m <sup>3</sup>	$\rho_m$	1200 kg/m <sup>3</sup>
Modulus of elasticity	$E_f$	240 GPa	$E_m$	3.3 GPa
Poisson coefficient	$\nu_f$	0.3	$\nu_m$	0.4
Tensile strength at break	$X_f$	4000 MPa	$X_m$	350 MPa
Volumetric fraction	$V_f$	0.6	$V_m$	0.35



**Fig. 4** Section through a composite material layer and deformation in the x direction

$S_p$  surface of the porosity

- Density

$$\rho = \rho_f V_f + \rho_m V_m = 1800 + 0.6 + 1200 \times 0.35 = 1500 \text{ kg/m}^3 \quad (3)$$

- Longitudinal Young modulus in forces direction  $E_1$

$$E_1 = K E_f V_f + E_m V_m = 0.9 \times 240 \times 0.6 + 3.3 \times 0.35 = 130.75 \text{ GPa} \quad (4)$$

$K = 0.9$  (pot life coefficient)

- Longitudinal Young modulus perpendicular to forces direction  $E_2$

$$E_2 = E_f \times E_m / (E_f V_m + E_m V_f) = 240 \times 3.3 / (240 \times 0.35 + 3.3 \times 0.6) = 9.2 \text{ GPa} \quad (5)$$

- Poisson coefficient  $\nu_{12}$  and  $\nu_{21}$

$$\nu_{12} = V_f \cdot \nu_f + V_m \cdot \nu_m = 0.6 \times 0.3 + 0.35 \times 0.4 = 0.32 \quad (6)$$

$$\nu_{21} = \nu_{12} \cdot \frac{E_2}{E_1} = 0.32 \times 9.2 / 130.75 = 0.02 \quad (7)$$

- Transversal elastic modulus  $G_{12}$

$$G_f = \frac{E_f}{2(1 + \nu_f)} = \frac{240}{2(1 + 0,3)} = 92.3 \text{ GPa} \quad \text{and} \quad (8)$$

$$G_m = \frac{E_m}{2(1 + \nu_m)} = \frac{3.3}{2(1 + 0,4)} = 1.18 \text{ GPa}$$

$$G_{12} = \frac{G_f \cdot G_m}{V_f \cdot G_m + V_m \cdot G_f} = \frac{92.3 \cdot 1.18}{0.6 \cdot 1.18 + 0.35 \cdot 92.3} = 3.3 \text{ GPa.} \quad (9)$$

- Longitudinal tensile strength

It is based on the following hypothesis: breakage of the fibers when the tension grows, involves breaking of the composite because matrix can't sustain employment growth results.

– Deformation at brake for matrix

$$\varepsilon_{mR} = \frac{X_m}{E_m} = \frac{350 \cdot 10^{-3}}{3.3} = 0.1 \quad (10)$$

– Deformation at brake for fibers

$$\varepsilon_{fR} = \frac{X_f}{E_f} = 4000 \cdot 10^{-3} / 240 = 0.016 \quad (11)$$

$$\varepsilon_{mR} > \varepsilon_{fR} \gg X = V_f \cdot X_f + V_m \cdot \sigma_m^* = 0.6 \cdot 4000 \cdot 10^{-3} + 0.1 = 2.5 \text{ GPa} \quad (12)$$

$V_m \cdot \sigma_m^* = 0.1$  the average stress at break of the matrix  
 $X$  tension at break of the composite

Because  $X > X_m$  ( $V_f > V_{fcrit}$ ) we can say that we met reinforcement condition

- Longitudinal compressive strength

Analysis of the longitudinal compression composite is conducted in reaction to buckling fibers embedded in the matrix.

**Localized shear buckling** it occurs when the matrix is rigid (ceramic or epoxy), or if the reinforcement is multidirectional. Buckling fibers starts in matrix rich areas, in areas with large pores or where fibers are arranged parallel with compressive stress.

Because fiber volume fraction is high

$$X_{c1} = \frac{G_m}{1 - V_f} = \frac{1.18}{1 - 0.6} = 2.95 \text{ GPa} \quad (13)$$

Buckling is propagated at  $45^\circ$  to the effort of compression, resulting in a rupture of the fibers double bent.

Taking into account the of localized shear mode, longitudinal compression strength is:

$$X_{c2} = 2 \cdot (V_f \cdot S_f + V_m \cdot S_m) = 2 \cdot (0.6 \cdot 2.31 + 0.35 \cdot 0.2) = 2.91 \text{ GPa} \quad (14)$$

$$S_f = \frac{X_f}{\sqrt{3}} = 4000 \cdot 10^{-3} \frac{1}{\sqrt{3}} = 2.31 \text{ GPa} \quad (15)$$

$$S_m = \frac{X_m}{\sqrt{3}} = 350 \cdot 10^{-3} \frac{1}{\sqrt{3}} = 0.2 \text{ GPa} \tag{16}$$

$S_f, S_m$ —are the fiber shear strength and matrix shear strength

$$X_c = \min(X_{c1}, X_{c2}) = 2.91 \text{ GPa} \tag{17}$$

- Transversal compressive strength

Depending of fibers disposal, it lead to the concentration of stress on the matrix in areas between fibers. Once produced, the crack propagates in the interface matrix, perpendicular to stretch effort in the locations of the nearest fibers.

The breaking occurs by matrix shear. Considering matrix as being homogeneous and isotropic material,  $Y_c$  becomes:

$$Y_c = \frac{X_m}{\sqrt{3}} = 350 \cdot 10^{-3} / \sqrt{3} = 0.2 \text{ GPa} \tag{18}$$

### Comparison Between Calculation and FEM Analysis Results

We considered composite structure in the form of a beam.

The force acting on the structure was considered, according to the manufacturer’s specifications is

$$F = 500 \text{ N}$$

For comparison, I used a finite element analysis program ANSYS to simulate the behavior of the structure to the action of force (Figs. 5, 6, 7 and 8).

FEA test results showed us a displacement of 0.503 mm to 0.306 for horizontal forces and vertical forces.



Fig. 5 Components of the stress—horizontal forces

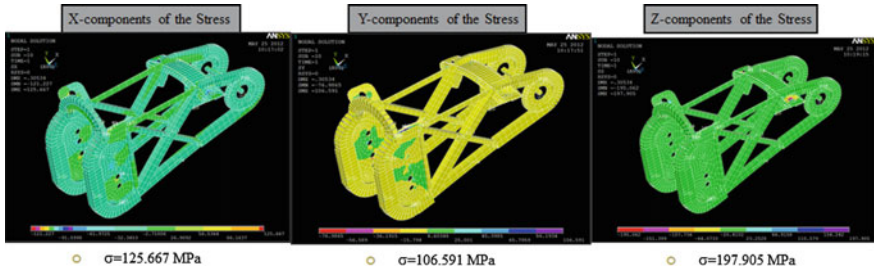


Fig. 6 Components of the stress—vertical forces

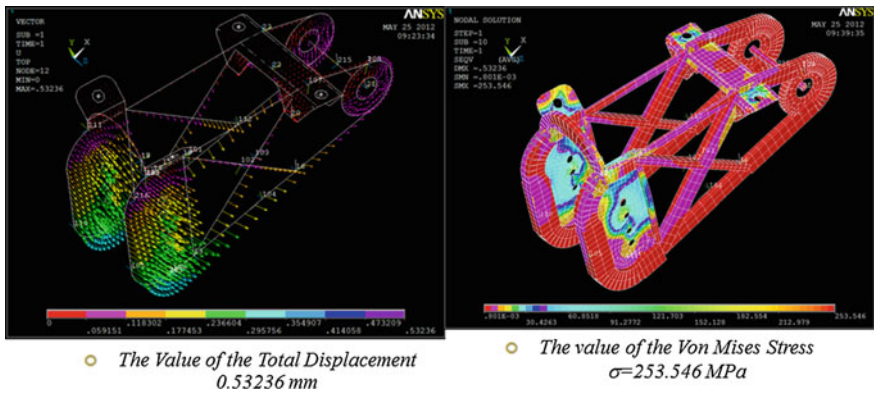


Fig. 7 Results for total displacement and von Mises Stress for horizontal forces

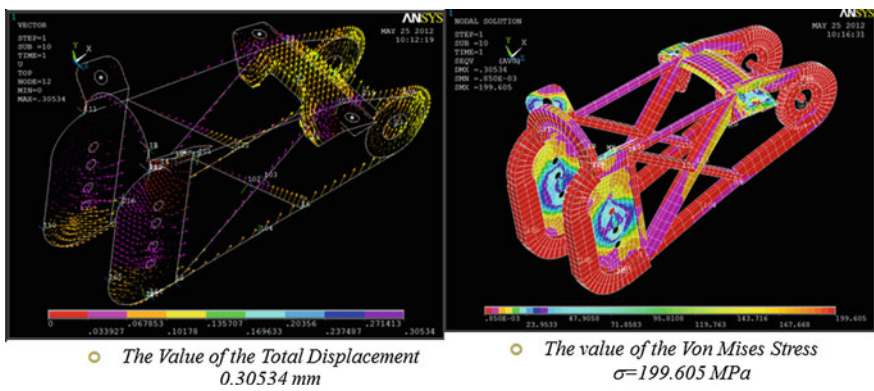


Fig. 8 Results for total displacement and von Mises Stress for vertical forces

If we compare the calculated displacement traction (1.16 mm), we conclude that the differences between results are very large and therefore not conclusive.

The next steps are for recalculate with different model and modification of the beam:

- change the position of applying force
- change sizes of the beam sections
- change type of connection between elements
- build complete model with column jacket.

## References

- ASTM Annual Book of ASTM Standards, Volume 15.03, Space Simulation; Aerospace and Aircraft; Composite Materials
- ASTM D 4762, "Standard Guide for Testing Polymer Matrix Composite Materials
- Curtis PT (1988) CRAG test methods for the measurement of the engineering properties of fibre reinforced plastics. Royal Aircraft Establishment, Technical Report 88012, Farnborough, UK
- Donald F (2014) Adams-CMH-17, composite materials handbook. In: Carlsson LA, Pipes RB (eds) Experimental characterization of advanced compositematerials, vol 1. CRC Press, Boca Raton, FL
- Heitz T (2013) The physical-mechanical properties of structural components made of fiber composite materials in the application of steering columns in cars. Doctoral Thesis, Brasov, Romania
- Heitz T, Chiru A (2011) Analysis of using CFK material for steering columns components in passenger vehicles—Part 2. FISITA, 13 EAEC Automotive Congress, Valancia
- Iosipescu N (1967) Journal of Materials, pp 537–566
- T Heitz-Performantele fizico-mecaniceale pieselor din materiale compozite utilizate pentru coloana de direcție a autovehiculului, Teză de doctorat, 2013, Brasov,România
- Taca C, Paunescu (2012) Composite materials. MatrixRom, Bucuresti, ISBN 9789737558440

# A Method for 3D Geometry Scanning of a Combustion Chamber

Dan Mihai Dogariu, Ciprian Andrei, Bogdan Tiberiu Vieru,  
Radu Adrian Plămădeală and Anghel Chiru

**Abstract** In order to perform virtual analyses, especially for gas exchange and thermodynamic simulations, and to compare the results obtained with the measured data on the research engine, the virtual geometry should match accurately the one of the real engine. For this reason, the objective of the paper is to present a method for obtaining a high accurate 3D model of a real combustion chamber and other supplementary geometry due to the particular shape required for virtual simulations. The paper presents a method for obtaining an accurate 3D model of the combustion chamber using high end touch probe 3D scanning technology. The results obtained represent cloud point data available to be imported in most of the 3D design software. From here, the 3D model was reconstructed. Methods for reverse engineering are also presented, where complex, numerous points had to be managed.

**Keywords** 3D scanning · 3D model · Internal combustion engine · Metrology

---

D.M. Dogariu (✉) · A. Chiru  
Department of Automotive and Transport Engineering, Transilvania University of Brasov,  
Brasov, Romania  
e-mail: dan.dogariu@gmail.com

A. Chiru  
e-mail: achiru@unitbv.ro

C. Andrei · B.T. Vieru · R.A. Plămădeală  
Technical Analysis, SC Schaeffler Romania SRL, Cristian, Romania  
e-mail: andreopr@schaeffler.com

B.T. Vieru  
e-mail: vierubgd@schaeffler.com

R.A. Plămădeală  
e-mail: plamardu@schaeffler.com

## Introduction

The combustion chamber of a classic internal combustion engine is the place where the fuel—air mixture burns, resulting in a volumetric expansion at high temperatures and pressures, which will generate power through the reciprocating mechanism. The volume of the combustion chamber is the remaining domain when the piston reaches TDC. However, in order to analyze a complete gas exchange cycle or to perform a combustion simulation, the entire volume of the cylinder swept by the piston must be considered supplementary to the combustion chamber volume. This is the reason for the necessity of a high accurate 3D model of the entire combustion chamber.

The combustion chamber belongs to a research gasoline single cylinder engine used for thermodynamic tests at the Research Institute of Transilvania University of Brasov.

In order to perform virtual analyses and to compare the results obtained with the measured data on the research engine, the virtual geometry should match accurately the one of the real engine.

The 3D model of the actual interior surfaces of the studied engine was achieved by 3D scanning. The technique used in this paper implies a high end touch probe Coordinate Measuring Machine (CMM).

## Description of the Used 3D Scanning Methodology

For determining the geometry of the interior surfaces of the engine, which are exposed to the burning process, a touch probe bridge-type CMM was used. The methodology for 3D scanning is based on the general metrology principles and operating procedures of a high end touch probe 3D scanner, equipment used in a special measurement laboratory.

A CMM is a measuring system with the means to move a probing system and the capability to determine spatial coordinates on the surface of the part being measured (Leach 2014). The CMM used to scan the required engine components is illustrated in Fig. 1.

The CMM may collect spatial information through many ways. One of the common ways are either through discrete probing, where data from single points on the surface are collected, or by scanning, where points are collected automatically, in a continuous manner, as the stylus tip is dragged across the measured surface (Leach 2014).

There are different probing systems that can be attached to a CMM, such as (Leach 2014):

- Analogue or a scanning probe;
- Touch trigger probe;
- Probes that employs optical technology.



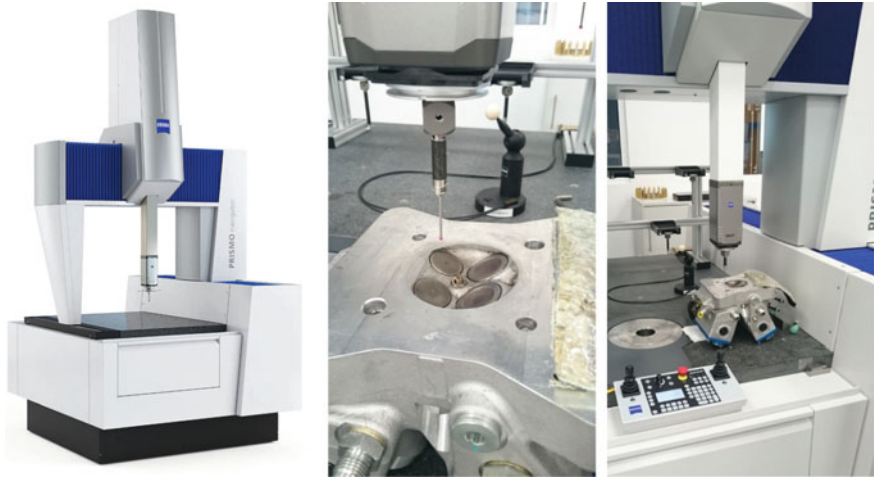


**Fig. 1** The bridge-type CMM used to measure the engine components

**Table 1** Main characteristics of the CMM and touch probes used (CMM product overview, PRISMO overview, Touch probe specifications)

Length measuring error	$0.9 + L/350 \mu\text{m}$
Repeatability range	$0.8 \mu\text{m}$
Scanning error	$3.0 \mu\text{m}$
Sensor overview	Active scanning probe
Probing force	Constant—it can be programmed between 50 and 1000 mN
Smallest stylus tip diameter	$0.3 \text{ mm}$
Travel speed	$0\text{--}70 \text{ mm/s}$ , when motorized

For this measuring study a touch probe with various ball diameters was used.

The main characteristics and parameters of the CMM and touch probes used are presented in Table 1 (CMM product overview,<sup>1</sup> PRISMO overview,<sup>2</sup> Touch probe specifications<sup>3</sup>).

The CMM is controlled from a PC, from where the strategies are programmed. The scanning software allows specifying for each path the starting, ending point and number of points/unit length to be collected.

Because there are several components involved in the construction of the proposed combustion chamber, the engine was dismantled and the parts were scanned individually. Some parts had to be scanned preassembled for a better reproduction of assembly dimensions, such as valve lift, spark plug geometry and injector nozzle.

<sup>1</sup>Industrial Metrology in Focus, Carl Zeiss brochure.

<sup>2</sup>PRISMO navigator sensor and accuracy overview. [www.optecgroup.com](http://www.optecgroup.com).

<sup>3</sup>[www.zeiss.com/industrial-metrology/en\\_us/products/sensors](http://www.zeiss.com/industrial-metrology/en_us/products/sensors).

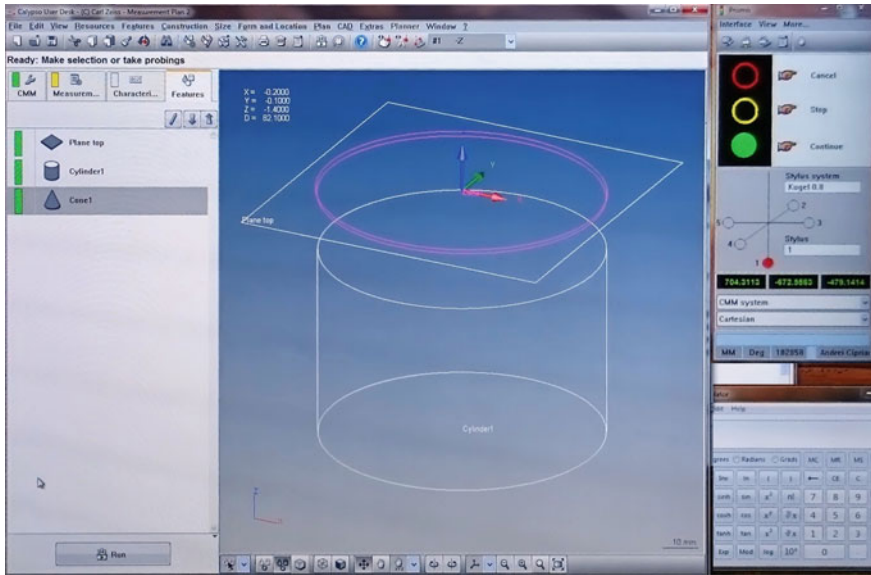


**Fig. 2** The control window of the CMM

In order to measure a component, its alignment relative to the coordinate system of the machine needs to be described. The alignment is usually made using datum features of the part, or when these are difficult to find or missing, auxiliary datum have to be created.

Depending on the shape of the object that must be scanned, different scanning approaches can be adopted. For the engine components, a free-form strategy for scanning was used, where the scanned surface was contacted at a large number of points by using grids, linear elements, circular elements and also singular point sets (Leach 2014).

For instance the liner, a relatively simpler component than the piston head surface, was scanned with several cross-sections with a defined axial pitch, to cover the entire piston stroke, especially the chamfer at TDC. This chamfer was scanned with the cone strategy of the 3D scanner (Zeiss Calypso documentation 2014). A snapshot of the predefined cone strategy on the control computer, can be seen in Fig. 2.

The rest of the complex geometries, like piston and the interior of the cylinder head were scanned with a strategy for unknown profiles. For this strategy, the touch probe is advancing with a smaller velocity on prescribed paths, like lines, circles and arches. More complex paths can be used, but they must be programmed first. For a simpler, efficient method, grid lines were drawn over the piston head surface. This method is known as digitization and is frequently used for industrial reverse engineering applications, when precision is the most important factor (About 3D scanning<sup>4</sup>).

<sup>4</sup><http://www.dirdim.com>.

As for the cylinder head, it was placed upside down on the bed of the 3D scanner and grid lines were also drawn, except for the center point, where the spark plug was placed. Here, other strategies were applied, as single point collection.

All the data collected, as cloud point data, needs to be imported into CAD software, in order to create a 3D geometry.

### Reconstruction of the 3D Model

After importing the cloud point data into individual cloud points for each feature which define a geometrical entity, the reconstruction begins. The main step is to interpret the cloud points into 3D smooth curves.

Figure 3 presents the original measured points, with certain dispersion, superimposed with the filtered cloud point data and the resulted 3D curve, which represents the interior of the cylinder liner.

The piston shows a more complex geometry, which had to be measured by aligning a grid, such that key elements of the surface to pass through this grid, relative to a symmetry plane. In Fig. 4, there is presented the piston on the CMM bed ready to be scanned, at left, and the reconstructed 3D model, at right. During measuring, a  $7 \times 15$  grid was collected, but also arc entities were collected over the surface of the valve emboss area.

Results of the 3D reconstruction are presented in Fig. 5. At left, the resulted 3D model of the piston, respectively at right, the 3D model of the cylinder head. The model of the cylinder head includes the intake and exhaust valves together with the

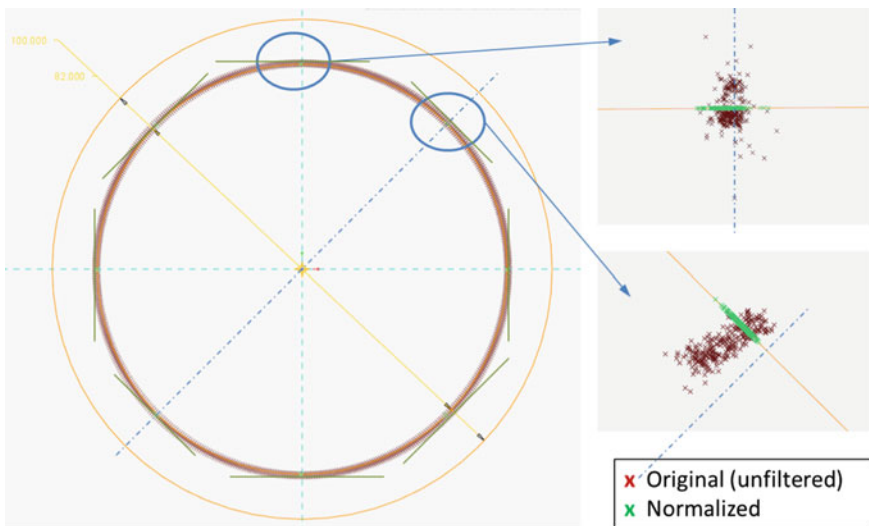
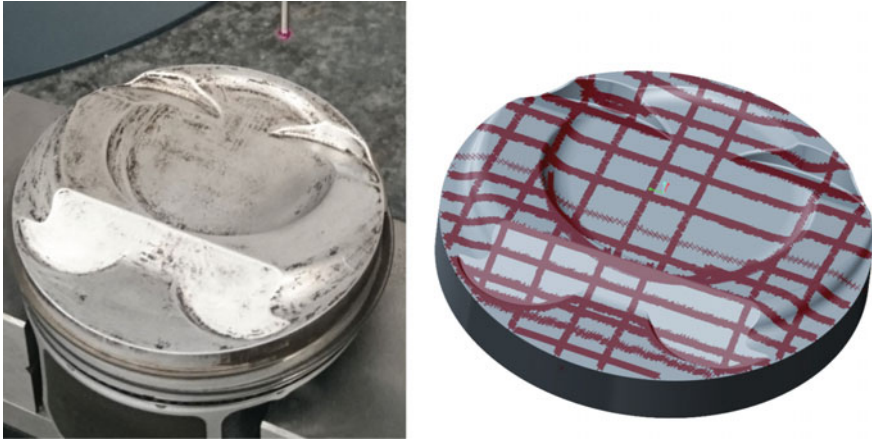
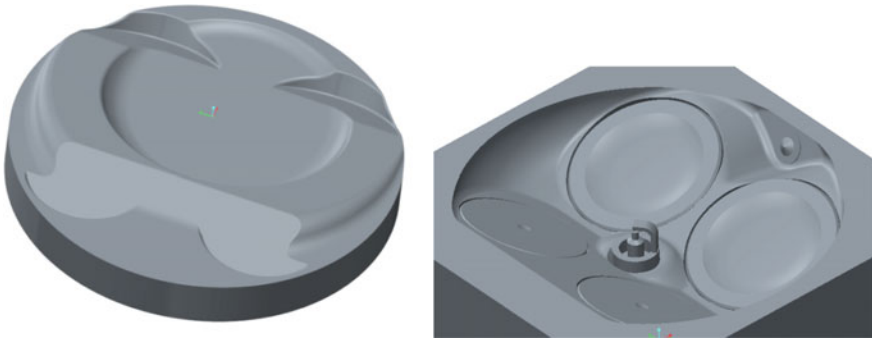


Fig. 3 The strategy used to measure the cylinder liner



**Fig. 4** The piston head surface, during measuring *left*, point cloud in CAD *right*



**Fig. 5** The resulted piston head *left*, cylinder head *right*

spark plug and injector. These elements had to be scanned while being assembled, for a better reproduction of the real situation. The 3D model also includes all these elements. The exact geometry is required for further thermodynamic simulation studies. Having an exact 3D replica of the existing and firing engine, one could compare the results obtained in the simulation with the results on the test bench, having a better equivalence.

## The Resulted 3D Model for a FEA

After having the complete 3D models of the components and assemblies that build the combustion chamber scanned and reconstructed, the first step for a finite element analysis is following, that is preparation of the model.

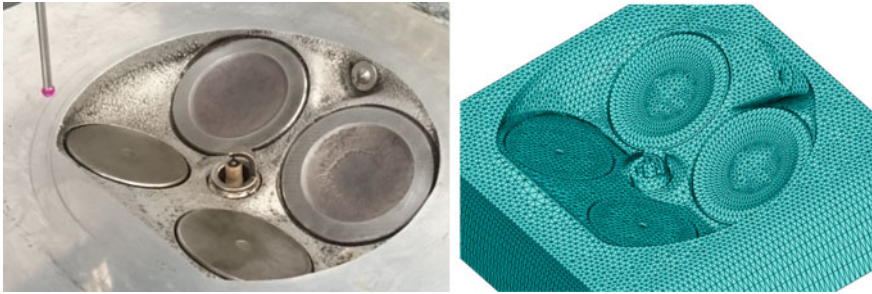


**Fig. 6** The cylinder head, during measuring *left*, 3D mesh in FEA *right*

The resulted 3D mesh of the cylinder head assembly, after importing the 3D model into a FEA software, can be seen in Fig. 6, at right and it reveals detailed regions of the model with a finer mesh. As a similarity to the real geometry, the real geometry and its corresponding 3D mesh are presented one next to another in Fig. 6.

This similarity confirms the accuracy of the 3D model comparing to the real geometry, thus the accuracy of the scanning method used for this study. This allows the use of this 3D model for further computational analyses, which can later be compared to actual laboratory measurements.

## Conclusions

Comparing to laser cloud point 3D scanners, the Coordinate Measuring Machine (CMM) does not require additional surface preparation in case of shiny surfaces and it provides comparable accuracy (Zheng 2012). This CMM has offered valuable information on special components of the research engine, like the cylinder liner.

There are always imperfections and small differences between the finished parts and the original, ideal 3D models, which the designer builds. Depending on the type of simulation, these differences might have an influence on the results, regarding swirl and tumble flow dynamic phenomena.

The scanned geometry offers a great accuracy of the 3D model with respect to the finished parts. For this reason, especially because original 3D models were unavailable, the parts were scanned. It is possible for the research engine to be modified for improvements.

When using the models for a CFD analysis, the level of detail for geometry is very important. Thus, the 3D model used for analysis must show a level of detail correspondingly to the case situation.

Limitations of the proposed study came from the difficulty in reproducing the 3D model of complex components based on the cloud point data.

## References

- Leach R (2014) Fundamental principles of engineering nanometrology, 2nd edn. William Andrew, New York, pp 295–321
- Zeiss Calypso documentation (2014)
- Zheng S (2012) A method of 3D measurement and reconstruction for cultural relics in museums. XXII ISPRS Congress, Melbourne

# Researches to Improve the Reliability of Clutches with Dual-Mass Flywheel

Valentin Nişulescu, Gheorghe Bancă, Marius Bâzgă  
and Alexandru Boroiu

**Abstract** The paper presents a qualitative and quantitative analysis of the reliability of the dual mass flywheels used in the clutches, based on the collection, analysis and modeling of technical data from the post-sale life of the road vehicles. In all cases the distribution of the malfunctioning times can be modeled using the normal law and that shows that the malfunctions are caused by the normal damaging processes: wearing processes and material ageing processes. The two most common faults malfunctions are not caused by the improper quality of one of the components. So, an excessive sliding between the clutch disk and the two metallic disks composing the dual mass flywheel is it determined by the design of the dual mass flywheel or by the improper driving style, and the grooves generated by the rivets of the clutch disk worn above the limit could be avoided if the clutch disk is replaced before exceeding the wear limit state—process depending on the maintenance system. The conclusions show the fact that based on the reliability can be redesigned the maintenance schedule for each type of vehicle (according to the established concept of “maintenance based on reliability”), which will ensure the improvement of the reliability and, as a result, the reduction of the ownership costs for the vehicle.

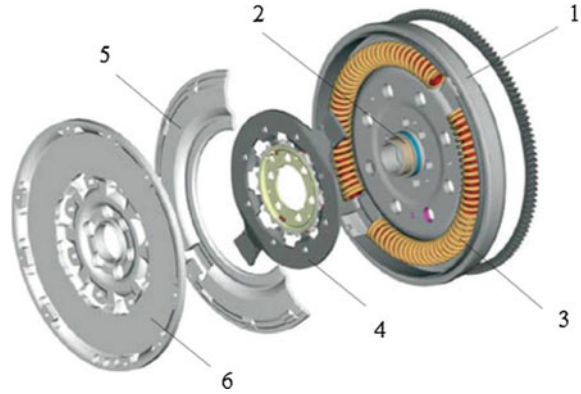
**Keywords** Clutch · Dual mass flywheel · Malfunction process · Reliability modeling

---

V. Nişulescu (✉) · G. Bancă  
University Politehnica Bucureşti, Bucharest, Romania  
e-mail: nisulescu.valentin@yahoo.com

M. Bâzgă · A. Boroiu  
University of Piteşti, Piteşti, Romania

**Fig. 1** Dual mass flywheel. 1 primary flywheel; 2 bearing; 3 helical spring; 4 flange; 5 cover; 6 secondary flywheel



## Introduction

By analyzing the data obtained from more than 40,000 service charts for vehicles (with various mileages, from 1 to 756,243 km) was observed that the highest frequency of the malfunction of the components occurs in the clutches with dual mass flywheel (962 malfunctions). As a result, in order to improve the reliability of the vehicles, the studies must be focused mainly on those vehicles equipped with an actuating assembly that contains a clutch with dual mass flywheel, like in Fig. 1 (Bâzgă 2013).

For this, the available data was further studied and it was observed that the frequency of the malfunctions is different depending on the engine. As such, the number of malfunctions (ordered decreasingly) depending on the engine (the codes vary for engines with varied functional characteristics, maximum power and maximum engine torque) are presented in Table 1.

**Table 1** Frequent breakdowns of dual mass flywheel

Engine code	Cylinder capacity/maximum power	Maximum torque	Number failure
A	1.9 TDI PD/77 kW	250 Nm at 1900 rpm	157
B	2.0 TDI PD/103 kW	320 Nm at 1750 rpm	142
C	1.6 TDI CR/77 kW	250 Nm at 1500 rpm	90
D	1.9 TDI PD/77 kW	250 Nm at 1900 rpm	46
E	1.9 TDI PD/66 kW	210 Nm at 1800 rpm	41
F	2.0 TDI CR/103 kW	320 Nm at 1750 rpm	32
G	2.0 TDI PD/103 kW	320 Nm at 1750 rpm	29
H	2.0 TDI CR/81 kW	250 Nm at 1500 rpm	17
I	2.0 TDI CR/100 kW	320 Nm at 1750 rpm	16
J	2.0 TDI CR/103 kW	320 Nm at 1750 rpm	11



**Table 2** Malfunctions observed in the service charts for the dual mass flywheel

Number	The malfunctions observed, their causes and consequences
1	Grooves on the friction surface of the flywheel caused by the rivets of the worn clutch disk, limiting the transmitted power
2	Extensive dark color stains and fissures on the friction surface, caused by overheating
3	Worn bearing/abnormal operating clearance ⇒ tightness losses ⇒ grease leaks from the flywheel ⇒ springs damage
4	Broken flywheel ⇒ tightness losses ⇒ grease leaks from the flywheel ⇒ springs damage
5	Flywheel seized due to the dust generated by the friction material
6	Stress relieving springs flywheel, reducing torsional vibration damping level

In addition, in Table 2, are presented the main types of malfunctions observed in the service charts for the dual mass flywheel and their causes and consequences. The malfunctions observed, their causes and consequences:

### Experimental

Was observed that the data are sufficient in number for statistical processing for the first 5 engine codes, and as a result they were further analyzed. As can be seen in the following paragraphs, the histograms created for the frequency of malfunction times present for all five engines the known Gauss bell shape, as such the experimental distributions were modeled using the usual law.

The two parameters for the malfunction times were calculated (Boroiu 2014):

- *mean of the operating time*, calculated with the formula (1):

$$m = \frac{\sum_{i=1}^{N_0} t_i}{N_0} \tag{1}$$

where  $t_i$  are the malfunction times, and  $N_0$  is the number of recorded malfunctions.

- *the average square deviation  $\sigma$  or the standard deviation  $s$* , when calculating based on the mean, determined with formula (2):

$$s = \sqrt{\frac{\sum_{i=1}^{N_0} (t_i - m)^2}{N_0 - 1}} \tag{2}$$

Next, was employed the special sub-routine from the software Microsoft Excel to represent the normal functions defined by the calculated parameters  $m$  and  $s$ ,

according to the analytical formula (3) for the probability density of the operating time.

$$f(x) = \frac{1}{\sigma\sqrt{2\pi}} \cdot e^{-\frac{(x-m)^2}{2\sigma^2}} \tag{3}$$

At the same time, were considered the malfunctions observed in the service charts (numbered at 6), and their causes and consequences, presented in Table 2, it becomes interesting to analyze the distribution of the malfunctions observed for each type of engine.

### Results and Discussion

Considering the calculation of the *mean of the operating time*, the *average square deviation*  $\sigma$  or the *standard deviation*  $s$ , and the *probability density of the operating time* by using the formulas (1), (2) and (3) were obtained the histograms and diagrams 1, 2, 3, 4, 5 (Figs. 2, 3, 4, 5 and 6) for the engine codes A, B, C, D, E modeled as follows (Boroiu 2013):

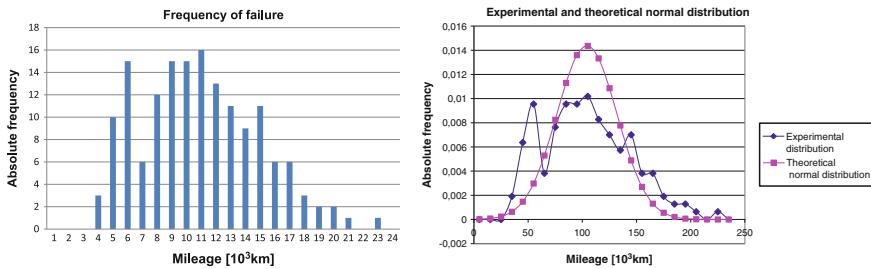


**Fig. 2** Histogram 1: Engine code A: 157 malfunction. Distribution 1:  $m = 104,235$  km;  $s = 27,757$  km

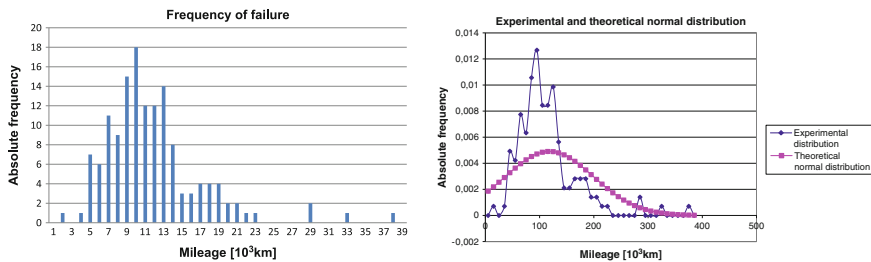


**Fig. 3** Histogram 2: Engine code B: 142 malfunction. Distribution 2:  $m = 11,3028$  km;  $s = 81,153$  km

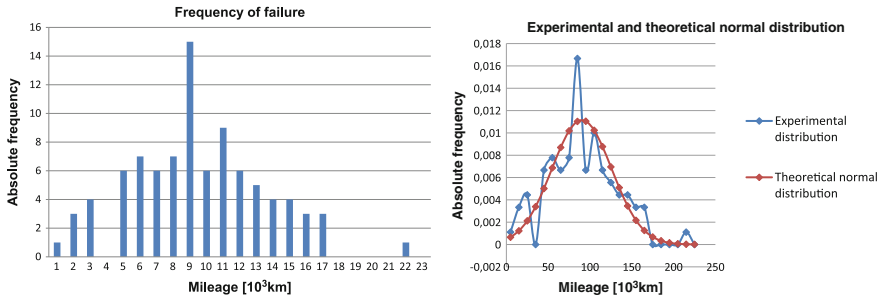


**Fig. 4** Histogram 3: Engine code C: 90 malfunction. Distribution 3:  $m = 90222$  km,  $s = 35795$  km

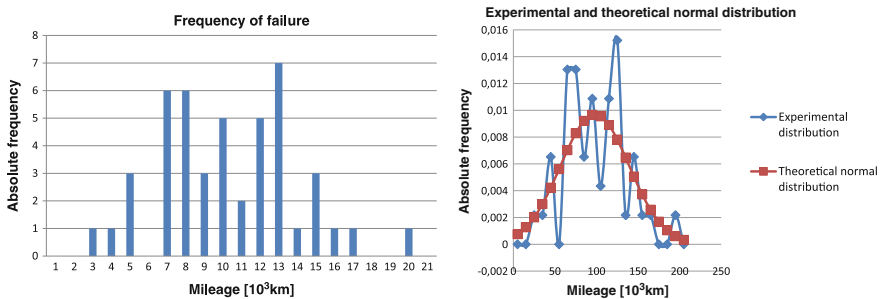


**Fig. 5** Histogram 4: Engine code D:46 malfunction. Distribution 4:  $m = 98043$  km,  $s = 41182$  km

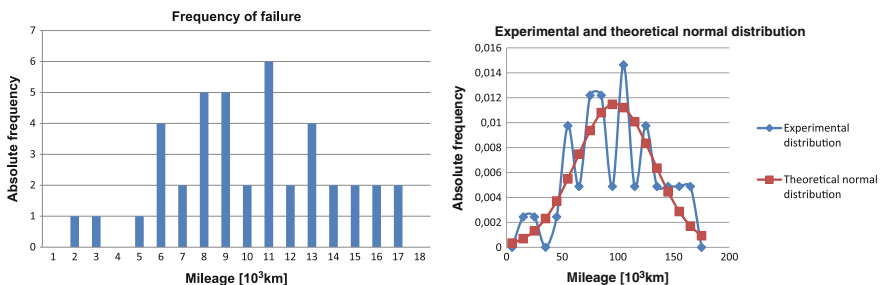


**Fig. 6** Histogram 5: Engine code E: 41 malfunction. Distribution 5:  $m = 97195$  km,  $s = 34704$  km

Representing on the same graph, for each type of engine, the experimental distribution and the normal theoretical distribution, can be observed in all cases that the distribution of the malfunction times can be modeled with the normal law. The fact that the reliability can be described by the normal model shows that the malfunctions are caused by the normal damaging processes: Wearing processes and material ageing processes (O’Connor 1991). By comparison, the two parameters of the statistic distributions are presented in Table 3.

**Table 3** Values of the reliability parameters for the dual mass flywheel determined for various engines

Engine code	Number malfunction	Average of car mileage (10 <sup>3</sup> km)	Standard deviations (10 <sup>3</sup> km)
A	157	104	27
B	142	113	81
C	90	90	35
D	46	98	41
E	41	97	34

Can be observed that the values of the means are approximately the same for all 5 engines analyzed (the highest value is for engine B), but the values of the standard deviations show a high variation (the smallest value for the standard deviation is shown for engine E). The malfunctions observed in the service charts (numbered at 6), and their causes and consequences, presented in Table 2, were highlighted with the graphs 6, 7, 8, 9, 10 (Figs. 7, 8, 9, 10 and 11) representing the distribution of the types of malfunctions, as follows:

**Fig. 7** Graphic 6: Distribution of the malfunctions types based on the malfunctions frequency for engine A

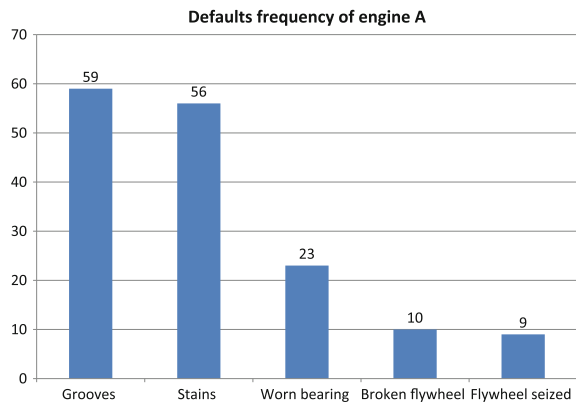


**Fig. 8** Graphic 7: Distribution of the malfunctions types based on the malfunctions frequency for engine C

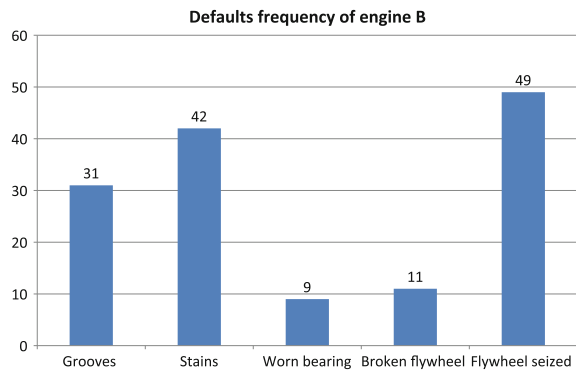


**Fig. 9** Graphic 8:  
Distribution of the malfunctions types based on the malfunctions frequency for engine C

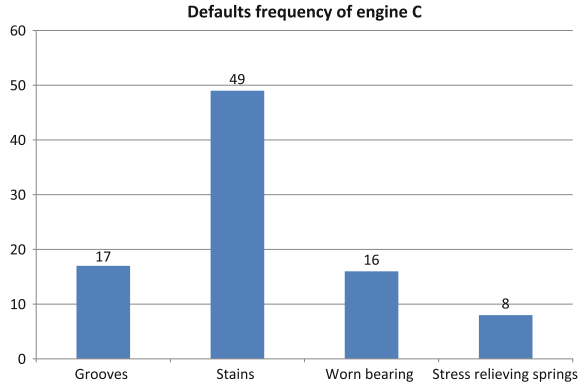


**Fig. 10** Graphic 9:  
Distribution of the malfunctions types based on the malfunctions frequency for engine D

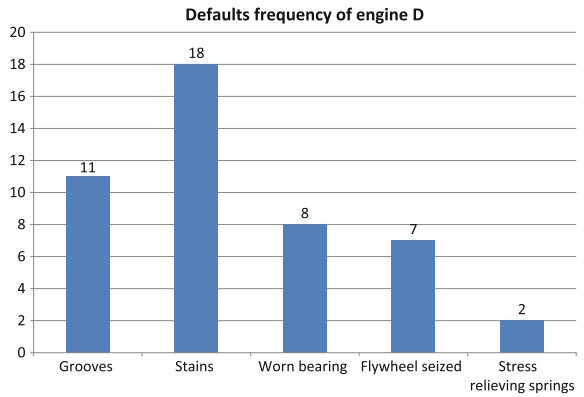
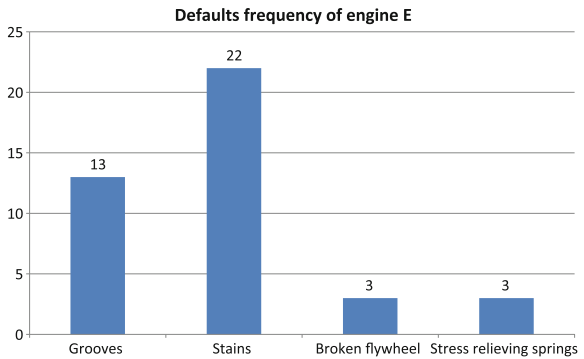


**Fig. 11** Graphic 10:  
Distribution of the malfunctions types based on the malfunctions frequency for engine E



The most frequent malfunctions for the 5 types of engines can be observed to be the “*Extensive dark color stains and fissures on the friction surface, caused by overheating*” followed by “*Grooves on the friction surface of the flywheel caused by the rivets of the worn clutch disk, limiting the transmitted power*”.

It is interesting to notice that these two malfunctions are not caused by the improper quality of one of the components. As such, the overheating indicates an excessive sliding between the clutch disk and the two metallic disks composing the dual mass flywheel—process depending on the design of the dual mass flywheel or the improper driving style, and the grooves generated by the rivets of the clutch disk worn above the limit could be avoided if the clutch disk is replaced before exceeding the wear limit state—process depending on the maintenance system.

Knowing the normal model for each distribution of the malfunction times for the dual mass flywheel (mean  $m$  and the standard deviation  $\sigma$ ) and imposing a minimum reliability level for this component of the clutch, using the tables for the Laplace function can be determined for each engine actuating the vehicles the mileage for which it becomes required to examine the technical state of the dual mass flywheel, which will impose the changing of the maintenance schedule. Thus will be ensured the highest reliability level, while minimizing the maintenance costs and, as a result, the ownership costs for the vehicle (an advantage for the owner).

For example, according to the tables for the Laplace function (Andreescu 1996), for a value of the mileage of  $(m - 2\sigma)$ , the reliability decreases with the value of 2.27 %. Thus, if it is imposed a minimum reliability level of 97.73 % (which is a good enough level) this means that the preventive replacement of the dual mass flywheel must be conducted before the mileage of  $(m - 2\sigma)$ .

Considering the values for  $m$  and  $s$  statistically determined and presented in Table 3, in order to ensure this minimum reliability level must be conducted maintenance interventions before or near the mileages of  $(m - 2\sigma)$ —Table 4.

Can be observed that the operation for checking the technical state of the dual mass flywheel can be provided in the technical checks presented in Table 4.

It presents a concern the fact that for the engine type B resulted that this check must be conducted even while preparing for sale such a situation is unacceptable and thus imposes the mandatory solving by design or manufacturing of this serious reliability problem. The status of the other engines can not be considered as acceptable, but at least this type of check can be applied conditionally (replacement depending on the observed state): the technical state of the dual mass flywheel is checked and is decided if the replacement is not required or the immediate replacement is required.

**Table 4** Mileages  $(m - 2\sigma)$  for the 5 types of engines

Engine code	Mileage $(m - 2\sigma)$ ( $10^3$ km)	Mileage of proper technical inspection ( $10^3$ km)
A	50	45
B	0 (the resulting negative value is not allowed: $-38$ )	0
C	20	15
D	14	15
E	29	30

## Conclusions

As a conclusion, in all cases the distribution of the malfunctioning times can be modeled using the normal law. The fact that the reliability can be described by the normal model shows that the malfunctions are caused by the normal damaging processes: wearing processes and material ageing processes.

The most frequent malfunctions for the dual mass flywheel as can be observed from graphs 6, 7, 8, 9, 10 (Figs. 7, 8, 9, 10 and 11) representing the distribution of the types of malfunctions depending on the frequency of the malfunctions are “Extensive dark color stains and fissures on the friction surface, caused by overheating” and “Grooves on the friction surface of the flywheel caused by the rivets of the worn clutch disk, limiting the transmitted power”.

To avoid the generation of grooves on the friction surfaces even at low values of the mileages, as can be observed in diagrams 1, 2, 3, 4, 5 (Figs. 2, 3, 4, 5 and 6) can be conducted a conditional maintenance ( $m - 2\sigma$ ) shown for each type of actuation in Table 4, where will be checked the wear degree of the clutch disk (visual check or actual measuring) during the regular technical checks using a viewing window provided for this in the crankcase of the clutch, followed by the decision to replace the clutch if it will not be reliable until the next technical check.

In the long run, considering the fact that the damaging processes at the level of the dual mass flywheels for the studied actuation systems and respectively their occurrence according to the diagrams 1, 2, 3, 4, 5 (Figs. 2, 3, 4, 5 and 6) for low mileages suggest that these components do not observe the normal law, must be identified the causes that cause such a fast wear of the friction gaskets of the clutch disk in order to remove them (those that depend on the design processes or the manufacturing processes), in order to obtain a wear with reduced intensity, acceptable.

As such, based on the reliability can be redesigned the maintenance schedule for each type of vehicle (according to the established concept of “*maintenance based on reliability*”), which will ensure the improvement of the reliability and, globally, the reduction of the ownership costs for the vehicle.

**Acknowledgments** The work has been funded by the Sectoral Operational Programme Human Resources Development 2007–2013 of the Ministry of European Funds through the Financial Agreement POSDRU/187/1.5/S/155536.

## References

- Andreescu C (1996) Aplicații numerice la studiul fiabilității automobilelor. București  
Bâzga M (2013) Thesis essay number 3: automotive maintenance optimization based on reliability. University of Pitesti  
Boroiu A (2013) Modelarea fiabilității autovehiculelor. Ed. Universității din Pitești, pp 25–27

- Boroiu A (2014) Utilizarea legii Gauss-Laplace pentru determinarea proporției de produse neconforme obținute în procesele de fabricație. *Revista Mentenanță și Distribuție Industrială*, pp 33–35
- O'Connor P (1991) *Practical reliability engineering*. Wiley, New York



# Theoretical and Practical Analysis of the in-Cylinder Tumble Motion

Dan Moldovanu and Adela Ioana Borzan

**Abstract** The present paper presents a comparative analysis of the in-cylinder tumble motion of the fluid (and because it is a SIE, the fluid is actually air mixed with gasoline) using an existing design from a Volkswagen Polo engine (type AWY), and introducing it to a CFD simulation software (AVL FIRE). The objective of the paper is first of all to compare the practical testbench measurements to the simulation results and see the differences. Then, modify the standard testbench by mounting a tumble flaps and also modify the intake port angle (larger with  $5^\circ$  and smaller with  $5^\circ$ ) to see the in-cylinder tumble movement and alignment. The existent controlled motions inside the cylinder were presented, like tumble, swirl and squish, along with the methods and ways to analyze all these motions. There are more methods of analyzing the motion of the air inside the cylinder, like using a cross-correlation digital Particle Image Velocimetry (PIV) (non-intrusive, but most expensive), or by using a paddle wheel mounted inside the cylinder (highly intrusive, low cost), or by mounting an anemometer inside the cylinder (moderately intrusive but the influence is the same for all measurements—systematic error, low cost), and the most equilibrated from the indication precision/cost point of view, a point-like built anemometer (low intrusiveness and low cost).

**Keywords** Tumble · Practical testbench · Theoretical comparison · AVL FIRE

## Introduction

There are many papers that studied the effects of in-cylinder motion of the air/mixture, like (Badami et al. 2004; He et al. 2013; Langrish et al. 2004), but many use CFD, because in a prototyping phase, CFD offers many advantages, such as low simulation time in comparison to measurements, lower costs, and the opportunity to better optimization (Gaikwad et al. 2009; Mariasiu 2013; Turrell et al. 2004).

---

D. Moldovanu (✉) · A.I. Borzan  
Technical University of Cluj-Napoca, Cluj-Napoca, Romania  
e-mail: dan.moldovanu@auto.utelj.ro

By default, the precision of the CFD simulation relies on the input data provided, therefore, another simulation is recommended, in software like AVL BOOST, for some early input data, or real measurements on the simulated engine.

This paper was focused on the tumble motion, and its influencing factors. Firstly, measurements had to be made to analyze the tumble motion, and then the CFD simulation was made using AVL FIRE v 2009.

## Objectives

The analysis of the tumble motion is important because, as seen in (Heywood 1988; Iclodean et al. 2013; Özener et al. 2013), the air-fuel mixture has an important role on the pollutant emissions, on both spark ignited engines and compression ignited engines.

## Methodology

The tumble testbench was made from the components of an AWY Volkswagen engine (Figs. 1 and 2), and then, as an input the air flow was calculated by using the diameter of the pipe and the measured velocity, using an anemometer for the working engine (at idle speed, at torque speed and at power speed), in order to know the airflow that must be ensured for the testbench.

The anemometer that was used to measure the air velocity is a YK 2004AH anemometer, but inside the cylinder, a pointlike anemometer was needed, so by using a Wheatstone bridge, and a 9 V battery, with a sensible wolfram pointlike resistor, the airflow measuring device was calibrated. The calibration graph is presented in Fig. 3.

To know the exact position of the measurements, the cylinder liner was made out of Perspex. After knowing the necessary airflow, it must be ensured using an air compressor. For the intake valve open at  $\frac{1}{2}$  max opening and max opening, the speed of the air was measured in the cylinder (open cylinder, no piston mounted) in 12 points on four planes perpendicular to the cylinder axis (Fig. 4 and Table 1).

The measurements were made for an opening of the intake valve of 3.5 and 7 mm, and the results compared in Fig. 5.

After knowing the tumble motion, a further analysis presumes the CFD simulation validated by these measurements. To do that, the intake pipe, the intake valve and the cylinder liner were built in CATIA and exported as `.stl` files that are recognized by AVL FIRE (Figs. 6 and 7).

**Fig. 1** Testbench made from AWY engine components

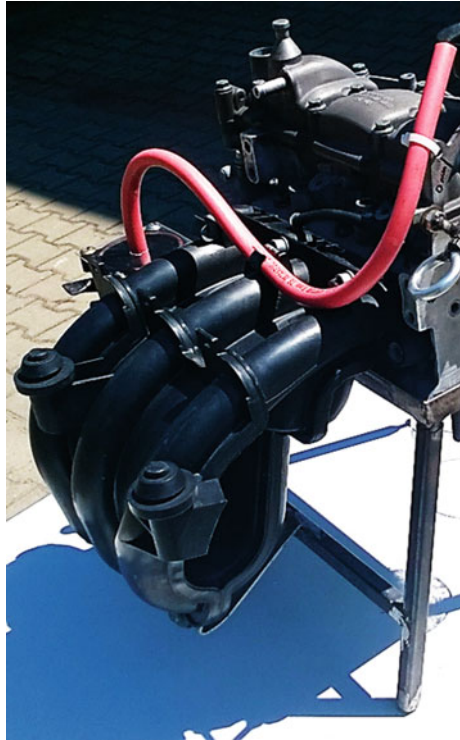


**Fig. 2** Valve opening adjustment mechanism



After importing the surface in AVL FIRE, the edge mesh was built, and the dimensions for the cells were chosen, so that the final mesh is as fine as possible but with minimum build time (if the build time is small, the simulation time is also

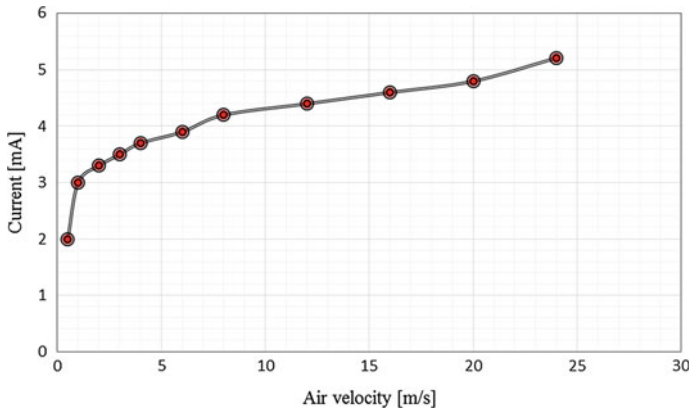


Fig. 3 Air speed measuring device calibration table

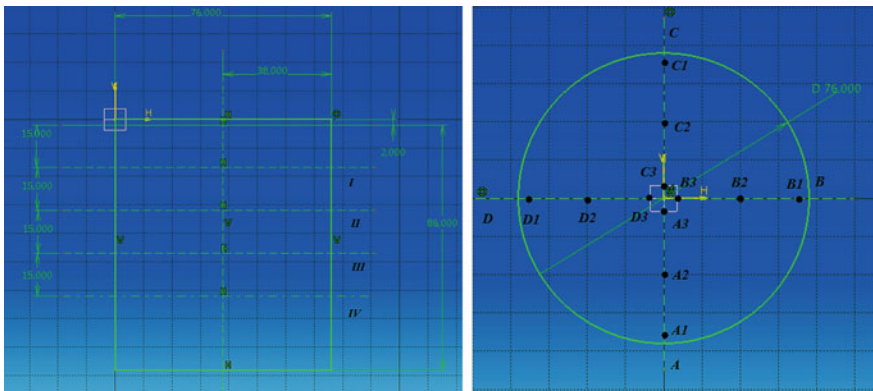


Fig. 4 Sections where measurements were made

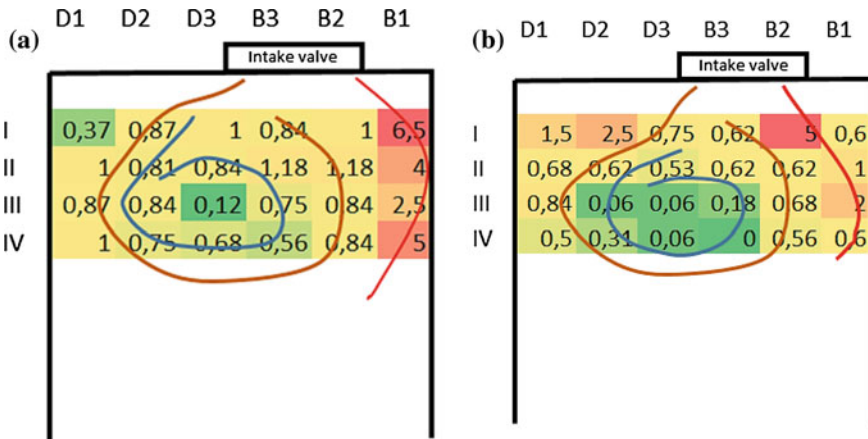
small, due to the complexity of the model). Intake and Outlet boundaries were created, and the input data for intake was the measured airflow and for the outlet, atmospheric pressure was set (Fig. 8).

The simulations were made for standard intake port, smaller angle of the intake port and bigger angle of the intake port.

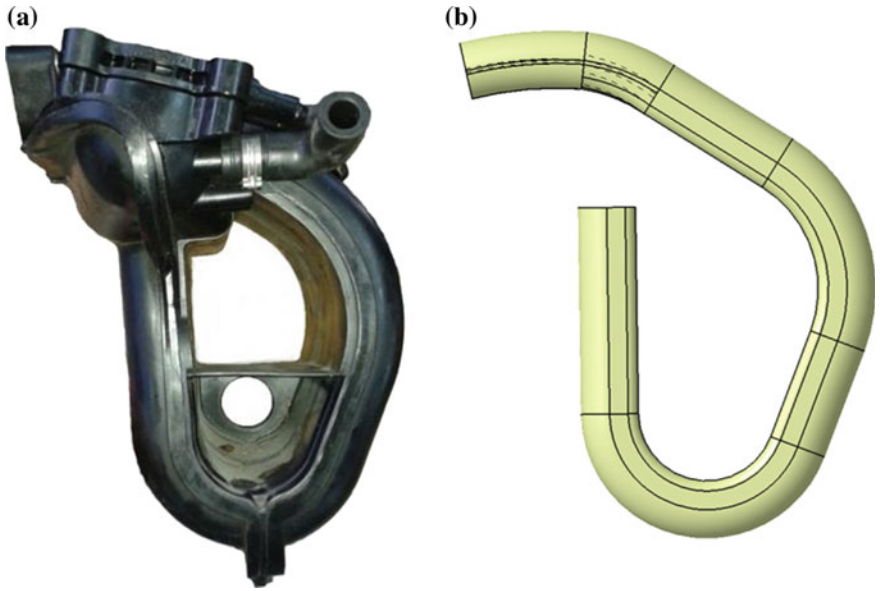
The results were compared and if the intake airflow is introduced correctly, the measurements on the real testbench indicate lower values (5 % smaller) for the tumble coefficient than the simulation, but that is explained by the air friction with the walls of the intake pipe. By introducing a tumble flaps, the tumble coefficient is slightly bigger (7 %) (Fig. 9).

**Table 1** Measurements of the air velocity at all the sections and all points

Section	Intensity (mA)	Velocity (m/s)	Intensity (mA)	Velocity (m/s)	Intensity (mA)	Velocity (m/s)
	A1		A2		A3	
I	3.8	5	2.7	0.81	2.3	0.62
II	2.2	0.56	3.3	2	2.5	0.68
III	1.2	0.12	2.4	0.65	1.5	0.25
IV	0.8	0	1.6	0.31	1	0.062
	B1		B2		B3	
I	2.3	0.62	3.8	5	2.3	0.62
II	3	1	2.3	0.62	2.3	0.62
III	3.3	2	2.5	0.68	1.4	0.18
IV	2.3	0.62	2.2	0.56	0.8	0
	C1		C2		C3	
I	2.4	0.65	2.9	0.87	1.5	0.25
II	2.2	0.56	2.4	0.65	2.3	0.62
III	1.4	0.18	1.8	0.37	1.3	0.15
IV	1.5	0.25	1.3	0.15	0.8	0
	D1		D2		D3	
I	3.2	1.5	3.4	2.5	2.6	0.75
II	2.5	0.68	2.3	0.62	2.1	0.53
III	2.8	0.84	1	0.062	1	0.062
IV	2	0.5	1.6	0.31	1	0.062

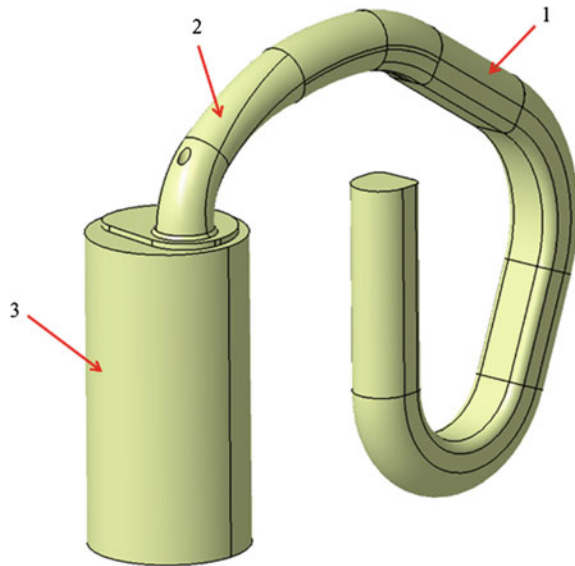


**Fig. 5** Tumble motion comparison for different valve openings. **a** Valve opening at 3.5 mm. **b** Valve opening at 7 mm



**Fig. 6** The intake pipe comparison. **a** Real intake pipe. **b** Virtual intake pipe

**Fig. 7** Intake model (1 cylinder liner, 2 cylinder head part of the intake, 3 intake pipe)



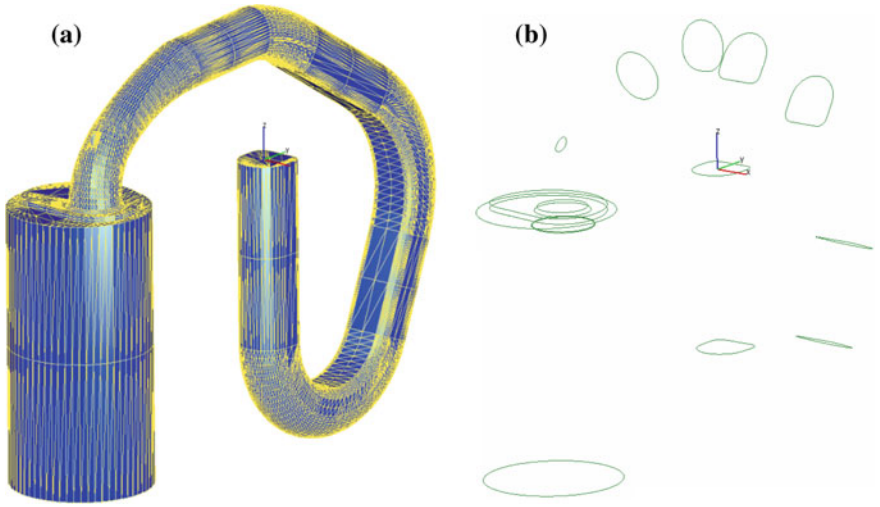


Fig. 8 The mesh and edge mesh of the model. **a** Mesh. **b** Edge mesh

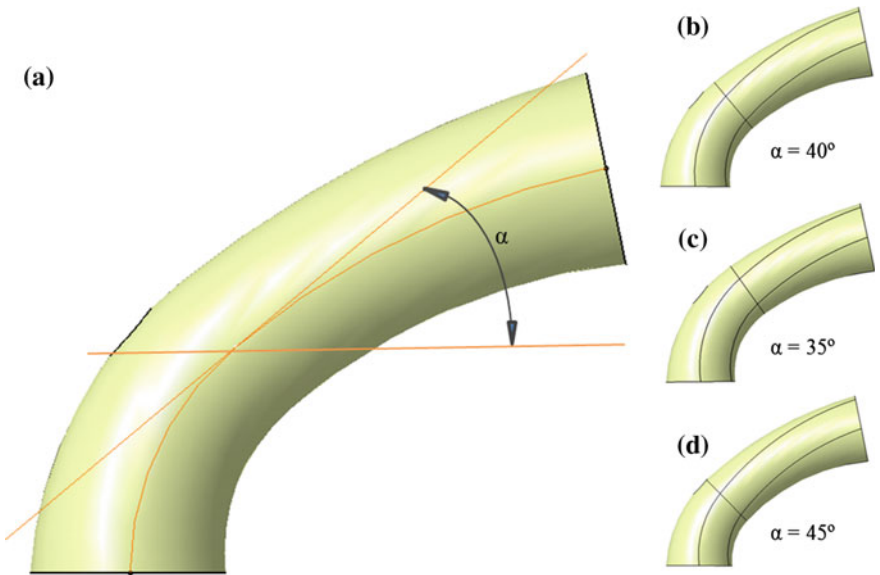


Fig. 9 Standard intake port ( $\alpha = 35^\circ$ ) and comparison versions at  $\alpha = 40^\circ$  and  $45^\circ$

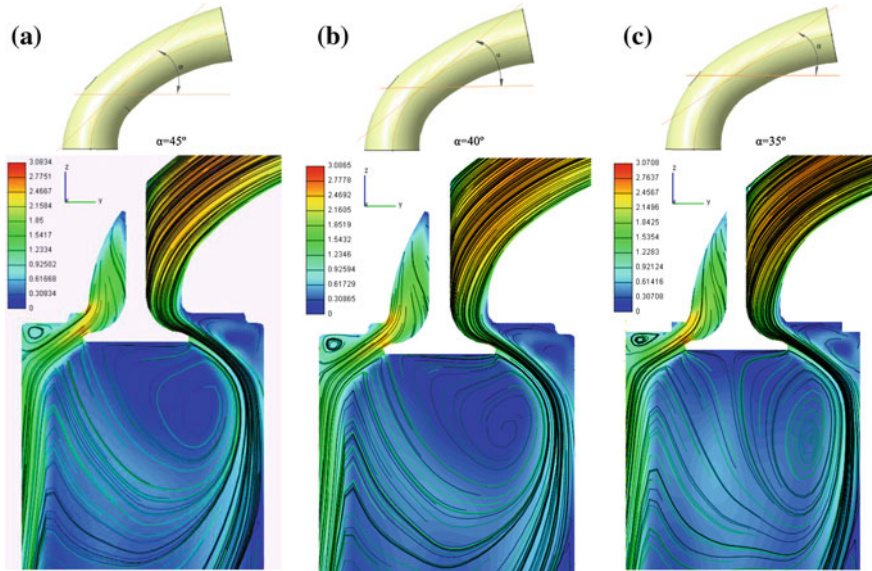


Fig. 10 Tumble analysis for the three versions of the intake pipe

## Results and Discussions

The results of the simulation are presented in Fig. 10. The representations show the influence of the angle of the intake pipe on the tumble motion inside the cylinder.

## Conclusions

From the simulations, when modifying the angle of the intake port the center of the in-cylinder tumble motion changes, if the angle is smaller with  $5^\circ$ , the center moves away from the center of the cylinder, where the spark plug is mounted, and if the angle is with  $5^\circ$  bigger, the center moves more towards the center of the cylinder but still away from the spark plug.

In conclusion, the tumble coefficient can be modified by mounting a tumble flaps, and the position of the center of the in-cylinder tumble motion can be controlled by modifying the angle of the intake pipe or (a method that was not tested) by having a profiled piston, towards the spark plug.

This paper shows the tight bond between simulation and real measurements made on a testbench.

The authors, previously studied swirl motion inside a CIE, with the paper: **Computational fluid dynamics simulation of a single cylinder research engine working with biodiesel**, published at Thermal Science.



**Acknowledgments** This paper was possible with the unconditioned help of Eng. Balea Bogdan Aurel and Eng. Bordas Lorant-Tibor.

## References

- Badami M, Bevilacqua V, Millo F, Chiodi M et al (2004) GDI swirl injector spray simulation: a combined phenomenological-CFD approach. SAE Technical Paper 2004-01-3005. doi:[10.4271/2004-01-3005](https://doi.org/10.4271/2004-01-3005)
- Gaikwad S et al (2009) Steady and transient CFD approach for port optimization. SAE Int J Mater Manuf 1(1):754–762
- He J et al (2013) Continuous nanofiber yarns twisted through three-dimensional high-speed swirling airflow. Therm Sci 17(5):1269–1276
- Heywood JB (1988) Internal combustion engine fundamentals, vol 930. McGraw-Hill, New York
- Iclodean C, Nicolae B, Bogdan V (2013) Simulation of pollutant emission for compression ignition engine fueled with biofuels using computer simulation with two combustion models. Annals of the Oradea University, Fascicle of Management and Technological Engineering, ISSUE #1, MAY 2013. <http://www.imtuoradea.ro/auo.fimte/>
- Langrish TAG, Williams J, Fletcher DF (2004) Simulation of the effects of inlet swirl on gas flow patterns in a pilot-scale spray dryer. Chem Eng Res Des 82(7):821–833
- Mariasiu F (2013) Numerical Investigation of the effects of biofuel characteristics on the injector nozzle erosion process. Tribol Trans 56(2):161–168
- Özener O, Yüksek L, Özkan M (2013) Artificial neural network approach to predicting engine-out emissions and performance parameters of a turbo charged diesel engine. Therm Sci 17(1):153–166
- Turrell MD et al (2004) CFD simulation of the flow within and downstream of a high-swirl lean premixed gas turbine combustor. In: ASME turbo expo 2004: power for land, sea, and air. American Society of Mechanical Engineers, New York

# Optimized Automotive Spark Ignition Engine

Edward Rakosi, Sorinel Talif and Gheorghe Manolache

**Abstract** A way to preserve the natural resources and lowering the pollution level is the improving of the thermal engine efficiency in order to reduce the fuel consumption. For this purpose, the authors propose a combined solution to improve the performances of the automotive engine. In order to improving the combustion efficiency, we tried to get a more close approach to ideal combustion cycle at constant volume, specific to the spark ignition engine, by developing an engine with sequentially variable compression ratio. Also, the theoretical and physical model developed allows the determination of a transversal new profile of the compression ring in order to obtain better lubrication conditions. By modifying the architecture of the compression ring the ware of friction is reduced, thereby increasing mechanical efficiency. Also, the paper present the results of an analysis concerning the main factors affecting the cam-follower contact conditions, emphasizing the lubrication regime influence on the wear of elements in contact. An original technical solution is proposed for the improvement of the lubrication regime, in order to avoid the starvation phenomenon. This theoretical and experimental study concerns the modification of some parameters of the internal combustion engine in various situations, aimed at optimizing a friendly environmental propulsion engine.

**Keywords** Spark ignition engines · Variation of the compression ratio · Cam-follower contact · Optimized engine

---

E. Rakosi (✉) · S. Talif · G. Manolache  
Technical University “Gheorghe Asachi” of Iasi,  
Prof. Dr. Doc. Dimitrie Mangeron St. 43, Iasi, Romania  
e-mail: edwardrakosi@yahoo.com

S. Talif  
e-mail: tsorinel@yahoo.ro

G. Manolache  
e-mail: gmanolache@yahoo.com

## Introduction

The spark ignition engines for automotive propulsion still represent about 65–70 % of the world market. On the other side, although the alternative propulsion solutions (called also hybrid) become more and more popular, they are not widely spread. The medium-large sized spark ignition engines with high fuel consumption have been improved step by step. The fueling systems have been optimized; improved solutions for gases distribution system have been used, the compression ratio has been modified, etc. This is an old area of interest and specialists have proposed several solutions. On the other hand, in the purpose of improving the spark ignition engines efficiency, the actual researches have taken into account the amelioration of the constructive and technological solutions.

## Engine Solutions, Analysis, Modeling, Simulation

### *Proposed Engine Solution*

The proposed solution by authors achieves the variation of the compression ratio by moving a small piston in the opposite direction to the main piston, during of 90° angular interval after the TDC, thus achieving an almost constant volume for the main part of the burning process (Rakosi et al. 2010). In the Fig. 1 this solution is shown for a position near the TDC.

Aiming to obtain results that would allow a comparison between real conditions and the proposed solution (in terms of differences between efficiencies), we developed a detailed analysis of this engine solutions (Gray 2004). For improving the basic efficiency of operating cycle, two separate cases were taken into account. The first presumes a constant bore for the small piston, while displacing it is between 1 and 10 mm. The second case preserves the stroke for this small piston, while its bore varies between 44 and 97 mm. A analyze of obtained efficiencies led us to the optimization of the mechanical parameters.

Momentary volume of the cylinder:

$$V(\alpha_m) = V_c + V_p(\alpha_m) \quad (1)$$

and momentary volume of the cylinder, as is affected by the movement of the small piston during the angular interval of its stroke, becomes:

$$V_2(\alpha_m, S_m) = V(\alpha_m) - V_m(\alpha_m, S_m) \quad (2)$$

and is shown in Fig. 2, in comparison with the one of standard engine (unmodified). Further on, this engine solution will be called short: **VSCR** (**V**ariable **S**equential **C**ompression **R**ation). The momentary compression ratio, for the standard engine is given by the expression:

**Fig. 1** Position near the TDC

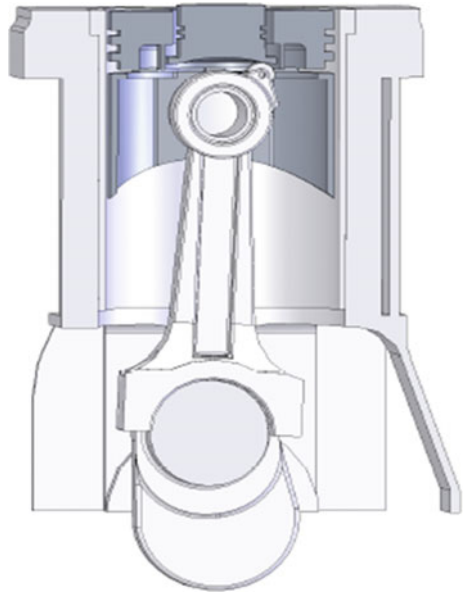
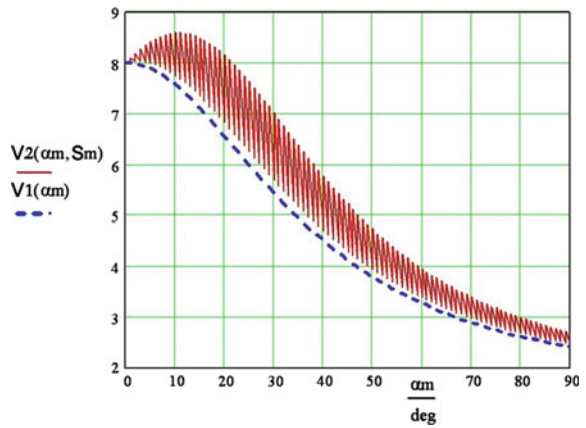


**Fig. 2** Variation of the cylinder volume as is it affected by the movement of the small piston, for different strokes

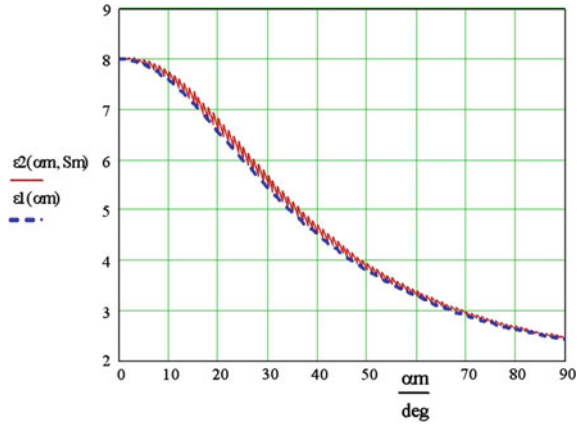


$$\varepsilon_1(\alpha_m) = 1 + \frac{V_s}{V(\alpha_m)} \tag{3}$$

while, for the **VSCR** engine, we get:

$$\varepsilon_2(\alpha_m, S_m) = 1 + \frac{V_s}{V_2(\alpha_m, S_m)} \tag{4}$$

**Fig. 3** The overlapped variations of the compression ratios



For a comparative view of effects, the overlapped variation curves of these two compression ratios, in the working domain of small piston, are shown in Fig. 3. Considering an adiabatic coefficient  $k = 1.3$ , the efficiency equations in these two studied cases become:

$$\eta_{tv1}(\alpha_m) = \left( 1 - \frac{1}{\varepsilon_1(\alpha_m)^{k-1}} \right) \cdot 100 \quad (5)$$

$$\eta_{tv2}(\alpha_m, S_m) = \left( 1 - \frac{1}{\varepsilon_2(\alpha_m, S_m)^{k-1}} \right) \cdot 100 \quad (6)$$

For the working range of the small piston, the gained thermal efficiency of the **VSCR** solution is:

$$\Delta\eta_{tv}(\alpha_m, S_m) = |\eta_{tv2}(\alpha_m, S_m) - \eta_{tv1}(\alpha_m, S_m)| \% \quad (7)$$

The variation range of the efficiency gain for different strokes or diameters of the small piston are shown in Figs. 4 and 5. In this case, the modeling uses the highest value for the stroke of the small piston (10 [mm]), which leads to the most significant increase of efficiency. In this analyze, the diameter of the small piston is modified, starting with the lowest value,  $D_m = 44$  mm, and ending when the diameter of main piston is reached ( $D_m = D = 97$  mm). The previous formulae are modified accordingly, only the intermediate and final results being presented. For the both cases, the stresses and the strains of the main piston of the **VSCR** engine were evaluated using the **FEM** (Finite Element Method) and some results are shown in Fig. 6.

In order to obtain a better lubrication conditions, to lower friction ware and to increase the mechanical efficiency, the authors studied and optimized also the architecture of the compression ring, obtaining a new transversal profile of the compression ring.

**Fig. 4** The variation range of the efficiency gain for different strokes of the small piston

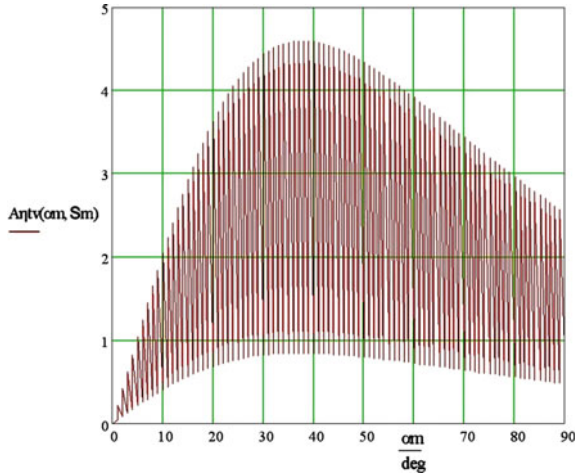
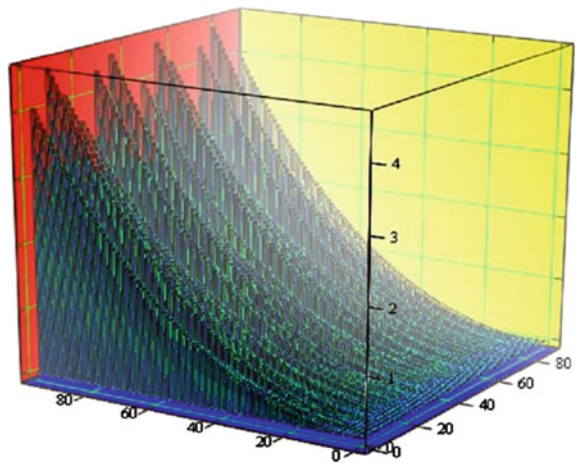


**Fig. 5** Efficiency gain by modifying the diameter of the small piston



When the peripheral surface of the piston ring is correctly aligned with the cylinder liner surface, the piston-piston rings-cylinder assembly acts as a labyrinth, insuring an efficient seal (Heisler 1995). Starting from the pressure  $p_0$  inside the combustion chamber, the pressure decreases to  $p_{s1}$  behind of the first compression ring, to  $p_1$  after the first ring, to  $p_{s2}$  and  $p_2$  behind and after of the second ring etc. Due to the high value of the chamfer angles  $h_1$ , only the surface with the length  $h_r = h - 2h_1$  [m] is considered as the hydrodynamic active surface of the piston ring. The specific relations for the hydrodynamic lubrication regime, correlated with the combustion chamber pressure, are used in order to establish the conditions of the oil intake and exhaust inside the piston ring-cylinder liner couple, thus leading to the best values for the angles of the conical surfaces that insure a preponderant hydrodynamic lubrication regime. The oil flow through the cylinder liner-piston

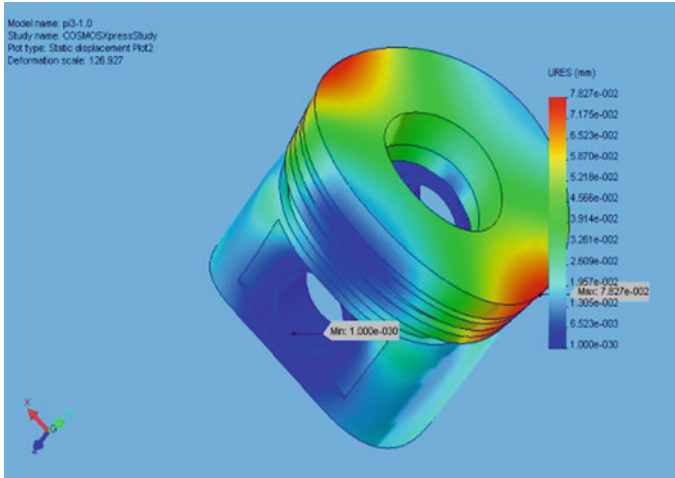


**Fig. 6** Strain for the main piston of the VSCR engine obtained using FEM

ring is calculated using the flow equation for the hydrodynamic reciprocating couples (Taylor 1993).

The equations are for the downward stroke:

$$Q_{L(d)} = \pi \cdot D \cdot \left[ \frac{h_1 h_2}{h_1 + h_2} v_p + \frac{1}{6} \frac{(h_1 h_2)^2 (p_1 - p_0)}{\eta (h_2^2 - h_1^2)} \right] [\text{m}^3/\text{s}] \quad (8)$$

and for the upward stroke:

$$Q_{L(u)} = \pi \cdot D \cdot \left[ \frac{h_1 h_2}{h_1 + h_2} v_p + \frac{1}{6} \frac{(h_1 h_2)^2 (p_0 - p_1)}{\eta (h_2^2 - h_1^2)} \right] [\text{m}^3/\text{s}]. \quad (9)$$

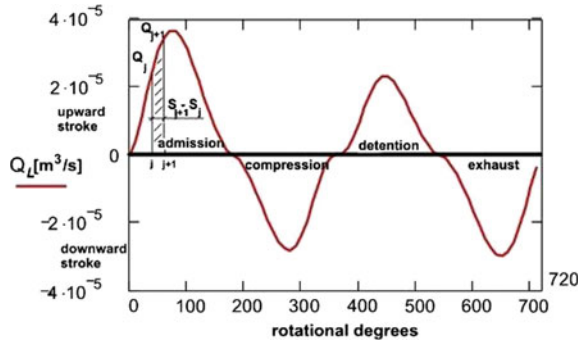
In order to evaluate the overall oil flow during one engine cycle we define the overall oil circulation  $Q_{Lt}$  [ $\text{m}^3/\text{s}$ ], calculated by graphical integration of the oil flow according to Fig. 7. The relation of the overall oil circulation is:

$$Q_{Lt} = \sum_{j=0}^{71} \frac{Q_{Li+1} + Q_{Li}}{2S} |S_{i+1} - S_i| [\text{m}^3/\text{s}] \quad (10)$$

A positive value of the overall oil circulation means that the oil flow is directed towards the combustion chamber.

Starting from the shear forces in the reciprocating couple for the hydrodynamic lubrication regime (Zhu and Cheng 1989), we evaluate the friction forces inside the cylinder liner-piston ring couple using the equations:

**Fig. 7** The oil flow through the cylinder liner-piston ring and the overall oil circulation Q<sub>Lt</sub> calculated by graphical integration



– for the downward stroke:

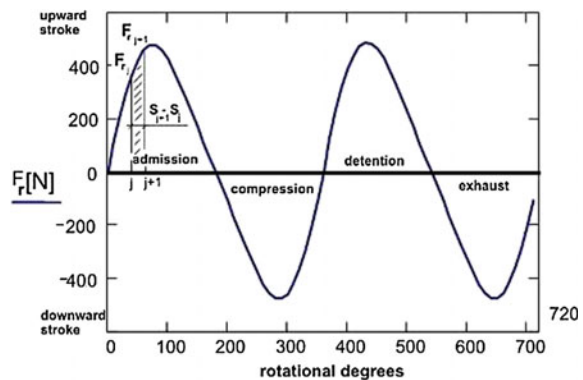
$$F_{f(d)} = \frac{2 \cdot \pi \cdot D \cdot \eta \cdot v_p}{k_d} \cdot \left[ 3 \cdot \frac{h_2 - h_1}{h_1 + h_2} - 2 \cdot \ln \frac{h_2}{h_1} \right] + \dots + \pi \cdot D \cdot k_d \cdot \frac{h_1 \cdot h_2}{h_1 + h_2} \cdot (p_1 - p_0) \text{ [N]} \tag{11}$$

– for the upward stroke:

$$F_{f(u)} = \frac{2 \cdot \pi \cdot D \cdot \eta \cdot v_p}{k_u} \cdot \left[ 3 \cdot \frac{h_2 - h_1}{h_1 + h_2} - 2 \cdot \ln \frac{h_2}{h_1} \right] + \dots + \pi \cdot D \cdot k_u \cdot \frac{h_1 \cdot h_2}{h_1 + h_2} \cdot (p_0 - p_1) \text{ [N]} \tag{12}$$

Defining mechanical work of the friction forces Lfr [J] for the piston ring, we may evaluate the mechanical losses using a graphical integration method for the variation shown in Fig. 8.

**Fig. 8** The friction forces inside the cylinder liner-piston ring couple and the mechanical work of the friction forces Lfr [J] for the piston ring calculated by graphical integration





Using the general expression of the mechanical work, we get the relation:

$$L_{fr} = \sum_{j=0}^{71} \frac{|F_{ri+1} + F_{ri}|}{2} |S_{i+1} - S_i| [J]. \quad (13)$$

A high value of this mechanical work means high friction forces inside the couple and diminishes the engine's mechanical efficiency.

### ***Computational Procedure***

The theoretical model developed allows the determination of the transversal profile of the first and the second compression ring in order to maintain similar lubrication conditions, to reduce oil consumption, to obtain lower friction forces and to increase the mechanical efficiency of the piston ring—cylinder line coupling. So, the slope repartition will be optimized in order to reduce oil flow towards the combustion chamber. Using the relation (8), (9) and (10) and giving values comprised between 0 and 1 for repartition X of the slope, the calculus are made in order to obtain a zero value for the overall oil circulation QLt. In that case, the oil flow towards the combustion chamber and the oil consumption is reduced to the minimum values. The upper slope angle and the bottom slope angle of the peripheral surface of the rings will be optimized in order to insure a lubrication regime preponderant hydrodynamic, to diminish friction forces and lowering the wear of piston rings and cylinder liner. Calculus, using the relation (11), (12) and (13), are made starting at 0 value for the upper and bottom slope angle and is considered ended when we obtain a maximum percentage from entire engine cycle with the hydrodynamic lubrication regime for the piston ring and a minimum value for the piston ring mechanical work of the friction forces Lfr [J]. We calculate also oil flow through cylinder liner-piston ring couple and the friction forces variation inside this couple for the entire engine cycle, for the both compression piston ring.

To find a unitary way to analyze and study the cam-follower contact conditions and to render evident solutions for wear reduction of this couple, the authors took into account a complex physical-mathematical model, which could allow the emphasis of the most important factors affecting the contact conditions. Simulation of the characteristic phenomena, in order to define a procedure for improving the contact conditions, was also considered.

### ***Mathematical and Physical Model for the Optimization of Cam-Follower Contact Conditions***

Up to now there is no unitary approach of the phenomena occurring during the working process of distribution system; due to the complexity of the processes

involved, the cam-follower contact state concept was developed in order to evaluate the distribution system of the internal combustion engines. This concept takes into account the multitude of processes occurring inside the cam-follower couple, emphasizing on their complexity and interdependence, facilitating thus in the mean time the analysis and improvement of the contact conditions. In order to define the previously mentioned concept the following processes were taken into account. The contact state  $\Gamma$  may be defined using the array:

$$\Gamma = (\Gamma_1, \Gamma_2, \Gamma_3, \Gamma_4) \tag{14}$$

with:

$$\Gamma_1 = \left( \begin{array}{l} Ax^2 + By^2 = D \\ D = z_1 + z_2 = const \\ A = \frac{1}{4} \left[ (c_{11} + c_{12}) + (c_{21} + c_{22}) + \sqrt{(c_{11} - c_{12})^2 + (c_{21} - c_{22})^2 + \dots} \right. \\ \quad \left. + 2(c_{11} - c_{12})(c_{21} - c_{22}) \cos 2\omega \right] \\ B = \frac{1}{4} \left[ (c_{11} + c_{12}) + (c_{21} + c_{22}) - \sqrt{(c_{11} - c_{12})^2 + (c_{21} - c_{22})^2 + \dots} \right. \\ \quad \left. + 2(c_{11} - c_{12})(c_{21} - c_{22}) \cos 2\omega \right] \\ C = \begin{pmatrix} c_{11} & 0 & c_{12} \\ c_{21} & 0 & c_{22} \end{pmatrix} \\ \omega \end{array} \right)$$

$$\Gamma_2 = \left( \begin{array}{l} \sigma_x = -p_0 \cdot 2\mu \frac{z}{b} \left[ \sqrt{\frac{b^2 + \lambda}{\lambda}} - 1 \right] \\ \sigma_y = -p_0 \cdot \frac{z}{b} \left[ \sqrt{\frac{b^2 + \lambda}{\lambda}} \left( 2 - \frac{b^2 z^2}{\lambda^2 + b^2 z^2} \right) - 2 \right] \\ \sigma_z = -p_0 \cdot \frac{bz^3}{\lambda^2 + b^2 z^2} \sqrt{\frac{b^2 + \lambda}{\lambda}} \\ \tau_{yz} = \tau_{zy} = -p_0 \cdot \frac{byz^2}{\lambda^2 + b^2 z^2} \sqrt{\frac{\lambda}{b^2 + \lambda}} \\ \tau_{xz} = \tau_{zx} = 0 \\ \tau_{xy} = \tau_{yx} = 0 \end{array} \right)$$

$\Gamma_1$  is the geometrical parameter of the cam-follower contact state,  $\Gamma_2$  is parameter of the principal stresses for the contact state; for the case of the cam-roller follower and cam-plane follower, with linear type contact,  $\Gamma_3$  is defined as a parameter of the thermal stresses for the cam-follower contact state,  $\Gamma_4$  is the parameter taking into account the lubrication state of the cam-follower couple, where: x, y—xOy coordinates; D—distance between the two points on the Oz axis ( $D = 0$  for the points in the common plane xOy);  $z_1$ —distance between a point on body 1 (cam) and the common plane xOy;  $z_2$ —distance between a point on body 2 (follower) and the common plane xOy; A, B—parameters of the contact ellipse; C—curvature matrix;  $\omega$ —between the axis of the initial coordinate systems  $Ox_1$  and  $Ox_2$ ;  $\lambda$  is the upper root of the equation  $\frac{y^2}{b^2 + \lambda} + \frac{z^2}{\lambda} = 1$  and a, b are the semi-axes of the pressure

ellipsoid;  $\bar{\varepsilon}$  and  $\bar{\sigma}$  are the strains and stresses given by the peculiar root of the thermo elasticity equation as a function of strain,  $h_{\min}$ —minimum film thickness;  $h_{\text{cen}}$ —central film thickness;  $\lambda$ —specific film thickness;  $Q_T$ —thermal correction coefficient;  $Q_{St}$ —coefficient for the reduction of the film thickness due to starvation;  $g_e$ —elasticity parameter;  $g_v$ —viscosity parameter.

$$\Gamma_3 = \begin{pmatrix} \bar{\varepsilon}_{xx} = \frac{\partial^2 \Phi}{\partial x^2} \\ \bar{\varepsilon}_{yy} = \frac{\partial^2 \Phi}{\partial y^2} \\ \bar{\varepsilon}_{zz} = 0 \\ \bar{\varepsilon}_{xy} = \frac{\partial^2 \Phi}{\partial x \partial y} \\ \bar{\varepsilon}_{yz} = 0 \\ \bar{\varepsilon}_{zx} = 0 \\ \bar{\sigma}_{xx} = -2G \frac{\partial^2 \Phi}{\partial y^2} \\ \bar{\sigma}_{yy} = -2G \frac{\partial^2 \Phi}{\partial x^2} \\ \bar{\sigma}_{zz} = -2G \nabla^2 \Phi = -2G \frac{1+\mu}{1-\mu} \alpha T \\ \bar{\sigma}_{xy} = 2G \frac{\partial^2 \Phi}{\partial x \partial y} \\ \bar{\sigma}_{yz} = 0 \\ \bar{\sigma}_{zx} = 0 \end{pmatrix}$$

$$\Gamma_4 = \begin{pmatrix} h_{\min} = a \cdot R_x \cdot U_e^b \cdot G^c \cdot W_e^d \\ h_{\text{cen}} = a' \cdot R_x \cdot U_e^{b'} \cdot G^{c'} \cdot W_e^{d'} \\ \lambda = \frac{h_{\min}}{1.15 \sqrt{R_{a1}^2 + R_{a2}^2}} \\ Q_T = \frac{1 - 13.2 \left( \frac{\rho_0}{\rho_{ef}} \right) \cdot Bk^{0.42}}{1 + 0.213 \left( 1 + 2.323 \cdot C_i^{0.83} \right) Bk^{0.64}} \\ Q_{St} = 1 - \frac{1}{\exp \left\{ \left[ \exp \left( \frac{0.78 \ln \psi_{1L}}{1 + 10^{-3} L_t} \right) \right] \ln(4.6 + 1.15 \cdot L_t^{0.6}) \right\}} \\ g_e = W_e \cdot U_e^f \\ g_v = G \cdot W_e^{e'} \cdot U_e^{f'} \end{pmatrix}$$

## Simulations

The specific parameters  $\Gamma_1$ ,  $\Gamma_2$ ,  $\Gamma_3$ ,  $\Gamma_4$ , and contact type they were evaluated through virtual models (Carra et al. 2004) shown in Fig. 9 and through simulations of the lubrication and wear phenomena in the cam-follower couple; in order to achieve this goals, the CATIA design media and MathCAD analytical program were used. The analysis of these models revealed the main factors (Tournier 2007) affecting the wear of the cam-follower couple and the specific effects of different contact conditions. As a result of these studies and simulations, a original method for reducing wear of the cam-follower couple has been developed, using an additional lubrication with oil jets directed over the contact area this method to avoids starvation was named **LUJET** (Lubrication Jet). Implementation of the **LUJET**

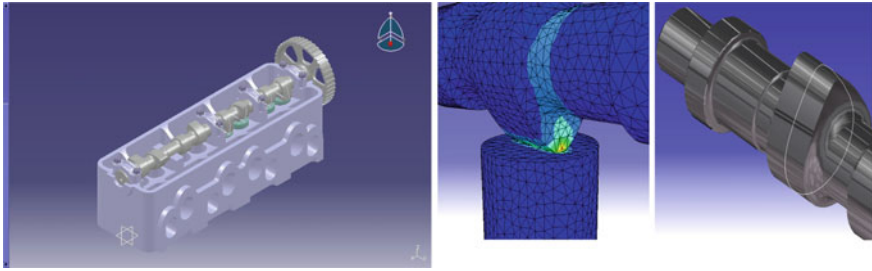
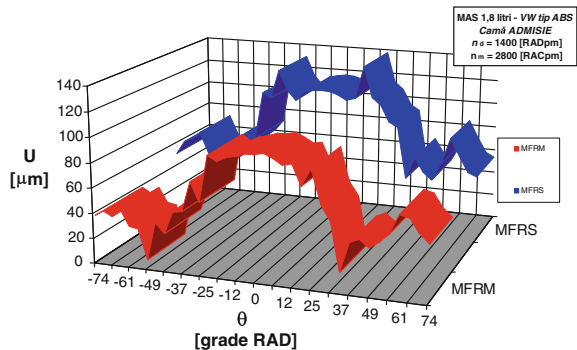


Fig. 9 Virtual model

has allowed the development of a **Modified Real Physical Model (MRPM)**, starting from an existing engine, widely used in the automotive construction, which does not imply expensive constructive changes of the base version of the engine (Standard Real Physical Model).

Through successive measurements, before and after the working cycles, according to the test program, wear was evaluated by the means of the changes in the follower stroke. The results of the experimental tests are shown in Figs. 10 and 11. The effect of wear over other cinematic parameters was also studied. Thus, wear diminished achieved by the solution developed led to lower rates of speed and acceleration follower, with favorable effects over the inertia stresses in the distribution system shown in Figs. 12 and 13. An overall conclusion is that the developed solutions led to a reduction of the average wear by 25  $\mu\text{m}$ , on the ascending side of the intake cam and by 23  $\mu\text{m}$ , on the descending side. Similar results were obtained for the exhaust cam, with a 30  $\mu\text{m}$  reduction on the ascending side and 22  $\mu\text{m}$  on the descending side. Using these absolute values we obtained the wear reductions percentages shown in Figs. 14 and 15. For the intake cam, wear reduction reached 30 % for the ascending profile and 26 % for the descending profile, while for the exhaust cam a 34 % wear reduction was registered for the ascending profile and 24.5 % for the descending profile. Because the effect of surface roughness over wear was not taken into account in the theoretical model, the authors tried to evaluate its effect during the experiments. The changes in the

Fig. 10 Wear for the intake valve



**Fig. 11** Wear for the exhaust valve

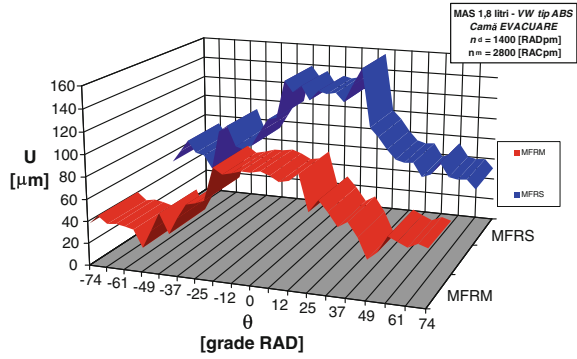


**Fig. 12** Effect of wear over the acceleration of the intake cam follower

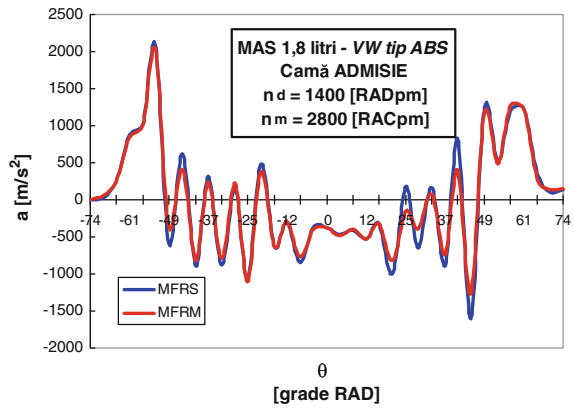


**Fig. 13** Effect of wear over the acceleration of the exhaust cam follower

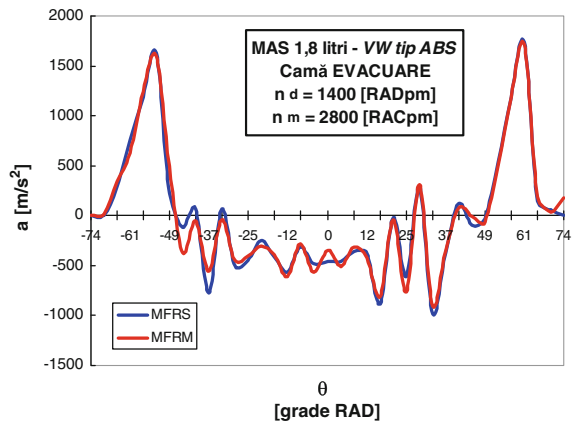


**Fig. 14** Wear reduction of the MFRM compared to MFRS for the intake cam

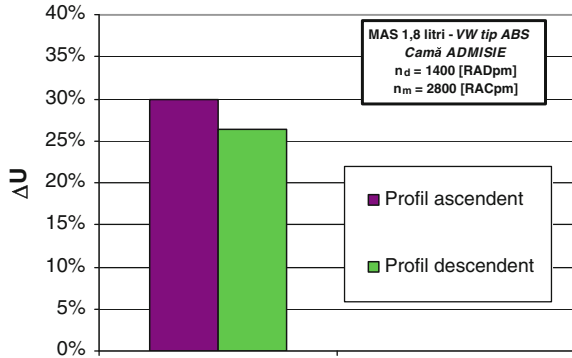
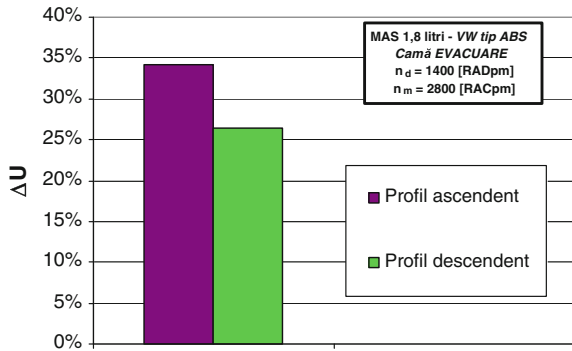
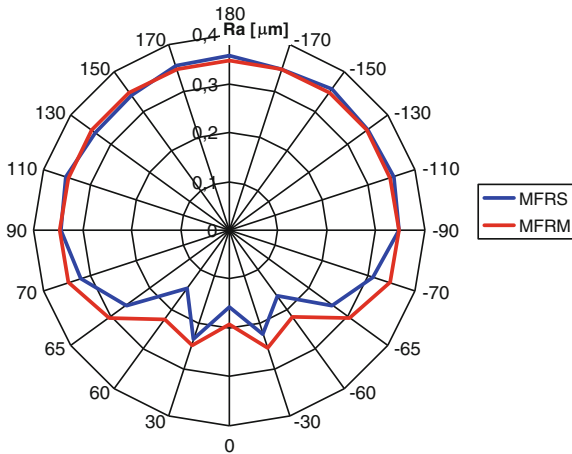


**Fig. 15** Wear reduction of the MFRM compared to MFRS for the exhaust cam



surfaces roughness are visible in Fig. 16. A more smooth variation of surface roughness was recorded for the modified real physical model **MFRM** compared to **SRPM**, thus confirming the mutual conditioning between lubrication and wear.

**Fig. 16** Average profile surface roughness of the intake and exhaust cam



## Conclusion

- For all the studied cases, the models have revealed a smoother drop in the thermal efficiency gain of the **VSCR** engine, during the combustion process.
- In the meantime, higher values of the thermal efficiency were recorded during the main phase of the combustion process and towards its end (the maximum thermal efficiency increase up to 4 %).
- A study of the efficiency increase shows that, in the first case, its maximum value is obtained at 35° CA after the TDC, while for the second case, the maximum value is attained at 37°–38° CA after the TDC. Thus is showing the advantage of this method in terms of a fuel consumption decrease.
- Several new notions were defined (*overall oil circulation* and *mechanical work of the piston ring friction forces*), in order to improve the profile of the compression rings of an internal combustion engine, to reduce oil consumption, to insure a predominantly hydrodynamic lubrication regime and to diminish piston rings and cylinder liner wear.
- The tests carried out with modified rings showed a decrease in gas pressure escaped in the crankcase and lower consumption of lubrication oil.
- The use of the **LUJET** solution has led to an effective reduction of the cams profile wear comprised between 22 and 30 µm; in the meantime, the experimental results shown a correlation between wear development and the surface roughness of the active profiles.
- In conclusion, the modification of those parameters leads to an optimized engine solution for lowering the fuel consumption and the pollution level, *an environmental friendly propulsion engine*.

## References

- Carra S, Garziera R, Pellegrini M (2004) Synthesis of cams with negative radius follower and evaluation of the pressure angle. *Mech Mach Theory* 39:p1017–p1032
- Gray Jr (2004) Piston in piston variable compression ratio engine. U S Patent, No. 6,752,105 B2
- Heisler H (1995) *Advanced engine technology*, SAE International
- Rakosi E, Manolache Gh, Talif S, Roşca R (2010) Solutions for reducing fuel consumption and pollution potential of automotive spark ignition engines. *Environ Eng Manage J* 9(10):1351–1355
- Taylor CM (1993) *Engine tribology*, tribology series 26, pp 75–88. Elsevier, Amsterdam
- Tournier JC (2007) Tribological analysis of injection cams lubrication in order to reduce friction and wear, SET Halstad
- Zhu D, Cheng HS (1989) An analysis and computational procedure for EHL film thickness, friction and flash temperature in line and point contacts. *STLE Tribol Trans* 32(3):364–370 (Park Ridge, IL, USA)

# Aspects Regarding the Evolution of the Depollution Norms and Test Cycles in Order to Determine Polluting Emissions

Gheorghe Bancă, Valentin Nişulescu and Gheorghe Frăţilă

**Abstract** This paperwork presents the evolution of depollution norms from Euro5 to Euro6 presenting at the same time the technologies used in order to meet their requirements and a comparative analysis of the NMVEG (New European Motor Vehicle Emissions Group) and WLTC (World Harmonized Light Vehicles Test Cycle) test cycles respectively, test cycles used in order to establish the level of polluting emissions for homologating the road vehicles equipped with thermal and hybrid engines, as well as for establishing the autonomy of the electric vehicles. It also describes the new WLTC test cycles to be adopted in the EU (European Union) starting with the Euro6c depollution norm.

**Keywords** Depollution · Emissions · Test cycles · NMVEG · WLTC

## Introduction

The climatic changes and the awareness on the damaging effects of the pollutants generated by the internal combustion engines have determined the international organizations to introduce legislative measures concerning the control of polluting emissions generated by road vehicles. Therefore, the American State of California announced the first regulations in 1961, then Japan in 1968, while the EU brought them up in discussion at the beginning of the 1970s, thus resulting “three major international norms” whose stages from the past 3 decades are schematically shown in Fig. 1.

The challenge brought by the international organizations made that the evolution of the limits provided by the norms be updated every 4–5 years, thus preserving and improving the dynamic performances, and the reliability of the thermal engines, concomitant with the evolution of the depollution norms throughout the vehicles lifespan, which forced the automotive manufacturers to come up with new tech-

---

G. Bancă (✉) · V. Nişulescu · G. Frăţilă  
University Politehnica of Bucharest, Bucharest, Romania  
e-mail: banca\_2004@yahoo.com



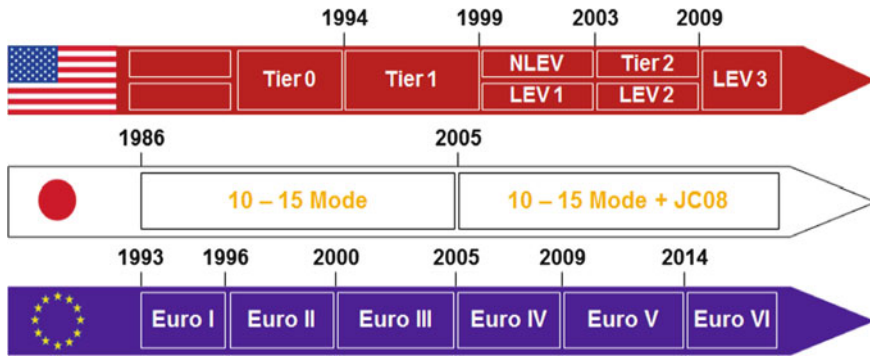


Fig. 1 Stages of the “three major international norms”

nologies in order to meet such limits, increasingly drastic. For the Euro norms, the technical development of the depollution systems faced several stages, each stage being associated to a certain norm from Euro1, Euro2, to Euro6, namely:

- for vehicles with SI engines (Spark-Ignition engines)—Fig. 2;
- for vehicles with CI engines (Compression-Ignition engines)—Fig. 3.

Nowadays, it is difficult to make a comparative analysis of the stringency of the regulations given that the test procedures and cycles are different (NMVEG for UE, JC-08 for Japan and FTP-75 for the USA) (Oprean 2003). In order to eliminate such shortcomings, UNECE (United Nations Economic Commission for Europe) proposed a new polluting emissions testing procedure for the light vehicles, called WLTP (Worldwide harmonized Light vehicles Test Procedure), procedure which shall adopt a new WLTC reference cycles, Fig. 4, to be implemented towards the end of 2017.

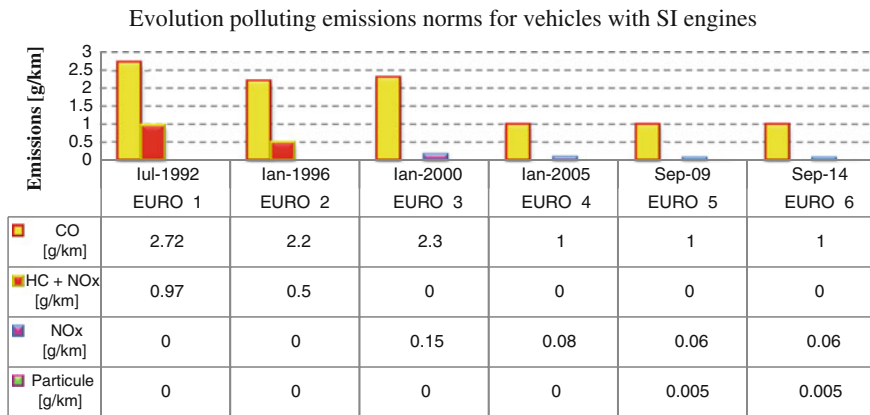


Fig. 2 Evolution of Euro norms for vehicles with SI engines

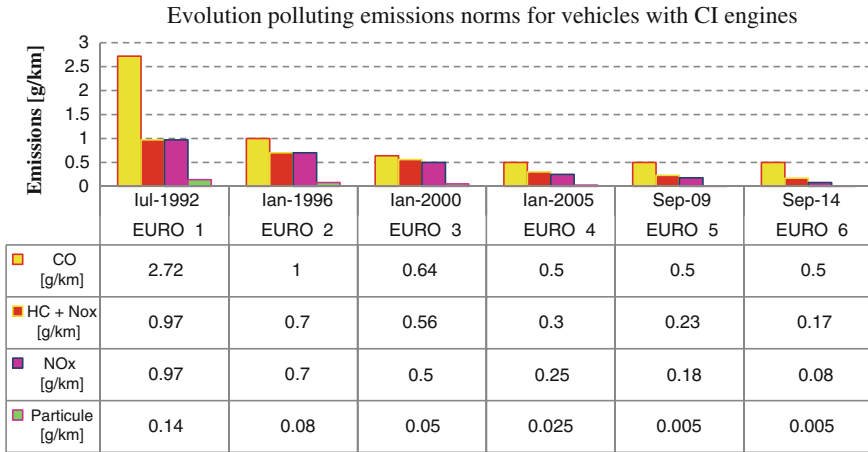


Fig. 3 Evolution of Euro norms for vehicles with CI engines

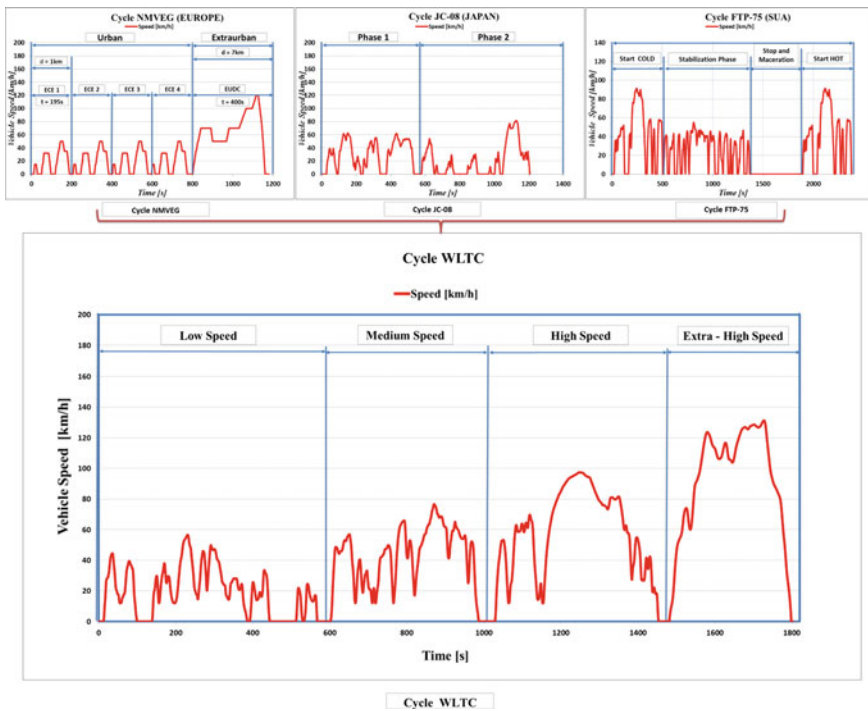


Fig. 4 Types of test cycles for determining the polluting emissions (NMVEG, JC-08, FTP-75 and WLTC)

The WLTC (Worldwide harmonized Light-duty Test Cycle) cycle, Fig. 4, is the cycle dedicated to testing the light vehicles in order to establish the polluting emissions, being proposed to replace the current NMVEG cycle, and it represents the base of the new test procedure, a procedure initially proposed by the UNECE, to be implemented since 2017.

With regard to the test procedure, it imposes additional restrictions concerning the tests carried out on the dynamometric benches and of running resistance, ambient temperature, the fuel quality, the gearbox shifting, choosing the tyres model and tyres pressure, charging the storage battery, the total weight of the vehicle (including the optional pieces of equipment, the loading and number of passengers), etc.

The WLTC cycle comprises 4 stages (low speed, medium speed, high speed and very high speed) and depending on the PMR ratio (power-to-mass ratio) of the vehicles—where the rated power is expressed in W, idle running weight in kg, the following test classes were defined and shown in Table 1.

In continuation, Table 2, summarizes the main characteristics of the NMVEG and WLTC cycles.

To determine the characteristics of Table 2 were used the relations:

– total time:

$$T_{total} = t_2 - t_1 + \sum_{i=2}^n (t_i - t_{i-1}) \tag{1}$$

**Table 1** Test classes used on the WLTC cycle depending on the PMR ratio

Category	PMR (W/kg)	Speed	Comment
Class 3	PMR > 34	Low, medium, high, very high	If v_max < 135 km/h, the ‘very high’ stage is replaced and the ‘low’ stage is repeated
Class 2	34 ≥ PMR > 22	Low, medium, high	If v_max < 90 km/h, the ‘high’ stage is replaced and the ‘low’ stage is repeated
Class 1	PMR ≤ 22	Low, medium	If v_max ≥ 70 km/h, the ‘low’ stage is repeated after the ‘medium’ stage
			If v_max < 70 km/h, the ‘medium’ stage is replaced and the ‘low’ stage is repeated

**Table 2** The main characteristics of the NMVEG and WLTC cycles

Characteristics of the cycles	Unit	NMVEG	WLTC
Total time	s	1180	1800
Total distance run	km	10.993	23.262
Idle time	s	267	242
Average speed (incl. stops)	km/h	33.538	46.4
Average speed (excl. stops)	km/h	43.157	53.8
Maximum speed	km/h	120	131.3
Average acceleration	m/s <sup>2</sup>	0.592	0.41
Maximum acceleration	m/s <sup>2</sup>	1.042	1.67

- total distance run:

$$d_{total\ run} = (t_2 - t_1) \frac{v_1}{3.6} + \sum_{i=2}^n (t_i - t_{i-1}) \frac{v_i}{3.6} \quad (2)$$

where  $v_i$  represents the vehicle's speed in m/s for the time step  $i$ ;

- average speed (incl. stops):

$$\dot{v}_{medium\ with\ stop} = 3.6 \frac{d_{total\ parc}}{T_{total}} \quad (3)$$

- average speed (excl. stops):

$$\dot{v}_{medium\ no\ stop} = 3.6 \frac{d_{total\ parc}}{T_{total}} \quad (3')$$

- max speed:

$$v_{max} = \max(v) \quad (4)$$

- average acceleration:

$$a_{medie} = \frac{1}{T_{total}} \sum_{i=1}^n a_i \quad (5)$$

- maximum acceleration:

$$a_{maxi} = \max(a_i) \quad (6)$$

where  $a_i$  represents the vehicle's acceleration in  $m/s^2$  for the time step  $i$ , if  $a_i > 0$ .

An important parameter requiring a particular attention when analysing a depollution cycle is the so-called relative positive acceleration or RPA (Relative Positive Acceleration) since it can provide data about how loaded is the respective cycle ([http://siar.ro/wp-content/uploads/2015/06/RIA\\_35.pdf](http://siar.ro/wp-content/uploads/2015/06/RIA_35.pdf)). The formula is given by the relation:

- relative acceleration:

$$RPA = \left( \frac{1}{d_{total\ parcursa}} \right) \sum_{i=1}^n \begin{cases} \frac{a_i v_i}{3.6} & \text{if } (a > 0) \\ 0 & \text{(otherwise)} \end{cases} \quad (7)$$

## Experiment

The case study is based on the upstream project study involving on identifying the operational points of the two cycles and the estimation of the polluting emissions for a vehicle equipped with a 1.5 dCI 81 kW Euro6 engine, using the simulation platform AMESim (Advanced Modelling Environment for Simulation of Engineering Systems).

The method of building the AMESim calculation model involves: generating an “ISO Camp” at the engine’s bench, choosing the model architecture—functional/dysfunctional (understanding the physical phenomena, defining the captors and actuators), creating and simplifying the model (formal—linear or nonlinear model), validation based on the initial test at the engine’s bench.

As far as the WLTC cycle is concerned, during simulation, just like when testing a vehicle on the roller bench, an important aspect is represented by the calculation of the time when shifting the velocity steps for each vehicle, which is a new aspect as compared against the NMVEG cycle, where the time for shifting the velocity steps is fixed. The purpose is to reflect the practical use and an efficient driving behaviour (low fuel consumption). The indications related to the shifting of the velocity steps per WLTC cycle are based on the balance between the power necessary to overcome resistances to advance in acceleration and the power supplied by the engine in all gears ratio possible, in a specific phase of the driving cycle.

The power necessary is calculated for each second  $i$  of the speed profile of the cycle, considering the power required in order to overcome the resistances to advance and provided that the vehicle accelerates using the relation 8:

$$P_{required,i} = \frac{f_0 \cdot v_i + f_1 \cdot (v_i)^2 + f_2 \cdot (v_i)^3 + (k_r \cdot a_i \cdot v_i \cdot m_t)}{3600}, \quad (8)$$

where:

- $f_0$  the load factor, represents the advanced resistance caused by the contact between the tyre and the rolling track (N);
- $f_1$  the load parameter, represents the frictions with in the kinematic chain of the transmission depending on speed [N/(km/h)];
- $f_2$  the load coefficient, represents the stressed caused by the aerodynamic resistance depending on the squared speed [N/(km/h)<sup>2</sup>];
- $P_{required,i}$  the power necessary in kW at second  $i$ ;
- $a_i$  vehicle acceleration at the second  $i$ , with  $a_i = \frac{v_{i+1} - v_i}{3.6 \cdot (t_{i+1} - t_i)}$  in m/s<sup>2</sup> and  $t$  — —time in s;
- $v_i$  vehicle speed at the second  $i$  in km/h;
- $m_t$  the vehicles mass in kg;
- $k_r$  coefficient that considers the inertial resistance values from the running gear during acceleration.

Description of the model: In order to study the influence of the transition from the NMVEG cycle at the WLTC cycle, the realization of the AMESIm simulation involve to model a vehicle equipped with a CI engine (compression ignition engine) turbocharged, a clutch, a gearbox, the after-treatment system exhaust (DOC—Diesel Oxidation Catalyst, NOx-Trap and DPF—Diesel Particulate Filter) and the cycles profiles (where the WLTC cycle should be defined in terms of speed and time-based ratio). The model also includes the basic accessories, he starter and the alternator, Fig. 5.

Since, in the event of using the HIL (Hardware in the Loop) model, we are constrained by the calculation time of the model in order to run in real time, we have used the DRVICE01D component (Driver internal combustion engine), a function specific for AMESIM which uses 8 files as inputs (necessary to be known and parameterized):

- the engine torque is calculated from the cartography “torque.data” or “BMEP.data” in inside the model and the engine temperature impact is taken into account by using the water temperature or the oil temperature and the “FMPEP.data” file, after relation 9:

$$T = T_{table} + T_{losses, T_{hot}} - T_{losses, temp} \tag{9}$$

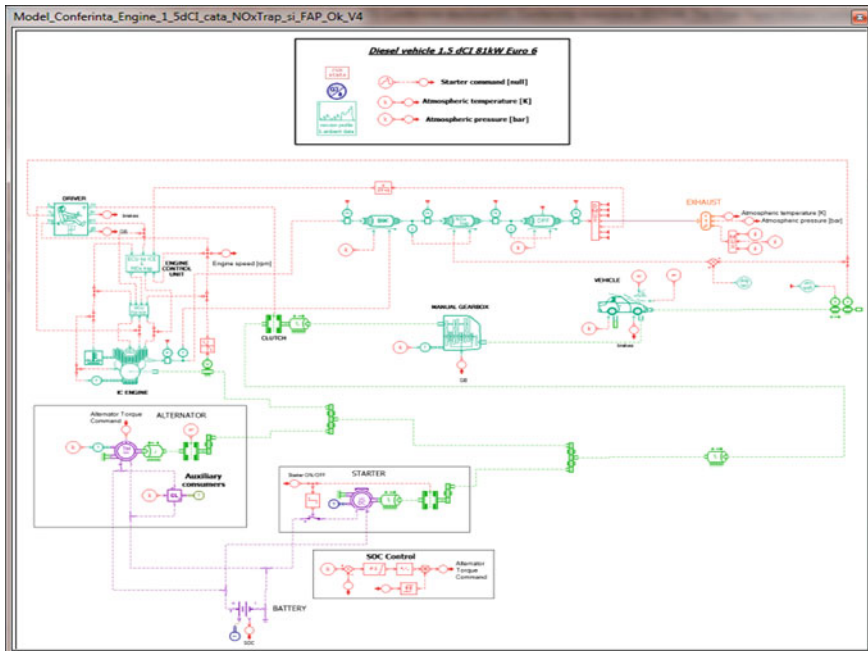


Fig. 5 A drawing of the proposed model

where:

- $T$  means the corrected torque (Nm);  
 $T_{table}$  means the torque (Nm) taken from the cartography “torque.data”;  
 $T_{losses}$  means the friction torque (Nm) at hot engine temperature  $T_{hot}$  taken from the cartography “FMEP.data”;  
 $T_{hot}$  means the parameter “hot engine temperature” (°C);  
 $T_{losses,temp}$  means the friction torque (Nm) at water temperature or oil temperature taken from the Table 1D “FMEP.data” (temp =  $T_{water}$  or temp =  $T_{oil}$ );  
 $T_{water}$  means the temperature of the water coming through the port 7 (°C);  
 $T_{oil}$  means the temperature of the oil through the port 8 (°C).

- at the end, a correction is applied on the output torque during the acceleration stages, in order to consider the environment conditions, as follows, relation 10:

$$T_{out,1} = T_{dyn} \cdot \frac{\rho_{air}}{1.205} \quad (10)$$

with:

- $T_{out,1}$  output torque at port 1 (Nm);  
 $T_{dyn}$  dynamic engine torque (Nm);  
 $\rho_{air}$  air density ( $\text{kg/m}^3$ ).

- for the output torque, the brakes medium effective pressure (BMEP) is calculated using the relation 11:

$$BMEP = \frac{4 \cdot \pi \cdot T_{out,1} \cdot 10^{-2}}{V} \quad (11)$$

where:

- $BMEP$  means the Brakes Medium Effective Pressure (bar);  
 $T_{out,1}$  means the torque at the engine shaft (Nm);  
 $V$  means the engine’s cylinder capacity (L).

- in the end, the real power is calculated using the relation 12:

$$P = T_{out,1} \cdot \omega \cdot 10^{-3} \quad (12)$$

where:

- $P$  means the real power (kW);  
 $T_{out,1}$  means the torque at the engine shaft (Nm);  
 $\omega$  means the angular speed at the shaft (rad/s).

## Results and Explanation

In order to validate the results, compliance with the speed profile on the roller bench is an important criterion in declaring the test as valid or invalid, the accepted tolerance being of  $\pm 2$  km/h (or 0.56 m/s) at  $\pm 1$  s. Both in Fig. 6 (simulated NMVEG cycle), and in Fig. 7 (simulated WLTC cycle) it could be noticed that this condition is fulfilled, therefore we can further analyse the results.

Considering the dynamics of the WLTC cycle, where the speeds and accelerations are significantly higher to the NMVEG cycle, there was a first comparative analysis between cycles made in Table 3 over the CO<sub>2</sub> emissions, emissions that render the fuel consumption bigger picture. The simulation results show that, although the WLTC cycle is more severe from the point of view of the speed—and loading respectively, the cumulated CO<sub>2</sub> emissions generated by the engine are approximately 103 % higher for the WLTC cycle, fact explained by the longer distance run  $\sim 23$  km, the global emissions of the engine expressed in g/km remained at the same level or even dropped by  $\sim 2$  %.

The logical explanation for which the CO<sub>2</sub> emission on the WLTC cycle are the same as on the NMVEG cycle is given by the fact that, although the engine load is higher on the WLTC cycle, the engine exploitation does make in an optimum operating condition close to the economical pole of the engine, where the range of operational points of the WLTC cycle is higher than the operational points of the NMVEG cycle. This fact is confirmed by the chart in Fig. 8, where the characteristic speed-torque in the WLTC cycle is at the edge of maximum torque

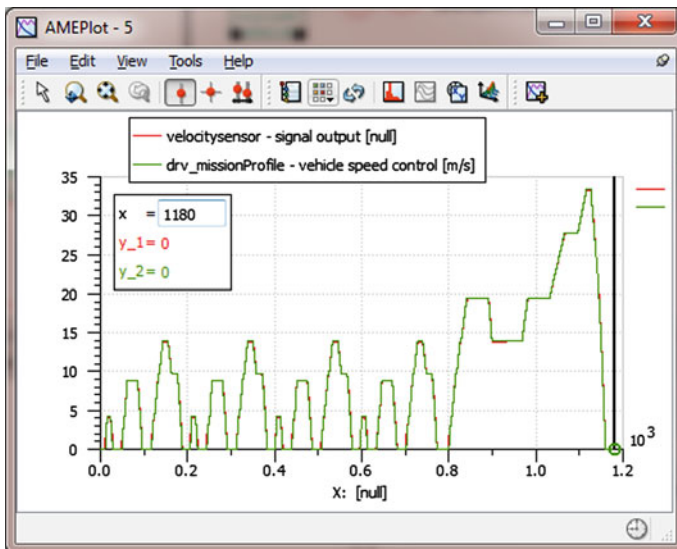


Fig. 6 Speed simulation in NMVEG cycle



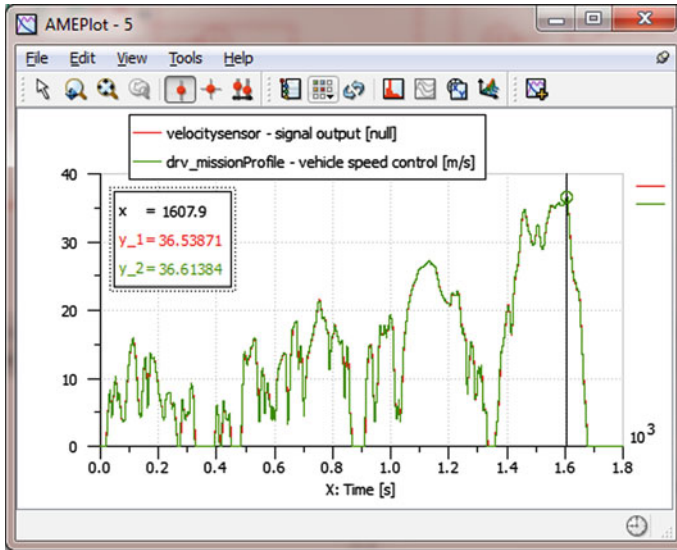


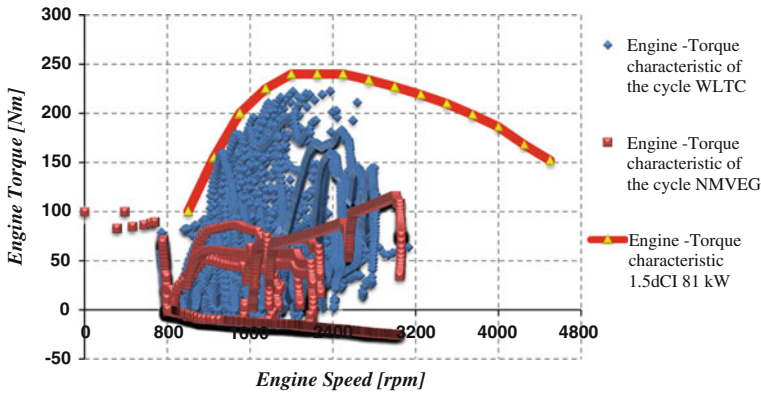
Fig. 7 Speed simulation in WLTC cycle

Table 3 Comparative analysis of CO<sub>2</sub> emissions

CO <sub>2</sub> emissions by the engine				
Cycle	Unit	NMVEG	WLTC	Variation (NMVG–WLTC) (%)
Norma	g/km	–	–	0
Distance run	km	11.08	22.866	106
Cumulated emissions from the engine	g	1287.37	2610.5	103
Emissions from the engine	g/km	116.19	114.16	–2

generated by the engine, the manufacturer having the freedom to calculate the moment for shifting the velocity steps for each vehicle.

For the particles emissions, Table 4, the shifting to the WLTC cycle faced a growth of the cumulated emissions by relatively up to 433 %, caused by violent accelerations, which lead to a richness >0.6 (richness = 1/lambda)—where the growth of the particles emissions becomes exponential, and a relative growth of 160 % of the global emissions, however, the limits of the Euro6c norm is met due to the DPF (Diesel Particulate Filter) technology, whose efficiency reached up to 99 %. Although the norm limits are met, increasing the loading speed by 160 % leads to triggering more frequent regenerations, reason for which special attention should be given when calibrating the Diesel engines and recalculating the Ki (regenerative coefficient), or re-dimensioning the DPF.



**Fig. 8** Engine torque characteristic—operational points

**Table 4** Comparative analysis of particles emissions

Mechanical particles emissions				
Cycle	Unit	NMVEG	WLTC	Variation (NMVG–WLTC) (%)
Norma	g/km	0.005	0.005	0
Distance run	km	11.08	22.866	106
Cumulated emissions from the engine	mg	923	4923.96	433
Emissions from the engine	g/km	0.0833	0.21534	159
Cumulated exhaust emissions	mg	9.23	49.24	433
Exhaust emissions (with FaP)	g/km	0.00083	0.00215	159
FaP efficiency	%	0.99	0.99	0

The analysis of NO<sub>x</sub> (Nitrogen Oxides), Table 5, shows an important degradation of the cumulated emissions, of approximately 350 % in relatively, degradation caused particularly by the higher temperatures (over 2000 K) in the combustion room, because of the higher charge in the WLTC cycle. In this particular case, although the simulation was made with an engine whose DT (Technical Definition) complied with the Euro6b norm (Cata + NO<sub>x</sub>-Trap and DPF), we could notice that the norm provisions were met for the NMVEG cycle, but not for the WLTC cycle, therefore, a re-optimization of the calibration as well as of the NO<sub>x</sub>-Trap re-dimensioning might be considered.

For HC emissions (unburned hydrocarbons)—Table 6 and CO emissions (Carbon Monoxide)—Table 7, the norm is complied with. We even notice an improvement of the HC emissions by approximately 20 %, and the same level of CO emissions in the WLTC cycle, according to ISO standards, this fact being explained by a quicker heating of the catalyser given the high loads throughout the WLTC cycle.

**Table 5** Comparative analysis of NO<sub>x</sub> emissions

NO <sub>x</sub> emissions				
Cycle	Unit	NMVEG	WLTC	Variation (NMVG–WLTC) (%)
Norma	g/km	0.08	0.08	0
Distance run	km	11.08	22.866	106
Cumulated emissions from the engine	mg	1478.949	6675.71	351
Emissions from the engine	g/km	0.13348	0.29195	119
Cumulated exhaust emissions	mg	650.7376	2937.31	351
Exhaust emissions	g/km	0.05873	0.12846	119

**Table 6** Synthesis of HC emissions

HC emissions				
Cycle	Unit	NMVEG	WLTC	Variation (NMVG–WLTC) (%)
Norma	g/km	0.05	0.05	0
Distance run	km	11.08	22.866	106
Cumulated emissions from the engine	mg	5100.186	8506.36	67
Emissions from the engine	g/km	0.46031	0.37201	–19
Cumulated exhaust emissions	mg	408.0149	680.509	67
Exhaust emissions	g/km	0.03682	0.02976	–19

**Table 7** Synthesis of CO emissions

CO emissions				
Cycle	Unit	NMVEG	WLTC	Variation (NMVG–WLTC) (%)
Norma	g/km	0.5	0.5	0
Distance run	km	11.08	22.866	106
Cumulated emissions from the engine	mg	30416.34	63575.2	109
Emissions from the engine	g/km	2.74516	2.78034	1
Cumulated exhaust emissions	mg	3649.961	7629.02	109
Exhaust emissions	g/km	0.32942	0.33364	1

## Conclusions

The evolution of the depollution norm from Euro5 to Euro6 involves reduction of the NO<sub>x</sub> polluting emissions limits (0.18–0.08 g/km) only for the vehicles equipped with CI engines, however, the stringency of the Euro6c norm is given by the new type of WLTP test procedure and the new type of WLTC cycle adopted;

As far as the are CO<sub>2</sub> emission, for the studied engine, although the WLTC cycle shows a higher constraining from the loading point of view, the global CO<sub>2</sub> emissions expressed in g/km remained at the same level, with even a slight decrease;

The engine speed torque characteristic for the WLTC cycle is at limit between of the maximum torque delivered by the engine, thus rendering the engine to operate on optimum operating points close to economical pole of the engine, where the engine efficiency is optimum;

Although the norm limits are met for the particles emissions, increasing the loading speed leads to triggering more frequent regenerations, reason for which special attention should be given when recalculating the Ki factor (regenerative coefficient).

Considering the simulation results, there might be considered a re-optimization of the calibration from the MAP (Mise au point) point of view, as well as a NO<sub>x</sub>-Trap re-dimensioning in order to comply with the Euro6c norm in relation to the emissions of nitric oxides.

With regard to the HC/CO emissions, the WLTC cycle shows zero non-conformity risks, with “iso” CO emissions, being favourable for reducing the HC emissions given of a high load on cycle, which leads to the quick heating of the catalyser.

**Acknowledgements** The results presented in this article were obtained with the support of the Ministry of European Funds through the Sectorial Operational Program for Human Resources Development 2007–2013, Contract No. POSDRU 187/1.5/S/155420.

## Reference

Oprean IM (2003) Modern automobile. Romanian Academy Publishing House, Bucharest

# Measurement Equipment for Research of the Pressure Wave Compressors

Cristian-Ioan Leahu, Dan Mihai Dogariu, Anghel Chiru,  
George-Radu Toganel and Gabriel Mitroi

**Abstract** The performances of the supercharged internal combustion engines are depending significantly on the efficiency of the compressors, but also on the quality of tuning of the compressors with the engines. Such an example may be the pressure wave compressor. This compressor requires a careful tuning with the engine, in order to assure a high working efficiency. More precisely, the driving speed of the compressor must be identified, for every engine speed and load domain. Researches in this direction are required, both for the pressure wave compressor separately to the engine, but also for the whole assembly mounted on the engine. Through pressure wave compressors exhaust gas and intake air is flowing. For this reason, it is necessary to evaluate the evolution in time of the two gases parameters, at different speeds of the compressor's rotor. The measurements can be realized with special and precise equipment. Therefore, in this paper are presented such equipment, with the mounting places on the pressure wave compressor.

**Keywords** Measurement equipment · Pressure wave compressor · Engine · Intake air pressure

---

C.-I. Leahu (✉) · D.M. Dogariu · A. Chiru · G.-R. Toganel · G. Mitroi  
Transilvania University of Brasov, Eroilor Boulevard, no. 29, 500036 Brasov, Romania  
e-mail: leahu.cristian@unitbv.ro

D.M. Dogariu  
e-mail: dan.dogariu@gmail.com

A. Chiru  
e-mail: achiru@unitbv.ro

## Introduction

The supercharging process realized by the pressure wave compressor is far more complex than the supercharging process made by the turbochargers. Inside the turbocharger the exhaust gases are flowing through the turbine and the intake air through the blower. These two parts of the turbocharger are isolated from each other. This means that the exhaust gases and the intake gases do not meet at any time (Rakopoulos and Giakoumis 2009).

Instead, within the pressure wave compressor, the exhaust gases and intake gases successively occupy the same areas. More specifically, through the rotor channels, the intake air and the exhaust gases are constantly in direct contact (Heisler 1995). Therefore, in the interface zone between the exhaust gases and intake air under certain conditions, it can produce a process mixture of the two gases.

To minimize the negative effects of this mixing process, the drive speed of the pressure waves compressor must be correlated with the parameters of the exhaust gases, which entering in compressor (Hirceaga and Radu 2012). Correlation would be achieved in each operating mode of the supercharged engine (Leahu et al. 2015a, b). In this way, to a certain pressure of the exhaust gases, will correspond a certain drive speed of the pressure waves compressor.

Through this correlation is aimed mainly at achieving three objectives: obtaining the intake air pressure higher compared with the exhaust gases pressure; the entering inside the intake manifold only of the compressed air, and not the air mixed with the exhaust gases; filling the whole volume of fresh air channels at the beginning of the functional cycle.

To achieve these objectives, the experimental research equipment must be used to determine among others, the pressure and temperature variation of the exhaust gases at various drive speeds of the compressor. Therefore, in this paper are presented such equipment, with the mounting places on the pressure wave compressor.

## Theoretical Aspects

The pressure waves compressor is composed of a rotor placed between two stators, one through which the exhaust gases are flowing (warm stator), and one through which the intake air is flowing (cold stator). The rotor is passed from one end to the other by longitudinal channels. At a single rotation speed of the rotor, each channel is successively passing by the ports in the stators. Inside the cold stator are located the intake and evacuation ports of the air, and in the warm stator are located the intake and evacuation ports of the exhaust gases.

It can be considered that inside a channel is beginning a new functional cycle, when it is filled with fresh air (Leahu 2013). According to Fig. 1, by rotating the rotor, the channel that is filled with fresh air, reaches the port 3. Thus, exhaust gases enter in the channel, compressing directly the intake air. When the channel reaches

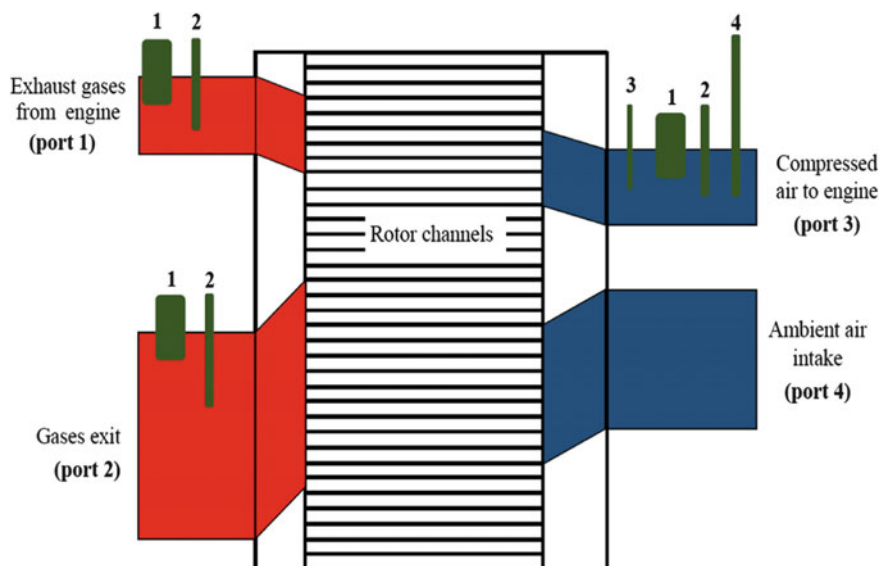


**Fig. 1** Mounting the measure equipment used at the research of the pressure wave compressor: 1 pressure sensor, 2 temperature sensor, 3 anemometer, 4 sampling for gas analyzer

port 1, the compressed air will be evacuated to the engine. It is important that the channel passes port 1 before the exhaust gases reach the end of the channel, at the cold stator.

Further, by moving the channel, the exhaust gases will return through port 4 in the warm stator, where they will be evacuated in the exhaust system of the vehicle. The evacuation process is based on the exhaust gases high pressure. Simultaneously with the emptying of the channel of exhaust gases, the channel is filled with fresh air, and the operating cycle is resumed. To have only intake air at the ending of the functional cycle, it is necessary that with the evacuation of the exhaust gases (through port 4) will be evacuated a part of the intake air (through the port 2). This will ensure emptying a channel of gases.

In the processes of compression and expansion carried inside the rotor channels are formed the pressure waves. These waves may improve, in certain circumstances, the quality of the compression and expansion processes (Leahu 2013).

The efficiency of a pressure wave compressor depends significantly on the pressure of the exhaust gases generated by the supercharged engine. At a certain pressure of the exhaust gases, the value of the drive speed influences the moment in which the intake air-exhaust gases interface reaches the end of the channel, at the cold stator. If the speed is too low then exhaust gases can reach the supercharged engine's intake manifold. If the rotation speed is too high, the interface is reaching only a part of the length of the channel, resulting a reduced compression level.

Also the drive speed may influence the fresh air fill level of the channels. In this case, if the exhaust gases speed is low, a too high drive speed won't allow a satisfying fill of the channels with air.

## Measurement Equipment for the Research

To streamline an existing pressure wave compressor model, is needed that it's driving speed to have an optimal value through each engine operation mode (Hirceaga and Radu 2012). In this way, there would be a high quality supercharging process that will improve the ecological end energetical performances of the supercharged engine (Leahu and Radu 2011). Improving the quality of supercharger process reduce emissions during engine operation at low-medium speeds and loads, which are characterized higher polluting emissions (Tarulescu 2011).

To achieve this objective, it is necessary to identify the drive speed at which is obtained the highest air pressure. This pressure that corresponds to a certain value of the exhaust gases pressure. Experimental researches are carried out with the compressor at different speeds driving to the same functional regime of the engine. According to (Leahu et al. 2013; Leahu et al. 2015a, b), this is achievable if the pressure wave compressor is powered by an electric motor with variable drive speed.

As we can see in Fig. 1, to measure the exhaust gases pressure is used a pressure sensor which is mounted at the entrance of the gases inside the warm stator. Also, in that area is mounted a temperature sensor. Such sensors are shown in Fig. 2.

The piezo electrical sensor shown in Fig. 2b can operate up to 400 °C, therefore, when measuring the exhaust gas pressure it must be cooled. In this sense the sensor is mounted on the exhaust manifold through an adaptor for cooling (Fig. 2c). Between the pressure sensor and the adaptor is circulating cooling liquid (Merker et al. 2012).

In order to obtain information related to velocity of the gases inside the rotor channels, is measured the velocity of the air that is exiting the compressor. Velocity measurement can be realized with a hot wire anemometer (Fig. 2d). By the usage of this anemometer can also be identified the air flow that the pressure waves compressor provides the engine.

Also at the exiting of the compressed air from the compressor is mounted a pressure and a temperature sensor. This way we can compare the intake air and exhaust gases pressure. As the difference between the two pressures is more reduced, the efficiency of the compressor is higher. At the same time the temperature sensor indicates the need or not to use an intercooler. According to (Leahu et al. 2015a, b), the intake air that is evacuating the pressure wave compressors has a higher temperature than in the case of turbochargers, according to the same degree of compression air.

For example, in Fig. 3 is shown the efficiency that has a compressor during the supercharging of a compression ignite engine. Presented experimental results are



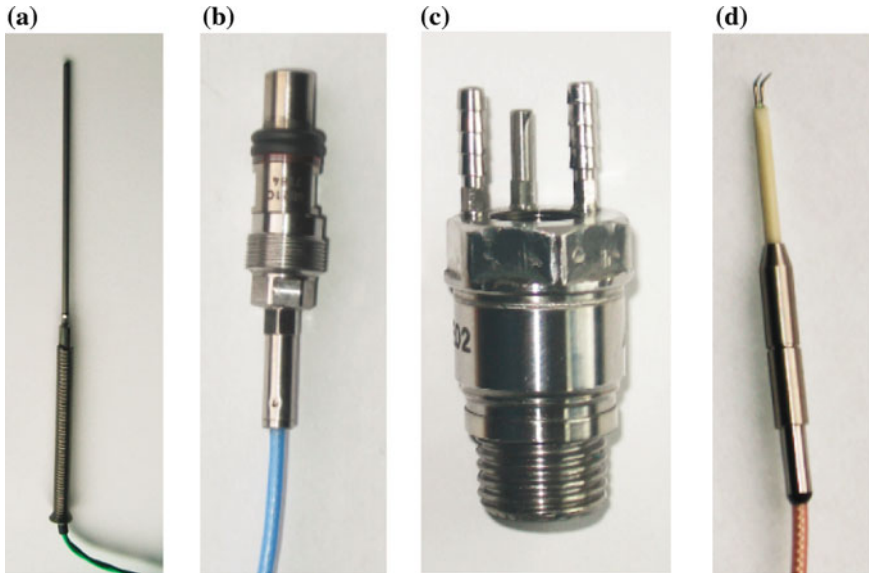


**Fig. 2** Types of sensors used in research of the pressure wave compressor: **a** thermocouple NiCrNi, **b** piezo electric pressure sensor, **c** hotwire anemometer, **d** cooled adapter for pressure sensor

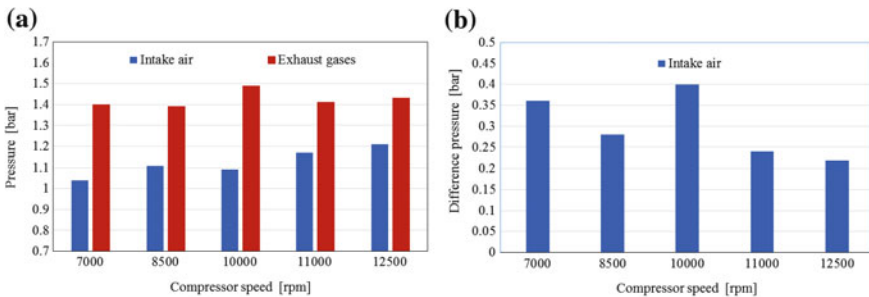


**Fig. 3** Variation of the intake air and exhaust gases pressure according to compressor speed: **a** air and gases pressure values, **b** the difference between the intake air and exhaust gases pressures

obtained with the engine operating at the same load and speed. During this time the pressure wave compressor was driven by an electric motor at different drive speeds.

In Fig. 3a it is shown that at the same operation regime of the compression ignite engine, the compressor was driven at various rotating speeds variable from 7000 to 12,500 rpm. The intake air pressure and the exhaust gases pressure were changed with the drive speed. According to Fig. 3b, the smallest difference between the intake air and the exhaust gases is obtained at the 12,500 rpm drive speed. It also notes that the rotation speed of 10,000 rpm will generate the biggest difference in

pressure between the two gases. However intake air pressure is above the pressure obtained at the drive speed of 7000 rpm. This indicates that a particular importance in ensuring a higher quality of the supercharging and the pressure with which the exhaust gases enter the pressure wave compressor.

As stated optimum drive speed of the pressure wave compressor implies among others that the exhaust gases do not reach the supercharged engine's intake manifold. Therefore, as shown in Fig. 2 in the output of the air of the compressor is connected a gas analyzer. This measure all pollutant emissions in the intake air, which indicated that a part of the exhaust gases located in the rotor channels reached the cold stator. In this situation the drive rotation speed will be modified so that the exhaust gases in the intake air to be minimal.

At the exit exhaust gases from pressure wave compressor can mount a pressure sensor and a temperature sensor. This way can be compared the exhaust gases at the entering and the exit of the compressor.

The maximum rotation speed of some pressure wave compressors can exceed 20,000 rpm. To measure such speeds it can be used an optical tachometer. Such tachometers can measure up to 100,000 rpm speeds with a resolution of 1 rpm.

## Conclusions and Discussions

The efficiency of an existing model of the pressure wave compressor may be increased if its driving speed is correlated with each value of the exhaust gases pressure of the supercharged engine. The correlating of these two parameters is made with difficulty because inside the compressor the intake air is in direct contact with the exhaust gases. Also the compression and expansion processes carried out inside the channels of the rotor are accompanied by pressure waves. These pressure waves, which cross the channels from one end to the other, can improve quality processes, if they reach the stators at the right times.

Correlating speed with the exhaust gases pressure has as primary objective obtaining a high as possible intake air pressure according to the exhaust gases pressure, and minimize the level of exhaust gases from the compressed air that is entering the supercharged engine.

To achieve these objectives, during research must be used equipment that measures pressure and temperature with the exhaust gases enter in the compressor. Equally important is to measure pressure, temperature, flow rate and the composition of the compressed air, evacuated by the compressor to the internal combustion engine.

It can be considered that the compressor efficiency is all the greater as the intake air pressure is closer to the exhaust gases pressure. But it is necessary that the exhaust gases pressure will be a high one. When choosing the optimal compressor rotation speed will take into account that the compressed air should be as less as possible contaminated with exhaust gases. In this regard one method is to use

during experimental research a gas analyzer that could measure any emission concentration in the intake manifold of the engine.

Compressed air velocity measurement can provide information on the speed of the moving interface between intake air and exhaust gases. It can also calculate air flow consumed by the internal combustion engine. Air consumption of the internal combustion engine it is desirable to directly measure the manifold between the compressor and the engine, because a part of fresh air entering the compressor is evacuated together with the exhaust gas.

**Acknowledgments** 1. This paper is supported by the Sectoral Operational Programme Human Resources Development (SOP HRD), financed from the European Social Fund and by the Romanian Government under the project number POSDRU/159/1.5/S/134378.

2. We hereby acknowledge the structural funds project PRO-DD (POS-CCE, O.2.2.1., ID 123, SMIS 2637, ctr. No 11/2009) for providing the infrastructure used in this work.

## References

- Heisler H (1995) Advanced engine technology. SAE Int, Warrendale
- Hirceaga M, Al Radu Gh (2012) Analysis of the influencing factors on the optimal driving speed of a pressure wave supercharger—PWS. *Ingenieria Automobilului* 6:14–15
- Leahu CI, Al Radu Gh (2011) Optimisation of joint operation of pressure waves compressors of type complex with diesel engines. *Bull Transilvania Univ Brasov* 53:7–12
- Leahu CI (2013) Theoretical and experimental researches as regards raising the efficiency of the supercharging process achieved by the pressure wave compressors. *Bull Transilvania Univ Brasov* 55:7–12
- Leahu CI, Abăitancei H, Radu S (2013) Drive with rotative speed independent from the engine, of the pressure wave compressors. *Recent J* 37:29–35
- Leahu CI, Chiru A, Tarulescu S (2015a) A modality to optimize common functioning of a pressure wave supercharger with an internal combustion engine. *Appl Mech Mater* 772:350–354
- Leahu CI, Dogariu DM, Chiru A (2015b) Researches on the influence of pressure wave compressor on the intake air temperature at the supercharged engines. *Bull Transilvania Univ Brasov* 57:7–12
- Merker GP, Schwarz C, Teichmann R (eds) (2012) Combustion engines development. In: Mixture formation, combustion, emissions and simulation. Springer, London
- Rakopoulos CD, Giakoumis EG (2009) Diesel engine transient operation, principles of operation and simulation analysis. Springer, London
- Tarulescu S, Tarulescu R (2011) Chemical pollution produced by the diesel vehicles in Brasov city. In: Chiru A (ed) *The automobile and the environment*. Cambridge Scholars Publishing, Newcastle-upon-Tyne, pp 475–486

# Friction Analysis of a Two Stroke Engine

Sebastian Radu, Horia Abăitancei, Adrian Tuşinean,  
Gheorghe-Alexandru Radu and Marton Iakab-Peter

**Abstract** Internal combustion engines continue to be the vehicles main propulsion system. For all engines, low friction levels are extremely important for the overall efficiency. Components and sub-systems where friction reduction can take place are: crankshaft main bearings, conrod bearings, cam shaft bearings, balancer shafts (if present), auxiliary drives (chains, alternator etc.), valve trains and pistons/pistons ring with liners. This paper describes how the bearings were calculated and assesses motor mechanism friction losses in the engine mechanism.

**Keywords** Two stroke · Engine · Simulation · Amesim

## Introduction

In the case of the internal combustion engines, only a part of the mechanical energy produced by the load within the cylinders during the combustion process and transferred to the driving mechanism is available at the crankshaft flange. A certain percentage of the energy generated by the load of the cylinders is lost by friction of components that are in relative motion. The amount of mechanical losses depends on the engine type and the operating conditions. To raise the engine performance it is necessary that the value of the mechanical energy, consumed to overcome the friction forces, to be as low as possible. Therefore action is taken to reduce the friction forces, within the driving mechanism, either via constructive measures (peripheral speed of the journal, materials, tolerances, etc.) either via technological measures (antifriction material addition, etc.)

---

S. Radu (✉) · H. Abăitancei · G.-A. Radu · M. Iakab-Peter  
Transilvania University of Brasov, Brasov, Romania  
e-mail: s.radu@unitbv.ro

A. Tuşinean  
ThermoLift, Inc., New York, USA

**Table 1** Two stroke engine specific geometry data

Bore	79.5	mm
Stroke	95.5	mm
Nr. of cylinders	4	
Total cylinder volume	1.9	l
Stroke/bore ratio	1.2	
Medium piston speed	12.73	m/s
Con rod length	166	mm

## Objectives

The main objective is to design a friction calculus for a two stroke diesel engine with the following input data: 4 cylinders in line, Power = 100 HP, Speed = 4000 rpm, maximum pressure in the cylinder = 200 bar. The main parameters of the engine mechanism are given in Table 1.

Necessary output data:

- Dimensioning engine's bearings system: B/D ratio, peripheral speed of the journal, clearance value, and minimum thickness of the lubrication oil film.
- Evaluation of power losses due to friction, friction coefficient calculus at various operating regimes of engine speed.

In order to meet this scope, the model was developed in that way that it can identify the friction conditions and losses for each pair of parts that have a relative motion. In this respect, the model is able to simulate a complete running cycle considering rotation angle dependent load and load application direction for the:

- piston/liner friction;
- piston/connecting rod bearing friction;
- connecting rod/crank friction;
- crank/crankcase.

Considering following running variables:

- different engine speeds;
- different engine/oil temperatures
- engine warm up period;
- engine transient speed variation.

A scheme of the overall analysis procedure is given in Fig. 1.

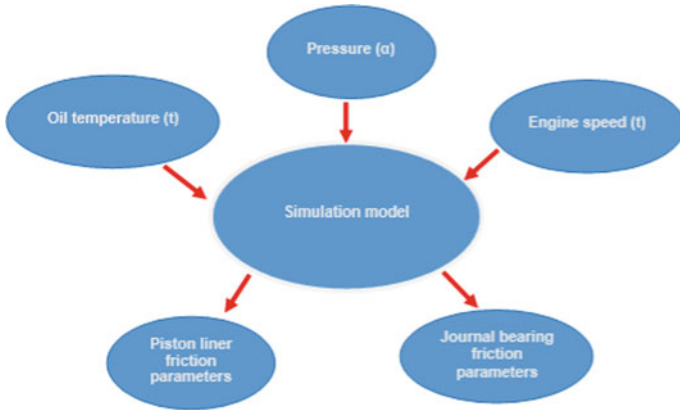


**Fig. 1** Scheme of the analysis procedure

## Basics of Physical Model

### *Piston/Liner Friction Basics*

Friction conditions of the piston/liner assembly are influenced, as presented in Fig. 1, by:

- material pair assembly;
- lubrication conditions;
- system geometry;
- time dependent boundary conditions.

### *Speed Dependent Flow Friction Coefficient*

Viscous friction between two surfaces that have relative motion between them depends on dimensional parameters such as contact area and clearance between the

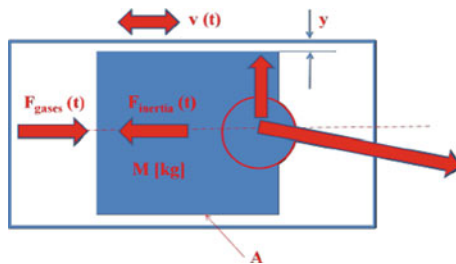


**Fig. 2** Forces acting in the conventional engine mechanism

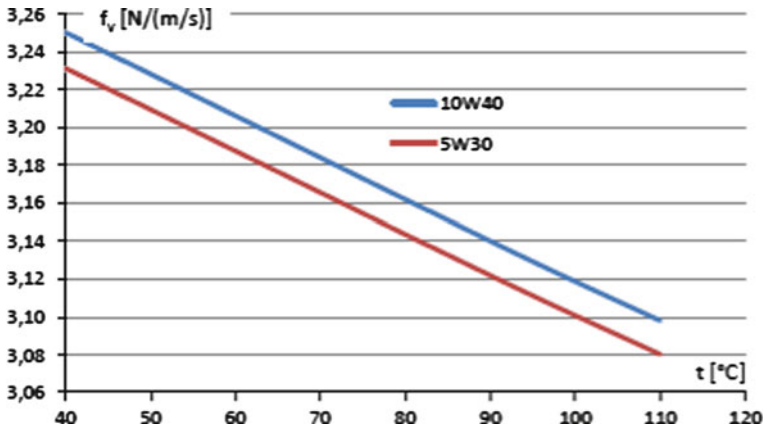


Fig. 3 Influence of temperature on viscous friction coefficient

two surfaces, and also depends on fluid properties, e.g. fluid density and viscosity. The flow friction coefficient is a measure of the damping of the movement of the oscillating mass, described by the Eq. 1.

$$M\ddot{x} + f_v \dot{x} + kx = F(t) \quad (1)$$

Viscous friction is, after (Küntschler 1987), linearly proportional to:

- fluid viscosity;
- fluid density;
- contact area between the two meeting surfaces; inversely proportional to:
- the clearance between the two meeting surfaces.

The viscous friction influence on piston group dynamics is described, considering the computation scheme in Fig. 2, by equation:

$$f_v = \frac{A\mu\rho}{y} \quad (2)$$

Influence of temperature on viscous friction coefficient is given in Fig. 3.

It can be observed that assuming a constant friction coefficient may alter the computation results.

## Methodology

To achieve the objectives of this paper were the following steps are:

- Input data computation considering overall engine parameters (given in Table 1). Computation of power, torque and mean effective pressure at rated power speed and rated torque speed.

- Computation of crank angle dependent piston speed and speed dependent friction force and power.
- Journal bearing dimensioning.
- Journal bearing friction power computation for each rated power and torque speed for each pair of elements in relative displacement.
- Computation of additional specific friction parameters: Friction mean effective pressure, Peripheral speed, Specific journal pressure.

For the evaluation of the losses caused by friction, a simulation program developed by LMS's multiple 1D Image Lab was used. The AMESim Software permits the common analysis of different physical systems that are functioning by different physical principles. The driving mechanism analysis was done using dedicated mathematical models that takes in account both hydraulic and mechanical components.

Planar mechanical library is used to model the crank mechanism:

- The engine bloc is considered as fixed and connected to the crank through a pivot junction (main bearing),
- The velocity of the crank body is imposed by an actuator. The crank is connected to the conrod through a pivot junction (conrod bearing),
- The conrod is connected to the piston through a pivot junction,
- The piston is connected to the engine bloc through a pivot junction. The ignition force is directly applied on it.

THH library is used to model the lubrication system:

- This oil groove feeds the main bearing. A hole in the crank collects one part of the oil,
- In the crank this oil is centrifuged before to reach the feeding hole of the conrod bearing (Fig. 4).

The connection between mechanical and lubrication systems is facilitated by sensors transferring load and velocity signals to the bearings. Bearing boundary conditions must be defined in such way that:

- Velocity input is the sum of the journal and the bearing velocities,
- Load and velocity inputs are expressed in the same absolute frame,
- The load to be used is the load applied by the bearing on the journal.

Figure 5 describes the way in which components are interconnected hydraulic and mechanical components.

The crankshaft rotary velocity is imposed. It starts from 0 to a constant fixed velocity. Two velocities are applied using a batch runs: 2000, 4000 rpm.

The piston force is computed from an in-cylinder pressure at full load. It is function of the crankshaft angle RPM and rotary velocity as shown Fig. 6.



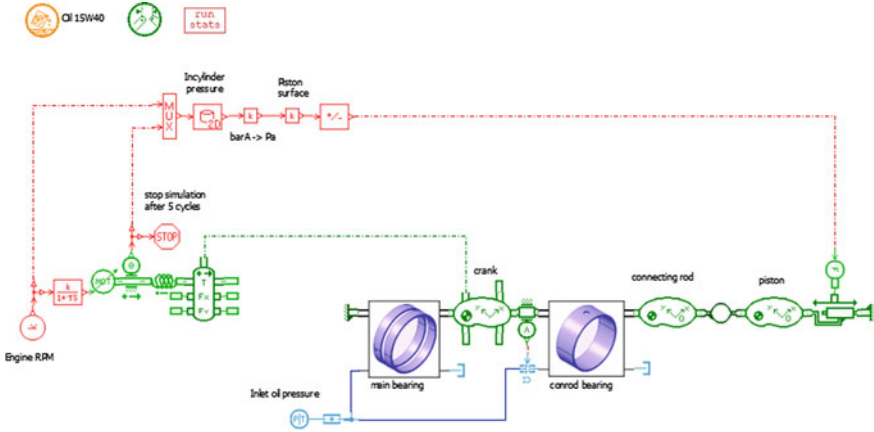
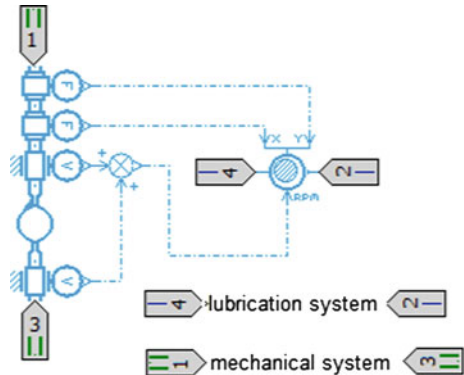


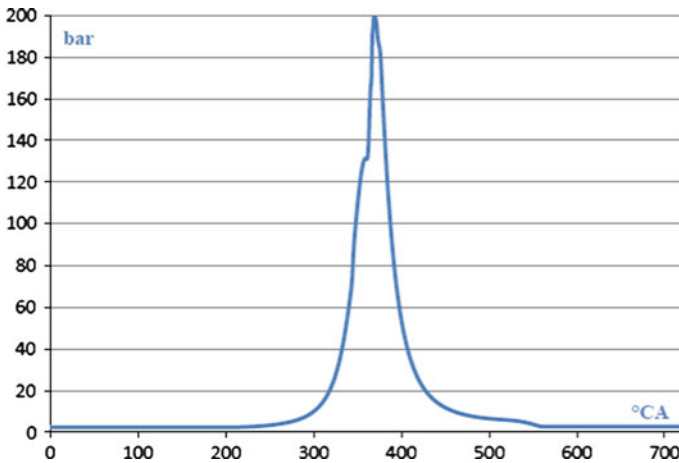
Fig. 4 AMESim model

Fig. 5 Sketch of mechanical/lubrication connection



The journal bearing is modeled using the model TFBEAPET11—thermal-hydraulic bearing (b. f.) with Petroff friction with partial groove with modulated rotary speed and load. This is a *bearing* submodel with a partial circumferential groove. The load can vary in intensity and direction. The *bearing* is fed by the *bearing* housing. Heat due to friction is computed with Petroff equation. The variation of radial clearance is also taken into account. The user has also access to the average temperature of oil film. Use this submodel to model bearings with a partial under varying load conditions.

Hydrodynamic effects can be taken in account. They are usually important in connecting rod bearings. Given  $D$  the *bearing* diameter and  $L$  its width, use Ocvirk solutions for  $L/D < 1$  and Warner-Sommerfeld for  $L/D > 1$  (Küntschler 1987). Up to



**Fig. 6** Cylinder pressure

$L/D = 0.5$ , the groove can extend at an angle up to  $270^\circ$ . For  $L/D$  from 0.5 up to 1, the submodel is accurate for a groove angle of up to  $180^\circ$ . Given  $C$  the radial clearance and  $D$  the bearing diameter, use this submodel if  $C/D < 0.05$ . Otherwise use hydraulic annular pipe submodel.

## Simulation Results

The simulation results are given below, considering piston and journal bearings. Following crank—angle dependent data are presented: Piston velocity (Fig. 7a), Piston friction power (Fig. 7b), Journal relative eccentricity (Fig. 7c), Minimum oil film thickness (Fig. 7d).

Friction analysis between piston and cylinder, piston ring versus cylinder, and connecting-rod versus piston bolt versus piston are presented in Table 2.

In the column total piston assembly there are summed the power losses for the elements grouped for an cylinder (piston-linear, piston-conrod and conrod-crank assemblies). In column “total engine” the crank-housing losses are added.

A time dependent analysis of the engine mechanism is considered for the crank/conrod journal for two conditions, engine acceleration and warm up. The simulation parameters were:

- speed increase from 2000 to 4000 rev/min 10 s (Fig. 8),
- engine temperature increases from 30 to  $90^\circ$  in 25 s (Fig. 9).

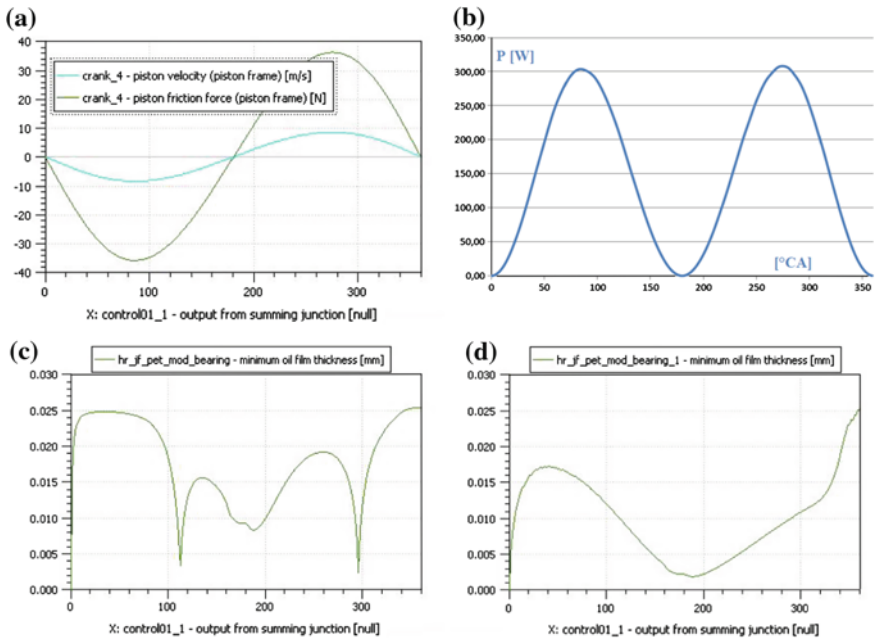


**Fig. 7** Simulation results. **a** Piston cylinder friction force and velocity **b** piston/cylinder friction power **c** piston/conrod journal bearing **d** conrod/crank bearing

**Table 2** Friction analysis results

	Piston-liner	Piston-conrod	Conrod-crank	Crank-housing	Total piston assembly	Total engine loss
Friction power loss (W)	908	240	976	1269	8496	14210
Min oil film thickness (p, m)		7.10	1.1	3.5		
Friction mean effective pressure (bar)	0.14	0.04	0.15	0.20	1.34	2.24
Journal peripheral speed (m/s)		4.19	10.89	12.57		

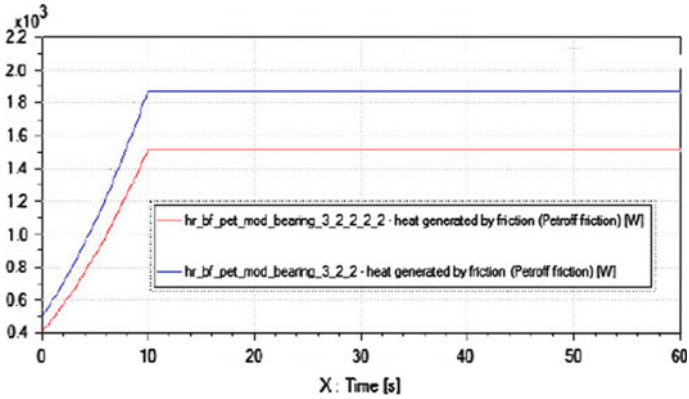


Fig. 8 Engine friction power loss during engine acceleration

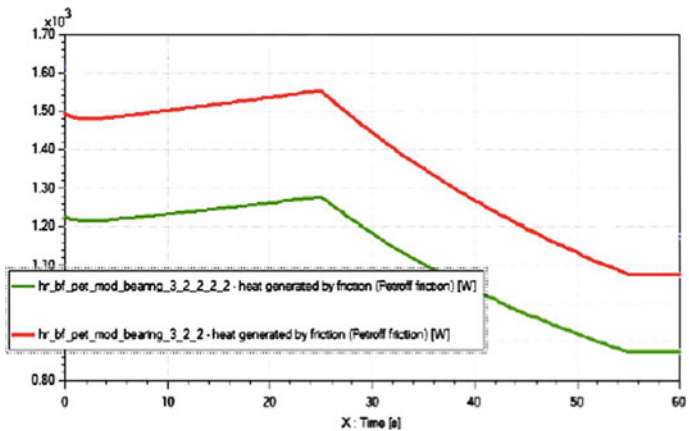


Fig. 9 Engine friction power loss during warm up at 4000 1/min

### Conclusions

The calculus of the losses due friction was done by considering the contribution of each joint within the driving mechanism depending on engine load and crankshaft angle.

The engine load and speed is directly influencing the losses due friction.

It can be observed that after the engine reached the working temperature the losses due friction are dominated by approximately 30 %.

The crankshaft bearings were designed so that the minimum thickness of the lubricant to be at least 1  $\mu\text{m}$ .

The changing the width of the bearing has a more significant influence on the minimum oil film thickness than the bearing diameter growth.

**Acknowledgment** 1. This paper is supported by the Sectoral Operational Programme Human Resources Development (SOP HRD), financed from the European Social Fund and by the Romanian Government under the project number POSDRU/159/1.5/S/134378.

## References

Küntsch V (1987) Kraftfahrzeugmotoren—Auslegung und Konstruktion. VEB Verlag Technik, Berlin  
LMS Amesim Software library

# Independent Suspension—The Equivalence of Model and Vehicle Parameters

Ion Preda

**Abstract** The vehicle suspension design starts with studies on simple models, needing few input data. The aim of the initial model simulations is to choose the suspension parameters able to ensure a good compromise between comfort and dynamic vehicle qualities, at different travelling speeds and loads. The result of this stage is the setup on the model of the needed suspension parameters, from which the stiffness of the suspension springs and tires and the damping coefficient are the most important. After starting the design with initial layouts and dimensions of the suspension linkage, the model parameters must be “translated” to the real vehicle. This paper primarily deals with the suspension model—real vehicle suspension translation process. For the MacPherson, short-long arm and swing arm suspensions, it is emphasizing the equivalence between a displacement or a force at the wheel or ground level and its corresponding displacement/force at the suspension spring or shock absorber (motion ratio and mechanical advantage).

**Keywords** Passive suspension · Suspension linkage · Independent suspension · Suspension design · Model parameters

## Introduction

The main functions of the vehicle suspension system are: *to cushion* the shocks transmitted from the ground to the body; *to dampen* the oscillations of the body; *to control* and limit the relative wheel-body positions in order to optimize the wheel-ground interactions and to protect the parts that connect the running gear with the drive train and vehicle body.

---

I. Preda (✉)

Automotive and Transport Department, Transilvania University of Brasov,  
29 Eroilor Blvd, 500036 Brasov, Romania  
e-mail: pion@unitbv.ro

There are different possibilities to realize these functions: without an amount of external energy (in which case the suspension is called *passive suspension*); with the help of a large amount of external energy—but with large possibilities to accomplish the suspension tasks (*active suspension*); with the use of a small amount of external energy (*semi-active suspensions* and *self-levelling suspensions*).

The functions of a passive suspension are realized by elastic elements, shock absorbers, and guiding mechanisms. The cushioning function is done by the elastic elements (*suspension springs, tires, anti-roll bars, and bushings*), able to store the energy of the mechanical shocks (induced by the ground unevenness) and to release that later, in a longer time interval. This way, the forces transmitted to the body and, consequently, its accelerations, will be smaller.

The damping function of a passive suspension is realized mainly by the *shock absorbers* and, in a smaller measure, by the *tires* and the bushings. These dampers generate frictional forces opposing to the relative body-wheels movements, thus consuming the kinetic energy of the mechanical system and leading to the decrease of the oscillations amplitude.

The position control function of the suspension is realized by mechanisms with different complexities, which are named *wheel guiding mechanisms* or, commonly, *suspension linkages*. Theirs main tasks are to ensure a good placement of the wheels with respect to the ground (so that to obtain maximal summative tires grip) and to limit, with the help of spring buffers, the up or down wheel travel relative to the body.

The main characteristics of a real suspension (the stiffness  $k_{sv}$  of the spring and the damping coefficient  $c_{sv}$  of the shock absorber) will be adopted with respect to the results obtained after the simulation based on mathematical models. An important question is how to realize the equivalence (transfer or relationship) between the model and true suspension characteristics (and vice versa). This study's intention is to provide answers to this question.

## Motor Vehicle Suspensions

The layouts of various motor vehicle suspensions are very different and there are many criteria to classify them. A first criterion is the construction of the axle. With respect to that, the axles can be *articulated* (made by more parts with relative movement possibilities, as seen in Fig. 1), *rigid* (one piece and very stiff) or *semi-rigid* (one piece, but more compliant for torsional efforts as for bending efforts). The behavior of the semi-rigid axle fits between the articulated and the rigid axles.

Each of the three axle types presented will make a wheel to influence in a different way the other wheel on the same axle. Considering that, the movement of one wheel with respect to the body can be *independent*, *dependent*, or *semi-dependent*, respectively. These three types of wheels influence are extended to the classification of the suspensions. Thus, an *independent suspension*, such as the one schematized in

**Fig. 1** Schemes of strut and arm independent suspension (MacPherson suspension): *left* primary scheme; *right* actual scheme

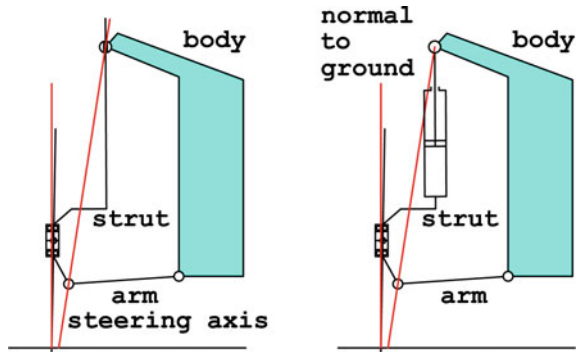


Fig. 1, is characterized by a wheel-guiding mechanism ensuring a single degree of freedom (DoF) to the wheel: the bounce (jounce and rebound) movement.

The independent suspensions can have guiding mechanisms (linkages) with different complexities. The simplest linkage consist of only one triangular (A-shaped or wishbone) arm, which has the possibility to oscillate (rotate) in a plane disposed laterally, longitudinally, or diagonally with respect to the vehicle: swing arm, trailing (or leading) arm, or semi-trailing arm, respectively. Of course, due to the simplicity of those linkages with a single arm, the vehicle's dynamic performances may be penalized.

A second category consists of linkages with medium complexity, the so-called “classical” guiding mechanisms. These include the short-long arm and the strut-and-arm linkages.

The last category of guiding mechanisms for independent suspensions uses three, four, or even five control arms. This means those are the most complex, but are also the most performant suspension types. Having so many arms, the wheel bounce (theoretically impossible in the case of a mechanism with constant dimension elements) is permitted only due to the joints compliance.

The *short-long (transverse) A-arm suspension* has a guiding mechanism with four elements: the vehicle body as base, two transverse control arms (a shorter one in the upper side) attached to the body by rotation joints and the knuckle (wheel hub carrier) connected through ball-joints to the other ends of the arms, as seen in Fig. 2. The spring and the shock absorber can be mounted between an arm and the body (as shown in Fig. 2) or between the knuckle and the body. Often, the spring and the shock absorber may form an assembly (coil-over shock absorber).

An early layout of the strut-and-arm wheel guiding mechanism consisted of an arm disposed in the lower side of the vehicle and in a strut jointed to the arm at the bottom side and to the monocoque body or to the frame at the upper side, as seen in Fig. 1, left. The knuckle (wheel carrier) is firmly attached to the strut and sustains the wheel through the bearings. Together with the spring and the shock absorber, this forms the basic design of the *strut-and-arm independent suspension*. In the case of a steerable axle, the upper joint permits four DoF (a translation and three



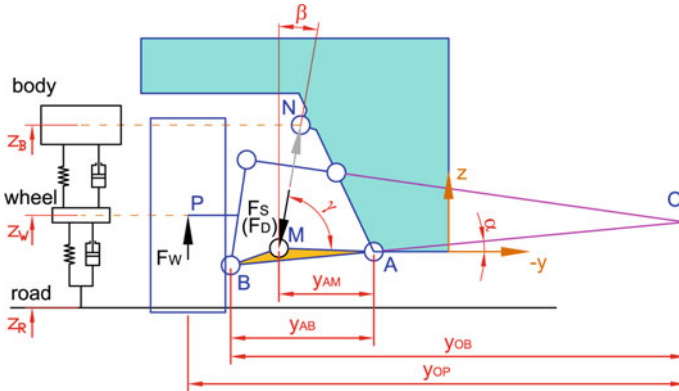


**Fig. 2** Calculus scheme of the short-long-arm suspension linkage with the spring or damper attached to the lower arm and the associated ride “quarter-vehicle model” with two DoFs

rotations, even though only two rotations are theoretically necessary). The arm must be triangular, with a rotational joint at the body and with a spherical joint (ball joint) at the other end.

Modern implementations of the MacPherson suspension replace the track and radius arms with a single triangular control arm. This type is known as *pseudo-MacPherson suspension* and is shown in Fig. 1, right. The steering axis (a false pivot) passes through the center points of the upper strut-mount and of the arm’s inelastic ball-joint and defines a constant kingpin offset at ground (scrub radius).

From the previous discussion about the independent suspension it can be concluded that, even though most of the wheel guiding mechanisms are spatial (three dimensional), most of them can be considered very close to planar mechanisms, which simplifies their predesign.

The relations presented next between the suspension model and real vehicle suspension parameters refer mainly to the short-long A-arm, strut-and-arm and swing arm independent suspensions, but these can be easily adapted for other suspension types.

## Quarter-Car Suspension Model

Even though the simulation is largely used for the study of vehicle suspensions, there are few studies in the literature (Untaru et al. 1981; Genta and Morello 2009 or Jazar 2008) about how to create or synthesize the models or how to equate the parameters of a true vehicle with the ones of the model.

The study of the low-frequency vertical oscillations can be realized with simple models, considering the vehicle as a system consisting of undeformable bodies connected by massless springs and dampers (Untaru et al. 1981; Gillespie 1992; Pandrea et al. 2001).

Based on the principle that the best model is a simple one ensuring good results, the most often adopted model for the study of vehicle’s ride behavior and quality is the so-called “quarter-vehicle model” or “vehicle-corner model” (Untaru et al. 1981; Genta and Morello 2009; Gillespie 1992; Pandrea et al. 2001; Fenton 1998; Rahnejat 1998; Wong 2001; Dixon 2009; Mitschke and Wallentowitz 2004). This includes only two elements with concentrated inertial properties: one for a wheel and the other for the part of the body supported by that wheel. Because in general the up-and-down movement presents most interest, only the mass properties of those inertial elements will be considered (neglecting the moments of inertia involved in rotations) and only one DoF, the vertical translation, will be taken into account for each body.

The result is the model presented in Fig. 2, left, with a sprung mass (the vehicle body) and an unsprung mass (the wheel). The body is linked to the wheel through massless spring and damper, while the tire (represented here as a spring-damper combination) makes the connection between the wheel and the ground. This model is suited for frequencies up to 30–50 Hz, that are over the natural frequency of the unsprung mass.

The excitation of the system is the force induced by the irregularities of the ground (road) surface. Thus,  $z_R$  is the elevation of the surface profile and  $\dot{z}_R$  represents the vertical velocity of the tire at the ground contact point.

The reference system is usually adopted in two variants: having a single origin (displacement  $z = 0$ ) for ground, wheel and body or having separate origins for the ground and masses. In that second case, shown in Fig. 2, left, the positions  $z_i = 0$  will correspond to the equilibrium positions, that must be previously calculated. This way, the gravitational forces of the wheel and the body will not appear explicitly in the movement equation.

By applying the Newton’s second law to the sprung and unsprung masses, the system’s equations of motion can be obtained:

$$\begin{aligned} m_B \cdot \ddot{z}_B &= F_{IS} + F_D - W_B \\ m_W \cdot \ddot{z}_W &= F_{IT} - (F_{IS} + F_D) - W_W \end{aligned} \tag{1}$$

in the case of the absolute coordinate system, and respectively

$$\begin{aligned} m_B \cdot \ddot{z}_B &= F_S + F_D \\ m_W \cdot \ddot{z}_W &= F_T - (F_S + F_D) \end{aligned} \tag{2}$$

in the case of the relative coordinate systems, with origins at the static equilibrium positions.

Here, the indices W, B, S, D and T stand respectively for wheel, body, spring, damper, and tire (capital letters); so,  $m_W$  and  $m_B$  are the lumped masses of the wheel and body;  $W_W$  and  $W_B$  are the weights of the wheel and body;  $F$  is a force produced by spring or damper or tire.

The forces  $F_T$ ,  $F_S$  and  $F_D$  depend on displacements  $z$ , on velocities  $\dot{z}$  and, possibly, on time  $t$ . Considering the forces are linearly depending on the springs deflections and dampers piston-tube relative velocities, the system of Eq. (2) takes the well-known shape (Untaru et al. 1981; Genta and Morello 2009; Gillespie 1992; Pandrea et al. 2001; Fenton 1998; Wong 2001; Dixon 2009; Mitschke and Wallentowitz 2004):

$$\begin{aligned} m_B \cdot \ddot{z}_B &= k_S \cdot (z_W - z_B) + c_D \cdot (\dot{z}_W - \dot{z}_B) \\ m_W \cdot \ddot{z}_W &= \ddot{z} k_T \cdot (z_R - z_W) + c_T \cdot (\dot{z}_R - \dot{z}_W) - k_S \cdot (z_W - z_B) - c_D \cdot (\dot{z}_W - \dot{z}_B) \end{aligned} \quad (3)$$

where the constant values  $k_S$  and  $k_T$  are the stiffness coefficients of the model's spring and tire, while  $c_D$  and  $c_T$  are the viscous damping coefficients of the model's damper and tire.

## Parameter Translation Between the Real Suspension and the 2-DoF Model

After the tuning of the “quarter-car” model [as is presented, for example, in (Preda 2015)], it is necessary to realize the correspondence between all the parameters of the model and real vehicle. The author observed that little specific information exists about the correlation between model and particular suspension solutions.

To obtain (almost) similar dynamic behaviors for the model and vehicle, the mechanical energy (both, kinetic and potential components) and their rates of change must be equal at any moment for both systems—the dynamic model and the real vehicle. The parameters needed to be “translated” are the ones entering in the system of Eqs. (1) or (2).

Even though it is not entirely true, most of the suspension linkages can be approximated and primarily analyzed as planar mechanisms. This assumption will be considered further.

### *The Spring Stiffness Coefficient and the Shock Absorber Damping Coefficient*

To obtain the relationship between the stiffness and damping coefficients of the model and those of the real vehicle, the principle of the *virtual mechanical work* will be applied (Olariu et al. 1982). That means the elementary mechanical work (and instantaneous mechanical power) realized on the model and on the real vehicle must be equal.

In the beginning, the case of the short-long arm suspension will be analyzed, as presented schematically in Fig. 2; the force element (spring or shock absorber) is

attached to the lower arm. In the Fig. 2, that arm makes the angle  $\alpha$  with the vehicle's  $y$  axis (lateral direction) and the direction of the force makes the angle  $\beta$  with the vehicle  $z$  axis. The point  $P$  is the center of the wheel, the points  $A$  and  $B$  are the inner and outer ends of the lower arm and  $M$  and  $N$  are respectively the points where the force element it is articulated to the lower arm and to the body.

At a particular relative wheel-body position, any part of the suspension linkage will have a certain center of rotation with respect to the vehicle body (Dudiță and Diaconescu 1981; Alexandru et al. 2005; Simionescu et al. 2010). The movement of any part of the linkage will be a rotation about this center. For example, the point  $A$  is the rotation center for the lower arm and the point  $O$  is the rotation center for the wheel assembly. The wheel instantaneous center  $O$  is placed at the intersection of the perpendiculars on the velocity directions of the outer ends of the arms (which is similar with the intersection of the arms directions). Designing the suspension linkage with an inward point  $O$ , as seen in Fig. 2, may lead to a benefic wheel camber change and to a higher roll-axis position (ensuring a better vehicle dynamics during cornering) and, for that, it is generally adopted for common or sport vehicles (Adams 1993; Milliken and Milliken 1997; Reimpell et al. 2001; Heisler 2002).

Further, an elementary (infinite small) rotation angle  $\delta\alpha$  of the lower arm about the point  $A$  will be considered. This will generate an elementary spring deflection  $\delta d_S$  (change of the distance  $MN$ ) and elementary displacements on the vehicle's  $z$  axis:  $\delta z_M$  for the point  $M$ ,  $\delta z_B$  for the point  $B$  and also  $\delta z_P$  for the point  $P$  (the last being equal with the elementary displacement  $\delta z_W$  on the model). Also, the projections on the vehicle's  $y$  axis of the segments  $OP$ ,  $OB$ ,  $AB$  and  $AM$  will be noted respectively with  $y_{OP}$ ,  $y_{OB}$ ,  $y_{AB}$  and  $y_{AM}$  (Fig. 2).

Because the points  $P$  and  $B$  are on the wheel assembly and rotate about the instantaneous center  $O$ , the elementary displacements  $\delta z_P$  and  $\delta z_B$  are proportional with the lengths  $y_{OP}$  and  $y_{OB}$ . Thus, it results that the wheel's vertical elementary displacement on the model is

$$\delta z_W = \delta z_P = (y_{OP}/y_{OB}) \cdot \delta z_B, \quad (4)$$

Also, the points  $B$  and  $M$  are on the lower arm and rotate about the instantaneous center  $A$  and so the elementary displacements  $\delta z_B$  and  $\delta z_M$  are proportional with the lengths  $y_{AB}$  and  $y_{AM}$ . It yields:

$$\delta z_B = (y_{AB}/y_{AM}) \cdot \delta z_M, \quad (5)$$

The elementary displacement of the point  $M$  is perpendicular to the direction  $AM$  and has the magnitude

$$\delta \alpha \cdot AM = \delta z_M / \cos \beta = \delta d_S \cdot \sin \gamma, \quad (6)$$

where  $AM$  is the distance between the points  $A$  and  $M$  and  $\gamma = \angle AMN$  is the angle between that segment and the spring force direction.

Introducing Eqs. (5) and (6) into Eq. (4) it results the final relationship between the elementary displacement  $\delta z_W$  of the wheel on the model and the elementary deflection  $\delta d_S$  of the vehicle spring:

$$\delta z_W = (y_{OP}/y_{OB}) \cdot (y_{AB}/y_{AM}) \cdot \cos \beta \cdot \sin \gamma \cdot \delta d_S. \quad (7)$$

The ratio

$$R_K = \delta z_W / \delta d_S = (y_{OP}/y_{OB}) \cdot (y_{AB}/y_{AM}) \cdot \cos \beta \cdot \sin \gamma = \delta F_S / \delta F_W \quad (8)$$

is named *spring motion ratio* and indicates how many times the wheel's elementary displacement on the model is bigger as the elementary deflection of the vehicle spring. Due to the fact that the mechanical energy is conserved, this ratio exists also, in a reversed way, between the force change  $\delta F_S$  of the vehicle spring and the force change  $\delta F_W$  of the model's wheel,  $R_K = \delta F_S / \delta F_W$ , and is named *mechanical advantage* (leverage or amplification of force).

Starting from the definition of the stiffness coefficient, the stiffness coefficient  $k_S$  of the spring in the model can be obtained from Eq. (8) as function of vehicle spring's stiffness coefficient  $k_{Sv}$ :

$$\begin{aligned} k_S &= \delta F_W / \delta z_W = (\delta F_S / \delta d_S) / R_K^2 = k_{Sv} / R_K^2 \\ &= k_{Sv} / [(y_{OP}/y_{OB}) \cdot (y_{AB}/y_{AM}) \cdot \cos \beta \cdot \sin \gamma]^2 \end{aligned} \quad (9)$$

This equation shows that the stiffness  $k_{Sv}$  of the real spring must be bigger than the suspension stiffness  $k_S$  adopted for the model.

The results from (Adams 1993) or (Jazar 2008) appear as particular cases and can be obtained from the previous equation if the angle  $\gamma = \angle AMN$  (Fig. 2) is equal with  $90^\circ$  ( $\sin \gamma = 1$ ).

To obtain the *motion ratio of the shock absorber*,  $R_D$ , it is enough to repeat the previous reasoning for the spring, but replacing the force changes  $\delta F_S$  and  $\delta F_W$  with real forces  $F_D$  and  $F_W$  and the elementary displacements  $\delta z_W$  and  $\delta d_S$  with the velocity of the model's wheel  $\dot{z}_W$  and with the relative velocity  $v_D$  of the shock absorber (relative velocity of points M and N, as seen in Fig. 2). Almost similar with the Eq. (8) it is obtained that:

$$R_D = \dot{z}_W / v_D = (y_{OP}/y_{OB}) \cdot (y_{AB}/y_{AM}) \cdot \cos \beta \cdot \sin \gamma = F_D / F_W. \quad (10)$$

Further, starting from the definition of the damping coefficient, from the Eq. (10) it can be obtained the damping coefficient  $c_D$  in the model as function of the shock absorber's (constant) damping coefficient  $c_{Dv}$ :

$$\begin{aligned} c_D &= F_W / \dot{z}_W = (F_D / v_D) / R_D^2 = c_{Dv} / R_D^2 \\ &= c_{Dv} / [(y_{OP}/y_{OB}) \cdot (y_{AB}/y_{AM}) \cdot \cos \beta \cdot \sin \gamma]^2 \end{aligned} \quad (11)$$

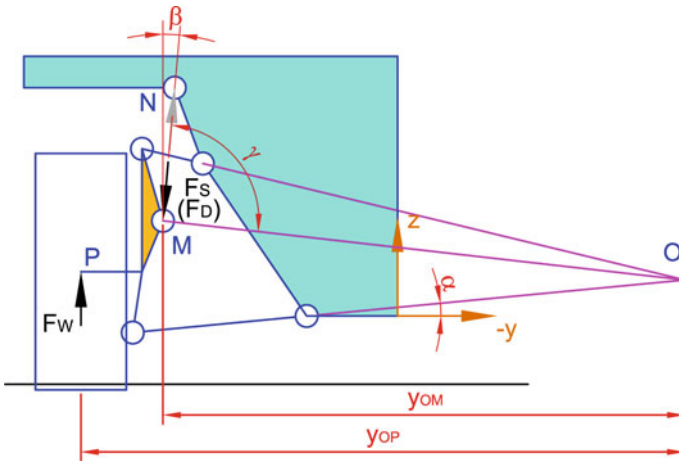


**Fig. 3** Calculus scheme of the short-long-arm suspension linkage with the spring or shock absorber attached to the knuckle

If the short-long A arm suspension has a force element (spring or shock absorber) attached to the upper arm, it is necessary only to move the points A, B and M from the lower arm (as seen in Fig. 2) to the upper arm, and the Eqs. (6)...(8) remain valid.

Another design layout may attach the force elements directly to the wheel carrier (knuckle), as in Fig. 3. That means the point M will be on the wheel assembly and will have the point O (not the point A) as rotation instantaneous center.

That means the spring- or damper motion-ratio R will be

$$R = (y_{OP}/y_{OM}) \cdot \cos \beta \cdot \sin \gamma \tag{12}$$

where the angle  $\beta$  is the angle of the force element with the vehicle's z axis and  $\gamma$  is now the angle  $\angle OMN$  (because the point M rotates about the point O).

In the case of the MacPherson suspension (Vieru 2001; Merel and Deschaume 2003; Preda et al. 2010), the Eq. (12) can be also applied because both the spring and shock absorber are attached to the wheel carrier, Figs. 1 and 3. The point N is the center of the spring-damper supporting bearing, while the points  $M_S$  for the spring and  $M_D$  for the shock absorber must be positioned respectively on the spring axis and shock absorber axis (indicated in green and brown in these figures). The point positions on those axes don't matter (in Fig. 4 these were taken on the wheel spining axis). The instantaneous center of rotation O of the wheel assembly will be found at the intersection of the control arm direction with the perpendicular on the pivoting axis (BN), per Fig. 4. The angle  $\beta$  is the angle of the force element ( $M_SN$  or  $M_DN$ ) with the vehicle's z axis and  $\gamma$  is now the angle  $\angle OM_DN$  or  $\angle OM_SN$ .

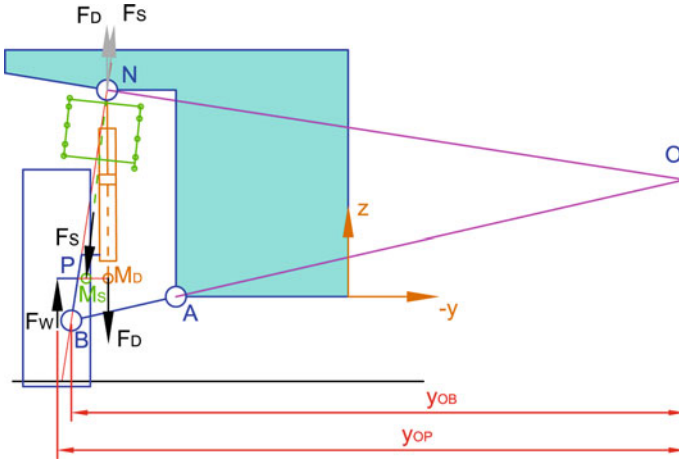


**Fig. 4** Calculus scheme of the MacPherson suspension linkage

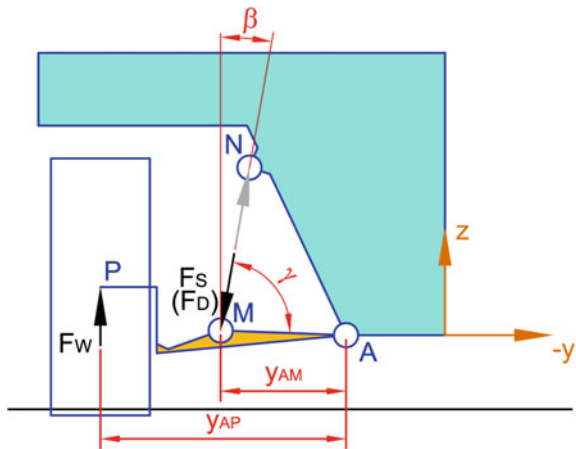
In the case of the *swing arm suspension*, the wheel is mounted on the single control arm, Fig. 5, and also the force elements are articulated to that wheel-arm assembly.

That means the spring- or damper motion-ratio  $R$  will be

$$R = (y_{AP}/y_{AM}) \cdot \cos \beta \cdot \sin \gamma \tag{13}$$

where the angle  $\beta$  is the angle of the force element with the vehicle's  $z$  axis and  $\gamma$  is now the angle  $\angle AMN$  (because the point  $M$  rotates about the point  $O$ ).

**Fig. 5** Calculus scheme for the swing-arm suspension linkage



Similar reasoning can be made for the other simple suspension linkages (as trailing or semi-trailing arm suspension or semi-independent suspension), but the analysis plane must be taken perpendicular to the control arm's oscillating axis.

In this section, only the influence of the suspension spring over the stiffness coefficient used in the model was presented. In practice, one must also take into account the contribution of the anti-roll bar, as presented in (Rill 2007), or even the one of the bushing used to attach the control arms to the vehicle body. Those supplementary springs will make the suspension stiffer when the wheels of the same axle are passing over different obstacles as in the case of equal bounce of the two wheels.

One of the conclusions to be drawn here is that the mounting on the knuckle of the force elements needs smaller forces but bigger bounce-rebound travels.

Another conclusion is that the spring- or shock-absorber motion-ratio  $R$  depends on the vertical wheel travel, because some of the lengths  $y$  and the angles  $\beta$  and  $\gamma$  will change on the wheel bounce. To have a good idea about the change of the motion-ratio  $R$ , at least five different linkage positions must be studied (out of which one should be for the vehicle static load and two for the extreme positions). The calculation of the motion-ratio can be realized based on scale drawings, on matrix calculation (Simionescu et al. 2010), vectorially (Alexandru et al. 2005), or using multibody dynamics systems (MBS) software.

In the absence of damping forces and based on the values of the spring motion-ratio  $R_k$ , the static characteristic of the suspension may be obtained. Taking different wheel-body positions, the spring deflection will be calculated first, then its force  $F_S$  and the correspondent force  $F_W$  at the wheel. Remembering Eq. (3) and the wheel displacements between the considered positions will result the contribution of the spring to the tire load versus wheel displacement curve. Adding the influences of the buffer-springs that curve may be corrected, as presented in Reimpell et al. (2001), Crolla (2009).

The static forces appearing in the linkage elements (in equilibrium condition) may be obtained using the method of the force polygon (Fenton 1998; Olariu et al. 1982; Vieru 2001).

## *The Masses*

During the suspension oscillations, the parts in relative motion are rotating against their instantaneous centers. To distribute their inertial properties to the model wheel and body masses ( $m_W$  and  $m_B$ ), the kinetic energy of the rotating parts (depending on the moments of inertia and rotary speeds) must be equivalent with the kinetic energy of the model masses in translation. That means that the values  $m_W$  and  $m_B$  of the model masses depend not only on the real system masses of the vehicle parts, but also on how these masses are distributed (on the moments of inertia of these parts) and even on the instantaneous position of the suspension linkage. In other words, to be fully equivalent with the real vehicle, the model masses may be



variable! This aspect will not be further developed here; instead, an approximate method, with constant model masses, will be used.

The wheel mass  $m_W$  in the model must be in fact equivalent with the masses sum of the next vehicle elements:

- entire: wheel (tire and rim), hub, brake, bearing;
- part of: arm (or arms), shock absorber, anti-roll bar and axle shaft (if exists).

The mass of the elements in the last list (contributing both to the model's wheel and body masses) may be calculated so that the static moments over the part's center of gravity of the mass fractions to be equal:

$$m_{W_i} \cdot L_{W_i} = m_{B_i} \cdot (L_i - L_{W_i}) \quad m_i = m_{W_i} + m_{B_i}. \quad (14)$$

where index  $i$  indicates a certain vehicle part;  $m_i$ ,  $m_{W_i}$  and  $m_{B_i}$  are respectively the full mass and the fractions distributed to the model's wheel and body of the part  $i$ ;  $L_i$  is the length between the part's articulations (or ends) attached to the vehicle's wheel and body;  $L_{W_i}$  is the length between the part's center of gravity and the articulation (or ends) attached to the vehicle's wheel.

If computer-aided design (CAD) models are available and the material densities of those parts are known, the calculation of the model wheel and body masses become a simple problem (Bujoaica et al. 2014). Also, there are relatively simple experimental methods to determine the center of mass and moment of inertia of the existing parts and also their mass fractions  $m_{W_i}$  and  $m_{B_i}$  (Preda 1993). Today, manufacturers have very good estimations of the inertial properties of the previously listed parts, that contribute to the model's masses (Baggio and Arnoux 2004).

## ***The Tire***

The main component of the vehicle tire is rubber, a material with elasto-plastic behavior. Due to this and also to the pressured air inside, the tire presents both elastic and damping characteristics, depending on many factors, such as inflation pressure, construction, frequency of vertical oscillation, rotational speed, temperature, and others.

In order of importance, the inflation pressure and the tire material contribute to the tire stiffness. Even very simple models, as the one presented in (Preda and Ciolan 1997), indicate a regressive stiffness characteristic (the stiffness coefficient reduces as the deflection increases), experimental determinations shows that the stiffness coefficient is almost constant (the characteristic is nearly linear), except for very small tire deflections (Wong 2001; Rill 2007).

Also, it must be noted that the stiffness coefficient is practically directly proportional with the inflation pressure, which means the coefficient can be easily modified with 10...20 % by a pressure change during a normal tire operation (without compromising the tire span life).

Working in the same way on the model and on the real vehicle, the stiffness coefficients of the real tire will be equal with the one in the model, and the same situation exists for the damping coefficients. At the ride frequency, less than 30 Hz, the damping of the tire is relatively insignificant and thus it is rarely considered in such studies (Gillespie 1992; Mitschke and Wallentowitz 2004).

## Conclusions

For the study of the ground vehicles independent suspensions, simple dynamic and mathematic models are used, mainly in the first stages of the design process. In the literature there are few studies presenting a systematic approach for realizing models and especially for a correct bi-directional parameter translation between the model and the real vehicle.

This article discusses the main aspects involved in the model-vehicle equivalence, analyzing some of the most preferred suspension types by the light-vehicle manufacturers.

## References

- Adams H (1993) Chassis engineering: chassis design, building and tuning for high performance handling. HPBooks, New York
- Alexandru P, Vișa I, Talabă D, Alexandru C, Antonya C (2005) Modelarea statico-dinamică a mecanismelor de ghidare ale roților automobilelor. Editura Lux Libris, Brasov
- Baggio P, Arnoux P (2004) Notion fondamentales de confort. In: Renault Automobiles (eds), Ecole de la Liaison au Sol, vol. 3
- Bujoaica R, Nicolae V, Vieru I, Mitran G, Ilie S (2014) Model and simulation for the behavioral assessment of a car rear suspension fitted on with the trim corrector, presented at the SMAT. Craiova, Romania
- Crolla D (2009) Automotive engineering: powertrain, chassis system and vehicle body. Butterworth-Heinemann, Oxford
- Dixon JC (2009) Suspension geometry and computation. Wiley, Chichester
- Dudiță F, Diaconescu DV (1981) Mecanisme: cinematică. Transilvania University, Dinamica. Brasov
- Fenton J (1998) Handbook of automotive powertrains and chassis design. Professional Engineering Publishing, Trowbridge
- Genta G, Morello L (2009) The Automotive Chassis. Syst Des 2
- Gillespie TD (1992) Fundamentals of vehicle dynamics. SAE, Warrendale, USA
- Heisler H (2002) Advanced vehicle technology. Elsevier
- Jazar RN (2008) Vehicle dynamics: theory and application. Springer
- Merel J, Deschaume A (2003) Filtrage d'une jambe de force de type Mac Pherson. *Ingénieurs de l'Automobile*, 44–48
- Milliken WF, Milliken DL (1997) Race car vehicle dynamics: SAE
- Mitschke M, Wallentowitz H (2004) Dynamik der Kraftfahrzeuge, 4. Auflage edn. Springer, Berlin
- Olariu V, Sima P, Achiriloaie V (1982) Mecanica tehnică. Editura Tehnică, Bucharest

- Pandrea N, Pârlac S, Popa D (2001) Modele pentru studiul vibrațiilor automobilelor. TipArg, Pitesti, Romania
- Preda I (1993) Studiul solicitărilor din transmisia autoturismelor de teren, în vederea optimizării acesteia. Ph.D. Thesis, Transilvania University of Brasov, Brasov
- Preda I (2015) Model based algorithm for the study of the vehicle suspension, presented at the international conference of mechanical engineering ICOME. Craiova, Romania
- Preda I, Ciolan G (1997) Modelarea interacțiunii dintre roata și sol, presented at the CAR conference, Pitesti
- Preda I, Ciolan G, Ispas N (2010) Optimization study of a car suspension-steering linkage, presented at the international conference of mechanical engineering ICOME. Craiova, Romania
- Rahnejat H (1998) Multi-body dynamics: vehicles, machines and mechanisms. Wiley, New York
- Reimpell J, Stoll H, Betzler JW (2001) The automotive chassis, engineering principles, 2nd edn. Butterworth-Heinemann, Oxford
- Rill G (2007) Vehicle dynamics—fundamentals and modeling aspects. Fachhochschule, Regensburg
- Simionescu PA, Talpasanu I, Di Gregorio R (2010) Instant-center based force transmissivity and singularity analysis of planar linkages. ASME—J Mech Rob 2
- Untaru M, Poțincu G, Stoicescu A, Peres G, Tabacu I (1981) Dinamica autovehiculelor pe roți. Editura Didactica și Pedagogica, Bucharest
- Vieru I (2001) Studiul solicitărilor din elementele punților autoturismelor în vederea optimizării constructive. Ph.D. Thesis, Transilvania University of Brasov, Brasov
- Wong JY (2001) Theory of ground vehicles, 3rd edn. Wiley, Ottawa

# Studies About Behavior of the Human Cervical—Head System During Frontal Crash Impact

Stefanita Ciunel and Bebe Tica

**Abstract** Concerned challenge of road safety, in terms of research and development, most automotive companies develops more than 50 years, technologies that improve the safety posed by their vehicles. Most research is based on studies conducted in the laboratory of accidentology and studying human behavior to improve biofidelity of these dummies in order to develop the most efficient equipment in real situations that may arise at the wheel. Today, the automotive companies do not cease to develop new safety devices which prevent an accident or to protect passengers. The choices made in terms of safety is based on greater prevention, more anticipation, the driver is still responsible factor for the act of driving. It is extremely complex, however, and the body structure and reactivity shock. The reaction of shock is extensive and consists of biomechanical response and neuro major spending in the immediate medical assistance and recovery.

**Keywords** Frontal collision · Biofidelity · Cranio-cervical system

## Introduction

Because must take into account the many factors involved in impact dynamics studies<sup>1</sup> have sequenced the impact of: pre-impact, impact and post-impact (Korteling 1990).

*Pre-impact factors* occupants attitude and physical, pathological and behavioral thereof: anthropometric data (age, sex, weight, body index); data about the

---

<sup>1</sup><http://www.ircobi.com>.

---

S. Ciunel (✉) · B. Tica  
Faculty of Mechanical Engineering, University of Craiova, Craiova, Romania  
e-mail: ciunel\_stefanita@yahoo.com

B. Tica  
e-mail: ticabebe@yahoo.com

pathophysiology victim (personal history pathological muscle tone, biological content of internal organs); data on the victim's behavior (alcohol, drugs, medicines, clothes); vehicle occupants data (position in the vehicle, posture, or not wearing a seat belt).

*Impact factors* check occupants attitude and physical concerns, are most technical in nature and relate to vehicle operation parameters snapshots in time of the accident: the direction, strength, impact duration; vehicle deceleration; passive safety of passengers (loading belt interactions with airbag, board or wheel contact) interaction with other occupants of the car interior or objects (Mackay et al. 1990).

*Factors post-impact* are of a medical nature and aimed almost exclusively complexity and severity of injuries, duration of impact until the first medical competence of medical personnel in providing first aid, accurate diagnosis, treatment quality, short-term consequences and long. The science of biomechanics, still in the initial phase, required the use of several types of subjects in testing, consisting first of these bodies. The basic information was obtained about the resilience of human bodies under the forces of the typical external impact collisions at high speeds.

Main features of the test dummies were sustainability, utility, and the possibility of reduced repeatability of tests. Their biofidelity was limited to the external shape, weight and degrees of freedom of joints, all similar to human. Lately, computer programs to reconstruct traffic accidents prove to be invaluable in the work of the expert. The computer allows, on the one hand modeling of the wearer inside the passenger compartment, on the other hand offers a simulation conditions as close to the real trajectory of the victim's body and, ultimately, creates prerequisites determining the impact speed of the vehicle.

## The Anatomy of Human Cervical Spine

The movement of crano-cervical complex are, Fig. 1:

1. Flexion-extension, having motions are performed in the sagittal plane, the axis Oy; Flexion-extension, the very low degree, maximum 30° occurs in atlanto-occipital joint around a transverse shaft. Flexion-extension movements of greater amplitude drive the rest of the cervical spine, reaching the final at an angle of 60° flexion and 50° on the active extension. C1–C2 complex in its structure and the links between them ensures rotation of the skull majority, and with C0 achieved 60 % of the axial rotation of the head. Less mobile in rotation is the torque C0–C1, which provides the weight in the flexion-extension movements. This is justified by the particular structure of C1 (Axis), which is made up of a “tooth”, which articulates with C2 (Atlas) and C0 penetrating it through a musculo-ligamentous important functional context. C1 traumatic tooth fracture leads to sudden death through bulbar nerve fascicles involvement.

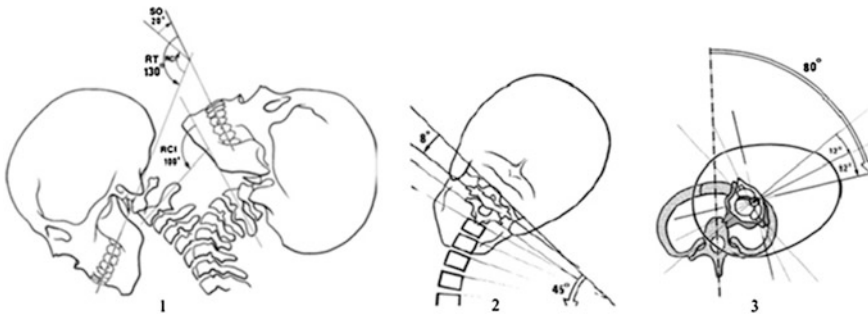


**Fig. 1** Craniocervical mobility amplitude in the 3 plans (Franck and Netter 2008)

2. Laterality movements which is realized in frontal plane, the axis Ox. Laterality runs in the sagittal plane, passing through each condyle is very limited and maximum 15°. The amplitude can be increased up to 40°–45° in training sub-jacent cervical spine (below the level C2).
3. Axial rotation movement which is carried out in a horizontal plane, the axis Oz. The rotation about the articulation atlanto axoidiană is unique and runs around a vertical axis passing through the tooth axis. The maximum 30° strictly to the C1–C2. Greater rotation is possible by training other spinal joints can be increased up to 80°–85°.

It began studying computer cervical tomography area by craniocervical area of a patient, male, 43 years old adult at Helios Clinic, Craiova, using the Siemens brand equipment consisting of a Magnetom Avanto MRI machine and a 1.5 T multislice computed tomography machine Somatom Spirit type, 2009.

We have used three scanning schemes: a cross-scan planes parallel with distance of 10 mm (see Fig. 2a), a scanning plane parallel to the front with the distance of 1.7 mm (Fig. 4b) a scan parallel to the sagittal plane having a distance of 1.1 mm (Fig. 2c).

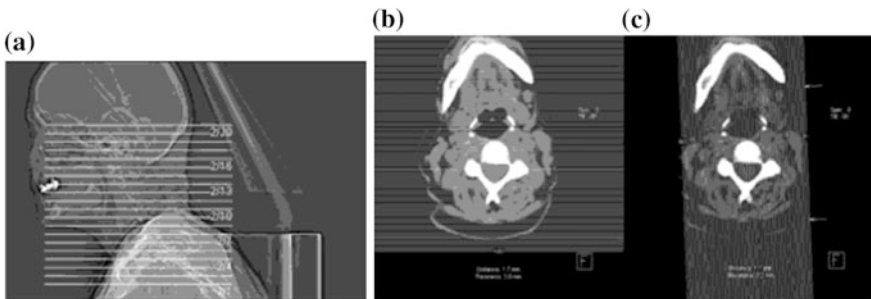


**Fig. 2** Tomography scanning schemes used in craniocervical area

## Simulation Collision with the Front of a Virtual Vehicle with a Crash Test Dummy Inside, at Different Impact Speeds

An auto accident simulation is a virtual recreation of a destructive impact test using a computer simulation to examine the safety of the car. Simulations of “crash” are used by researchers using the analysis CAE (Computer Aided Engineering) for resistance calculations in the modeling CAD (Computer Aided Design) vehicles. During a simulation of this kinetic energy—the energy of movement, which has a car before impact is converted into energy of deformation, mostly plastic deformation of the material body at the end impact, Fig. 3.

The dummy was introduced car system consists of automobile, ground and obstacle. Figure 5 presented the dummy attached studied system.

The complete system crash test was exported to analysis software which keep geometric (constraints of movement) (Yan 2006).<sup>2,3</sup>

They were filled with (Claessens et al. 1997):

- Connect cinematic required additional (geometric links) to ensure consistency and movement of the studied system.
- To solids transferred were similar material attached real model;
- Starting the movement (the initial speed of the vehicle) was carried out using a linear actuator acting. Its action takes place over a very short initial printing speed of the car, are expected to run freely on the ground until he meets the obstruction (Im and Nilsson 1990);
- The dummy belt is attached to the seat by a virtual resort to simulate the flexibility of the system protection (Dejeammes et al. 1990);
- Dummy components were found masses of the various components based on data from literature (Gabriel 2009);
- The vehicle’s weight is 1500 kg;
- Integration algorithm is kind Kutta Merson (integrated into the simulation program);
- Were established and other initial parameters according to the literature (Gabriel 2009; Simms et al. 2005).

To simulate the impact of the car with initial speed of 30–100 km/h were established following initial parameters:

- Speed linear actuator printed is 8.33–27.8 m/s.
- The total duration of the simulation is 2.4 s.
- Maximum duration of action of the actuator is 0.3–1.5 s.

<sup>2</sup>SAE J211—Instrumentation for Impact Tests.

<sup>3</sup>VisualNastran—User Guide and Tutorials—2001–2004.

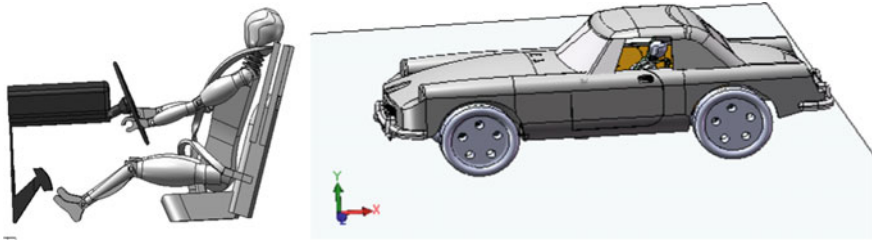
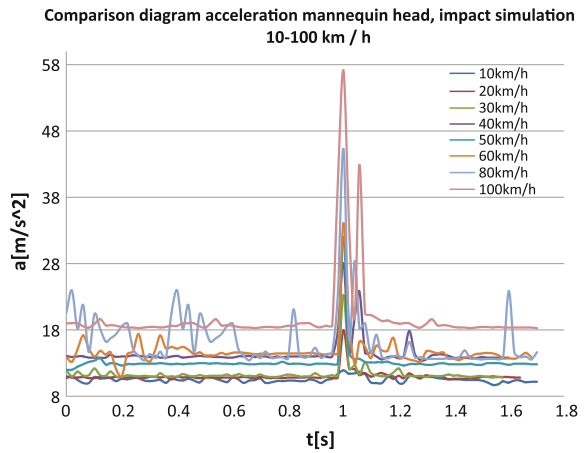


Fig. 3 The dummy model introduced in car model

Fig. 4 Comparative chart of the accelerations obtained in the center of mass of the dummy's head



The program determines behavior through the entire system kinematics and dynamics studied through data tables and diagrams automatically generated. In this case, we determined the following important parameters: speed vehicle development, vehicle acceleration, and acceleration the dummy's head. Accelerations in the center of mass of the dummy's head to impact simulations generated from the virtual vehicle with speeds between 10 and 100 km/h can be analyzed on a comparative diagram shown in Fig. 4.

Mitigate the consequences of post-traumatic driver led to the need to study the area cranio-cervical so through research and system modeling cranio-cervical completed by experimental research in the laboratory, can be determined key dynamic parameters appearing in such situations.



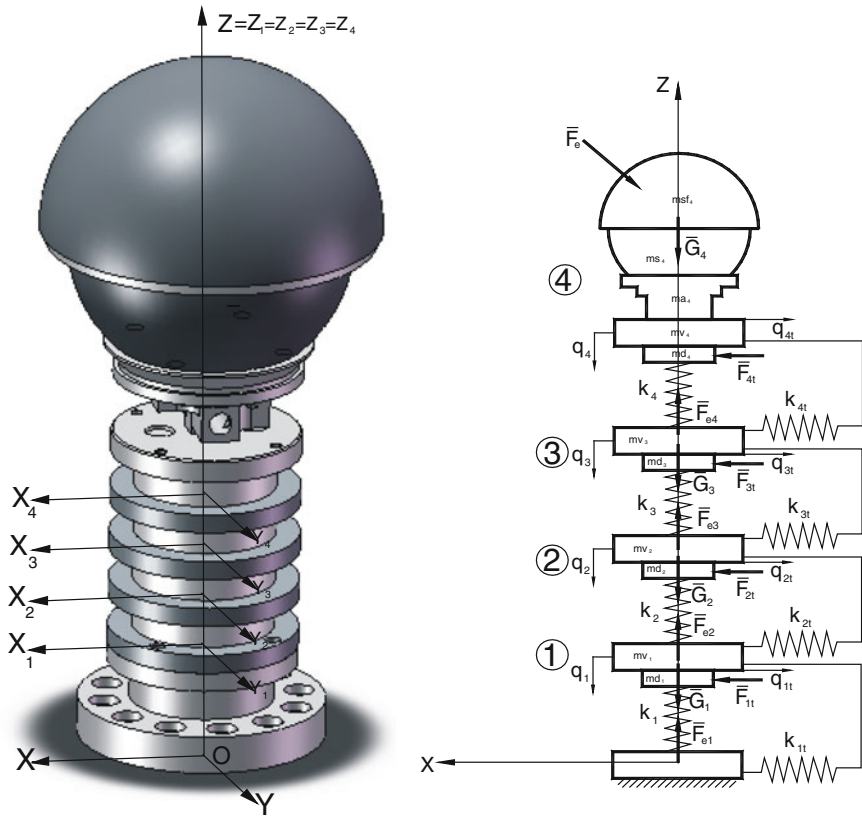


Fig. 5 Mechanic and mathematic of assembly studied

### Mathematical Model of Cervical—Head System Test Dummy

For the study was considered system consists of three-dimensional model used to design the test stand (Tarniță et al. 2010). The assembly of the dummy's neck flanges basic (considered fixed) and two spherical metal has mechanical and mathematical model shown in Fig. 8 on the whole model operates 13 external forces:

- an external force  $F_e$  system that simulates the force acting on the head (impact force) as:

$$\overline{F_e}(t) = \begin{cases} (F_{ex} \cdot \frac{t}{t_1}) \cdot \bar{i} + (F_{ez} \cdot \frac{t}{t_1}) \cdot \bar{k}, & \text{for } t \in [0; t_1] \\ (F_{ex} \cdot \frac{t_2 - t}{t_2 - t_1}) \cdot \bar{i} + (F_{ez} \cdot \frac{t_2 - t}{t_2 - t_1}) \cdot \bar{k}, & \text{for } t \in (t_1; t_2] \\ 0 \cdot \bar{i} + 0 \cdot \bar{j} + 0 \cdot \bar{k}, & \text{for } t \in (t_2; t_3] \end{cases} \quad (1)$$

where:  $F_{ex}$ —maximum component on  $Ox$  acting on the dummy’s head;  $F_{ez}$ —maximum axle component  $Oz$  acting on the dummy’s head;  $t_1$ —the time for which the impact force increases to the maximum;  $t_2$ —the time for which the impact force decreases to the minimum;  $t_3$ —time interval that studies the system studied by the force of impact.

- The forces of gravity  $G_1, G_2, G_3, G_4$ , the components of the mechanical system, as:

$$\begin{aligned} \overline{G_1}(t) &= -(mv_1 + md_1) \cdot g \cdot \bar{k} \\ \overline{G_2}(t) &= -(mv_2 + md_2) \cdot g \cdot \bar{k} \\ \overline{G_3}(t) &= -(mv_3 + md_3) \cdot g \cdot \bar{k} \\ \overline{G_4}(t) &= -(mv_4 + md_4 + mf_4 + ms_4 + msf_4) \cdot g \cdot \bar{k} \end{aligned} \quad (2)$$

$mv_1$ —metal disc Table 1;  $md_1$ —one disc mass elastic (rubber or silicone);  $mv_2$ —metal disc Table 2;  $md_2$ —elastic disc Table 2 (rubber or silicone);  $mv_{3-3}$  metal disc mass;  $md_3$ —3 disc mass elastic (rubber or silicone);  $mv_4$ —metal disc Table 4;  $md_{4-4}$  disc mass elastic (rubber or silicone);  $ma_4$ —joint table Item 4;  $ms_4$ —lower spherical mass of key 4;  $ms_4$ —upper spherical mass of key 4;  $k$ —versor  $Oz$  axis.

- Longitudinal forces due to elastic rubber or silicone discs, like:

$$\begin{aligned} \overline{F_{e1}}(t) &= k_1 \cdot q_1 \cdot \bar{k} \\ \overline{F_{e2}}(t) &= k_2 \cdot q_2 \cdot \bar{k} \\ \overline{F_{e3}}(t) &= k_3 \cdot q_3 \cdot \bar{k} \\ \overline{F_{e4}}(t) &= k_4 \cdot q_4 \cdot \bar{k} \end{aligned} \quad (3)$$

where:

$k_i$ —elastic constants corresponding longitudinal elastic forces  $F_{ei}$ ;  $q_i$  - generalized longitudinal coordinates ( $i = 1-4$ ).

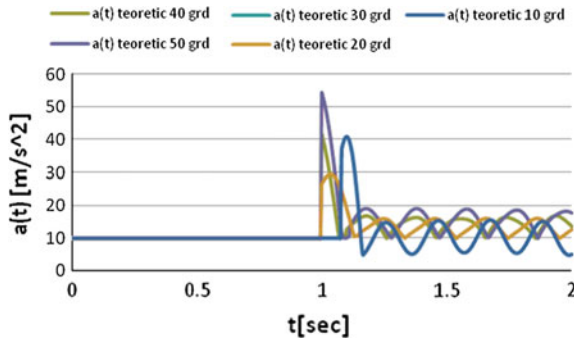


**Fig. 6** Evolution acceleration versus time for different angles of the pendulum initial conditions dummy head accelerations in different angles initial pendulum

- The transverse forces due to elastic rubber or silicone discs, like:

$$\begin{aligned}
 \overline{F_{1t}}(t) &= k_{1t} \cdot q_{1t} \cdot \vec{i} \\
 \overline{F_{2t}}(t) &= k_{2t} \cdot q_{2t} \cdot \vec{i} \\
 \overline{F_{3t}}(t) &= k_{3t} \cdot q_{3t} \cdot \vec{i} \\
 \overline{F_{4t}}(t) &= k_{4t} \cdot q_{4t} \cdot \vec{i}
 \end{aligned}
 \tag{4}$$

where:

$k_{it}$ —elastic constants corresponding transverse cross elastic forces  $F_{it}$ ;  $q_{it}$ —cross generalized coordinates ( $i = 1-4$ ). The mechanical assembly is shown in Fig. 5, studied were chosen as coordinates generalized coordinates  $q_{1t}$ ,  $q_{2t}$ ,  $q_{3t}$ ,  $q_{1t}$ ,  $q_{2t}$ ,  $q_{3t}$ . Coordinate systems  $O_1x_1y_1z_1$ ,  $O_2x_2y_2z_2$ ,  $O_3x_3y_3z_3$  and  $O_4x_4y_4z_4$  are fixed to the elements.

Looking at the graphics allure obtained by solving mathematical model for acceleration of cranio-cervical system head is found that, by stepping on the pendulum charts are almost identical in the range (0–1 s.). And after the impact force is made form is likely attenuated sine graphs. This aspect can be explained by the fact that the mathematical model was considered as instantaneous collision. It also notes that in the interval (0–1 s.) the acceleration is  $9.81 \text{ m/s}^2$  for all particular situations (initial angle of the pendulum 0–50°), which coincides with reality because the entire system studied acting only gravitational acceleration. If not overlap on a single plot of the accelerations obtained for different angles of the pendulum is obtained compared to the chart of Fig. 6.

## The Experimental Device for Laboratory Testing of Cranio—Cervical System of Crash Test Dummies

The technical problem solved by this device consists of designing a technical system by which construction is possible a wide range of tests for all types of mannequins for experiments, but also for conducting experimental determinations particular subject technical expertise judicial road events. The technical system of shuttle overcomes the drawbacks mentioned above, in that it is provided with a movable frame that can move in three directions (vertical, transverse and longitudinal), and the rotation of the grade level of the area or areas tested, Fig. 7.

The vertical displacement is performed four columns end, each mounted cylindrical cross-guide joints in the middle of two screws threaded frame is square.

Longitudinal displacement will be done using two columns longitudinal joints fastened themselves cylindrical in cross—directions—operated screw thread and a square with two nuts, and mutually centered within the cell. Traverse is executed by a slide-type device mounted on a board in turn by four bearings integral with movable table.

Several tests were performed using several angles original pendulum, which can be divided into two large groups: cranio-cervical classic system testing and system testing cranio-cervical biofidelity that can be used in the composition test dummies auto accidents.



**Fig. 7** Experimental stand with cranio-cervical classic system ready for testing : 1 electromagnetic brakes; 2 pendulum; 3 classic cranios-cervical system, 4 rotational system for cranio-cervical system; 5 vertical and horizontal translation system (3 axes); 6 guide cable; 7 position winch pendulum

Cranio-cervical test system used mannequins classic car was done for initial angles of the pendulum between  $10^\circ$  and  $50^\circ$ . These angles were determined using accelerometer placed no.4 pendulum arm and acquisition program of Arduino board. In determining the desired angle to the electromagnetic brake for locking the pendulum arm.

## **Biofidelic Cranio-Cervical System Loaded by Shape Memory Alloys Springs and Rotation Mechanism at Pendulum Device**

The cranio-cervical test dummies biofidelity the composition of crash test dummy, the subject of this study is shown in Fig. 8.

Interested, in particular, changes in the absolute acceleration of the dummy head during the experiment. Thus, organizing data from ACC3 accelerometer obtained comparative diagram shown in Fig. 9.

Analyzing graphics acceleration system simulation obtained at car with virtual mannequin impact barrier for different vehicle speeds, but also diagrams and mathematical model obtained by experimental testing, found a similarity, at least for the maximum.

Thus, in Fig. 10 are given comparative charts of accelerations obtained mathematical model dummy skull, classic cranio-cervical system and biofidelic cranio-cervical system, and system simulation car model for different vehicle speeds.



**Fig. 8** The cranio-cervical artificial muscles biofidelity driven based on shape memory springs ready for experimental testing

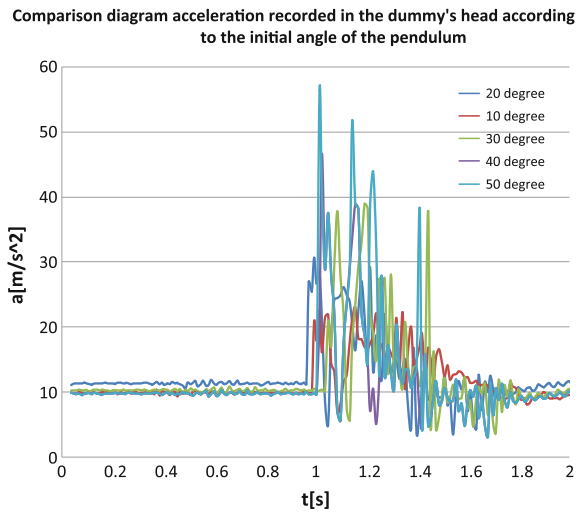


**Fig. 9** Acceleration absolute comparison chart of the dummy's head (ACC3) according to the initial angle of the pendulum biofidelity cranio-cervical system

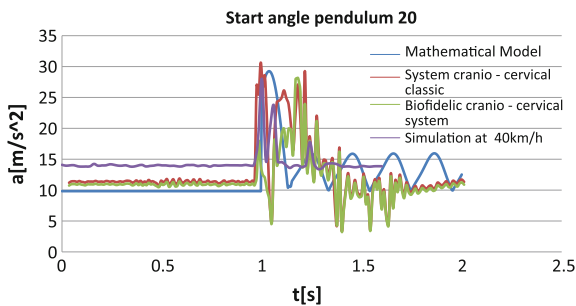


**Fig. 10** Comparison chart peak accelerations recorded in the dummy's head to the mathematical model, cranio-cervical system biofidelic classic and original pendulum angle 20° and system test dummy virtual car on impact with an obstacle at speeds of 30 km/h

## Conclusions

The analysis of diagrams and tables can be extracted, at least, the following conclusions:

- Using the experimental device pendulum can study different impact conditions in the automotive field;
- Cranio-cervical system with artificial musculature is close to the actual behavior by simulating natural reactions;

- Can get a calibration device for different experimental situations in reality, if studied;
- Comparative graphics components are similar and have similar values after the moment of impact;
- Graphics acceleration for different speeds of impact achieved by simulating collision system auto barrier until the moment of impact, are different from those obtained by using the mathematical model proposed, or by testing the experimental stand, because the dummy is requested by simply moving the car running virtual support.

It appears that the system (complex) cranio—cervical biofidelic designed and experimental device testing present in our work, both made basically represents an innovative system for studying the behavior of different components of the structure of a mannequin testing different types of impact in the field of passive safety vehicles. In general, it is considered that the development of automotive mannequins to test different types of impact will lead to continuous improvement of safety of the driver and passengers.

## References

- Abedrabbo G (2009) Simulation of a frontal crash test using multibody dynamics. Universite catholique de Louvain, Center for Research in Mechatronics, Belgium
- Claessens M, Sauren F, Wismans J (1997) Modelling of the human head under conditions: a parametric study. In: Proceedings of the 41st STAPP car crash conference, Florida, pp 3829–3848
- Dejeammes M, Alauze A, Trauchessec R (1990) Comfort of passive safety devices in car. Methodology of a long term follows-up survey. SAE Paper 905199/1990
- Franck H, Netter HD (2008) Atlas de anatomia a omului. Calysto Publicing, Bucharest
- Korteling TE (1990) Perception—response speed and driving capabilities of brain-damaged and older drivers. *Human Factors*, pp. 95–108
- Mackay M, Cheng L, Smith M (1990) Restrained front seat car occupant fatalities. In: AAAA proceedings p 34
- Im H, Nilsson L (1990) The effects of a mobile telephone task on driver behaviour in a car following situation. *Accid Anal Prev* 27:707–715
- Simms C, Van Loocke M, Lyons G (2005) Computational modelling of the head and jaw for OOP frontal impact applications. In: 5th European MADYMO User Conference, Cambridge, September 26th–27th
- Tarniță D, Boborelu C, Popa DL, Tarniță C, Rusu L (2010) The three-dimensional modeling of the complex virtual human elbow joint. *Rom J Morphol Embriology* 51(3):489–495, ISSN 1220-0522 (Ed. Academiei Romane)
- Yan JA (2006) A computer simulation model of the human head-neck musculoskeletal system. PhD Thesis, The University of Tennessee and The University of Memphis, December

# Considerations on the Vehicles Identification and Classification in Traffic by the Length Criterion

Nicolae Filip, Adrian Dohotari and Jacint Kovacs

**Abstract** Vehicle identification in traffic using the criterion of length is more often used in the development of automatic detection equipment. Two classic examples are relevant: Doppler radar detection and video detection. Let's not forget laser detector that provides a vehicle quite accurate shape. The disadvantage of these methods of the traffic participants classifying is the error of determining the length of vehicles that exceed 10 %. The work is the result of almost 10 years of experience conducting traffic studies using automatic vehicles detection equipments. For a better classification of traffic participants we proposed an algorithm for processing the primary data files collected from counting equipments which compare values: length and speed. This allows the identification of certain categories of vehicles impossible otherwise to be classified (bike/motorcycle, or Tractor trailer/Trucks & Derivatives 2 axles, etc.). The efficiency of the proposed classification algorithm was tested in urban mobility projects carried out this year. In this way, we could detail more specifically road users, resulting in a more efficient mobility analysis.

**Keywords** Radar · Vehicle · Length · Classification · Algorithm

---

N. Filip (✉) · A. Dohotari · J. Kovacs  
Department Road Vehicle and Transportation,  
Technical University of Cluj Napoca, 103–105 Muncii Street,  
400641 Cluj-Napoca, Romania  
e-mail: Nicolae.Filip@auto.utcluj.ro

A. Dohotari  
e-mail: jacintkovacs@gmail.com

J. Kovacs  
e-mail: doh.adrian@yahoo.com



## Introduction

The need for automatic classification of road users is obvious and required to perform traffic studies. Automatic detection of vehicles on the road consists in identification of the vehicle presence and the speed with which it passes through the detection area. If these two parameters are collected directly by detection equipment, the third parameter: the category to which the vehicle belongs is subsequently determined by an analytical method using raw data recorded (speed) and some constants resulted from the settings of detection conditions (Shyr-Long et al. 2014).<sup>1</sup> Identification of the class of which the registered vehicle belongs is a requirement for traffic analysis, which provides information to:

- Determination of the traffic basic parameters calculated for road design in terms of bearing capacity and traffic capacity;
- Development of urban mobility plan in municipalities and cities;
- Identify the traffic participants share on the traffic count area;
- Determining the vehicles equivalent numbers of road users using the equivalence coefficients of each category.

According to current regulations in traffic censuses, traffic participants are classified in 11 categories, as follows<sup>2</sup>:

- Bicycles, motorcycles;
- Cars;
- Minibuses with max 8 + 1 seats;
- Pick ups and trucks with maximum laden weight  $\leq 3.5$  t;
- Two axle Trucks and Derivatives;
- Trucks and Derivatives with 3 or 4 axles;
- Articulated vehicles (TIR), with more than 4 axles;
- Buses;
- Tractors with/without trailers and special vehicles;
- Trucks with 2, 3 or 4 axle trailer;
- Horse wagon.

The techniques used to identify the traffic participants category covering two measurable characteristics: axle weight and total vehicle length. Vehicles classification using length criteria is quite frequently and it is applied for radar detection, video detection and in the case of traffic surveys with rubber tubes.

The length criterion does not provide an accurate differentiation between vehicles of different categories having similar lengths. Often the following classification indecisions it happens regarding the type of road users:

---

<sup>1</sup>User Manual for SDRtraffic/ SDRtraffic + Smartphone Edition 8.2\_1503.

<sup>2</sup>Ordinul nr. 617 din 23 octombrie 2003 pentru aprobarea reglementării tehnice „Normativ pentru determinarea traficului de calcul pentru proiectarea drumurilor din punct de vedere al capacității portante și al capacității de circulație” Indicativ AND 584–2002.

- Bicycles/motorcycles;
- Pick ups and trucks with maximum laden weight  $\leq 3.5$  t/horse wagon;
- Tractor trailer/Trucks and Derivatives 2 axles.

In this context, based on experience in the use of detection equipments we develop software enabling the identification of these categories in indecision regarding the road users.

## Traffic Parameters Identification Using Radar Equipments

Radar equipment to measure traffic parameters are part of non intrusive type of detection. They are mounted either side of the road using street furniture elements (columns for fixing road signs or traffic light pole, lighting poles fixing, etc.), or cantilevered above the road (Fig. 1).

A radar equipment to measure traffic parameters differs from the traffic safety one, used by police patrols, by several characteristics as follows (Filip 2010):

- Measures both the vehicle speed and its length;
- Identify the presence of the vehicle relative to the basis of time (date, hour, minute), which determines the hourly flow;
- Allow simultaneous detection of vehicles traveling in both directions of road travel;
- Are usually discrete measurement equipment that are more difficult to see by the road users (this does not induce the driver behavior prevention and kept going so normal traffic characteristics);

In order to assure measurement of this parameters, some adjusting must be made for assure the wave propagation positioning incidents from the road. According to the road specific conditions, there are two angles for positioning the setting emission direction:

- The angle in the horizontal plane ( $\alpha$ ), it is a constant depending on the type of device and it can have a value of  $45^\circ$  (most devices) or  $30^\circ$ ;
- Vertically angle  $\beta$  whose value is variable depending on the location of the equipment (height above the ground and distance from the road) and the number of lanes in each direction of travel as well as their width (Fig. 2), (User Manual).

If the Doppler principle used for measure the speed of the vehicles is well known, less is known about how it can be measure the specific vehicle length. For length detection, the system emits a pulse of radar survey (frequency modulated emission) and then receives reflections of the pulse from the target to the next emission pulse survey. The time from the beginning of a pulse survey and beginning of the next pulse is called pulse repetition period and it represents the basis of determining the vehicle length (Mark and Goodson 1985).



**Fig. 1** Mobile traffic data count in different work conditions (Road traffic laboratory of UTCN projects for develop urban mobility plan in different cities from country)

### **The Developed Algorithm for Vehicles Traffic Classification Using the Criterion of Length**

However, vehicles classification criterion using their length is exposed to errors quite common, as mentioned in Chap. 1.

Most often, the software utility which accompanied the detection equipment allows the identification of 4–8 categories of road users.

Taking as reference the CNADR requirements and ARX classification procedure (recently increasingly used in Europe), we proposed an algorithm and soft for processing the traffic data to classify vehicles in 12 categories. Additional the developed soft application allow setting the thirteen classes for vehicles with

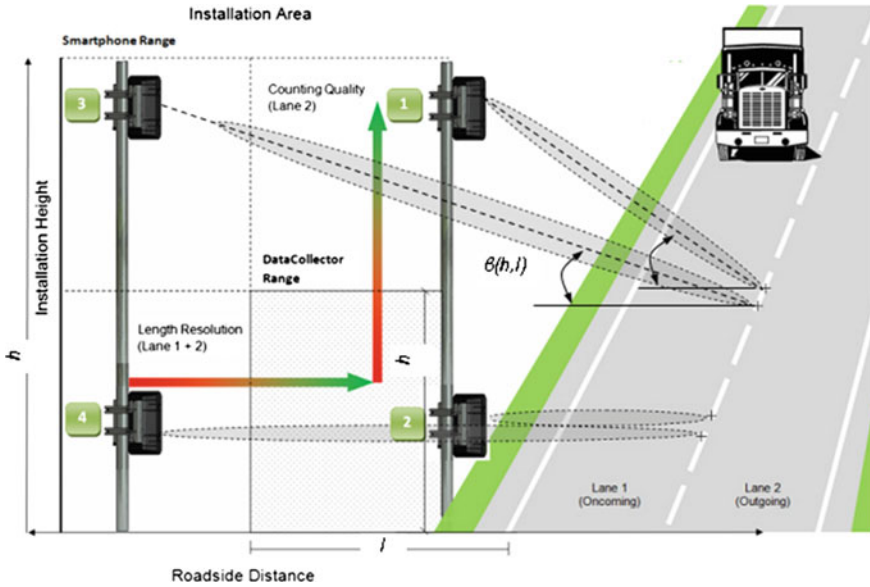


Fig. 2 Traffic radar different  $\beta$  setup angle

atypical lengths with a significant presence in traffic (e.g. new trams in cities whose length is up to 31.5 m) (Moldovan and Filip 2014; Shyr-Long et al. 2014).

Because most equipment provides detected measurement data files in txt. format, we used this format as a data source very friendly which could be imported in various media software for traffic data processing. Thus we developed in Ms-Excel an application that allowed statistical basic traffic files processing in order to obtain the following parameters (Fig. 3a, b):

- Vehicle flow peaks in [veh./h];
- Average speed in [km/h];
- Absolute frequency distribution of velocities within 10 km/h minimum speed to maximum speed recorded;
- Classification of road users in the 12 (extended to 13) categories.

It was further considered necessary to eliminate indecision classification for vehicles with lengths close, but with different dynamic features, through an additional filtration of available data (Nguyen et al. 2002).

In this way it was considered two registered parameters: length and speed, for a supplementary evaluation. Also, based on observations and dynamic characteristics of different vehicle type, we established maximum speeds for vehicles from indecision categories in terms of accurate identification of the type.

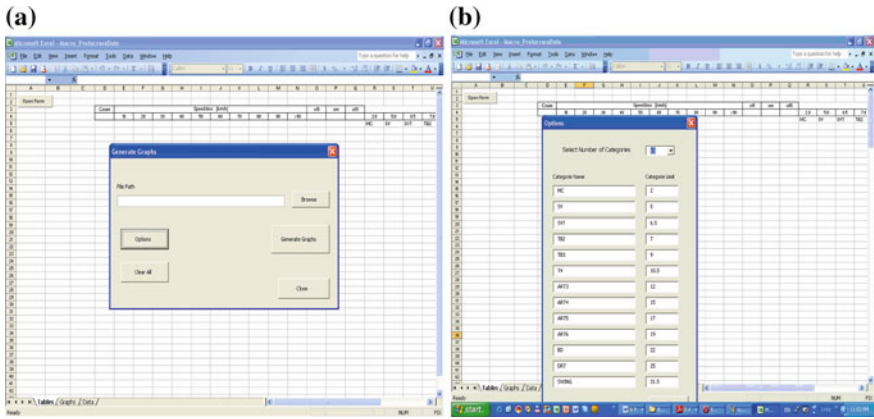


Fig. 3 The traffic data processing developed soft, a data upload and processing interface; b the interface for number of classification category selection

The result is a data processing algorithm developed on the basis of the flowchart shown in Fig. 4.

It is noted that it has been considered that these additional filtering of the data can be used only for the traffic measurement on roads in suburban areas around cities entry. In conditions of slow traffic due to large flows of vehicles in busy areas, this additional filtering may not be applied with acceptable results.

### Testing the Proposed Algorithm

In order to tests the proposed algorithm were used traffic data files collected from measurements taken during the seven days in a city with a population of up to 100,000 inhabitants. The measurements were performed with a device SDR (Radar Traffic Classifier) (User Manual).

Measured data files were processed using software offered by the company producing equipment (Collect Data) and with own computer software.

Comparing data tables and graph reports, we found that data processing was complete a similarly in the case of using both software, which also results in Fig. 5. In addition we obtained a more detailed classification of road users, because our software allows distributing traffic participants in 12 classes.

The vehicles classification in more detailed categories has benefits regarding the future traffic analyses. In this respect, this make possible a more precisely evaluation of participant categories rate.

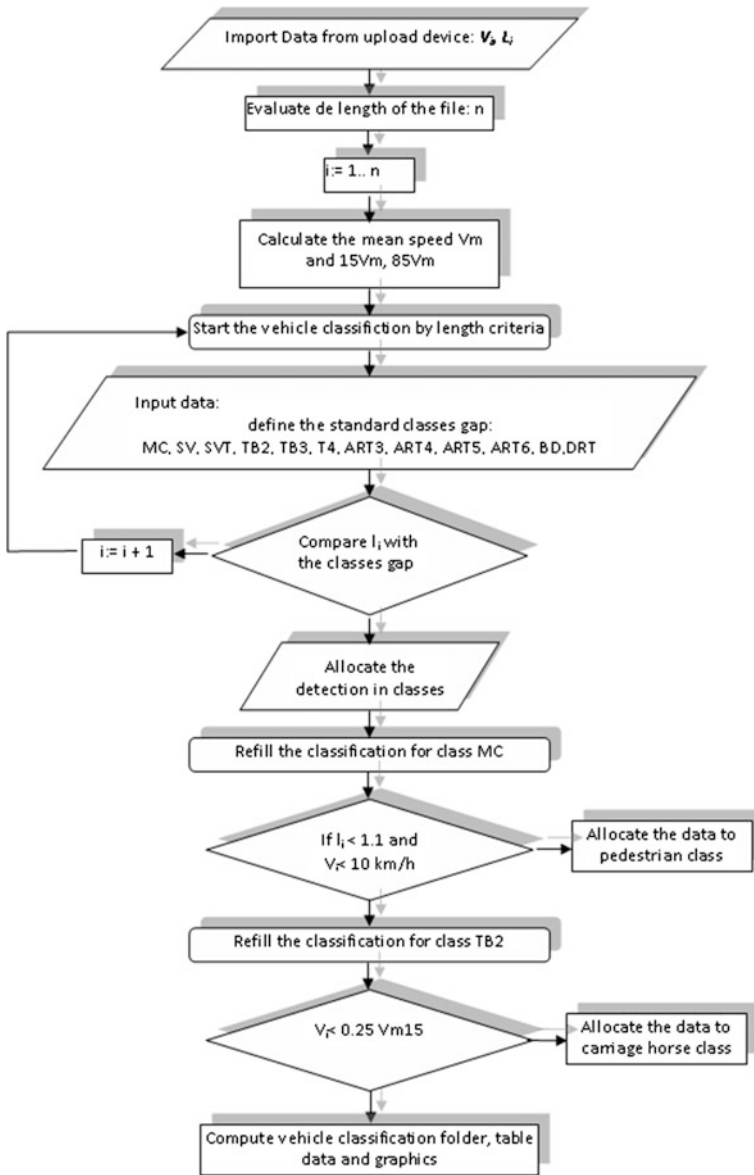


Fig. 4 The logical flowchart of the proposed algorithm

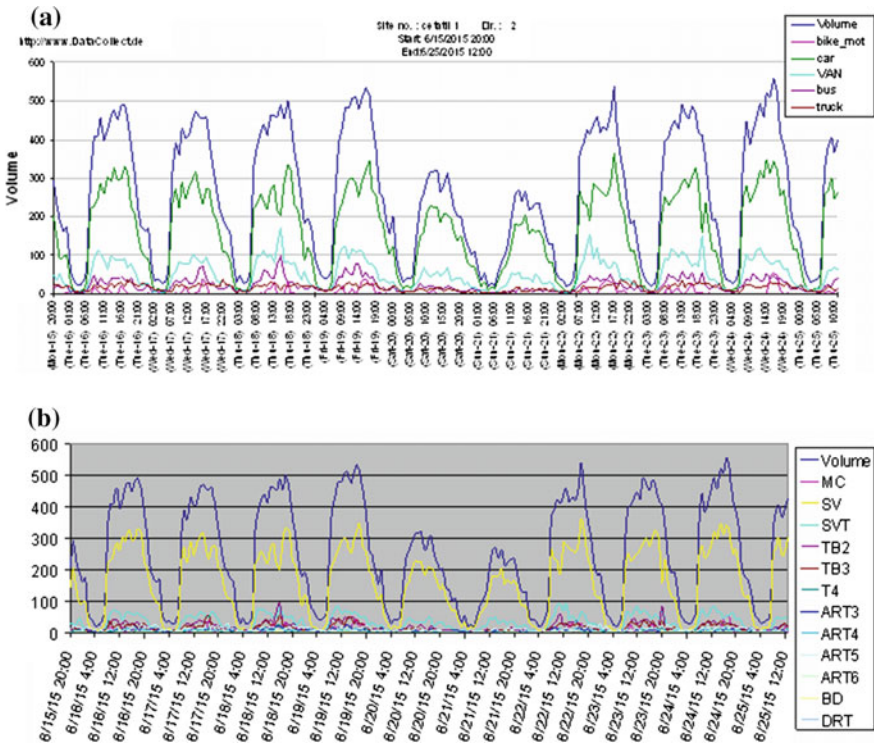


Fig. 5 Traffic flow for 24 h; data processed with: **a** processed with data collect soft, **b** processed with proposed software

If we take into consideration the possibility to identify registered bikes in traffic, this represent an useful information in developing mobility plans, where a priority is to encourage their use as an alternative ecological displacement.<sup>3</sup>

Then the algorithm was applied also to identify the bikes from Bicycle and Motorcycle category in traffic. The results are shown in Table 1.

<sup>3</sup>Guidelines Developing And Implementing A Sustainable Urban Mobility Plan. <http://www.eltis.org>.

**Table 1** Filtering data results for bike and motorcycle

Date	Time	Common class bike + motorcycle		Detailed classes	
		Data collect soft source	Owen soft source	Bike	Motorcycle
6/16/2015	1:00:00 AM	4	4	0	4
6/16/2015	2:00:00 AM	0	0	0	0
6/16/2015	3:00:00 AM	0	0	0	0
6/16/2015	4:00:00 AM	0	0	0	0
6/16/2015	5:00:00 AM	0	0	0	0
6/16/2015	6:00:00 AM	0	0	0	0
6/16/2015	7:00:00 AM	0	0	0	0
6/16/2015	8:00:00 AM	1	1	0	1
6/16/2015	9:00:00 AM	16	16	4	12
6/16/2015	10:00:00 AM	10	10	7	3
6/16/2015	11:00:00 AM	0	0	0	0
6/16/2015	12:00:00 PM	0	0	0	0
6/16/2015	1:00:00 PM	15	15	8	7
6/16/2015	2:00:00 PM	2	2	2	0
6/16/2015	3:00:00 PM	0	0	0	0
6/16/2015	4:00:00 PM	1	1	1	0
6/16/2015	5:00:00 PM	24	24	11	13
6/16/2015	6:00:00 PM	10	10	4	6
6/16/2015	7:00:00 PM	0	0	0	0
6/16/2015	8:00:00 PM	1	1	1	0
6/16/2015	9:00:00 PM	1	1	0	1
6/16/2015	10:00:00 PM	0	0	0	0
6/16/2015	11:00:00 PM	0	0	0	0
6/16/2015	12:00:00 AM	0	0	0	0
6/16/2015	06:00-09:00	17	17	4	13
6/16/2015	15:00-19:00	35	35	16	19
6/16/2015	06:00-22:00	81	81	38	43
6/16/2015	00:00-24:00	85	85	38	47

## Conclusion

Traffic studies made on the basis of continuous measurements are a necessary requirements for optimizing the movement of vehicles, but also for determining traffic for road design calculation in terms of bearing capacity and traffic capacity.

Detailing the traffic participants by proposed filtering method give better information's for analyze the contribution of each vehicles type to the traffic flow. In the case of the cross rods lights optimization, the vehicles category is taking into consideration to calculate the number of equivalent vehicles.



In the European context of the requirement realization of urban mobility plans in the major cities, traffic studies remain a requirement too. If we take into consideration the possibility to identify registered bikes in traffic, this represent an useful information in developing mobility plans, where a priority is to encourage their use as an alternative ecological displacement (See Footnote 3).

We test the soft during last months regarding the quality of data recorded and final results delivered and the results were acceptable.

It is now undergoing the procedure for obtaining copyright for software application developers.

## References

- Filip N (2010) Ingineria traficului rutier. Ed. Mediamira, Cluj-Napoca, pp 253–291
- Mark E, Goodson BS (1985) Technical shortcomings of doppler traffic radar. *J Forensic Sci JFSCA* 30(4):1186–1193
- Moldovan M, Filip N (2014) Increasing of the urban traffic surveillance by automatic information device. *Central Eur J Eng* 4(2):133–141
- Nguyen DH, Kay JH, Orchard BJ, Whiting RH (2002) Classification and tracking of moving ground vehicles. *Lincoln Laboratory Journal* 13(2):275–304
- Shyr-Long J, Wei-Hua C, Hsiang-Pin L (2014) Estimating speed using a side-looking single-radar vehicle detector. *IEEE Trans Intell Transp Syst* 15(2):607–614

# Aspects Regarding Priority Settings in Unsignalized Intersections and the Influence on the Level of Service

Dumitru Ilie, Matei Lucian, Vîntorur Matei, Racilă Laurențiu  
and Oprica Theodor

**Abstract** The authors study in this paper mathematical models that rely on input data type like: intersection type, access stages and duration, approach grade, number of branches, number of lanes, types of tapes, flared approaches, etc. After establishing a mathematical algorithm based on the detailed characteristics of different types of priority intersections we determine the potential capacity those intersections types as basis for subsequent development of the area as well as testing factor for the optimum conditions of road traffic. The results allow the development of models and simulations in software platforms (ex. AIMSUN, VISSUM) that can be quantified in optimization solutions.

**Keywords** Level of service · Uncontrolled intersection · Movement capacity · Queue length · Four-leg intersection · Traffic priority

---

D. Ilie (✉) · M. Lucian · V. Matei · R. Laurențiu · O. Theodor  
Faculty of Mechanics, University of Craiova, Craiova, Romania  
e-mail: dumitru\_ilie@yahoo.com

M. Lucian  
e-mail: mateiclucian@gmail.com

V. Matei  
e-mail: mvinatoru2000@yahoo.com

R. Laurențiu  
e-mail: racila\_laurentiu@yahoo.com

O. Theodor  
e-mail: oprica\_theodor@yahoo.com

## Introduction

Intersections and interchanges are major points of conflict for road users and are the frequent site of injuries and fatalities. Intersections also have a significant impact on the mobility of pedestrians and bicyclists (Andrews et al. 1998).

The speed and ease with which they can move through an intersection is affected by the signal timing scheme, the number and configuration of lanes, width of the traveled way, presence of a median or refuge islands, traffic calming configurations, roadsides, landscaping features, traffic volumes, and other factors.

Transport problem today comes under new forms due to natural desire that need to meet the needs of safe travel, speed, comfort, economy and environmental protection (Andrews et al. 1998; Box et al. 1994).

Meeting these needs today we need to address a few areas like:

- Infrastructure, designed in the past and no longer correspond to current standards, and to the future needs;
- Lack of funds due, at present, to difficult economic situation;
- The need to maintain old constructions makes widening of some streets impossible and arranged the streets along major traffic flows (Robertson and Bretherton 1991).

## Priority of Streams in Intersections

An intersection is a road junction where two or more roads either meet or cross at grade. This intersection includes the areas needed for all modes of travel: pedestrian, bicycle, motor vehicle, and transit. Thus, the intersection includes not only the pavement area, but typically the adjacent sidewalks and pedestrian curb cut ramps. All the road junctions designated for the vehicles to turn to different directions to reach their desired destinations. Traffic intersections are complex locations in any cities. This is because vehicles moving in different direction want to occupy same space at the same time (Stewart and Aerde 1998).

Basically, there are four types of intersections, determined by the number of road segments and priority usage.

- Priority Intersection: Occur where one of the intersecting roads is given definite priority over the other;
- Space sharing intersection: Are intended to permit fully equally priority and to permit continuous movement for all intersecting vehicle flows;
- Time Sharing Intersection: Are those at which alternative flows are given the right of way at different point in time (Transportation Research Board 2010);
- Uncontrolled intersection: are the most common type of intersection usually occurs where the intersecting roads are relatively equal importance and found in areas where there is not much traffic shown.

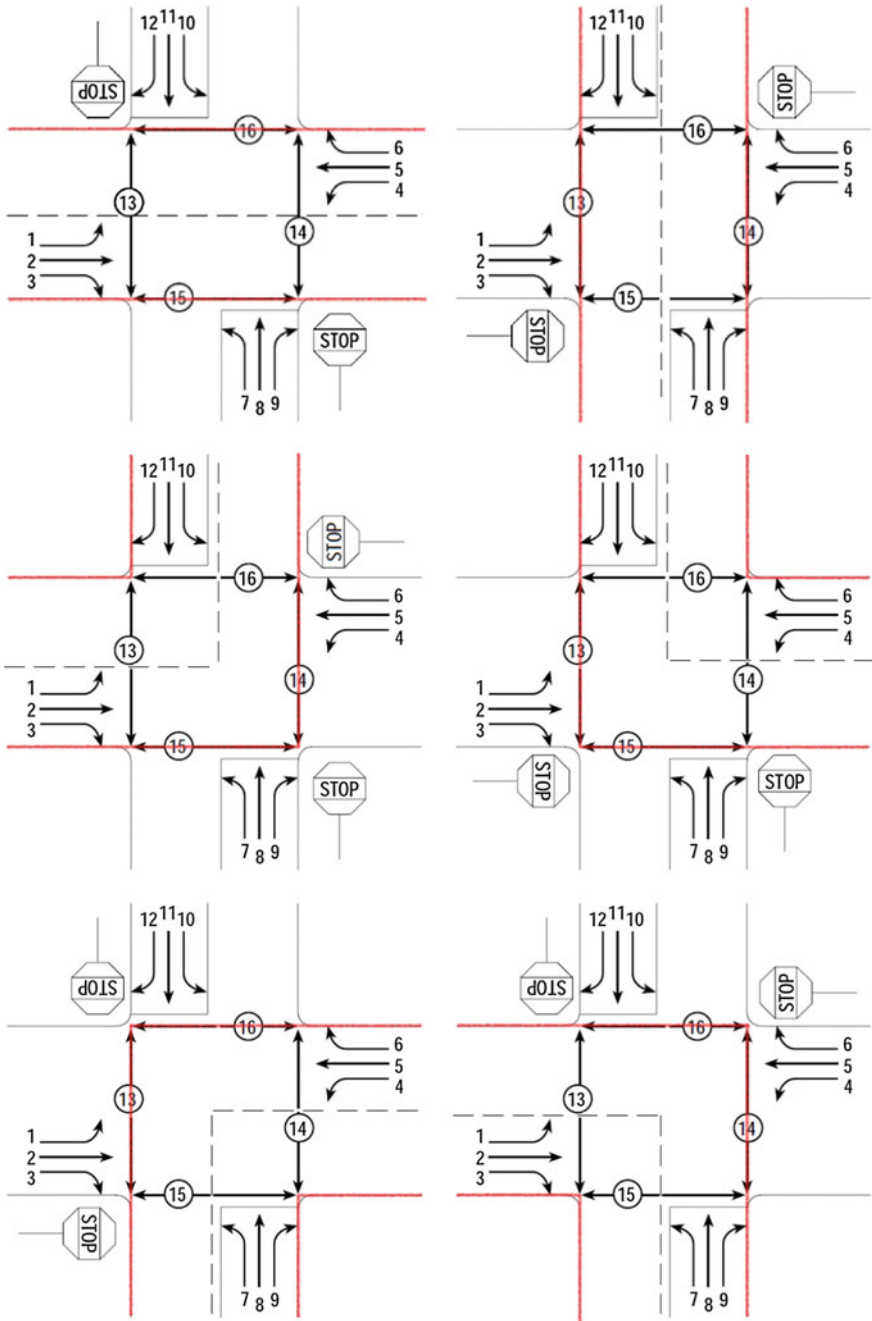


Fig. 1 Four-leg intersection priority type 1, 2, 3, 4, 5 and 6

The paper study the influence of potential capacity of four-leg priority controlled intersection on the level of service of the intersection. The methodology provides, beside the current studied TWSC Intersections and AWSC Intersections, a method to calculate the potential capacity of the road for all types of priority's in intersection given by the Romanian legislation. So for a four-leg intersection we can identify 6 types of priorities based on the conflict traffic movements in the intersections (Fig. 1).

## Potential Capacity Calculation

Priority matrix constants. In the mathematical model, the priority of right-of-way given to each traffic stream must be identified. Some streams have absolute priority, whereas others have to give way or yield to higher-order streams so it has been identified for a four-leg intersection 4 movement ranks:

- Movements of Rank 1 includes the priority movement of the major streets.
- Movements of Rank 2 (subordinate to 1) include the traffic movements that will give way or stop to and only to Rank 1 movements (can be movements from the major streets and movements from the minor streets).
- Movements of Rank 3 (subordinate to 1 and 2) include the traffic only from the minor street and the movements will give way or stop to and only to Rank 1 and Rank 2 movements.
- Movements of Rank 4 (subordinate to all others) include the traffic only from the minor street and the movements will give way or stop to and only to Rank 1, Rank 2 and Rank 3 movements. Rank 4 movements only occur at four-leg intersections.

Starting from this we needed to isolate the type of movement realized in all types of intersection and introduce it into a constant priority matrix based on the movement rank and geometrical characteristics of the intersection (Robertson and Bretherton 1991; Stewart and Aerde 1998; Transportation Research Board 2010). The priority constants matrix can be seen in the Figs. 2 and 3.

**Geometrical characteristics of the intersection.** Road conditions include geometric and other elements on which the traffic rely on so it will be without congestions (Transportation Research Board 2010). In some cases, these influence the capacity of a road; in others, they can affect a performance measure such as speed, but not the capacity or maximum flow rate of the facility.

Geometric factors include the following (Transportation Research Board 2010):

- Number of lanes from the major and minor streets;
- The type of facility and its development environment;
- Lane widths;
- Shoulder widths and lateral clearances;
- Design speed;

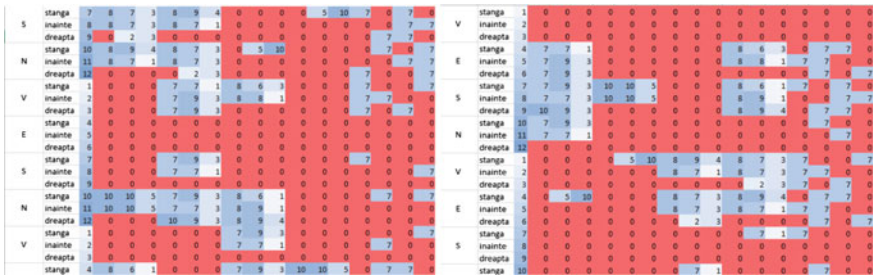


Fig. 2 Priority constant matrix for every type of four-leg intersection movement

Prioritati	V			E			S			N			V	E	S	N
	stanga	inainte	dreapta	stanga	inainte	dreapta	stanga	inainte	dreapta	stanga	inainte	dreapta	P1	P2	P3	P4
P1	1	0	0	1	0	0	4	3	2	4	3	2	0	0	0	0
P2	3	3	2	0	0	0	1	1	0	4	4	3	0	0	0	0
P3	1	1	0	4	4	3	0	0	0	3	3	2	0	0	0	0
P4	4	4	3	1	1	0	3	3	2	0	0	0	0	0	0	0
P5	0	0	0	3	3	2	4	4	3	1	1	0	0	0	0	0
P6	4	3	2	4	3	2	1	0	0	1	0	0	0	0	0	0

Fig. 3 Movement rank matrix

- Flared approaches;
- Horizontal and vertical alignments;
- Traffic from nearby intersections does not back up into the subject intersection;
- A separate lane is provided for the exclusive use of each minor-street movement;
- An upstream signal does not affect the arrival pattern of the major-street traffic;
- No other movements of Rank 2, 3, or 4 impede the subject movement;

Taking into account that the potential capacity of the intersection is subject to all the geometrical characteristics of the intersection and to all the changes that are made to it the formula for the geometrical factors takes into account all of this and can be seen in the Fig. 4.

**Conflicting volume calculation.** Each movement at a four-leg priority intersection faces a different set of conflicts that are directly related to the nature of the movement (Brilon 2011).

The conditions that are integrated as factors into the mathematical model are calculated based on the geometrical characteristics of the intersection and are based on the following criteria:

- The right-turning traffic from the major street is separated by a triangular island.
- The number of lanes one lane on the major street for every stream.

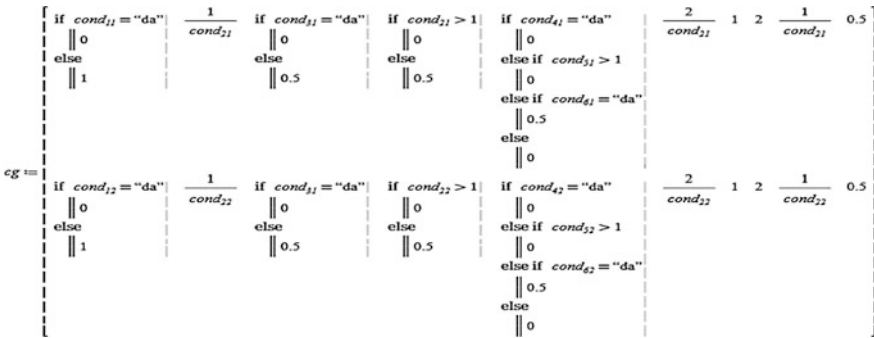


Fig. 4 Geometrical characteristics of the intersection

- The right-turn lane on the major street is separated from the rest of the movements.
- The minor approach is flared.
- The access from the minor movements is done in two separate stages.

Again in the mathematical model the conflict traffic volumes are calculated based on the real traffic volumes and the geometrical characteristics of the intersection that is added into the formula based on the priority constant matrix, see Figs. 5 and 6.

**Potential capacity.** Capacity is defined as the maximum number of vehicles, passengers, or the like, per unit time, which can be accommodated under given conditions with a reasonable expectation of occurrence. Potential capacity describes

Fig. 5 Traffic volumes based on the geometrical factor of the intersection

```

P_f := || k ← 0
        || for i ∈ 0 .. rows(P_f) - 1
        ||   || if (i = 12) ∨ (i = 24) ∨ (i = 36) ∨ (i = 48) ∨ (i = 60)
        ||   ||   || k ← k + 1
        ||   || for j ∈ 0 .. cols(P_f) - 1
        ||   ||   || if P_{i,j} = 0
        ||   ||   ||   || vec_{i,j} ← 0
        ||   ||   || else if (M_{P_k,j} = "a") ∨ (M_{P_k,j} = "c") ∨ (M_{P_k,j} = 0)
        ||   ||   ||   || vec_{i,j} ← c_{G_0, P_{i,j}-1} · V_{0,j}
        ||   ||   || else if (M_{P_k,j} = "b") ∨ (M_{P_k,j} = "d")
        ||   ||   ||   || vec_{i,j} ← c_{G_1, P_{i,j}-1} · V_{0,j}
        ||   ||   ||
        ||   ||   ||
        ||   ||
        || vec
    
```

Fig. 6 Conflicting volume

```
V_c := || i ← 0
      || for k ∈ 0 .. rows (P_i) - 1
      ||   || if k = o_{i+1, 0}
      ||     || i ← i + 1
      ||     || vec_{i, k - o_i} ← ∑_{i=0}^{15} P_{f_{k, i}}
```

the capacity of a minor stream under ideal conditions assuming that it is unimpeded by other movements and has exclusive use of a separate lane (Mueller and Claudio 2014).

Once the conflicting volume, critical gap and follow up time are known for a given movement its potential capacity can be estimated using gap acceptance models. The concept of potential capacity assumes that all available gaps are used by the subject movement i.e.; there are no higher priority vehicular or pedestrian movements and waiting to use some of the gaps it also assumes that each movement operates out of an exclusive lane. The potential capacity of is calculated using the formula shown in the Fig. 7.

Fig. 7 Potential capacity

```
c_p := || for i ∈ 0 .. rows (V_c) - 1
      ||   || for j ∈ 0 .. cols (V_c) - 1
      ||     || if V_{c_{i, j}} = 0
      ||       || vec_{i, j} ← 0
      ||     || else
      ||       || vec_{i, j} ← V_{c_{i, j}} * \frac{e^{-V_{c_{i, j}} \cdot t_{c_{i, j}}}}{1 - e^{-\frac{V_{c_{i, j}} \cdot t_{f_{i, j}}}{3600}}}
```



## Conclusion

The potential capacity calculation for every type of priority in a four-leg intersection is important in the evaluation of traffic based on the following:

- We can juggle with the geometrical characteristics of the intersection so we can maintain a lower delay for the intersection or approach priority desired and this can be seen in the Level of Service calculation;
- The priority effect for an independent intersection can be evaluated based on the potential capacity and LOS calculation. Thus the correct measures for decongesting the intersection can be taken;
- We can analyze the traffic flow and the delay for multiple intersection in a zone based on different scenarios for upstream intersection priority.

**Acknowledgements** This research article was supported by: (1) Grant no. P09003/1138/31.03.2014—“Virtual design of mechatronic and robotic applications specific to the automotive industry and transportation-PV-AMR”—Competitiveness Pole “Automotive Sud-Vest Oltenia”; (2) Grant no. 12P09002/08.05.2013—“Research to implement an advanced maintenance system in automotive industry in order to increase the degree of competitiveness”, Competitiveness Pole “Automotive Sud-Vest Oltenia”.

## References

- Andrews CM, Elahi SM, Clark JE (1998) Traffic-Control System in Transportation Research Record, pp 150–155
- Box GP, Jenkins G, Reisel G (1994) Time series analysis: forecasting and control. Prentice Hall, Englewood Cliffs, NJ
- Brilon W (2011) Delay at unsignalized intersections. D 44 780 Bochum, Germany
- Robertson DI, Bretherton RD (1991) Optimizing networks of traffic signals in real time—the SCOOT method. *IEEE Trans Veh Technol* 40(1)
- Stewart JA, Aerde MV (1998) An assessment of adaptive co-ordination of traffic signal offsets within integration. *Traffic Eng Control* 39:435–443
- Transportation Research Board (2010) American Association of State Highway and Transportation Officials (AASHTO) and Federal Highway Administration. Highway Capacity Manual 2010
- Mueller J, Claudio D (2014) Simulating unsignalized intersection right-of-way. Department of Mechanical and Industrial Engineering, Montana State University Bozeman, MT pp 59717–3800

# Influence of Tyre Pressure and Weight Distribution on Axles on the Theoretical Speed Ratio in the Running Gear System of Four-Wheel Drive Tractors

Mircea Nastasoiu and Nicolae Ispas

**Abstract** The paper presents a mathematical model used to evaluate the theoretical speed ratio in the running gear system of four-wheel drive tractors, taking account of tyres pressure. This model emphasizes situations when the parasite power phenomenon occurs in tractor's transmission, the criterion being the negative slip of wheels on one axle. Likewise, the paper addresses the influence of redistributing the tractor's weight on the two axles upon the theoretical speed ratio. The authors present applications of the mathematical model elaborated for the tractor MAT 81, manufactured by MAT Craiova, Romania.

**Keywords** Four-wheel drive tractors · Theoretical speed ratio in the running gear system · Mathematical model

## Mathematical Modelling of Theoretical Speed Ratio in the Running Gear System of Four-Wheel Drive Tractors

The operation of four-wheel-drive tractors with rigid interaxial coupling shows that they reach maximum efficiency under conditions of equality of theoretical, peripheral speeds of front and rear wheels, that is to say when

$$\omega_{m1}r_1 = \omega_{m2}r_2,$$

where  $\omega_{m1}, \omega_{m2}$  are the angular speeds of front and rear wheel, respectively, expressed in 1/s;  $r_1, r_2$ —are the corresponding dynamic radii.

The tractor-related literature reveals that the study of the kinematic non-concordance calls for the use of the theoretical speed ratio which is defined

---

M. Nastasoiu (✉) · N. Ispas

Department of Automotive and Transport Engineering, Transilvania University of Brasov,  
B-Dul Eroilor Nr.29, 500036 Brasov, Romania  
e-mail: m.nastasoiu@unitbv.ro

through the ratio of the peripheral speeds of the wheels on the two axles:  $K = v_{r1}/v_{r2}$ . However, we state that by using this coefficient the simultaneous influence of all factors upon the kinematic non-concordance cannot be taken into account; in addition, the  $K$  coefficient cannot be generalized in view of characterizing the kinematic non-concordance of the tractor under various operation conditions. In other papers, this coefficient is defined through the ratio of slip coefficients of the two axles (Nastasoiu et al. 1983):

$$K = \frac{\eta_{\delta 2}}{\eta_{\delta 1}} = \frac{1 - \delta_2}{1 - \delta_1}, \tag{1}$$

where:  $\delta_1$ —slip of front wheel;  $\delta_2$ —slip of rear wheel.

The  $K$  ratio is called theoretical speed ratio.

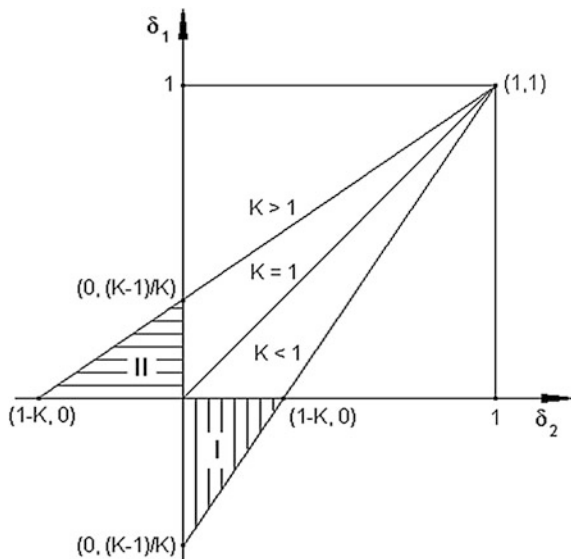
For a particular value of the  $K$  coefficient, there is a linear dependence between the slips of the two axles:

$$\delta_1 = \frac{\delta_2}{K} + \frac{K - 1}{K}. \tag{2}$$

Figure 1 graphically presents Eq. 2 for three particular values of the  $K$  coefficient:  $K > 1$ ,  $K = 1$ ,  $K < 1$ .

The graph shows that the tractor is operated at equal wheel slips and, consequently, the traction qualities of the wheels will be used at a similar efficiency level only under the conditions of a perfect theoretical speed ratio between the front and

**Fig. 1** Dependence between the slips of the driven axles for different values of the theoretical speed ratio coefficient



rear wheels, that is to say when  $K = 1$ . Provided such a theoretical speed ratio does not exist, in certain cases one axle is a driven axle and the other axle is braked (it will be pushed by the tractor’s body). Tractor’s operation in area I (marked with horizontal lines in Fig. 1) indicates that only the rear axle is driven ( $\delta_2 > 0$ ), whereas the front axle is pushed ( $\delta_1 < 0$ ). In area II, it is the front axle that is driven ( $\delta_1 > 0$ ), whereas the rear axle is braked ( $\delta_2 < 0$ ). The greater the theoretical speed ratio, the more common the situation when only one axle is driven. Likewise, we mention that both axles may be driven under the conditions of theoretical speed ratio in the running gear system ( $\delta_{1, 2} > 0$  on both axles); yet, in this case the wheels on two axles have different slip values and, therefore, their traction qualities will be unequally used. The greater the inequality, the lower is the theoretical speed ratio. The unequal use of the traction qualities of front and rear wheels negatively influence the tractive performance of the tractor.

The theoretical speed ratio in case of rectilinear travel of the tractor becomes (Nastasoiu et al. 1983; Guskov 1977; Wong 1993):

$$K_r = \frac{1 - \delta_2}{1 - \delta_1} = \frac{i_2}{i_1} \cdot \frac{r_1}{r_2}, \tag{3}$$

where:  $i_1$  is the gear ratio of the front axle drive;  $i_2$ —is the gear ratio of the rear axle drive;  $r_1$  and  $r_2$ —corresponding wheels radii.

Taking account of tyres radial deformation, which has the greater influence upon the change of wheels radius, we obtain the following relation for the  $K_r$  coefficient:

$$K_r = \frac{i_2}{i_1} \cdot \frac{r_{01} - Z_1/2\lambda_{r1}}{r_{02} - Z_2/2\lambda_{r2}}, \tag{4}$$

where:  $r_{01}$  and  $r_{02}$  are the free radii of the wheels with no load to act upon (not even the wheels’ own weight), expressed in m;  $Z_1$  and  $Z_2$  are the normal load on the front and rear axle, expressed in N;  $\lambda_{r1}$  and  $\lambda_{r2}$ —radial elastic constant of tyres, expressed in N/m.

The elastic constant  $\lambda$  may be determined with *Hedekel* formula (Nastasoiu et al. 1983), written under the form:

$$\lambda_r = 2\pi p_a \sqrt{r_0 r_b}, \tag{5}$$

where:  $p_a$ —tyre pressure, expressed in Pa;  $r_b$ —tyre rolling radius in cross section, expressed in m;

Using relation (2), we can determine the front axle slip  $\delta_1$ :

$$\delta_1 = \frac{\delta_2}{K_r} + \frac{K_r - 1}{K_r}. \tag{6}$$

In case the total vertical load of the tractor is redistributed on the two axles, the normal load  $Z_1$  and  $Z_2$ , from relation (4), are replaced with:

$$Z_1 = Z_{01} - \Delta_G; \quad Z_2 = Z_{02} + \Delta_G. \tag{7}$$

where:  $Z_{01}$  and  $Z_{02}$  are the static normal load on the two axles of the tractor;  $\Delta_G$ —change (increase) of total vertical load acting upon the tractor.

### Applications of the Mathematical Model Developed

The following 7 figures graphically illustrate the applications of the mathematical model developed. The applications are for tractor MAT 81 which has a nominal power of 58 kW (manufactured at MAT Craiova, Romania), with front tyres 11.2 R 24 and rear tyres 16.9 R 30, with total mass of 3627 kg, distributed as follows: 1540 kg on the front axle, 2087 kg on the rear axle. For this tractor we have the ratio  $i_2/i_1 = 17.0769/12.2172 = 1.3978$ .

The coefficient  $K_r$  has been determined for different values of tyre pressure (pressure deviations of  $\pm 0.05$  bar as compared to the values recommended by the manufacturer). We have also determined the slip values considering the theoretical speed ratio. We underscore that the negative slip values show that the corresponding axle is braked, which reveals the so-called parasite power phenomenon in tractor’s transmission.

Figures 2 and 5 illustrate that tyres pressures,  $p_1$  and  $p_2$ , significantly influence the values of the theoretical speed ratio  $K_r$ , and some contradictory aspects occur (Figs. 3 and 4). Therefore, as pressure  $p_2$  continues to grow in rear tyres, the values

**Fig. 2** Variation of theoretical speed ratio, with pressure in rear tyres

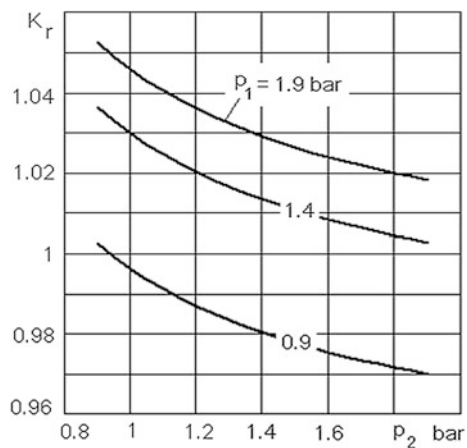


**Fig. 3** Variation of front wheels slip, with pressure in rear tyres

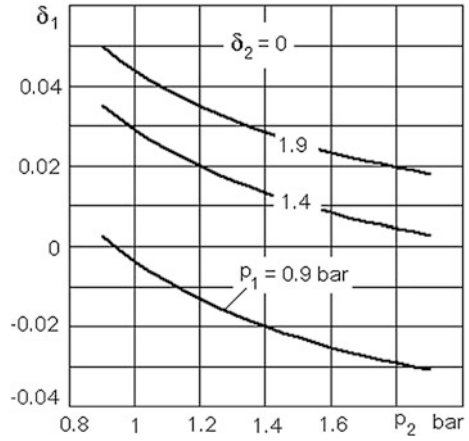


**Fig. 4** Variation of rear wheels slip, with pressure in rear tyres

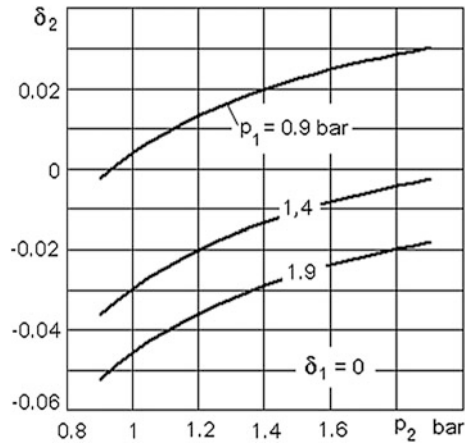
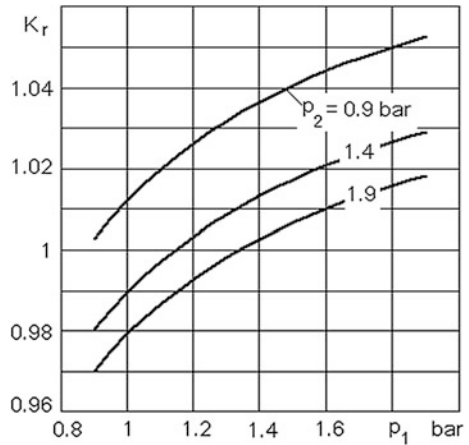


**Fig. 5** Variation of theoretical speed ratio, with pressure in front tyres



of the  $K_r$  coefficient decrease; at the same pressure  $p_2$ , the value of this coefficient increases along with the increase of pressure  $p_1$  in front tyres (see Fig. 2). On the other hand, as pressure  $p_1$  continues to grow in front tyres, the values of the  $K_r$  coefficient increase; at the same pressure  $p_1$ , the value of this coefficient decreases along with the increase of pressure  $p_1$  in rear tyres (see Figs. 5, 6, 7 and 8).

This application has also emphasized the influence of redistributing the tractor's weight on the two axles upon the theoretical speed ratio. In this case the coefficient ranges between 1.03 and 1.09. The weight redistribution is significant especially when the agricultural equipment is hauled.

**Fig. 6** Variation of front wheels slip, with pressure in front tyres

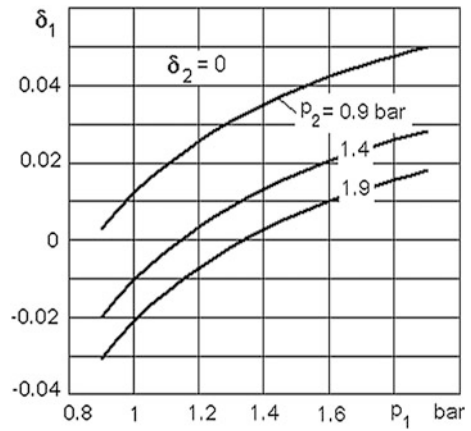


**Fig. 7** Variation of rear wheels slip, with pressure in front tyres

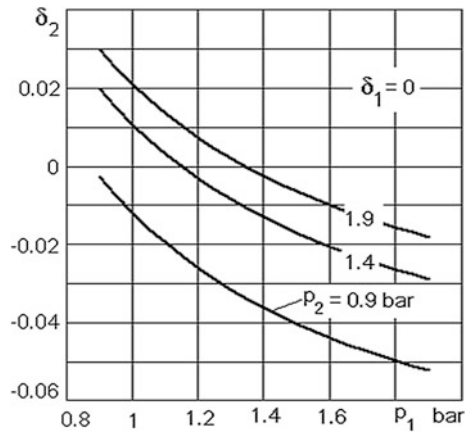
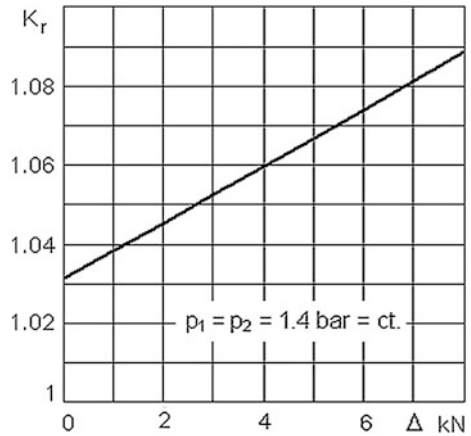


**Fig. 8** Variation of theoretical speed ratio, with redistribution of tractor's weight on the two axles



## Conclusions

The mechanics of four-wheel-drive tractors with rigid interaxial coupling has important particularities. An important particularity consists in the fact that the inequality of theoretical speeds of both front and rear wheels may considerably influence the tractor's mechanics, namely a driven axle may turn into a braked axle. In this situation it is the phenomenon of interior power flow that occurs in tractor's transmission, known as parasite power. The mathematical model developed in this paper enables us to show the conditions for the occurrence of the parasite power phenomenon in tractor's transmission.

The negative consequences of the theoretical speed ration in the running gear system explains the manufacturer's recommendations to rigorously consider the values prescribed for tyre pressure and not to operate the tractor with the coupled front axle on roads with good adhesion. As for the roads with bad adhesion the theoretical speed ratio is counterbalanced by different slip of wheels on the two axles.

## References

Guskov BB (1977) Tractori, Teoria, cisti II. Vişeişia Şkola, Minsk  
 Năstăsoiu S, Andreescu C, Popescu S, Frăţilă G, Cristea D (1983) Tractoare. Editura Didactică şi Pedagogică, Bucureşti  
 Wong JY (1993) Theory of ground vehicles. Wiley, New York



# The Development of a New Thermal Comfort Indexes

Catalin Adrian Neacsu and Mariana Ivanescu

**Abstract** Temperature inside the vehicle cabin is very important to provide comfortable conditions to the car passengers. The aim of this paper is to define an index that will be used in the evaluation of the thermal comfort for the whole car. Given that, to evaluate the thermal comfort we will need to realize a numerical simulation. In this paper, we will define two general comfort indexes: *General Thermal Comfort Index (GTCI)* and *General Absolute Thermal Comfort Index (GATCI)*. Those indexes are evaluated as an area of a surface, and are represented as graphs. The graphs are constructed taking into account the value of the thermal comfort indexes for the car occupants, and the GATCI is defined by the area of the surface and by the evaluated values. A better definition of the thermal comfort index is given by the GTCI, defined in the same way as the GATCI, but with the specification that if the individual index (PMV, PPD or DTS).

**Keywords** Thermal comfort · Vehicle · Numerical simulation · PMV—PPD · DTS

## Introduction

According to ISO 7730 (1984), the thermal is defined as “that condition of mind which expresses satisfaction with thermal environment”.

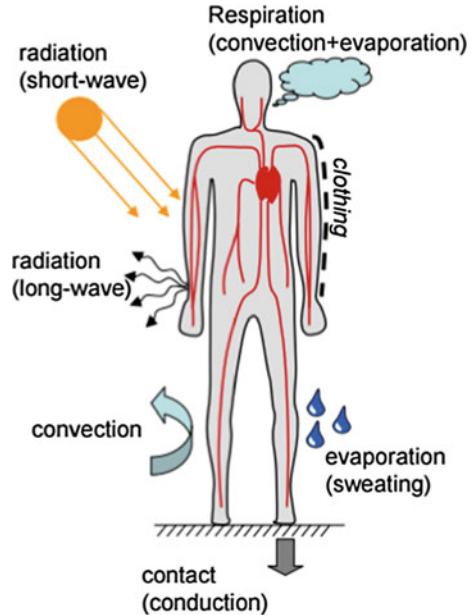
Human body’s thermoregulatory system allows adjustment of physiological heat load and thermal comfort of the body in different conditions, in Fig. 1 being presented the processes that characterize the heat transfer between the human body and the environment (Paulke 2008). We can state that the thermal comfort is affected by the three existent types of heat transfer: conduction, convection and radiation.

---

C.A. Neacsu (✉)  
SC Automobile Dacia SA, Mioveni, Romania

M. Ivanescu  
University of Pitesti, Pitești, Romania

**Fig. 1** Heat transfer between human body and the environment (Paulke 2008)



The human thermal comfort can be influenced by six parameters that are divided in environmental and personal factors (ISO/TS 14505-1:2007 2007).

- *environmental factors*: air temperature, air relative humidity, air velocity, mean radiant temperature.
- *personal factors*: clothing isolation metabolic rate.

To describe the thermal comfort, we must consider a link between these factors, link defined by the thermal comfort index.

Today we can find a variety of thermal comfort indexes, but they can be divided in:

- global indexes: **PMV (Predicted Mean Vote)**, **PPD (Predicted Percentage of Dissatisfied)**, **DTS (Dynamic Thermal Sensation)**.
- local factors (defined according to ISO 14505-2 2006).

The PMV/PPD model was developed by Fanger (1970) using heat balance equations and empirical studies about skin temperature to define comfort. Standard thermal comfort surveys ask subjects about their thermal sensation on a seven point scale from cold (-3) to hot (+3). To calculate the Predicted Mean Vote (PMV) of a large group of subjects for a particular combination of environmental and personal factors we use the Fanger's equations. Thermal neutrality is represented by zero, and the comfort zone is defined by the combinations of the six parameters for which the PMV is within the recommended limits ( $-0.5 < \text{PMV} < +0.5$ ). More useful than predicting the thermal sensation of a population is to consider whether or not people will be satisfied. For this Fanger has developed another equation to relate the PMV

to the Predicted Percentage of Dissatisfied (PPD), relation that is based on studies that observed persons in a room with indoor conditions precisely controlled.

This method treats all occupants the same and disregards location and adaptation to the thermal environment. It basically states that the indoor temperature should not change as the seasons do. Rather, there should be one set temperature year-round. This is taking a more passive stand that humans do not have to adapt to different temperatures since it will always be constant.

ASHRAE Standard 55-2010 (1981) uses the PMV model to set the requirements for indoor thermal conditions. It requires that at least 80 % of the occupants be satisfied.

Thermal comfort models allow to assess the thermo-physiologic interaction of a human body with its environment in terms of feeling cold, neutral or warm, comfortable or un-comfortable. On the other hand, simple global comfort models (like PMV) make an advanced simulation based on Fiala's (1998) manikin more or less dispensable.

Stationary comfort models typically assess the thermal sensation level (cold-hot) using given boundary conditions. Such suggestions hold for moderate boundary conditions that change in a quite slow manner. Dynamic models (like Fiala) consider time-changing reactions on thermal boundary conditions, typically human skin temperatures and their derivations in time. A well-known phenomenon is the following: A cold human entering a warm bath feels hot during the first period of time, later on, the thermal sensation gets moderate and the feeling changes from "to hot" to "warm". Dynamic effects remain completely unconsidered in stationary models.

Today, the most advanced model is based on Zhang and considers time-dependent skin temperatures as an input for different body parts. That's why it is an ideal extension to Fiala's thermal manikin that guarantees high quality for local thermal response functions, like skin temperatures. This model is based on a huge number of climate chamber test that helped to obtain correlations between human temperatures and local thermal comfort indices.

## Validation of the Numerical Model

To be able to evaluate the numerical simulation results we must first conduct an experiment to see if the obtained results by numerical simulation are similar to those obtained in real life. For this, the vehicle has equipped with 12 thermocouples and we conducted a series of experiments in a given situation and the boundary conditions for experiment are showed in Table 1 (Neacsu 2011).

For the numerical simulation we have used two software programs: Ansys Fluent and Theseus FE, whilst the linking was done using different Matlab programs and Excel charts. The main advantage of the Theseus-FE software is that it include a thermal manikin (Baker et al. 2009; Nillson 2004), and that will help us to evaluate the thermal comfort index for the vehicle occupants.

**Table 1** Boundary conditions for experiment

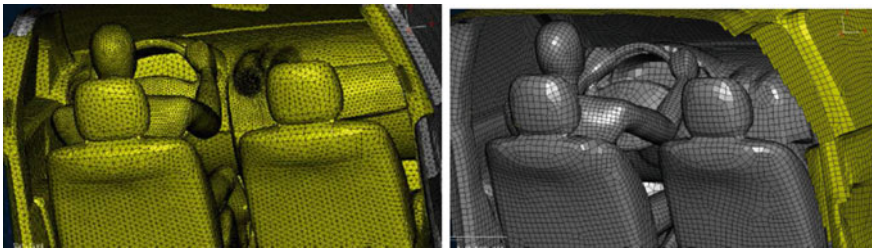
Parameter	Value
Environmental temperature (°C)	38
Environment relative humidity (%)	50

Starting from the car CAD geometry we will create a shell finite element model that comprises the car interior components. The obtained shell mesh will be used as it is to realize the Theseus-FE calculus. For the Ansys Fluent calculus we will need the air inside the car cockpit, so we will create the volume mesh of the inside of the car (Fig. 2).

We will realize a coupled numerical simulation between Ansys Fluent and Theseus FE, the results for air velocity near boundaries obtained in Fluent being used for the Theseus FE simulation.

The results obtained in the simulation, compared with those obtained from the experiment are present in Table 2.

As we can see, the numerical simulation results are similar to those obtained in the experiment, so we can conclude that the numerical simulation will give us concluding results.

**Fig. 2** Finite element model of the car cockpit**Table 2** Experimental results compared with numerical simulation results

Time (s)	Simulation temperature (°C)	Experimental temperature (°C)	Time (s)	Simulation temperature (°C)	Experimental temperature (°C)
0	55.24	54.4	960	29.64	30.0
120	46.04	48.3	1080	28.94	29.1
240	40.47	41.5	1200	28.18	28.3
360	36.74	37.7	1320	27.44	27.6
480	34.84	35.5	1440	26.72	27.0
600	33.25	33.8	1560	26.36	26.6
720	31.78	32.4	1680	26.08	26.3
840	30.66	31.2	1800	25.56	25.5

### Development of the New Thermal Comfort Indexes

The numerical simulation consist in nine cases each one characterized by an air-flow inlet distribution inside the cockpit and the air inlets positions are presented in Fig. 3.

In the Table 3 are presented the airflow rate values at right side inlets specifying that for the left side the values are the same.

The boundary conditions used for numerical simulation are presented in Table 4 and the values of the air temperature versus time when the air conditioning system operates are presented in Table 5.

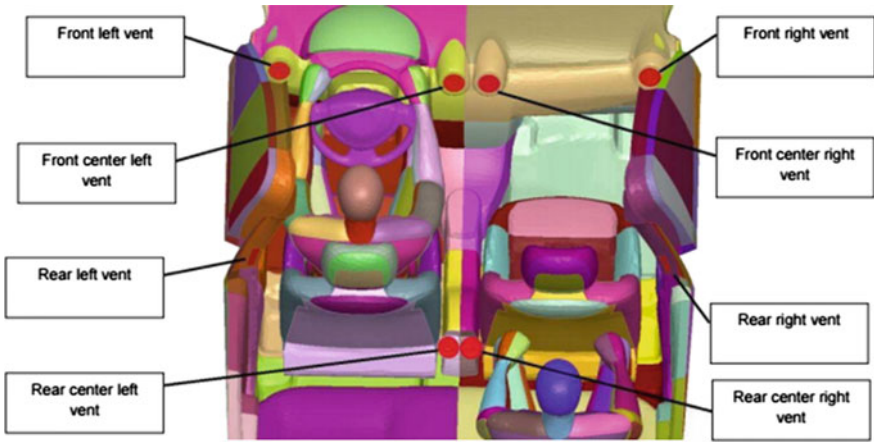


Fig. 3 Air inlets positions

Table 3 Airflow rate values

Case	Front (kg/s)		Rear (kg/s)	
	Central inlet	Side inlet	Central inlet	Side inlet
Case 1	0.024440	0.027560	0.01300	0
Case 2	0.024440	0.027560	0.00650	0.00650
Case 3	0.024440	0.027560	0	0.01300
Case 4	0.021385	0.024115	0.01950	0
Case 5	0.021385	0.024115	0.00975	0.00975
Case 6	0.021385	0.024115	0	0.01950
Case 7	0.018330	0.020670	0.02600	0
Case 8	0.018330	0.020670	0.01300	0.01300
Case 9	0.018330	0.020670	0	0.02600
Reference	0.030050	0.034450	0	0

**Table 4** Boundary conditions

Parameter	Value
Solar radiation intensity (W/m <sup>2</sup> )	1000
Sun azimuth angle (°)	330
Sun altitude angle (°)	45
Environmental temperature (°C)	38
Environment humidity (%)	50
Sky mean radiant temperature (°C)	25

**Table 5** Air temperature value

Time (s)	Temperature (°C)	Time (s)	Temperature (°C)	Time (s)	Temperature (°C)
0	51.9	600	12.1	1200	8.5
120	29.8	720	11.1	1320	8.0
240	18.2	840	10.2	1440	7.5
360	15.2	960	9.7	1560	7.2
480	13.4	1080	9.0	1680	7.0
				1800	6.7

The values from Table 3 will be used in the *Ansys Fluent* calculus and we will obtain the velocity near occupant's heads. In Fig. 4 are presented the velocity profiles for the case 9 and in Table 6 the maximum velocity values in the vicinity of occupants heads.

In terms of air speed velocity the maximum value reached at rear passenger head is 0.50 m/s in the 9th case, and for the front passenger, in the reference case the maximum airspeed is 0.91 m/s.

Using the *Ansys Fluent* results we will conduct a *Theseus FE* calculus for each case using the boundary conditions from Table 4 and AC temperatures from Table 5. The obtained values are presented in Table 7 at the end of the simulation for each airzone (front and rear).

The graphic representation of the values from Table 7 gives us a better understanding of the obtained data (Fig. 5).

Looking at Fig. 5 we can observe that the air introduction on the rear side of the cockpit gives us lower temperatures, compared to the reference case, where red represents the rear part of the cockpit and blue the front part.

*Theseus FE* is used also for its ability to evaluate the thermal comfort and the thermal comfort indexes at the end of the simulation are presented in Fig. 6.

Because the thermal comfort is characterized by different indexes, we must define a link between those indexes and the general thermal comfort.

To evaluate the thermal comfort degree for the entire car cockpit we will define an index that will allow us to sum the PMV, PPD and DTS thermal comfort index for each car occupant.

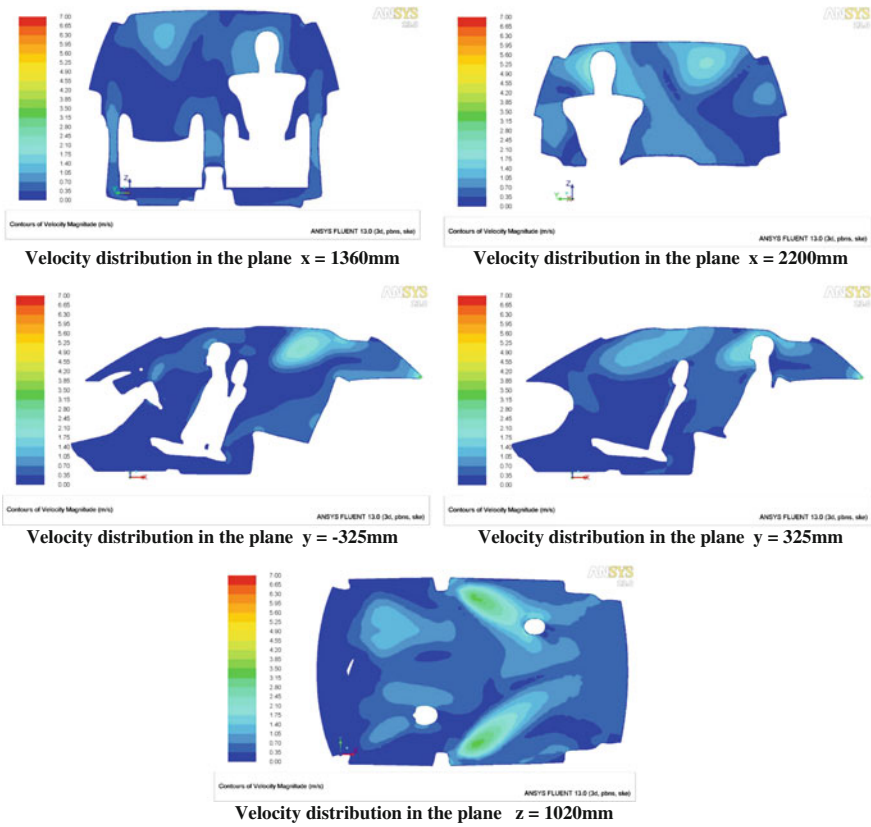


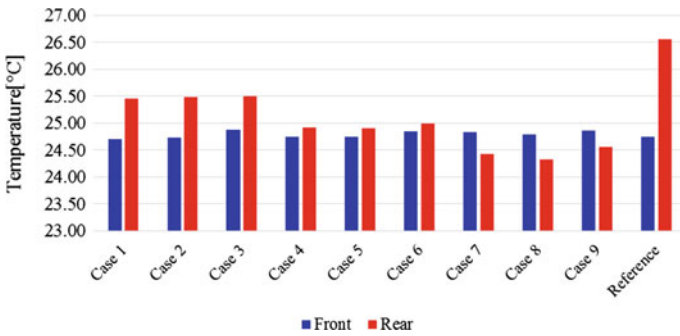
Fig. 4 Velocity distribution for case 9

Table 6 Maximum velocities values in the vicinity of occupant’s head

Case	Driver (m/s)	Rear right passenger (m/s)	Case	Driver (m/s)	Rear right passenger (m/s)
Case 1	0.53	0.31	Case 6	0.46	0.45
Case 2	0.55	0.31	Case 7	0.40	0.40
Case 3	0.52	0.38	Case 8	0.40	0.34
Case 4	0.47	0.35	Case 9	0.39	0.50
Case 5	0.48	0.32	Reference	0.91	0.28

**Table 7** Temperature values for each airzone at the end of the simulation

Time (s)	Temperature (°C)			
	Front		Rear	
	600	1800	600	1800
Case 1	32.43	24.70	33.15	25.45
Case 2	32.46	24.73	33.18	25.48
Case 3	32.58	24.87	33.17	25.50
Case 4	32.48	24.75	32.62	24.92
Case 5	32.46	24.75	32.59	24.91
Case 6	32.53	24.84	32.66	24.99
Case 7	32.57	24.83	32.15	24.43
Case 8	32.49	24.79	32.01	24.33
Case 9	32.58	24.86	32.27	24.56
Reference	32.45	24.74	34.25	26.56



**Fig. 5** Temperature values at the end of the simulation

The PMV and PPD values are between  $-3$  and  $+3$  where the negative value characterize the discomfort produced by low temperatures and positive values the discomfort produced by high temperatures, where 0 value characterize the thermal neutrality.

We will define the **PMV<sub>G</sub>** (Predicted Mean Vote <sub>Global</sub>), and **DTS<sub>G</sub>** Dynamic Thermal Sensation <sub>Global</sub>) that have the values equal to PMV module and respectively DTS module. This values allows us to evaluate how close we are to the thermal neutrality without taking into account the hot or cold sensation.

$$DTS_G = |DTS| \tag{1}$$

$$PMV_G = |PMV| \tag{2}$$



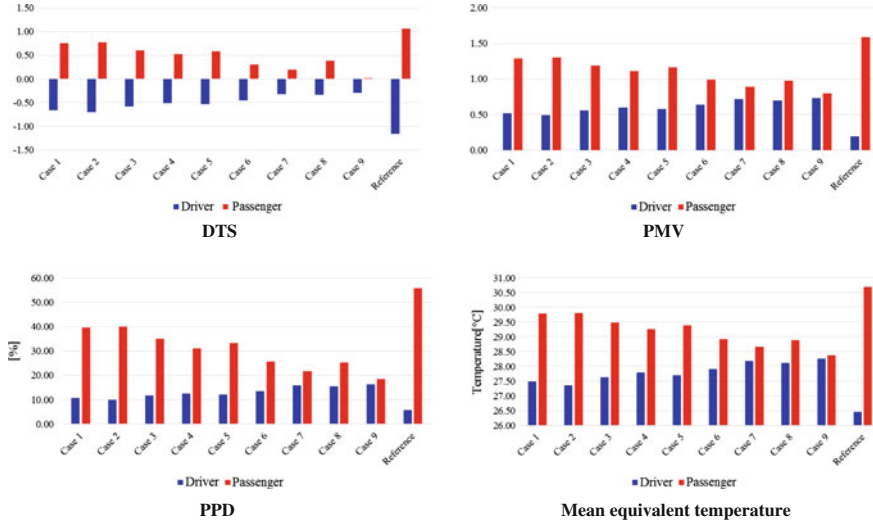


Fig. 6 Thermal comfort indexes at the end of the simulation

The **PPD<sub>G</sub>** (**Predicted Percentage of Dissatisfied<sub>Global</sub>**) value is calculated using the formula

$$PPD_G = \frac{PPD \cdot 3}{100\%} \tag{3}$$

From the obtained values for the indexes we will observe that those are included in [0.0,3], where 0 is the neutrality and 3 the maximum discomfort.

To evaluate the comfort degree we will define, as we stated previously, two thermal comfort indexes. The first we will allow us to say if we have obtained or not the thermal comfort inside the car cockpit and the second to evaluate how close we are from the thermal neutrality.

According to ASHRAE, it's considered that thermal comfort is acquired when at least 80 % of the occupants are satisfied with the thermal sensation. So, the PPD value will be equal to 20 %, this will conduct to an PPD target, noted with PPD<sub>T</sub> equal to 0.6.

Because PPD is correlated with PMV, the **PMV<sub>T</sub>** (**Predicted Mean Vote<sub>Target</sub>**), will be equal to 0.85. For the DTS index, the DTS<sub>T</sub> will be equal to 1.

The thermal comfort indexes that we will define, have values equals with the surface of a radar type graph on which we will use the values of PMV<sub>G</sub>, PPD<sub>G</sub> and DTS<sub>G</sub> to of the vehicle occupants for which we have evaluate them.

The first index that we will define is the **General Thermal Comfort Index (GTCI)**, and this index will allow us to see if we have obtained or not the thermal

comfort state for all the vehicle occupants. To construct this graph we will consider the following thing: in the case that one of the values for  $PMV_G$ ,  $PPD_G$  and  $DTS_G$  is smaller than the target value for that index, we will use the target temperature for that index. The obtained value for the area of the surface will be compared with the GTCI value calculated for the case in which we will have all the indexes equals to the target.

The second index that we will define is **GATCI (General Absolute Thermal Comfort Index)** is defined by the area of the surface and by the evaluated values. The smaller is the value of the area; the better is the thermal comfort.

In Table 8 are presented the values for GTCI and GATCI thermal comfort indexes and the graphic evaluations of these indexes are shown in Fig. 7.

Analyzing the obtained results we will observe that in case 9 all the passenger are in the thermal comfort state, and also, the case 9 provide us the best solution (from those analyzed) to obtain a better thermal comfort.

**Table 8** GTCI and GATCI thermal comfort indexes

Case	GTCI	GATCI	Case	GTCI	GATCI
Case 1	2.072	1.748	Case 6	1.942	0.905
Case 2	2.609	1.787	Case 7	1.765	0.706
Case 3	2.359	1.430	Case 8	1.921	0.906
Case 4	2.180	1.219	Case 9	1.697	0.520
Case 5	2.282	1.335	Reference	3.646	2.911
			Target	1.697	

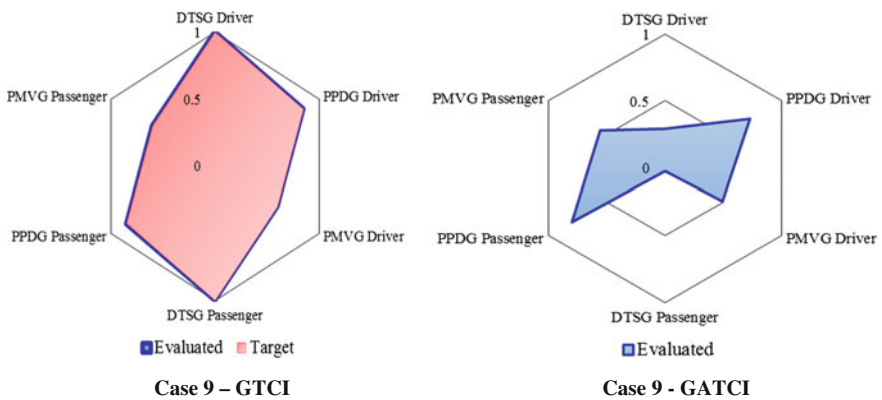


**Fig. 7** Thermal comfort evaluation, GTCI and GATCI

## Conclusions

The thermal comfort is characterized by different indexes, we must define a link between those indexes and the general thermal comfort.

The aim of this paper is to define an index that will be used in the evaluation of the thermal comfort for the whole car. Given that, to evaluate the thermal comfort we will need to realize a numerical simulation. After a bibliographical study, we have decided that the best way to realize the calculus is to use two programs: one that will solve the CFD equation of the air flow inside the cabin, and the other that will solve the thermal transfer between the car interior's components, and also contain a numerical thermal manikin.

The graphs are constructed taking into account the value of the thermal comfort indexes for the car occupants, and the **GATCI (General Absolute Thermal Comfort Index)** is defined by the area of the surface and by the evaluated values. The smaller is the value of the area; the better is the thermal comfort.

A better definition of the thermal comfort index is given by the *General Thermal Comfort Index (GTCI)*, defined in the same way as the GATCI, but with the specification that if the individual index (PMV, PPD or DTS) is inferior at the target value, it's value is taken by the target.

The GTCI gives us the answer to the question: "Does all the car occupants have reached thermal comfort?". If the values of GTCI is equal to the target, the answer is YES, if it is bigger than the target, the answer is NOT.

In conclusion, this work presents a new approach of the thermal comfort index inside of the passenger compartment, taking into account the air temperature, the most important parameter that influence thermal comfort.

**Acknowledgements** This work was supported by Grant of the Romanian National Authority for Scientific Research, MEN—UEFISCDI, project no. 264/2014, PN-II-PT-PCCA-2013-4-0569.

## References

- ASHRAE Standard 55 (1981) Thermal environment for human occupancy, Atlanta
- Baker P, Jenkins M, Wagner S, Ellinger M (2009) An optimized thermal design and development process for passenger compartments. In: European automotive simulation conference, Munich
- Fanger PO (1970) Thermal comfort: analysis and applications in environmental engineering, McGraw-Hill
- Fiala D (1998) Dynamic simulation of human heat transfer and thermal comfort PhD Thesis, De Montfort University Leicester
- ISO 7730 (1984) Moderate thermal environments—determination of the PMV and PPD indices and specification for thermal comfort. International Standards Organization, Geneva
- ISO/TS 14505-1:2007 (2007) Ergonomics of the thermal environment—evaluation of thermal environments in vehicles—part 1: principles and methods for assessment of thermal stress
- ISO 14505-2:2006 (2006) Ergonomics of the thermal environment—evaluation of thermal environments in vehicles—part 2: determination of equivalent temperature

- Neacsu C (2011) Contributions to the car cockpit thermal comfort optimization using numerical simulation, PhD Thesis, University of Pitesti
- Nillson H (2004) Comfort climate evaluation with thermal manikin method and computer simulation models. ISBN 91-7283-693-8
- Paulke S (2008) Thermal comfort design and assessment of vehicle cabins with THESEUS-FE, HdT seminar. München (14.10.08)

# The Correlation Between the Tests and the Calculation Method in the Case of an Engine Mount

Gîrbovan Daniel, Nicolae Viorel and Vieru Ionel

**Abstract** The paper presents the study of the impact on the behavior of an engine mount. The objective of the work was to achieve a correlation between calculations and the impact behavior on the test, to highlight its breaking areas. They were made several numerical simulations whose results were compared with the experimental determinations made on test bench. FEM (Finite Element Method) was used as method of calculation and the software used was PAMCRASH.

**Keywords** Impact · Engine mount · Breaking · FEM

## Introduction

The engine mount is part of the engine and gearbox mounting and suspension system. Due to the weight of the engine and the gearbox, these mount have a robust shape and significant weight.

The mount are undergoing severe and complex stresses such as successive turns, more or less close, and various types of shock (frontal impact, side impact). These stresses may produce immediate or progressive deterioration of its structure. The objective of our work was to achieve a correlation between calculations and the impact behavior on the test, to highlight its breaking areas.

---

G. Daniel (✉)  
RTR, Voluntari, Romania  
e-mail: girbovan\_daniel@yahoo.com

N. Viorel · V. Ionel  
University of Pitesti, Pitesti, Romania  
e-mail: viorel.nicolae@upit.ro

V. Ionel  
e-mail: ionel.vieru@upit.ro

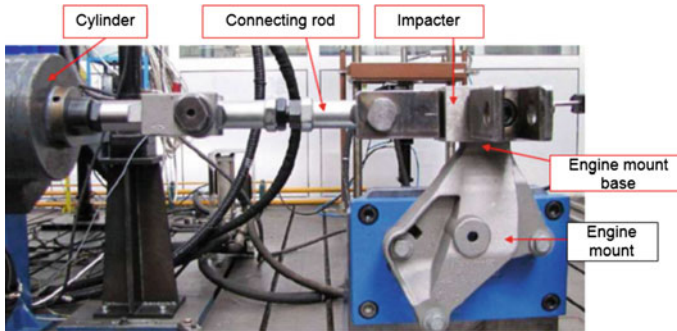


**Fig. 1** The experimental test bench

## The Methodology of the Experimental Tests

Two trials were conducted in the same manner traction, namely the engine mount is secured by bolts on the test bench (2013 RENAULT documentation). The impactor was placed at the mount level, so that the application center of the force to be coaxial with the center of the base, as shown in Fig. 1. The impactor and the hydraulic cylinder are connected by a connecting rod. This connecting rod allows to protect the cylinder to prevent a cutting moment during installation.

## Make of the Virtual Models

ANSA software was used for preprocessing and PAMCRASH software was used for analysis, the post-processing of results being done with METAPOST software (2014 PAMCRASH documentation).

Meshing of the engine mount is a very important phase and can greatly influence the results. As the element size is larger, the results are far from reality. By clearing, the fine elements greatly increase the computing time. It has to be found a compromise between the computing time and the size of the item in order to obtain optimal efficacy (Imbert 1995).

After achieving the numerical discretization, model preparation is just as important. Moreover, our objective was to realize a simple model, easy to modify, allowing simulation of real phenomena recorded on the test bench. For this reason, the impact simulation programs provide a wide range of database functions, that can be incorporated into each analysis to improve the probability of the calculation— attempts correlation.

The first numerical model of the engine mount was carried out using CATIA V5 and is shown in Fig. 2, and the properties of the material used in the calculation are shown in Table 1.



**Fig. 2** The first numerical model of the engine mount

**Table 1** Properties of the material used for calculations

Symbol	Characteristics	Value	Measurement units
E	Young modulus	75,000	MPa
$\mu$	Poisson coefficient	0.3	–
$\rho$	Density	2700	kg/m <sup>3</sup>
Rp 0.2	Elastic limit	170	MPa
Rm	Breaking limit	250	Mpa

Modelisation of the impactor was done to simulate the contact of this part with the engine mount. 3D modeling was used to create a solid-solid contact with a gap of 0, so it is automatically generated all the interferences between the parts during the physical contact.

The speed is applied to a rigid created on the impactor, comprising the nodes of the side placed on the direction of the force, as shown in Fig. 3.

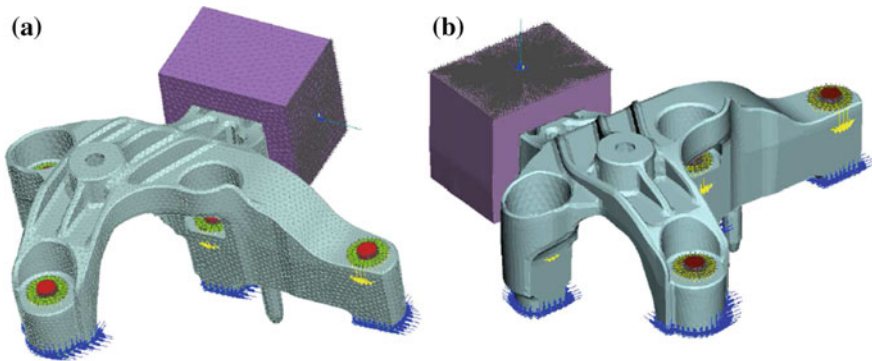


**Fig. 3** Modelisation of stresses. **a** The stress on OX axis. **b** The stress on OZ axis

### Results and Conclusions

The results of the first experimental tests are summarized in Fig. 4 and the results obtained by the first numerical analysis are presented in Fig. 5.

These first results are not acceptable for the case of the force applied on OZ axis. In both cases it could be observed a rupture zone at the boundary between the engine mount base and the impactor, which was not obtained in the real situation.

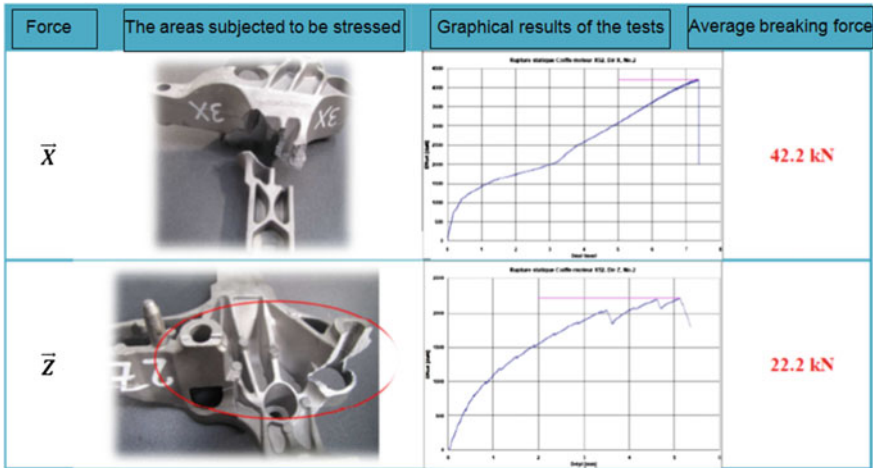


Fig. 4 The results of the tests done with the stresses applied on OX and OZ axis

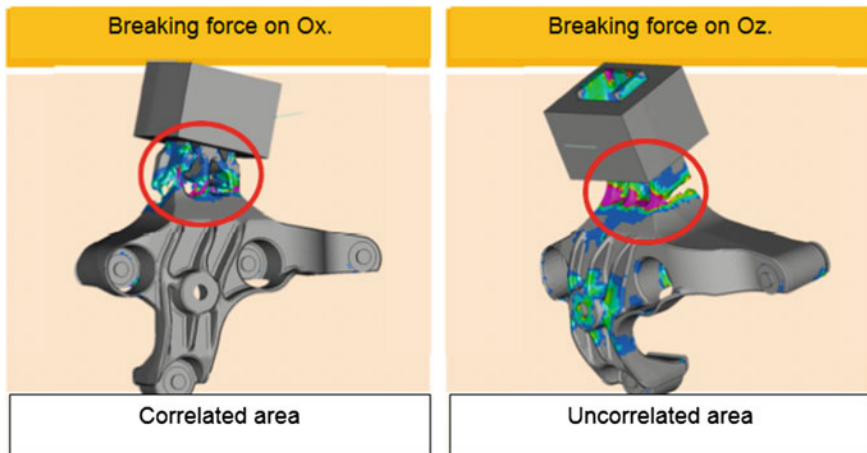


Fig. 5 The results obtained by numerical analysis with the stresses applied on OX and OZ axis



The second identified issue is the slipping that occurs between the impactor and the engine mount because, during computing, nothing prevents this. This phenomenon is not observed during the experiments on the test bench.

In the next iterations this movement will be blocked. We can choose to use a TIED contact-type or a resort with infinite stiffness on the mount axis linking the two rigids on each part. These two simulations will be done simultaneous (Fig. 6).

Moreover, the calculation was stopped by the solver due to the occurrence of the elements with negative volume. The solver is unable to solve the system of equations and because of this the calculation stops. Adding this type of contact allows increasing the calculation time and avoid this type of error as the contact is made between elements.

It was observed a deformation of the mount base during calculation, issue which does not appear during experiments. In fact, instead of having a rectilinear trajectory, the engine mount performs an uncontrolled rotation. We therefore decided to fully guide the impactor for future calculations.

Two models were made, having different only the contact between the engine mount and the impactor (Fig. 7).

Moreover, the contact between elements is added as the guide of the main node of the rigid on the impactor side. Otherwise, all other dates remain unchanged.

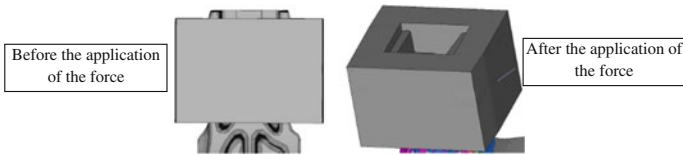


Fig. 6 Slipping of the impactor before and after the numerical simulation

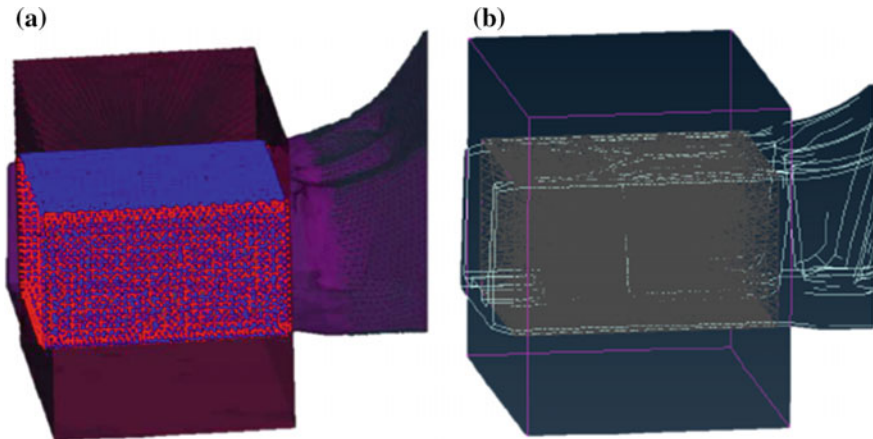


Fig. 7 Modelisation of the impactor—engine mount contact. **a** TIED contact impactor—mount. **b** SPRING contact impactor—mount

The results of the calculation performed in these conditions are shown in Fig. 8.

It could be observed that the strains are quasi-identical: the rupture zone always occurs at the boundary between the impactor and the mount surface. In fact, the load is high between the rigid constrained surfaces and the free ones whose geometry accentuates the appearance of the stress.

As a result of further testing, we found that we are dealing with two different and very closed breaking modes and a slight change in testing conditions lead to different results.

Following these conclusions, it was done a new modeling of the kneecap and the steering power link. This will allow the reproduction in the best way of the whole assembly movement. The spring was used to block the impactor, which is much less constrained than a TIED contact, as shown in Fig. 9.

Figure 10 presents the final results.

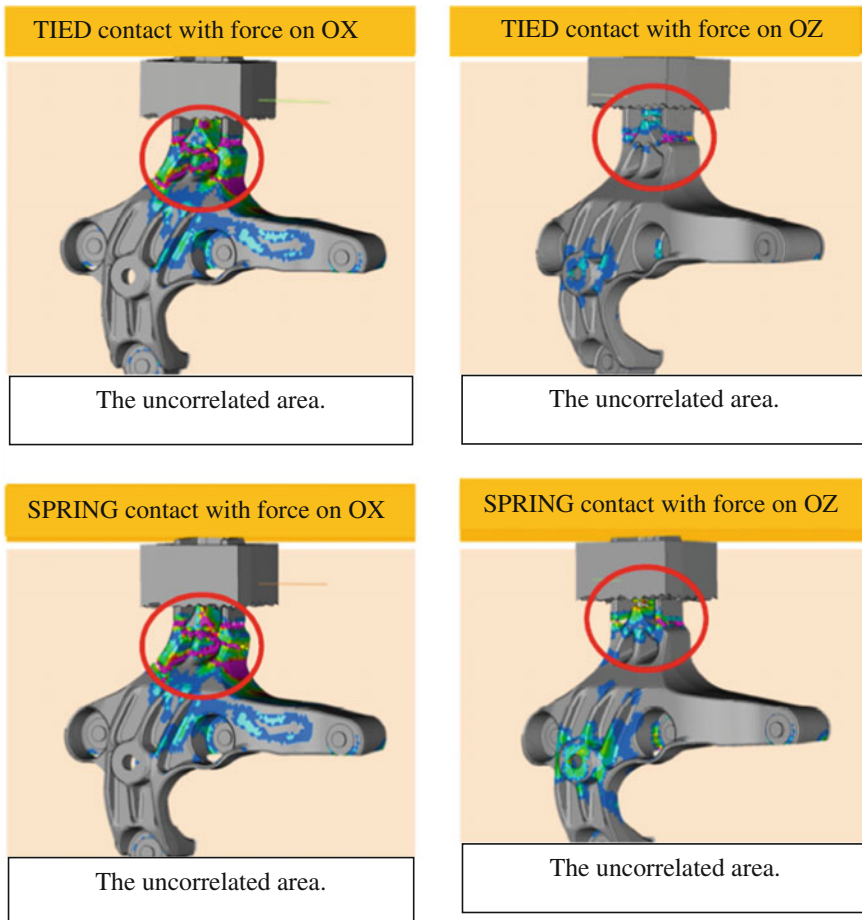


Fig. 8 The results of the computing for the engine mount in the new conditions

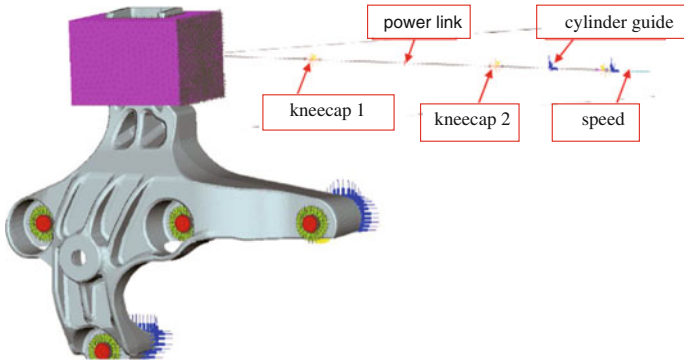


Fig. 9 Final model of the engine mount

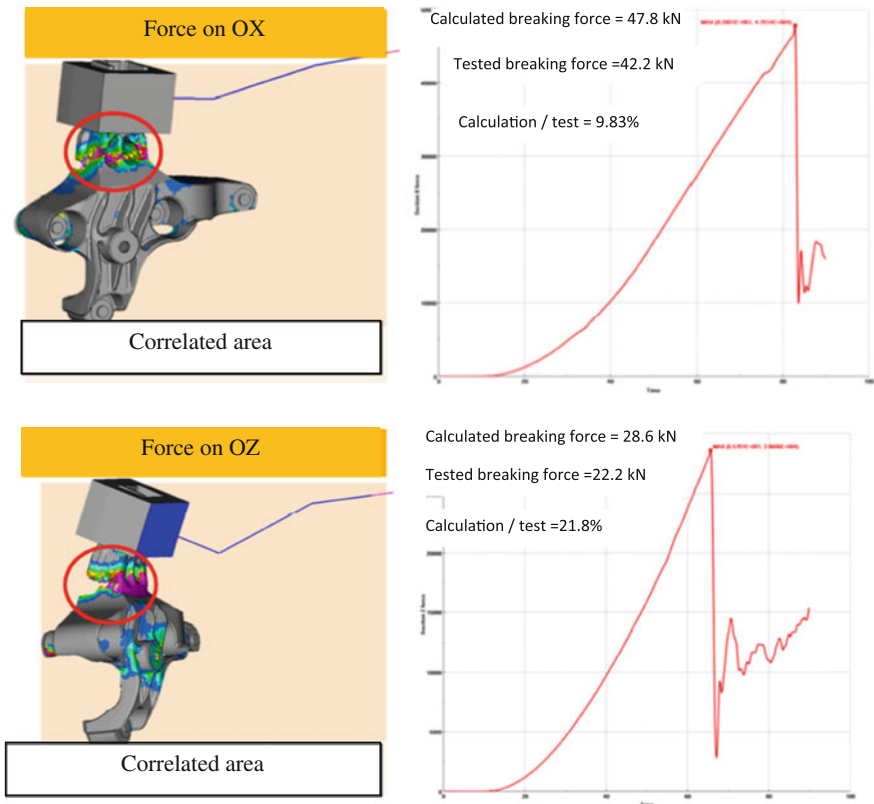
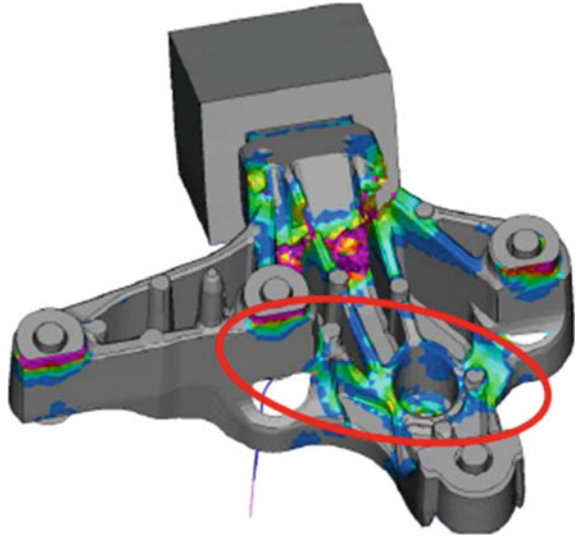


Fig. 10 Final results obtained by numerical simulations for the engine mount

**Fig. 11** The position of the second breaking area



It could be noticed that the correlation is good for the force applied on OX with 10 % less error for the breaking force. For the force applied on OZ, the difference is significant, i.e. 22 %. It is also easy to identify the second potential rupture zone, as shown in Fig. 11.

Taking into consideration the complexity of the piece and test conditions is deemed as valid the entire approach done in order to validate the methodology of calculation.

It could be noticed that, in order to achieve results in accordance with the experimental data it must take care that the modeling and simulation will be done in conditions as close to the real ones. The calculation methodology developed in this case can be used for any other type of mount that operate under similar conditions.

## References

Imbert J-F (1995) *Analyse des structures par éléments finis*. Cépaduès, Paris

# Dummy Kinematic Behaviour and Head Injuries Analysis in Frontal Collisions

Oana Victoria Oțăt, Ștefan Cristian Castravete and Victor Oțăt

**Abstract** Within the present research study we aim at running a frontal collision virtual simulation in order to establish the driver's kinematic and dynamic behavior at the impact moment by means of LS-DYNA software. Hence, our research study further underpins a contrastive analysis regarding the driver's injury degree in the head region versus the riskiest positions to cause the highest injury degree in frontal collisions. Thus, we have considered several situations in which the dummy is first sited in its normal position, and then, in turns, it is incorrectly positioned on the driver seat so as to analyze the action of the passive safety systems, i.e. the safety belt and the airbag system. Our kinematic and dynamic behavior analysis at the impact moment was carried out starting from the driver's normal position, when the Hybrid III—5th percentile dummy female was positioned with the thorax area centered to the steering wheel at a distance of 350 mm.

**Keywords** Frontal collision · Out of position · Head injury criteria · LS-DYNA

## Introduction

Within the last decades, both nationally and internationally, a steadily interest has been paid to road accidents research, in terms of their dynamics and of vehicles' active and passive safety improvement alike, thus aiming at preventing or minimizing negative consequences due to vehicle collision.

---

O.V. Oțăt (✉) · V. Oțăt

Faculty of Mechanical Engineering, University of Craiova, Craiova, Romania  
e-mail: otatoana@yahoo.com

V. Oțăt

e-mail: otatvictor@yahoo.com

Ș.C. Castravete

Caelynx Europe, Craiova, Dolj, Romania  
e-mail: scastravete@caelynx.ro

Muhammad (2002) puts forwards a comparative analysis of the bodywork damages and the injury degree suffered by the vehicle occupants during a collision with a pole or a barrier.

The development and the validation of a simulation and analysis model regarding the occupant's behavior in a front-rear-type impact is endorsed by Deter et al. (2007)

The preoccupation for the development and the optimization of virtual analysis models concerning the driver's behavior during the collision is highlighted by a series of research studies carried out by Takeo et al. (2012), Stahlschmidt et al. (2014), Ming-Pei et al. (2014), and Pradeep et al. (2010).

The Hybrid III—5th percentile dummy female has been previously used in frontal collision studies, as mentioned by Ming-Pei et al. (2014), and Pradeep et al. (2010). Admittedly, following the comparative analysis of experimental tests results and the numerical modelling by means of the LS-DYNA software, we can conclude that this dummy type stands as a viable cost-effective alternative to determine the injury degree in vehicles frontal collisions.

## The Vehicle Law of Motion at the Impact Moment

The kinematics parameters required for the dynamic analysis of the collision have been established by means of the LS-DYNA software. In order to determine the motion curve of the vehicle during the pre-crash, crash and post-crash phases and to determine the kinematic parameters required for the dynamic impact analysis, a frontal-type collision simulation carried out by means of the LS-DYNA software.

Under the circumstance, a frontal collision between a mid-size sedan (<http://www.ncac.gwu.edu/vml/models.html>) and a rigid wall has been considered. Thus, the main force direction (PDoF) has been oriented in a 12-o'clock-position and a 100 % overlapping degree. The initial vehicle velocity during the pre-crash phase has been set up at 40 km/h (Fig. 1).

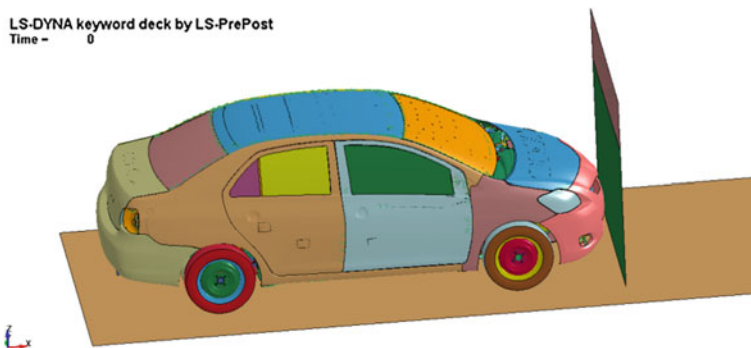


**Fig. 1** Frontal collision between a vehicle and a rigid wall in LS DYNA

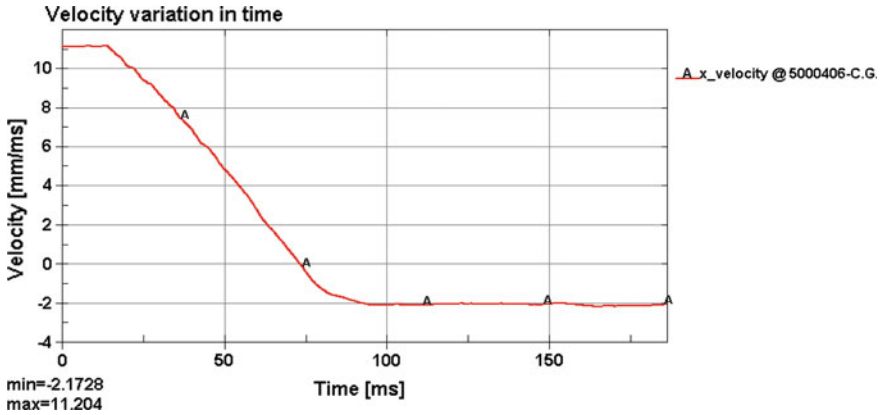


Fig. 2 The velocity variation curve for vehicle’s movement

The LS-DYNA software provides the users with an option that generates a velocity diagram in relation to time diagram, thus enabling us to record the velocity variation before and after the frontal collision.

Following the velocity versus time variation analysis we found as representative for our research study the velocity values within the time interval from 0.0 to 200 ms, during which the velocity ranged from an initial value of 11.2 mm/ms, i.e. the maximum value, up to the  $v_f = 0.0$  mm/ms, at the final moment  $t_f = 200$  ms (Fig. 2).

### The Dummy—Vehicle Model

In order to analyze the influence of the frontal collision upon the driver, we have designed both a kinematic and dynamic model consisting of the dummy-seat-airbag system. Aiming at achieving as accurate as possible results, besides these elements, we have also added to our model design the following elements: the dashboard, the steering wheel and the steering column, as illustrated in Fig. 3. These elements have been integrated to our model design in order to position the dummy in compliance with the driver’s real-life position. Moreover, another reason to introduce these elements is motivated by the fact that at the impact moment a considerable number of injuries occur due to the interaction with the elements found in the passenger compartment. Similar to the passive safety elements, we have also modelled the three-point restraint system, i.e. the seat belt as well as the driver’s airbag system located on the steering wheel.

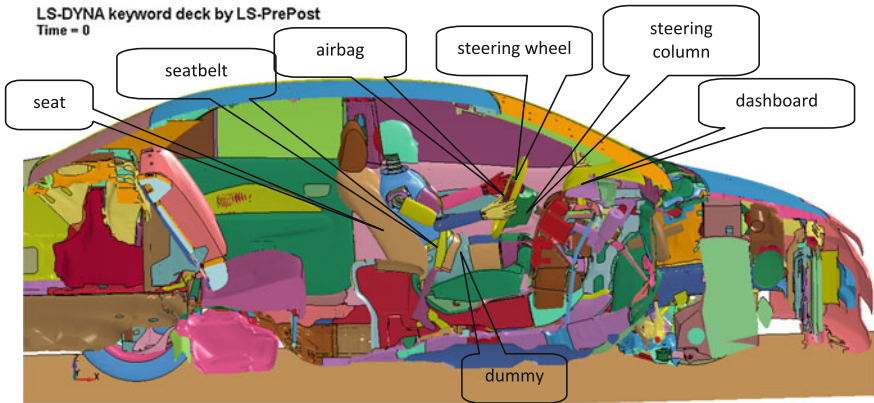
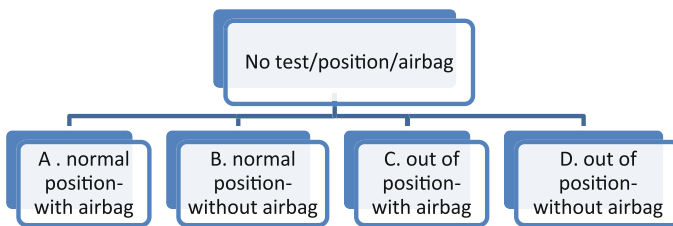


Fig. 3 The dummy-vehicle passive safety elements system

### The Analysis and the Numerical Simulation of the Frontal Collision

Aiming to study the kinematics and dynamics behavior of the driver during a frontal collision, we have carried out several series of tests. In all the situations considered the prescribed displacement was defined by the motion curve described previously. Thus, we have undertaken four series of tests that envisaged changes in the driver’s position as well as the influence of the passive safety system, i.e. of the airbag system.

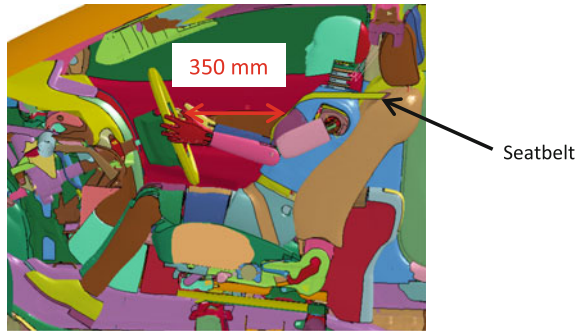


The first test focused on the driver’s normal position, so that the Hybrid III—5th percentile dummy female was positioned with a centered thorax in relation to the wheel, at a distance of 350 mm from the steering wheel. In order to position the dummy, the knee joint was set up at an angle of 110° while the hands were placed on the wheel by bending the elbow joint at an angle of 130°.

As illustrated in Fig. 4, the dummy was fixed in this position by means of a restraint system, i.e. a three-point fastened safety belt.



**Fig. 4** Normal position of the dummy



Seeking to establish a comparative relation of the driver’s kinematic and dynamic behaviour at the collision moment, the second series of tests focused on the incorrect positioning of the dummy (out of position) in relation to the distance from the steering wheel. According to Bass et al. (1998), in the ISO-2 position the dummy thorax is placed in the close proximity of the airbag and steering wheel and the dummy spine is parallel to the plane of the steering wheel.

The incorrect positioning of the dummy applied in the study involved its placing in an ISO-2 position, at a distance about of 50 mm between the thorax and the steering wheel. For this position two tests have been carried out, thus, test vehicle was first equipped with an airbag system, and, then, in the second test, no airbag system was activated.

### An Overview of the Results Obtained in the Dummy’s Head Area Following a Frontal Collision

A review of the specialized literature within this research field pinpoints that most of the automotive crash tests based on different types of dummies regard the HIC factor—Head Injury Criteria as the benchmark in assessing the injury degree in the head area (Table 1).

**Table 1** HIC, AIS code and head injury

HIC	AIS code	Head injury
135–519	1	Headache or dizziness
520–899	2	Unconscious less than 1 h; linear fracture
900–1254	3	Unconscious 1–6 h; depressed fracture
1255–1574	4	Unconscious 6–24 h; open fracture
1575–1859	5	Unconscious more than 24 h; large hematoma
>1860	6	Non-survivable

The highest values of the acceleration can be tolerated only for very short durations (200 g of 2 ms), while lower accelerations for longer time spans (80 g of 200 ms) are not tolerated. To establish the injuries degree in the complex curve of acceleration in the head area, we have established as a reference factor the Head Injury Criteria, defined by Salwan et al. (2014) as follows:

$$HIC = \left\{ (t_2 - t_1) \left[ \frac{1}{t_2 - t_1} \int_{t_1}^{t_2} a(t) dt \right]^{2.5} \right\} max \tag{1}$$

where  $t_1$  and  $t_2$  indicate the initial time and the final time (in seconds) and  $a(t)$  is the acceleration resulted (in g), measured in the head area gravity center.

According to the Directive 96/79/EC (1996) and FMVSS 208 (1998) Regulations, in case of frontal collisions, the maximal values of HIC, compatible with the driver’s survival are as follows:

$$HIC_{36} \text{ (throughout a 36 ms interval)} < 1000$$

In order to reveal the results obtained in the head area, we have predefined a node of interest, i.e. node 56961404. This node coincides with the mass center of the head, where an accelerometer was defined and placed.

A first set of results observed following the completion of the simulation regarded the time variations of the linear acceleration, recorded in the driver’s head area. In compliance with FMVSS 208 Regulation, the maximum acceleration in the head area is 80 g.

Hence, as illustrated in Fig. 5, the maximum acceleration cannot be achieved for a normal position of the dummy, protected by the vehicle’s passive safety systems, i.e. the seat belt and the airbag system, thus, resulting a lower injury degree in the

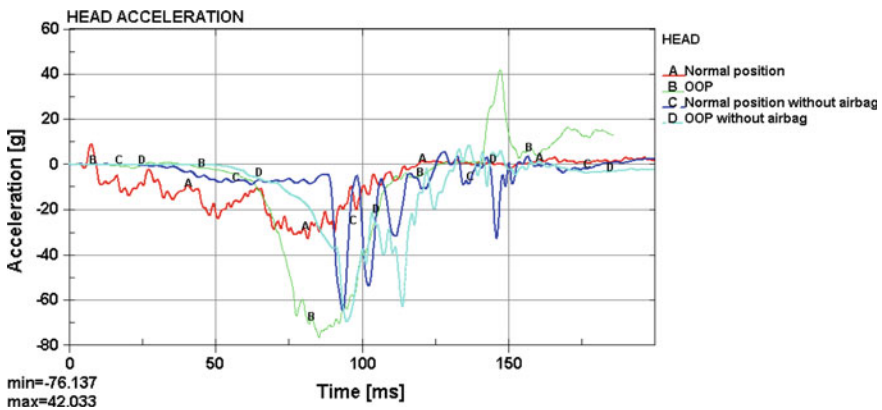


Fig. 5 Time variation of linear acceleration

head area. The maximum acceleration value in the head area, for the first situation analyzed, reaches the maximum value of 39 g at a time  $t = 90$  ms.

Conversely, for the following three situations considered we have recorded far higher acceleration values in the head area. Thus, if the dummy is incorrectly positioned in relation to the steering wheel, the acceleration value reaches the limit imposed by 80 g.

Figure 5 also illustrates that the absence of the airbag system influences considerably the acceleration value. Accordingly, for a correct position of the dummy, though without an airbag system, the maximum acceleration reaches 77 g.

The injury degree in the head area can be quantified by means of the head trauma criterion called HIC—Head Injury Criteria.

In accordance with the results obtained, the maximum HIC 36 (within a time interval of 36 ms) in the head region gravity center is 1082 for an incorrect positioning of the dummy in relation to the steering wheel while the airbag system keeps active. We could thus note that this value exceeds the superior limit of 1000, and in compliance with the AIS code, it falls under level 3 injury category, involving even the fracture. Similarly, in case the dummy is incorrect positioned and the airbag system is deactivated, the HIC value is above the limit regulated by FMVSS 208, falling also in the AIS Level 3 category (Fig. 6).

The results obtained following the four positions of the driver investigated throughout this present research study, are indicated in Table 2.

In case the dummy is correctly positioned, no matter whether the airbag system is activated or not, we have established that the HIC value is below the enforced limit, framed within AIS Level 1, i.e. minimal injury in the head area.

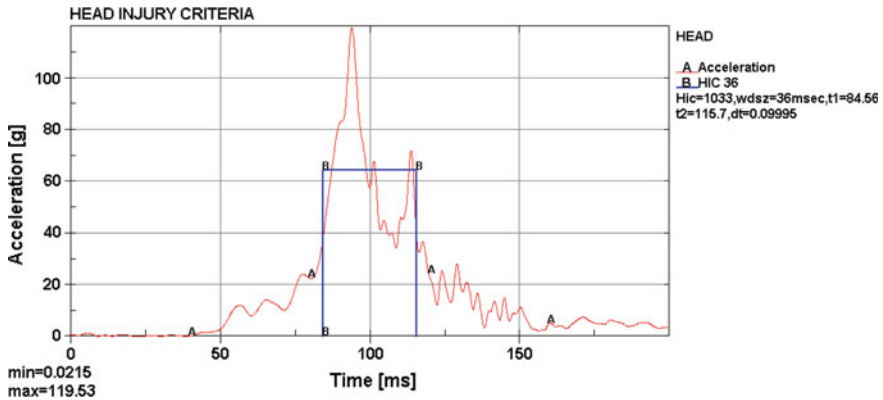


Fig. 6 Head injury criteria—OOP without airbag system

**Table 2** HIC and acceleration values

Dummy component–head–node 56961404				
Test	Parameter			
	Acceleration (g)		HIC 36	
	Max	FMVSS 208	Max	FMVSS 208
A	39	80	139.5	1000
B	80	80	1082	1000
C	78.6	80	273	1000
D	119	80	1033	1000

## Conclusion

Based on the results established for HIC 36 we can conclude that in a frontal collision, if the driver is sited in the normal driving position and the airbag system is active, the injuries suffered in the head area are compatible with survival.

For the same impact speed, from a correct position of the dummy versus an incorrect one, in compliance with the AIS scale, the injury degree in the head area is 1 AIS, in the first case, while reaching level three in the second situation.

According to the undertaken comparative analysis we could reach the conclusion that the predominant influence upon the injury degree in the head area is determined by the position of the dummy in relation to the steering wheel. Also, the airbag system displays some influences in this respect, though considerably lower as related to the injuries suffered.

## References

- Bass CR, Crandall JR, Pilkey WD (1998), Out-of-position occupant testing (OOPS3 Series), University of Virginia, Automobile Safety Laboratory
- Deter T, Malczyk A, Kuehn M (2007), Validation of a seat-dummy simulation model for rear-impact. Paper number 07-0151, Society of Automotive Engineers, Inc.
- Directive 96/79/EC of the European Parliament and of the Council of 16 December 1996 on the protection of occupants of motor vehicles in the event of a frontal impact
- Federal Motor Vehicle Safety Standard (FMVSS) No. 208 (1998), Occupant Crash Protection
- Ming-Pei L, Chih-Min C, Cho-Hsuan T, Chia-Hui T, Chun-Te L (2014) Usage of the LSTC\_NCAC hybrid III 50th dummy in frontal occupant simulation. In: 13th international LS-DYNA users conference, Session: Occupant Safety
- Muhammad AH (2002) Comparison of structural damage and occupant injuries corresponding to a vehicle collision onto a pole versus a flat barrier. Bachelor of Engineering, NED University of Engineering and Technology, Karachi, Pakistan
- Pradeep M, Chung-Kyu P, Dhafer M, Cing-Dao K (2010) LSTC/NCAC dummy model development. In: 11th international LS-DYNA users conference, Session: Occupant Safety
- Salwani MS, Sahari BB, Ali A, Nuraini AA (2014) The effect of automotive side member filling on car frontal impact performance. *J Mech Eng Sci (JMES)* 6:873–880. ISSN (Print): 2289-4659; e-ISSN: 2231-8380

- Stahlschmidt S, Gromer A, D'Souza R, Franz U (2014) Update in dummy model enhancements and effective pre-processing. In: 13th international LS-DYNA users conference, Session: Occupant Safety
- Takeo U, Yasuhito T, Toshikazu N (2012) Applications of occupant safety simulation using MADYMO, vol 58, No. 165, Komatsu Technical Report

# Theoretical and Experimental Research on the Torque Variation of the Body Passing Through Landmarks

Dumitru Neagoe, Dumitru Bolcu, Loreta Simniceanu and Mario Trotea

**Abstract** This paper presents analytical expressions of the vertical reactions of the car wheels. These mathematical expressions take into account the inertia forces which are expressed by two main components of acceleration of the reference system chosen. The vertical reactions of the wheels and the torque acting on the body are determined by analytical and experimental methods in case of movement among the landmarks when the vehicle speed is 25 km/h. Theoretical results are compared with data obtained from experimental tests. Approximation values of the two data sets validates the theoretical model adopted.

**Keywords** Body · Torque variation · Landmarks passing

## Introduction

In the moving vehicle the forces appear in areas of tread contact, that are generally variable in time and which are generated by:

- Inertia forces due to movements that are not straight;
- Inertia forces generated by speed changes;
- The additional friction forces during braking;
- Defects of the runway;

---

D. Neagoe (✉) · D. Bolcu · L. Simniceanu · M. Trotea  
Faculty of Mechanics, University of Craiova, Calea Bucuresti Nr. 107, Craiova, Romania  
e-mail: neagoe\_dumitru@yahoo.com

D. Bolcu  
e-mail: dbolcu@yahoo.com

L. Simniceanu  
e-mail: lsimniceanu@yahoo.com

M. Trotea  
e-mail: mtrotea@yahoo.com

- External forces generated by atmospheric factors;
- Forces generated by uneven loading of the vehicle.

That forces are not symmetrical leads to the torque appears who subjected the body to torsion (produces a torque on the body). This leads to the deformation body and the additional deformations acting on it. In addition, because of frequent occurrence of this torque, for some of body parts the fatigue phenomena occur.

## Theoretical Considerations

If the vehicle is moving on rectilinear trajectories the forces of inertia occur leading to a variable distribution of interaction forces between the wheels and tread.

In Mitschke (1990) are presented the vertical reactions of the wheels. The customization is obtained by considered only the inertia forces:

$$\begin{aligned}
 F_1 &= \frac{bmg}{2(a+b)} - \frac{bhm}{e(a+b)}a_y - \frac{mh'}{2(a+b)}a_x \\
 F_2 &= \frac{bmg}{2(a+b)} + \frac{bhm}{e(a+b)}a_y - \frac{mh}{2(a+b)}a_x \\
 F_3 &= \frac{bmg}{2(a+b)} - \frac{bhm}{e(a+b)}a_y + \frac{mh}{2(a+b)}a_x \\
 F_4 &= \frac{bmg}{2(a+b)} + \frac{bhm}{e(a+b)}a_y + \frac{mh'}{2(a+b)}a_x
 \end{aligned} \tag{1}$$

where:

- $m$  is the vehicle mass;
- $h$  is the height of mass center of the vehicle;
- $e$  is the track;
- $a$  is the distance between the mass center and the front axle;
- $B$  is the distance from the center of mass to rear axle;
- $a_x$  is the longitudinal acceleration;
- $a_y$  is the transversal acceleration.

Vehicle reference system was chosen with the origin in its center of mass, horizontal  $Ox$  axis in the longitudinal plane, the horizontal  $Oy$  axis in the transverse plane and  $Oz$  axis vertical. With this reference system chosen, acceleration components are (if the vehicle is moving with constant speed):

$$\begin{aligned}
 a_x &= \frac{-v_0^2 \sin \gamma}{\sqrt{f'^2(\theta) + g'^2(\theta)}} \left[ \text{arctg} \left( \frac{g'(\theta)}{f'(\theta)} \right) \right]' \\
 a_y &= \frac{v_0^2 \cos \gamma}{\sqrt{f'^2(\theta) + g'^2(\theta)}} \left[ \text{arctg} \left( \frac{g'(\theta)}{f'(\theta)} \right) \right]'
 \end{aligned} \tag{2}$$

where:

- $f(0)$  and  $g(0)$  are functions that give parameterization trajectory described by the center of mass of the vehicle;
- $v_0$  is the velocity of mass center;
- $\gamma$  is the angle between the speed of the center of mass of the vehicle and its longitudinal plane.

The  $\gamma$  angle is the solution of the differential equation:

$$\frac{d\gamma}{d\theta} + \frac{1}{b} \sqrt{f'^2(\theta) + g'^2(\theta)} \cdot \sin \gamma = \left[ \operatorname{arctg} \left( \frac{g' \cdot (\theta)}{f' \cdot (\theta)} \right) \right]' \tag{3}$$

Because the vertical reactions are not equal for front and rear axle, the next torque will appear:

- for the front axle:

$$M_f = \frac{e}{2} (F_1 - F_2) \tag{4}$$

- for the rear axle:

$$M_t = \frac{e}{2} (F_3 - F_4) \tag{5}$$

In this way over the body acts a torque:

$$M_t = M_f - M_S \tag{6}$$

This torque is proportional to vehicle mass, with height of mass center and with the transversal acceleration. The body twisting can be highlighted very well in moving through landmarks because the vertical reactions have a large variation around steady values. Moving among landmarks can be treated as a sinusoidal trajectory with the next parametric equations:

$$\begin{aligned} f(\theta) &= \theta = vt \\ g(\theta) &= A \sin \frac{\pi\theta}{S} = A \sin \frac{\pi vt}{S} \end{aligned} \tag{7}$$

where:

- $v$  is the vehicle's speed on the axis milestone direction;
- $t$  is time;
- $S$  is the distance between two landmarks (or the distance between two successive points of intersection between the trajectory and the landmarks line);
- $A$  is the amplitude of movement.



In Figs. 1, 2, 3 and 4 are shown the vertical displacements. Those vertical displacements are calculated using the next relationships:

$$D_1 = \frac{1}{k_f} \left( F_1 - \frac{bmg}{2(a+b)} \right)$$

$$D_2 = \frac{1}{k_f} \left( F_2 - \frac{bmg}{2(a+b)} \right)$$

$$D_3 = \frac{1}{k_f} \left( F_3 - \frac{amg}{2(a+b)} \right)$$

$$D_4 = \frac{1}{k_f} \left( F_4 - \frac{amg}{2(a+b)} \right)$$

where:

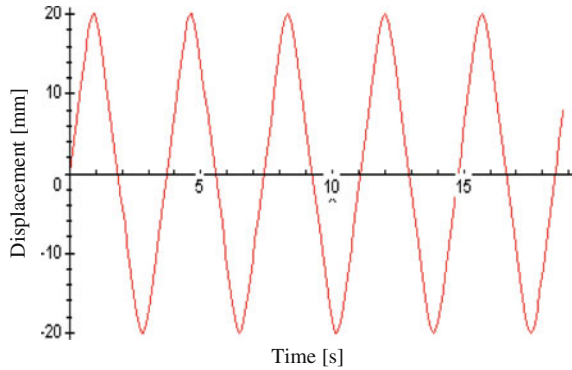
$k_f$  is the elastic constant for the front suspension;

$k_s$  is the elastic constant for the rear suspension.

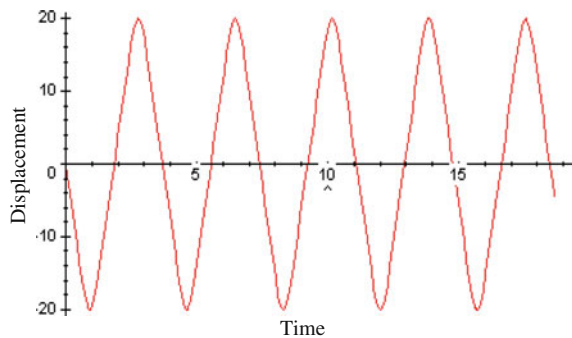
Graphs were made for a car with the next characteristics:  $m = 1440$  kg;  $a = 1233$  mm;  $b = 1337$  mm;  $e = 1464$  mm. Were considered:  $S = 10$  mm;  $A = 2.5$  mm and  $v = 25$  km/h.

In Fig. 5 is presented the variation of body torque.

**Fig. 1** The vertical displacement for the front right wheel



**Fig. 2** The vertical displacement for the front left wheel



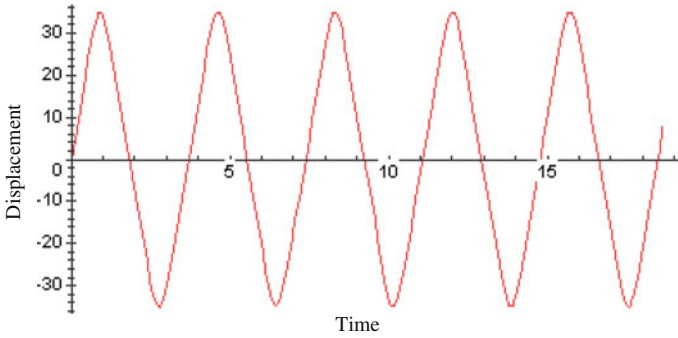


**Fig. 3** The vertical displacement the rear right wheel

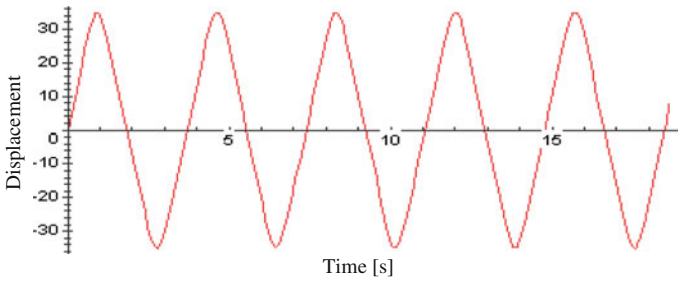


**Fig. 4** The vertical displacement the rear left wheel

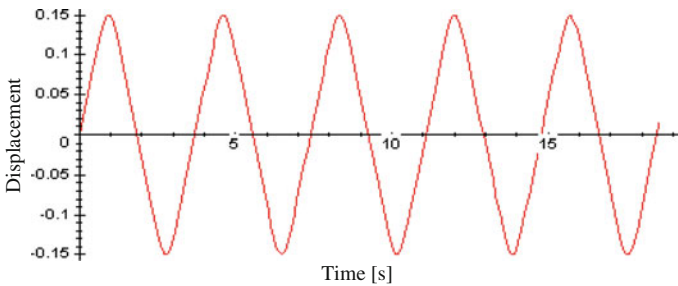


**Fig. 5** The variation of vehicle body torque

## Experimental Verifications

Experimental tests were done on a road with landmarks (travels slalom). This route has the plan shape and dimensional data presented in Fig. 6 and photo in Fig. 7.

As you can see this road consists of eight landmarks placed collinear with the axis of the runway width of 10 cm,  $S = 10$  m distance from each other (for passenger cars with a wheelbase less than 2.7 m).

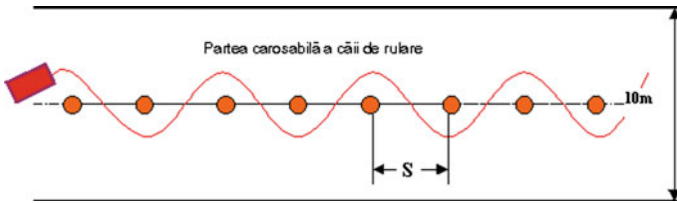


Fig. 6 Plan shape and dimensional data

Fig. 7 Road with landmarks (travels slalom)

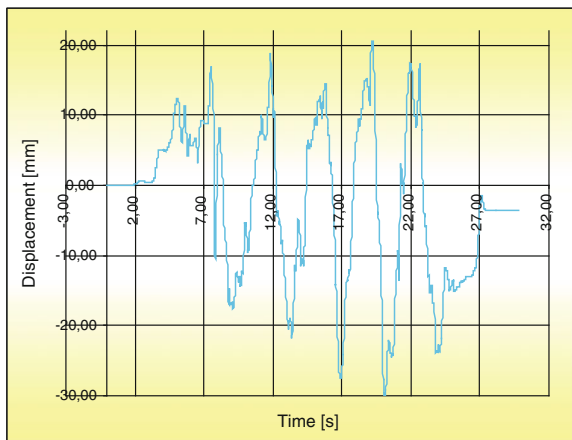


Vehicle moving on a sinusoidal trajectory enables the dynamic cornering ability. During the experiences the car is passing through landmarks, as closed as possible, with constant speed (25 km/h).

In Figs. 8, 9, 10 and 11 are presented the vertical displacements at the four wheels.

In Fig. 12 the variation of body torque is presented.

Fig. 8 The vertical displacement for the front right wheel landmarks passing, 25 Km/h



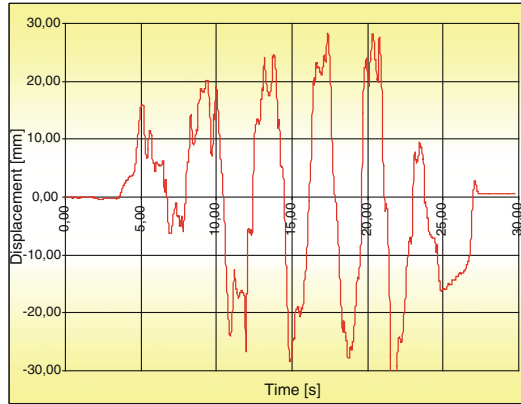


Fig. 9 The vertical displacement for the front left wheel landmarks passing, 25 Km/h

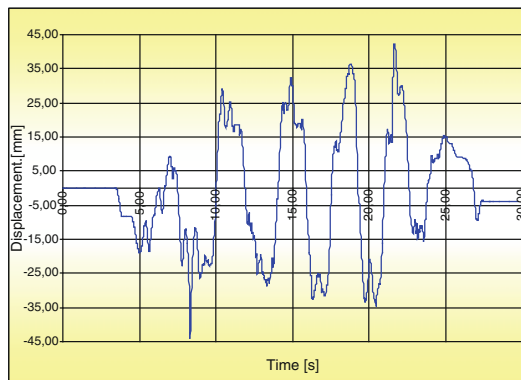


Fig. 10 The vertical displacement for the rear right wheel landmarks passing, 25 Km/h

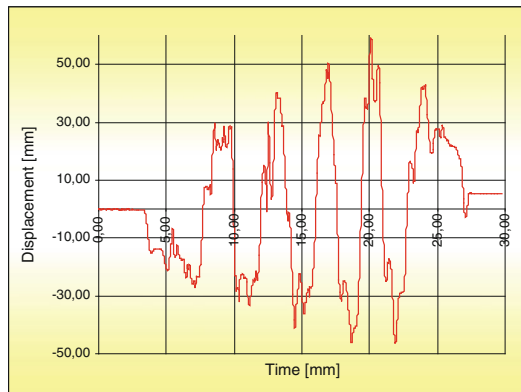
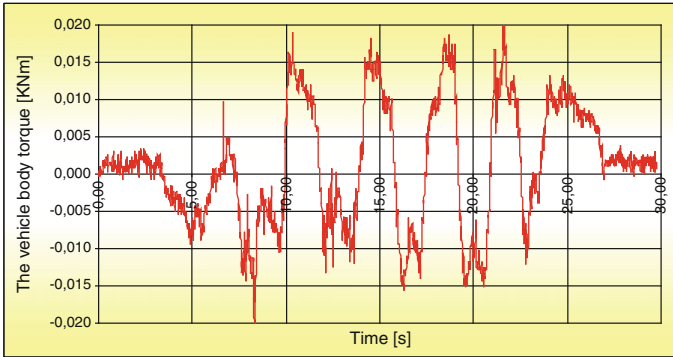


Fig. 11 The vertical displacement for the rear left wheel landmarks passing, 25 Km/h



**Fig. 12** The variation of vehicle body torque landmarks passing, 25 Km/h

## Conclusions

The body torque is increases proportionally to the square travel speed of the car. The size of route also influences the body torque. This is proportional increasing with  $\left(\frac{\Delta}{S}\right)^{0.5}$ .

## Reference

Mitschke M (1990) Dynamik de Kraftfahrzeug. Schwingungen. Springer, Heidelberg, Berlin

# The Simulation of the Vehicle Motion Based on Generalized Mathematical Model of Vehicle Motion

Loreta Simniceanu, Victor Otat, Trotea Mario and Mihaela Bogdan

**Abstract** The paper presents a numerical simulation of the motion of a car based on a mathematical model that takes into account the lateral and longitudinal forces from the contact stain, forces given by suspension system, aero-dynamical force and weight force. In the paper is also presented the mechanical model for a vehicle upon which it was built a mathematical model. Considering the mechanical model and the mathematical model vehicle dynamics numerical simulations were made using the computing environment Matlab. Numerical simulations presented in this paper are obtained at relatively constant speeds of the car, taking into consideration a sinusoidal variation of the steering angle of the wheel: the variation of steering angle was with amplitude equal to  $5^\circ$  and period equal to 3 s. The results refers to the linear and angular movement and velocity, linear and angular accelerations, deformations of the tires, lateral forces.

**Keywords** Automotive moving · Mathematical model · Numerical simulation

## The Vehicle Motion Mathematical Model

The vehicle motion equations are obtained by application of the following two theorems: the theorem of impulse derivative and the theorem of kinetic moment derivative for an vehicle considered as a rigid body.

---

L. Simniceanu (✉) · V. Otat · T. Mario · M. Bogdan  
Faculty of Mechanics, Calea Bucuresti Nr. 107, Craiova, Romania  
e-mail: lsimniceanu@yahoo.com

V. Otat  
e-mail: otatvictor@yahoo.com

T. Mario  
e-mail: mtrotea@yahoo.com

M. Bogdan  
e-mail: bogdan.mihaela@hotmail.com

These equations are particularized for studied cases. The forces which act on automotive are presented in the Fig. 1.

It is considered two reference frames:

- one named proper frame associated to rigid body which replace vehicle suspended mass, having the origin  $O$  into its center of mass and  $Ox$  and  $Oy$  axes make the plane of advancement principal direction. The  $Oz$  axe is chosen perpendicular to two mentioned axes;
- other fixed frame named  $O_1X_1Y_1Z_1$  presented in Fig. 1.

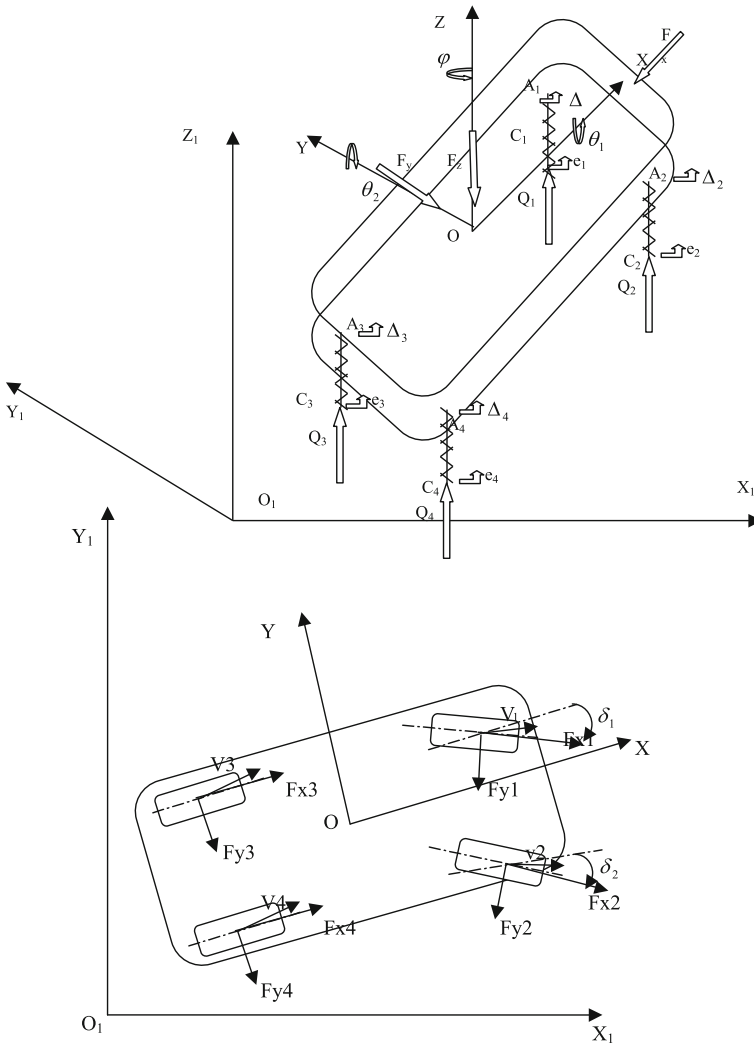


**Fig. 1** Forces on vehicle

Also, it is noted with:

- $A_1, A_2, A_3, A_4$ , the contact points of joints with suspended mass;
- $C_1, C_2, C_3, C_4$  the centers of the contact areas between tires and road;
- $F_{x1}, F_{x2}, F_{x3}, F_{x4}$  longitudinal tangential forces for each wheel;
- $F_{y1}, F_{y2}, F_{y3}, F_{y4}$  lateral tangential forces for each wheel;

Named  $x_{A1,A2,A3,A4}; y_{A1,A2,A3,A4}; z_{A1,A2,A3,A4}$  the coordinates of points  $A_1, A_2, A_3, A_4$  above chosen proper frame.

For automotive it is considered the following freedom degrees:

- $x$ , describes the motion on longitudinal axis;
- $y$ , describes the motion on transversal axis;
- $u$ , describes the motion on vertical axis;
- $\theta_1$ , describes the rotative motion of suspended mass around Ox axis;
- $\theta_2$ , describes the rotative motion of suspended mass around Oy axis;
- $\varphi$ , describes the rotative motion of suspended mass around Oz axis.

The system of equations which results by taking into account of these forces has a following matriceal form (Simniceanu 2005):

$$\dot{X} = f(X) \tag{1}$$

where

$$X = (y, u, v_x, v_y, v_z, \theta_1, \theta_2, \varphi, \omega_x, \omega_y, \omega_z, \delta_s)^t$$

Also, it is used the following notations:

- $v_x, v_y, v_z$ —the velocity projections on the axes of the considered frame;
- $\omega_x, \omega_y, \omega_z$ —the angular velocity projections on the axes of the considered frame;

In the system of Eq. (1) are neglected centrifugal moments of inertia. The centrifugal moments of inertia  $J_{xy}$  and  $J_{xz}$  are zero because of vehicle symmetry, but, generally,  $J_{xz}$  are different to zero. However, by comparison between experimental results and results of numerical simulation, it is observed that effect of terms which comprises is too small so that they can be neglected even in an enough precisely study.

Because the velocity of the motion is kept approximatively constant during numerical simulations, the only parameter which influences the forces from contact area is tires slip angle. It is considered that the tires slip angle influences only lateral forces after following law:

$$F_{yk} = c_{k1} \cdot \alpha_k - c_{k3} \cdot \alpha_k^3, \quad k = 1, 2, 3, 4 \tag{2}$$

$c_{k1}, c_{k3}$  (N/rad)—cornering stiffness coefficients of each wheel which characterize the tire slip deformation;

$\alpha$ —tire slip angle.

This dependence is valuable until the values of angles to 7–10°.



## The Numerical Simulation Scheme

The numerical simulation is realized in MATLAB and it is obtained the scheme from Fig. 2.

The calculation blocks from Fig. 2 implement the (1) equations.

These blocks are not presented in this paper. The simulation method used is Dormand/Prince with fixed step equal to  $10^{-3}$  s. The simulation time necessary to a motion during 10 s was about 8 s.

## The Motion Cases Studied and Results

It is studied three vehicle motion cases. In all cases, the x velocity, named  $v_x$ , is kept approximatively constant to 30 km/h. The rolling resistance of rear wheels (forces  $F_{3x}$  and  $F_{4x}$ ) was resulted to 60.15 N on each wheel. In the first case, the variation of steering angle was sinusoidal with amplitude equal to  $5^\circ$  and period equal to 3 s (Fig. 3a). In the second case, it is used an linear signal with slope equal to 6.67 degrees/second during 1.5 s followed to a constant signal at  $10^\circ$  (Fig. 3a).

The parameters of studied vehicle are the following:  $m = 1442$  kg,  $J_x = 340$  kg m<sup>2</sup>,  $J_y = 2002$  kg m<sup>2</sup>,  $J_z = 2644$  kg m<sup>2</sup>,  $e = 1.46$  m,  $a = 1.135$  m,  $b = 1.435$  m,  $u_0 = 0.585$  m,  $Q_{s1} = Q_{s2} = 3948$  N,  $Q_{s3} = Q_{s4} = 3124$  N,  $k_1 = k_2 = 19,072$  N/m,  $k_3 = k_4 = 23,502$  N/m,  $f_1 = f_2 = 576.92$  Ns/m,  $f_3 = f_4 = 692.3$  Ns/m,  $F_{x3} = F_{x4} = 60.15$  N,  $c_1 = 28,650$  N/rad,  $c_3 = 110,000$  N/rad,  $v_{x0} = 30$  km/h, where:

$m$	is the mass of vehicle;
$J_x, J_y, J_z$	are the axial moments of inertia;
$e$	is the gauge;
$a, b$	are the coordinates of the center of mass;
$u_0$	is the initial coordinate on Oz axis of the center of mass;
$Q_{s1}, Q_{s2}, Q_{s3}, Q_{s4}$	are the statically vertical reactions of each wheel;
$k_1, k_2, k_3, k_4$	are the elastic constants of the suspension;
$f_1, f_2, f_3, f_4$	are the damping coefficients of the suspension

It is considered the expression for aerodynamic forces (Oțăt et al. 2005):

$$F = 0.5 \cdot \rho \cdot c_x \cdot A \cdot v^2, \quad (3)$$

where

$$\rho = 1.225 \text{ kg/m}^3, \quad A = 2\text{m}^2, \quad C_x = 0.35.$$

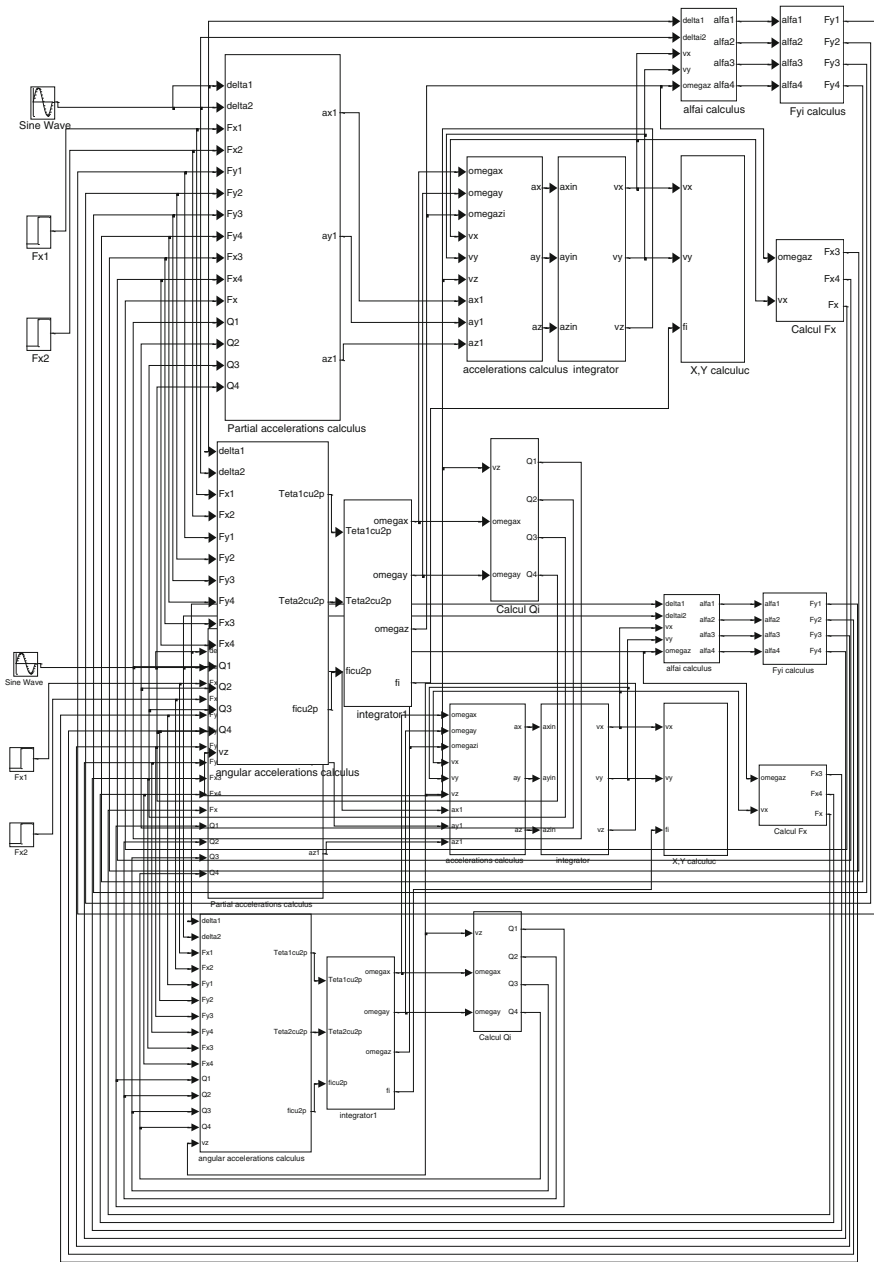
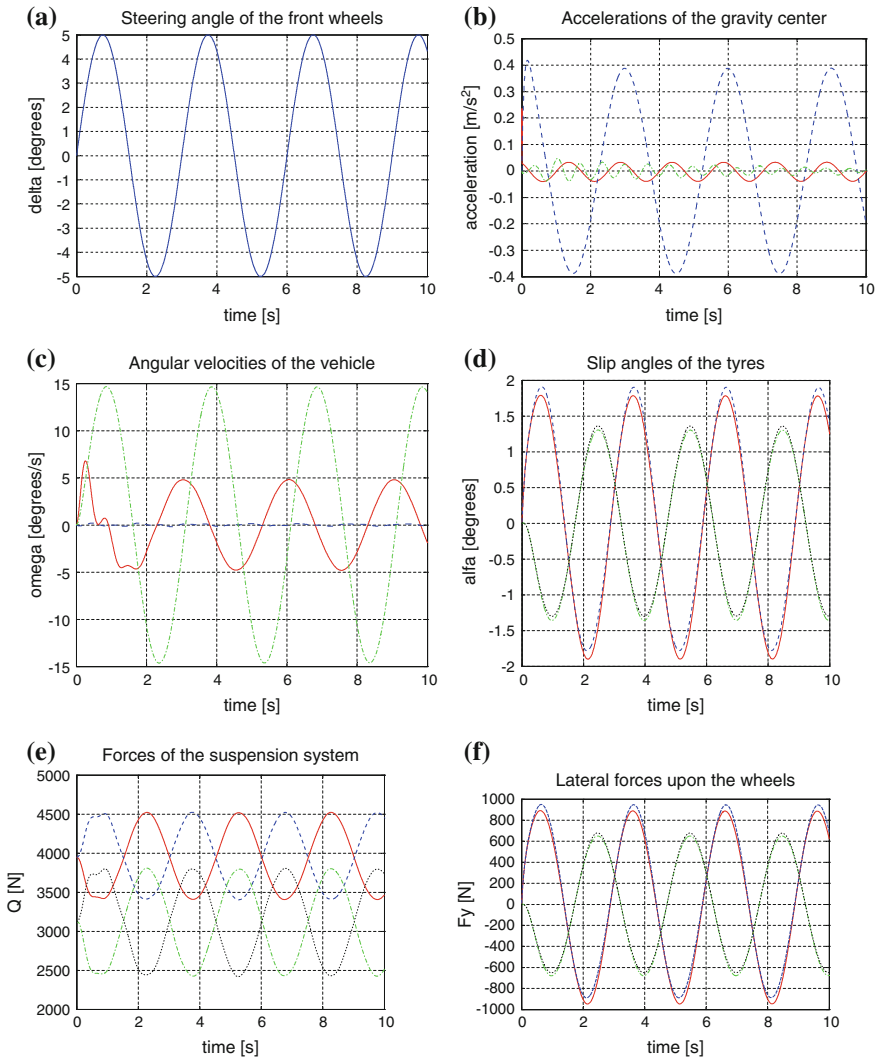


Fig. 2 The numerical simulation scheme



**Fig. 3** The results obtained in the first simulation case

In Fig. 3 are the results from the first case. In the graphs that represent the linear or angular speeds or displacements, with continuous red line are represented the sizes on the x-axis, with blue are represented the sizes on the y-axis and the green dot line are represented the sizes on the z-axis.

In the case of graphics that represent characteristic values of the four wheels, the solid line red are the sizes of wheel 1 according to Fig. 3d–f, with a blue discontinue line are represented the sizes for the wheel 2, with a dotted green line are represented the sizes for the wheel 3 and with a dotted black line are represented the sizes

for the wheel 4. The same significance of the types of line are kept for the other cases results.

In the first case, it is remarked the fact that the accelerations along z axis are small resulting the very small displacements of mass center on this axis. The y axis accelerations have the biggest values with amplitudes until  $0.37 \text{ m/s}^2$ , between these are comprised the x axis accelerations with values until  $0.03 \text{ m/s}^2$ . The damping presence and automotive inertia make to appear the phase difference between these accelerations.

About the vehicle's angles, it is remarked a neglected pitching angle, but the rolling angle has the amplitudes about  $2.3^\circ$ . The slip angles and lateral forces upon wheels have the same aspect.

It is appeared a phase difference between lateral forces variations on front wheels and rear wheels, but the forces on the wheels from interior turning are smaller than those on the wheels from exterior. The values of  $1.7^\circ$  of tires slip angles and 900 N of lateral forces are close to the values obtained in the case of the experimental studies.

Because the pitching angle is neglected, the forces variations given by suspension system follows the steering angle. The trajectory obtained is sinusoidal like a move between poles, but with smaller amplitude.

## Conclusions

For this motion case previous studied, it comes out that these theoretical results are in concordance to the values obtained by testing, not only as form, but also as values. The data resulted by the numerical simulation validate the mathematical model of vehicle motion which allows this model to be used for numerical simulation and analysis of other cases of movement of vehicles.

## References

- Oțăt V et al (2005) *Dinamica autovehiculelor*. Editura Universitaria, Craiova  
Simniceanu L (2005) *Contribuții la aplicarea teoriei sistemelor dinamice in dinamica autovehiculelor*. Universitatea Politehnica Bucuresti, Bucuresti

# Research Regarding Night-Time Pedestrian Visibility

Bogdan Tolea, Daniel Trusca and Csaba Antonya

**Abstract** The main objective of the paper is to determine the night-time visibility of a pedestrian on public road, using clothing articles with different colors. In order to achieve the main objective, luminance measurements were made, using different colored clothing articles at various distances from the vehicle. During the testing procedures, photos were taken, which were processed with specialized software in order to determine the visibility of the pedestrian at different distances. Experimental data together with the data obtained by image processing can lead to a clear conclusion regarding the night-time pedestrian visibility and the influence of the clothing articles color.

**Keywords** Data · Luminance · Pedestrian · Vehicle · Visibility

## Introduction

Pedestrians are the road users which are the most vulnerable in case of an accident. Proper visibility of pedestrian reduces the chance of being involved in a vehicle collision. Human visual system has to accommodate from daylight sensitivity to darkness sensitivity. In order to drive during nighttime, the detection and perception of the objects on the road is critical (Hankey et al. 2005).

To travel safely in darkness, the pedestrians have to make sure that the drivers can see them relatively far ahead. For the task of driving in the dark, the detectability of objects on the roadway becomes critical. The distance to the possible obstacle or pedestrian must be long enough to allow the time for the driver to avoid an accident by pressing the brake or steering.

It was researched that the most frequent pedestrian accidents occur during night (Owens and Sivak 1996). It was reported that approximately 20 % of the drivers involved in a vehicle-pedestrian accident, during nighttime, did not realized the

---

B. Tolea (✉) · D. Trusca · C. Antonya  
University “Transilvania” of Brasov, Brasov, Romania

presence of the pedestrian (Hazlett and Allen 1968). An important parameter that influences visibility during night is the headlamps glare from the oncoming vehicle. This parameter decreases the pedestrian visibility during nighttime (Borzendowski et al. 2015).

In a recent study conducted by Wood et al. (2012), the participants had to drive and detect pedestrians in three different testing conditions: hazy vision, normal vision and simulated cataracts. In some of the tests the headlight glare was present, while in some of them a lighting source was located near the pedestrian. After completing tests, was reported that the response time decreased in the presence of glare, leading to the conclusion that the pedestrians are difficult to see at night when glare occurs due to the oncoming traffic headlamps (Wood et al. 2012).

Another important parameter that may influence the visibility of a pedestrian is the clothing color. Some of the colors are more visible, while others are difficult to see. According to Alred et al. (2015) was not established the evidence of safety benefit of wearing high-visibility clothing (Aldred and Woodcock 2015).

## Methodology

To achieve the proposed objective, a vehicle equipped with halogen headlights was used, positioned at different distances from a static pedestrian.

For the measurements were used both low beam and high beam of the vehicle in order to measure the luminance reflected on the pedestrian. The testing procedure started with positioning the pedestrian at 0.5 m of the verge of the road, while the vehicle was positioned at 10 m away of the pedestrian on the right lane. In order to measure the distance accurately, a laser measuring device was used. When the vehicle and the pedestrian were positioned at the desired location, the value of the luminance was measured on different type of shirts and at different lighting conditions (high beam, low beam) from the driver seat. The next step was to take pictures with a calibrated. This procedure was repeated at steps of 10 m, until the distance of 100 m was reached between the car and the pedestrian (Fig. 1).

By definition, luminance is the light intensity transmitted from a surface per unit area in a given direction.<sup>1</sup>

For the experiment different clothing colors for the shirts of the pedestrian were used in order to determine its visibility. The tested colors for the shirts were red, blue, yellow and a reflecting jacket.

Once the testing procedure was completed, the photos were processed in photogrammetry software, PC-Rect. This software is able to calculate the luminance values on each pixel of the picture using Adrian's diagram. The points chosen for evaluation were positioned in the lower part of the t-shirts, respectively of the reflecting jacket (Fig. 2).

---

<sup>1</sup><http://www.oxforddictionaries.com/definition/english/luminance>. Accessed in 21 July 2015.



Fig. 1 Conducting of the experiment

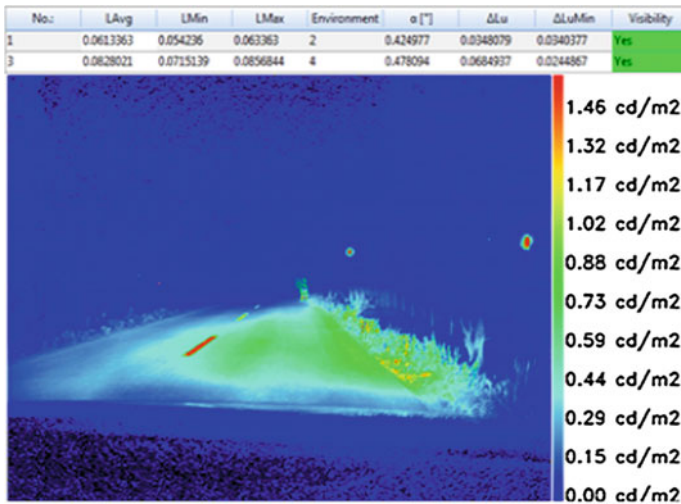


Fig. 2 Example of photo processing in PC-Rect

## Results

In Fig. 3 is shown the luminance diagram for the high beam, respectively the low beam, obtained by measurement.

The peak value of the luminance for the high beam case is obtained by the reflecting jacket, having a value of  $3.3 \text{ cd/m}^2$ , at a distance of 10 m of the pedestrian. This value is linearly decreasing until the distance of 50 m is reached. From this distance to the distance of 70 m, the luminance value remains almost constant. The interval 70-90 presents a linear decreasing of the luminance, until the minimum value of  $1.3 \text{ cd/m}^2$  is achieved.

For the low beam, the peak value of the luminance in the case of reflecting jacket is lower, obtaining a value of  $2.2 \text{ cd/m}^2$ , at a distance of 10 m. The luminance value decreases with the increasing of the distance between the vehicle and the pedestrian,

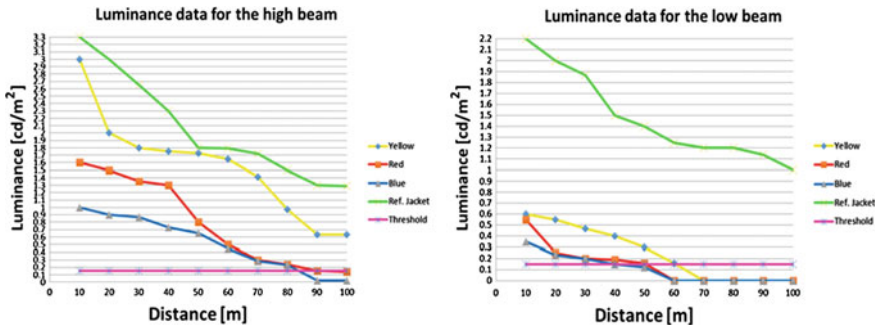


Fig. 3 Luminance diagram obtained after measurements

reaching a minimum value of 1. In both cases the reflecting jacket was visible on all distances, representing the best option of clothing article during night-time.

In the first case, the yellow t-shirt was visible in all test conditions, while in the second case was visible only until the distance of 60 m was reached.

For the first case, the red color was visible at a distance of 90 m, while for the second case the maximum distance from where the color was visible was 50 m.

The less visible color was the blue one. In the first case was visible at a distance of 80 m, whereas for the second case, the blue color was no longer visible after 40 m.

In Fig. 4 are presented two luminance diagrams for the high beam respectively low beam, obtained after image processing.

The visibility of the colors used in the test was similar with the one obtained after data collection, but the values of the luminance was slightly different. One of the reasons of the differences is due to the position of the points chosen for analysis in the software. When these points are moved, the luminance value may vary. In order to obtain accurate values of the luminance, we tried to use the same points on the analysis surface, with the ones used in the measurement process.

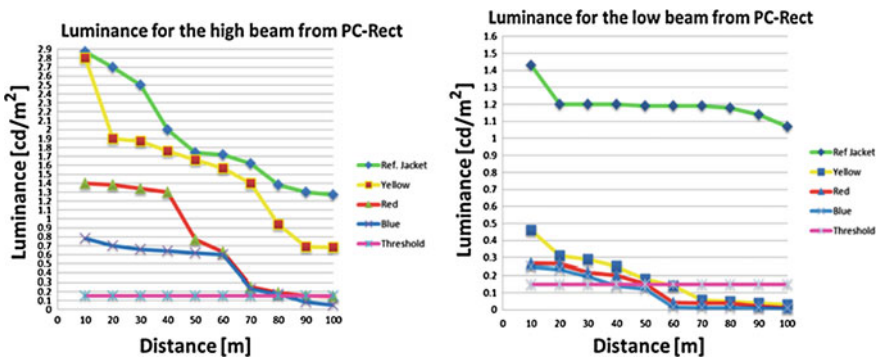


Fig. 4 Luminance diagrams for low beam and high beam obtained from PC-Rect



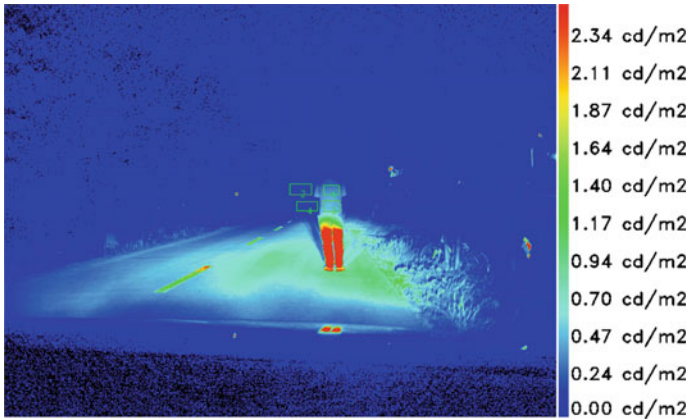


Fig. 5 Analysis surface in PC-Rect

The “threshold” line represents the visibility threshold, obtained in PC-Rect.

The squares number 1 and 3 presented in Fig. 5 represent the analyzed surface on the pedestrian, whereas the squares number 2 and 4 represent the associated background area. PC-Rect is able to measure not only the contrast between the associated background color and the analysis surface but also measures accurate values of the luminance.

PC-Rect is calculating luminance after Adrian’s Diagram and shows the visibility in a table (Fig. 6). In the Fig. 6, the columns represent:

- No.—number of rectangles used as analysis surface
- LAvg—average luminance
- LMin, LMax—minimum and maximum value of the luminance

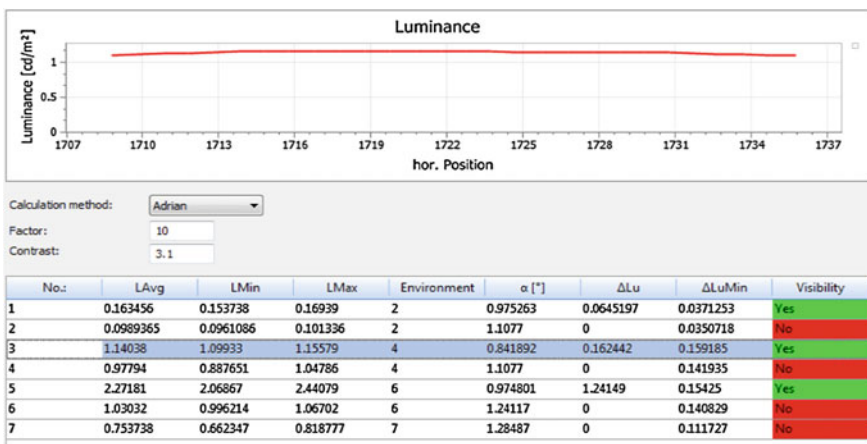


Fig. 6 Luminance diagram obtained in PC-Rect

- $\Delta Lu$ —difference between  $L_{avg}$  of the analysed area and  $L_{avg}$  of the background area
- $\Delta Lu_{Min}$ —luminance threshold difference
- Visibility: exists if  $\Delta Lu > \Delta Lu_{Min}$

Visibility level (VL) was introduced by Adrian, and represents a measure of the capability to detect objects as pedestrians, vehicles etc., depending on the contrast between the background and the object (Adrian and Jobanputra 2005).

$$VL = \Delta Lu / \Delta Lu_{Min} \quad (1)$$

$$\Delta L = |L_T - L_B| \quad (2)$$

$$L_T = (E_V / \pi) \times \rho \quad (3)$$

$$L_B = (E / \pi) \times \rho \quad (4)$$

where:

$L_T$  target luminance

$L_B$  background luminance

$E_V$  vertical luminance

$\rho$  surface reflectivity

$E$  illuminance [lux]

The luminance threshold difference ( $\Delta Lu_{Min}$ ) represents the theoretical difference of the luminance, such that observers can detect targets in specific time (Adrian and Jobanputra 2005).

## Limitations

One of the limitations is that during the experiment there was not taken into account the upcoming traffic, which may influence the visibility of a pedestrian (glare effect).

Another limitation is the weight distribution in the vehicle, which can influence the angle of the light cone of the headlights.

The third limitation was the fact that the color of the pedestrian's trousers was neglected.

In the test procedure was used only one type of headlights.

The obtained data is valid only for similar weather conditions.

## Conclusions

The novelty of the paper is introducing the image processing in order to determine pedestrians visibility. The measurements were performed from driver's seat taking into account the position of the driver.

After analyzing theoretical and experimental data presented in the paper is observed that the risk of driving during night-time is influenced to a great extent on the level of visibility. The performance of the human eye is limited in adapting to darkness or the sudden transition from darkness to light, which can influence the visibility of pedestrian, as emerges from this paper.

According to the measurements, reflective vest had the best visibility, for both, short distances respectively long distances compared with other colors.

Without the use of reflective vest, yellow is the most visible color in the hierarchy of colors used in this study, being visible on a distance of 60 m for the low beam test, respectively 100 m for the high beam test.

The blue shirt was the less visible color, being visible only at a distance of 40 m while driving with the low beams respectively a distance of 80 m for the high beams.

## References

- Adrian W, Jobanputra R (2005) Influence of pavement reflectance on lighting for parking lots. Portland Cement Association, Skokie
- Aldred R, Woodcock J (2015) Reframing safety: an analysis of perceptions of cycle safety clothing. *Transp Policy* 42:103–112
- Borzendowski SAW et al (2015) Drivers' judgments of the effect of headlight glare on their ability to see pedestrians at night. *J Saf Res* 53:31–37
- Hankey JM, Blanco M, Gibbons RB, McLaughlin SB, Dingus TA (2005) Enhanced night visibility series, volume I: executive summary. No. FHWA-HRT-04-132
- Hazlett RD, Allen MJ (1968) The ability to see a pedestrian at night: the effects of clothing, reflectorization and driver intoxication. *Am J Optom Arch Am Acad Optom* 45(4):246–258
- Owens DA, Sivak M (1996) Differentiation of visibility and alcohol as contributors to twilight road fatalities. *Hum Factors* 38(4):680–689
- Wood JM, Tyrrell RA, Chaparro A, Marszalek RP, Carberry TP, Chu BS (2012) Even moderate visual impairments degrade drivers' ability to see pedestrians at night. *Invest Ophthalmol Vis Sci* 53(6):2586–2592

# Research Regarding the Effects of Emergency Vehicle Braking upon Its Occupants

Alexandru-Ionut Radu, Daniel-Dragos Trusca, Bogdan-Adrian Tolea and Corneliu Cofaru

**Abstract** The purpose of this study is to determine the effects of emergency vehicle's braking on its occupants, and to determine the possibility of injury using one human test subject and an experimental dummy, in an actual vehicle's braking test at certain speed values, with and without seatbelts.

**Keywords** Brake · Occupant · Dummy · Seatbelt · Acceleration

## Introduction

To better understand the phenomenon of braking the car, the necessary of determining the interconnection between elements of human-vehicle-road system. The relationship between man and vehicle can be described as a link among thinking, analysis and action. The connection between the car and the environment is characterized by the interaction of the road environment and vehicle traffic on that entity integrated into a system action–reaction. Such a vehicle is conditioned by the quality and road functions, the environment and the actions of other road users (Nakamura et al. 2002).

One of the important elements influencing the passenger vehicle's occupant is ergonomics. Vehicle's occupant's comfort is influenced by the shape and design of the vehicle's interior elements that support its position during movement, but also the elements of passive safety and interior elements that can occur in outstanding dynamic braking, cornering, traveling on a bumpy road, collision, rollover, etc.

Along with vehicle ergonomics there are several passive element systems, like the airbags and seat belts, designed to protect the occupants from harmful movement during vehicle's handling. In the case of emergency braking, if the seatbelt is

---

A.-I. Radu (✉) · D.-D. Trusca · B.-A. Tolea · C. Cofaru  
University of "TRANSILVANIA", Brasov, Romania  
e-mail: raduionut\_2008@yahoo.com

not used, the car occupants risk injury by hitting the car interior elements such as dashboard or steering wheel.

Usually when the driver reacts to the oncoming threat on the road, and when the maximum brake force is applied, the vehicle's occupants are unaware of what happens and do not have time to prepare him/herself to the act of braking (tightening the body muscles).

The braking system is a mechanical device which inhibits motion, slowing or stopping a moving object or preventing its motion. Most brakes commonly use friction between two surfaces pressed together to convert the kinetic energy of the moving object into heat, though other methods of energy conversion may be employed. The braking system of a motor vehicle consists of the components shown in Fig. 1 (Nice 2000).

In addition to the normal components, there are two more systems that help the vehicle decelerate: a braking device and the retarder.

The braking device helps to reduce the vehicle's speed to a value desired by the driver or to stop and immobilize it on a level road and on slopes when climbing and descending.

Retarders help to stabilize the vehicle's speed when descending on long hills without using the braking devices, or to stabilize the vehicle. The use of these devices reduces the driver's fatigue and the wear of the friction linings on the service brakes is reduced by 25–30 % (Hogan 1973).

To collect data from the human and dummy occupants, an acquisition equipment was used, PIC DAQ, produced by DSD Austria. This device was a data acquisition platform for recording dynamic data, where accelerations and angular velocities described the movement (vehicle driving performance, braking tests, and vehicle crash tests). The device has three axial acceleration and angular velocity sensors for vehicle measurements and the acquisition time can be up to 300 s at the highest sampling rate per channel (1 kHz), as the channel sampling rate is reduced the acquisition time increases. It also has a storage capacity on storage card for more than 500 brake tests (Steffan 2014).

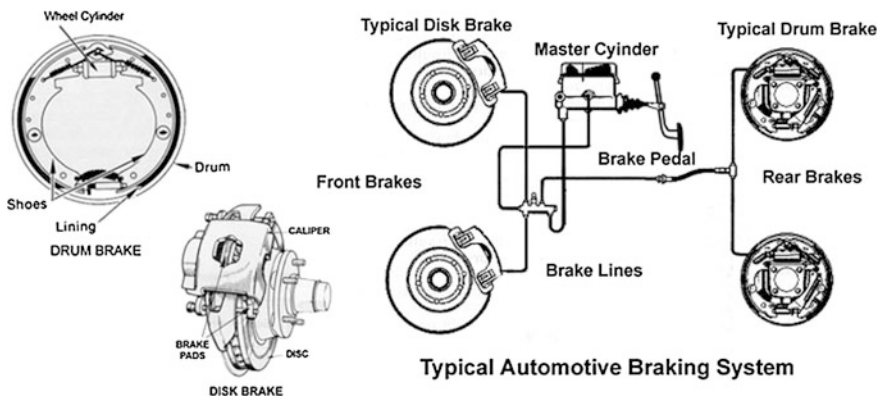


**Fig. 1** Braking system of a motor vehicle

The dummy was equipped with a newer, smaller version of the PIC DAQ system, called DAQ5, provided with 15 channels instead of 8 channels compared to the older version DAQ3.

The vehicle was also equipped with GPS acquisition systems, called the GARMIN 18× USB and a ASUS EEE Laptop and software to collect data regarding the speed, position and acceleration of the vehicle.

A Nikon Coolpix L22 camera was also used to capture images of the movement of the occupants during the braking phase.

The vehicle used was a 2012 VW Jetta, 1.6 TDI, equipped with ventilated brake disks on the front axle, non-ventilated disks on the rear axle, ABS and ESP electronic systems, and 6.5 J R16 rim size, with Pirrelli P7 205/55 R16 summer tires with minimal wear level, standard suspension, independent McPherson strut with stabilizer spring on the front axle and on the rear axle independent suspension with spring multi-point stabilizer.

• **Objectives**

The main objectives are:

- To determine the acceleration values on the head and torso of the occupant in the case of emergency vehicle braking;
- To determine the difference between using and not using the seatbelt by the occupants;
- To determine the biofidelity of the dummy occupant by comparison of the movement with the human occupant in the same test;

• **Methodology**

The purpose of the experiment was to determine the acceleration values recorded on the occupant’s head in case of a vehicle’s emergency braking situation, with and without seatbelts attached, and also to analyze the difference in movement and acceleration between a human occupant and a dummy occupant.

The test involved mounting data acquisition systems on the human and dummy occupants, placing them in a vehicle and braking the vehicle at a certain speed until the vehicle is completely stopped. Also a GPS system was mounted on the vehicle to record the vehicle’s speed and direction.

Two test scenarios were conducted, involving 4 tests, 2 at 50 km/h with and without seatbelts and 2 at a speed of 70 km/h, with and without seatbelts.

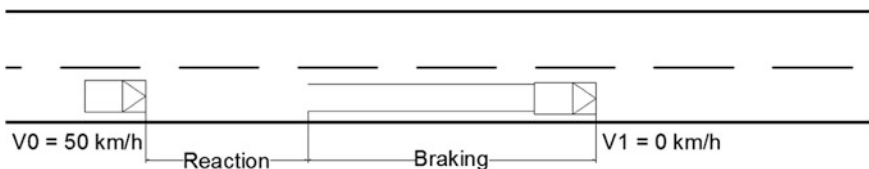


Fig. 2 First test scenario

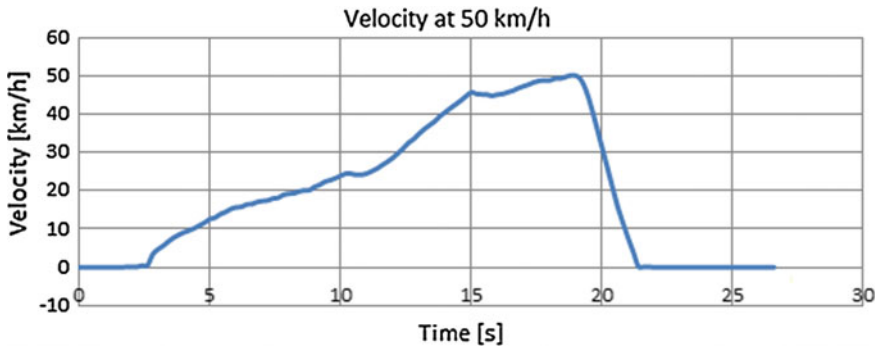


Fig. 3 Second test scenario

**First Test Scenario**

As shown in the figure, the vehicle was accelerated and maintained at the initial speed,  $V_0 = 50 \text{ km/h}$ , with the acceleration of  $a_0 = 0 \text{ m/s}^2$ . At a certain point the vehicle was braked violently until it reaches the final speed  $v_1 = 0 \text{ km/h}$ . There is a time of reaction of the driver, this time was usually  $t_r = 0.8 \text{ s}$  until the actual braking occurred. As a standard feature, the vehicle was equipped with an ABS (Antilock Braking System) (Fig. 2).

In Fig. 3, the vehicle’s velocity from 0 up to 50 km/h and the braking phase, from 50 to 0 km/h is presented.

**Second Test Scenario**

In this figure, the braking was acted from the initial speed of  $V_0 = 70 \text{ km/h}$ , until the vehicle’s speed reaches  $v_1 = 0 \text{ km/h}$  is presented. The reaction time was the same as previously presented,  $t_r = 0.8 \text{ s}$ . The test was made on a dry good quality pavement of the road surface (Fig. 4).

The vehicle’s velocity, from 0 to 70 km/h and the braking phase, from 70 to 0 km/h is presented (Fig. 7).

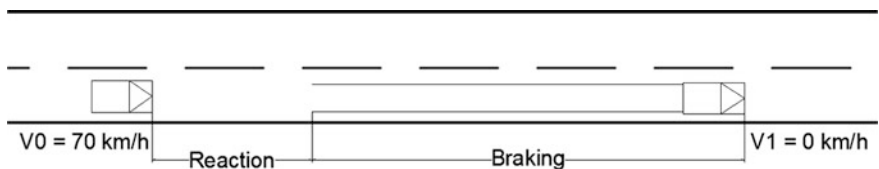


Fig. 4 Velocity graph

## Results

### *First Test Scenario*

In Fig. 5, the head acceleration during the braking phase, of both occupants is presented. The results show that the human has a greater acceleration than the dummy, for the dummy's head and neck has a greater rigidity than the volunteer passenger. During the braking phase the center of gravity shifted forward because of inertia, on the timeline between second 1.5 and 4, and after the vehicle completely stopped, the center of gravity shifted back, this can be observed following the phenomenon between the second 4 and 4.5. In this test the seatbelts were used, and they provided the retention needed to keep the occupant restraint in the seat, so the acceleration on the head was at a low value, in this case the maximum value was 0.15 G's on the human head and 0.1 G's on the dummy.

In Fig. 6, the acceleration during braking without seatbelts is presented. Similar to previous tests, the human has a greater acceleration value, maximum of 2.6 g's and 1.2 for the dummy. The difference in acceleration values was stated when using the seatbelts (Fig. 7).

### *Second Test Scenario*

In Fig. 8 the head acceleration of both occupants, similar to the previous test is presented. The acceleration was greater on the human occupant compared to the dummy, having a maximum value of 0.2 G's, and 0.12 G's on the dummy. After the braking phase when the vehicle stopped the center of gravity shifted back

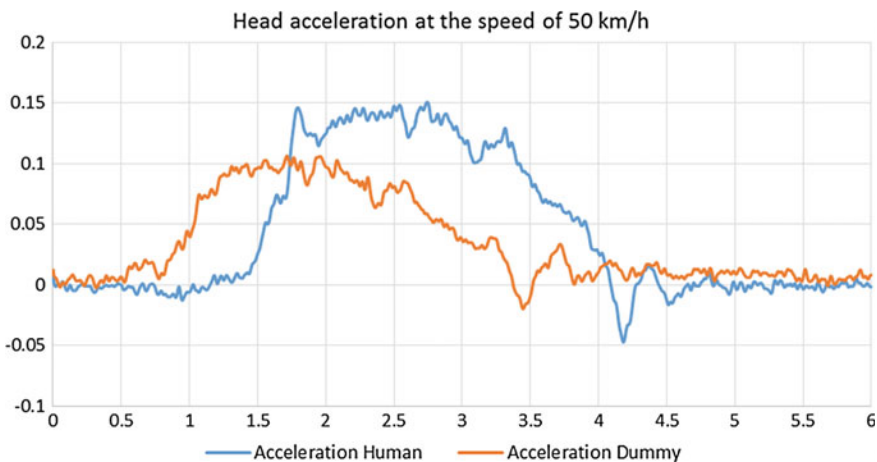


Fig. 5 Head acceleration



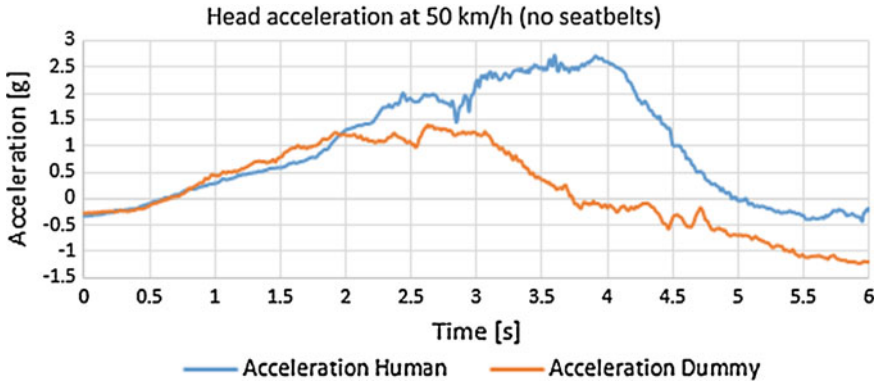


Fig. 6 Head acceleration without seatbelts

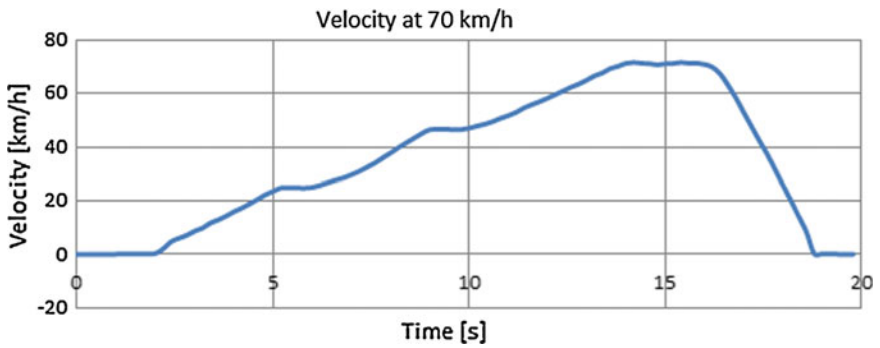


Fig. 7 Vehicle velocity

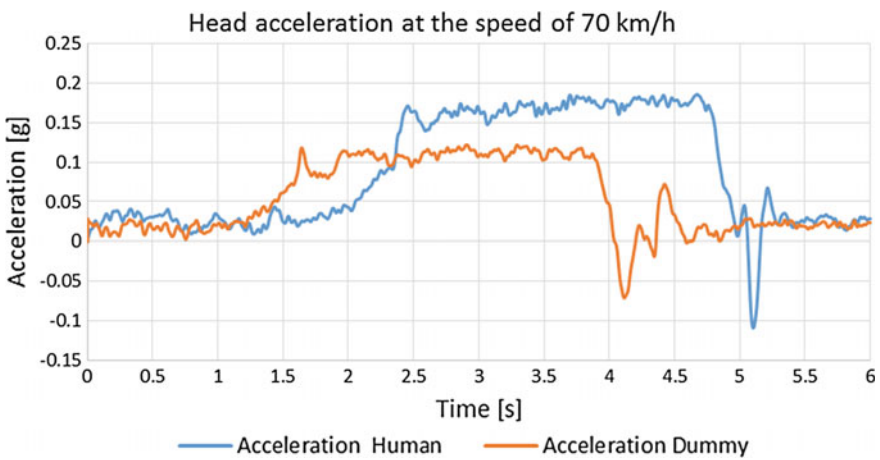


Fig. 8 Head acceleration graph

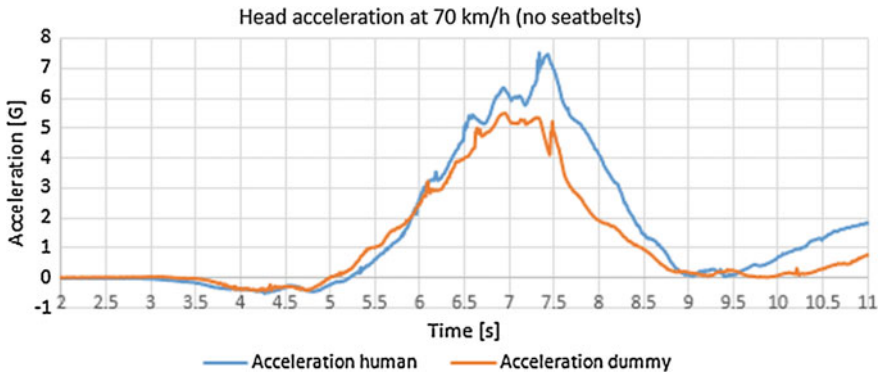


Fig. 9 Head acceleration graph

generating an extra acceleration that could be observed in the timeline between second 5 and 5.5 for the human with the value of 0.1 G’s, and 4 and 4.5 for the dummy having the value of 0.06 G’s. Also, in this case, one can state that this acceleration was higher for the human than for the dummy.

In Fig. 9 the acceleration values of the occupant during the test, without seatbelts is presented. The maximum value of acceleration in this test was 7 G’s for the human occupant and 5 G’s for the dummy, difference made by the rigidity of the dummy’s components.

• **Limits on the proposed study**

- The limits are generated by the accelerometers that cannot be mounted on the center mass of the torso and head;
- Another limit taken into account is the reduced number of tests for the biofidelity of the test dummy requires a large variety of tests;
- The measurements parameters used are for normal driving condition and not applied in a particular crash case.

• **The novelty of the paper**

- The novelty in this paper is represented by the comparison between the human occupants and crash test dummies on a dynamic condition of the same vehicle;
- Another novelty in represented by the testing condition that frequently occur in urban and extra urban traveling condition caused by different traffic conditions.

## Conclusions

The braking tests demonstrate that the restrain systems of the vehicle, the seatbelts, keep the occupants of the vehicle locked in the seats so that that the acceleration values on the head are low, and that the occupants do not hit any parts of the vehicle's interior.

The test shows that there is a major difference between using and not using the seatbelts of the vehicle, the difference in acceleration is about 7 G's, and also the risk of the occupants hitting the inside of the vehicle (the rear passengers have the risk of hitting the front seats). For the occupants are not restrained to the seats, and because of inertia, they tend to continue moving when the vehicle brakes suddenly.

Taking into account the test's results, one can conclude that the biofidelity of the crash test dummy will be similar to the human counterpart's, the difference is made by the rigidity of the body parts, the human has a more flexible neck while the dummy that has a more rigid one.

The results of this test demonstrate how important the seatbelts are to the vehicle's occupants and without using them, sudden braking of a vehicle can endanger them.

## References

- Hogan CM (1973) Analysis of highway noise. *J Water Air Soil Pollut* 2(3):387–392. ISSN 0049-6979
- Nakamura E, Soga M, Sakai A, Otomo A et al (2002) Development of electronically controlled brake system for hybrid vehicle. SAE technical paper 2002-01-0300. doi:10.4271/2002-01-0300
- Nice K (2000) How power brakes work. HowStuffWorks.com <http://auto.howstuffworks.com/auto-parts/brakes/brake-types/power-brake.html>
- Steffan H (2014) "Dr. Steffan Datentechnik Ges.m.b.H. DSD at [http://www.dsd.at/index.php?option=com\\_content&view=article&id=16:picdaq&catid=37&Itemid=207&lang=en](http://www.dsd.at/index.php?option=com_content&view=article&id=16:picdaq&catid=37&Itemid=207&lang=en)

# Effect of Water Injection at Inlet of Turbocharger on Compressor Performances

Podevin Pierre, Périlhon Christelle, Danlos Amélie, Punov Plamen, Nouri Hussain, Wagner Marc, Massouh Fawaz and Mansilla Raul

**Abstract** In experiments on water injection conducted on internal combustion engines, water injection is generally performed in the intake manifold upstream of the engine intake. The cooling effect is used to increase power in spark ignition engines or to reduce  $\text{NO}_x$  emissions in compression engines. The present paper studies the effect of water injection upstream of the compressor and discusses its influence on turbocharger performances. Experiments were conducted on a standard turbocharger with a mist system and an air-water injection system. Test bench features are indicated and the characteristics of the water injection systems are described. Calculation of the compressor power in presence of water injection is explained. Some significant results are presented.

**Keywords** Turbocharger · Water injection · Compressor

## Nomenclature

### Symbol

$\eta$  Efficiency

$\gamma$  Cp/Cv

### Letters

Cp Specific heat capacity at constant pressure (J/kg.K)

Cv Specific heat capacity at constant volume (J/kg.K)

---

P. Pierre (✉) · P. Christelle · D. Amélie

Cnam—Conservatoire national des arts et métiers, Laboratoire CMGPCE, Paris, France  
e-mail: pierre.podevin@cnam.fr

P. Plamen

Faculty of Transport, Technical University of Sofia, Sofia, Bulgaria

N. Hussain · W. Marc

AIR LIQUIDE—Research & Development, Paris-Saclay, France

M. Fawaz · M. Raul

ENSAM—Ecole Nationale Supérieure d'Arts et Métiers, Laboratoire Dynfluid,  
Paris, France

Qm	Flow rate (kg/s)
p	Pressure (Pa)
P	Power (W)
r	Ratio
T	Temperature (K)
t	Temperature (°C)
Tauxc	Compression ratio

### Subscript

c	Compressor
comp	Compressor
t	Turbine
turb	Turbine
da	Dry air
wa	Wet air
is	Isentropic
a	Air
air	Air
w	Water
m	Mechanical
i	Impact or total
1	Inlet
2	Outlet

## Introduction

The cooling capacity of air by water evaporation is a widely used technique. Applications in the field of air conditioning for buildings exist (evaporative cooling, adiabatic cooling), and can be extended to industrial vehicles for economic purposes (Lacour et al. 2015).

This technique is also used in the area of industrial gas turbines and automotive engines.

For gas turbines, it is a means used to improve, or at least maintain, the performance of large power gas turbines when the ambient temperature is significantly greater than the nominal operating temperature. Fogging technology has been widely described by (Bhargava et al. 2007a, b, c): an amount of water is injected until it reaches the vapor saturation limit (100 % humidity). Wet compression, or so-called “overfogging” or “overspray” is also used and allows a further cooling with evaporation of the water droplets in the compressor (Bracco et al. 2007).

For the internal combustion engine, the injection of water is used to reduce the maximum temperature in the combustion chamber on large vehicles (aircraft, buses, etc.) or competition vehicles.

BMW currently uses this technology on spark ignition engines fitted in an M4 Pacecar vehicle used for the MotoGP championship, and it is planned to equip standard vehicles (BMW 118i prototype—3 cylinder 1.5 l).

At present, studies on water injection mainly focus on diesel engines in order to reduce NOx.

On recent automotive engines, (Tauzia et al. 2010) presented a study on the injection of water into the intake manifold and provided an extensive literature survey of previous work on this subject. Similarly (Sahin et al. 2014) reported a study with a very simple water injection system, upstream of the compressor (carburetor). While gains in Nox were achieved, higher PM emissions were noted by Tauzia while a decrease in the smoke number K was recorded by Salin.

However, it appears important to study separately the influence of water injection on an automotive compressor on a specific bench because it is difficult to understand this influence on a complete gas turbine or turbocharged engine which involve many interlinked tuning parameters.

It is common to consider fluid compression in a compressor as adiabatic. This is generally acceptable as the quantity of heat released to the ambient environment is negligible compared to the compression power. In this case, it can be easily demonstrated from a thermodynamic point of view that cooling the fluid during compression reduces the compression work. This is what is expected by the vaporization of water.

## Test Bench

In our laboratory dry compressed air at a pressure of 10 bar with an air-flow up to 0.5 kg/s is available. This allows us to run the turbocharger with cold air instead of hot gas, which proved to be particularly interesting for the present tests.

A scheme of the test bench is given in Fig. 1. The turbine is fed with dry compressed cold air and a valve is used to adjust the speed of the turbocharger to the requirement. Another valve on the compressor downstream of the circuit is used to adjust the resistance of the circuit. By acting on these two valves, an iso-speed can be relatively easily achieved.

The center housing is fed by the lubricating unit with SAE 5–30 W oil. Oil temperature and pressure are adjustable respectively from 20 to 120 °C and from 0.5 to 4 bar.

Figure 2 is a picture of the compressor arrangement. The turbocharger is a model used for racing cars and it is fitted with ball bearings.

As shown in Fig. 1, a heat exchanger is placed on the turbine circuitry. This heat exchanger was used to cool down the air at the inlet of the turbine for another study. For the experiments presented in this paper it was not useful and was removed for the experiments with air-water injection system.

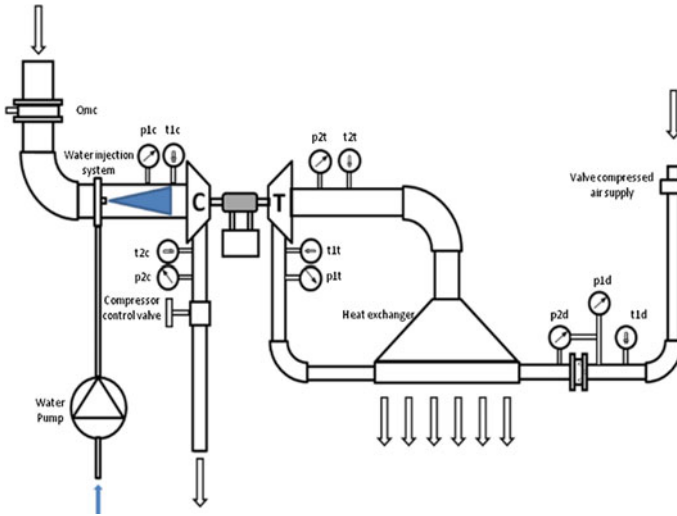


Fig. 1 Scheme of test bench

Fig. 2 Compressor arrangement



## Measurements

The main measurements done are the following:

- Compressor and turbine upstream-downstream: pressure: strain gauge transducers
- Compressor and turbine upstream-downstream: temperature: platinum resistance thermometers
- Rotational Speed: detection of the influence of metal on inductance parameters

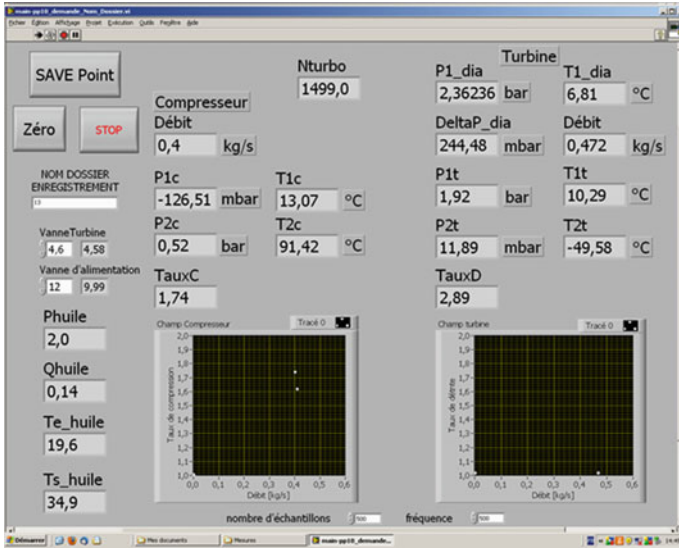


Fig. 3 Data acquisition window

- Compressor air flow: thermal mass flow meter
- Turbine air flow: sharp edge orifice

All the sensor signals are converted to 0–10 voltage and sent to a USB data acquisition device. The device is controlled by Labview. For each signal 500 measurements were done at a scanning speed of 500 Hz. Two files were created, one with detailed values (for checking purposes), and one with mean values.

The measurements are displayed on the computer screen in order to check the stabilization of the tested point. When stabilization is reached, the data are stored. Before testing, a measurement point is performed at idle in order to identify the initial voltage of each sensor. A picture of the data acquisition window is given in Fig. 3.

### Calculation

The recorded data are transferred to an Excel file and a macro converts the voltage values into physical values. Calculation of the compression ratio and flow rate do not present any particular difficulties.

Since it is impossible to measure the compressor power or turbine power directly, they can be calculated, as usual, according to the first law of thermodynamics assuming no heat exchange, i.e., an adiabatic process.



This calculation seems correct for the compressor in dry air operation and leads to a realistic isentropic compressor efficiency.

$$P_{cda} = \dot{Q}m_c \cdot C_{p_{air}} \cdot (T_{i2c} - T_{i1c}) \quad (1)$$

With the injection of water, compression power cannot be calculated with Eq. (1). The calculation is no longer valid and leads to meaningless results. It would be necessary to know the enthalpy of the water evaporation, but this enthalpy variation cannot be measured.

In this configuration the compressor power is calculated from the power of the turbine and a mechanical efficiency estimated in dry air tests.

$$P_t = \dot{Q}m_t \cdot C_{p_{air}} \cdot (T_{i1t} - T_{i2t}) \quad (2)$$

$$\eta_m = \frac{P_{cda}}{P_t} \quad (3)$$

$$P_{cwa} = \eta_m \cdot P_t \quad (4)$$

Note. Mechanical efficiency can reach values greater than one, especially when tests are done with the heat exchanger on the turbine circuitry. This is due to the fact that heat exchange on the turbine side is neglected. Nevertheless, as experiments with dry air or wet test are done in the same conditions, the calculation of  $P_{cwa}$  can be considered to be satisfactory.

The compressor power is compared with respect to isentropic compression.

$$P_{cis} = \dot{Q}m_c \cdot C_{p_{air}} \cdot (T_{i2cis} - T_{i1c}) \quad (5)$$

with:

$$T_{i2cis} = T_{i1c} \left( \frac{p_{i2c}}{p_{i1c}} \right)^{\frac{\gamma-1}{\gamma}} \quad (6)$$

and compressor isentropic efficiency is:

$$\eta_{isc} = \frac{P_{cis}}{P_{cda}} \text{ for dry air} \quad (7)$$

$$\eta_{isc} = \frac{P_{cis}}{P_{cwa}} \text{ for wet air} \quad (8)$$

## Water Injection Results

Tests were done with a mist system and an air-water injection system. Measurements are rather sensitive, so when an iso-speed was performed, for the same operating point (same compressor downstream valve opening), a dry air test, a test with water injection and a second dry air test were successively done. The first and last tests have to be identical.

### *Mist System*

Upstream of the compressor, a water injection device is installed. The spray can be visualized thanks to the transparent tube, Fig. 4.

This mist system consists of injection nozzles supplied with water by a pump under a pressure of 50 bar.

Three configurations were tested:

1. injector nozzle centered B01 (red mark) rate 0.08 l/min, Fig. 5
2. centered injector nozzle B04 (green mark) rate 0.20 l/min
3. two injector centered nozzles B01 total flow rate 0.16 l/min, Fig. 6

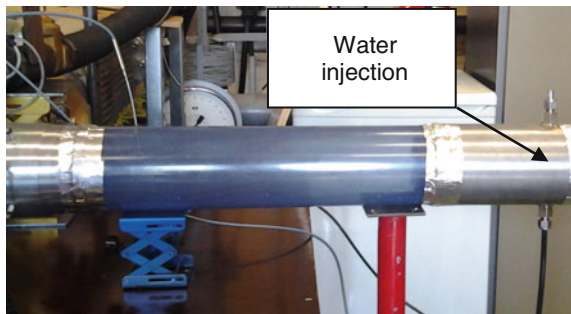
Spraying was performed in the direction of flow. Some tests were conducted with configuration 2 by injecting the water in the opposite direction of flow. No significant effect was recorded.

Figure 7 was recorded during the experiment to characterize the angle and the length of the spray. Drop size was about 20  $\mu\text{m}$ .

In some configurations, i.e. with a low-speed compressor, a deposit of water droplets was observed on the periphery of the inlet duct. These droplets coalesce and form a trickle. A scoop system was put in place to recover this water to prevent it from directly entering the compressor.

First, in order to demonstrate the effect of the injection of water, a preliminary test on a compressor orifice line is presented (the position of the compressor output valve is kept constant). Figure 8 shows the evolution of the operating point for a

**Fig. 4** Water mist injection



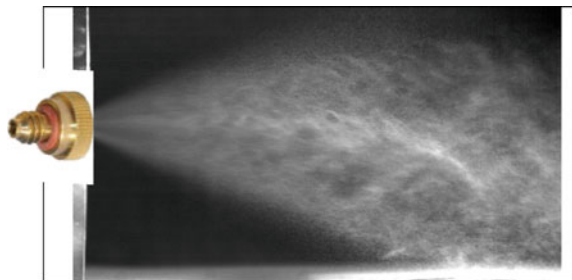
**Fig. 5** One nozzle configuration



**Fig. 6** Two nozzle configuration



**Fig. 7** Spray in free field—50 bar



rotational speed of 70,000 rpm. For an air inlet temperature of 22 °C and a reference temperature of 15 °C, the relevant corrected speed must be set to 70,845 rpm.

Point 1 is a stabilized point without water injection. After injecting water at 0.08 l/min, a drop in the rotation speed of about 700 rpm was observed. After stabilization, points 2 and 3 were obtained. The change in the compressor flow, compression ratio and turbine power was very low (theoretically unchanged on the turbine side). Point 4 corresponds to the readjustment of the rotational speed close

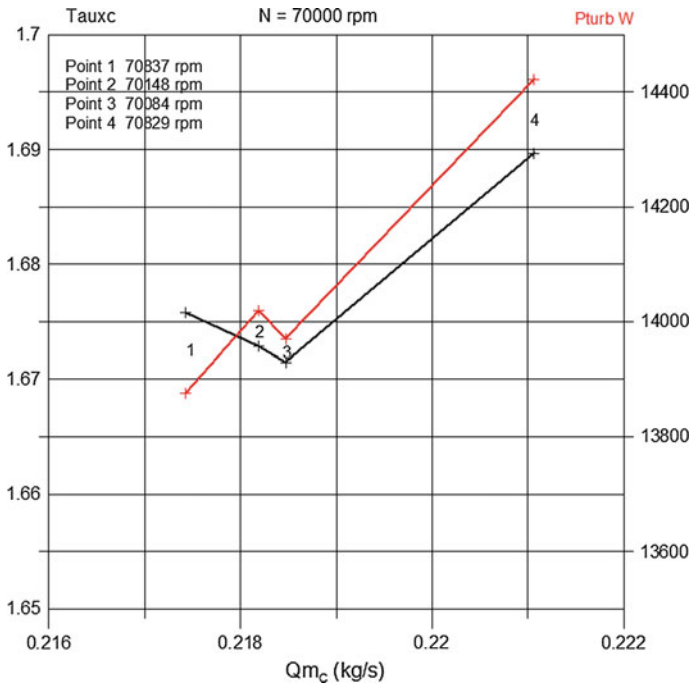


Fig. 8 Water injection evolution of the operating point

to 70,845 rpm. As a result, an increase in the compression ratio and the turbine power were observed.

Experiments were conducted for iso-speeds of 70,000, 80,000, and 90,000 rpm. In this paper we will present only the results for 80,000 rpm and for water injection at 0.08 and 0.20 l/min.

Figure 9 shows that an appreciable rise in the compression ratio is observed when water is injected, and a weak increase in turbine power, Fig. 10, at high air flow. This results in an increase of compressor efficiency with water injection at high flow, Fig. 11, and about the same efficiency at low flow.

Figure 12 shows that with a greater water flow, there is a clear increase in compression ratio and we obtain a high turbine power increase when water is injected, Fig. 13, especially at low air flow. This leads to a drop in compressor efficiency with water injection at low flow, Fig. 14, and about the same efficiency at high flow. Probably, at low flow rates, not all the water is sprayed, thus affecting the proper operation of the compressor.

Note: In calculating the power supplied to the compressor in wet conditions, energy supplied to the fluid being sprayed was not taken into account. This energy is relatively low, 7 W for a water flow of 0.08 l/min and 17 W at 0.2 l/min.

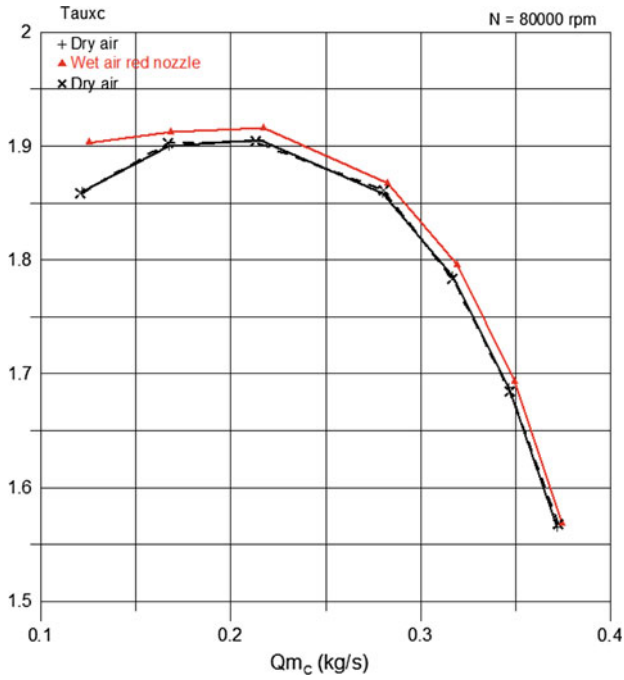


Fig. 9 Compression ratio versus air flow. Water injection 0.08 l/min

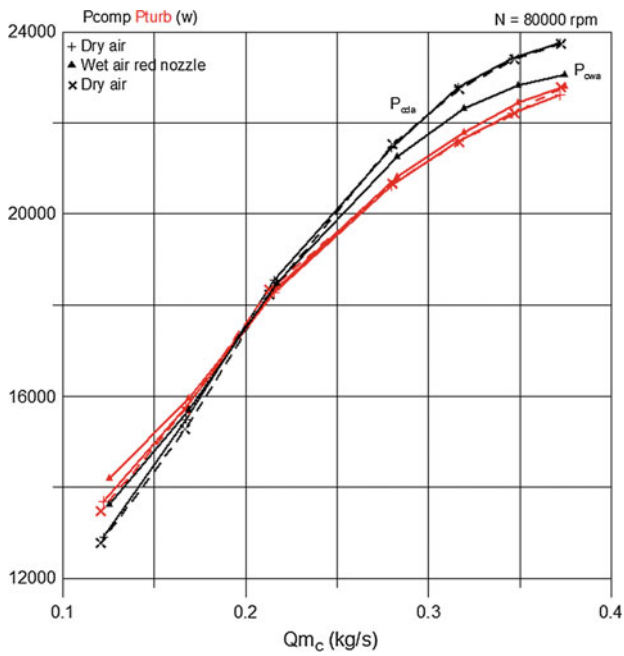


Fig. 10 Compressor power and turbine power. Water injection 0.08 l/m

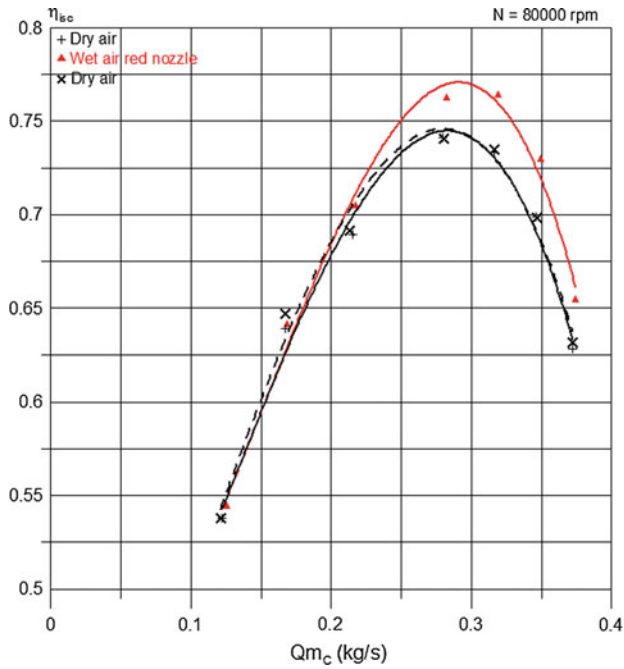


Fig. 11 Isentropic efficiency versus air flow. Water injection 0.08 l/min

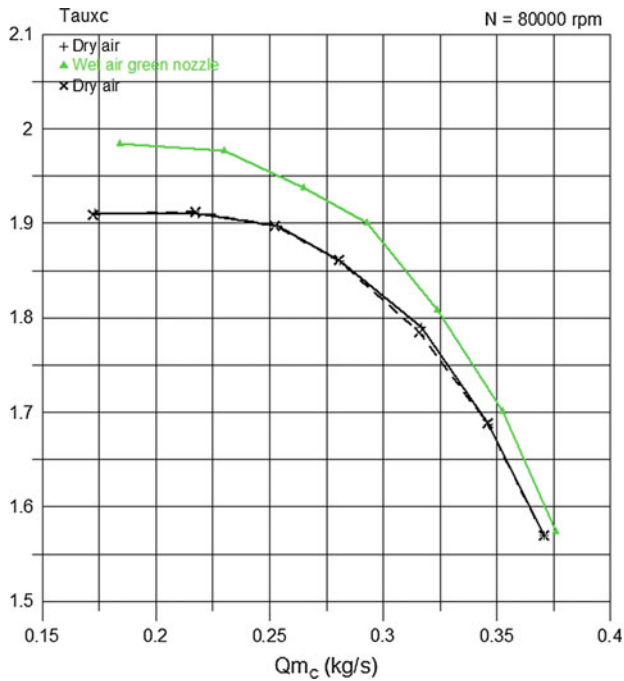


Fig. 12 Compression ratio versus air flow. Water injection 0.2 l/min

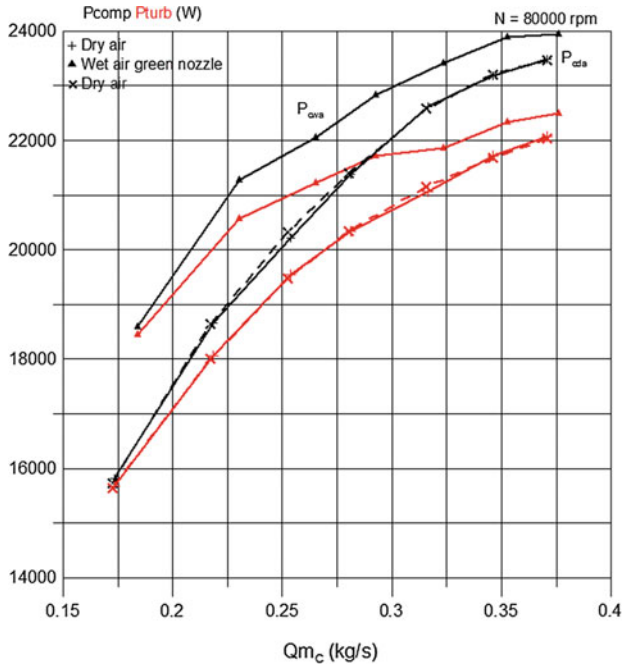


Fig. 13 Compressor power and turbine power. Water injection 0.2 l/m

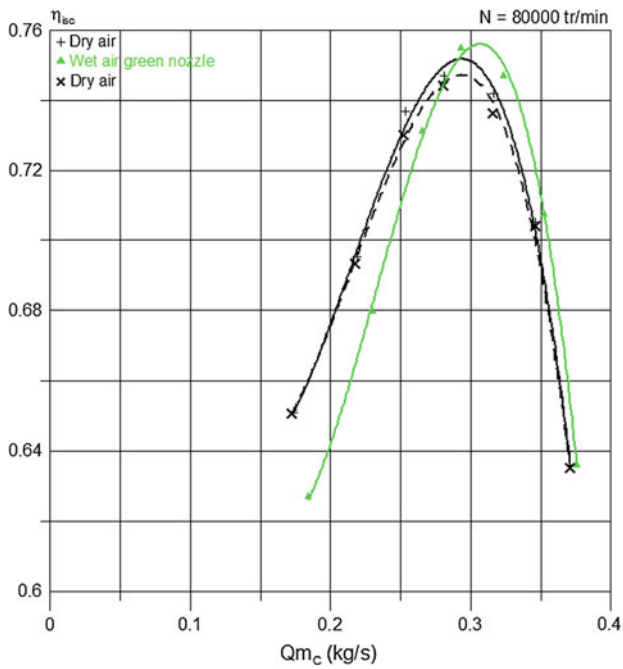


Fig. 14 Isentropic efficiency versus air flow. Water injection 0.2 l/min

### ***Air-Water Injection System***

The water is injected in the center of the device and pulverized into fine droplets through the air injected peripherally. The general arrangement of the test bench is presented on Fig. 15. This device makes it possible to have a thinner jet angle than with a mist system. Figure 16 represents the spray in free field. The air and water ratio was adjusted to obtain a water drop of about 20  $\mu\text{m}$ .

Air and water flows are measured and can be adjusted.

Experiments were conducted for a turbocharger speed of 70,000 rpm. The first test was done with a constant injected air-water ratio and a water flow of 0.18 l/min. At low compressor flow the isentropic efficiency was significantly less with water injection than with dry air. It was therefore decided to conduct a further test keeping the ratio  $r_{wa}$ : constant at 1 %.  $r_{wa}$  is the ratio of water flow to compressor flow.

$$r_{wa} = \frac{Qm_w}{Qm_c} \quad (9)$$

The injected air flow was kept constant at 4.7  $\text{Nm}^3/\text{h}$ . Results are presented in Figs. 17, 18, and 19. Comparing these experiments with a constant water flow

**Fig. 15** General arrangement of the test bench with air-water injection system

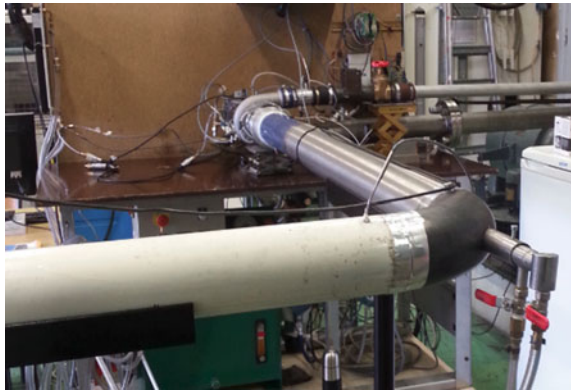


**Fig. 16** Spray in free field, air-water injection system





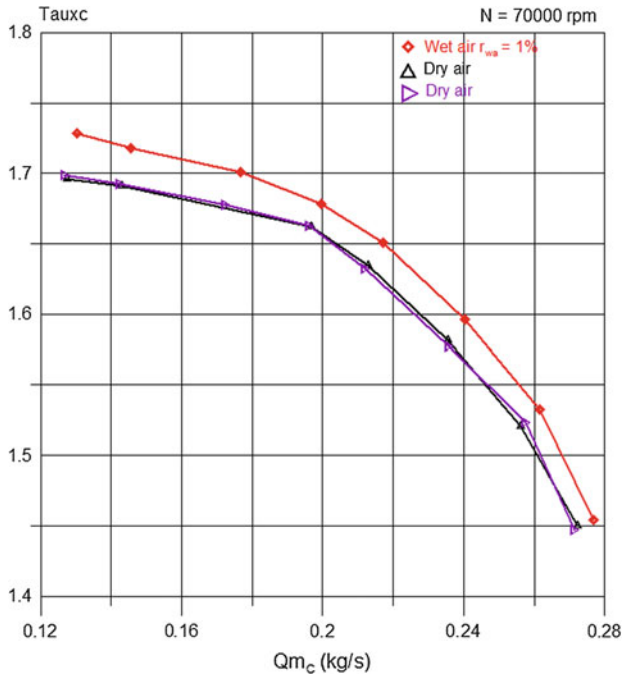


Fig. 17 Compression ratio versus air flow  $r_{wa} = 1 \%$

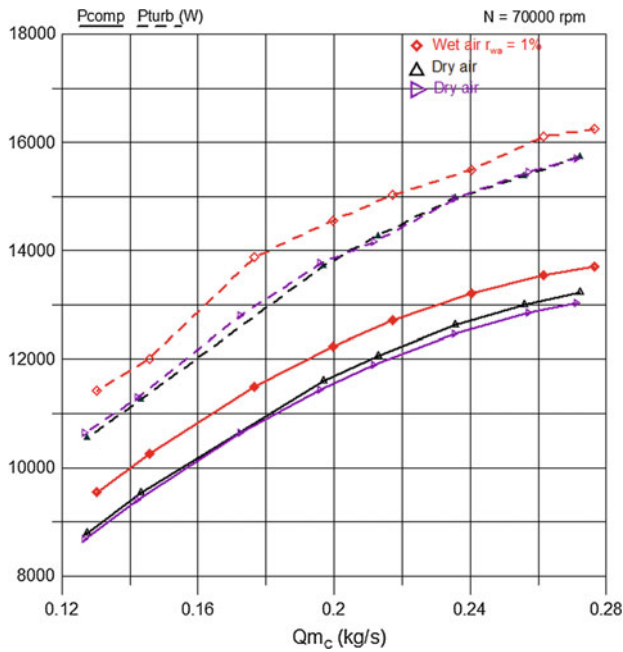


Fig. 18 Compressor power and turbine power  $r_{wa} = 1 \%$

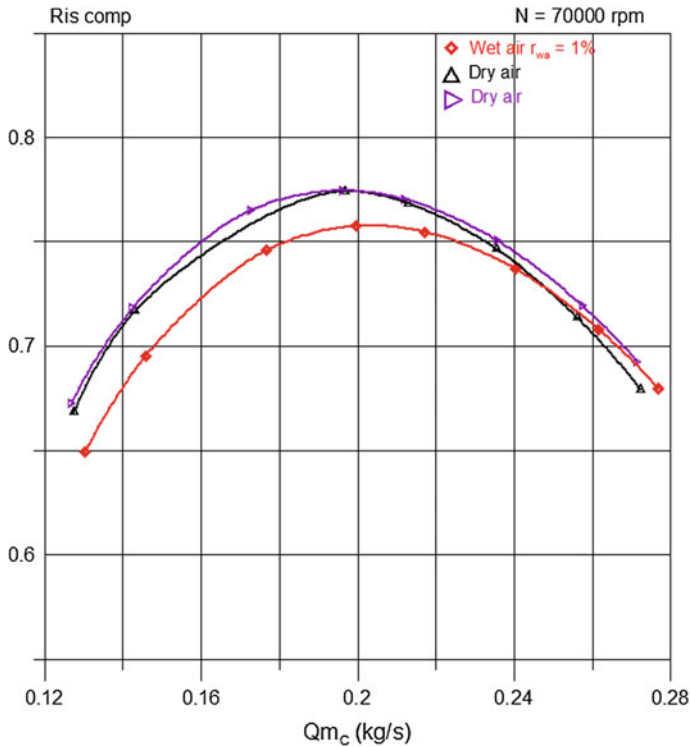


Fig. 19 Isentropic efficiency versus air flow  $r_{wa} = 1 \%$

of 0.18 l/min, it was observed that there was an increase in isentropic efficiency at low compressor flow, but that the efficiency remained lower than with dry air. The results below are similar to those obtained with mist air injection.

Another test was done in order to find an optimum  $r_{wa}$  ratio at 70,000 rpm. We selected a point close to the maximum isentropic efficiency for this speed.

The first point was done with dry air, and for the following points we gradually increased the amount of water per pitch by approximately 0.5 %, till  $r_{wa}$  reached about 5 %. Then two dry air points were done to validate the test series. For each point the value of the speed was adjusted by acting on the turbine valve. The compressor valve remained in the same position.

The test results are shown in Figs. 20, 21 and 22. The scales have been enlarged to clearly show the evolution of performances. Overall, the maximum variation was about 4 % on the flow rate, 2.5 % on the compression ratio and 14 % on the power.

Injecting water up to an amount of 1.5 % led to an increase in the compression ratio, its power as well as a slight decrease in the isentropic efficiency. Above, particularly for quantities greater than 2.5 %, the compression ratio drops and the power thus stagnates, causing the isentropic efficiency to fall.

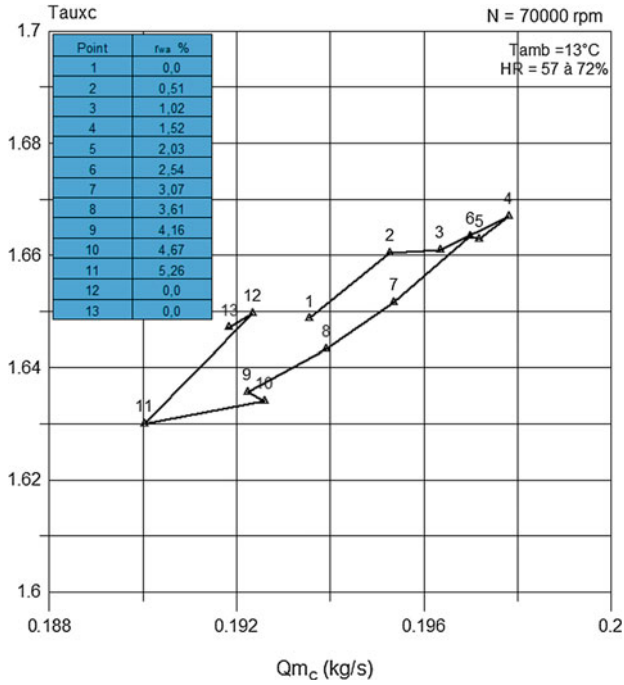


Fig. 20 Compression ratio versus air flow r<sub>wa</sub> variable

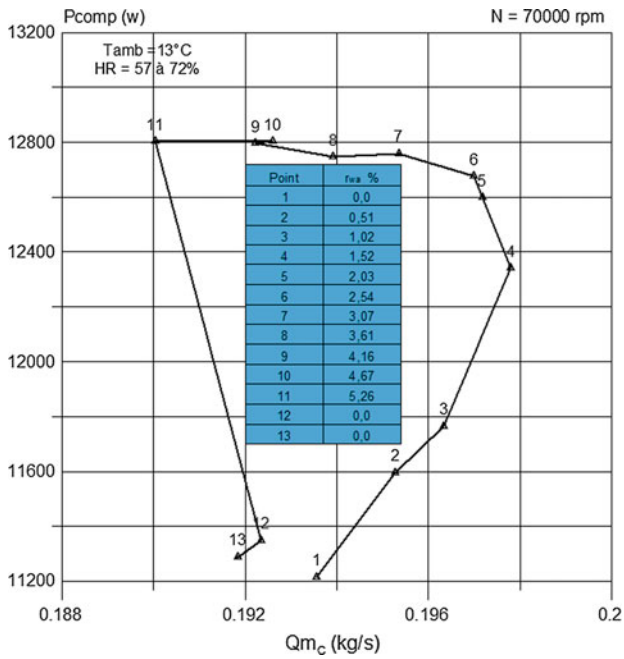


Fig. 21 Compressor power r<sub>wa</sub> variable

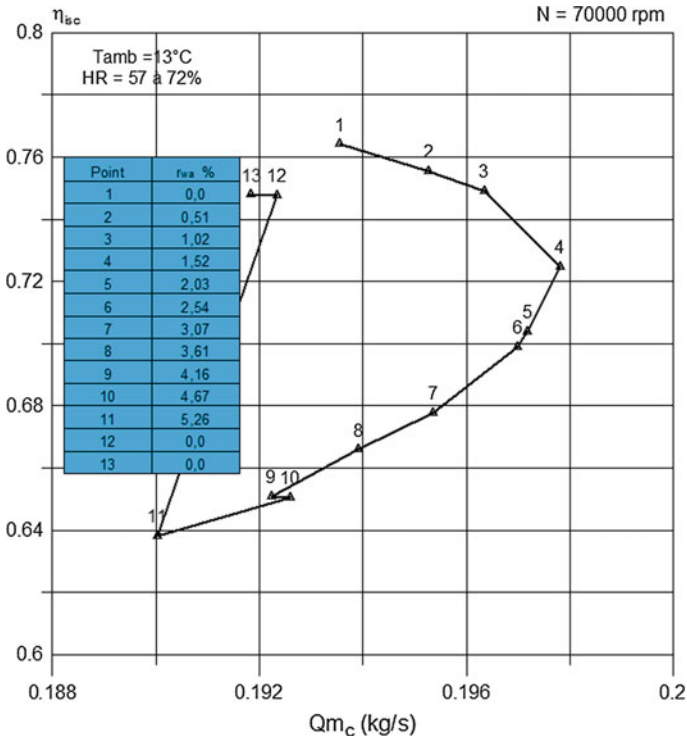


Fig. 22 Isentropic efficiency versus air flow  $r_{wa}$  variable

### Conclusions

Upstream water injection allows the compressor to increase the compression ratio for a fixed rotation speed. Contrary to expectations, experiments did not reveal any increase in compressor efficiency. The efficiency remained about the same and generally decreased for low flow rates, probably due to the weak homogeneity of the air-water mixture and too much water injected.

For water injection during the tests, “standard” equipment was used. It is likely that better results could be obtained by using more efficient means of injection that allow variation of the water flow, control of the droplet size and spray angle. For automobile engines, a compressor upstream of the water injection is a potentially interesting technology but much more difficult to implement than injection downstream. It requires strict control of the injection quality in order to prevent droplets from impacting the compressor blades and damaging them.

## References

- Bhargava RK, Meher-Homji CB, Chaker MA, Bianchi M, Melino F, Peretto A, and Ingistov S (2007a) Gas Turbine Fogging Technology: a state-of-the-art review-part I: inlet evaporative fogging-analytical and experimental aspects. *ASME J Eng Gas Turbines Power* 129:443–453
- Bhargava RK, Meher-Homji CB, Chaker MA, Bianchi M, Melino F, Peretto A, Ingistov S (2007b) Gas turbine fogging technology: a state-of-the-art review-part II: overspray fogging-analytical and experimental aspects. *ASME J Eng Gas Turbines Power* 454–460
- Bhargava RK, Meher-Homji CB, Chaker MA, Bianchi M, Melino F, Peretto A, Ingistov S (2007c) Gas turbine fogging technology: a state-of-the-art review-part III: practical considerations and operational experience. *ASME J Eng Gas Turbines Power* 461–472
- Bracco S, Pierfederici A, Trucco A (2007) The wet compression technology for gas turbine power plants: thermodynamic model. *Appl Therm Eng* 27(2007):699–704
- Lacour S, Podevin P, Punov P (2015) Fuels saving using direct adiabatic cooling instead conventional air conditioning for a tractor cabin. In: *BulTrans international scientific conference*. Sozopol Bulgaria, Sept 2015
- Sahin Z, Tuti M, Durgun O (2014) Experimental investigation of the effects of water adding to the intake air on the engine performance and exhaust emissions in a DI automotive diesel engine. *Fuel* 115(2014):884–895
- Tauzia X, Maiboom A, Shah SR (2010) Experimental study of inlet manifold water injection on combustion and emissions of an automotive direct injection. *Diesel engine Energy* 35 (2010):3628–3639